Published in Journals: Applied Sciences, Drones,
Energies, Machines, Materials and Sensors

Topic Reprint

Design, Simulation and New Applications of Unmanned Aerial Vehicles

Volume II

Edited by
Andrzej Łukaszewicz, Wojciech Giernacki, Zbigniew Kulesza,
Jaroslaw Alexander Pytka and Andriy Holovatyy

mdpi.com/topics

Design, Simulation and New Applications of Unmanned Aerial Vehicles—Volume II

Design, Simulation and New Applications of Unmanned Aerial Vehicles—Volume II

Editors

Andrzej Łukaszewicz
Wojciech Giernacki
Zbigniew Kulesza
Jaroslaw Alexander Pytka
Andriy Holovatyy

MDPI

Basel • Beijing • Wuhan • Barcelona • Belgrade • Novi Sad • Cluj • Manchester

Editors

Andrzej Łukaszewicz
Bialystok University of Technology
Bialystok
Poland

Wojciech Giernacki
Poznan University of Technology
Poznan
Poland

Zbigniew Kulesza
Bialystok University of Technology
Bialystok
Poland

Jaroslaw Alexander Pytka
Lublin University of Technology
Lublin
Poland

Andriy Holovatyy
Lviv Polytechnic National University
Lviv
Ukraine

Editorial Office
MDPI
St. Alban-Anlage 66
4052 Basel, Switzerland

This is a reprint of articles from the Topic published online in the open access journals *Applied Sciences* (ISSN 2076-3417), *Drones* (ISSN 2504-446X), *Energies* (ISSN 1996-1073), *Machines* (ISSN 2075-1702), *Materials* (ISSN 1996-1944), and *Sensors* (ISSN 1424-8220) (available at: https://www.mdpi.com/topics/UAV).

For citation purposes, cite each article independently as indicated on the article page online and as indicated below:

Lastname, A.A.; Lastname, B.B. Article Title. *Journal Name* **Year**, *Volume Number*, Page Range.

Volume II
ISBN 978-3-7258-0979-0 (Hbk)
ISBN 978-3-7258-0980-6 (PDF)
doi.org/10.3390/books978-3-7258-0980-6

Set
ISBN 978-3-7258-0975-2 (Hbk)
ISBN 978-3-7258-0976-9 (PDF)

Contents

About the Editors

Andrzej Łukaszewicz

Andrzej Łukaszewicz, Ph.D., has a position as an Assistant Professor at the Institute of Mechanical Engineering in the Faculty of Mechanical Engineering at Bialystok University of Technology, Poland (October 1997–present). He holds a Ph.D. degree in solid mechanics from the Warsaw University of Technology, Warsaw, Poland. He is interested in UAV design, CAx, CAD, topology optimization, lattice structures, the mechanics of materials, fracture mechanics, and material testing. His main research area is mechanical engineering. He has co-authored more than 170 publications in journals, conference proceedings, or book chapters and has reviewed more than 50 papers in 20 international journals. He is also a member of the Topical Advisory Panel of six international journals.

Wojciech Giernacki

Wojciech Giernacki, Ph.D., D.Sc. (Eng.), is an Associate Professor at the Institute of Robotics and Machine Intelligence of Poznan University of Technology. He received his Ph.D. degree in control engineering and robotics from the Poznan University of Technology in 2011 and his D.Sc. in 2019. He founded and heads the PUT AeroLab and Unmanned Aerial Vehicles Research Group, as well as the Division of Control and Optimization at the Institute of Robotics and Machine Intelligence. His scientific interests are focused on the issues of UAVs, especially robust and adaptive control, optimization techniques, and data fusion from sensors.

Zbigniew Kulesza

Zbigniew Kulesza, Ph.D., D.Sc., is an Associate Professor at the Faculty of Electrical Engineering, Bialystok University of Technology, Poland. His practical and theoretical results pertain to the area of control theory and robotics. His domain of interest includes control theory methods for rotor crack detection, damage detection filters, rotor dynamics, parametric and nonlinear vibrations, dynamics and control of robot manipulators and mobile robots, the design and programming of real-time control systems, the modeling and simulation of pneumatic drive systems, and the aerodynamics of micro aerial vehicles. Currently, he is involved in building an observation system for agricultural machines as well as in a robot manipulator fast path planning project.

Jaroslaw Alexander Pytka

Jaroslaw Alexander Pytka, D.Sc., Ph.D., M.S., Automotive Engineer, is working at the Department of Motor Vehicles, Lublin University of Technology, Poland, as a Researcher and Educator for undergraduate and graduate students of Automotive Technology. He has a position as an Associate Professor. He received his M.S. degree in Automotive Engineering in 1992 from the Lublin University of Technology. He earned his Ph.D. in Soil Physics from the Institute of Agrophysics, Lublin, Poland. His major research interest is wheel–soil interaction analysis with a focus on experimental studies.

Andriy Holovatyy

Andriy Holovatyy, Ph.D., is an Assistant Professor at the Department of Computer-Aided Design Systems at Lviv Polytechnic National University (Ukraine). He obtained his PhD degree with a specialisation in Computer-Aided Design Systems at Lviv Polytechnic National University (Ukraine) in 2010. He is the co-author of more than 60 publications in journals, conference proceedings, and book and monograph chapters. His domain of interest includes the simulation of complex heterogeneous

systems using VHDL-AMS and Verilog-AMS, the automated design of microelectromechanical systems, the application of MEMS devices in intelligent systems, the development of microcontroller-based devices, software engineering, and hardware and software development for embedded systems. He is also interested in CAx systems for UAV design, FEA and CFD analysis in UAV design, MEMS application in UAS, embedded systems design for UAVs, and the development of algorithms and software for UAV/UAS. Currently, he is also a co-editor for the MDPI (Switzerland, Basel) Topic: "Innovation and Inventions in Aerospace and UAV Applications".

Preface

This collection is dedicated to presenting the current state of the art in UAV research. It explores the application of advanced methods, algorithms, and technologies, using, for example, artificial intelligence, neural networks, sensors, modern materials, and techniques.

This Topic reprint provides a platform for scientists and engineers to present the latest progresses, challenges, and opportunities in the field of multidisciplinary UAV system development.

The main goal is to emphasize the potential of integrating numerical simulations and design methods to achieve better autonomous unmanned flying platforms for a range of applications and to foster knowledge exchange and innovative research for effective UAV design, control, and exploitation.

Volume I contains 25 papers published in MDPI journals: *Drones* (15 papers), *Sensors* (5), *Energies* (3), *Applied Sciences* (2) in the period from 21.02.2022 to 13.10.2022.

Volume II contains 25 papers published in MDPI journals: *Drones* (16 papers), *Applied Sciences* (5), *Materials* (2), *Energies* (1), and *Machines* (1) in the period from 01.11.2022 to 31.10.2023.

The Editors would like to thank the authors of the 50 papers (Volume I and Volume II) featured in Topic "Design, Simulation and New Applications of Unmanned Aerial Vehicles" for their contributions to UAV advancement.

Andrzej Łukaszewicz, Wojciech Giernacki, Zbigniew Kulesza, Jaroslaw Alexander Pytka, and Andriy Holovatyy
Editors

applied sciences

MDPI

Article

Sliding Mode Path following and Control Allocation of a Tilt-Rotor Quadcopter

Chih-Chen Yih * and Shih-Jeh Wu

Department of Mechanical & Automation Engineering, I-Shou University, Kaohsiung 84001, Taiwan
* Correspondence: ccyih@isu.edu.tw; Tel.: +886-7-657-7711 (ext. 3229)

Abstract: A tilt-rotor quadcopter (TRQ) equipped with four tilt-rotors is more agile than its under-actuated counterpart and can fly at any path while maintaining the desired attitude. To take advantage of this additional control capability and enhance the quadrotor system's robustness and capability, we designed two sliding mode controls (SMCs): the typical SMC exploits the properties of the rotational dynamics, and the modified SMC avoids undesired chattering. Our simulation studies show that the proposed SMC scheme can follow the planned flight path and keep the desired attitude in the presence of variable deviations and external perturbations. We demonstrate from the Lyapunov stability theorem that the proposed control scheme can guarantee the asymptotic stability of the TRQ in terms of position and attitude following via control allocation.

Keywords: tilt-rotor quadcopter (TRQ); sliding mode control (SMC); control allocation; path following

Citation: Yih, C.-C.; Wu, S.-J. Sliding Mode Path following and Control Allocation of a Tilt-Rotor Quadcopter. *Appl. Sci.* **2022**, *12*, 11088. https://doi.org/10.3390/app122111088

Academic Editors: Jaroslaw Pytka, Andrzej Łukaszewicz, Zbigniew Kulesza, Wojciech Giernacki and Andriy Holovatyy

Received: 27 September 2022
Accepted: 30 October 2022
Published: 1 November 2022

Publisher's Note: MDPI stays neutral with regard to jurisdictional claims in published maps and institutional affiliations.

1. Introduction

Due to advancements in microprocessors and sensors, quadrotors have recently received much attention, playing an increasingly important role in unmanned aerial vehicles (UAVs). Now, quadrotors can easily hover indoors or outdoors and fly fast with global positioning system (GPS) devices or tiny cameras. Generally, changing the velocities of rotors [1,2] can generate lift and steering torque to control the attitude and position of the quadcopter.

Scholars and engineers have proposed several methods to solve the control problem for a quadrotor. These methods can be divided into: PID control [3–5], feedback linearization [6], optimal control [7], back-stepping [8,9], SMC [10–13], robust control [14], neural control [15,16], and nonlinear control [17]. To handle uncertainty systematically, researchers have extensively applied SMCs to address the robust control problem of quadrotors.

The super-twist control algorithm [18–20], a second-order SMC, has been studied to alleviate harmful chattering and maintain the robust capability of first-order SMCs. The studies in [21–23] demonstrate the stability and finite-time convergence of the super-twist control algorithm for single-variable systems through a Lyapunov stability analysis. For instance, Xu et al. [11] studied an adaptive terminal sliding mode for a quadrotor attitude control with specified capability and input saturation. In addition, Besnard et al. [12] proposed an observer-based SMC to address model uncertainty and wind perturbation. The recent work in [24,25] introduced the perturbation observer incorporating enhanced SMC for application in quadrotor UAV control.

Recently, several control methods have been proposed to solve the localization or following problem of under-actuated quadrotors, but these methods are still insufficient and have many shortcomings. For example, if the actuator fails or the rotor is damaged, the quadrotor will crash due to a lack of actuator redundancy to restore attitude and position. Tilt-rotor quadrotors [26] can increase the degree of control freedom and provide control redundancy. Compared with under-actuated quadrotors, full-drive quadrotors have more flexibility than under-actuated quadrotors and have recently attracted the research community's attention. Ryll et al. [27] proposed a modeling approach for an

overdrive quadrotor UAV. They provide a dynamic linearization control that uses higher-order derivatives of the measured output. Hua et al. [28] studied the control of vertical take-off and landing (VTOL) vehicles with bank thrust angle limitation. The proposed control can achieve the primary and secondary goals of asymptotically stabilizing position and direction. Recently, Rashad et al. [29] reviewed various UAV designs with fully actuated multi-rotors, in the literature. They introduced the control allocation matrix to categorize the proposed hardware framework and discussed the criteria for optimizing the UAV design. Zheng et al. [30] introduced the hardware design of an experimental tilt-rotor drone that uses linear servo motors to control the tilt mechanism. The authors also implemented and tested their PD-based translation and attitude control scheme on the fully actuated prototype quadrotor. To control the hovering and fixed-wing flight of a tilt-rotor UAV and the transition between them, Willis et al. [31] proposed a control scheme, which includes a low-level angular rate controller and a variable mixer, and an LQR following control

We propose a TRQ model based on translational and rotational dynamics, perturbation, and model uncertainty. Note that the SMC presented for an under-actuated quadrotor cannot be directly applied to a tilt-rotor quadrotor. We propose an SMC scheme with control allocation, exploiting the structural features of rotational dynamics and avoiding chattering in translational dynamics to further enhance the robustness and capability of TRQ systems.

The paper is organized as follows: Section 2 discusses the TRQ's dynamics and various drive modes. Section 3 presents the proposed SMC scheme and control assignment. Section 4 provides a stability analysis. In Section 5, the proposed SMC scheme is applied to a TRQ for numerical simulation. Section 6 gives some conclusions.

2. Dynamic Model of a Tilt-Rotor Quadcopter (TRQ) with Various Actuation Modes

This section will establish a dynamic model from the Newton–Euler equation. First, we present the dynamics of the TRQ (Figure 1). Using the variables defined in the nomenclature, we propose various actuation modes from over-actuated, to fully actuated, to under-actuated modes.

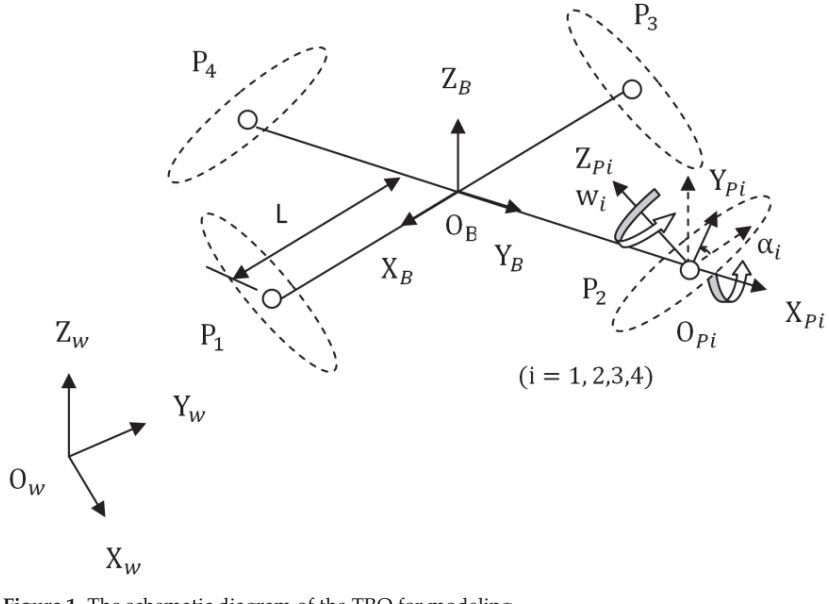

Figure 1. The schematic diagram of the TRQ for modeling.

2.1. Rotational and Translational Dynamics

The rotation matrix ${}^{B}R_{P_i}$ from the ith rotor frame to the body frame is

$$ {}^{B}R_{P_i} = R_Z(\beta_i)R_X(\alpha_i) \tag{1} $$

$$ R_X(\alpha_i) = \begin{bmatrix} 1 & 0 & 0 \\ 0 & \cos\alpha_i & -\sin\alpha_i \\ 0 & \sin\alpha_i & \cos\alpha_i \end{bmatrix}, $$

and

$$ R_Z(\beta_i) = \begin{bmatrix} \cos\beta_i & -\sin\beta_i & 0 \\ \sin\beta_i & \cos\beta_i & 0 \\ 0 & 0 & 1 \end{bmatrix}, \ \beta_i = (i-1)\frac{\pi}{2}, \ i = 1,\ 2,\ 3,\ 4. $$

The angular velocity is

$$ w_{Pi} = {}^{P_i}R_B w_B + \begin{bmatrix} \dot{\alpha}_i & 0 & w_i \end{bmatrix}^T \tag{2} $$

We define

$$ sgn(x) = \begin{cases} 1 & if \ x > 0 \\ -1 & if \ x < 0 \end{cases} $$

where

$$ w_1 < 0,\ w_3 < 0\ ,\ w_2 > 0,\ w_4 > 0 $$

The rotational dynamics of the TRQ can be formulated as:

$$ \tau_B = I_B\dot{w}_B + w_B \times I_B w_B + \sum_{i=1}^{4} {}^{B}R_{P_i}\tau_{Pi} \tag{3} $$

where

$$ \tau_{Pi} = I_{Pi}\dot{w}_{Pi} + w_{Pi} \times I_{Pi}w_{Pi} - \tau_{di} \tag{4} $$

$$ \tau_{di} = \begin{bmatrix} 0 & 0 & -k_m w_i^2 sgn(w_i) \end{bmatrix}^T \tag{5} $$

The force in the rotor frame is

$$ T_{pi} = \begin{bmatrix} 0 & 0 & k_f w_i^2 \end{bmatrix}^T \tag{6} $$

and the toque in body frame is

$$ \tau_B = \sum_{i=1}^{4} ({}^{B}O_{P_i} \times {}^{B}R_{P_i}T_{Pi}) \tag{7} $$

The transform between body angular rates to the Euler rates is

$$ \dot{r} = R_T w_B \tag{8} $$

where

$$ R_T = \begin{bmatrix} 1 & s_\phi \tan\theta & c_\phi \tan\theta \\ 0 & c_\phi & -s_\phi \\ 0 & s_\phi \sec\theta & c_\phi \sec\theta \end{bmatrix} \tag{9} $$

and $r = \begin{bmatrix} \phi & \theta & \psi \end{bmatrix}^T \in R^3$ is the attitude vector of the roll, the pitch, and the yaw angle. We denote $s_{q_i} = \sin q_i$ and $c_{q_i} = \cos\ q_i$.

Taking the derivative of (8) and ignoring I_{Pi} in (4), we have

$$ \ddot{r} = \dot{R}_T R_T^{-1}\dot{r} + R_T I_B^{-1}(\tau_B - w_B \times I_B w_B + \sum_{i=1}^{4} {}^{B}R_{P_i}\tau_{di}) \tag{10} $$

We denote

$$\tau = \sum_{i=1}^{4} ({}^{B}O_{P_i} \times {}^{B}R_{P_i} T_{Pi}) + \sum_{i=1}^{4} {}^{B}R_{P_i} \tau_{di} \tag{11}$$

Define the transform matrix

$$\Psi = R_T^{-1} \tag{12}$$

From (8), we have

$$w_B = \Psi \dot{r} \tag{13}$$

It follows from (10) and (12) that

$$\begin{aligned} \Psi^T I_B \Psi \ddot{r} &= -\Psi^T I_B \dot{\Psi} \dot{r} - \Psi^T w_B \times I_B w_B + \Psi^T \tau \\ &= -\left[\Psi^T I_B \dot{\Psi} + \Psi^T \left(\Psi \dot{r} \times I_B \Psi\right)\right] \dot{r} + \Psi^T \tau \end{aligned} \tag{14}$$

Considering the perturbation torque τ_d, we obtain

$$H(r)\ddot{r} + C\left(r, \dot{r}\right)\dot{r} = \Psi^T(\tau + \tau_d) \tag{15}$$

where

$$H(r) = \Psi^T I_B \Psi \tag{16}$$

$$C\left(r, \dot{r}\right) = \left[\Psi^T I_B \dot{\Psi} + \Psi^T \left(\Psi \dot{r} \times I_B \Psi\right)\right] \tag{17}$$

$$\Psi(r) = \begin{bmatrix} 1 & 0 & -s_\theta \\ 0 & c_\phi & c_\theta s_\phi \\ 0 & -s_\phi & c_\theta c_\phi \end{bmatrix} \tag{18}$$

and $H(r) \in R^{3\times 3}$ is the inertia matrix, $C\left(r, \dot{r}\right)\dot{r} \in R^3$ represents the centrifugal and Coriolis forces. $\tau = \begin{bmatrix} \tau_\phi & \tau_\theta & \tau_\psi \end{bmatrix}^T \in R^3$ is the vector of torques and $\tau_d \in R^3$ is the perturbation torque.

The velocity in F_w is

$$\dot{p} = {}^{W}R_B V_B \tag{19}$$

The derivative of velocity in F_B can be expressed as

$$\dot{V}_B = -w_B \times V_B + {}^{W}R_B^T \begin{bmatrix} 0 & 0 & -g \end{bmatrix}^T + \frac{f}{m} \tag{20}$$

where

$${}^{W}R_B = \begin{bmatrix} c_\theta c_\psi & s_\phi s_\theta c_\psi - c_\phi s_\psi & c_\phi s_\theta c_\psi + s_\phi s_\psi \\ c_\theta s_\psi & s_\phi s_\theta s_\psi + c_\phi c_\psi & c_\phi s_\theta s_\psi - s_\phi c_\psi \\ -s_\theta & s_\phi c_\theta & c_\phi c_\theta \end{bmatrix}$$

and

$$f = \sum_{i=1}^{4} {}^{B}R_{P_i} T_{Pi} \tag{21}$$

where $p = \begin{bmatrix} x & y & z \end{bmatrix}^T \in R^3$. $f = \begin{bmatrix} f_x & f_y & f_z \end{bmatrix}^T \in R^3$ is the vector of forces.

Taking the derivative of (19), ignoring ${}^{W}\dot{R}_B$ and using (20), the translational dynamics becomes

$$m\ddot{p} = {}^{W}R_B = (-w_B \times V_B + f) - \begin{bmatrix} 0 & 0 & mg \end{bmatrix}^T + u_d \tag{22}$$

where $u_d \in R^3$ is the perturbation force in F_w.

2.2. Over-Actuated, Fully Actuated, and Under-Actuated Modes

Denote $\alpha = [\alpha_1 \quad \alpha_2 \quad \alpha_3 \quad \alpha_4]^T$,$w = [w_1 \quad w_2 \quad w_3 \quad w_4]^T$, $s_i = \sin\alpha_i$, and $c_i = \cos\alpha_i$, one can arrange (21) and (11) as

$$\begin{bmatrix} f \\ \tau \end{bmatrix} = \begin{bmatrix} K_1(\alpha) \\ K_2(\alpha) \end{bmatrix} U(w) \tag{23}$$

where

$$U = [w_1^2 \quad w_2^2 \quad w_3^2 \quad w_4^2]^T$$

$$K_1(\alpha) = \begin{bmatrix} 0 & k_f s_2 & 0 & -k_f s_4 \\ -k_f s_1 & 0 & k_f s_3 & 0 \\ k_f c_1 & k_f c_2 & k_f c_3 & k_f c_4 \end{bmatrix} \tag{24}$$

$$K_2(\alpha) = \begin{bmatrix} 0 & Lk_f c_2 - k_m s_2 & 0 & -Lk_f c_4 + k_m s_4 \\ -Lk_f s_1 - k_m s_1 & 0 & Lk_f c_3 + k_m s_3 & 0 \\ -Lk_f s_1 + k_m c_1 & -Lk_f s_2 - k_m c_2 & -Lk_f s_3 + k_m s_3 & -Lk_f s_4 - k_m s_4 \end{bmatrix} \tag{25}$$

Remark 1. *Over-actuated and fully actuated modes.*

For over-actuated mode, the vector of tilt angles is

$$\alpha = [\alpha_1 \quad \alpha_2 \quad \alpha_3 \quad \alpha_4]^T$$

By setting $\alpha_3 = -\alpha_1$, $\alpha_4 = -\alpha_2$, the vector of tilt angles for fully actuated mode is

$$\alpha = [\alpha_1 \quad \alpha_2 \quad \alpha_1 \quad \alpha_2]^T$$

Remark 1. *Under-actuated mode.*

By setting $\alpha = [0 \quad 0 \quad 0 \quad 0]^T$, the force and the torque in (23) for the under-actuated mode can be reduced as

$$\begin{bmatrix} f_z \\ \tau_\phi \\ \tau_\theta \\ \tau_\psi \end{bmatrix} = \begin{bmatrix} k_f & k_f & k_f & k_f \\ 0 & Lk_f & 0 & -Lk_f \\ -Lk_f & 0 & Lk_f & 0 \\ k_m & -k_m & k_m & -k_m \end{bmatrix} U(w) \tag{26}$$

3. Sliding Mode Path following and Control Allocation

In this section, we first propose the sliding mode-based attitude and position following control via torque and force in (23). Then, we present the control allocation from the control torque and force to the speed and tilt angle of four rotors. Figure 2 illustrates the TRQ control scheme.

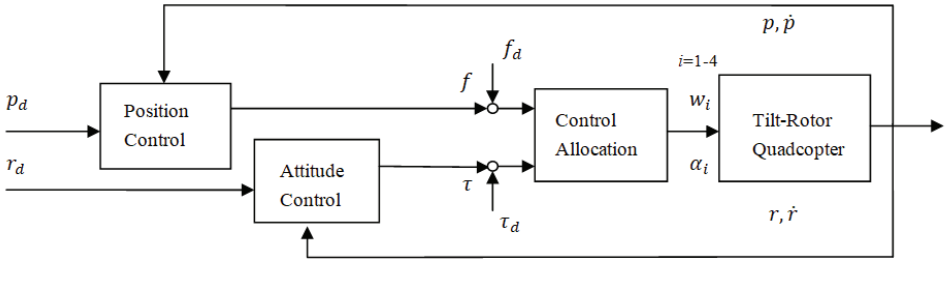

Figure 2. The TRQ control scheme.

3.1. Attitude and Position following SMC

Define $s_1 \in R^3$

$$\dot{r}_r = \dot{r}_d - \Lambda_1(r - r_d) \tag{27}$$

and

$$s_1 = \dot{r} - \dot{r}_r = \dot{r} - \dot{r}_d + \Lambda_1(r - r_d) \tag{28}$$

where r_d is the desired attitude and $\dot{r}_d$ is the desired angular velocity.

Now, we propose the following control for attitude following to exploit the structure of the rotational dynamics:

$$\tau = \Psi^{-T}\left[\hat{H}\ddot{r}_r + \hat{C}\dot{r}_r - K_1\, SGN(s_1) - K_3 s_1 - K_4\tilde{r}\right] \tag{29}$$

where $\tilde{r} = r - r_d$ and $\widehat{(\cdot)}$ denotes the nominal of $(\cdot)$. K_1, K_3, K_4 are positive diagonal matrices, $sgn(\cdot)$ is the sign function, and

$$SGN\left([x_1 \;\; x_2 \;\; x_3]^T\right) = [sgn(x_1) \;\; sgn(x_2) \;\; sgn(x_3)]^T \tag{30}$$

We can now define $s_2 \in R^3$

$$s_2 = \dot{p} - \dot{p}_d + \Lambda_2(p - p_d) \tag{31}$$

where p_d is the desired position and $\dot{p}_d$ is the desired velocity.

The position following control is proposed to alleviate the chattering effects as follows:

$$f = {}^{W}R_B^{-1}\left(u + \begin{bmatrix} 0 \\ 0 \\ mg \end{bmatrix}\right) \tag{32}$$

where u is designed as follows:

$$\dot{u} = -(K_2 + \Lambda_2)u + \hat{m}\left((K_2 + \Lambda_2)\ddot{p}_d + \dddot{p}_d - K_2\Lambda_2\left(\dot{p} - \dot{p}_d\right) - \Lambda_3 s_2 - \Lambda_4\, SGN(s_2)\right) \tag{33}$$

where K_2, Λ_2, Λ_3, Λ_4 are positive diagonal matrices.

3.2. Control Allocation

3.2.1. Fully Actuated Mode

We use the following assumption for the fully actuated quadcopter system

$$\alpha_3 = -\alpha_1, \quad \alpha_4 = -\alpha_2 \tag{34}$$

Now, we propose the following steps to compute α_i and w_i:
Step 1: Initially, set the tilt angles ($\alpha_1 = \alpha_2 = 0$).
Step 2: Compute f and τ from (32) and (29).
Step 3: Compute the rotor velocities.

$$\begin{bmatrix} w_1^2 \\ w_2^2 \\ w_3^2 \\ w_4^2 \end{bmatrix} = \begin{bmatrix} k_f c_1 & k_f c_2 & k_f c_3 & k_f c_4 \\ 0 & Lk_f c_2 - k_m s_2 & 0 & -Lk_f c_4 + k_m s_4 \\ -Lk_f c_1 - k_m s_1 & 0 & Lk_f c_3 + k_m s_3 & 0 \\ -Lk_f s_1 + k_m c_1 & -Lk_f s_2 - k_m c_2 & -Lk_f s_3 + k_m c_3 & -Lk_f s_4 - k_m c_4 \end{bmatrix}^{-1} \begin{bmatrix} f_z \\ \tau_\phi \\ \tau_\theta \\ \tau_\psi \end{bmatrix} \tag{35}$$

where $s_i = \sin\alpha_i$ and $c_i = \cos\alpha_i$ $(i = 1,\ 2,\ 3,\ 4)$.

Step 4: Compute the tilt angles from (23) and (24) using (34) as follows:

$$\alpha_1 = \sin^{-1}\left(\frac{-f_y}{k_f\left(w_1^2 + w_3^2\right)}\right) = -\alpha_3 \tag{36}$$

$$\alpha_2 = \sin^{-1}\left(\frac{f_x}{k_f\left(w_2^2 + w_4^2\right)}\right) = -\alpha_4 \tag{37}$$

Step 5: Go to Step 2 to continue the iteration.

3.2.2. Over-Actuated Mode

We propose the steps to compute α_i and w_i:
Step 1: Initially, set the tilt angles $\alpha_i = 0$ ($i = 1, 2, 3, 4$).
Step 2: Compute f and τ from (32) and (29).
Step 3: Compute the rotor velocities from (35).
Step 4: Compute the tilt angles from (23)–(25) as follows:

$$\left(k_f s_2\right) w_2^2 + \left(-k_f s_4\right) w_4^2 = \tau_\phi \tag{38}$$

$$\left(Lk_f c_2 - k_m s_2\right) w_2^2 + \left(-Lk_f c_4 + k_m s_4\right) w_4^2 = \tau_\phi \tag{39}$$

$$\left(-k_f s_1\right) w_1^2 + \left(k_f s_3\right) w_3^2 = \tau_\theta \tag{40}$$

$$\left(-Lk_f c_1 - k_m s_1\right) w_1^2 + \left(Lk_f c_3 + k_m s_3\right) w_3^2 = \tau_\theta \tag{41}$$

where $s_i = \sin\alpha_i$ and $c_i = \cos\alpha_i (i = 1,\ 2,\ 3,\ 4)$. Using the triangular identities $s_i^2 + c_i^2 = 1$ $(i = 1,\ 2,\ 3,\ 4)$, one can use the numerical method to solve for α_i in the system of nonlinear equations.

Step 5: Go to Step 2 to continue the iteration.

3.2.3. Under-Actuated Mode

Notice that, due to the lack of control degrees of freedom, the desired attitude ϕ_d and θ_d is not arbitrary for the under-actuated quadrotor.

One can obtain ϕ_d and θ_d by

$$\phi_d = \sin^{-1}\left(\frac{u_x s_{\psi d} - u_y c_{\psi d}}{\sqrt{u_x^2 + u_y^2 + (u_z + mg)^2}}\right) \tag{42}$$

$$\theta_d = \tan^{-1}\left(\frac{u_x c_{\psi d} + u_y s_{\psi d}}{u_z + mg}\right) \tag{43}$$

The vector of w_i^2 is

$$\begin{bmatrix} w_1^2 \\ w_2^2 \\ w_3^2 \\ w_4^2 \end{bmatrix} = \begin{bmatrix} k_f & k_f & k_f & k_f \\ 0 & -Lk_f & 0 & Lk_f \\ -Lk_f & 0 & Lk_f & 0 \\ k_m & -k_m & k_m & -k_m \end{bmatrix}^{-1} \begin{bmatrix} f \\ \tau_\phi \\ \tau_\theta \\ \tau_\psi \end{bmatrix} \tag{44}$$

4. Stability Analysis

This section presents the stability analysis of the SMC scheme. Let us use $\lambda_M(A)$, $\lambda_m(A)$ for the largest and smallest eigenvalue of a matrix A. We denote the Euclidean norm for an $n \times 1$ vector x by $\|x\| = \sqrt{x^T x}$. The inertia matrix is symmetric, positive definite, and bounded by $0 < \lambda_m(H) \leq \|H(r)\| \leq \lambda_M(H)$. The matrix $\dot{H}(r) - 2C\left(r, \dot{r}\right)$ is skew-symmetric.

4.1. Sliding Mode Attitude following Control

Theorem 1. *Consider the dynamic model described in (15) and the control for attitude following in (29). The attitude following error dynamics is exponentially stable if the switching gain satisfies the following condition.*

$$\lambda_m(K_1) \geq \left(\|\widetilde{H}\| \|\ddot{r}_r\| + \|\widetilde{C}\| \|\dot{r}_r\| + \|\tau_d\| \right) + \varepsilon_1 \tag{45}$$

where ε_1 is a positive constant.

Proof. $\widehat{H}$ and $\hat{C}$ represent the nominal H and C, where $\widetilde{H} = H - \widehat{H}$ and $\widetilde{C} = C - \hat{C}$.

The rotational dynamics can be expressed as follows:

$$\widehat{H}(q)\ddot{r} + \hat{C}(r,\dot{r})\dot{q} = \Psi^T(\tau + \tau_d) + h_1(r,\dot{r},\ddot{r}) \tag{46}$$

$$h_1(r,\dot{r},\ddot{r}) = -\widetilde{H}(r)\ddot{r} - \widetilde{C}(r,\dot{r})\dot{r}$$

Define

$$\dot{r}_r = \dot{r}_d - \Lambda_1(r - r_d) \tag{47}$$

and

$$s_1 = \dot{r} - \dot{r}_r = \dot{r} - \dot{r}_d + \Lambda_1(r - r_d) \tag{48}$$

It follows from (48) that

$$\dot{s}_1 = \ddot{r} - \ddot{r}_r = \ddot{r} - \ddot{r}_d + \Lambda_1(\dot{r} - \dot{r}_d) \tag{49}$$

Now, we propose the control

$$\tau = \Psi^{-T}\left[\hat{H}\ddot{r}_r + \hat{C}\dot{r}_r - K_1\, SGN(s_1) - K_3 s_1 - K_4\tilde{r}\right] \tag{50}$$

where $\tilde{r} = r - r_d$ and $K_1,\ K_3,$ and K_4 are diagonal matrices. □

Define the Lyapunov function

$$V_1 = \frac{1}{2}s_1^T M(r) s_1 + \frac{1}{2}\tilde{r}^T K_4 \tilde{r} \tag{51}$$

Using (50) and taking derivative of V_1 yield

$$\dot{V}_1 = s_1^T H \dot{s}_1 + \frac{1}{2}s_1^T \dot{H} s_1 + \tilde{r}^T K_4 \dot{\tilde{r}} \tag{52}$$

If the switching gain meets the condition as follows

$$\lambda_m(K_1) \geq \left(\|\widetilde{H}\| \|\ddot{r}_r\| + \|\widetilde{C}\| \|\dot{r}_r\| + \|\tau_d\| \right) + \varepsilon_1 \tag{53}$$

where ε_1 is a positive constant.

From (52), we have

$$\dot{V}_1 \leq -\varepsilon_1\, s_1^T SGN(s_1) - s_1^T K_3 s_1 - \tilde{r}^T K_4 \tilde{r} < 0\ ,\ s_1 \neq 0 \tag{54}$$

The following adaptation law can replace the switching gain K_1

$$K_1 = diag([k_1\ \ k_2\ \ k_3]) \tag{55}$$

$$k_i(t) = k_{ci}|\eta_i| + k_{mi}$$

where $k_{ci} > 0$, $k_{mi} > 0$ and η_i is the obtained by filtering the $sgn(s_{1i})$ using a low-pass filter

$$\zeta_i \dot{\eta}_i + \eta_i = sgn(s_{1i}),\ \eta_i(0) = 0 \tag{56}$$

where ζ_i is a positive constant.

4.2. Sliding Mode Position following Control

Theorem 2. *Consider the translational dynamic model described in (21) and the control for position following in (32)–(33). The position following error dynamics is then asymptotically stable.*

Proof. The translational dynamics is

$$\ddot{p} = \frac{1}{m}u + \frac{u_d}{m} \tag{57}$$

where

$$u = \begin{bmatrix} u_x \\ u_y \\ u_z \end{bmatrix} = {}^{W}R_B f - \begin{bmatrix} 0 \\ 0 \\ mg \end{bmatrix} \tag{58}$$

The nominal dynamics is

$$\ddot{p} = \frac{1}{\widehat{m}}u + \frac{\hat{u}_d}{\widehat{m}} \tag{59}$$

where $\widehat{m}$ is the nominal mass and $\hat{u}_d = 0$.

The sliding surface $s_2 \in R^3$ is

$$s_2 = \dot{p} - \dot{p}_d + \Lambda_2(p - p_d) \tag{60}$$

Using (57) yields

$$\dot{s}_2 = \frac{1}{\widehat{m}}u - \ddot{p}_d + \Lambda_2(\dot{p} - \dot{p}_d) \tag{61}$$

and

$$\dot{s}_2 = \frac{1}{\widehat{m}}\dot{u} - \dddot{p}_d + \Lambda_2(\dot{s}_2 - \Lambda_2(\dot{p} - \dot{p}_d)\ ) \tag{62}$$

Define the Lyapunov function

$$V_2 = \frac{1}{2}s_2^T\Lambda_3 s_2 + \frac{1}{2}\dot{s}_2^T\dot{s}_2 + \gamma ABS(s_2) \tag{63}$$

where

$$\gamma = [\gamma_1\ \gamma_2\ \gamma_3]$$

It follows from (63) that

$$\dot{V}_2 = \dot{s}_2^T\big(\ddot{s}_2 + \Lambda_3 s_2 + \Lambda_4\ SGN(s_2)\big) \tag{64}$$

where Λ_4 is a diagonal matrix with diagonal elements $[\gamma_1\ \gamma_2\ \gamma_3]$.

Then

$$\ddot{s}_2 + \Lambda_3 s_2 + \Lambda_4\ SGN(s_2) = -K_2\dot{s}_2 \tag{65}$$

and

$$\dot{V}_2 = -K_2\dot{s}_2^T\dot{s}_2 \tag{66}$$

Using (62) and (65) yields

$$\dot{u} = \widehat{m}\big(-(K_2 + \Lambda_2)\dot{s}_2 - \Lambda_3 s_2 - \Lambda_4\ SGN(s_2) + \dddot{p}_d + \Lambda_2^2(\dot{p} - \dot{p}_d)\big) \tag{67}$$

Substituting $\dot{s}_2$ from (61) into (64), we have

$$\dot{u} = -(K_2 + \Lambda_2)u + \widehat{m}\big((K_2 + \Lambda_2)\ddot{p}_d + \dddot{p}_d - K_2\Lambda_2\big(\dot{p} - \dot{p}_d\big) - \Lambda_3 s_2 - \Lambda_4\, SGN(s_2)\big) \quad (68)$$

We can derive from LaSalle-Yoshizawa theorem and (66) that $\dot{s}_2 \to 0$. On the basis of (62) and the Barbalat's lemma, one can conclude that $\ddot{s}_2 \to 0$. Therefore, we have the following from (65)

$$\Lambda_3 s_2 = -\Lambda_4\, SGN(s_2) \quad (69)$$

which ensures that

$$s_2 = 0 \quad (70)$$

□

5. Numerical Simulation

To illustrate the proposed control scheme's design, we give an example of a fully actuated TRQ.

5.1. Simulation Parameters

Assuming $s_{q_i} = \sin q_i,\ c_{q_i} = \cos q_i,$ we have

$$H_{11} = I_x, H_{12} = 0,\ H_{13} = -I_x s_\theta$$
$$H_{22} = I_y c_\phi^2 + I_z s_\phi^2,\ H_{23} = c_\theta c_\phi s_\phi \big(I_y - I_z\big)$$
$$H_{33} = I_x s_\theta^2 + I_y c_\theta^2 s_\phi^2 + I_z c_\theta^2 c_\phi^2$$

The matrix of $C\big(r, \dot{r}\big)$ is

$$C_{11} = 0$$
$$C_{12} = -I_x\dot{\psi}c_\theta + \big(I_y - I_z\big)\Big(\dot{\theta}s_\phi c_\phi + \dot{\psi}c_\theta s_\phi^2 - \dot{\psi}c_\theta c_\phi^2\Big)$$
$$C_{13} = -I_y\dot{\psi}c_\theta^2 s_\phi c_\phi + I_z\dot{\psi}c_\theta^2 s_\phi c_\phi$$
$$C_{21} = I_x\dot{\psi}c_\theta - \big(I_y - I_z\big)\Big(\dot{\theta}s_\phi c_\phi + \dot{\psi}c_\theta s_\phi^2 - \dot{\psi}c_\theta c_\phi^2\Big)$$
$$C_{22} = -I_y\dot{\phi}s_\phi c_\phi + I_z\dot{\phi}s_\phi c_\phi$$
$$C_{23} = -I_x\dot{\psi}s_\theta c_\theta + I_y\dot{\psi}s_\theta c_\theta s_\phi^2 + I_z\dot{\psi}s_\theta c_\theta c_\phi^2$$
$$C_{31} = -I_x\dot{\theta}c_\theta + I_y\dot{\psi}c_\theta^2 s_\phi c_\phi - I_z\dot{\psi}c_\theta^2 s_\phi c_\phi$$
$$C_{32} = I_x\dot{\psi}s_\theta c_\theta + (I_z - I_y)\Big(\dot{\theta}s_\theta s_\phi c_\phi + \dot{\phi}c_\theta s_\phi^2 - \dot{\phi}c_\theta c_\phi^2\Big) - I_y\dot{\psi}s_\theta c_\theta s_\phi^2 - I_z\dot{\psi}s_\theta c_\theta c_\phi^2$$
$$C_{32} = I_x\dot{\psi}s_\theta c_\theta + (I_z - I_y)\Big(\dot{\theta}s_\theta s_\phi c_\phi + \dot{\phi}c_\theta s_\phi^2 - \dot{\phi}c_\theta c_\phi^2\Big) - I_y\dot{\psi}s_\theta c_\theta s_\phi^2 - I_z\dot{\psi}s_\theta c_\theta c_\phi^2$$
$$C_{33} = I_x\dot{\theta}s_\theta c_\theta + I_y\Big(-\dot{\theta}s_\theta c_\theta s_\phi^2 + \dot{\phi}c_\theta^2 s_\phi c_\phi\Big) - I_z\Big(\dot{\theta}s_\theta c_\theta c_\phi^2 + \dot{\phi}c_\theta^2 s_\phi c_\phi\Big)$$

We employ the following variables for simulation:

$$m = 2\text{kg},\ L = 0.275\text{m}, g = 9.81\text{m/s}^2,$$
$$I_x = 0.025\text{kgm}^2,\ I_y = 0.025\text{kgm}^2, I_z = 0.040\text{kgm}^2,$$
$$k_m = 2.67{\cdot}10^{-7}\text{Ns}^2,\ k_f = 1.5{\cdot}10^{-5}\text{Nms}^2.$$

with initial conditions

$$\begin{bmatrix} x(0) & y(0) & z(0) \end{bmatrix} = \begin{bmatrix} 0 & 0 & 0 \end{bmatrix}$$

and the desired positions

$$\begin{bmatrix} x_d(t_f) & y_d(t_f) & z_d(t_f) \end{bmatrix} = \begin{bmatrix} 20 & 10 & 5 \end{bmatrix}$$

where $t_f = 20$. The desired attitudes are

$$\phi_d = 0,\ \theta_d = 0,\ \psi_d = 0$$

The desired path is defined as

$$x_d(t) = 2.5{\cdot}10^{-2}\, t^3 - 1.875{\cdot}10^{-3}\, t^4 + 3.75{\cdot}10^{-5}\, t^5$$
$$y_d(t) = 1.25{\cdot}10^{-2}\, t^3 - 9.375{\cdot}10^{-4}\, t^4 + 1.875{\cdot}10^{-5}\, t^5$$
$$z_d(t) = 6.25{\cdot}10^{-3}\, t^3 - 4.6875{\cdot}10^{-4}\, t^4 + 9.375{\cdot}10^{-6}\, t^5$$

Now, we use the following control parameters for simulation:

$$\Lambda_1 = 10\ I_2\ , \Lambda_2 = 4I_3,\ \Lambda_3 = 40\ I_3,\ \Lambda_4 = I_3, K_1 = I_3,$$
$$K_2 = 4I_3, K_3 = 4I_3, K_4 = 10I_3, k_{ci} = 4I_3,\ \ k_{mi} = 0.1I_3,\ \ (i = 1, 2, 3).$$

5.2. Simulation Results

We present the simulation results of the proposed attitude and position following SMC control in Figures 3–8. Figures 3 and 4 show the attitude and position trajectories of the quadrotor with variable changes (weights increased to 125%). The simulation results in Figures 3 and 4 show that the proposed SMC can successfully drive the quadrotor from the initial position through the desired path to the final destination while maintaining the desired attitude. Figures 5 and 6 show the lift and steering torque produced by the four tilt-rotors of the TRQ. Figure 7 shows the path of the tilt angle with parameter deviation. The corresponding quadrotor speeds are shown in Figure 8.

Because the stability analysis in the previous section demonstrated robustness with respect to parameter uncertainty and external perturbations, we then further evaluated the impact of external perturbations on the TRQ. We used perturbation force [sin(4*t*) − sin(4*t*) 2sin(4*t*)] N and perturbation torque [0.1sin(2*t*) 0.1sin(2*t*) 0.1sin(2*t*)] Nm applied to TRQ for simulated motion. As shown in Figures 9–14, we can see that the perturbation has little effect on the capability of the quadcopter because the proposed control and control assignment can reject the perturbation and return the state variables to the sliding surface.

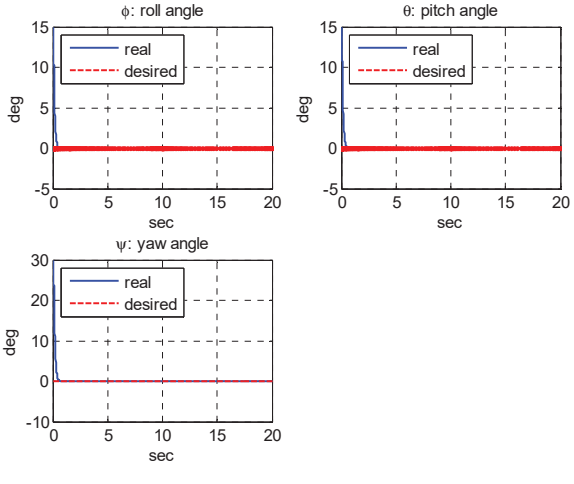

Figure 3. The attitude path with variable deviations.

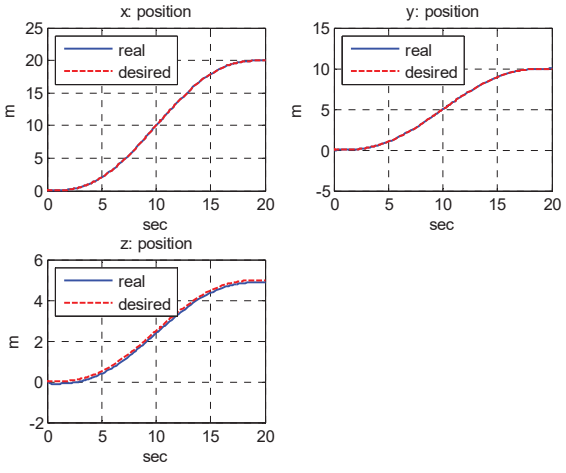

Figure 4. The position path with variable deviations.

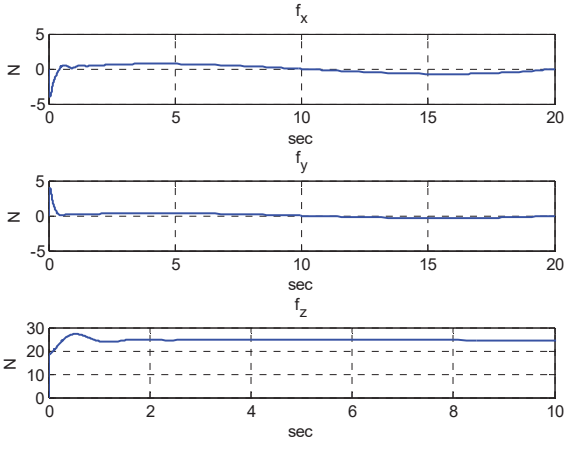

Figure 5. The propelling force with variable deviations.

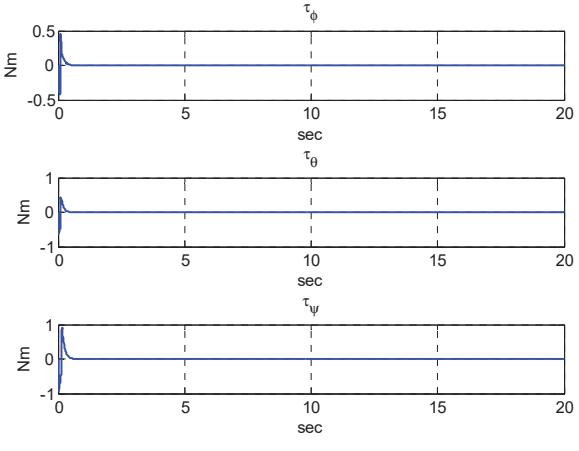

Figure 6. The turning torque with variable deviations.

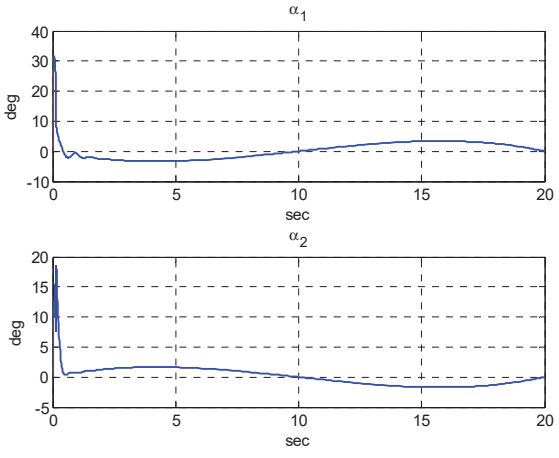

Figure 7. The tilt angle path with variable deviations.

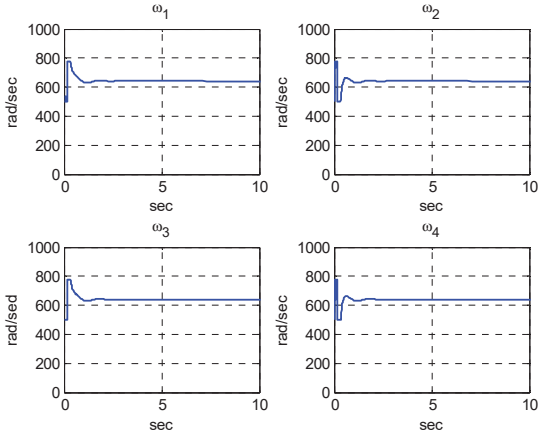

Figure 8. The rotor velocity with variable deviations.

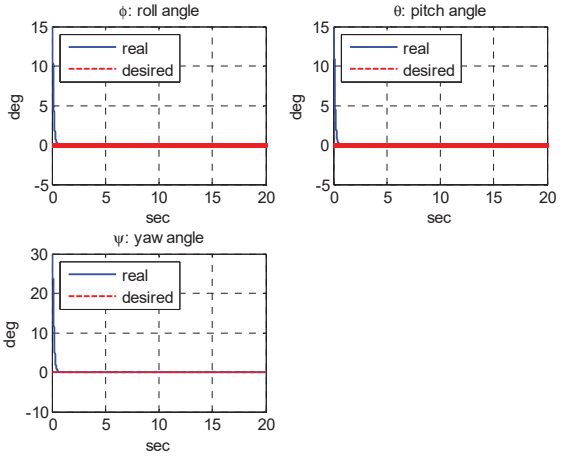

Figure 9. The attitude path with variable deviations and perturbations.

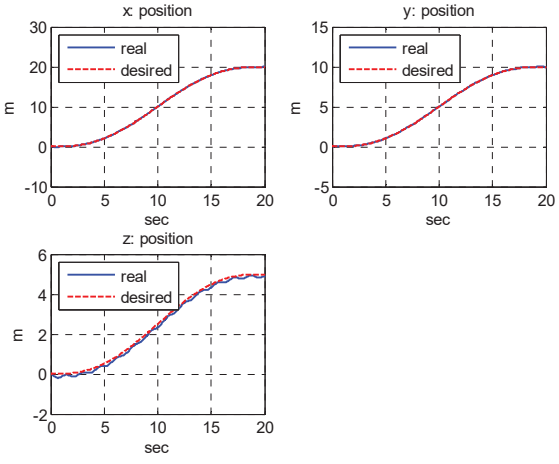

Figure 10. The position path with variable deviations and perturbations.

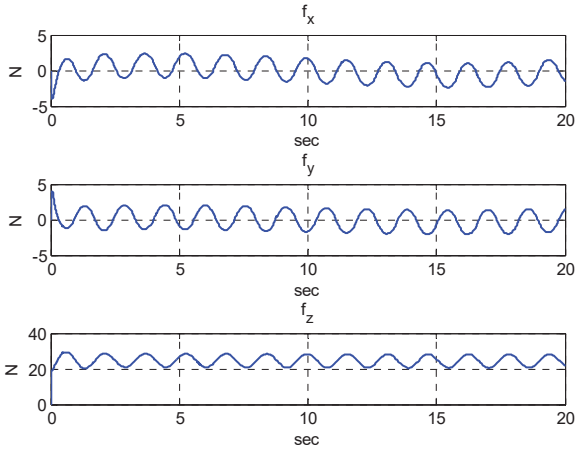

Figure 11. The propelling force with variable deviations and perturbations.

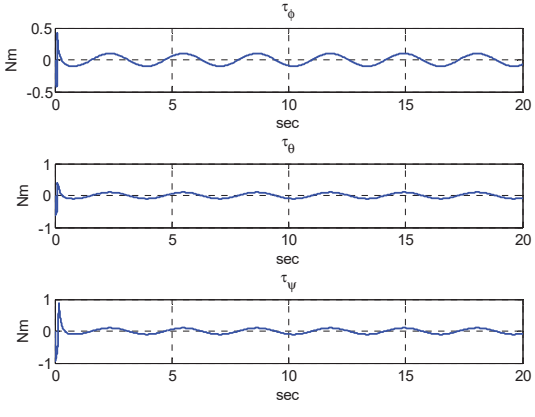

Figure 12. The turning torque with variable deviations and perturbations.

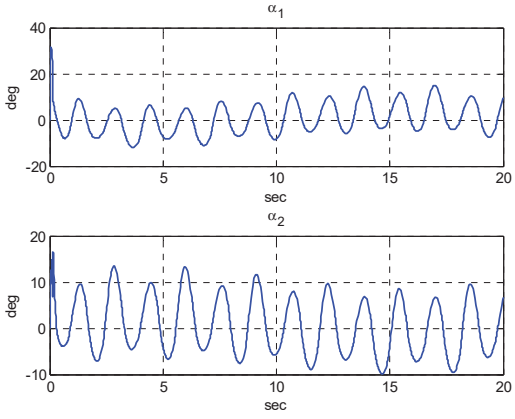

Figure 13. The tilt angle path with variable deviations and perturbations.

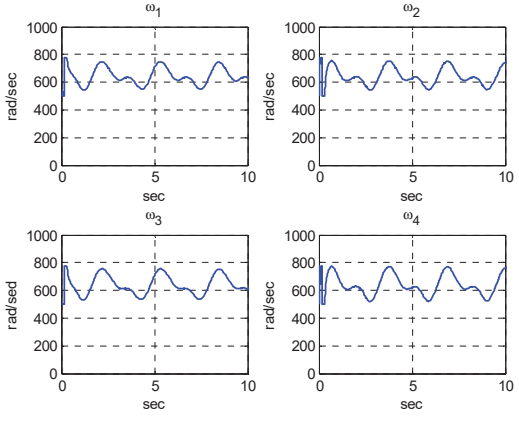

Figure 14. The rotor velocity with variable deviations and perturbations.

In summary, the numerical simulation results clearly show that the proposed SMC schemes can accomplish the goal of trajectory tracking and counter the parametric variation and external disturbances in the rotation and translation of TRQ via control allocation.

6. Conclusions

This paper presents the dynamic modeling, path following, and control allocation of a TRQ. Two types of SMC are proposed to enhance the robustness and capability: one is the first-order sliding mode for attitude following and the other is the second-order sliding mode for position following. Considering the parameter changes and external perturbation, we show the stability analysis based on the Lyapunov theory that the proposed control scheme can ensure the error dynamics' asymptotic stability for the position and attitude following. In the numerical simulation of the fully actuated mode, we demonstrated that the proposed SMC could achieve path following and attitude regulation goals in the presence of variable changes and external perturbations. The tilt-rotor quadrotor has more control degrees of freedom than the under-actuated quadrotor and, therefore, can make full use of the control redundancy to complete the simultaneous trajectory tracking and attitude control that a traditional quadrotor cannot do, and thus has a certain degree of actuator fault tolerance. In the future, we will integrate the sliding mode path following and control allocation into a fault-tolerant flight control.

Author Contributions: Conceptualization, C.-C.Y. and S.-J.W.; methodology, C.-C.Y. and S.-J.W.; software, S.-J.W.; validation, C.-C.Y. and S.-J.W.; formal analysis, C.-C.Y.; investigation, S.-J.W.; writing—original draft preparation, C.-C.Y. and S.-J.W.; writing—review and editing, C.-C.Y.; visualization, S.-J.W. All authors have read and agreed to the published version of the manuscript.

Funding: This research received no external funding.

Institutional Review Board Statement: Not applicable.

Informed Consent Statement: Not applicable.

Data Availability Statement: No new data were created or analyzed in this study. Data sharing is not applicable to this article.

Conflicts of Interest: The authors declare no conflict of interest.

Nomenclature

B	quadrotor body
P_i	propeller i
F_w	inerita world frame
F_B	body frame
F_{P_i}	ith propeller frame
R_T	transform matrix from body angular rates to Euler rates
p	position of B in F_w
q	Euler angle of B in F_w
${}^W R_B$	rotation matrix from F_B to F_w
${}^B R_{P_i}$	rotation matrix from $F_{P_i}$to F_B
w_i	ith propeller spinning velocity about Z_{Pi}
w_{P_i}	the angular velocity in the ith propeller frame
α_i	ith propeller tilting angle about X_{Pi}
T_{P_i}	the force in the ith propeller frame
w_B	angular velocity of B in F_B
v_B	velocity of B in F_B
τ_B	torque in F_B
τ_{P_i}	torque in F_{P_i}
τ_{di}	ith propeller air drag torque about Z_{Pi}
T_i	ith propeller thrust along Z_{Pi}
τ_{w_i}	motor torque along Z_{Pi}
m	total quadrotor mass
I_{Pi}	inertia of the ith propeller P_i
I_B	inertia of the quadcopter body B
k_f	propeller thrust coefficient
k_m	propeller drag coefficient
L	distance of F_{P_i} to F_B
g	gravity constant

References

1. Mahony, R.; Kumar, V.; Corke, P. Multirotor Aerial Vehicles: Modeling, Estimation, and Control of Quadrotor. *IEEE Robot. Autom. Mag.* **2012**, *19*, 20–32. [CrossRef]
2. Quan, Q. *Introduction to Multicopter Design and Control*; Springer: Berlin/Heidelberg, Germany, 2017.
3. Miranda-Colorado, R.; Aguilar, L.T. Robust PID control of quadrotors with power reduction analysis. *ISA Trans.* **2020**, *98*, 47–62. [CrossRef] [PubMed]
4. Gomes, L.L.; Leal, L.; Oliveira, T.R.; Cunha, J.P.V.S.; Revoredo, T.C. Unmanned Quadcopter Control Using a Motion Capture System. *IEEE Lat. Am. Trans.* **2016**, *14*, 3606–3613. [CrossRef]
5. Shankaran, V.P.; Azid, S.I.; Mehta, U.; Fagiolini, A. Improved Performance in Quadrotor Trajectory Tracking Using MIMO PI-D Control. *IEEE Access* **2022**, *10*, 110646–110660.
6. Lee, D.; Kim, H.J.; Sastry, S. Feedback Linearization vs. Adaptive SMC for a Quadrotor Helicopter. *Int. J. Control Autom. Syst.* **2009**, *7*, 419–428. [CrossRef]
7. Satici, A.C.; Poonawala, H.; Spong, M.W. Robust Optimal Control of Quadrotor UAVs. *IEEE Access* **2013**, *1*, 79–93. [CrossRef]

8. Koksal, N.; An, H.; Fidan, B. Backstepping-based adaptive control of a quadrotor UAV with guaranteed following capability. *ISA Trans.* **2020**, *105*, 98–110. [CrossRef]
9. Young-Cheol, C.; Hyo-Sung, A. Nonlinear Control of Quadrotor for Point Following: Actual Implementation and Experimental Tests. *IEEE/ASME Trans. Mechatron.* **2015**, *20*, 1179–1192.
10. Perozzi, G.; Efimov, D.; Biannic, J.-M.; Planckaert, L. Path following for a quadrotor under wind perturbations: SMC with state-dependent gains. *J. Frankl. Inst.* **2018**, *355*, 4809–4838. [CrossRef]
11. Xu, G.; Xia, Y.; Zhai, D.-H.; Ma, D. Adaptive prescribed capability terminal sliding mode attitude control for quadrotor under input saturation. *IET Control Theory Appl.* **2020**, *14*, 2473–2480. [CrossRef]
12. Besnard, L.; Shtessel, Y.B.; Landrum, B. Quadrotor vehicle control via SMCler driven by sliding mode perturbation observer. *J. Frankl. Inst.* **2012**, *349*, 658–684. [CrossRef]
13. Ricardo, J.A., Jr.; Santos, D.A.; Oliveira, T.R. Attitude Tracking Control for a Quadrotor Aerial Robot Using Adaptive Sliding Modes. In Proceedings of the XLI Ibero-Latin-American Congress on Computational Methods in Engineering (ABMEC), Foz do Iguaçu, Brazil, 16–19 November 2020.
14. Islam, S.; Liu, P.X.; El Saddik, A. Robust Control of Four-Rotor Unmanned Aerial Vehicle With Perturbation Uncertainty. *IEEE Trans. Ind. Electron.* **2015**, *62*, 1563–1571. [CrossRef]
15. Dierks, T.; Jagannathan, S. Output Feedback Control of a Quadrotor UAV Using Neural Networks. *IEEE Trans. Neural Netw.* **2010**, *21*, 50–66. [CrossRef] [PubMed]
16. Wu, H.; Ye, H.; Xue, W.; Yang, X. Improved Reinforcement Learning Using Stability Augmentation With Application to Quadrotor Attitude Control. *IEEE Access* **2022**, *10*, 67590–67604. [CrossRef]
17. Yang, S.; Xian, B. Exponential Regulation Control of a Quadrotor Unmanned Aerial Vehicle With a Suspended Payload. *IEEE Trans. Control Syst. Technol.* **2020**, *28*, 2762–2769. [CrossRef]
18. Levant, A. Principles of 2-sliding mode design. *Automatica* **2007**, *43*, 576–586. [CrossRef]
19. Levant, A. Sliding order and sliding accuracy in SMC. *Int. J. Control* **1993**, *58*, 1247–1263. [CrossRef]
20. Utkin, V.I.; Poznyak, A.S. Adaptive SMC with application to super-twist algorithm: Equivalent control method. *Automatica* **2013**, *49*, 39–47. [CrossRef]
21. Moreno, A.; Osorio, M. Strict Lyapunov functions for the super-twisting algorithm. *IEEE Trans. Autom. Control* **2012**, *57*, 1035–1040. [CrossRef]
22. Pico, J.; Pico-Marco, E.; Vignoni, A.; De Battista, H. Stability preserving maps for finite-time convergence: Super-twisting sliding-mode algorithm. *Automatica* **2013**, *49*, 534–539. [CrossRef]
23. Utkin, V. On convergence time and perturbation rejection of super-twisting control. *IEEE Trans. Autom. Control* **2013**, *58*, 2013–2017. [CrossRef]
24. Mokhtari, A.; Benallegue, A.; Orlov, Y. Exact linearization and sliding mode observer for a quadrotor unmanned aerial vehicle. *Int. J. Robot. Autom.* **2006**, *21*, 39–49. [CrossRef]
25. Beballegue, A.; Mokhtari, A.; Fridman, L. High-order sliding-mode observer for a quadrotor UAV. *Int. J. Robust Nonlinear Control* **2008**, *18*, 427–440. [CrossRef]
26. Bauersfeld, L.; Spannagl, L.; Ducard, G.J.J.; Onder, C.H. MPC Flight Control for a Tilt-Rotor VTOL Aircraft. *IEEE Trans. Aerosp. Electron. Syst.* **2021**, *57*, 2395–2409. [CrossRef]
27. Ryll, M.; Bülthoff, H.H.; Giordano, P.R. A Novel Overactuated Quadrotor UnmannedAerial Vehicle: Modeling, Control, and Experimental Validation. *IEEE Trans. Control Syst. Technol.* **2015**, *23*, 540–556. [CrossRef]
28. Hua, M.-D.; Hamel, T.; Morin, P.; Samson, C. Control of VTOL vehicles with thrust-tilting augmentation. *Automatica* **2015**, *52*, 1–7. [CrossRef]
29. Rashad, R.; Goerres, J.; Aarts, R.; Engelen, J.B.C.; Stramigioli, S. Fully Actuated Multirotor UAVs: A Literature Review. *IEEE Robot. Autom. Mag.* **2020**, *27*, 97–107. [CrossRef]
30. Zheng, P.; Tan, X.; Kocer, B.B.; Yang, E.; Kovac, M. TiltDrone: A Fully-Actuated Tilting Quadrotor Platform. *IEEE Robot. Autom. Lett.* **2020**, *5*, 6845–6852. [CrossRef]
31. Willis, J.; Johnson, J.; Beard, R.W. State-Dependent LQR Control for a Tilt-Rotor UAV. In Proceedings of the 2020 American Control Conference (ACC), Denver, CO, USA, 1–3 July 2020; pp. 4175–4181.

drones

MDPI

Article

Aerodynamic Performance Analysis of VTOL Arm Configurations of a VTOL Plane UAV Using a Computational Fluid Dynamics Simulation

Gesang Nugroho *, Yoshua Dwiyanson Hutagaol and Galih Zuliardiansyah

Department of Mechanical and Industrial Engineering, Faculty of Engineering, Universitas Gadjah Mada, Yogyakarta 55284, Indonesia
* Correspondence: gesangnugroho@ugm.ac.id

Abstract: A vertical take-off and landing plane (VTOL plane) is a fixed-wing unmanned aerial vehicle (FWUAV) configuration with the ability to take off and land vertically. It combines the benefits of fixed-wing and multirotor configurations, which gives it a high cruising range and independence from a runway. This configuration requires arms as mountings for the VTOL's motors. This study discusses the design of a VTOL Plane with various VTOL arm configurations, and a computational fluid dynamics (CFD) simulation was conducted to find out which configuration performs the best aerodynamically. The VTOL arm configurations analyzed were a quad-plane, a twin-tail boom, a tandem wing, and a transverse arm. The interpreted performances were the lift and drag performances, stall conditions, flight efficiency, stability, and maneuverability. The relative wind directions toward the longitudinal axis of the UAV, which are the sideslip angle and the angle of attack, were varied to simulate various flying conditions. The results showed that the twin tail-boom is the most advantageous based on the interpreted performances.

Keywords: VTOL plane UAV; VTOL arm configuration; computational fluid dynamics

Citation: Nugroho, G.; Hutagaol, Y.D.; Zuliardiansyah, G. Aerodynamic Performance Analysis of VTOL Arm Configurations of a VTOL Plane UAV Using a Computational Fluid Dynamics Simulation. *Drones* **2022**, *6*, 392. https://doi.org/10.3390/drones6120392

Academic Editors: Andrzej Łukaszewicz, Wojciech Giernacki, Zbigniew Kulesza, Jaroslaw Pytka and Andriy Holovatyy

Received: 7 November 2022
Accepted: 30 November 2022
Published: 2 December 2022

1. Introduction

As the development of unmanned aerial vehicle (UAV) technology is becoming rapid, new demands from countless fields are emerging due to its advantages of having small dimensions, low operating cost, and minimal risk to the environment and human life. UAVs are already commonly used in the military [1]. Furthermore, they have a promising future in forestry [2], medical [3], and meteorology [4]. Ever-growing demands mean that UAVs need to be developed in a variety of shapes and sizes to satisfy and achieve limitless kinds of mission.

Despite being relatively new entrants to the airspace, UAVs have already come in a variety of configurations. UAVs are generally classified into two configurations, namely rotary-wing and fixed-wing. Each configuration has its advantages and disadvantages. A vertical take-off and landing plane (VTOL plane) is a combination of those two configurations, affording the benefit of high cruising range and efficiency from a fixed wing and the capability of taking off and landing in a limited area from a rotary wing [5]. VTOL Planes are ideal for usage in a remote area, rough terrain, or a vast body of water, making it excellent for application to monitoring and surveillance.

Numerous design concepts for VTOL plane UAVs are available, such as a fixed-wing VTOL and a tiltrotor. The main difference between the two is how the UAV transitions from the VTOL phase to the cruising phase, and vice versa. However, the tiltrotor concept uses a complicated mechanism to change the orientation of the rotors with a control system too complex to be used as a design reference. On the other hand, the fixed-wing VTOL is simpler to manufacture and operate, making it easier to develop and expand further.

VTOL plane design requires arms to mount its rotary-wing rotors. Many UAV designs and configuration concepts can be utilized as a VTOL plane design by placing arms as mountings for the VTOL motors, namely a quad-plane [6], a twin-tail boom [7–9], a tandem wing [10,11], and a transverse arm. Moreover, the quad-plane, twin-tail boom, and tandem wing configurations are already available on the market [6–9,11]. The transverse arm is a newly proposed idea based on the configuration's geometry that could work as a VTOL plane configuration. As such, it is not a common configuration and can not be found in the market.

Even though there are already CFD simulations [12–14] and experimental studies [10,15] of those configurations' performances, no research has been conducted to compare and determine which arm configuration performs the best aerodynamically. Furthermore, different missions demand different performances of the UAV. Even though the configurations being compared are already developed and quite mature, the comparison result could work as a basis for customers or users to choose which configuration to develop based on the mission's need. As a result, this study will discuss each configuration's advantages and disadvantages, determine which configuration performs the best overall, and what kind of mission each is suitable for.

Each configuration has its characteristics. Quad-plane configuration is the most common because it resembles the conventional fixed-wing configuration the most with the addition of VTOL arms. However, due to the fuselage stretching to the tailplane, it has more drag than the twin-tail boom configuration. The tandem wing configuration uses its two wings to support the VTOL motors, so it does not require additional beams. The drawbacks include being more prone to wind gusts or less stable in crosswind conditions due to its two wings [16]. The transverse arm configuration has two horizontal stabilizer surfaces, in the forward and aft fuselage, as supports to mount the VTOL motors, making it stable but susceptible to higher drag.

The arm configurations mentioned are all acceptable for a VTOL plane design. However, the design geometries are quite different. To determine which configuration performs the best, all four configurations' designs were analyzed using a CFD approach to find out their aerodynamic performance in various wind situations to simulate real flight conditions.

2. Research Methods

The UAV is designed through several steps, beginning with conceptual design, preliminary design, and detailed design [17–22]. These steps are necessary to ensure that the UAV being designed is reliable and satisfies the DR&O. The performances being compared are the lift and drag characteristics, stall conditions, efficiency, stability, and maneuverability. To ensure that the performances are comprehended in various flight conditions, the angle of attack and sideslip angle need to be considered since they influence stability [23]. The angle of attack, α, is the angle between the longitudinal axis x and the projection of the vector speed $\vec{V}$ on the plane of symmetry x, z. The sideslip angle, β, is the angle between the vector of speed relative to the air $\vec{V}$ and the plane of the aircraft x, z [24]. Both angles are illustrated in Figure 1.

A computational fluid dynamics approach was used to analyze the overall design because it is more feasible than using a wind tunnel as an experimental approach. Furthermore, it does not require excessive cost. The simulation was conducted using an accurate turbulence model to acquire accurate data.

The VTOL plane was designed to be hybrid, where the VTOL propulsion uses electric motors, and the fixed-wing propulsion uses an internal combustion engine (ICE) with gasoline to increase the cruise range and energy efficiency. The conversion to other configurations follows several processes to make each configuration work based on similar studies or comparison planes. We attempted to keep the variables, including the aircraft weight, the cruise speed, the wing area, the wing planform design, horizontal and vertical stabilizer volume coefficient, fuselage geometry, and the forward propulsion system intake and exhaust geometry the same in all configurations. The following arm configurations were used in the comparison:

a. Quad-plane [6];
b. Twin-tail boom [7–9];
c. Tandem wing [10,11];
d. Transverse arm.

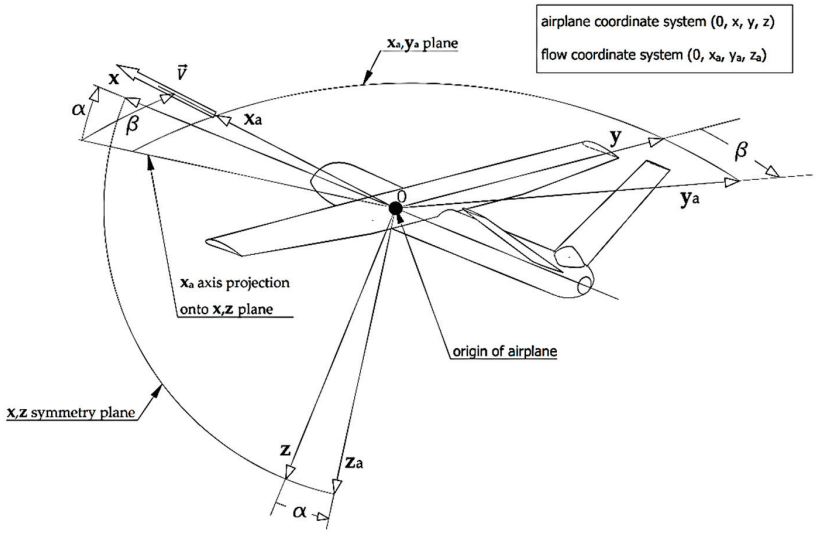

Figure 1. Definition of angle of attack and angle of sideslip.

2.1. Design Requirements and Objectives

The VTOL plane is designed to fly at low speed with low stall speed to accommodate the transition from the vertical take-off phase to the cruising phase and then to the vertical landing phase. The VTOL plane must not stall until the VTOL motors take over the lifting duty and fully support the aircraft's weight so the transition from forward flight to hovering remains stable and smooth [25]. The civil aviation safety regulation (CASR) [26] was also used to determine the requirements to ensure the aircraft conformed to governing body regulations so it could be certified. Table 1 lists the DR&O, followed by Figure 2, which shows the mission profile of the VTOL plane.

Table 1. Design requirements and objectives (DR&O).

No	Requirement	Value
1	Take-off transition distance	80 m
2	Landing transition distance	150 m
3	Cruising altitude	300 m
4	Cruising velocity	23 m/s
5	Stall speed	14 m/s
6	Load Weight	1 kg
7	Flight time	6 h
8	Rate of climb	5.5 m/s
9	Maximum take-off weight	10 kg
10	Wingspan	2 m

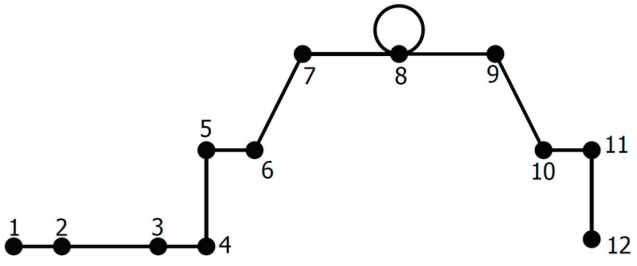

Figure 2. VTOL plane mission profile. Note: 1—ground test; 2—engine start and warm up; 3—VTOL take-off preparation; 4—VTOL take-off; 5—VTOL transition to forward flight; 6—Climb; 7—cruise; 8—loiter and cruise back; 9—descent; 10—forward flight transition to VTOL; 11—VTOL landing; 12—engine shutdown and ground test.

2.2. Conceptual Design

The conceptual design step configures the wing configuration, fuselage geometry, empennage, and propulsion systems. To fulfill the requirement of a low stall speed, a high-lift wing configuration is needed. Therefore, the high-wing configuration was chosen due to its superior lift-to-drag ratio (L/D) to the mid-wing and the low-wing configurations [27]. The wing was designed without dihedral angles to simplify the geometries in the CFD simulation.

The geometry of the fuselage is a combination of several comparison planes. The dimensions of the fuselage were adapted to the electronic components and fuel tank volume requirements. The propulsion system configuration chosen was a pusher with the ICE mounted in the aft fuselage, to avoid obstructing the pitot tube, camera, and sensors mounted at the nose of the fuselage. In a twin-tail boom design, the fuselage does not need to be stretched to the tailplane because the tailplane is mounted on the twin-boom, which shortens the fuselage length but still accommodates enough room for the necessary electronic components and the fuel tank.

ALTI Ascend [7], ALTI Transition [8], and Foxtech Great Shark 330 [9] have similar DR&O to the designed VTOL plane, so they were chosen as comparison planes in this study. Those comparison planes were used as a reference to determine the fuselage geometry and their specifications were needed as reference data to solve equations in the sizing step.

2.3. Preliminary Design

Preliminary design was divided into two steps, namely weight sizing and performance sizing. In weight sizing, several values such as take-off weight, empty weight, fuel weight, and fuel fraction were calculated. Data from comparison planes were used as a reference to calculate those values, according to the equations provided by [18]. Fuel fraction is the amount of fuel weight needed for a mission phase divided by the empty weight of the aircraft.

In performance sizing, the values to be calculated are the power loading (*W*/*P*) and wing loading (*W*/*S*). They are obtained by calculating each phase's performance equations provided by [18] to obtain every phase's range of accepted wing loadings and power loadings based on the DR&O. The wing loading and power loading are then plotted in one (*W*/*P*) vs. (*W*/*S*) graph to obtain an area where all design points within that area are acceptable to fulfill the aircraft's mission profile.

2.3.1. Weight Sizing

Table 2 shows the fuel fractions of each phase of the mission and Table 3 shows the calculated weight sizing.

Table 2. Fuel fraction [17].

Phase	Value
Engine start and warm-up	0.998
VTOL take-off preparation	0.998
VTOL transition to forward flight	0.998
Climb	0.995
Cruise	0.998
Loiter	0.938
Cruise back	0.998
Descent	0.995
Landing, taxi, and shutdown	0.995

Table 3. Weight sizing.

VTOL Plane Weight Sizing	
Maximum take-ff weight (MTOW)	10.04 kg
Empty airframe weight	3.5 kg
Ready to fly (RTF) dry weight	6.15 kg
Ready to fly (RTF) including fuel and batteries	9 kg
Maximum payload	1 kg
Fuel weight	1.1 kg

2.3.2. Performance Sizing

Figure 3 shows the (*W*/*P*) vs. (*W*/*S*) matching plot of every phase's performance curve, which resulted in an area where all points within are considered acceptable and capable of fulfilling the DR&O. The white area shows the acceptable range for a design point. A design point was then picked considering the optimum wing area and power needed. The wing loading and the power loading values were provided by the selected design point, shown as a red dot in Figure 3. The results of the performance sizing are listed in Table 4.

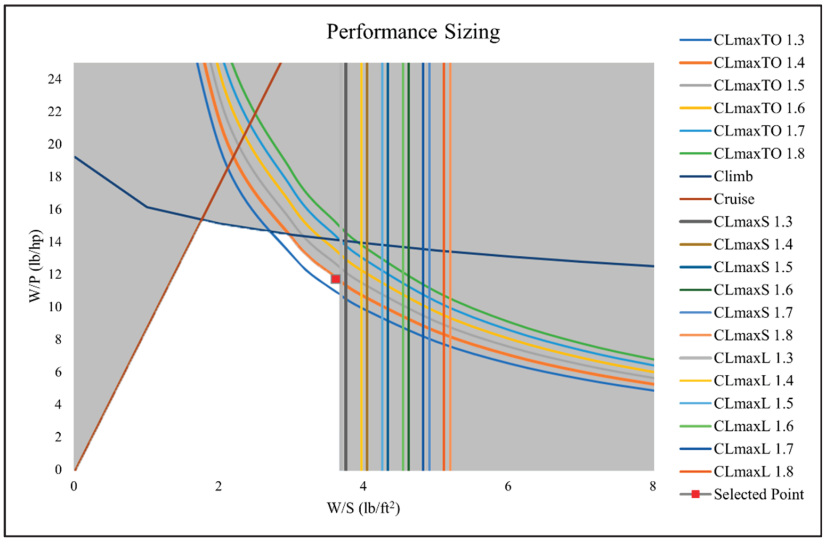

Figure 3. Performance sizing graph.

Table 4. Performance sizing.

VTOL Plane Performance Sizing	
Wing loading (*W*/*S*)	3.6 lb/ft^2 = 17.6 kg/m^2
Power loading (*W*/*P*)	11.8 lb/hp = 5.4 kg/hp
C_{LmaxTO}	1.4
C_{LmaxL}	1.3
C_{LmaxS}	1.3

2.4. Detailed Design

Data that were obtained through the preliminary design step were used to design the wing, VTOL arm, and empennage. After the calculations to obtain the dimensions had been completed, a 3D design was created. Several simplifications had been carried out to the design as it was solely used for simulation purposes, which means manufacturing processes were not taken into consideration.

2.4.1. Wing Detailed Design

The planform of the wing was designed using equations from [18]:

$$s = \frac{W_{TO}}{\left(\frac{W}{S}\right)} \quad (1)$$

$$AR = \frac{b^2}{s} \quad (2)$$

$$Cr = \frac{2}{1+\lambda} \times \frac{s}{b} \quad (3)$$

$$Ct = \lambda \times Cr \quad (4)$$

where: s = wing area (m^2), b = wingspan (m), Cr = root chord (m), Ct = tip chord (m), AR = aspect ratio.

According to Table 4, the required coefficient of lift (C_L) was 1.4, so the NACA 4412 was selected as the wing airfoil because it had a C_L of 1.6 [28]. Table 5 shows the results of the wing design calculated using Equations (1)–(4). Figure 4 shows the wing planform design.

Table 5. Wing design.

Wing Design	
s	0.57 m^2
AR	7.01
b	2 m
Cr	0.315 m
Ct	0.215 m

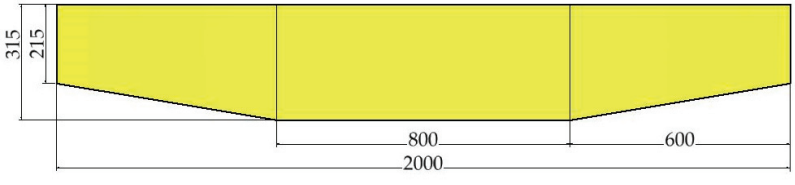

Figure 4. Wing planform design in mm.

2.4.2. VTOL Arm Design

The VTOL arm design determines the position of the VTOL motors. The VTOL motors used were Brushless DC Motors 490KV with 16-inch propellers, so the arms were designed

with enough clearance so the propellers would not hit the fuselage. The stability of the VTOL plane was the next consideration, as it is affected by the motors' position relative to the plane's center of gravity. It was determined that the angle range should be between 30° and 60°. Figure 5 schematically shows the position of the VTOL motor.

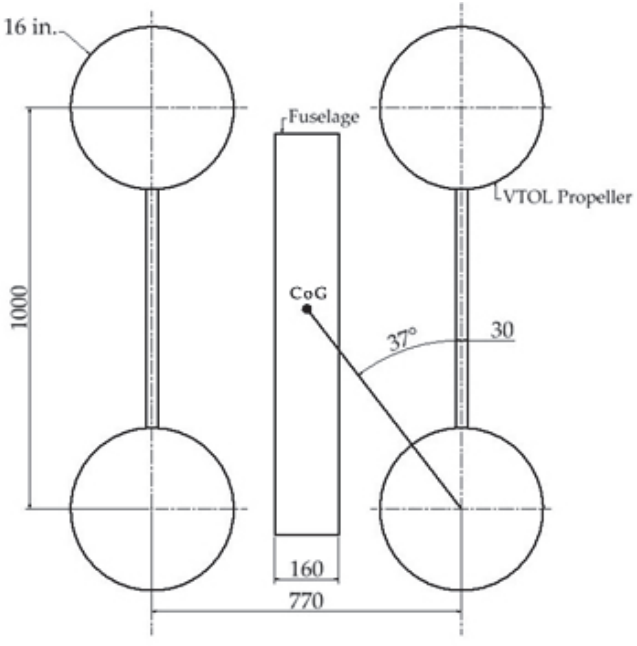

Figure 5. Schematic drawing of the VTOL motors' position.

2.4.3. Empennage Detailed Design

In a twin-tail boom configuration, the tail boom is an extension of the VTOL arm. As such, the horizontal stabilizer span is constrained. NACA 0006 was chosen for the empennage airfoil as it has zero C_L at 0° angle of attack [28]. Using equations provided by [20], the necessary values and dimensions to design the empennage were calculated, such as the vertical tail volume coefficient (V_v), the horizontal tail volume coefficient (V_h), the vertical tail moment arm (L_v), and the horizontal tail moment arm (L_v). The tail moment arm is the distance from 25% wing mean aerodynamic chord (MAC) to 25% tail mean aerodynamic chord (MAC). Table 6 shows the results of the empennage design calculations.

$$V_v = \frac{l_V \times S_V}{s \times b} \tag{5}$$

$$V_v = \frac{l_V \times S_V}{s \times b} \tag{6}$$

2.4.4. Twin-Tail Boom Final Design

After all the size data had been obtained, a three-dimensional model was created. The model was created using Autodesk Inventor Professional 2022 software. Figure 6 shows a three-dimensional model of the VTOL plane with a twin-tail boom configuration.

2.5. Conversion to Other Configurations

The twin-tail boom design acted as a reference for other configurations, namely the quad-plane, the tandem wing, and the transverse arm.

Table 6. Empennage design.

Empennage Design	
V_v	0.025
V_h	0.6
L_v	0.9 m
L_h	1 m
Vertical stabilizer root chord ($Cr_{vertical}$)	0.23 m
Vertical stabilizer tip chord ($Ct_{vertical}$)	0.157 m
Vertical stabilizer span ($b_{vertical}$)	0.17 m
Horizontal stabilizer root chord ($Cr_{horizontal}$)	0.157 m
Horizontal stabilizer tip chord ($Ct_{horizontal}$)	0.157 m
Horizontal stabilizer span ($b_{horizontal}$)	0.662 m

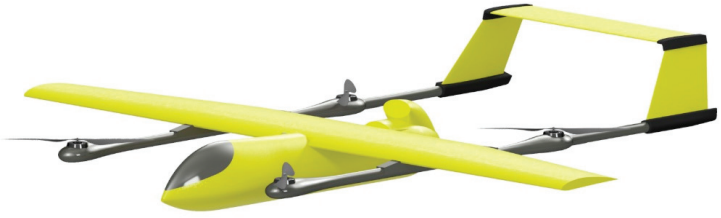

Figure 6. Three-dimensional model of the VTOL plane with a twin-tail boom configuration.

2.5.1. Quad-Plane Design

The difference between the twin-tail boom and the quad-plane configuration is mainly in the empennage configuration. V-tail was selected as the empennage configuration for the quad-plane design. The V-tail was found to be a stable configuration in crosswind conditions [28]. The fuselage was extended to the V-tail as the tails needed to be mounted on it. The V-tail geometry used the same V_v, V_h, L_v, and L_h values as the twin-tail boom configuration. Those values were then used to determine the V-tail dimensions using the equation provided by [20].

$$S_{V-tail} = S_v + S_h \tag{7}$$

$$\Gamma = \tan^{-1}\sqrt{\frac{S_v}{S_h}} \tag{8}$$

where Γ is the dihedral angle from the horizontal plane. Table 7 shows the results of the V-tail geometry calculations, and Figure 7 shows the three-dimensional model of the quad-plane configuration.

Table 7. V-tail design for the quad-plane configuration.

V-Tail Design.	
Γ	36.54°
V-tail root chord ($Cr_{V\text{-}tail}$)	0.2 m
V-tail tip chord ($Ct_{V\text{-}tail}$)	0.14 m
V-tail span ($b_{V\text{-}tail}$)	0.53 m

2.5.2. Tandem Wing Design

The tandem wing configuration is unlike the other configurations in several parameters. The CoG of a tandem wing is located between the fore and the hind wings, not at the wing, like a classic fixed-wing configuration. Moreover, the hind wing acts as a horizontal stabilizer and a lifting surface, causing major concerns for stability and controllability [16]. The aerodynamic performance of the hind wing is also heavily affected by the downwash

of the forewing. The effect of longitudinal and vertical gaps between the two wings was reported in [29].

Figure 7. Three-dimensional model of the VTOL plane with a quad-plane configuration.

Creating a gap vertically would mean creating a gap in the vertical positions of the front and the rear VTOL motors because the motors were to be mounted at the tip of the wings. The gap would cause stability problems in the hovering phase, so no vertical gap was created between the forewing and the rear wing. Nonetheless, a bigger longitudinal gap, also called a stagger (St), was created to minimize the downwash effect, with the angle of the VTOL motors' positions against the CoG taken into consideration. Specifically, stagger is the longitudinal distance from the 25% forewing MAC to the 25% hind wing MAC. The taper ratio of the forewing also has a significant effect on the aerodynamic performance of the hind wing [30].

A V-tail configuration was chosen as the empennage configuration to help with the pitch stability of the VTOL plane despite the hind wing acting as a horizontal stabilizer. Nonetheless, the need for a horizontal stabilizer was diminished, and the horizontal area of the V-tail was relatively small. Table 8 shows the tandem wing sizing. Figure 8 shows the schematic drawing of the configuration, and Figure 9 shows a three-dimensional model of the tandem wing configuration.

Table 8. Tandem wing sizing.

Tandem Wing Sizing	
Stagger (S_t)	0.86 m
Γ	35°
V-tail root chord ($Cr_{V\text{-}tail}$)	0.1 m
V-tail tip chord ($Ct_{V\text{-}tail}$)	0.07 m
V-tail span ($b_{V\text{-}tail}$)	0.256 m

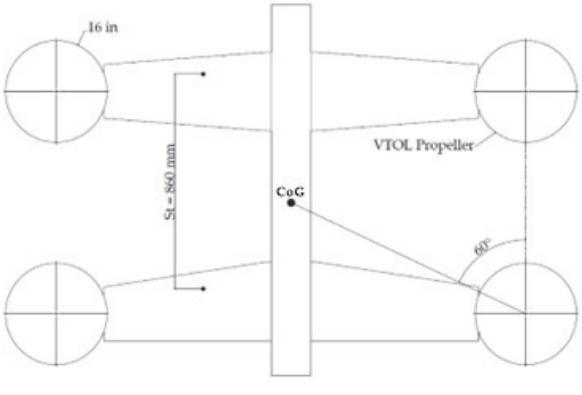

Figure 8. Schematic drawing of the tandem wing configuration.

Figure 9. Three-dimensional model of the VTOL plane with the tandem wing configuration.

2.5.3. Transverse Arm Design

In the transverse arm configuration, there are two horizontal stabilizers, a canard, and a horizontal tailplane. This configuration is also known as a three-surface aircraft. The VTOL motors were to be mounted at the tip of the horizontal stabilizers. The parameters needed to be calculated to make the conversion were the tailplane geometry and the VTOL motors' position. Table 9 shows the results of the tailplane sizing. Figure 10 shows a schematic drawing of the configuration and Figure 11 shows a three-dimensional model.

Table 9. Transverse arm sizing.

Transverse Arm Sizing	
Canard area (S_c)	0.077 m^2
Canard chord (C_c)	0.13 m
Canard span (b_c)	0.59 m
Horizontal tailplane area (S_h)	0.107 m^2
Horizontal tailplane chord (C_h)	0.18 m
Horizontal tailplane span (b_h)	0.59 m
Vertical tailplane area (S_v)	0.021 m^2
Vertical tailplane root chord (Cr_v)	0.13 m
Vertical tailplane tip chord (Ct_v)	0.1 m
Vertical tailplane span (b_v)	0.21 m

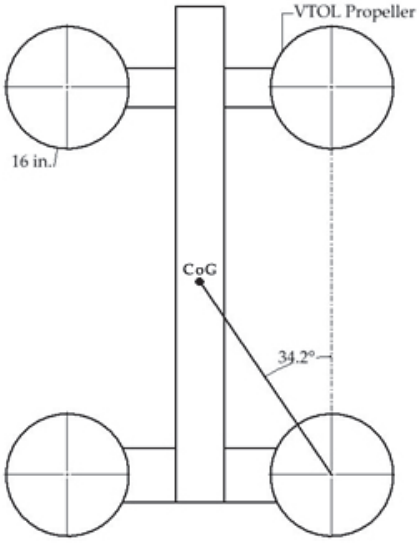

Figure 10. Schematic drawing of the transverse arm configuration.

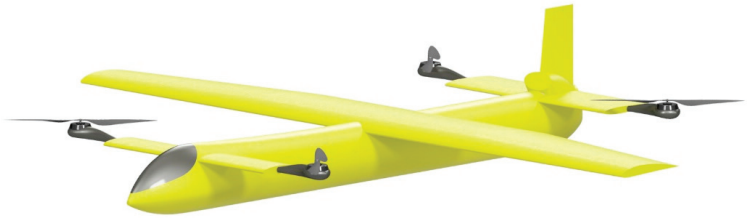

Figure 11. Three-dimensional model of the VTOL lane with a transverse arm configuration.

2.6. CFD Simulation

A CFD simulation was run after all the configurations had been designed to determine the parameters needed to compare the aerodynamic performances of the configurations. The parameters sought were the coefficient of lift (C_L), the coefficient of drag (C_D), the lift-to-drag ratio (L/D), the stall speed, the coefficient of pitch moment (C_p), the coefficient of roll moment (C_r), the coefficient of yaw moment (C_y), and the turn radius (r). the parameters for lift, drag, stall conditions, efficiency, and stability could be obtained using equations provided by [31].

$$C_L = \frac{F_L}{\frac{1}{2} \times \rho \times V^2 \times A} \tag{9}$$

$$C_D = \frac{F_D}{\frac{1}{2} \times \rho \times V^2 \times A} \tag{10}$$

$$C_p = \frac{M_p}{\frac{1}{2} \times \rho \times V^2 \times A \times C} \tag{11}$$

$$C_r = \frac{M_r}{\frac{1}{2} \times \rho \times V^2 \times A \times C} \tag{12}$$

$$C_y = \frac{M_y}{\frac{1}{2} \times \rho \times V^2 \times A \times C} \tag{13}$$

$$L/D = \frac{F_L}{F_D} \tag{14}$$

Parameters for maneuverability could be obtained by parsing the resultant force acting on the aircraft. Figure 12 shows a free-body diagram of the aircraft. Good maneuverability means the aircraft can make a small turning radius without stalling.

$$\sum F = m \times a \tag{15}$$

$$F_L \times \sin\theta = \frac{m \times v^2}{r} \tag{16}$$

$$F_L \times \cos\theta \geq m \times g \tag{17}$$

2.6.1. Simulation Parameters

In this study, various flight conditions were simulated. The sideslip angle variations were 0°, 15°, and 30° to simulate headwind and crosswind conditions. The angle of attack also varied between 0° and 24° with an interval of 4° for the headwind condition, and between 0° and 15° with an interval of 5° for crosswind conditions. The bank angle simulated was varied between 0° and 40° with an interval of 10°. The wind speed was set to 23 m/s (the aircraft's designed cruising speed) and the air density was set to 1.225 kg/m^3.

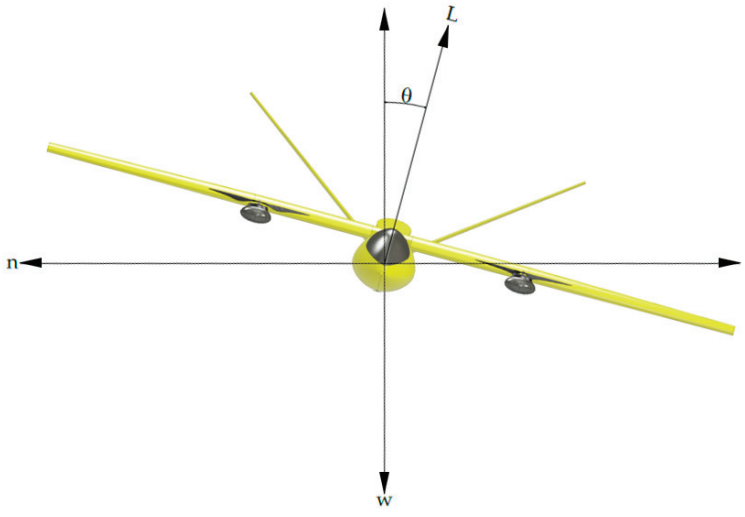

Figure 12. Free-body diagram of the aircraft.

2.6.2. Simulation Setup

In the headwind simulations, the fluid domain of the CFD only used half of the plane to reduce processing time. Unfortunately, the crosswind simulations could not do so because of the asymmetrical airflow direction between the right side and the left side of the aircraft.

After creating the fluid domain model, the next step was to mesh the model. The global mesh size was 0.8 m. To improve accuracy, further mesh sizing was added to the domain, such as a body of influence sizing of the domain with 0.05 m. The body of influence enveloped a small area within the fluid domain, which included the aircraft. A face sizing of 0.005 m was added to the aircraft's faces. For the simulation of the boundary layer and surrounding airflow to be accurate, inflation of an 8e-5 m thick first layer was added.

To validate the mesh quality, the orthogonal quality and skewness were checked. The average value of the orthogonal quality of the mesh was 0.74, and the average value of the skewness was 0.25. The mesh quality was considered acceptable for further simulations [32]. Figures 13–15 shows the results of the mesh.

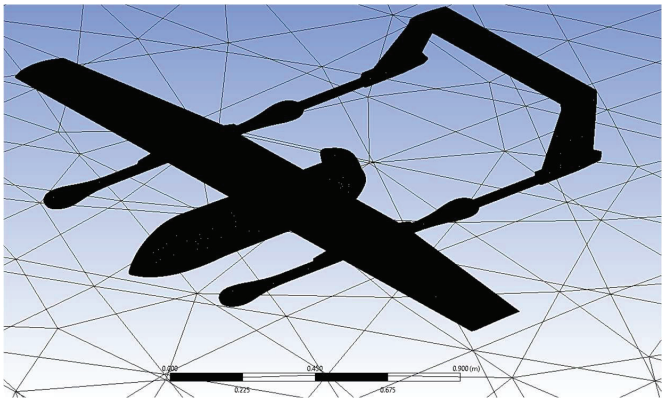

Figure 13. Mesh results visualization.

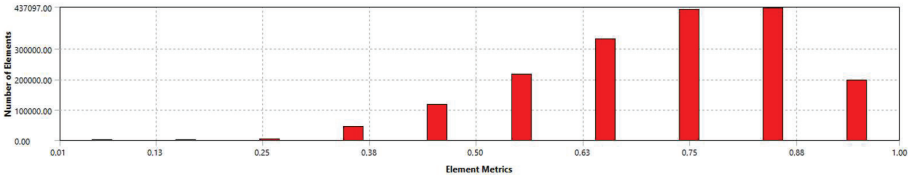

Figure 14. Orthogonal quality distribution.

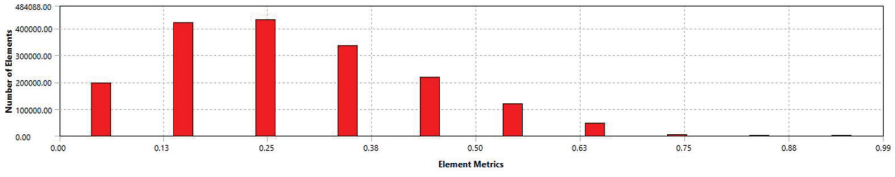

Figure 15. Skewness quality distribution.

A turbulent SST k-Omega was applied in this simulation. This model uses the k-Epsilon model's advantage in simulating free-stream conditions and the k-Omega model's advantage in simulating areas near the wall [33]. As the simulation's Mach number was less than 0.36, the fluid was incompressible, and the simulation was steady-state. The determined convergence criteria were 10^{-3} for all the residuals and the force reports.

3. Results

3.1. Lift, Drag, and Efficiency

This study analyzed the performance of the lift force, drag force, and flight efficiency. The greater the angle of attack, the bigger the lifting force is. However, the drag also increases because the air encounters more surface area as the aircraft pitches up. Figure 16 shows the pressure contour of the VTOL plane at 0° AoA and 16° AoA, which visualizes the lift and drag phenomenon. The bottom of the VTOL plane has greater pressure than the top, which generates lift. The bigger the difference between the pressure at the bottom and the top of the VTOL lane, the bigger the lift being generated, as well as the drag.

Using Equations (9) and (10), the C_L and C_D values for all configurations were obtained. Figure 17 shows the C_L and C_D of all configurations at the simulated angles of attack in headwind conditions. Figure 17a depicts that the C_L increases as the AoA increases, which is consistent with the prediction and the data that the pressure contours in Figure 16 depict. With the same consistency, Figure 17b depicts that the C_D also increases as the AoA increases.

At lower AoA, the twin-tail boom had the highest C_L, while the other three configurations did not differ significantly. However, at AoA higher than 12°, the tandem wing had the highest C_L overall. The twin-tail boom, the quad-plane, and the transverse arm configurations started to lose lifting capabilities after 16° AoA, as could be seen in Figure 17a, where the three configurations' C_L values started to drop. The tandem wing configuration's C_L continued to increase and only started to drop at 20° AoA.

All four configurations' drag did not differ significantly, although the tandem wing configuration had the highest overall C_D, as predicted, due to the extra wing compared to the other configurations. The transverse arm had the second-highest overall C_D because of its extra surface, the canard. Meanwhile, the quad-plane had the lowest C_D overall.

In crosswind conditions, the wing generates less lift than in the headwind condition because one side of the wing does not receive clean air, as the air is already disturbed by the fuselage. Figure 18 depicts the coefficient of lift in crosswind conditions. In crosswind conditions with a sideslip angle of 15°, the coefficients of lift were almost the same at lower AoA. Even so, the phenomenon remained that at lower AoA, the twin-tail boom configuration had the highest C_L than the others, and then after a certain angle the tandem wing generated more lift and the highest C_L value.

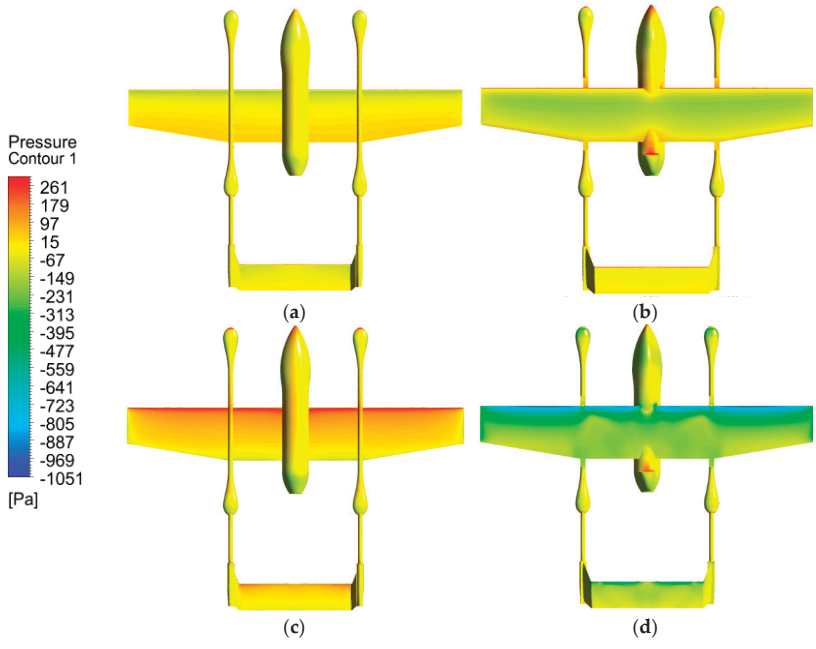

Figure 16. Pressure contours; (**a**) bottom view at 0° AoA, (**b**) top view at 0°AoA, (**c**) bottom view at 16° AoA, and (**d**) top view at 16° AoA.

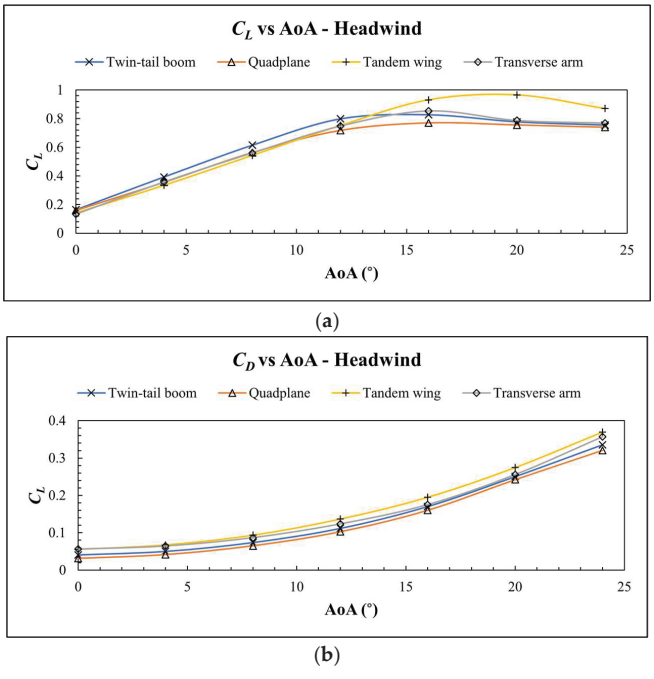

Figure 17. C_L and C_D in headwind conditions; (**a**) C_L vs. AoA, and (**b**) C_D vs. AoA.

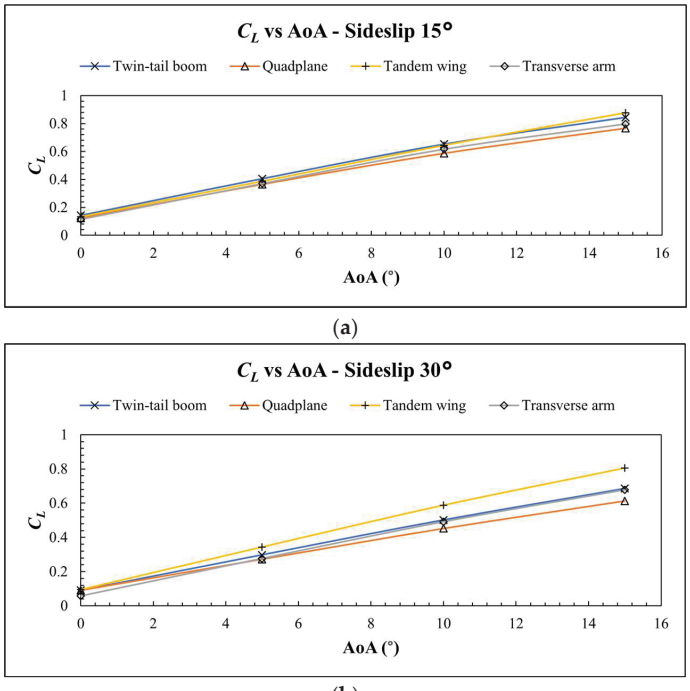

Figure 18. C_L vs. AoA; sideslip angle: (**a**) 15°, and (**b**) 30°.

When the sideslip angle was 30°, the tandem wing had the highest C_L value overall, as predicted, because it had an extra surface on either side of the wing. Meanwhile, data of the twin-tail boom and the transverse arm configuration were almost matching. Overall, the twin-tail boom had better lifting capabilities at lower AoA until the sideslip angle reached 15°. Meanwhile, the tandem wing was better at higher AoA and sideslip angle. The quad-plane configuration was found to be poor in all conditions in terms of lifting capabilities, but it was the better one in drag as it had the lowest C_D value. In contrast, the tandem wing had the highest C_D value because of the two-wing configuration.

As the drag force is directly opposite to the thrust, the propulsion system has to work harder to generate more thrust as the drag increases, causing inefficiency. Using Equation (14), the L/D data could be obtained and used as a parameter to analyze efficiency in the headwind and crosswind conditions. A higher L/D value means higher efficiency. Figure 19 shows the L/D data.

Based on Figure 19a, it was found that the quad-plane configuration had the highest efficiency in the headwind condition between 0° and 10° and then the twin-tail boom was the most efficient from 10° to 16° even though the quad-plane was not far below the twin-tail boom in that AoA range. In contrast, the tandem wing configuration was the most inefficient at low AoA (0°–16°). At AoA higher than 16° though, the tandem wing was the most efficient mostly because of its superior lifting capabilities.

In the crosswind condition with a 15° sideslip angle depicted by Figure 19b, the only difference was that the twin-tail boom configuration was the most efficient. This was caused by the lower drag of the twin-tail boom configuration because the fuselage is shorter than the quad-plane configuration.

At a 30° sideslip angle, the tandem wing was far superior in efficiency because of its far greater lifting capabilities. In contrast, the quad-plane configuration was found to be

the least efficient than the others even though at level flight (0° AoA), every configuration besides the tandem wing had almost the same efficiency.

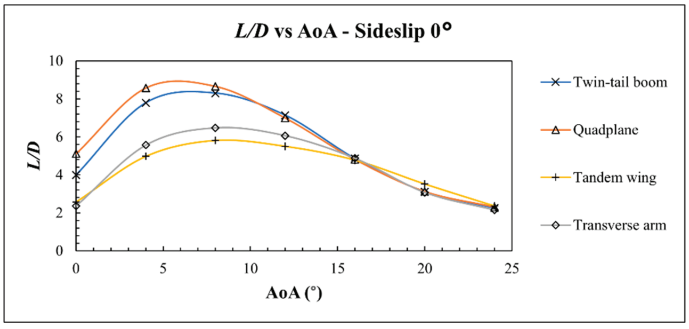

(**a**)

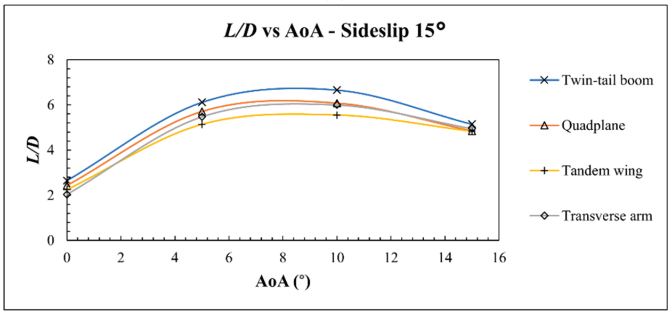

(**b**)

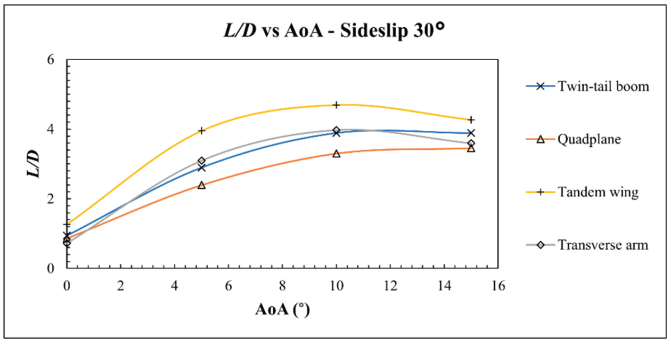

(**c**)

Figure 19. L/D vs. AoA; sideslip angle: (**a**) 0°, (**b**) 15°, and (**c**) 30°.

3.2. Stalling Performance

A stall is the loss of the wing's capabilities to generate lift. It can be visualized as the breakdown of the smooth airflow over the wing, suddenly changing into turbulent airflow. Figure 20 visualizes the stall phenomenon occurring on the twin-tail boom configuration, where it can be seen that the airflow over the wing at 0° AoA is smooth, but at 24°, the airflow does not stick to the wing surface anymore and becomes turbulent and violent.

To understand the stalling performance of each configuration, the critical angle and the stall speed need to be analyzed. The critical angle is an angle of attack at which the VTOL plane generates the greatest amount of lift force. Beyond the critical angle, the C_L value drops, meaning the aircraft has stalled. According to Figure 17a, the twin-tail boom, the quad-plane, and the transverse arm configuration had the same critical angle, which is

16°. The tandem wing configuration had a higher critical angle, 20°, meaning the aircraft could pitch with a greater angle before it stalled.

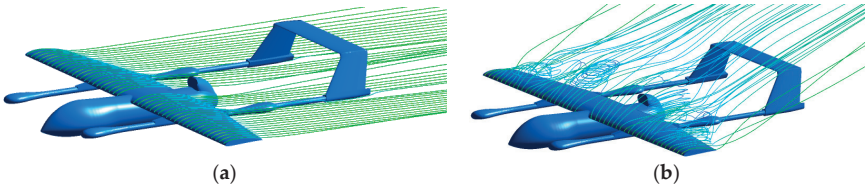

(**a**) (**b**)

Figure 20. The stall phenomenon visualized by the airflow over the wing at (**a**) 0° AoA and (**b**) 24° AoA.

The stall speed refers to the transition of the VTOL plane from hovering mode to forward flight mode. A low stall speed is determined as a good performance. The stall speed data could be necessary for flight controller input or for monitoring the flight. The stall speed value was obtained by using Equation (9), using the weight of the aircraft (98.5 N) as the lift force variable. In doing so, the speed variable is the speed required to support the aircraft's weight. Figure 21 shows the stall speed data in headwind and crosswind conditions.

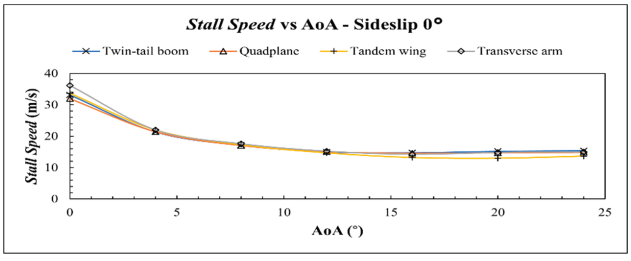

(**a**)

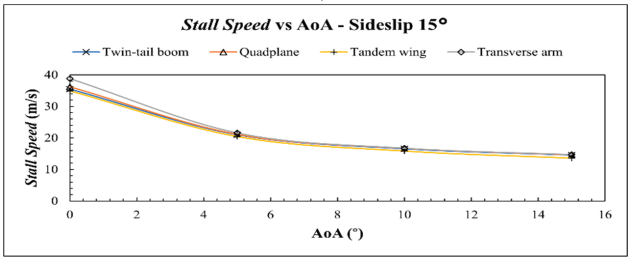

(**b**)

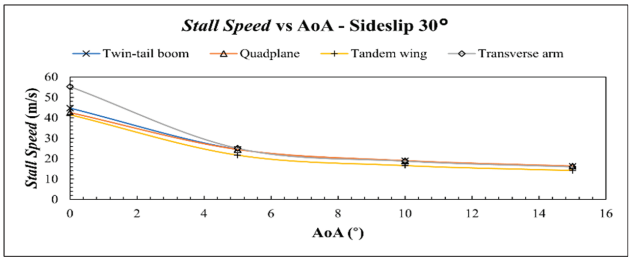

(**c**)

Figure 21. Stall speed vs. AoA; sideslip angle: (**a**) 0°, (**b**) 15°, (**c**) 30°.

In the headwind condition depicted by Figure 21a, it was found that all configurations had fulfilled the stall speed DR&O, which is 15 m/s, at 12° AoA. As the C_L values dropped after the critical angle, the stall speed increased. Besides the tandem wing, all configurations had similar stall speed values at every AoA. The tandem wing performed the best as it had the lowest stall speed, but only at AoA greater than 8°.

Figure 21b shows the stall speed data of the crosswind condition with a 15° sideslip angle. The VTOL plane fulfilled the stall speed DR&O at 15° AoA. The tandem wing outperformed the other configurations, as predicted. Once again, the stall speed value of other configurations did not differ significantly. Although at 0° AoA, the transverse arm differed and had the highest stall speed value overall, meaning this configuration performed the worst.

The tandem wing also performed the best at a 30° sideslip angle as depicted by Figure 21c and had already fulfilled the DR&O at 15° AoA. Meanwhile, the twin-tail boom and the quad-plane configuration were still similar. The transverse arm performed the worst again at 0° AoA as it had a significantly higher stall speed than other configurations.

3.3. Stability Performance

An aircraft has three types of stability: longitudinal, lateral, and directional stability. In this study, longitudinal stability was represented by the coefficient of pitch moment (C_p). In crosswind conditions, the left and right sides of the aircraft have different pressure because of the airflow direction. These differences cause a tendency for an aircraft to roll or yaw, making lateral and directional stability a necessary parameter to analyze to determine each configuration's stability performance. The lateral stability can be determined by analyzing the C_r value, while the directional stability can be determined by analyzing the C_y value. The closer those values are to 0, the better the stability performance is. Having 0 coefficient of moment means the aircraft maintains its position, and is stable and level, without any tendency to pitch, roll, or yaw.

Figure 22 depicts the C_p of all configurations in headwind and crosswind conditions. The quad-plane configuration had a positive C_p value between 0° and 8°, causing the aircraft to pitch up. However, the quad-plane had a zero C_p value, which means the aircraft reached longitudinal stability. The further the C_p value, the worse the stability performance is, requiring the elevator to work harder to counteract the aircraft's tendency to pitch up or down, only to keep the aircraft level. As can be seen in Figure 22a, the tandem wing had the worst performance in longitudinal stability, mainly because its two wings were generating lift far away from the CoG.

The twin-tail boom and the quad-plane configuration performed well in longitudinal stability in crosswind conditions as depicted by Figure 22b,c. However, the quad-plane performed better because the C_p approached zero as the angle of attack became greater. Because the aircraft generates less lift in crosswind conditions, there are more instances where the aircraft must pitch up to generate more lift, which makes the quad-plane the most longitudinally stable. In contrast, the tandem wing continued to perform poorly in longitudinal stability in crosswind conditions.

The tendency of an aircraft to roll and yaw in crosswind conditions is mostly because of the difference in the lift force being generated between one side and the other. The fuselage is also a disturbance for the airflow, causing one side of the wing not to receive clean air. To determine the lateral stability, the C_r values were analyzed. The smaller the C_r value, the more an aircraft can maintain its position on the longitudinal axis in crosswind conditions.

Figure 23 depicts the C_r values of the VTOL plane. Figure 23a shows the 15° sideslip angle condition. It explains that the twin-tail boom and the quad-plane configuration had similar C_r values, although the twin-tail boom slightly outperformed the quad-plane. While the transverse arm performed poorly, the tandem wing had the worst longitudinal stability; as predicted before, the tandem wing configuration had problems in stability and controllability. Figure 23b shows the 30° sideslip angle condition, which does not depict

any significant difference from the 15° sideslip angle condition. The twin-tail boom still outperformed the rest, while the tandem wing was the most unstable longitudinally.

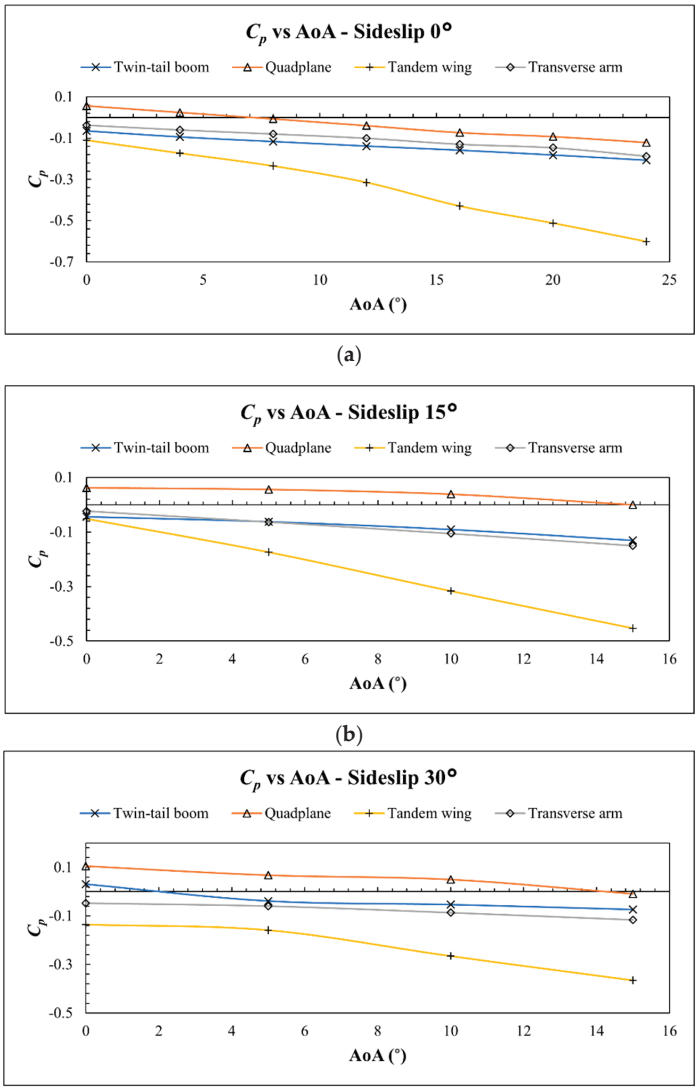

Figure 22. C_p vs. AoA; sideslip angle: (**a**) 0°, (**b**) 15°, and (**c**) 30°.

The ability of an aircraft to retain its position on the vertical (yaw) axis is called lateral directional stability. The configurations' directional stability performance could be determined by analyzing the coefficient of yaw moment (C_y). The closer the C_y is to zero, the more stable the aircraft is on the vertical axis. Figure 24 depicts the C_y values of the VTOL plane. It was found that in crosswind conditions, C_y values generally decreased as the AoA increased. This means that a higher AoA leads to better stability of the aircraft on the vertical axis. The sideslip angle also affected this phenomenon, as depicted in Figure 24; in the 15° sideslip angle, C_y values decreased as the AoA increased, but not significantly. In contrast, C_y values decreased quite significantly as the AoA increased at a 30° sideslip angle.

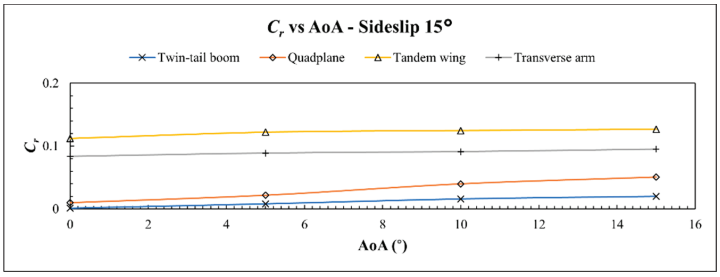

(**a**)

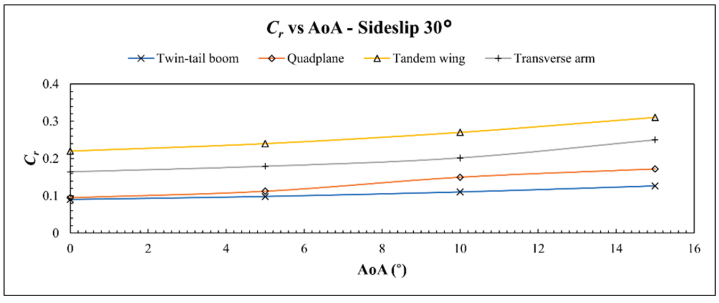

(**b**)

Figure 23. C_r vs. AoA; sideslip angle: (**a**) 15°, and (**b**) 30°.

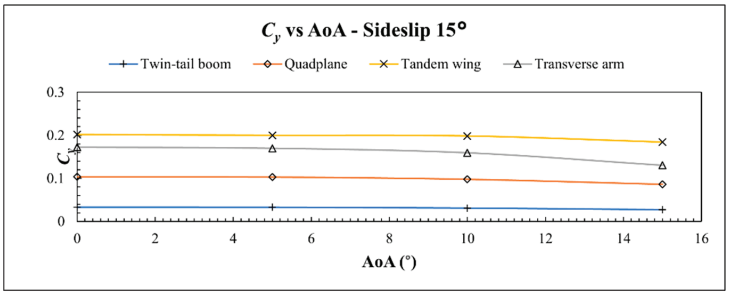

(**a**)

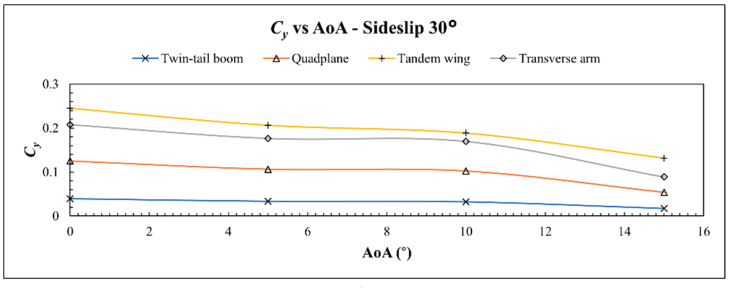

(**b**)

Figure 24. C_y vs. AoA; sideslip angle: (**a**) 15°, and (**b**) 30°.

As depicted by Figure 24a, the twin-tail boom was the most directionally stable in a crosswind condition with a 15° sideslip angle, followed by the quad-plane configuration, although the difference was quite significant, which means that the twin-tail boom was

far superior. The tandem wing was the most unstable configuration, caused by the extra wing. The transverse wing also performed poorly, not far off from the C_y values of the tandem wing. However, at 15° AoA in both 15° and 30° sideslip angles, the transverse arm's C_y values dropped, which means the aircraft became more stable. Nevertheless, it was still outperformed by the twin-tail boom and quad-plane configurations. Figure 24b shows the C_y values in a crosswind condition with a 30° sideslip angle. It further validates that the performance ranking from the most stable to the least was the twin-tail boom, the quad-plane, the transverse arm, and the tandem wing configuration.

After analyzing the coefficients of moment acting on the aircraft on the longitudinal, lateral, and vertical axis and comparing the stability performance, it was determined that the twin-tail boom configuration was the most stable overall in headwind and crosswind conditions. The extra surface of the tandem wing and the transverse arm resulted in a less stable aircraft. However, the transverse arm's extra surface was a stabilizer that granted better control authority and could be used to counteract the aircraft's tendencies to pitch, roll, and yaw. On the other hand, the extra surface on the tandem wing configuration was a lifting surface, and it became a problem for stability and controllability, as predicted.

3.4. Maneuverability Performance

Maneuverability is an aircraft's ability to maneuver. An aircraft with better maneuverability can execute more extreme maneuvers without stalling. Determining good maneuverability can be executed by analyzing the turn radius an aircraft makes. An aircraft turns by moving the aileron in opposite directions on the right and the left side of the wing, generating different lifting forces. The difference in lifting forces banks the aircraft depending on which way the aircraft wants to turn. In this study, the VTOL plane was analyzed at 10°, 20°, 30°, and 40° bank angles.

Before the turn radius was calculated, the ability of the aircraft to turn at the predetermined bank angles must be analyzed. Using Equation (17), the maximum bank angle of the VTOL plane was determined. The maximum bank angle was described as the bank angle at which the aircraft's lifting forces could still fully support the aircraft's weight. If the aircraft's maximum bank angle was more than the predetermined bank angles, the turn radius was calculated using Equation (16).

Figure 25 depicts each configuration's turn radius data in headwind conditions. The twin-tail boom and quad-plane configuration had the tightest turn radius at low AoA. Meanwhile, the tandem wing outperformed both configurations with an AoA greater than 12°. The tandem wing and the transverse arm did not have sufficient lifting force at 4° AoA and 30° bank angle, while the twin-tail boom and the quad-plane already had a sufficient lift in the same condition. The smallest turn radius was 26.5 m, made by the tandem wing configuration at a 40° bank angle and 20° AoA.

Figure 26 depicts the maneuverability performance of the VTOL plane in crosswind conditions. The results in Figure 26a show that at a 15° sideslip angle, the VTOL plane needed to pitch up to 5° AoA to execute the turn at 0°–30° bank angles without stalling. Furthermore, the transverse arm needed to pitch up more to 10° AoA to turn at a 30° bank angle. To turn at a 40° bank angle, the VTOL plane needed a 10° AoA to generate enough lift. The smallest turn radius, 29.2 m, was made by the tandem wing and occurred at a 40° bank angle and a 15° AoA. The transverse arm had poor maneuverability performance in this condition, already stalling at a 30° bank angle and 5° AoA, while the other configurations could turn in the same conditions without stalling.

Figure 26b shows the superiority of the tandem wing further as it could execute 10° and 20° bank angle turns at 5° AoA in crosswind conditions with a 30° sideslip angle without stalling. The other configurations could not complete this feat and needed a 10° AoA to execute a turn at the same bank angle and crosswind conditions. The smallest turn radius at a 30° sideslip angle in crosswind conditions was 31.9 m by the tandem wing at a 40° bank angle and a 15° AoA.

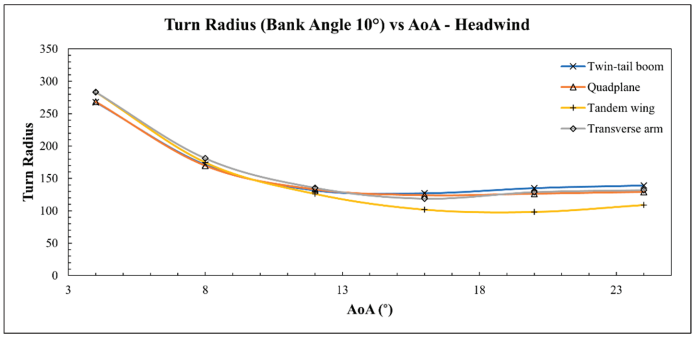

(**a**)

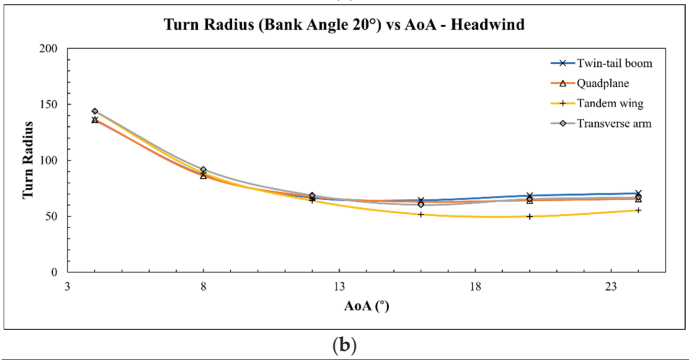

(**b**)

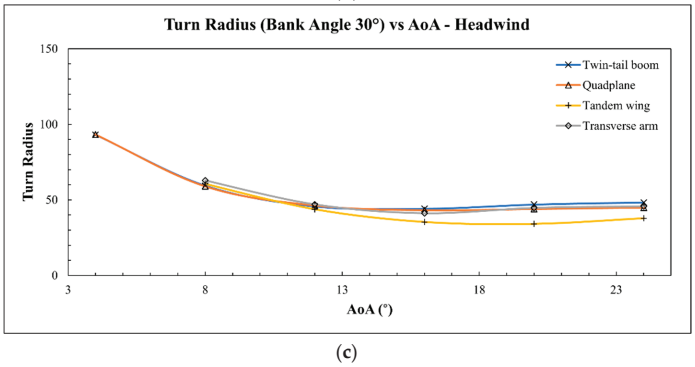

(**c**)

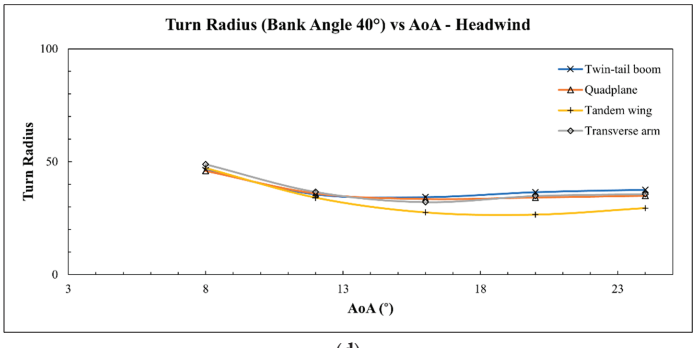

(**d**)

Figure 25. Maneuverability in headwind conditions; bank angles: (**a**) 10°, (**b**) 20°, (**c**) 30°, and (**d**) 40°.

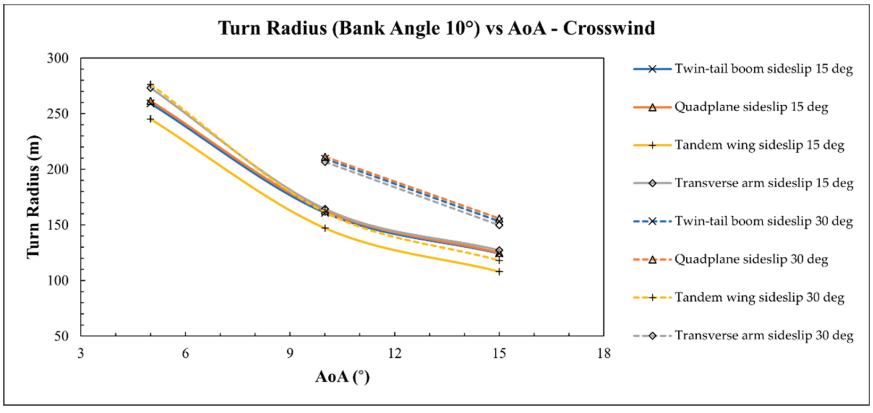

(**a**)

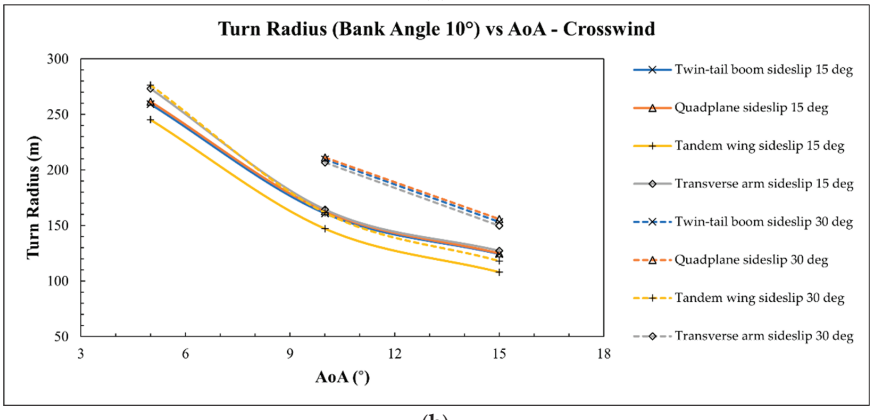

(**b**)

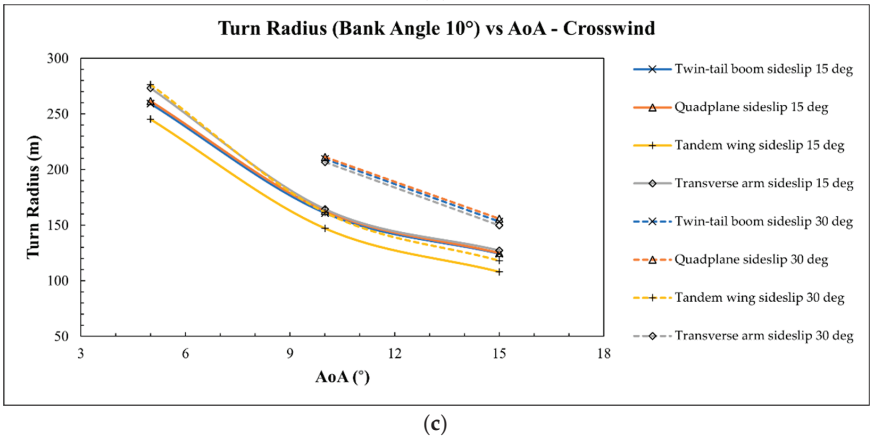

(**c**)

Figure 26. *Cont.*

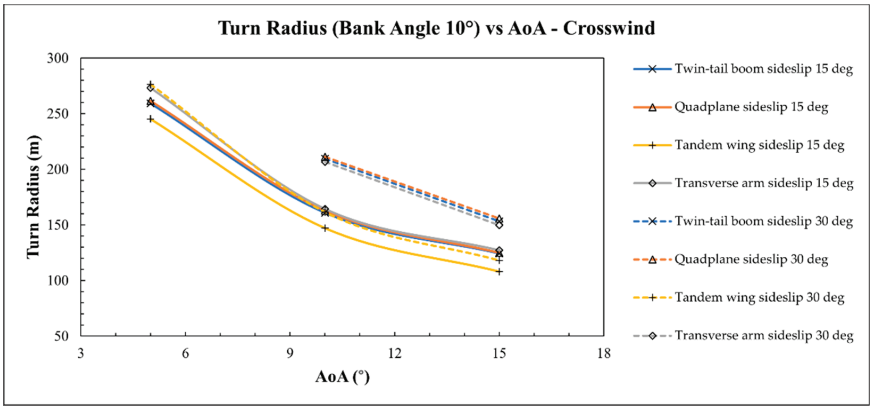

(**d**)

Figure 26. Maneuverability in crosswind conditions; bank angle: (**a**) 10°, (**b**) 20°, (**c**) 30°, and (**d**) 40°.

Overall, the tandem wing was far superior to the other configurations in terms of maneuverability. As could be seen in Figure 26b, at a 30° sideslip angle, where all configurations generated less lift, the tandem wing matched the turn radius of other configurations at the same bank angle but at a 15° sideslip angle. The tandem wing and the quad-plane exhibited good maneuverability performance in headwind conditions at lower AoA but struggled in crosswind conditions. The transverse arm performed poorly in headwind conditions but outperformed the twin-tail boom and the quad-plane in crosswind conditions with a 30° sideslip angle.

4. Discussion

This study compared the aerodynamic performance of a VTOL plane with different VTOL arm configurations. The twin-tail boom had the best lifting performance at lower AoA in headwind and crosswind conditions but was outperformed by the tandem wing at high AoA. Overall, the tandem wing had the best lifting performance due to an extra lifting surface, especially at greater AoA where the hind wing gets clean air, unobstructed by the forewing. That superior lifting performance gave the tandem wing good maneuverability. However, the extra surface generated more drag and caused inefficiency in headwind conditions.

In terms of efficiency, the quad-plane performed the best at low AoA in headwind conditions, as could be seen by the L/D values. The twin-tail boom matched the quad-plane's efficiency starting from 8° AoA. The quad-plane and the twin-tail boom were superior in efficiency because of the streamlined geometry that does not have any extra surfaces as in the transverse arm and the tandem wing. However, in crosswind conditions, the quad-plane, the twin-tail boom, and the transverse arm lost a lot of lift force, so the tandem wing was more efficient due to the extra wing generating high lifting forces capable of overcoming the drag force.

As the stall speed was directly affected by the generated lifting force, the tandem wing had the lowest stall speed. Low stall speed was needed to stabilize the aircraft during the transition from hovering to forward flight and vice versa. The twin-tail boom and the quad-plane matched the tandem wing's stall speed at low AoA in all conditions. The transverse arm had the highest stall speed at 0° AoA, which made it a poor performance as the VTOL plane's wing needs level (0° AoA) to make a smooth and stable transition.

Stability is crucial for every aircraft. The simulation results showed that the quad-plane configuration was the most stable longitudinally in headwind and crosswind conditions, although the twin-tail boom and the transverse arm also did not perform poorly. On the other hand, the tandem wing was the most unstable. Due to the center of gravity being in

between the fore- and hind wings, any difference in lift generated by the two wings could cause major longitudinal stability problems.

The difference between the transverse arm and the tandem wing is the extra surface in the transverse arm configuration is a stabilizer with symmetrical airfoil. Symmetrical airfoil generates less lift than asymmetrical airfoil. Hence, the extra surface of the tandem wing configuration, which is a wing with an asymmetrical airfoil, generates more lift at a distance from the center of gravity, causing stability problems. Moreover, a control surface, namely the elevator, could be used to counter-moment the aircraft and keep the aircraft stable while cruising. Even so, the pitch moment of the tandem wing was bigger to begin with. An elevator needs to generate sufficient moment only to counter it, reducing the pitching authority of the controller.

In crosswind conditions, the twin-tail boom was the most stable. Contrarily, the tandem wing was the most unstable on the lateral and vertical axes. High C_r and C_y meant that the tandem wing tended to roll and yaw extremely because of the crosswind and was unable to maintain its position. Overall, having an extra lifting surface would cause an unstable flight.

Depending on the mission, maneuverability could be important as well, although the fixed-wing VTOL is an unlikely configuration choice for a UAV with a high maneuverability requirement. Analysis of maneuverability is still crucial, though, to understand the designed aircraft's capabilities so that risky flight parameters can be avoided. A too extreme bank angle could end in the aircraft stalling. A banking aircraft also generates less lift than a level one, which means an aircraft would need to pitch up more to generate sufficient lift, adding risks of stalling.

The simulation showed that in headwind conditions and low AoA, the twin tail boom and the quad-plane performed the best. At AoA greater than 10°, the tandem wing outperformed both. The transverse arm had the worst maneuverability in headwind conditions and was the most prone to stalling. In crosswind conditions, the tandem wing was far superior and outperformed the other configurations. Moreover, the transverse arm was better at a 30° sideslip angle than the twin-tail boom and the quad-plane. Overall, the tandem wing had the best maneuverability due to its superior lifting capabilities. The twin-tail boom performed well in a headwind condition but quite poorly in a high sideslip angle crosswind condition.

In general, the twin-tail boom configuration had the most favorable aerodynamic performance. The twin-tail boom had good lifting capabilities at low AoA and low drag overall. The twin-tail boom was also efficient according to its L/D data. Furthermore, even though the tandem wing had extra lifting surface, the twin-tail boom matched the tandem wing's stall speed at low AoA in headwind and crosswind conditions. A VTOL plane rarely needs to pitch up to a big AoA for climbing because the VTOL motors take the aircraft vertically to or nearly to its cruising altitude. As could be seen from the simulation results, the twin-tail boom generally had good aerodynamic performance at low AoA, which made it a suitable arm configuration for a VTOL plane. As such, many VTOL plane UAVs using the twin-tail boom configuration can be found in the public market [7–9] because it is suitable for monitoring missions in the agriculture and forestry fields.

The quad-plane performed slightly worse than the twin-tail boom in lateral and directional stability, but had better efficiency in level flight. As such, the quad-plane is suitable for surveillance missions [6], such as in a military or a search-and-rescue operation, which require longer range but still stable flight. The tandem wing could be chosen for missions that demand extreme maneuverability in exchange for its efficiency and stability. The transverse arm did not perform outstandingly relative to the other configuration. It is not as mature an idea as the others, but it showed promising performance in longitudinal stability. Future revision to and development of the concept is needed to make it feasible for a VTOL-plane design.

5. Conclusions

This study examined four arm configurations for a VTOL plane and compared their aerodynamic performance. A CFD simulation was carried out to obtain the data in headwind and crosswind conditions. The data were used to calculate several parameters, such as the aerodynamic coefficients, moment coefficients, stalling conditions, and maneuverability performance. Upon analyzing the parameters, it was found that the twin-tail boom is the most suitable configuration for a VTOL plane, especially at a low angle of attack. The twin-tail boom has desirable lifting capabilities, efficiency, maneuverability, and stability in crosswind conditions. The quad-plane and the tandem wing are suitable for some specific demanding missions. Meanwhile, the transverse arm still needs further development to be implemented. Each configuration has its own infirmity, which could be increased by proper tuning and control input.

Author Contributions: Conceptualization, G.N.; data curation, Y.D.H.; formal analysis, G.Z.; funding acquisition, G.N.; investigation, G.Z.; methodology, G.N.; project administration, G.Z.; software, Y.D.H.; supervision, G.N. and G.Z.; validation, Y.D.H.; visualization, Y.D.H.; writing—original draft, Y.D.H.; writing—review and editing, G.N. All authors have read and agreed to the published version of the manuscript.

Funding: This research was funded by Penelitan Terapan Unggulan Perguruan Tinggi (PTUPT), grant number: No. 1692/UN1/DITLIT/Dit-Lit/PT.01.03/2022.

Data Availability Statement: Not applicable.

Acknowledgments: The authors would like to thank the Department of Mechanical and Industrial Engineering, Faculty of Engineering, Universitas Gadjah Mada and Penelitian Terapan Unggulan Perguruan Tinggi (PTUPT), Directorate-General of Higher Education, Ministry of Education, Culture, Research, and Technology.

Conflicts of Interest: The authors declare no conflict of interest.

References

1. Miller, C.; Chadwick, S. *Military Unmanned Aerial Vehicles and Diversification Opportunities*; Mississippi Defense Diversification Initiative–Technical Report; United States Department of Defense Office of Economic Adjustment: Arlington, VA, USA, 2018; pp. 4–7. [CrossRef]
2. Banu, T.P.; Borlea, G.F.; Banu, C. The Use of Drones in Forestry. *J. Environ. Sci. Eng. B* **2016**, *5*, 557–562. [CrossRef]
3. Kotlinski, M.; Calkowska, J.K. U-Space and UTM Deployment as an Opportunity for More Complex UAV Operations Including UAV Medical Transport. *Intell. Robot. Syst.* **2022**, *106*, 12. [CrossRef]
4. Sziroczak, D.; Rohacs, D.; Rohacs, J. Review of Using Small UAV Based Meteorological Measurements for Road Weather Management. *Prog. Aerosp. Sci.* **2022**, *134*, 100859. [CrossRef]
5. Filippone, A. *Flight Performance of Fixed and Rotary Wing Aircraft; In Elsevier Aerospace Engineering Series*, 1st ed.; Butterworth-Heinemann: Boston, MA, USA, 2006; ISBN 978-0-7506-6817-0.
6. ViewPro AZH2600V. Available online: https://www.viewproonline.com/products/azh2600v-vtol-drone-vertical-take-off-and-landing-industry-application-uavs-more-than-3-hours-flight-time (accessed on 25 September 2022).
7. ALTI Ascend. Available online: https://www.ssass.co.za/alti-ascend (accessed on 25 September 2022).
8. ALTI Transition. Available online: https://www.ssass.co.za/alti-transition (accessed on 25 September 2022).
9. Foxtech Great Shark 330. Available online: https://www.foxtechfpv.com/foxtech-great-shark-330-vtol.html (accessed on 25 September 2022).
10. Okulski, M.; Ławryńczuk, M. A Small UAV Optimized for Efficient Long-Range and VTOL Missions: An Experimental Tandem-Wing Quadplane Drone. *Appl. Sci.* **2022**, *12*, 7059. [CrossRef]
11. Foxtech Altair 370. Available online: https://www.foxtechfpv.com/foxtech-altair-370-tandem-wing-hybrid-vtol.html (accessed on 25 September 2022).
12. Czyba, R.; Lemanowicz, M.; Gorol, Z.; Kudala, T. Construction Prototyping, Flight Dynamics Modeling, and Aerodynamic Analysis of Hybrid VTOL Unmanned Aircraft. *J. Adv. Transp.* **2018**, *2018*, 7040531. [CrossRef]
13. Min, K.-M.; Chia, F.-Y.; Kim, B.-H. Design and CFD Analysis of A Low-Altitude VTOL UAV. *Int. J. Mech. Prod. Eng. Res. Dev.* **2019**, *9*, 555–562. [CrossRef]
14. Rosid, N.H.; Lukman, E.I.; Fadlillah, M.A.; Moelyadi, M.A. Aerodynamic Characteristics of Tube-Launched Tandem Wing Unmanned Aerial Vehicle. *J. Phys. Conf. Ser.* **2018**, *1005*, 012015. [CrossRef]

15. Gigacz, R.; Mohamed, A.; Poksawat, P.; Panta, A.; Watkins, S. Exploring Tandem Wing UAS Designs for Operation in Turbulent Urban Environments. *Int. J. Micro Air Veh.* **2018**, *10*, 254–261. [CrossRef]
16. Brinkworth, B.J. On the Aerodynamics of the Miles Libellula Tandem-Wing Aircraft Concept, 1941–1947. *J. Aeronaut. Hist.* **2016**, *2*, 10–58.
17. Austin, R. *Unmanned Aircraft Systems: UAVs Design, Development and Deployment; In AIAA Education Series*, 1st ed.; American Institute of Aeronautics and Astronautics; Wiley: Reston, VA, USA; Chichester, UK, 2010; ISBN 978-1-60086-759-0.
18. Roskam, J. *Airplane Design Part I: Preliminary Sizing of Airplanes*, 1st ed.; DARcorporation: Lawrence, KS, USA, 1986; ISBN 978-1-884885-42-6.
19. Roskam, J.; Lan, C.-T.E. *Airplane Aerodynamics and Performance*, 1st ed.; DARcorporation: Lawrence, KS, USA, 1997; ISBN 978-1-884885-44-0.
20. Raymer, D.P. *Aircraft Design: A Conceptual Approach; In AIAA Education Series*, 6th ed.; American Institute of Aeronautics and Astronautics, Inc.: Reston, VA, USA, 2018; ISBN 978-1-62410-490-9.
21. Sadraey, M.H. *Aircraft Design: A Systems Engineering Approach; In Aerospace Series*, 1st ed.; Wiley: Chichester, West Sussex, UK, 2013; ISBN 978-1-119-95340-1.
22. Anderson, J.D. *Aircraft Performance and Design*, 1st ed.; WCB/McGraw-Hill: Boston, MA, USA, 1999; ISBN 978-0-07-001971-3.
23. Van Nguyen, N.; Tyan, M.; Lee, J.W.; Kim, S. Investigations on Stability and Control Characteristics of a CS-VLA Certified Aircraft Using Wind Tunnel Test Data. *Proc. Inst. Mech. Eng. Part G J. Aerosp. Eng.* **2016**, *230*, 2728–2743. [CrossRef]
24. Popowski, S.; Dąbrowski, W. Measurement and Estimation of the Angle of Attack and the Angle of Sideslip. *Aviation* **2015**, *19*, 19–24. [CrossRef]
25. Yu, S.; Kwon, Y. Development of VTOL Drone for Stable Transit Flight. *J. Comput. Commun.* **2017**, *05*, 36–43. [CrossRef]
26. Civil Aviation Safety Regulation (CASR) Part 107. Available online: https://terra-drone.co.id/wp-content/uploads/2020/04/CASR-Part-107.pdf (accessed on 13 September 2022).
27. Heitmeyer, J.C. *Effect of Vertical Position of the Wing on the Aerodynamic Characteristics of Three Wing-Body Combinations*; Research Memorandum, National Advisory Committee for Aeronautics: Washington, DC, USA, 1953.
28. Musa, N.A.; Mansor, S.; Ali, A.; Omar, W.Z.W.; Latif, A.A.; Perumal, K. Effects of Aircraft Tail Configurations on Sensitivity to Yaw Disturbances. *Appl. Mech. Mater.* **2014**, *629*, 197–201. [CrossRef]
29. Minardo, A. The Tandem Wing: Theory, Experiments and Practical Realisations. Master's Thesis, Politecnico DI Milano, Milan, Italy, 2014.
30. Cheng, H.; Wang, H. Prediction of Lift Coefficient for Tandem Wing Configuration or Multiple-Lifting-Surface System Using Prandtl's Lifting-Line Theory. *Int. J. Aerosp. Eng.* **2018**, *2018*, 3104902. [CrossRef]
31. Clancy, L.J. *Aerodynamics*, 1st ed.; Wiley: New York, NY, USA, 1975; ISBN 978-0-470-15837-1.
32. Mesh Quality & Advance Topics 2022. Available online: https://featips.com/wp-content/uploads/2021/05/Mesh-Intro_16.0_L07_Mesh_Quality_and_Advanced_Topics.pdf (accessed on 18 October 2022).
33. ANSYS Inc. *ANSYS Fluent User's Guide*; Release 19.2; ANSYS Inc.: Canonsburg, PA, USA, 2018.

materials

MDPI

Article

Efficiency Decreases in a Laminated Solar Cell Developed for a UAV

Krzysztof Mateja [1,2,*], Wojciech Skarka [1,2] and Aleksandra Drygała [3]

[1] Department of Fundamentals of Machinery Design, Silesian University of Technology, Stanisława Konarskiego 18A, 44-100 Gliwice, Poland
[2] SkyTech eLab LLC, Stanisława Konarskiego 18C, 44-100 Gliwice, Poland
[3] Department of Engineering Materials and Biomaterials, Silesian University of Technology, Stanisława Konarskiego 18A, 44-100 Gliwice, Poland
* Correspondence: krzysztof.mateja@polsl.pl

Abstract: Achieving energy autonomy in a UAV (unmanned aerial vehicle) is an important direction for aerospace research. Long endurance flights allow for continuous observations, taking of measurements and control of selected parameters. To provide continuous flight, a UAV must be able to harvest energy externally. The most popular method to achieve this is the use of solar cells on the wings and structure of the UAV. Flexible solar cells mounted on the surface of the wings can be damaged and contaminated. To prevent these negative changes, it is necessary to apply a protective coating to the solar cells. One of the more promising methods is lamination. To properly carry out this process, some parameters have to be appropriately adjusted. The appropriate selection of temperature and feed speed in the laminator allows a PV (photovoltaic) panel to be coated with film, minimizing any defects in the structure. Covering PV panels with film reduces the performance of the solar cells. By measuring the current–voltage characteristics, data were obtained showing the change in the performance of solar cells before and after lamination. In the case of testing flexible PV panels, the efficiency decreased from 24.29 to 23.33%. This informed the selection of the appropriate number of solar cells for the UAV, considering the losses caused by the lamination process.

Keywords: renewable energy; flexible solar cell; lamination; energy harvesting; UAV power supply system

Citation: Mateja, K.; Skarka, W.; Drygała, A. Efficiency Decreases in a Laminated Solar Cell Developed for a UAV. *Materials* **2022**, *15*, 8774. https://doi.org/10.3390/ma15248774

Academic Editors: Andrzej Łukaszewicz, Wojciech Giernacki, Zbigniew Kulesza, Jaroslaw Pytka and Andriy Holovatyy

Received: 29 September 2022
Accepted: 6 December 2022
Published: 8 December 2022

Publisher's Note: MDPI stays neutral with regard to jurisdictional claims in published maps and institutional affiliations.

1. Introduction

External energy harvesting allows for standalone power supply systems to extend their working time and even achieve full energy autonomy [1–3]. PV (photovoltaic) panels allow electricity to be obtained from solar energy, and surplus energy can be stored in batteries [4,5]. The use of such systems is gaining more and more popularity in the electromobility industry in use, among others, in charging stations for electric cars, and in aviation as an element of the wings or other parts of the vehicle structure. In the case of UAVs (unmanned aerial vehicles), the operation of a solar cell under the conditions in which it will be operated should be verified [2]. Currently, UAVs are used for, amongst other functions, distributing shipments, mapping, surveillance, and monitoring of borders and crops [6,7]. The biggest research area associated with UAVs is increasing flight duration without unnecessary landing. For this purpose, systems should be developed to increase flight duration, optimize the system in terms of weight and provide functionality in all weather conditions. Obtaining external energy allows for energy autonomy; however, it is closely related to the location and time of flight [8]. The use of solar cells allows for an increase in flight duration, but it also has numerous limitations that have to be taken into account during the design of power supply systems [9–11].

The sun is the largest source of free energy on Earth. Solar energy is a renewable, pollution-free, sustainable, and inexhaustible resource. A solar cell is a device that converts solar energy into electricity through the photovoltaic effect. The most-used material for

solar cells is silicon. Other materials used for the construction of photovoltaic cells are gallium arsenide, cadmium telluride, and copper indium gallium selenide. However, these technologies are restricted by resource scarcity. The highest efficiency is provided by GaAs solar cells, but these cost as much as ten times more than silicon-based devices [7,12,13]. Although different solar cell types on the market exist, very few are applied to UAVs due to their energy conversion efficiency, cost considerations, environmental compliance, weight, and flexibility.

Standard silicon solar cells are brittle and breakable, so this type is not suitable for UAVs [14,15]. In the case of aircraft, solar cells must be able to distort due to the numerous curvatures of the wing surfaces and also due to the stresses that occur on the UAV during flight [16–18]. Solar cells used in aviation and space applications should be flexible to better conform to the surface of the wings, tail, and hull [8,19,20].

Currently, solar cells convert most of the visible light spectrum and about half of the ultraviolet and infrared light spectrum to usable energy. The efficiency of a solar cell is a measure of its performance in converting sunlight into electricity [21]. The electrical properties of solar cells are determined from measured current–voltage (I–V) characteristics and power–voltage (P–V) characteristics.

The energy conversion is driven by the absorption of light (photon) energy, producing electron–hole pairs in a semiconductor and charge carrier separation. A p–n junction is used for charge carrier separation. For photovoltaic devices, reflection and transmission are typically considered loss mechanisms, as photons that are not absorbed do not generate power. To protect solar cells from external conditions, thin films that are resistant to mechanical damage are used [20]. Solar panel lamination is one of the processes crucial to ensuring a long lifespan, but it does affect the amount of light entering the device. In this work, the influence of a protective film application on optical properties was investigated via spectrophotometer. A spectrophotometer allows for the observation of changes in the range of UV, visible, and infrared light transmitted, and to analyze if within these ranges the characteristics of the tested samples are constant or variable [22].

Each protective layer on a solar cell's surface together with the effects of ambient temperature and irradiation variations cause the parameters of PV panels to change [23–26]. To perform tests on solar cells, it is necessary not only to measure the current–voltage and power–voltage characteristics for different irradiation and temperatures of the solar cell, but also to check the solar cell structure and protective layers on its surface [27,28].

During the lamination process, the microstructure of the solar cell may experience changes [29]. Microfractures can be caused by environmental conditions such as thermal cycling and humidity. Another cause of micro-cracks are mechanical stresses. This kind of damage can be caused by choosing incorrect parameters for the lamination process, e.g., by using too much pressure. Micro-cracking causes a reduction in output power resulting in deterioration of the efficiency of the solar cell.

To strengthen solar cells and prevent mechanical damage, various protective coatings are used on their upper surface: films, resins, and composite materials. This process is also intended to improve the aerodynamics of the UAV. The coating protection extends the service life of the system. It allows for quick cleaning of PV panels and also prevents the ingress of moisture and dust into the system. The process of mounting solar cells on the wing can be divided into several types of technology [20] using the following methods:

- Adhering to an existing wing—this method is good for retrofitting an existing UAV. Aerodynamics are normally not affected as modules are extremely thin. The biggest advantage of this solution is it allows the possibility of replacing PV cells in the event of damage. Wiring between modules is time-consuming with large wings, as strings of solar cells run from root to tip. The biggest disadvantage of this solution is the sealing of the gap between two modules [20,30].
- Placed into a mold—the challenge is to fix the modules in their exact position and to ensure no resin leaks onto the front of the module. The advantage of this solution is the wiring, which is easy to arrange. The effects of PV modules on aerodynamics are

largely eliminated but modules cannot be swapped in case of damage. One variation of this method is to place solar cells inside the wing structure with a transparent coating, e.g., transparent film. This technology is mainly practiced within hobby modeling circles and the production process can be seen on models that are often developed by enthusiasts, e.g., on YouTube channels. Due to the labor-intensive nature of this method and the impossibility of replacing damaged elements, it is rarely used in commercial UAVs.

- As the wing surface—lightweight solar modules need more ribs; more sturdy solar modules need fewer ribs but have more weight. The wiring arrangements are easy in this solution [31–34].

This article details aspects of the development of a solar-powered UAV which is designed to be able to fly in the stratosphere—TwinStratos (TS) UAV [35–37]. The goal of this research was to obtain an understanding of the laminated solar cells used in the first, smaller prototype of TS (Figure 1). Decreases in efficiency and changes in the parameters of solar cells can affect energy produced by the system. For the purposes of this experiment, the UAV was equipped with SunPower Maxeon Ne3 solar cells, which are flexible and allow for adaptation to curved surfaces. The manufacturer of the SunPower Maxeon Ne3 cells ensured efficiency at a level of 24.3% [38]. Data received from a test stand allowed us to calculate if the number of solar cells assumed in the initial assumption was able to perform the assumed flight mission. Data obtained in the test allowed the development of a simulation model for a power supply system of the envisioned solar-powered UAV. In previous works, this integrated design approach based on model-based system engineering developed by the project team was applied to the design and testing of ultra-efficient racing vehicles [39], automated guided vehicles (AGVs) [40], as well as for the design of general aviation class aircraft [41].

Figure 1. The first prototype of TwinStratos.

2. Materials and Methods

2.1. Lamination Process

In this study, we decided to laminate solar cells and glue PV panels to the UAV's wings. This method of mounting was chosen due to the fact it allowed application onto an existing aircraft. The second reason was related to the proof-of-concept stage of the UAV being developed. If there were any changes needed, these could be made relatively easily.

Solar cell lamination has two purposes:

- Improving the aerodynamics of the wing with elimination of sharp edges;
- Protection against scratching of the solar cell, action of chemicals, and harmful effects of weather conditions.

A disadvantage of lamination is the reduction in efficiency of solar cells in relation to the efficiency of uncovered solar cells. The test plan relating to lamination has been divided into individual stages:

1. Testing of films of various thicknesses involving local damage to samples and then checking their reaction to external forces. This study enables the selection of a suitable film ultimately used in the UAV.

2. Examination of the selected film with a spectrophotometer to find out its characteristics of reflection, absorption, and transmission.
3. Covering the solar cell with the selected film. During lamination of the solar cells, an important aspect is the selection of appropriate process parameters.
4. Testing the current–voltage characteristics of solar cells before and after the lamination process.

2.2. Film for Lamination

There are a few types of film with different thicknesses that can be used as protective surfaces for solar cells. In aerospace, one of the most widely used encapsulating materials is EVA (ethylene–vinyl acetate) [42]. The advantages of this material are high transmission and resistance to UV radiation [43]. The disadvantage in the case of EVA is the method required in the lamination process. To provide a smooth connection between the film and the solar cell, it is necessary to use a vacuum, ensuring that no air or humidity will be in contact with the solar cells. This requires advanced equipment that increases the cost of making the prototype of the UAV.

Another kind of film that can be used for solar cell lamination is PVC (polyvinyl chloride) film. PVC and EVA are similar materials. EVA is more flexible, lighter, and stronger than PVC, but the advantage of PVC is its ease of application to the solar cell. In this case, use of vacuum is not necessary. The time needed to prepare PVC-laminated solar cells is shorter than in the case of EVA.

For our prototype solution, we decided to use PVC film due to the simplicity of its application to the solar cell's surface. The films tested ranged from 60 to 250 microns in thickness. The inner side of the film is covered with glue, allowing adhesion to the laminated elements. The thinnest films were characterized by high flexibility but low mechanical strength, thick films the inverse. To select the appropriate film thickness, we decided to conduct several tests to check the strength of the films. Films were tested primarily in terms of their actual application and the typical working conditions. For this reason, at this stage of the work, no research was carried out with the use of advanced equipment, but only with the use of simple tools—knives, drills, needles, and files. Prepared damages are the most common defect that can occur during UAV flight operations. The performed tests were to show whether the damage caused by the system would allow further operation of the UAV or not. A visual method was used to check for defects appearing after film failure.

Tests have been carried out on laminated films. A laminator was used to prepare the samples. For lamination, we used a Laminator OPUS ProfiLAM (OPUS, Gliwice, Poland) A3. For the PVC film method of solar cell lamination, it was found that during the welding of the film, the guide rollers removed air just before the lamination process. With such a laminating process, there was no need to control the pressure to facilitate getting rid of air bubbles. The preparation of samples for testing began with laminating paper as a precursor to laminating solar cells. Due to its hygroscopicity, the paper allowed the adhesive to be absorbed, thanks to which no stains or air bubbles were formed. The use of paper additionally allowed us to obtain a rigid surface like the surface of a laminated solar cell. In the case of double lamination (film–paper–film), the second layer of film additionally stiffened the whole, making the sample similar to the structure of the UAV's laminate surface.

2.3. Initial Film Thickness Tests

In the case of testing the mechanical strength of the film against damage in real conditions, three tests were carried out. The first test consisted of cutting the film lengthwise and then bending it. The purpose of the test was to show the reaction of the longitudinally torn film to the stress on the wing of the UAV. Defects of this type may appear in the case of incorrect performance during manufacturing. The second test consisted of creating spot damage to the film and then checking whether the defect due to bends would enlarge. The

purpose of this test was to present an example of films being damaged in flight. The final test tested damage to the edges of the film and then analyzed how stresses and external forces affected this damage. This test was similar to the second test, but the film was damaged at the end of the sample. This type of damage may occur when the film is detached from the UAV structure.

Every test was conducted several times on each film type with the number of bends to the film occurring around a dozen repetitions. This number of repetitions made it possible to observe changes in the structure of the samples. In the case where changes were not noticeable, the test time and/or a change of method of loading the samples using stretching and bending along other axes were added.

The incision test followed by the bend test yielded the observations in Table 1. Figure 2 presents the results of the incision test.

Table 1. Incision test results.

Film Thickness (μm)	Effect
≤100	The incision damaged the inner side of the film. Due to the high flexibility of the film, the incision did not enlarge.
125–200	The incision damaged the inside of the film, enlarging the gap due to prolonged bending.
≥250	The incision did not damage the inner side of the film. However, due to bending, the gap burst.

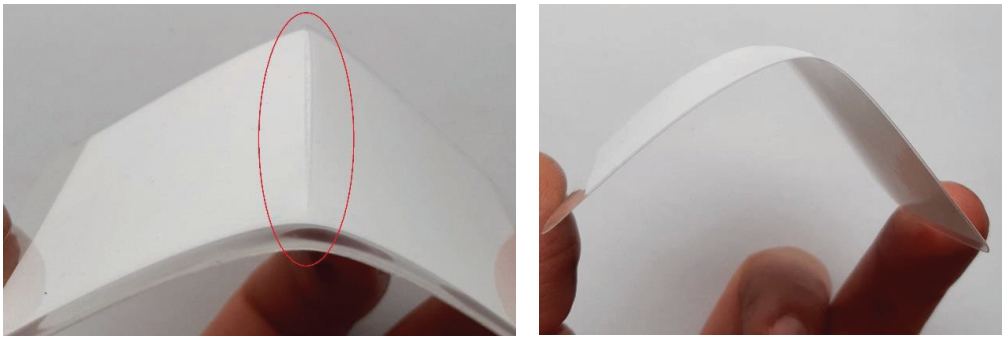

(**a**) (**b**)

Figure 2. Samples tests: (**a**) incision test of a film with a thickness of 250 μm with a burst gap; (**b**) incision test of a film with a thickness of 100 μm, which does not enlarge the damage.

In the second test, related to spot damage, all film thickness did not show any enlargement of defects, even under the influence of prolonged stresses as a result of bending or applying tensile stress.

The third test, related to end damage to the film, showed the effects listed in Table 2.

Table 2. End damage results.

Film Thickness (μm)	Effect
<100	In the case of thin film, the defect easily increased due to its delicate surface.
100–200	In the case of the intermediate films, the defect increased, but more slowly than in the case of thin and thick films.
≥250	In the case of thick films, the defect increased easily due to their greater brittleness/fragility.

Thinner films allow flexibility over a low radius equal to a few centimeters. This feature of thin films allows for their use on small UAV elements such as hulls, ailerons, and flaps. Thick films do not allow the same flexibility over a low radius as thin films do, but they are more durable. Thick films provide higher resistance to mechanical damage. However, the thicker film, the lower the efficiency of the solar cells. Thicker films are heavier than thinner films, which is another point in favor of using the thinnest possible film.

After the lamination process, solar cells are soldered. Soldered joints stiffen the PV panel, increasing its brittleness. Analyzing the research carried out on possible damage of laminated solar cells during the flight of the test UAV and its response to defects, it was decided that the thinnest film that could be used was a film with a thickness of 100 μm.

2.4. Parameters of the Lamination Process

While testing the film samples, the parameters of the lamination process were of less importance due to the use of absorbent paper, to which the film adhered easily. In the case of solar cells, these parameters are more important due to the non-absorptive nature of solar cells. The parameters that played the greatest role in an optimized process were temperature and speed of lamination.

An optimized lamination process should create a smooth texture on the surface of the solar cell without visible defects (Figure 3a). The laminator used allowed 9 lamination speeds, allowing a feed rate from 200 to 1800 mm/min with increments of 200 mm/min for each speed. High feed rates (lamination speed) caused the film to peel off the solar cell. A second disadvantage of high feed rates was the formation of adhesive stains on the solarcell's surface (Figure 3b). Feed rates over 1400 mm/min produced these defects.

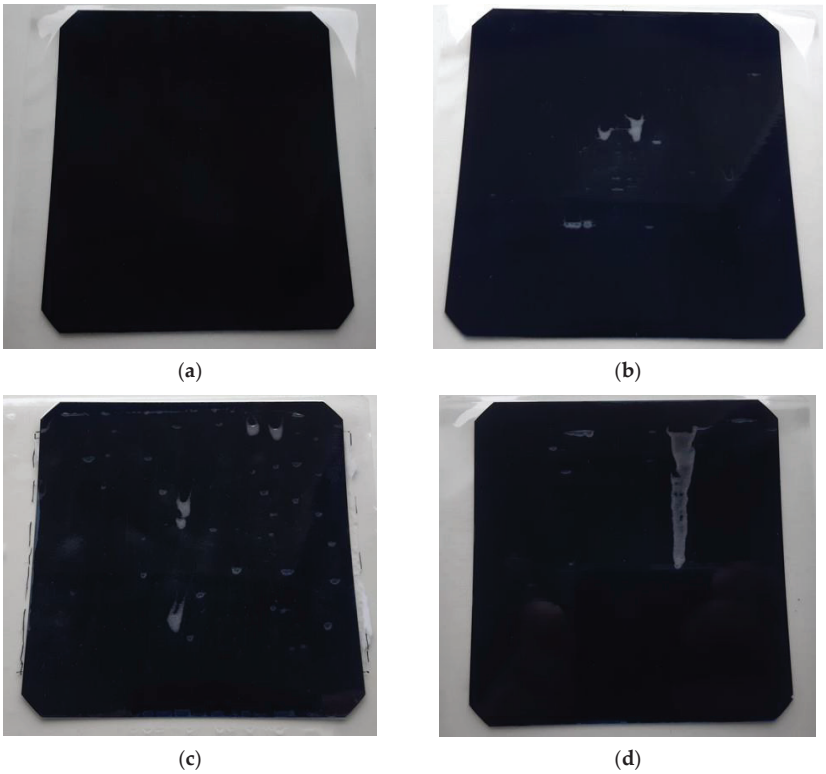

(**a**) (**b**)

(**c**) (**d**)

Figure 3. Laminated solar cells: (**a**) without defects; (**b**) adhesive stains on the surface caused by too fast feed; (**c**,**d**) damp patches from the adhesive caused by too low temperature of lamination.

Another variable parameter was the temperature of lamination. The temperature range of the lamination process was between 70–140 °C. Low temperatures caused ineffective lamination, characterized by the formation of damp patches from the adhesive (Figure 3c,d).

Feed rates of 800–1000 mm/min and temperatures in the range of 90–105 °C produced optimal results.

The selection of the appropriate lamination process parameters made it possible to obtain a homogeneous PV panel surface free from flaws. Prepared samples were subjected to tests that examined their electrical properties before and after lamination.

Parallel to the lamination of the chosen solar cells, a different type of flexible solar cells was also laminated. For each type, the optimal parameters of temperature and lamination speed determined for that type were used.

3. Test Stands

3.1. Test Stand for Collecting the Characteristics of Transmission, Absorption, and Reflection

During the research, we used an Evolution 220 spectrophotometer (Thermo Fisher Scientific, Waltham, MA, USA) to measure the characteristics of transmission, absorption, and reflection of the film. The spectrophotometer allowed for the determination of the characteristics in wavelengths ranging from 190 to 1100 nm.

3.2. Microscale Characterization Method

To obtain images of the monocrystalline surface topography of solar cells we used a scanning electron microscope (SEM). Images were obtained using a Supra 35 (Zeiss, Thornwood, NY, USA) SEM using an acceleration voltage of 10 kV. The secondary electron (in-lens) detector was used to obtain images of the surface topography.

3.3. Test Stand for Collecting Current–Voltage Characteristics of a Solar Cell

The test stand (Figure 4a) for measuring the current–voltage characteristics of solar cells allowed measurements to be obtained for the tested solar cells for STC (standard test conditions)—irradiated with a power of 1000 W/m^2 at a temperature of 25 °C, and Air mass 1.5 spectrum (AM 1.5) defined by European standard IEC 60904-3 [44]. This system for I-V characteristic measurements of solar cells meets all the requirements of the IEC 60904-1 standard [45].

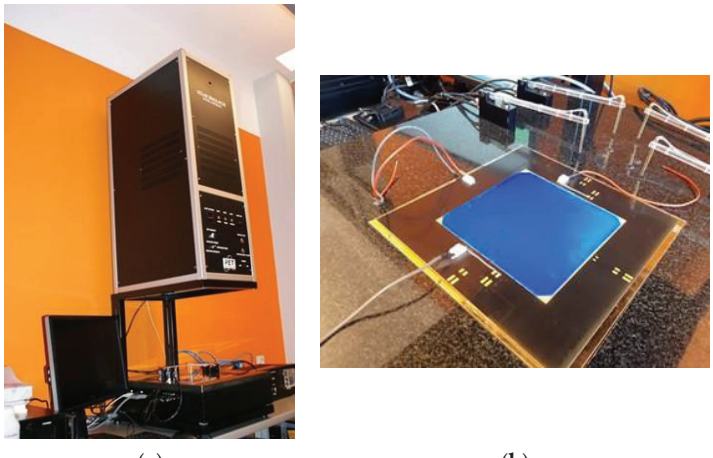

(**a**) (**b**)

Figure 4. Test stand: (**a**) solar simulator with a xenon flash lamp, measuring table, and computer for downloading current–voltage characteristics; (**b**) research conducted on flexible solar cells placed on the measuring table.

The device consists of a light source in the form of a xenon flash lamp with a power of 1430 watts. After passing through the filter ("Air Mass Filter") and the optical system, it uniformly illuminates the measuring table (Figure 4b).

4. Results and Discussion

4.1. Transmission, Absorption, and Reflection of the Film

The characteristics of absorption, reflection, and transmission are presented in Figure 5b–d for both films before and after the lamination stage were tested. The SunPower Maxeon Ne3 datasheet contains the spectral response of solar cells [38], which is presented in Figure 5a. The spectral response is the ratio of current generated by the solar cell to the power incident on the solar cell [46]. These characteristics make it possible to observe changes in the spectral response depending on the wavelength. When analyzing the graphs, the main observations were made of the wavelength range and places where the changes in characteristics occurred. In terms of the solar energy supplied to solar cells, the changes in the UV and infrared range are not as significant as in the visible light range.

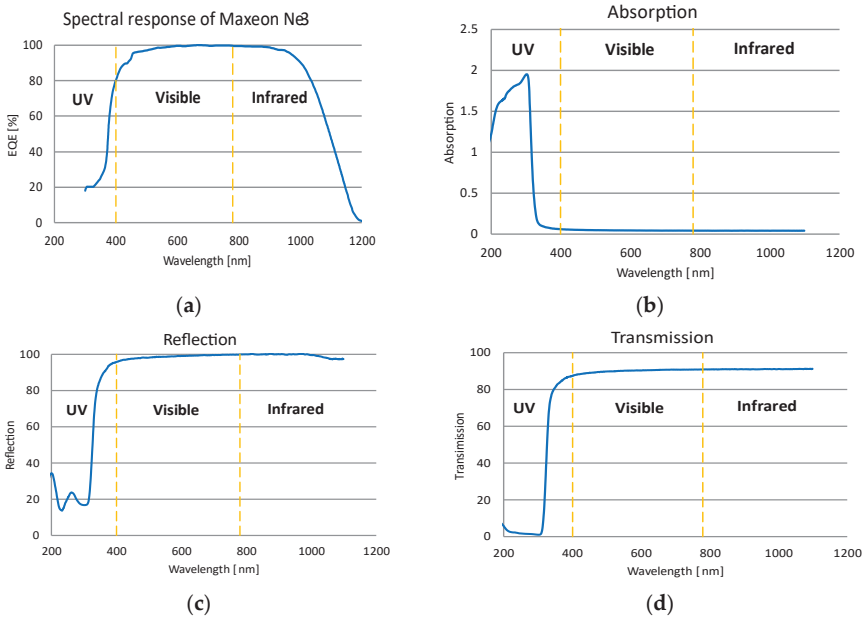

Figure 5. Characteristics of: (**a**) spectral response of Maxeon Ne3; (**b**) 100 μm film absorption; (**c**) 100 μm film reflection; (**d**) 100 μm film transmission.

There are some changes in the UV wavelength range for transmission, absorption, and reflection. From a value of about 300 nm, the characteristics stabilize at one level over the entire range of visible light up to a final value of 1100 nm. The research carried out on laminated film elucidated changes in reflection, absorption, and transmission in the visible light range. A uniform value of the characteristics in the range from 300 to 780 nm demonstrates that the parameters of the solar cell in the visible light range will be constant. This information allows the conclusion to be made that the system will operate with similar performance across the entire range of visible light.

4.2. Microscopic Scale Observations of the Solar Cell

Figure 6 shows the surface topography of a monocrystalline silicon solar cell. It was observed that there are randomly distributed pyramids on the surface, which may indicate the etching of the substrate in alkaline solutions. This chemical treatment of monocrystalline

silicon significantly reduces the reflectance from the front surface of the solar cells. The texturization of the silicon surface is a key element in the production of photovoltaic cells, enabling the formation of an appropriate microstructure on the surface of the substrate, trapping solar radiation inside the material by repeated reflection [47–49].

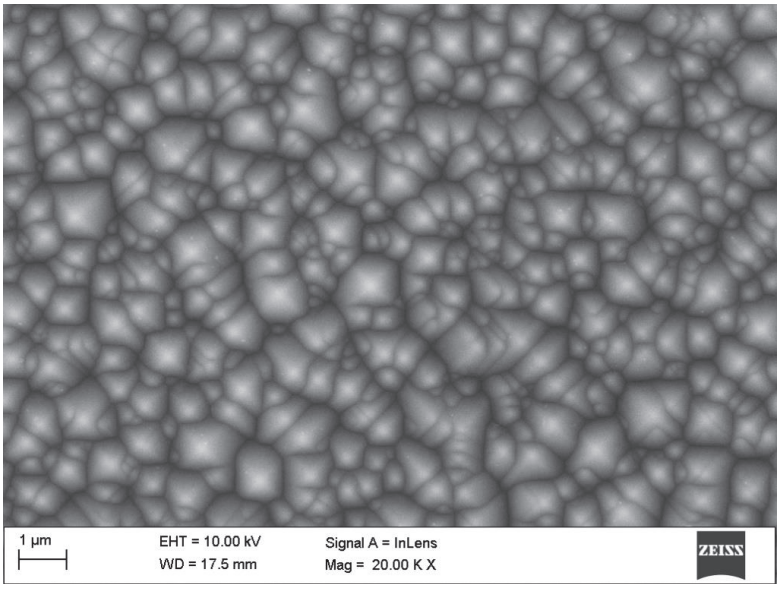

Figure 6. SEM textured surface topography of the N-type monocrystalline silicon solar cell.

All leads in the tested N-type solar cells are on the rear surface of the samples (Figure 7). The electrode topography of a monocrystalline silicon photovoltaic cell is shown in Figure 8a,b.

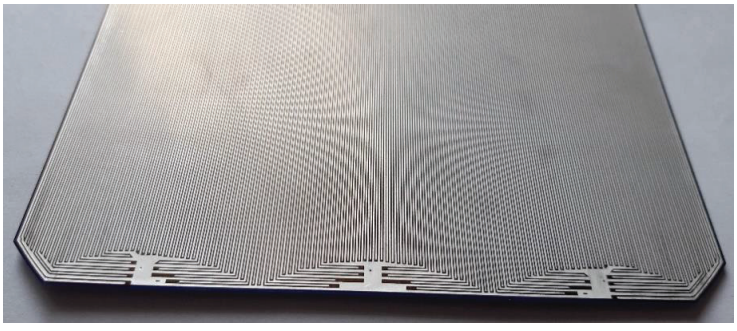

Figure 7. Rear surface of Maxeon Ne3 with visible connectors in the lower part.

When analyzing the structure of the solar cell before and after the lamination process, no traces of microcracks were observed. The temperature changes during lamination and the force generated by rollers pressing the film to the solar cell did not damage the upper surface layer and the electrical connections of the solar cell. The decrease in the efficiency of the solar cell is therefore not due to microcracks, but only due to the properties of the layer of film applied during lamination. The lower efficiency and deterioration of electrical parameters are related to the light transmittance factor of the film.

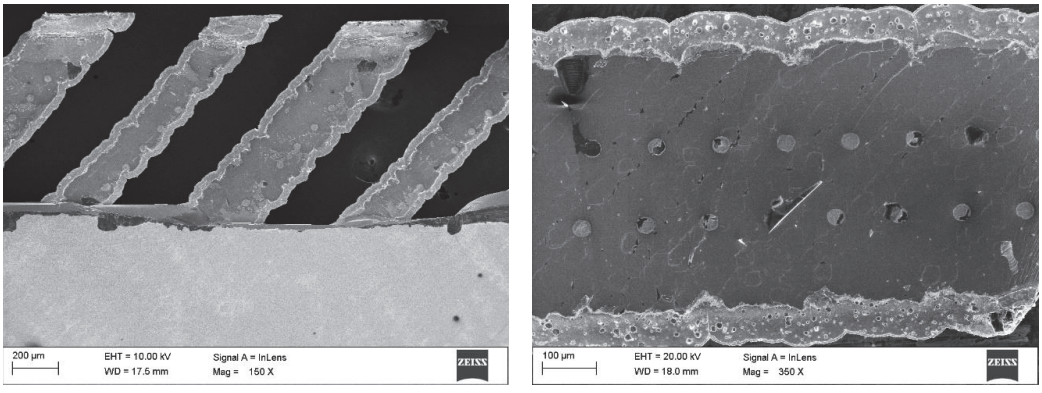

(**a**) (**b**)

Figure 8. Topography of the electric contact surfaces of a monocrystalline silicon photovoltaic cell of the N-type: (**a**) contact of fingers (grid lines) with connectors; (**b**) finger (grid line).

4.3. Solar Cell Characteristics

The test stand allowed the determination of the electrical specification of the solar cells (Table 3). These values, as a mean of all measurements, I–V (current–voltage) and P–V (power–voltage) characteristics are presented in Figure 9.

Table 3. Electrical specifications of tested SunPower Maxeon Ne3 solar cells.

Data	Manufacturer Data (Non-Laminated)	Non-Laminated	Laminated (100 µm Film)
V_{oc} (V)	>0.731	0.733	0.726
I_{sc} (A)	>6.382	6.330	6.061
V_{mp} (V)	>0.625	0.627	0.624
I_{mp} (A)	>6.050	5.92	5.747
P_{mpp} (Wp)	>3.77	3.71	3.589
Fill Factor (%)	80.8	80.8	81
Efficiency (%)	>24.34	24.29	23.33

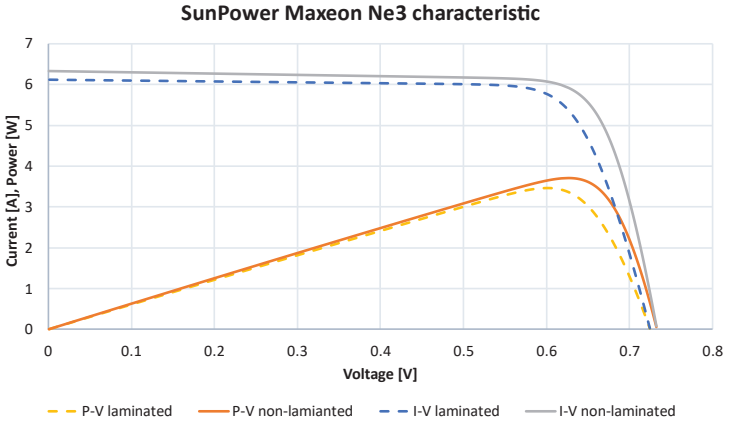

Figure 9. I–V and P–V characteristics of the SunPower Maxeon Ne3 cells.

For each type (laminated and non-laminated) we used 25 samples of solar cells to conduct research. The relative standard deviation (RSD) as well as the minimum and maximum values obtained during tests are presented in Table 4.

Table 4. Specification of tested SunPower Maxeon Ne3 solar cells.

Data	Non-Laminated			Laminated (100 μm Film)		
	Min	**Max**	**RSD (%)**	**Min**	**Max**	**RSD (%)**
V_{oc} (V)	0.728	0.738	0.77	0.725	0.731	1.81
I_{sc} (A)	6.109	6.33	0.28	6.032	6.421	0.24
V_{mp} (V)	0.616	0.639	1.04	0.604	0.629	1.47
I_{mp} (A)	5.793	6.039	0.79	5.724	6.05	1.15
P_{mpp} (Wp)	3.619	3.82	1.32	3.51	3.7	1.27
Fill Factor (%)	79.9	84.2	1.23	77.1	82.2	1.9
Efficiency (%)	24	24.77	1.12	23.01	23.79	0.85

The test stand allowed for an irradiation intensity with a power equal to 1000 W/m^2 to be provided to cells. To obtain the characteristics for the lower range of irradiation intensity, the commonly used generic simulation model using a MATLAB/Simulink system was applied. Data obtained during the STC tests of the solar cell were used as inputs in the simulation model. Data from the tested solar cells and different irradiation levels are presented in Table 5. I–V and P–V characteristics are presented in Figures 10 and 11.

Table 5. MPPT data of tested solar cell.

Non-Laminated				
Irradiation (W/m^2)	**Voltage (V)**	**Current (A)**	**Power (W)**	**Fill Factor (%)**
1000	0.627	5.92	3.709	80.8
750	0.626	4.439	2.779	59.9
500	0.622	2.961	1.842	39.7
250	0.611	1.482	0.906	19.5
Laminated				
Irradiation (W/m^2)	**Voltage (V)**	**Current (A)**	**Power (W)**	**Fill Factor (%)**
1000	0.624	5.748	3.588	81
750	0.622	4.317	2.684	61
500	0.618	2.872	1.776	40
250	0.606	1.437	0.871	19.8

The data introduced into the system allowed for the determination of current–voltage (Figure 12) and power–voltage (Figure 13) characteristics of solar cells for different temperatures. Using temperature coefficients of the SunPower Maxeon Ne3 cells, the following values were applied: voltage: −1.74 mV/°C, current: 2.9 mA/°C, power: −0.29%/°C.

Temperature coefficient data obtained in the simulation model allowed for the comparison of these data with analytical calculations. Comparing these values, it can be concluded that the simulation model results are consistent with the calculations. The data of a solar cell for different temperatures are presented in Table 6.

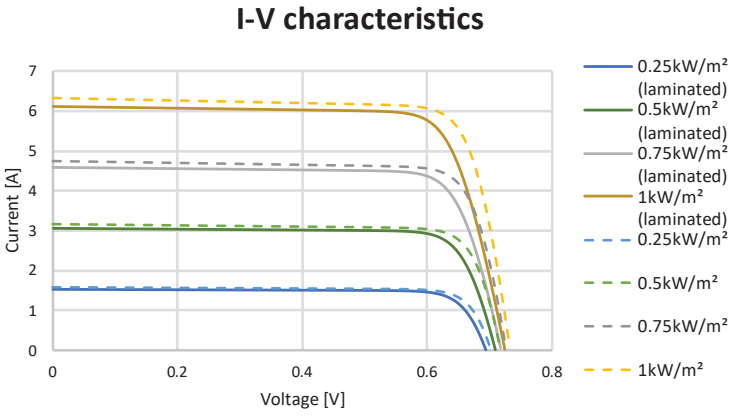

Figure 10. I–V curve at different irradiation levels for SunPower Maxeon Ne3 cells.

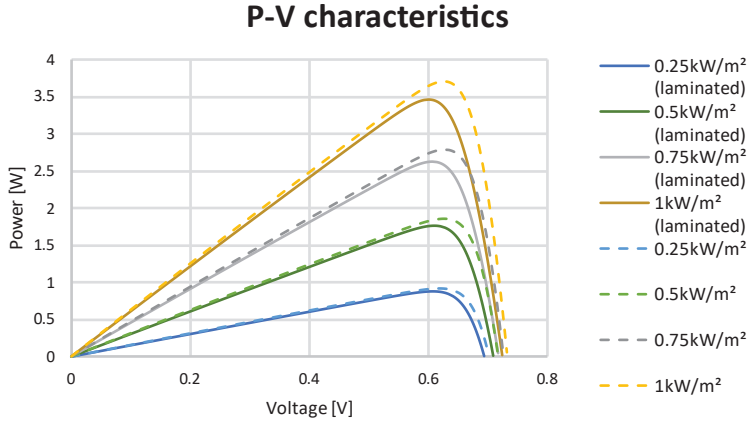

Figure 11. P–V curve at different irradiation levels for SunPower Maxeon Ne3 cells.

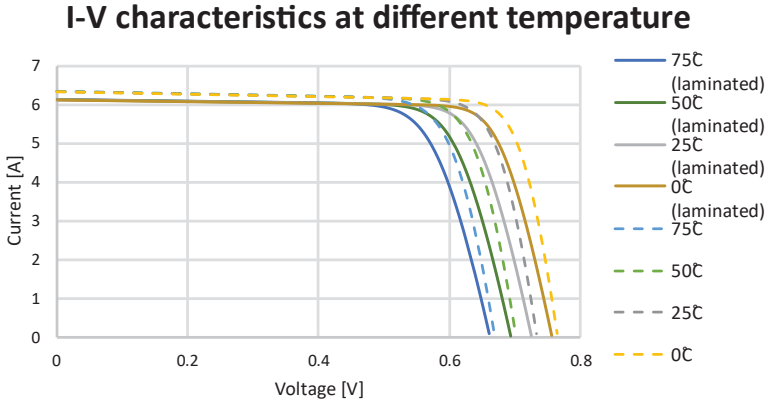

Figure 12. I–V curve at different temperatures for a SunPower Maxeon Ne3 cell.

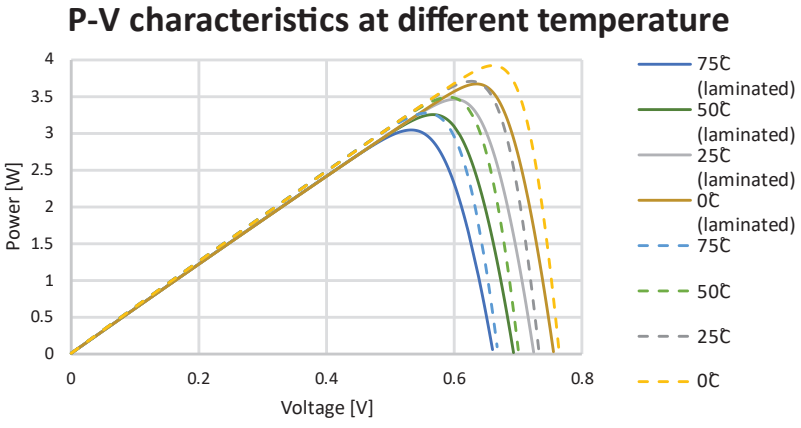

Figure 13. P–V curve at different temperatures for a SunPower Maxeon Ne3 cell.

Table 6. MPPT data for tested solar cells in different temperatures.

Non-Laminated				
Temperature	**Voltage (V)**	**Current (A)**	**Power (W)**	**Fill Factor (%)**
0	0.673	5.876	3.952	85.1
25	0.627	5.92	3.709	80.8
50	0.58	5.964	3.458	74.5
75	0.534	5.992	3.201	69
Laminated				
Temperature	**Voltage (V)**	**Current (A)**	**Power (W)**	**Fill Factor (%)**
0	0.671	5.706	3.827	87
25	0.624	5.748	3.588	81
50	0.578	5.779	3.343	76
75	0.532	5.813	3.092	70.2

5. Conclusions

SunPower Maxeon Ne3 solar cells were selected for testing present repeatable electrical and physical parameters. The flexibility of the solar cell allows it to be bent and influenced by external forces without fear that the solar cell will be broken or damaged. These features of the cell make it suitable for aerospace applications.

Flexible solar cells were covered with a thin film to provide protection and enhancement of the solar cell and to improve the aerodynamics of the UAV structure. The reduction in the solar cells' efficiency because of the lamination process reduced the energy supplied to the UAV power supply system. Tests carried out on test stands allowed for the determination of the efficiency of laminated and non-laminated solar cells. It was found that the optimal film thickness for lamination, a PVC film of 100 µm, reduced efficiency by 4%. Spectrophotometric characteristics of transmission, absorption, and reflection allowed the conclusion that in the full range of visible light, these values are constant. This data demonstrates that losses of efficiency are constant for the visible light range. Reductions in efficiency precipitate the need to use more solar cells to obtain the same energy value. Reduced efficiency in relation to non-laminated solar cells, together with the benefits of enhanced protection of cells that film lamination confers, result in the need to change the design of the UAV, to optimize the energy consumption or redefine the battery capacity.

Simulations that include the different parameters of solar cells in different temperatures allow for the determination of the response of the system in conditions when solar cells are exposed to frosty surroundings and to high temperatures. In the case of a specific UAV being designed as part of this work, with an optimal flight time of over 24 h, this reduction in efficiency due to lamination equal to 4% will be significant.

Further work is planned to validate the simulation models of the laminated PV panels by testing the UAV in a real environment. The simulation model will allow predictions for the control of the energy balance of the UAV. Data related to solar cells, such as sun exposure, cloud cover, location, day duration, angular variation of the aircraft, flight scenarios, and energy consumption will also be considered. These data, in combination with the development of a power supply system, will allow for the calculation of the energy balance and planning of optimal flight paths in the stratosphere.

The methods developed for lamination of solar cells and data obtained will be used in the first prototype of the TS UAV. Subsequent improved iterations of TS will be able to fly in the stratosphere and achieve a cruising altitude of 20 km. These extreme conditions will allow verification of the initial assumptions with regard to the laminated PV systems meeting the requirements of this demanding environment.

Author Contributions: Conceptualization, K.M.; methodology, K.M. and A.D.; validation, W.S.; formal analysis, K.M.; investigation, K.M.; resources, A.D.; data curation, K.M.; writing—original draft preparation, K.M.; writing—review and editing, W.S. and A.D.; visualization, K.M.; supervision, W.S.; project administration, W.S.; funding acquisition, K.M. and W.S. All authors have read and agreed to the published version of the manuscript.

Funding: This research was partially funded from EEA and Norway Grants 2014–2021 and was partially carried out in the framework of project No. 10/60/ZZB/153 "Long-endurance UAV for collecting air quality data with high spatial and temporal resolutions". This work has also been supported by Silesian University of Technology (grant no. 10/060/BKM22/2025) and co-financed by the European Union from the European Social Fund in the framework of the project "Silesian University of Technology as a Center of Modern Education based on research and innovation" POWR.03.05.00-71300-Z098/17. The APC was funded by Silesian University of Technology.

Institutional Review Board Statement: Not applicable.

Informed Consent Statement: Not applicable.

Data Availability Statement: Not applicable.

Acknowledgments: The authors would like to express our thanks to the following researchers for their contribution to the research and carrying out some of the preparatory work as part of Project-Based Learning—the supervisors: Tomasz Rogala, Roman Niestrój, and the students: Justyna Sobiech, Kamil Świątek, Dominik Lipok, Robert Lipka, Bartłomiej Ciupka, Daniel Czernecki.

Conflicts of Interest: The authors declare no conflict of interest.

Abbreviations

AM	Air mass
EVA	Ethylene–vinyl acetate
GaAs	Gallium arsenide
I-V	Current–voltage
IR	Infrared
P-V	Power–voltage
PV	Photovoltaics
PVC	Polyvinyl chloride
RSD	Relative standard deviation
STC	Standard test conditions
TS	TwinStratos
UAV	Unmanned aerial vehicle
UV	Ultraviolet

References

1. McEvoy, A.; Markvart, T.; Castañer, L. *Practical Handbook of Photovoltaics Fundamentals and Applications*, 2nd ed.; Elsevier: Waltham, MA, USA, 2011.
2. Zhang, J.; Lou, M.; Xiang, L.; Hu, L. Power cognition: Enabling intelligent energy harvesting and resource allocation for solar-powered UAVs. *Future Gener. Comput. Syst.* **2020**, *110*, 658–664. [CrossRef]
3. Bakar, A.; Ke, L.; Liu, H.; Xu, Z.; Wen, D. Design of Low Altitude Long Endurance Solar-Powered UAV Using Genetic Algorithm. *Aerospace* **2021**, *8*, 228. [CrossRef]
4. Rydh, C.J.; Sandén, B.A. Energy analysis of batteries in photovoltaic systems. Part I: Performance and energy requirements. *Energy Convers. Manag.* **2005**, *46*, 1957–1979. [CrossRef]
5. Rydh, C.J.; Sandén, B.A. Energy analysis of batteries in photovoltaic systems Part II: Energy return factors and overall battery efficiencies. *Energy Convers. Manag.* **2005**, *46*, 1980–2000. [CrossRef]
6. Doskocz, J.; Kardasz, P.; Hejduk, M.; Wiejkut, P. The possibilities of using drones in the courier services. *World Sci. News* **2016**, *48*, 119–132.
7. Papež, N.; Dallaev, R.; Ţălu, Ş.; Kaštyl, J. Overview of the Current State of Gallium Arsenide-Based Solar Cells. *Materials* **2021**, *14*, 3075. [CrossRef] [PubMed]
8. Oettershagen, P.; Melzer, A.; Mantel, T.; Rudin, K.; Lotz, R.; Siebenmann, D. A Solar-Powered Hand-Launchable UAV for Low-Altitude Multi-Day Continuous Flight. In Proceedings of the IEEE International Conference on Robotics and Automation (ICRA), Seattle, WA, USA, 26–30 May 2015; pp. 3986–3993.
9. Aktaş, A.; Kirçiçek, Y. *Solar Hybrid Systems: Chapter 13—Examples of Solar Hybrid System Layouts, Design Guidelines, Energy Performance, Economic Concern, and Life Cycle Analyses*; Elsevier: San Diego, CA, USA, 2021; pp. 331–349.
10. Kalogirou, S.A. *Solar Energy Engineering*; Academic Press: Cambridge, MA, USA, 2009.
11. Qazi, S. *Standalone Photovoltaic (PV) Systems for Disaster Relief and Remote Areas: Chapter 7—Solar Thermal Electricity and Solar Insolation*; Elsevier: Amsterdam, The Netherlands, 2017; pp. 203–237.
12. Li, J.; Aierken, A.; Zhuang, Y.; Xu, P.Q.; Wu, H.Q.; Zhang, Q.Y.; Wang, X.B.; Mo, J.H.; Yang, X.; Chen, Q.Y.; et al. 1 MeV electron and 10 MeV proton irradiation effects on inverted metamorphic GaInP/GaAs/InGaAs triple junction solar cell. *Sol. Energy Mater. Sol. Cells* **2021**, *224*, 111022. [CrossRef]
13. Singh, A. SunPower: A Path toward Strategic Development. *Emerg. Econ. Cases J.* **2021**, *3*, 77–86. [CrossRef]
14. Omazic, A.; Oreski, G.; Halwachs, M.; Eder, G.C.; Hirschl, C.; Neumaier, L.; Pinter, G.; Erceg, M. Relation between degradation of polymeric components in crystalline silicon PV module and climatic conditions: A literature review. *Sol. Energy Mater. Sol. Cells* **2019**, *192*, 123–133. [CrossRef]
15. Xue, B.; Li, F.; Song, M.; Shang, X.; Cui, D.; Chu, J.; Dai, S. Crack Extraction for Polycrystalline Solar Panels. *Energies* **2021**, *14*, 374. [CrossRef]
16. Blakers, A.W.; Armour, T. Flexible silicon solar cells. *Sol. Energy Mater. Sol. Cells* **2009**, *93*, 1440–1443. [CrossRef]
17. Li, X.; Li, P.; Wu, Z.; Luo, D.; Yu, H.Y.; Lu, Z.H. Review and perspective of materials for flexible solar cells. *Mater. Rep. Energy* **2021**, *1*, 100001. [CrossRef]
18. Kim, S.; Hoang, V.Q.; Bark, C.W. Silicon-Based Technologies for Flexible Photovoltaic (PV) Devices: From Basic Mechanism to Manufacturing Technologies. *Nanomaterials* **2021**, *11*, 2944. [CrossRef] [PubMed]
19. Oettershagen, P.; Melzer, A.; Mantel, T.; Rudin, K.; Stastny, T.; Wawrzacz, B.; Hinzmann, T.; Leutenegger, S.; Alexis, K.; Siegwart, R. Design of small hand-launched solar-powered UAVs: From concept study to a multi-day world endurance record flight. *J. Field Robot.* **2017**, *34*, 1352–1377. [CrossRef]
20. Kokkos, S.; Morfidis, E. Aerodynamic Design and Analysis of Solar Powered UAV (Unmanned Aerial Vehicle). Master's Thesis, University of Thessaly, Volos, Greece, 2020.
21. Fegade, U.A.; Jethave, G.N. *Interface Science and Technology, Chapter 15—Photocatalytic Reduction of CO2 in Hydrocarbon: A Greener Approach for Energy Production*; Elsevier: Amsterdam, The Netherlands, 2021; pp. 871–915.
22. Brochure: Evolution 201 and 220 UV-Visible Spectrophotometers. Available online: https://assets.thermofisher.com/TFS-Assets%2FMSD%2Fbrochures%2FBR51944-evolution-201-220.pdf (accessed on 29 September 2022).
23. Liu, Y.; Xu, Z.; Du, H.; Lv, M. Multidisciplinary Optimization of Thermal Insulation Layer for Stratospheric Airship with a Solar Array. *Aerospace* **2022**, *9*, 83. [CrossRef]
24. Feister, U.; Cabrol, N.; Häder, D. UV Irradiance Enhancements by Scattering of Solar Radiation from Clouds. *Atmosphere* **2015**, *6*, 1211–1228. [CrossRef]
25. Brizon, M. Solar Energy Generation Model for High Altitude Long Endurance Platforms. Master's Thesis, KTH—Royal Institute of Technology, Stockholm, Sweden, 2016.
26. Han, X.T.; Xie, A.Y.; Bi, X.C.; Liu, S.J.; Hu, L.H. Effects of altitude, ambient temperature and solar radiation on fasting heat production in yellow cattle (Bos taurus). *Br. J. Nutr.* **2003**, *89*, 399–408. [CrossRef]
27. Semenova, O.V.; Yuzova, V.A.; Patrusheva, T.N.; Merkushev, F.F.; Railko, M.Y.; Podorozhnyak, S.A. Antireflection and protective films for silicon solar cells. In Proceedings of the IOP Conference Series Materials Science and Engineering, Tomsk, Russia, 14–18 April 2014.
28. Swatowska, B.; Stapinski, T.; Drabczyk, K.; Panek, P. The role of antireflective coatings in silicon solar cells—The influence on their electrical parameters. *Opt. Appl.* **2011**, *41*, 487–492.

29. Microfractures in Solar Modules: Causes, Detection and Consequences. GSES Technical Papers. Available online: https://www.gses.com.au/wp-content/uploads/2016/03/GSES_microfractures.pdf (accessed on 29 September 2022).
30. Tsach, S.; Ankri, L.; Cohen, M.; Ehrlich, Y.; Goldenberg, T.; Levy, H.; Regev, I.; Vladimirsky, A.; Weider, A.; Yossef, Z. Sunsailor: Solar Powered UAV. In Proceedings of the 47th Israel Annual Conference on Aerospace Sciences, Tel Aviv, Israel, 21–22 February 2007.
31. Sousa, J.C. Solar System for a Long Endurance Electric UAV. Master's Thesis, University of Beira Interior, Covellian, Portugal, 2015.
32. Oettershagen, P. Solar-Powered Unmanned Aerial Vehicles: Design and Environment-Aware Navigation for Robust Low-Altitude Multi-Day Continuous Flight. Doctor Thesis, ETH Zurich, Zurich, Switzerland, 2018.
33. Energy to Cross Oceans and Continents. Available online: https://aroundtheworld.solarimpulse.com/adventure (accessed on 15 June 2022).
34. Polymers Aiding Solar Impulse 2's Round-the-World Adventure. Available online: https://knowledge.ulprospector.com/4541/polymers-aiding-solar-impulse-2s-round-world-adventure/ (accessed on 15 June 2022).
35. Mateja, K.; Skarka, W. Towards energetic autonomy of UAV. In Proceedings of the 27th ISTE International Conference on Transdisciplinary Engineering, Warsaw, Poland, 1–10 July 2020; pp. 423–432.
36. Zenowicz, K.; Skarka, W. Verification of Flutter Method for the Purposes of Building a Very Flexible Wing Generative Model. In Proceedings of the 27th ISTE International Conference on Transdisciplinary Engineering, Warsaw, Poland, 1–10 July 2020; pp. 383–392.
37. Skarka, W.; Jałowiecki, A. Automation of a Thin-Layer Load-Bearing Structure Design on the Example of High Altitude Long Endurance Unmanned Aerial Vehicle (HALE UAV). *Appl. Sci.* **2021**, *11*, 2645. [CrossRef]
38. Datasheet SunPower Maxeon Ne3. Available online: https://www.makeyoursolar.com/ (accessed on 29 September 2022).
39. Targosz, M.; Skarka, W.; Przystałka, P. Model-based optimization of velocity strategy for lightweight electric racing cars. *J. Adv. Transp.* **2018**, *2018*, 3614025. [CrossRef]
40. Niestrój, R.; Rogala, T.; Skarka, W. An Energy Consumption Model for Designing an AGV Energy Storage System with a PEMFC Stack. *Energies* **2020**, *13*, 3435. [CrossRef]
41. Peciak, M.; Skarka, W. Assessment of the Potential of Electric Propulsion for General Aviation Using Model-Based System Engineering (MBSE) Methodology. *Aerospace* **2022**, *9*, 74. [CrossRef]
42. Dwivedi, V.S.; Patrikar, J.; Addamane, A.; Ghosh, A.K. MARAAL: A Low Altitude Long Endurance Solar Powered UAV for Surveillance and Mapping Applications. In Proceedings of the 23rd International Conference on Methods & Models in Automation & Robotics (MMAR), Miedzyzdroje, Poland, 27–30 August 2018; pp. 449–454. [CrossRef]
43. Sisanth, K.S.; Thomas, M.G.; Abraham, J.; Thomas, S. General Introduction to Rubber Compounding. In *Progress in Rubber Nanocomposites*; Elsevier: Amsterdam, The Netherlands, 2017; pp. 1–39. ISBN 978-0-08-100409-8.
44. *IEC 60904-3*; Photovoltaic Devices—Part 3: Measurement Principles for Terrestrial Photovoltaic (PV) Solar Devices with Reference Spectral Irradiance Data. IEC: Geneva, Switzerland, 2019.
45. *IEC 60904-1*; Photovoltaic Devices—Part 1: Measurement of PV Current-Voltage Characteristics. IEC: Geneva, Switzerland, 2019.
46. Leitão, D.; Torres, J.P.N.; Fernandes, J.F.P. Spectral Irradiance Influence on Solar Cells Efficiency. *Energies* **2020**, *13*, 5017. [CrossRef]
47. Sankarasubramaniam, S.; Saud, G.K.; Shashikala, M.; Suratkar, P.; Saravanan, S. Impact of surface texturization on overall performance of mono-crystalline silicon solar cells. *ECS Trans.* **2015**, *66*, 9–17. [CrossRef]
48. Dobrzański, L.A.; Drygała, A. Laser application in photovoltaics for surface texturization of silicon and front electrode deposition. *Mater. Perform. Charact.* **2019**, *8*, 1136–1146. [CrossRef]
49. Kulesza-Matlak, G.; Gawlińska, K.; Starowicz, Z.; Sypień, A.; Drabczyk, K.; Drabczyk, B.; Lipiński, M.; Zięba, P. Black silicon obtained in two-step short wet etching as a texture for silicon solar cells—Surface microstructure and optical properties studies. *Arch. Metall. Mater.* **2018**, *63*, 1009–1017.

drones

MDPI

Article

Sensorless and Coordination-Free Lane Switching on a Drone Road Segment—A Simulation Study

Zhouyu Qu †,‡ and Andreas Willig *,‡

Department of Computer Science and Software Engineering, University of Canterbury, Christchurch 8140, New Zealand
* Correspondence: andreas.willig@canterbury.ac.nz
† Current address: Private Bag 4800, Christchurch 8140, New Zealand.
‡ These authors contributed equally to this work.

Abstract: Copter-type UAVs (unmanned aerial vehicles) or drones are expected to become more and more popular for deliveries of small goods in urban areas. One strategy to reduce the risks of drone collisions is to constrain their movements to a drone road system as far as possible. In this paper, for reasons of scalability, we assume that path-planning decisions for drones are not made centrally but rather autonomously by each individual drone, based solely on position/speed/heading information received from other drones through WiFi-based communications. We present a system model for moving drones along a straight road segment or tube, in which the tube is partitioned into lanes. We furthermore present a cost-based algorithm by which drones make lane-switching decisions, and evaluate the performance of differently parameterized versions of this algorithm, highlighting some of the involved tradeoffs. Our algorithm and results can serve as a baseline for more advanced algorithms, for example, including more elaborate sensors.

Keywords: drones; wireless communications; path planning; collision avoidance; performance evaluation

Citation: Qu, Z.; Willig, A. Sensorless and Coordination-Free Lane Switching on a Drone Road Segment—A Simulation Study. *Drones* **2022**, *6*, 411. https://doi.org/10.3390/drones6120411

Academic Editors: Andrzej Łukaszewicz, Wojciech Giernacki, Zbigniew Kulesza, Jaroslaw Pytka and Andriy Holovatyy

Received: 16 October 2022
Accepted: 10 December 2022
Published: 14 December 2022

1. Introduction

Unmanned aerial vehicles (UAV) or drones are increasingly becoming an interesting alternative for the delivery of small goods, in particular in densely populated urban environments [1–3]. Rotary-wing or copter-type drones are advantageous for this class of applications due to their manoeuvrability, their ability to hover and their vertical take-off and landing capability. Drone-based delivery has important advantages: (i) drones can move in three dimensions and can often take a much more direct route than possible on a street network, reducing the distance to travel and speeding up the delivery of time-critical items; (ii) they are less likely to be hampered by traffic congestion and in turn, do not contribute to the congestion of passenger-carrying vehicles on the ground; (iii) delivery of small goods via drones is potentially more environmentally sustainable, as the mass of a drone to be moved is orders of magnitude lower than the mass of cars or vans (even though the drone additionally has to work against gravity) [4–7]. We expect that delivery drones will become more autonomous and will be used in increasingly large numbers. At the same time, flying drones present a safety hazard for humans, particularly when a drone loses control and crashes, when two or more drones collide fatally, or when a drone enters an airspace also occupied by manned aircraft (e.g., close to an airport or in the operational area of a rescue helicopter). One approach to manage safety risks is to confine drones to move along pre-planned airspaces most of the time. Therefore, we envisage the introduction of a *drone road system* similar to a road network for vehicles, a network of straight cylindrical segments (or *tubes*) meeting at intersections, which drones can enter and leave either at pre-planned on- and offramps or at arbitrary locations. A drone road

network can be partially overlaid with the street network so that a crashing drone hits the ceiling of a car instead of a human.

In this paper, we explore how drones can move along a drone tube such that most of the time they fly at their preferred speed, stay within the tube, and above all avoid collisions with other drones (and subsequent crashes). To cater to a wide variety of drone models and drone operating procedures we make only minimal assumptions about the sensing and communications capabilities of drones. We assume that drones are only equipped with a GPS receiver and a WiFi adapter, and we express this by saying that drones are *sensorless*. Drones continuously measure their own position and broadcast this and other operational data (e.g., speed) regularly to a local neighbourhood—in other words, our communications model for drones is very similar to the communications model in vehicular networks, which is critically based on the frequent transmission of safety messages [8]. We refer to these periodic transmissions (which are similar in spirit to the WAVE/SAE J2735 protocol's *basic safety messages* used in vehicular networking [9]) as *beacons*. A drone can use beacons received from other drones to estimate their trajectory, identify the risk of upcoming collisions and take corrective actions. Similar to the case of vehicular networks, beacons can get lost through packet collisions and other channel phenomena [10–13], leading to potentially significant uncertainty about the position and speed of neighbouring drones. These communication-induced uncertainties come on top of other uncertainties, e.g., from noisy GPS receivers or weather conditions [14].

Fundamentally, to move in a tube, drones have to make decisions about their speed and their position relative to the tube, such that they eventually reach their final destination, avoid collisions with other drones or obstacles and do all that at a speed as close as possible to their preferred speed. Drones have to achieve this in the presence of uncertainty about other drones' positions, resulting from packet losses. In this paper, we report on the design and performance evaluation of a simple, computationally inexpensive, yet flexible autonomous decision-making algorithm for controlling the movements of drones in a drone tube. We make the following contributions:

- We present a system model for a drone tube, in which the space within the tube and outside of it is subdivided into lanes, and in which drones exchange basic position and velocity information through frequent broadcasting of beacons.
- We present a simple, computationally inexpensive, de-centralized and *coordination-free* decision algorithm, by which drones decide the lane and speed to use, based on information about neighboured drones received through beacons. The algorithm is "greedy", i.e., it is based on an internal and parameterizable cost model which takes into account both the deviation from the preferred speed and the drone's position relative to the tube. The algorithm aims to minimize short-term costs. By adjusting the algorithm parameters it becomes possible to choose appropriate tradeoffs between deviations from the preferred speed and temporary movements out of the tube. By "coordination-free", we mean that drones can make use of the position and speed information gathered from beacons of other drones, but no further data is included in beacons that would allow them to inform (or even actively negotiate with) other drones about any planned movements. Despite its simplicity, the algorithm is parameterizable and can achieve a substantial range of different behaviours. To demonstrate this, we define four noticeably different variants of our algorithm.
- We perform a simulation-based performance analysis of these four variants, reporting results for the average number of drone collisions, average speed, and average distance to the tube when moving out of the tube. The focus of our evaluation is the impact of the underlying communications subsystem on key performance measures such as the number of drone collisions. We, therefore, do not consider other sources of uncertainty, such as GPS noise.

Our results show that: (i) The drone collision rate depends strongly on the density of drones (very likely caused by excessive packet collisions and therefore uncertainty about positions and speeds of neighboured drones), on the beacon sending rate and, broadly, on

how "cautious" the algorithm is in its decision-making. (ii) There is a tradeoff between the collision rate and the (reduction of) speed. To avoid frequent slowdowns, drones need to switch lanes to maintain their preferred speed, but this increases the risk of having a collision with other drones.

Our decision algorithm makes only minimal assumptions—it requires no sensors other than GPS and it only relies on simple position and velocity reporting without elaborate coordination. As such, it can serve as a baseline for more advanced algorithms relaxing one or both of these restrictions. (The source code of the simulator is available at https://github.com/zqu14/Drone-lane-switching (accessed on 13 October 2022)).

The remaining paper is structured as follows. In Section 2, we briefly discuss related work. In Section 3, we introduce our system model, including tubes and lanes, drones and drone arrival process, communications and key performance measures. Following this, in Section 4 we introduce the greedy lane-switching (GreedyLS) algorithm, by which drones frequently make decisions on the lane and speed to take over the next short time window. In Section 5, we present and discuss our simulation results and in Section 6 we conclude the paper and discuss potential avenues for future work.

2. Related Work

In this section, we present related studies about path planning and packet loss problems for drones.

2.1. Drone Road Systems

Using drones for deliveries in urban areas is an idea that is gaining traction, ranging from mundane items such as pizzas (https://dronedj.com/2022/01/27/dominos-pizza-drone-delivery-new-zealand/ (accessed on 13 October 2022)) to more critical items such as medications or blood samples [15,16]; see also [17] for a survey drone applications and their communications properties. To simplify air traffic management, drone road systems or drone highways (https://www.altitudeangel.com/news/uk-government-gives-the-green-light-for-worlds-longest-drone-superhighway (accessed on 13 October 2022)) are seen as attractive options and have started to gain traction in the research literature. For example, in [18] a microscopic piecewise-continuous traffic flow model for drones moving in a tube-like "channel" is proposed and analyzed from a stability perspective. In [19], the risk generated by drones moving in a corridor is modelled and an airspace capacity analysis is being carried out, which takes into consideration the collision rate and failure rate of drones. In [20], the modelling of collision risks including risks arising from positional uncertainty is discussed. The required ground infrastructure for urban air mobility and related regulatory aspects are reviewed in [21].

2.2. Dynamic Path Planning for Drones

In our system model, a key challenge for drones is collision avoidance. To achieve that, drones need to continuously detect the position, speed and heading of other drones and plan their own path based on that. Dynamic path planning algorithms [22] address this class of problems. In general, they generate several candidate paths and then choose the optimal one based on a pre-established cost function. In our paper, we benefit from the properties of our system model, which restricts the path decisions a drone can make to a finite (and small) set, limiting computational complexity.

Path conflicts and inconsistency of wireless communication are typical problems for drones when coordinating movements with others. In [23], Zhenyu et al. propose a method to address these issues. The first step is to calculate the probability of a collision by considering a random error vector to simulate the inaccuracy of the position information of other drones, then a Kalman filter [24] is used to predict the state and plan the path. The simulation results show the great effectiveness of the Kalman-filtering-based algorithm to reduce the collision possibility among several drones.

Several papers investigate dynamic path planning in different situations. Ragi and Chong [25] present a partially observable Markov decision process (POMDPs) [26] approach to allow drones to track the positions of others and a target, and avoid collisions with each other. Hu et al. [27] employ reinforcement learning to guide drones while avoiding obstacles. Yu et al. [28] consider target tracking in an urban environment and propose a cooperative path-planning algorithm integrating both aerial and ground-based autonomous vehicles. Xiaolei et al. [29] provide a solution using an improved evolutionary optimization algorithm. It can effectively solve the path planning problem at the cost of high computational complexity.

2.3. Congestion Control in Vehicular Networks

The setup considered in this paper has some similarities to the case of vehicular networks, where vehicles periodically send local broadcasts to inform their neighbourhood about their position, speed and heading. If the underlying wireless technology is based on IEEE 802.11p, then these periodic packets experience both direct and hidden-terminal collisions and this can negatively increase the uncertainty about the position and direction of neighbours and possibly increase collision rates. This is known as the congestion control problem in the context of vehicular ad hoc networks (VANETs) [30,31].

In [32], a simple VANET model is constructed to explore the possible approaches to solve the congestion problem. Their results suggest three key factors: transmit power, packet transmission duration/packet size and packet transmission rate. These can be adapted to reduce the network load and hence control the congestion. There are also many further proposals in the literature to solve the problem by adapting these factors; see [33–36]. While the effects of congestion in vehicular networks (and by our adoption of related communications technologies also in our drone network) are well understood on a packet level (for example, rates of hidden-terminal and direct collisions), the impact on physical collisions of drones or vehicles is less well studied. This is one of the key problems addressed in this paper.

2.4. Packet Loss in Drone Communications

Packet loss is a crucial problem in drone communications, it can be caused by many reasons. In [37], Fabra et al. investigated several parameters that can affect the packet loss rate between drones. With increasing distance between two drones, the packet loss rate tends to become larger. Furthermore, the degree of change is decided by the on/off status of the engine. When the engine is off, the degree is high. Conversely, the degree becomes low once the engine is turned on. Other parameters such as the remote control proximity and the packet size affect the communication quality between drones only slightly.

In [38], Khalifeh et al. designed experiments to explore the influence of some factors on the packet loss rate between the drones and the ground stations. One interesting finding of this paper is that the height of the drones can have a great impact on the packet loss rate under the utilized ZigBee protocol [39]. The packet loss rate stays at 0% when the height is less than 150 m, and it will rapidly increase to 65% if the height reaches 200 m.

There also exists a rich literature exploring the impact of packet loss. In [40], James et al. examine how the packet loss rate can affect the performances of three drone swarm path planning algorithms [41,42]. The results show that a higher packet loss rate leads to an increased rate of separation violations, thus requiring a larger minimum safety distance to maintain the safety of the drone swarm. In addition, Buonocore et al. [43] have evaluated the impact of some packet loss models on the drone formation control [44]. Results show that even the simplest packet loss models can lead to some abnormal behaviours and collisions under a centralized drone control algorithm [45], and the outcomes become worse when more realistic loss models are used.

3. System Model

In this section, we present our system model, starting with our model for drone tubes and their internal structure, followed by our model for the drones themselves and the drone arrival process, then introducing the communications protocols and channel model used in this work and finally presenting the key performance measures.

3.1. Tube, Lanes and Tiers

For the purposes of this paper, we fix a three-dimensional coordinate system with orthogonal axes, which we simply refer to as the x-, y- and z-axes. We assume that the tube and all lanes (see below) run in parallel to the y-axis, which in turn runs parallel to the surface of the earth. The tube is of finite length L meters. The coordinate origin is placed at one end of the tube such that the y-coordinates of a drone moving in the tube run from 0 (where drones are being injected into the tube) to the length of the tube (where they are removed). The tube itself and the entire space around it is partitioned into *lanes*, similar to the way a one-way street can be partitioned into lanes. A lane is a hexagonal cylinder wide enough to contain any drone under consideration. A drone will fly in such a way that it is completely within its current lane, with the exception of lane-switching operations—while a drone flies in a lane, its centre point will be on the centre line of the lane. We fix a particular lane to be at the centre of the tube and refer to it as *tier-0* or centre lane (shown in grey in Figure 1). Further lanes are packed around the centre lane in the manner indicated in Figure 1, creating a hexagonal tiling. The lanes immediately neighbouring the centre lanes are tier-1 lanes (shown in orange), the lanes immediately neighbouring tier-1 lanes that are not themselves tier-0 or tier-1 lanes are tier-2 lanes (shown in lime), and so on. Note that in this arrangement the centre point of each lane has the same distance as the centre point of each of its six neighboured lanes. As an example, in this paper we assume that tiers 0 and 1 are within the tube, all further tiers are considered to be outside the tube. The GreedyLS algorithm allows drones to move in lanes outside the tube, depending on how its cost model assigns cost to out-of-tube lanes. It is important to point out that our algorithm as such can work with arbitrary numbers of in-tube tiers, including partial tiers.

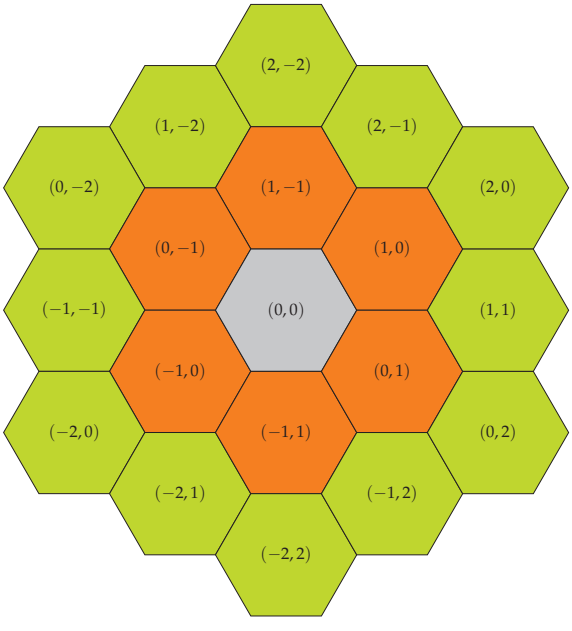

Figure 1. Lane layout when looking along the tube in the y-direction.

Across its lifetime, the drone will move in parallel to the y-axis in a positive direction. A drone might change its lane, which corresponds to changes in its x- and z-coordinates. Restricting to these two axes, we can conveniently represent the coordinates of lane centre points and tiers in the following way: if we denote by r the distance between the centre points of neighboured lanes and introduce two basis vectors $\mathbf{e}_1$ and $\mathbf{e}_2$ in the $x-z$-plane such that $\mathbf{e}_1$ points from the centre point of the centre lane (the grey lane in Figure 1, marked as $(0,0)$) to the centre point of the upper right neighbour lane (the orange lane marked as $(1,0)$), and $\mathbf{e}_2$ points from the centre point of lane $(0,0)$ to the centre point of the lower right neighbour lane marked as $(0,1)$. With this, the centre points of all lanes can be represented in the form $i \cdot \mathbf{e}_1 + j \cdot \mathbf{e}_2$ with $(i,j) \in \mathbb{Z}^2$; compare this with Figure 1. We will frequently refer to a particular lane through these (i,j) integer coordinates. Note that in this setting the centre lane has coordinates $(0,0)$, the lanes on the first tier are given by $(1,0)$, $(-1,0)$, $(0,1)$, $(0,-1)$, $(1,-1)$ and $(-1,1)$, and generally the lanes of the n-th tier are given by:

- Corners: $(n,0)$,$(-n,0)$,$(0,n)$,$(0,-n)$,$(n,-n)$,$(-n,n)$.
- The points $(x, n-x)$ for $x \in \{1,\ldots,n-1\}$.
- The points $(-x,-(n-x))$ for $x \in \{1,\ldots,n-1\}$.
- The points $(-x,n)$ for $x \in \{1,\ldots,n-1\}$.
- The points $(x,-n)$ for $x \in \{1,\ldots,n-1\}$.
- The points $(n,-x)$ for $x \in \{1,\ldots,n-1\}$.
- The points $(-n,x)$ for $x \in \{1,\ldots,n-1\}$.

(consider the lanes on tier 2 in Figure 1 as an example). Conversely, to work out to which tier τ a given point (i,j) belongs, the following formula is helpful:

$$\tau(i,j) = \begin{cases} \operatorname{abs}(j) & : \quad i = 0 \\ \operatorname{abs}(i) & : \quad j = 0, i \neq 0 \\ \operatorname{abs}(i) + \operatorname{abs}(j) & : \quad \operatorname{sign}(i) = \operatorname{sign}(j), i \neq 0, j \neq 0 \\ \max\{\operatorname{abs}(i), \operatorname{abs}(j)\} & : \quad \text{otherwise.} \end{cases} \tag{1}$$

3.2. Drones

We assume all drones to be copter-type, due to their manoeuvrability and their ability to hover and perform vertical take-off and landing. In this paper, we assume that each drone has a *preferred speed*, which the drone operator can pick as a compromise between required delivery speed and drone energy consumption. The drone will not exceed its preferred speed, but it may travel temporarily at a slower speed when circumstances call for it. We assume that each drone randomly picks its preferred speed from the interval $[20\,\mathrm{m/s}, 30\,\mathrm{m/s}]$, independently and from a uniform distribution.

For this paper we have decided to not model the drone dynamics in any detail, we assume that drones can change their speeds instantaneously and that at any given speed lane switching between neighboured lanes takes a constant amount of time T_{switch}, which is identical for all drones. Furthermore, for reasons of simplicity we have also decided not to model the size of drones in any detail. Instead, we regard two drones as colliding when the distance of their centre points falls below a threshold of d_{safety} meters. This threshold is also referred to as the *safety distance* and we assume it to be 0.5 m in this paper. In general, d_{safety} should be smaller than the distance r between centre points of neighboured lanes, so that drones in different lanes do not collide.

Each drone has an accurate GPS receiver, i.e., it can determine its position as well as the current time with sufficiently high accuracy—we do not consider measurement noise. Furthermore, we are not concerned with the power/energy consumption of drones.

3.3. Drone Arrival Process

Drones only arrive at the starting end of the tube ($y = 0$) and only leave the system when they collide or reach the other end of the tube. Drones only arrive at intra-tube lanes, and we model arrivals by assigning to each intra-tube lane a separate and stochastically independent random drone arrival process—using random arrivals reflects the indepen-

dence of drones and the lack of centralized control. In this paper, the arrival process for each intra-tube lane is a Poisson process of rate $\lambda > 0$, so that the inter-arrival times of drones are independent and identically distributed with an exponential distribution of parameter λ.

If we were to insert each arrived drone into its lane unconditionally, we would distort drone collision statistics by a number of unwanted drone collisions, which occur independently of any decision algorithm. The first reason for this is that the inter-arrival times may with a certain probability be so small that the geographical distance between a newly arriving and a previous drone on the same lane is smaller than the safety distance d_{safety}. Furthermore, immediately after its arrival, a drone has not yet received any beacon from others, it has no position and speed information about them and therefore cannot take any corrective action such as speeding down.

To deal with this, we distinguish between the arrival and the actual insertion of a drone into its lane, which is subject to certain conditions. If these conditions are not met, an arrived drone is discarded without any further consequences.

Specifically, we check for each generated drone whether it is likely to not experience a collision for at least the first T_S seconds, which we refer to as the *insertion safety time*. When a drone arrives on lane $l \in \mathbb{Z}^2$, it will be inserted when the distance between the new drone and the ahead drone on the same lane is larger than the safety distance d_{safety}, and furthermore, one of the following conditions is true:

- Its preferred speed v_{pref} does not exceed the current speed of the drone ahead in the same lane.
- Its preferred speed v_{pref} is larger than the current speed of the drone ahead, but the distance to the drone ahead is large enough for any collision to occur only at a time larger than T_S.

Under these assumptions (and in the absence of drones from neighbouring lanes suddenly switching onto lane l) the candidate drone will have at least T_S seconds time to receive beacons and learn where the other drones are. If the conditions are not fulfilled, the generated drone is dropped. We assume this insertion safety time to be $T_S = 0.5$ s. The actual GreedyLS algorithm starts running within an inserted drone a little earlier (at 0.4 s) so that it can make adjustments to speed or position before the insertion safety time expires.

3.4. Communications Protocols and Channel Model

We view the requirements for drone communications to be quite similar to the requirements for safety-related communications in vehicular networks [8,9]. We assume that all drones are equipped with a WiFi network adapter [46], operating with similar settings as known from the former IEEE 802.11p amendment. Specifically, they operate in the 5 GHz band over a 10 MHz wide channel, using OFDM with 16-QAM modulation on individual sub-carriers and using a rate-1/2 encoder. These settings result in a 12 Mbps data rate. On the MAC layer, we use the IEEE802.11 EDCA access function, with access class `AC_BE`, $CW_{\min} = 31$, $CW_{\max} = 1023$ and $AIFS = 7$.

Drones frequently send *beacons* to their local neighbourhood using a MAC-layer broadcast. We assume that these beacons are the only type of messages that drones send on the considered channel. The beacons contain safety-related information conveying the current position and speed of the sending drone. The beacon size is fixed to a total length of 152 bytes, the beacon contents are shown in Figure 2. In this figure, the "LocalBroadcastHeader" belongs to an enclosing protocol allowing to multiplex different types of local broadcasts, the magic number is a fixed value that helps the receiver to confirm that the beacon contents include a safety message, the version field encodes the version or structure of the safety message being used (this allows to include different types of safety messages), the identifier field is a unique identifier for the sending node, the sequence number is generated by the sending node to allow receivers to estimate packet loss rates and the safety message contains information such as the position and speed of the sending drone. The beacons are being generated almost periodically, with an average rate of β beacons per second.

The beacons are not generated strictly periodically, but with a jitter of 10% around the average inter-beacon time of $1/\beta$ seconds. The beacon rate parameter β will be varied in our experiments. Furthermore, all drones use the same fixed transmit power P_t, which we keep fixed at 5 mW (as an indication of transmission range, this setting leads to a 50% reception rate for our standard beacons at a distance of 119 m).

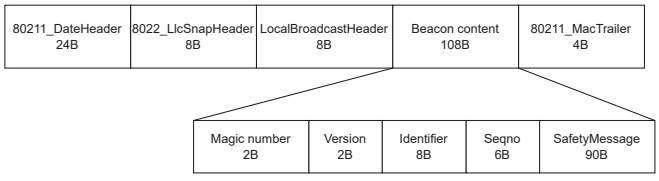

Figure 2. Beacon contents.

Each drone stores the information from received beacons in a *neighbour table*. The neighbour table contains for each currently known neighbour drone the contents of the last correctly received beacon as well as the local timestamp for the time this last beacon was received. The timestamp allows a drone to assess the amount of uncertainty in a neighbours position, but most importantly, the timestamp is critical for the *soft-state* operation of the neighbour table: the table entries are checked frequently, and when too much time has passed since the last beacon was received, the entry is dropped. The timeout value has been set to ten seconds.

For the wireless channel, we use a simple log-distance channel model with variable path loss exponent γ [47], i.e., the received power at distance d meters (for d being at least as large as the reference distance d_0, which here we assume to be one meter) is given by

$$P_r(d) = \frac{P_t}{PL_0} \cdot \left(\frac{d_0}{d}\right)^{\gamma} \tag{2}$$

where PL_0 is the path loss at the reference distance, which we assume to be 40 dB. This is a reasonable model when drones operate sufficiently far away from any reflecting surfaces and any shadowing from the drone's body is ignored. We have used a path loss exponent of $\gamma = 2.5$ for our simulations. Furthermore, we assume that there is no external interference.

3.5. Key Performance Measures and Problem Formulation

We use three key performance measures to assess the algorithms proposed in this paper. They are:

- The average number of collisions per kilometre, where the average is taken over a number of replications for a given set of parameters.
- The average speed of drones, taken over all inserted drones within a replication (sampled regularly) and all replications for a given set of parameters. Note that, due to the fact that preferred speeds are drawn uniformly from $[20\text{m/s}, 30\text{m/s}]$ and that drones are not allowed to go above their preferred speed, the average speed will not exceed 25 m/s, and will often be below that.
- Average out-of-tube tier of drones, taken over all inserted drones within a replication (sampled regularly) and all replications for a given set of parameters. In this statistic the in-tube lanes will enter with a contribution of zero, the second tier (the first tier out of the tube) will enter with a contribution of one, and so forth.

In our system model the key control knobs for a drone are the lane and the speed to use, and it decides these dynamically based on the current neighbourhood. For real deployments, a decision algorithm for speed and lane generally will attempt to maximize both the average speed and the drone density, subject to constraints on the average number of collisions and occupancy of out-of-tube lanes. Instead of maximizing the average speed, one might be interested in minimizing the maximum deviation from the preferred

speed. However, as the focus of this paper is more on exploring the tradeoffs achievable with one particular algorithm, in our experiments we vary the drone density (or drone generation rate) and obtain results for the number of collisions, the average speed and the lane occupancy for different parameterizations or variants of the algorithm, so that we can understand their tradeoffs.

3.6. Summary of All Fixed Parameters

The key fixed parameters for this paper are summarized in Table 1.

Table 1. Key parameters.

Parameter	Explanation	Value
Tube parameters		
r	Distance of neighbour lane centre points	1 m
L	Tube length	1 km
Drone and drone arrival parameters		
d_{safety}	Minimal safety distance	0.5 m
	Preferred speed distribution	U [20 m/s, 30 m/s]
T_{switch}	Time required for switching to a neighbouring lane	1 s
λ	Drone arrival rate to an in-tube lane	$\lambda \in \{0.1, 0.3, \ldots, 1.5\}$
T_S	Insertion safety time	0.5 s
Communications and channel parameters		
	Beacon length (total)	152 B
	PHY data rate	12 Mbps
β	Beaconing rate	$\beta \in \{10\,\text{Hz}, 20\,\text{Hz}\}$
P_t	Transmit power	5 mW
PL_0	Path loss at reference distance	40 dB
γ	Path loss exponent	2.5
	Neighbour table timeout	10 s

Our parameter settings are not in all cases completely realistic (e.g., lanes would normally be wider than one meter), and we have also chosen to ignore the noise in parameters such as the GPS position readings. This is for two reasons. First, our parameters have been chosen to achieve a higher rate of collisions, helping to more clearly highlight the performance difference between the considered algorithms and displaying their relative performance merits, and also avoiding rare-event simulation. Secondly, by restricting the position uncertainty in the system to the effects of packet losses, we can clearly investigate and display their impact, avoiding confounding the effects of packet losses with other sources of uncertainty.

4. The Greedy Lane-Switching (GreedyLS) Algorithm

In this section, we first give a generic description of the greedy lane-switching (or GreedyLS) decision algorithm, followed by presenting a number of algorithm variants with specific choices for the cost parameters, expressing different tradeoffs between speed and position cost.

4.1. Algorithm Description

We now describe the decision algorithm by which each drone decides the lane and speed to use in the next few seconds. The decision algorithm runs periodically. The (average) period needs to be significantly larger than the time required to switch to a neighboured lane or to change the speed to a given setting. This allows us to treat lane switching and speeding up/down as elementary actions and avoids the need to maintain state information that would be necessary when these actions took multiple periods. We also refer to the (average) period as the *unit time*.

Our decision algorithm is "stateless". i.e., a decision is always made only based on current circumstances, not based on previously stored state information (other than the contents of the neighbour table), and it is "greedy" in that it seeks to minimize costs in the short-term, over only the next unit time. The algorithm does not allow drones to operate at speeds higher than their preferred speed, only at lower speeds.

The cost model used for the algorithm employs two different types of cost. The drone knows for every tier $\tau \in \{0, 1, 2, \ldots\}$ the position cost for spending one unit of time at tier τ, we refer to this unit position cost as $c_p(\tau)$. The mapping $c_p(\cdot)$ is known and identical for all drones. Similarly, for a given speed v and preferred speed v_{pref} there is a mapping $c_s(\cdot)$ which gives the speed cost $c_s(v, v_{pref})$ of operating at speed v for one unit time when the preferred speed is v_{pref}.

The GreedyLS algorithm runs on each drone separately and independently. It has the following inputs:

- The current lane $l \in \mathbb{Z}^2$ and tier $\tau = \tau(l)$ (cf., Equation (1)).
- The speed v_{ahead} of the drone ahead in the same lane l. If there is no (known) ahead drone, then $v_{ahead} = \infty$.
- The distance d_{ahead} to the ahead drone in the same lane l. If there is no (known) ahead drone, then $d_{ahead} = \infty$.
- For all available neighbour lanes:
  - Their lane number $l_i \in \mathbb{Z}^2$ and tier $\tau_i = \tau(l_i)$.
  - The distance $d_{i,ahead}$ to the closest drone ahead of us (taken in the y-coordinate only) and having a y-coordinate at least as large as our own in lane l_i, and its speed $v_{i,ahead}$.
  - The distance $d_{i,behind}$ to the closest drone behind us in lane l_i, and its speed $v_{i,behind}$.

  If we want to also consider "concurrent collisions" (see below) then the neighbour lane information above must be extended to include all lanes in the first two tiers around the current lane.

  Note that $d_{i,ahead}$, $d_{i,behind}$, $v_{i,ahead}$ and $v_{i,behind}$ are all inferred from the neighbour table. The GreedyLS algorithm proceeds in the following steps:
- First step: build the list $\mathcal{L} = \{(l'_1, \tau'_1, v'_1), \ldots, (l'_k, \tau'_k, v'_k)\}$ of eligible lanes l'_i (and their tiers τ'_i) and allowable speeds v'_i on them:
  - The current lane l in tier τ is always eligible, its allowable speed is

    $$v' = \min\left\{v_{ahead}, v_{pref}\right\} \tag{3}$$

    where v_{pref} is the own preferred speed.
  - A neighbour lane m is eligible when both the following conditions are true:
    - $d_{m,behind} \geq \epsilon_1$, i.e., the distance to the behind drone must be at least as large as a given threshold ϵ_1.
    - $d_{m,ahead} \geq \epsilon_2$, i.e., the distance to the ahead drone must be at least as large as a given threshold ϵ_2.

    These conditions together express that we only consider a neighbour lane eligible when there is a sufficiently large "gap" around our current position.
  - The previous eligibility conditions can be extended to better address a particular type of collision, which we loosely refer to as "concurrent collisions". These can occur if two (or more) drones on different lanes find the same target lane m eligible and decide to switch to it at the same time and position. To prevent this, the previous eligibility conditions for neighbour lane m can be extended to require that all neighbour lanes m' of m excluding our own current lane l (we refer to these as *indirect neighbours* of lane l) have a sufficiently large "gap", i.e.,:

  - $\forall m' \neq l, m'$ is neighbour of m : $d_{m',behind} \geq \epsilon_3$, i.e., the distance to the behind drone in lane m' must be at least as large as ϵ_3 for all neighbour lanes $m' \neq l$ of target lane m.
  - $\forall m' \neq l, m'$ is neighbour of m : $d_{m',ahead} \geq \epsilon_4$, i.e., the distance to the ahead drone in lane m' must be at least as large as ϵ_4 for all neighbour lanes $m' \neq l$ of target lane m.
- The allowable speed on the eligible neighbour lane m is given as

$$v'_m = \min\left\{v_{pref}, v_{m,ahead}\right\} \tag{4}$$

- Second step: From $\mathcal{L}$ determine the target lane/tier and speed as

$$(l^*, \tau^*, v^*) = \underset{(l',\tau',v')\in\mathcal{L}}{\arg\min} \left(c_s(v', v_{pref}) + c_p(\tau') + c_x(l, l')\right) \tag{5}$$

  i.e., the lane/tier and speed combination giving the smallest total position, speed and switching cost per unit of time. The term $c_x(l, l')$ allows to model a cost for switching into a neighboured lane, it is of the form $c_x(l, l') = \epsilon_5 \cdot \mathbf{1}_{\{l'\}}(l)$, where $\mathbf{1}_{\{l'\}}(l) = 1$ if $l = l'$ and 0 otherwise. The parameter $\epsilon_5 \geq 0$ represents lane switching cost.
- Third step: Switch to lane l^* and adjust speed to v^*.

  A pseudo-code summary of this algorithm can be found in Figure 3.

```
// Inputs
Current lane l and tier τ(l)
Preferred speed v_pref
For all lanes m: distance d_{m,ahead} to ahead drone on lane m
For all lanes m: distance d_{m,behind} to behind drone
For all lanes m: speed v_{m,ahead} of ahead drone

// Auxiliary functions and predicates
Let N(m) be the neighbour lanes of lane m ∈ Z^2, not including m
Let V(m) = min{v_pref, v_{m,ahead}}
Let I(m,l) = ∀m' ∈ N(m), m' ≠ l : d_{m',behind} ≥ ε3 ∧ d_{m',ahead} ≥ ε4

// First step: determine eligible lanes
L0 = {l} ∪ {m : m ∈ N(l) ∧ d_{m,behind} ≥ ε1 ∧ d_{m,ahead} ≥ ε2 ∧ I(m,l)}
L = {(m, τ(m), V(m)) : m ∈ L0}

// Second step: determine target lane/tier and speed as
(l*, τ*, v*) = arg min_{(l',τ',v')∈L} (c_s(v', v_pref) + c_p(τ') + c_x(l,l'))

// Third step: switch lane and change speed as determined
```

Figure 3. Pseudocode of the GreedyLS algorithm.

For the purposes of this paper, we assume that

$$c_p(\tau) = \begin{cases} 0 & : \quad \tau \leq 1 \\ \kappa_1(\tau - 1)^2 & : \quad \tau > 1 \end{cases} \tag{6}$$

for some $\kappa_1 \geq 0$, i.e., we assume that the intra-tube part consists of the centre lane and only one tier around it. We furthermore assume that

$$c_s(v, v_{pref}) = \kappa_2(v - v_{pref})^2 \tag{7}$$

for some $\kappa_2 \geq 0$. Both speeds v and v_{pref} are assumed to be given in units of m/s. Note that the two functions $c_p(\cdot)$ and $c_s(\cdot)$ are not considered part of the GreedyLS algorithm proper, but are just examples chosen for the purposes of this paper. By changing the cost function $c_p(\cdot)$ we can model other tube layouts, e.g., we can include more tiers, or we can rule out lanes that would collide with buildings by assigning them infinite costs. The remaining GreedyLS algorithm can remain unchanged.

Note that the behaviour of this algorithm is determined by the five constants ϵ_1 to ϵ_5 as well as the position and speed cost per unit time mappings $c_p(\cdot)$ and $c_s(\cdot)$ (in our case, in particular the constants κ_1 and κ_2). In addition to and independently of this algorithm, each drone should nearly continuously monitor the distance to the ahead drone on the same lane. This distance can change instantaneously, for example, when another drone switches into our lane ahead of us. In response to such a change, we need to adapt our own speed immediately to the speed of the new ahead drone (by adjusting our own speed to the minimum of the ahead drone speed and our own preferred speed).

4.2. Baseline Algorithm and GreedyLS Variants

To limit the scope of the evaluation in this paper we make some preliminary choices for some of the GreedyLS parameters, and then define a baseline algorithm and a number of GreedyLS variants to compare.

With one exception, we will set $\epsilon_5 = 0$, i.e., in this paper we ignore lane-switching costs. We set $\epsilon_1 = \epsilon_2 = \epsilon_1^*$, i.e., we assume that in neighboured lanes the required gap has the same size ahead and behind. In our experiments, we only vary ϵ_1^*. We also set $\epsilon_3 = \epsilon_4 = \epsilon_2^*$, i.e., we assume that the required gap in the neighbour lanes (to avoid concurrent collisions) has the same size ahead and behind. In our experiments, we vary only ϵ_2^*. In particular, we choose either $\epsilon_2^* = 0$, effectively disabling the check for concurrent collisions, or we set ϵ_2^* to be the same as ϵ_1^*, and only the latter is varied.

The baseline algorithm considered in this paper is referred to as the Blind algorithm. In this, an inserted drone never changes its lane or speed at all, i.e., it reflects the situation where drones do nothing at all to avoid collisions. In addition, we define the following four GreedyLS variants:

- Defensive algorithm: pick $\kappa_1 = \kappa_2 = 1$, $\epsilon_1^* = \epsilon_2^* = 10^9$ and $\epsilon_5 = 10^9$. These settings effectively rule out any lane switching but allow for adaptation to the speed of the ahead node on the current lane.
- Crowded-$(\epsilon_1^*, \epsilon_2^*)$ algorithm: restrict to intra-tube lanes by setting $\kappa_1 = 10^9$ (cf. Equation (6)), $\kappa_2 = 1$ and ϵ_1^*, ϵ_2^* to the given values.
- PreferInside-$(\epsilon_1^*, \epsilon_2^*)$: set $\kappa_1 = 25$ and $\kappa_2 = 1$. With these settings, an out-of-tube lane becomes preferable only when the best achievable speed difference to the preferred speed v_{pref} on any eligible intra-tube lane exceeds 5 m/s.
- PreferOutside-$(\epsilon_1^*, \epsilon_2^*)$: set $\kappa_1 = \kappa_2 = 1$. With these settings already modest speed differences to the preferred speed will make out-of-tube lanes more preferable.

For the last three algorithms, we have simulated the following combinations for $(\epsilon_1^*, \epsilon_2^*)$:

- $(10, 0)$, $(20, 0)$, $(50, 0)$;
- $(10, 10)$, $(20, 20)$, $(50, 50)$.

We have summarized all relevant GreedyLS parameters (general decision algorithm parameters, parameters for example cost functions, and restrictions of general parameters used in this paper) in Table 2.

Table 2. Key adjustable parameters of GreedyLS.

Parameter	Explanation	Value
Basic GreedyLS Decision Parameters		
ϵ_1	Required minimum distance to behind drone on a neighbour lane	varied
ϵ_2	Required minimum distance to ahead drone on a neighbour lane	varied
ϵ_3	Required minimum distance to behind drone on an indirect neighbour lane	varied
ϵ_4	Required minimum distance to ahead drone on an indirect neighbour lane	varied
ϵ_5	Lane-switching cost	0
Timing parameters		
	Unit time	3 s
	Neighbour table timeout	10 s
Example cost function parameters		
κ_1	Position cost coefficient	varied
κ_2	Speed cost coefficient	varied
GreedyLS parameter choices for this paper		
ϵ_1^*	Common value of ϵ_1 and ϵ_2 (required minimum distance to ahead and behind drones on neighbour lanes)	varied
ϵ_2^*	Common value of ϵ_3 and ϵ_4 (required minimum distance to ahead and behind drones on indirect neighbour lanes)	varied

4.3. Further Comments

Algorithm Scope: It is important to point out that the GreedyLS algorithm is not limited to the case with just two in-tube tiers of lanes, but rather can accommodate arbitrary layouts of in-tube, allowed out-of-tube and completely forbidden lanes (e.g., ones that would go through a building). This can be achieved through proper choice of the position cost function $c_p(\cdot)$, which in general can be made location- or time-dependent, and which may even be adapted over time. A reliable system then needs to be in place to ensure that drones always have access to the most recent position cost function relevant for their movements.

Algorithm Complexity: Fix a particular drone x and denote by M the number of current neighbour drones of x. For each of these neighbour drones we know its position, its lane, and its speed from the beacons we have received from it and which have been entered into the neighbour table. There are three key operations for the neighbour table: enumerating all neighbours and finding those on a particular lane, adding a new neighbour and periodically checking the timers associated with each neighbour (and possibly deleting a timed-out neighbour from the table). Each of these operations is $O(M)$ at worst. If we denote by $L = 1 + 6 + 12 = 19$ the number of lanes that the algorithm considers (the current lane, the six neighbour lanes and the 12 indirect neighbour lanes), then for each of these L lanes the GreedyLS algorithm needs to find out which drones are on that lane and in particular the position and speed of the ahead and behind drones, which for each of the L lanes is an $O(M)$ operation at worst (and better with suitable data structures). The first step of the decision algorithm is $O(1)$, since for each of the six neighbour lanes we test the distance to the ahead and behind drones on that lane and its six neighbours (indirect neighbour check). The first step produces a result list with up to six candidate lanes, and in the second step we evaluate the cost function (Equation (5)) for each of the candidate lanes, which is an $O(1)$ operation per candidate lane.

Handling Uncertainty: In a drone road system there will be various and substantial uncertainties and disturbances, for example, wind gusts or noise in GPS position readings. Addressing these uncertainties explicitly will be the subject of future research, in this paper, we focus solely on the uncertainty induced by the underlying communications system (and the packet losses it induces). We clearly expect that new decision algorithms will

be developed that account for such uncertainty, but they will also be addressed in many other ways, e.g., through advances in GPS receiver technology, through appropriate system settings (for example, making lanes wider), and through specifying minimum technical quality requirements for participating drones.

5. Results

We have built a discrete-event simulation model using the OMNeT++ simulation framework (https://www.omnetpp.org (accessed on 13 October 2022)) and using the IEEE 802.11 EDCA implementation provided by the INET framework in version 4.3.2. (https://inet.omnetpp.org (accessed on 13 October 2022)).

In our simulations, we ran 50 independent replications for each considered parameter combination, and we present averaged results. We have also checked the 95% confidence intervals of our calculated averages. These are sufficiently tight, and we have not included them in the figures to avoid visual clutter. Each replication ran for 200 simulated seconds.

5.1. Average Number of Collisions

In Figure 4, we show results for the average number of collisions per kilometre for varying drone generation rate λ, a tube length of $L = 1$ km and all considered variants, including the Blind variant. The curve shown for each variant is its average performance over all combinations of beaconing rate β and $(\epsilon_1^*, \epsilon_2^*)$ combinations. Obviously, the Blind variant is substantially worse than all the other variants, so we will not discuss it any further. In Figure 5, we show results for the average number of collisions for all schemes except the blind one, and for three different beaconing rates $\beta \in \{5\,\text{Hz}, 10\,\text{Hz}, 20\,\text{Hz}\}$. For each of the Crowded, PreferInside and PreferOutside algorithms we have selected a $(\epsilon_1^*, \epsilon_2^*)$ combination with (close to) the lowest number of collisions for inclusion in the graph.

The first (and quite obvious) conclusion is that all considered algorithms provide vast improvements over the Blind algorithm, which we only included as a baseline in the first place. Its performance in the other metrics is clear from its construction: surviving drones will always fly at their preferred speed (hence producing an average speed of 25 m/s) and they will never leave the tube.

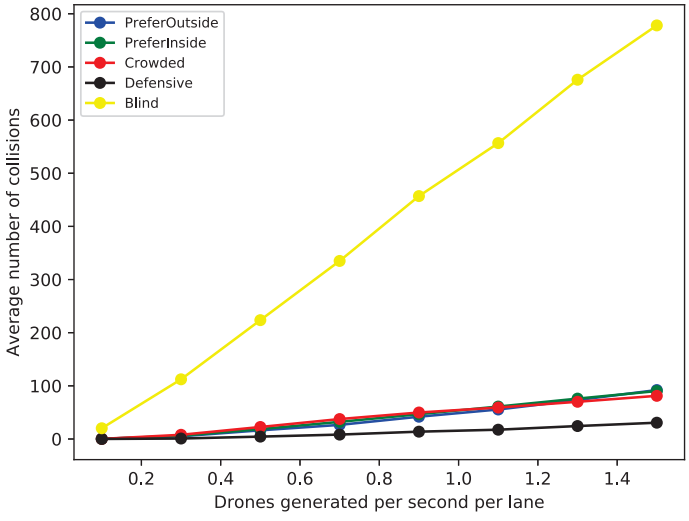

Figure 4. Average number of collisions per kilometre for varying drone generation rate λ and beaconing rate β. $L = 1$ km. With the Blind algorithm.

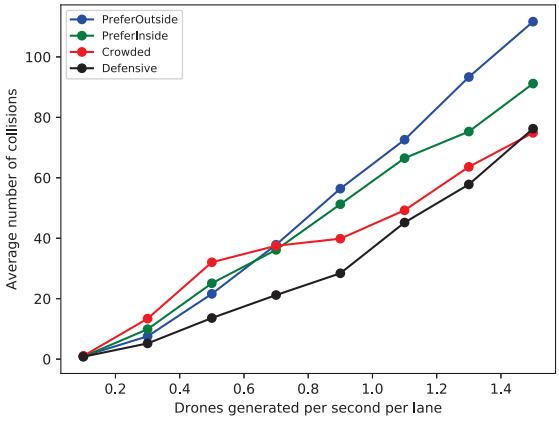

(**a**) 5 Hz beaconing rate.

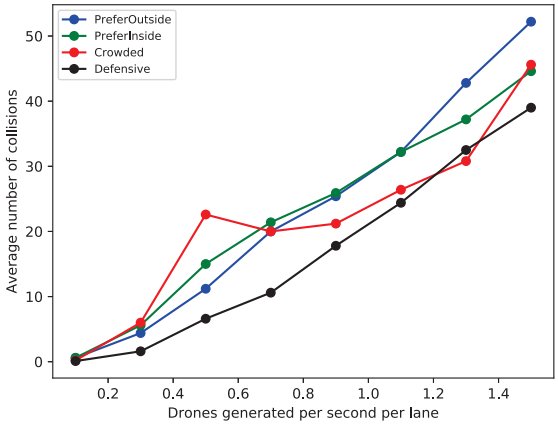

(**b**) 10 Hz beaconing rate.

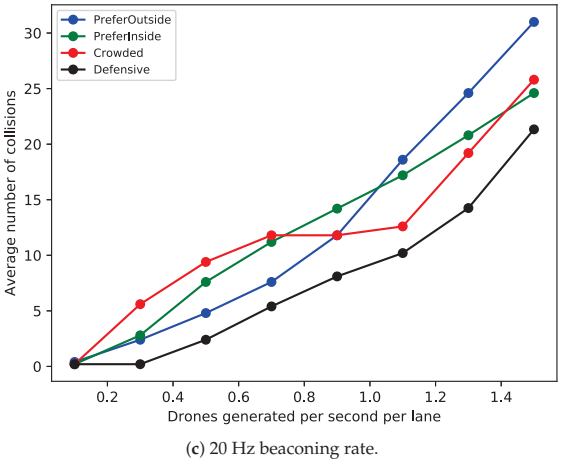

(**c**) 20 Hz beaconing rate.

Figure 5. Average number of collisions per kilometre for varying drone generation rate λ and beaconing rate β, without the Blind algorithm. $L = 1$ km.

The Defensive algorithm shows consistently the best performance, having a genuinely lower average collision rate than any other algorithm. Note that the Defensive algorithm effectively forbids any lane switching, whereas all the other algorithms allow it (either restricted to in-tube lanes or not). This suggests that allowing lane switching increases collision risk. To investigate this further, in Figure 6 we show the average number of lane-switching operations per drone for selected algorithms. The figure confirms that the algorithm allowing the most lane switching operations (PreferOutside) is also the algorithm showing the highest average number of collisions for higher values of the drone generation rate. The Crowded algorithm shows a "non-monotonic" behaviour in Figure 5, its collision rate actually decreases at some point for increasing λ. This can also be explained with reference to Figure 6. The Crowded algorithm is effectively limited to in-tube lanes, and these leave fewer and fewer options for lane switching, so that as λ increases the Crowded algorithm behaves more and more like the Defensive algorithm, leading to a reduction in collisions.

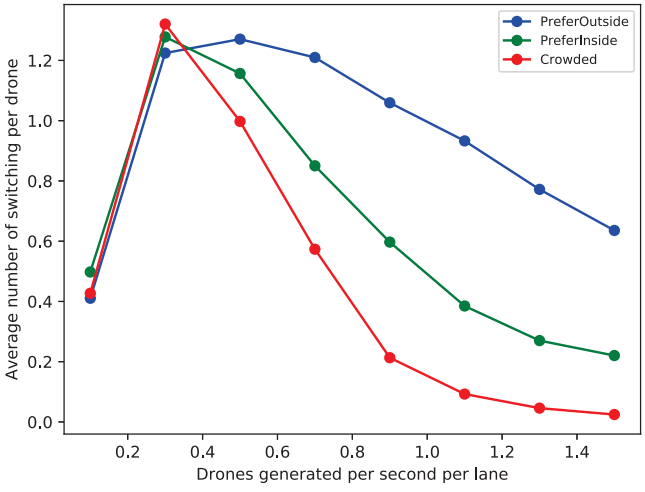

Figure 6. Average number of lane switching operations per drone per kilometre for selected algorithms.

It is also noteworthy to point out the differences between the beaconing rates in Figure 6. The relative performance of the considered algorithms changes, but clearly the overall average collision numbers increase for decreasing beaconing rate.

To investigate the role that concurrent collisions play (see Section 4.1), in Figure 7 we show the average collision count for the considered combinations of $(\epsilon_1^*, \epsilon_2^*)$ and an average beaconing rate of $\beta = 20$ Hz for the for Crowded, PreferOutside and PreferInside algorithms (cf., Section 4.2). It can be observed that for all three algorithms, the variants which disable the check for concurrent collisions show much higher collision counts than the variants which do check for the risk of concurrent collisions and the difference can be quite substantial. Note that for each of these three algorithms we have included the overall (close-to) top-performing variant (with $(\epsilon_1^*, \epsilon_2^*) = (10\,\text{m}, 10\,\text{m})$) in Figure 5 and in all subsequent figures.

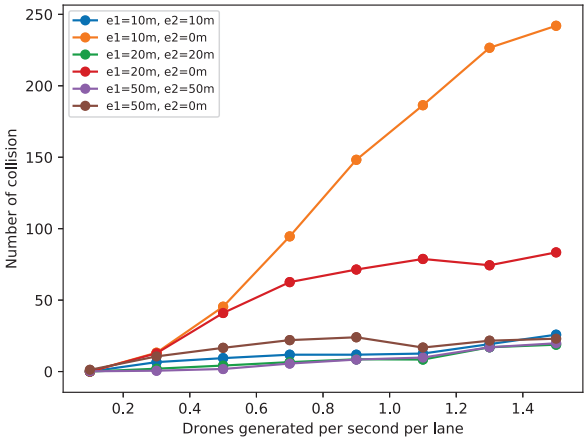

(**a**) Crowded Algorithm.

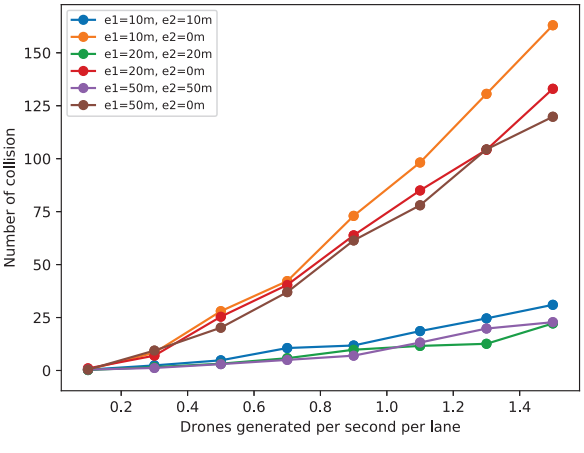

(**b**) PreferOutside Algorithm.

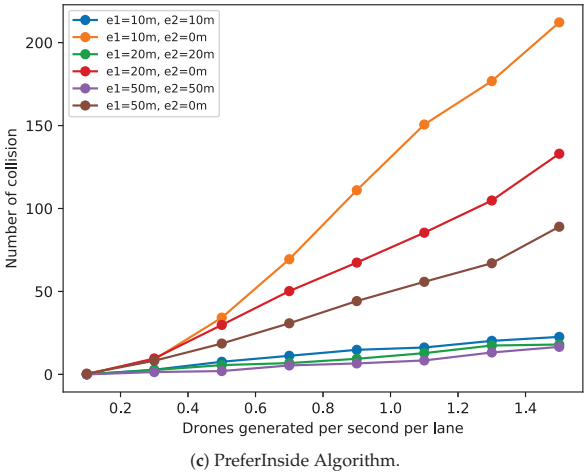

(**c**) PreferInside Algorithm.

Figure 7. Average number of collisions per kilometre for varying drone generation rate λ and different choices for $(\epsilon_1^*, \epsilon_2^*)$, for Crowded, PreferOutside and PreferInside algorithms. $L = 1$ km.

The number of drone collisions increases for all algorithms as the drone generation rate λ increases. Clearly, the higher drone density packs drones more closely and also leads to more packet collisions (either direct or hidden-terminal collisions), which in turn leads to higher uncertainty about the position and speed of neighboured drones, including the ones that are close and pose the highest collision risk. To shed further light on this, in Figure 8 we show the average number of packet losses (as a proxy for packet collision rates), which we have inferred from sequence number gaps observed by receiving nodes. In this figure, we have used a beaconing rate of 20 Hz. As expected, the number of packet losses increases quickly for increasing drone density. The observation that the Defensive, Crowded and PreferInside variants show a higher packet loss count than PreferOutside is likely due to the fact that these variants produce fewer drone collisions than PreferOutside, leading to a higher drone density and, therefore, more packet losses.

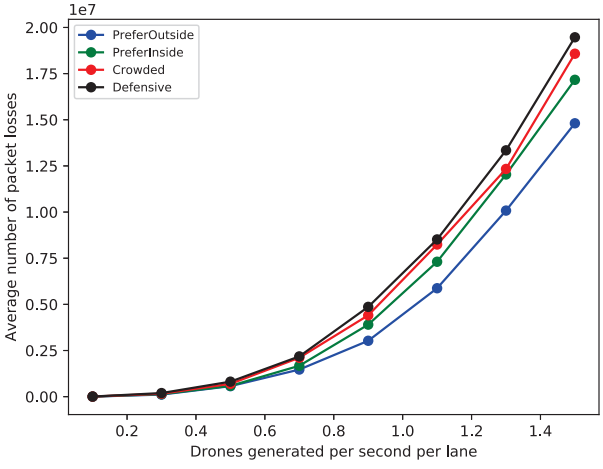

Figure 8. Average number of packet losses per kilometre for selected algorithms at a 20 Hz beaconing rate.

It can also be observed that in general the curves for the higher beaconing rate $\beta = 20\,\text{Hz}$ show better performance over the lower rate $\beta = 10\,\text{Hz}$. Likely, the higher beacon generation rate, while increasing channel congestion, still reduces the average time between receiving beacons from a neighbour, therefore, reducing uncertainty about its position and collision risk. It can be expected though that further increases the beaconing rate are going to increase the collision risk, due to increasing hidden-terminal packet collisions [12].

5.2. Average Speed

In Figure 9 we show the average speed of drones for varying drone generation rate λ, for the Defensive algorithm and the best variants of the Crowded/PreferOutside/PreferInside algorithms as identified in the previous section. As the preferred speeds are drawn from the interval $[20\,\text{m/s}, 30\,\text{m/s}]$, we would expect this average to be 25 m/s if drones avoid slowing down.

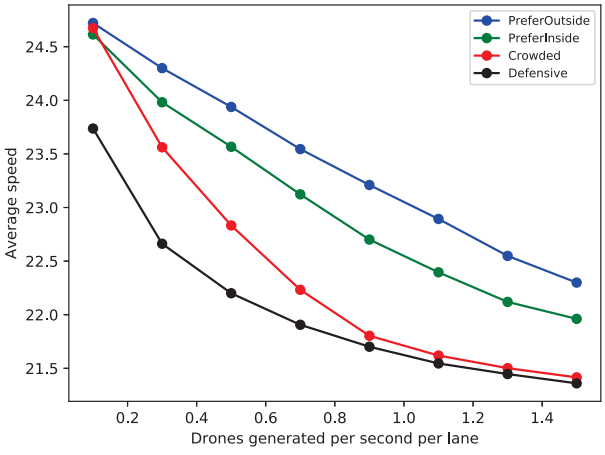

Figure 9. Average speed per kilometre for selected algorithms.

As expected, for all algorithms the average speed decreases as the drone generation rate increases, as there is a higher chance that a drone might have to slow down to adapt to the speed of an ahead drone, while simultaneously having fewer options for lane switching. The Defensive algorithm shows this effect most strongly, as lane switching is effectively ruled out. The Crowded algorithm has second-worst performance, followed by PreferInside, as both algorithms have a tendency to restrict drones to intra-tube lanes. With the PreferOutside algorithm, drones have a stronger tendency to move into out-of-tube lanes, leading to an overall larger number of lanes being used and a lower drone density per lane, which in turn allows for higher speeds. However, recall from Section 5.1 that the PreferOutside algorithm also tends to have the highest collision count for large λ.

We have also investigated the average speed for the different choices of $(\epsilon_1^*, \epsilon_2^*)$ for the Crowded, PreferOutside and PreferInside algorithms (cf., Section 4.2). The results are shown in Figure 10. It can be observed that for all three algorithms the variant that was the best in terms of collision count also had the lowest average speeds, particularly as λ increases.

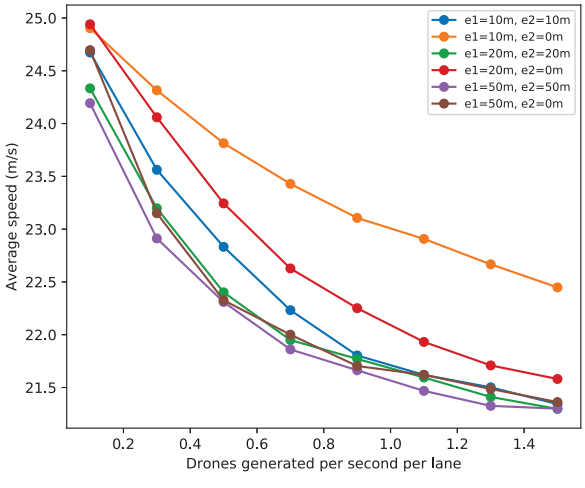

(**a**) Crowded algorithm.

Figure 10. *Cont.*

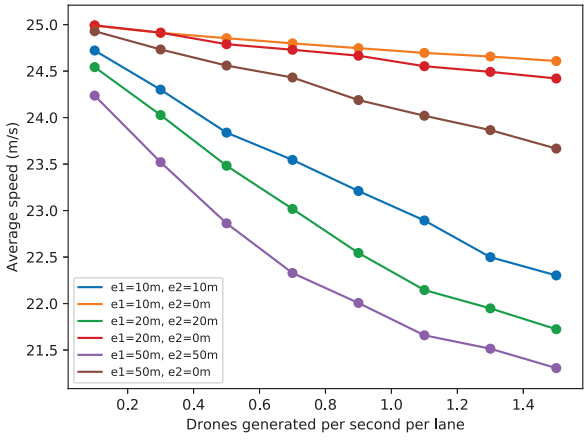

(**b**) PreferOutside algorithm.

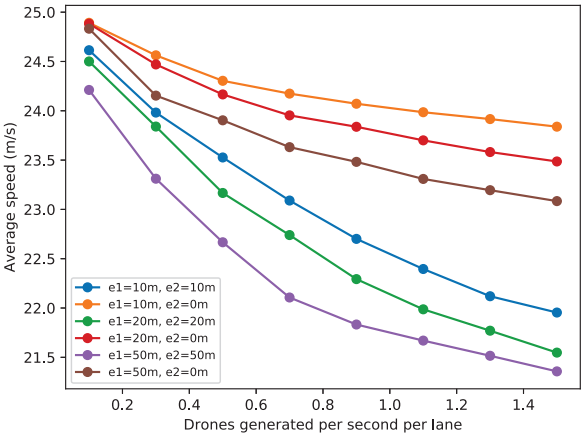

(**c**) PreferInside algorithm.

Figure 10. Average speed for varying drone generation rate λ and different choices for $(\epsilon_1^*, \epsilon_2^*)$, for Crowded, PreferOutside and PreferInside algorithms. $L = 1$ km.

5.3. Average Out-of-Tube Tier

In Figure 11, we show the average out-of-tube tier of drones for the varying drone generation rate λ. Note that algorithms forcing drones to stay inside the tube (Defensive and Crowded) incur a cost of zero, as confirmed in the figure. For the PreferOutside and PreferInside algorithms, the figure confirms that it is indeed possible to achieve different positional behaviours through careful selection of algorithm parameters.

We have investigated the average out-of-tube tier values for the different choices of $(\epsilon_1^*, \epsilon_2^*)$ for the PreferOutside and PreferInside algorithms. For both algorithms, the variant with the lowest average collision count also had the lowest average out-of-tube tier values as λ increases. This is because the variant that includes the most conservative concurrent collision checks is also the most reluctant to switch lanes overall, which also reduces lane-switching operations to out-of-tube lanes.

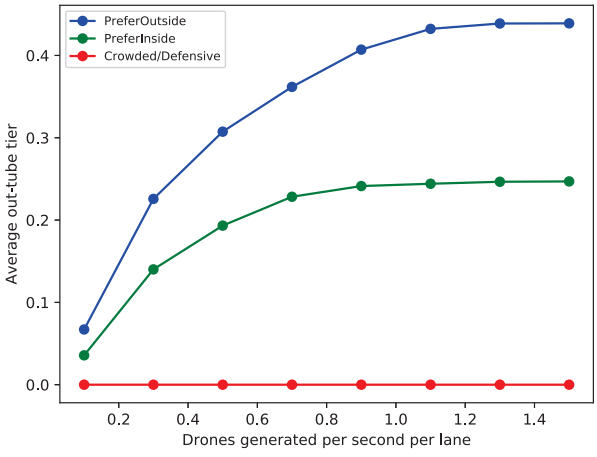

Figure 11. Average out-of-tube tier per kilometre for selected algorithms.

5.4. Discussion

Our results already allow drawing some conclusions. The observation that collision rates increase as the drone density increases is quite expected, and this can certainly in parts be attributed to increased packet loss rates and the resulting increased uncertainty about the positions and speed of neighboured drones.

The presence or absence of a check for concurrent collisions can have a substantial impact on collision rates, and on the willingness of drones to switch lanes. Related to this is the observation that lane switching generally increases the collision risk, even when drones might move out of the tube. At the same time, avoiding lane switching comes at the cost of average speed. Interestingly, the completely rigid Defensive algorithm has a much lower collision count than the much more flexible PreferOutside algorithm, which ought to have plenty of opportunities for drones to avoid collisions by leaving the tube and reducing drone density.

Our results also show a tradeoff between collision count and speed or drone density and one can expect that these tradeoffs will be experienced by any decision algorithm.

Finally, as explained in Section 3.6, for the simulation results presented so far we have chosen parameters that "stress" the system, leading to a perhaps heightened number of collisions. To give a glimpse at the impact of this choice, as an example we show in Figure 12 the average number of collisions for the PreferOutside, PreferInside and Crowded algorithms, in both a "stressed" setting (using the same parameters as previously) and a "normal" setting with more relaxed parameters. In the normal setting, we have used a generation rate of 0.1 drones generated per second per lane, $\epsilon_1^* = \epsilon_2^* = 10\,\mathrm{m}$, a distance of 10 m between lane centre points, a uniform distribution between 10 m/s and 15 m/s for the preferred speed, a 20 Hz beaconing rate and a 10 minimum safety distance d_{safety} between inserted drones. It can be seen that indeed the average collision numbers are substantially lower for the normal setting, while relative performance trends between schemes are broadly preserved.

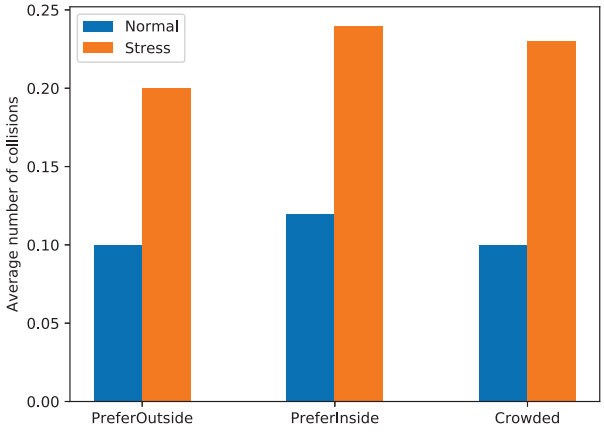

Figure 12. Average number of collisions for selected algorithms under "stressed" and "normal" settings, for a low drone generation rate of 0.1 Hz.

6. Conclusions and Future Work

The construction of a drone road system offers a principled way forward to use drones on a larger scale for deliveries of small goods and other applications in urban environments. Controlling the movements of drones in such a system should follow a distributed approach for scalability reasons. We believe that any decision algorithm by which a drone decides its lane and speed will face the tradeoffs that we have observed, for example, the tradeoff between collision risk and speed or drone density.

Besides its ability to let users adjust their operating points in these tradeoffs by careful parameter selection, the simple decision algorithm presented in this paper is mainly useful as a baseline for more advanced algorithms incorporating additional sensor modalities or additional information exchanged between drones (including active negotiation).

There are many opportunities for future research. The first is to extend the system model for a drone road system by intersections, on- and offramps, arbitrarily curved and oriented tubes and location-dependent cost functions for the speed and position cost, $c_p(\cdot)$ and $c_s(\cdot)$, to accommodate differences in built infrastructure in various parts of a city. Building on such an extended system model, there are then opportunities to design suitable decision algorithms for turning at an intersection or zipping in at onramps. An important addition to the system model (and perhaps to future decision algorithms) will be the explicit consideration of system uncertainty, e.g., positional uncertainty from noisy GPS readings or wind gusts. The system model can also be extended to include a more realistic model of drone dynamics and decision algorithms then can express more fine-grained behaviour for acceleration and deceleration, perhaps including more aspects of the behaviour of human drivers. Beyond this, we can optimize important system parameters such as the beaconing rate, physical layer parameters such as transmit power or the modulation and coding scheme and the parameters of the GreedyLS algorithm, and perform a sensitivity study for these parameters. Besides offline optimization, it is also very interesting to find dynamic adaptation algorithms for particularly important parameters such as the beaconing rate. Finally, since serious experimental work in the construction of drone road systems is still far ahead in the future, it will be quite important to develop simulation tools allowing the efficient simulation of large-scale road systems while preserving important properties of the wireless communications technology and sensors.

Author Contributions: Conceptualization, Z.Q. and A.W.; methodology, Z.Q. and A.W.; software, Z.Q.; validation, Z.Q. and A.W.; formal analysis, Z.Q. and A.W.; investigation, Z.Q. and A.W.; resources, A.W.; data curation, Z.Q.; writing—original draft preparation, A.W. and Z.Q.; writing—review and editing, A.W.; visualization, Z.Q.; supervision, A.W.; project administration, A.W.; funding acquisition, A.W. All authors have read and agreed to the published version of the manuscript.

Funding: This research received no external funding.

Conflicts of Interest: The authors declare no conflict of interest.

References

1. Brunner, G.; Szebedy, B.; Tanner, S.; Wattenhofer, R. The Urban Last Mile Problem: Autonomous Drone Delivery to Your Balcony. In Proceedings of the 2019 International Conference on Unmanned Aircraft Systems (ICUAS), Atlanta, GA, USA, 11–14 June 2019; pp. 1005–1012. [CrossRef]
2. Scott, J.E.; Scott, C.H. Models for drone delivery of medications and other healthcare items. *Int. J. Healthc. Inf. Syst. Informatics* **2018**, *3*, 20–34. [CrossRef]
3. Park, J.; Kim, S.; Suh, K. A comparative analysis of the environmental benefits of drone-based delivery services in urban and rural areas. *Sustainability* **2018**, *10*, 888. [CrossRef]
4. Hong, I.; Kuby, M.; Murray, A. A deviation flow refueling location model for continuous space: A commercial drone delivery system for urban areas. In *Advances in Geocomputation*; Springer: Berlin/Heidelberg, Germany, 2017; pp. 125–132.
5. Li, Y.; Yang, W.; Huang, B. Impact of UAV delivery on sustainability and costs under traffic restrictions. *Math. Probl. Eng.* **2020**, *2020*, 9437605. [CrossRef]
6. Baldisseri, A.; Siragusa, C.; Seghezzi, A.; Mangiaracina, R.; Tumino, A. Truck-based drone delivery system: An economic and environmental assessment. *Transp. Res. Part Transp. Environ.* **2022**, *107*, 103296. [CrossRef]
7. Rashidzadeh, E.; Molana, S.M.H.; Soltani, R.; Hafezalkotob, A. Assessing the sustainability of using drone technology for last-mile delivery in a blood supply chain. *J. Model. Manag.* **2021**, *16*, 1376–1402.
8. Karagiannis, G.; Altintas, O.; Ekici, E.; Heijenk, G.; Jarupan, B.; Lin, K.; Weil, T. Vehicular Networking: A Survey and Tutorial on Requirements, Architectures, Challenges, Standards and Solutions. *IEEE Commun. Surv. Tutorials* **2011**, *13*, 584–616. [CrossRef]
9. Kenney, J.B. Dedicated Short-Range Communications (DSRC) Standards in the United States. *Proc. IEEE* **2011**, *99*, 1162–1182. [CrossRef]
10. Shen, X.; Cheng, X.; Zhang, R.; Jiao, B.; Yang, Y. Distributed Congestion Control Approaches for the IEEE 802.11p Vehicular Networks. *IEEE Intell. Transp. Syst. Mag.* **2013**, *5*, 50 – 61. [CrossRef]
11. Sahoo, J.; Wu, E.H.K.; Sahu, P.K.; Gerla, M. Congestion-Controlled-Coordinator-Based MAC for Safety-Critical Message Transmission in VANETs. *IEEE Trans. Intell. Transp. Syst.* **2013**, *14*, 1423–1437. [CrossRef]
12. Hassan, M.I.; Vu, H.L.; Sakurei, T. Performance Analysis of the IEEE 802.11 MAC Protocol for DSRC Safety Applications. *IEEE Trans. Veh. Technol.* **2011**, *60*, 3882–3896. [CrossRef]
13. Yao, Y.; Rao, L.; Liu, X. Performance and Reliability Analysis of IEEE 802.11p Safety Communication in a Highway Environment. *IEEE Trans. Veh. Technol.* **2013**, *62*, 4198–4212. [CrossRef]
14. Hu, J.; Erzberger, H.; Goebel, K.; Liu, Y. Probabilistic Risk-Based Operational Safety Bound for Rotary-Wing Unmanned Aircraft Systems Traffic Management. *J. Aerosp. Inf. Syst.* **2019**, *17*, 171–181. [CrossRef]
15. Niglio, F.; Comite, P.; Cannas, A.; Pirri, A.; Tortora, G. Preliminary Clinical Validation of a Drone-Based Delivery System in Urban Scenarios Using a Smart Capsule for Blood. *Drones* **2022**, *6*, 195. [CrossRef]
16. Valencia-Arias, A.; Rodriguez-Correa, P.A.; Patino-Vanegas, J.C.; Benjumea-Arias, M.; Cruz-Vargas, J.D.L.; Moreno-Lopez, G. Factors Associated with the Adoption of Drones for Product Delivery in the Context of the COVID-19 Pandemic in Medellin, Colombia. *Drones* **2022**, *6*, 225. [CrossRef]
17. Hayat, S.; Yanmaz, E.; Muzaffar, R. Survey on Unmanned Aerial Vehicle Networks for Civil Applications: A Communications Viewpoint. *IEEE Commun. Surv. Tutorials* **2016**, *18*, 2624–26621. [CrossRef]
18. Gharibi, M.; Gharibi, Z.; Boutaba, R.; Waslander, S.L. A Density-Based and Lane-Free Microscopic Traffic Flow Model Applied to Unmanned Aerial Vehicles. *Drones* **2021**, *5*, 116. [CrossRef]
19. Kim, Y.; Bae, J. Risk-Based UAV Corridor Capacity Analysis above a Populated Area. *Drones* **2022**, *6*, 221. [CrossRef]
20. Bijjahalli, S.; Gardi, A.; Pongsakornsathien, N.; Sabatini, R.; Kistan, T. A Unified Airspace Risk Management Framework for UAS Operations. *Drones* **2022**, *6*, 184. [CrossRef]
21. Schweiger, K.; Preis, L. Urban Air Mobility: Systematic Review of Scientific Publications and Regulations for Vertiport Design and Operations. *Drones* **2022**, *6*, 179. [CrossRef]
22. Zhou, Y.; Rao, B.; Wang, W. UAV Swarm Intelligence: Recent Advances and Future Trends. *IEEE Access* **2020**, *8*, 183856–183878. [CrossRef]
23. Wu, Z.; Li, J.; Zuo, J.; Li, S. Path Planning of UAVs Based on Collision Probability and Kalman Filter. *IEEE Access* **2018**, *6*, 34237–34245. [CrossRef]
24. Li, Q.; Li, R.; Ji, K.; Dai, W. Kalman filter and its application. In Proceedings of the 2015 8th International Conference on Intelligent Networks and Intelligent Systems (ICINIS), Tianjin, China, 1–3 November 2015; pp. 74–77.

25. Ragi, S.; Chong, E.K.P. UAV Path Planning in a Dynamic Environment via Partially Observable Markov Decision Process. *IEEE Trans. Aerosp. Electron. Syst.* **2013**, *49*, 2397–2412. [CrossRef]
26. Miller, S.A.; Harris, Z.A.; Chong, E.K. A POMDP framework for coordinated guidance of autonomous UAVs for multitarget tracking. *Eurasip J. Adv. Signal Process.* **2009**, *2009*, 1–17. [CrossRef]
27. Hu, J.; Yang, X.; Wang, W.; Wei, P.; Ying, L.; Liu, Y. Obstacle Avoidance for UAS in Continuous Action Space Using Deep Reinforcement Learning. *IEEE Access* **2022**, *10*, 90623 – 90634. [CrossRef]
28. Yu, H.; Meier, K.; Argyle, M.; Beard, R.W. Cooperative Path Planning for Target Tracking in Urban Environments Using Unmanned Air and Ground Vehicles. *IEEE/ASME Trans. Mechatronics* **2015**, *20*, 541–552. [CrossRef]
29. Liu, X.; Du, X.; Zhang, X.; Zhu, Q.; Guizani, M. Evolution-algorithm-based unmanned aerial vehicles path planning in complex environment. *Comput. Electr. Eng.* **2019**, *80*, 106493. . [CrossRef]
30. Wischhof, L.; Rohling, H. Congestion control in vehicular ad hoc networks. In Proceedings of the IEEE International Conference on Vehicular Electronics and Safety, Shaanxi, China, 14–16 October 2005, pp. 58–63. [CrossRef]
31. Zhang, W.; Festag, A.; Baldessari, R.; Le, L. Congestion control for safety messages in VANETs: Concepts and framework. In Proceedings of the 2008 8th International Conference on ITS Telecommunications, Phuket, Thailand, 24 October 2008; pp. 199–203. [CrossRef]
32. Bouassida, M.S.; Shawky, M. On the congestion control within VANET. In Proceedings of the 2008 1st IFIP Wireless Days, Dubai, United Arab Emirates, 24–27 November 2008; pp. 1–5. [CrossRef]
33. Le, L.; Baldessari, R.; Salvador, P.; Festag, A.; Zhang, W. Performance Evaluation of Beacon Congestion Control Algorithms for VANETs. In Proceedings of the 2011 IEEE Global Telecommunications Conference-GLOBECOM, Houston, TX, USA, 5–9 December 2011; pp. 1–6. [CrossRef]
34. Kolte, S.R.; Madankar, M.S. Adaptive congestion control for transmission of safety messages in VANET. In Proceedings of the International Conference for Convergence for Technology, Pune, India, 6–8 April 2014; pp. 1–5. [CrossRef]
35. Sangaiah, A.K.; Ramamoorthi, J.S.; Rodrigues, J.J.; Rahman, M.A.; Muhammad, G.; Alrashoud, M. LACCVoV: Linear adaptive congestion control with optimization of data dissemination model in vehicle-to-vehicle communication. *IEEE Trans. Intell. Transp. Syst.* **2020**, *22*, 5319–5328. [CrossRef]
36. Bansal, G.; Cheng, B.; Rostami, A.; Sjoberg, K.; Kenney, J.B.; Gruteser, M. Comparing LIMERIC and DCC approaches for VANET channel congestion control. In Proceedings of the 2014 IEEE 6th International Symposium on Wireless Vehicular Communications (WiVeC 2014), Vancouver, BC, Canada, 14–15 September 2014, pp. 1–7. [CrossRef]
37. Fabra, F.; Calafate, C.T.; Cano, J.C.; Manzoni, P. On the impact of inter-UAV communications interference in the 2.4 GHz band. In Proceedings of the 2017 13th International Wireless Communications and Mobile Computing Conference (IWCMC), Valencia, Spain, 26–30 June 2017, pp. 945–950. [CrossRef]
38. Khalifeh, A.F.; AlQudah, M.; Tanash, R.; Darabkh, K.A. A Simulation Study for UAV- Aided Wireless Sensor Network Utilizing ZigBee Protocol. In Proceedings of the 2018 14th International Conference on Wireless and Mobile Computing, Networking and Communications (WiMob), Limassol, Cyprus, 15–17 October 2018; pp. 181–184. [CrossRef]
39. Ramya, C.M.; Shanmugaraj, M.; Prabakaran, R. Study on ZigBee technology. In Proceedings of the 2011 3rd International Conference on Electronics Computer Technology, Kanyakumari, India, 8–10 April 2011; Volume 6, pp. 297–301.
40. James, S.; Raheb, R.; Hudak, A. Impact of Packet Loss to the Motion of Autonomous UAV Swarms. In Proceedings of the 2020 AIAA/IEEE 39th Digital Avionics Systems Conference (DASC), Virtual Conference 2020; pp. 1–9. [CrossRef]
41. James, S.; Raheb, R. Path Planning for Critical ATM/UTM Areas. In Proceedings of the 2019 IEEE/AIAA 38th Digital Avionics Systems Conference (DASC), San Diego, CA, USA, 8–12 September 2019; pp. 1–6.
42. Berg, J.v.d.; Guy, S.J.; Lin, M.; Manocha, D. Reciprocal n-body collision avoidance. In *Robotics Research*; Springer: Berlin/Heidelberg, Germany, 2011; pp. 3–19.
43. Buonocore, L.R.; Lippiello, V.; Manfredi, S.; Ruggiero, F.; Siciliano, B. Effects of Packet Losses on Formation Control of Unmanned Aerial Vehicles. *IFAC Proc. Vol.* **2014**, *47*, 1234–1240. [CrossRef]
44. Anderson, B.; Fidan, B.; Yu, C.; Walle, D. UAV formation control: Theory and application. In *Recent Advances in Learning and Control*; Springer: Berlin/Heidelberg, Germany, 2008; pp. 15–33.
45. Shiyou, D.; Xiaoping, Z.; Guoqing, L. The null-space-based behavioral control for swarm unmanned aerial vehicles. In Proceedings of the 2011 First International Conference on Instrumentation, Measurement, Computer, Communication and Control, Beijing, China, 21–23 October 2011; pp. 1003–1006.
46. IEEE Computer Society, Sponsored by the LAN/MAN Standards Committee. *IEEE Standard for Information technology—Telecommunications and Information Exchange between Systems—Local and Metropolitan Area Network—Specific Requirements—Part 11: Wireless LAN Medium Access Control (MAC) and Physical Layer (PHY) Specifications*; IEEE: New York, NY, USA, 2016.
47. Rappaport, T.S. *Wireless Communications—Principles and Practice*; Prentice Hall: Upper Saddle River, NJ, USA, 2002.

drones

MDPI

Article

RF Source Localization Using Multiple UAVs through a Novel Geometrical RSSI Approach

Nurbanu Güzey

Department of Electrical-Electronics Engineering, Sivas University of Science and Technology, Sivas 58000, Turkey; nurbanu.guzey@sivas.edu.tr

Abstract: In this paper, a novel geometrical localization scheme based on the Received Signal Strength Indicator (RSSI) is developed for a group of unmanned aerial vehicles (UAVs). Since RSSI-based localization does not require complicated hardware, it is the correct choice for RF target localization. In this promising work, unlike the other techniques given in the literature, transmit power or path loss exponent information is not needed. The procedure depends on the received power difference of each receiver in UAVs. In the developed scheme, four UAVs forming two groups fly in perpendicular planes. Each UAV in the group moves in a circle, keeping its distance from the plane's center until it gets equal power with the other members of its group. Using this movement rate, lines passing through the source position are calculated. The intersection of these lines gives the position of the RF target. However, in a noisy environment, the lines do not intersect at one point. Therefore, the algorithm given in the manuscript finds a point that has a minimum distance to all lines and is also developed. Simulation results are provided at the end of the manuscript to verify our theoretical claims.

Keywords: localization; received signal strength indicator; unmanned aerial vehicles

Citation: Güzey, N. RF Source Localization Using Multiple UAVs through a Novel Geometrical RSSI Approach. *Drones* **2022**, *6*, 417. https://doi.org/10.3390/drones6120417

Academic Editors: Andrzej Łukaszewicz, Wojciech Giernacki, Zbigniew Kulesza, Jaroslaw Pytka and Andriy Holovatyy

Received: 9 November 2022
Accepted: 12 December 2022
Published: 15 December 2022

1. Introduction

Unmanned Aerial Vehicles (UAVs) and other new smartly linked platforms have become increasingly integrated into the Internet of Things, which is a vast global network (IoT). UAVs not only provide a practical solution to the drawbacks of fixed terrestrial IoT infrastructure, but also new ways to supply value-added IoT services through a variety of applications ranging from monitoring and surveillance to on-demand last-mile deliveries and people transport. UAVs are predicted to soon be a vital component of our cities and rule the common low-altitude airspace if they live up to their potential [1].

Localization and tracking are crucial issues to be solved in commercial and military applications such as air traffic control, remote sensing, and intelligence, surveillance, and reconnaissance (ISR) [2]. Initially, ground-based methods were used to conduct localization. However, due to the fast development of UAVs and sensor technology, UAVs are now able to be used as airborne sensing devices. Furthermore, some applications, such as search and rescue missions, may require only aerial localization. The aerial vehicles' mobility and extensive eyesight allow for successful and fast localization. Furthermore, flying above ground level decreases signal propagation uncertainty due to obstacles and enhances RF target identification. However, when the UAV wanted to follow a trajectory to track a target, a control methodology was required. In [3], a vector-field method is proposed that does not require knowledge of course dynamics or wind. In [4,5], an autopilot control system is proposed.

Apart from search, rescue, and surveillance operations, UAVs are also used in smart city applications where high technologies such as IoT and deep learning are used. In [6], it is recommended to use computer vision and deep learning techniques in UAVs to improve the quality of life of visually impaired individuals. UAVs are also used to detect, locate,

and track unauthorized UAVs, which have been identified as of the utmost priority both in military and civilian settings. In [7], an intermittent RF source is tracked with a UAV swarm.

2. Related Work

The localization of an RF target by using UAVs is studied in the literature in a number of different ways. Some of the existing approaches include visual characteristics [8], RF time of arrival [9], angle of arrival [10], time difference of arrival [11], Doppler and direction of arrival [12,13], and received signal strength indicator (RSSI) [14–16]. Additionally, there are techniques that directly track the target using GPS or range and angle sensors [17,18]. In [19], Bluetooth is used instead of GPS, and localization is enhanced with an intelligent camera module.

Visual feature-based algorithms are effective in locating an item in a variety of situations; however, they may suffer in long-range localization operations, particularly when vision is obscured, or light conditions are poor [20]. Thermal cameras can help with this problem, but when the weather is hot, they can produce a lot of false positives. Time of arrival and angle of arrival techniques require more complicated antennas and synchronization challenges that might arise owing to the mobility of UAVs. Thus, in some circumstances, the hardware configuration for determining the signal's direction may not be accessible, and the UAVs may be forced to depend only on the signal strength to locate the target. Furthermore, because of the importance of energy restrictions in UAVs, a simpler method is typically used to ensure that flight duration is increased, and the mission is accomplished within the time constraints. RSSI techniques may yield promising outcomes in this scenario.

Because of this, RSSI-based localization and tracking have been studied in the literature. For example, [16] introduces an RSSI tracking method that makes use of the law of cosines along with estimated distances from the RF source to determine the steering angle that points the tracking agent toward the target. However, they presuppose a fixed transmit power that cannot always be met. A particle filter approach [21] and RSSI-based method are presented in [22], where the transmit power is estimated with an artificial neural network before the localization process, which makes the procedure more complicated.

Particularly, UAVs flying in a predefined formation can locate and follow a target of interest in order to gather information or deliver critical services [23]. In [24], it outlines a set of UAVs with RSSI sensors that conduct trilateration, with the target's position established by a fusion center and the distances from the RF source approximated using the log-normal shadowing model. For the localization of stationary RF targets in non-convex settings, estimation and control techniques for a team of robots were presented in [25]. In [26], differential RSSI (DRSSI) model is used for localization. The difference in received signal powers by the UAVs is used to calculate the heading angles of the UAVs. Furthermore, DRSSI measurements are enhanced with an Extended Kalman Filter for more accurate results.

In our previous study, UAV groups used the signal strength difference received by the UAVs for target localization. The UAV group was positioned above the target on the x and y axes by preserving the formation. Since the position of the formation center is known, the position of the target is determined [27]. Table 1 gives a summary of selected localization methods.

This study examines a swarm of cooperative UAVs that are outfitted with basic RSSI sensors and coordinate their movements to localize an object that emits radio waves. The system is based on comparing the signal strengths received by the antennas carried by four UAVs, which are divided into two groups. Each group consists of two UAVs. In each group, UAVs move in a circular manner in the plane they fly to receive equal signal power with their group mate. The UAV that is closer to the source moves away from the source, and the UAV that is far from the source approaches the source at the same rate, and they acquire equal power. By using the moving rate for each group, the location of the RF source is calculated geometrically. Further, no time synchronization of transmitter and receiver

antennas is required in this approach. Two circles are designed, one in the *x*-*y* plane and the other in the *x*-*z* plane, which are perpendicular to each other, and their centers are fixed. The desired trajectories of the UAVs are calculated in real-time so that they remain on these circles. The movements of the UAVs on the circle are calculated according to the difference in the signal strength they receive. With the PID logic, the UAVs are moved so that the difference in the received signal power will be zero. In the developed algorithm, a total of four UAVs were used, two in the *x*-*y* plane and two in the *x*-*z* plane. These are the minimum numbers for the algorithm to work. Target localization accuracy can be increased by using more UAVs. In addition, using more than four UAVs will increase the cost in practice.

Table 1. Comparison of different localization techniques.

Study	Method	Advantages	Limitation/Disadvantages
S. M. Denghan et al. [26]	Differential RSSI	Transmit power value is not required	Nonlinear modeling for FIM and EKF
Hasanzade et al. [22]	RSSI with EKF	Noise reduction with EKF	Transmit power value required, it is estimated with NN
Hasanzade et al. [22]	RSSI with Particle Filter	Only one UAV is requied	High computational complexity of Partical Filter
Zhou et al. [19]	Both RSSI and Visual localiation	Localization with Bluetooth	Images can be poor for some circumtances

The research objective in this study is:

- Ability to do localization in GPS-denied environments.
- Ability to do localization without knowing the output power of the target and without the need for time synchronization between the transceiver and receiver antennas

The contribution of this article can be summarized as follows:

- For environments with weak GPS signals, a novel geometry-based localization method has been developed.
- Since the receiving antennas are on the UAVs, a method has been developed that will make it possible to detect the target location more precisely by increasing the distances between the UAVs.
- An augmented point on the sphere is calculated where the line passing through this point and sphere center also passes through the target position.

The rest of the paper is organized as follows: in Section 3, background on RSSI and methodology of the proposed method are given, simulation results to verify the given method are mentioned in Section 4, and the conclusion of this study and future work are offered in Section 5.

3. Materials and Method

The details of RSSI-based localization using UAVs are given in this section. RSSI is the technique that calculates the power of the signal strength at the receiver as a function of different parameters, such as transmitting power, characteristics of the receiver and transmitter antennas, distance between the receiver and transmitter, etc. [28]. Measured signal strength can be converted to the distance between the transmitter and the receiver. In space, as the distance between the transmitter and receiver changes, the signal strength also changes. This can be measured by using the following Friis equation [28]:

$$P_r = P_t D_r D_t \left(\frac{\lambda}{4\pi d}\right)^{\gamma} + N(0, \sigma) \quad (1)$$

where P_t is the transmitted signal power from the transmitter, d is the distance between the emitter and receiver, γ is the path loss exponent, and λ is the wavelength of the transmitted signal. An additive Gaussian noise N is included within the equation to model error caused

by reflections, measurements, and so on. The path loss exponent γ can take a value between the range 2 and 4 due to different environmental conditions. It can also exceed this bound under some special conditions [29].

In this manuscript, an RSSI-based geometrical solution is proposed to the localization problem of RF devices in a GPS-denied environment.

The algorithm is derived in the presence of two major challenges:

- There is no prior information on the target's location.
- Signal strength is all that is measured by UAVs; there is no time stamp or other useful information in the signal. There is no direction-finding hardware on board.

To solve the problem, the following two conditions are assumed:

- There is always a clear line of sight between the UAVs and the target.
- There are no communication limitations; UAVs may send and receive data without losing information.

The details of the method are given in the following subsections. In the first subsection, the desired posture (3D Cartesian location) of each UAV is calculated so that the UAVs would move on two perpendicular circles. One of the circles is in the *x*-*y* plane and at a distance *r* from the center, and the other is chosen in the *x*-*z* plane and at a distance *r* from the center. In the second subsection, rotating angles are calculated that will allow the UAVs to rotate on the circle while maintaining the 2*r* distance between them. The derivatives of the rotating angles are calculated using the difference in received signal powers.

3.1. Desired Initial Posture Derivation of Four UAVs

Suppose there are four UAVs equipped with RSSI receivers in arbitrary initial locations. Their initial desired locations are derived as follows:

$$\begin{array}{lll} x_1^d(t_0) = x_c - r\cos(\alpha(t_0)) & y_1^d(t_0) = y_c - r\sin(\alpha(t_0)) & z_1^d = z_c \\ x_3^d(t_0) = x_c + r\cos(\alpha(t_0)) & y_3^d(t_0) = y_c + r\sin(\alpha(t_0)) & z_3^d = z_c \\ x_2^d(t_0) = x_c - r\sin(\beta(t_0)) & y_2^d = y_c & z_3^d(t_0) = z_c - r\cos(\beta(t_0)) \\ x_4^d(t_0) = x_c + r\cos(\beta(t_0)) & y_4^d = y_c & z_4^d(t_0) = z_c + r\sin(\beta(t_0)) \end{array} \quad (2)$$

where $C(x_c, y_c, z_c)$ is the center of the formation, r is the radius of the circles, $\alpha(t_0)$ and $\beta(t_0)$ are the initial rotation angles, given as in Figure 1, defined by the user, and t_0 is the initial time. D1 and D3 UAVs form a group in the *x*-*y* plane, while D2 and D4 UAVs form another group in the *x*-*z* plane.

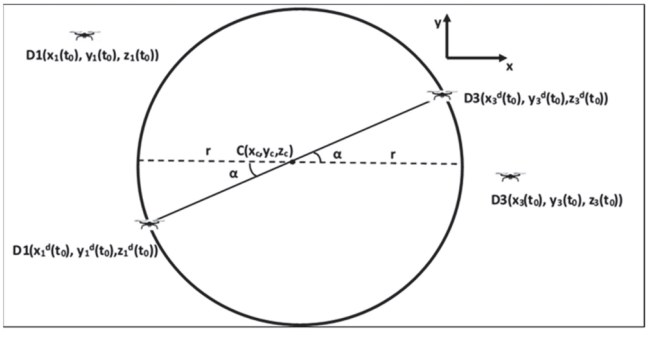

Figure 1. *Cont.*

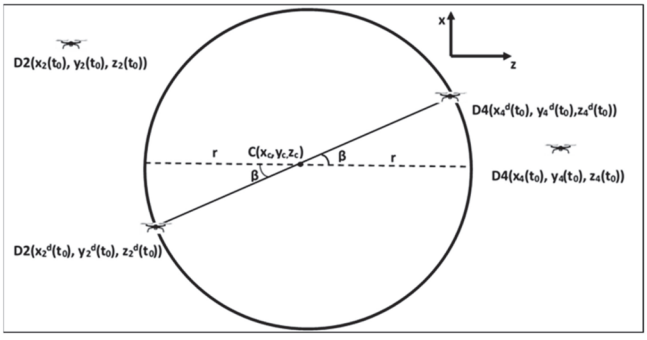

Figure 1. Initial and desired locations of the UAVs.

The desired initial postures (2) of the UAVs moving both in the *x-y* axis and in the *x-z* axis are calculated in a way that satisfies two basic constraints: (i) Both UAVs are at a distance of r from the center; (ii) the distance between two UAVs is 2*r*. Thus, UAVs move on the predetermined circle, and the distance between the UAVs is fixed. Derivation of the rotating angle dynamics is given in the next subsection.

3.2. Rotating Angle Calculation

To find the direction of the target in both vertical and horizontal planes, the signal power differences are defined as follows:

$$\begin{aligned} e_1 &= P_3 - P_1 \\ e_2 &= P_4 - P_2 \end{aligned} \tag{3}$$

where $P_1, \ldots, P_4$ are the received signal powers by $D_1, \ldots, D_4$, respectively, while e_1 is obtained from the difference in signal strengths of the 3rd UAV and the 1st UAV, e_2 is obtained from the power differences of the 4th UAV and the 2nd UAV. Then the error dynamics are given as follows:

$$\begin{aligned} \dot{e}_1 &= \dot{P}_3 - \dot{P}_1 \\ \dot{e}_2 &= \dot{P}_4 - \dot{P}_2 \end{aligned} \tag{4}$$

Two UAVs moving in the *x-z* axis are used to find the horizontal direction of the target, whereas UAVs moving in the *x-y* plane are used to find the vertical direction of the target. Derivation of α and β are calculated to make the difference of the signal strength received by the two UAVs zero. PID controller logic is used, and derivative of α was defined as the function of e_1 and derivative β as the function of e_2. The desired rotating angle dynamics are defined as:

$$\begin{aligned} \dot{\alpha} &= k_P e_1 + k_I \int_{t_0}^{t} e_1(\tau) d\tau + k_D \dot{e}_1 \\ \dot{\beta} &= k_P e_2 + k_I \int_{t_0}^{t} e_2(\tau) d\tau + k_D \dot{e}_2 \end{aligned} \tag{5}$$

where $k_P > 0$, $k_I > 0$, and $k_D > 0$ are design parameters. Then the current rotating angles are found as:

$$\begin{aligned} \alpha(t) &= \alpha(t_0) + \int_{t_0}^{t} \dot{\alpha}(\tau) d\tau \\ \beta(t) &= \beta(t_0) + \int_{t_0}^{t} \dot{\beta}(\tau) d\tau \end{aligned} \tag{6}$$

Changing the α and β in time (6) will automatically change the desired locations of the UAVs according to (7). This change continues until e_1 and e_2 converges to zero or a pre-defined and tolerable error bound.

$$\begin{array}{lll} x_1^d(t) = x_c - r\cos(\alpha(t)) & y_1^d(t) = y_c - r\sin(\alpha(t)) & z_1^d = z_c \\ x_3^d(t) = x_c + r\cos(\alpha(t)) & y_3^d(t) = y_c + r\sin(\alpha(t)) & z_3^d = z_c \\ x_2^d(t) = x_c - r\sin(\beta(t)) & y_2^d = y_c & z_3^d(t) = z_c - r\cos(\beta(t)) \\ x_4^d(t) = x_c + r\cos(\beta(t)) & y_4^d = y_c & z_4^d(t) = z_c + r\sin(\beta(t)) \end{array} \tag{7}$$

Remark: Consider the scenario shown in Figure 2, they detect a target while flying. The received signal power in each group is compared by itself, and UAVs move in their planes until they receive equal signal power. In this scenario, D4 gets more power than D2, so D4 moves away from the target and D2 moves towards the target. Same as for D1 and D3, D1 receives less power than D3, therefore D1 approaches to the target while D3 moves away from the target, as given in Figure 3.

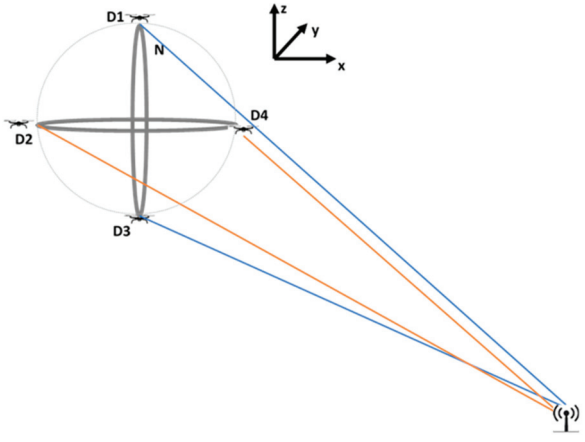

Figure 2. UAVs fly in the desired initial location with different received signal strengths.

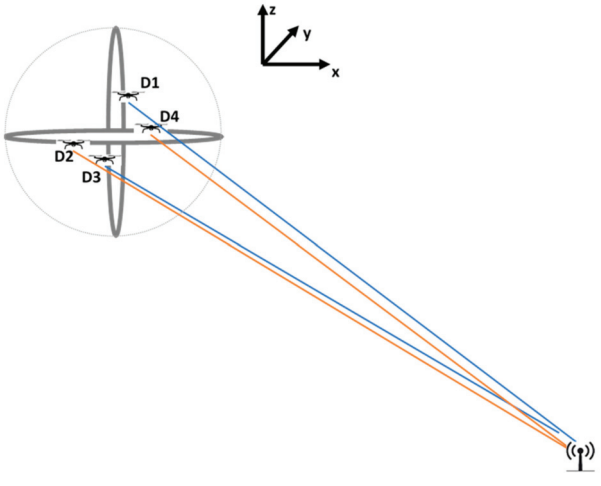

Figure 3. UAVs move in a circular formation to receive the same RSSI value.

Next, the augmented point and the lines that pass through the target position are calculated.

3.3. Augmented Point and Direction Calculation

When power errors are within a tolerable error range, the plane formed by the line through the D1–D3 and the line through the D2–D4 is calculated. The line that will be perpendicular to this plane and pass through the center is determined. As the first step in calculating the line, an augmented point is calculated on the sphere formed by the perpendicular circles.

An augmented point, $A(x_{aug}, y_{aug}, z_{aug})$, is defined on the sphere, which has equal distance to each UAV and satisfies the criteria below:

$$\begin{aligned}
&\sqrt{(x_a - x_c)^2 + (y_a - y_c)^2 + (z_a - z_c)^2} = r \\
&da_1 = \sqrt{(x_a - x_1^d)^2 + (y_a - y_1^d)^2 + (z_a - z_1^d)^2} \\
&da_2 = \sqrt{(x_a - x_2^d)^2 + (y_a - y_2^d)^2 + (z_a - z_2^d)^2} \\
&da_3 = \sqrt{(x_a - x_3^d)^2 + (y_a - y_3^d)^2 + (z_a - z_3^d)^2} \\
&da_4 = \sqrt{(x_a - x_4^d)^2 + (y_a - y_4^d)^2 + (z_a - z_4^d)^2} \\
&da_1 = da_2 = da_3 = da_4
\end{aligned} \tag{8}$$

with these criteria (8), the augmented point is calculated as follows:

$$\begin{aligned}
r_a &= |r\cos(\beta)| \\
z_{aug} &= z_c + r\sin(\alpha)\sin(\beta) \\
x_{aug} &= x_c - r_a\sin(\alpha) \\
y_{aug} &= y_c - r_a cos(\alpha)
\end{aligned} \tag{9}$$

Claim: The line passes through the sphere's center $C(x_c, y_c, z_c)$ and the augmented point $A(x_{aug}, y_{aug}, z_{aug})$ also intersects the target position. The definition of the line passing through the $A(x_{aug}, y_{aug}, z_{aug})$ and $C(x_c, y_c, z_c)$ is derived as follows:

$$\begin{aligned}
y &= \tfrac{x - x_{aug}}{x_c - x_{aug}}\left(y_c - y_{aug}\right) + y_{aug} \\
z &= \tfrac{y - y_{aug}}{y_c - y_{aug}}\left(z_c - z_{aug}\right) + z_{aug}
\end{aligned} \tag{10}$$

This line is in the direction of the source. For the sake of localization, the group of UAVs is moved while keeping the consensus to receive equal signal power. In their new location, a new line is generated with new angles. This procedure is conducted multiple times. Since all the lines are directed through the source, their intersection will give the location of the source. In a noise-free environment, two lines are enough to locate the target. However, since signal power may be seriously influenced by the environment and may have a high level of noise, the lines may not intersect at one point. In a noisy environment, the lines may not go through the source. Therefore, the point that has the shortest distance to all lines is assigned as the source location. The Algorithm 1 that gives the minimum distance to all lines is given in below. The overall framework of the proposed localization process is given in the flowchart given in Figure 4.

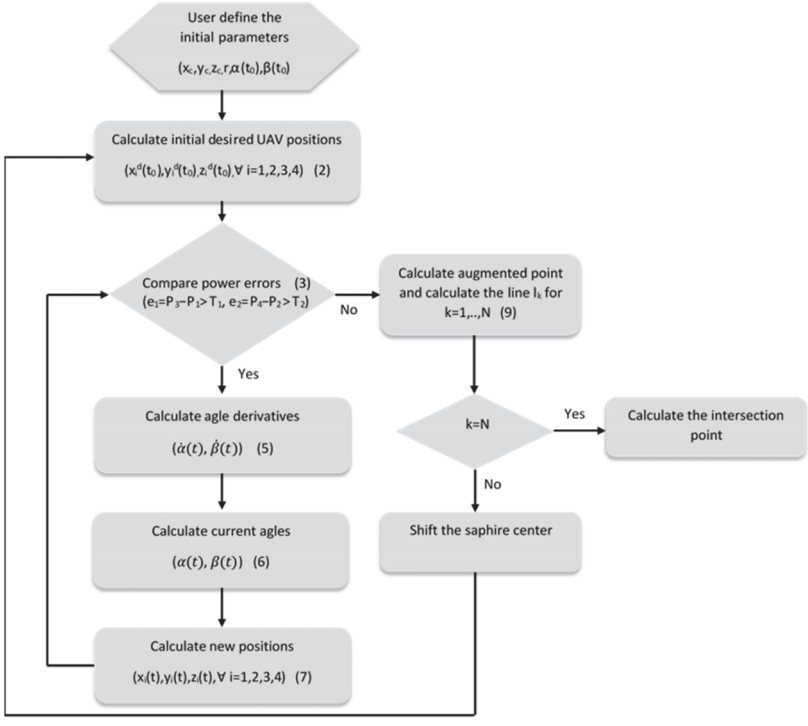

Figure 4. Flowchart of proposed localization method.

Algorithm 1: Minimum distance to lines calculation (x_{est_f},y_{est_f},z_{est_f}).

Set n = length of line segments, N = number of line segments; P is a very large constant
$p = 1$;
for $k = 1$ *to* N;
  for $m = 1$ *to* N
    if $m \neq k$
  $d_{\min} = P$
  for $i = 1$ *to* n
    for $j = 1$ *to* n
      $d = \sqrt{(x(k,i) - x(m,j))^2 + (y(k,i) - y(m,j))^2 + (z(k,i) - z(m,j))^2}$
        if $d < d_{min}$
          $d_{min} = d, i_{min} = i, j_{min} = j,$
        end if
      end for
    end for
  $x_{est}(p) = \frac{x(k,i_{\min}) + x(m,j_{\min})}{2}$, $y_{est}(p) = \frac{y(k,i_{\min}) + y(m,j_{\min})}{2}$, $z_{est}(p) = \frac{z(k,i_{\min}) + z(m,j_{\min})}{2}$
    $p = p + 1$
    end for
  end for
end for

4. Results

In this section, the performance of the proposed method is given. Localization of a target in a 1×1 km^2 search area was considered for simulation studies. The target is assumed to be on the ground. In the beginning, UAVs search the GPS-denied area until

they receive an RF signal. Then they rotate on the given circles until the UAVs in each group receive equal power.

As mentioned above, the line intersects the augmented point, and the formation center will also intersect the source position as given in Figure 5. Movements of UAVs on the sphere and the angles are also demonstrated in Figure 5. One line is not enough to find the source's location. By moving the UAV group and keeping the formation, multiple lines are generated, as demonstrated in Figure 6. The intersection of these lines gives the source's location.

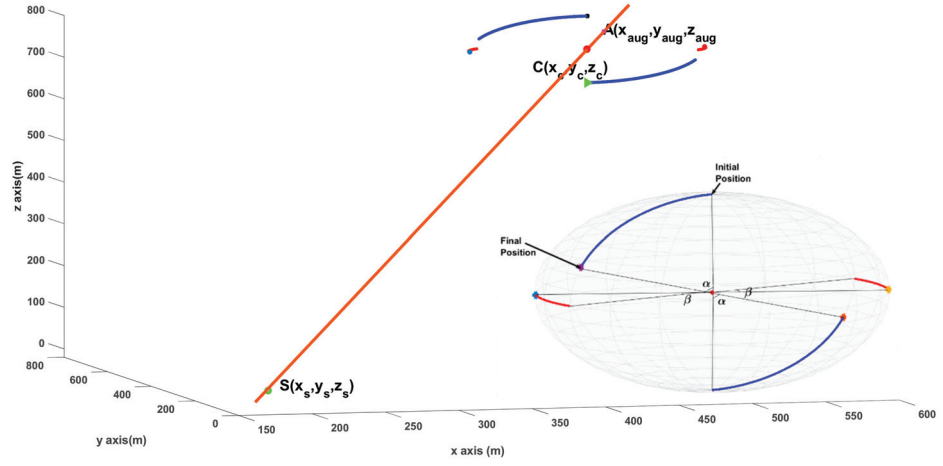

Figure 5. Rotation of UAVs and a line passing through augmented point and formation center.

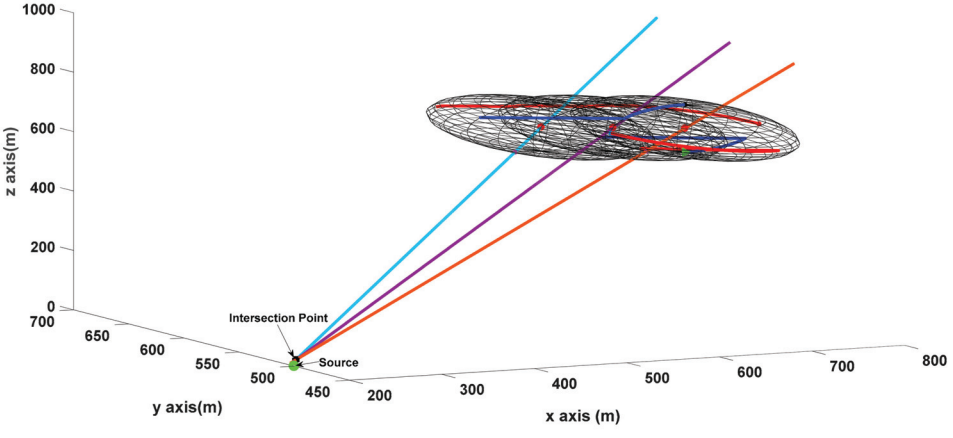

Figure 6. Intersection of multiple lines, which gives the source location.

As shown in Figure 6, UAVs with different received signal powers initially act in a way to equalize the received power. When the center of gravity moves, the procedure starts again and the received signal powers are equalized again. New augmented points with new angle values are calculated, and the location of the target is determined by the intersection lines passing through the center and the augmented points. Figure 7 demonstrates the received power difference of the UAVs in each group.

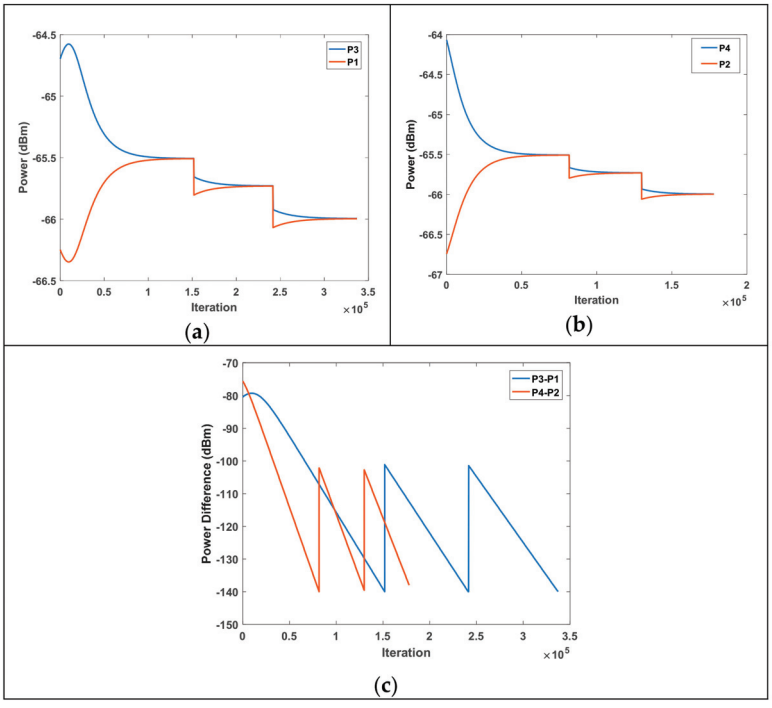

Figure 7. (**a**) Received power by D1 and D3, (**b**) received power by D2 and D4, and (**c**) power differences of each group.

However, due to the noise effects, the received signal power values may vary from their originals. Although the mean of multiple RSSI values is used in the algorithm, the lines may not intersect at one point. In this situation, in order to find the point that has a shortest distance to all lines the algorithm given in previous section is utilized. The point that has a minimum distance to all lines is referred to as the source location, and the result is demonstrated in Figure 8.

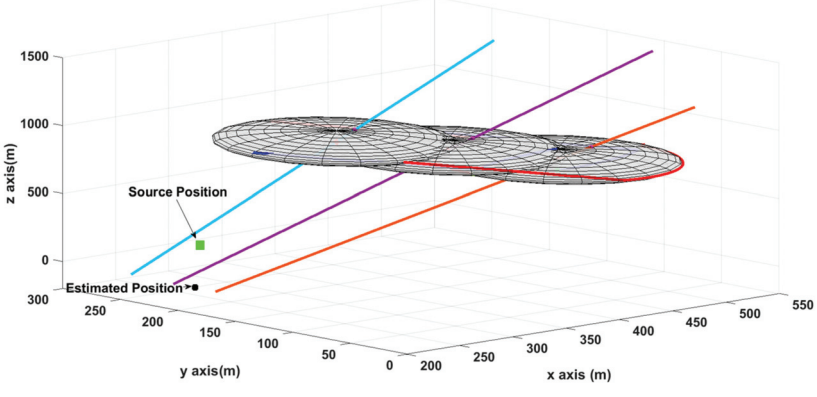

Figure 8. Source localization in a noisy environment.

Figure 8 shows target detection when the received signal strength is different from the theoretically calculated signal power (1). Scanning is performed when the sphere center is at three different points. After 100 Monte Carlo simulations, the mean error value is found

to be 52.66 m when a noise with a 4% standard deviation over the signal power is added. Table 2 shows localization errors for different noise values.

Table 2. Localization error of RF source with different noise ratios.

Standard Deviation Ratio	Mean Error
2%	28.3 m
4%	52.66 m
8%	145.7 m

As can be seen from the table, localization error increases when the noise level increases. As a continuation of this study, it is aimed to reduce the noise level by using nonlinear filters. Thus, the proposed localization method will provide more accurate results.

5. Conclusions

A novel localization method that can work in GPS-denied environments which can occur due to tall buildings, trees, canyon walls blocking the GPS satellite signals, or a lack of coverage was proposed. This powerful geometrical solution performs the localization process without the need for transmit power and path loss exponent information. The procedure depends on the difference in received signal power measured by RSSI sensors. UAVs move until each UAV receives equal power while keeping the formation. With this movement rate, lines intersecting at the source location are calculated. In a noise-free environment, two lines are enough to calculate the position. However, in a noisy environment, these lines do not intersect. Therefore, generating more lines will improve localization performance. An algorithm that finds a point which has a minimum distance to all lines is also given in this manuscript.

In this study, the source location is calculated as the point that has a minimum distance to all lines. Nonlinear filtering methods will be considered to find the source location with minimum error will be considered as a future study. Furthermore, results are given based on computer simulations. With the real-time application of the algorithm, the performance of the method will be examined more precisely.

Funding: This research received no external funding.

Data Availability Statement: Not applicable.

Conflicts of Interest: The author declares no conflict of interest.

References

1. Labib, N.S.; Brust, M.R.; Danoy, G.; Bouvry, P. The Rise of Drones in Internet of Things: A Survey on the Evolution, Prospects and Challenges of Unmanned Aerial Vehicles. *IEEE Access* **2021**, *9*, 115466–115487. [CrossRef]
2. Laoudias, C.; Moreira, A.; Kim, S. A survey of enabling technologies for network localization tracking and navigation. *IEEE Commun. Surv. Tutor.* **2018**, *20*, 3607–3644. [CrossRef]
3. Wang, X.; Roy, S.; Farì, S.; Baldi, S. Adaptive Vector Field Guidance without a Priori Knowledge of Course Dynamics and Wind. *IEEE/ASME Trans. Mechatron.* **2022**, *27*, 4597–4607. [CrossRef]
4. Baldi, S.; Roy, S.; Yang, K.; Liu, D. An Underactuated Control System Design for Adaptive Autopilot of Fixed-Wing Drones. *IEEE/ASME Trans. Mechatron.* **2022**, *27*, 4045–4056. [CrossRef]
5. Wang, X.; Roy, S.; Farì, S.; Baldi, S. The problem of reliable design of vector-field path following in the presence of uncertain course dynamics. *IFAC-Pap. OnLine* **2020**, *53*, 9399–9404. [CrossRef]
6. Nasralla, M.M.; Rehman, I.U.; Sobnath, D.; Paiva, S. Computer Vision and Deep Learning-Enabled UAVs: Proposed Use Cases for Visually Impaired People in a Smart City. In Proceedings of the Computer Analysis of Images and Patterns CAIP 2019, Salerno, Italy, 6 September 2019. Communications in Computer and Information Science Springer.
7. Koohifar, F.; Guvenc, I.; Sichitiu, M.L. Autonomous Tracking of Intermittent RF Source Using a UAV Swarm. *IEEE Access* **2018**, *6*, 15884–15897. [CrossRef]
8. Bi, F.; Lei, M.; Wang, Y. Context-aware MDNet for target tracking in UAV remote sensing videos. *Int. J. Remote Sens.* **2020**, *41*, 3784–3797. [CrossRef]
9. He, J.; Geng, Y.; Pahlavan, K. Toward accurate human tracking: Modeling time-of-arrival for wireless wearable sensors in multipath environment. *IEEE Sens. J.* **2014**, *14*, 3996–4006.

10. Nguyen, N.H.; Doğançay, K. Instrumental Variable Based Kalman Filter Algorithm for Three-Dimensional AOA Target Tracking. *IEEE Signal Process. Lett.* **2018**, *25*, 1605–1609. [CrossRef]
11. Fletcher, F.; Ristic, B.; Mušicki, D. Recursive estimation of emitter location using TDOA measurements from two UAVs. In Proceedings of the 10th International Conference on Information Fusion, Québec, QC, Canada, 9–12 July 2007.
12. Lin, A.; Ling, H. Doppler and direction-of-arrival (DDOA) radar for multiple-mover sensing. *IEEE Trans. Aerosp. Electron. Syst.* **2007**, *43*, 345–361. [CrossRef]
13. Guzey, N.; Xu, H.; Jagannathan, S. Localization of Near-Field Radio Controlled Unintended Emitting Sources in the Presence of Multipath Fading. *IEEE Trans. Instrum. Meas.* **2014**, *63*, 2696–2703. [CrossRef]
14. Viani, F.; Lizzi, L.; Rocca, P.; Benedetti, M.; Donelli, M.; Massa, A. Object tracking through RSSI measurements in wireless sensor networks. *Electron. Lett.* **2008**, *44*, 653–654. [CrossRef]
15. Lagias, A.E.; Lagkas, T.D.; Zhang, J. New RSSI-based tracking for following mobile targets using the law of cosines. *IEEE Wirel. Commun. Lett.* **2017**, *7*, 392–395. [CrossRef]
16. Uluskan, S.; Filik, T.A. Geometrical Closed Form Solution for RSS Based Far-Field Localization: Direction of Exponent Uncertainty. *Wirel. Netw.* **2019**, *25*, 215–227. [CrossRef]
17. Zengin, U.; Dogan, A. Real-Time Target Tracking for Autonomous UAVs in Adversarial Environments: A Gradient Search Algorithm. *IEEE Trans. Robot.* **2007**, *23*, 294–307. [CrossRef]
18. Haoran, S.; Faxing, L.; Hangyu, W.; Junfei, X. Optimal observation configuration of UAVs based on angle and range measurements and cooperative target tracking in three-dimensional space. *J. Syst. Eng. Electron.* **2020**, *31*, 996–1008. [CrossRef]
19. Zhou, M.; Lin, J.; Liang, S.; Du, W.; Cheng, L. A UAV patrol system based on Bluetooth localization. In Proceedings of the 2nd Asia-Pacific Conference on Intelligent Robot Systems (ACIRS), Wuhan, China, 16–18 June 2017; pp. 205–209.
20. Zhang, W.; Song, K.; Rong, X.; Li, Y. Coarse-to-Fine UAV Target Tracking with Deep Reinforcement Learning. *IEEE Trans. Autom. Sci. Eng.* **2019**, *16*, 1522–1530. [CrossRef]
21. Hasanzade, M.; Herekoğlu, Ö.; Yeniçeri, R.; Koyuncu, E.; İnalhan, G. RF Source Localization using Unmanned Aerial Vehicle with Particle Filter. In Proceedings of the 9th International Conference on Mechanical and Aerospace Engineering (ICMAE), Budapest, Hungary, 10–13 July 2018.
22. Hasanzade, M.; Herekoglu, O.; Ure, N.K.; Koyuncu, E.; Yeniceri, R.; Inalhan, G. Localization and tracking of RF emitting targets with multiple unmanned aerial vehicles in large scale environments with uncertain transmitter power. In Proceedings of the International Conference on Unmanned Aircraft Systems (ICUAS), Miami, FL, USA, 13–16 June 2017.
23. Spyridis, Y.; Lagkas, T.; Sarigiannidis, P.; Zhang, J. Modelling and simulation of a new cooperative algorithm for UAV swarm coordination in mobile RF target tracking. *Simul. Model. Pract. Theory* **2021**, *107*, 102232. [CrossRef]
24. Liang, J.; Liang, Q. RF Emitter Location Using a Network of Small Unmanned Aerial Vehicles (SUAVs). In Proceedings of the IEEE International Conference on Communications (ICC), Kyoto, Japan, 8–9 June 2011.
25. Charrow, B.; Michael, N.; Kumar, V. Cooperative multi-robot estimation and control for radio source localization. *Int. J. Robot. Res. (IJRR)* **2014**, *33*, 569–580. [CrossRef]
26. Dehghan, S.M.; Moradi, H.; Shahidian, S.A. Optimal path planning for DRSSI based localization of an RF source by multiple UAVs. In Proceedings of the 2014 Second RSI/ISM International Conference on Robotics and Mechatronics (ICRoM), Tehran, Iran, 15–17 October 2014; pp. 558–563.
27. Güzey, H.M.; Güzey, N. Adaptive hybrid formation-search and track controller of UAVs. *Int. J. Syst. Sci.* **2022**, *53*, 2301–2317. [CrossRef]
28. Lee, J.H.; Buehrer, R.M. Fundamentals of received signal strength-based position location. In *Handbook of Position Location: Theory, Practice, and Advances*; Zekavat, R., Buehrer, R.M., Eds.; Wiley: Singapore, 2012; pp. 359–394.
29. Chan, Y.T.; Lee, B.H.; Inkol, R.J.; Chan, F. Estimation of emitter power, location, and path loss exponent. In Proceedings of the CCECE Montreal, Quebec, Canada, 29 April–2 May 2012.

drones

MDPI

Article

Exploring the Feasibility of Mitigating Flood Hazards by an Existing Pond System in Taoyuan, Taiwan

Kuo-Hsin Tseng [1,2,3,*], Tsun-Hua Yang [4], Pei-Yuan Chen [3], Hwa Chien [3], Chi-Farn Chen [1] and Yi-Chan Hung [2]

[1] Center for Space and Remote Sensing Research, National Central University, 300 Zhongda Rd., Zhongli Dist., Taoyuan City 32001, Taiwan
[2] Department of Civil Engineering, National Central University, 300 Zhongda Rd., Zhongli Dist., Taoyuan City 32001, Taiwan
[3] Institute of Hydrological and Oceanic Sciences, National Central University, 300 Zhongda Rd., Zhongli Dist., Taoyuan City 32001, Taiwan
[4] Department of Civil Engineering, National Yang Ming Chiao Tung University, 1001 Daxue Rd., East Dist., Hsinchu City 30010, Taiwan
* Correspondence: khtseng@csrsr.ncu.edu.tw

Abstract: Changes in the global climate have induced densified rainfall and caused natural hazards across the world in recent years. Formed by a central mountain range and a corridor of alluvial plains to the west, Taiwan is at risk of flood hazards owing to its low-lying lands as well as the distinct seasonality of rainfall patterns. The rapid discharge of surface runoff and a growing number of impervious surfaces have also increased flood hazards during recent typhoon landfalls. A century ago, ancestors in Taoyuan City constructed a system of water channels composed of thousands of ponds to fulfill the needs of agriculture and aquaculture. During the expansion of urban areas, land reformation replaced a majority of earlier ponds with residential and industrial zones. However, the remaining ponds could potentially serve as on-site water detention facilities under the increasing risk of floods. In this research, we first renewed an outdated pond database by deploying a novel unmanned aerial vehicle (UAV) system with a micro-sonar to map the bathymetry of 80 ponds. Next, a simplified inundation model (SPM) was used to simulate the flood extent caused by different scenarios of rainfall in Bade District of Taoyuan City. Assuming that extremely that heavy rainfalls at 25, 50, 75, and 100 mm occurred in a very short period, the flood area would decrease by 96%, 75%, 52%, and 37%, respectively, when the ponds were preparatorily emptied.

Keywords: mobile mapping; UAV; sonar; simplified inundation model

Citation: Tseng, K.-H.; Yang, T.-H.; Chen, P.-Y.; Chien, H.; Chen, C.-F.; Hung, Y.-C. Exploring the Feasibility of Mitigating Flood Hazards by an Existing Pond System in Taoyuan, Taiwan. *Drones* **2023**, *7*, 1. https://doi.org/10.3390/drones7010001

Academic Editors: Andrzej Łukaszewicz, Wojciech Giernacki, Zbigniew Kulesza, Jaroslaw Pytka and Andriy Holovatyy

Received: 15 November 2022
Revised: 16 December 2022
Accepted: 16 December 2022
Published: 20 December 2022

1. Introduction

A network of ponds scattered over a 30 × 30 km area is an iconic landscape in northern Taiwan (Figure 1). The ancient Shihmen river, flowing through the center of current Taoyuan City and forming the alluvial plain, was captured by the northbound river and reduced water levels at lower reaches more than 30,000 years ago [1]. The ancestors who arrived here centuries ago had settled along the river bank or areas with accessible groundwater. Along with the growing population, residents who in the early stage farmed with precipitation and natural watercourses had to build water facilities in the last century [2]. Freshwater supply had become an issue, so the ancestors irrigated with ponds and ditches. Although Taoyuan's geographical environment is unsuitable for dams as the average slope of streams is 1/40–1/120 [2], the soil type composed of laterite and loess is conducive to constructing artificial water storage facilities. As time went on, some of the ponds functioned as small reservoirs in the water source management system and were linked with rivers and streams. These ponds' functionalities have become an intricate system for irrigation, drainage, wetland conservation, and aquafarming [3] (Figure 1, inset figures).

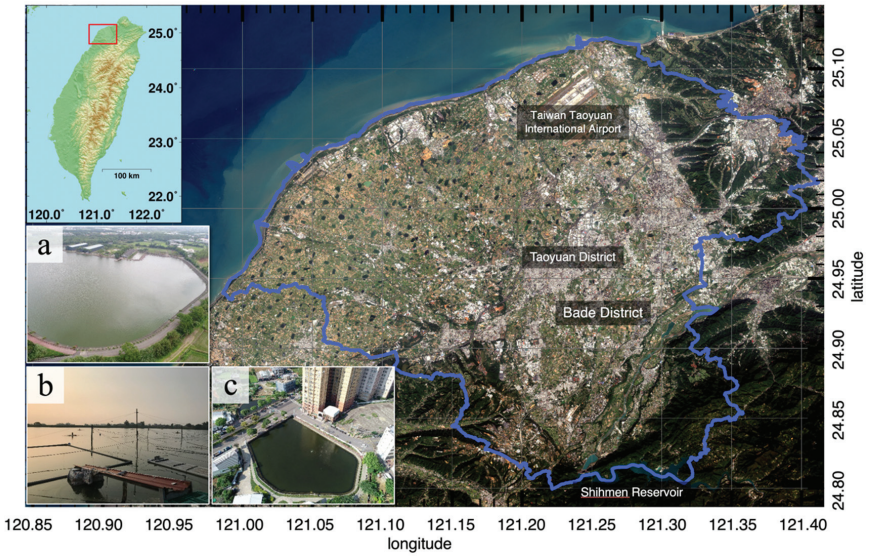

Figure 1. (Overview map) Taoyuan city in the red box is located in northern Taiwan. (Main) The pond system in Taoyuan City (blue) is a multipurpose water facility for various applications, for example: (**a**) irrigation; (**b**) fish farming; and (**c**) ecology parks.

1.1. Pond Network in Taoyuan

Recently, the demands for agricultural production decreased, and the rice fields in many irrigated areas were progressively replaced by urban areas [2,4], due primarily to the rapid development of industry and commerce. From 2002 to 2018, the area of cultivated land decreased from 39,608 to 31,896 ha in Taoyuan [5]. According to the latest mapping in 2011, there are still 2851 existing ponds, as delineated by the Department of Water Resources, Taoyuan (TYWR) from aerial photography. Because of the cutback of water demand for agriculture, some channel sectors within the network gradually disintegrated where ponds were abandoned. These diminishing ponds have limited storage capacity due to sedimentation. Wang (2013) [6] suggested that converting fish ponds into flood detention basins could mitigate flood hazards regardless of whether the accumulated precipitation is 150 mm or as high as 1200 mm. Wang & Chang (2016) [7] also explored the spatial connection between the ponds in Taoyuan and investigated the possibility of flood detention. They assumed an average depth of 3.4 m for 497 ponds and concluded that using this existing configuration could effectively reduce flood risks. For a daily accumulated rainfall of 200 mm, the ponds in Dayuan District, near Taiwan Taoyuan International Airport in Figure 1, could reduce 55% of the water from a simulated flood event [7].

Unfortunately, most ponds have very limited information, even in the government database. Incomplete background knowledge is a major drawback for an overall assessment and planning. Therefore, to fully explore the potential usage of their capacities, detailed geometric parameters are needed. This study, therefore, first intended to develop a complete digital elevation model (DEM) to seamlessly connect the pond floor and the neighboring land for later use in flood simulation. As demonstrated in Bade District of Taoyuan City in Figure 2a, the DEM from the Ministry of the Interior (Taiwan) is unable to reveal detailed pond shapes. As the close-up in the orange box in Figure 2a demonstrates, the water surface is hydro-flattened during the editing of airborne LiDAR data, and thus the elevation is similar to that of the neighboring land (Figure 2b). Therefore, as demonstrated in Figure 2c, the DEM used in the following simulation was modified according to either a single depth value in the database or the bathymetric maps updated by our fieldwork.

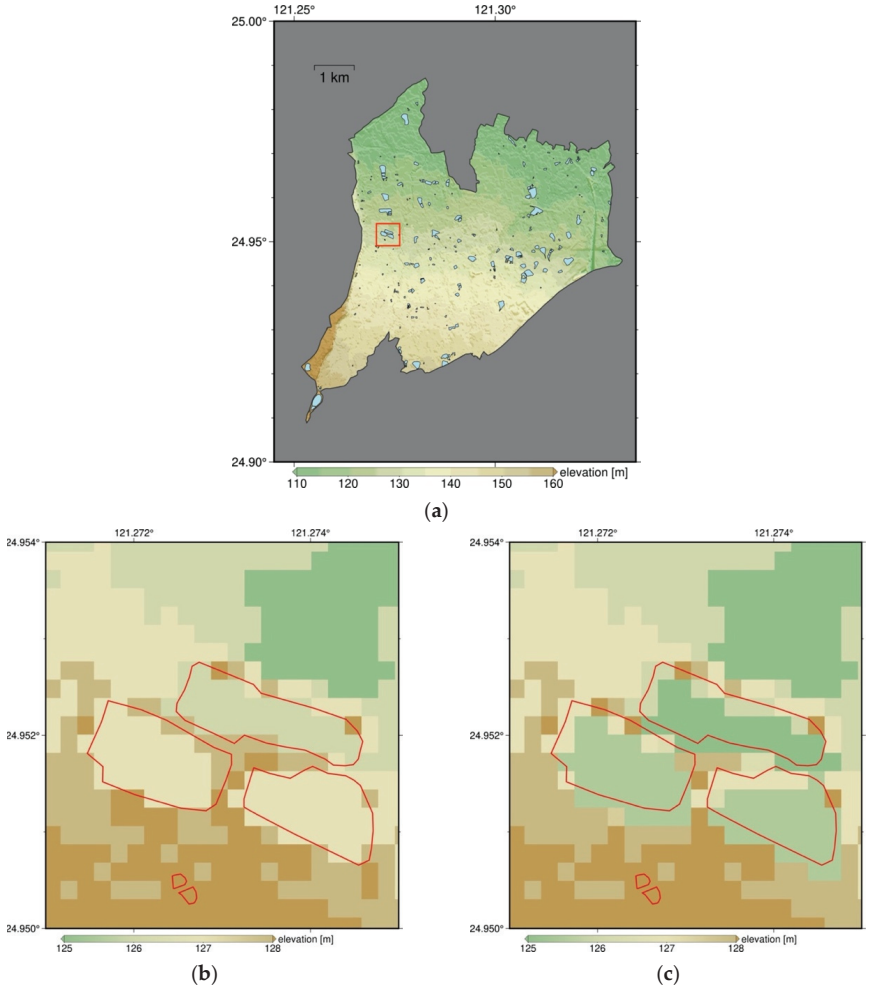

Figure 2. Bade District in Taoyuan City is the demonstration site for flood detention simulation: (**a**) an overview of Bade District and pond locations (black polygon); (**b**) a blow-up view of the orange box in panel (**a**). The 20-m resolution elevation model from MOI does not appropriately reveal bathymetry in pond locations (red); and (**c**) The DEM is modified within ponds by depth information from the government database or our fieldwork.

1.2. Methods for Measuring Inland Waterbodies

To measure point depth over a lake, surveyors used to deploy sounding rods, sounding leads and other tools lowered from a vessel. Lately, optical and acoustic sounding sensors were developed by counting the elapsed time of wave propagation. There are active and passive mechanisms in optical sounding [8]. The most popular device for shallow water areas is the airborne laser bathymetry (ALB) system, which estimates the range based on the bidirectional propagation time of short pulses between the surface and bottom. ALB can nominally survey depths to 60 m depending on the water clarity [9]. The laser is split by an optical coupler into an infrared beam and a green beam. The infrared beam is used to detect water surfaces because of its poor penetration, while the green beam zig-zagging across-track aims to measure depths. The advantage of active ALB is the insensitivity of sunlight angles and the reflections of wave surfaces as compared with passive optical sounding, as

well as its workability under insufficient light sources [10,11]. Hilldale and Raff (2008) [12] collected 220 km of ALB data at the Yakima Basin in Washington and the Trinity River Basin in Texas to perform surveys of two riverbeds. Comparing LiDAR data and the single-beam echosounder with the real time kinematic technique of the global positioning system (RTK-GPS), the results showed that the standard deviation is at 0.3–0.42 m level when the slope is less than 20%, and it may be up to 0.63 m otherwise.

In contrast, passive optical sensor onboard satellites can estimate water column thickness from the light attenuation between spectral bands. This approach reduces costs in the field and avoids the inaccessibility of remote areas. Stumpf et al. (2003) [13] proposed a log-ratio transformation utilizing spectral attenuation based on the Beer–Lambert Law. By comparing IKONOS satellite images with depth measurements, a linear variation algorithm and an empirical proportional variation algorithm are constructed. An alternative way to exploit optical images is based on the hypsometric approach. Getirana et al. (2018) [14] used Landsat historical images and SARAL/AltiKa altimetry satellite to build a slope elevation model for Lake Mead, USA. They further used flow direction and neighboring hydrological formations to derive full reservoir bathymetry. In their results, interpolated DEM in consideration of the upstream and downstream elevation agreed well with surveys from scan-sonar and chirp seismic reflection.

Besides, acoustic methods had also been widely used to detect and locate objects/obstacles in the water. Sound navigation and ranging (Sonar) can be divided into active and passive types based on function and mode. Sonar systems are categorized as, for example, side-scan sonar, multibeam sonar, acoustic communication system, positioning system, acoustic Doppler system, and acoustic tomography network. Active sonar is mostly operated for bathymetric mapping, fish detection, and sediment profiling [15]. However, these systems are primarily used in waterbodies where the cruising of vessels allows. For a small pond or a narrow channel, the mobility of ships is constrained and the cost of a survey campaign may not be economically reasonable.

1.3. A Novel Bathymetry Technique

With the boom in commercial-grade drones, various ingenious applications have been developed thanks to their outstanding maneuverability in the field. The unmanned aerial vehicle (UAV) has been used to broaden research areas in agriculture, forestry, flood monitoring, and geohazard assessment [16,17]. The DEM generated from aerial photos using the structure from motion (SFM) technique has a high degree of conformity with aerial LiDAR data [18]. Javemick et al. (2014) [19] used stereo-paired images taken at 600 m and 800 m above the ground and performed SFM to construct a DEM. The geolocation errors were 0.04 m in planar, and 0.10 m in vertical directions. UAVs have also been utilized for bathymetric mapping, outperforming traditional approaches in efficiency and accessibility. Alvarez et al. (2018) [20] conducted shallow water depth mapping in a small reservoir in Oklahoma, USA, where the study area was about 28,000 m^2. An echosounder mounted onboard a floating platform was towed by a UAV to measure water depth. They retrieved scattered point depths and applied cluster analysis to distinguish areas with large standard deviations. The underwater topography map was obtained by spatial fitting of the measured depth points, and a standard deviation of 0.37 m was reached between the fitted terrain and reference data. Bandini et al. (2018) [21] combined a UAV, a sonar, an inertial measurement unit (IMU), a SONY RX-100 camera, and a GNSS module to correct the distortion and tilt. Similarly, the entire sonar system was towed by a UAV and the result showed an accuracy of ~2.1% of actual depth with a maximum depth of 35 m. Many innovative approaches developed in the abovementioned experiments considerably reduce costs compared with traditional methods.

Due to the inaccessibility of several unmanaged ponds in Taoyuan, we also needed a mobile platform with good flexibility when hovering above a pond. Therefore, a novel measuring system was developed to map the depth of ponds. This research first renewed the outdated depth of ponds with a mobile sounding system comprising a UAV, a smart-

phone, and a micro-sonar. The innovation of this UAV module was to hang the sonar by an aerial vehicle to skim the surface of the water, without the floating platform that is usually restricted by launching and mobility in a small pond of a few thousand square meters. Also, this is the first time that a group of pond models was integrated with an adjacent DEM to simulate the overland flow under different rainfall scenarios using the simplified inundation model (SPM) [22].

2. Methodology

2.1. Workflow

The workflow of this study is outlined in Figure 3. The first step was to select the study area and ponds to be measured. Here, we picked 80 ponds in Taoyuan City, of which 15 ponds are located in Bade District. To update the geometry of each site, four main tasks were conducted, including the deployment of control points, operation of aerial photography, UAV bathymetry, and other ground surveys. To model the neighboring land, aerial photos taken within a 200 m buffer were stereo-paired to build a DEM constrained by GNSS control points with precise point positioning (PPP) solutions. To model the underwater part, the measured depth points were used to interpolate a mesh grid of bathymetry in consideration of slope and channel geometry. For the land area outside the buffer or for the pond without fieldwork, the 20 m digital terrain model (DTM) released by the Ministry of the Interior (MOI), Taiwan (https://dtm.moi.gov.tw (accessed on 1 July 2022), version 2018) was used. The DTM was produced by a nationwide airborne LiDAR campaign, and the specified accuracy of LiDAR measurement was 0.25 m in vertical for each 1 m grid comprising more than 2 LiDAR points. The joint terrain model, composed of an underwater DEM, a land DEM, and the MOI DEM, was assembled and bilinearly resampled into a 0.5 m resolution. The next step was to use this integrated DEM for SPM flood simulation. Finally, the floodwater was assumed to be dissipated into the ponds via a virtual network, and the contribution of the ponds to flood detention was assessed.

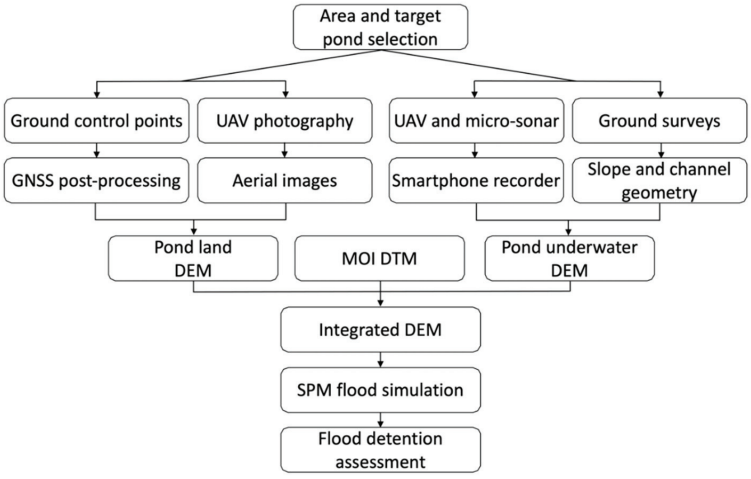

Figure 3. Workflow for pond measurements and to build an integrated digital elevation model with neighboring terrain.

2.2. Fieldwork Procedure

2.2.1. Modeling of Terrain DEM

For fieldwork in the selected pond, one operator controlled a DJI Phantom 4 Pro (DJI-P4P) UAV to take aerial photos for reconstructing DEM over the land area. A flight height of 60 m and an overlap rate of 70% were set with a ~200 m buffer area outside the pond. To ensure the quality of geolocation for the orthorectified images, 3–5 ground

control points were positioned by a u-blox C94-M8P GNSS receiver for more than 30 min. This GNSS chip provides single-frequency phase pseudo-ranges compatible with GPS, GLONASS, and Galileo. GNSS observation files are imported to RTKLIB [23] open-source software to solve Precise Point Positioning (PPP) coordinates. With PPP, the accuracy could be increased to a decimeter level for phase pseudo-ranges, owing to the reduction of biases and clock/orbital errors.

2.2.2. Modeling of Pond DEM

A DJI Phantom 3 Advanced (DJI-P3A) UAV was deployed to carry a bathymetric module along the planned route above the water surface. Under moderate environmental conditions, including good GPS visibility, calm wind speed, and low RF interference, the UAV can stay within 1.5 m in horizontal and 0.1 m in vertical directions. The maximum load under DJI-P3A is limited to ~500 g based on previous tests [24]. Hence, a lightweight (89 g) Ling-Hui micro-sonar and a smartphone can be hung by the UAV with a fishing string 1.5 m long (Figure 4). The ranging capability of this leisure-grade fish finder is between 0.6 m and 30 m and the working temperature is <40 °C. Although the main application of this low-cost (~70 USD) micro-sonar is for fish detection, it is possible to estimate the depth owing to its sensitivity at ~10 cm level [24]. The sonar data were transmitted to the smartphone through Wi-Fi, with a maximum transmission distance of 50 m.

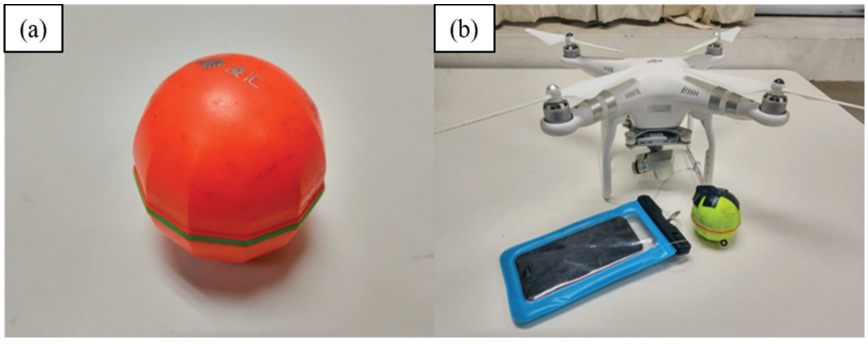

Figure 4. (**a**) A sample of micro-sonar that can measure water depth in 0.6–40 m; and (**b**) the entire module combines a DJI-P3A UAV, a micro-sonar, and an Android phone in a waterproof bag.

The operator first planned a grid of points on the pond where the UAV could stay for 1 min. Water depths displayed in the mobile application (App) that came with the sonar were screenshotted every 2 s, with a total of 25–30 repetitions for each point. After removing the first and last 15 s when sonar readings were not yet stabilized, approximately 10–12 redundant measurements were retained for computing water depth. As this low-cost sonar does not have a positioning module, the smartphone-recorded National Marine Electronics Association (NMEA) file was used for geolocations. The assisted global positioning system (A-GPS), with good coverage of cellular networks, outperforms the code positioning by GPS [25]. This approach also avoids positioning errors due to the obscured sky visibility and ionospheric effects. The images screenshotted in the mobile App contains the resolved depth information. Here, we used an automatic recognition module coded in MATLAB to digitize water depth and timestamps recorded in each image. To produce DEM over the land area, a Pix4D Mapper was adopted to process aerial photos and control points to establish DEM and a mosaicked image. The water area mask was visually delineated from the mosaic image.

Among several interpolation strategies for modeling terrain, the inverse weighted distance (IDW) and the ordinary Kriging (OK) are most commonly favored to estimate continuous surfaces [26]. A study in Saldanha Bay further suggested that IDW consistently performed better than OK across multiple interpolation tests [27]. Based on the assumption

that the bottom sedimentation of the ponds is smooth and the depth points are evenly distributed, IDW is reasonable in the presentation of floor topography. Hence, to fit the surface of underwater terrain from pointwise measurements, we adopted IDW as the spatial interpolation method. The formula of IDW [28,29] is

$$D(i,j) = \frac{\sum_{x=1}^{n} \frac{D_x}{d(i,j)_x}}{\sum_{x=1}^{n} \frac{1}{d(i,j)_x}} = \frac{\sum_{x=1}^{n} D_x W(i,j)_x}{\sum_{x=1}^{n} W(i,j)_x} \quad (1)$$

where $D(i,j)$ is the depth of an unknown point, D_x is the value of a measured point and $d(i,j)_x$ is the Euclidean distance from the unknown point $D(i,j)$ to the x^{th} measured point. The weight in IDW is thus W_i, such as 1 divided by $d(i,j)_x$. IDW searches adjacent data at the pixel to be interpolated, and calculates the weighted average inversely proportional to the distance. Following that, the slope of the enclosing dyke is considered in generating an underwater model. We assumed that the dyke had a uniform slope as they were mostly renovated by a precast concrete form (Figure 5). The combination of slope measurement and IDW can present a completely seamless model rather than just using one of them. Finally, the joint pond model can be obtained by combining the underwater model with the land model.

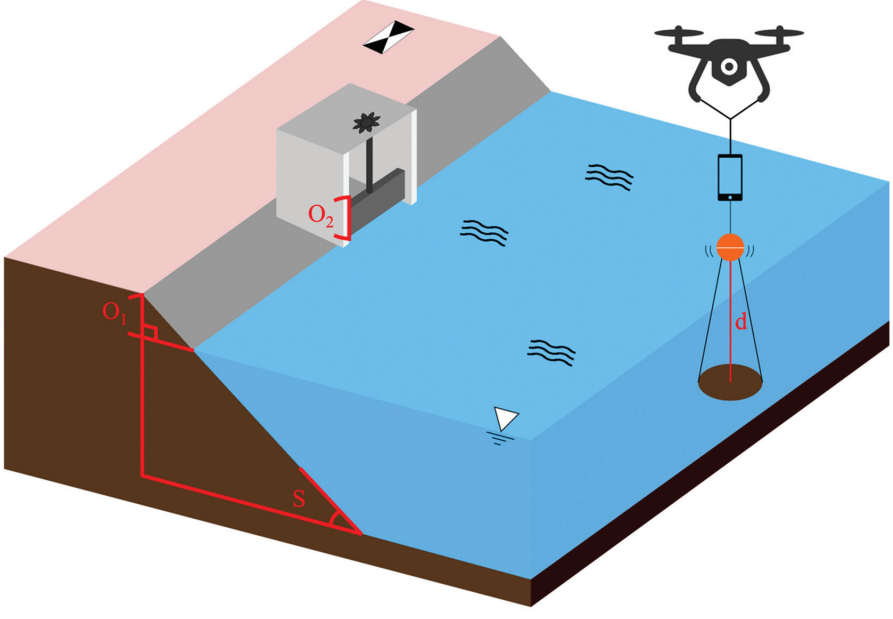

Figure 5. A schematic diagram of surveying parameters in the target pond, where d is the depth from sonar, O_1 is the highest water level without a water gate, and O_2 is the highest water level when a water gate exists. The slope along the pond edge is assumed a constant S.

To calculate the maximum storage (V_{max}) of each site, dyke or water gate height measured in situ was considered as the maximum water level. Equation (2) calculates water storage for each 0.5 × 0.5 m pixel (row i from 1 to n and column j from 1 to m) falling within the pond mask:

$$V_{max} = \sum_{j=1}^{n} \sum_{i=1}^{m} A(i,j) \times [D(i,j) + O_k] \times M(i,j) \quad (2)$$

where A is the unit area of each pixel (0.25 m^2), D is the depth, O_k ($k \in \{1,2\}$) is the extra height measured in Figure 5, which is the lower one of height to the top of concrete dyke

(O_1) or the slab height of the water gate (O_2). M is the pond mask, set to 1 within the pond and 0 for the land area. Figure 6 displays two examples of pond model in Yangmei District (YM145) and Bade District (BD033).

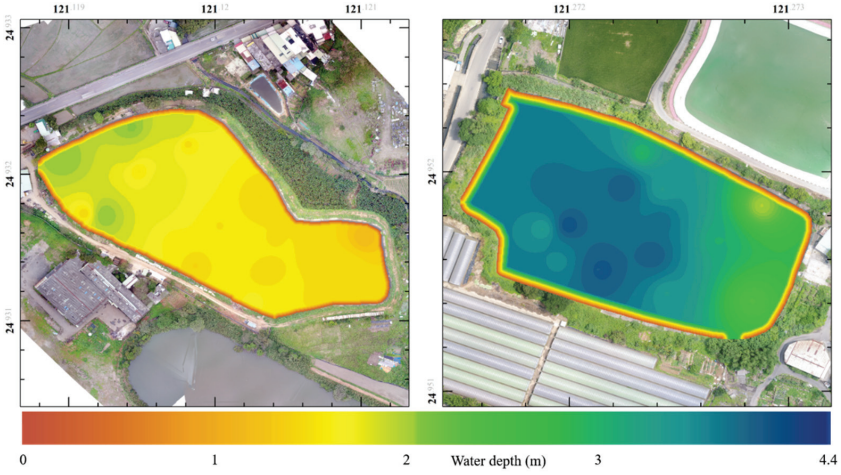

Figure 6. Two examples of the integrated pond model in YM145 (**left**) and BD033 (**right**). Color code indicates water depth based on the highest water level.

2.3. Flood Simulation

2.3.1. Simplified Inundation Model (SPM)

SPM [23] refers to a set of simple physical properties that were developed to simulate flooding extent by using DEM as the sole input parameter. The model requires rainfall and a threshold that represents the acceptable difference between total flood and simulated flood. It is suggested to set 10% of the rainfall remaining on the ground to calculate the extent and depth of a flooding event [22]. Compared to other simulation methods, SPM produces results promptly. The flow direction is first calculated and the rows of cell arrays are sequenced, and cells located at the end of arrays would be considered a high contribution. The flood would be drained to a lower elevation or a higher contribution, and the amount of water is in line with the preset rainfall and threshold. D-infinity [30] is used to transport water from flooding cells to surrounding cells. When the flow direction is between two cells, water is distributed according to the slope as weight because the downstream areas also have a higher risk of flood. As demonstrated in Figure 7a, a model with nine cells represents the main terrain formation. As the water level increases from cell #5 in panel (b), eight possible flowing directions are displayed as orange arrows while the steepest slope is marked as the red arrow. Angles a and b between two flowing directions to cell #1 and #2 are used as the weight to allocate water from the center cell, in terms of b/(a + b) and a/(a + b), respectively (Figure 7b). This process will continue until the water level is balanced among surrounding cells (Figure 7c) [22,30].

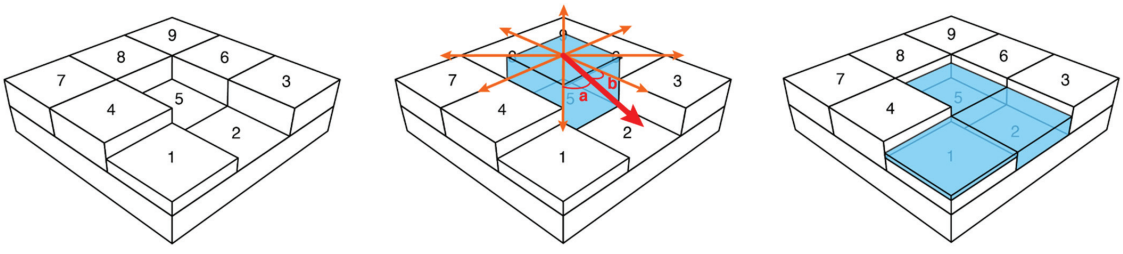

Figure 7. A schematic of SPM redrawn from [22,30]: (**a**) the terrain is illustrated as nine cells with varying elevations; (**b**) the flood occurs at cell #5 and the steepest slope in this region is shown as the red arrow, between two (cell #1 and #2) out of eight possible flowing directions (orange arrows); the planar angles between the red arrow and directions to cell #1 and #2 (angle a and b) are used as weights to allocate water accumulated in cell #5; and (**c**) the allocation process is iterated among cells until reaching a balanced water level.

The convenience and outstanding speed of SPM have been demonstrated in the literature [31], highlighting that SPM using only elevation data for simulation was superior in areas without detailed hydrological parameters. SPM is much faster than other models in both data collection and processing efficiency, and the precision when performing on the town- and village-scale could reach an acceptable level, where the fit indicator (the overlapped flooded area divided by the total flooded area) is greater than 0.69 [31].

2.3.2. A Virtual Channel Scheme to Dissipate Floodwater

After simulation using SPM, the initial flood zones and their depths were estimated. However, if we assumed a virtual channel network existed between the flood-prone areas and the neighboring ponds, the flooded area might be further reduced based on a redistribution scheme. First, we assumed that the pond collocated with a flooded area would be filled. Next, the disconnected flooded areas in the SPM results were divided into patches. Starting from the lowest elevation, the flooded patches, one by one, the ponds not full and located downslope were searched. The flooded patch was first drained to the candidate with the shortest Euclidean distance. When the pond was full, the flooded patch found the next closest one to share floodwater, until no more successors located downslope had room to accommodate them. It should be understood that although the virtual channels do not exist in the field at this moment, based on our simulation, the demand for a drainage system could be visualized and the route could be considered for future plans.

3. Result

3.1. Validation of UAV Depth Measurements

A ship survey campaign was conducted in a pond #GI215 in Guanyin District Taoyuan. The Otter Unmanned Surface Vehicle (USV) carrying a Norbit iWBMS multibeam echosounder was deployed to scan the bathymetry. As shown in Figure 8a, the detailed elevation from the top of the dyke is revealed in USV sidescan results, with a range resolution of <1 cm. To compare the depth with measurements from our UAV module, 14 points skimmed by UAV are marked as black circles in Figure 8a,b, while the bathymetry in Figure 8b was modeled by the IDW strategy. The accuracy of UAV data, in terms of standard deviation and correlation coefficient as compared against USV data over those 14 depth points, achieved 0.12 m and 0.86, respectively. The error is about 4.8% of depth if we took 2.5 m of the averaged depth as a benchmark.

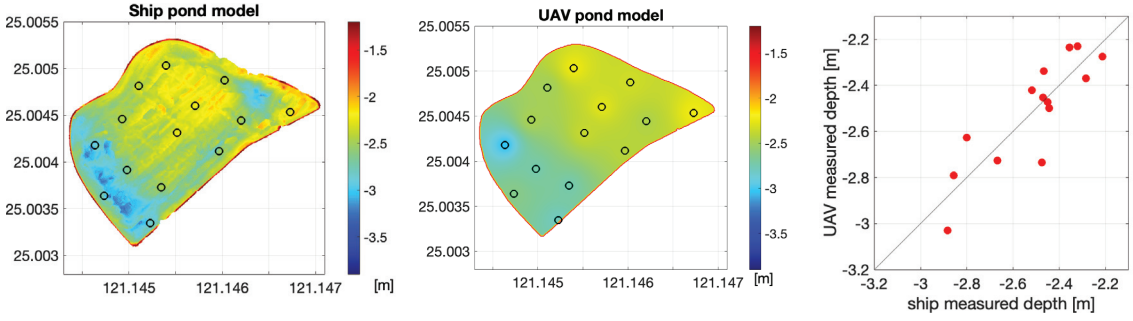

(**a**) (**b**) (**c**)

Figure 8. (**a**) The Otter Unmanned Surface Vehicle (USV) and a Norbit iWBMS multibeam echosounder scanning bathymetry; (**b**) Our UAV and a micro-sonar measurement (14 points), and the IDW-interpolated bathymetry; and (**c**) Scatterplot of depth values over 14 points.

3.2. Validation of Integrated Pond Models

In 2019, 80 ponds over the entire Taoyuan City were selected for fieldwork. Each location required 3–4 onsite staff to take 1–1.5 h of measurement. The detailed data processing and validation procedure can be found in [24,32]. The 80 models, as shown in Figure 9, have a range of water depth from 0.7 to 4.4 m and a range of storage from 2191 m^3 to 155,564 m^3. For comparing the configuration of ponds with historical data from TYWR, the correlation coefficient of water extent reached 0.99 (Figure 10a). However, in the comparison of water storage, two (CL143 and YM051, see #8 and #53 in Appendix A) had extraordinarily mismatched values. The depth calculated roughly from storage and the area in the TYWR record was just 0.07 m and 0.27 m for CL143 and YM051, respectively, which was far shallower than the common depth ranging between 1.2 m and 2.0 m. Therefore, the outliers were attributed to the significant underestimate of storage in the database. The correlation coefficient of storage without those two sites was improved from 0.70 to 0.83 (Figure 10b).

The results shown here have two-fold implications. First, the fidelity of our pond models should satisfy the needs of SPM simulation. Some depths in the database may be unreliable due to an inaccurate taping observation or a lack of updating recent dredging processes. The UAV sensing module introduced herein is flexible in cost, accuracy, and coverage. Second, the historical data need to be routinely updated to grasp the current status of bathymetry. Severe sedimentation is of great concern to some kinds of functionalities, for example, aquafarming and irrigation water storage.

3.3. Design of Drainage Channels from Virtual Network Dissipating Scheme

In this research, Bade District in Taoyuan City (Figure 1) was chosen for flood simulation because of its high level of urban development and the history of frequent flooding events. During short periods of heavy rainfall, floods often took place owing to an inadequate drainage system, even though the number and scale of ponds in Bade are larger than in other districts [33]. To assess the potential usage of the current infrastructure as a floodwater detention facility, SPM was applied in Bade with rainfall amounts of 25 mm, 50 mm, 75 mm, and 100 mm. Because no drainage conditions other than elevation are required in SPM, it has the great advantage of presenting short periods of heavy rainfall.

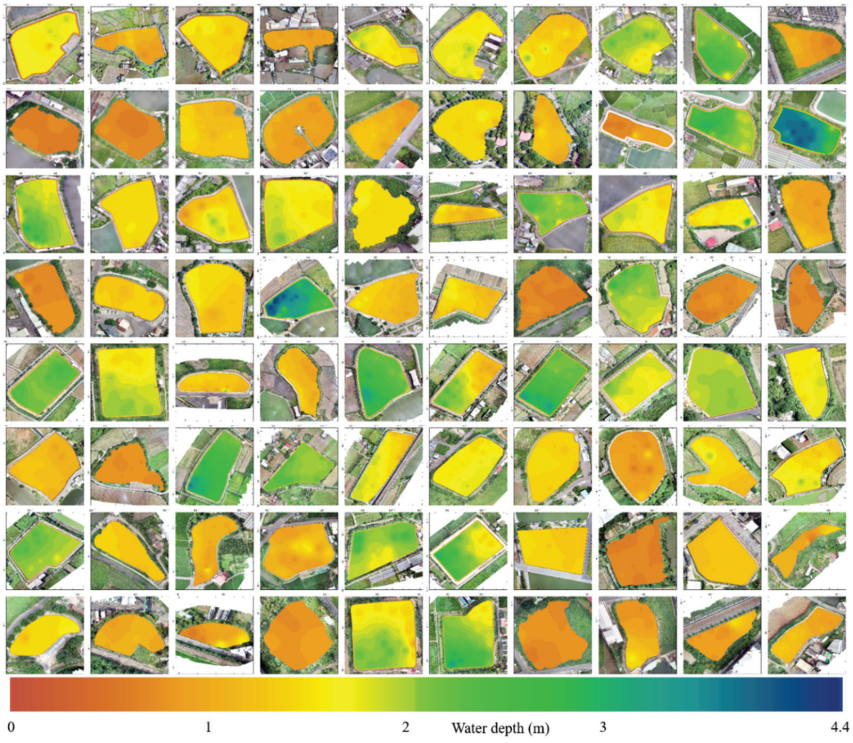

Figure 9. The 80 selected pond models. Each pond has an area greater than 2500 m^2 and at least 10 measurement points.

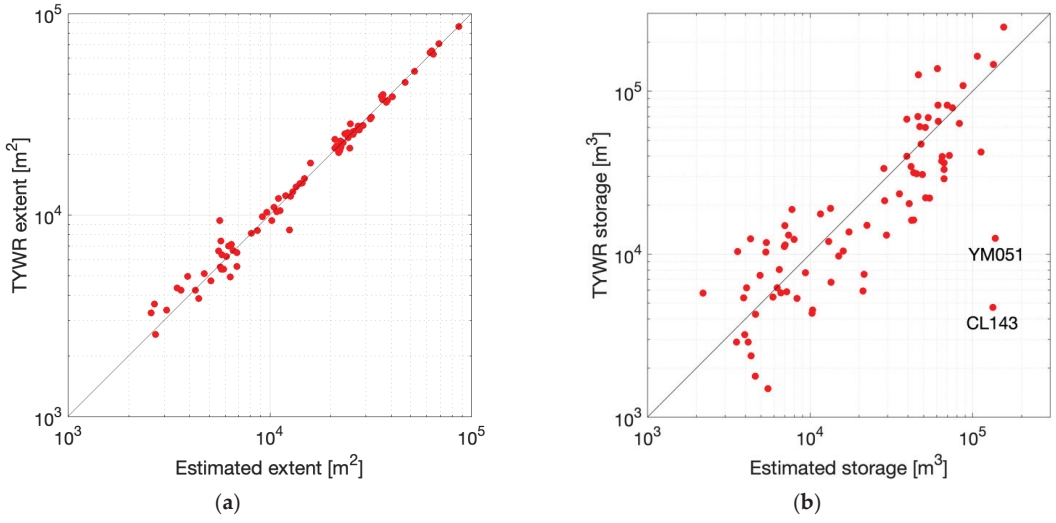

Figure 10. A log scale comparison of: (**a**) water extent; and and (**b**) water storage in 80 selected ponds.

The initial flooded area and redistribution procedure of floodwater was exemplified by the 75 mm rainfall case. As the flood just happened, the area simulated by SPM was shown as blue patches in Figure 11a. Those submerged areas could be further dissipated

through a virtual channel scheme defined in Section 2.3.2. Following the algorithm, the virtual network, or the lines connecting flooded patches to those ponds with unfilled space, is visualized as black lines in Figure 11a. It is noted that because some detention basins have been filled in the low-to-high elevation order, several flood patches need to be drained across the main slope direction (south to north). If the floodwater could be successfully redirected to the target ponds, the flooded areas could be reduced, as indicated by the red patches in Figure 11b. The flooded extent is much smaller than its initial form, since many ponds situated outside of flood-prone areas could potentially share stormwater under the assumption of appropriate drainage facilities. However, considering the actual constructional and operational difficulties of this virtual network, the black lines in panel (a) are simplified as three main channels, such as A to A′, B to B′, and C to C′ in panel (c), indicating three routes representative of the most demands in the simulation. It is observed that a cross-tributary design in the upstream (A-A′) and a new channel linking flooded areas to a huge pond (C-C′) or to a pond cluster (B-B′) are preferred for this purpose.

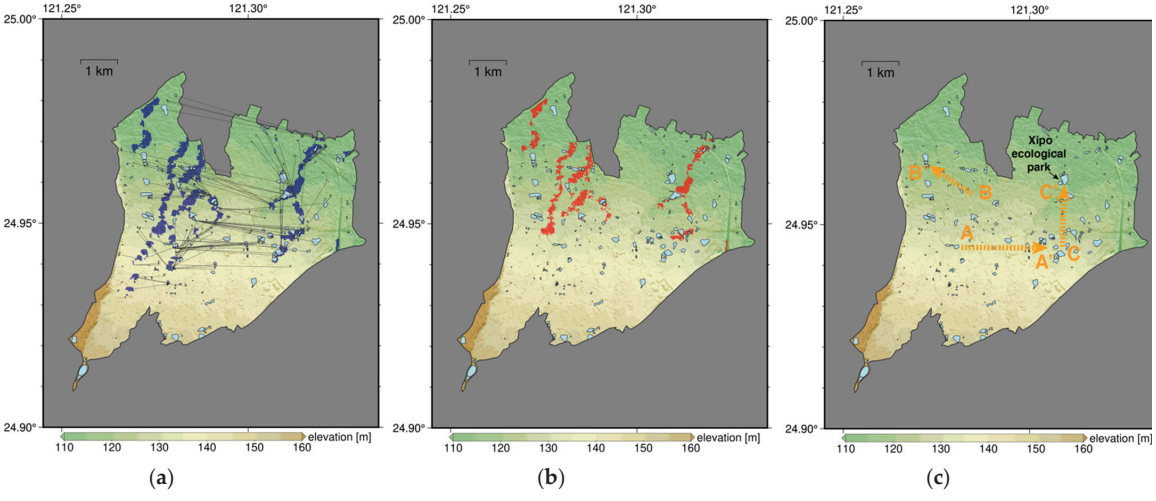

Figure 11. SPM flood simulation under 75 mm rainfall scenario by using pre-emptied ponds: (**a**) flood patches (blue) and their links to the unfilled ponds (black line); (**b**) reduced flood patches (red) after floodwater redistribution; and (**c**) three main routes of water redirection to reduce flood hazard.

A similar simulation of the dissipating procedure was conducted for the other three rainfall scenarios and the results are illustrated in Figure 12. In this figure, the blue plus red patches indicate flooded areas initially simulated by SPM and the red patches are the ones left after virtual channel dissipating scheme, similar to an overlap of panel *a* and *b* in Figure 11. Another symbol introduced in this figure is the green patch, which is used to highlight the difference between using depth in the historical data (with green) and using the updated pond model (without green) in simulations. For example, in the 25 mm case, the green patches in the middle exist because old data underestimate pond storage, and thus the floodwater cannot be shared by the neighboring ponds. In contrast, by updating several ponds through our fieldwork (yellow filling) to the west, most sites were found bigger in their storage and hence could accommodate floodwater from those green patches. It is clear, especially in 25 mm and 50 mm rainfall scenarios. However, as rainfall increases, the water storage capacity is minor in the portion of floodwater, so the DEM correctness becomes less important. As a result, almost no green patches can be seen in 75 mm and 100 mm cases.

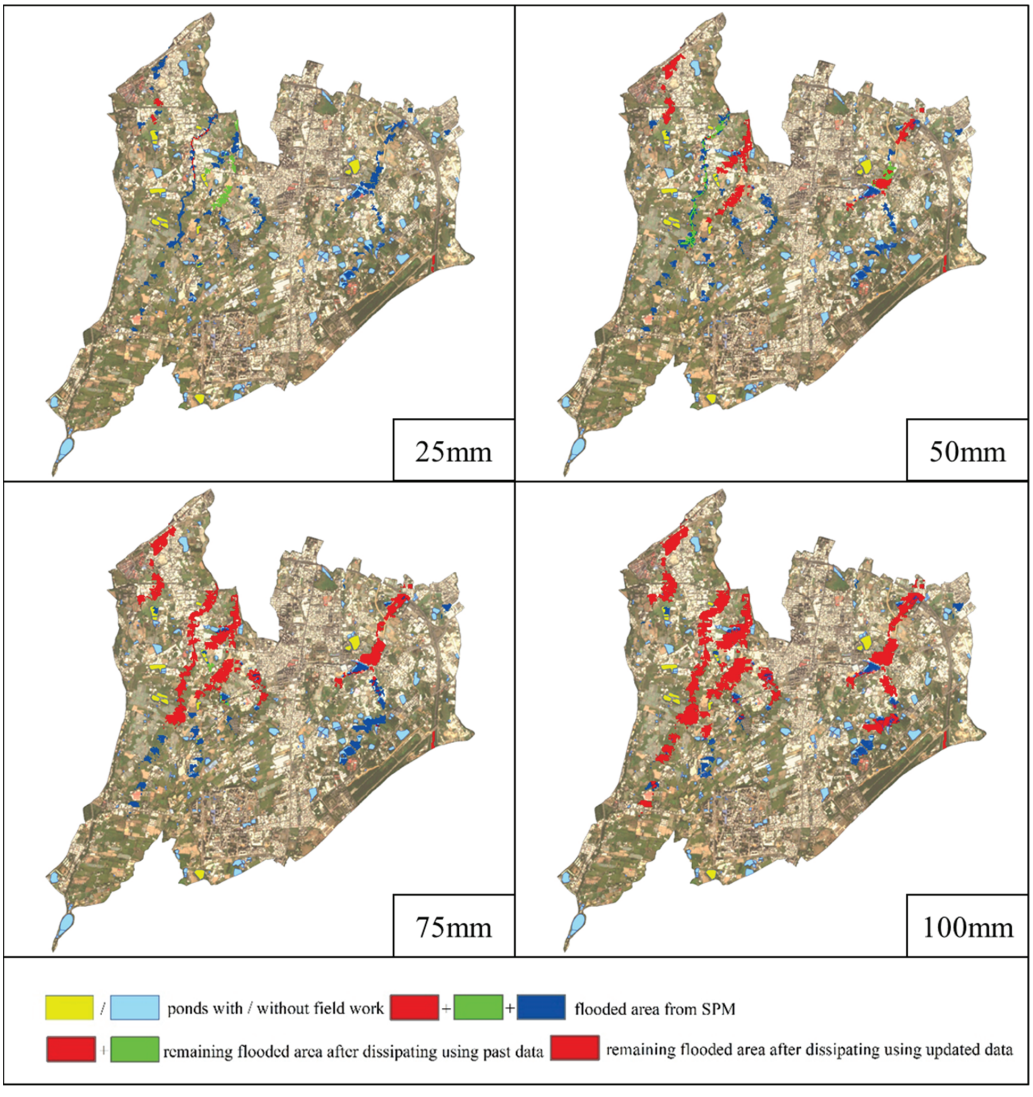

Figure 12. Simulation of the flooded area in Bade District (north up). The terrain declined from south to north. Four panels represent rainfall simulations from 25 mm to 100 mm. The base map adopts Sentinel-2 natural color composite on 17 November 2019.

Because SPM gives the highest contribution to the lowest elevation in this region, the flood accumulates from the top (north) to the bottom (south) direction. When the rainfall amount is 25 mm, most of the flooded areas could be dissipated if there was a channel system linking ponds downslope of the flood hotspots. When rainfall amount reaches 50 mm, there could still be a significant reduction in the flooded areas. However, when rainfall amount reaches 75 mm or 100 mm, the contribution of ponds becomes progressively insignificant. Figure 13 shows the reduction percentage in flood areas and water volumes, based on four rainfall scenarios. The red solid/dashed line and blue solid/dashed line indicate the simulated flood area with/without our fieldwork and the simulated water volume with/without our fieldwork, respectively. When rainfall amounts increase from

25 mm to 50 mm, 75 mm, and 100 mm, reductions of flood area by the pond model updated in this study are 96%, 75%, 52%, and 37%, respectively. A similar trend is found in flood volume. When rainfall amounts increase in those four scenarios, reductions of flood volume by the updated pond model are 93%, 56%, 28%, and 14%, respectively. Overall, results from the updated pond model show up to 10% less flooded area and 3 to 7% less floodwater volume than the old model (TYWR) in four rainfall scenarios. Based on this simulation, the administrative agencies could have an overview of the first-order flood-prone areas in this district, and plan/renovate inter-pond channels that are close to the flooded patches. Meanwhile, those on-site tenants must carry out desilting work regularly, once the ponds are requisitioned to the flood detention network.

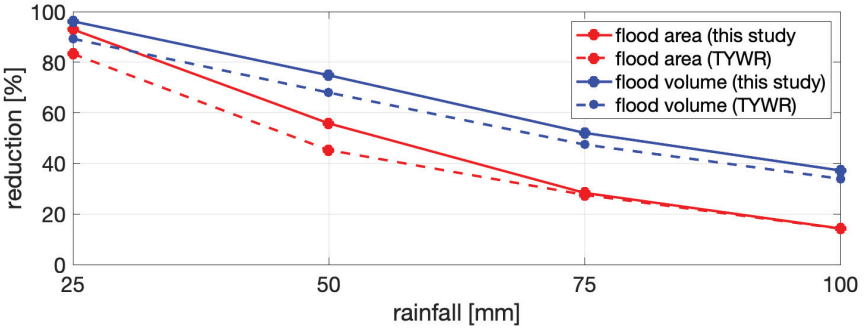

Figure 13. The percentage of the reduced flood area and volume based on the TYWR database and the ones based on our fieldwork.

4. Discussion

This study utilized a novel water depth measuring module that could apply to small waterbodies difficult to be accessed or to be surveyed with traditional equipment. Meanwhile, the accuracy of UAV-assisted depth measurement was comparable with the reference data. The advantage of this approach is the capability of recovering underwater terrain of a pond insensible by optical remote sensing methods, or the ones full of aerators and wires unable to operate a ship. The method is particularly handy for quickly verifying the renovation of a pond. For example, the Xipo ecological park (labeled in Figure 11c, a combination of BD089 and BD090 in Appendix A) has 88,092 m^3 of the estimated storage, which is close to the nominally new storage announced onsite (88,000 m^3) [34] than the record in the outdated TYWR database (40,543 m^3). It is also the main reason why several black lines in Figure 11a connect between flooded patches to the Xipo ecological park, such as the route C-C′ in Figure 11c. Actually, the three main routes suggested in Figure 11c are in accordance with a majority of built-up areas in Bade District, as shown in Figure A1 of Appendix B. It affirms the need for a new drainage system to reduce the risk of flood hazards over the densely populated area. In the future, when this procedure could be regularly operated, the tenant and owner (administrative agencies) should systematically monitor the timely change of pond sedimentation.

Moreover, the actual storage is crucial for the first crop of paddy rice cultivation (January–June) for irrigation purposes. Taiwan experienced a severe drought event in 2021 [35], which was the worst in 56 years, and forced almost all farmers to leave their land fallow in April and May. Therefore, preparatory storage of water in the pond system could mitigate the impact of drought events under any prompt water rationing schemes from the reservoir upstream. Based on Appendix A, the sum of estimated storage (2,928,301 m^3) is greater than the TYWR record (2,647,510 m^3) by 280,791 m^3. If we took the 2500:1 as the ratio of water supply for rice cultivation [36], the storage estimation uncertainty is 112 tons of rice production in equivalent, which highlights the need for accurate quantification of capacity in this regard.

On the other hand, the pond system has an advantage in flood prevention. Although the terrain of Taoyuan city belongs to the tableland, for the time being, historical flood hazards had not caused a disastrous impact. Flood events in the record showed that regional flooding was mainly caused by insufficient drainage and large amounts of precipitation in a short period, which makes SPM applicable in this case. In this research, after updating the storage of 15 ponds in Bade District, as the ones starting with "BD" in Appendix A, the total water storage in Bade increases by 127,216 m^3 (from 252,475 m^3 to 379,691 m^3), about 10% of the previous total volume. Our analysis shows that the virtual detention system could effectively reduce 83–93% and 45–56% of flood areas under 25 mm and 50 mm precipitation scenarios, respectively. However, the flooded area is much less reduced when the rainfall is 75 mm (28% reduction) and 100 mm (14% reduction) by using either new or old pond DEM. Another simulation (not shown here) indicates that if a total of 224 ponds larger than 400 m^2 in Bade could increase by 20% of its storage, the ratio of remaining flooded areas and volumes could be further decreased by 4% and 3.4%, respectively when rainfall is 100 mm.

Compared with various depth mapping methods at present, traditional methods such as surveying instruments are time-consuming and laborious or require the navigation of ships. Although the precision and resolution of LiDAR are more attractive, the instrument is expensive (updated every six years in Taiwan) and the operation is highly restricted by water quality. In this study, a UAV combined with sonar was proven to reduce time and labor costs [24]. Meanwhile, the UAV module shows high mobility characteristics that undoubtedly provide a novel method for water storage estimation. Although a few estimates in our research deviated from those in TYWR, attributed to seasonal and anthropogenic factors, the study showed that most results match well with the planned storage.

5. Conclusions

Flood hazard has become a deepening problem because of urban development and the loss of natural pervious surfaces. Asphalt in urban reduces seepage and allows heavy rainfall runoff to flood. Ancestors built thousands of ponds around current Taoyuan City to collect precipitation for irrigation. However, with the transformation from an agricultural to an industrial society, the watercourse has been deserted because of the lack of appropriate management and operation. The basic information of waterbodies, i.e., area and storage, has been poorly investigated and thus put huge uncertainty when using them for data analysis and simulation. In this research, a novel bathymetry technique, UAV with sonar and smartphone, was developed to perform bathymetry. Easily implementated with a few operators at each site, the fully integrated pond model with the neighboring land can be built for updating the outdated database. The system successfully detected two anomalies (CL143 and YM051) whose storages were apparently incorrect in the record. In the future, this system can be used to rapidly verify ponds whose single geometric parameter (area, depth, and volume) is not convertible by others.

In flood simulation, SPM showed the potential of a >70% reduction in flood areas in Bade when a sudden heavy rain of <50 mm occurred. The existing pond network in Bade may assist in retaining floodwater and mitigating the severity of flood hazards. However, it should be emphasized that the flood maps derived herein depend on the assumption of virtual channels between flood patches and ponds located downslope. The results could be a good reference for administrative agencies to optimize or reinvigorate abandoned channels/pipelines currently in the field.

Author Contributions: Conceptualization, K.-H.T. and C.-F.C.; methodology, K.-H.T., T.-H.Y. and Y.-C.H.; software, T.-H.Y. and P.-Y.C.; validation, H.C. and Y.-C.H.; investigation, H.C., P.-Y.C. and Y.-C.H.; data curation, K.-H.T. and Y.-C.H.; writing, K.-H.T., T.-H.Y., P.-Y.C. and Y.-C.H. All authors have read and agreed to the published version of the manuscript.

Funding: This research is supported partially by grants from the National Science and Technology Council of Taiwan (108-2621-M-008 -008 - and 106-2410-H-305 -003 -), and partially by grants from the Department of Water Resources, Taoyuan City Government (1071205-P1 and 1081202-P1).

Data Availability Statement: Not applicable.

Acknowledgments: We thank Chung-Yen Kuo in the Department of Geomatics, National Cheng Kung University, Taiwan, to provide the Otter Unmanned Surface Vehicle data.

Conflicts of Interest: The authors declare no conflict of interest.

Appendix A

Table A1. Pond parameters of 80 cases surveyed by the UAV module.

NUM	ID	S [°]	Min Depth [m]	Max Depth [m]	Estimated Area [m^2]	TYWR Area [m^2]	O_k [m]	Estimated Storage [m^3]	TYWR Storage [m^3]
1	GI275	20	1.0	2.0	68,737	71,039	0.2	106,664	163,711
2	CL086	60	0.5	1.5	36,456	39,632	0.6	51,313	22,194
3	BD293	25	1.2	1.8	24,394	24,219	0.7	45,185	31,152
4	BD027	60	0.7	1.1	25,922	25,975	0.8	39,370	39,890
5	YM145	25	1.1	2.2	21,350	22,033	0.5	39,399	67,300
6	GI277	25	1.2	2.2	64,744	62,735	0.7	134,353	145,900
7	CL170	30	0.9	2.1	31,474	29,986	0.2	43,348	16,200
8	CL143	27	1.3	2.5	62,326	64,182	0.5	133,196	4705
9	HW256	30	1.4	2.9	22,477	21,696	0.5	54,315	22,060
10	HW279	60	0.5	1.2	5732	7413	0	4303	12,416
11	GI278	60	0.5	0.7	9187	9824	0	4915	7398
12	GI279	60	0.5	0.8	23,608	25,315	0	13,343	19,063
13	GI281	30	0.8	1.5	25,078	28,369	0.6	40,726	20,450
14	GI283	60	0.5	1.2	36,175	37,414	0	28,719	21,290
15	CL186	60	0.7	1.5	5693	5529	0	5497	1493
16	PZ159	60	1.1	1.8	8068	8104	0	10,349	4537
17	PZ160	60	0.5	1.5	4289	4239	0	4338	2373
18	BD031	30	0.5	1.4	11,026	12,093	1.5	22,346	15,001
19	BD032	23	1.8	3.1	11,216	10,548	0.7	29,465	13,085
20	BD033	23	1.9	4.1	13,007	13,006	0.4	42,129	16,134
21	GI260	30	1.0	3.2	27,918	26,917	0.6	64,578	37,331
22	BD089	30	1.2	1.7	38,247	36,961	0.5	66,582	33,027
23	BD090	30	0.7	2.1	12,514	8411	0.5	21,510	7516
24	YM421	27	1.4	2.2	8661	8402	0.1	13,431	6715
25	YM422	60	1.4	1.8	2683	3610	0	3530	2885
26	YM427	30	0.9	1.8	6378	4918	0	6985	14,990
27	PZ047	28	1.4	2.7	12,712	12,427	0.4	28,408	33,626
28	PZ048	30	1.3	2.0	6846	6510	0.3	11,599	17,616
29	CL233	35	0.8	3.5	5648	9360	0.3	9371	7696
30	BD025	25	0.7	1.3	11,983	12,441	0	10,278	4336
31	BD026	25	0.5	1.0	4745	5118	0.4	4602	1784
32	BD010	30	1.0	1.4	5788	6340	0	6619	5790
33	BD011	30	1.0	1.9	23,093	22,898	1	48,102	47,323
34	YM187	30	2.2	4.4	40,608	38,727	0	112,656	42,380
35	YM189	30	0.9	1.7	24,959	21,433	0.4	35,428	23,454
36	YM344	22	0.7	1.9	86,244	86,085	0.7	155,564	247,140
37	CL128	60	0.5	0.8	13,516	13,763	0	7378	13,073
38	CL120	26	1.5	3.0	28,955	27,882	0.5	64,892	39,693

Table A1. *Cont.*

NUM	ID	S [°]	Min Depth [m]	Max Depth [m]	Estimated Area [m^2]	TYWR Area [m^2]	O_k [m]	Estimated Storage [m^3]	TYWR Storage [m^3]
39	YM346	25	0.5	0.9	63,450	65,130	0.4	60,790	137,743
40	HW251	60	0.5	0.7	6560	6670	0.6	7169	5870
41	YM049	25	2.1	2.7	21,001	21,473	0.3	47,260	60,638
42	YM300	30	1.3	2.2	21,921	20,457	0.6	46,038	70,000
43	CL158	30	0.9	2.2	14,476	14,385	0	15,972	10,450
44	YM029	25	0.8	1.5	35,804	38,775	0.5	51,139	59,900
45	YM030	25	1.9	3.4	22,437	23,245	0.8	66,584	29,072
46	YM330	25	0.9	2.7	25,951	25,184	1	61,341	65,300
47	YM375	23	2.1	3.5	22,264	20,916	0	49,162	30,800
48	YM377	25	1.5	2.4	15,931	18,164	1.5	46,481	126,000
49	PZ144	30	1.9	2.2	2587	3261	0.6	5918	5454
50	PZ145	30	1.4	1.9	2712	2557	0.3	4618	4276
51	PZ175	30	0.9	1.3	5752	5391	0.5	8314	5355
52	PZ172	60	0.6	0.8	9652	10,337	0	6267	6206
53	YM051	30	2.1	3.8	46,761	45,493	0.6	137,851	12,495
54	YM052	27	1.9	2.5	31,836	30,557	0.4	71,891	40,334
55	YM343	30	0.8	2.0	37,884	36,331	0.5	69,664	82,160
56	YM082	35	1.4	1.9	14,798	15,159	0	21,119	5940
57	HW294	30	1.2	1.5	10,794	10,408	0	13,006	11,980
58	YM076	25	0.5	1.5	52,130	51,825	1	87,449	108,110
59	YM095	23	1.1	2.0	24,241	25,701	0.6	41,776	34,469
60	YM350	25	1.1	2.1	24,434	24,433	0.5	43,389	31,618
61	YM352	25	1.7	2.5	27,336	27,713	1	75,154	79,000
62	BD075	60	1.1	1.4	3639	4237	0	4154	2892
63	BD036	30	0.8	1.6	10,233	9402	0.6	15,025	9750
64	BD165	30	0.7	1.7	10,464	10,945	0.8	17,381	13,672
65	YM378	30	1.5	2.9	36,501	37,547	0.5	82,852	63,390
66	YM379	25	1.4	3.2	21,051	23,766	0.8	53,320	68,865
67	BD012	30	1.2	1.5	5894	5382	0	6943	11,123
68	CL273	60	0.5	0.7	14,079	14,365	0	7722	18,810
69	CL313	30	0.9	1.3	3906	4960	0	4060	6205
70	YM542	30	0.5	1.4	6108	6214	0.3	7016	11,380
71	YM520	30	0.9	1.7	3074	3379	0	3965	3210
72	YM462	30	0.8	1.2	5580	6647	0.6	7979	12,330
73	YM461	60	0.5	1.8	6256	7037	0	5392	11,776
74	YM147	60	0.6	0.9	5090	4703	0	3576	10,380
75	YM310	20	0.8	2.4	26,442	26,155	0.8	61,280	82,000
76	YM313	20	1.5	3.4	27,814	26,497	0.5	66,586	36,329
77	HW259	60	0.5	0.9	3462	4333	0	2192	5769
78	HW260	60	0.7	1.6	4444	3856	0	3904	5400
79	YM120	60	0.7	1.5	6448	7145	0	5347	10,298
80	YM163	30	0.8	1.5	6870	5573	0	6469	8034

Appendix B

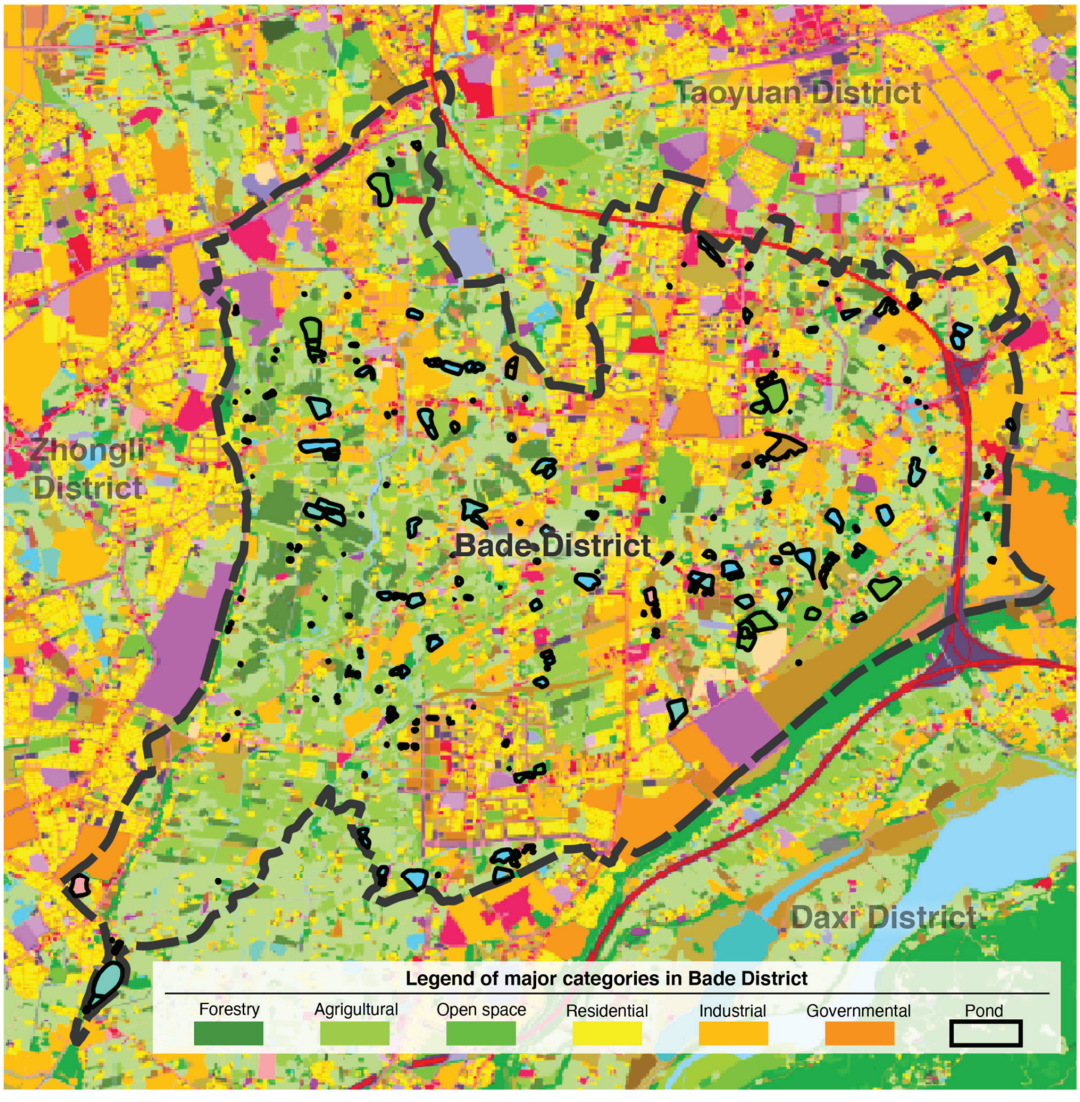

Figure A1. Land use map of Bade District. (modified from Taiwan MAP Service, National Land Surveying and Mapping Center, https://maps.nlsc.gov.tw (accessed on 1 July 2022)).

References

1. Fang, W.T.; Chu, H.J.; Cheng, B.Y. Modeling waterbird diversity in irrigation ponds of Taoyuan, Taiwan using an artificial neural network approach. *Paddy Water Environ.* **2009**, *7*, 209–216. [CrossRef]
2. Shih, N.J.; Qiu, Y.T. The Morphology of Evolved Urban Fabric around Farm Ponds. *Remote Sens.* **2021**, *13*, 437. [CrossRef]
3. Hakka Affairs Council. Taoyuan Tableland and Ponds. Available online: https://english.hakka.gov.tw/Content/Content?NodeID=692&PageID=42603&LanguageType=ENG (accessed on 1 August 2022).
4. Fang, W.; Huang, Y. Modelling Geographic Information System With Logistic Regression In Irrigation Ponds, Taoyuan Tableland. *Procedia Environ. Sci.* **2012**, *12*, 505–513. [CrossRef]
5. Department of Budget, Accounting and Statistics, Taoyuan. Available online: https://dbas.tycg.gov.tw/home.jsp?id=206&parentpath=0,13,47 (accessed on 1 August 2022).

6. Wang, J.J. Feasibility Analysis of Using Farm Ponds as Adaptation Tools for Stormwater Management. *Int. J. Clim. Chang. Impacts Responses* **2013**, *4*, 71–90. [CrossRef]
7. Wang, J.J.; Chang, S.S. Detention Analysis of Farm Pond and Ditch Network in Taoyuan City. *J. City Plan.* **2016**, *43*, 157–187. (In Chinese)
8. Kasvi, E.; Salmela, J.; Lotsari, E.; Kumpula, T.; Lane, S. Comparison of remote sensing based approaches for mapping bathymetry of shallow, clear water rivers. *Geomorphology* **2019**, *333*, 180–197. [CrossRef]
9. Xing, S.; Wang, D.D.; Xu, Q.; Lin, Y.Z.; Li, P.C.; Jiao, L.; Zhang, X.L.; Liu, C.B. A Depth-Adaptive Waveform Decomposition Method for Airborne LiDAR Bathymetry. *Sensors* **2019**, *19*, 5065. [CrossRef]
10. Wang, C.K.; Philpot, W.D. Using airborne bathymetric lidar to detect bottom type variation in shallow waters. *Remote Sens. Environ.* **2007**, *106*, 123–135. [CrossRef]
11. Costa, B.M.; Battista, T.A.; Pittman, S.J. Comparative evaluation of airborne LiDAR and ship-based multibeam SoNAR bathymetry and intensity for mapping coral reef ecosystems. *Remote Sens. Environ.* **2009**, *113*, 1082–1100. [CrossRef]
12. Hilldale, R.C.; Raff, D. Assessing the ability of airborne LiDAR to map river bathymetry. *Earth Surf. Proc. Land* **2008**, *33*, 773–783. [CrossRef]
13. Stumpf, R.P.; Holderied, K.; Sinclair, M. Determination of water depth with high-resolution satellite imagery over variable bottom types. *Limnol. Oceanogr.* **2003**, *48*, 547–556. [CrossRef]
14. Getirana, A.; Jung, H.C.; Tseng, K.H. Deriving three dimensional reservoir bathymetry from multi-satellite datasets. *Remote Sens. Environ.* **2018**, *217*, 366–374. [CrossRef]
15. Lurton, X. *Introduction to Underwater Acoustics*; Springer: Berlin, Germany, 2016.
16. Nex, F.; Remondino, F. UAV For 3D Mapping Applications: A Review. *Appl. Geomat.* **2013**, *6*, 1–15. [CrossRef]
17. Liu, P.; Chen, A.Y.; Huang, Y.N.; Han, J.Y.; Lai, J.S.; Kang, S.C.; Wu, T.H.; Wen, M.C.; Tsai, M.H. A review of rotorcraft Unmanned Aerial Vehicle (UAV) developments and applications in civil engineering. *Smart Struct. Syst.* **2014**, *13*, 1065–1094. [CrossRef]
18. Fonstad, M.A.; Dietrich, J.T.; Courville, B.C.; Jensen, J.L.; Carbonneau, P.E. Topographic structure from motion: A new development in photogrammetric measurement. *Earth Surf. Proc. Land* **2013**, *38*, 421–430. [CrossRef]
19. Javemick, L.; Brasington, J.; Caruso, B. Modeling the topography of shallow braided rivers using Structure-from-Motion photogrammetry. *Geomorphology* **2014**, *213*, 166–182. [CrossRef]
20. Alvarez, L.V.; Moreno, H.A.; Segales, A.R.; Pham, T.G.; Pillar-Little, E.A.; Chilson, P.B. Merging Unmanned Aerial Systems (UAS) Imagery and Echo Soundings with an Adaptive Sampling Technique for Bathymetric Surveys. *Remote Sens.* **2018**, *10*, 1362. [CrossRef]
21. Bandini, F.; Olesen, D.; Jakobsen, J.; Kittel, C.M.M.; Wang, S.; Garcia, M.; Bauer-Gottwein, P. Technical note: Bathymetry observations of inland water bodies using a tethered single-beam sonar controlled by an unmanned aerial vehicle. *Hydrol. Earth Syst. Sci.* **2018**, *22*, 4165–4181. [CrossRef]
22. Yang, T.H.; Chen, Y.C.; Chang, Y.C.; Yang, S.C.; Ho, J.Y. Comparison of Different Grid Cell Ordering Approaches in a Simplified Inundation Model. *Water* **2015**, *7*, 438–454. [CrossRef]
23. Takasu, T.; Yasuda, A. Development of the low-cost RTK-GPS receiver with an open source program package RTKLIB. In Proceedings of the International Symposium on GPS/GNSS, 2009, International Convention Center, Jeju, Republic of Korea, 4–6 November 2009; Volume 1.
24. Hung, Y.C.; Wan, H.H.; Tsai, P.Y.; Liao, W.T.; Tseng, K.H. Using UAV with Low-cost Sonar to Measure Parameters of Ponds. *J. Photogramm. Remote Sens.* **2019**, *24*, 135–146. (In Chinese)
25. Kong, S.H. Fast Multi-Satellite ML Acquisition for A-GPS. *IEEE T Wirel Commun.* **2014**, *13*, 4935–4946. [CrossRef]
26. Curtarelli, M.; Leão, J.; Ogashawara, I.; Lorenzzetti, J.; Stech, J. Assessment of spatial interpolation methods to map the bathymetry of an Amazonian hydroelectric reservoir to aid in decision making for water management. *ISPRS Int. J. Geo-Inf.* **2015**, *4*, 220–235. [CrossRef]
27. Henrico, I. Optimal interpolation method to predict the bathymetry of Saldanha Bay. *Trans. GIS* **2021**, *25*, 1991–2009. [CrossRef]
28. Bartier, P.M.; Keller, C.P. Multivariate interpolation to incorporate thematic surface data using inverse distance weighting (IDW). *Comput. Geosci.* **1996**, *22*, 795–799. [CrossRef]
29. Lu, G.Y.; Wong, D.W. An adaptive inverse-distance weighting spatial interpolation technique. *Comput. Geosci.* **2008**, *34*, 1044–1055. [CrossRef]
30. Tarboton, D.G. A new method for the determination of flow directions and upslope areas in grid digital elevation models. *Water Resour. Res.* **1997**, *33*, 309–319. [CrossRef]
31. Bulti, D.; Abebe, B. A Review Of Flood Modeling Methods For Urban Pluvial Flood Application. *Model. Earth Syst. Environ.* **2020**, *6*, 1293–1302. [CrossRef]
32. Hung, Y.C. Using Mobile Bathymetry System to Produce Bathymetry Model in Shallow Water Area. Master's Thesis, National Central University, Taoyuan City, Taiwan, 2020.
33. Zheng, S.T. It Rained Heavily in Afternoon in Taoyuan, and Serval Road Sections in Bade Were Flooded. *Liberty Times Net*. 25 June 2019. Available online: https://news.ltn.com.tw/news/life/breakingnews/2833370. (accessed on 1 August 2022). (In Chinese).
34. Department of Public Information, Taoyuan. Available online: https://news.tycg.gov.tw/home.jsp?id=2&parentpath=0&mcustomize=news_view.jsp&dataserno=201708220001&aplistdn=ou=news,ou=chinese,ou=ap_root,o=tycg,c=tw&toolsflag=Y#U (accessed on 1 August 2022). (In Chinese)

35. Chou, C.; Weng, M.; Huang, H.; Chang, Y.; Chang, H.; Yeh, T. Monitoring The Spring 2021 Drought Event In Taiwan Using Multiple Satellite-Based Vegetation And Water Indices. *Atmosphere* **2022**, *13*, 1374. [CrossRef]
36. Bouman, B. How much water does rice use. *Management* **2009**, *69*, 115–133.

applied sciences

MDPI

Article

An Aeromagnetic Compensation Algorithm Based on Radial Basis Function Artificial Neural Network

Shuai Zhou [1], Changcheng Yang [1], Zhenning Su [2], Ping Yu [1] and Jian Jiao [1,*]

[1] College of GeoExploration Science and Technology, Jilin University, Changchun 130012, China
[2] Institute of Geophysical and Geochemical Exploration, Chinese Academy of Geoscience, Langfang 065000, China
* Correspondence: jiaojian001@jlu.edu.cn

Abstract: Aeromagnetic exploration is a magnetic exploration method that detects changes of the earth's magnetic field by loading a magnetometer on an aircraft. With the miniaturization of magnetometers and the development of unmanned aerial vehicles (UAV) technology, UAV aeromagnetic surveying plays an increasingly important role in mineral exploration and other fields due to its advantages of low cost and safety. However, in the process of aeromagnetic measurement data, due to the ferromagnetic material of the aircraft itself and the change of flight direction and attitude, magnetic field interference will occur and affect the measurement of the geomagnetic field by the magnetometer. The work of aeromagnetic compensation is to compensate for this part of the magnetic interference and improve the magnetic measurement accuracy of the magnetometer. This paper focused on the problems of UAV aeromagnetic survey data processing and improved the accuracy of UAV based aeromagnetic data measurement. Based on the Tolles–Lawson model, a numerical simulation experiment of magnetic interference of UAV-based aeromagnetic data was carried out, and a radial basis function (RBF) artificial neural network (ANN) algorithm was proposed for the first time to compensate the aeromagnetic data. Compared with classical backpropagation (BP) ANN, the test results of the synthetic data and real measured magnetic data showed that the RBF-ANN has higher compensation accuracy and stronger generalization ability.

Keywords: aeromagnetic compensation; radial basis function; deep learning; unmanned aerial vehicles (UAV); local minimum

Citation: Zhou, S.; Yang, C.; Su, Z.; Yu, P.; Jiao, J. An Aeromagnetic Compensation Algorithm Based on Radial Basis Function Artificial Neural Network. *Appl. Sci.* **2023**, *13*, 136. https://doi.org/10.3390/app13010136

Academic Editors: Andrzej Łukaszewicz, Wojciech Giernacki, Zbigniew Kulesza, Jaroslaw Pytka and Andriy Holovatyy

Received: 22 November 2022
Revised: 16 December 2022
Accepted: 16 December 2022
Published: 22 December 2022

1. Introduction

With the development of the global economy, the demand for mineral resources in all countries in the world is also increasing. However, due to complex terrain conditions, many areas rich in mineral resources cannot be explored. In order to increase the detection range and improve exploration efficiency, aeromagnetic measurement technology has been rapidly developed. Airborne magnetic surveying is an important airborne geophysical exploration method, which can be used for magnetic data acquisition under various complex terrain conditions.

Moreover, UAV technology has developed very rapidly and has been well used in all walks of life, so UAV survey technology has gradually developed, and is now widely used in resource exploration, regional survey and other fields [1,2]. With the development of UAV technology, more and more countries have carried out the research and development of UAV aeromagnetic measurement equipment technology and achieved remarkable results. The available information indicates that the first company in the world to develop UAV aeromagnetic survey equipment was Magsurvey in the United Kingdom, which developed the PrionUAV aeromagnetic survey system in 2003 [3]. Since then, many companies around the world have conducted research and development of UAV aeromagnetic survey systems, such as the GeoRanger-I of the Dutch company Fugro [4], the Canadian company Universal Wing Geophysical (UWG) Venturer [5], the Japanese RMAX-G1 [6], the Swiss and German

jointly developed reconnaissance B1-100 [7], the German MD4-1000 [8], CH-3 [9] from the Institute of Geophysical and Geochemical Exploration (IGGE) of the Chinese Academy of Geological Science, and an integrated multi-rotor aeromagnetic survey system at Queen's University in Canada [10].

Due to the ferromagnetic material inside the UAV and its various influences during flight, it will inevitably cause certain interference to the data collected by the magnetometer sensor; if we want to obtain high-quality aeromagnetic data, we must study the appropriate aeromagnetic compensation technology [11,12].The compensation methods of aeromagnetic interference are mainly divided into hardware compensation and software compensation. The hardware compensation method is to first calculate the magnetic interference of the detection platform, and then add several coils to the detection platform to counteract the magnetic interference generated by the aircraft. In the late 20th century, high-cost, low-precision hardware compensation began to be slowly replaced by software compensation [11]. According to the nature and causes of magnetic interference, Tolles and Lawson divided it into constant interference, induced interference, and eddy current interference, and established the classic Tolles–Lawson model (T-L model) [13], which is the foundation on which current aeromagnetic compensation methods are built. Based on the T–L model, Leliak established an aeromagnetic compensation method based on FOM compensation flight [14]. The variables in the T–L equation are not independent of each other, and the linear relationship between the variables affects the stability of the solution, and the linear relationship between the variables is called multicollinearity. Bickel proposed a small-signal method to weaken the linear relationship between variables, resulting in a more stable solution [15]. Leach first proposed to overcome the multicollinearity problem of equations by introducing regularization terms through the linear regression method [16], Hardwick et al. proposed a compensation algorithm for total field gradients [17]. Dou proposes a new real-time method based on recursive least squares, and the simulation results showed that the method has a good ability to compensate for magnetic interference caused by an aircraft and its maneuvering [18]. Wu et al. use principal component analysis (PCA) to reduce the multicollinearity of the T-L model [19]. Xu applied deep learning to magnetic anomaly detection and noise cancellation [20].

Considering the lack of computational accuracy and generalization ability of linear regression methods, people began to explore new aeromagnetic compensation algorithms through neural networks. Williams successfully established an aeromagnetic compensation model based on a neural network for the first time, but his model had the problem of overfitting [21]. Zhang proposes a new compensation method that used a one-dimensional convolutional neural network to perform secondary compensation on the data that were compensated by the T–L model to eliminate the influence of tail boom swing, which has a significant compensation effect on aeromagnetic noise [22]. Ma proposed a dual estimation method for aeromagnetic compensation, combining a linear model with a neural network to improve the accuracy of magnetic compensation [23]. Although the above two methods improved the accuracy of aeromagnetic compensation, there were also problems, such as difficult parameters selection and complex network structures in design. Yu et al. proposed an aeromagnetic compensation algorithm based on deep autoencoder (DAE) [24], which reduced the multicollinearity between variables in the T–L equation, but it was not perfect for the feature extraction of high-dimensional complex data in the training process of the autoencoder network, and the local minimum problem easily occurred. They then proposed to use a generalized regression neural network (GRNN) to establish an aeromagnetic compensation model, which had a fast calculation speed, high compensation accuracy, and no backpropagation [25]. Although they solved the problem of over fitting, the problem of gradient disappearance was not considered.

The aeromagnetic compensation method based on a neural network still has some problems to be solved, such as local minimum problems in backpropagation, difficult parameters selection, and complex network structures. In order to further improve the accuracy of aeromagnetic compensation, this paper proposed, for the first time, a magnetic

compensation method based on BRF-ANN, which is widely used in function approximation, pattern recognition, and signal processing [26]; it is also widely used in aerospace, such as the longitudinal channel flight control of small UAVs [27], the navigation of UAVs [28], issues related to the optimization of UAV [29], and so on. The hidden nodes of RBF-ANN adopted the distance between the input mode and the center vector (such as the Euclidean distance) as the independent variable of the function and used the radial basis function (such as the Gaussian function) as the activation function, which is a local approximation network with better generalization ability and a simple network design. The paper is divided into five chapters. The first and last chapters present the introduction and conclusion. The second chapter discusses compensation models and methods, introducing the T–L model and the principles of BP-ANN and RBF-ANN, including the characteristics of RBF-ANN. The third chapter introduces data simulation and testing, and the fourth chapter shows the testing of the measured data; the results are displayed in graphs and tables and a method effectiveness analysis was also carried out. The application and analysis of theoretical synthetic data and real measured aeromagnetic compensation data showed that the proposed method effectively solved the problem of high-precision compensation of aeromagnetic survey data based on rotary wing UAV platform, and greatly improved the error compensation accuracy of aeromagnetic dynamic measurement data.

2. Compensation Models and Methods

2.1. T-L Model

The conversion relationship between the local coordinate system and the aircraft coordinate system is shown in Figure 1. The center of the magnetometer probe mounted on the drone is set as the origin of the coordinate system O, x_b, y_b, and z_b are the coordinate axes of the aircraft coordinate system, and their distribution direction is parallel to the direction of the three axes of the magnetometer. x, y, and z are the spatial axes of the local coordinate system at the same origin as the aircraft coordinate system. The y_c axis is the projection of the y_b axis on the xOy plane. The flight attitude during the flight of the drone can be divided into three parts: side sliding, roll and pitch. Where, is the angle between xb axis and plane xOy, is the angle between y_b axis and y_c axis, and is the angle between y axis and y_c axis. The local coordinate system can be rotated according to the sequence of yaws ψ, pitches λ and rolls θ. The rotation sequence cannot be replaced at will [5].

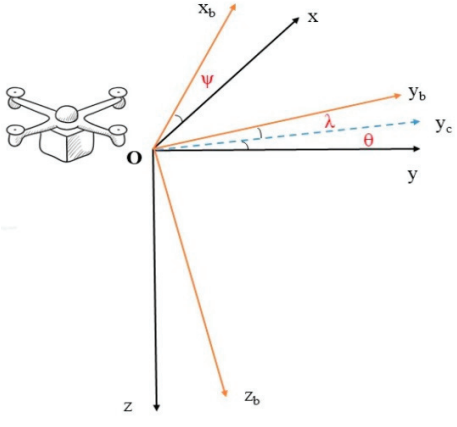

Figure 1. Coordinate system conversion relationship.

Tolles and Lawson divide interference fields into constant interference fields, induced interference fields, and eddy current interference fields, according to their nature and causes [9]. The constant interference field (H_p) is caused by direct current in the ferromagnetic material and wires inside the aircraft, and its value and direction are independent of

the flight attitude of the aircraft, and the interference value is constant for the same aircraft. The induced interference field (H_i) is produced by the magnetization of soft magnetic or paramagnetic substances inside the aircraft by the geomagnetic field, and its magnitude and direction are closely related to the flight attitude of the aircraft and the changes of the local geomagnetic field. The eddy current interference field is generated by the metal body cutting the geomagnetic field magnetic induction line during the flight of the aircraft, and its size and direction change with the change of the geomagnetic field gradient, flight acceleration and flight action [5]. They can be represented in the aircraft coordinate system as:

$$H_P = c_1u_1 + c_2u_2 + c_3u_3 \tag{1}$$

$$H_i = T(c_4u_1^2 + c_5u_1u_2 + c_6u_1u_3 + c_7u_2^2 + c_8u_2u_3 + c_9u_3^2) \tag{2}$$

$$\begin{array}{c} H_{ec} = T(c_{10}u_1u_1' + c_{11}u_2u_1' + c_{12}u_3u_1' + c_{13}u_1u_3' \\ +c_{14}u_2u_3' + c_{15}u_3u_3' + c_{16}u_1u_2' + c_{17}u_2u_2' + c_{18}u_3u_2') \end{array} \tag{3}$$

$$u_1 = \frac{T_{bx}}{T_t}, u_2 = \frac{T_{by}}{T_t}, u_3 = \frac{T_{bz}}{T_t} \tag{4}$$

$$T_t = \sqrt{T_{bx}^2 + T_{by}^2 + T_{bz}^2}, \tag{5}$$

where T represents the geomagnetic field, c_1, c_2, ..., c_{18} represents the compensation coefficient, u_1, u_2, and u_3 are the cosine values of the angle between the three axes of the aircraft coordinate system and the geomagnetic field direction, u_1', u_2', u_3' are the differentiation of u_1, u_2, u_3 with respect to time t, T_t represents the total geomagnetic field data measured by the optical pump magnetometer, T_{bx}, T_{by} and T_{bz} represent the three components of the fluxgate. The accuracy of the measured data of the triaxial fluxgate magnetometer is far inferior to that of the optical pump magnetometer, and it also needs to be corrected accordingly during its installation, resulting in errors in the measured fluxgate three-component data, which indirectly affects the compensation effect. Therefore, this paper needs to make corresponding corrections to the measured fluxgate three-component data, and the correction formula is as follows:

$$\begin{bmatrix} T_{bx} \\ T_{by} \\ T_{bz} \end{bmatrix} = D \begin{bmatrix} T_{gx} \\ T_{gy} \\ T_{gz} \end{bmatrix} \tag{6}$$

$$D = \begin{bmatrix} \cos\theta\cos\psi & \sin\theta\cos\psi & -\sin\psi \\ \cos\theta\sin\lambda\sin\psi - \sin\theta\cos\lambda & \sin\theta\sin\lambda\sin\psi + \cos\theta\cos\lambda & \sin\lambda\cos\psi \\ \cos\theta\cos\lambda\sin\psi + \sin\theta\sin\lambda & \sin\theta\cos\lambda\sin\psi - \cos\theta\sin\lambda & \cos\lambda\cos\psi \end{bmatrix} \tag{7}$$

$$T_{gx} = T\cos\varphi\cos\mu \tag{8}$$

$$T_{gy} = T\cos\varphi\sin\mu \tag{9}$$

$$T_{gz} = T\cos\varphi\sin\varphi, \tag{10}$$

where Ψ is the side roll angle when the aircraft is flying, λ is the pitch angle when the aircraft is flying, θ is the side slip angle when the aircraft is flying, μ is the magnetization bias angle, and φ is the magnetization tilt angle

Finishing Formulas (1)~(5) can be obtained, the total interference magnetic field (H_t) of the aircraft is:

$$\begin{array}{l} H_t = H_p + H_i + H_{ec} \\ = T(c_1u_1/T + c_2u_2/T_t + c_3u_3/T \\ +c_4u_1^2 + c_5u_1u_2 + c_6u_1u_3 + c_7u_2^2 + c_8u_2u_3 + c_9u_3^2 \\ +c_{10}u_1u_1' + c_{11}u_2u_1' + c_{12}u_3u_1' + c_{13}u_1u_3' + c_{14}u_2u_3' \\ +c_{15}u_3u_3' + c_{16}u_1u_2' + c_{17}u_2u_2' + c_{18}u_3u') \end{array}, \tag{11}$$

According to the relationship between u_1, u_2, and u_3

$$\begin{array}{c} u_1^2 + u_2^2 + u_3^2 = 1 \\ u_1 u_1' + u_2' u_2' + u_3 u_3' = 0 \end{array}', \tag{12}$$

After sorting out Equations (11) and (12), we get:

$$H_t = \begin{bmatrix} b_1 \\ b_2 \\ b_3 \\ b_4 \\ b_5 \\ b_6 \\ b_7 \\ b_8 \\ b_9 \\ b_{10} \\ b_{11} \\ b_{12} \\ b_{13} \\ b_{14} \\ b_{15} \\ b_{16} \end{bmatrix}^T \begin{bmatrix} u_1/T \\ u_2/T \\ u_3/T \\ u_1^2 \\ u_1 u_2 \\ u_1 u_3 \\ u_2 u_3 \\ u_2^2 \\ u_1 u_1' \\ u_2 u_1' \\ u_3 u_1' \\ u_1 u_3' \\ u_2 u_3' \\ u_3 u_3' \\ u_1 u_2' \\ u_3 u_2' \end{bmatrix}, \tag{13}$$

where b_1, b_2, ..., b_{16} represent 16 compensation coefficients.

2.2. BP Artificial Neural Network

BP-ANN is an algorithm that can learn and store the relationship between input data and output data without knowing the relationship between the two; it is currently the neural network with the highest application frequency and the widest application field. The calculation process of BP-ANN mainly consists of two parts: forward propagation of information and backpropagation of error. The process of forward propagation is to conduct the input data in the order of the input layer, the hidden layer, and the output layer, and then compare the output data with the expected output. If the error reaches the specified range, or the number of training times reaches a certain number of times, the training can be stopped, otherwise it will be transferred to the backpropagation process of error. The backpropagation of error refers to the process of finding the parameters corresponding to the minimum value of the loss function of the neural network by continuously and iteratively optimizing the weights and biases in the neural network. At present, gradient descent is the most widely used optimization method in the backpropagation process. The BP-ANN structure diagram is shown in Figure 2.

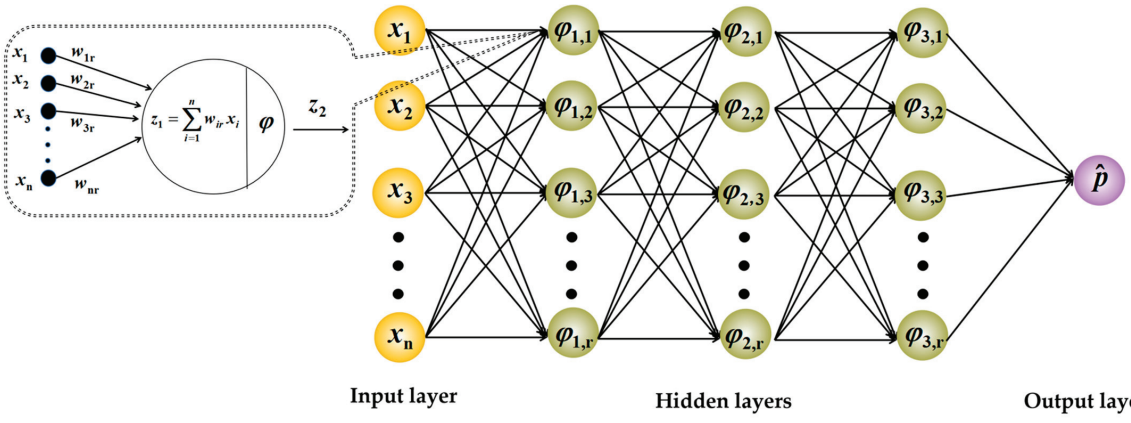

Figure 2. Structure diagram of BP-ANN.

In the process of aeromagnetic compensation, the causes of aeromagnetic interference were analyzed to determine the training parameters of BP-ANN, the same goes for RBF-ANN, the compensation model had 9 input parameters, which consists of the fluxgate three components, the directional cosine and its derivative to time. In addition, the output layer is magnetic interference (H_t), and the number of hidden layers of BP-ANN and the number of nodes per hidden layer can be determined by trial and error and the following empirical formula:

$$r = \sqrt{nl} + \delta, \tag{14}$$

where δ take the integer (experience value) of 1~10, r is the number of hidden layer nodes, n is the number of input layer nodes, l is the number of output layer nodes. In this paper, the number of hidden layers of BP-ANN is 3, and the number of hidden layer nodes is 4.

The training process of BP-ANN is:

(1) The weights and bias vectors of the neural network are initialized, and the weights and biases from the input layer to the hidden layer and the hidden layer to the output layer are denoted as $\omega^{(0)}$, $b_1^{(0)}$, $v^{(0)}$ and $b_2^{(0)}$, respectively.

(2) The forward propagation process of information is carried out to calculate the output value of each layer and its corresponding loss function:

$$E(\theta) = \frac{1}{n}\sum_{i=1}^{n}(y_i - \phi(v_i\phi(w_i + b_{i-1}) + b_i), \tag{15}$$

where θ represents the parameter collection of the neural network, y_i represents the true value in the data, ω_i represents the weight of the neural network, b_i represents the bias of the neural network and φ represents the activation function;

(3) Calculate the error terms of the output and hidden elements based on the loss function. The error terms of the output unit are:

$$\nabla_{(k)}v = \frac{\partial E}{\partial v} = \frac{\partial z_2}{\partial v}\frac{\partial E}{\partial z_2}\frac{\partial E}{\partial p} \tag{16}$$

$$\nabla_{(k)}b_2 = \frac{\partial E}{\partial b_2} = \frac{\partial z_2}{\partial b_2}\frac{\partial p}{\partial z_2}\frac{\partial E}{\partial p}, \tag{17}$$

The error terms of the hidden cell are:

$$\nabla_{(k)}w = \frac{\partial E}{\partial w} = \frac{\partial z_2}{\partial w}\frac{\partial h}{\partial z_1}\frac{\partial z_2}{\partial h}\frac{\partial p}{\partial z_2}\frac{\partial E}{\partial p} \tag{18}$$

$$\nabla_{(k)} b_1 = \frac{\partial E}{\partial b_1} = \frac{\partial z_1}{\partial b_1}\frac{\partial h}{\partial z_1}\frac{\partial z_2}{\partial h}\frac{\partial p}{\partial z_2}\frac{\partial E}{\partial p} \nabla_{(k)} b_1 = \frac{\partial E}{\partial b_1} = \frac{\partial z_1}{\partial b_1}\frac{\partial h}{\partial z_1}\frac{\partial z_2}{\partial h}\frac{\partial p}{\partial z_2}\frac{\partial E}{\partial p}, \tag{19}$$

where z_1 represents the input value of the hidden layer, z_1 represents the output layer, h represents the output value of the hidden layer, and p represents the model predicted value;

(4) Update weights and biases in the neural network. The updated output unit is:

$$v^{(k)} = v^{(k-1)} - \eta \nabla_{(k)} v \tag{20}$$

$$b_2^{(k)} = b_2^{(k-1)} - \eta \frac{\partial E}{\partial b_2}, \tag{21}$$

The updated hidden unit is:

$$w^{(k)} = w^{(k-1)} - \eta \nabla_{(k)} w \tag{22}$$

$$b_1^{(k)} = b_1^{(k-1)} - \eta \frac{\partial E}{\partial b_1}, \tag{23}$$

where η represents the learning rate and k represents the number of iterations;

(5) Repeat the above steps repeatedly, when the loss function is less than a given threshold or the number of iterations is greater than the set number of times, stop the iteration; this article believes that the parameters obtained at this time are the best parameters.

Before feeding data into the neural network, it is important to normalize the data. This can not only speed up the calculation of the neural network, but also improves the accuracy of the algorithm. In order to facilitate the calculation, this paper normalized the data to the interval of [−1,1], and the normalization method is:

$$y = -1 + \frac{2(x - x_{\min})}{x_{max} - x_{\min}}, \tag{24}$$

where x is the data before normalization and y is the normalized data.

2.3. RBF Artificial Neural Network

Compared with BP artificial neural network, RBF artificial neural network is an effective feed forward neural network, which has significant advantages such as strong global approximation ability, no local minimum problems and fast learning speed [30]. It usually consists of an input layer, hidden layer, and output layer, in which it can be adjusted according to the actual need for the number of neurons in the hidden layer. In this paper, the number of RBF-ANN neurons in the hidden layer was the same as the number of input samples, and its network structure diagram is shown in Figure 3.

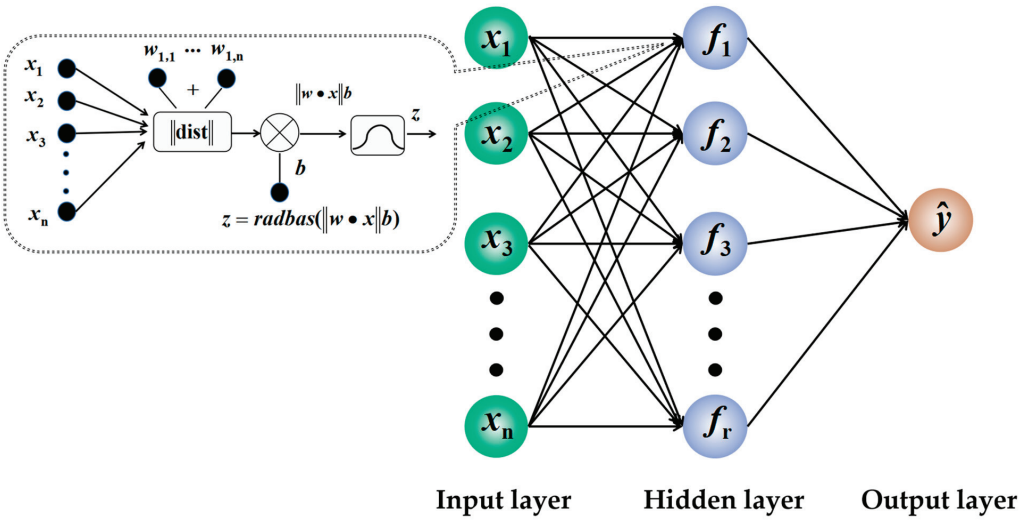

Figure 3. Structure diagram of RBF-ANN.

BP-ANN can have one or multiple hidden layers, while BRF-ANN have only one hidden layer. The first layer of the BRF-ANN is the input layer, which only plays the role of transmitting information and does not do any transformation processing on the input data. The second layer is a hidden layer, the number of nodes of the hidden layer is not fixed, it can be adjusted according to actual need, and based on the task goal is constantly changing, the activation function of the hidden layer is a non-negative linear function symmetrical along the center point and constantly decaying rapidly to both sides, with local response characteristics. The third layer is the output layer, which will linearly transform the input data and then the output.

The activation function of the hidden layer of the BP-ANN calculates the inner product of the input data and connection weights, while the independent variable of the activation function in the hidden layer of the BRF-ANN is the Euclidean distance between the input data and the center vector, and the activation function is the radial basis function. The farther the input data is from the center of the radial basis function, the less active it is. It can be seen that the output of the BRF-ANN is not related to all parameters, but only to a small number of parameters, and this article calls this characteristic of the BRF-ANN a local response characteristic. Therefore, BRF-ANNs are local approximation networks, while BP-ANNs are global approximation networks.

The hidden and output layers of a BP-ANN can be linear or nonlinear, while the hidden layer of an BRF-ANN is nonlinear, and the output layer is linear. The basic idea of BRF-ANN is that the radial basis function is used to construct a hidden layer space for the data in hidden nodes in the hidden layer, and the hidden layer converts the input data to a certain extent, and converts the low-dimensional mode input data into the high-dimensional space, so that the linear indivisible problem in the low-dimensional space becomes linearly separable in the high-dimensional space.

In the learning process of BRF-ANN, the most critical problem is how to determine the expansion coefficient of the hidden layer activation function. The common method is to select directly from a given set of training samples according to a certain method, or to determine by clustering. In this paper, the center point was randomly selected from the input sample using the direct selection method.

The activation function of the BRF-ANN is generally the Gaussian function:

$$f(x) = e^{-\frac{r^2}{2\sigma^2}}, \tag{25}$$

In the above equation, r is the Euclidean distance of the input data to the center point, σ represents the rate at which the function falls to 0, also known as the expansion factor. As can be seen from Figure 4, the smaller the expansion factor, the narrower the image.

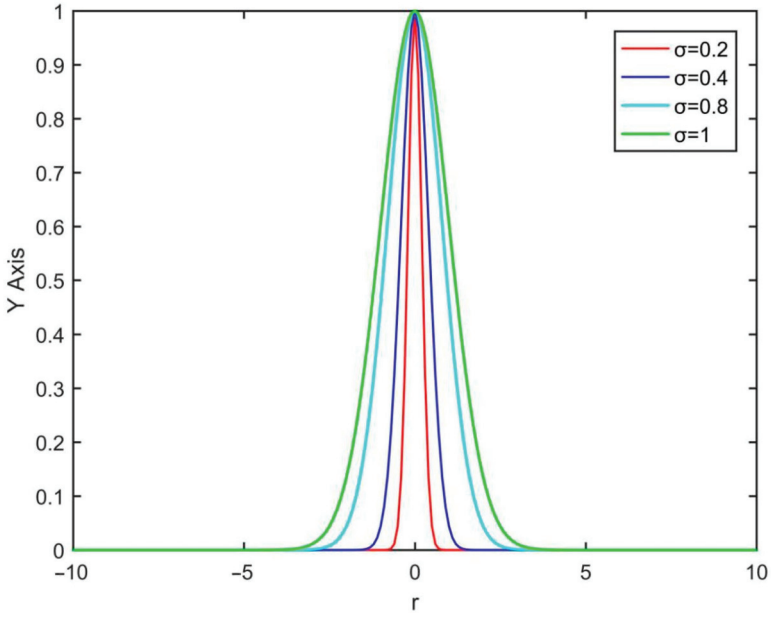

Figure 4. Gaussian radial basis function.

The training process of the BRF-ANN is as follows:

(1) Determine the parameters. Initialize the connection weights between the hidden layer and the output layer:

$$w_{kj} = k_{\min} + j\frac{k_{\max} - k_{\min}}{q+1}, \tag{26}$$

where k_{min} is the minimum value of the output of the k-th neuron, k_{max} is the maximum value of the output of the k-th neuron, and q is the number of output layer units.

Initialize the center parameters of each neuron in the hidden layer: In order to reflect the characteristics of the input information to the greatest extent, the values of the centers of neurons in different hidden layers should be as different as possible and should correspond to the width vector. In order to show the characteristics of the input information more obviously, this paper changes the initial value of the central component of each neuron in the hidden layer from small to large equal spacing, so that the weaker input information produces a stronger response near the smaller center. The size of the spacing is determined by the number of neurons in the hidden layer. Finally, the initial value of the central parameter of each neuron in the hidden layer of the BRF-ANN can be expressed as:

$$c_{ji} = i_{\min} + \frac{i_{max} - i_{\min}}{2p} + (j-1)\frac{i_{max} - i_{\min}}{p}, \tag{27}$$

where i_{min} is the minimum value entered for the i-th feature value i_{max} is the maximum value entered in the i-th feature, and p is the number of neurons in the hidden layer.

Initialize the width vector: As can be seen from Figure 4, the smaller the width vector, the narrower the image of the activation function, and the smaller the response of other neuron centers in this neuron. Its calculation formula is:

$$d_{ji} = d_f \sqrt{\frac{1}{N}\sum_{k=1}^{N}(x_i^k - c_{ji})}, \tag{28}$$

(1) Input layer to hidden layer calculation:

$$z_i = e^{-\| \frac{x - c_j}{D_j} \|^2}, \tag{29}$$

where c_j is the center vector corresponding to the j-th hidden layer neuron and D_j is the width vector of the j-th hidden layer neuron.

(2) Calculation of the output layer:

$$y_k = \sum_{j=1}^{p} w_{kj} z_j, \tag{30}$$

(3) Updated iteration of weight:

$$w_{kj}(t) = w_{kj}(t-1) - \eta \frac{\partial E}{\partial w_{kj}(t-1)} + \alpha[w_{kj}(t-1) - w_{kj}(t-2)] \tag{31}$$

$$c_{ji}(t) = c_{ji}(t-1) - \eta \frac{\partial E}{\partial c_{ji}(t-1)} + \alpha[c_{ji}(t-1) - c_{ji}(t-2)] \tag{32}$$

$$d_{ji}(t) = d_{ji}(t-1) - \eta \frac{\partial E}{\partial d_{ji}(t-1)} + \alpha[d_{ji}(t-1) - d_{ji}(t-2)], \tag{33}$$

where is η the learning rate and E represents the loss function.

In the training process, this paper first initializes the weight from the hidden layer to the output layer, the central parameters of each neuron in the hidden layer, and the width vector, and then calculates the loss function, when the loss function is less than the given threshold or the number of iterations is greater than the set number of times, stop the iteration, otherwise the gradient descent method is used to recalculate each weight until the conditions are met.

3. Data Simulation and Testing

3.1. Data Simulation

In order to solve the T-L model, this paper simulated the magnetic interference generated by the UAV during flight according to a standardized flight method (FOM) designed by Leliak and used the corresponding compensation algorithm to solve the simulated data, calculate the corresponding 16 compensation coefficients, and apply them to another set of data simulated by the standardized flight method to test the generalization ability of the model.

The FOM flight method is as follows: the aircraft flies sequentially in the order of north, east, south and west, each of which includes three $\pm 5^\circ$ yaws, three $\pm 5^\circ$ pitches and three $\pm 10^\circ$ rolls, and the duration of each group of maneuvers is about 5~10 s, and 5 s of flat flight are interspersed between each group of maneuvers. The magnetic field in the flight area changes steadily, and in order to reduce the interference of shallow geological bodies on the aircraft, the flight altitude is generally set to 2000~3000 m.

This paper simulated two different sets of FOM flight data, denoted as Flight A and Flight B. Assuming that the aircraft is compensated in strict accordance with the FOM flight method, the geomagnetic field T is 46,862 nT, the magnetization inclination angle

is $-1.298°$, and the magnetization declination angle is $36.663°$, T_{gx}, T_{gy} and T_{gz} can be calculated according to Formulas (8)~(10), and then the fluxgate three-component, T_{bx}, T_{by} and T_{bz} can be calculated by correcting the obtained data according to Formulas (6) and (7). The three-axis fluxgate and the corresponding aeromagnetic interference model obtained by simulation are shown in Figures 5 and 6.

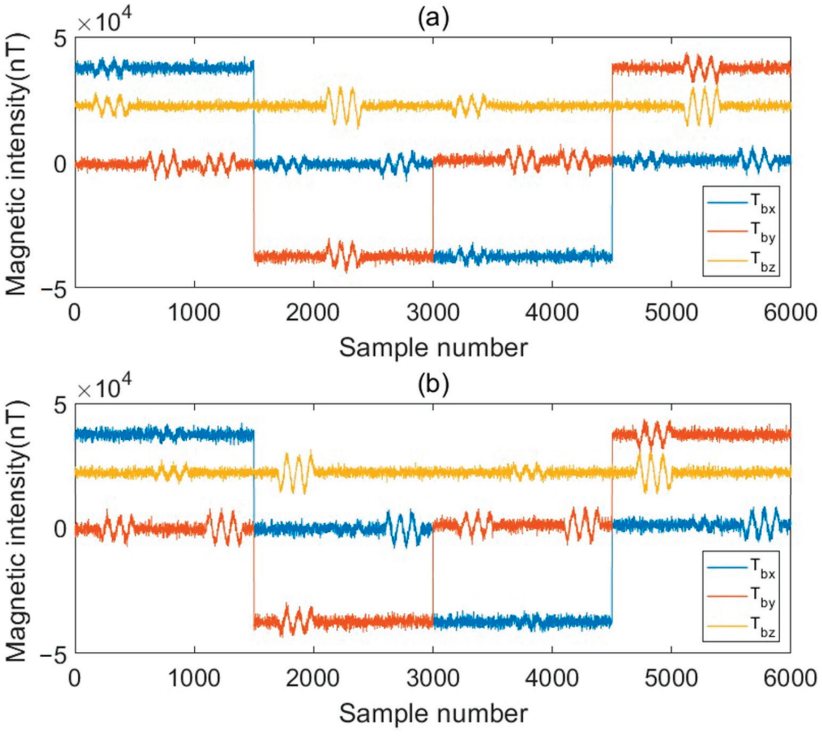

Figure 5. Simulation model of a three-axis fluxgate: (**a**) flight A; and (**b**) flight B.

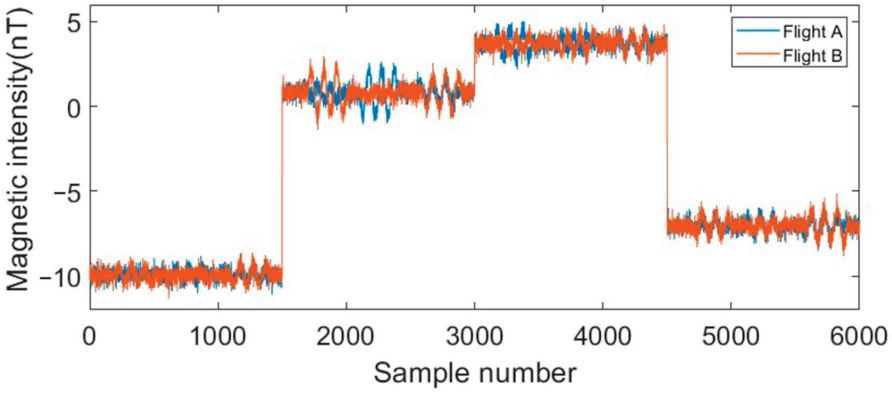

Figure 6. Aeromagnetic interference model corresponding to FOM flight.

3.2. Compensation Results

In order to verify the performance of the algorithm, this paper records two sets of simulation data, Flight A and Flight B, as training and test sets, respectively. As shown in Table 1, in the test set Flight A, the standard deviation of the raw data is 5.5873, the BP-ANN reduces the standard deviation to 0.0792, the IR is 70.5465, and the BRF-ANN reduces the standard deviation to 0.0649 and the IR is 86.1052. In the test set Flight B, the standard deviation of the raw data is 5.5927, the BP-ANN reduces the standard deviation to 0.0828 and the IR to 69.5160, and the BRF-ANN reduces the standard deviation to 0.0651 and the IR to 85.9473. The result after compensation is shown in Figure 7.

Table 1. Comparison of compensation results of BP-ANN and BRF-ANN.

Test Set	Training Set	Method/Model	STD_p	STD_f	IR
Flight A	Flight B	BP-ANN	5.5873	0.0792	70.5465
		BRF-ANN		0.0649	86.1052
Flight B	Flight A	BP-ANN	5.5927	0.0828	67.5160
		RBF-ANN		0.0651	85.9473

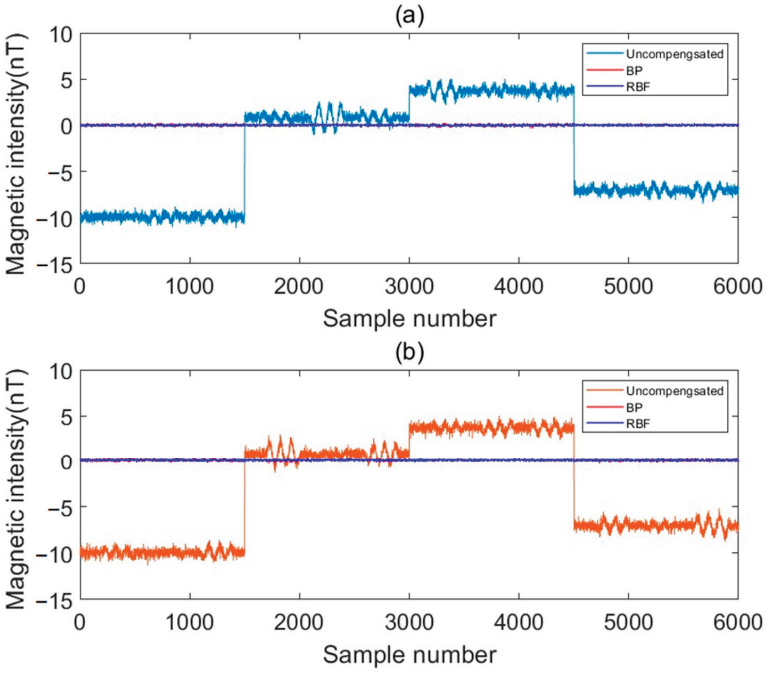

Figure 7. Simulation data compensation results: (**a**) test set flight A; and (**b**) test set flight B.

4. Real Measured Data Test

4.1. UAV Compensation Flight

In order to establish a suitable UAV aeromagnetic compensation model, this paper used a rotor UAV to carry out a compensation flight in Ma'anshan City, Anhui Province, China. The terrain is flat, there are no interference factors such as high-voltage power poles around, and the surrounding geomagnetic field does not change much, which is very in line with the hypothetical conditions set by the T–L model. This paper developed a UAV magnetic survey system, as shown in Figure 8, which is mainly composed of two parts: UAV platform and aeromagnetic survey equipment. The selected UAV platform is a

fuel-powered unmanned helicopter SU-H2M, which can take off and fly autonomously, and has the characteristics of long endurance, fast speeds, and a large cruising distance. The maximum payload is 45 kg, the battery life is 2 h, and the general cruising speed is 60 km/h. The aeromagnetic measurement equipment is mainly composed of five parts, as shown in Figure 9: (1) a high-precision potassium pump magnetometer (GSMP-35U used to measure the total magnetic field strength of the geomagnetic field; (2) a triaxial fluxgate magnetometer (TFM100-G2) used to record aircraft attitude change information; (3) a laser altimeter from the MDL company with a range of 0.05 m~200 m; (4) an inertial navigation module, using OEM 62 GPS locator, with a static plane positioning accuracy within ±2 m; and (5) the data collector and data processing platform, as shown in Figure 10 (detailed parameters are shown in Table 2).

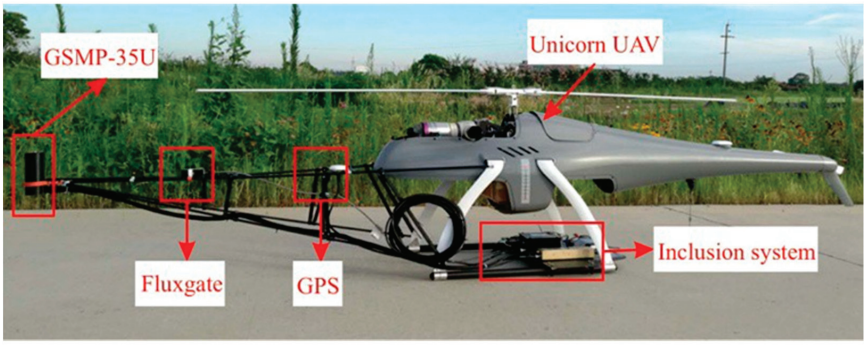

Figure 8. UAV detection platform.

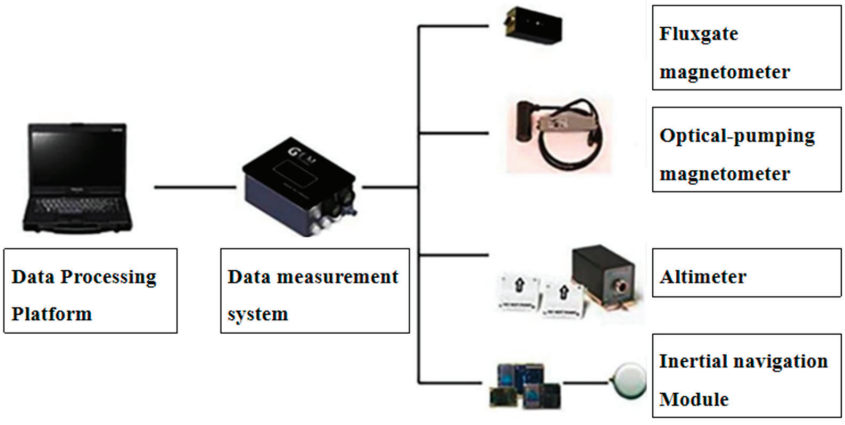

Figure 9. Aeromagnetic measurement equipment.

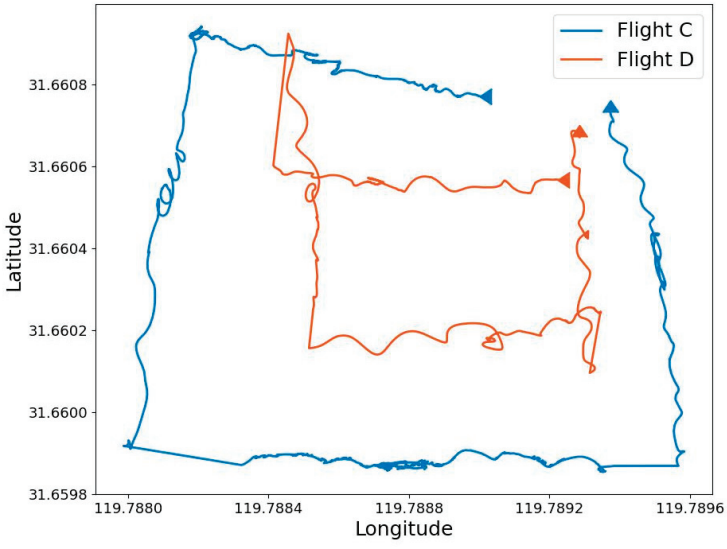

Figure 10. Flight C and Flight D flight paths.

Table 2. Main technical parameters of GSMP-35U high-precision potassium optical pump magnetometer.

Measuring Range	**20,000 nT~120,000 nT**
Gradient capacity	50,000 nT/m
Sensitivity	0.0003 nT@1Hz
Resolution	0.0001 nT
Measurement accuracy	±0.05 nT
Sample rate	1, 2, 5, 10, 20 Hz
Operating temperature	−20 °C~+55 °C

A total of two flights were carried out in this experiment, and the aeromagnetic interference data measured in the two compensation flight experiments are named Flight C and Flight D. The flight data of the two compensated flights are shown in Figures 10 and 11.

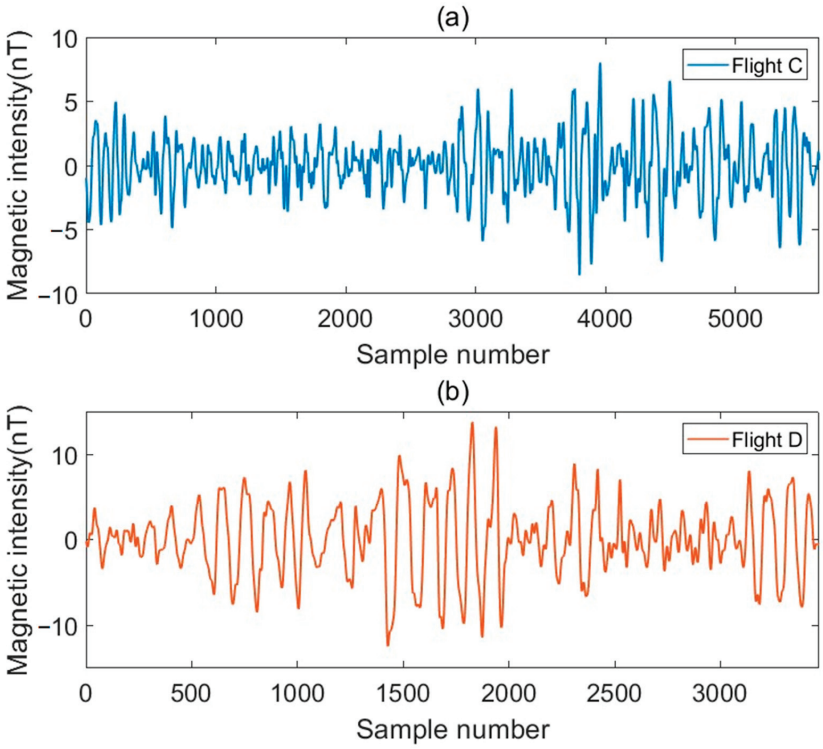

Figure 11. Aeromagnetic interference model: (**a**) Flight C; (**b**) Flight D.

4.2. Compensation Results

At present, the ratio (*IR*) of the standard deviation of magnetic interference before and after aeromagnetic compensation is commonly used in the industry to evaluate the compensation effect of aeromagnetic compensation methods.

$$IR = \frac{STD_p}{STD_f} \tag{34}$$

$$STD = \sqrt{\frac{1}{n}\sum_{i=1}^{n}(x_i - \mu)^2}, \tag{35}$$

where STD_p is the standard deviation of the magnetic interference before compensation, and STD_f is the standard deviation of the residual magnetic interference after compensation, μ is the arithmetic mean of the data.

In order to verify the aeromagnetic compensation effect of the above two methods, the data of Flight D and Flight C are used as training sets to compensate for Flight C and Flight D, respectively. The compensation result is shown in Figures 12 and 13. Table 3 shows the comparison of the compensation effects of BP-ANNs and BRF-ANNs. In Flight C, the BP-ANN reduced the standard deviation from 2.2804 to 0.3376 with an IR of 6.7547, and the BRF-ANN reduced the standard deviation from 2.2804 to 0.3091 with an IR of 7.3775. In Flight D, the BP-ANN reduced the standard deviation from 4.2558 to 0.5734 with an IR of 7.4220, and the BRF-ANN reduced the standard deviation from 4.25584 to 0.4734 with an IR of 8.9899. From the compensation results, it can be seen that the compensation effect of BRF-ANN is better than that of BP-ANN, which proves the superiority of BRF-ANN compensation method.

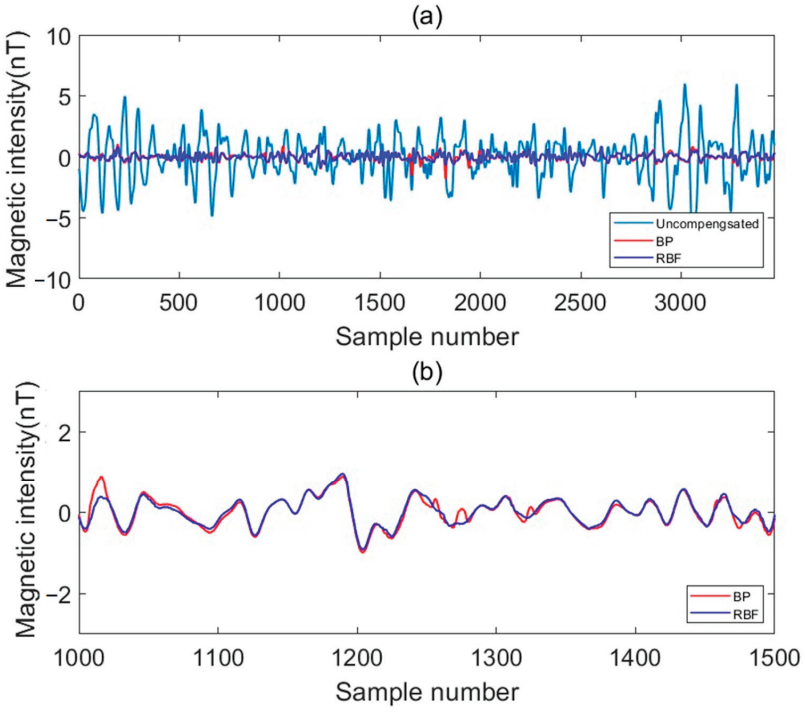

Figure 12. Flight C compensation results: (**a**) BP-ANN and BRF-ANN compensation results; and (**b**) compensation for the resulting sampling points 1000 to 1500.

Table 3. Comparison of compensation results of BP-ANN and BRF-ANN.

Test Set	Training Set	Method/Model	STD_p	STD_f	IR
Flight C	Flight D	BP-ANN	2.2804	0.3376	6.7547
		BRF-ANN		0.3091	7.3775
Flight D	Flight C	BP-ANN	4.2558	0.5734	7.4220
		RBF-ANN		0.4734	8.9899

This section may be divided by subheadings. It should provide a concise and precise description of the experimental results, their interpretation, as well as the experimental conclusions that can be drawn.

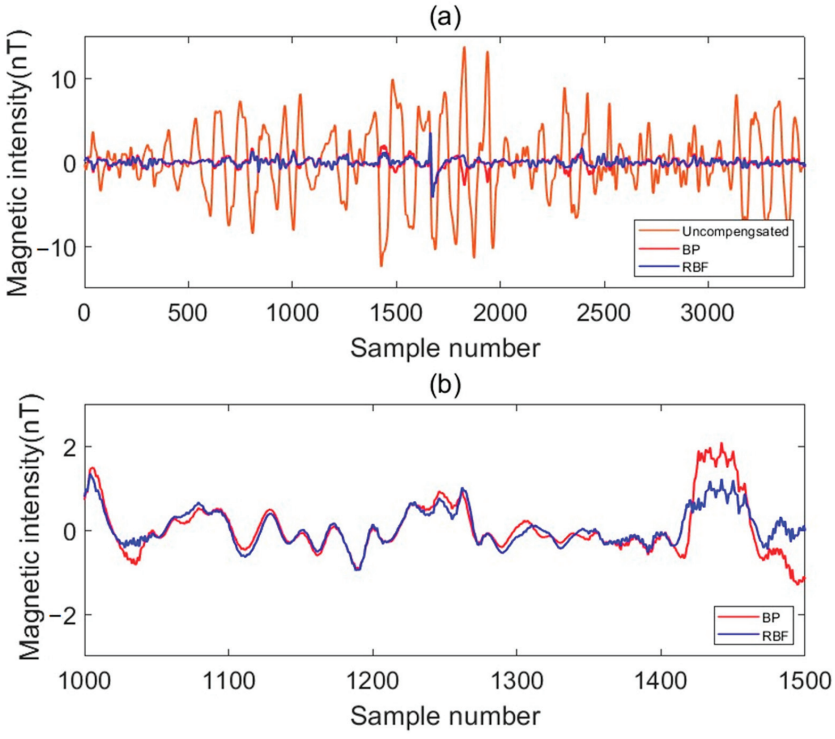

Figure 13. Flight D compensation results: (**a**) BP-ANN and BRF-ANN compensation results; and (**b**) compensation for the resulting sampling points 1000 to 1500.

5. Conclusions

In the previous aeromagnetic compensation work, although the classical BP-ANN is stronger than traditional regression algorithms in terms of fitting ability, the BP-ANN is a global approximation network, with limited generalization ability, and there are problems, such as falling into a local minimum easily, gradient disappearance, and an overfitting problem in magnetic compensation which affects the accuracy of aeromagnetic compensation. In order to improve the accuracy of compensation, on the basis of the T–L model, we proposed a compensation algorithm based on BRF-ANN, in which the hidden layer node uses the distance between the input mode and the central vector as the independent variable of the function, and uses the radial basis function as the activation function, which has the characteristics of local approximation and better generalization ability, avoids the problem of local minimum effectively, and improves the accuracy of magnetic compensation to a certain extent. We verified the feasibility of this method in simulated data and measured data experiments.

Author Contributions: Z.S., J.J. and C.Y.: Conceptualization, Methodology, Software; J.J. and S.Z.: Resources Data curation; C.Y.: Writing—Original draft preparation; C.Y. and Z.S.: Visualization; Z.S., C.Y., P.Y. and S.Z.: Writing—Reviewing and Editing. All authors have read and agreed to the published version of the manuscript.

Funding: This work was supported by National Key R&D Program of China (No. 2020YFE0201300), National Natural Science Foundation of China (No. 42204141), the Natural Science Foundation of Jilin Province (No. 20210508033RQ), National Natural Science Foundation of China (No. 42274187), Interdisciplinary training Program for Young teachers and students of Jilin University (415010300086).

Conflicts of Interest: The authors declare no conflict of interest.

References

1. Zheng, Y.; Li, S.; Xing, K.; Zhang, X. Unmanned Aerial Vehicles for Magnetic Surveys: A Review on Platform Selection and Interference Suppression. *Drones* **2021**, *5*, 93. [CrossRef]
2. Yang, J.; Chen, J.; Yang, Z. Energy Efficient UAV Communication with Trajectory Optimization. In Proceedings of the 2021 2nd International Conference on Big Data & Artificial Intelligence & Software Engineering (ICBASE), Zhuhai, China, 24–26 September 2021; pp. 508–514.
3. Cui, Z.; Xu, Z.; Li, J. Development and application status and exhibition of the UAV aerogeophysical technology. *Calc. Tech. Geophys. Geochem. Explor.* **2016**, *38*, 740–745.
4. Richard, P. GeoRanger Aeromagnetic UAV—From development to commercial survey. *Preview Aust. Soc. Explor. Geophys.* **2006**, *125*, 28–29.
5. Wu, T.; Xu, X.; Ren, L. Progress and prospect of UAV marine aeromagnetic survey technology. *Hydrogr. Surv. Charting* **2017**, *37*, 17–20.
6. Kaneko, T.; Koyama, T.; Yasuda, A.; Takeo, M.; Yanagisawa, T.; Kajiwara, K.; Honda, Y. Lowaltitude Remote Sensing of Volcanoes Using an Unmanned Autonomous Helicopter: An Example of Aeromagnetic Observation at IzuOshima Volcano, Japan. *Int. J. Remote Sens.* **2011**, *32*, 1491–1504. [CrossRef]
7. Eck, C.; Imbach, B. Aerial Magnetic Sensing with an UAV Helicopter. In Proceedings of the ISPRS International Archives of the Photogrammetry, Remote Sensing and Spatial Information Sciences, Zurich, Switzerland, 14–16 September 2011; pp. 81–85.
8. Stoll, J.; Moritz, D. Unmanned Aircraft Systems for Rapid near Surface Geophysical Measurements. In Proceedings of the Conference on Unmanned Aerial Vehicles in Geomatics (UAV-g), Rostock, Germany, 4–6 September 2013; pp. 391–394.
9. Li, W.; Xuwen, Q.; Xinping, G. The IGGE UAV Aero Magnetic and Radiometric Survey System. In Proceedings of the 20th European Meeting of Environmental and Engineering Geophysics, Athens, Greece, 14–18 September 2014; pp. 1–5.
10. Walter, C.; Braun, A.; Fotopoulos, G. Highresolution Unmanned Aerial Vehicle Aeromagnetic Surveys for Mineral Exploration Targets. *Geophys. Prospect.* **2020**, *68*, 334–349. [CrossRef]
11. Yang, S.L.; Li, F.L.; Huang, J.J.; Wang, J.; Huang, M.N.; Wang, X.; Zhou, Q. History and Prospects of Aeromagnetic Compensation Technologies Used in China and Abroad. *Geophys. Geochem. Explor.* **2017**, *41*, 694–699.
12. Xiong, S.Q. Innovation and application of airborne geophysical exploration technology. *J. Geomech.* **2020**, *26*, 791–818.
13. Tolles, W.E.; Lawson, J.D. *Magnetic Compensation of MAD Equipped Aircraft*; Airborne Instruments Lab. Inc.: Mineola, NY, USA, 1950; pp. 201–211.
14. Leliak, P. Identification and Evaluation of Magnetic-Field Sources of Magnetic Airborne Detector Equipped Aircraft. *IRE Trans. Aeronaut. Navig. Electron.* **1961**, *ANE-8*, 95–105. [CrossRef]
15. Bickel, S. Small Signal Compensation of Magnetic Fields Resulting from Aircraft Maneuvers. *IEEE Trans. Aerosp. Electron. Syst.* **1979**, *AES-15*, 518–525. [CrossRef]
16. Leach, B. Aeromagnetic Compensation as a Linear Regression Problem. 2010. Available online: https://doi.org/10.1016/B97801 26287509.500176 (accessed on 20 November 2022).
17. Hardwick, C.D. Important Design Considerations for Inboard Airborne Magnetic Gradiometers. *Geophysics* **1984**, *49*, 2004–2018. [CrossRef]
18. Dou, Z.; Ren, K.; Han, Q.; Niu, X. A Novel RealTime Aeromagnetic Compensation Method Based on RLSQ. In Proceedings of the 2014 Tenth International Conference on Intelligent Information Hiding and Multimedia Signal, Kitakyushu, Japan, 27–29 August 2014; pp. 243–246.
19. Wu, P.; Zhang, Q.; Chen, L.; Zhu, W.; Guangyou, F. Aeromagnetic Compensation Algorithm Based on Principal Component Analysis. *J. Sens.* **2018**, *2018*, 5798287. [CrossRef]
20. Xu, X.; Huang, L.; Liu, X. DeepMAD: Deep Learning for Magnetic Anomaly Detection and Denoising. *IEEE Access* **2020**, *8*, 121257–121266. [CrossRef]
21. Williams, P.M. Aeromagnetic Compensation Using Neural Networks. *Neural Comput. Appl.* **1993**, *1*, 207–214. [CrossRef]
22. Zhang, D.; Liu, X.; Qu, X.; Zhu, W.; Huang, L.; Fang, G. Analysis of Aeromagnetic Swing Noise and Corresponding Compensation Method. *IEEE Trans. Geosci. Remote Sens.* **2022**, *60*, 1–10. [CrossRef]
23. Ma, M.; Zhou, Z.; Cheng, D. A Dual Estimate Method for Aeromagnetic Compensation. *Meas. Sci. Technol.* **2017**, *28*, 115904. [CrossRef]
24. Yu, P.; Zhao, X.; Jiao, J. An Aeromagnetic Compensation Algorithm Based on a Deep Autoencoder. *IEEE Geosci. Remote Sens. Lett.* **2022**, *19*, 1–5. [CrossRef]
25. Yu, P.; Zhao, X.; Jiao, J.; Jia, J.; Zhou, S. An Improved Neural Network Method for Aeromagnetic Compensation. *Meas. Sci. Technol.* **2020**, *32*, 045106. [CrossRef]
26. Casasent, D.; Chen, X. Radial Basis Function Neural Networks for Nonlinear Fisher Discrimination and Neyman–Pearson Classification. *Neural Netw.* **2003**, *16*, 529–535. [CrossRef]
27. Wang, S.; Li, B.; Geng, Q. IEEE Research of RBF Neural Network PID Control Algorithm for Longitudinal Channel Control of Small UAV. In Proceedings of the 2013 10th IEEE International Conference on Control and Automation (ICCA), Hangzhou, China, 12–14 June 2013; pp. 1824–1827.
28. Yuan, D.; Yan, J.; Wang, X.; Xi, Q. A Study of Information Fusion for UAV Based on RBF Neural Network. *IEEE Int. Conf. Control. Autom.* **2007**, *17*, 2839–2842.

29. Phiboon, T.; Khankwa, K.; Petcharat, N.; Phoksombat, N.; Kanazaki, M.; Kishi, Y.; Bureerat, S.; Ariyarit, A. Experiment and Computation Multifidelity Multiobjective Airfoil Design Optimization of Fixedwing UAV. *J. Mech. Sci. Technol.* **2021**, *35*, 4065–4072. [CrossRef]
30. Deng, Y.; Zhou, X.; Shen, J.; Xiao, G.; Hong, H.; Lin, H.; Wu, F.; Liao, B. New Methods Based on Back Propagation (BP) and Radial Basis Function (RBF) Artificial Neural Networks (ANNs) for Predicting the Occurrence of Haloketones in Tap Water. *Sci. Total Environ.* **2021**, *772*, 145534. [CrossRef] [PubMed]

energies

MDPI

Article

Energy Autonomy Simulation Model of Solar Powered UAV

Krzysztof Mateja [1,2,*], Wojciech Skarka [1,2,*], Magdalena Peciak [1,3], Roman Niestrój [2,4] and Maik Gude [3]

[1] Department of Fundamentals of Machinery Design, Silesian University of Technology, Stanisława Konarskiego 18A, 44-100 Gliwice, Poland
[2] SkyTech eLab LLC, Stanisława Konarskiego 18C, 44-100 Gliwice, Poland
[3] Institute of Lightweight Engineering and Polymer Technology, Technische Universitat Dresden, Holbeinstraße 3, 01307 Dresden, Germany
[4] Department of Electrical Engineering and Computer Science, Silesian University of Technology, Bolesława Krzywoustego 2, 44-100 Gliwice, Poland
* Correspondence: krzysztof.mateja@polsl.pl (K.M.); wojciech.skarka@polsl.pl (W.S.)

Abstract: The energy autonomy of UAVs is an important direction in the field of aerospace. Long-endurance aerial vehicles allow for continuous flight; however, to meet the guidelines, the power supply system has to be able to harvest energy from outside. Solar cells allow the production of electricity during the day when the sun shines on their surface. Depending on the location, time, weather, and other external factors, the energy produced by PV panels will change. In order to calculate as accurately as possible the energy obtained by solar cells, we developed a simulation model that took into account all of the external restrictions and the UAV's limits during flight. The conducted analysis made it possible to obtain information for the specific input data on whether the UAV is able to fly for 24 h in a specific flight scenario. The UAV powered by solar cells developed by us and the performed aviation missions have shown that the UAV is capable of continuous flight without the need to land.

Keywords: renewable energy; solar cell; Model-Based Design; energy harvesting; energy autonomy; UAV power supply system

Citation: Mateja, K.; Skarka, W.; Peciak, M.; Niestrój, R.; Gude, M. Energy Autonomy Simulation Model of Solar Powered UAV. *Energies* **2023**, *16*, 479. https://doi.org/10.3390/en16010479

Academic Editors: Jaroslaw Pytka, Andrzej Łukaszewicz, Zbigniew Kulesza, Wojciech Giernacki and Andriy Holovatyy

Received: 30 November 2022
Revised: 23 December 2022
Accepted: 27 December 2022
Published: 1 January 2023

1. Introduction

Unmanned Aerial Vehicles (UAVs) are increasingly used in everyday life. The scope of their work is constantly enlarged from casual filming [1] to advanced military use [2]. UAVs are used for distributing shipments, mapping, surveillance, and monitoring borders or crops [3,4]. The limited duration of the UAV flight causes the necessity to land and the resulting loss of time in terms of interrupting the mission, charging or replacing the batteries. Designers of UAVs are looking for opportunities to obtain energy from outside; if this is achieved, the time of flight will be extended [5]. The goal is to achieve full energy autonomy. The energy autonomy of UAVs is an important direction in the field of aerospace because, in addition to the possibility of continuous operation, another advantage is the lower cost of this kind of application in comparison to using a satellite. One of the most used sources is a solar cell [4,5].

Solar-powered UAVs are not a new concept of aerial vehicles. We can distinguish many types of solar-powered UAVs, for example: Atlantic Solar [5,6], Solar Impulse 2 [7], Airbus zephyr [8], PHASA-35 [9], and Odysseus [10]. Each of these aircrafts is based on a lightweight composite structure and is equipped with photovoltaic (PV) panels. Depending on the purpose of the UAV, the payload aspect, as well as the weight of the measuring, detection, and control devices should be taken into account. A UAV's weight should be as low as possible. The load-bearing structure then enables a larger payload or an increase in the capacity of the batteries, which allows for an extension in the applications of the UAV [3,5].

The possibility of obtaining electricity from solar cells makes them the main substitute or complementary source of energy [11]. The use of PV panels can be found in small devices, such as lights or toys, on the roofs of houses to provide partial electricity to houses, or in a large area of desert, lake or farmland where they play the role of new power plants [11,12]. The ease of generating electricity, the relatively low cost of such a power supply system, and the newer materials of solar cells have seen them gain recognition in new technology industries.

There are a number of different technologies are used for manufacturing solar cells with different materials that are used in various industries [4]. The most commonly used material for solar cells is silicon. Other materials used for the construction of photovoltaic cells are gallium arsenide, cadmium telluride, and copper indium gallium selenide. However, this technology is restricted by the scarcity of the required materials. The most popular silicon PV panels are rigid and breakable [13,14]. These kinds of solar cells are not resistant to working under stresses where forces act on the PV panel. The wings, fuselages, tail are curved surfaces. This makes it impossible to fit the silicon solar cell into the construction of the UAV. For UAVs, aerospace, and aviation, we have to take into account flexible solar cells, which are able to bend and are more durable than standard silicon solar cells [15,16]. Under the influence of stresses and forces during operation, the PV panel will not break and will still be able to produce electricity. In this group, we can distinguish several types of solar cells that could be used in the aviation industry. The most popular is the GaAs (Gallium arsenide) solar cell, which provides the highest efficiency, exceeding 30% [4,17]. The disadvantage of GaAs is the high cost, meaning designers often cannot afford to build a prototype. GaAs is used primarily in the space industry as probes, satellites and in the military industry due to their flexibility, efficiency and weight. Another kind of solar cell that can be used in aviation is flexible silicon solar cells [18]. This kind of PV panel provides an efficiency of around 25%, at a much lower cost compared to GaAs. A DSSC (Dye-sensitized solar cell) is a type of solar cell that has different properties than the previous two types [19]. Their maximum efficiency is around 13%, but they make up for this with long service life, low production costs, high resistance to mechanical damage, and a wide-angle range of sunlight [19,20]. In addition to low efficiency, another is its poor resistance to operation at low and high temperatures [19,20].

To strengthen solar cells mounted on the UAV structure and to prevent mechanical damage, various protective coatings are used on their upper surface, e.g., films and resins to extend the service life of the system. Solar cells can be mounted to the wing via several types of technology [21]:

- Adhering to the existing wing—this method is good for the retrofit of existing UAVs. The advantage is the possibility of replacement in case of damage. The disadvantage of this solution is sealing the gap between the two modules [21,22].
- Solar modules into the mold—this method is good for new UAVs. Solar cells are a direct part of the wing. The advantage is its easy to arrange wiring, however, the PV modules cannot be swapped in case of damage.
- Solar modules as wing surface—PV panels are used as the upper surface of the wings. The advantage is its easy to arrange wiring, however, it requires additional ribs inside the structure of the wing to strengthen the structure of the UAV [8,23–25].

UAV's power supply system can be built using many different storage sources. The current predominant battery energy storage technology for UAVs is the Li-ion battery [3,5,22,24]. The type of battery cell should take into account temperature range, lifespan, energy density, safety, and performance. Another issue is the shape of the battery cell. We can distinguish three main shapes of battery cells: prismatic, cylindrical, and pouch [26,27]. The cylindrical cell has good mechanical strength, specific energy, and energy density. The disadvantage of the cylindrical cell is its bad heat management. The prismatic cell has good mechanical strength, heat management, specific energy, and energy density but they have a heavy shell, which leads to certain restrictions on the energy density

of the battery pack. Pouch cells have good heat management, energy density, and specific energy. The disadvantage is its low mechanical strength [26,27].

To provide solar cells and battery cells that are fully functional, the power supply system should be equipped with MPPT (Maximum Power Point Tracking) and a BMS (Battery Management System). MPPT ensures the continuous supply of the maximum power generated by the PV [28]. A photovoltaic module has non-linear I–V (current–voltage) characteristics and its P–V (power–voltage) characteristics show that it possesses only one point (P_{mpp}). This point also varies with the change in insolation and temperature. MPPT is used to maximize the value of the solar energy produced by the PV module. BMS is responsible for the proper work of the batteries. The BMS controls the charging and discharging currents, the uniform voltage of cells, and the overall temperature of the system [29].

As part of the research work, a team of scientists and designers developed and built a family of UAVs called TwinStratos (TS), which are suitable for continuous flight missions.

As part of this work, several scale-up units have been built so far and are intended to be built for the testing and verification of individual subsystems, as well as for the implementation of planned research missions.

1. TwinStratos 110 (TS110) scaled 1:10—UAV for testing general layout and specific simplified control system;
2. TS17 scaled 1:7—UAV for testing the power supply system, energy consumption simulation model, and technology of manufacturing;
3. TS12 scaled 1:2—UAV for long endurance tests, verification flight parameters and performance ranges in operation mode, designated for service use and research tests;
4. TS—target UAV intended for the research and implementation of commercial services.

The correct selection of solar cells, batteries, energy converters and energy management devices with the simultaneous use of energy-saving propulsion systems should enable the long-endurance flight of the UAV [5,6,30]. The aim of this article is to illustrate the complexity of the issues of a solar-powered UAV. The simulation model developed as part of this work was used to verify whether the aircraft is able to fly over 24 h under the given conditions. In this research, the Model-Based Design (MBD) methodology was used. The approach is characterized by placing the simulation models of the analyzed system in the center of the development process. Using MBD is beneficial, particularly in designing dynamic and complex systems, as it allows for a better understanding and reduction of the complexity of UAVs [31,32]. Additionally, the MBD allows us to design and optimize the technical parameters, work more efficiently in designing systems and ease cooperation between specialists in different fields [33]. Such an integrated design approach based on the MBD methodology was developed by the project team and applied to the design and testing of ultra-efficient racing vehicles [34], Automated Guided Vehicles AGVs [33], as well as for the design of General Aviation class aircraft [35].

2. Solar Energy Production

2.1. Irradiation

Irradiation is a key element in obtaining solar energy for PV cells. Solar cells can produce energy when the sun is shining on the upper surface. The value of the energy differs and depends on several factors. The most important factors, which cause the most significant differences, are location and date (time) [11,12,36]. Whilst the sun always produces the same value of energy, the circular and rotational movement of the earth means that we cannot obtain this same value of energy in one place for 24 h. To calculate the volume of energy we can produce in solar cells, we have to use equations that allow us to calculate the value of the energy that can be transferred to the solar cells [36–39]. Solar constant G_{SC} = 1367 W/m^2. To calculate the energy to the specific location, we have to use

equations connected with the position of the earth, relative to the sun [39]. Declination (δ) is the angle between the line to the sun and the equatorial plane.

$$\delta = 23.45 \times \sin\left(360 \times \frac{284 + \mathrm{n}}{365}\right) \tag{1}$$

where n is the day of the year. The range of declination is $-23.45^\circ \ll \delta \ll 23.45^\circ$. The maximum positive value is during the summer solstice and the maximum negative value is during the winter solstice. The declination is the same across the world. The hour angle (ω) changes all the time, by 15° per hour. We can write it with the following formula:

$$\omega = 15^\circ \times (Solar\ time - 12) \tag{2}$$

The range of the hour angle is $-180^\circ \ll \omega \ll 180^\circ$. The negative value is before solar noon. Zenith angle θ_z is the angle between the line to the sun and the horizontal surface. The formula of the zenith angle can be written as:

$$\theta_z = \cos(\varphi) \times \cos(\delta) \times \cos(\omega) + \sin(\varphi) \times \sin(\delta) \tag{3}$$

where φ = latitude $\times\ \pi/180$. The range of the zenith angle is $0^\circ \ll \theta_z \ll 90^\circ$. When zenith angle $\theta_z = 0^\circ$ is sunrise, $\theta_z = 90^\circ$ is sunset. Day length (N) can be calculated by the formula:

$$\mathrm{N} = \frac{2}{15} \times \mathrm{Arccos}(-\tan\varphi \times \tan\delta) \tag{4}$$

The irradiation on surface G_{on} when θ_Z = 0 just outside the atmosphere is calculated from constant G_{SC} and the day number as follows:

$$\mathrm{G_{on}} = \mathrm{G_{sc}} \times \left[1 + 0.033 \times \cos\frac{360 \times \mathrm{n}}{365}\right] \tag{5}$$

The solar constant G_{SC} is a mean value. The earth's orbit is elliptical and the distance between the sun and earth varies by 3.3%.

The hourly radiation I_o and the daily radiation H_o can be calculated by the formulas below:

$$\begin{aligned} \mathrm{I_o} &= \tfrac{12\times3600}{\pi} \times \mathrm{G_{sc}} \times \left[1 + 0.033 \times \cos\tfrac{360\times\mathrm{n}}{365}\right] \\ &\times \left[\cos(\varphi) \times \cos(\delta) \times (\sin\omega_2 - \sin\omega_1) + \tfrac{\pi\times(\omega_2-\omega_1)}{180} \times \sin\varphi \times \sin\delta\right] \end{aligned} \tag{6}$$

where ω_2, ω_1 is the hour angle in the considered hours.

$$\mathrm{H_o} = \frac{24 \times 3600}{\pi} \times \mathrm{G_{sc}} \times \left[1 + 0.033 \times \cos\frac{360 \times \mathrm{n}}{365}\right] \times \cos(\varphi) \times \cos(\delta) \times \sin\omega_s + \frac{\pi \times \omega_s}{180} \times \sin\varphi \times \sin\delta \tag{7}$$

The unit of the hourly radiation is J/m^2. The daily radiation unit is $J/day \times m^2$. To calculate these values to watt-hours (Wh), we had to convert this unit.

Air mass (AM) is the distance travelled by the atmosphere by the sun's rays on the Earth and can be calculated by the below formula [36,39]:

$$\mathrm{AM} = \frac{\text{path length travelled}}{\text{vertical depth of the atmosphere}} = \frac{1}{\cos\theta_z} \tag{8}$$

An explanation of air mass is posted below in Figure 1.

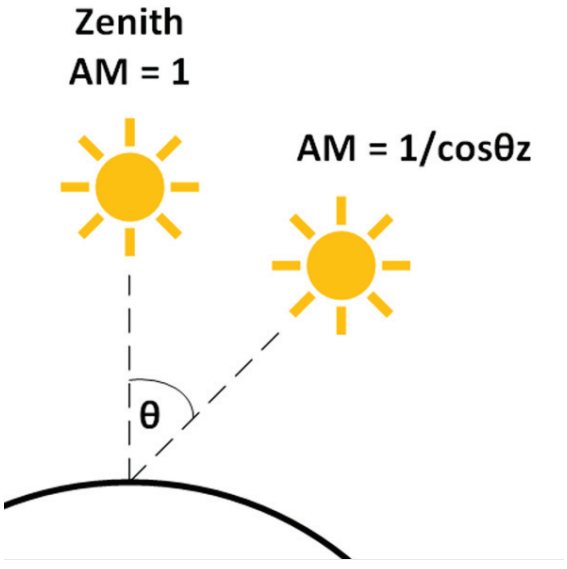

Figure 1. Explanation of air mass notion.

Hottel [40] has presented a method for estimating the beam radiation transmitted through clear atmospheres, which takes into account the zenith angle and altitude for a standard atmosphere and for four climate types [39].

Beam and diffuse radiation are the two types of radiation that are the most important in the case of irradiance solar cells. Beam (direct) radiation is the solar radiation that falls straight to the surface. This radiation is not scattered by the atmosphere. Diffuse radiation is scattered by the atmosphere in all directions. Only some of this radiation arrives at the Earth's surface. Beam radiation can be calculated by the following formula:

$$G_{cb} = \tau_b \times G_{on} \times [\cos(\varphi) \times \cos(\delta) \times \cos(\omega) + \sin(\varphi) \times \sin(\delta)] \quad (9)$$

where τ_b is the ratio of the transmitted direct radiation to the total radiation incident at the top of the atmosphere. This ratio can be calculated as follows:

$$\tau_b = \frac{G_{cb}}{G_o} = a_0 + a_1 \times e^{\left(\frac{-k}{\cos\theta_z}\right)} \quad (10)$$

where $G_o = G_{on} \times \cos\theta_z$ and a_0, a_1, k are the constant, calculated using next equations:

$$a_0 = r_0 \times \left(0.4237 - 0.00821 \times (6 - A)^2\right) \quad (11)$$

$$a_1 = r_1 \times \left(0.5055 - 0.00595 \times (6.5 - A)^2\right) \quad (12)$$

$$k = r_k \times \left(0.2711 - 0.01858 \times (2.5 - A)^2\right) \quad (13)$$

where A is the altitude of the site above sea level. These equations can be used only for A < 2.5; r_0, r_1, r_k are constant values from Table 1. Data for the Table 1 was develop based on the Hottel estimation method [40].

Table 1. Coefficients for climate type and sample location.

Climate Type	r_0	r_1	r_k	Sample location
Tropical	0.95	0.98	1.02	Nairobi
Midlatitude summer	0.97	0.99	1.02	Rome
Subarctic summer	0.99	0.99	1.01	Ny-Ålesund
Midlatitude winter	1.03	1.01	1.00	Gliwice

The diffuse radiation can be calculated by the following formula:

$$G_{cd} = \tau_d \times G_{on} \times [\cos(\varphi) \times \cos(\delta) \times \cos(\omega) + \sin(\varphi) \times \sin(\delta)] \tag{14}$$

where τ_d is the ratio of the transmitted diffuse radiation to the total radiation incident at the top of the atmosphere. This coefficient can be calculated as follows:

$$\tau_d = \frac{G_{cd}}{G_o} = 0.271 - 0.294 \times \tau_b \tag{15}$$

Using all of the previous equations, we can calculate the total radiation, which is necessary to calculate the energy, which can be obtained by solar cells. The total radiation received on a horizontal surface at the ground surface can be calculated as follows:

$$\begin{aligned} G_c = G_{cb} + G_{cd} = (\tau_b + \tau_d) \times G_{sc} \times \left[1 + 0.033 \times \cos \tfrac{360 \times n}{365}\right] \\ \times [\cos(\varphi) \times \cos(\delta) \times \cos(\omega) + \sin(\varphi) \times \sin(\delta)] \end{aligned} \tag{16}$$

The hourly radiation on a horizontal surface is written as follows:

$$\begin{aligned} I_c = \tfrac{12 \times 3600}{\pi} \times (\tau_b + \tau_d) \times G_{sc} \times \left[1 + 0.033 \times \cos \tfrac{360 \times n}{365}\right] \\ \times [\cos(\varphi) \times \cos(\delta) \times (\sin \omega_2 - \sin \omega_1) \\ + \tfrac{\pi \times (\omega_2 - \omega_1)}{180} \times \sin \varphi \times \sin \delta\Big] \end{aligned} \tag{17}$$

The above equations will be the basis for the source code, which will then be implemented into the simulation environment. The equations allow us to obtain the value of irradiation for a given time and location.

2.2. External Restrictions on Solar Energy Production

In the case of UAVs powered by solar energy, the power supply system is subject to many dependencies and limitations. It can be divided into two groups. The first is related to factors that are beyond human control, i.e., weather conditions, temperature, cloud cover, air pollution. The second is related to the variable parameters that can be changed in the UAV, e.g., electric motor power, mass, payload, flight path planning. The individual elements are divided into subsequent components and each of them has an impact on the energy balance. The general diagram of dependencies is presented in Figure 2.

Obtaining a negative energy balance makes it necessary to change the flight conditions or the construction of the drone, reduce energy consumption, and reduce the weight of the UAV [41]. Energy harvesting, in the case of solar powered UAVs, primarily depends on the irradiation level. During the flight, we also have to take into account other external restrictions, such as cloudiness, temperature, solar and air pollution.

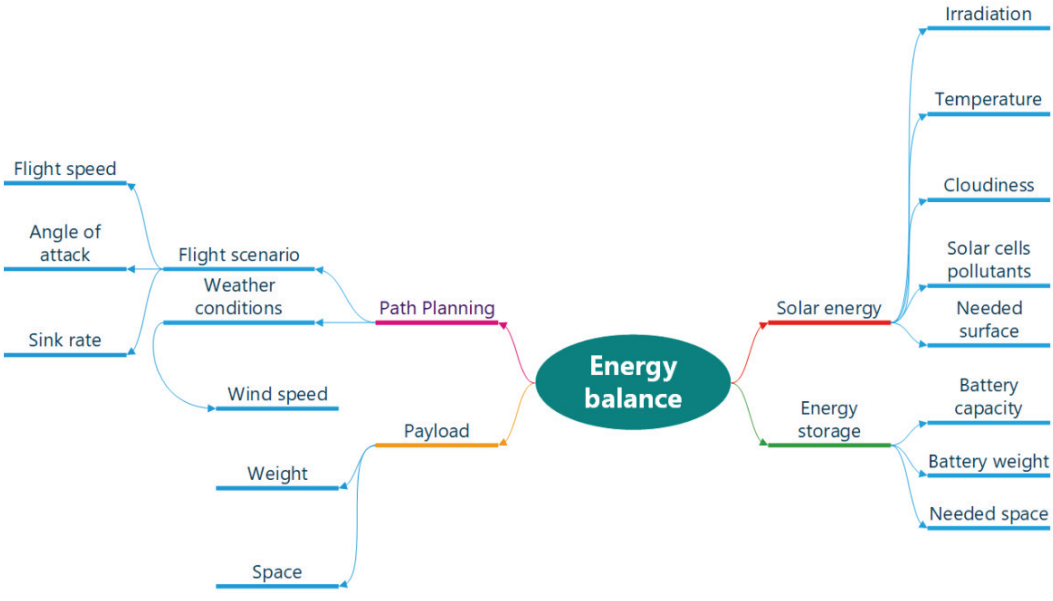

Figure 2. Energy balance general diagram.

2.2.1. Cloudiness

The calculations related to irradiation allow us to obtain the results for a given location and on a specific day. This value shows the results for perfect conditions. In a real environment, clouds often restrict the available sunlight. There are three main types of clouds [42]:

1. cirrus clouds;
2. cumulus clouds;
3. stratus clouds.

Different types of clouds cause the scale of cloudiness to change. The cloudiness is measured on the okta scale (from 0—no cloud cover, to 8—full cloud cover). The percentage value that lowers the obtained energy can be written as: 0—100%, 1—98%, 2—94%, 3—88%, 4—79%, 5—70%, 6—54%, 7—50%, 8—27%. Cloudiness scale equal 9/8 is sky obscured—9—0% [43–45].

2.2.2. Temperature

Temperature is a variable that is important in the case of the efficiency of solar cells. The higher the temperature, the lower the efficiency [36,39,46]. Every solar cell has a temperature coefficient, which is connected with the voltage, current, and power [39]. The increase in temperature causes the deterioration of the solar cell parameters, reducing its power and efficiency (Figure 3).

For the UAV, we used a drop of air temperature between 0.5–1 °C, every 100 m [47]. The air temperature distribution depends mainly on: latitude, altitude, season, and topography. This kind of calculation for the temperature drop we can use up to the tropopause. Tropopause has this same temperature in the vertical section and amounts to −51 °C [47]. This temperature is maintained up to an altitude of 20 km.

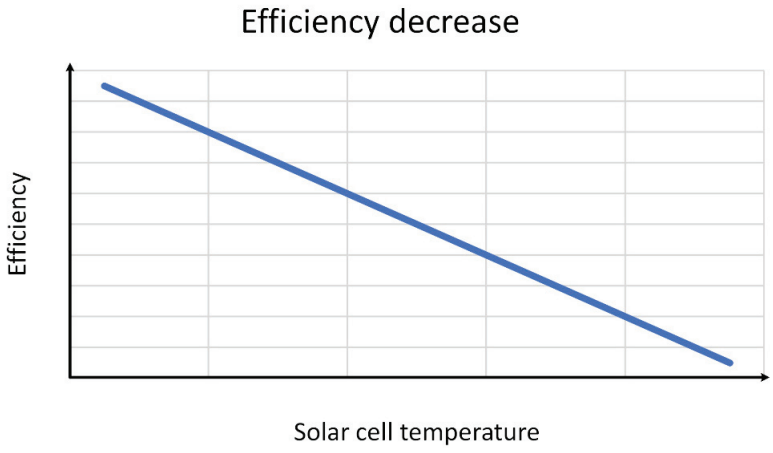

Figure 3. Efficiency decrease in solar cells.

The efficiency decrease in the solar cell with the increase in temperature is related to the heating of the solar cell under the influence of sunlight and the reduction in the heat dissipation capacity of the solar cell in the case of operation in high ambient temperature. The operation of the PV panels at high temperatures not only results in lower electrical power but also accelerates the degradation process of the solar cells.

In the simulation model, the current ambient temperature is connected with the height of the flight. To calculate the current temperature we can use the below formula.

$$T_C = T_I - [H_R \times (T_D \times 100)] \quad (18)$$

where T_C is the current temperature on the height of the flight, T_I is the temperature on the ground, H_R—is the relative height of the flight in meters, and T_D is the temperature drop. We can assume ~1 °C for a dry-adiabatic temperature gradient and ~0.6 °C for a humid adiabatic temperature gradient [48].

2.2.3. Air and Solar Cell Pollutions

Air pollution and pollutions on the solar cells' surfaces reduce the efficiency of the solar cells. These data are difficult to measure. The dust layer, smog from chimneys, soot, and hoarfrost cannot be precisely defined, particularly in the still changing conditions. In order to define more precisely the pollutants that may appear on the surface of the PV panels, it is necessary to group them. The purpose of this grouping is to facilitate the identification of the locations and seasons of such pollution. The intensity and impact on the operation of the solar-powered UAV power supply system should also be defined. Sometimes, these kinds of pollutions are momentary and, in terms of the entire mission, will not be of significant importance.

3. Materials and Methods—Numerical Model Data

The factors that were presented in the previous section are the first group of the numerical model. These data can help us to calculate the energy balance, but we have no influence on these variables. The second group is directly related to the power supply system components; namely, the solar cells and battery cells. We can freely change these elements and modify their connections in such a way as to obtain an energy surplus that allows for a continuous UAV flight of at least 24 h.

To provide a flight for 24 h we have to take into account both the outside data (e.g., weather) and the inside data (e.g., battery capacity, UAV design, solar cells). All of the

requirements should be fulfilled to allow us to complete the planned flight scenario. The process of carrying out the concept selection is presented in Figure 4.

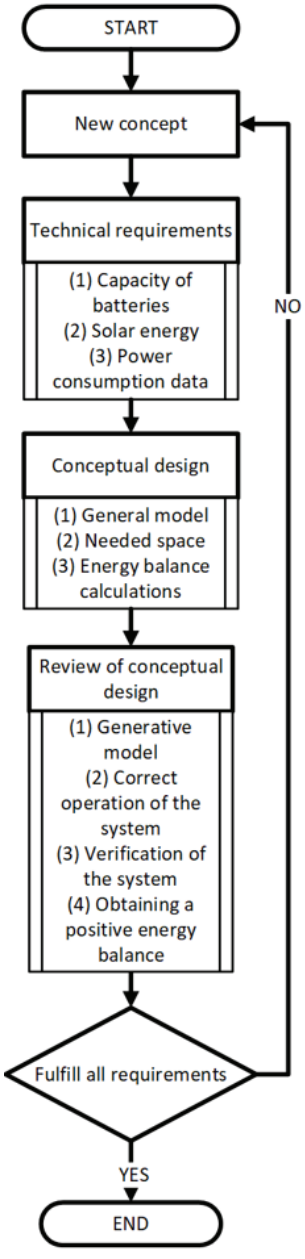

Figure 4. Flow chart of choosing the parameters of the power supply system.

To verify the numerical model, we took into account two types of TwinStratos: TS17 (Figure 5) and TS12. The parameters of both UAVs are given in Table 2, below:

Figure 5. TwinStratos 17 prototype.

Table 2. Parameters of TS17 and TS12.

Parameter	TS17	TS12
Mass [kg]	9.4	45
Wingspan [m]	3.6	12.4
Payload [kg]	2.5	2.5
Wing area [m^2]	0.896	8.6
Rate of Climb (ROC) [m/s]	0.999	1.5
Rate of Descent (ROD) [m/s]	0.41	0.26
Climb speed [m/s]	13.3	11.1
Cruise speed [m/s]	13	13.9
Descend speed [m/s]	6.5	9.5
Angle of Attack range [°]	−3 to 8	−3 to 5
Maximum altitude [km]	8	20
Power supply system parameters—described in the below subchapters		
Battery capacity [kWh]	0.622	2.797
Battery connection	4S12P	12S18P
Battery mass [kg]	2.4	10.8
Number of solar cells	40	350
Solar cell connection	40S1P	70S5P

3.1. Power Consumption

The UAV requires energy for its propulsion and additional systems, e.g., navigation, control, safety, measurement. Electric motors consume the majority of the energy. This value range can be wide due to the operational state of the flight. Take-off and climbing consume the most energy during flight at this same height and descent lower. During gliding, the electric motors do not consume energy; therefore, this stage of flight can be used as an energy buffer.

When the power consumption of the motors is variable, for the peripheral devices (control, navigation), we can use a constant value as the power consumption. The power consumption of the system on the UAV board is difficult to define. Due to the low percentage of the whole energy consumption, we can take into account the maximum value of the power consumption of the additional systems. In our case, this value is equal to 20 W for TS17 and 50 W for TS12. To assess the energy consumption of the analyzed UAVs, we used the simulation model developed in our previous study on the potential of General Aviation electric aircrafts, which is widely described [35]. Due to the higher altitudes reached by the UAVs, the COESA Atmosphere Model block responsible for calculating the changes in the atmospheric parameters was replaced by the ISA Atmosphere Model block. The model uses a backward approach. This approach allows us to assess the energy demand in order to perform the movement of the vehicle with the predefined parameters and it does not require control. Additionally, this approach performs calculations faster than the forward approach [49].

The model consists of the following subsystems, which are responsible for different calculations and behavior simulations (Figure 6):

- Flight Control Module (FCM): controls the UAV and carries out the prepared mission scenario;
- Environment: calculates the changes in the atmospheric parameters due to changes in the UAV altitude;
- Airframe: calculates, based on the information from Flight Control Module and Environment, the required torque and energy demand of the UAV to fly with the given parameters;
- Power Subsystem: consists of the following subsystems: Battery, Electric Motor and Loads, which are responsible for simulating the power demand for avionics.

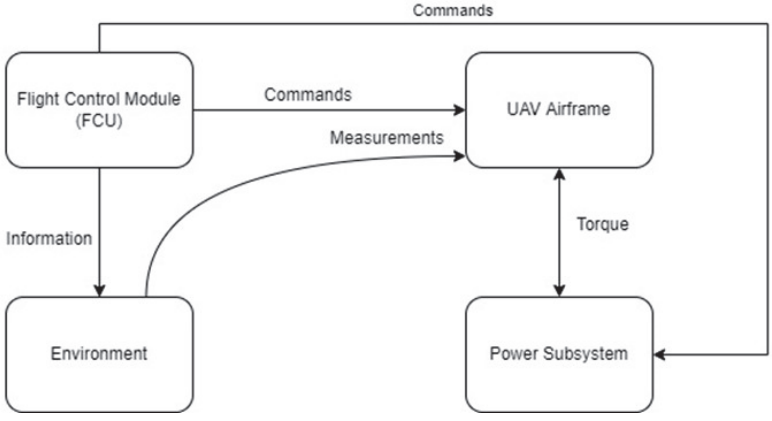

Figure 6. The simulation model and the flow of data.

The model's working principle can be described as follows: the Flight Control Module passes the information regarding the changes in the UAV altitude to the Environment to calculate the changes in the atmospheric parameters. Then, these subsystems send the flight and atmospheric parameters to the Airframe, which, after calculating the torque demand, "forces" the electric motor to produce the ordered value, which affects the battery power consumption.

In our simulation model, we used the following simplifications:

1. The electric motor runs on a direct current;
2. The flight takes place in nonthermal and nonwind conditions;
3. The battery operation is not affected by the temperature;
4. The UAV is considered to be a mass point;
5. The UAV is not equipped with solar cells.

In the case of the last simplification, the task of this model is only to assess the energy demand of the UAV, not its flight performance (e.g., range).

3.2. Power Supply System Elements

3.2.1. Solar Cells

As a base for our UAV, we decided to use flexible SunPower Maxeon Ne3 solar cells [50]. The manufacturer ensures that the efficiency of this solar cell is over 24.34% and the generated power is around 3.77 W. To check if the parameters included in the datasheet are reliable, we decided to check the current-voltage (I-V) and power-voltage (P-V) characteristics on the test stand. The tests were carried out both for the non-laminated solar cells and for the solar cells laminated with 100 μm PVC (Polyvinyl Chloride) film (Figure 7). Lamination decreases the efficiency of the solar cell but this coating increases its durability and resistance to the mechanical damage that may occur during UAV flight [51].

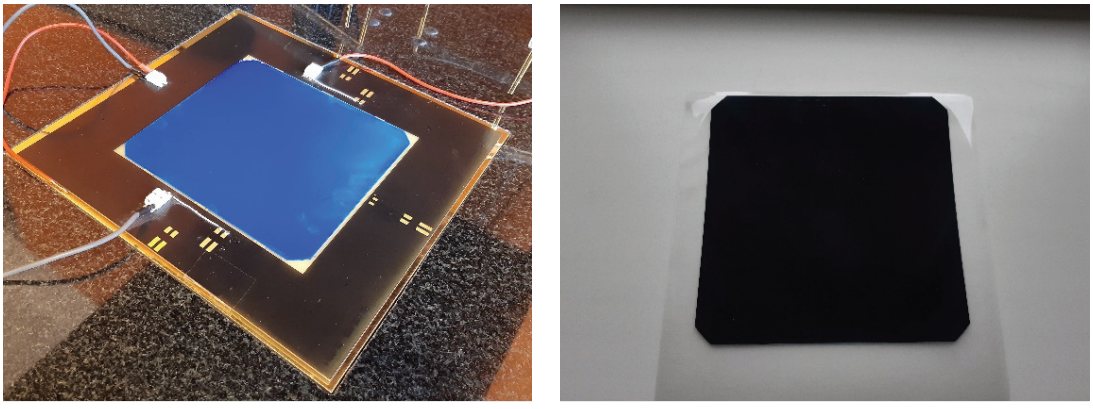

(**a**) (**b**)

Figure 7. Solar cells samples: (**a**) Non-laminated solar cell in the test stand table; (**b**) Laminated solar cell coated with 100 µm PVC film.

The test stand allows us to test solar cells in the STC (Standard Test Conditions): irradiate with the power 1000 W/m^2 in the temperature 25 °C, and Air mass 1.5 spectrum (AM 1.5) defined by European standard IEC 60904-3 [52]. The system for the I-V characteristic measurements of the solar cells meets all of the requirements of the IEC 60904-1 standard [53].

On the wings of the TS17, we could place a maximum of 40 pcs solar cells and, on the TS12, 350 pcs. The exact type of solar cell connection also took into account the nominal voltage of the battery and the voltage range of the MPPT converters. We decided to use a connection 40S1P for TS17, and 70S5P for TS12. In a parallel connection, the disadvantage is that, in case of damaging a single solar cell and lowering the current value, the whole chain will generate this low current. By increasing the number of parallel connections, we increased the redundancy of the system, and in the event of a single cell failure, we increased the value of the generated energy.

3.2.2. Battery Cells

The battery was selected in such a way as to best meet the following criteria: the lowest possible weight with the highest possible specific energy and energy density. The initial parameters of the power supply system were determined on the basis of simplified analytical calculations. Taking into account the number of solar cells and the energy that can be obtained, the capacity of the battery was calculated. We chose Gliwice as the location for the calculation. The vernal equinox was used for the irradiation equations.

For TS17 and TS12, we decided to use this same battery cell: Samsung INR18650-35E (Figure 8). The chosen battery cell generates 3.7 V, with a capacity of 3.5 Ah. The weight is equal to 50 g. As the connection, we used 4S12P for TS17 and 12S18P for TS12. A wide range of operating temperatures is essential in case of wide varying temperatures during flight. The Samsung INR18650-35E continues to work, even at −20 °C. The storage system was designed in such a way as to provide battery heating for long flights at high altitudes and at low temperatures. The heater starts to heat up the battery pack space if the temperature drops below the set level.

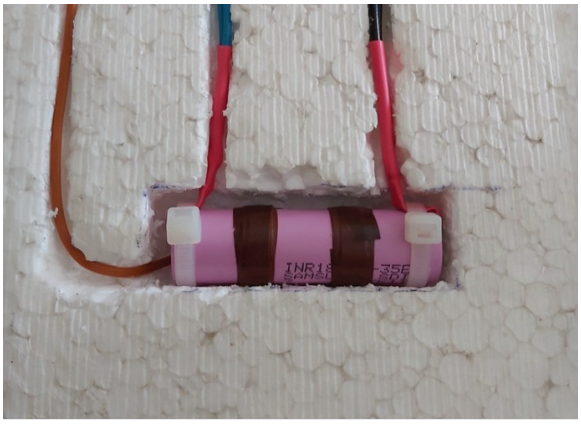

Figure 8. Samsung INR18650-35E tested in the insulation layer.

3.3. Simulation Model

A simulation model of the TwinStratos power supply system was prepared analogically, similar to the general diagram in Figure 2 (Figure 9). The main goal of the simulation model is to obtain the output data, such as the energy from the PV, the SoC (State of Charge), and time to discharge. Simulation allows us to check whether the given parameters in the adopted scenario will be feasible.

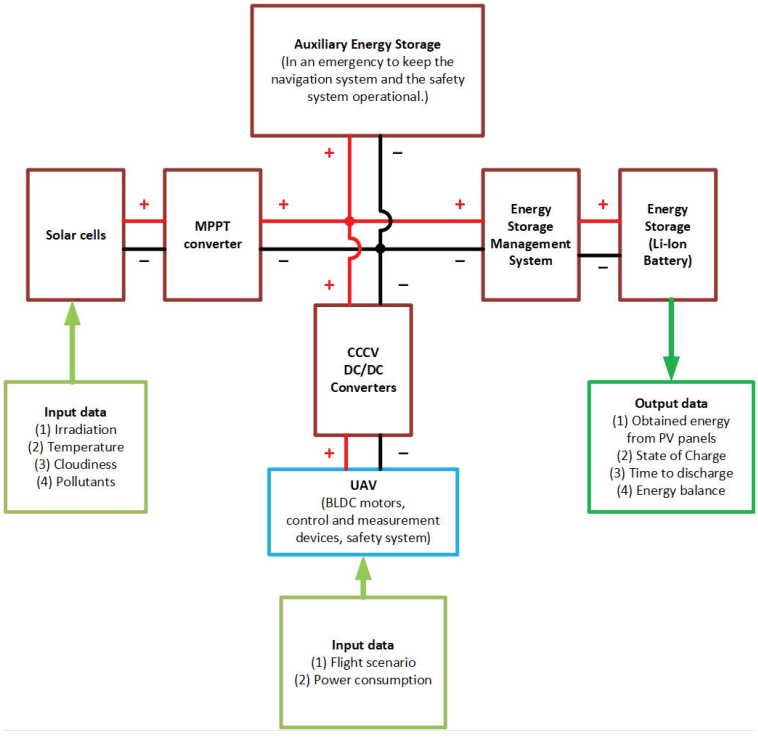

Figure 9. General diagram of the TwinStratos power supply system.

The scenarios that took into consideration time and location were either able or not able to achieve a 24 h flight. The flow chart (Figure 10) shows the change procedure for achieving a 24 h flight.

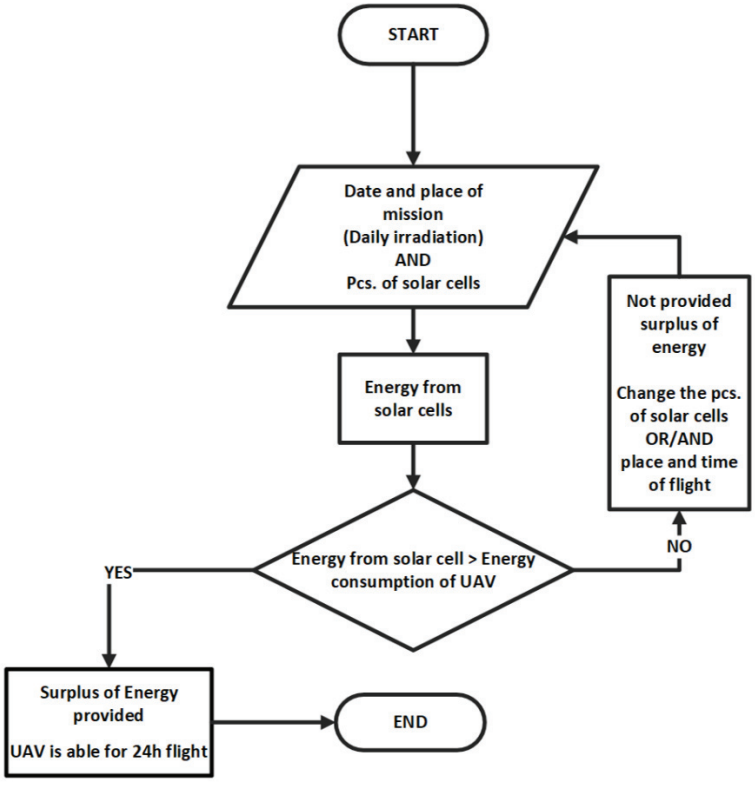

Figure 10. Flow chart of the energy balance of the UAV.

3.4. Scenarios of Path of Flight

To develop the UAV flight scenarios, we took into account the basic operations: take-off, climbing, gliding. The scenario helps to define the UAV energy demand so that it is possible to determine the power needed for each stage of flight. In the simulation model, we decided to prepare two main flight scenarios. Flight paths allow us to optimize the power consumption during the flight and increase the working time of the power supply system. The properly prepared scenarios for the UAV, in combination with the properly selected solar cells, batteries, and power consumption devices, allow for obtaining long endurance, which should ultimately achieve full energy autonomy of the UAV. The flight planning paths are mainly based on reaching the set altitude and then, depending on the needs, we can start the gliding or supporting the flight at a certain altitude. The goal of the simulation is to achieve a milestone in the form of a flight over 24 h. All of the scenarios were developed to take-off at sunrise. The single scenario is 24 h and it repeats every day thereafter.

The TwinStratos 1:7 scenarios were divided into two parts (Figure 11):

1. Ascending to a height of 5 km and then holding that ceiling. We start gliding to 1 km in this way to finish gliding in 24 h from the take-off
2. Ascending to a height of 8 km and then holding that ceiling. We start gliding to 1 km in this way to finish gliding in 24 h from the take-off

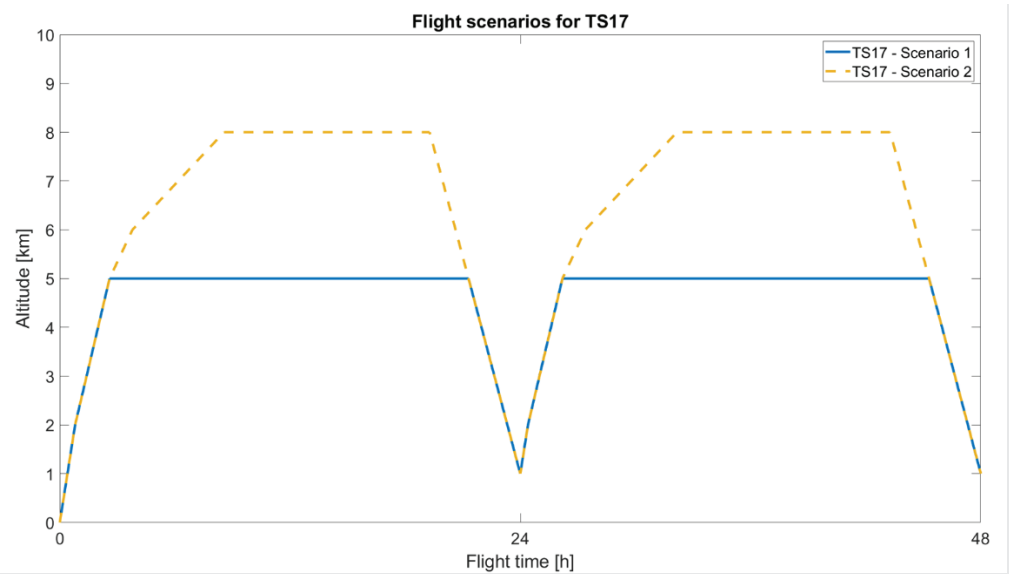

Figure 11. Flight scenarios for TS17.

The TwinStratos 1:2 scenarios were divided for three parts (Figure 12):

1. Ascending to a height of 10 km and then holding that ceiling. We start gliding to 1 km in this way to finish gliding in 24 h from the take-off.
2. Ascending to a height of 15 km and then holding that ceiling. We start gliding to 1 km in this way to finish gliding in 24 h from the take-off.
3. Ascending to a height of 20 km and then gliding to 1 km.

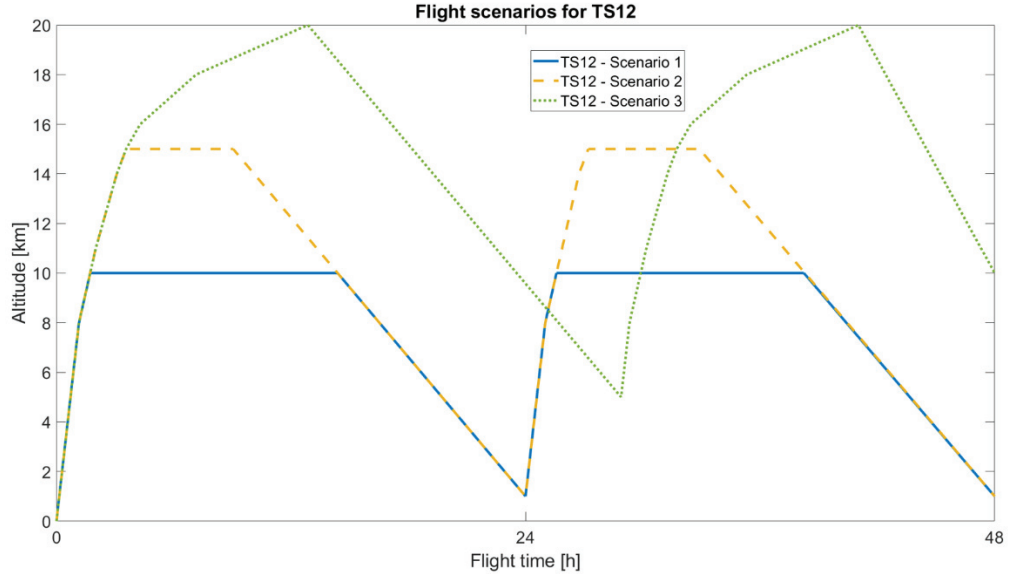

Figure 12. Flight scenarios for TS12.

For the initial scenarios, we used a location of Gliwice. At the time of the first flights, we decided to set to the vernal equinox. If the UAV was unable to fly in this season, we

would change the time to summer solstice to compare the results. As the temperature for the vernal equinox, we take a temperature of 15 °C, and for the summer solstice, 25 °C.

The data (partially included in Table 2) for the simulation model of the power consumption were developed by aviation designers. These parameters were entered into the model. In the simulation model, we used data where the flight path angle is 4.3° for TS17 and 7.7° for TS12. To provide enough lift force, the angle of attack is equal to 6° for TS17 and 3.5° for TS12.

As in the initial stage of flight (take-off), we can climb fast with a high flight path angle; in further climbing to the higher levels, this value will be lower due to the air density decrease and pressure decrease. It can cause lower energy consumption.

The lower the air density, the higher the speed required by the UAV to fly. We assumed that to simplify the simulation model, the power consumption data will be the same as in the simulation model of the propulsion system. Increasing the airspeed at a reduced flight path angle should, to some degree, increase the power consumption. Table 3 contains the flight path angle used in the power supply system simulation model.

Table 3. Flight path angle included in the simulation.

Altitude [km]	TS17	Altitude [km]	TS12
From 0 to 2	3°	From 0 to 10	5°
From 2 to 5	2°	From 10 to 15	4°
From 5 to 6	1°	From 15 to 17	2°
From 6 to 8	0.5°	From 17 to 20	1°

4. Results and Discussion

4.1. Irradiation Value in the Model

The irradiation, which is able to reach the solar cells, depends on time, location, and weather conditions. The formulas included in Section 2 allowed us to prepare a script that calculates the value of irradiation for the given parameters. We are planning to perform the first flights of TS12 and TS12 in Gliwice (Poland). As the initial assumption, we chose the vernal equinox as the time point for the mission. Depending on the season, we obtain different values of irradiation for Gliwice (Figure 13).

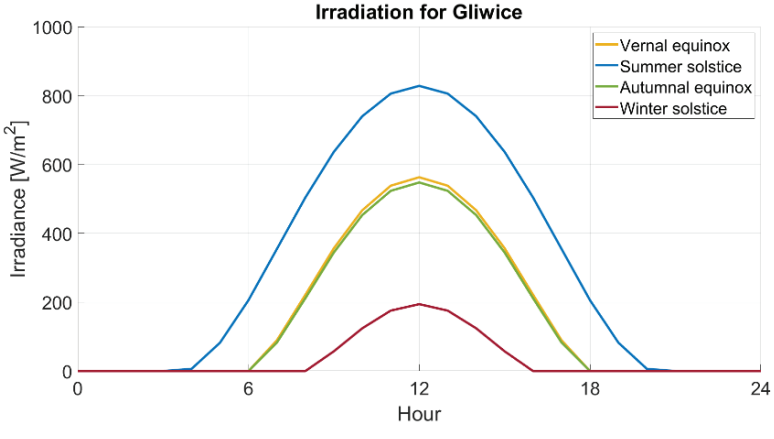

Figure 13. Irradiation for Gliwice for different days beginning seasons of the year.

In the case of different places of flight at this same time, we obtain an irradiance parabola with a different peak value and time of solar insolation. To compare the location of Gliwice with different places—in both directions to the equator and to the pole—we

chose four additional locations to see results. The geographical coordinates of all of the places are presented below:

- Ny-Ålesund—latitude: 78°55′0″ N; longitude: 11°56′0″ E;
- Gliwice—latitude: 50°17′32″ N; longitude: 18°40′3″ E;
- Rome—latitude: 41°53′0″ N; longitude: 12°29′0″ E;
- Mexico City—latitude: 19°26′0″ N; longitude: 99°8′0″ W;
- Nairobi—latitude: 1°16′0″ S; longitude: 36°48′0″ E;

For each location, we prepared an irradiation plot for the vernal equinox (Figure 14). On this day, across the globe, the day lasts 12 h. Figure 14 shows how important the location of a flight with a solar-powered UAV is.

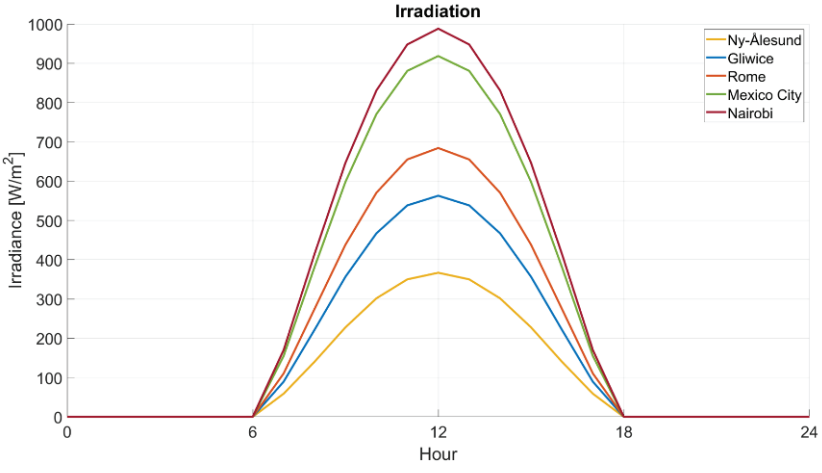

Figure 14. Irradiation for different location in the Vernal equinox.

In all of these places, we use a 0 level as height above sea level. The results will vary if the data take into account the altitude above sea level. To show how the altitude affects the irradiation, we prepared another analysis. Figure 15 shows the difference between 0 and 2.5 km altitude for Gliwice in the vernal equinox. For the 0–2.5 km range of height, the peak values were as follows:

- 0 km—563 W/m^2
- 0.5 km—596 W/m^2
- 1 km—623 W/m^2
- 1.5 km—644 W/m^2
- 2 km—660 W/m^2
- 2.5 km—670 W/m^2

The difference is the highest in the first 0.5 km and 1km. It is equal to 6 and 10.5%, respectively. In the last range, between 2 and 2.5 km, the difference is significantly smaller, and it is equal to 1.5%. The difference between the peak values from 0 and 2.5 km is equal to 19%.

In our simulation model, we used 0-level data as the input for the solar-powered power supply system. More precise data will be used in the model after the first flights.

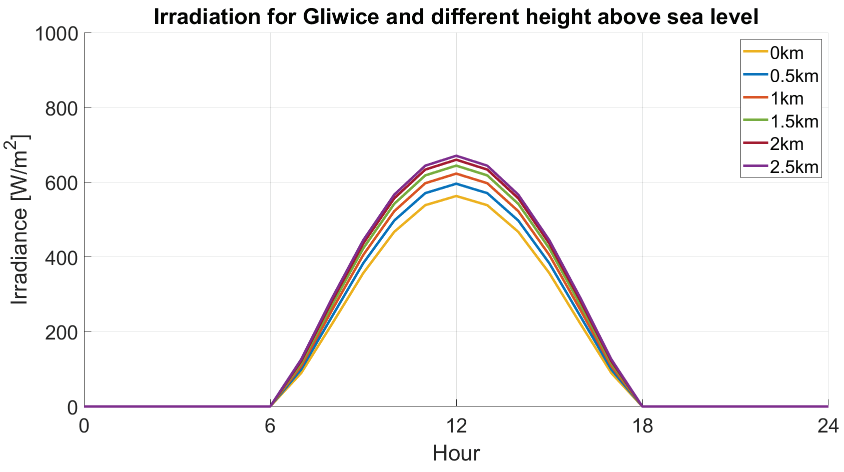

Figure 15. Irradiation for Gliwice in vernal equinox for different altitude.

4.2. Solar cells

The P-V and I-V characteristics of the solar cells allow us to obtain the exact parameters of the SunPower Maxeon Ne3. The obtained data are shown in Table 4. The I-V and P-V characteristics are presented in Figure 16.

Table 4. Electrical specification of tested solar cells.

Data	Manufacturer Data (Non-Laminated)	Non-Laminated	Laminated (100 µm Film)
V_{oc} [V]	>0.731	0.733	0.726
I_{sc} [A]	>6.382	6.330	6.061
V_{mp} [V]	>0.625	0.627	0.624
I_{mp} [A]	>6.050	5.92	5.747
P_{mpp} [Wp]	>3.77	3.71	3.589
Efficiency [%]	>24.34	24.29	23.33

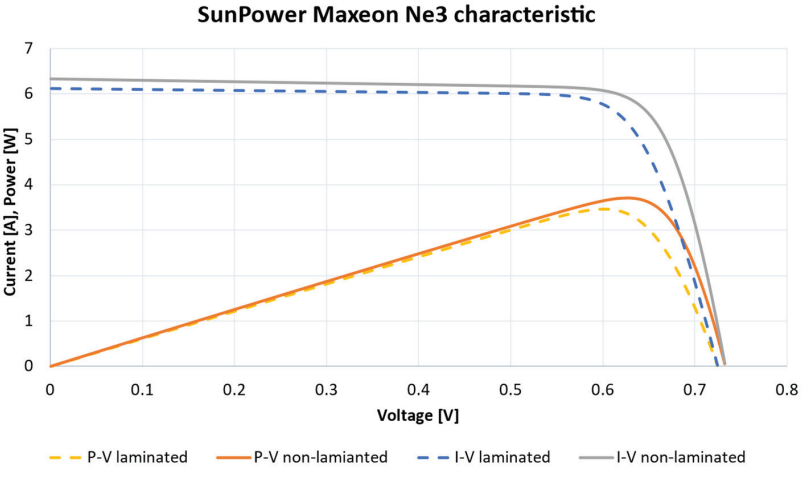

Figure 16. I-V and P-V characteristics of the SunPower Maxeon Ne3.

We researched non-laminated and laminated solar cells. In the case of TS17 and TS12, we used laminated solar cells, which have lower efficiency than non-laminated ones. In the simulation model, we used parameters of this type of solar cell. Figure 17 shows the characteristics with a different irradiation level, Figure 18 shows the characteristics of a different temperature solar cell. Tables 5 and 6 present the parameters of the laminated solar cells.

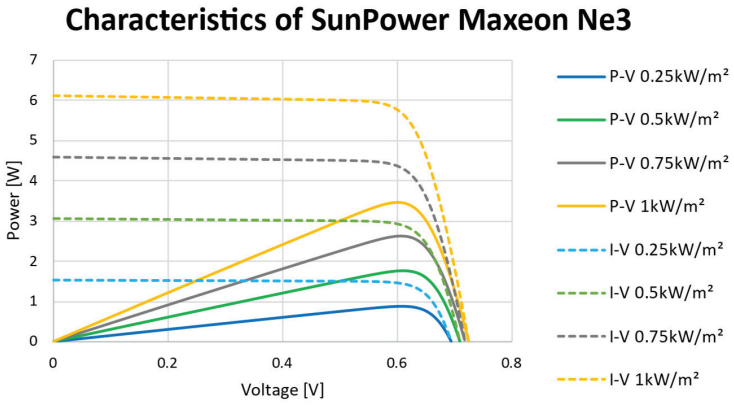

Figure 17. P-V and I-V characteristics of the laminated SunPower Maxeon Ne3 for different irradiance.

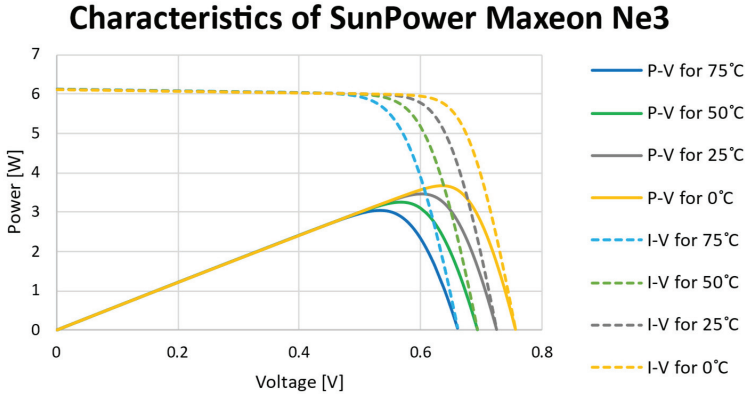

Figure 18. P-V and I-V characteristics of the laminated SunPower Maxeon Ne3 for different temperatures.

Table 5. MPPT data of tested solar cell.

Laminated SunPower Maxeon Ne3				
Irradiation [W/m²]	**Voltage [V]**	**Current [A]**	**Power [W]**	**Fill Factor [%]**
1000	0.624	5.748	3.588	81
750	0.622	4.317	2.684	61
500	0.618	2.872	1.776	40
250	0.606	1.437	0.871	19.8

Table 6. MPPT data for tested solar cell in different temperatures.

Laminated SunPower Maxeon Ne3				
Temperature	**Voltage [V]**	**Current [A]**	**Power [W]**	**Fill Factor [%]**
0	0.671	5.706	3.827	87
25	0.624	5.748	3.588	81
50	0.578	5.779	3.343	76
75	0.532	5.813	3.092	70.2

4.3. Power Consumption

The power consumption data for climbing are shown in Figure 19 for TS17 and in Figure 20 for TS12. The data obtained by the simulation model allows us to obtain the value of the power consumption of the electric motors. The low power of the electric motors is caused by a specific and very light UAV.

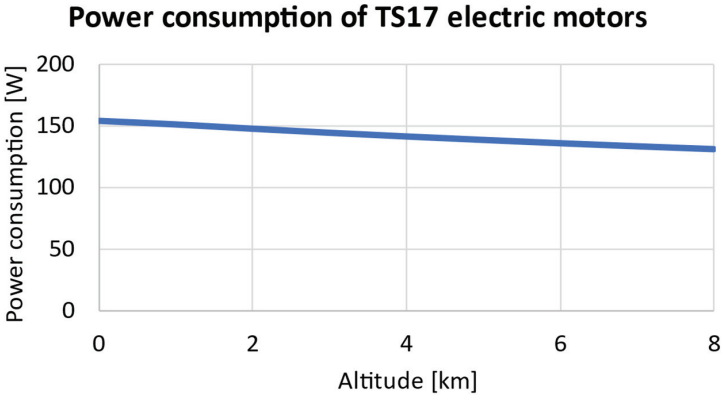

Figure 19. Power consumption of TS17 electric motors during climbing.

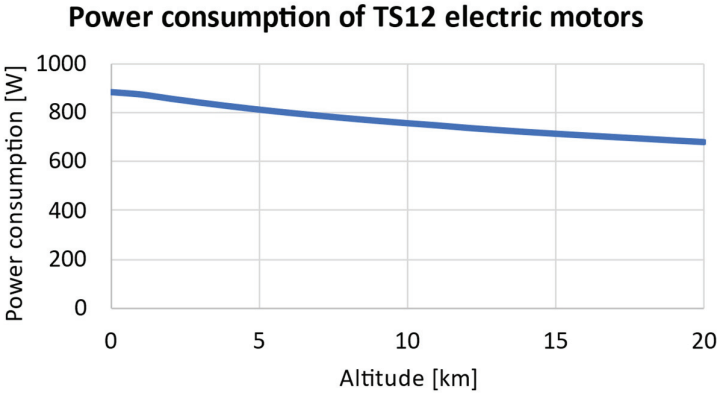

Figure 20. Power consumption of TS12 electric motors during climbing.

The cruise speed for TS17 was defined as 13 m/s and 13.9 m/s for TS12. Changes to the Angle of Attack (AoA) cause either greater or less aerodynamic drag. Figures 21 and 22 show the differences in the power consumption caused by changing AoA. Depending on the altitude, the range of the cruise speed may be significantly wider; to simplify the calculations, we present the data on the power consumption for these cruise speeds.

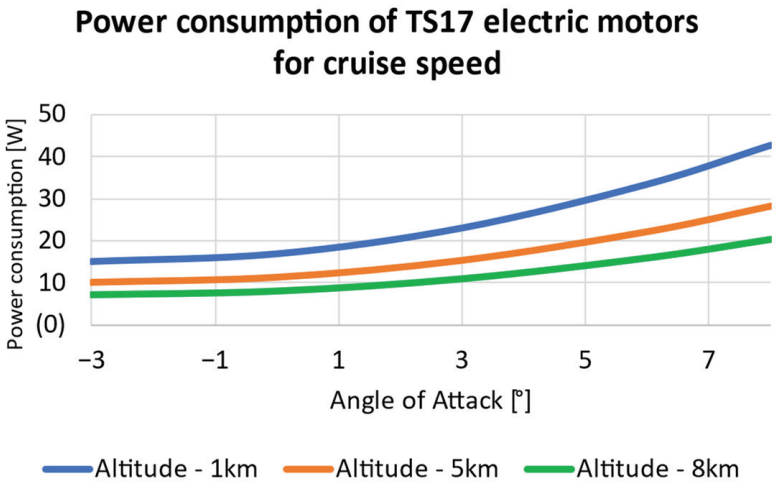

Figure 21. Power consumption of TS17 electric motors for cruise speed.

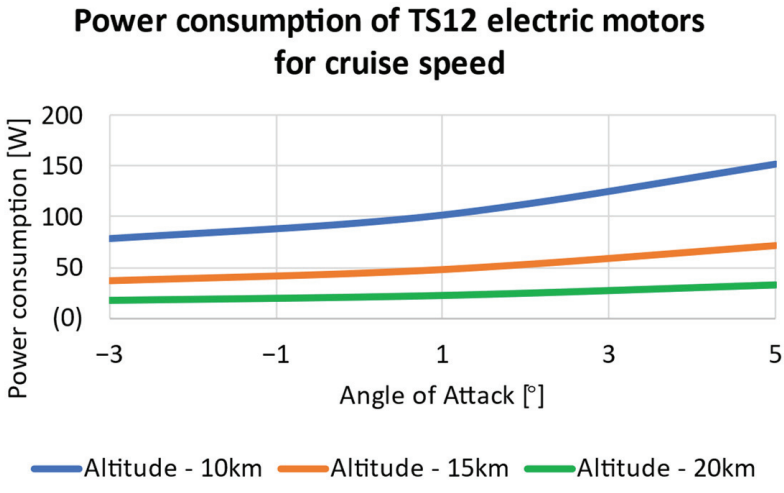

Figure 22. Power consumption of TS12 electric motors for cruise speed.

In the simulation model of the power supply system, the value of the power consumption was additionally multiplied by the efficiency of the electric motors. The climbing efficiency of the electric motors was 90% both for TS17 and TS12; the cruise efficiency was 50%.

4.4. Battery Cell

To obtain the precise parameters of the power supply system, the model was adjusted to the parameters obtained on real systems. On the test stand, we received the data and tuned the simulation model. For each range of the discharge current, the model is adjusted separately due to significant changes in the discharge characteristics of the battery cells. The research was conducted for six discharge currents in the range 0.2–5 A (Figure 23).

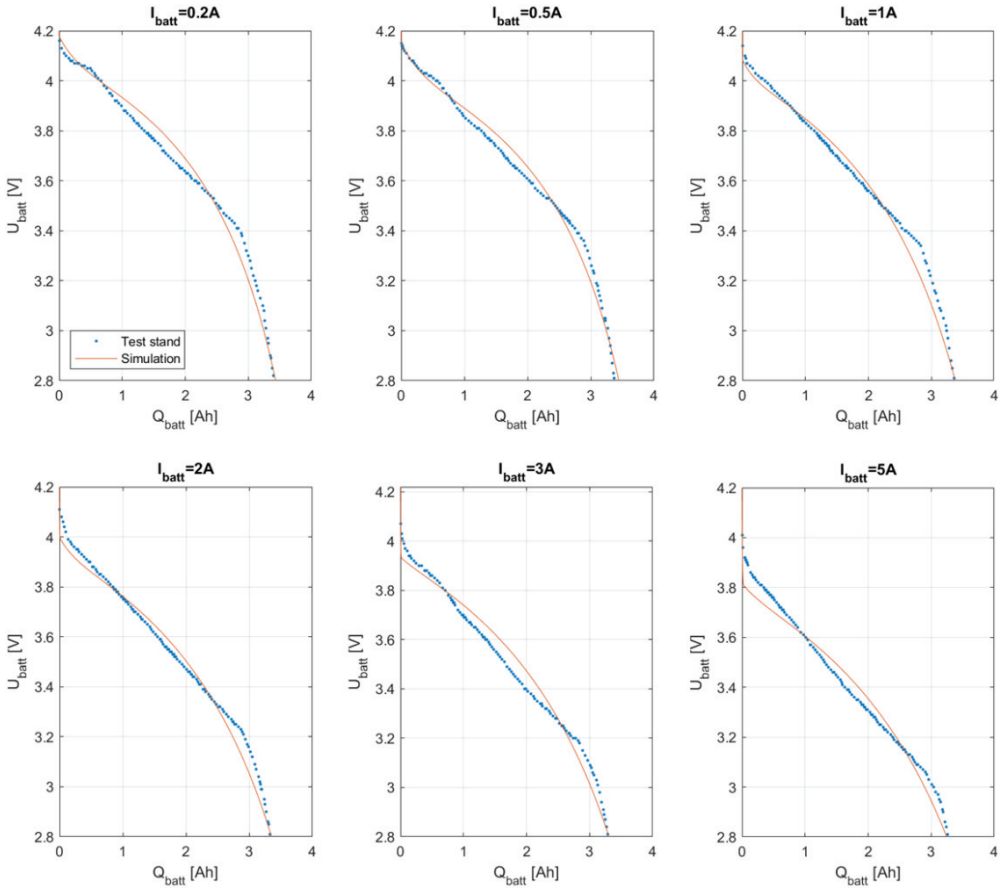

Figure 23. Tuned characteristics of the Samsung INR18650-35E battery simulation model.

To simplify the simulation model, we did not use a temperature effect and an ageing effect. By using the heater in the battery pack, we want to provide the optimal condition of work for the batteries. The ageing effect was omitted. When building the prototype, the decrease in the capacity after a few hundred charging cycles is redundant.

The developed calculations of the power consumption show that the power supply system will be discharged with low currents. For both of the UAVs, these values are similar and they are presented in Table 7.

Table 7. Discharging currents during the flight.

Stage of Flight	TS17	TS12
Cruise flight	0.28 A	0.25 A
Climbing	~1.1 A	~1.1 A
Descend—without work of electric motors (avionics)	0.11 A	0.06 A

4.5. Power Supply System Simulation Model

4.5.1. Twin Stratos 17

We have a three main points for changing the power consumption. At these points, there is a fundamental change in the flight state. The UAV goes from climbing to cruise flight and then to gliding.

The power consumption for the 5 km and 8 km scenarios reflects the scenario shown in Figure 11. During the climb, the power supply system drew the most energy with a gradual decrease in the power consumption (reflection of Figure 19). Flight at a certain altitude (5 km or 8 km) allows for a reduction in energy consumption. Both the climb and cruise values take into account the efficiency of the electric motors. Starting gliding saves energy, then only the control measuring devices consume energy.

MPPT power is the power that is provided to the power supply system from the PV panels. We can see a significant difference between the energy delivered at the vernal equinox and the summer solstice. The power obtained by the PV panels during the summer solstice is 92% higher than in the vernal equinox for Gliwice.

In the vernal equinox, TS17 is not able to ensure full energy autonomy (Figure 24). The battery was drained after 14 h and 30 min from take-off. The battery is discharged at a height of 5 km. This gives the UAV time for gliding, but it is a dangerous situation because the UAV is not able to rotate and change the direction of descent. To ensure the continuity of the mission, the battery cannot become entirely unloaded.

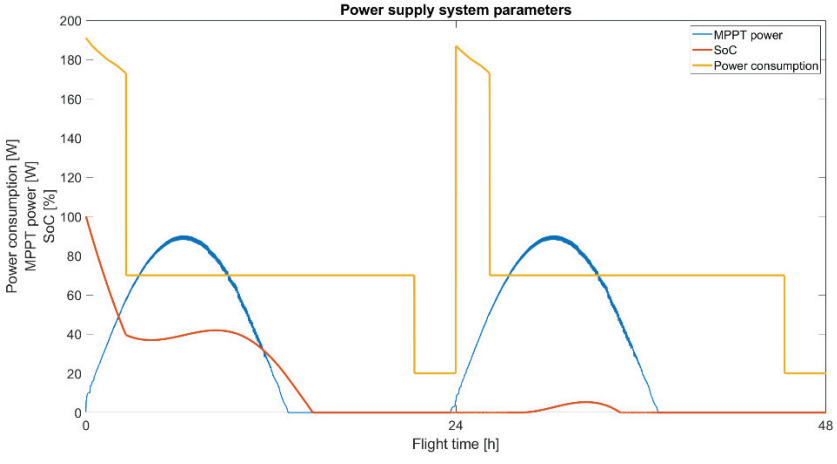

Figure 24. TwinStratos 17 5 km scenario in the vernal equinox.

During the summer solstice, TS17 was able to fly for over 24 h at the maximum altitude of 5 km (Figure 25). The lowest SOC was equal to 11.5% and it occurred in the morning of the second day, at an altitude of 5 km. At this height, the UAV starts charging the battery because the energy from the PV is higher than the power consumption during cruising.

In the case of the flight to the highest altitude equal to 8 km, TS17 was not able to achieve this height (Figure 26). This was a result of the PV providing less energy and less energy storage and this caused the battery to be drained after 6 h and 30 min from take-off.

In Figures 24 and 26, we can see recharging the battery on the second day. This shows that the simulation model of the power supply system works correctly, but the position of the UAV in space is not noticeable through this system. The system only recognizes the energy demand and the energy balance.

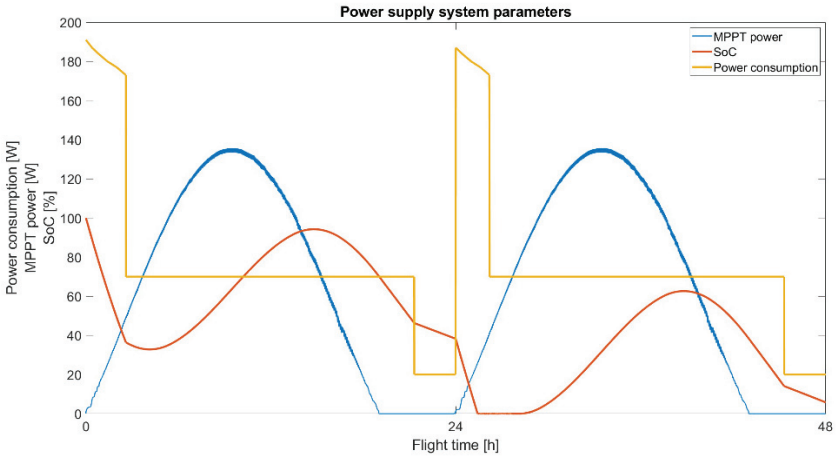

Figure 25. TwinStratos 17 5 km scenario in the summer solstice.

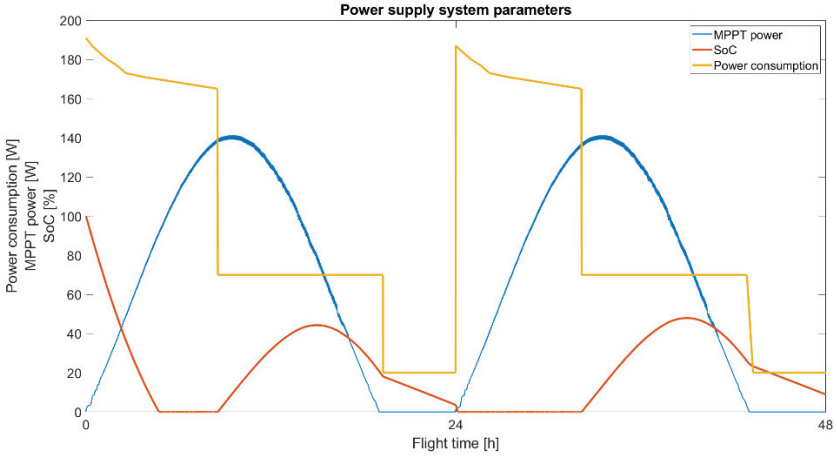

Figure 26. TwinStratos 17 8 km scenario in the summer solstice.

4.5.2. Twin Stratos 12

For TS12, the energy consumption was analogous to Figure 12. The climb values were taken from Figure 20. All of the values include the efficiency of the electric motors. During the vernal equinox, we can observe that the power from the PV is higher than the power consumption in the 10 km (Figure 27) and 15 km (Figure 28) scenarios, when the TwinStratos begin cruising. Higher flight altitude and longer gliding time allows for longer energy saving than in the case of the TS17. The power consumption spikes again after the glide phase ends and the climb phase resumes. We can observe it returning to the set altitude. Then, the SoC of the battery reaches its lowest value. The value of the SoC was correspondingly equal to 29% for the 10 km scenario and 20.5% for the 15 km scenario. In the TS12 scenarios, during flights up to altitudes of 10 km and 15 km, the UAV obtained its energy autonomy in the vernal equinox.

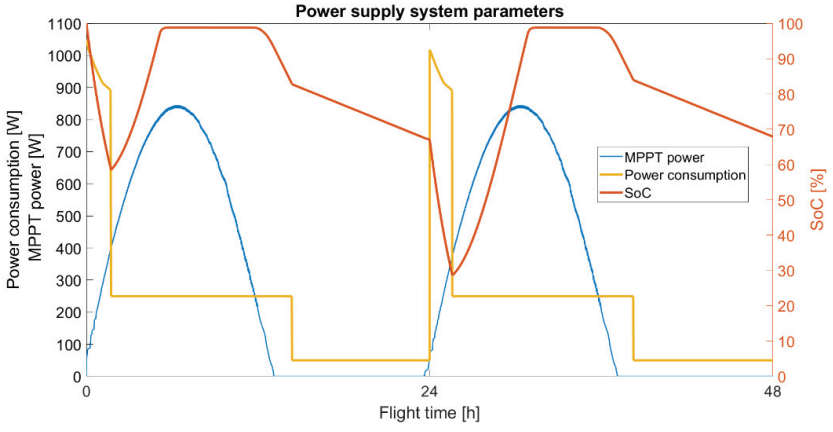

Figure 27. TwinStratos 12 10 km scenario in the vernal equinox.

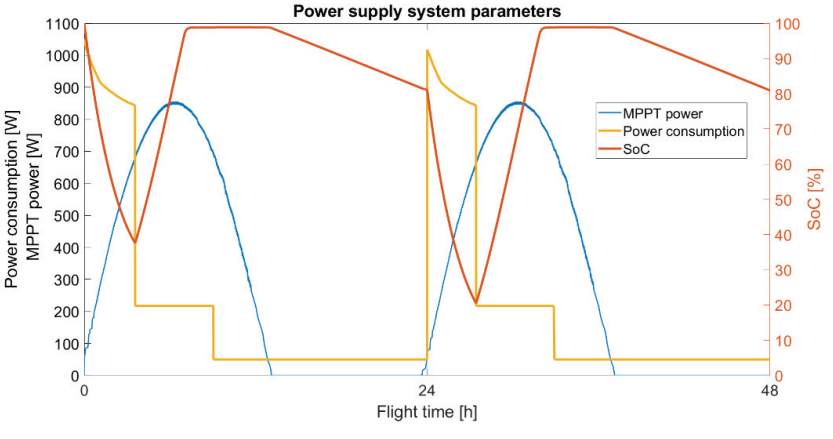

Figure 28. TwinStratos 12 15 km scenario in the vernal equinox.

For the flight up to 20 km, the energy accumulated in the batteries and produced by the PV were not able to provide a surplus energy balance in the vernal equinox. The energy needed to achieve an altitude of 20 km was too high at the stage of climbing; 11 h after take-off, the battery was drained (Figure 29). The last two kilometers were achieved with a low degree of climb, equal to 1°. To achieve an altitude equal to 20 km, we had to change the time of the flight.

During the summer solstice, TS12 was able to fly for over 24 h (Figure 30). The lowest SoC was at the beginning of the flight, up to the moment when the power from the PV was higher than the current power consumption, which occurred about 4 h and 30 min after take-off. The lowest value of SoC was equal to 22.5%. On the second day, the battery began to lower the SoC when the power from the PV was lower than the power consumption.

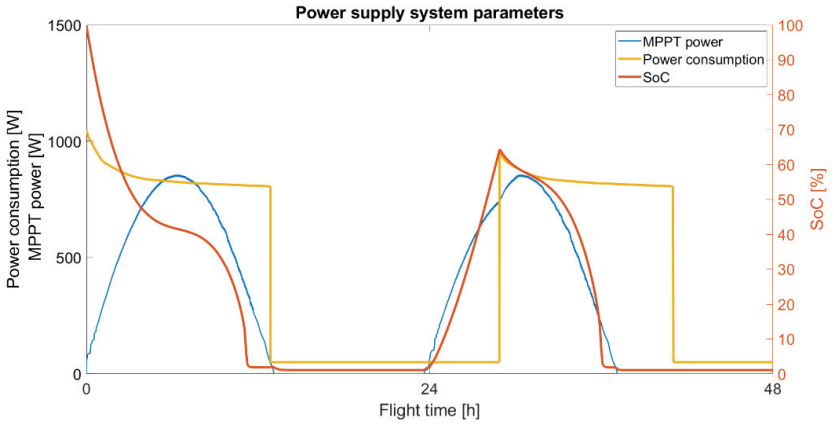

Figure 29. TwinStratos 12 20 km scenario in the vernal equinox.

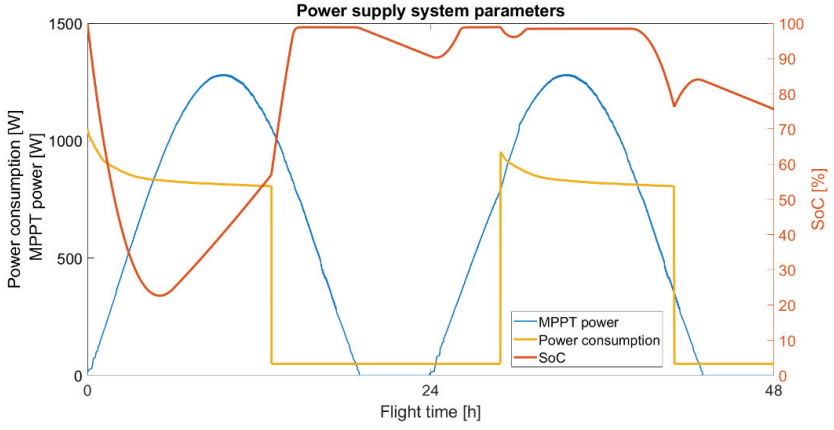

Figure 30. TwinStratos 12 20 km scenario in the summer solstice.

As it was written in the previous case (for TS17), the power obtained by the PV panels during the summer solstice is 92% higher than in the vernal equinox for Gliwice. For our location, almost twice as much energy from the PV allows for a flight to an altitude of 20 km. Changing the flight time to the summer solstice allowed us to obtain a positive energy balance for the 20 km scenario.

5. Conclusions

By analyzing the simulation graphs, it can be concluded that the most important issue when planning a long-endurance flight is the flight path and the appropriate weather conditions. The simulations show that a 24 h flight is feasible for the location of Gliwice during the spring equinox for TS12 and during the summer solstice for TS17. For both scenarios, sunny weather was adopted without cloud cover, which additionally allowed the UAVs to obtain more energy from the PV.

As the altitude increases, the energy obtained from the solar cells increases. However, due to the impossibility of obtaining the data from the real environment, the increase in this value was omitted and the data from 0 m above sea level were adopted.

The falling speed of TS12 and TS17 depends on the altitude, but for the calculations, this value has been simplified to one constant value for TS12 — 0.26 m/s — and0.41 m/s for TS17.

By analyzing the numerical simulations and the prepared flight scenarios, it can be concluded that the best ways to achieve a long endurance flight (at least 24 h) are the following elements:

- The flight begins at sunrise. Take-off and climb are the stages that consume the most energy, so it is good to compensate for high energy consumption with energy produced from the photovoltaic system;
- The potential energy accumulated in the form of height should be used as a time buffer, which is best used at night, when the photovoltaic system does not produce energy and the drive system does not consume energy from the power supply system;
- Continuous, gradual increase in altitude during the day and keeping the altitude as high as possible until sunset or even more depending on the type of mission;
- Commencement of the UAV gliding stage with sunset or supporting a specific altitude in such a way as to complete the stage of gliding to a given altitude with sunrise or later depending on the type of mission;
- Flight sustain should be performed at the highest altitudes due to the lower energy demand of UAV propulsion systems;
- When it is not possible to obtain a long endurance flight for the UAV, it may be necessary to change the flight duration, location, time of flight, or flight path;
- If it is not possible to obtain flight-long endurance for the key set parameters, it may be necessary to change the design of the UAV, the number of solar cells, the capacity of the battery, or the weight of the payload.

It can be concluded that the TS17 scale is a bit too small for full energy autonomy. TS12 shows a greater degree of energy autonomy by achieving higher ceilings and a lower value of the ROD (Rate of Descent) than in the case of TS17. The TS12 has almost ten times more wing area than the TS17, as a result of which it is able to obtain ten times more energy during the flight than the TS17. An additional advantage in the energy balance of the TS12 is that the maximum power consumption is seven times higher than in the case of TS17. Comparing the energy that can be produced by the TwinStratos 1:2 and 1:7 and their energy demand, it can be seen that a better energy balance is achieved by TS12.

Another milestone that our team has taken into account is the highest possible altitude to be achieved. When analyzing the flight duration, we noticed that sometimes the maximum altitude of TS is not possible to reach, particularly when starting the flight at sunrise (e.g., Figures 26 and 29), or during the not appropriate period. In the event that the energy demand during take-off and climb is the highest, and the PV energy is insufficient at some point, the battery discharges, preventing the UAV from continue to climb.

By analyzing the energy demand and PV power, it can be concluded that the best time to complete the mission aimed at achieving the highest ceiling is not sunrise, but around noon, when the sun is at its highest. In this case, the energy obtained from the PV will partially cover the energy demand of the electric motors and the UAV's control systems. The limitations are also related to the time needed to reach a given altitude. These considerations should be taken into account when we are choosing the time of the UAV's take-off.

The full set of equipment depends on the mission being performed, which is not fully defined at this stage of the work; therefore, simplifications have been made in the model after defining the mission and the various sets of measuring/observation devices. Another reason for simplifying the model is the lack of detailed data for many on-board subsystems with energy consumption characteristics. For many, only the maximum power of the device is given and the load characteristics are not analyzed. In laboratory tests, it is also difficult to confirm the characteristics of many subsystems. The team is planning intensive work on the problem indicated by the reviewer during the flight tests. Therefore, the entire power supply system has been measured in detail and is equipped with controllers and accessories that allow for connecting and disconnecting individual power supply systems.

TS17 and TS12 will be made with the technology of ultra-light composite structures. Currently, TS17 is at the construction stage and the prototype is shown in Figure 5. Only

flights in the real environment will allow the correctness of the simulation and its results to be verified. The completed missions will provide the necessary data to fine-tune the simulation model. Another stage will be the intended use of the UAV, taking into consideration its equipment and the weight of its on-board devices. In the event that, in a given mission, it is not possible to perform a long-endurance flight, the mission can be postponed until the summer solstice or the 24 h flight stage can be avoided, with an emphasis on the implementation of a specific mission.

Author Contributions: Conceptualization, K.M. and M.P.; methodology, K.M. and M.P.; software, K.M., M.P. and R.N.; validation, W.S. and M.G.; formal analysis, W.S. and M.G.; investigation, K.M.; resources, K.M., M.P. and R.N.; data curation, K.M. and M.P.; writing—original draft preparation, K.M.; writing—review and editing, W.S. and M.G.; visualization, K.M.; supervision, W.S.; project administration, K.M. and W.S.; funding acquisition, W.S. All authors have read and agreed to the published version of the manuscript.

Funding: This research was partially funded by the EEA and Norway Grants 2014–2021 and was partially carried out in the framework of the project No. 10/60/ZZB/153 "Long-endurance UAV for collecting air quality data with high spatial and temporal resolutions" and co-financed by the European Union from the European Social Fund in the framework of the project "Silesian University of Technology as a Center of Modern Education based on research and innovation" POWR.03.05.00-00-Z098/17.

Data Availability Statement: Not applicable.

Acknowledgments: The authors would like to thank Aleksandra Drygała for her support during the research. In addition, the authors would like to express our thanks to the following researchers for their contribution to the research and carrying out some of the preparatory work as part of Project-Based Learning—Anna Romańska, Michał Sobota, Paweł Paszka, Michał Wądek, Weronika Chaberska, Kaja Orzechowska.

Conflicts of Interest: The authors declare no conflict of interest.

Abbreviations

δ	Declination angle
θ_z	Zenith angle
φ	Latitude angle
τ_b	Ratio of the transmitted direct radiation to the total radiation incident at the top of the atmosphere
τ_d	Ratio of the transmitted diffuse radiation to the total radiation incident at the top of the atmosphere.
ω	Hour angle
A	Altitude of the site above sea level
AGV	Automated Guided Vehicle
AM	Air mass
AoA	Angle of Attack
BMS	Battery Management System
DSSC	Dye-sensitized solar cell
FCM	Flight Control Module
G_c	Total radiation
G_{cb}	Beam radiation
G_{cd}	Diffuse radiation
G_{on}	Irradiation on surface
G_{SC}	Solar constant
GaAs	Gallium arsenide
H_o	Daily radiation
H_R	Relative height of the flight in meters,
I_c	Hourly radiation on a horizontal surface
I_{mp}	Optimum Operating Current
I_o	Hourly radiation

I_{sc}	Short Circuit Current
I-V	Current-Voltage
MBD	Model-Based Design
n	Day of the year
N	Day length
P_{mpp}	Nominal Maximum Power
P-V	Power-Voltage
PV	Photovoltaics
PVC	Polyvinyl Chloride
r_0, r_1, r_k	Coefficients for climate type
ROC	Rate of Climb
ROD	Rate of Descent
SoC	State of Charge
T_C	Current temperature on the height of the flight
T_D	Temperature drop
T_I	Temperature on the ground
TS12	TwinStratos 1:2
TS17	TwinStratos 1:7
UAV	Unmanned Aerial Vehicle
V_{oc}	Open Circuit Voltage
V_{mp}	Optimum Operating Voltage

References

1. Li, X.; Yang, L. Design and Implementation of UAV Intelligent Aerial Photography System. In Proceedings of the 2012 4th International Conference on Intelligent Human-Machine Systems and Cybernetics, Nanchang, China, 26–27 August 2012; pp. 200–203.
2. Chadwick, S.; Miller, C.R. Military Unmanned Aerial Vehicles and Diversification Opportunities. Mississippi Defense Diversification Initiative. 2018, pp. 1–70. Available online: https://aquila.usm.edu/fac_pubs/16830 (accessed on 2 November 2022).
3. Doskocz, J.; Kardasz, P.; Hejduk, M.; Wiejkut, P. The possibilities of using drones in the courier services. *World Sci. News* **2016**, *48*, 119–132.
4. Papež, N.; Dallaev, R.; Ţălu, Ş.; Kaštyl, J. Overview of the Current State of Gallium Arsenide-Based Solar Cells. *Materials* **2021**, *14*, 3075. [CrossRef] [PubMed]
5. Oettershagen, P.; Melzer, A.; Mantel, T.; Rudin, K.; Lotz, R.; Siebenmann, D. A Solar-Powered Hand-Launchable UAV for Low-Altitude Multi-Day Continuous Flight. In Proceedings of the IEEE International Conference on Robotics and Automation (ICRA), Seattle, DC, USA, 26–30 May 2015; pp. 3986–3993.
6. Oettershagen, P.; Melzer, A.; Mantel, T.; Rudin, K.; Stastny, T.; Wawrzacz, B.; Hinzmann, T.; Leutenegger, S.; Alexis, K.; Siegwart, R. Design of small hand-launched solar-powered UAVs: From concept study to a multi-day world endurance record flight. *J. Field Robot.* **2017**, *34*, 1352–1377. [CrossRef]
7. Zephyr-UAV-Airbus. Available online: https://www.airbus.com/defence/uav/zephyr.html (accessed on 1 November 2022).
8. Solar Impulse. Available online: https://aroundtheworld.solarimpulse.com/ (accessed on 1 November 2022).
9. PHASA-35 First Flight | Newsroom | BAE Systems | International. 2020. Available online: https://www.baesystems.com/en/article/ground-breaking-solar-powered-unmanned-aircraft-makes-first-flight (accessed on 1 November 2022).
10. High Altitude, Ultra-Long Endurance, Pseudo-Satellite—HAPS—Odysseus—Aurora Flight Sciences. Available online: https://www.aurora.aero/odysseus-high-altitude-pseudo-satellite-haps/ (accessed on 1 November 2022).
11. Rydh, C.J.; Sandén, B.A. Energy analysis of batteries in photovoltaic systems Part II: Energy return factors and overall battery efficiencies. *Energy Convers. Manag.* **2005**, *46*, 1980–2000. [CrossRef]
12. Rydh, C.J.; Sandén, B.A. Energy analysis of batteries in photovoltaic systems. Part I: Performance and energy requirements. *Energy Convers. Manag.* **2005**, *46*, 1957–1979. [CrossRef]
13. Omazic, A.; Oreski, G.; Halwachs, M.; Eder, G.C.; Hirschl, C.; Neumaier, L.; Pinter, G.; Erceg, M. Relation between degradation of polymeric components in crystalline silicon PV module and climatic conditions: A literature review. *Sol. Energy Mater. Sol. Cells* **2019**, *192*, 123–133. [CrossRef]
14. Xue, B.; Li, F.; Song, M.; Shang, X.; Cui, D.; Chu, J.; Dai, S. Crack Extraction for Polycrystalline Solar Panels. *Energies* **2021**, *14*, 374. [CrossRef]
15. Li, X.; Li, P.; Wu, Z.; Luo, D.; Yu, H.Y.; Lu, Z.H. Review and perspective of materials for flexible solar cells. *Mater. Rep. Energy* **2021**, *1*, 100001. [CrossRef]
16. Blakers, A.W.; Armour, T. Flexible silicon solar cells. *Sol. Energy Mater. Sol. Cells* **2009**, *93*, 1440–1443. [CrossRef]
17. Li, J.; Aierken, A.; Zhuang, Y.; Xu, P.Q.; Wu, H.Q.; Zhang, Q.Y.; Wang, X.B.; Mo, J.H.; Yang, X.; Chen, Q.Y.; et al. 1 MeV electron and 10 MeV proton irradiation effects on inverted metamorphic GaInP/GaAs/InGaAs triple junction solar cell. *Sol. Energy Mater. Sol. Cells* **2021**, *224*, 111022. [CrossRef]

18. Kim, S.; Hoang, V.Q.; Bark, C.W. Silicon-Based Technologies for Flexible Photovoltaic (PV) Devices: From Basic Mechanism to Manufacturing Technologies. *Nanomaterials* **2021**, *11*, 2944. [CrossRef]
19. Szindler, M.; Szindler, M.; Drygała, A.; Lukaszkowicz, K.; Kaim, P.; Pietruszka, R. Dye-Sensitized Solar Cell for Building-Integrated Photovoltaic (BIPV) Applications. *Materials* **2021**, *14*, 3743. [CrossRef]
20. Ezhov, A.; Zhdanova, K.A.; Bragina, N.A.; Mironov, A.F. Approaches to Improve Efficiency of Dye-Sensitized Solar Cells. *Macroheterocycles* **2016**, *9*, 337–352. [CrossRef]
21. Kokkos, S.; Morfidis, E. *Aerodynamic Design and Analysis of Solar Powered UAV (Unmanned Aerial Vehicle)*; University of Thessaly: Volos, Greece, 2020.
22. Tsach, S.; Ankri, L.; Cohen, M.; Ehrlich, Y.; Goldenberg, T.; Levy, H.; Regev, I.; Vladimirsky, A.; Weider, A.; Yossef, Z. Sunsailor: Solar Powered UAV. In Proceedings of the 47th Israel Annual Conference on Aerospace Sciences, Tel Aviv, Israel, 21–22 February 2007.
23. Sousa, J.C. Solar System for a Long Endurance Electric UAV. Master's Thesis, University of Beira Interior, Covilhã, Portuguese, 2015.
24. Oettershagen, P. Solar-Powered Unmanned Aerial Vehicles: Design and Environment-Aware Navigation for Robust Low-Altitude Multi-Day Continuous Flight. Ph.D. Thesis, ETH Zurich, Zurich, Switzerland, 2018.
25. Polymers Aiding Solar Impulse 2's Round-the-World Adventure. Available online: https://knowledge.ulprospector.com/4541/polymers-aiding-solar-impulse-2s-round-world-adventure/ (accessed on 1 November 2022).
26. Miao, Y.; Hynan, P.; von Jouanne, A.; Yokochi, A. Current Li-Ion Battery Technologies in Electric Vehicles and Opportunities for Advancements. *Energies* **2019**, *12*, 1074. [CrossRef]
27. Horiba, T. Lithium-Ion Battery Systems. *Proc. IEEE* **2014**, *102*, 939–950. [CrossRef]
28. Verma, D.; Nema, S.; Shandilya, A.M.; Dash, S.K. Maximum power point tracking (MPPT) techniques: Recapitulation in solar photovoltaic systems. *Renew. Sustain. Energy Rev.* **2016**, *54*, 1018–1034. [CrossRef]
29. Hannan, M.A.; Hoque, M.M.; Hussain, A.; Yusof, Y.; Ker, P.J. State-of-the-art and energy management systems of Li-ion batteries in EV applications: Issues and recommendations. *IEEE Access* **2018**, *6*, 19362–19378. [CrossRef]
30. Pham, K.L.; Leuchter, J.; Bystricky, R.; Andrle, M.; Pham, N.N.; Pham, V.T. The Study of Electrical Energy Power Supply System for UAVs Based on the Energy Storage Technology. *Aerospace* **2022**, *9*, 500. [CrossRef]
31. Skarka, W. Methodology for The Optimization of An Energy Efficient Electric Vehicle. In Proceedings of the IRF 2018 6th International Conference Integrity-Reliability-Failure, Lisbon, Portugal, 22–26 July 2018.
32. Mateja, K.; Skarka, W. Towards energetic autonomy of UAV. In Proceedings of the 27th ISTE International Conference on Transdisciplinary Engineering, Warsaw, Poland, 6–10 July 2020; pp. 423–432.
33. Niestrój, R.; Rogala, T.; Skarka, W. An Energy Consumption Model for Designing an AGV Energy Storage System with a PEMFC Stack. *Energies* **2020**, *13*, 3435. [CrossRef]
34. Targosz, M.; Skarka, W.; Przystałka, P. Model-based optimization of velocity strategy for lightweight electric racing cars. *J. Adv. Transp.* **2018**, *2018*, 3614025. [CrossRef]
35. Peciak, M.; Skarka, W. Assessment of the Potential of Electric Propulsion for General Aviation Using Model-Based System Engineering (MBSE) Methodology. *Aerospace* **2022**, *9*, 74. [CrossRef]
36. Kalogirou, S. *Solar Energy Engineering: Processes and Systems*; Elsevier: Amsterdam, The Netherlands; Academic Press: Burlington, MA, USA, 2009.
37. Page, J. Chapter IIA-1-The Role of Solar-Radiation Climatology in the Design of Photovoltaic Systems. In *Practical Handbook of Photovoltaics*, 2nd ed.; Academic Press: Cambridge, MA, USA, 2012; pp. 573–643. [CrossRef]
38. Aktaş, A.; Kirçiçek, Y. Chapter 13-Examples of Solar Hybrid System Layouts, Design Guidelines, Energy Performance, Economic Concern, and Life Cycle Analyses. In *Solar Hybrid Systems*; Academic Press: Cambridge, MA, USA, 2021; pp. 331–349. [CrossRef]
39. Duffie, J.A.; Beckman, W.A. *Solar Engineering of Thermal Processes*, 4th ed.; John Wiley & Sons, Inc.: Hoboken, NJ, USA, 2013. [CrossRef]
40. Hottel, H.C. A simple model for estimating the transmittance of direct solar radiation through clear atmospheres. *Solar Energy* **1976**, *18*, 129–134. [CrossRef]
41. Zhang, L.; Li, J.; Wu, Y.; Lv, M. Analysis of attitude planning and energy balance of stratospheric airship. *Energy* **2019**, *183*, 1089–1103. [CrossRef]
42. Cloud Classifications and Characteristics. Available online: https://www.weather.gov/media/lmk/soo/cloudchart.pdf (accessed on 1 November 2022).
43. Wacker, S.; Gröbner, J.; Zysset, C.; Diener, L.; Tzoumanikas, P.; Kazantzidis, A.; Vuilleumier, L.; Stöckli, R.; Nyeki, S.; Kämpfer, N. Cloud observations in Switzerland using hemispherical sky cameras. *J. Geophys. Res.* **2015**, *120*, 695–707. [CrossRef]
44. Smith, C.J.; Bright, J.M.; Crook, R. Cloud cover effect of clear-sky index distributions and differences between human and automatic cloud observations. *Solar Energy* **2017**, *144*, 10–21. [CrossRef]
45. Myers, D.R. *Solar Radiation: Practical Modeling for Renewable Energy Applications*; CRC Press: Boca Raton, FL, USA, 2017.
46. Most Efficient Solar Panels 2022. Available online: https://www.cleanenergyreviews.info/blog/most-efficient-solar-panels (accessed on 1 November 2022).
47. Layers of the Atmosphere. Available online: https://www.weather.gov/jetstream/layers (accessed on 1 November 2022).

48. Hemond, H.F.; Fechner, E.J. Chapter 4-The Atmosphere. In *Chemical Fate and Transport in the Environment*, 3rd ed.; Academic Press: Cambridge, MA, USA, 2015; pp. 311–454. [CrossRef]
49. Horrein, L.; Bouscayrol, A.; Delarue, P.; Verhille, J.N.; Mayet, C. Forward and Backward simulations of a power propulsion system. *IFAC Proc. Vol.* **2012**, *45*, 441–446. [CrossRef]
50. Datasheet SunPower Maxeon Ne3. Available online: https://www.makeyoursolar.com/ (accessed on 8 December 2022).
51. Mateja, K.; Skarka, W.; Drygała, A. Efficiency Decreases in a Laminated Solar Cell Developed for a UAV. *Materials* **2022**, *15*, 8774. [CrossRef]
52. *IEC 60904-3*; Photovoltaic devices—Part 3: Measurement Principles for Terrestrial Photovoltaic (PV) Solar Devices with Reference Spectral Irradiance Data. IEC: Geneva, Switzerland, 2019.
53. *IEC 60904-1*; Photovoltaic Devices—Part 1: Measurement of PV Current-Voltage Characteristics. IEC: Geneva, Switzerland, 2019.

drones

MDPI

Article

Strapdown Celestial Attitude Estimation from Long Exposure Images for UAV Navigation

Samuel Teague [1,*] and Javaan Chahl [1,2]

[1] School of Engineering, University of South Australia, Mawson Lakes, SA 5095, Australia
[2] Joint and Operations Analysis Division, Defence Science and Technology Group, Melbourne, VIC 3207, Australia
* Correspondence: samuel.teague@mymail.unisa.edu.au

Abstract: Strapdown celestial imaging sensors provide a compact, lightweight alternative to their gimbaled counterparts. Strapdown imaging systems typically require a wider field of view, and consequently longer exposure intervals, leading to significant motion blur. The motion blur for a constellation of stars results in a constellation of trails on the image plane. We present a method that extracts the path of these star trails, and uses a linearized weighted least squares approach to correct noisy inertial attitude measurements. We demonstrate the validity of this method through its application to synthetically generated images, and subsequently observe its relative performance by using real images. The findings of this study indicate that the motion blur present in strapdown celestial imagery yields an a posteriori mean absolute attitude error of less than 0.13 degrees in the yaw axis, and 0.06 degrees in the pitch and roll axes ($3\,\sigma$) for a calibrated wide-angle camera lens. These findings demonstrate the viability of low-cost, wide-angle, strapdown celestial attitude sensors on lightweight UAV hardware.

Keywords: celestial; stellar; navigation; strapdown; attitude

Citation: Teague, S.; Chahl, J. Strapdown Celestial Attitude Estimation from Long Exposure Images for UAV Navigation. *Drones* **2023**, *7*, 52. https://doi.org/10.3390/drones7010052

Academic Editors: Andrzej Łukaszewicz, Wojciech Giernacki, Zbigniew Kulesza, Jaroslaw Pytka and Andriy Holovatyy

Received: 13 December 2022
Revised: 9 January 2023
Accepted: 9 January 2023
Published: 12 January 2023

1. Introduction

The use of stabilized celestial navigation sensors for uncrewed aerial vehicle (UAV) attitude determination is well documented [1]. With recent demand for size, weight and power constrained systems, strapdown celestial sensors have become more common. A strapdown [2] celestial navigation sensor is rigidly mounted to the airframe, causing imagery to be subjected to motion artefacts from the aircraft, such as actuation, vibration and turbulence. The length of the exposure window is the primary factor governing the severity of the resultant motion blur. For wide-angled lenses, it is necessary to use longer exposure windows so as to increase the total light energy incident on the sensor. Under stable flight conditions, longer exposure windows enable the detection of higher magnitude stars, and consequently provide a more accurate attitude estimate. Under motion, however, the longer exposure window results in "smearing" of star images, leaving a trail as seen in Figure 1. This image shows a region of interest (ROI) containing a single star trail captured in-flight from a strapdown celestial imaging system. We can see from this ROI that the resultant trail tends to be noisy, and the angular velocity tends to change throughout the exposure interval.

The premise for this research comes from the hypothesis that the observed star trails contain high-resolution information pertaining to the attitude of the aircraft during the exposure window. We present a method which estimates high-resolution attitude data from long-exposure images, provided availability of a low resolution approximation from the autopilot (e.g., from an inertial measurement unit). This method makes use of long-exposure strapdown imagery simulation, presented in [3], to provide an initial approximation of the star trail location and orientation, and corrects for attitude and attitude rate errors from the

inertial unit. We demonstrate the effectiveness of this method in estimating aircraft attitude under high motion conditions.

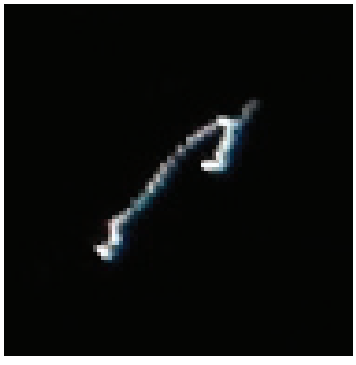

Figure 1. A region of interest containing a single star trail, captured from a strapdown celestial imaging sensor (Pi Camera HQ, 500 ms exposure interval). The shape of the star trail indicates that the camera was subjected to significant changes in attitude throughout the exposure interval.

The method presented in this paper is unique in the domain of drone navigation. Similar research has been conducted in the field of satellite navigation for the removal of motion blur. A common technique for the removal of motion blur includes estimation of the blur kernel. Knowledge of the kernel enables methods such as inverse filtering and Wiener filtering to correct the motion-blurred image. Estimation of the blur kernel is typically straightforward when analyzing stellar imagery, due to the sparsity of the stars; thus, it is is common practice to estimate the kernel parameters as seen in [4] and apply filters that utilize this kernel, as seen in [5,6]. While offering an effective means of removing motion blur in satellite imagery, such approaches tend not to capture rotational motion about the optical axis, due to the assumption that the blur kernel is spatially invariant. The method presented in [7] does explicitly take into account rotation about the boresight; however, the linear approximation used in this method is not applicable for UAV applications.

The work presented in [8] estimates the motion parameters of a given image, and uses this information to estimate the centroid of a blurred star. This assumes that there exists a global degradation function, which tends not to be the case for UAV navigation. The method presented in [9] uses an attitude correlated frames approach, in which the attitude between frames is measured with a gyroscope to within 1 arcsecond precision. This work also assumes that the rotation about the optical axis is negligible. The approach in [10] identifies correlation between subsequent short-exposure frames, and superimposes these frames to generate a long exposure image. This approach is limited by the sensor sensitivity, however, due to the need to identify stars from the shorter exposure images.

We can see in Figure 1 that the assumption of a spatially invariant blur kernel does not hold true when factors such as turbulence and aircraft control are taken into consideration. The aircraft will typically experience rotation about the yaw axis to some extent, leading to spatial variations in the motion blur on the imaging plane. Additionally, correlated frames approaches, such as those seen in [9,10], require levels of sensitivity from the imaging equipment that are not achievable with lightweight hardware at low altitudes. Furthermore, inertially aided approaches to noise removal tend to assume that gyroscope measurements contain negligible error, as seen in [9]. We observe that, especially with low-cost UAV hardware, angular rate measurements tend to be subjected to multiple sources of noise, and thus do not offer the level of precision required to perform image stabilization.

The method presented here is unique in that no attempt is made at denoising the image. Rather, we detect points from each star trail that are correlated, and infer the attitude by using a least-squares approximation that corrects the noisy inertial navigation system (INS) attitude measurements. This approach gives rise to potential use cases such

as in-flight magnetometer calibration and thermal photogrammetry. Additionally, this may be used to correlate points from different star trails within a single frame, enabling the use of traditional point-source celestial imaging techniques, such as camera calibration [11] and star identification/tracking [12].

2. Methods

The methodology outlined in this section assumes that the camera orientation, relative to the aircraft body frame, is calibrated and fixed throughout the flight. It also assumes that the camera calibration matrix is known. These calibrations are conducted prior to takeoff.

The following steps are performed in attitude estimation:

1. Estimate the theoretical curve of the star trail on the image plane by using INS measurements.
2. Apply a smoothing filter, morphological operations, and clustering to extract the star trail for each star with brightness above a given magnitude threshold.
3. Apply a thinning algorithm on each star trail to remove the effects of Gaussian point-spread diffusion.
4. Identify the endpoints of each star trail given the INS-simulated approximation.
5. Use the endpoints of the thinned star trails, along with the endpoints of the INS approximation, to compute the weighted least squares approximation for the mean attitude offset throughout the exposure window.
6. For each point in the mean-error corrected INS approximation, compute the least squares approximation of the precise attitude offset.

This method is valid for star trails which form a simple curve with observable endpoints on the image plane. Complex curves create ambiguity in the apparent motion of the airframe.

2.1. Image Processing

We denote the series of n INS attitude measurements (pertaining to a long-exposure image) as

$$\mathbf{r}_i = \begin{bmatrix} \phi \\ \theta \\ \psi \end{bmatrix} \tag{1}$$

for attitude measurement i with roll ϕ, pitch θ and yaw ψ. We compute the theoretical curve of the star trails on the image plane following the methodology in [3], denoted $\mathbf{s}_j$, for star j. Initial corrections to right ascension and declination are applied given annual proper motion, precession, nutation, and aberration given the location of the aircraft and time of flight. These corrections are only applied once per flight, prior to further calculations.

Given the hour-angle of a star, ω, the local elevation El of a celestial body given declination δ and latitude Lat is computed:

$$El = \operatorname{asin}\big(\sin(\delta)\ \sin(Lat)\ +\ \cos(\delta)\cos(Lat)\cos(\omega)\big) \tag{2}$$

and the local azimuth, Az, is given by:

$$Az = \operatorname{atan2}\big(\sin(\omega)\ ,\ \cos(\omega)\sin(Lat)\ -\tan(\delta)\cos(Lat)\big) + \pi. \tag{3}$$

We subsequently correct for refraction, given by

$$R = \frac{1.02}{\tan\left(El + \dfrac{10.3}{El + 5.11}\right)}, \tag{4}$$

where R is the refractive distance, expressed in arcminutes; thus, the apparent elevation of a star El' is then given by

$$El' = El + R. \tag{5}$$

Given the azimuth and elevation of a star, the corresponding unit vector in northeast-down (NED) coordinates is given by

$$\begin{aligned} X &= \cos(Az)\cos(El') \\ Y &= \sin(Az)\cos(El') \\ Z &= -\sin(El') \end{aligned}. \tag{6}$$

The rotation from the local NED frame to the aircraft frame is computed from the roll, pitch, and yaw of attitude measurement i, represented as matrix $\mathbf{C}_{a/ned}$. The transformation from aircraft to camera frame, $\mathbf{C}_{c/a}$, remains constant, and is determined by the orientation of the camera with respect to the inertial unit. The unit vector in local NED coordinates $\mathbf{v}^l$ is then transformed to the camera frame of reference, $\mathbf{v}^c$:

$$\mathbf{v}^c = \mathbf{C}_{c/a}\mathbf{C}_{a/l}\mathbf{v}^l. \tag{7}$$

For components x, y and z of unit vector $\mathbf{v}^c$, we compute the homogeneous point $\mathbf{P}$ in the camera frame of reference:

$$\mathbf{P} = \begin{bmatrix} \frac{X}{Z} \\ \frac{Y}{Z} \\ 1 \end{bmatrix}. \tag{8}$$

The camera intrinsic matrix, $\mathbf{K}$, is assumed to be known, given by

$$\mathbf{K} = \begin{bmatrix} f_x & 0 & x_0 \\ 0 & f_y & y_0 \\ 0 & 0 & 1 \end{bmatrix}, \tag{9}$$

where f_x and f_y are the focal lengths in the x and y axes, respectively, and x_0 and y_0 are the x and y locations of the principal point on the image plane. Thus, the pixel location, $\mathbf{s}_j[i]$, of the star for attitude measurement i is computed:

$$\mathbf{s}_j[i] = \mathbf{KP}. \tag{10}$$

Each $\mathbf{s}_j$ contains n two-dimensional points on the image plane, corresponding with the n attitude measurements. The prior calculations are performed n times for each star visible in the theoretical camera field of view to produce the array $\mathbf{s}_j$. Reference stars are selected based on their intensity, such that the brightest o stars in the frame are chosen. For each theoretical star trail, we apply a series of image-processing operations on the real image, as shown in Figure 2.

We first extract the ROI from the real image, given the theoretical star trail. A buffer is applied to the height and width of the ROI to allow for INS errors, typically corresponding to 2–3° of angular deviation. Gaussian blur is applied to the image with a 3×3 kernel, so as to reduce the magnitude of the image noise. A binary threshold is applied at five standard deviations above the average pixel value, as measured from the original full-scale image. This threshold is typical of stellar imaging sensors [13]. Image opening is performed with a 3×3 kernel to remove any remaining noise. The remaining contours are clustered, originating with the centre-most contour, and accumulating additional contours which are within 0.25° angular separation of the clustered set. Finally, the clustered contours are thinned by using the method presented in [14], so as to extract the centre-line from the star trail. Disjoint sections in the thinned image are connected by a straight line segment.

The thinned image is reduced to an array of two-dimensional points that are ordered from endpoint to endpoint. We denote this array as $\mathbf{p}_j$, for star j.

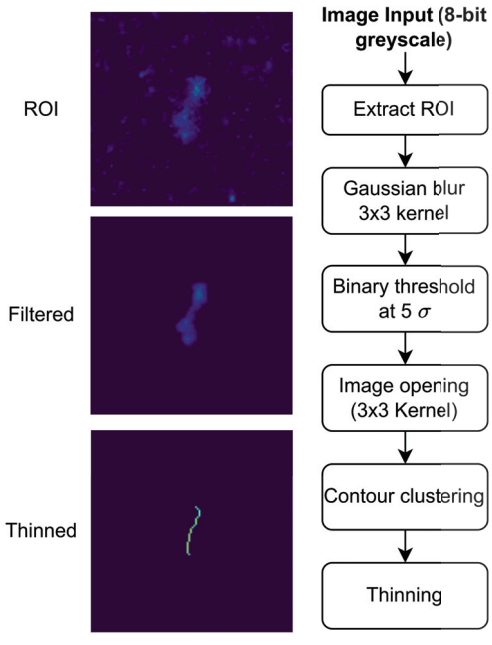

Figure 2. Flow diagram of image processing chain, with example images (black and white images converted to a perceptually uniform colour scale).

There is a possibility that the correspondence between endpoints in $\mathbf{p}_j$ and $\mathbf{s}_j$ is reversed. We use the approximate orientation from $\mathbf{s}_j$ to resolve the polarity of $\mathbf{p}_j$. We measure the angle on the image plane, θ_s, between the first and last elements of $\mathbf{s}_j$, as well as θ_p, the angle between the first and last elements of $\mathbf{p}_j$. If the magnitude of the difference between these angles exceeds $\frac{\pi}{2}$, we reverse the indices of array $\mathbf{p}_j$ to match the orientation of $\mathbf{s}_j$.

2.2. Orientation Estimation

Orientation estimation is performed in two steps. We first compute the mean attitude correction required to correlate the endpoints in $\mathbf{s}$ with the endpoints in $\mathbf{p}$. Once aligned, we compute the individual offsets for each of the n INS attitude measurements.

The rotation which transforms a vector from real-world coordinates to camera coordinates via a yaw-pitch-roll Euler sequence, is given by

$$\mathbf{R} = \begin{bmatrix} \mathrm{c}(\theta)\mathrm{c}(\psi) & \mathrm{c}(\theta)\mathrm{s}(\psi) & -\mathrm{s}(\theta) \\ -\mathrm{c}(\phi)\mathrm{s}(\psi) + \mathrm{s}(\phi)\mathrm{s}(\theta)\mathrm{c}(\psi) & \mathrm{c}(\phi)\mathrm{c}(\psi) + \mathrm{s}(\phi)\mathrm{s}(\theta)\mathrm{s}(\psi) & \mathrm{s}(\phi)\mathrm{c}(\theta) \\ \mathrm{s}(\phi)\mathrm{s}(\psi) + \mathrm{c}(\phi)\mathrm{s}(\theta)\mathrm{c}(\psi) & -\mathrm{s}(\phi)\mathrm{c}(\psi) + \mathrm{c}(\phi)\mathrm{s}(\theta)\mathrm{s}(\psi) & \mathrm{c}(\phi)\mathrm{c}(\theta) \end{bmatrix}, \quad (11)$$

where $\mathrm{c}(x)$ and $\mathrm{s}(x)$ represent $\cos(x)$ and $\sin(x)$, respectively.

Stars are framed in the celestial coordinate system; thus, translation is negligible. Therefore, the image coordinates, $\mathbf{x}$, for infinitely distant objects, is given by

$$\mathbf{x} = \mathbf{KRX}, \quad (12)$$

where **X** is the vector containing the local NED world coordinates at a given point:

$$\mathbf{X} = \begin{bmatrix} X \\ Y \\ Z \end{bmatrix}. \tag{13}$$

We expand the vector **x** into its components to get the image coordinates x, y, and z:

$$\begin{aligned} x = f_x\big[&(\cos\theta\cos\psi)X + (\cos\theta\sin\psi)Y - (\sin\theta)Z\big] \\ &+ p_x\big[(\sin\phi\sin\psi + \cos\phi\sin\theta\cos\psi)X \\ &+ (-\sin\phi\cos\psi + \cos\phi\sin\theta\sin\psi)Y + (\cos\phi\cos\theta)Z\big] \end{aligned} \tag{14}$$

$$\begin{aligned} y = f_y\big[&(-\cos\phi\sin\psi + \sin\phi\sin\theta\cos\psi)X \\ &+ (\cos\phi\cos\psi + \sin\phi\sin\theta\sin\psi)Y + (\sin\phi\cos\theta)Z\big] \\ &+ p_y\big[(\sin\phi\sin\psi + \cos\phi\sin\theta\cos\psi)X \\ &+ (-\sin\phi\cos\psi + \cos\phi\sin\theta\sin\psi)Y + (\cos\phi\cos\theta)Z\big] \end{aligned} \tag{15}$$

$$\begin{aligned} z = &\big(\sin\phi\sin\psi + \cos\phi\sin\theta\cos\psi\big)X + \big(-\sin\phi\cos\psi + \\ &\cos\phi\sin\theta\sin\psi\big)Y + \big(\cos\phi\cos\theta\big)Z. \end{aligned} \tag{16}$$

The two-dimensional homogeneous image pixel coordinates, are subsequently given by

$$\mathbf{u} = \begin{bmatrix} u \\ v \end{bmatrix};\ u = \frac{x}{z},\ v = \frac{y}{z}. \tag{17}$$

The Jacobian containing partial derivatives of pixel location with respect to changes in orientation is then given by (see Appendix A.1 for partial derivative equations):

$$\mathbf{J} = \begin{bmatrix} \dfrac{\partial u}{\partial \phi} & \dfrac{\partial u}{\partial \theta} & \dfrac{\partial u}{\partial \psi} \\ \dfrac{\partial v}{\partial \phi} & \dfrac{\partial v}{\partial \theta} & \dfrac{\partial v}{\partial \psi} \end{bmatrix}. \tag{18}$$

Thus, the first order Taylor series expansion gives

$$\mathbf{u}' = \mathbf{u} + \mathbf{J}\Delta\mathbf{r}, \tag{19}$$

where $\Delta\mathbf{r}$ is the vector containing the change in roll, pitch, and yaw required to translate pixel **u** to $\mathbf{u}'$:

$$\Delta\mathbf{r} = \begin{bmatrix} \Delta\phi \\ \Delta\theta \\ \Delta\psi \end{bmatrix}.$$

The linearized relationship between change in pixel location and change in orientation can be expressed as

$$\Delta\mathbf{u} \ = \ \mathbf{J}\Delta\mathbf{r}. \tag{20}$$

We extend this notation for multiple observations, $\Delta\hat{\mathbf{u}}$, where each observation $\Delta\mathbf{u_i} = [\Delta u_i,\ \Delta v_i]^T$ is vertically stacked to give a vector of length $2m$:

$$\Delta\hat{\mathbf{u}} = \big[\Delta u_1,\ \Delta v_1,\ \ldots\ \Delta u_m,\ \Delta v_m\big]^T \tag{21}$$

and similarly the Jacobian $\mathbf{J_i}$ for each observation is vertically stacked to give the matrix of size $[2m \times 3]$:

$$\hat{\mathbf{J}} = \begin{bmatrix} \mathbf{J_1} \\ \vdots \\ \mathbf{J_m} \end{bmatrix}. \tag{22}$$

Thus, provided a minimum of $m = 2$ points, we can apply the weighted least squares solution for $\Delta\mathbf{r}$,

$$\Delta\mathbf{r} = \left(\hat{\mathbf{J}}^T\mathbf{W}\hat{\mathbf{J}}\right)^{-1}\hat{\mathbf{J}}^T\mathbf{W}\Delta\hat{\mathbf{u}}, \tag{23}$$

where the diagonal weight matrix $\mathbf{W}$ with size $[2m \times 2m]$ contains the weighting for each observation

$$\mathbf{W} = \begin{bmatrix} w_1 & 0 & \dots & 0 & 0 \\ 0 & w_1 & \dots & 0 & 0 \\ \vdots & \vdots & \ddots & \vdots & \vdots \\ 0 & 0 & \dots & w_m & 0 \\ 0 & 0 & \dots & 0 & w_m \end{bmatrix}, \tag{24}$$

where w_i is calculated from the signal strength of observation i, such that salient stars are weighted more heavily,

$$w_i = \log_{10}\left(\frac{p_i - \mu}{\sigma}\right), \tag{25}$$

and p_i is the peak pixel intensity for observation i, μ is the mean value across the image ($p_i \gg \mu$), and σ is the standard deviation in pixel intensity in the image. Note that the weightings for the u and v components of a given observation are equal.

The mean-offset corrected camera attitude is computed iteratively, such that

$$\Delta\mathbf{r}_k = \Delta\mathbf{r}_{k-1} + \left(\hat{\mathbf{J}}_{k-1}^T\mathbf{W}\hat{\mathbf{J}}_{k-1}\right)^{-1}\hat{\mathbf{J}}_{k-1}^T\mathbf{W}\Delta\hat{\mathbf{u}}_{k-1} \tag{26}$$

until $|\Delta\mathbf{r}_k - \Delta\mathbf{r}_{k-1}| \leq 10^{-6}$ rad. Values $\Delta\hat{\mathbf{u}}_{k-1}$ and $\hat{\mathbf{J}}_{k-1}$ are recomputed at each iteration from Equations (17) and (18), given the updated attitude:

$$\mathbf{r}_i' = \mathbf{r}_i - \Delta\mathbf{r}_k. \tag{27}$$

Equation (26) yields the mean attitude offset throughout a given exposure window. In some cases, this level of precision is satisfactory (for example, for online magnetometer calibration). The long exposure image typically contains higher-resolution attitude information pertaining to the aircraft orientation throughout the exposure window. This information can be obtained by aligning elements from the mean-corrected array $\mathbf{s}_j'$ with elements from observation $\mathbf{p}_j$. An example demonstrating the difference between mean and fine alignment can be seen in Figure 3.

A similar process to the mean attitude correction is followed for the high-resolution attitude estimation. For each star, the theoretical curve of the trail is recomputed with the mean attitude offset applied to obtain $\mathbf{s}_j'$, and the polarity once again checked to ensure that the elements of $\mathbf{p}_j$ are in the correct order. We make the following assumptions when mapping $\mathbf{s}_j'$ to $\mathbf{p}_j$:

1. The INS sampling period, T_s, is constant.
2. The photon flux density incident on the sensor from a given luminary is constant.
3. The path taken by the airframe results in a simple curve on the image plane (i.e., the star trail does not cross itself at any point).

From these assumptions, it is evident that for each successive point in the fine-attitude corrected set, $\mathbf{s}''$, the rate of increase in the cumulative intensity must be constant,

$$\mathbf{I}\left(\mathbf{s}_j''[i]\right) - \mathbf{I}\left(\mathbf{s}_j''[i-1]\right) = C, \tag{28}$$

given pixel intensity $\mathbf{I}(x)$ at location x in the frame. Thus, the location of pixel $\mathbf{s}''[i]$ should be chosen to satisfy

$$\mathbf{I}\left(\mathbf{s}_j''[i]\right) = \mathbf{I}\left(\mathbf{s}_j''[i-1]\right) + C, \tag{29}$$

where the first element, $\mathbf{s}_j''[0]$ is equal to $\mathbf{p}_j[0]$, and C is chosen to ensure the last element in $\mathbf{s}_j''$ is equal to the last element in $\mathbf{p}_j$:

$$C = \frac{1}{n}\sum_{i=0}^{p}\mathbf{I}(\mathbf{p}_j[i]) \tag{30}$$

given n elements in $\mathbf{s}_j$, and p elements in $\mathbf{p}_j$.

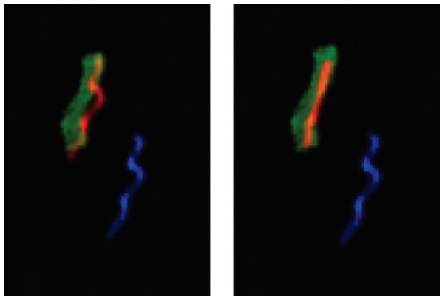

Figure 3. An example of attitude correction, displaying a region of interest for a single star. Greyscale images are overlaid onto a three-channel image. **Left**: mean-only alignment, **Right**: fine attitude alignment. Green, real image; blue, synthetic image from INS; red, reprojection after corrections.

The candidates for $\mathbf{s}_j''[i]$ are contained in the ordered set of thinned points from the real image, $\mathbf{p}_j$. We use a cumulative sum of real image intensities along the skeleton to solve for $\mathbf{s}_j''$ empirically, as shown in Algorithm 1:

Algorithm 1 Mapping from INS points to real image points.

$\mathbf{s}_j''[0] \leftarrow \mathbf{p}_j[0]$
$n \leftarrow 1$
$sum \leftarrow 0$
for $i = 1; i < p$ **do**
  $sum \leftarrow sum + \mathbf{p}_j[i]$
  if $sum \geq C$ **then**
    $overshoot \leftarrow (sum - C)$
    $\mathbf{s}_j''[n] \leftarrow Interpolate\left(\mathbf{p}_j[i], \mathbf{p}_j[i-1], overshoot\right)$
    $sum \leftarrow overshoot$
    $n \leftarrow n + 1$
  end if
end for

For each observed star, there exists a set of mean attitude corrected points, $\mathbf{s}_j'$, and a set of fine attitude corrected points, $\mathbf{s}_j''$. For each of the n INS attitude measurements, we apply the least squares solution from Equation (26). The Jacobian $\mathbf{J}$ is computed for each attitude by using Equation (18), and the change in pixel location, $\Delta\mathbf{u}$, is computed as $\mathbf{s}_j' - \mathbf{s}_j''$. The updated attitudes, $\mathbf{r}_i''$, are given by

$$\mathbf{r}_i'' = \mathbf{r}_i' - \Delta\mathbf{r}_{ik}. \tag{31}$$

The updated direction cosine matrices (DCM), $\mathbf{R''}_i$, are constructed from the Euler angles $\mathbf{r}''_i$ similarly to Equation (11). Given the rotational transformation $\mathbf{C_{c/a}}$ which relates the aircraft frame of reference to the camera frame of reference, the aircraft DCM for each attitude, expressed in NED coordinates is calculated:

$$\mathbf{C}_{a/ned}[i] = \mathbf{C}^T_{c/a}[i]\mathbf{R''}_i. \tag{32}$$

Thus, we use Equation (32) to compute the updated aircraft DCM for each attitude measurement from the INS.

In theory, two endpoints from a single star are sufficient to estimate attitude. In practice, however, there does not exist enough angular resolution to accurately correct for aircraft yaw (under normal flight conditions, with the camera facing upward). For this reason, we limit estimation to images containing three or more salient stars, separated by at least one third of the image width.

3. Results

Due to limitations in the accuracy of INS estimation with the available hardware, we are unable to acquire a ground-truth attitude reference for images captured in flight at the level of precision required. Consequently, we use the methodology presented in [3] to generate high-quality simulation images from real flight data for quantitative analysis. We treat the INS attitude measurements as ground truth, and apply two forms of noise to these measurements:

1. A random-valued constant offset, and
2. Perlin noise.

The random valued constant offset is applied to every attitude measurement throughout the exposure interval, and is representative of attitude/estimation bias. The gradient-based Perlin noise is generated for each individual measurement, and is representative of attitude drift from the INS estimator. We selected Perlin noise due to its gradient-based nature, and zero-crossing properties, which are typical of iterative estimators. Both sources of noise are applied together. We measure the efficacy of the methodology presented in Section 2 based on its ability to correct for these sources of noise and recover the true attitude of the aircraft.

Real imagery and INS attitude data was captured from a single test flight. A Pixhawk version 2 autopilot was used for vehicle control and attitude estimation. Attitude data was logged from the autopilot's extended Kalman filter (EKF) at a rate of 30 Hz. The camera was mounted to the autopilot via a rigid plastic 3D-printed structure, such that all autopilot attitudes were coupled with the aerial imagery. We used a Raspberry Pi 4 companion computer for image storage, and a Raspberry Pi high-quality camera sensor fitted with the official 6-mm wide-angle lens for image capture. The sensor resolution was set to 3280×2464, with an ISO of 800. The flight was conducted at a height of 150 m above ground level with an exposure interval of 500 ms. No clouds were present, and the trial was conducted under moonless conditions. The airframe used for this study was a Zeta Science FX61 with 1.5 m wingspan, with an approximate mass of 1.5 kg, as seen in Figure 4.

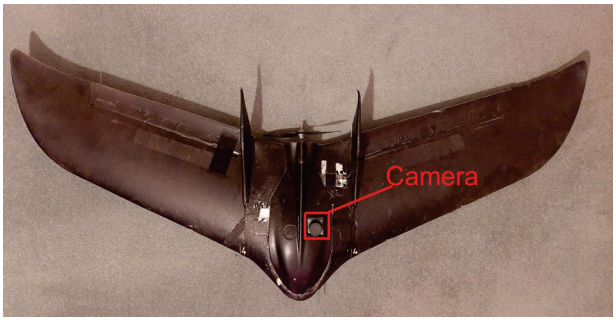

Figure 4. Zeta Science FX61 airframe used for capturing in-flight imagery.

3.1. Simulation Results

For each image captured, a series of attitude measurements were stored to disk corresponding with the exposure interval. We used a static ground image to calibrate the simulation, and subsequently generate each synthetic image from the log data. A uniformly distributed random offset between -1° and 1° was applied to the roll and pitch channels, and a uniformly distributed random offset between -3° and 3° was applied to the yaw channel. We applied a greater offset to the yaw channel to replicate the magnetometer bias typically seen in low-cost INS systems. A sequence of Perlin noise of length n was generated for the roll, pitch, and yaw channels, with number of octaves uniformly randomly selected between 0.1° and 2°, and magnitude less than 0.5°. This noise is representative of angular rate errors, as can be seen in Figure 5.

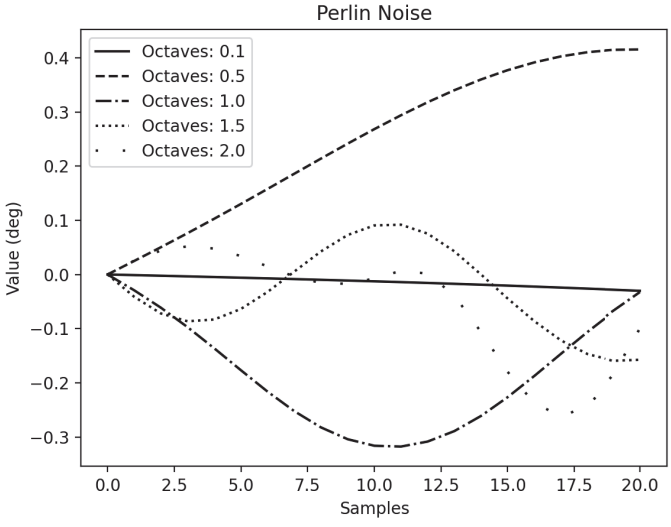

Figure 5. An example of Perlin gradient-based noise generation across various octaves (frequencies).

The methodology from Section 2 was applied, given the synthetic images (ground truth) and noisy attitude data (INS). Points $\mathbf{p}_j$ were extracted by using the presented image processing methods, and points $\mathbf{s}_j$ were computed by using the noisy attitude data.

A total of 110 images were simulated and processed. From these, 56 images contained a sufficient number of salient stars to perform attitude estimation (in accordance with the constraints set in Section 2). Each image had $n = 14$ noisy attitude estimates. Figure 6 shows histograms of mean absolute errors. Table 1 shows detailed results from this test. For each image captured, the mean, mean absolute, and max errors were recorded from the

attitude correction output. We can see from these results that the mean errors were close to zero, indicating that bias in the estimation process is low. The three standard deviation limit indicates that 99.7% of yaw errors are less than 0.2828°, pitch errors less than 0.1453°, and roll errors less than 0.1366°. Similarly, 99.7% of mean absolute yaw errors fell within ±0.1294°, pitch errors within ±0.0591°, and roll errors within ±0.0604°. The residual mean absolute error in the least squares approximation was 1.246 pixels, and an average of 6.036 stars were used for each estimation.

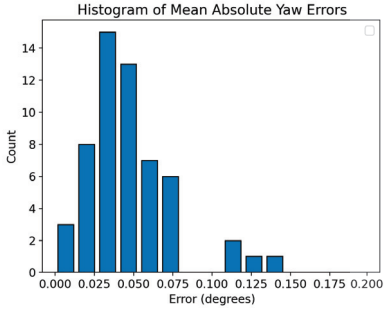

(**a**)

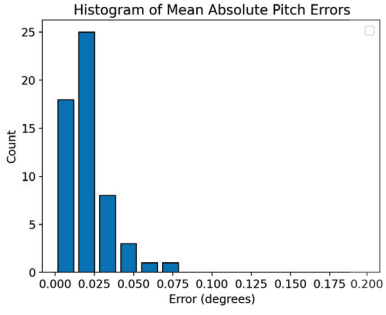

(**b**)

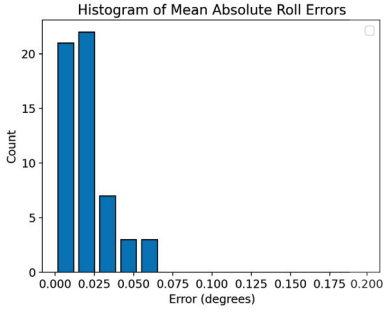

(**c**)

Figure 6. Histogram of mean absolute errors from each simulated image containing $n = 14$ attitude references. (**a**) Yaw. (**b**) Pitch. (**c**) Roll.

We can see from testing that the corrected attitude contained significantly reduced errors. Yaw errors with average magnitude 1.5° were typically corrected to within approximately 0.05°, and roll and pitch errors with average magnitude 0.5° were corrected to within approximately 0.02°. The maximum errors were also significantly lower than the average Perlin noise of 0.2°, highlighting the efficacy of this algorithm in removing both sources of noise. A graphic showing the simulated attitude correction can be seen in Figure 7.

Table 1. Simulated flight results. All units in degrees.

	Mean	**Median**	**Std**	**Mean + 3σ**
Max yaw error	0.1053	0.0903	0.0856	0.2828
Max pitch error	0.0503	0.0414	0.0317	0.1453
Max roll error	0.0506	0.0418	0.0286	0.1366
Mean absolute yaw error	0.0428	0.0442	0.0274	0.1294
Mean absolute pitch error	0.0205	0.0167	0.0128	0.0591
Mean absolute roll error	0.0217	0.0207	0.0129	0.0604
Mean yaw error	0.0118	0.01076	0.0322	-
Mean pitch error	−0.0080	−0.0061	0.0138	-
Mean roll error	−0.0078	−0.0061	0.02124	-

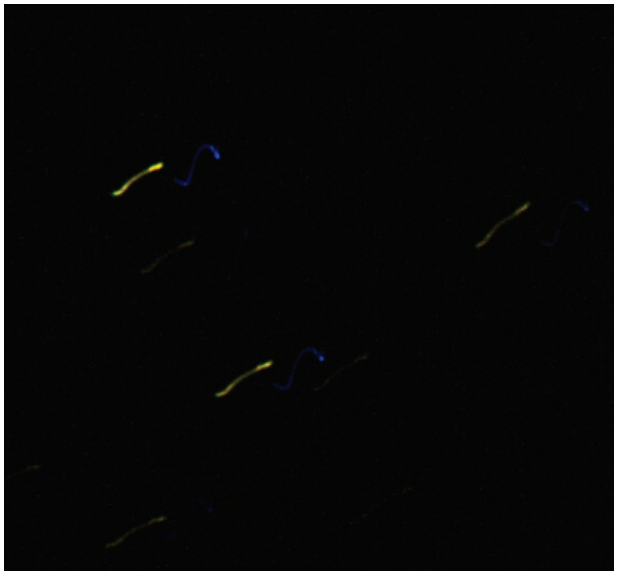

Figure 7. An example of simulation attitude correction, displaying superimposed regions of interest. Green channel, baseline simulation image; blue channel, synthetic image from noisy INS; red channel, synthetic image after corrections. Max yaw error: 0.0727°, max pitch error: 0.0286°, max roll error: 0.0226°.

3.2. Real Imagery

To supplement the simulation results, we observe the output of our methodology when applied directly to a real image. Although no ground truth was available, we assess the resulting reprojection in a qualitative manner, so as to validate the efficacy of the image-processing techniques. The real images are subjected to small errors in the camera matrix **K**, which are most prevalent at maximal radial distance from the principal point, as well as other minor unmodeled sources of noise.

From the 110 images captured, 49 satisfied the requirements for attitude estimation. The mean residual error of the least squares estimation was 3.945 pixels, as compared with 1.264 pixels in simulation. The average number of stars used for estimation was 5.510, as compared to 6.036 in simulation. Figures 8 and 9 demonstrate the efficacy of this method in practice. We show the ROI for each star used in the attitude estimation process. The green channel contains the real image, the blue channel contains the uncorrected INS data, and the red channel is a reprojection of the corrected INS data. We can see that our method corrected for both types of noise. Some bias remains present in some stars, which is more prominent at greater distances from the optical centre.

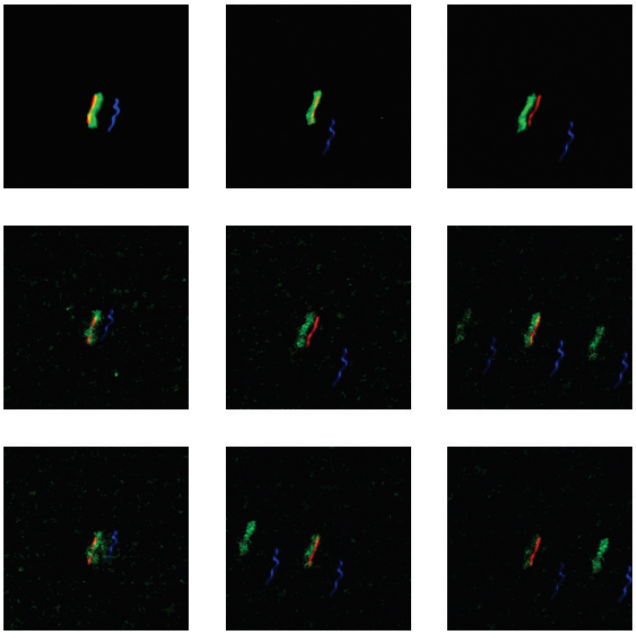

Figure 8. ROIs of stars used for attitude correction on a real image. Green channel, real image; blue channel, synthetic image from raw INS data; red channel, synthetic image from corrected INS data. The intensity of each ROI is amplified such that the peak pixel intensity is 255.

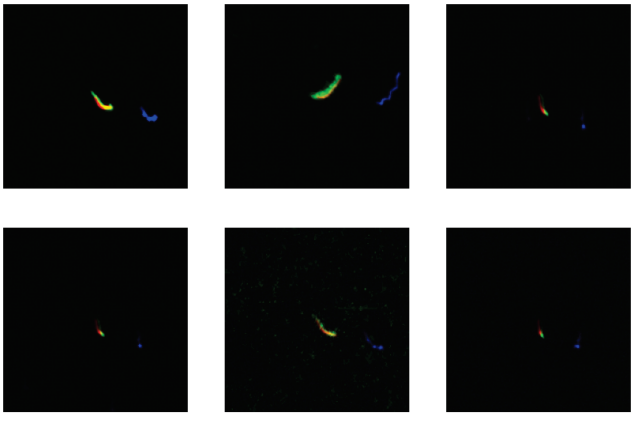

Figure 9. ROIs of stars used for attitude correction on a real image. Green channel, real image; blue channel, synthetic image from raw INS data; red channel, synthetic image from corrected INS data. The intensity of each ROI is amplified such that the peak pixel intensity is 255.

4. Discussion

The assumptions made in Section 2 may limit potential use cases for this approach. Assumption 2, constant photon flux density from a given luminary, disqualifies the use of rolling shutter cameras, and indicates that the performance will be hindered if the image is subjected to obscurities such as partial cloud cover. Assumption 3, that the star forms a simple curve on the image plane, may become limiting for imaging systems with longer exposure intervals, due to the increased likelihood of complex curves forming on the image plane. Interestingly, it may be possible to plan aircraft trajectories, which reduces the likelihood of this occurring.

It is evident in the results that some re-projection bias remains when performing attitude correction on the real images (3.945 pixels, as compared with 1.264 in simulation). There are two potential causes for this value being significantly higher than in simulation.

1. The camera calibration matrix, **K** does not perfectly characterize the camera.
2. Unmodeled sources of noise caused the image processing techniques not to transfer from simulation to reality.

Our observation is that the former is the most likely cause of this error. It is evident that certain areas on the imaging plane are defocused and do not conform with a Gaussian point-spread distribution, which may be contributing to the delocalization of pixels during the image processing stage. The image-thinning algorithm preserves the endpoints of the simulated stars (which are drawn from a sequence of Gaussian point-spread functions); however it tends to truncate the endpoints of the real stars. We postulate, however, that this effect is less significant than the effect caused by camera calibration. We see in Figures 8 and 9 that the fine-attitude correction appears to remove both the high- and low-frequency components of noise, but the bias offset remains for some stars. If the image-processing techniques were failing, we would not observe the removal of noise, particularly with the lower signal-to-noise ratio stars seen in Figure 8. We also observe that the bias tends to be greater for stars located further from the optical centre. These effects are indicative of residual nonlinear errors, such as radial and tangential distortion. Despite our efforts to remove the sources of distortion, this is a practical limitation of low-cost hardware. Interestingly, if this bias is caused by nonlinear distortion, then the residual error is not a good indicator of attitude error. This is evident when considering that a perfect attitude estimate will still yield reprojection errors.

The geometry of the camera tends toward a greater error in yaw than for pitch and roll. Under stable flying conditions (minimal roll and pitch), the yaw angle of the aircraft is measured from the angle of arc between stars about the principal point. When only a small number of observations are made, the dispersion of stars about this principal point is unlikely to be uniform, and consequently the resolution is decreased. In theory, this could be offset by applying a higher weight to stars that are further displaced from the principal point. In practice, however, the effects of lens distortion are most prominent at points farthest from the principal point, and these observations are likely to be more erroneous.

In this study we seldom encountered multiple stars within the same ROI. With more sensitive optical equipment, or less accurate attitude sensors, the occurrence of multiple stars may increase. We have not explored the possibility of outlier removal; however, we expect that the use of a random sample consensus (RANSAC) [15] algorithm may be beneficial for the selection of stars under such circumstances.

5. Conclusions

We have demonstrated a novel use for long-exposure imagery captured from a low-cost strapdown celestial sensor mounted to a lightweight, low-altitude, fixed-wing airframe. The captured imagery contains high-resolution data pertaining to the attitude of the aircraft. Standard image processing techniques were used on the long exposure images, in conjunction with a linearized weighted least squares approximation, so as to produce a corrected attitude estimate for each attitude reported by the INS. Through simulation, we demonstrated that attitude is estimated with means absolute error less than 0.13 degrees in

the yaw axis, and less than 0.06 degrees in the pitch and roll axes ($3\,\sigma$). We subsequently demonstrated that this algorithm translates to real imagery, with some additional noise due to calibration. Future work will explore the use of this technique for the online calibration of magnetometer offsets.

Author Contributions: Conceptualization, S.T. and J.C.; methodology, S.T.; software, S.T.; validation, S.T.; formal analysis, S.T.; investigation, S.T.; resources, J.C.; data curation, S.T. and J.C.; writing—original draft preparation, S.T.; writing—review and editing, J.C.; visualization, S.T.; supervision, J.C.; project administration, J.C. All authors have read and agreed to the published version of the manuscript.

Funding: This research received no external funding.

Informed Consent Statement: Not applicable.

Data Availability Statement: Not applicable.

Acknowledgments: This work was supported by Scope Global Pty Ltd. under the Commonwealth Scholarships Program, and the Commonwealth of South Australia under the Australian Government Research Training Program.

Conflicts of Interest: The authors declare no conflict of interest.

Appendix A

Appendix A.1. Jacobian Matrix Entries

The partial derivatives of the image coordinates with respect to the aircraft Euler angles are given by:

$$\begin{aligned}\frac{\partial x}{\partial \phi} =& p_x\big[\cos\phi\big(\sin\psi X - \cos\psi Y\big)\\ &- \sin\phi\big(\sin\theta\cos\psi X + \sin\theta\sin\psi Y + \cos\theta Z\big)\big]\end{aligned} \tag{A1}$$

$$\begin{aligned}\frac{\partial x}{\partial \theta} =& -f_x\big(\sin\theta\cos\psi X + \sin\theta\sin\psi Y + \cos\theta Z\big)\\ &+ p_x\cos\phi\big(\cos\theta\cos\psi X + \cos\theta\sin\psi Y - \sin\theta Z\big)\end{aligned} \tag{A2}$$

$$\begin{aligned}\frac{\partial x}{\partial \psi} =& f_x\cos\theta\big(-\sin\psi X + \cos\psi Y\big)\\ &+ p_x\sin\phi\big(\cos\psi X + \sin\psi Y\big)\\ &+ p_x\cos\phi\big(-\sin\theta\sin\psi X + \sin\theta\cos\psi Y\big)\end{aligned} \tag{A3}$$

$$\begin{aligned}\frac{\partial y}{\partial \phi} =& f_y\big[\big(\sin\phi\sin\psi + \cos\phi\sin\theta\cos\psi\big)X\\ &+ \big(-\sin\phi\cos\psi + \cos\phi\sin\theta\sin\psi\big)Y\\ &+ \big(\cos\phi\cos\theta\big)Z\big] + p_y\big[\big(\cos\phi\sin\psi - \sin\phi\sin\theta\cos\psi\big)X\\ &+ \big(-\cos\phi\cos\psi - \sin\phi\sin\theta\sin\psi\big)Y - \big(\sin\phi\cos\theta\big)Z\big]\end{aligned} \tag{A4}$$

$$\begin{aligned}\frac{\partial y}{\partial \theta} =& f_y\big[\big(\sin\phi\cos\theta\cos\psi\big)X\\ &+ \big(\sin\phi\cos\theta\sin\psi\big)Y + \big(-\sin\phi\sin\theta\big)Z\big]\\ &+ p_y\big[\big(\cos\phi\cos\theta\cos\psi\big)X\\ &+ \big(\cos\phi\cos\theta\sin\psi\big)Y + \big(-\cos\phi\sin\theta\big)Z\big]\end{aligned} \tag{A5}$$

$$\begin{aligned}\frac{\partial y}{\partial \psi} =& f_y\big[\big(-\cos\phi\cos\psi-\sin\phi\sin\theta\sin\psi\big)X\\ &+\big(-\cos\phi\sin\psi+\sin\phi\sin\theta\cos\psi\big)Y\big]\\ &+p_y\big[\big(\sin\phi\cos\psi-\cos\phi\sin\theta\sin\psi\big)X\\ &+\big(\sin\phi\sin\psi+\cos\phi\sin\theta\cos\psi\big)Y\big]\end{aligned} \tag{A6}$$

$$\begin{aligned}\frac{\partial z}{\partial \phi} =& \big[\cos\phi\sin\psi-\sin\phi\sin\theta\cos\psi\big]X\\ &+\big[-\cos\phi\cos\psi-\sin\phi\sin\theta\sin\psi\big]Y+\big[-\sin\phi\cos\theta\big]Z\end{aligned} \tag{A7}$$

$$\begin{aligned}\frac{\partial z}{\partial \theta} =& \big[\cos\phi\cos\theta\cos\psi\big]X+\big[\cos\phi\cos\theta\sin\psi\big]Y\\ &+\big[-\cos\phi\sin\theta\big]Z\end{aligned} \tag{A8}$$

$$\begin{aligned}\frac{\partial z}{\partial \psi} =& \big[\sin\phi\cos\psi-\cos\phi\sin\theta\sin\psi\big]X\\ &+\big[\sin\phi\sin\psi+\cos\phi\sin\theta\cos\psi\big]Y\end{aligned} \tag{A9}$$

and the 2-dimensional homogeneous image coordinates are given by:

$$u=\frac{x}{z},\ \ v=\frac{y}{z} \tag{A10}$$

then by applying the quotient rule, we compute the partial derivatives:

$$\frac{\partial u}{\partial \phi}=\frac{z\frac{\partial x}{\partial \phi}-x\frac{\partial z}{\partial \phi}}{(z)^2} \tag{A11}$$

$$\frac{\partial u}{\partial \theta}=\frac{z\frac{\partial x}{\partial \theta}-x\frac{\partial z}{\partial \theta}}{(z)^2} \tag{A12}$$

$$\frac{\partial u}{\partial \psi}=\frac{z\frac{\partial x}{\partial \psi}-x\frac{\partial z}{\partial \psi}}{(z)^2} \tag{A13}$$

$$\frac{\partial v}{\partial \phi}=\frac{z\frac{\partial y}{\partial \phi}-y\frac{\partial z}{\partial \phi}}{(z)^2} \tag{A14}$$

$$\frac{\partial v}{\partial \theta}=\frac{z\frac{\partial y}{\partial \theta}-y\frac{\partial z}{\partial \theta}}{(z)^2} \tag{A15}$$

$$\frac{\partial v}{\partial \psi}=\frac{z\frac{\partial y}{\partial \psi}-y\frac{\partial z}{\partial \psi}}{(z)^2} \tag{A16}$$

References

1. Kayton, M.; Fried, W.R. *Avionics Navigation Systems*; John Wiley & Sons: Hoboken, NJ, USA, 1997.
2. Titterton, D.; Weston, J.L.; Weston, J. *Strapdown Inertial Navigation Technology*; IET: Stevenage, UK, 2004; Volume 17.

3. Teague, S.; Chahl, J. Imagery Synthesis for Drone Celestial Navigation Simulation. *Drones* **2022**, *6*, 207. [CrossRef]
4. Chen, X.; Liu, D.; Zhang, Y.; Liu, X.; Xu, Y.; Shi, C. Robust motion blur kernel parameter estimation for star image deblurring. *Optik* **2021**, *230*, 166288. [CrossRef]
5. Wei, Q.; Weina, Z. Restoration of motion-blurred star image based on Wiener filter. In Proceedings of the 2011 Fourth International Conference on Intelligent Computation Technology and Automation, Shenzhen, China, 28–29 March 2011; Volume 2, pp. 691–694.
6. Wang, S.; Zhang, S.; Ning, M.; Zhou, B. Motion blurred star image restoration based on MEMS gyroscope aid and blur kernel correction. *Sensors* **2018**, *18*, 2662. [CrossRef] [PubMed]
7. Zhang, W.; Quan, W.; Guo, L. Blurred star image processing for star sensors under dynamic conditions. *Sensors* **2012**, *12*, 6712–6726. [CrossRef] [PubMed]
8. Sun, T.; Xing, F.; You, Z.; Wei, M. Motion-blurred star acquisition method of the star tracker under high dynamic conditions. *Opt. Express* **2013**, *21*, 20096–20110. [CrossRef] [PubMed]
9. Ma, L.; Zhan, D.; Jiang, G.; Fu, S.; Jia, H.; Wang, X.; Huang, Z.; Zheng, J.; Hu, F.; Wu, W.; et al. Attitude-correlated frames approach for a star sensor to improve attitude accuracy under highly dynamic conditions. *Appl. Opt.* **2015**, *54*, 7559–7566. [CrossRef] [PubMed]
10. He, Y.; Wang, H.; Feng, L.; You, S. Motion-blurred star image restoration based on multi-frame superposition under high dynamic and long exposure conditions. *J. Real-Time Image Process.* **2021**, *18*, 1477–1491. [CrossRef]
11. Klaus, A.; Bauer, J.; Karner, K.; Elbischger, P.; Perko, R.; Bischof, H. Camera calibration from a single night sky image. In Proceedings of the 2004 IEEE Computer Society Conference on Computer Vision and Pattern Recognition, 2004. CVPR 2004, Washington, DC, USA, 27 June–2 July 2004; Volume 1, p. I.
12. Rijlaarsdam, D.; Yous, H.; Byrne, J.; Oddenino, D.; Furano, G.; Moloney, D. A survey of lost-in-space star identification algorithms since 2009. *Sensors* **2020**, *20*, 2579. [CrossRef] [PubMed]
13. Liebe, C.C. Accuracy performance of star trackers-a tutorial. *IEEE Trans. Aerosp. Electron. Syst.* **2002**, *38*, 587–599. [CrossRef]
14. Zhang, T.Y.; Suen, C.Y. A fast parallel algorithm for thinning digital patterns. *Commun. ACM* **1984**, *27*, 236–239. [CrossRef]
15. Fischler, M.A.; Bolles, R.C. Random sample consensus: A paradigm for model fitting with applications to image analysis and automated cartography. *Commun. ACM* **1981**, *24*, 381–395. [CrossRef]

machines

MDPI

Article

Path Planning of Unmanned Aerial Vehicle in Complex Environments Based on State-Detection Twin Delayed Deep Deterministic Policy Gradient

Danyang Zhang, Zhaolong Xuan *, Yang Zhang, Jiangyi Yao, Xi Li and Xiongwei Li

Equipment Simulation Training Center, Shijiazhuang Campus, Army Engineering University, Shijiazhuang 050003, China
* Correspondence: youngzhxm@aeu.edu.cn

Abstract: This paper investigates the path planning problem of an unmanned aerial vehicle (UAV) for completing a raid mission through ultra-low altitude flight in complex environments. The UAV needs to avoid radar detection areas, low-altitude static obstacles, and low-altitude dynamic obstacles during the flight process. Due to the uncertainty of low-altitude dynamic obstacle movement, this can slow down the convergence of existing algorithm models and also reduce the mission success rate of UAVs. In order to solve this problem, this paper designs a state detection method to encode the environmental state of the UAV's direction of travel and compress the environmental state space. In considering the continuity of the state space and action space, the SD-TD3 algorithm is proposed in combination with the double-delayed deep deterministic policy gradient algorithm (TD3), which can accelerate the training convergence speed and improve the obstacle avoidance capability of the algorithm model. Further, to address the sparse reward problem of traditional reinforcement learning, a heuristic dynamic reward function is designed to give real-time rewards and guide the UAV to complete the task. The simulation results show that the training results of the SD-TD3 algorithm converge faster than the TD3 algorithm, and the actual results of the converged model are better.

Keywords: unmanned aerial vehicle; deep reinforcement learning; TD3; dynamic reward function; state detection

Citation: Zhang, D.; Xuan, Z.; Zhang, Y.; Yao, J.; Li, X.; Li, X. Path Planning of Unmanned Aerial Vehicle in Complex Environments Based on State-Detection Twin Delayed Deep Deterministic Policy Gradient. *Machines* **2023**, *11*, 108. https://doi.org/10.3390/machines11010108

Academic Editors: Wojciech Giernacki, Andrzej Łukaszewicz, Zbigniew Kulesza, Jaroslaw Pytka and Andriy Holovatyy

Received: 12 December 2022
Revised: 6 January 2023
Accepted: 10 January 2023
Published: 13 January 2023

1. Introduction

In recent years, UAVs have been widely used in the military by virtue of their stealth and high maneuverability. The small and medium-sized UAVs are widely used on the battlefield to attack important enemy targets because of their small size and the ability to evade radar detection by flying at low or ultra-low altitudes [1–4]. In addition, under the original technology, UAVs were controlled by rear operators for all operations and did not achieve unmanned operation in the true sense. Further, with the advancement of artificial intelligence technology, UAV intelligent pilot technology has also been rapidly developed, and UAV autonomous control can be realized in many functions. However, in order to further enhance the UAV's autonomous control capability, research on UAV path planning, real-time communication, and information processing needs to be strengthened. Among them, UAV autonomous path planning is a hot issue attracting current researchers' attention [5–8].

The path planning problem can be described as finding an optimal path from the current point to the target point under certain constraints, and many algorithms have been used so far to solve UAV path planning problems in complex unknown environments. Nowadays, the common path planning algorithms are the A*algorithm, the artificial potential field algorithm, the genetic algorithm, and the reinforcement learning method [9,10]. In recent years, deep learning (DL) and reinforcement learning (RL) have achieved a lot of results in many fields. Deep learning (DL) has strong data fitting ability, and reinforcement

learning (RL) can model the process reasonably and can be trained without labels [11–13] combined the advantages of DL and RL to obtain deep reinforcement learning (DRL), which provides a solution to the problem of perception and decision-making for UAVs in complex environments [14].

The DRL can effectively solve problems with both continuous and discrete spaces. Therefore, many researchers proposed using DRL to solve the path planning problem. Mnih, V., et al. proposed the deep Q-network (DQN) algorithm [15] by combining Q-learning and deep learning to solve the problem of dimensional explosion triggered by high-dimensional inputs. The DQN algorithm has achieved greater results in discrete action and state spaces but cannot effectively solve the continuous state and action spaces. In addition, when the changes of states and actions are infinitely partitioned, the amount of data for states and actions will show exponential growth with the increase of degrees of freedom, which can significantly impede the training and ultimately result in the algorithm failing [16]. Moreover, the discretized state and action space actually removes a large amount of important information, which will eventually lead to poor control accuracy, which will not meet the requirements for UAV control accuracy in air warfare. The actor-critic (AC) algorithm has the ability to handle the continuous action problem and is therefore widely used to solve problems in the continuous action space [17].The network structure of the AC algorithm includes an actor network and a critic network, actor network is responsible for outputting the action, and the critic network evaluates the value of the action and uses a loss function to continuously update the network parameters to get the optimal action strategy [18]. However, the effect of the AC algorithm relies heavily on the judgment of the value of the critic network, and the critic network converges slowly, which leads to the actor network. Lillicrap, T.P. et al. [19] proposed the deep deterministic policy gradient (DDPG) algorithm. The DDPG builds on the DQN algorithm's principles and combines the Actor-Critic algorithm's framework with several enhancements over the original AC algorithm to more effectively tackle the path planning problem in static environments. However, when applying the DDPG algorithm to solve path planning problems in dynamic environments, there is the problem of overvaluation of the value network, which leads to slow model convergence and a low training success rate. Scott Fujimoto [20] et al. improved on the deep deterministic policy gradient (DDPG) algorithm to obtain the twin delayed deep deterministic policy gradient (TD3) algorithm, which is the TD3 algorithm that incorporates the idea of the double DQN algorithm [21] into the DDPG algorithm, which effectively solves the problem of difficult algorithm convergence in a dynamic environment.

In this paper, a state detection method is proposed and combined with a dual-delay deep deterministic policy gradient (TD3) to form the SD-TD3 algorithm, which can solve the global path planning problem of a UAV in a dynamic battlefield environment and also identify and avoid obstacles. The main contributions of this paper are as follows:

(1) After combining the battlefield environment information, the information interaction mode between UAV and the battlefield environment is analyzed, a simulation environment close to the real battlefield environment is built, and the motion model of UAV autonomous path planning is constructed.

(2) The network structure and parameters most suitable for the SD-TD3 algorithm model are determined through multiple experiments. A heuristic dynamic reward function and a noise discount factor are also designed to improve the reward sparsity problem and effectively improve the learning efficiency of the algorithm.

(3) A state detection method is proposed that divides and compresses the environment state space in the direction of the UAV and encodes the space state by a binary number, so as to solve the problem of data explosion in the continuous state space of the reinforcement learning algorithm.

(4) The simulation experiments are carried out to verify the performance of the SD-TD3 algorithm, and the simulation experiments are based on the model of a UAV performing a low airspace raid mission. The results show that the SD-TD3 algorithm can help the UAV

avoid radar detection areas, mountains, and random dynamic obstacles in low-altitude environments so that it can safely and quickly complete the low-altitude raid mission.

(5) By analyzing the experimental results, it can be concluded that the SD-TD3 algorithm has a faster training convergence speed and a better ability to avoid dynamic obstacles than the TD3 algorithm, and it is verified that the SD-TD3 algorithm can further refine the environmental state information to improve the reliability of the algorithm model, so that the trained algorithm model has a higher success rate in practical applications.

The rest of the paper is structured as follows, with related work presented in Part II. The third part models and analyzes the battlefield environment. Part IV describes the state detection scheme, the specific structure of the SD-TD3 algorithm, and the setting of the heuristic reward function, and Part V verifies the performance of the SD-TD3 algorithm through a simulation environment and analyzes the experimental results. The conclusion is given in the sixth part.

2. Related Work

In recent years, a lot of research on autonomous UAV path planning has been carried out at home and abroad, which can be divided into four categories of algorithms according to their nature: graph search algorithms, linear programming algorithms, intelligent optimization algorithms, and reinforcement learning algorithms.

The graph search algorithm mainly contains the Dijkstra algorithm, the RRT algorithm, the A* algorithm, the D* algorithm, etc. The most classical Dijkstra algorithm shows higher search efficiency than depth-first search or breadth-first search in the problem of finding the shortest path. However, the execution efficiency of the Dijkstra algorithm gradually decreases as the map increases. Ferguson, D. et al. [22] optimized Dijkstra and proposed the A* and D* algorithms. Zhan et al. [23] proposed an UAV path planning based on the improved A* algorithm for the path planning problem of low altitude UAVs in a 3D battlefield environment that satisfies UAV performance constraints such as safe lift and turn radii. Saranya, C. et al. [24] proposed an improved D* algorithm for the path planning problem in complex environments, which introduced slope into the reward function. The simulations and experiments proved the effectiveness of the method, which can be used to guarantee the flight safety of UAVs in complex environments. Li, Z. et al. [25] applied the RRT algorithm to the unmanned ship path planning problem, and an improved fast extended random tree algorithm (Bi-RRT) is proposed. The simulation results show that the optimized RRT algorithm can shorten the planning time and reduce the number of iterations, which has better feasibility and effectiveness.

The linear programming algorithm is a mathematical theory and method to study the extremum of a linear objective function under linear constraints that is widely used in the military, engineering technology, and computer fields. Yan, J. et al. [26] proposed a mixed-integer linear programming-based UAV conflict resolution algorithm that establishes a safety separation constraint for pairs of conflicting UAVs by mapping the nonlinear safety separation constraint to sinusoidal value-space separation linear constraints, then constructs a mixed-integer linear programming (MILP) model, mainly to minimize the global cost, and finally conducts simulation experiments to verify the effectiveness of the algorithm. Yang, J. et al. [27] proposed a cooperative mission assignment model based on mixed integer linear programming for multiple UAV formations against enemy air defense fire suppression. The algorithm represents the relationship between UAVs and corresponding missions by decision variables, introduces continuous time decision variables to represent the execution time of missions, and establishes the synergistic relationship among UAVs and between UAVs performing missions by mathematical descriptions of linear equations and inequalities between decision variables. The simulation experiments show the rationality of the algorithm.

The intelligent optimization algorithms are developed by simulating or revealing certain phenomena and processes in nature or the intelligent behaviors of biological groups, and they generally have the advantages of simplicity, generality, and ease of parallel

processing. In UAV path planning, genetic algorithms, particle swarm algorithms, ant colony algorithms, and hybrid algorithms have been applied more often. Hao, Z. et al. [28] proposed an UAV path planning method based on an improved genetic algorithm and an A* algorithm for system positioning accuracy in the UAV path planning process, considering the UAV obstacle constraints and performance constraints, and taking the shortest planned trajectory length as the objective function, which achieved the goal of accurate positioning with the goal of the least number of corrected trajectories. Lin, C.E. [29] established an UAV system distance matrix to solve the multi-target UAV path planning problem and ensure the safety and feasibility of path planning, used genetic algorithms for path planning, and used dynamic planning algorithms to adjust the flight sequence of multiple UAVs. Milad Nazarahari et al. [30] proposed an innovative artificial potential field (APF) algorithm to find all feasible paths between a starting point and a destination location in a discrete grid environment. In addition, an enhanced genetic algorithm (EGA) is developed to improve the initial path in continuous space. The proposed algorithm not only determines the collision-free path but also provides near-optimal solutions for all robot path planning problems.

Reinforcement learning is an important branch of machine learning that can optimize decisions without a priori knowledge and by continuously trying to iterate to obtain feedback information based on the environment. Currently, many researchers combine reinforcement learning and deep learning to form deep reinforcement learning (DRL), which can effectively solve path planning problems in dynamic environments. Typical DRL algorithms include the deep Q-network (DQN) algorithm, the actor-critic (AC) algorithm, the deep deterministic policy gradient (DDPG) algorithm, and the twin delayed deep deterministic policy gradient (TD3) algorithm. Cheng, Y. et al. [31] proposed a deep reinforcement learning obstacle avoidance algorithm under unknown environmental disturbances that uses a deep Q-network architecture and sets up a comprehensive reward function for obstacle avoidance, target approximation, velocity correction, and attitude correction in dynamic environments, overcoming the usability problems associated with the complexity of control laws in traditional parsing methods. Zhang Bin [32] et al. applied the DDPG algorithm. The improved algorithm has significantly improved efficiency compared with the DDPG algorithm. Hong, D. [33] et al. proposed an improved double-delay deep deterministic policy gradient (TD3) algorithm to control multiple UAV actions and also utilized the frame superposition technique for continuous action space to improve the efficiency of model training. Finally, simulation experiments showed the reasonableness of the algorithm. Li, B. [34] et al. combined meta-learning with the dual-delay depth-deterministic policy gradient (TD3) algorithm to solve the problem of rapid path planning and tracking of UAVs in an environment with uncertain target motion, which improved the convergence value and speed. Christos Papachristos et al. [35] proposed an off-line path planning algorithm for the optimal detection problem of an a priori known environment model. The actions that the robot should take if no previous map is available are iteratively derived to optimally explore its environment.

In summary, many approaches for autonomous path planning have been proposed in the field of UAVs, but relatively little work has been done to apply these approaches to battlefield environments. In the previous experiment, we selected the DQN algorithm, the DDPG algorithm, and the TD3 algorithm. The experimental results show that the DQN algorithm and the DDPG algorithm are difficult to converge, and the training results are not ideal. In this paper, the double-delay deep deterministic policy gradient (TD3) algorithm is selected for UAV path planning because TD3 not only has powerful deep neural network function fitting capability and better generalized learning capability but also can effectively solve the problem of overestimation of Q-value during the training process for algorithmic models with actor-critic structure. The TD3 also has the advantage of fast convergence speed and is suitable for acting in continuous space. However, the original TD3 algorithm usually only takes the current position information of the UAV as the basis for the next behavior judgment, and the training effect is not ideal in a dynamic environment. In

this paper, we provide a state detection method to detect the environmental space in the direction of UAV flight so that the algorithm model can have stronger environmental awareness and make better decisions during the flight process.

3. Environmental Model

3.1. Description of the Environmental Model

Figure 1 illustrates the battlefield environment of an UAV on a low-level raid mission, where the UAV is assigned to attack a radar position 50 km away. In order to avoid flying too high and being detected by radar, the UAV must take a low-altitude flight below 1 km. During low-altitude flight, the UAV needs to autonomously avoid static ground obstacles such as mountains and buildings. At the same time, because the low-altitude environment is susceptible to dynamic obstacles such as flying birds and civilian low-altitude vehicles, the UAV also needs to make accurate and timely responses to random dynamic obstacles.

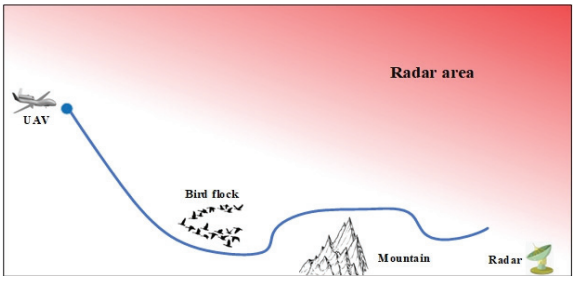

Figure 1. Schematic of battlefield environment.

3.2. Environment Parameters Setting

The simulation experimental environment is set as a low-altitude area of 50 km long and 1 km high, and the radar position $Radar_{(x,y)}$ and the UAV initial position $UAV_{(x_0,y_0)}$ can be expressed as:

$$Radar_{(x,y)} = [50\text{ km}, 0.2\text{ km}] \tag{1}$$

$$UAV_{(x_0,y_0)} = [0\text{ km}, 1\text{ km}] \tag{2}$$

The velocity v of the UAV can be divided into horizontal velocity $v_{xi} \in (0\text{ m/s},\ 100\text{ m/s})$ and vertical velocity $v_{yi} \in (-3\text{ m/s}, 3\text{ m/s})$, and the UAV real-time position $uav(t_i)$ can be expressed as

$$uav(t_i) = [x_{t_i}, y_{t_i}] = [\sum_i (v_{xi} * \Delta t), \sum_i (v_{yi} * \Delta t)] \tag{3}$$

The UAV should avoid collision with static ground obstacles such as mountains and buildings during low-altitude flight. In addition, the assumption is that the height of the ground obstacle is 100 m and the coordinates of its lowest center point $Static\_obstacle_{(x,y)}$ can be expressed as:

$$Static\_obstacle_{(x,y)} = [20\text{ km}, 0\text{ km}] \tag{4}$$

In the process of low-altitude flight, the UAV should also avoid dynamic obstacles such as flying birds, low-altitude civil vehicles, etc. Assuming that dynamic obstacles are randomly generated in the area below 300 m in height and the initial position is expressed as (x_0, y_0), its dynamic real-time position $Dynamic\_obstacle_{(x,y)}$ can be expressed as follows:

$$Dynamic\_obstacle_{(x,y)} = [x_d, y_d] = \left[x_0 + v_{dx} * \Delta t, y_0 + v_{dy} * \Delta t\right] \tag{5}$$

The initial position (x_0, y_0) in Equation (5), $x_0 \in (0\text{ km}, 50\text{ km})$, $y_0 \in (0\text{ km}, 0.3\text{ km})$, dynamic obstacle moving speed $v_{dx} \in (-10\text{ m/s}, 10\text{ m/s})$, $v_{dy} \in (-1\text{ m/s}, 1\text{ m/s})$.

A safe distance of more than 50 m should be maintained between the UAV and the dynamic obstacle.

$$d_{safe} = \left| uav(t_i) - Dynamic_{obstacle(x,y)} \right| = \sqrt{(x_{t_i} - x_d)^2 + (y_{t_i} - y_d)^2} \geq 0.05 \text{ km} \quad (6)$$

The maximum firing range of the air-to-ground missile on the UAV is 10 km. Assuming that the missile has a 100% hit rate within the firing range, the UAV is considered to have completed its mission when it safely reaches a position 10 km from the radar. The UAV is equipped with a radar warning device to determine if it is locked by the radar, and the maximum radius of the guided radar is 40 km. However, the probability P of an UAV being detected by radar in the airspace below 1 km in altitude is related to the distance d between radars and the current flight altitude h due to factors such as the curvature of the earth, detection angle, ground obstructions, and ground clutter. If the UAV is flying at too low an altitude, there is a low altitude blind zone that is completely undetectable by radar. Assuming that the radar blind zone is an airspace with an altitude less than 300 m, the radar detection probability model can be expressed as:

$$P = \begin{cases} 0 & d > 50 \text{ km} \\ 0 & h < 0.3 \text{ km} \\ 1 & d \leq 50 \text{ km},\ h \geq 1 \text{ km} \\ \frac{1}{0.01+2e^{-5h+5}} - \frac{d^2}{3200} + \frac{1}{2} & d \leq 50 \text{ km},\ 0.3 \text{ km} \leq h \leq 1 \text{ km} \end{cases} \quad (7)$$

Equation (7) can be obtained from the radar detection probability model as shown in Figure 2.

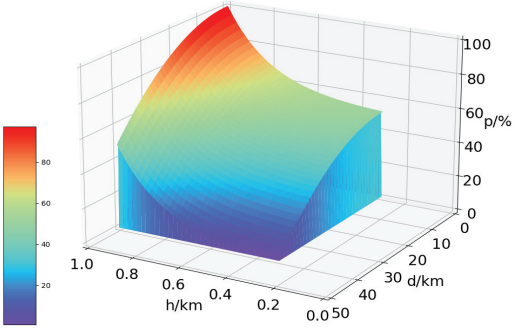

Figure 2. Probability model of radar detection.

From Figure 2, we can see that the d-axis is the distance between the UAV and radar, the h-axis is the flight height of the UAV, and the p-axis is the probability of the UAV being detected by radar. In addition, through the analysis, it can be seen that the UAV can effectively avoid the detection of radar when it flies below 300 m but the probability of being detected by radar is not 100% in the range of flight altitude $h \in (0.3 \text{ km},\ 1 \text{ km})$, which makes it difficult for the UAV to accurately identify the radar-covered airspace during the training process. In summary, this path planning experiment is challenging.

4. TD3-Based UAV Path Planning Model

In this section, we will describe the origin and development of the TD3 algorithm and improve it to better solve this path planning problem. The improvements are twofold. First, a dynamic reward function is set up to solve the problem of sparse rewards in the traditional deep reinforcement learning algorithm model, which can provide real-time feedback to the corresponding rewards according to the state of the UAV and speed up the convergence of the algorithm model in the training process. Secondly, the SD-TD3 algorithm is proposed, which mainly sets the segmentation of the region in the flight direction of the UAV, detects

and encodes the states at different regional locations with binary numbers, and adds the detected environmental state values to the input of the algorithm model to improve the UAV's obstacle avoidance capability.

4.1. Deep Reinforcement Learning Model

Deep reinforcement learning (DRL) is a learning method combining DL and RL that combines the data processing capability of DL with the decision-control capability of RL. In recent years, DRL has achieved great results in continuous space motion control and can effectively solve the UAV path planning problem. The deep deterministic policy gradient (DDPG) algorithm is a representative algorithm in DRL for solving continuous motion space problems, which can lead to deterministic actions based on state decisions. The idea of the DDPG algorithm is derived from the Deep Q Network (DQN) algorithm, and the update function of DQN can be expressed as:

$$Q(s,a) = Q(s,a) + \alpha\left(r + \gamma \underset{a'}{\max} Q(s',a') - Q(s,a)\right) \tag{8}$$

where $\alpha \in (0,1]$ is the learning rate, which is used to control the proportion of future rewards during learning. In addition, $\gamma \in (0,1)$ is the decay factor, which indicates the decay of future rewards. r denotes the reward after performing action a. From Equation (8), it can be seen that DQN is updated using the action currently considered to be of the highest value at each learning, which results in an overestimation of the Q-value, and thus DDPG also suffers from this problem. In addition to this, DDPG is also very sensitive to the adjustment of hyperparameters [36].

The double-delay deep deterministic policy gradient (TD3) algorithm solves these problems. The TD3 makes three improvements over the DDPG: first, it uses two independent critic networks to estimate Q values and selects smaller Q values for calculation when calculating the target Q values, which can effectively alleviate the problem of overestimation of Q values; second, the actor network uses delayed updates. The critic network is updated more frequently compared with the actor network, which can minimize the error; third, smoothing noise is introduced in the action value output from the actor target network to make the valuation more accurate, but no noise is introduced in the action value output from the actor network.

The pseudo-algorithm of TD3 can be expressed as Algorithm 1:

Algorithm 1: The Pseudo-Algorithm of TD3

1. Initialize critic networks Q_{θ_1}, Q_{θ_2}, and actor network with random parameters θ_1,θ_2,$\emptyset$
2. Initialize target networks $\theta_1' \leftarrow \theta_1$, $\theta_2' \leftarrow \theta_2$, $\emptyset' \leftarrow \emptyset$
3. Initialize replay buffer B
4. **for** t = 1 **to** T **do**
5. Select action with exploration noise $a \sim \pi_\emptyset(s) + \epsilon, \epsilon \sim N(0,\sigma)$ and observe reward r and new state s'
6. Store transition tuple (s,a,r,s') in B
7. Sample mini-batch of N transitions (s,a,r,s') from B
8. Compute target action $\widetilde{a} \leftarrow \pi_{\emptyset'}(s') + \epsilon, \epsilon \sim \mathrm{clip}(N(0,\widetilde{\sigma}), -\mathrm{c}, \mathrm{c})$
9. Compute target Q value $y \leftarrow \mathrm{r} + \gamma \min_{i=1,2} Q_{\theta_i'}(s', \widetilde{a})$
10. Update critics $\theta_i \leftarrow argmin_{\theta_i} N^{-1} \sum \left(y - Q_{\theta_i}(s,a)\right)^2$
11. **if** t mod d **Then**
12. Update $\emptyset$ by the deterministic policy gradient:
13. $\nabla_\emptyset J(\emptyset) = N^{-1} \sum \nabla_a Q_{\theta_1}(s,a)\big|_{a=\pi_\emptyset(s)} \nabla_\emptyset \pi_\emptyset(s)$
14. Update target networks:
15. $\theta_i' \leftarrow \tau\theta_i + (1-\tau)\theta_i'$
16. $\emptyset' \leftarrow \tau\,\emptyset + (1-\tau)\emptyset'$
17. **end if**
18. **end for**

4.2. State Detection Method

The conventional TD3 algorithm takes the current position information (*x*,*y*) of the UAV as input, outputs the action to the environment, and continuously learns from the environment with rewards for interaction. When trained enough times, the UAV is able to take the corresponding correct action at any position to reach the destination. In this method, it is difficult to effectively achieve the purpose of avoiding obstacles through the current position information of the UAV when dynamic obstacles appear in the environment. In order to be able to effectively complete the path planning task in a complex dynamic environment, the UAV must be able to identify the environmental state of the forward region, and when an obstacle appears in the forward region, the UAV can immediately identify the location of the obstacle and make a decision to avoid the obstacle. Therefore, in this paper, a state detection coding method is designed to encode the environmental state of the UAV's forward area.

The UAV is usually equipped with various sensors for detecting the surrounding environment. Suppose the UAV is equipped with sensors that can detect the state of the area ahead, and the working maximum distance of the sensors is 100 m. In addition, through these sensors, the UAV can detect whether there is an obstacle in the area ahead. We use the binary number 1 or 0 to indicate the presence or absence of obstacles. Further, through the state detection code, we can get a set of current environment state information arrays; this array will be added to the input of the algorithm model. In this way, the UAV can make the correct decision based on the environmental state information of the forward area.

By the state detection coding method, the environment space of the UAV advance region needs to be divided. Since the current environment is a continuous space, it can theoretically be divided an infinite number of times, but it will cause an increase in the training computation. Therefore, our scheme takes a limited number of divisions, which can also be regarded as the compression of the environmental state space in front of the UAV. Taking Figure 3 as an example, it can be seen that the region in front of the UAV is divided into six parts on average, and there are seven location points for encoding. The state input information of the UAV, S_{UAV}, can be expressed as follows:

$$S_{UAV} = [s_0, s_1, s_2, s_3, s_4, s_5, s_6, x, y], s_i \in [0, 1] \tag{9}$$

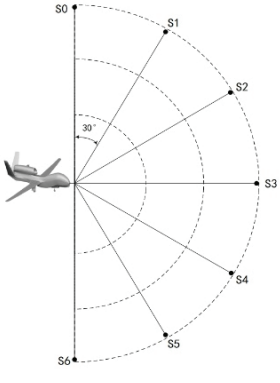

Figure 3. Schematic diagram of status detection code.

In Equation (9) s_i represents the environmental state information about each direction; $s_i = 0$ means there is no obstacle in the corresponding direction, and s_i = 1 means there is an obstacle in the corresponding direction. In addition, by inputting S_{UAV} to the algorithm model, after training the UAV can make correct decisions based on environmental state information in the forward direction, and thus accomplish the task of avoiding various

obstacles. In order to verify the effectiveness of the state detection coding method, this experiment will also further refine the state and divide the area in front of the UAV into 12 parts on average; the location points for coding will then be 13, and the state input information S_{UAV} can be expressed as:

$$S_{UAV} = [s_0, s_1, s_2, s_3, s_4, s_5, s_6, s_7, s_8, s_9, s_{10}, s_{11}, s_{12}, x, y], s_i \in [0, 1] \tag{10}$$

4.3. Heuristic Dynamic Reward Function

The reward functions, also known as immediate rewards, are an important component of deep reinforcement learning algorithm models. When an UAV performs an action, the environment generates feedback information for that action and evaluates the effect of that action. In traditional reinforcement learning algorithms, intelligence is rewarded when it completes a task and is not rewarded in other states. However, such rewards are prone to the reward sparsity problem in the face of complex environments [37]. The effective rewards are not available in a timely manner, and the algorithm model will be difficult to converge, which can be solved by setting up a heuristic reward function with guidance. The heuristic reward function designed in this paper can be expressed as follows:

$$R = \begin{cases} \frac{\beta(D-d_{t+1})}{D}, & d_t > d_{t+1} \\ -\frac{\beta(D-d_{t+1})}{D}, & d_{t+1} \geq d_t \end{cases} \tag{11}$$

In Equation (11) $\beta \in (0, +\infty)$ is the reward coefficient, D is the initial distance of 50 km between the UAV and radar position, d_t is the distance between the UAV and radar position at the current moment, and d_{t+1} is the distance between the UAV and radar position at the next moment. In analyzing Equation (11), we can see that when the UAV performs each action, if it is closer to the target at the next moment, it gets a positive reward, and the closer it is to the radar position, the greater the positive reward value it gets; if it is further away from the radar position at the next moment, it gets a negative reward, and the further it is from the radar position, the greater the negative reward value it gets.

In addition to the heuristic reward, when the distance between UAV and a dynamic obstacle is less than the safe distance d_{safe} or when there is a collision with a static obstacle, the reward of 300 dollars will be obtained, the environment will be reset, and UAV will start training from the initial position again. In addition, when the distance between the UAV and the radar is less than 10 km, the mission is completed, the reward of 300 dollars will be given, the environment is reset, and the UAV starts training again from its initial position.

In general, the reward function in this study is a dynamic reward function generated by combining the current state of the UAV. The dynamic nature of the reward function has two main points. One is that the reward generated by the environment interaction is generated in real time when the UAV is trained in the environment, which solves the problem of sparse reward compared to traditional reinforcement learning. Second, the reward value obtained during the training process of UAV and environment interaction will change with the current location information. According to the change in reward value, the UAV can be guided to move in the appropriate direction, which can promote the convergence of the algorithm model. The reward function has the role of heuristic guidance for UAVs, so it can be called the heuristic reward function.

4.4. State Detection Double-Delay Depth Deterministic Policy Gradient Algorithm Model

In combining the TD3 algorithm model with the above-mentioned heuristic reward function and the state detection method, it is possible to design the state detection double-delay depth deterministic policy gradient (SD-TD3) algorithm model. The UAV detects the state information s of the environment in the forward region, encodes it as the input of the algorithm model, and outputs the action after calculating it with the TD3 model. Figure 4 shows the specific algorithm. During the process, the UAV executes a and the environment's state changes to the next state, s'; while executing a, the environment will

feedback a reward r, according to the reward function, and the quadratic information set (s, a, r, s') is obtained. The quaternion information reaches the experience pool, and when the experience pool is stored to a certain number, random samples are drawn for training, and by inputting these sample data, they are used to update the network of actor-critic. The existence of the experience pool helps UAV learn from previous experiences and improve the efficiency of sample utilization. The random sampling can break the correlation between samples and make the learning process of the UAV more stable [38].

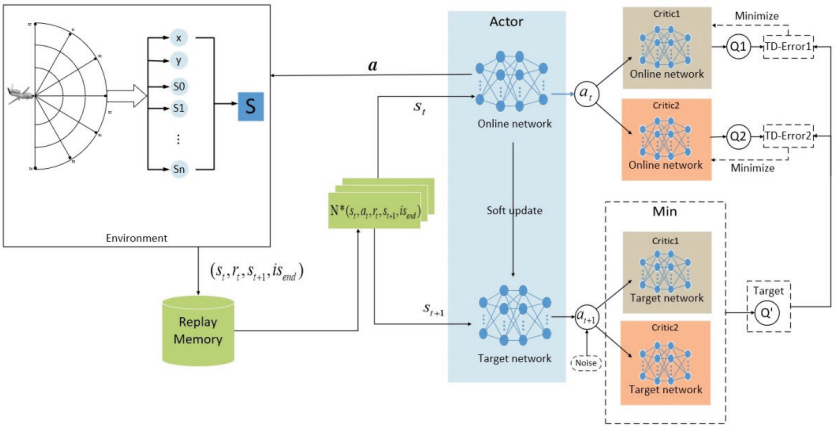

Figure 4. The combination of the state probing method and the TD3 model.

The TD3 algorithm model sets up a total of six neural networks based on the actor-critic structure, which are actor network $\pi_{\emptyset}$, actor target network $\pi_{\emptyset'}$, critic network Q_{θ_1}, critic network Q_{θ_2}, critic target network $Q_{\theta_1'}$, critic target network $Q_{\theta_2'}$. The roles and updates of these networks can be expressed as:

1. Actor network $\pi_{\emptyset}$: input the current state s of the UAV, output the current action a and then interact with the environment to reach the next state s' and the obtained reward r. The actor network parameters $\emptyset$ are updated iteratively in this process.
2. Actor target network $\pi_{\emptyset'}$: s' in the quaternion is used as input after random sampling from the experience pool, and the next action a' is generated after adding noise ϵ to the output result. The actor target network parameter $\emptyset'$ is based on the actor network parameter $\emptyset$ for delayed soft update, $\theta_i' = \tau\theta_i + (1-\tau)\theta_i'$.
3. Critic network Q_{θ_i}: input current state s and current action a, output current Q value $Q_{\theta_i}(s, a)$, and iteratively update critic network parameter θ_i in this process. in calculating the target Q value, take the smallest of $Q_{\theta_1'}(s', a')$ and $Q_{\theta_2'}(s', a')$ is calculated, $y = \mathrm{r} + \gamma \min_{i=1,2} Q_{\theta_i'}(s', a')$.
4. Critic target network $Q_{\theta_i'}$: After random sampling from the experience pool, s' in the quaternion and the next action a' generated by the Actor target network are used as input, and $Q_{\theta_1'}(s', a')$ and $Q_{\theta_2'}(s', a')$ are output. The critic target network parameter θ_i' is delayed soft update based on critic network parameter θ_i, $\emptyset' = \tau\emptyset + (1-\tau)\emptyset'$.

For the Critic network, the loss function is expressed as:

$$J(\theta_i) = N^{-1} \sum \left(y - Q_{\theta_i}(s, a)\right)^2 \tag{12}$$

For actor networks, a deterministic strategy is used to optimize the parameters, and the loss function is expressed as

$$\nabla_{\emptyset} J(\emptyset) = N^{-1} \sum \nabla_a Q_{\theta_1}(s, a)\Big|_{a=\pi_{\emptyset}(s)} \nabla_{\emptyset} \pi_{\emptyset}(s) \tag{13}$$

5. Simulation Experiment Setup and Result Analysis

In order to test the effectiveness of SD-TD3 algorithm performance, this experiment set up two simulation experimental environments for training Environment 1 is a static environment, set up with a radar detection area and a mountain range as static obstacles. Environment 2 is a dynamic environment, in which a random low-altitude dynamic obstacle is added to Environment 1, and the relevant environmental parameters are described in Section 3.2. The TD3 algorithm and SD-TD3 algorithm are verified in these two environments. All training experiments were conducted on a computer with an Intel(R) Core(TM) i7-10700 CPU and an NVIDIA GeForce RTX3060Ti GPU, using Python 3.9 as the project interpreter. The deep learning framework Pytorch-1.12.1 is used for neural network training under Windows.

5.1. Algorithm Hyperparameter Settings

The hyperparameters of TD3 and SD-TD3 algorithms are: neural network structure parameters, learning rate α, discount factor γ, experience pool size R, number of samples B, target network soft update factor τ, noise attenuation factor k. These parameters have different effects on the performance of the algorithms. If the number of hidden layers and hidden layer neurons in the neural network is too small, the neural network cannot fit the data well, and if the number of hidden layers and hidden layer neurons in the neural network is too large, the increase in the calculation amount of the algorithm cannot effectively learn. The larger the value of learning rate α, the faster the training speed of the algorithm, but prone to oscillation; the smaller the value, indicating that the slower the training speed model is difficult to converge. The larger the discount factor γ, the more the algorithmic model focuses on past experience; the smaller the value, the more it focuses on current experience. In addition, both the size of the experience pool R and the number of samples sampled B affect the learning efficiency of the algorithm; if the value is too small, the learning efficiency will be low, and if the value is too large, the algorithm tends to converge to a local optimum. The smaller the soft update coefficient τ of the target network, the more stable the algorithm is, and the smaller the change of the target network parameters, the slower the algorithm will converge. Since the action values of the actor target network output in the algorithm model is added with smoothing noise ϵ

$$\epsilon \sim \mathrm{clip}(N(0, \widetilde{\sigma}), -\mathrm{c}, \mathrm{c}) \tag{14}$$

In Equation (14), $\widetilde{\sigma}$ is the standard deviation of the normal distribution, and the larger the value, the larger the value of the added noise. However, as the model gradually converges with the training process, it is not easy to converge if the noise value is too large to produce oscillations. Therefore, the noise attenuation factor $k \in (0, 1)$ is set in this experiment, and the standard deviation $\widetilde{\sigma}$ is multiplied by the noise attenuation factor k to reduce the noise whenever the UAV completes a task during training. The specific hyperparameter settings are shown in Table 1.

Due to the fact that both TD3 algorithm and SD-TD3 algorithm use the actor-critic framework, the learning rates α_a and α_c of the Actor module network and Critic module network are important hyperparameters. Where α_a corresponds to actor network π_ϕ and actor target network $\pi_{\phi'}$, α_c corresponds to critic network Q_{θ_1}, critic network Q_{θ_2}, critic target network $Q_{\theta_1'}$ and critic target network $Q_{\theta_2'}$. so, α_c has a large impact on the convergence effect of the model. In order to select a suitable α_c, we set five different α_c for training in environment 1 and environment 2 through several experiments, and compare the convergence of the TD3 algorithm and SD-TD3 algorithm in different environments by analyzing the results.

Table 1. Hyperparameter settings.

Hyperparameters	Symbol	Value
Hidden layers	-	2
Hidden layer units	-	256
Max episodes	-	3000
Max steps per episode	-	400
Actor network learning rate	α_a	0.0001
Critic network learning rate	α_c	0.001
Discount factor	γ	0.99
Replay buffer size	R	6400
Batch size	B	128
Soft update rate	τ	0.005
Noise attenuation factor	k	0.999

5.2. Analysis of Experimental Results

5.2.1. TD3 Algorithm Model

Figures 5 and 6 show the training effects achieved by the TD3 algorithm after setting five different critic module network learning rates α_c in environments 1 and 2, respectively. From Figure 5, it can be seen that the most suitable α_c for the TD3 algorithm model in Environment 1 is 0.0009, and the model starts to converge at a round number of 660 No oscillation occurs after the model converges. From Figure 6, it can be seen that in environment 2, the most suitable α_c for the TD3 algorithm model is 0.0001, and the model starts to converge when the number of rounds is 710. Due to the dynamic obstacles of random appearance and random motion in environment 2, the model can converge, but there are still more obvious oscillations.

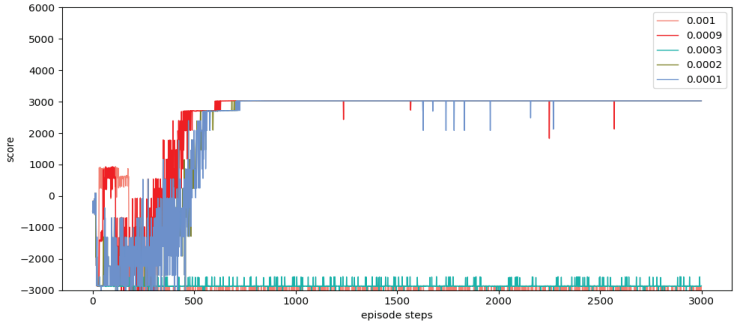

Figure 5. Training result of TD3 algorithm model in environment 1.

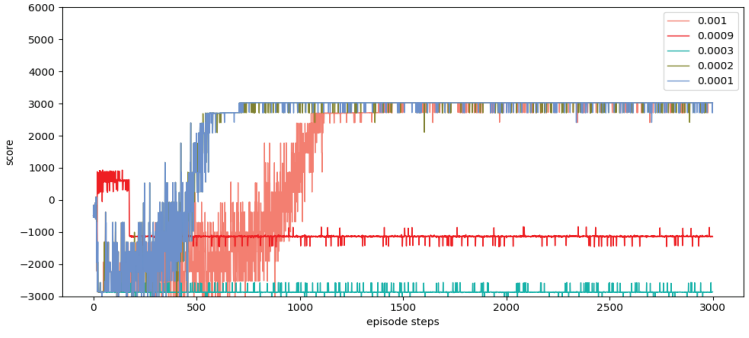

Figure 6. Training result of TD3 algorithm model in environment 2.

5.2.2. SD-TD3 Algorithm Model

To verify the performance of the SD-TD3 algorithm model, the area in front of the UAV is divided equally into six parts. Figures 7 and 8 show the training results achieved by the SD-TD3 (6) algorithm with five different critic module network learning rates α_c set in environment 1 and environment 2, respectively. From Figure 7, it can be seen that the most appropriate α_c for the SD-TD3 (6) algorithm model is 0.0003 in Environment 1, and the model starts to converge at a round number of 410. From Figure 8, it can be seen that under environment 2, the most suitable α_c for the SD-TD3 (6) algorithm model is 0.001, and the model starts to converge at a number of rounds of 635. At this point, it can be seen that the SD-TD3 (6) algorithm model converges faster compared to the TD3 algorithm model.

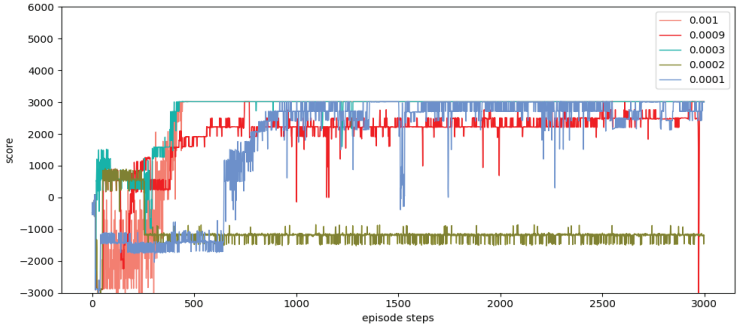

Figure 7. Training result of SD-TD3 (6) algorithm model in environment 1.

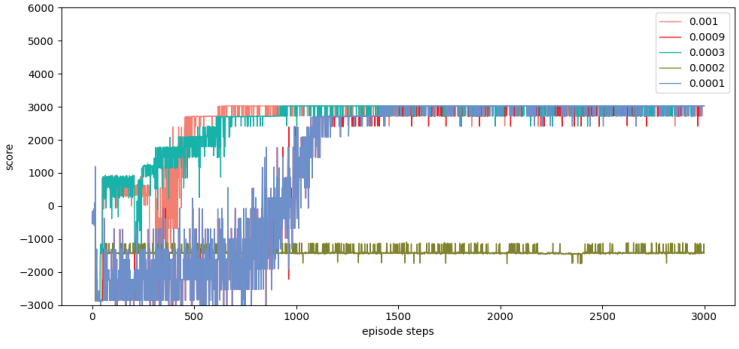

Figure 8. Training results of SD-TD3 (6) algorithm model in Environment 2.

In order to further validate the performance of the SD-TD3 algorithm model, the area in front of the UAV's travel was divided equally into 12 sections. Figures 9 and 10 show the training results achieved by the SD-TD3 (12) algorithm in Environment 1 and Environment 2 after setting five different Critic module network learning rates α_c, respectively. From Figure 9, it can be seen that the most appropriate α_c for the SD-TD3 (12) algorithm model is 0.0009 in Environment 1, and the model starts to converge at a round number of 90. From Figure 10, it can be seen that under environment 2, the most suitable α_c for the SD-TD3 (12) algorithm model is 0.0009, and the model starts to converge at the number of rounds of 210. At this point, it can be seen that the SD-TD3 (12) algorithm model converges faster compared to the SD-TD3 (12) algorithm model.

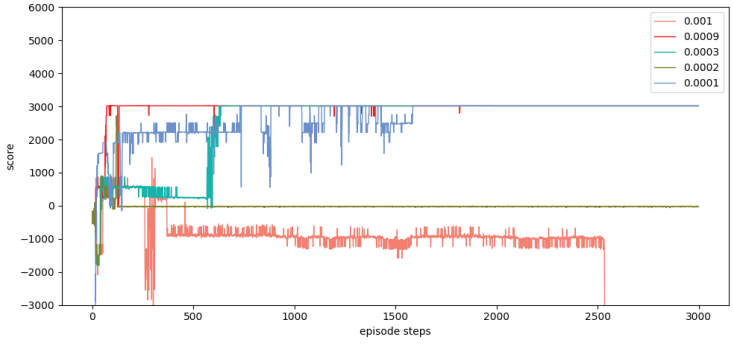

Figure 9. Training result of SD-TD3 (12) algorithm model in environment 1.

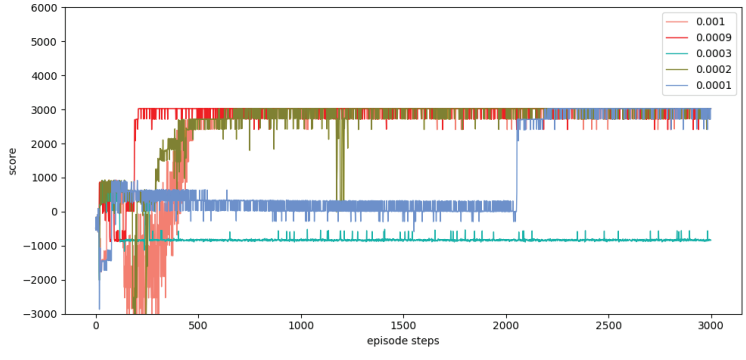

Figure 10. Training result of SD-TD3 (12) algorithm model in environment 2.

5.2.3. Comprehensive Analysis

Figure 11 compares the best training results of the three algorithmic models in the two environments.

In analyzing all the training results, it is clear from them that the TD3 algorithm model and the SD-TD3 algorithm model eventually obtain the same reward value in both static and dynamic environments, and both can reach convergence, but the convergence speed in the dynamic environment is slower than that in the static environment. In comparison with the convergence speed of the three models, the SD-TD3(12) algorithm model converges faster than the SD-TD3(6) algorithm, and the SD-TD3(6) algorithm model converges faster than the TD3 algorithm. Therefore, the convergence speed of the SD-TD3 algorithm model is higher than that of the TD3 algorithm model in both static and dynamic environments.

Further observation of the training results shows that the oscillation amplitude of the three models in the dynamic environment is larger than that in the static environment. In order to verify the robustness of the model, the model that had been trained and reached convergence was run for 30,000 rounds in two environments, and the analysis was carried out by comparing the probability of successfully completing the task.

In Figure 12, the blue color indicates the probability in environment 1, and the orange color indicates the probability in environment 2. The actual success rates of the three algorithm models in the static environment are similar and close to 1. The actual success rates of the three models in the dynamic environment are lower compared to those in the static environment, but the SD-TD3 algorithm's performance is higher compared to the TD3 algorithm, and the performance of the SD-TD3 algorithm model can be improved with further refinement of the spatial states, thus improving the actual success rates.

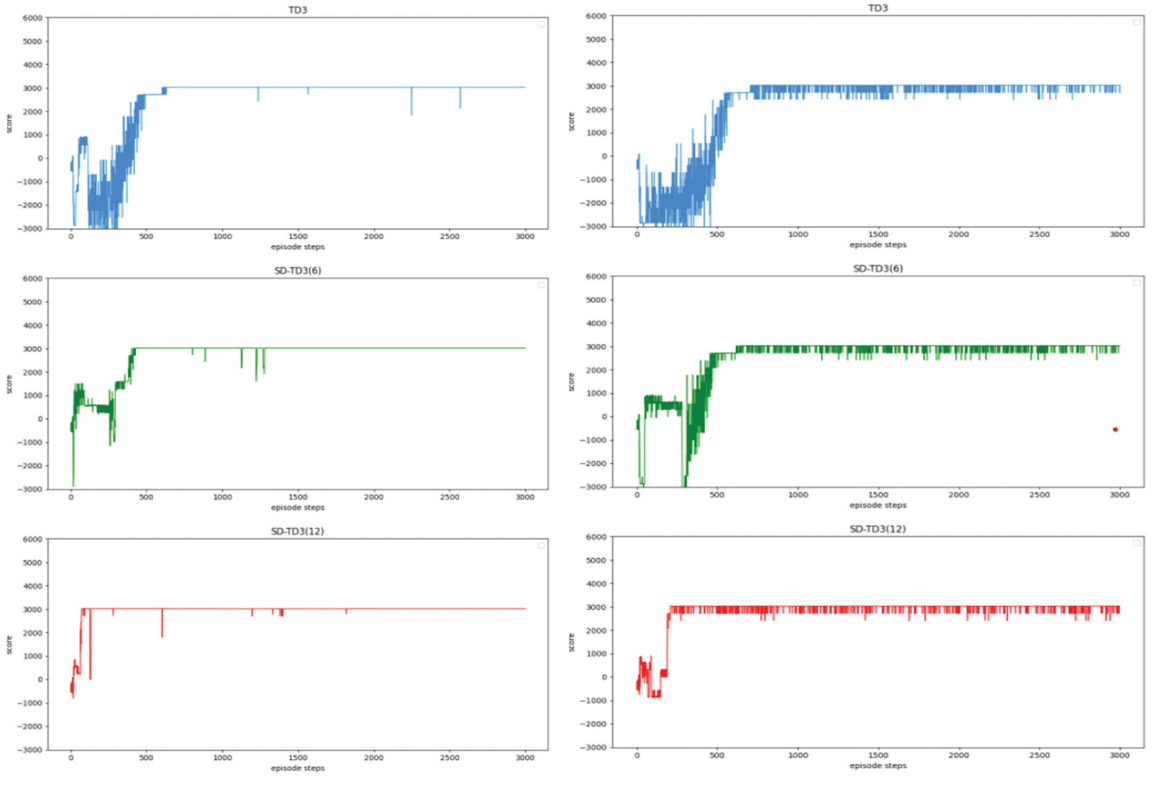

Figure 11. The best training results of the three algorithmic models. (**a**) Best training results of the model in environment 1; (**b**) Best training results of the model in environment 2.

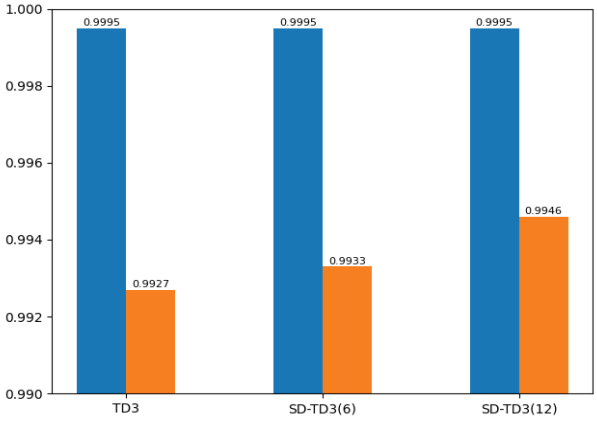

Figure 12. Success rate of all algorithmic models in both environments.

6. Conclusions

In this paper, we propose a state detection method based on the TD3 algorithm to solve the autonomous path planning problem of UAVs in low-altitude conditions. Firstly, the process of a UAV raid mission in a complex low-altitude environment was modeled, as were

the static environment and dynamic environment of low-altitude flight. Similarly, in order to solve the problem of sparse reward in traditional reinforcement learning, a dynamic reward function with heuristic guidance is set up, which can make the algorithm model converge faster. On the basis of these works, combined with the state detection method, the SD-TD3 algorithm is proposed. The simulation results show that the convergence speed of the SD-TD3 algorithm model is faster than that of the TD3 algorithm model in both a static and a dynamic environment. In the static environment, the actual task completion rate of the SD-TD3 algorithm is similar to that of the TD3 algorithm, but in the dynamic environment, the success rate of the SD-TD3 algorithm model to complete the raid task is higher than that of the TD3 algorithm, and with the detailed division of the space state information in the direction of UAV travel, the success rate of the SD-TD3 algorithm model will also improve. In general, the SD-TD3 algorithm has a faster training convergence speed and a better ability to avoid dynamic obstacles than the TD3 algorithm. The SD-TD3 algorithm needs to accurately extract environmental information to determine the position of obstacles, but in practical applications, many sensors are needed to extract and process environmental information. This paper does not study the collaborative processing method of these sensors, so it will be challenging in practical applications. In future work, it can be further studied to change the input mode of the algorithm model and input more effective environmental information to promote the algorithm model's ability to make correct decisions. At the same time, the SD-TD3 algorithm is combined and compared with other DRL algorithms, such as the PPO (proximal policy optimization) algorithm and SAC (soft actor critic) algorithm.

Author Contributions: Conceptualization, D.Z.; methodology, D.Z.; software, D.Z.; validation, D.Z., Z.X. and X.L. (Xiongwei Li).; formal analysis, D.Z.; investigation, Z.X.; resources, X.L. (Xiongwei Li), Y.Z., J.Y. and X.L. (Xi Li).; data curation, X.L. (Xi Li); writing original draft preparation, D.Z.; writing—review and editing, D.Z., J.Y., Z.X., X.L. (Xiongwei Li), Y.Z. and X.L. (Xi Li).; visualization, D.Z. and J.Y.; supervision, Z.X., X.L. (Xiongwei Li) and Y.Z.; project administration, Z.X.; funding acquisition, Y.Z. and X.L. (Xiongwei Li). All authors have read and agreed to the published version of the manuscript.

Funding: This research was funded by the National Natural Science Foundation of China, grant number 62071483, and the National Natural Science Foundation of China, grant number 61602505.

Institutional Review Board Statement: Not applicable.

Informed Consent Statement: Not applicable.

Data Availability Statement: The data used to support the findings of this study are available from the corresponding author upon request.

Conflicts of Interest: The authors declare that they have no conflict of interest or personal relationships that could have appeared to influence the work reported in this paper.

References

1. Aggarwal, S.; Kumar, N. Path planning techniques for unmanned aerial vehicles: A review, solutions, and challenges. *Comput. Commun.* **2020**, *149*, 270–299. [CrossRef]
2. Tsourdos, A.; White, B.; Shanmugavel, M. *Cooperative Path Planning of Unmanned Aerial Vehicles*; John Wiley & Sons: Hoboken, NJ, USA, 2010.
3. Chen, Y.; Mei, Y.; Yu, J.; Su, X.; Xu, N. Three-dimensional unmanned aerial vehicle path planning using modified wolf pack search algorithm. *Neurocomputing* **2017**, *266*, 445–457.
4. Zhang, H.; Xin, B.; Dou, L.-H.; Chen, J.; Hirota, K. A review of cooperative path planning of an unmanned aerial vehicle group. *Front. Inf. Technol. Electron. Eng.* **2020**, *21*, 1671–1694. [CrossRef]
5. Cabreira, T.M.; Brisolara, L.B.; Paulo, R.F.J. Survey on coverage path planning with unmanned aerial vehicles. *Drones* **2019**, *3*, 4. [CrossRef]
6. Yao, P.; Wang, H.; Su, Z. Real-time path planning of unmanned aerial vehicle for target tracking and obstacle avoidance in complex dynamic environment. *Aerosp. Sci. Technol.* **2015**, *47*, 269–279. [CrossRef]
7. Liang, X.; Meng, G.; Xu, Y.; Luo, H. A geometrical path planning method for unmanned aerial vehicle in 2D/3D complex environment. *Intell. Serv. Robot.* **2018**, *11*, 301–312. [CrossRef]

8. Dolicanin, E.; Fetahovic, I.; Tuba, E.; Hrosik, R.C.; Tuba, M. Unmanned combat aerial vehicle path planning by brain storm optimization algorithm. *Stud. Inform. Control* **2018**, *27*, 15–24. [CrossRef]
9. Sun, P.; Guo, Z.; Lan, J.; Hu, Y.; Baker, T. ScaleDRL: A Scalable Deep Reinforcement Learning Approach for Traffic Engineering in SDN with Pinning Control. *Comput. Netw.* **2021**, *190*, 107891. [CrossRef]
10. Roberge, V.; Tarbouchi, M.; Labonté, G. Comparison of parallel genetic algorithm and particle swarm optimization for real-time 865 UAV path planning. *IEEE Trans. Ind. Inform.* **2012**, *9*, 132–141. [CrossRef]
11. Liu, Z.; Zhang, Y.; Yu, X.; Yuan, C. Unmanned surface vehicles: An overview of developments and challenges. *Annu. Rev. Control* **2016**, *41*, 71–93. [CrossRef]
12. Zhang, S.; Zhou, Y.; Li, Z.; Pan, W. Grey wolf optimizer for unmanned combat aerial vehicle path planning. *Adv. Eng. Softw.* **2016**, *99*, 121–136. [CrossRef]
13. Zhang, X.; Duan, H. An improved constrained differential evolution algorithm for unmanned aerial vehicle global route planning. *Appl. Soft Comput.* **2015**, *26*, 270–284. [CrossRef]
14. Guo, S.; Zhang, X.; Zheng, Y.; Du, Y. An autonomous path planning model for unmanned ships based on deep reinforcement learning. *Sensors* **2020**, *20*, 426. [CrossRef] [PubMed]
15. Mnih, V.; Kavukcuoglu, K.; Silver, D.; Rusu, A.A.; Veness, J.; Bellemare, M.G.; Graves, A.; Riedmiller, M.; Fidjeland, A.K.; Ostrovski, G.; et al. Human-level control through deep reinforcement learning. *Nature* **2015**, *518*, 529–533. [CrossRef] [PubMed]
16. Wang, Y.; Gao, Z.; Zhang, J.; Cao, X.; Zheng, D.; Gao, Y.; Ng, D.W.K.; Di Renzo, M. Trajectory design for UAV-based internet of things data collection: A deep reinforcement learning approach. *IEEE Internet Things J.* **2021**, *9*, 3899–3912. [CrossRef]
17. Han, M.; Zhang, L.; Wang, J.; Pan, W. Actor-critic reinforcement learning for control with stability guarantee. *IEEE Robot. Autom. Lett.* **2020**, *5*, 6217–6224. [CrossRef]
18. Li, B.; Wu, Y. Path planning for UAV ground target tracking via deep reinforcement learning. *IEEE Access* **2020**, *8*, 29064–29074. [CrossRef]
19. LLillicrap, T.P.; Hunt, J.J.; Pritzel, A.; Heess, N.; Erez, T.; Tassa, Y.; Silver, D.; Wierstra, D. Continuous control with deep reinforcement learning. *arXiv* **2015**, arXiv:1509.02971.
20. Fujimoto, S.; Hoof, H.; Meger, D. Addressing function approximation error in actor-critic methods. In Proceedings of the International Conference on Machine Learning, Stockholm, Sweden, 10–15 July 2018; pp. 1587–1596.
21. Wang, Z.; Schaul, T.; Hessel, M.; Hasselt, H.; Lanctot, M.; Freitas, N. Dueling network architectures for deep reinforcement learning. In Proceedings of the International Conference on Machine Learning PMLR, New York, NY, USA, 19–24 June 2016; pp. 1995–2003.
22. Ferguson, D.; Stentz, A. Using interpolation to improve path planning: The Field D* algorithm. *J. Field Robot.* **2006**, *23*, 79–101. [CrossRef]
23. Zeiwei, Z.; Wei, W.; Nengcheng, C.; Chao, W. An improved A* algorithm using unmanned aerial vehicle (uav) flight path planning. *Geomat. Inf. Sci. Wuhan Univ.* **2015**, *40*, 315–320. [CrossRef]
24. Saranya, C.; Unnikrishnan, M.; Ali, S.A.; Sheela, D.; Lalithambika, V. Ter-rain based D algorithm for path planning. *IFAC Pap.* **2016**, *49*, 178–182. [CrossRef]
25. Li, Z.; Li, L.; Zhang, W.; Wu, W.; Zhu, Z. Research on Unmanned Ship Path Planning based on RRT Algorithm. *J. Phys. Conf. Ser.* **2022**, *2281*, 12004. [CrossRef]
26. Yan, J.; Li, X.; Liu, B.; Liu, L. Multi UAV suppression of on enemy air defense based on MILP. *J. Nav. Aeronaut. Astronaut. Univ.* **2014**, *29*, 6.
27. Yang, J.; Xu, X.; Yin, D.; Ma, Z.; Shen, L. A space mapping based 01 linear model for onboard conflict resolution of heterogeneous unmanned aerial vehicles. *IEEE Trans. Veh. Technol.* **2019**, *68*, 7455–7465. [CrossRef]
28. Zhou, H.; Xiong, H.-L.; Liu, Y.; Tan, N.-D.; Chen, L. Trajectory Planning Algorithm of UAV Based on System Positioning Accuracy Constraints. *Electronics* **2020**, *9*, 250. [CrossRef]
29. Lin, C.E.; Syu, Y.M. GA/DP Hybrid Solution for UAV Multi-Target Path Planning. *J. Aeronaut. Astronaut. Aviat.* **2016**, *48*, 203–220.
30. Nazarahari, M.; Khanmirza, E.; Doostie, S. Multi-objective multi-robot path planning in continuous environment using an enhanced genetic algorithm. *Expert Syst. Appl.* **2019**, *115*, 106–120. [CrossRef]
31. Cheng, Y.; Zhang, W. Concise deep reinforcement learning obstacle avoidance for underactuated unmanned marine vessels. *Neurocomputing* **2018**, *272*, 63–73. [CrossRef]
32. Zhang, B.; He, M.; Chen, X.; Wu, C.; Liu, B.; Zhou, B. Application of Improved DDPG Algorithm in Automatic Driving. *Comput. Eng. Appl.* **2019**, *55*, 264–270.
33. Hong, D.; Lee, S.; Cho, Y.H.; Baek, D.; Kim, J.; Chang, N. Energy-Efficient Online Path Planning of Multiple Drones Using Reinforcement Learning. *IEEE Trans. Veh. Technol.* **2021**, *70*, 9725–9740. [CrossRef]
34. Li, B.; Gan, Z.; Chen, D.; Aleksandrovich, D.S. UAV maneuvering target tracking in uncertain environments based on deep reinforcement learning and meta-learning. *Remote Sens.* **2020**, *12*, 3789. [CrossRef]
35. Papachristos, C.; Kamel, M.; Popović, M.; Khattak, S.; Bircher, A.; Oleynikova, H.; Dang, T.; Mascarich, F.; Alexis, K.; Siegwart, R. Autonomous exploration and inspection path planning for aerial robots using the robot operating system. In *Robot Operating System (ROS)*; Springer: Cham, Switzerland, 2019; pp. 67–111.
36. Zhang, F.; Li, J.; Li, Z. A TD3-based multi-agent deep reinforcement learning method in mixed cooperation-competition environment. *Neurocomputing* **2020**, *411*, 206–215. [CrossRef]

37. Memarian, F.; Goo, W.; Lioutikov, R.; Niekum, S.; Topcu, U. Self-supervised online reward shaping in sparse-reward environments. In Proceedings of the 2021 IEEE/RSJ International Conference on Intelligent Robots and Systems (IROS), Prague, Czech Republic, 27 September–1 October 2021; pp. 2369–2375.
38. Wu, Y.H.; Yu, Z.C.; Li, C.-Y.; He, M.J.; Hua, B.; Chen, Z.M. Reinforcement learning in dual-arm trajectory planning for a free-floating space robot. *Aerosp. Sci. Technol.* **2020**, *98*, 105657. [CrossRef]

drones

MDPI

Article

Research on Aerodynamic Characteristics of Trans-Media Vehicles Entering and Exiting the Water in Still Water and Wave Environments

Jun Wei, Yong-Bai Sha, Xin-Yu Hu, Zhe Cao, De-Ping Chen, Da Zhou and Yan-Li Chen *

Key Laboratory of CNC Equipment Reliability, Ministry of Education, School of Mechanical and Aerospace Engineering, Jilin University, Changchun 130022, China
* Correspondence: chenyanli@jlu.edu.cn

Abstract: The problem of aircraft entering and exiting water is a complex, nonlinear, strongly disturbed, and multi-coupled multiphase flow problem, which involves the precise capture of the air/water interface and the multi-coupling interaction between aircraft, water, and air. Moreover, due to the large difference in medium properties during the crossing, the load on the body will suddenly change. In this paper, the VOF (volume of fluid) algorithm is used to capture the liquid surface at the air/water interface, and since body movement is involved in this process, the overset grid technology is used to avoid the traditional dynamic grid deformation problem. In the process of this numerical simulation prediction, the effects of different water-entry angles and different water-entry heights on the body load and attitude of the trans-medium aircraft, as well as the cavitation evolution law of the body water entry are analyzed. On this basis, to simulate the authenticity and complexity of the water-entry environment, numerical wave-making technology was introduced to analyze the water-entry load, posture, and cavitation evolution law of the body under different wave environments. The numerical parameters under the condition of wave and no wave are compared, and the difference in water-entry performance under the condition of wave and no wave is analyzed.

Keywords: transmedia aircraft; multiphase flow; overset grid; cavitation evolution; numerical wave making

Citation: Wei, J.; Sha, Y.-B.; Hu, X.-Y.; Cao, Z.; Chen, D.-P.; Zhou, D.; Chen, Y.-L. Research on Aerodynamic Characteristics of Trans-Media Vehicles Entering and Exiting the Water in Still Water and Wave Environments. *Drones* **2023**, *7*, 69. https://doi.org/10.3390/drones7020069

Academic Editors: Andrzej Łukaszewicz, Wojciech Giernacki, Zbigniew Kulesza, Jaroslaw Pytka and Andriy Holovatyy

Received: 7 December 2022
Revised: 13 January 2023
Accepted: 13 January 2023
Published: 18 January 2023

1. Introduction

With the rapid development of small aircraft, ships, underwater submersibles, and other intelligent mobile platforms in search and rescue, detection, communications, combat reconnaissance, combat, and other types of military activities [1], civilian fields are widely used. However, the three-dimensional process of modern warfare is accelerating, and the environment in which combat equipment is located is gradually changing from the original single type to the multi-phase type [2]. To better adapt to the operational needs of modern warfare, the study of trans-media vehicles has become crucial.

The dynamic model of the trans-medium aircraft [3] is the basis for analyzing its motion characteristics and studying flight stability control. As the core key link of the dynamic model, the numerical prediction of the outlet/inlet section plays a vital role in the accurate response of the dynamic model. The water-entry process is a complex fluid phenomenon with strong nonlinear and unsteady characteristics [4]. From a mechanical point of view, the water-entry process of an object passing through the water surface at a relative speed mainly includes three stages [5]: the slamming when it contacts the free surface, the open cavity with large deformation of the free surface, and the underwater movement after the open cavity closes [6]. The first slamming stage is mainly a matter of impact dynamics, while the last two water-entry stages involve fluid–structure interaction of hydrodynamics and structural dynamics coupling [7]. In the initial stage of water entry, due to the large difference in the characteristics of the liquid and gas media, the slamming

process will instantly generate a large load on the airframe, causing the part of the trans-medium aircraft in contact with the free surface to suffer a short-term, high-intensity pressure shock wave [8]. This propagates inside the body, causing the body to produce plastic deformation and have an oscillation effect. After entering the water, due to the large deformation of the free surface and the fluid–solid coupling between the hydrodynamic force and the body [9], cavitation evolution will occur on the surface of key components such as the body rotor, and the unsteady evolution and collapse of the cavitation will produce corresponding damage on the surface of the structure. Pressure pulsations cause significant dynamic responses in the body structure.

A crucial step in the numerical prediction of water entry is the simulation of large deformation of the free interface and the boundary conditions of the dynamic mesh [10]. The simulation of large deformation of free interface mainly includes two types: one is the interface tracking technology, and the other is the interface capture technology [11]. Typical free interface simulation methods include the level-set and VOF methods. The level-set method is a grid-based interface tracking method proposed by Osher and Sethian [12]. This method expresses the free interface as a continuous function, which is convenient for directly using mathematical tools The geometric characteristic parameters and surface tension of the interface are solved, and this method can also be extended to higher-order spaces [13]. The applicable scenarios of the level-set method are mainly distributed in the simulation of the movement of water droplets, the fusion of water droplets on the air-water free interface, and the evolution of bubbles in water [14–17]. Since this method does not consider the function of the continuity equation, it does not have the property of volume conservation [18]. Therefore, it often faces the problem of mass non-conservation when the numerical simulation is used to track free interfaces [19]. To solve the problem of the non-conservation of mass, Hirt, and Nichols [20] proposed the VOF method. The VOF (volume of fluid) method is an interface tracking method based on the Euler grid. In this method, the mutually incompatible fluid components share a set of momentum equations, and the phase interface tracking in the calculation domain is realized by introducing the variable of phase volume fraction ζ [21,22]. ζ represents the volume of one phase as a percentage of the mesh volume in which it is located. The VOF method can construct the interface by calculating the phase fraction of each grid unit in the entire computational domain [23]. It has very good and accurate numerical prediction results for dam breaks, surf waves, and Rayleigh Taylor instability. Ashgriz and Poo [24] proposed the FLAIR (flux line-segment model for advection and interface reconstruction) technology based on the traditional VOF method. The basic principle is to construct a straight-line segment with an inclination angle to approximately replace the physical free interface. Then calculate the fluid volume flow through the mesh approximation surface per unit of time and use it as a correction value of the numerical flux as a function of fluid volume. The PLIC (piecewise linear interface calculation) reconstruction technology proposed by Youngs [25] is also based on the traditional VOF method. The principle of the PLIC reconstruction technology is similar to that of the FLAIR reconstruction technology. This method is also widely used in liquid surface capture [26,27]. Sussman and Puckett [28] combined the superiority of level-set to calculate the curvature and the conservation of VOF to propose the CLSVOF (coupled level-set volume of fluid) method, which is widely used in numerical simulations of other gas–liquid two-phase interfaces, such as oceans, water conservancy, hydropower, liquid jets, etc. [29–32].

2. Airframe Design Scheme for Trans-Media Aircraft

Because of its ability to span multiple media, the trans-medium aircraft must adapt to the differences in physical properties of multiple media at the same time. Such prerequisites bring inevitable contradictions to its airframe structure design, but in general, the design concept of the cross-medium aircraft is to balance the difficulties that need to be overcome when the multi-medium crosses under the premise of satisfying the stable operation of the single-medium function, such as (1). However, in the underwater navigation stage, due to

the nonlinear disturbance of water flow, to obtain sufficient steering stability, the aircraft should ensure that the aircraft body has considerable weight and structural strength. (2). In terms of the shape of the fuselage, based on the similarity principle of Reynolds number, the speed of the same fuselage shape in water and air media is quite different, which causes instability in the medium transition process of the trans-medium aircraft, which leads to the failure of crossing. (3). In terms of wing layout, when the aircraft is flying in the air, the pressure difference between the upper and lower surfaces of the wing generates lift to overcome gravity. When the flight speed is constant, the lift is related to the wing area. Influenced by airframe drag, the wing surface has a relatively short span and narrow chord. (4). In terms of pressure and tightness, underwater navigation has high requirements for pressure and tightness, while in air flight, especially in low-altitude flight, sealing and pressure performance are hardly considered. Even the pressure-resistant hulls used in high-altitude flights are no match for cabins used in underwater voyages.

Through the analysis of the above difficult problems, this paper proposes a water–air dual-power ducted structure scheme based on the multi-rotor aircraft architecture based on the basic principles of the trans-medium aircraft, as shown in Figure 1. By taking into account the design of the structure and power system, the detailed design of the airframe of the trans-medium aircraft is carried out.

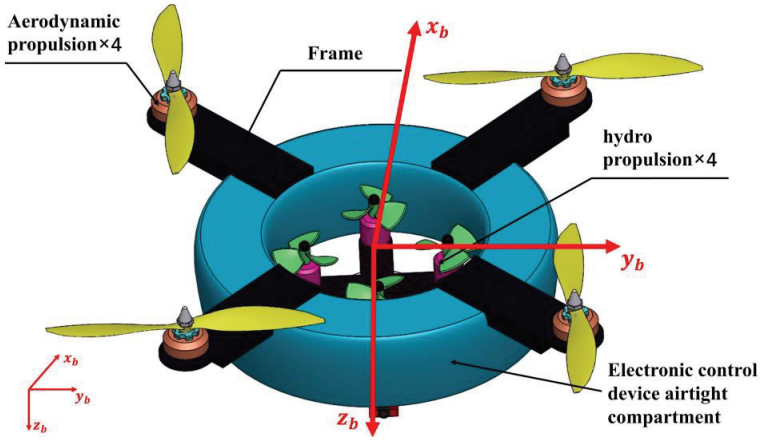

Figure 1. Schematic diagram of the overall structure of the water–air dual-power ducted trans-medium aircraft.

As shown in the figure above, the overall structure of the trans-medium aircraft is based on the "X" layout of the four-rotor aircraft. The air flight and the vertical medium transition between water and air are realized through the air rotors. It has strong operational stability. The structural design of the cross-section duct realizes the reduction in water-entry slamming during the medium transition process and the duct-collection effect on the power of the underwater propeller. The underwater propellers are arranged in pairs in the center of the duct body in a "cross" shape to provide power for underwater multi-directional movement.

2.1. Layout and Principle of Airframe Propulsion System

This design combines the advantages of the layout of the four-rotor unmanned aerial vehicle. The air rotor power propeller adopts the "X" layout scheme, and the underwater propeller power adopts the "cross" layout scheme. The propeller types and their layout are shown in Figure 2, the red triangle represents the forward direction of the aircraft, and the front and back blades of the rotor are distinguished by different colors.

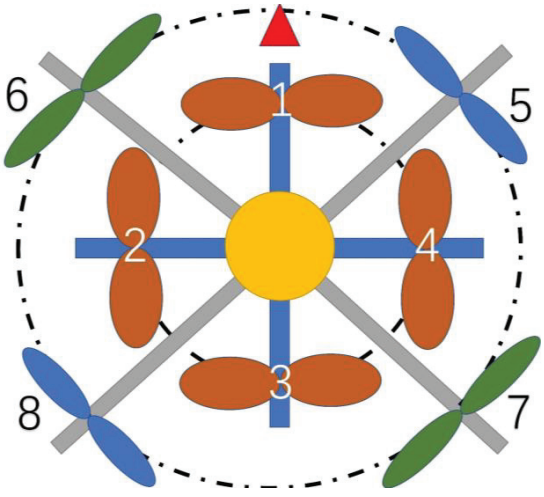

Figure 2. Schematic diagram of thruster type and its arrangement.

Through the description of the propeller types and their arrangement above, a brief introduction will be given to the working principles of the different missions of the trans-medium aircraft described in this paper, as shown in Figure 3. The four aerodynamic propellers are mainly responsible for the air flight mission of the aircraft. The basic propulsion principle is consistent with the drive mode of the quadrotor aircraft, and the purpose of flying in six degrees of freedom in space is achieved by changing the speed input of the four motors. Arrows of different sizes in the figure represent the differences in motor speed resulting in differences in the lift, thereby achieving the purpose of changing the aircraft's motion attitude.

2.2. Internal Structure Design of Trans-Media Aircraft

2.2.1. Conduit Shape Design

For the layout design of the underwater propeller, the presence of the culvert body can effectively increase the efficiency of underwater propulsion. The duct body of the water–air dual-power ducted system mainly plays the role of protecting the propeller (underwater turbulence impact), supporting the body structure, and storing the integrated electronic control system inside the aircraft. Due to the existence of the duct body, the impact noise of the propeller tip is reduced, and the induced resistance is small so that the operating efficiency of the propeller is improved and greater thrust will be generated under the same power consumption condition, which greatly improves the aerodynamic performance of the ducted system. In the basic shape of the duct body design, a part of the cylindrical duct body section resembles a curved airfoil. The performance enhancement of ducted propellers has three geometrical features: a properly designed air inlet accelerates the flow of the propeller rotating medium, the gap between the propeller blades and the duct wall (tip clearance) improves the blade tip flow, and the diffuser partially suppresses the shrinkage of the flowing medium [33].

As shown in Figure 4, the duct is generally divided into three parts, the inlet section, the middle section, and the expanded outlet section. Its main shape and structure parameters are the inlet curvature R, the inner diameter D_c, the expanded outlet diameter D_e, the duct expansion angle Φ, and the culvert road height H. The above geometric variables can be dimensionless through the inner diameter or propeller diameter.

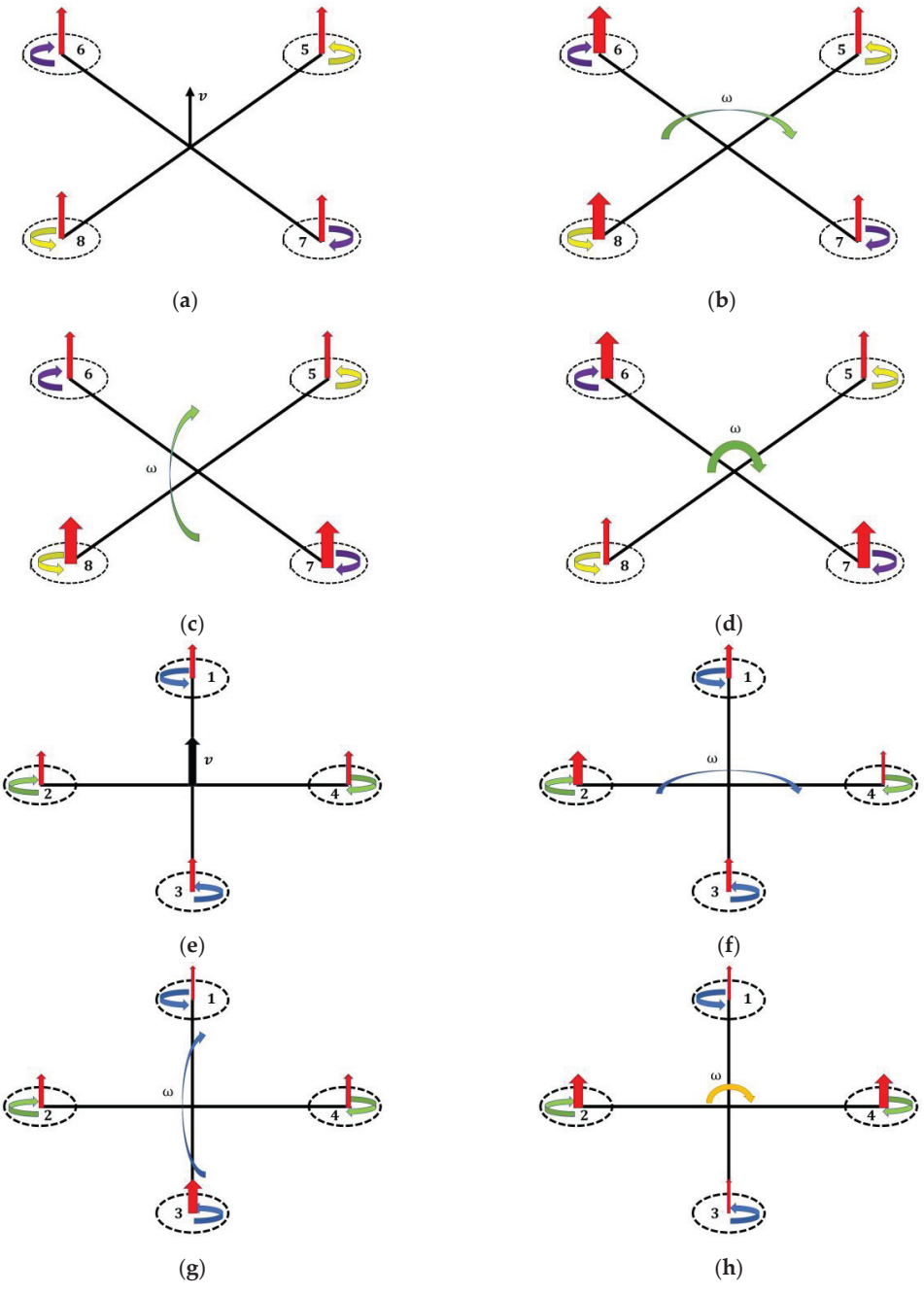

Figure 3. Schematic diagram of the working principle of the power system of the trans-medium aircraft: (**a**–**d**) translation, roll, pitch, yaw (air layout); (**e**–**h**) translation, roll, pitch, yaw (underwater layout).

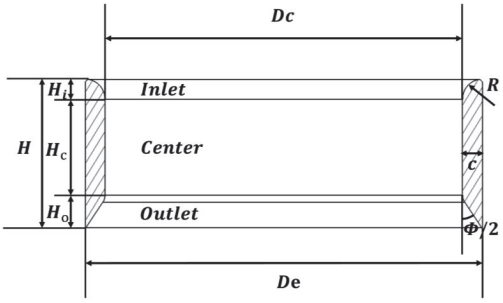

Figure 4. Schematic diagram of the cross-sectional structure of the duct body.

By placing the propeller inside the duct, the trans-medium aircraft has unparalleled safety for the operator and the surrounding environment, and through its VOTL capability, it can take off and land and operate in a narrow environment. With the support of the designed duct, the duct wall can effectively convert the propeller slipstream into thrust, thereby generating additional thrust.

2.2.2. Frame Structure Design

The frame structure is the bearing platform of the aircraft. According to the core, internal components of the trans-media aircraft and the overall layout structure under different media conditions, the air four-rotor support frame, and the underwater four-propeller thrust support frame are respectively designed. The air-supported frame only uses a wheelbase of 500 mm and is directly connected to the duct body in a rigid body. The frame layout adopts an "X" shape, as shown in Figure 5a, and the material is mainly carbon fiber, which greatly reduces the weight of the body and enhances the water entry of the aircraft, its anti-slamming ability. The main supporting component of the underwater support frame is the propeller drive motor. To realize the internal layout of the culvert body of the propeller, a cross-shaped frame body is used, and its material is also carbon fiber. The propeller support base and the cross-shaped frame are fixed to realize the culvert body. The layout of the four propellers in the "ten" shape inside the channel body is shown in Figure 5b,c. The propeller support base and the cross-shaped frame are fixed by pipe clamps. The design form of the overall aircraft frame is shown in Figure 5d. The frame bears the load of the underwater thrust device and is driven by independent power systems to complete single-medium and multi-medium crossing and multi-modal movements.

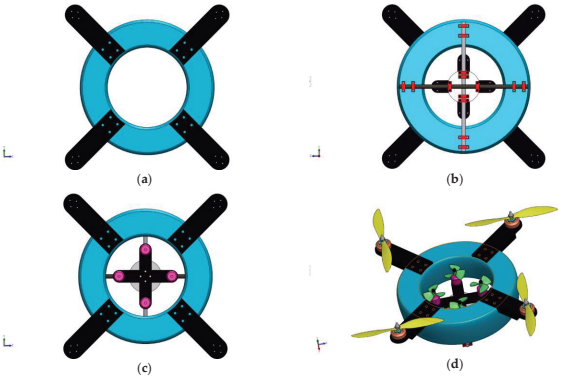

Figure 5. Schematic diagram of the frame structure design of the trans-media aircraft: (**a**) air quad-copter support frame; (**b**) cross frame structure; (**c**) underwater propeller support rack; (**d**) aircraft overall rack layout design.

3. Based on OpenFOAM Numerical Calculation Theory

3.1. Numerical Water/Gas Two-Phase Flow Mathematical Model

For the numerical simulation of water–air two-phase flow, its solution models are mainly divided into two categories: high-phase fraction models and interface capture models [34]. In this study, the trans-medium vehicle is used to cross the water–air two-phase flow medium. Such a fluid–fluid problem with a clear boundary can be well-applied to the interface capture model. The two key issues of the interface capture idea are: (1) the interface should be as thin as possible; (2) the algorithm should be as stable as possible when the interface is unstable [35]. The interFOAM solver based on the VOF method is used to solve the interface of water–gas two-phase flow in OpenFOAM [36]. The interFOAM solver is based on incompressible, adiabatic, insoluble, non-mixing (mixing refers to the distribution of one fluid in another fluid, such as the movement of bubbles in liquid) two-phase interface capture to solve. The volume fraction method (VOF) is used to capture the free interface of two-phase flow, while the finite volume method [37] (FVM) is used for spatial discretization.

The complex flow conditions in nature are controlled by three basic physical principles, namely the law of conservation of mass, Newton's second law, and the law of conservation of energy. These three basic physical principles correspond to three governing equations, that is, the governing equations of fluid mechanics (continuity equation, momentum equation, and energy equation), and these three equations are the mathematical description of the corresponding physical principles. According to the above three basic physical principles, the governing equation of the incompressible Newtonian fluid is as follows:

$$\begin{cases} \nabla \cdot \boldsymbol{U} = 0 \\ \frac{\partial \boldsymbol{U}}{\partial t} + \nabla \cdot (\boldsymbol{U}\boldsymbol{U}) = -\nabla \frac{p}{\rho} + \nabla \cdot (\upsilon \nabla \boldsymbol{U}) \end{cases} \tag{1}$$

where ρ is the density, $\boldsymbol{U}$ is the velocity of the control body, ρ is the pressure, and υ is the viscosity.

Through the above basic incompressible N-S equation, the momentum equation of the insoluble multiphase system can be obtained under the condition of gravity and source term:

$$\frac{\partial \rho \boldsymbol{U}}{\partial t} + \nabla \cdot (\rho \boldsymbol{U}\boldsymbol{U}) - \nabla \cdot \boldsymbol{\tau} = -\nabla p + \rho g + \boldsymbol{F} \tag{2}$$

where $\boldsymbol{F}$ is the surface tension. The continuity equation can be expressed as:

$$\frac{\partial \rho}{\partial t} + \nabla \cdot (\rho \boldsymbol{U}) = 0 \tag{3}$$

If two kinds of fluids are considered to be incompressible, that is to say, the fluid element of a certain fluid motion is considered, and its material derivative is 0, that is:

$$\frac{D\rho}{Dt} = \frac{\partial \rho}{\partial t} + \boldsymbol{U} \cdot \nabla p = 0 \tag{4}$$

The density in Equation (4) can be solved for the pure convection equation when the velocity $\boldsymbol{U}$ is known. In the volume of fluid (VOF) method, ζ is defined to represent the phase fraction of the fluid. Consider a gas–liquid two-phase system of a certain grid unit, if the grid unit is filled with fluid, then $\zeta = 1$; if the grid unit is filled with gas, then $\zeta = 0$. If the value of ζ is between 0 and 1, there is gas–liquid mixing in this grid cell.

As shown in Figure 6, if the phase fraction of the entire grid is calculated to construct the interface, it will be found that the volume fraction is a step function in space and is discontinuous in space, so the reconstructed phase interface is discontinuous. The interface between two adjacent grids is discontinuous, and the physical quantity is also discontinuous when passing through the interface. This phenomenon is called parasitic

current. The main work of the VOF method at present is to alleviate the parasitic flow phenomenon caused by the numerical method.

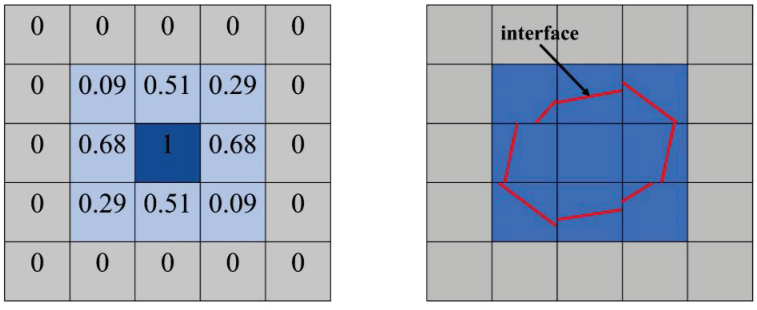

Figure 6. Spatial distribution of phase fraction and its interface reconstruction by VOF method.

Next, the surface tension equation in the momentum equation of the insoluble multi-phase system is deduced. The most important feature of the surface tension is that there is a sharp pressure drop Δp at the interface. Take the fluid microelement of the two-phase interface, and let p_1 be the downward pressure exerted by the air above the element; p_2 is the upward pressure exerted by the liquid below the surface microelement, so $\Delta p = p_1 + p_2$ can be obtained, and the surface tension of the curved surface microelement is defined as $\boldsymbol{F}$. As shown, Figure 7 is a schematic diagram of the force on the surface micro-element at the two-phase interface.

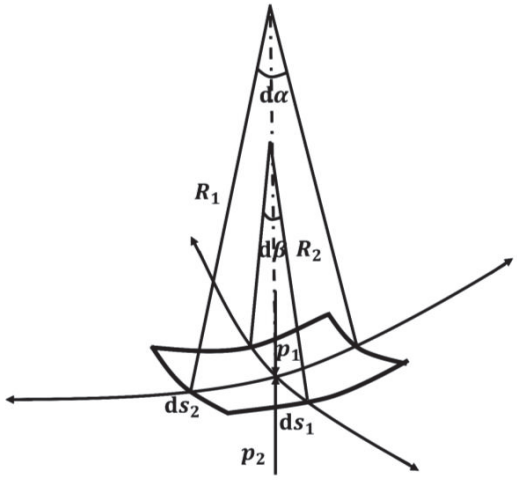

Figure 7. Schematic diagram of the force on the surface microelement at the interface of two phases.

In the figure, s_1 and s_2 are the lengths of the sides of the surface micro-element, so the area of the surface micro-element is $ds_1 ds_2$. $d\alpha$ and $d\beta$ are the curvature angles of different curves on the surface micro-element, and R_1 and R_2 are the radii of curvature of different curves on the surface micro-element, respectively. The magnitude of the combined force on the surface micro-element is:

$$\boldsymbol{F}_p = (p_1 - p_2) ds_1 ds_2 \tag{5}$$

The definition of surface tension shows that it acts on the four edges of the surface micro-element and that the combined force of tension is vertical and balanced with $\boldsymbol{F}_p$ above. Defining the coefficient of surface tension as σ, the magnitude of the tension on the s_1-edge is σds_1, and the magnitude of its component in the vertical direction is $\sigma ds_1 \sin(d\beta/2)$.

In the case of small β, $\sigma ds_1 \sin(d\beta/2) \approx \sigma ds_1 (d\beta/2)$. Similarly, the tension acting on the s_2-edge is $\sigma ds_2 (d\alpha/2)$. Thus, the surface tension acting on the surface micro-element is:

$$\boldsymbol{F}_\sigma = \sigma(ds_1 d\beta + ds_2 \alpha) = \sigma(\frac{d\beta}{ds_1} + \frac{d\alpha}{ds_2}) ds_1 ds_2 \tag{6}$$

Now denote by $\boldsymbol{n}$ the unit normal to the surface differential element, which points from a higher phase fraction to a lower phase fraction, modulo 1. Then we have:

$$\frac{\partial \boldsymbol{n}_x}{\partial x} = \frac{d\alpha}{dx} = \frac{1}{R_1} \tag{7}$$

$$\frac{\partial \boldsymbol{n}_y}{\partial y} = \frac{d\beta}{dy} = \frac{1}{R_2} \tag{8}$$

$$\frac{\partial \boldsymbol{n}_z}{\partial z} = 0 \tag{9}$$

So the surface tension expression can be translated as:

$$\boldsymbol{F}_\sigma = \sigma(\frac{1}{R_1} + \frac{1}{R_2}) ds_1 ds_2 \tag{10}$$

In addition because:

$$\nabla \cdot \boldsymbol{n} = \frac{\partial \boldsymbol{n}}{\partial x} + \frac{\partial \boldsymbol{n}}{\partial y} + \frac{\partial \boldsymbol{n}}{\partial z} = \frac{1}{R_1} + \frac{1}{R_2} \tag{11}$$

Therefore:

$$\boldsymbol{F}_\sigma = \sigma \nabla \cdot \boldsymbol{n} ds_1 ds_2 \tag{12}$$

With the surface micro-element in force equilibrium, then we have:

$$\Delta p = p_1 - p_2 = \sigma(\frac{1}{R_1} + \frac{1}{R_2}) = \sigma \nabla \cdot \boldsymbol{n} \tag{13}$$

Next, the surface tension is modeled according to the continuum surface force model to obtain:

$$\nabla p = \sigma \kappa \nabla \zeta \tag{14}$$

where $\boldsymbol{K}$ represents the curvature at the interface.

Next, to solve the pressure term and body force term in the momentum conservation equation, define p_{rgh} in OpenFOAM as follows:

$$p_{rgh} = p - \rho \boldsymbol{g} \cdot \boldsymbol{h} \tag{15}$$

where the p_{rgh} is the reference pressure, which is obtained by splitting the pressure p. It has very good stability during the solution calculation; therefore, in general form, the reference pressure is used as the variable for the iterative calculation.

Since the two-phase flow problem is involved, the density in the basic governing equation is related to the physical properties of water and gas, so for the unification of the equations, ρ is defined as follows:

$$\rho = \zeta \rho_1 + (1 - \zeta) \rho_2 \tag{16}$$

where ρ_1 and ρ_2 are different phase densities, respectively.

Therefore, by substituting the previously derived expressions for each variable into the incompressible N-S Equation (1), the fluid micro-element control equation under the VOF method is obtained as follows:

$$\frac{\partial \zeta}{\partial t} + \boldsymbol{U} \cdot \nabla \zeta = 0 \tag{17}$$

$$\frac{\partial \rho \boldsymbol{U}}{\partial t} + \nabla \cdot (\rho \boldsymbol{U}\boldsymbol{U}) - \nabla \cdot (\boldsymbol{v} \nabla \boldsymbol{U}) - \nabla \boldsymbol{U} \cdot \nabla \boldsymbol{v} = -\nabla p_{rgh} - \boldsymbol{g} \cdot \boldsymbol{h} \nabla p + \sigma \kappa \nabla \zeta \tag{18}$$

$$\nabla \cdot \boldsymbol{U} = 0 \tag{19}$$

It can be seen from the above governing equations that there is no essential difference between the VOF equation and the single-phase flow equation, both of which contain a momentum equation and a continuity equation. The continuity equations are exactly the same. The momentum equation, the VOF model is supplemented with a space-varying viscosity and an additional surface tension term. In addition, a phase transport equation is included. To sharpen the free interface, OpenFOAM uses the method proposed by Waller [38] to add artificial convection terms to the phase equation to squeeze the phase fraction near the phase interface to counterbalance the solution. The equation causes the ambiguity of the phase boundary caused by numerical dissipation to ensure the clarity of the interface. According to the idea of adding an artificial convection term, the VOF model can be expressed as:

$$\frac{\partial \zeta}{\partial t} + \nabla \cdot (\zeta \boldsymbol{U}) + \nabla \cdot (\zeta (1 - \zeta) \boldsymbol{U}_c) = \zeta \nabla \cdot \boldsymbol{U} \tag{20}$$

The third item in Equation (20) is an artificially added compressible item. According to the mathematical properties of this item, when ζ = 0 or 1, the calculated value is 0; that is, its value is 0 in pure phase (non-interface). A non-zero value exists when ζ is between 0 and 1. $\boldsymbol{U_c}$ is the compression velocity, the direction is the same as the phase gradient, so:

$$\boldsymbol{U}_c = c|\boldsymbol{U}| \frac{\nabla \zeta}{|\nabla \zeta|} \tag{21}$$

where $\boldsymbol{c}$ represents a controllable compression factor. When $\boldsymbol{c}$ = 0, there is no compression effect. The larger $\boldsymbol{c}$ is, the faster and more obvious the compression effect will be. The final phase equation embedded in the OpenFOAM solver is as follows:

$$\frac{\partial \zeta}{\partial t} + \nabla \cdot (\zeta \boldsymbol{U}) + \nabla \cdot (\zeta (1 - \zeta) c |\boldsymbol{U}| \frac{\nabla \zeta}{|\nabla \zeta|}) = \zeta \nabla \cdot \boldsymbol{U} \tag{22}$$

3.2. Trans-Medium Aircraft Multi-Medium Spanning Moving Mesh Technology

It is very convenient to use dynamic overset grids for complex structures with relative motion. The relative motion between subdomains does not require grid deformation, let alone regenerate the grid, and only needs to define the law of grid motion under the condition that the subdomains overlap each other.

The advantage of the overset grid method is that it allows complex integrated or separated geometries to be processed using multiple overlapping meshes. Each component grid can handle a part of the domain and can be moved freely or as specified. Before solving the flow-governing equations, all component meshes need to be assembled to determine the information connectivity between different domains. This process includes the following key steps: (1) cutting holes, (2) overlapping boundary search, and (3) contribution unit search. The specific schematic diagram is shown in Figure 8.

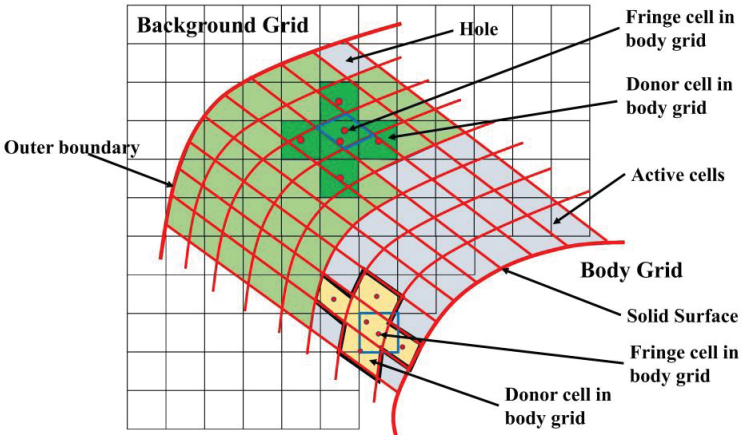

Figure 8. Schematic diagram of the assembly principle of overset grid.

3.3. Numerical Wave Making

The application scenario of modern numerical wave-making technology is the simulation of buildings in the marine environment. In this paper, to verify the ability of the medium-crossing medium of the trans-medium aircraft in the wave environment and compare the load impact on the body with the data under the condition of still water, the aerodynamic performance of the trans-media aircraft entering and exiting water under different external environments is obtained.

The numerical wave-making technology in this paper is still the numerical solution of the two-phase flow, and the solver used is the same as that of the aircraft entering the water under still water conditions, which is overInterDyFoam, which uses finite volume discretization and the volume fraction of fluid (VOF) method to solve the 3D Reynolds-averaged Navier–Stokes (RANS) equations for two incompressible phases and handle dynamic meshes. The calculation domain of numerical wave-making is shown in Figure 9.

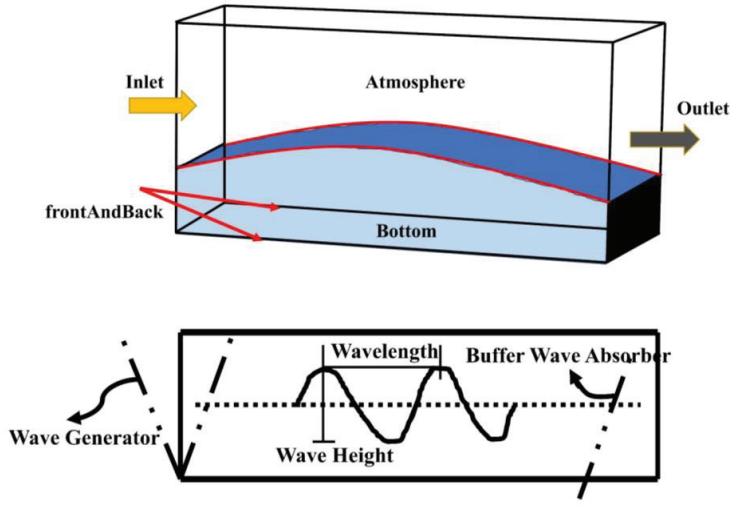

Figure 9. Schematic diagram of the numerical wave-making calculation domain.

4. Numerical Prediction of Aircraft Entering and Exiting the Water

4.1. Mesh Independence Test

To verify the grid independence, the trans-medium aircraft is selected as the research object, and different levels of grids are calculated under the condition of the air rotor of the aircraft at 2000 r/min. The air rotor model is APC-1047SF.

Figure 10a–c are the rotor thrust curves, the tip speed curve when R/r = 1.1, and the tip speed curve when R/r = 1.2 under different grid levels, respectively. R is the air rotor radius and r is the sampling radius.

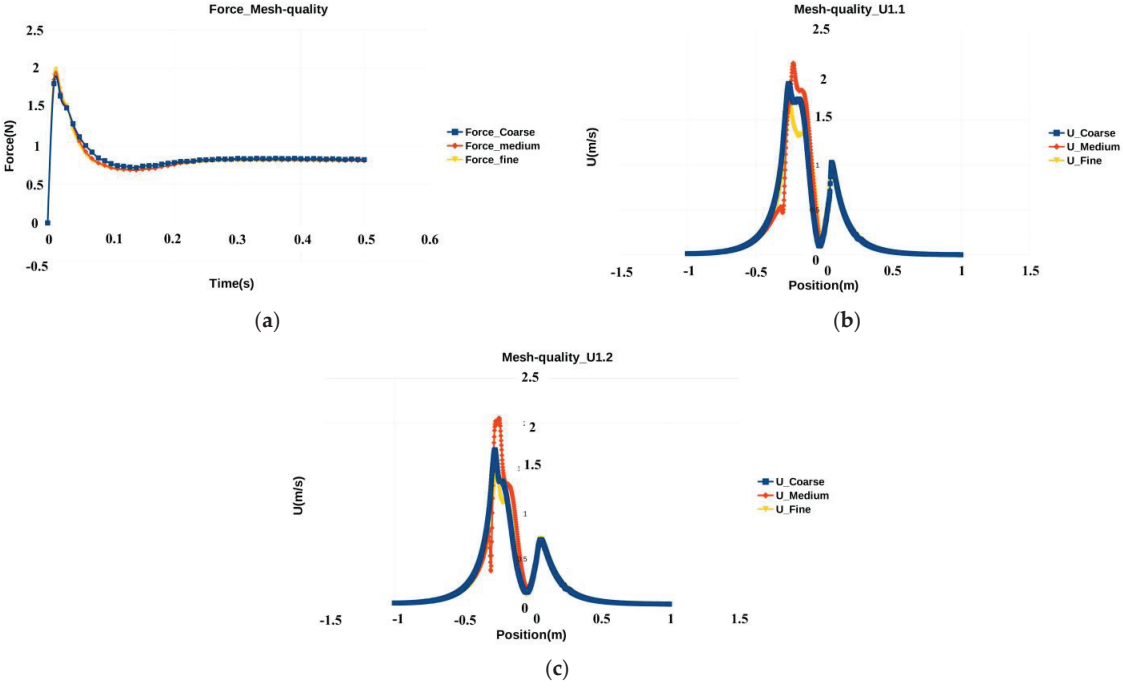

Figure 10. Schematic diagram of variable curves under different grid levels: (**a**) rotor thrust curve; (**b**) the tip speed curve when R/r = 1.1; (**c**) the tip speed curve when R/r = 1.2.

From the above schematic diagram of the curve change, it can be seen that better computational accuracy can also be obtained when the grid is controlled at a medium level. Therefore, in this study, the computational grid level for the numerical prediction of aircraft entry and exit is controlled at a medium level, which can effectively save computational power and obtain more accurate results with limited computational resources.

To verify the convergence of the solution iteration process, the residual curves of the turbulence parameters involved in the RANS modeling method are extracted by sampling in this paper, and the curves are shown in Figure 11.

By observing the above curves, it can be found that each parameter gradually converges to a constant value as the solution time increases. By such a trend of functional variation, it can be judged that the numerical simulation converges during the computational solution of the grid-independent numerical experimental validation. The simulated debugging parameters are shown in Tables 1–3.

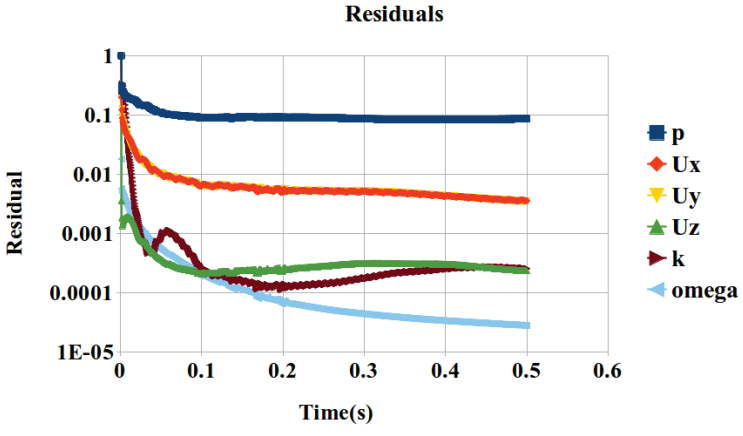

Figure 11. Residual curve.

Table 1. Mesh convergence analysis.

Mesh Type	Number of Grid Cells	Grid Base Size/m	
		Background Area	Overlapping Area
coarse	1,554,953	0.13	0.06
medium	3,663,283	0.10	0.05
fine	4,437,138	0.07	0.04

Table 2. Boundary Conditions.

Turbulence Parameters	Inlet	Outlet	Wall	Blades
k	fixedValue	inletOutlet	kqRWallFunction	kqRWallFunction
nut	calculated	calculated	nutUSpaldingWallFunction	nutUSpaldingWallFunction
omega	fixedValue	inletOutlet	omegaWallFunction	omegaWallFunction
p	fixedFluxPressure	totalPressure	fixedFluxPressure	fixedFluxPressure
U	fixedValue	pressureInletOutletVelocity	fixedValue	movingWallVelocity

Table 3. Simulation of debugging parameters.

Mesh Type	Turbulence Model	Physical Time Step	Maximum y+ Value	Whether to Use Wall Functions	Solving Time
coarse	k-omega two-equation model	3×10^{-4} s	40	YES	0.88 h (64 CPUs)
medium	k-omega two-equation model	2×10^{-4} s	35	YES	2.07 h (64 CPUs)
fine	k-omega two-equation model	1×10^{-4} s	32	YES	2.54 h (64 CPUs)

4.2. Mesh Generation Verification Analysis

Numerical prediction of trans-medium aircraft entering and exiting water involves body movement, so there is a dynamic grid problem. During the solution process, the movement and deformation of the grid will have a huge impact on the solution accuracy and solution convergence, so the overlapping grid method will be used in the pre-processing grid generation process for the numerical simulation of aircraft entering and exiting the water. The overlapping grid method needs to establish two sets of grids, in which the calculation domain of the external flow field of the trans-media aircraft is used as the

background grid, and the aircraft itself is used as a moving overlapping grid. The role of moving in the grid, the numerical communication between the two sets of grids adopts the Lagrange interpolation shape function method because this process does not involve the deformation of the moving grid, thus ensuring the stability and convergence of the solution process. However, the numerical communication in the solution process leads to a longer calculation time for this kind of mesh method than that of traditional deformable dynamic mesh. Figure 12 is a schematic diagram of the grid generation of the aircraft entering and exiting the water.

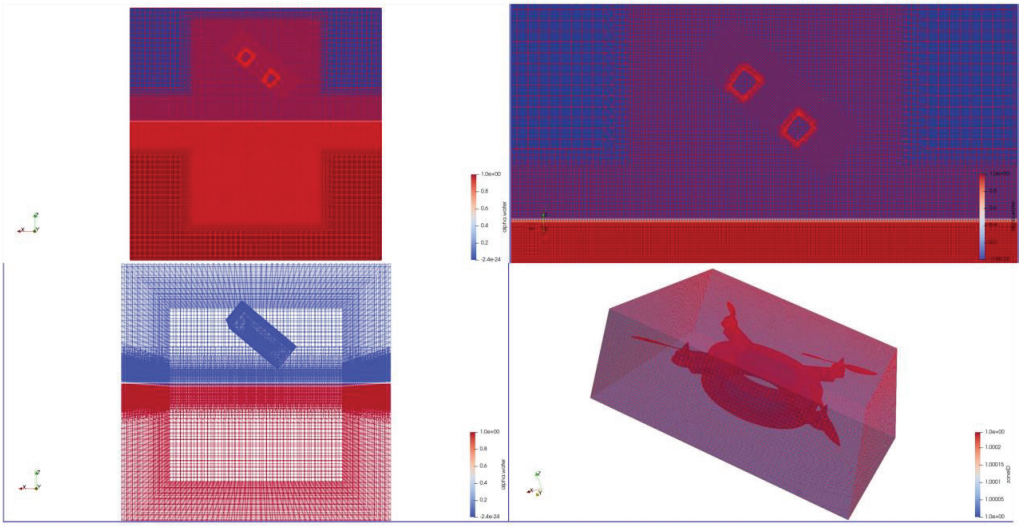

Figure 12. Schematic diagram of grid generation for numerical prediction of water inflow and outflow.

4.3. Research on the Water-Entry and -Exit Characteristics of the Aircraft in the Static Water State

4.3.1. Water-Entry Characteristics at Different Angles

In this paper, the initial conditions for the water-entry characteristics of the trans-media aircraft at different angles are set as follows: the water-entry height is 0.4 m, the initial velocity of water entry is 0, the free fall hits the water surface, and the body enters the water body under the action of gravity. To verify the water-entry performance of the aircraft at different angles, this paper sets its water-entry angles to 0°, 10°, 20°, 30°, and 40°, respectively. The angle of entry into the water is defined as the angle between the plane of the air rotor blades and the water surface. The vehicle is in the process of entering the water and is to turn off all power devices at a certain angle and height of free fall into the water.

To reveal the influence of the static water flow disturbance on the speed and impact load of the aircraft during the water-entry process, this paper takes the aircraft at a height of 0.4 m and an inclination angle of 40° as an example and obtains the phase change of the water flow field and the motion of the aircraft through numerical simulation calculations. The streamlined diagram is shown in Figure 13.

It can also be seen from the above water flow phase change diagram and body motion streamline diagram that at the moment of water entry and slamming, the high-speed zone is near the water/air interface, and as the water-entry process proceeds, the water flow buffers the body speed to gradually decrease; the kinetic energy of the body movement is transformed into the kinetic energy of water flow disturbance cavitation sputtering.

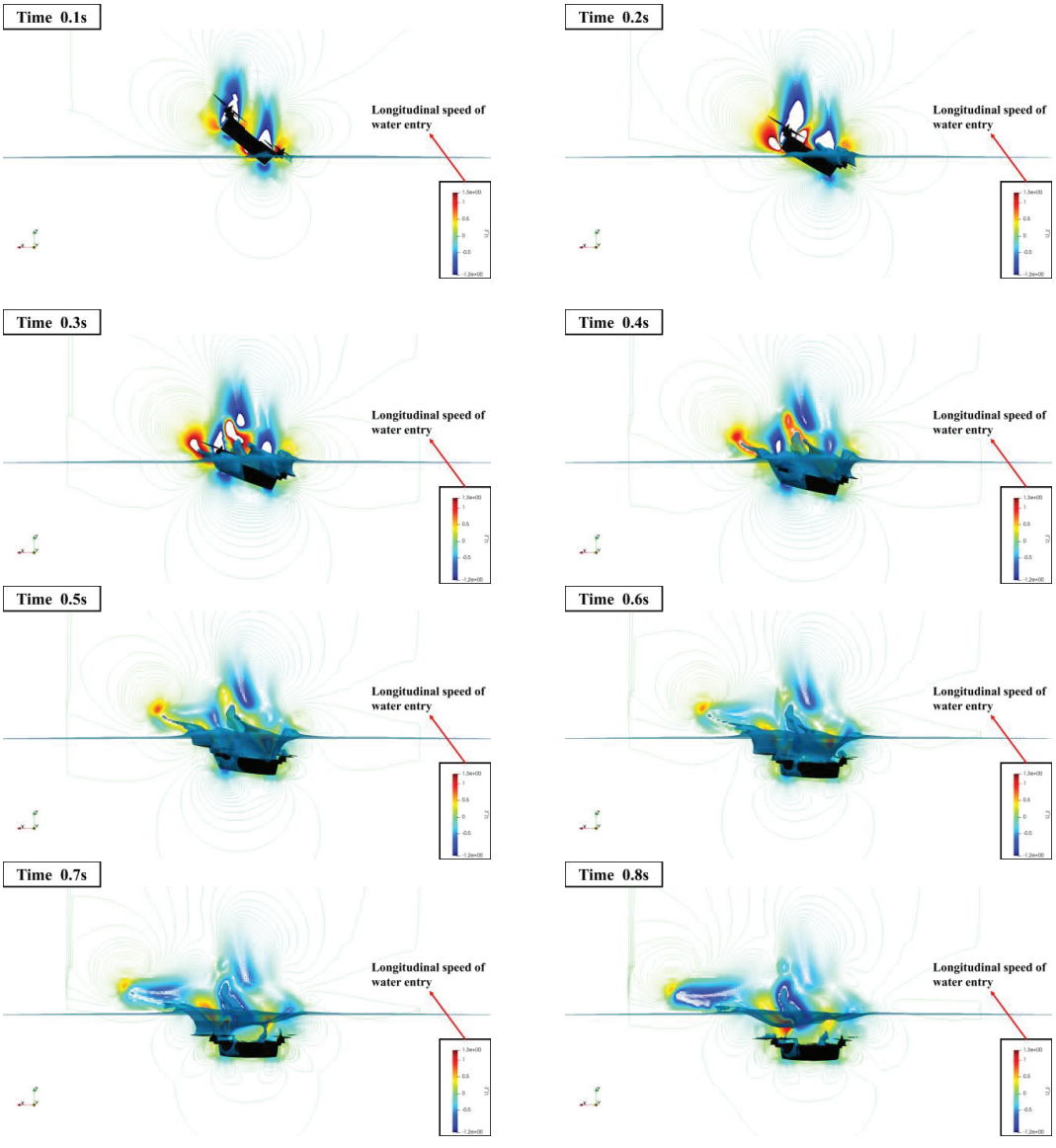

Figure 13. Water flow phase change and body motion streamline diagram of the inflow flow field.

Next, to analyze the vortex structure of the flow field during the water-entry process of the trans-medium aircraft, it is necessary to be able to identify and detect the vortex in the flow field through an effective visualization method. In this paper, the Q criterion [39] method is used for the above analysis.

The theory of the Q criterion comes from the velocity gradient tensor. The velocity gradient tensor expression is as follows:

$$\frac{\partial u_i}{\partial x_j} = 0.5[\frac{\partial u_i}{\partial x_j} + \frac{\partial u_j}{\partial x_i}] + 0.5[\frac{\partial u_i}{\partial x_j} - \frac{\partial u_j}{\partial x_i}] \tag{23}$$

Among them, the symmetric part is denoted as S, which is usually called the strain rate tensor; the antisymmetric part is denoted as Ω, which is usually called the rotation rate or vorticity tensor.

$$S = 0.5[\frac{\partial u_i}{\partial x_j} + \frac{\partial u_j}{\partial x_i}] \tag{24}$$

$$\Omega = 0.5[\frac{\partial u_i}{\partial x_j} - \frac{\partial u_j}{\partial x_i}] \tag{25}$$

The Q value is defined as the second invariant of the velocity gradient tensor, namely:

$$Q = 0.5[||\Omega||_F^2 - ||S||_F^2] \tag{26}$$

It can be seen from the above formula that the positive value of Q indicates the region where the vorticity is dominant in the flow field, and the negative value indicates the region where the strain rate or viscous stress is dominant. As shown in Figure 14, when the aircraft enters the water at 40°, the cloud diagram of the vorticity changes the Q criterion when entering the water.

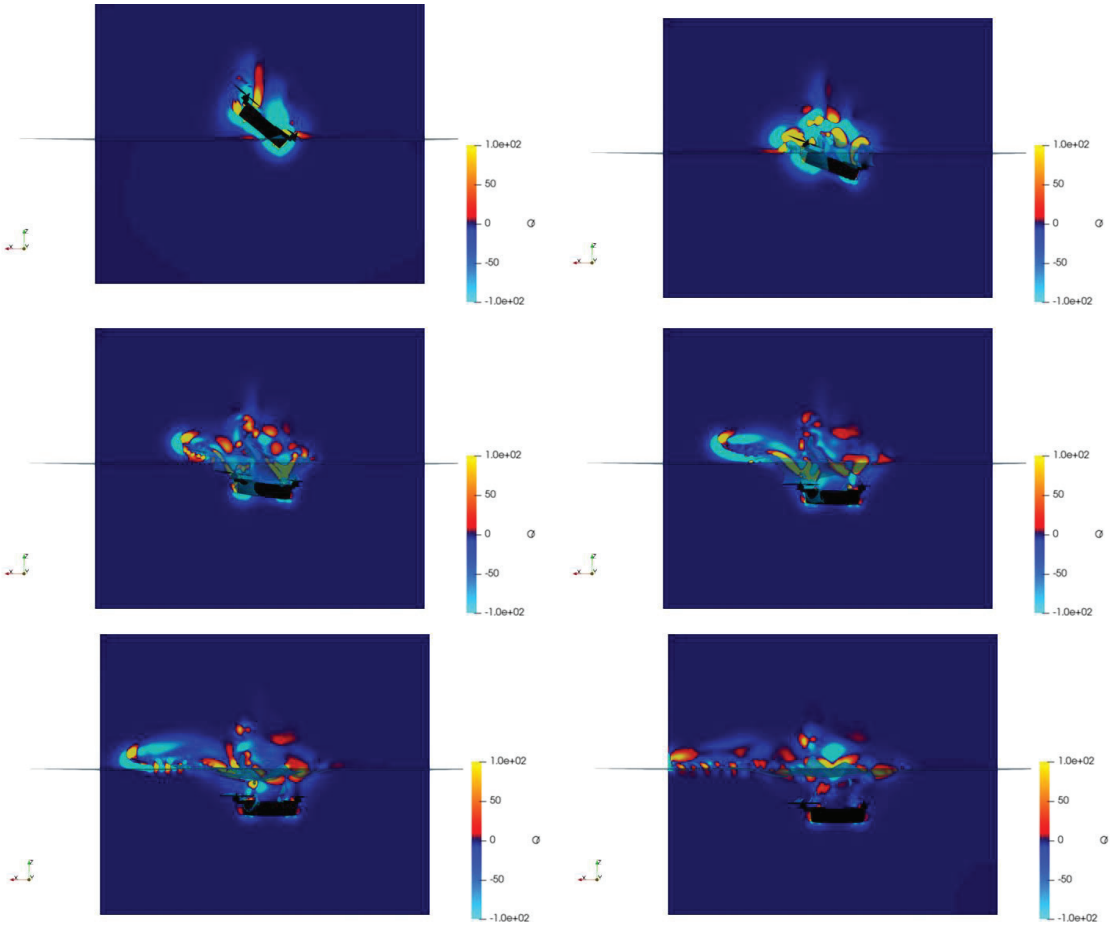

Figure 14. Q-value cloud chart when entering the water at 40°.

The flow mechanism of this changing cloud image reveals that the vortex at the boundary and front end of the aircraft body is mainly affected by shearing, and the continuous development of the cavity leads to the complexity and fragmentation of the positive and negative Q value alternating area of the cavity development. This indicates that the formation of the cavitation region is mainly affected by the joint action of rotation and shear.

4.3.2. Water-Entry Characteristics at Different Heights

This paper explores the aerodynamic characteristics of the vertical entry of the aircraft into the water at different altitudes. The initial conditions for the aircraft are set as follows: the aircraft maintains a vertical attitude and enters the water, and the initial heights of entering the water are set to 0.2 m, 0.3 m, and 0.5 m, respectively. Through the data sampling and analysis of the numerical results of the aircraft entering the water at different heights, the body load impact curves and speed curves suffered by the airframe in the process of entering the water at different heights are obtained, as shown in Figures 15 and 16.

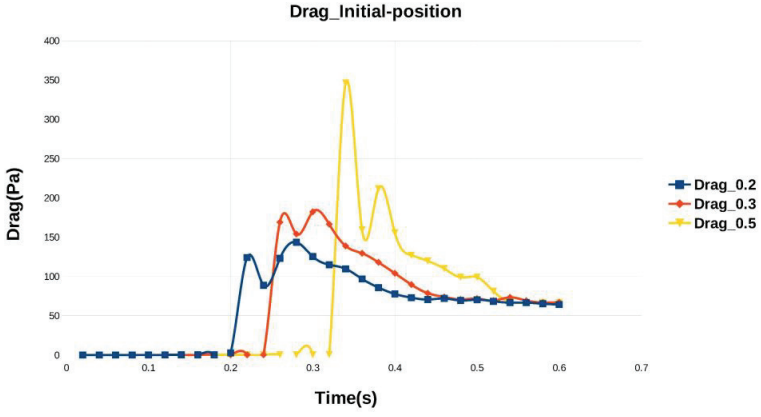

Figure 15. Variation curve of water load impact at different heights.

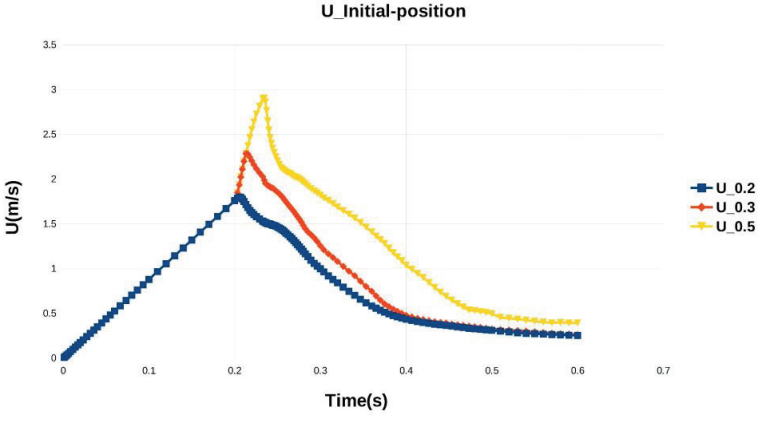

Figure 16. Velocity curves of the body entering the water at different heights.

It can be seen from the curve of load impact change that, when entering the water at different heights, there is a second extreme value in the peak value of the load impact on the body, indicating that in the process of entering the water, there is a periodical change in the load impact of the body in a part of a very short period. This process will produce alternating loads and stress mutations on the body structure, thus reflecting that the structural stability of the trans-medium aircraft needs to be extremely guaranteed.

According to the different water-entry heights, the peak value of the load impact is also different. It can be seen from the curve that as the initial height increases, the water-entry slamming is more severe and the load peak value is also higher. It can be seen from the graph of body speed change that because of the difference in the initial height, the speed at which the aircraft reaches the water–air interface is also different. The impact effect is also more obvious, so the rate of change of its velocity is also greater, and the momentum impact is also stronger.

The Figure 17 shows the cavitation phase transition diagram of the aircraft vertically entering the water at different heights.

Through the above cavitation phase transition diagram, it can be found that when different initial heights enter the water, the degree of fragmentation of the water flow cavitation is different at the moment of water collision. The higher the height, the greater the speed of water entry, and the stronger the degree of cavitation fragmentation. In addition, the bigger it is, the greater the kinetic energy of the body is converted into the kinetic energy of water flow. As mentioned above, the streamlined distribution map of the flow field body is obtained through numerical calculation, as shown in Figure 18.

Through the above-streamlined distribution diagram, it can be found that the velocity field of the overall calculation domain presents a dynamic unsteady change with the evolution of the cavitation phase transition. As the water-entry speed increases, the high-speed area at the tail also gradually moves up. This high-speed area will gradually expand upward and finally form a certain far-field airflow.

4.3.3. Aircraft Water-Exit Characteristics

After the aircraft completes the underwater diving mission, it transitions to the air medium to perform the air flight mission. This process must go through the water-exit action from water to air. The water and air media are quite different, so this process will lead to sudden changes in the body load at the moment of water exit. In addition, the airframe undergoes continuous and stable water resistance load until the load almost disappears, which will also lead to the imbalance of the control of the trans-medium aircraft. Therefore, the numerical prediction of the water-outlet characteristics of the aircraft can provide mechanical sensing analysis for the imbalance adjustment of the controller in the water-outlet stage.

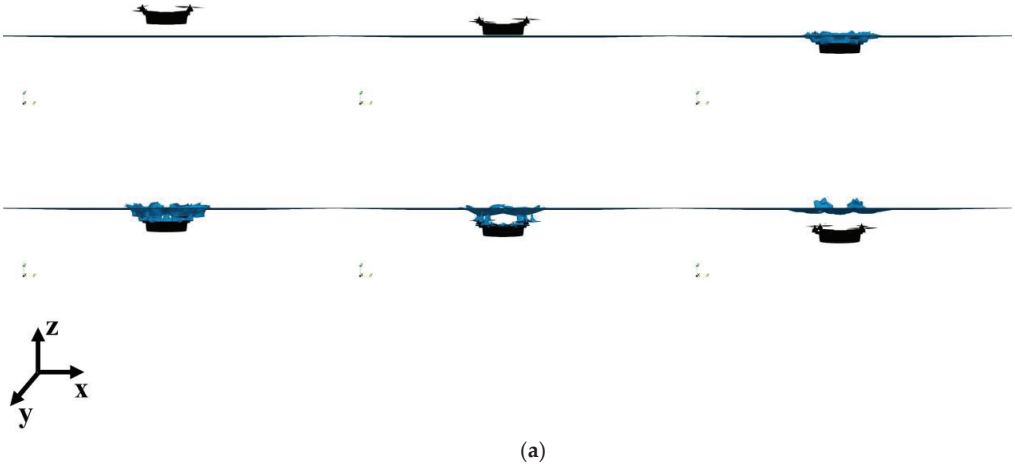

(**a**)

Figure 17. *Cont.*

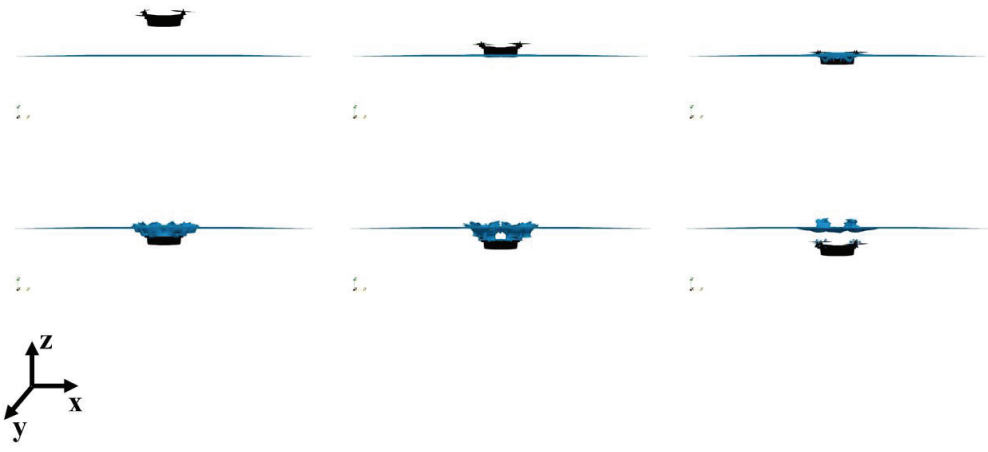

(**b**)

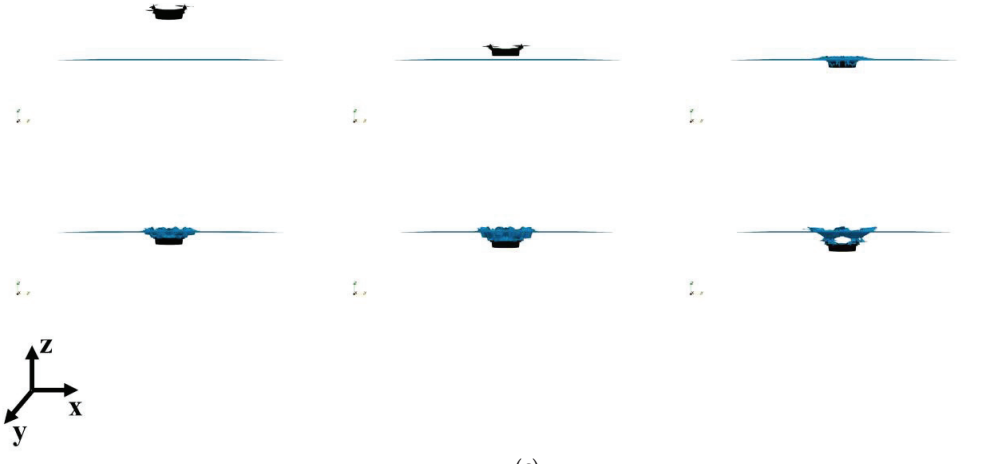

(**c**)

Figure 17. Phase transition diagram of water flows cavitation at different heights: (**a**) 0.2 m high into the water; (**b**) 0.3 m high into the water; (**c**) 0.5 m high into the water.

Consistent with the previous analysis method, based on the OpenFOAM open-source numerical platform, the numerical aerodynamic characteristics of the water-exit process are calculated using the overlapping grid method. The initial conditions are set as follows: the initial speed of the trans-media aircraft is 2 m/s, and the vertical water-exit attitude is used to complete the water-exit process. In the process of the aircraft out of the water, the underwater propellers' upward propulsion close to the water's surface, when the air rotor is exposed to the water's surface, starts the rotor, the underwater propeller, and the air rotor dual thrust to complete the role of leaving the water surface. In the simulation process, the underwater propeller and air rotor are divided into rotating areas, and the stationariness and motion of the rotating areas are controlled to achieve the above physical process. Figure 19 shows the water load change curve of the body.

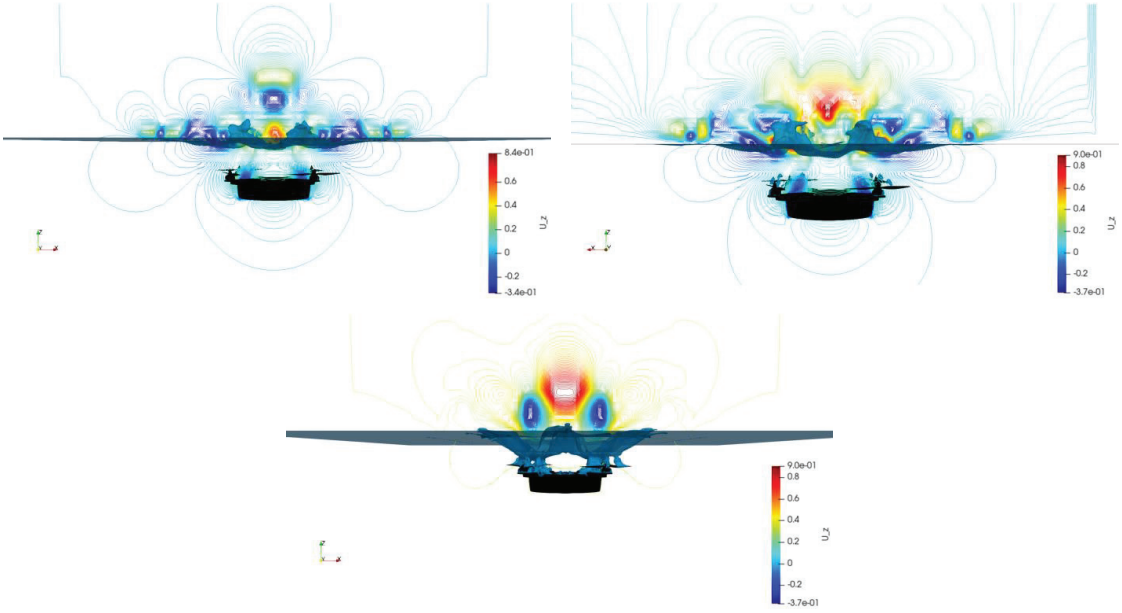

Figure 18. Velocity flow line diagram of the calculation domain under different altitude conditions.

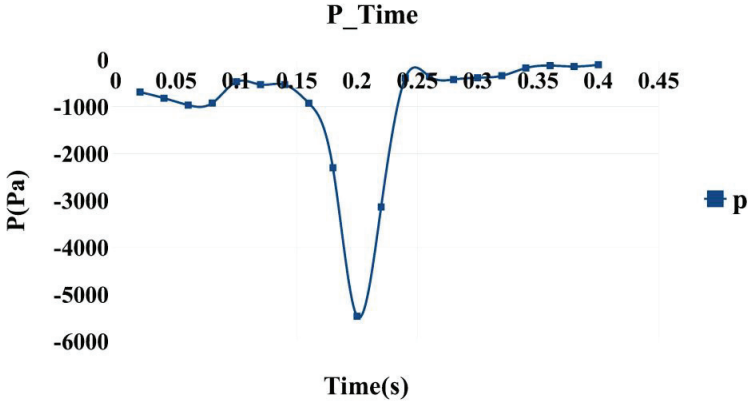

Figure 19. Body water load change curve.

It can be seen from the change curve that as the aircraft gradually moves from the deep-water area to the shallow-water area, the body load will decrease. When approaching the free water surface at a certain initial speed, the impact effect still exists, and the body load will reach the peak value in a short time. When the body jumps out of the water, the load of the body is gradually reduced until the body jumps out of the water completely and the load reaches a smaller value. Due to the inertia effect of the body and the viscosity effect of the water flow during the water exit, the body still entrains the water flow, so the load is still at the same level. The value underwater is almost the same. As it continues to rise, the water flow leaves the fuselage, and the load reaches a minimum value. At this time, the load on the aircraft is equal to that in the air flight stage.

Figure 20 shows the change curve of the attitude angular velocity of the trans-medium aircraft during the water exit.

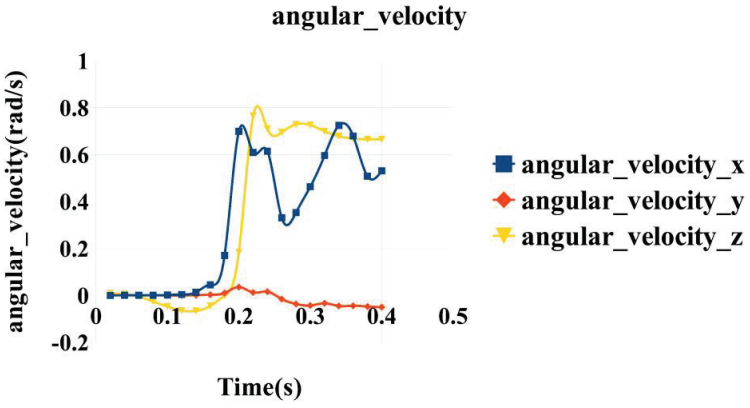

Figure 20. Angular velocity variation curve of aircraft out of water attitude.

Through the analysis of the above angular velocity change curve, it can be seen that the pitch attitude of the aircraft remains stable during the process of exiting the water, while the roll attitude and yaw attitude have some changes because of the disturbance of the water flow in this process, and the change range of the yaw attitude is larger than that of the roll. The attitude is a little bigger, but it remains stable after changing to the peak value, while the roll attitude is irregular and nonlinear under the wave disturbance because the water flow disturbance wave is consistent with the roll direction during the water-discharge process. According to the analysis of the simulated attitude change of the aircraft entering and exiting the water, the controller can be adjusted reasonably, effectively, and stably, thus providing a certain simulation practice basis for the control design of the trans-medium aircraft.

The generation of the above mechanical properties is related to the cavitation phase transition of the water flow during the water-exit process. Through the numerical calculation of the convection field, the schematic diagram of the cavitation phase transition of the water flow during the water exit of the aircraft is obtained, as shown in Figures 21 and 22.

Through the above longitudinal and top-down views of the water flow cavitation phase transition diagram of the aircraft's water-exit process, the analogy with the body load and attitude change results obtained above shows that since the aircraft body is close to the free surface of the water, the influence of the free surface on the water-exit process cannot be ignored. When the aircraft passes through the free surface, the water resistance will suddenly decrease, and it is often asymmetrical concerning the body, which will cause the body to deflect, which is consistent with the attitude change results mentioned above. In addition, the water discharge hits the free liquid surface to cause the liquid level to fluctuate, which further increases the randomness of the water-discharge process. The influence of water flow cavitation on the viscosity of the fuselage during water discharge cannot be ignored, just like the load results of the fuselage mentioned above.

4.4. Research on Water-Entry Characteristics in Wave State

In the real physical environment, the trans-medium aircraft will be impacted by strong nonlinear waves during the process of entering and exiting the water. Therefore, to be close to the real physical scene, the water column impact nonlinear wave is used in the numerical prediction of the aircraft entering and exiting the water in the wave environment. The basic method is as follows: set a water column with a certain height and width in the calculation domain, and these water columns will hit the free water surface under the action of gravity, thereby generating strong nonlinear wave disturbance. The schematic diagram of the shock wave generation is shown in Figure 23.

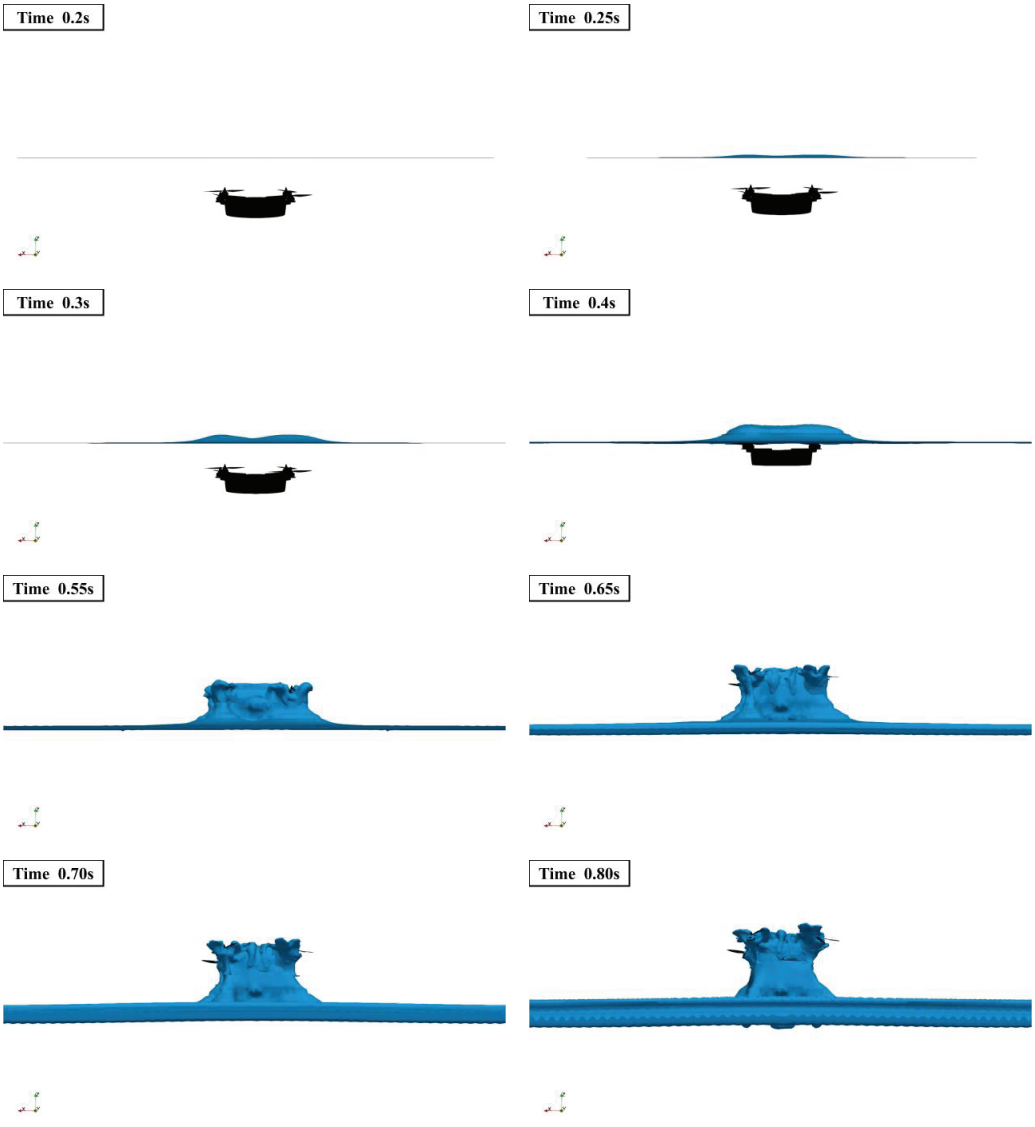

Figure 21. Schematic diagram of cavitation phase transition of water flow in water-outlet process (portrait).

As shown in the figure above, this paper uses a fixed water-column width of 0.7 m and different water-column heights to simulate the wave intensity variable. The idea of variable parameter analysis in this paper has two aspects. On the one hand, under the condition of fixed wave intensity, the aircraft enters the water at different angles. On the other hand, under the condition that the aircraft enters the water at a fixed angle, the water-entry characteristics of the aircraft are analyzed with different wave intensities.

4.4.1. Fixed Wave Intensity (the Height of the Water Column Is a Fixed Value)

Set the height of the water column to 0.2 m, and the aircraft enters the water at 0°, 10°, 20°, 30°, and 40°, respectively. Through numerical calculation, the schematic diagram of the wave height change curve at the central axis position of the calculation domain under different water-entry angles is shown in Figure 24.

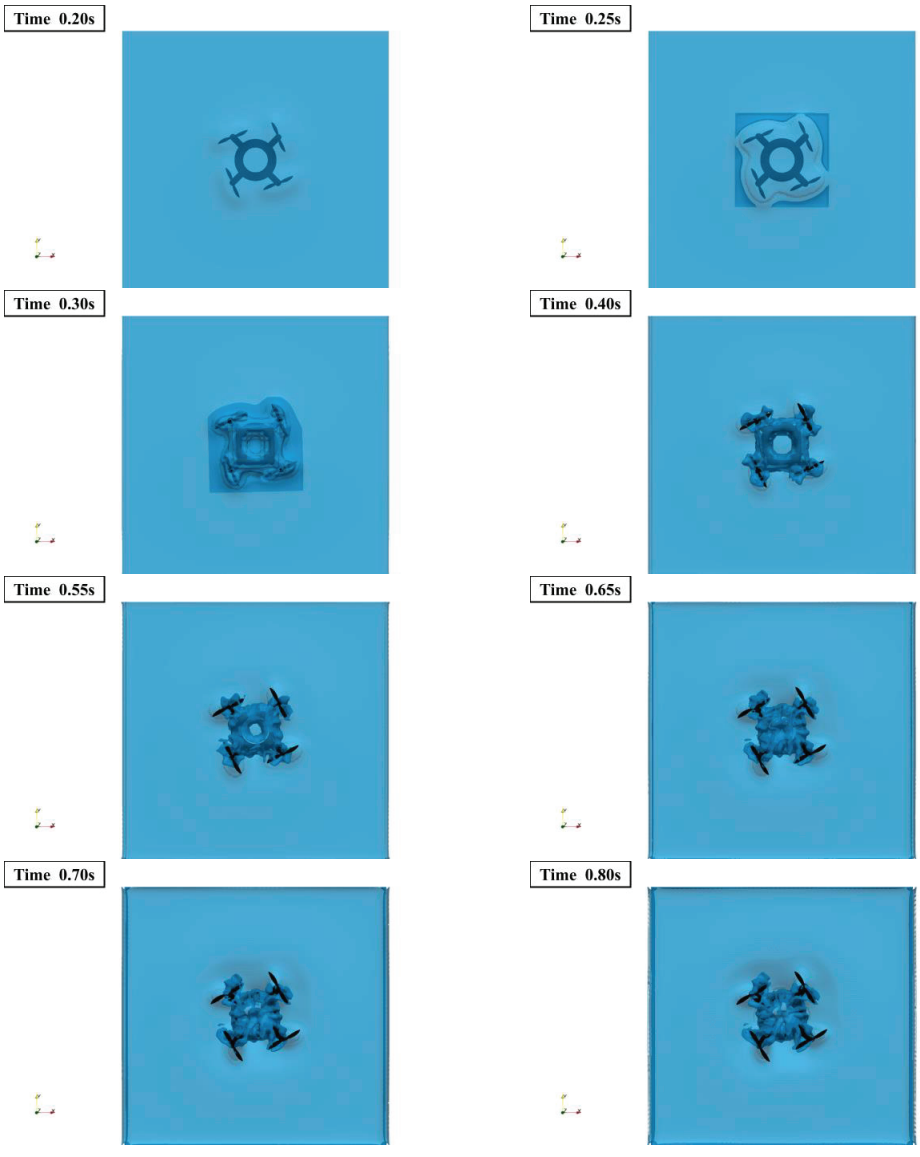

Figure 22. Schematic diagram of cavitation phase transition of water flow in water-outlet process (overlook).

From the changing trend of the above curves, it can be judged that the nonlinearity produced by the water-column impact wave-making method is very strong, which is closer to the real physical scene. It can also be seen from the figure that the wave disturbance on the water surface when entering the water vertically is stronger than that when entering the water obliquely.

By visualizing the calculation results, a schematic diagram of the cavitation evolution of the phase volume fraction of the aircraft entering the water at different angles is obtained, as shown in Figure 25.

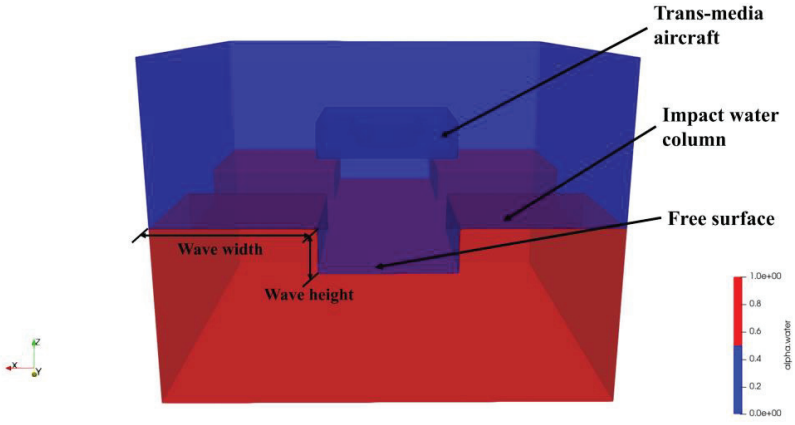

Figure 23. Schematic diagram of shock wave generation.

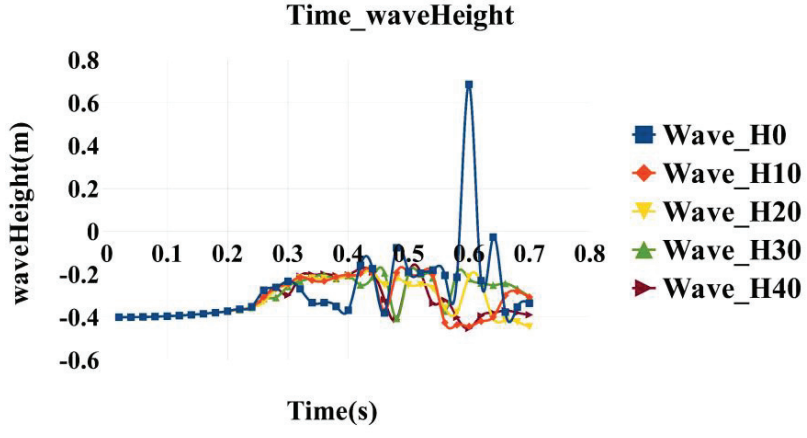

Figure 24. Schematic diagram of wave height curve changes under different water-entry angles.

It can be seen from the schematic diagram of the cavitation evolution of the volume fraction of the water-entry phase from the above-mentioned angles that when the body enters the water vertically, the degree of wave interference is the largest, and the cavitation evolution of the water flow is the most severe; when the body is inclined into the water, the impact of wave disturbance on the body posture is larger. In the case of a small inclination angle, the body posture can naturally achieve self-warming, but as the inclination angle increases, the body posture loses its self-stabilization condition and rolls significantly during the water-entry process because of the drooping impact of waves. Therefore, when it comes to the controller, external interference should be added to make the aircraft perform feedback adjustments under the drooping impact of the wave to achieve stability of the body attitude.

To quantitatively analyze the attitude change of the aircraft, the angular velocity change curves of the aircraft entering the water at different angles are obtained through numerical simulation, as shown in Figure 26.

It can be seen from the above curves that the yaw attitude of the airframe changes significantly in the state of vertical entry into the water, while the pitch and roll attitudes do not change significantly. In the case of entering the water at a small angle, the roll attitude of the body changes slightly because of the impact of waves, and the change in the pitch attitude is a necessary change because of the influence of the restoring moment of the body. After the water-entry process is completed, the body can still achieve stability. When the

body enters the water at a relatively large angle, there is a second peak phenomenon in the pitching angular velocity. The generation of the initial peak value is still affected by the restoration torque. With the completion of the water-entry process, the body cannot achieve self-stabilization conditions because of the excessive water-entry angle under the sagging impact of the waves, resulting in the loss of balance of the body posture, roll posture, and yaw. Attitude will change significantly

Figure 27 is a schematic diagram of the change of the mechanical parameter curve during the body's entry into the water, showing the changing trend of the body's load impact, body speed, and body movement displacement when entering the water at different angles.

It can be seen from the load curve that the load of the body entering the water vertically is greater than the load impact of the oblique entry into the water, and the load under the small angle of the water entry will gradually tend to balance, while the load of the large angle of the water entry will show a nonlinear change that is due to instability. When the body speed enters the water vertically or at a small angle, after the water-entry process is completed, the speed will increase linearly because of the drooping impact of the wave. The large-angle water-entry velocity curve also has a secondary peak phenomenon, which is still caused by the drooping impact of the wave, which causes the body to become unstable, so that the body moves downward in the form of a rollover, which greatly reduces the resistance on the body; thus, this makes the body obtain greater downward speed. It can be seen from the displacement curve that after the body rolls over, the speed increases, resulting in a greater displacement of the body at the same time.

Figure 28 is a binary diagram of the phase volume fraction. Through the binary diagram, we can observe the generation and closure of cavitation under different angles of water entry.

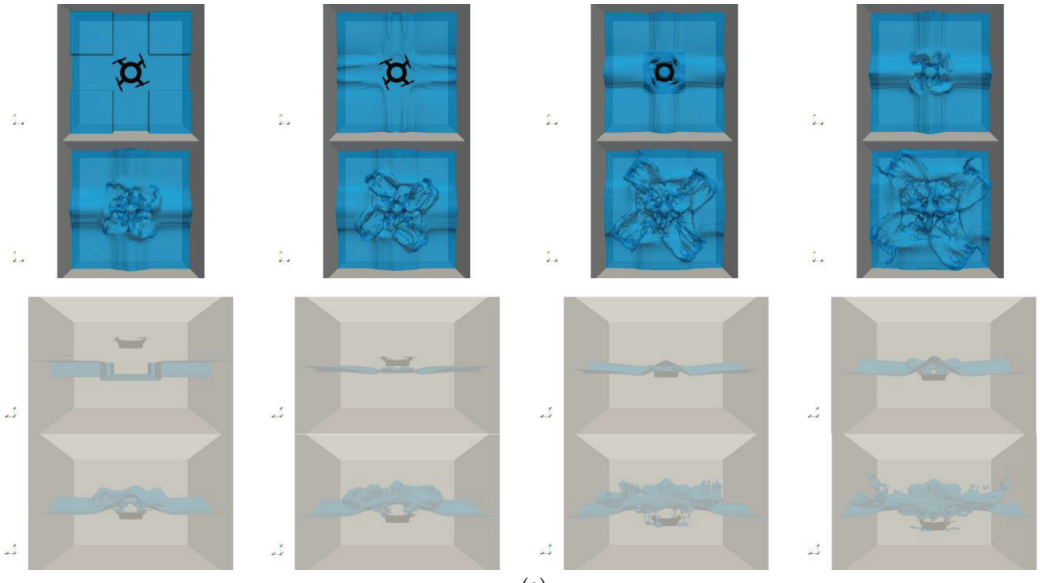

(**a**)

Figure 25. *Cont.*

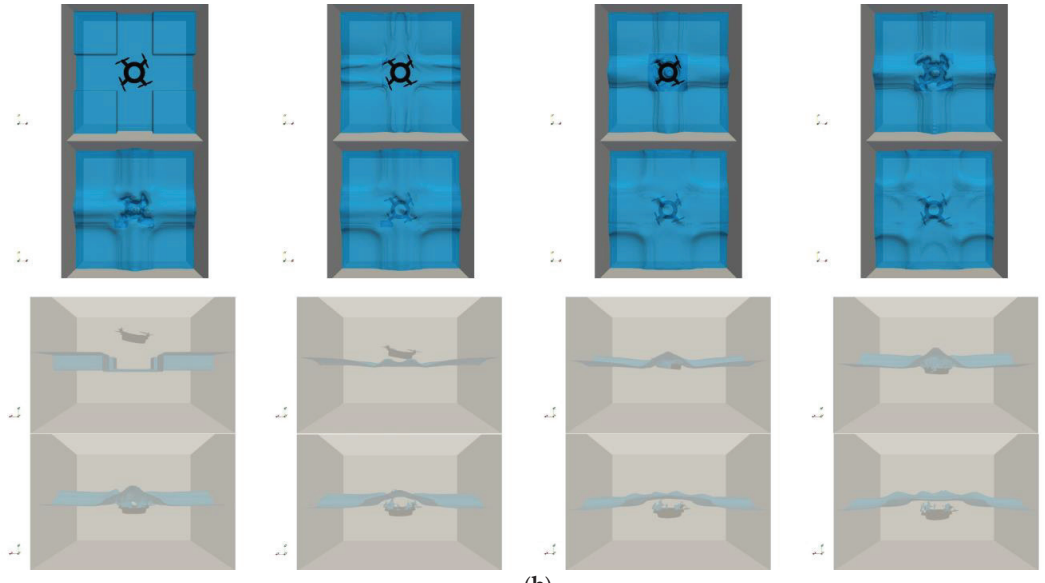

(**b**)

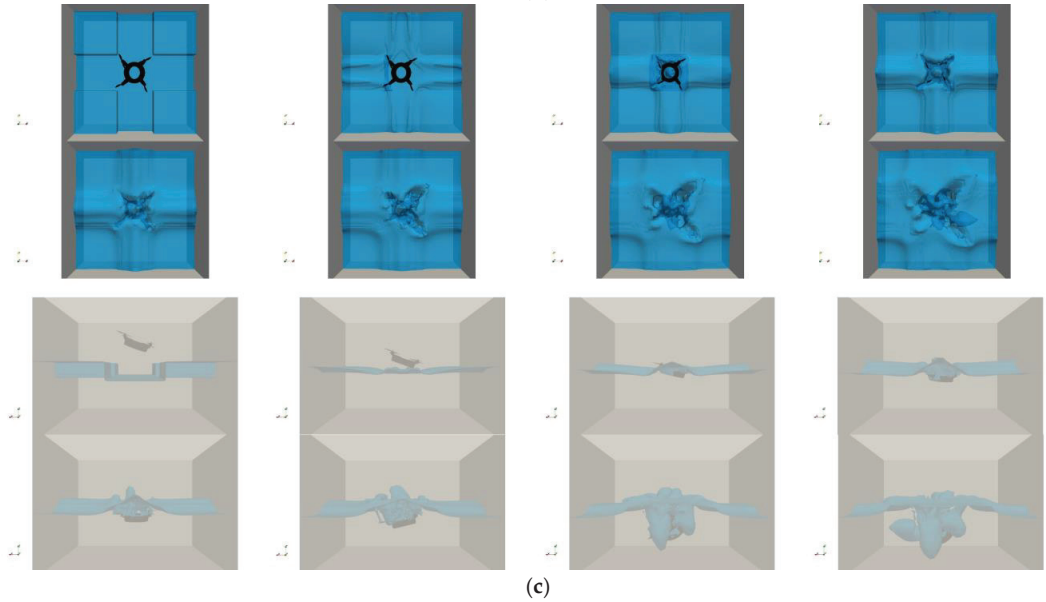

(**c**)

Figure 25. *Cont.*

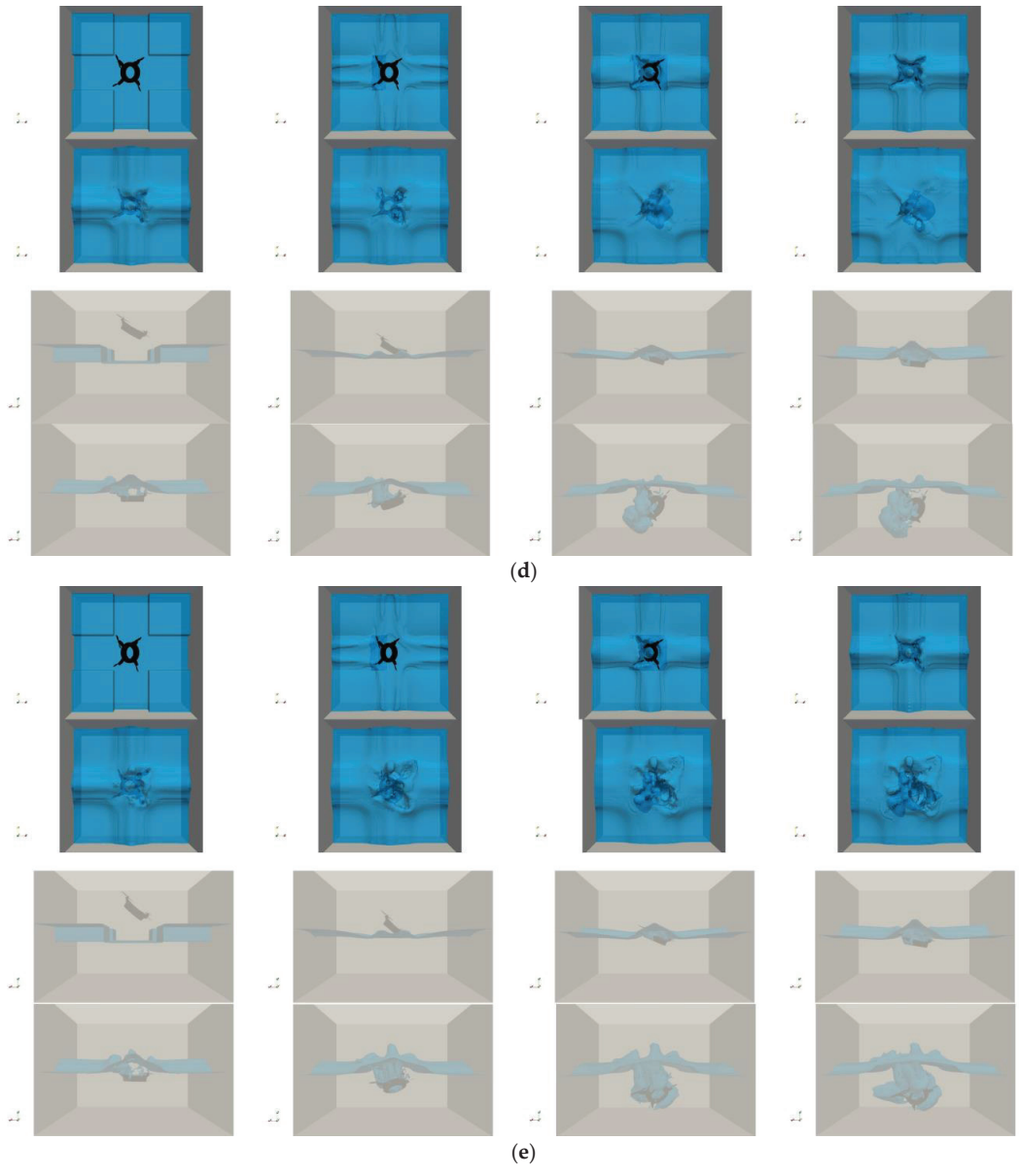

Figure 25. Schematic diagram of cavitation evolution of water phase volume fraction at different angles: (**a**–**e**) are, respectively, 0°, 10°, 20°, 30°, and 40° into the water.

To visualize the impact of wave drooping on the body, this paper performs post-processing on the velocity flow field in the calculation domain to obtain the flow field velocity streamline diagram in the vertical direction, as shown in Figure 29.

Through the visual streamline diagram processing, under the condition of large-angle water entry, the impact of wave drooping impact on the rollover of the body can be seen. When the angle of the body deviates to one side, the drooping force of the wave will form a flow around this place, so that the body that is already inclined cannot maintain its original state. This is the root cause of the body rollover.

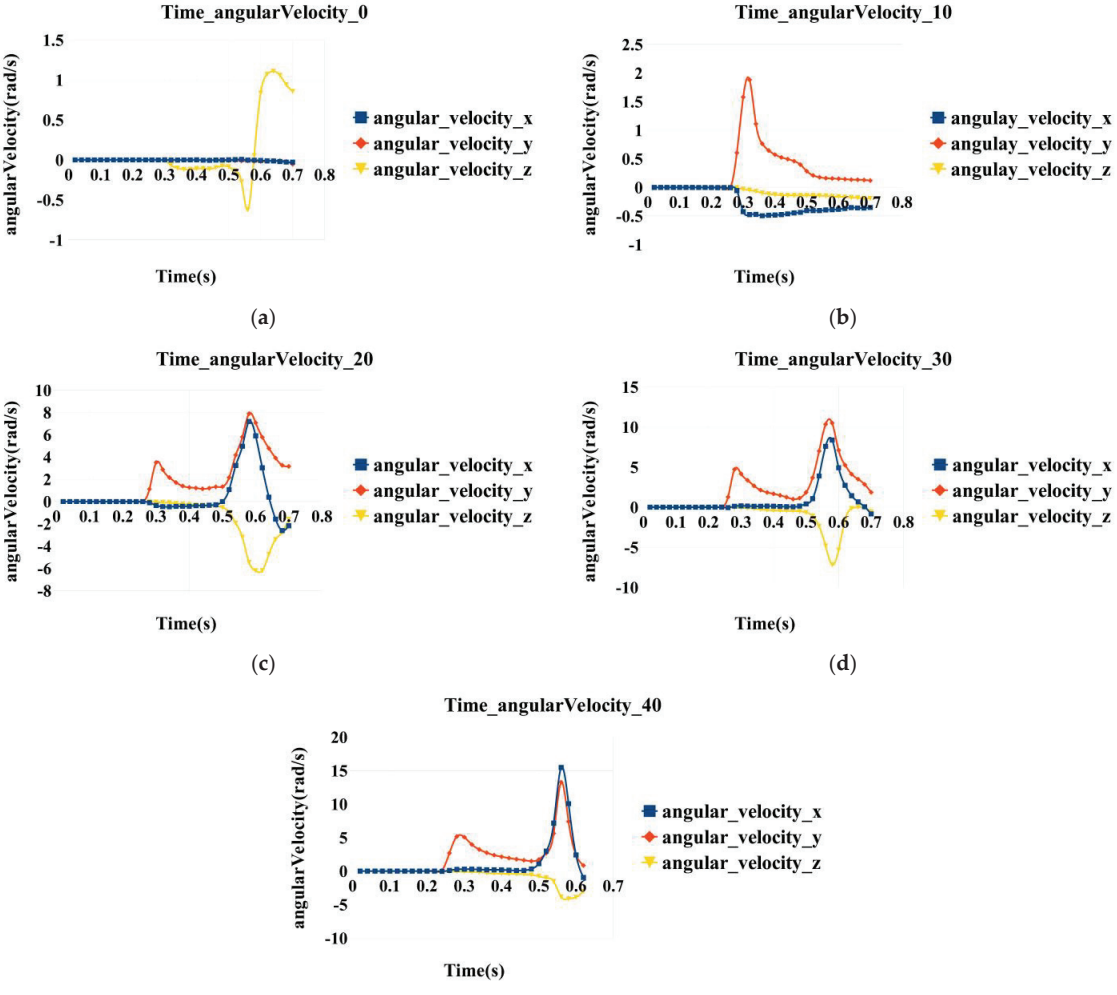

Figure 26. Schematic diagram of the angular velocity change curve of entering the water at different angles: (**a**–**e**) are, respectively, 0°, 10°, 20°, 30°, and 40° into the water.

4.4.2. Fixed Water-Entry Angle (Changes Wave Intensity)

Enter the water at a fixed angle of 40° and create waves of different intensities by changing the height of the impacting water column. In this paper, the heights of the impacting water columns are set to be 0.2 m, 0.3 m, and 0.4 m, respectively. Under different wave intensities, the wave height curves at the central axis of the calculation domain are obtained, as shown in Figure 30.

Similar to the previous ones, the generated waves have strong nonlinearity, which is close to the scene of real aircraft entering the water.

Figure 31 is a schematic diagram of the cavitation evolution of the phase volume fraction caused by the body entering the water at an angle of 40° under different wave intensities.

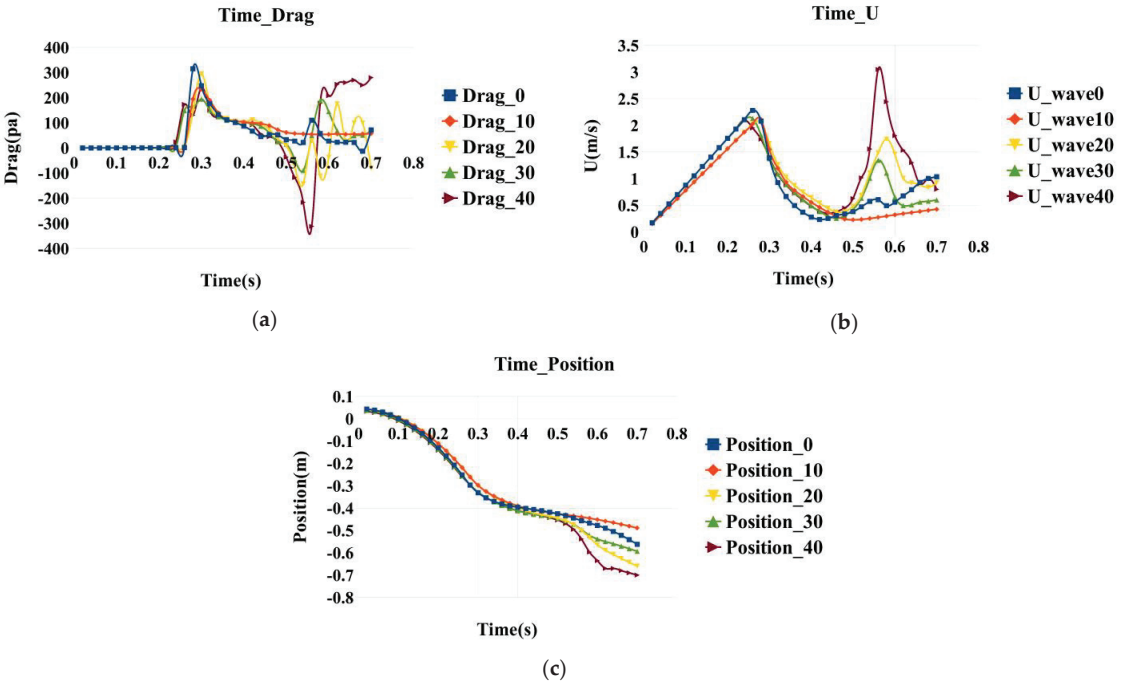

Figure 27. Schematic diagram of the change curve of the mechanical parameters of the body: (**a**) body load impact; (**b**) body movement speed; (**c**) body motion displacement.

From the figure above, it can be seen that in the calculation time of 0.6 s, the aircraft was unstable when the height of the water column was 0.2 m, but it was not unstable when the height of the water column was 0.3 m and 0.4 m. This is because, with the increase in the height of the impacting water column, the wave strength is too large, so that when the water column initially sinks, the weight of the body cannot overcome the influence of the wave force, so that the body obtains an upward moment, which cancels out the rollover moment. Therefore, the aircraft can still realize the self-stabilizing condition in a short time. With the arrival of the next wave-dropping moment, the body will still roll over and become unstable.

The Figure 32 shows the change curve of the mechanical characteristics of the body, which is similar to the previous one. They are the change curve of the body load, the change curve of the body motion speed, and the change curve of the body motion displacement.

It can also be seen from the above mechanical characteristic curve that when the wave intensity is too large, the body will be temporarily given an upward wave moment to maintain the posture balance. Through the speed curve, it can be seen that under the condition of the highest wave intensity, such an upward wave moment will temporarily change the speed direction of the body and make the body move upward.

To show the evolution law of water flow cavitation more intuitively, similar to the above, a binary map of the phase volume fraction of the body entering the water is extracted, as shown in Figure 33.

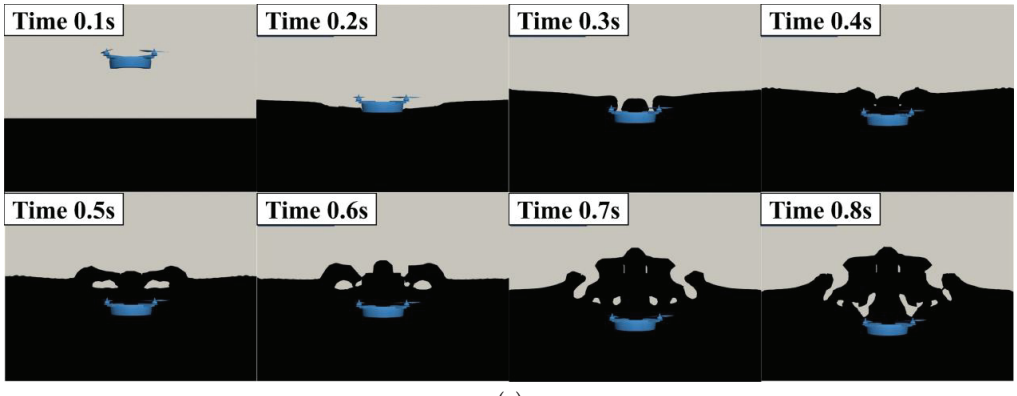

(**a**)

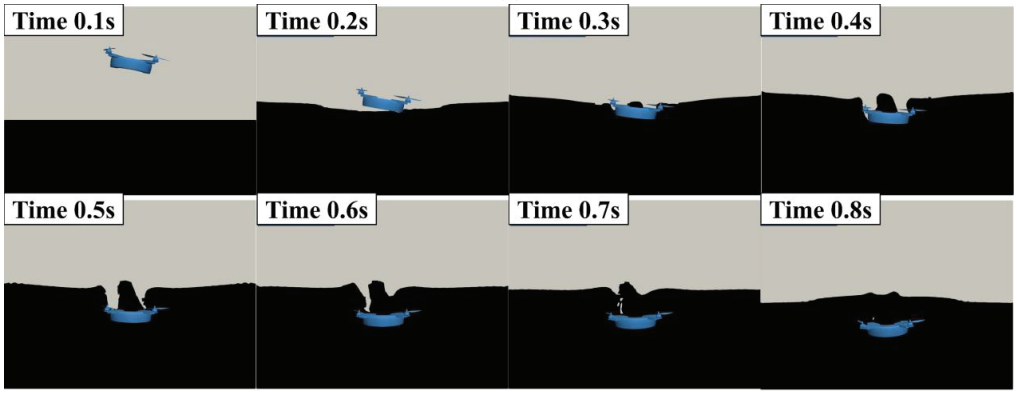

(**b**)

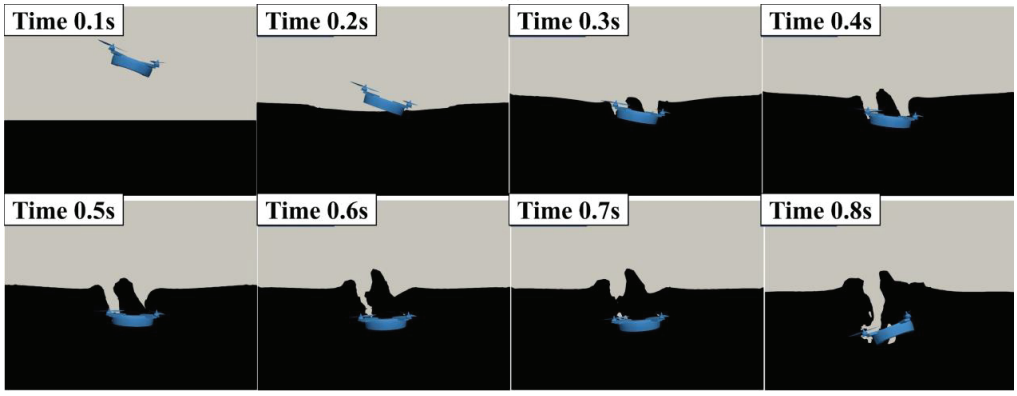

(**c**)

Figure 28. *Cont.*

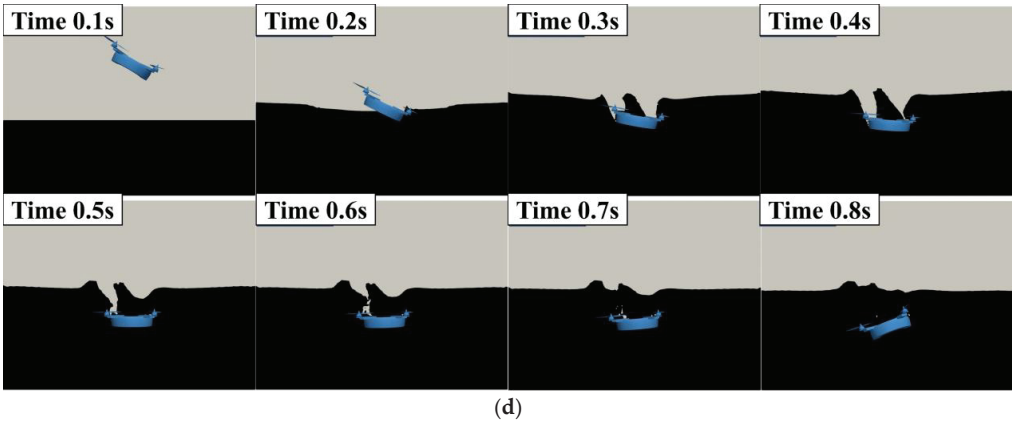

(**d**)

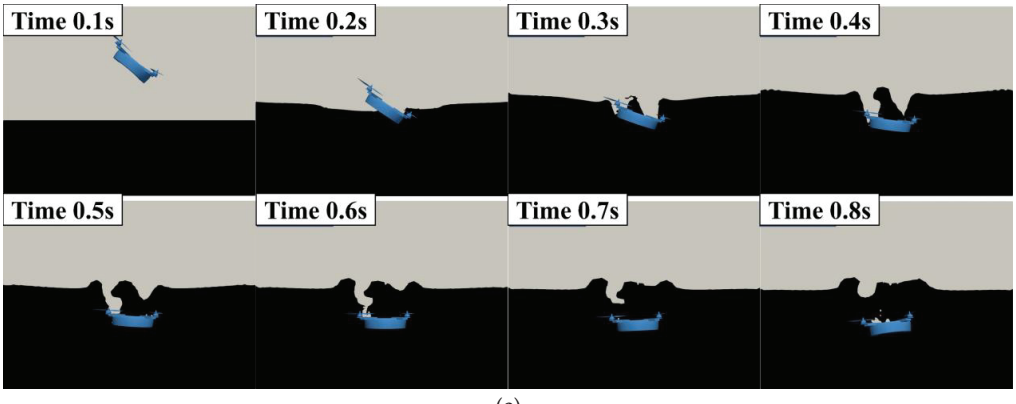

(**e**)

Figure 28. Phase volume fraction binary map: (**a**–**e**) are, respectively, 0°, 10°, 20°, 30°, and 40° into the water.

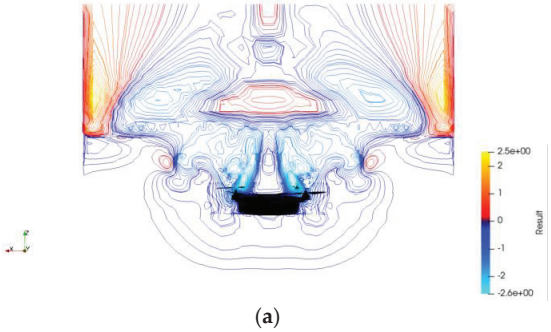

(**a**)

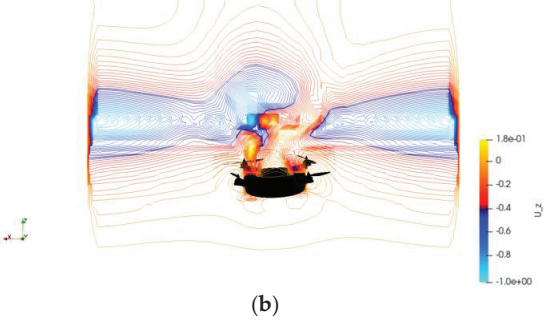

(**b**)

Figure 29. *Cont.*

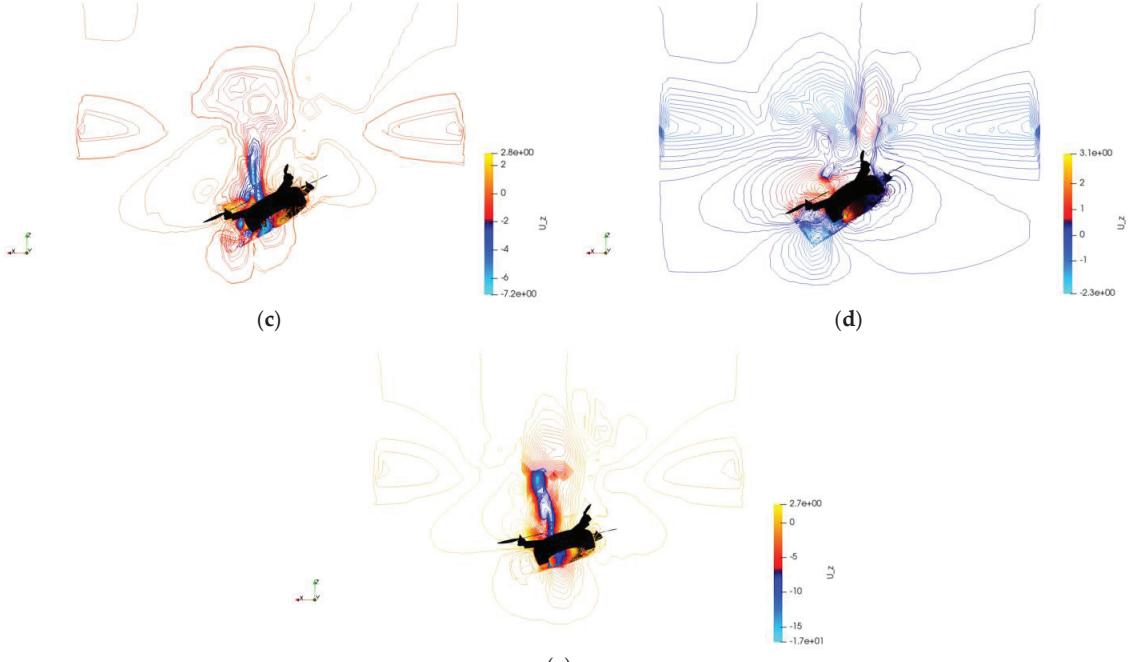

(**c**) (**d**)

(**e**)

Figure 29. Schematic diagram of vertical velocity streamlines in the computational domain flow field: (**a**–**e**) are, respectively, 0°, 10°, 20°, 30°, and 40° into the water.

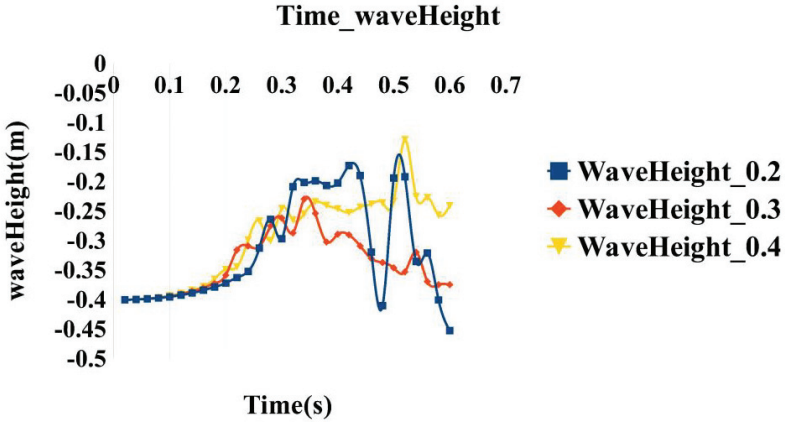

Figure 30. Variation curves of wave height at the central axis position under different wave intensities.

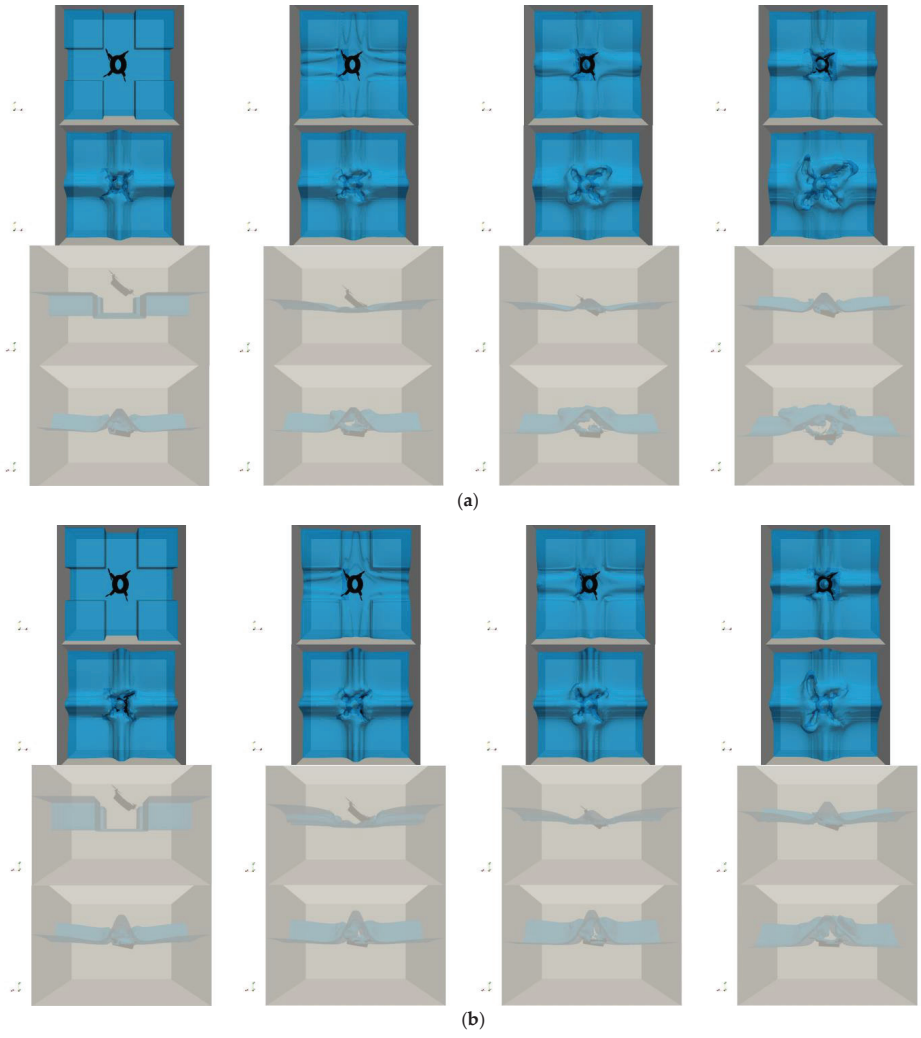

(**a**)

(**b**)

Figure 31. Schematic diagram of cavitation evolution: (**a**) 0.3 m; (**b**) 0.4 m.

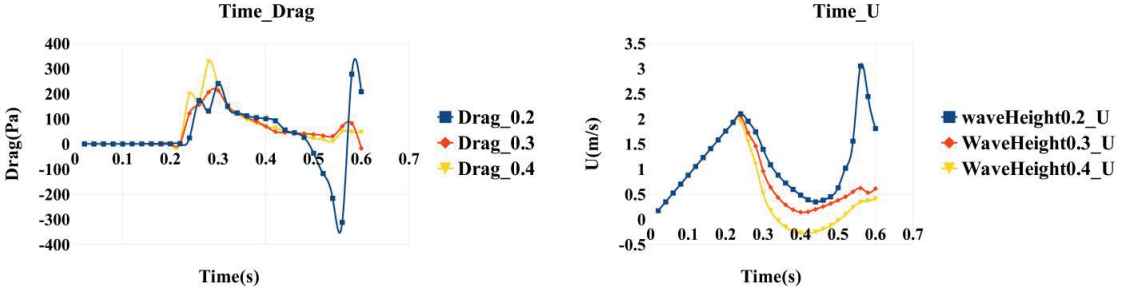

(**a**) (**b**)

Figure 32. *Cont.*

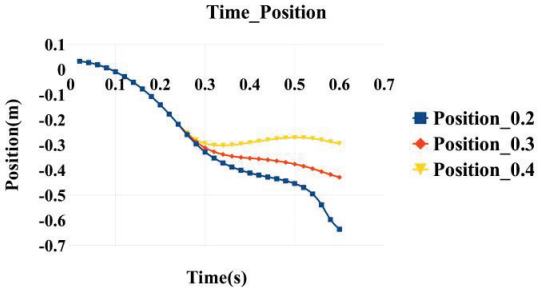

(**c**)

Figure 32. The mechanical characteristic curves of the body: (**a**) load curve; (**b**) speed curve; (**c**) displacement curve.

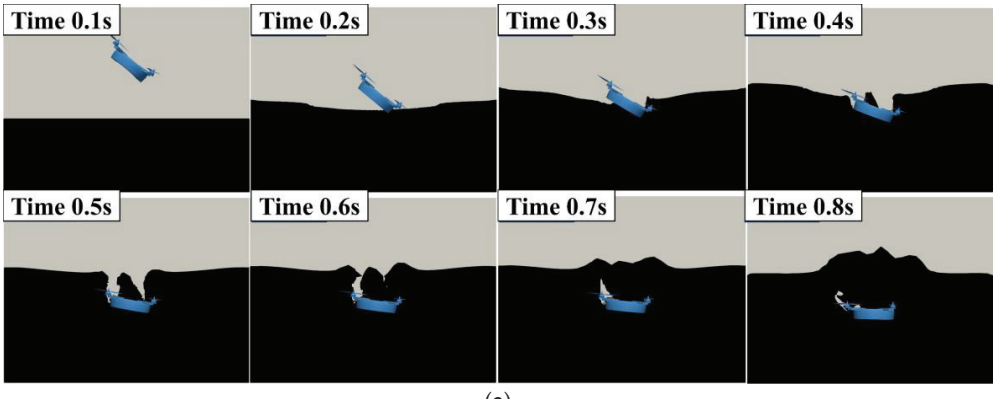

(**a**)

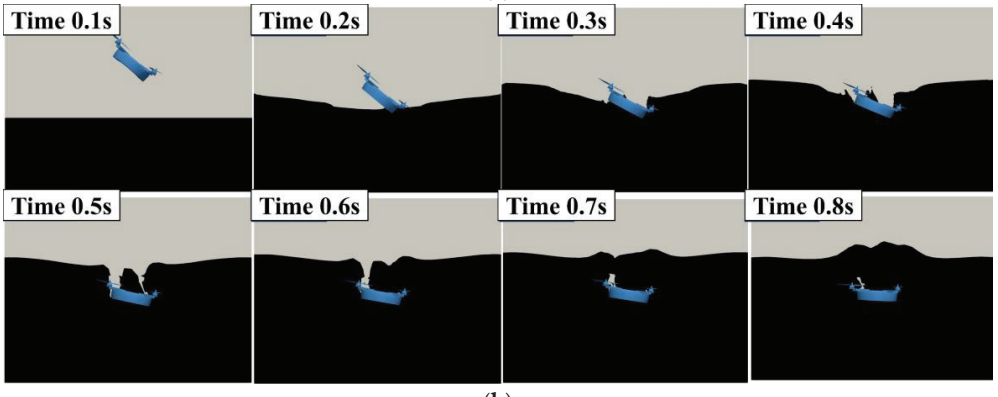

(**b**)

Figure 33. Phase volume fraction binary map: (**a**) 0.3 m; (**b**) 0.4 m.

The above binary diagram clearly shows the evolution diagram of water-entry cavitation under two different wave intensities. As mentioned above, under the action of upward wave torque, the body gradually achieves self-stabilization in a short period. The expansion and closure of the cavity during the water-entry process have also been displayed.

5. Conclusions

In this paper, the VOF method with overset meshes is used to capture the air–water interface for vehicle entry into the water, and the results of mechanical properties are obtained for different angles and different heights under static water conditions and different angles and different wave intensities under wave conditions. Under still water conditions, due to the great disparity of the water–air medium, a restoring moment opposite to the tilt direction will be generated during the tilt angle entering the water, resulting in obvious changes in the pitching attitude of the aircraft. Under the condition of small wave intensity, after the body enters the water at a large angle, due to the influence of the wave-dropping moment, the attitude of the body will be unstable and rollover will occur. Under the condition of large wave intensity, due to the large drooping moment squeezing the fluid around the body, the body generates an upward moment, which cancels out the rollover moment, so that the body can achieve attitude balance in a short time. Through the analysis of the load curve graph of the body into the water and the horizontal projection view of the phase volume fraction, we know that in the horizontal projection, the area of the water bubble evolution of the vertical water entry is larger, resulting in the vertical resistance to the body also being larger, and the submersion speed also being slower. Therefore, the vertical resistance to water entry can be reduced by tilting the water entry at a certain angle. The above research on the hydraulic mechanism of entry and exit provides a theoretical basis for the design of the medium-crossing controller of trans-medium aircraft.

The different stages through which the trans-media vehicle enters the water are analyzed by the schematic diagram of the evolution of the water bubble for different operating conditions as follows:

(1) At the beginning of the water entry, the wet water area of the vehicle increases rapidly, and if the speed of entry is relatively large, there will be a relatively stable vacuole separation line; the water is separated from the surface of the body, and the entry vacuole begins to form.
(2) After the vehicle enters the water for a period of time, the vacuole will be connected to the atmosphere; air continues to fill the rear space of the object entering the water, and the vacuole continues to increase, which is partly air and partly steam. As the vacuole increases, the buoyancy force on the vehicle increases.
(3) The next step in the development of the incoming vacuole is the closure of the vacuole, where the air on the surface of the water no longer enters the vacuole. When the forces that determine vacuole closure (hydrostatic pressure, dynamic pressure of air flowing in the vacuole, and surface tension) dominate, the vacuole begins to narrow, neck, and finally close. When the bubble closes, the waters moving inward collide together and produce upward and downward water jets.
(4) After the bubble is closed, as the object continues to move, the bubble, due to the water hostage effect, gradually reduces to completely disappear. After the disappearance of the air bubble, the object in the water begins to enter the full wetting motion; at this time, the object is far from the free surface of the water, and the free surface of the flow of the impact can be disregarded. The flow is unbounded.

Author Contributions: Conceptualization, J.W. and Y.-L.C.; methodology, J.W.; software, D.Z.; validation, D.-P.C.; formal analysis, J.W.; investigation, Z.C.; resources, J.W. and Y.-L.C.; data curation, J.W.; writing—original draft preparation, J.W.; writing—review and editing, J.W.; visualization, J.W.; supervision, Y.-L.C.; project administration, X.-Y.H.; funding acquisition, Y.-B.S. All authors have read and agreed to the published version of the manuscript.

Funding: This research received no external funding.

Data Availability Statement: Not applicable.

Acknowledgments: This work is supported by the Jilin Province Key Science and Technology R&D project under Grant No. 20210203175SF, the Aeronautical Science Foundation of China under Grant No. 2019ZA0R4001, the National Natural Science Foundation of China under Grant No. 51505174,

the Foundation of Education Bureau of Jilin Province under Grant No. JJKH20220988KJ, and the Interdisciplinary Integration, Innovation, and Cultivation Project of Jilin University under Grant No. JLUXKJC2020105.

Conflicts of Interest: The authors declare no conflict of interest.

References

1. Ma, Z.; Chen, D.; Li, G.; Jing, X.; Xiao, S. Configuration Design and Trans-Media Control Status of the Hybrid Aerial Underwater Vehicles. *Appl. Sci.* **2022**, *12*, 765. [CrossRef]
2. Zhang, X.; Huang, J.; Huang, Y.; Huang, K.; Yang, L.; Han, Y.; Wang, L.; Liu, H.; Luo, J.; Li, J. Intelligent amphibious ground-aerial vehicles: State of the art technology for future transportation. *IEEE Trans. Intell. Veh.* **2022**, 1–19. [CrossRef]
3. Bi, Y.; Lu, D.; Zeng, Z.; Lian, L. Dynamics, and control of hybrid aerial underwater vehicle subject to disturbances. *Ocean Eng.* **2022**, *250*, 110933. [CrossRef]
4. Shi, Y.; Pan, G.; Yim, S.C.; Yan, G.; Zhang, D. Numerical investigation of hydroelastic water-entry impact dynamics of AUVs. *J. Fluids Struct.* **2019**, *91*, 102760. [CrossRef]
5. Zhou, D.-H.; Shi, H.-H.; Jia, H.-X. Characteristics of the multiphase flow field with super-cavitation induced by successively fired projectiles under-water and cross-medium. *J. Mech. Sci. Technol.* **2022**, *36*, 247–258. [CrossRef]
6. Shi, Y.; Pan, G.; Yan, G.-X.; Yim, S.C.; Jiang, J. Numerical study on the cavity characteristics and impact loads of AUV water entry. *Appl. Ocean Res.* **2019**, *89*, 44–58. [CrossRef]
7. Huang, L.; Ren, K.; Li, M.; Tuković, Ž.; Cardiff, P.; Thomas, G. Fluid-structure interaction of a large ice sheet in waves. *Ocean Eng.* **2019**, *182*, 102–111. [CrossRef]
8. Shi, F.; Xin, J.; Jin, Q. A Cartesian grid based multiphase flow model for water impact of an arbitrary complex body. *Int. J. Multiph. Flow* **2019**, *110*, 132–147. [CrossRef]
9. Wu, Q.; Ni, B.; Bai, X.; Cui, B.; Sun, S. Experimental study on large deformation of free surface during water exit of a sphere. *Ocean Eng.* **2017**, *140*, 369–376. [CrossRef]
10. Peng, B.; Zhou, C. An approach of dynamic mesh adaptation for simulating 3-dimensional unsteady moving-immersed-boundary flows. *Int. J. Numer. Methods Fluids* **2018**, *87*, 180–201. [CrossRef]
11. Xin, J.; Shi, F.; Fan, S.; Jin, Q.; Chang, X. Parametric studies on the water impact of one and twin free-falling wedges by a Cartesian grid multiphase flow model. *Ocean Eng.* **2022**, *249*, 110854. [CrossRef]
12. Osher, S.; Sethian, J.A. Fronts propagating with curvature-dependent speed: Algorithms based on Hamilton-Jacobi formulations. *J. Comput. Phys.* **1988**, *79*, 12–49. [CrossRef]
13. Osher, S.; Fedkiw, R.P. Level set methods: An overview and some recent results. *J. Comput. Phys.* **2001**, *169*, 463–502. [CrossRef]
14. Chang, Y.-C.; Hou, T.; Merriman, B.; Osher, S. A level set formulation of Eulerian interface capturing methods for incompressible fluid flows. *J. Comput. Phys.* **1996**, *124*, 449–464. [CrossRef]
15. Sussman, M.; Fatemi, E.; Smereka, P.; Osher, S. An improved level set method for incompressible two-phase flows. *Comput. Fluids* **1998**, *27*, 663–680. [CrossRef]
16. Yang, C.; Mao, Z.-S. An improved level set approach to the simulation of drop and bubble motion. *Chin. J. Chem. Eng. Engl. Version* **2002**, *10*, 263–272.
17. Marchandise, E.; Remacle, J.-F. A stabilized finite element method using a discontinuous level set approach for solving two phase incompressible flows. *J. Comput. Phys.* **2006**, *219*, 780–800. [CrossRef]
18. Sethian, J.A.; Smereka, P. Level set methods for fluid interfaces. *Annu. Rev. Fluid Mech.* **2003**, *35*, 341–372. [CrossRef]
19. Olsson, E.; Kreiss, G. A conservative level set method for two phase flow. *J. Comput. Phys.* **2005**, *210*, 225–246. [CrossRef]
20. Hirt, C.W.; Nichols, B.D. Volume of fluid (VOF) method for the dynamics of free boundaries. *J. Comput. Phys.* **1981**, *39*, 201–225. [CrossRef]
21. Rider, W.J.; Kothe, D.B. Reconstructing volume tracking. *J. Comput. Phys.* **1998**, *141*, 112–152. [CrossRef]
22. Harvie, D.J.; Fletcher, D.F. A new volume of fluid advection algorithm: The stream scheme. *J. Comput. Phys.* **2000**, *162*, 1–32. [CrossRef]
23. Cifani, P.; Michalek, W.; Priems, G.; Kuerten, J.G.; van der Geld, C.; Geurts, B.J. A comparison between the surface compression method and an interface reconstruction method for the VOF approach. *Comput. Fluids* **2016**, *136*, 421–435. [CrossRef]
24. Ashgriz, N.; Poo, J. FLAIR: Flux line-segment model for advection and interface reconstruction. *J. Comput. Phys.* **1991**, *93*, 449–468. [CrossRef]
25. Youngs, D.L. Time-dependent multi-material flow with large fluid distortion. In *Numerical Methods in Fluid Dynamics*; Academic Press: Cambridge, MA, USA, 1982.
26. Yang, A.-S.; Yang, J.-C.; Hong, M.-C. Droplet ejection study of a Picojet printhead. *J. Micromechanics Microengineering* **2005**, *16*, 180. [CrossRef]
27. Meier, M.; Yadigaroglu, G.; Smith, B.L. A novel technique for including surface tension in PLIC-VOF methods. *Eur. J. Mech. -B/Fluids* **2002**, *21*, 61–73. [CrossRef]
28. Sussman, M.; Puckett, E.G. A coupled level set and volume-of-fluid method for computing 3D and axisymmetric incompressible two-phase flows. *J. Comput. Phys.* **2000**, *162*, 301–337. [CrossRef]

29. Lv, X.; Zou, Q.; Reeve, D. Numerical simulation of overflow at vertical weirs using a hybrid level set/VOF method. *Adv. Water Resour.* **2011**, *34*, 1320–1334. [CrossRef]
30. Wang, Z.; Yang, J.; Koo, B.; Stern, F. A coupled level set and volume-of-fluid method for sharp interface simulation of plunging breaking waves. *Int. J. Multiph. Flow* **2009**, *35*, 227–246. [CrossRef]
31. Liu, D.; Tang, W.; Wang, J.; Xue, H.; Wang, K. Modelling of liquid sloshing using CLSVOF method and very large eddy simulation. *Ocean Eng.* **2017**, *129*, 160–176. [CrossRef]
32. Sun, D.; Tao, W. A coupled volume-of-fluid and level set (VOSET) method for computing incompressible two-phase flows. *Int. J. Heat Mass Transf.* **2010**, *53*, 645–655. [CrossRef]
33. Zhao, L.; Shkarayev, S. Characterization of ducted contra-rotating propeller propulsions. *Int. J. Micro Air Veh.* **2019**, *11*, 1756829319837661. [CrossRef]
34. Noh, W.F.; Woodward, P. SLIC (simple line interface calculation). In Proceedings of the Fifth International Conference on Numerical Methods in Fluid Dynamics, Twente University, Enschede, The Netherlands, 28 June–2 July 1976; pp. 330–340.
35. Lopez, J.; Hernandez, J.; Gomez, P.; Faura, F. An improved PLIC-VOF method for tracking thin fluid structures in incompressible two-phase flows. *J. Comput. Phys.* **2005**, *208*, 51–74. [CrossRef]
36. Roenby, J.; Larsen, B.E.; Bredmose, H.; Jasak, H. A new volume-of-fluid method in OpenFOAM. In Proceedings of the MARINE VI: Proceedings of the VI International Conference on Computational Methods in Marine Engineering, Nantes, France, 5–17 May 2017; pp. 266–277.
37. Eymard, R.; Gallouët, T.; Herbin, R. Finite volume methods. *Handb. Numer. Anal.* **2000**, *7*, 713–1018.
38. Weller, H. *A Code Independent Notation for Finite Volume Algorithms*; Technical Report TR/HGW/02; Nabla Ltd.: Port Louis, Mauritius, 2002.
39. Dubief, Y.; Delcayre, F. On coherent-vortex identification in turbulence. *J. Turbul.* **2000**, *1*, N11. [CrossRef]

drones

MDPI

Article

A Computational Investigation of the Hover Mechanism of an Innovated Disc-Shaped VTOL UAV

Samia Shahrin Ahmed Snikdha * and Shih-Hsiung Chen

Department of Aeronautics and Astronautics (DAA), College of Engineering, National Cheng Kung University, No. 1, University Rd, East District, Tainan City 701, Taiwan
* Correspondence: p48087065@gs.ncku.edu.tw

Abstract: Inventive approaches are constantly being revealed in the field of vertical take-off and landing (VTOL) unmanned aerial vehicle (UAV) configuration concepts and designs. To date, a body-associated configuration of UAVs for augmented lift remains unclear among other approached designs. The current paper investigates the mechanism of a high-lift ducted fan mounted in the central body for VTOL UAV designs. We report an unresolved design of a disc-shaped UAV with a single rotor that aims to enhance the cost-effectiveness of fuel consumption with a substantial contribution of body lift to hover thrust. The convex upper surface curvature was applied to generate a significant lift contribution from the body during hover. The computational fluid dynamics (CFD) approach based on unstructured discretization followed by three-dimensional steady Reynolds-averaged Navier–Stokes (RANS) flow was applied in ANSYS CFX to mechanistically investigate the underlying design considerations. The disc-shaped UAV uses the lip curvature on the duct inlet to generate a vertical force that demonstrates a significant contribution of 95% of the rotor thrust during hovering. The UAV's upper surface generates prolonged flow entrainment free from momentum losses in swirling flows. This phenomenon is followed by reduced power consumption in hovering and vertical flight, making the UAV aerodynamically stable and environmentally safe.

Keywords: computational fluid dynamics (CFD); VTOL UAV; disc-shaped drone; hover; vertical flight

Citation: Ahmed Snikdha, S.S.; Chen, S.-H. A Computational Investigation of the Hover Mechanism of an Innovated Disc-Shaped VTOL UAV. *Drones* **2023**, *7*, 105. https://doi.org/10.3390/drones7020105

Academic Editors: Andrzej Łukaszewicz, Wojciech Giernacki, Zbigniew Kulesza, Jaroslaw Pytka and Andriy Holovatyy

Received: 22 December 2022
Revised: 24 January 2023
Accepted: 31 January 2023
Published: 3 February 2023

1. Introduction

From the beginning of the 21st century, researchers and industries have been coming forward to model the innovative engineering designs of effective flying drones with improved aerodynamic performances and capabilities. A recent review report [1], gave an overview of the types of UAVs and their subsystems and evaluated different applications related to remote sensing, spraying of liquids, and logistics. Another study [2], reported a classification, a broad spectrum of applications, and the existing challenges of UAV designs. Some of the most common applications of flying drones are remote sensing; aerial photography for completing intelligence, surveillance, and reconnaissance missions; environmental protection; mailing and delivery; and other miscellaneous applications.

The rotary wing design of UAVs or drones allows them to fly at high speeds and perform VTOL and hovering flight; however, to date, challenges associated with efficient performance in cruise flight are being faced [3]. Although rotary-wing drones have simple control systems and they are maneuverable, their main disadvantage is power consumption [4,5]. The aerodynamic interactions between multiple rotors, fuselage, and lifting bodies add further complexities. The SUI endurance simulations of forward flight in [6] have provided insight into better designs during cruise; under-mounting the fore rotors and over-mounting the aft rotors improves the aerodynamic efficiency of the vehicle. The hybrid SUI increases the forward horizontal force by 63% compared to the standard SUI. However, even with mild rotor–rotor interactions, the aerodynamic performance of the vehicle is affected, thus requiring design improvements. The authors of [6] conducted a

study on the flight phases of the classic commercial quadcopter DJI Phantom and reported that an octa-rotor (coaxial quadrotor) not only increases the thrust but also the power required to fly it. The authors of [7] showed that, at the same power consumption, the thrust is significantly greater than the simple superposition of the thrust generated by the eight small single rotors. However, the power consumption of the rotor is affected by the inward interaction from the rotor wake. The difficulties associated with the rotor–rotor interactions of the quadrotor aircraft were further analyzed by [8] through numerical simulations, both in hover and forward flight. They reported that the inflow caused by interaction between rotors during hover was higher than that of a single rotor; additionally, the tip vortex and downwash flow of the upstream rotors have a strong impact on the downstream rotors during forward flight.

Another appealing branch of multirotor drones is the design of coaxial rotor systems. The authors of [9] reported that there is a peak in the total rotor efficiency (thrust-to-power ratio) for coaxial rotors, and that the efficiency can be increased by 2% to 5% by increasing the pitch of the lower rotor. However, the thrust of a coaxial rotor system is reduced compared to having the rotors in line or having a single octa-rotor.

The aerodynamic behaviors of UAVs make it difficult to demonstrate the maximum efficiency with minimum power consumption. The authors of [10] reported wind tunnel experiments of the small-scale rotor used in multirotor vehicles, in forward flight at various inflow angles. Their investigation pointed out that, at larger angles of attack, an increase in the freestream advance ratio results in a decrease in thrust and power, whereas, at angles of attacks of less than 15°, the thrust and power follow the increasing trend with increasing advance ratios. However, their results did not report ways to compensate the power consumption at high-speed edgewise flows. In this paper, our simpler comprehensive design approached the disadvantage of high-power consumption from the propellers of multirotor flying drones.

Considering all these challenges of rotorcraft designs in respect to energy resource limitations, in this paper, we propose an innovated design of a disc-shaped VTOL UAV concentrating on energy saving due to the upper surface flow speeding up, leading to lower pressure for extra lift other than rotor thrust. The momentum theory of rotors in hover and vertical flight, first addressed by Glauert [11], is applied to evaluate the thrust, as stated in earlier studies [12]. The lifting rotor is mechanized by achieving lift force and thrust force through the momentum change based on the concept of the induced velocity normal to the disc plane. Moreover, the induced velocity in the far wake is twice that at the rotor disc. The body generates a significant portion of hover thrust to reduce the load of the rotor, resulting in less energy consumption along with longer endurance. The design of the body was modulated by applying the concept of the upper surface curvature on the disc-shaped UAV. Such a curvature effect is an important fluid mechanics phenomenon that has not yet been utilized at its full potential and capabilities. Hatton [13] introduced a family of Coanda UAVs named Geoff's Flying Saucers (GFS), which have a circular canopy as a housing for the propulsion system with an orthogonal arrangement of the Coanda surfaces. Many engineers [14] have applied their own innovative approaches to Coanda-based UAVs, such as the addition of helium chambers and tandem rotor arrangements to extract higher thrust. The proposed innovative design, based on the upper surface curvature, addresses three key design limitations of conventional Coanda UAVs. Firstly, these designs suffer from thrust losses due to radially broadened geometry. The authors of [15] reported this limitation by developing a mathematical model; however, their model used for the flight mechanics of a Coanda UAV could not contribute to the lift in the spanwise direction. Similarly, [16] reported that the radially broadened structure of Coanda UAVs averts the convex surfaces from high lift contribution along the linear spanwise direction. Moreover, another design limitation is the baseplate of the Coanda UAV that generates negative lift due to propeller downwash. The authors of [17] approached the limitation of negative lift generation with an effective thrust reduction of 34% and 17%, respectively. However, unlike the previous studies, we approached mitigating the net

thrust reduction by considering a suck-in configuration with a spherical flat lower surface and achieved significant improvement in thrust reduction.

Thirdly, another limitation with such VTOL designs is an alternate to high thrust requirement from the propellers while hovering. Based on the hover performance study [18,19] mechanistic investigations on the hover power compensation of quadcopters, hex copters, or octocopters represent an underdeveloped area of research. Considering the precedent studies, we simulated the conditions of UAV body contribution to hover thrust compensation with the ring-wing airfoil concept [20] by inhaling the air at the center of the craft. The authors of [12] approached the hovering by considering a disc-shaped annular-ducted lift fan system with two fans of 36 blades. However, they did not mention the ways to compensate for the high thrust requirement while hovering. Interestingly, [21] achieved a smooth transition to forward flight by tilting the toroidal fuselage of 'Cypher', an unmanned aerial vehicle with two coaxial counter-rotating rotors in a ducted fan arrangement. Their study used the cyclic path of the rotors to reduce the excessive pitching moment generation from the inlet-nose flow separation and the drag penalty on the aft part of the shroud. However, it required a considerable amount of power and did not eliminate the drag generation on the trailing side of the rotor.

This paper presents the aerodynamic behavior of a disc-shaped UAV and aims to investigate the feasibility and flyability of this concept in both vertical flight and hover modes. This system aims to present a substitute for a conventional multirotor propeller-based UAVs, with its body ducting the octa-bladed rotor to improve the propulsive efficiency and lower energy consumption. The proposed VTOL UAV design suggests a minimum energy usage (at a lower RPM) with a compensation of thrust contribution from the body during hover.

2. The Disc-Shaped VTOL UAV at a Glance

The engineering design software tool *Solidworks2018* was used to design the 3D CAD model of the lifting vehicle. We designed the fan blades by considering the NACA 4424 airfoil profile for its satisfactory lift-to-drag ratio. The undertaken drone was a VTOL aircraft with a doughnut shape and a ducted rotor in its center that drove the lifting vehicle. The UAV body diameter equaled 3 m. The simpler comprehensive geometry made the UAV lighter than conventional anuloid UAVs [22]. Both the lift and cruise were generated by a single propulsion system. Figure 1 represents different views of the 3D diagram of the lifting vehicle, with an octa-bladed rotor placed in the inner section of the UAV. The upper surface curvature was designed to apply the lip effect to maintain prolonged flow entrainment during VTOL and the hover mode of the UAV. This geometry belongs to a new class of UAV configuration, where the disc-shaped body essentially makes a significant contribution to the rotor's thrust.

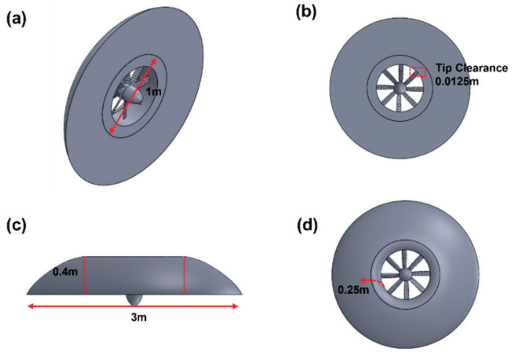

Figure 1. Design parameters of the lifting UAV; (**a**) isometric view, (**b**) bottom view, (**c**) side view, and (**d**) top view.

3. Computational Method

3.1. Mathematical Modeling and Governing Equations

High-fidelity computational fluid dynamics (CFD) simulations are performed to evaluate the aerodynamic characteristics of the vehicle in hover and vertical flight. Fluid dynamic simulations were performed using the general-purpose code [23] ANSYS CFX. The equations that govern the motion of the Newtonian fluid are the continuity, the momentum (Navier–Stokes equations), and the energy equation expressed in terms of surface integrals using Gauss' divergence theorem over the control volume, V. More often, the solver describes the flow field of the governing equations with the mean values by taking a time-averaged form of the equations known as the Reynolds averaged Navier–Stokes (RANS) equations. With the approach of the eddy viscosity principle after Boussinesq (1877), the general time-averaged RANS equations can be expressed in the tensor form as:

$$\frac{\partial \overline{\rho}}{\partial t} + \frac{\partial \overline{\rho}\widetilde{u_i}}{\partial x_i} = 0 \tag{1}$$

$$\rho\left(\frac{DU_i}{Dt}\right) = F_i - \frac{\partial P}{\partial x_j} + \frac{\partial}{\partial x_j}\tau_{ij} \tag{2}$$

where $\tau_{ij} = \mu\frac{\partial u_i}{\partial x_j} + \rho\left(v_T\left(\frac{\partial u_i}{\partial x_j} + \frac{\partial u_j}{\partial x_i}\right) - \frac{2}{3}\kappa\delta_{ij}\right)$ corresponds to the total shear stress or the Reynold's stress.

$$\frac{\partial \overline{\rho}\widetilde{E}}{\partial t} + \frac{\partial \overline{\rho}\widetilde{u}_j\widetilde{H}}{\partial x_j} = \frac{\partial}{\partial x_j}\left[-\overline{q_j} - \overline{\rho u j'' h''} + \overline{\tau_{ij}'' u_i''} - \overline{\rho u_j''\frac{1}{2}u_i'' u_i''}\right] + \frac{\partial}{\partial x_j}\left[\left(\overline{\tau}_{ij} - \overline{\rho u_i'' u_j''}\right)\right] \tag{3}$$

However, the RANS equation requires a turbulence model for its closure in order to approximate the real-world flow field. In this paper, we applied one of the most popular turbulence models, the $SST\ k-w$ model developed by Menter. The $SST\ k-w$ model is advantageous for its good behavior in adverse pressure gradients and separating flow. The SST formulation also switches to a $k-\epsilon$ behavior, developed by Wisconsin, in the freestream and thereby avoids the common $k-w$ problem of becoming too sensitive to the inlet freestream turbulence properties. It solves two transport equations, one for the turbulent kinetic energy and one for the turbulent frequency, w.

Turbulent kinetic energy: $\frac{\partial k}{\partial t} + U_j\frac{\partial k}{\partial x_j} = P_k - \beta^* k\omega + \frac{\partial}{\partial x_j}\left[(v + \sigma_k v_T)\frac{\partial k}{\partial x_j}\right]$, where the kinematic eddy viscosity, $v_T = \frac{a_1 k}{max(a_1\omega, SF_2)}$ and P_k is the production rate of turbulence. w—equation:

$$\frac{\partial \omega}{\partial t} + U_j\frac{\partial \omega}{\partial x_j} = aS^2 - \beta w^2 + \frac{\partial}{\partial x_j}\left[(v + \sigma_\omega v_T)\frac{\partial \omega}{\partial x_j}\right] + 2(1 - F_1)\sigma_{\omega 2}\frac{1}{\omega}\frac{\partial k}{\partial x_i}\frac{\partial \omega}{\partial x_i}$$

The closure coefficients and auxiliary relations of the model are given by:

$$F_2 = \tanh\left[\left[max\left(\frac{2\sqrt{k}}{\beta^*\omega y}, \frac{500v}{y^2\omega}\right)\right]^2\right],\ P_k = min\left(\tau_{ij}\frac{\partial U_i}{\partial x_j}, 10\beta^* k\omega\right),$$

$$F_1 = \tanh\left\{\left\{min\left[max\left(\frac{\sqrt{k}}{\beta^*\omega y}, \frac{500v}{y^2\omega}\right), \frac{4\sigma_{\omega 2}k}{CD_{k\omega}y^2}\right]\right\}^4\right\}, CD_{k\omega} = max\left(2\rho\sigma_{\omega 2}\frac{1}{\omega}\frac{\partial k}{\partial x_i}\frac{\partial \omega}{\partial x_i}, 10^{-10}\right),$$

$\varphi = \varphi_1 F_1 + \varphi_2(1 - F_1)$, $\alpha_1 = \frac{5}{9}$, $\alpha_2 = 0.44$, $\beta_1 = \frac{3}{40}$, $\beta_2 = 0.0828$, $\beta^* = \frac{9}{100}$, $\alpha_{k1} = 0.85$, $\alpha_{k2} = 1$, $\sigma_{\omega 1} = 0.5$, and $\sigma_{\omega 2} = 0.856$, where y is the distance to the nearest wall. $F_1 = 1$ is applied inside the boundary layer and 0 in the free stream. Similarly, $F_2 = 1$ is applied for the boundary layer flows and 0 for the free shear flows. The structure of the turbulent boundary layer exhibits large velocity gradients and quantities characterizing turbulence rising to a need for near-wall treatment. The finite volume code in the CFX solver imple-

ments the wall functions by adding source terms in the momentum equations and by using the log-law, $\frac{U}{u_\tau} = \frac{1}{k} lmEy^+$, where $E = 9.8$ is equivalent to the additive constants. Using $\tau_\omega = \rho {u_\tau}^2$, we obtain $\tau_\omega = \frac{\rho u_\tau kU}{lnEy^+}$. For the wall treatment at the viscous sublayer, the first computational wall is generated with its centroid at $y^+ \approx 1$. This requires a fine mesh adjacent to the wall. However, a higher y^+ is acceptable as long as it is well inside the viscous sublayer.

The volume and surface integrals of the flow equations are discretized in ICEM CFD by using unstructured mesh. The mesh is then imported to the CFX pre-solver, which utilizes the element-based finite volume method [24] to solve the Navier–Stokes equations, the turbulent kinetic energy, and the turbulent dissipation rate. A fully coupled solver scheme between momentum and pressure equations resolve the pressure–velocity coupling with the second order upwind discretization of the pressure equation.

3.2. Generating Computational Mesh

The computational cylindrical domain is a 11D radius measured by a 17D height flow field containing the rotational domain with a height of 120 mm and a radius of 506.25 mm. The UAV in the domains is imported to the widely used commercial software ANSYS ICEM 19.0 for generating the mesh topology. From the experience of many other researchers [25], the unstructured mesh technique is successfully applied to the geometry as depicted in Figures 2 and 3. CFD methods with unstructured grid techniques offer the advantage of handling complex aero geometries with high accuracy results through locally refining the cells as required. Tetrahedral-based volume mesh (Figure 4) is generated by the quick Delaunay method, which provides a fine mesh quality with a smoother transition in the volume element size. The mesh contains 8M cells with 30 prismatic layers in each domain. Previously published reports [26] established high-quality mesh with 20–40 prism layers (each with an expansion ratio of 1.2). The complex flow-oriented zone in the rotational domain contains 5M cells for the sake of solution accuracy. The first layer height of the boundary layer is measured to be 0.006 mm to ensure $y^+ \approx 0.7$ on most of the surface area, depending on the freestream velocity in the cruise mode. In CFD modeling, a $y+$ value near unity with a greater number of prism layer elements accurately predicts the flow separation, surface pressure, and aerodynamic forces [27]. Hence, a high resolution of prism mesh is needed to fully resolve the thin boundary layer or the viscous sublayer.

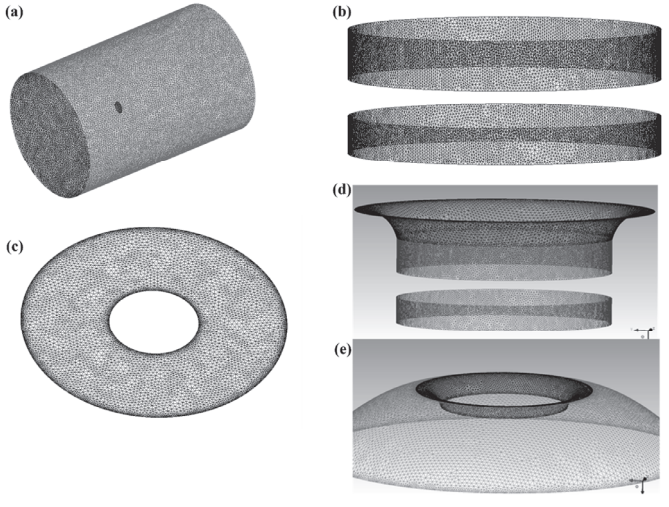

Figure 2. (**a**) Surface mesh on the UAV body inside the stationary domain, (**b**) duct, (**c**) lower surface, (**d**) lip curvature, and (**e**) upper surface.

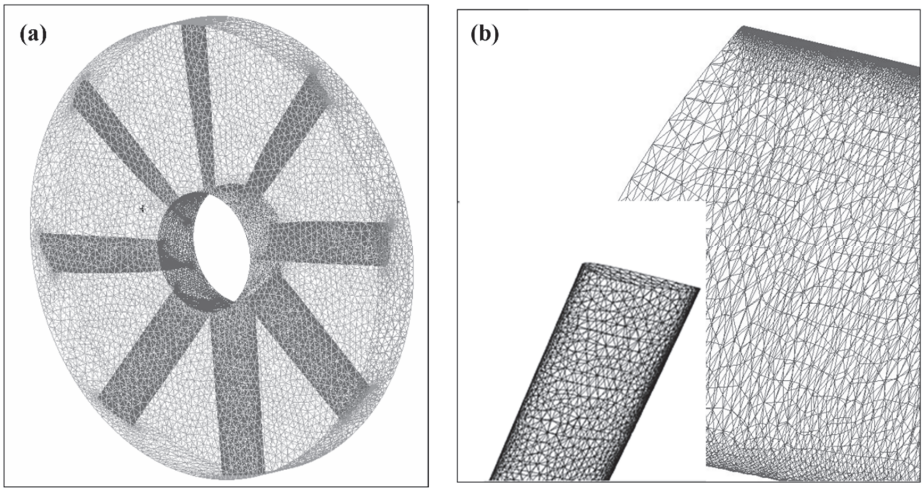

Figure 3. (**a**) Surface mesh on the UAV parts in the rotating domain, (**b**) zoomed-in view of the mesh on the blades.

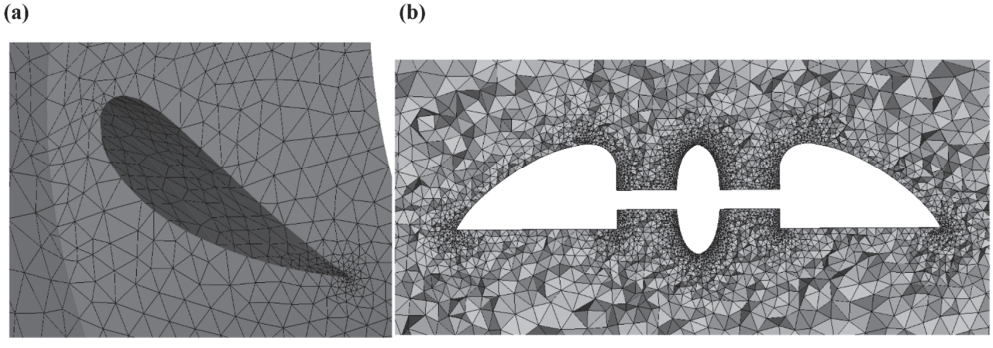

Figure 4. (**a**) Hub showing the blade section, (**b**) volume mesh through the mid-section of the UAV in the density zone.

3.3. Boundary Conditions and Physical Modeling

This paper addresses the following features of ANSYS CFX (Table 1). Steady state simulations are carried out in CFX solver with the physical model as explained in Figure 5. For the simulation of the UAV in hover, the computational domain is divided into stationary (inlet and outlet regions) and rotational (rotating fan blades with hub) domains. The steady state physics of the analysis is set up with a velocity inlet (velocity in hover, $U = 0$ m/s) and pressure outlet definitions. On the side surface, an opening boundary condition is assumed for an opening boundary condition allowing the flow to both enter and leave the fluid domain across the boundary with zero pressure offset during the course of the solution. Air density, dynamic viscosity, and ambient temperature were defined at standard ideal gas states. The solid surfaces of the UAV and the shroud surface of the rotating zone are set as no-slip walls at the adiabatic heat transfer.

Table 1. Physical modeling in CFX.

Component	Feature	Details
ANSYS CFX—Pre	Simulation type	Steady state
	Fluid type	Air ideal gas
	Domain type	Multiple domain Rotating frame of reference Stationery frame of reference
	Turbulence model	SST
	Heat transfer	Total energy
	Boundary conditions	Velocity inlet (Subsonic) Pressure outlet (Subsonic) Wall: no-slip Wall: adiabatic Far-field: opening
	Domain interfaces	General connection Frozen rotor Specified pitch angles (360°)
	Timestep	Physical timescale: $\frac{0.1}{\omega}$
ANSYS CFX—Solver Manager	Start	Double Precision
ANSYS CFX—Post	Plots	Contour: pressure, and velocity Streamlines Velocity vector

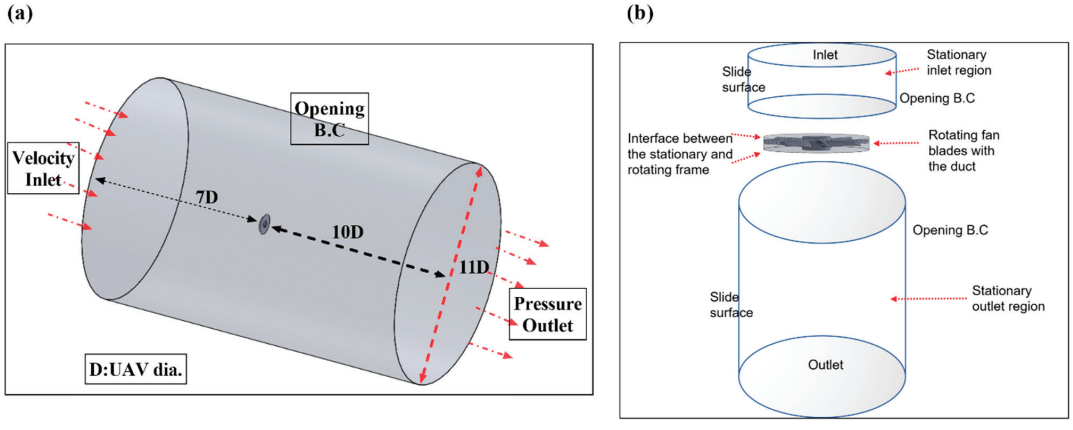

Figure 5. (**a**) Computational domain interpreting boundary conditions; (**b**) interface between the rotational and stationary domains.

For multi-reference domains, the stationary and the rotational reference frames are bridged by an interface connection. A 'frozen rotor' type interface model is used in calculations for modeling the frame change with specified pitch angles of 360° on each side. A frozen-rotor interface model can significantly reduce the computational effort and provide reasonably accurate results for steady-state simulations [28,29]. When a frozen rotor is selected, the rotating blades and the body are both frozen, for the actual incoming flow is axisymmetric. Moreover, the attitude of the rotating blades is relative to the rotor and is almost unchanged. With the limited computational effort, the high accuracy and acceptance rate of the frozen rotor model has already been established by many aerodynamics experts [17,18,30]. With this setting, the solid structure of the rotor itself remains fixed; hence, this approach is proposed by many authors [18] due to its

reliable accuracy in simulating propeller flow for small-scale multirotor UAVs. The general grid interface (GGI) is used for mesh connections between interfaces. GGI connections refer to gluing the meshes where faces do not match or when a frame change occurs. Menter's shear stress transport (*SST*) version of the $k - \omega$ turbulence model, known for its reliability [31–33] and robustness, is applied to solve the boundary layer near the wall surface of the UAV. The zero gradient turbulence model is used for the steady developed flow [34]. Turbulent flows require a heat transfer model for simulation purposes. Accordingly, both the fluid domains were simulated by applying the total energy heat transfer model to characterize the transport of enthalpy, including the kinetic energy effects. The rotating fluid motion was simulated by adding source terms for Coriolis forces and centrifugal forces. Counter-rotating wall velocities were assigned at the shroud surface.

4. Results

4.1. Mesh Sensitivity Analysis

To validate the computational model, mesh sensitivity analysis was conducted considering the mesh element sizes from coarser to finer. A coarse grid topology with a global maximum element size of 6800 mm for stationary domain parts and 600 mm for rotational parts was selected for the first simulation of the UAV in vertical climb and hovering. The coarse grid topology generates 1M cells. The vehicle thrust coefficient is selected for the mesh independence test parameter. The simulation results led to insignificant results with the coarse grids. However, the thrust coefficient in hover converges to a significant value by refining the mesh elements. The finer mesh is generated by considering global maximum element sizes of 680 mm and 60 mm, respectively, for the stationary and rotational domain parts. Eventually, a negligible discrepancy in the thrust coefficient is achieved with 9M and 11M cells. The thrust coefficient is calculated following the normalized thrust coefficient equation of the momentum theory [35].

Therefore, to reduce the available computational resources, the mesh with 9M cells, containing 5M cells in the rotational domain and 4M cells in the stationery domain, is considered for further investigations in this study. This converged hover thrust coefficient (Figure 6) with a varied number of mesh elements hereby establishes the computational validity of this study.

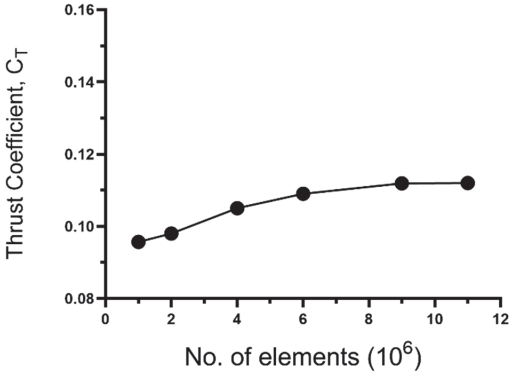

Figure 6. Mesh sensitivity analysis in hovering.

4.2. Hover and Vertical Flight Results

The drone was conceptually designed by combining the upper surface curvature effects and rotor propulsion for lift generation. The CFD tool was applied to validate the physical feasibility of the conceptual design. A curvature on the upper surface of the body and the inlet lip induced a larger and smoother flow into the rotor and created a favorable lower pressure (Figure 7). As the air passes through the rotor following a curved wall, the contact pressure on the curved wall is lower than the ambient pressure because of

the presence of viscous phenomena. The shape of such a surface lip plays an important role in improving hover efficiency by generating lower pressure on the contour of the upper surface. Positive pressure arises on the lower surface of the UAV body, adding to the driving pressure gradient and eventually suggesting a high lift contribution from the body. A low-pressure gradient is created on the upper convex lip surface, delineating a high lifting force induced by the curvature effect.

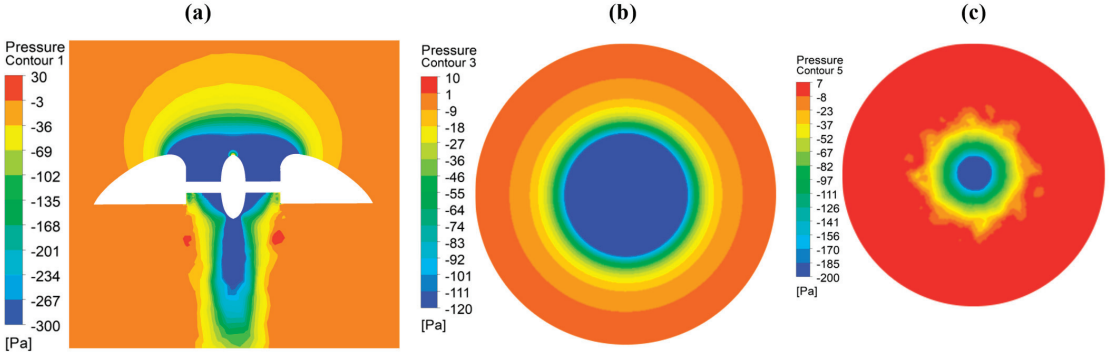

Figure 7. Pressure contour at hovering, $U_\infty = 0$ m/s. (**a**) XY, Z = 0 mid-plane, (**b**) YZ, X = −0.5 upper surface, and (**c**) YZ, X = 0.5 lower surface cross-sectional plane.

As shown in Figure 8, the air velocity passing over the upper surface of the drone is greater than that passing over the lower surface, leading to higher dynamic pressure on the upper surface compared to the lower surface. In particular, the rotor thrust, and body generated lift acting on the UAV, is increased with the high dynamic pressure, as indicated by the increased velocity gradient on the upper surface. The lower surface velocity profile resembles a star shape formation because of the rotation of the octa-bladed rotor.

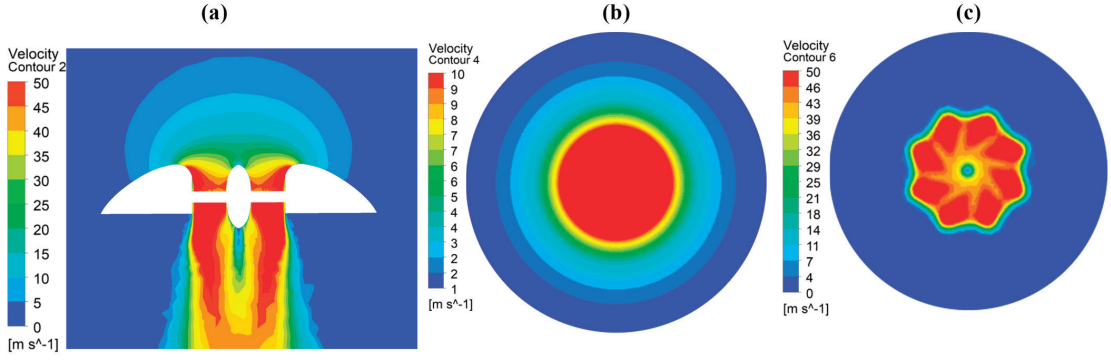

Figure 8. Velocity contour at hovering, $U_\infty = 0$ m/s. (**a**) XY, Z = 0 mid-plane, (**b**) YZ, X = −0.5 upper surface, and (**c**) YZ, X = 0.5 lower surface cross-sectional plane.

The velocity streamlines and the velocity vector plot in Figure 9 indicate a prolonged flow entrainment by the UAV body with stable symmetric flow patterns free from fluid momentum losses in the radial direction. One possible explanation for this innovative design's efficiency can be observed through the visual interpretation of velocity vector plots. Commonly, conventional saucer-shaped UAVs experience flow separations along the curvature of the upper surface [36]. To study the flow separation mechanism, the velocity vectors are plotted across the central cross-sectional plane, as depicted in Figure 9b, which describes a stable blanket of high velocity air remaining attached to the contours of the

upper surface convex curvature without experiencing flow separations. The stability of attached streamlines is achieved at a much lower RPM of 3800 than the investigation of Najafi et al. [37], who observed the stable flow at 8000 RPM on the considered UAV design. The upper body curvature and the spherical disc shape of the UAV account for maintaining attached flow at the aircraft's trailing edge. However, to study this phenomenon in more detail, future experimental setups would need to provide the ability to visualize the flow separations.

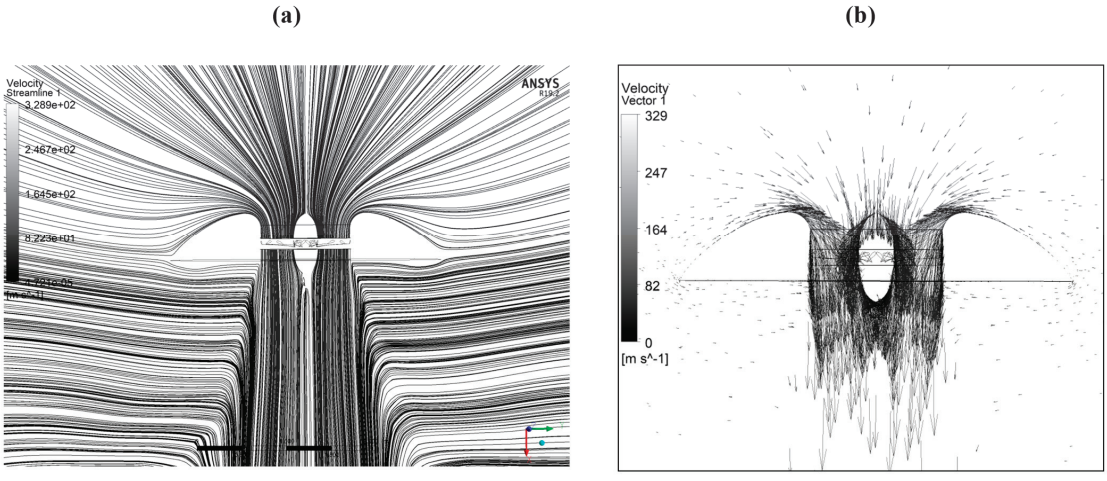

Figure 9. Mid-section plane plots of (**a**) surface streamlines, and (**b**) velocity vector in hovering, at $U_\infty = 0$ m/s.

Prolonged flow attachment augments the lift contribution from the body surfaces, which act as a wing to balance the aerodynamic stability of the UAV. As shown in Figure 10a, the upper surface acts as a wing and generates a significantly high lift of 0.96 of rotor thrust. This happens due to the flow speeding up by the convex curvature of the upper surface. However, the lower surface negligibly generates a negative lift of 0.01 of rotor thrust, which reduces the overall body lift by 1%. This negative lift or drag increment, caused by the lower surface due to the rotor downwash, is compensated by the body upper surface. Thus, while hovering, the effective lift from the body alone is 0.95 of the rotor thrust. This significant extra lift from the body augments the hover efficiency compared to the conventional UAVs because the lift contribution from the body makes the vehicle advantageous to the environment for reduced energy consumption. As the vertical wind speed increases, the overall thrust and body lift decreases due to the increasing drag from the lower surface, as shown in Figure 10b,c. During vertical flight, air approaches the UAV at a higher speed, which drags the vehicle towards the fluid flow direction. Thus, the lower surface generates more negative lift at an increasing vertical wind speed. Following the vertical climb theory, keeping a constant RPM, the thrust coefficient of the lifting system decreases with the increasing wind velocity (Figure 10d). This is because, with the increasing inflow speed the angle of attack of the blades decreases and the body contribution becomes less significant due to the force coming from the incoming vertical wind. When the vertical wind speed reaches 15 km/h, the body lift dwindles by 30% of the lift generated in hover mode. This body lift decreases further as the vertical wind speed reaches 30 km/h. Therefore, the specific disc-shaped configuration of the drone body and central position of the fan promoted the lift efficiency due to the low pressure in the upper surface curvature generating a significant thrust contribution from the body.

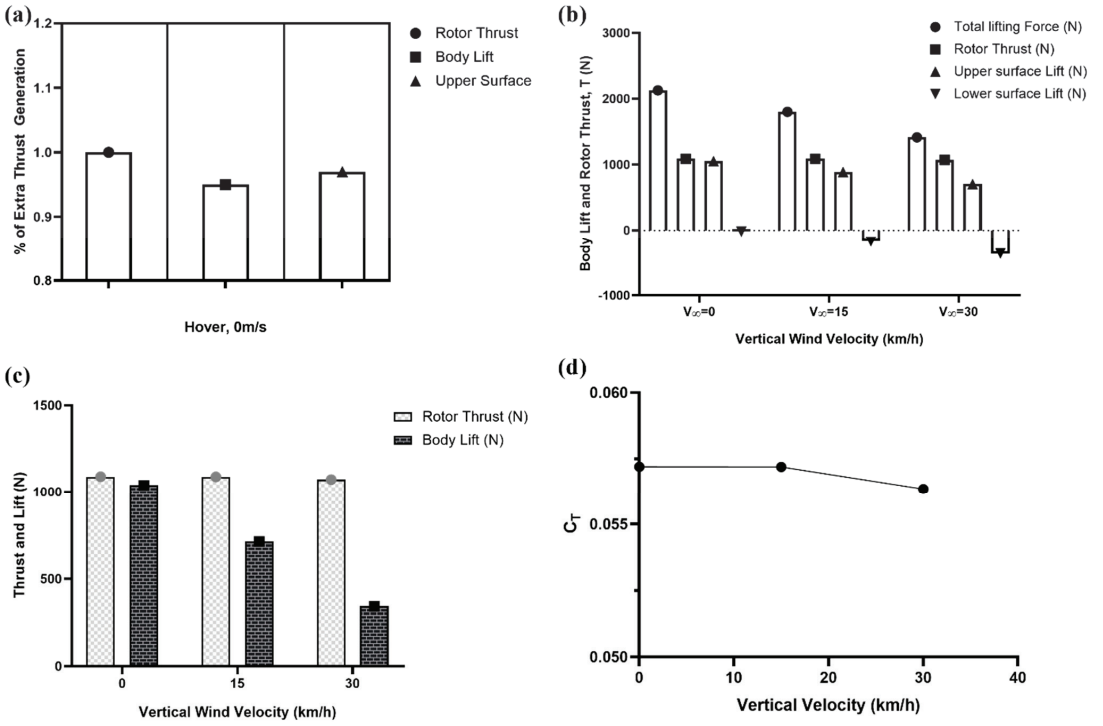

Figure 10. (**a**) Extra lift contribution from the body delineating the UAV hover efficiency, (**b**) discrete hover and vertical flight thrust with body lift, (**c**) percentage generation of body lift and rotor thrust in hover and vertical flight, and (**d**) thrust coefficient of the UAV with increasing vertical wind speed.

The simulation results show a hover thrust of $1090N$ with a significant contribution from the body lift of $1040N$. Therefore, the generated thrust gives the rotor efficiency $\eta = \frac{111.149}{95.05}\frac{kg}{hp} = 1.17$ kg/hp and the body lift efficiency $\frac{T}{P} = \frac{106.05}{95.05} = 1.12$ kg/hp.

The moment on the fan, produced by the aerodynamic force of the rotating blades, is obtained as 215 N m. Thus, the simulated mechanical power of the rotor in hover mode achieved 95.05 hp, which was used to accelerate the air going through the disc area of the rotating rotor. The low power required to run the fan reduces the corresponding drag on the fan blades, resulting in sufficiently less energy consumption. We aimed to design the UAV body to reduce the load on the rotor and then eventually reduce the power consumption. The current multirotor VTOL drones provide hover thrust only by the propellers, with substantial power consumption. In our strategy of a curvature body VTOL UAV, the body shares the lift required to hover by reducing the power consumption of the rotor.

As the UAV starts vertical climbing with the increasing inflow wind speed, the percentage of body lift contribution to the rotor thrust declines. Figure 11a portrays that, while hovering, the body contribution is 0.95 of rotor thrust. As the vertical wind speed reaches 15 km/h, the body lift contribution reduces to 0.66 of rotor thrust, which further decreases to 0.32 of rotor thrust at the wind speed of 30 km/h and constant RPM of 3800. This suggests that the body alone covers a considerable part of hover thrust. The significant portion of the body lift contribution comes from the UAV upper surface due to the curvature configuration. Because the body generates such a significant amount of lift force, unlike conventional multirotor UAVs, this extra lift contributes to the energy-saving potential of the propulsion system, leading to a longer endurance. As shown in the lift distribution of Figure 11b, with the increasing wind speed in vertical flight, the upper surface induces a higher percentage of lift out of the total lift. However, it associates an increasing negative

lift from the lower surface. The increasing wind force accounts for the rising drag of the lower surface. To approach the vertical windspeed of 30 km/h at a null incidence with constant RPM, a negative lift of 1.05 of total body lift is generated by the lower surface; nevertheless, this is compensated by the upper surface. The increasing downwash-induced velocity accounts for rising negative lift from the lower surface. The extra lift from the body accelerates the UAV to move vertically upwards toward the wind.

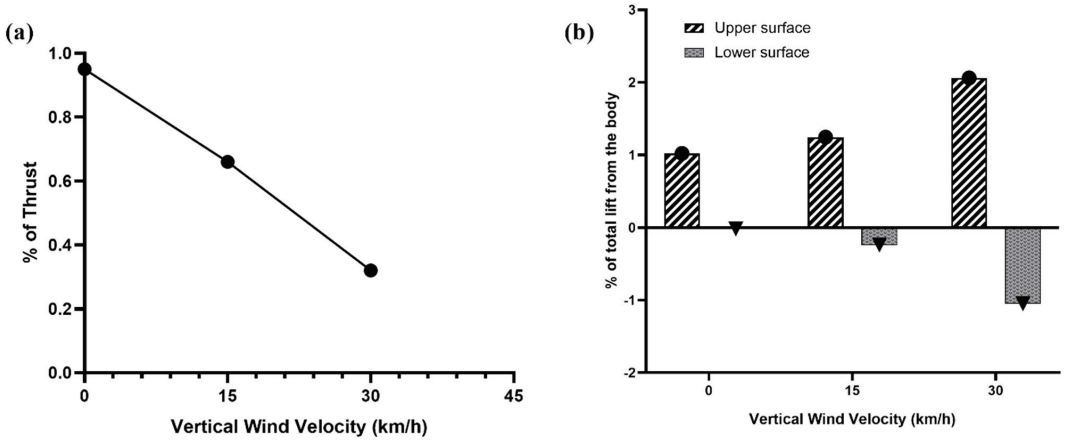

Figure 11. (**a**) The percentage of extra lift generated by the body compared to the rotor thrust, (**b**) lift distribution of the body from hover with 0 m/s to the vertical flight with increasing wind velocity.

The specific UAV design can save energy due to the following facts: (1) The elimination of rotor wake swirling loss and wake coning loss. The duct associated body eliminates the fan blade tip vortex and prevents the downstream flow from contraction. (2) The substantial amount of extra lift generated by the body as a significant contribution to the rotor thrust. (3) The additional body lift helps to reduce the corresponding power required to operate the UAV and increase the flight endurance. The CFD results of hovering showed that 0.95 of rotor thrust comes from the upper surface curvature lift. Moreover, a negligible drag or negative lift of 0.01 of the total thrust comes from the lower base surface.

5. Discussion

As the new design has demonstrated an effective hover and vertical flight performance with a significant lift contribution from the body, the next stage of the study would be comprised of conducting forward flight simulations. Presumably, in forward flight, the body would play the role of a wing to reduce the load on the rotor. This is because the disc-shaped body would act as a cross-section of the airfoil to generate more lift in forward flight. We attempted to address the reduction in the overall net lift due to the disc-shaped lower surface of the UAV in hover and vertical flight. Figure 11 exhibits a 1 % reduction in the overall net lift generated from the body while hovering at 0 m/s. This reduction percentage due to the flat lower surface is much less than body-associated UAVs with concave or convex lower surfaces, as presented by Nauddin's UAV in [17], where a 34% body lift reduction was obtained. Furthermore, Barlow et al.'s [20] application of a ring-wing airfoil on a radial UAV generated less than favorable results. However, the application of a ring-shaped upper surface in our inventive design achieved more than favorable results due to the recovery of thrust losses in the radial direction. The duct enclosing the rotor acts as the anti-noise material, resembling Shin et al.'s [38] observations of a reduced acoustic signature of UAV.

The surface streamlines and velocity vector plots depict an interesting behavior of flow attachment, complying with an annular disc of earlier studies [12]. However, inconsistent

with the previous study, we considered the upper surface in our geometry, which acts as the wing for the UAV. Generally, the aerodynamic challenges include flow separation from the wings. Nevertheless, our results show highly improved flow separation and swirling flows of the surface streamlines. This ensures reduced thrust losses with efficient energy consumption by the control systems and increases the aerodynamic performance of the UAV and proves to be of a greater potential interest to the industry.

One possible explanation for the innovated design's efficiency can be observed through the visual interference of velocity vector plots. In conventional saucer-shaped UAVs, flow separations along the convex surface are a common occurrence [36]. Many designers have used vortex generators and axial vanes to prevent or delay flow separations such that the flow remains attached to the curved surface [39]. Researchers in their investigations experienced flow separation characterized by a swirling vortex generated above the upper surface. However, our velocity vector plots show a stable blanket of high velocity attached to the contours of the convex upper surfaces and the flat lower surface without experiencing flow separations.

6. Conclusions

The aerodynamic characteristics of the disc-shaped lifting system for VTOL UAV from vertical climb to hover were investigated by applying the ANSYS CFX software. A significant lift contribution to the hover thrust was generated by the UAV body, with a negligible negative lift caused by the disc-shaped flat lower surface due to rotor downwash. This study proves the concept that the drone body can produce significant extra lift to the rotor, reducing the load on the rotor, both in vertical flight and in hover. This is caused by the pressure differential along the UAV body surfaces, particularly by the flow passing through the upper surface before entering the rotor and creating large negative pressure to lift up the vehicle. In addition to a substantial hover thrust, 95% of the rotor thrust is generated by the UAV body as an extra lift.

For an efficient design along with the energy resource limitations, an alternative lift of the UAV can be generated from the body. The drone body alone generated 0.95 of hover thrust, which significantly contributes to the energy-saving potential of the propulsion system. Thus, the innovative disc-shaped vehicle could eventually lead to longer endurance, which is a common limitation of multirotor UAVs. Additionally, in forward flight the body would play the role of a wing to reduce the load of the rotor to be studied in future. This would result in substantially reduced energy consumption in forward flight.

In future work, the model will be validated for transition to horizontal flight with control approaches to improve the stability of the control system. The predicted simulation data provide useful insights for future experimental studies of the disc-shaped UAV. The unique disc-shaped UAV has high lift efficiency and acceptable lift, generating characteristics of the body with great potential for future VTOL transportation.

Author Contributions: The current research presented in this paper was conceptualized and supervised by S.-H.C.; throughout the methodology the simulations were conducted, and the results were analyzed by S.S.A.S.; data analysis, writing—original draft preparation, S.S.A.S. All authors have read and agreed to the published version of the manuscript.

Funding: This research received no external funding.

Data Availability Statement: The data presented in this study are available on request from the corresponding author.

Conflicts of Interest: The authors declare no conflict of interest.

References

1. González-Jorge, H.; Martínez-Sánchez, J.; Bueno, M.; Arias, P. Unmanned Aerial Systems for Civil Applications: A Review. *Drones* **2017**, *1*, 2. [CrossRef]
2. Hassanalian, M.; Abdelkefi, A. Classifications, applications, and design challenges of drones: A review. *Prog. Aerosp. Sci.* **2017**, *91*, 99–131. [CrossRef]

3. Austin, R. *Unmanned Aircraft Systems: UAVS Design, Development and Deployment*; John Wiley & Sons: Hoboken, NJ, USA, 2011; Volume 54.
4. Aleksandrov, D.; Penkov, I. Energy Consumption of Mini UAV Helicopters with Different Number of Rotors. In Proceedings of the 11th International Symposium" Topical Problems in the Field of Electrical and Power Engineering, Estonia, Pärnu, 16–21 January 2012; pp. 259–262.
5. Bouabdallah, S.; Murrieri, P.; Siegwart, R. Towards Autonomous Indoor Micro VTOL. *Auton. Robot.* **2005**, *18*, 171–183. [CrossRef]
6. Diaz, P.V.; Yoon, S. Computational Analysis of Urban Air Mobility Vehicles. In Proceedings of the 8th European Conference for Aeronautics and Aerospace Sciences (EUCASS), NASA Ames Research Center, Moffett Field, Santa Clara, CA, USA, 1–4 July 2019; p. 359.
7. Lei, Y.; Huang, Y.; Wang, H. Aerodynamic Performance of an Octorotor SUAV with Different Rotor Spacing in Hover. *Processes* **2020**, *8*, 1364. [CrossRef]
8. Hwang, J.Y.; Jung, M.K.; Kwon, O.J. Numerical Study of Aerodynamic Performance of a Multirotor Unmanned-Aerial-Vehicle Configuration. *J. Aircr.* **2015**, *52*, 839–846. [CrossRef]
9. Giljarhus, K.E.T.; Porcarelli, A.; Apeland, J. Investigation of Rotor Efficiency with Varying Rotor Pitch Angle for a Coaxial Drone. *Drones* **2022**, *6*, 91. [CrossRef]
10. Kolaei, A.; Barcelos, D.; Bramesfeld, G. Experimental Analysis of a Small-Scale Rotor at Various Inflow Angles. *Int. J. Aerosp. Eng.* **2018**, *2018*, 1–14. [CrossRef]
11. Byham, G.M. The future of rotorcraft. *Aeronaut. J. -New Ser.* **2003**, *107*, 377–388. [CrossRef]
12. Jiang, Y.; Zhang, B.; Huang, T. CFD Study of an Annular-Ducted Fan Lift System for VTOL Aircraft. *Aerospace* **2015**, *2*, 555–580. [CrossRef]
13. Hatton, G. Thrust Generating Apparatus. US0213090A1, 4 September 2008.
14. Nedelcut, F. Coanda Effect UAV—A New Born Baby in the Unmanned Aerial Vehicles Family. *Rev. Air Force Acad.* **2010**, *17*, 21–28.
15. Ahmed, R.I.; Abu Talib, A.R.; Rafie, A.S.M.; Djojodihardjo, H. Aerodynamics and flight mechanics of MAV based on Coandă effect. *Aerosp. Sci. Technol.* **2017**, *62*, 136–147. [CrossRef]
16. Hibbeler, R. *Fluid Mechanics*, 2nd ed.; Pearson: London, UK, 2015.
17. Siddiqi, Z.; Lee, J.W. Experimental and numerical study of novel Coanda-based unmanned aerial vehicle. *J. Eng. Appl. Sci.* **2022**, *69*, 76. [CrossRef]
18. Lopez, O.D.; Escobar, J.A.; Pérez, A.M. Computational Study of the Wake of a Quadcopter Propeller in Hover. In Proceedings of the 23rd AIAA Computational Fluid Dynamics Conference, Denver, Colorado, 5–9 June 2017. [CrossRef]
19. Henricks, Q.; Wang, Z.; Zhuang, M. Small-Scale Rotor Design Variables and Their Effects on Aerodynamic and Aeroacoustic Performance of a Hovering Rotor. *J. Fluids Eng.* **2020**, *142*, 081209. [CrossRef]
20. Barlow, C.; Lewis, D.; Prior, S.D.; Odedra, S.; Erbil, M.A.; Karamanoğlu, M.; Collins, R. Investigating the Use of the Coanda Effect to Create Novel Unmanned Aerial Vehicles. In Proceedings of the International Conference on Manufacturing and Engineering Systems, Huwei, Yunlin, Taiwan, 17–19 December 2009; pp. 386–391.
21. Cycon, J.P.; Scott, M.W.; DeWitt, C.W. Method of Reducing a Nose-Up Pitching Moment on a Ducted Unmanned Aerial Vehicle. US6170778B1, 9 January 2001.
22. Petrolo, M.; Carrera, E.; D'Ottavio, M.; Visser, C.C.d.; Pátek, Z.; Janda, Z. On the development of the Anuloid, a disk-shaped VTOL aircraft for urban areas. *Adv. Aircr. Spacecr. Sci.* **2014**, *1*, 353–378. [CrossRef]
23. Stajuda, M.; Karczewski, M.; Obidowski, D.; Jóźwik, K. Development of a CFD model for propeller simulation. *Mech. Mech. Eng.* **2016**, *20*, 579–593.
24. van Leer, B. Towards the ultimate conservative difference scheme. V. A second-order sequel to Godunov's method. *J. Comput. Phys.* **1979**, *32*, 101–136. [CrossRef]
25. Xu, H.; Ye, Z.-Y.; Shi, A.-M. Numerical Study of Propeller Slipstream Based on Unstructured Dynamic Overset Grids. *J. Aircr.* **2012**, *49*, 384–389. [CrossRef]
26. Ryu, M.; Cho, L.; Cho, J. Aerodynamic Analysis of the Ducted Fan for a VTOL UAV in Crosswinds. *Trans. Jpn. Soc. Aeronaut. Space Sci.* **2016**, *59*, 47–55. [CrossRef]
27. Blocken, B.; Defraeye, T.; Koninckx, E.; Carmeliet, J.; Hespel, P. CFD simulations of the aerodynamic drag of two drafting cyclists. *Comput. Fluids* **2013**, *71*, 435–445. [CrossRef]
28. Kim, W.-Y.; Senguttuvan, S.; Kim, S.-M. Effect of Rotor Spacing and Duct Diffusion Angle on the Aerodynamic Performances of a Counter-Rotating Ducted Fan in Hover Mode. *Processes* **2020**, *8*, 1338. [CrossRef]
29. Thouault, N.; Breitsamter, C.; Adams, N.A. Numerical and Experimental Analysis of a Generic Fan-in-Wing Configuration. *J. Aircr.* **2009**, *46*, 656–666. [CrossRef]
30. Kutty, H.A.; Rajendran, P. 3D CFD Simulation and Experimental Validation of Small APC Slow Flyer Propeller Blade. *Aerospace* **2017**, *4*, 10. [CrossRef]
31. Pérez Gordillo, A.M.; Villegas Santos, J.S.; Lopez Mejia, O.D.; Suárez Collazos, L.J.; Escobar, J.A. Numerical and Experimental Estimation of the Efficiency of a Quadcopter Rotor Operating at Hover. *Energies* **2019**, *12*, 261.
32. Jiang, Y.; Zhang, B. Numerical Investigation of Effect of Parameters on Hovering Efficiency of an Annular Lift Fan Aircraft. *Aerospace* **2016**, *3*, 35. [CrossRef]

33. Min, K.-M.M.K.-M.; Tjprc. Design and CFD Analysis of A Low-Altitude VTOL UAV. *Int. J. Mech. Prod. Eng. Res. Dev. (IJMPERD)* **2019**, *9*, 555–562.
34. Prisacariu, V. CFD Analysis of UAV Flying Wing. *Incas Bull.* **2016**, *8*, 65–72. [CrossRef]
35. John Seddon, S.N. Rotor in Vertical Flight: Momentum Theory and Wake Analysis. In *Basic Helicopter Aerodynamics*; John Wiley & Sons: Hoboken, NJ, USA, 2011; pp. 23–61. [CrossRef]
36. Crivoi, O.; Doroftei, I. Some experimental results on Coanda effect with application to a flying vehicle. *IOP Conf. Ser. Mater. Sci. Eng.* **2016**, *147*, 012082. [CrossRef]
37. Najafi, M.; Jahanmiri, M. An Innovative Technique to Increase Lift of a Coanda UAV. *IOSR J. Mech. Civ. Eng.* **2017**, *14*, 27–35. [CrossRef]
38. Shin, D.; Kim, H.; Gong, J.; Jeong, U.; Jo, Y.; Matson, E.T. Stealth UAV through Coandă Effect. In Proceedings of the 2020 Fourth IEEE International Conference on Robotic Computing (IRC), Taichung, Taiwan, 9–11 November 2020; pp. 202–209.
39. Gad-el-Hak, M.; Bushnell, D. Separation Control: Review. *J. Fluids Eng.* **1991**, *113*, 5–30. [CrossRef]

drones

MDPI

Article

Semantic Scene Understanding with Large Language Models on Unmanned Aerial Vehicles

J. de Curtò [1,2,3,4,*], I. de Zarzà [1,2,3,4] and Carlos T. Calafate [2]

[1] Centre for Intelligent Multidimensional Data Analysis, HK Science Park, Shatin, Hong Kong
[2] Departamento de Informática de Sistemas y Computadores, Universitat Politècnica de València, 46022 València, Spain
[3] Informatik und Mathematik, GOETHE-University Frankfurt am Main, 60323 Frankfurt am Main, Germany
[4] Estudis d'Informàtica, Multimèdia i Telecomunicació, Universitat Oberta de Catalunya, 08018 Barcelona, Spain
* Correspondence: decurto@em.uni-frankfurt.de

Abstract: Unmanned Aerial Vehicles (UAVs) are able to provide instantaneous visual cues and a high-level data throughput that could be further leveraged to address complex tasks, such as semantically rich scene understanding. In this work, we built on the use of Large Language Models (LLMs) and Visual Language Models (VLMs), together with a state-of-the-art detection pipeline, to provide thorough zero-shot UAV scene literary text descriptions. The generated texts achieve a GUNNING Fog median grade level in the range of 7–12. Applications of this framework could be found in the filming industry and could enhance user experience in theme parks or in the advertisement sector. We demonstrate a low-cost highly efficient state-of-the-art practical implementation of microdrones in a well-controlled and challenging setting, in addition to proposing the use of standardized readability metrics to assess LLM-enhanced descriptions.

Keywords: scene understanding; large language models; visual language models; CLIP; GPT-3; YOLOv7; UAV

Citation: de Curtò, J.; de Zarzà, I.; Calafate, C.T. Semantic Scene Understanding with Large Language Models on Unmanned Aerial Vehicles. *Drones* **2023**, *7*, 114. https://doi.org/10.3390/drones7020114

Academic Editors: Diego González-Aguilera and Federico Tombari

Received: 16 December 2022
Revised: 31 January 2023
Accepted: 6 February 2023
Published: 8 February 2023

1. Introduction and Motivation

Unmanned Aerial Vehicles (UAVs) have proven to be an essential asset for practically addressing many challenges in vision and robotics. From surveillance and disaster response to the monitoring of satellite communications, UAVs perform well in situations where seamless mobility and high-definition visual capture are necessary. In this work, we focused on tasks that require a semantic understanding of visual cues and that could guide initial estimates in proposing an adequate characterization of a certain environment. Problems that are of interest include semi-adaptive filming [1] and automatic literary text description. In this setting, we propose a complete pipeline that provides real-time original text descriptions of incoming frames or a general scene description given some pre-recorded videos. The descriptions are well-suited to creating an automatic storytelling framework that can be used in theme parks or family trips alike.

Foundation models are techniques based on neural networks that are trained on large amounts of data and that present good generalization capabilities across tasks. In particular, Natural Language Processing (NLP) has seen a dramatic improvement with the appearance of GPT-2 [2] and its subsequent improvements (GPT-3 [3]). Indeed, Large Language Models (LLMs) and Visual Language Models (VLMs) have recently arisen as a resource for determining widespread problems in disciplines from robotics manipulation and navigation to literary text description, completion, and question answering. We attempt to introduce these techniques in the field of UAVs by providing the vehicle with enhanced semantic understanding. Our approach uses a captioning technique based on CLIP [4,5],

along with the YOLOv7 detector [6], which enhances the captioning output with the object annotations detected and then wires the text into GPT-3.

The descriptions provided are accurate and show a detailed understanding of the scene, and they introduce hallucinated elements that yield sound and consistent seed captions. The literary style allows for the system to be used in a wide variety of situations; for example, a human companion can use the generated text for assistance in writing a script.

The system can be used without fine-tuning in a wide variety of environments, as the base models are trained on large amounts of data. However, to further improve the consistency of the descriptive text, a proper fine-tuning of the detector could be useful when the objects that the system would normally encounter are not present in the COCO object classes [7,8], or when one wants to emphasize certain aspects of the visual cues; for instance, in an amusement park, a fine-tuning of the data could add specificity to the descriptions, e.g., providing captions that include trademark imaginary characters or specific attractions, rides, or games.

This article proposes, from the point of view of system integration, a novel zero-shot literary text description system using state-of-the-art large-language modules through the use of microdrones (RYZE Tello) and UAVs; additionally, a proposed set of measures is newly introduced in this context to assess the adequacy of the output text for the target audience.

One of the main technical issues of applying LLMs to UAVs is that the data have to be relayed to the computer, where either computation has to take place or a query has to be formulated to use an API. On-board processing is possible, but it is limited due to the amount of GPU memory that state-of-the-art models need. A high-definition camera, well-calibrated and possibly stabilized, is crucial for the optimal behavior of the overall system, as it mainly relies on visual cues for processing the entire pipeline. Another limitation is due to the object detector (YOLOv7) that is used to improve the query formulation prior to using GPT-3; in this particular setting, we used a pretrained model trained on the COCO dataset, but specific training data may be needed for a target application. Furthermore, the object detector could be integrated into the on-board processing using a CORAL board.

The main goal of this manuscript is to propose a system that could be used in many real-life applications. The majority of the techniques used have been thoroughly tested in standard datasets before, but there has been little experimentation in real settings with varying conditions and equipment. For testing the system, we used standardized measures originally used to assess texts written by human instructors in the context of the military, education, and so on.

2. Contribution and Paper Organization

A low-cost, highly efficient practical implementation of the system was performed through the use of microdrones (e.g., RYZE Tello), which perform real-time video streaming on a ground computer that controls the vehicle. The level of autonomy of the system could be further enhanced by performing part of the computation on-device; for example, by the attachment of a CORAL Dev Board Mini (Google), which only adds 26 g of payload, to the body of the microdrone. This endows the UAV with a TPU (2GB) that can process on-device real-time detections, for instance, through the use of state-of-the-art models such as SSD MobileNet V2 [9] and EfficientDet-Lite3x [10].

The RYZE Tello drone is a compact and lightweight quadrotor drone designed for use in educational and recreational applications. It is equipped with an Intel processor and a variety of sensors, including a camera, an IMU, and ultrasonic range finders. The drone is capable of autonomous flight using a pre-programmed set of commands and can be controlled remotely using a compatible device, such as a smartphone. It is also equipped with a number of interactive features, such as gesture control and throw-to-fly, which allow users to easily interact with the drone in a variety of ways; that is, the RYZE Tello drone is

a versatile and user-friendly platform that is well-suited for a wide range of applications, including education, entertainment, and research.

A more professionally driven, inexpensive prototype appropriate for outdoor use was attempted by the use of an NXP Hover Games Drone Kit with a CORAL Dev Board Mini (Google) and a high-definition camera (see Figure 1). It also includes GPS and a Flight Management Unit (FMU) that supports the PX4 autopilot flight stack. Autonomy could be enhanced by the use of a LiDAR lite-v3 for navigation purposes, a lightweight 23 g light-ranging device with a high accuracy and range (40 m). In a well-controlled situation, such as a film studio, a tethered UAV could be used to eliminate the limitation of the battery capacity of the vehicle.

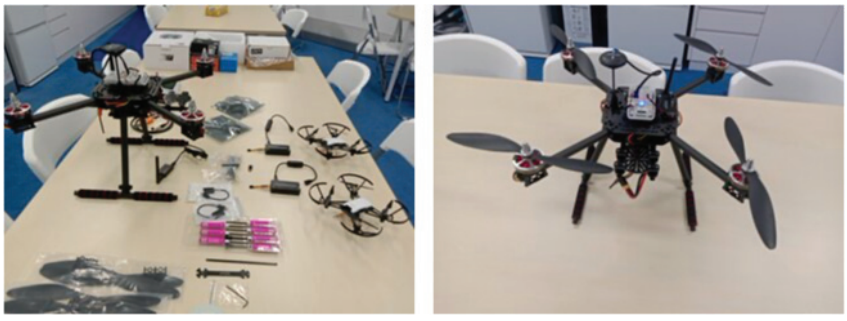

Figure 1. RYZE Tello Microdrones and the NXP Hover Games Drone Kit.

The NXP Hover Games Drone Kit is a hardware and software platform designed for the development and evaluation of autonomous drone systems. It includes a quadrotor drone equipped with an NXP S32 processor, a variety of sensors including an IMU, ultrasonic range finders, and stereo cameras, and a range of peripherals such as LED lights and a buzzer. The kit also includes a software library and sample code for implementing various autonomous flight behaviors such as hovering, takeoff, and landing. It is intended for use by researchers and developers working in the field of autonomous drone systems, and can be used for a wide range of applications, including drone racing, search and rescue, and aerial photography. Overall, the NXP Hover Games Drone Kit is a comprehensive and versatile tool for exploring the capabilities and limitations of autonomous drone systems.

Experimental results based on a UAV testbed show that the proposed pipeline is able to generate accurate state-of-the-art zero-shot UAV literary text descriptions.

The remainder of the paper is structured as follows: an overview of state-of-the-art approaches that entail the use of foundation models is provided. Next, Section 4 addresses the proposed methodology, as well as the background for the prior knowledge needed for the experimental assumptions, while experiments are presented in Section 5. Section 6 proposes standardized readability metrics to evaluate LLM-generated descriptions. Finally, Section 7 provides the conclusions and describes further work.

3. Overview and State of the Art

Large Language Models (LLMs) [11–13] and Visual Language Models (VLMs) [5] have emerged as an indispensable resource to characterize complex tasks and bestow intelligent systems with the capacity to interact with humans in an unprecedented way. These models, also called foundation models, are able to perform well in a wide variety of tasks, e.g., in robotics manipulation [14–16], and can be wired to other modules to act robustly in highly complex situations, such as in navigation and guidance [17,18].

LLMs are ML models that are trained on very large datasets of text and are capable of generating human-like text. These models are typically based on neural networks, which are composed of interconnected processing units that are able to learn and adapt through training. The goal of large language models is to learn the statistical patterns and

relationships present in the training data and use this knowledge to generate coherent and plausible text.

One of the key features of large language models is their ability to generate text that is difficult to distinguish from text written by humans. These models are trained on vast amounts of text and, as a result, are able to capture a wide range of linguistic patterns and structures, including syntax, grammar, and vocabulary. This enables them to generate text that is highly coherent and grammatically correct, and these models can thus be used for a variety of tasks, such as translation, summarization, and text generation.

In addition to their language generation capabilities, large language models have also been shown to be effective at a variety of natural language processing tasks, including language translation, question answering, and text classification. In essence, LLMs are a powerful and versatile tool for understanding and working with natural language data.

Visual Language Models (VLMs) are ML models that are trained on large datasets of text and images and are capable of generating natural language text that is coherent and grammatically correct. The goal of VLMs is to learn the statistical patterns and relationships present in the training data and use this knowledge to generate text that is descriptive and informative about the visual content of an image or a set of images.

One of the key features of visual language models is their ability to generate text that is grounded in the visual content of an image or a set of images. This means that the text generated by these models is specifically related to the objects, people, and events depicted in the image and provides descriptive and informative details about these elements. For example, a VLM could be used to generate a caption for an image depicting the occurrence of a particular action.

In addition to generating descriptive text, visual language models can also be used for a variety of other tasks, such as image classification, object detection, and image captioning. These models can be trained to recognize and classify different types of objects and events in an image and can also be used to generate coherent and grammatically correct captions that describe the content of an image.

VLMs are a powerful and versatile tool for understanding and working with both text and image data. By enabling the generation of descriptive and informative text that is grounded in the visual content of an image, these models have the potential to facilitate a wide range of applications, including image and video analysis, content generation, and natural language processing.

Drones, also known as unmanned aerial vehicles (UAVs), have the potential to be used for a wide range of applications involving semantic scene understanding, which refers to the ability of a system to analyze and interpret the meaning or significance of the objects, people, and events present in a scene. This capability is important for many applications, including robotics, surveillance, and autonomous driving.

One way in which drones can be used for this particular purpose is through the use of on-board sensors and cameras to capture visual data and other types of data about the environment. These data can then be processed and analyzed using ML algorithms to identify and classify the objects and events present in the scene. For example, a drone equipped with a camera and an object recognition algorithm could be used to identify and classify different types of objects in a scene, such as vehicles, pedestrians, and buildings.

In addition to object recognition, drones can also be used for other types of tasks, such as event detection and tracking. For example, a drone equipped with a camera and an event detection algorithm could be used to identify and track the movements of people or vehicles in a scene. This could be useful for applications such as surveillance or traffic monitoring. By enabling the analysis and interpretation of the meaning or significance of objects and events in a scene, drones can provide valuable insights and information for a variety of tasks and scenarios. In this work, we built on the improvements in object detection [19,20] and model reparameterization [21,22] to apply LLMs and VLMs in the field of Unmanned Aerial Vehicles (UAVs) [1]. State-of-the-art techniques of captioning [23–25] have allowed computers

to semantically understand visual data, while advances in automated storytelling can now generate realistic storylines from visual cues [26,27].

4. Methodology

UAV real-time literary storytelling refers to the use of Unmanned Aerial Vehicles (UAVs), also known as drones, to generate narrative stories in real-time based on data they collect. This could involve using the UAVs to capture visual data and other types of data about the environment and then processing and analyzing these data using ML algorithms to identify the objects and events present in the scene. The resulting data could then be used to generate a narrative story that describes and explains the objects and events in the scene coherently and grammatically.

One potential application of UAV real-time literary storytelling is in the field of journalism, where UAVs could be used to capture newsworthy events and generate narratives about these events in real time. For example, a UAV could be used to capture images and video of a natural disaster and then generate a narrative story about the disaster that is based on the data collected by the UAV. This could provide a more immersive and interactive way of reporting on events and could enable journalists to generate stories more quickly and efficiently.

Another potential application is in the field of entertainment, where UAVs could be used to capture data about live events and generate interactive narratives about these events in real time. For example, a UAV could be used to capture data about a sports game and then generate a narrative story about the game that is based on the data collected by the UAV. This could provide a more engaging and interactive way of experiencing live events and could enable users to experience events in a more immersive and interactive way.

UAV real-time literary storytelling offers potential for a wide range of applications, including journalism, entertainment, and education. By enabling the generation of narrative stories in real time based on data collected by UAVs, this technology has the potential to facilitate a more immersive and interactive way of experiencing and understanding events and situations.

CLIP (Contrastive Language-Image Pre-training) is a neural network architecture developed by researchers at OpenAI that can be used for image captioning and other natural language processing tasks. It is based on the idea of pre-training a model on a large dataset of images and text and then fine-tuning it for a specific task, such as image captioning.

CLIP uses a transformer architecture, which is a type of neural network that is particularly well-suited for tasks involving sequential data, such as natural language processing. The model is trained to predict the next word in a sentence given the previous words, using the images as additional context. One key feature of CLIP is that it is able to learn a continuous space of image and text representations, which allows it to generate high-quality captions for a wide range of images. It is also able to learn from a large amount of data, which helps it to generalize to new images and improve the performance in the image captioning task.

The problem of captioning can be formulated as follows: given a dataset of paired images and captions $\{x^z, c^z\}_{z=1}^{N}$, the aim is to be able to synthesize adequate captions given an unseen sample image. In our approach, we built on recent work that uses the embedding of CLIP as a prefix to the caption and that is based on the next objective, where the captions can be understood as a sequence of tokens $c^z = c_1^z, \ldots, c_\ell^z$, padded to a maximum length ℓ:

$$\max_{\theta} \sum_{z=1}^{N} \sum_{w=1}^{\ell} \log p_\theta(c_w^z |\, x^z, c_1^z, \ldots, c_{w-1}^z). \tag{1}$$

We consider, as in [4], an autoregressive language model that predicts the consequent token without considering future tokens.

The CLIP embedding is then projected by a mapping network, denoted as F:

$$p_1^z, \ldots, p_k^z = F(\text{CLIP}(x^z)). \tag{2}$$

where p_w^z is a vector with the same dimension as a word embedding and then concatenated with the caption embedding. A cross-entropy loss is used to train the mapping F.

YOLO (You Only Look Once) [19,20] is a real-time object detection algorithm. It is an end-to-end neural network model that is able to detect and classify objects in images and videos. YOLO works by dividing the input image into a grid of cells and predicting the class and location of objects within each cell. The model uses anchor boxes to make predictions at multiple scales, so it can detect objects of different sizes. The model also predicts the confidence of each detection, which helps to filter out false positives.

One of the main advantages of YOLO is its speed. It is able to process images and videos in real time, making it suitable for use in applications such as video surveillance and autonomous vehicles. YOLO has undergone several versions, with each version improving the accuracy and efficiency of the model. YOLOv7 is the latest version of YOLO and includes several enhancements over previous versions.

We propose a general pipeline for UAV real-time literary storytelling (see Figure 2) that is based on the previously described captioning technique that utilizes CLIP prefix captioning [4,5,28] and that combines the obtained sentence trained with Conceptual Captions [29] with detections given by YOLOv7 [6]. The output of the object detector is processed by a module of sentence formation such that it can be fed into a GPT-3 module, which provides an enhanced literary description. A query formulating the task to be determined by GPT-3 is needed. The system can work in real time on the streaming frames of the vehicle or as a post-processing module once the UAV has landed.

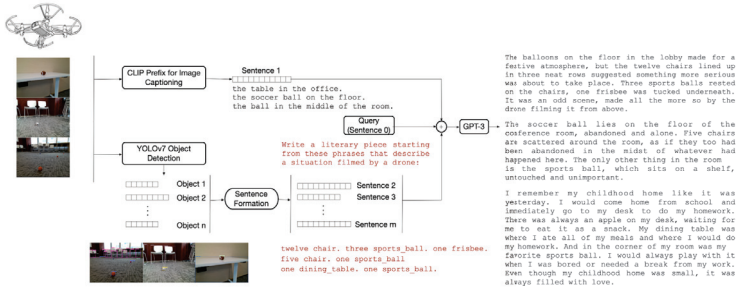

Figure 2. UAV real-time literary storytelling.

The pipeline does not require fine-tuning to specific tasks, although it would benefit from such tuning if used in a particular environment where some specific objects need to be identified, e.g., when there is a need to be specific in terms of trademark names.

The main blocks of the architecture are CLIP Prefix for Image Captioning, YOLOv7, and GPT-3.

CLIP Prefix for Image Captioning is a transformer-based architecture that enables the generation of captions while the CLIP and GPT-2 model are frozen. It consists of the training of a lightweight mapping network based on a transformer [30,31] that translates from the CLIP embedding space to GPT-2.

YOLOv7 is the state-of-the-art object detector in terms of speed and accuracy. It is a generalization of previous YOLO-based architectures with the use of Extended Efficient Layer Aggregation Networks (E-ELANs) [6]. E-ELANs address the problem of controlling the shortest longest gradient path so that the network converges effectively. It uses expand, shuffle, and merge cardinality to continue learning without losing the original gradient path.

GPT-3 is used to enhance the captions by the natural language instruction and prompt engineering. All of our experiments used the API of OpenAI, and the model is surprisingly effective with zero-shot prompts.

Having said that, the manuscript has the goal of deploying state-of-the-art LLMs to accomplish the task of zero-shot semantic scene understanding through the use of a low-cost UAV (RYZE Tello or a NXP Hover Games Drone Kit) that incorporates a high-definition camera. Further integration by the use of a Raspberry Pi Zero W or a CORAL board can move some of the computation on-device with the proper module adaptation, both for object detection and also for the LLM API. In the latter case, a call to OpenAI API is necessary at this stage but advances on the field will soon make it possible to test the trained models directly on-board (e.g., pruning the LLM model to make it fit on memory) without the need to relay the video frames to the computer for further processing. In either way, model pruning can be used to reduce the model size and thus reduce the computational requirements. Another technique would be to use model quantization to reduce the precision of the model and make it more efficient. Additionally, another viable approach is knowledge distillation, where the knowledge of a large teacher model is transferred to a smaller student model for the purpose of using it on a resource-constrained environment.

5. Results and Experiment Set-Up

Experiments were conducted on a well-controlled challenging environment with the use of RYZE Tello, streaming the data in real time to a ground computer that processes the frames one by one. Figures 3–6 illustrate all of the stages of the used methodology for a number of UAV captured stream frames, with contrasting levels of descriptive goodness. The drone captures a particular visual scene that is consequently sent to the ground computer, where a first caption is generated using CLIP Prefix for Image Captioning with beam search. The caption is improved by the output of a YOLOv7 object detector after sentence formation. Finally, a query is formulated together with the resultant caption to generate an enhanced text description by the GPT-3 module. The results are consistent and robust and exhibit original and genuine descriptions of the imagery, and the modules of captioning and object detection are effective and efficient.

CLIP Prefix for Image Captioning presents an average runtime of 206 ms and the YOLOv7 Object Detector presents one of 556 ms, using a GPU Tesla V100-SXM2 (16GB) and a two-core Intel(R) Xeon(R) CPU @ 2.00 GHz. Prompts to the OpenAI API take an average of 3.9 s using the completion model text-davinci-002, where max_tokens = 401 and temperature = 0.9.

Figure 3 shows the methodology when the CLIP captioning module and the YOLOv7 object detection produce accurate outputs, and the GPT-3 module produces a very good enhanced literary description.

Figure 4 shows the methodology when the CLIP captioning module and the YOLOv7 object detection produce relatively good outputs (detection of the majority of objects—not all or not completely accurate), and the GPT-3 generates a realistic literary description but with the presence of hallucinated elements that provide realism but are not actually in the scene.

Figure 5 shows the methodology when the CLIP captioning module and the YOLOv7 produce somewhat adequate outputs, but they are not particularly accurate, e.g., detecting objects but misclassifying some of them, or generating overly general caption descriptions. The GPT-3 then produces an enhanced description, but not a very accurate one.

Finally, Figure 6 shows the methodology when the CLIP captioning module or YOLOv7 object detection fail to describe the scene accurately, and the GPT-3 module generates an erroneous text description.

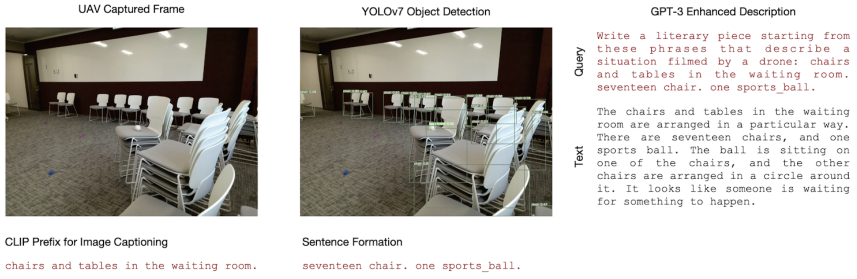

(a)

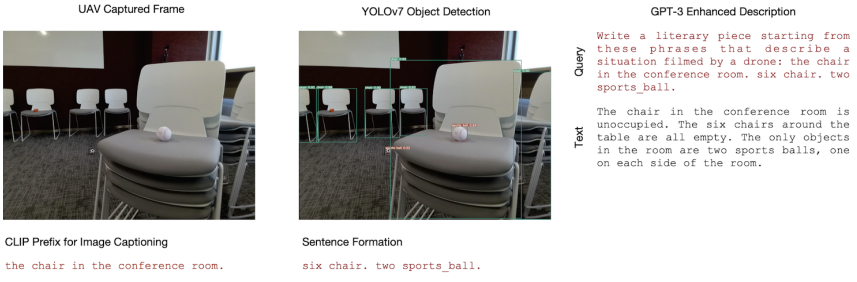

(b)

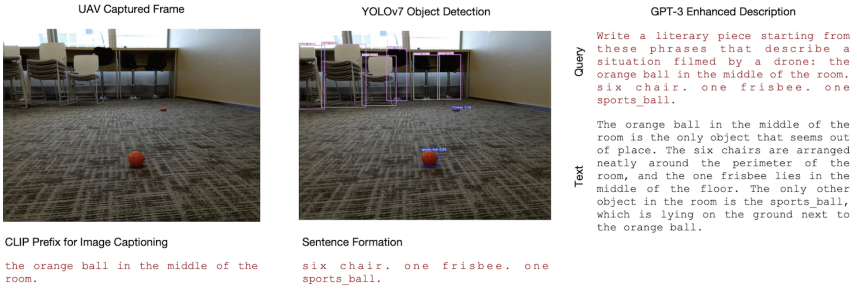

(c)

Figure 3. UAV captured frame processing and GPT-3. Very good GPT-3 descriptions of the scene.

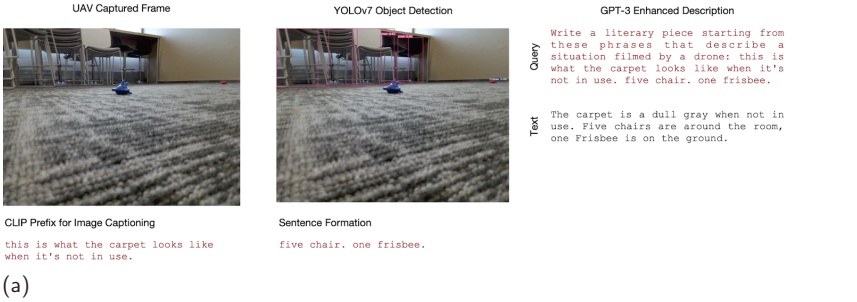

(a)

Figure 4. *Cont.*

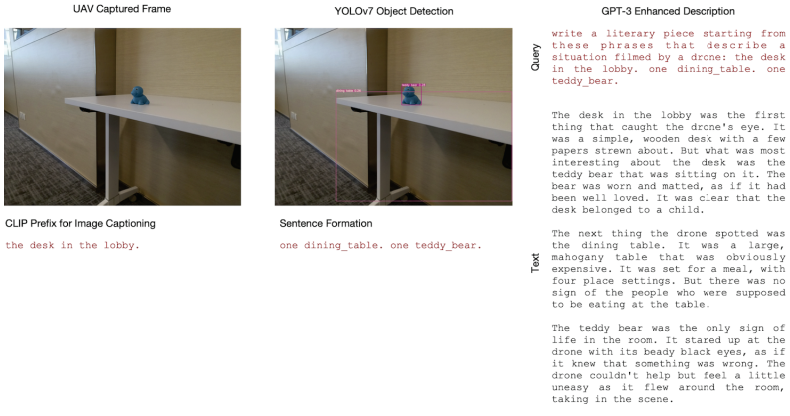

(b)

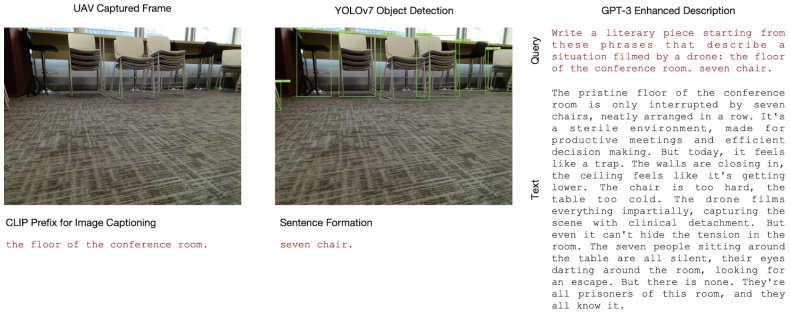

(c)

Figure 4. UAV captured frame processing and GPT-3. Adequate literary GPT-3 descriptions.

(a)

Figure 5. *Cont.*

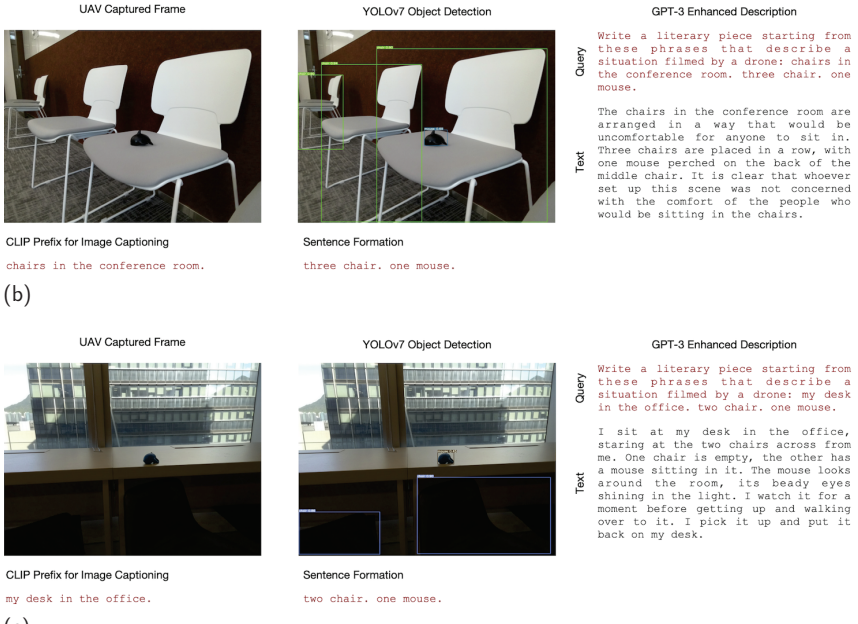

Figure 5. UAV captured frame processing and GPT-3. Somewhat good descriptions, but the CLIP captioning module and the YOLOv7 produce inaccurate outputs.

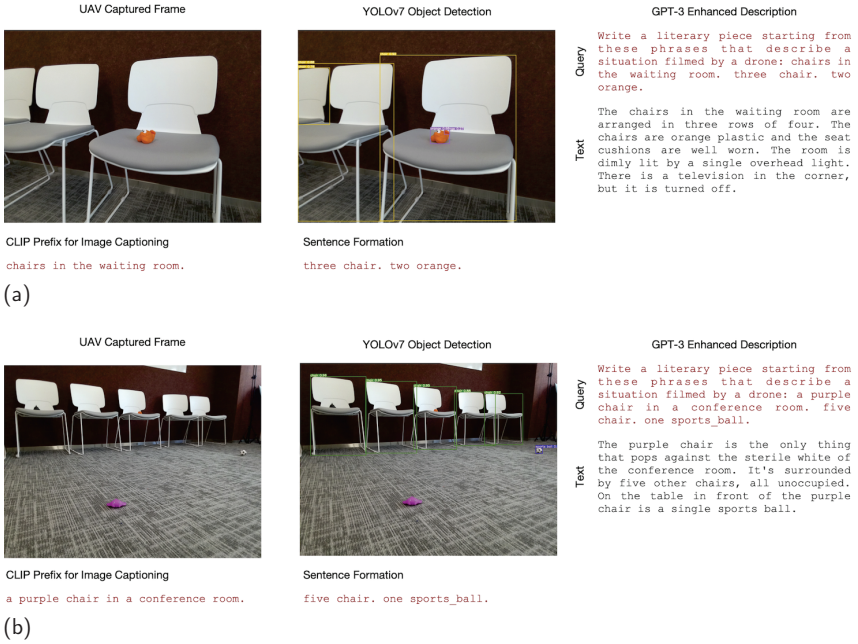

Figure 6. UAV captured frame processing and GPT-3. Failure cases.

6. Readability Analysis

GPT-3 (short for "Generative Pre-training Transformer 3") is a large language model developed by OpenAI that is trained on a very large dataset of text and is capable of

generating human-like text. It is based on a type of neural network called a transformer, which is composed of interconnected processing units that are able to learn and adapt through training. The goal of GPT-3 is to learn the statistical patterns and relationships present in the training data and use this knowledge to generate coherent and plausible text.

One of the key features of GPT-3 is its ability to generate text that is difficult to distinguish from text written by humans. It is trained on a dataset of billions of words and, as a result, is able to capture a wide range of linguistic patterns and structures, including syntax, grammar, and vocabulary. This enables it to generate text that is highly coherent and grammatically correct, and it can thus be used for a variety of tasks, such as translation, summarization, and text generation.

Readability measures are tools that are used to evaluate the complexity of written text and determine how easy or difficult it is for readers to understand. One common readability measure, for instance, is the GUNNING Fog index, which is a formula that estimates the number of years of education a reader would need to understand a piece of text. The GUNNING Fog index is based on the average number of words per sentence and the percentage of complex words (those with three or more syllables) in the text.

To calculate the GUNNING Fog index, the following steps are followed:

- Count the number of words in a sample of the text;
- Count the number of sentences in the sample;
- Divide the total number of words by the total number of sentences to calculate the average number of words per sentence;
- Count the number of complex words (those with three or more syllables) in the sample;
- Divide the number of complex words by the total number of words, and multiply the result by 100 to calculate the percentage of complex words in the sample;
- Add the average number of words per sentence and the percentage of complex words. The result is the GUNNING Fog index.

The GUNNING Fog index is typically used to evaluate the readability of written materials, such as reports, documents, and articles. It is a useful tool for determining the level of difficulty of a piece of text and ensuring that it is appropriate for a particular audience. For example, a text with a GUNNING Fog index of 8 would be considered suitable for readers with an eighth-grade education or higher.

Such readability measures are useful tools for evaluating the complexity of written text and ensuring that it is appropriate for a particular audience. This can help writers and editors to produce written materials that are clear, concise, and easy to understand and can help readers to more easily comprehend and retain information presented in a text.

A readability analysis of the GPT-3-enhanced text is provided by the use of standardized measures, the one introduced earlier being the most effective. In this manuscript, we propose analyzing LLM texts by the following metrics: FLESCH reading ease, DALE CHALL readability, the Automated Readability Index (ARI), the COLEMAN LIAU index, GUNNING Fog, SPACHE, and Linsear Write. The scores obtained by the use of these formulas were designed by linguists to assess the readability of texts to approximate their usability and have been extensively used by, for example, the Office of Education of the United States of America to calibrate the readability of textbooks for the public school system, daily newspapers and monthly magazines to target the appropriate audience, the Department of Defense to help assess the adequacy of technical manuals, and, in general, many US Government Agencies to evaluate the difficulty of a reading passage written in English.

FLESCH reading ease [32] is a simple approach used to assess the grade level of the reader. It is based on the average sentence length and the average number of syllables per word. It is a score in the set $[0, 100]$; the higher the number, the easier the text is to read. According to the scale, $[0, 30]$ means a text is easily understood by a college graduate, $[60, 70]$ means it is easily understood by eighth and ninth graders, and $[90, 100]$ means it is easily understood by a fifth grader.

DALE CHALL readability [33] calculates the grade level of a text sample based on the average sentence length in words and the number of difficult words according to a designated list of common words familiar to most fourth-grade students. Adjusted scores are as follows: <5: Grade 4 and below; $[5,6)$: Grades 5–6; $[6,7)$: Grades 7–8; $[7,8)$: Grades 9–10; $[8,9)$: Grades 11–12; $[9,10)$: College; ≥ 10: College Graduate.

The Automated Readability Index (ARI) consists of a weighted sum of two ratio factors: the number of characters per word, and the average number of words per sentence. It assesses the understandability of a text and outputs a value that approximates the grade level needed to grasp the text. For example, the tenth grade corresponds to 15–16 years old, the eleventh grade corresponds to 16–17 years old, the twelfth grade corresponds to 17–18 years old, and greater than twelve corresponds to the level of college.

The COLEMAN-LIAU index [34] is similarly based on the average number of letters per 100 words and the average number of sentences per 100 words. It is like the ARI, but unlike most of the other metrics that predict the grade level, it relies on characters instead of syllables per word.

GUNNING Fog [35] is based on the scaled sum of the average sentence length and the percentage of hard words. It measures the readability of a text passage, and the ideal value is 7 or 8. Texts with a score above 12 are too hard for most people to understand. The measure scores highly with short sentences written in simple language but penalizes long sentences with complicated words.

The SPACHE readability formula [36] is based on the average sentence length and the number of difficult words according to a third grader. It is similar to Dale Chall, but for primary texts until the third grade. To assess the readability of a text, SPACHE is first used, and if the result is higher than third grade, Dale Chall is used.

Linsear Write is a readability formula based on sentence length and the number of words with three or more syllables. Analogous to the previous formulations, it scores a text passage according to the grade level.

Table 1 shows the proposed metrics on several example frames. The metrics are computed on unique frames in Row 1–3 and on multi-frame configurations in Row 4–8. We can observe that the storylines generated exhibit a relatively consistent behavior among the statistical indices, where unique frames tend to be ranked at a lower grade level and multi-frame configurations are closer to college level. All SPACHE readability indices are higher than third grade, so Dale Chall has to be considered, where the frames are consistently ranked with a median grade level of $[7,8]$. Among the measures, GUNNING Fog presents an ideal behavior, as all values are in the range of [7–12], which means that the level of generated texts is comparable to that of established publications in magazines and books, and therefore can be understood by the general public while presenting a rich vocabulary.

Table 1. Readability analysis of a random stream of data captured by RYZE Tello. Score (upper row) and grade level (lower row) for each metric.

Frame(s) \ Metric	FLESCH Reading Ease	Dale Chall	ARI	Coleman Liau	GUNNING Fog	SPACHE	Linsear Write
00	68.36 [8, 9]	6.56 [7, 8]	6.29 [7]	9.10 [9]	9.47 [9]	4.56 [5]	6.1 [6]
01	84.22 [6]	6.06 [7, 8]	3.63 [9, 10]	4.36 [4]	8.18 [8]	3.91 [4]	7.14 [7]
02	84.57 [6]	5.67 [5, 6]	3.80 [9, 10]	5.04 [5]	7.40 [7]	4.18 [4]	6.46 [6]
03–05	71.11 [7]	6.82 [7, 8]	10.27 [16, 17]	7.89 [8]	11.81 [12]	5.82 [6]	13.14 [13]
06–07	82.08 [7, 8]	6.82 [5]	4.36 [8]	7.89 [8]	7.56 [4]	3.64 [7]	6.94
08–10	74.30 [7]	6.35 [7, 8]	7.05 [13, 14]	7.53 [8]	10.58 [11]	4.87 [5]	9.0 [9]
11–13	75.94 [7]	6.33 [7, 8]	8.54 [9]	7.47 [7]	10.76 [11]	5.33 [5]	11.5 [12]

7. Conclusions

An RIZE Tello drone is a small, lightweight, and low-cost quadrotor drone that is equipped with a camera and is capable of autonomous flight. In this system, the drone is used to capture video footage of a scene and transmit it to a ground computer in real time.

On the ground computer, the video stream is processed using state-of-the-art LLMs together with a module of object detection to produce accurate text descriptions of a scene in the form of captions. These captions can be used to provide a verbal description of the scene for individuals who are deaf or hard of hearing, or to provide additional context for individuals who are able to see the video footage.

A pipeline for semantic scene understanding given a stream of UAV data frames was proposed. The methodology does not require fine-tuning; rather, it provides zero-shot text descriptions. The modules consist of state-of-the-art architectures. A captioning module based on CLIP Prefix for Image Captioning is wired through sentence formation to a YOLOv7 object detector, and the generated text is enhanced by prompting GPT-3 natural language instructions. We are the first to provide zero-shot UAV literary storytelling that can stream to a ground computer in real time or after landing (in this latter case, the video would be stored on an SD card, and the RYZE Tello drone needs to be equipped with a board computer, e.g., a Raspberry Pi Zero W or a CORAL board) and that provides state-of-the-art accurate literary text descriptions. Metrics used to assess the readability of LLM texts are proposed, leveraging standardized measures from linguistics.

The system combines the capabilities of an RIZE Tello drone (or an NXP Hover Games Drone) with advanced techniques of computer vision to provide a rich and detailed description of a scene in real time. The system has potential applications in a wide range of fields, including surveillance, search and rescue, and environmental monitoring.

As further work, the trajectory of the drone could be optimized for a certain filming style to help the text description module to obtain better shots for particularly interesting events that need to be addressed in the storyline. That being said, in the current work, we did not take planning and trajectory issues into consideration and assumed that the UAV is being remotely controlled or is flying using an adequate autopilot policy. In addition, GPS coordinates and positioning information from other sensors such as IMU or LiDAR could be used to further improve the resultant text descriptions by prompting the GPT-3 module with the corresponding trajectories.

There are a number of other ways that the previously described system could be extended or improved upon. Some potential areas of further work include the following.

The accuracy and reliability of the algorithms that handle captioning and object detection can be improved: while current LLMs and object detection algorithms are highly accurate, there is always room for improvement. Further research could focus on developing new techniques or fine-tuning existing algorithms to increase their accuracy and reliability. Other sensors can be added: the RIZE Tello drone is equipped with a camera, but additional sensors, such as LiDAR or RADAR, could allow the system to gather more detailed and comprehensive data about the scene. The drone's autonomy could be enhanced: the RIZE Tello drone is capable of autonomous flight, but further work could focus on developing more advanced autonomy algorithms to enable the drone to navigate more complex environments and perform more sophisticated tasks. Real-time analysis could be implemented: at the moment, the system processes the video stream and generates captions and object detections after the fact. However, implementing real-time analysis could allow the system to provide updates and alerts in near-real time, making it more useful for applications such as surveillance or search and rescue. Finally, applications could be developed for specific domains: the system could be tailored to specific domains by training the captioning and object detection algorithms on domain-specific data and developing domain-specific applications. For example, the system could be used for agricultural monitoring by training the algorithms on data specific to crops and farm machinery.

The ultimate goal is to be able to confer autonomous systems (e.g., UAVs and self-driving cars) with literary capabilities comparable to those provided by human counterparts.

Specifically, the use of LLMs and VLMs push the boundaries of system perception and the understandability of events, situations, and contextual information.

Author Contributions: Conceptualization, J.d.C. and I.d.Z.; funding acquisition, C.T.C.; investigation, J.d.C. and I.d.Z.; methodology, J.d.C. and I.d.Z.; software, J.d.C. and I.d.Z.; supervision, C.T.C.; writing—original draft, J.d.C.; writing—review and editing, C.T.C., J.d.C. and I.d.Z. All authors have read and agreed to the published version of the manuscript.

Funding: This work is supported by the HK Innovation and Technology Commission (InnoHK Project CIMDA). We acknowledge the support of Universitat Politècnica de València; R&D project PID2021-122580NB-I00, funded by MCIN/AEI/10.13039/501100011033 and ERDF.

Institutional Review Board Statement: Not applicable.

Informed Consent Statement: Not applicable.

Data Availability Statement: Not applicable.

Conflicts of Interest: The authors declare that they have no conflict of interest. The funders had no role in the design of the study, in the collection, analyses, or interpretation of data, in the writing of the manuscript, or in the decision to publish the results.

Abbreviations

The following abbreviations are used in this manuscript:

ML	Machine Learning
NLP	Natural Language Processing
LLM	Large Language Models
VLM	Visual Language Models
GPT	Generative Pre-training Transformer
CLIP	Contrastive Language-Image Pre-training
YOLO	You Only Look Once
LiDAR	Light Detection And Ranging
RADAR	Radio Detection And Ranging

References

1. Bonatti, R.; Bucker, A.; Scherer, S.; Mukadam, M.; Hodgins, J. Batteries, camera, action! learning a semantic control space for expressive robot cinematography. In Proceedings of the 2021 IEEE International Conference on Robotics and Automation (ICRA), Xi'an, China, 30 May–5 June 2021.
2. Radford, A.; Wu, J.; Child, R.; Luan, D.; Amodei, D.; Sutskever, I. *Language Models Are Unsupervised Multitask Learners*; Technical Report; 2019. Available online: https://www.semanticscholar.org/paper/Language-Models-are-Unsupervised-Multitask-Learners-Radford-Wu/9405cc0d6169988371b2755e573cc28650d14dfe (accessed on 15 December 2022).
3. Brown, T.; Mann, B.; Ryder, N.; Subbiah, M.; Kaplan, J.D.; Dhariwal, P.; Neelakantan, A.; Shyam, P.; Sastry, G.; Askell, A.; et al. Language models are few-shot learners. *Neural Inf. Process. Syst.* **2020**, *33*, 1877–1901.
4. Mokady, R.; Hertz, A.; Bermano, A.H. ClipCap: CLIP prefix for image captioning. *arXiv* **2021**, arXiv:2111.09734.
5. Radford, A.; Kim, J.W.; Hallacy, C.; Ramesh, A.; Goh, G.; Agarwal, S.; Sastry, G.; Askell, A.; Mishkin, P.; Clark, J.; et al. Learning transferable visual models from natural language supervision. In Proceedings of the 38th International Conference on Machine Learning, Virtual, 18–24 July 2021.
6. Wang, C.-Y.; Bochkovskiy, A.; Liao, H.-Y.M. YOLOv7: Trainable bag-of-freebies sets new state-of-the-art for real-time object detectors. *arXiv* **2022**, arXiv:2207.02696.
7. Chen, X.; Fang, H.; Lin, T.-Y.; Vedantam, R.; Gupta, S.; Dollár, P.; Zitnick, C.L. Microsoft coco captions: Data collection and evaluation server. *arXiv* **2015**, arXiv:1504.00325.
8. Lin, T.-Y.; Maire, M.; Belongie, S.; Hays, J.; Perona, P.; Ramanan, D.; Dollár, P.; Zitnick, C.L. Microsoft coco: Common objects in context. In Proceedings of the Computer Vision—ECCV 2014: 13th European Conference, Zurich, Switzerland, 6–12 September 2014; Springer: Berlin/Heidelberg, Germany, 2014; pp. 740–755.
9. Sandler, M.; Howard, A.G.; Zhu, M.; Zhmoginov, A.; Chen, L. Inverted residuals and linear bottlenecks: Mobile networks for classification, detection and segmentation. *arXiv* **2018**, arXiv:1801.04381.
10. Tan, M.; Pang, R.; Le, Q.V. Efficientdet: Scalable and efficient object detection. *arXiv* **2020**, arXiv:1911.09070.
11. Alayrac, J.-B.; Donahue, J.; Luc, P.; Miech, A.; Barr, I.; Hasson, Y.; Lenc, K.; Mensch, A.; Millican, K.; Reynolds, M.; et al. Flamingo: A visual language model for few-shot learning. *arXiv* **2022**, arXiv:2204.14198.

12. Gu, X.; Lin, T.-Y.; Kuo, W.; Cui, Y. Open-vocabulary object detection via vision and language knowledge distillation. *arXiv* **2022**, arXiv:2104.13921.
13. Wei, J.; Tay, Y.; Bommasani, R.; Raffel, C.; Zoph, B.; Borgeaud, S.; Yogatama, D.; Bosma, M.; Zhou, D.; Metzler, D.; et al. Emergent abilities of large language models. *arXiv* **2022**, arXiv:2206.07682.
14. Cui, Y.; Niekum, S.; Gupta, A.; Kumar, V.; Rajeswaran, A. Can foundation models perform zero-shot task specification for robot manipulation? In Proceedings of the 4th Annual Learning for Dynamics and Control Conference, Stanford, CA, USA, 23–24 June 2022.
15. Nair, S.; Rajeswaran, A.; Kumar, V.; Finn, C.; Gupta, A. R3M: A universal visual representation for robot manipulation. *arXiv* **2022**, arXiv:2203.12601.
16. Zeng, A.; Florence, P.; Tompson, J.; Welker, S.; Chien, J.; Attarian, M.; Armstrong, T.; Krasin, I.; Duong, D.; Wahid, A.; et al. Transporter networks: Rearranging the visual world for robotic manipulation. *arXiv* **2022**, arXiv:2010.14406.
17. Huang, W.; Abbeel, P.; Pathak, D.; Mordatch, I. Language models as zero-shot planners: Extracting actionable knowledge for embodied agents. In Proceedings of the 39th International Conference on Machine Learning, Baltimore, MA, USA, 17–23 July 2022.
18. Zeng, A.; Attarian, M.; Ichter, B.; Choromanski, K.; Wong, A.; Welker, S.; Tombari, F.; Purohit, A.; Ryoo, M.; Sindhwani, V.; et al. Socratic models: Composing zero-shot multimodal reasoning with language. *arXiv* **2022**, arXiv:2204.00598.
19. Redmon, J.; Divvala, S.; Girshick, R.; Farhadi, A. You only look once: Unified, real-time object detection. In Proceedings of the IEEE/CVF Conference on Computer Vision and Pattern Recognition (CVPR), Las Vegas, NV, USA, 26 June–1 July 2016; pp. 779–788.
20. Redmon, J.; Farhadi, A. YOLO9000: Better, faster, stronger. In Proceedings of the IEEE/CVF Conference on Computer Vision and Pattern Recognition (CVPR), Honolulu, HI, USA, 21–26 July 2017; pp. 7263–7271.
21. Tan, M.; Le, Q.V. Efficientnet: Rethinking model scaling for convolutional neural networks. *arXiv* **2019**, arXiv:1905.11946.
22. Tan, M.; Le, Q.V. Efficientnetv2: Smaller models and faster training. *arXiv* **2021**, arXiv:2104.00298.
23. Anderson, P.; He, X.; Buehler, C.; Teney, D.; Johnson, M.; Gould, S.; Zhang, L. Bottom-up and top-down attention for image captioning and visual question answering. In Proceedings of the IEEE Conference on Computer Vision and Pattern Recognition, Salt Lake City, UT, USA, 18–23 June 2018; pp. 6077–6086.
24. Fang, H.; Gupta, S.; Iandola, F.; Srivastava, R.K.; Deng, L.; Dollár, P.; Gao, J.; He, X.; Mitchell, M.; Platt, J.C.; et al. From captions to visual concepts and back. In Proceedings of the IEEE Conference on Computer Vision and Pattern Recognition, Boston, MA, USA, 7–12 June 2015 ; pp. 1473–1482.
25. Xu, K.; Ba, J.; Kiros, R.; Cho, K.; Courville, A.; Salakhudinov, R.; Zemel, R.; Bengio, Y. Show, attend and tell: Neural image caption generation with visual attention. In Proceedings of the 32nd International Conference on International Conference on Machine Learning, Lille, France, 6–11 July 2015; pp. 2048–2057.
26. Fan, A.; Lewis, M.; Dauphin, Y. Hierarchical neural story generation. *arXiv* **2018**, arXiv:1805.04833.
27. See, A.; Pappu, A.; Saxena, R.; Yerukola, A.; Manning, C.D. Do massively pretrained language models make better storytellers? *arXiv* **2019**, arXiv:1909.10705.
28. Li, X.L.; Liang, P. Prefix-tuning: Optimizing continuous prompts for generation. *arXiv* **2021**, arXiv:2101.00190.
29. Sharma, P.; Ding, N.; Goodman, S.; Soricut, R. Conceptual captions: A cleaned, hypernymed, image alt-text dataset for automatic image captioning. In Proceedings of the 56th Annual Meeting of the Association for Computational Linguistics (Volume 1: Long Papers), Melbourne, Australia, 15–20 July 2018; pp. 2556–2565.
30. Dosovitskiy, A.; Beyer, L.; Kolesnikov, A.; Weissenborn, D.; Zhai, X.; Unterthiner, T.; Dehghani, M.; Minderer, M.; Heigold, G.; Gelly, S. et al. An image is worth 16x16 words: Transformers for image recognition at scale. *arXiv* **2021**, arXiv:2010.11929.
31. Vaswani, A.; Shazeer, N.; Parmar, N.; Uszkoreit, J.; Jones, L.; Gomez, A.N.; Kaiser, Ł.; Polosukhin, I. Attention is all you need. *arXiv* **2017**, arXiv:1706.03762.
32. Flesch, R. A new readability yardstick. *J. Appl. Psychol.* **1948**, *32*, 221–233. [CrossRef]
33. Dale, E.; Chall, J.S. A formula for predicting readability. *Educ. Res. Bull.* **1948**, *27*, 11–28.
34. Coleman, M.; Liau, T.L. A computer readability formula designed for machine scoring. *J. Appl. Psychol.* **1975**, *60*, 283–284. [CrossRef]
35. Gunning, R. *The Technique of Clear Writing*; McGraw-Hill: New York, NY, USA, 1952.
36. Spache, G. A new readability formula for primary-grade reading materials. *Elem. Sch. J.* **1953**, *53*, 410–413. [CrossRef]

drones

MDPI

Article

Acoustic SLAM Based on the Direction-of-Arrival and the Direct-to-Reverberant Energy Ratio

Wenhao Qiu, Gang Wang * and Wenjing Zhang

State Key Laboratory of Advanced Design and Manufacturing for Vehicle Body, Hunan University, Changsha 410082, China
* Correspondence: wangg@hnu.edu.cn

Abstract: This paper proposes a new method that fuses acoustic measurements in the reverberation field and low-accuracy inertial measurement unit (IMU) motion reports for simultaneous localization and mapping (SLAM). Different from existing studies that only use acoustic data for direction-of-arrival (DoA) estimates, the source's distance from sensors is calculated with the direct-to-reverberant energy ratio (DRR) and applied to eliminate the nonlinear noise from motion reports. A particle filter is applied to estimate the critical distance, which is key for associating the source's distance with the DRR. A keyframe method is used to eliminate the deviation of the source position estimation toward the robot. The proposed DoA-DRR acoustic SLAM (D-D SLAM) is designed for three-dimensional motion and is suitable for drones. The method is the first acoustic SLAM algorithm that has been validated on a real-world drone dataset that contains only acoustic data and IMU measurements. Compared with previous methods, D-D SLAM has acceptable performance in locating the drone and building a source map from a real-world drone dataset. The average location accuracy is 0.48 m, while the source position error converges to less than 0.25 m within 2.8 s. These results prove the effectiveness of D-D SLAM in real-world scenes.

Keywords: simultaneous localization and mapping; robot audition; direct-to-reverberant energy ratio; mobile robots

Citation: Qiu, W.; Wang, G.; Zhang, W. Acoustic SLAM Based on the Direction-of-Arrival and the Direct-to-Reverberant Energy Ratio. *Drones* **2023**, *7*, 120. https://doi.org/10.3390/drones7020120

Academic Editors: Andrzej Łukaszewicz, Wojciech Giernacki, Zbigniew Kulesza, Jaroslaw Pytka and Andriy Holovatyy

Received: 10 January 2023
Revised: 6 February 2023
Accepted: 8 February 2023
Published: 9 February 2023

1. Introduction

Recently, there has been renewed interest in simultaneous localization and mapping (SLAM). Many meaningful and excellent works in SLAM have been based on optical and visual sensors, such as VINS [1]. Different from visual SLAM, some works have focused on acoustic SLAM, where acoustic sensors are involved. Most works on acoustic SLAM have been conducted in underwater environments [2–4], while indoor acoustic SLAM [5–7], by contrast, has received scant attention. Conventional SLAM techniques based on optical and visual sensors are unsuitable for some special indoor environments, for example, foggy rooms where light and lasers cannot penetrate. Conversely, the indoor acoustic SLAM-based acoustic sensors can use continuous environmental sources as landmarks to assist the mapping of robots in such a foggy indoor environment. It is preferable to use acoustic SLAM in an indoor environment where light and lasers cannot penetrate and continuous environmental sources exist.

Based on the sensor type used, indoor acoustic SLAM can be classified as active or passive acoustic SLAM. Active indoor acoustic SLAM is usually based on active sonar, and a sonar beam is utilized in an active sonar sensor model to measure the positions of landmarks. To assist in localization, a motion sensor is required to generate motion reports. Passive indoor acoustic SLAM is usually based on microphone arrays for direction-of-arrival (DoA) estimates and motion sensors (such as an odometer) for motion reports. In 2009 Hu et al. [5] proposed an acoustic SLAM method based on a cross-shaped microphone array and odometry, and in 2013, Kallakuri et al. [6] developed a method based

on a microphone array and light detection and ranging (LiDAR). The two studies above were both capable of locating the robot and mapping the environment in experiments. However, highly accurate motion reports from odometry or LiDAR are necessary for acceptable results. For example, the robot's trace measured with only motion sensors (without information from acoustic sensors) coincided perfectly with the final estimation where all sensors were involved (see experimental results in Figure 4 of [5]). Thus, the accuracy of those methods is likely heavily dependent on the accuracy of motion sensors. Due to indoor reverberation, strong noise or even errors are common during DoA estimates. When the motion reports are inaccurate or even false, the above methods can hardly achieve acceptable results.

To facilitate robustness against false DoA estimates using motion sensors such as inertial measurement units (IMUs), Evers et al. [7,8] developed their own acoustic SLAM, "Acoustic SLAM" (aSLAM) with probabilistic source triangulation in 2018. However, aSLAM was only tested in simulations where the measurement noise of motion reports is ideal. Specifically, simple Gaussian noise was added to the true velocity of the robot to simulate the velocity measurement. However, the noise of a typical motion sensor, such as an IMU, is mainly non-Gaussian and nonlinear. It will be demonstrated in this paper that the result of feeding the aSLAM with practical datasets is undesirable.

As mentioned before, there are occasionally false DoA estimates due to reverberation in real indoor environments. At the same time, due to unavoidable integral error, motion sensors such as IMUs cannot provide accurate velocity logs or motion paths. Acoustic SLAM methods [5–7] that fuse DoA estimates and motion reports can be considered bearing only SLAM [9]. As the DoA estimates contain only directional information, highly accurate motion sensors are necessary to gain an acceptable overall positioning and mapping accuracy. However, low-price motion sensors, including IMUs, have an evident integral error, and their noise model is nonideal. If we want to obtain acceptable SLAM results with low-accuracy motion measurements in experiments, more information from acoustic sensors is vital in addition to the DoA. In addition to bearing information, the range that denotes the distance between the source and the robot should be beneficial for acoustic SLAM, especially when false DoA estimates are common and motion reports coming from low-accuracy IMU sensors suffer from severe drifting.

Several methods have been proposed for estimating the source's distance [10], including the time difference of arrival (TDOA), deep learning, triangulation, and the direct-to-reverberant energy ratio (DRR). The TDOA is sensitive to the array size [10], and the sound source distance estimation methods based on deep learning are unable to adapt to new environments unless retraining is carried out in advance for each new environment [11,12]. The distance estimations with triangulation vary considerably and are still affected by the accuracy of the motion sensors [13]. The DRR method, which is based on the phenomenon of indoor sound reflections, can be used to estimate the direct source's distance from the sensor in a reverberant field. Estimates with the DRR method are insensitive to the array size and do not rely on information from motion sensors [14], so it may be suitable to estimate the range to eliminate the error of motion sensors.

In 2018, M. Strauss, P. Mordel, V. Miguet, and A. Deleforge published the DREGON dataset, aiming at source localization research [15]. In this dataset, a drone with a microphone array and an IMU flies in an airtight room containing a loudspeaker. Publicly available data include the IMU data and the audio recordings during the entire flying period. Moreover, the airtight room was equipped with a motion capture system to obtain precise ground truth positions of the drone and the loudspeaker at all times. The DREGON dataset contains all the information needed for the evaluation and comparison of different acoustic SLAM algorithms and will be applied here to validate our proposed method.

In this paper, a DoA-DRR acoustic SLAM (D-D SLAM) is proposed for the situation when strong noise exists in IMU motion reports. The source's distance from the robot, which is estimated using the DRR method in different time frames, is added to acoustic SLAM as a new constraint of D-D SLAM. The critical distance, which is necessary for

associating the source's distance with the DRR, is estimated with an online method during the complete time period. Overcoming the deficiencies of Evers' aSLAM [7], the proposed D-D SLAM is validated using datasets generated from simulations and real-world indoor scenes drone measurements in the DREGON dataset. The continuous environmental source is required as a landmark in the D-D SLAM. The DRR metric is unsuitable for estimating sound source distance in a free field, so the D-D SLAM is only applicable to indoor scenarios. Generally, this paper proposes a new methodology for acoustic SLAM using only a microphone array and IMU. The essay has been organized in the following way. Section 2 is the problem formulation, and Section 3 introduces the necessary background knowledge. Section 4 derives the proposed D-D SLAM. Section 5 presents the setup of the simulation and experiment. Section 6 shows and analyses the results. Section 7 is the conclusion.

2. Problem Formulation

In previous acoustic SLAM research, the applied robot movement model always constrained the robot's velocity to be along the direction of orientation of the robot [5–7]. This constraint can be easily satisfied in simulation. Meanwhile, the coupling of the robot's orientation and its velocity direction simplified the mathematical deduction. However, it is only practical in a few kinds of real robots, for instance, two-wheel robots.

For the sake of generality, a three-dimensional robot movement model is applied in the proposed method. The model decouples the direction of the robot's velocity from its orientation; thus, it is suitable for most real robots, such as drones. As depicted in Figure 1, the robot's state at time t is considered as $\mathbf{r}_t = [\mathbf{p}_t^T, \mathbf{R}_t]$, where $\mathbf{p}_t = [u_{x,t,r}, u_{y,t,r}, u_{z,t,r}, v_{x,t,r}, v_{y,t,r}, v_{z,t,r}]$ is the position/velocity vector and $\mathbf{R}_t$ is the rotation matrix corresponding to the robot's orientation. Symbols *az*, *el*, and *r* in Figure 1 denote the azimuth, elevation, and radius of the sound source in the robot frame, respectively. The robot dynamics are given by:

$$\mathbf{p}_t = \mathbf{F}_t \mathbf{p}_{t-1} + d\mathbf{p}_{t-1|t} + \mathbf{v}_{t,\mathbf{p}},\ \mathbf{v}_{t,\mathbf{p}} \sim \mathcal{N}(\mathbf{0}_{\mathbf{6}\times\mathbf{1}}, \mathbf{\Sigma}_{t,\mathbf{p}}) \tag{1}$$

$$\mathbf{R}_t = \zeta\left([\theta, \psi, \varphi]^T + \mathbf{v}_{t,\mathbf{R}}\right),\ \mathbf{v}_{t,\mathbf{R}} \sim \mathcal{N}(\mathbf{0}_{\mathbf{3}\times\mathbf{1}}, \mathbf{\Sigma}_{t,\mathbf{R}}) \tag{2}$$

where $\mathbf{v}_{t,\mathbf{p}}$ denotes unbiased Gaussian noise with covariance $\mathbf{\Sigma}_{t,\mathbf{p}}$. $d\mathbf{p}_{t-1|t}$ is the small variation of $\mathbf{p}_t$ from time step $t-1$ to t, and $\zeta(\theta, \psi, \varphi)$ is a nonlinear function converting Euler angles, $[\theta, \psi, \varphi]$, to a rotation matrix. The matrix $\mathbf{F}_t$ and $d\mathbf{p}_{t-1|t}$ are given by:

$$\mathbf{F}_t = [\ \mathbf{I}_6\ ] \tag{3}$$

$$d\mathbf{p}_{t-1|\mathrm{t}} = [du_{x,t-1|t}, du_{y,t-1|t}, du_{z,t-1|t}, dv_{x,t-1|t}, dv_{y,t-1|t}, dv_{z,t-1|t}] \tag{4}$$

where $\mathbf{I}_n$ is the $n \times n$ identity matrix. It is clear that $du_{x,t-1|t}$, $du_{y,t-1|t}$, and $du_{z,t-1|t}$ are related to $dv_{x,t-1|t}$, $dv_{y,t-1|t}$, and $dv_{z,t-1|t}$. The method to estimate these values will be introduced in Section 3.

The measurements of the robot velocity $\boldsymbol{v}$ and orientation $\mathbf{R}$ are defined as $\mathbf{y}_t \triangleq [y_{t,v}, \boldsymbol{y}_{t,\mathbf{R}}]$ and modeled as:

$$y_{t,v} = \mathbf{h}\mathbf{p}_t + \mathbf{w}_{t,v} \tag{5}$$

$$y_{t,\mathbf{R}} = \zeta([\theta, \psi, \varphi]^T + \mathbf{w}_{t,\mathbf{R}})\ ,\ \mathbf{w}_{t,\mathbf{R}} \sim \mathcal{N}(\mathbf{0}_{3\times 1}, \sigma^2_{\mathbf{w},\mathbf{R}_t}) \tag{6}$$

where $\mathbf{w}_{t,v}$ is non-Gaussian noise, and $\mathbf{w}_{t,\mathbf{R}}$ denotes the measurement of Gaussian noise with covariance $\boldsymbol{\sigma}^{\mathbf{2}}_{\mathbf{w},\mathbf{R}_t}$. In addition, $\mathbf{h} \triangleq [\mathbf{0}_{3\times 3}, \mathbf{I}_3]$. In fact, robots equipped with a 9-axis IMU can provide accurate Euler angles with small errors. Therefore, D-D SLAM neglects the influence of the measurement noise on orientation, which means that $\sigma^2_{\mathbf{w},\mathbf{R}_t}$ is considered to be zero. Thus, (6) can be simplified to:

$$y_{t,\mathbf{R}} = y_{t-1,\mathbf{R}} \mathbf{\Delta R}_{t-1|t} \tag{7}$$

where $\Delta\mathbf{R}_{t-1|t}$ denotes the constraints of robot orientation from time step $t-1$ to t and is introduced in Section 3.

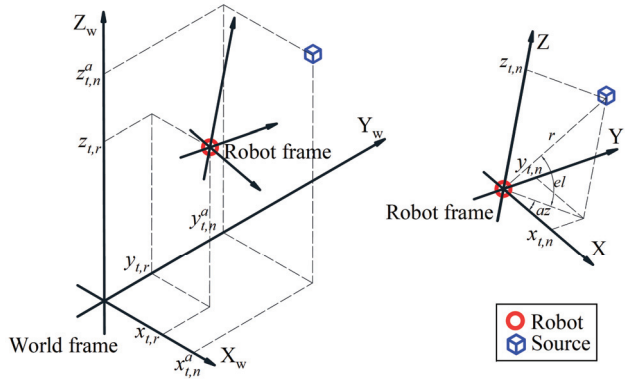

Figure 1. World frame and robot frame.

As the absolute positional state of the sound source is the landmark in mapping, the absolute state ($\mathrm{s}^a_{t,n} \triangleq [x^a_{t,n}, y^a_{t,n}, z^a_{t,n}]^T$) of source n in the world frame at time step t is defined as [7]:

$$\mathrm{s}^a_{t,n} = \mathrm{s}^a_{t-1,n} + \mathbf{n}_{t,n}, \quad \mathbf{n}_{t,n} \sim \mathcal{N}(\mathbf{0}_{3\times 3}, \mathbf{Q}) \tag{8}$$

where $n = 1, \ldots, N_t$ is the index of N_t sources, the superscript a stands for the world frame, and $\mathbf{n}_{t,n}$ is the process noise with covariance $\mathbf{Q}$. The transformation of the source's position in the world frame to that in the robot frame is given by:

$$\mathrm{s}_{t,n} = \mathbf{\Gamma}(\mathrm{s}^a_{t,n} - [u_{x,t,r}, u_{y,t,r}, u_{z,t,r}]^T), \ \mathbf{\Gamma} = \mathbf{R}_t \tag{9}$$

where $\mathrm{s}_{t,n} \triangleq [x_{t,n}, y_{t,n}, z_{t,n}]^T$ is the positional state of the source in the robot frame, and $\mathbf{\Gamma}$ is the rotation matrix between the world frame and the robot frame.

The bearing information of the source is estimated by the DoA algorithm and is modeled as [7]:

$$\Omega_t = [\bigcup_{n=1}^{Nt} D(\mathrm{s}_{t,n})] \cup K_t \tag{10}$$

where $D(\mathrm{s}_{t,n})$ is the process that models the missing DoAs and estimation errors, and K_t denotes the Poisson point process of N_t independent and identically distributed (IID) false DoA estimates distributed uniformly over a unit sphere.

The source's distance from the sensors is also estimated solely with the DRR. The DRR estimation method is developed using interaural magnitude-squared coherence (MSC), and the source's distance is estimated by computing the discrete Fourier transform (DFT) on overlapped windowed signal frames [16]. A small sound piece is sampled at time step t and divided into several parts by a sliding window. In each part of the sound piece, the source's distance from the sensors is estimated. The estimation is modeled by:

$$\hat{d}^n_{t,\mu} \sim \mathcal{N}(d^n_t, R_{t,d}) \tag{11}$$

where μ denotes the windowed signal frame indices, and d^n_t is the true source's distance from the sensors at time step t. In a short time, the estimated distances $\hat{d}^n_{t,\mu}$ in different window frames at time step t tend to follow a nearly normal distribution that is modeled with the mean d^n_t and the covariance $R_{t,d}$.

The positional state of the sources in the robot frame $s_{t,n}$ is associated with the DoA, and the distances of the sources are computed with the DRR. The relationship is as follows:

$$\begin{cases} [\boldsymbol{\omega}_{t,m}, r_{t,m}]^T = \mathcal{G}(s_{t,n}) + \mathbf{e}_{t,m} \\ \mathbf{e}_{t,m} \sim \mathcal{N}(\mathbf{0}_{3\times 1}, diag(R_{t,\mathrm{m}}, R_{t,\mathrm{d}})) \end{cases} \tag{12}$$

where $m = 1, \ldots, M_t$ denotes the index of DoA estimates, M_t is the number of DoA estimates in time step t, $\boldsymbol{\omega}_{t,m} = [\phi_{t,m}, \gamma_{t,m}]^T$, $\mathcal{G}(\bullet)$ is a function that is used to transform from Cartesian coordinates to spherical coordinates (azimuth $\phi_{t,m}$, elevation $\gamma_{t,m}$, and radius $r_{t,m}$), and $\mathbf{e}_{t,m}$ denotes the measurement error with covariance which consists of DoA estimation covariance $R_{t,m}$ and distance estimation covariance $R_{t,d}$.

Estimating $\mathbf{r}_t$ and $s^a_{t,n}$ using $\boldsymbol{\Omega}_t$, $\hat{d}^m_{t,\mu}$, and $\mathbf{y}_t$, presents more challenges than other methods.

(1) The robot's movement is nonuniform motion, and the velocity direction is decoupled from the robot's orientation. Therefore, the robot dynamics in this paper have more freedom of motion than in [5–7], meaning the movement estimation becomes more complex and difficult.
(2) The velocity and orientation are measured using an IMU, whose velocity measurement noise is non-Gaussian and nonlinear. This kind of noise is common in real instruments and cannot be simply removed with a traditional Kalman filter or even an extended Kalman filter (EKF) by fusing DoA measurements due to its strong nonlinearity.
(3) The distance estimation and the DoA measurement usually intermingle with strong noise and disturbances, causing a few incorrect estimations of the sound source position, leading to no convergence.
(4) The critical distance, which is essential for the estimation of the distance from the DRR, is usually calculated with the acoustic coefficients and geometry of the room. However, these parameters are unknown in our situation.

As mentioned before, new constraints, i.e., the source's distance from the sensor, are needed to overcome challenges 1 and 2. Based on a particle algorithm, a method for online estimation of the critical distance is designed to handle challenge 4, which will be introduced in Section 4. Regarding challenge 3, a filter based on a Gaussian mixture model is implemented, which will be discussed in Section 4.

3. Background Knowledge about IMU Preintegration and DRR

3.1. IMU Preintegration

To summarize hundreds of inertial measurements into a single relative motion constraint and update the robot states expediently, IMU preintegration [17] is used in this paper. The absolute robot state is updated by [17]:

$$\mathbf{R}_t = \mathbf{R}_{t-1}\Delta\mathbf{R}_{t-1|t} \tag{13}$$

$$\mathbf{V}_t = \mathbf{V}_{t-1} + \mathbf{g}\Delta t + \mathbf{R}_t\Delta\mathbf{V}_{t-1|t} \tag{14}$$

$$\mathbf{X}_t = \mathbf{X}_{t-1} + \mathbf{V}_{t-1}\Delta t + \frac{1}{2}\mathbf{g}\Delta t^2 + \mathbf{R}_t\Delta\mathbf{X}_{t|t-1} \tag{15}$$

where $\mathbf{X}_t = [u_{x,t,r}, u_{y,t,r}, u_{z,t,r}]^T$, $\mathbf{V}_t = [v_{x,t,r}, v_{y,t,r}, v_{z,t,r}]^T$, $\mathbf{g}$ denotes the gravitational acceleration, Δt is the time difference from time step $t-1$ to t, and $\Delta\mathbf{R}_{t-1|t}$, $\Delta\mathbf{X}_{t|t-1}$, and $\Delta\mathbf{V}_{t|t-1}$ represent the pre-integrated measurements calculated with Gaussian pre-integrated measurements (GPMs) [18]. To be specific, $\Delta\mathbf{R}_{t-1|t}$, $\Delta\mathbf{X}_{t|t-1}$, and $\Delta\mathbf{V}_{t|t-1}$ are estimated with Equations (20), (27), and (26) of Ref. [18], respectively, by feeding IMU measurements.

3.2. DRR Computing and Distance Estimator

For distance estimation, it is useful to determine how sound is reflected in reverberant fields. The DRR is a useful ratio to estimate a source's distance [19] and can be calculated using only acoustic data. The source's distance $d(\mu)$ is estimated by

$$d(\mu) = d_c(\sqrt{\eta_{\mathrm{MSC}}(\mu)})^{-1} \tag{16}$$

where $\eta_{\mathrm{MSC}}(\mu)$ is the broadband DRR calculated with the algorithm based on interaural MSC [16], and d_c is the critical distance that connects the source's distance and the DRR. The equivalent relative HRTF of the microphone array is used to apply the MSC [16] on drone data. The interaural level difference is estimated with the directivity indices of the microphone array, and the interaural time difference (ITD) is calculated with the DoA result and the array shape. The coherence of the reverberant components is set as a sinc function related to the frequency index and the pairwise distance between microphones [20]. The d_c is defined as [19]:

$$d_c = 0.1\sqrt{\rho_s\rho_r}\sqrt{V_R(\pi T_{60})^{-1}} \tag{17}$$

The accuracy of the proposed D-D SLAM is based on the source's distance estimation with the DRR. A large reverberation time, which indicates a small critical distance, contributes to the improvement of the source's distance estimation with the DRR, but larger reverberation times also make the estimation of ITD and ILD more distorted, which may affect the DRR estimation [16]. If the critical distance is too small, the reverberant energy received by the microphone array is much larger than the direct energy, and thus, the ITD and ILD would be seriously affected. If the critical distance is too large, the direct energy received by the microphone array is much larger than the reverberant energy, so the acoustical field of the room is similar to the free field. The acoustical free field does not meet the subject of the proposed D-D SLAM. Thus, the D-D SLAM cannot be used outdoors.

For common SLAM problems, the critical distance d_c is initially unknown because the source directivity indices ρ_s, the receiver directivity indices ρ_r, the room volume V_R and the reverberation time T_{60} cannot be measured in advance. Hence, an online method is proposed in Section 4 to estimate the critical distance during SLAM exploration.

4. Mapping and Locating

With the fundamental theory of SLAM [21], the acoustic SLAM problem can be modeled with the SLAM posterior probability density function (PDF), which is usually factorized into two parts:

$$p(\mathbf{r}_t, \mathbf{s}_t, d_c|\boldsymbol{\eta}_{1:t}, \boldsymbol{\Omega}_{1:t}, \mathbf{y}_{1:t}) = p(\mathbf{s}_t|\mathbf{r}_t, \boldsymbol{\Omega}_{1:t})p(\mathbf{r}_t, d_c|\boldsymbol{\eta}_{1:t}, \boldsymbol{\Omega}_{1:t}, \mathbf{y}_{1:t}) \tag{18}$$

where $\mathbf{s}_t$ is the set of all sound source positions, $p(\mathbf{s}_t \mid \mathbf{r}_t, \boldsymbol{\Omega}_{1:t})$ is a sound source's position posterior PDF corresponding to the mapping problem in SLAM, and $p(\mathbf{r}_t, d_c \mid \boldsymbol{\eta}_{1:t}, \boldsymbol{\Omega}_{1:t}, \mathbf{y}_{1:t})$ represents the robot posterior PDF corresponding to the locating problem in SLAM. The critical distance d_c is the random variable to be estimated. $\boldsymbol{\eta}_{1:t}$ denotes the DRR estimates from the beginning to time step t that are computed with the method based on interaural MSC [16].

4.1. Mapping

The sound sources are considered landmarks on the map, so the focus of the mapping procedure is the estimation of the source positions. To solve existing problems, including false DoA estimates, Evers et al. [7] proposed a mapping method based on probabilistic source triangulation and a random finite set. Their method performs well when the robot keeps moving and receiving a signal from the sound source. However, when the positions of both the robot and the sound source remain stationary, mapping mistakes may occur during the emerging process, which is often used to limit the number of Gaussian mixture

(GM) components. In this situation, the robot's position and DoA estimates do not change, resulting in the repeated emergence of the same new GM components located in the same zone. As the new GM components satisfy both the wrapped Gaussian distribution in angle and the uniform distribution in the radial direction [7], the component's distribution density in the sector region is uneven. The distance between any two GM components l can be calculated by:

$$l = \sqrt{2r^2 + \Delta r^2 + 2r\Delta r(1 - \cos(\Delta\gamma))} \tag{19}$$

where r is one of the component's distances from the robot, and Δr and $\Delta\gamma$ are the difference between the two components in radius and angle, respectively. With the same Δr and $\Delta\gamma$, the shorter the radius distance of the GM component is, the shorter the distance between different GM components is. Thus, the component density in the region closer to the robot is higher than others. Figure 2c reveals this false trend.

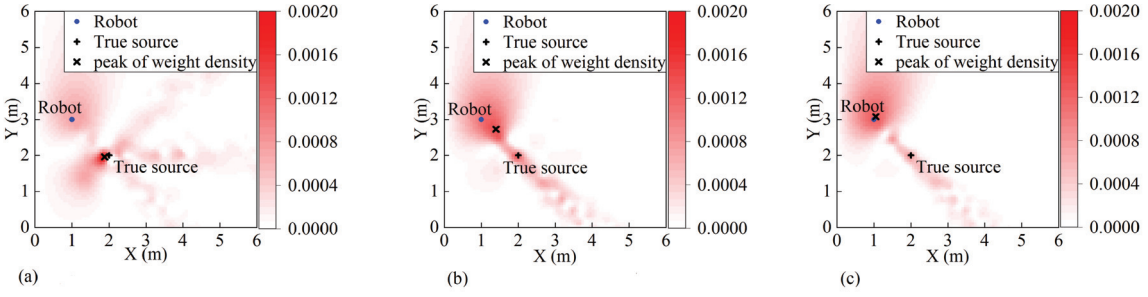

Figure 2. Extensive simulation of the origin method when the robot and the source remain still for (**a**) beginning (3 time steps), (**b**) 10 time steps, and (**c**) 17 time steps.

Before the clustering of GM components for source estimation, mixture reduction is usually applied to limit the number of components through merging. The criterion equation of merging components is given by [22]:

$$(m_k^i - m_k^j)^T (P_k^i)^{-1} (m_k^i - m_k^j) \leq U,\ i = 1, \ldots, J_k \tag{20}$$

where J_k is the number of GM components, j is the index of the component with the maximum weight, m_k^i denotes the position of the GM component in the robot frame, P_k^i is the covariance of the GM component's position, and U is the threshold of merging.

With the criterion Equation (20), it is found that the component merging is relevant to the covariance and the range between components. The new components are created with the same covariance and weight. Therefore, when they have a denser distribution (closer to the robot), they are more likely to be merged together, forming merged components with larger weights. When both the sound source and the robot remain stationary, new components will be created repeatedly in the same zone, and the distribution of weights (after merging) will become increasingly uneven over time. The area closer to the robot will receive much larger weights compared with that far from the robot. This trend has a negative influence on GM component clustering and may finally lead to a false estimation of the sound source position, indicating that it is much closer than the true value. Here, a simulation test is conducted to illustrate the problem mentioned above, while a solution will also be introduced in this section. The simulation test setup is basically the same as that of part C in Section 4 of [7], while an extra time segment is added when the robot remains stationary for several time steps.

Figure 2 is a heatmap of the source weight density calculated using the origin method [7] in the simulation setup with an extra time segment. A higher saturation level of red indicates a higher weight density. As shown in Figure 2a, just after the robot moved for three time

steps (same as that in the original simulation [7]), the GM components were clustered into the place close to the true source where the probability density peak is located. However, as shown in Figure 2b,c, the longer the robot remains stationary, the greater the peak of the probability density deviates toward the robot. The same trend can be found with the weighted centroid of the GM components. This deviation causes an incorrect estimation of the source position, leading to incorrect mapping.

To fix this problem, a solution is developed. The solution is the use of keyframes. When the robot and source remain stationary, new GM components are always created in the same region so that the new GM components are merged into a false component with a large weight. The weight of the false component increases over time, and the weighted centroid of the components is eventually shifted toward the robot. If the creation and merging of GM components stop when the robot and source remain stationary, a false component with a large weight is avoided. The basic idea is that a keyframe factor is calculated to evaluate the difference between the current frame and the last keyframe:

$$T = (\hat{T}_t^1 > T_{KF}^1) \| (\hat{T}_t^2 > T_{KF}^2) \| (\hat{T}_t^3 > T_{KF}^3) \tag{21}$$

$$\begin{cases} \hat{T}_t^1 = \| (u_{x,t,r}, u_{y,t,r}, u_{z,t,r})^T - (u_{x,KF,r}, u_{y,KF,r}, u_{z,KF,r})^T \| \\ \hat{T}_t^2 = \mathrm{OSPA}(\Omega_t, \Omega_{KF}) \\ \hat{T}_t^3 = \| \zeta^{-1}(R_t R_{KF}^T) \| \end{cases} \tag{22}$$

where the subscript *KF* denotes a keyframe, T_{KF}^k for $k = 1, 2, 3$ denotes the given threshold of the keyframe, $\| \bullet \|$ is the two-norm, $\zeta^{-1}(\bullet)$ is a function converting a rotation matrix to Euler angles, $\|$ indicates the OR operation, and OSPA is the Optimal Subpattern Assignment distance [23]. The correspondence of the DOA estimations between the two sets is unknown, so the OSPA is applied for the best match. The OSPA is defined as:

$$\mathrm{OSPA}(\Omega_t, \Omega_{KF}) = [\frac{1}{N} \min_{\pi \in \Pi_N} \sum_{i=1}^{M} l_c(\Omega_{t,i}, \Omega_{KF,\pi(i)}) + (N - M)c] \tag{23}$$

where $\Omega_t \triangleq \{\Omega_{t,1}, \ldots, \Omega_{t,N}\}$, $\Omega_{KF} \triangleq \{\Omega_{KF,1}, \ldots, \Omega_{KF,M}\}$, Π_N stands for the set of permutations of length M with elements from $\{1, \ldots, N\}$, $l_c(\Omega_{t,i}, \Omega_{KF,\pi(i)}) = \min(c, \| \Omega_{t,i} - \Omega_{KF,\pi(i)} \|)$ and c is a cutoff value of 30°.

When the robot and the source remain stationary, $\hat{T}_t^k$ will be less than T_{KF}^k, making T false. When T is false, the current frame in time step t is not a keyframe. In contrast, when the robot moves far enough, $\hat{T}_t^k$ becomes larger than T_{KF}^k, making T true. Thus, the current frame is considered a new keyframe, and the state of the keyframe is updated with the following equations:

$$\begin{cases} (u_{x,KF,r}, u_{y,KF,r}, u_{z,KF,r})^T = (u_{x,t,r}, u_{y,t,r}, u_{z,t,r})^T \\ \Omega_{KF} = \Omega_t \\ R_{KF} = R_t \end{cases} \tag{24}$$

When GM components are only created and merged in keyframes, a false merged component with a large weight is avoided. To eliminate accidental errors, a limiting filter is applied to the clustering of GM components. The limiting filter is modeled as:

$$\mathrm{LF}(\mathrm{s}_t) = \begin{cases} \mathrm{s}_t \quad , & \mathrm{OSAP}(\mathrm{s}_t, \mathrm{s}_{t-1}) \leq s_{LF} \\ \mathrm{s}_{t-1}, & \mathrm{OSAP}(\mathrm{s}_t, \mathrm{s}_{t-1}) > s_{LF} \end{cases} \tag{25}$$

where s_t is the source estimation which is calculated with the mapping method based on probabilistic source triangulation and random finite set [7] by feeding the data of keyframe, s_{LF} denotes the threshold value of the limiting filter, which is related to the maximal variation of the source position between time steps $t - 1$ and t. The OSAP is also applied, but the cutoff value c is changed to 0.5 m.

Using the probabilistic source triangulation in [7] and the keyframe method mentioned above, the source posterior PDF $p(\mathbf{s}_t \mid \mathbf{r}_t, \mathbf{\Omega}_{1:t})$ can be estimated using the evidence of the DoA estimation $\mathcal{L}(\mathbf{\Omega}_t \mid \mathbf{r}_t, d_c)$. The implementation is given by:

$$\mathcal{L}(\mathbf{\Omega}_t|\mathbf{r}_t, d_c) \triangleq e^{-N_{t,c}-p_d N_{t|t-1}} \prod_{m=1}^{M_t} \updownarrow(\boldsymbol{\omega}_{t,m}|\mathbf{r}_t, d_c) \tag{26}$$

where p_d denotes the probability of detection, $N_{t,c}$ is the number of false alarms, $N_{t\,|\,t-1}$ stands for the quantity of predicted features [7], and $\boldsymbol{\omega}_{t,m}$ is the DoA estimation computed from the GM components and the position of the robot. $\ell(\boldsymbol{\omega}_{t,m} \mid \mathbf{r}_t, d_c)$ is evaluated with Equation (34) in [7]. The mapping process is only fed with the data of the keyframe.

4.2. Locating

This section proposes a method to estimate the robot's location by fusing the IMU measurements and the DoA and DRR estimates. Additionally, the critical distance is estimated online. Because the relationship between the state of the robot and the sensor measurements is nonlinear and complicated, it is difficult to estimate the critical distance d_c and the state of the robot $\mathbf{r}_t$ directly from just the IMU measurements and the DoA and DRR estimates. Particle filters [24] are usually applied to model the robot posterior PDF of this nonlinear problem. With this method, the robot posterior PDF $p(\mathbf{r}_t, d_c \mid \boldsymbol{\eta}_{1:t}, \mathbf{\Omega}_{1:t}, \mathbf{y}_{1:t})$ is modeled as:

$$p(\mathbf{r}_t, d_c|\boldsymbol{\eta}_{1:t}, \mathbf{\Omega}_{1:t}, \mathbf{y}_{1:t}) \approx \sum_{i=1}^{I} \alpha_t^i \delta_{\hat{\mathbf{r}}_t^i, \hat{d}_c^i}(\mathbf{r}_t, d_c) \tag{27}$$

where I is the number of particles, α_t^i denotes the weight of a particle, and $\delta_{\hat{r}_t^i, \hat{d}_c^i}(\mathbf{r}_t, d_c)$ is the Dirac-delta function centered at $\mathbf{r}_t$, d_c and evaluated at $\hat{\mathbf{r}}_t^i$, $\hat{d}_c^i$. Because the state of the robot and the critical distance are estimated at the same time, there is a large amount of uncertainty, so large quantities of particles are required to model the robot posterior PDF.

Using (16) the source's distance from robot $\hat{d}$ can be computed with the DRR if the critical distance is known. As the source's distance is helpful in the estimation of the robot's position, it is easier to estimate the state of the robot when the critical distance is known. To simplify the robot posterior PDF, the marginalization [25] is adopted to decouple the posterior PDF into that of d_c and $\mathbf{r}_t$ separately, i.e., the robot posterior PDF $p(\mathbf{r}_t, d_c \mid \boldsymbol{\eta}_{1:t}, \mathbf{\Omega}_{1:t}, \mathbf{y}_{1:t})$ is factorized into two parts:

$$p(\mathbf{r}_t, d_c|\boldsymbol{\eta}_{1:t}, \mathbf{\Omega}_{1:t}, \mathbf{y}_{1:t}) = p(d_c|\boldsymbol{\eta}_{1:t}, \mathbf{\Omega}_{1:t}, \mathbf{y}_{1:t}) p(\mathbf{r}_t|d_c, \boldsymbol{\eta}_{1:t}, \mathbf{\Omega}_{1:t}, \mathbf{y}_{1:t}) \tag{28}$$

Using (15), the state of the robot can be computed from the IMU measures. Meanwhile, the source's distance from the robot computed from a given d_c, $\boldsymbol{\eta}_{1:t}$ using (16), and DoA estimates can be used to correct the state of the robot. Therefore, this paper takes the estimation of the robot's state $\mathbf{r}_t$ as a nonlinear substructure [25] of the estimation of critical distance d_c. Thus, for each d_c particle, there is a substructure corresponding to the robot state and the source position.

The critical distance is assumed to be within a certain range $\hat{d}_c \in [d_c^{min}, d_c^{max}]$ and obeys a uniform distribution:

$$\hat{d}_c^i \sim \mathcal{U}(d_c^{min}, d_c^{max}), \quad i = 1, \ldots, I \tag{29}$$

where d_c^{min} and d_c^{max} are the minimum and maximum of the critical distance, respectively, and I is the number of particles. A critical distance particle is drawn from the uniform distribution. For each critical distance particle and each source, the estimations of the source's distance at time step t can be calculated in the following formula according to (16):

$$\hat{d}_{t,m,\mu}^i = \hat{d}_c^i \left(\sqrt{\eta_{t,m,\mu}}\right)^{-1}, \quad \mu = 1, \ldots, B \tag{30}$$

where B denotes the number of windowed signal frames in time step t, $m = 1, \ldots, M_t$ and $\hat{d}^i_{t,m,\mu}$ is the source's distance corresponding to $\hat{d}^i_c$.

Theoretically, the state of the robot can be computed using iterative calculation of (13)–(15) as long as the initial value of the robot's state is given. In fact, a 9-axis acceleration gyroscope sensor can provide an accurate rotation matrix $\mathbf{R}_t$ that can be used to accurately describe the attitude of the robot. Therefore, $\mathbf{R}_t$ is computed directly from IMU measurements and the GPMs in this paper. However, the velocity and position of the robot cannot be computed using only the IMU measurements due to unacceptable integral error. Therefore, the DoA estimates and DRR are used to eliminate those errors by fusing all measures with an EKF [26]. For weakly nonlinear systems, an EKF has better performance than a Kalman filter. The sound source distance estimation from DRR is added as a constraint to suppress the noise of IMU measurements along the direction of sound arrival. With the addition of range information, the state of the robot has weaker nonlinearity than that of the robot which only contains bearing information and IMU measurements. Therefore, EKF is suitable for the estimation of the weakly nonlinear state of the robot in D-D SLAM. Using (13)–(15), the implementation of the EKF is given by:

$$\mathbf{X}'^i_t = \mathbf{X}^i_{t-1} + \mathbf{V}^i_{t-1}\Delta t + \frac{1}{2}\mathbf{g}\Delta t^2 + \mathbf{R}_t\Delta\mathbf{X}_{t-1|t} \tag{31}$$

where $\mathbf{X}'^i_t$ denotes the prediction of the robot's position in the EKF. The rotation matrix $\mathbf{R}_t$ and the velocity $\mathbf{V}_t$ are determined from Equations (13) and (14). The pre-integrated measurement of position $\Delta\mathbf{X}_{t-1|t}$ is estimated with Equation (27) of Ref. [18] by feeding IMU measurements. The prediction of covariance in the EKF is given by:

$$Cov'^i_{t,m} = \mathbf{F}_t Cov^i_{t-1,m}{\mathbf{F}_t}^T + \mathbf{Q}^i_{\mathbf{X}_t} \tag{32}$$

where $Cov^i_{t-1,m}$ denotes the covariance of the EKF, $\mathbf{F}_t$ is given by (3) and $\mathbf{Q}^i_{\mathbf{X}_t}$ is the process non-Gaussian noise of the robot position. $\mathbf{Q}^i_{\mathbf{X}_t}$ is associated with the process noise of the robot's velocity, according to (31) with the variance-covariance propagation law:

$$\mathbf{Q}^i_{\mathbf{V}_t} = \mathbf{Q}^i_{\mathbf{V}_{t-1}} + d\mathbf{Q}_{\mathbf{V}_{t-1|t}} \tag{33}$$

$$\mathbf{Q}^i_{\mathbf{X}_t} = \mathbf{Q}^i_{\mathbf{X}_{t-1}} + \Delta t\mathbf{Q}^i_{\mathbf{V}_{t-1}}\Delta t + d\mathbf{Q}_{\mathbf{X}_{t-1|t}} \tag{34}$$

where $d\mathbf{Q}_{\mathbf{X}_{t-1|t}}$ and $d\mathbf{Q}_{\mathbf{V}_{t-1|t}}$ denote the variances of the GPMs of the robot's position and velocity, respectively. For each source, the observational equation in the EKF is determined by:

$$[\hat{\omega}^i_{t,\mathrm{m}}, \hat{r}^i_{t,\mathrm{m}}]^T = \mathcal{G}(\mathbf{R}_t(\mathbf{X}'^i_t - \hat{\mathrm{s}}^i_{t-1,m})) \tag{35}$$

where $m = 1, \ldots, M_t$, $\mathbf{R}_t$ is estimated with Equation (13) and $\mathcal{G}(\bullet)$ is the Cartesian-to-spherical transformation. According to the mapping procedure (Section 4.1), the estimation of source $\hat{\mathrm{s}}^i_{t-1,m}$ is given using GM component clustering of the keyframe data. Hence, the Kalman gain and the correction of Kalman gain are given by:

$$\mathbf{K}^i_{t,m} = Cov'^i_{t,m}(\mathbf{H}^i_{t,m})^T(\mathbf{H}^i_{t,m}Cov'^i_{t,m}(\mathbf{H}^i_{t,m})^T + \mathbf{R}_{EKF})^{-1} \tag{36}$$

$$\hat{\mathbf{X}}^i_{t,m,\mu} = \mathbf{X}'^i_t + \mathbf{K}^i_{t,m}([\mathbf{\Omega}_{t,m}, \hat{d}^i_{t,m,\mu}]^T - [\hat{\omega}^i_{t,\mathrm{m}}, \hat{r}^i_{t,\mathrm{m}}]^T) \tag{37}$$

$$\hat{\mathbf{V}}^i_{t,m,\mu} = (\hat{\mathbf{X}}^i_{t,m,\mu} - \mathbf{X}^i_{t-1})/dt \tag{38}$$

$$Cov^i_{t,m} = (\mathbf{I}_3 - \mathbf{K}^i_{t,m}\mathbf{H}^i_{t,m})Cov'^i_{t,m} \tag{39}$$

where $\mathbf{H}$ is the Jacobian matrix of the observational equation, $\hat{\mathbf{V}}^i_{t,m,\mu}$ is the velocity of the robot corresponding to each output of the EKF, dt denotes the time difference between two adjacent keyframes, which is different from Δt, and $\mathbf{R}_{EKF}$ is the measurement noise,

which is assumed to be known. The output of the EKF, $\hat{\mathbf{X}}^i_{t,m,\mu}$, corresponds to each source's distance $\hat{d}^i_{t,m,\mu}$. As the estimation of the robot's position is nonlinear and the rotation matrix $\mathbf{R}_t$ is computed directly from IMU measurements, the Gaussian mixture model (GMM) is applied to model the robot posterior PDF $p(\mathbf{X}_t \mid d\ i\ c, \boldsymbol{\eta}_{1:t}, \boldsymbol{\Omega}_{1:t}, \mathbf{y}_{1:t})$:

$$p(\mathbf{X}_t|d^i_c, \boldsymbol{\eta}_{1:t}, \boldsymbol{\Omega}_{1:t}, \mathbf{y}_{1:t}) = \sum_{M_t}^{m} \sum_{\mathrm{B}}^{\mu} w^i_{t,m,\mu} \mathcal{N}(\mathbf{X}_t|\hat{\mathbf{X}}^i_{t,m,\mu}, Cov^i_{t,m}) \tag{40}$$

where $w^i_{t,m,\mu}$ denotes the weights of the GM components in the windowed signal frame indices μ of time step t and is given by:

$$w^i_{t,m,\mu} = \mathcal{N}(\hat{\mathbf{X}}^i_{t,m,\mu}|\mathbf{X'}^i_t, \mathbf{Q}^i_{\mathbf{X}_t}) \tag{41}$$

It is clear that the smaller the difference between the outputs of the EKF and GPMs is, the larger the component weight $w^i_{t,m,\mu}$ is. For the GMM, the estimation of the robot position, the robot velocity, the source's distance from the robot, and the covariance in the EKF are computed with the weighted average method

$$\mathbf{X}^i_t = \sum_{M_t}^{m} \sum_{B}^{\mu} w^i_{t,m,\mu} \hat{\mathbf{X}}^i_{t,m,\mu} \tag{42}$$

$$\mathbf{V}^i_t = \sum_{M_t}^{m} \sum_{B}^{\mu} w^i_{t,m,\mu} \hat{\mathbf{V}}^i_{t,m,\mu} \tag{43}$$

$$d^i_{t,m} = \|\mathbf{X}^i_t - \hat{\mathrm{s}}_{t,m}\| \tag{44}$$

$$Cov_{t,m} = \sum_{M_t}^{m} \sum_{B}^{\mu} w^i_{t,m,\mu} Cov^i_{t,\mu} \tag{45}$$

The weight of each critical distance and robot position particle is given by:

$$\alpha^i_t = \mathcal{N}(\mathbf{X}^i_t \Big| \mathbf{X'}^i_t, \mathbf{Q}^i_{\mathrm{X}_t}) \tag{46}$$

Equation (46) reflects the coincidence degree between the robot position corresponding to each critical distance particle and the GPM measurements. The GPMs of the IMU are used to evaluate each critical distance particle. The weights of the critical distance particle that fits the GPM measurements well will become larger. The final estimation of the robot and source position will be in the best interests of all measurements.

4.3. Posterior PDF of the D-D SLAM

This section provides the implementation of evaluating the SLAM posterior PDF. Because a rotation matrix can describe the attitude of the robot accurately with the GPMs of the IMU data and the source triangulation does not depend on velocity, (18) is reduced to:

$$p(\mathbf{X}_t, \mathbf{s}_t, d_c|\boldsymbol{\eta}_{1:t}, \boldsymbol{\Omega}_{1:t}, \mathbf{y}_{1:t}) = p(\mathbf{s}_t|\mathbf{X}_t, \boldsymbol{\Omega}_{1:t}) p(\mathbf{X}_t, d_c|\boldsymbol{\eta}_{1:t}, \boldsymbol{\Omega}_{1:t}, \mathbf{y}_{1:t}) \tag{47}$$

According to the Bayes rule, using (26) and (27), the posterior PDF $p(\mathbf{X}_t, d_c \mid \boldsymbol{\eta}_{1:t}, \boldsymbol{\Omega}_{1:t}, \mathbf{y}_{1:t})$ is given by:

$$p(\mathbf{X}_t, d_c|\boldsymbol{\eta}_{1:t}, \boldsymbol{\Omega}_{1:t}, \mathbf{y}_{1:t}) = \frac{\sum_{i=1}^{I} \alpha^i_t \ \mathcal{L}\left(\boldsymbol{\Omega}_t \Big| \hat{\mathbf{X}}_t, \hat{d}_c\right) \delta_{\hat{\mathbf{X}}_t, \hat{d}^i_c}(\mathbf{X}_t, d_c)}{\sum_{j=1}^{I} \alpha^j_t \ \mathcal{L}\left(\boldsymbol{\Omega}_t \Big| \hat{\mathbf{X}}_t, \hat{d}_c\right)} \tag{48}$$

Using (48) in (47), the SLAM posterior PDF is reduced to:

$$p(\mathbf{X}_t, \mathbf{s}_t, d_c|\boldsymbol{\eta}_{1:t}, \boldsymbol{\Omega}_{1:t}, \mathbf{y}_{1:t}) = \sum_{i=1}^{I} \beta_t^i \; \delta_{\hat{\mathbf{X}}_t, \hat{d}_c^i}(\mathbf{X}_t, d_c) \; p(\mathbf{s}_t|\mathbf{X}_t, \boldsymbol{\Omega}_{1:t}) \tag{49}$$

$$\beta_t^i = \frac{\alpha_t^i \; \mathcal{L}\left(\boldsymbol{\Omega}_t \middle| \hat{\mathbf{X}}_t, \hat{d}_c\right)}{\sum_{j=1}^{I} \alpha_t^j \; \mathcal{L}\left(\boldsymbol{\Omega}_t \middle| \hat{\mathbf{X}}_t, \hat{d}_c\right)} \tag{50}$$

where β_t^i is the weight and is used to evaluate the particle and estimate the position of the robot and the source. The D-D SLAM is summarized in pseudocode (see Algorithm 1).

Algorithm 1: D-D SLAM

```
Data: DoAs Ω_t, DRR η_t, IMU Measure y_t
for i = 1, ... , I do
    Compute r̂_t^i using (13)(14)(15);
    Compute KeyFrame factor using (21)(22);
    if KeyFrame then
        Compute Q_{X_t}^i, Cov'^i_{t,m} using (34)(33)(32);
        for m = 1, ... , M_t do
            Predict ω̂_{t,m}^i, r̂_{t,m}^i using (35);
            Compute K_{t,m}^i using (36);
            for μ = 1, ... , B do
                Evaluate X̂_{t,m,μ}^i, V̂_{t,m,μ}^i using (37)(38);
                Compute w_{t,m,μ}^i using (41);
            end
        end
        Update Cov_{t,m} using (45);
        Update X_t^i, V_t^i using (42)(43);
        Evaluate α_t^i using (46);
        Compute s_t^i using the mapping method [7] by
        feeding the date of keyframe;
        GM reduction of mapping [27];
        Evaluate L(Ω_t | r_t, d_c) using (26);
        Evaluate β_t^i using (50);
        Update particle state;
    else
        Update Q_{X_t}^i, Cov'^i_{t,m} using (34)(33)(32);
    end
end
Resampling [28];
```

Each particle is now evaluated by the evidence of mapping (26) and the weight of locating (46). When the velocity of the robot is updated with (43), first-order recursive temporal smoothing is applied to smooth the speed to minimize the jitter of the velocity:

$$\mathbf{V}_t^i = a_p \mathbf{V}_{t-1}^i + (1 - a_p) \sum_{M_t}^{m} \sum_{B}^{\mu} w_{t,m,\mu}^i \hat{\mathbf{V}}_{t,m,\mu}^i \tag{51}$$

where a_p is a smoothing parameter. In the procedure "Update particle state", the estimation of the robot and the source at time step t is computed with the weighted mean method.

5. Simulation and Experiment Setup

5.1. Simulation Setup

This simulation is designed to compare the performances of D-D SLAM and aSLAM [7] in a simulation room. In the simulation, the feasibility of the proposed online estimation algorithms for the critical distance used in D-D SLAM is also illustrated. The simulation room is similar to that in [7], i.e., a sealed 6 m $\times$ 6 m $\times$ 3 m room. A continuous signal source is placed in the center of the room (3 m, 3 m, 1.5 m), and the reverberation times T_{60} are set to 0.15 s and 0.5 s, respectively. The robot moves in the direction of a random orientation, similar to the movement in [7]. The magnitude of the velocity is set to 2 m/s with reference to the famous robot, TurtleBot2.

Under the condition of the reverberation times of 0.15 s, the signal of the source is a piece of music. The frequency of the music used in the simulation is time-varying and is within the range of 0–4000 Hz. A random path where the robot always keeps moving is used to test the proposed D-D SLAM (with the keyframe method) and the aSLAM. Another similar path where the robot keeps still for 10 times step during movement is used to justify the use of the proposed keyframes-based solution. The D-D SLAM with and without the keyframe method is tested in this path. The removal of the keyframe method means that each data frame is fed to the locating and mapping process.

Under the condition of the reverberation times of 0.5s, the signal of the source is white noise. The frequency range of the white noise sound source used in the simulation is 0–8000 Hz. Different levels of noise are added to the received signal of the microphone array, corresponding to different Signal-Noise Ratios (SNR). The D-D SLAM is tested with different SNRs, which contain 6 dB, 3 dB, 0 dB, and -3 dB.

The trajectory and IMU data are simulated using Robot Operating System (ROS) and Gazebo. A TurtleBot2 equipped with a microphone array and IMU is set in the room and moves randomly. The IMU data that are simulated by ROS contain only the numerical error. For vraisemblance, two types of Gaussian white noise are added artificially to the output data of the accelerometer and the gyroscope with variances of 1×10^{-3} and 1×10^{-2}, respectively, similar to that of the familiar low-cost IMU MPU6050. Therefore, the simulated IMU data contain both the nonlinear numerical error and the Gaussian measurement noise. The true trajectory data are recorded as the ground truth.

A sound record with eight channels is generated according to the image source method [29,30] using a room impulse response (RIR) simulator. The sample frequency is set to 16,000 Hz, and the microphone array shape is the same as in the DREGON dataset [15] mentioned above. The microphone array is fixed on the robot, and the transformation matrix between their positions and orientations is constant.

The DoA method based on SRP-PHAT [31] is applied to estimate the direction of the source, and the GPMs are applied to provide the observed values of the velocity, position, and orientation. With SRP-PHAT, the error of the DoA estimates is less than 2 degrees. The DRR computation is introduced in Section 3.

In [7], the measured velocity is simulated by adding Gaussian noise directly to the true velocity, which is different from the true IMU model. However, the velocity computed using IMU integration contains an accumulated error, which is nonlinear and cannot be eliminated simply by a Kalman filter. As a result, the accuracy of aSLAM with true IMU data will decrease over time. For comparison, three groups are developed under the condition of reverberation times of 0.15 s. Group I: aSLAM with motion reports, which is simulated by adding Gaussian noise to the true velocity directly, i.e., the same as in [7]. The noise signal is unbiased, and the root mean squared error (RMSE) of the noise signal is 0.75 m/s for velocity and 5 deg for azimuth. Group II: aSLAM with motion reports, which is computed with GPMs on the simulated IMU data that contain both nonlinear numerical error and Gaussian measurement noise. Group III: the proposed D-D SLAM with the same simulated IMU data as that in Group II. In all groups, the same DoA measurements are used, the robot starts in the same place, the number of particles is set to 10, the standard deviation of the DoAs is set to 2 deg, and the standard deviation of the source's distance

from the robot is set to 0.35 m. In this simulation, the time step, i.e., the time difference between nearby frames, is 1 s, and the total simulation time is 100 s (100 data frames).

5.2. Experiment Setup

To evaluate the effects of the algorithms on real indoor data, the DREGON dataset [15], which contains real data sampled with a drone flying in a real room, is applied. In the DREGON dataset, a MikroKopter unmanned aerial vehicle (UAV) equipped with a microphone array and IMU flew indoors. In this paper, the Free Flight-White Noise Source at High Volume case in the DREGON dataset is used. A continuous white noise sound source was placed in the room and sampled by an array of eight microphones (8SoundsUSB and ManyEars). The motion reports were measured with the onboard IMU (which is integrated with FlightCtrl 2.5). Meanwhile, the positions and orientations of the UAV and the source were recorded precisely by a 12-camera Vicon motion capture system and considered the ground truth. According to the dataset, the speed of the UAV is no faster than 1 m/s, and the flight contains hovering, a rectangle, spin, up and down.

It is clear that the magnitude of the UAV velocity is variable and that the direction of the UAV velocity is independent of the orientation of the UAV. To test aSLAM on the DREGON dataset, the robot dynamics must be updated for the flight patterns of the UAV. For comparison, three experimental groups were used. Group IV: aSLAM [7] with updated observer dynamics. Group V: the proposed D-D SLAM with the keyframe method. Group VI: the proposed D-D SLAM without the keyframe method. In both groups, the DoA estimates and motion reports are computed using the same method as in the simulation, and the particle number is set to 10. The UAV started in the same place and with the same posture. On the real indoor dataset, the elevation search boundaries are limited in $[-90^\circ, 20^\circ]$ to avoid the drone noise's influence, which has an elevation angle that is mostly 60°. The error of the DoAs estimated with SRP-PHAT is also less than 2 degrees. Then, the standard deviation of the DoA estimates is set to 2 degrees. The standard deviation of the source's distance estimation from the robot is set to 0.35 m. In this experiment, the time step, i.e., the time difference between nearby frames, is 0.0464 s, and the total simulation time is 46 s (993 data frames). Each data frame in the experiment contains 2048 audio sample points (0.0464 s) and 43 IMU measurements on average.

5.3. Performance Metric

To quantitatively analyze the accuracy, the error between the positional estimation and ground truth is evaluated with the Euclidean distance. The Euclidean distance is calculated by:

$$\mathrm{d}(\mathbf{X}_t^{gt}, \mathbf{X}_t^{est}) = \|\mathbf{X}_t^{gt} - \mathbf{X}_t^{est}\| \tag{52}$$

where the superscripts *gt* and *est* denote the ground truth and estimation, respectively, and $\mathbf{X}_t^{(\bullet)}$ is the position of the robot or the source.

6. The Results

6.1. Simulation Results

The results of the aSLAM and the proposed D-D SLAM in the simulation are shown in Figure 3. The results of the D-D SLAM under different conditions are shown in Figures 4 and 5, respectively. As shown in Figure 3 with the orange dashed-dotted line and solid circles, the trajectory and source position estimations of aSLAM with the true speed, which only contains Gaussian noise similar to that in [7], reach the expected effect, meeting the mean accuracies of 0.136 m and 0.14 m for estimations of the trajectory and source position, respectively.

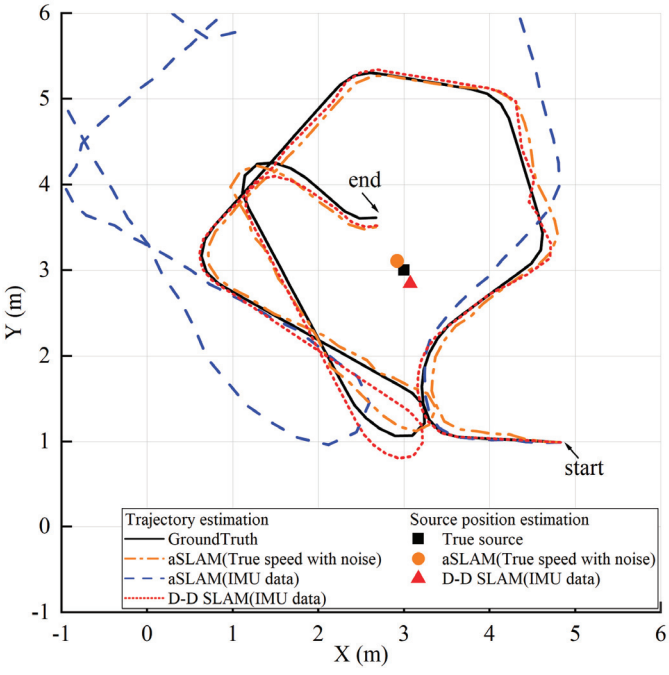

Figure 3. T_{60} = 0.15 s, Trajectory estimation on simulations for aSLAM with true speed plus noise (orange dash-dotted line), aSLAM with IMU data (blue dashed line), and the D-D SLAM with IMU data (red dotted line).

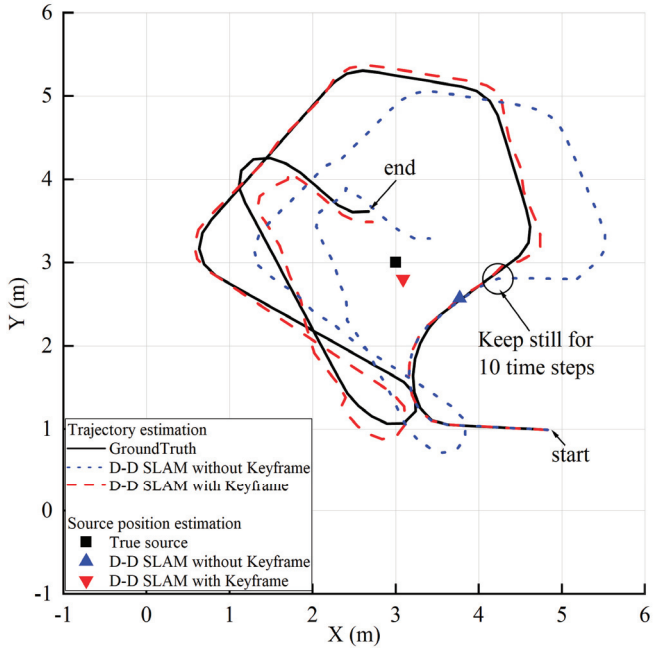

Figure 4. T_{60} = 0.15 s, Trajectory and source estimations on simulations for D-D SLAM with and without the keyframe method.

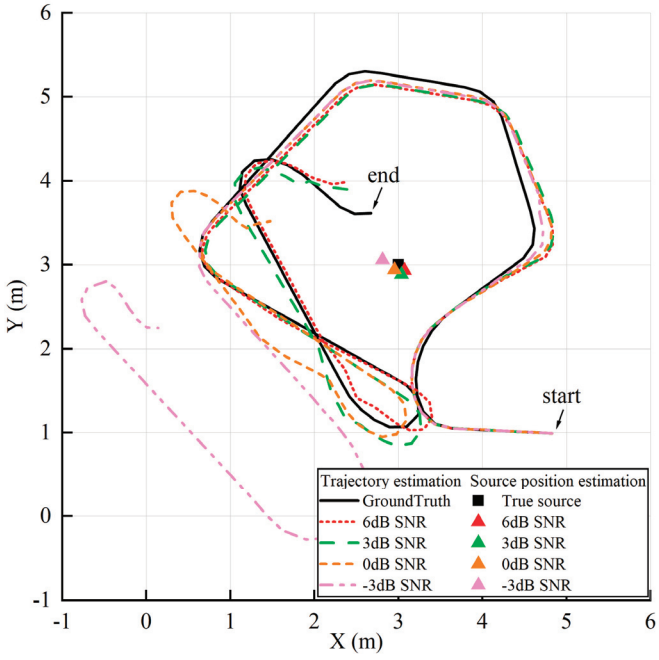

Figure 5. T_{60} = 0.5 s, Trajectory and source estimations on simulations for D-D SLAM under the condition of different SNRs.

However, when the simulated IMU data that contain nonlinear numerical error and Gaussian measurement noise are applied, aSLAM has poor performance. As shown by the blue dashed line in Figure 3, the trajectory estimation deviation increases with time. Within 29 s (29 time steps), the estimated position of the robot starts to be outside the room. The corresponding source position estimations are nonconvergent and sometimes even out of the room, so they cannot be marked as static points in Figure 3. In contrast, the proposed D-D SLAM with the same simulated IMU data performs well. As shown in Figure 3, the trajectory estimation of D-D SLAM in the red dotted line basically matches the ground truth, and the source position estimation in the red solid triangles is always close to the true source's position. During the whole process of 100 s (100 time steps), the estimation of the trajectory and source position with the proposed D-D SLAM is convergent and stable.

The poor performance of aSLAM with IMU data implies that additional constraints are needed in this situation. As the nonlinear noise is due to the integration error of the IMU, the DRR is used to compute the source's distance from the robot, which is applied as a new constraint. The result shown in Figure 3 demonstrates the different performances under the same conditions between aSLAM and the proposed D-D SLAM, proving the effectiveness of D-D SLAM. The use of the DRR for source distance estimations, which is considered an additional constraint, is key to eliminating the nonlinear error of IMU measurements.

Quantitative analysis of the accuracy using the Euler distance is illustrated in Figure 6. Under the condition of T_{60} = 0.15 s, the result of aSLAM is drawn as a blue line with solid squares, while that of the proposed D-D SLAM is drawn as a red line with solid squares.

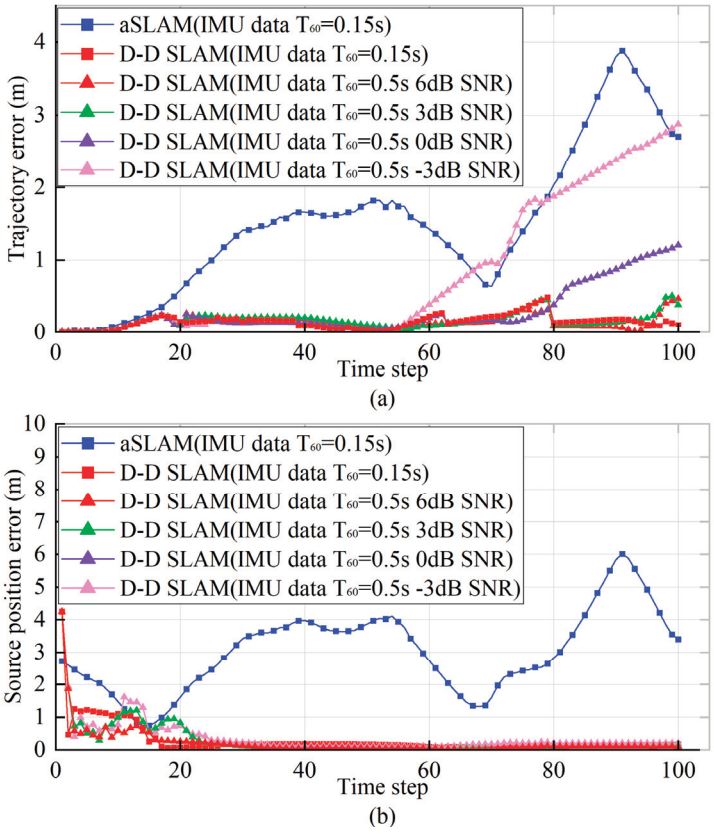

Figure 6. Simulation results for (**a**) the trajectory errors and (**b**) the source position errors over time steps.

For aSLAM with IMU data, the trajectory error reaches a maximum of 3.9 m at 91 s (91 time steps), and its mean value is 1.55 m, as shown in Figure 6a. Moreover, the overall trend of its trajectory error increases over time. With the random initial source position, the corresponding source position estimation error is unstable, as shown in Figure 6b. The error also reaches a maximum of 6.0 m at 91 s (91 time steps), and its average is 3.0 m. Within a room of 6 m $\times$ 6 m $\times$ 3 m, the trajectory and source position errors are unacceptable.

For the proposed D-D SLAM with IMU data, the maximum trajectory error is less than 0.48 m, and the mean value of the trajectory error is 0.14 m. Meanwhile, the source position error is less than 0.19 m just after 16 s (16 time steps), even though the source position error at the beginning is quite large due to the random initial source position. Compared with aSLAM, the source position error of D-D SLAM converges faster even with the larger initial value of the source position error. These results show that the proposed D-D SLAM has better performance using the same simulated IMU measurement, which proves that D-D SLAM has stronger robustness for the nonlinear noise of motion reports.

The good performance of the proposed D-D SLAM relies on reliable source distance estimates, which are based on the accurate estimate of the critical distance d_c. However, d_c is initially unknown. With the online estimation method in this paper, d_c is calculated during the SLAM process. Different particles of critical distance d_c are initialized in the beginning, and the weight of each d_c particle is evaluated with the coincidence degree between the robot position, which corresponds to each d_c particle and the IMU measurements. During the SLAM procedure, those d_c particles whose corresponding robot position matches poorly

with IMU measurements, DoA estimates, and sound source distance estimations from DRR are dropped. Figure 7 is the result of d_c at different time steps, where the different color dashed lines represent values of different d_c particles and the red solid line represents their weighted mean. The mean of d_c converges rapidly to a stable value in less than 27 s (27 time steps). The results show that the proposed online estimation method can obtain a convincing critical distance, even though the directivity of the source and receiver, the room size, and the reverberation time are unknown.

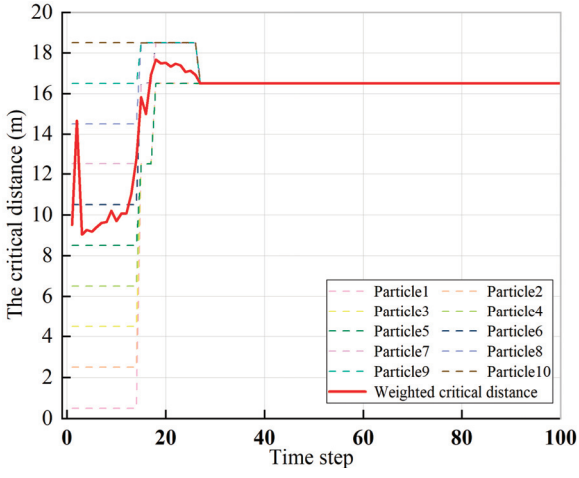

Figure 7. The state of different critical distance particles and the weighted critical distance with simulation data under the condition of T_{60} = 0.15 s.

The reverberation time T_{60} of the room is a general acoustic character of the environment. The simulation results of different reverberation times (T_{60} = 0.15 s and T_{60} = 0.5 s) are shown in Figures 3 and 5, respectively. As shown in Figure 6, the average errors of trajectory and source position are 0.14 m and 0.21 m, respectively, when T_{60} = 0. 5 s and SNR = 6 dB, while the average errors of trajectory and source position are 0.14 m and 0.29 m, respectively, when T_{60} = 0. 15 s. In different acoustic environments, the proposed D-D SLAM still gets small errors and has similar performances, showing its robustness against changing the environment.

As shown in Figures 3 and 5, the D-D SLAM can work with the continuous sound source of music or white noise, so the white noise sound source is unnecessary. The frequency ranges of the music and the white noise used in the simulation are different, and the frequency of the music is time-varying, so the D-D SLAM is insensitive to the frequency range.

The influences of different SNRs are studied. As shown in Figure 6, the average errors of trajectory and source position are 0.14 m and 0.21 m, respectively, when SNR = 6 dB, while the average errors of trajectory and source position are 0.16 m and 0.27 m, respectively, when SNR = 3 dB. The errors of trajectory estimation do not converge when SNRs are 0 dB and −3 dB. The trajectory error of −3 dB SNR grows faster than that of 0 dB SNR. Therefore, simulation results show that received signals whose SNR is bigger than 3 dB is necessary for the proposed technique.

In the simulation, the results of the D-D SLAM with and without the keyframe method are shown in Figure 4. The trajectory estimations of the D-D SLAM with and without the keyframe method are comparable before the robot remains stationary. The robot begins to remain stationary after moving for 20 time steps. After remaining stationary for 10 time steps, the trajectory estimations of the D-D SLAM without the keyframe method (blue line) go seriously wrong. And the source position estimations of the D-D SLAM without

the keyframe method (blue triangle) are much closer to the position where the robot remains stationary rather than the position of the true source. This result is similar to the phenomenon presented in Figure 2. On the contrary, the D-D SLAM with the keyframe method (red line) still performs well after remaining stationary for 10 time steps. It is possible for a robot to remain stationary for some time during the SLAM procedure, so the keyframe method is necessary to prevent false source and trajectory estimations when the robot keeps still.

6.2. Experimental Results

Figure 8 shows the estimated trajectory and source position using D-D SLAM and aSLAM for real indoor datasets [15]. Even worse than that in simulation Group II, the estimated trajectory of aSLAM in the experiment goes outside the boundary of the experiment room after 18.7 s (402 time steps) and never returns during the remainder of the experiment. Therefore, it is not fully shown in Figure 8. The gradual divergence of the estimated trajectory is because of the shifting integrated velocity from the IMU measurements. Due to the incremental error of trajectory estimation, the source estimation of aSLAM is also unstable, and out of the room, so it cannot be marked in Figure 8. In contrast, the estimated trajectory of the proposed D-D SLAM always converges to a small neighborhood of the ground truth, as shown in Figure 8. Meanwhile, the estimation of the source position also converges with the true source position.

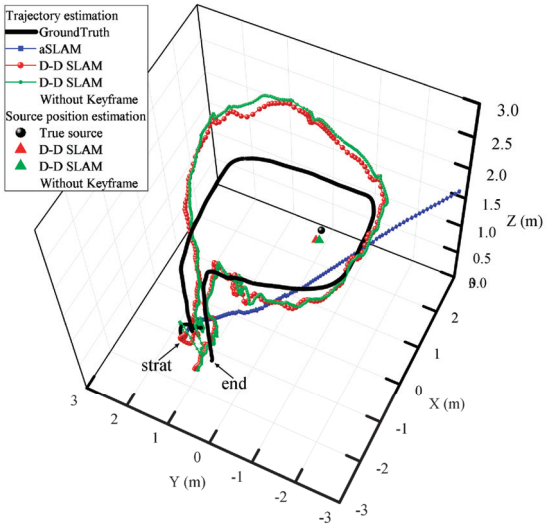

Figure 8. The estimation of trajectory and the source position using aSLAM and D-D SLAM with and without the keyframe method.

Figure 9 illustrates the estimation errors of the trajectory and source position. For aSLAM with real indoor data, the overall trajectory error tends to increase during the complete SLAM process, which is unacceptable. The source position error has the same trend as that of the trajectory error.

For the proposed D-D SLAM with the keyframe method, the maximum trajectory error reaches 1.18 m at 16.1 s (347 time steps), and its mean value is 0.48 m. In the meantime, the maximum error of the source position estimates of 0.66 m occurs at the beginning because the initial source position is random, and the error quickly converges to the stable value of 0.25 m after 2.8 s (60 time steps).

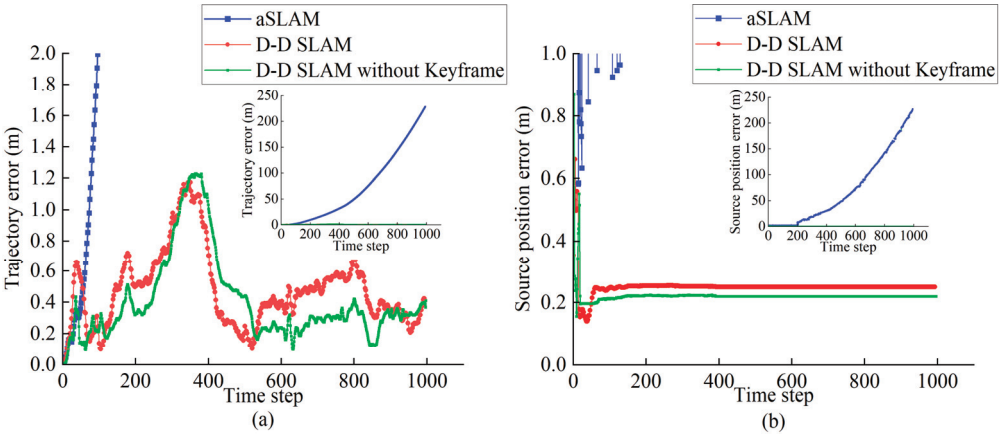

Figure 9. Dataset result for (**a**) the trajectory error and (**b**) the source position estimation error over time steps.

Compared with aSLAM, the proposed D-D SLAM has an acceptable performance in the trajectory and source position error, proving its validity for real world indoor scenes. The results in Figure 9 show the potential of the proposed D-D SLAM to work with an IMU in closed environments.

In the experiment, the results of the D-D SLAM with and without the keyframe method are shown in Figure 8, and the corresponding errors are shown in Figure 9. There are only small differences between the results of the D-D SLAM with and without the keyframe method. Thus, the keyframe method has a limited impact on the accuracy of estimations. Meanwhile, the use of the proposed D-D SLAM contributes to reducing the computing effort.

Figure 10 shows the critical distance estimation on the DREGON dataset. Similar to that in the simulation, the estimated critical distance converges rapidly to a stable value near 6.8 m.

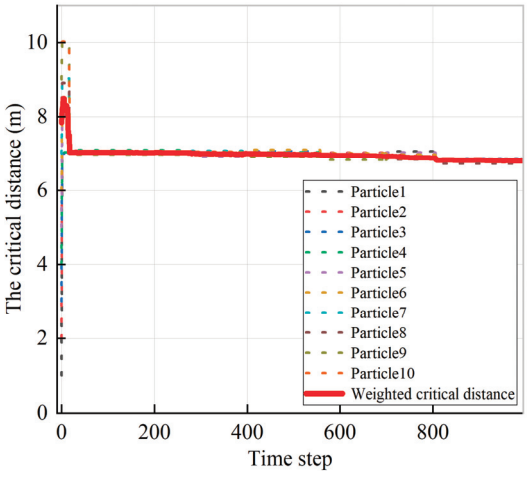

Figure 10. The state of different critical distance particles and the weighted critical distance with real data.

With Intel i5-7500 CPU (4 cores 3.40GHz), under the condition of 10 particles, the expected latency is 0.1392 s, and the D-D SLAM performs at a speed of 7.1 FPS. The received audio signals do not change significantly when the microphone on the robot moves slightly, so the FPS of 7.1 should be acceptable for acoustic SLAM.

6.3. Analysis

In this section, the reasons for the trajectory errors are analyzed. The trajectory errors are affected by the number of particles, the max number of GM components used in source mapping, the DoA estimates, the IMU measurements, and the robot's distance from the source.

The positional errors in different particle numbers are observed (as triangle and circle marks in Figure 11a). It is also important to determine the influence of the particle number on the critical distance estimation. The experiment in Section 5.2 is repeated for 5, 8, 10, 15, and 20 particles to investigate if a further improvement of the positional accuracy and the critical distance estimation can be achieved.

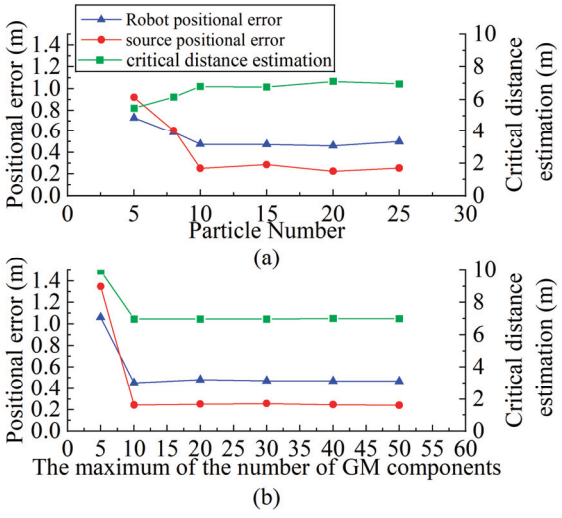

Figure 11. The positional error and the critical distance estimation with (**a**) different numbers of particles and (**b**) the max number of GM components.

When the number of particles increases from 5 to 10, the errors of source position and robot trajectory estimation decline quickly because the brute force strategy consists of increasing the number of particles and proves to be effective [32]. When the number of particles increases above 10, the errors of the source position and the robot trajectory estimation stabilize at values of 0.25 m and 0.48 m, respectively. The reason for this is that the contribution of increasing the particle number is negligible after a few iterations [33]. The critical distance estimation also quickly converges to a stable value for the same reason.

The experiment in Section 5.2 is also repeated for different max numbers of GM components used in source mapping (as triangle and circle marks in Figure 11b). With an increase in the maximum of GM components, the positional error and the critical distance estimates quickly converge to a stable value.

As mentioned before, the SRP-PHAT with limited elevation search boundaries has high-accuracy DoA results. Even if the direction of the drone noise is in the range of the source direction, the Wiener Filter with the noise sample can be applied for noise reduction [15]. Incidentally, the drone noise can only affect the ITD and the coherence of binaural signals in the calculation process of DRR. As the ITD is calculated with accurate

DoA estimates, the ITD is robust to drone noise. As the drone noise is diffuse and incoherent between different channels, it can be suppressed when calculating the coherence of binaural signals.

As the covariance of the DoA estimates and the IMU measurements are considered to be time-invariant while the trajectory errors have obvious variation with time, the time-varying robot's distance from the source is considered. In Figure 12, the true robot-source distance is represented with the blue dashed line, and the trajectory error of D-D SLAM is drawn with the solid red line. What Figure 12 clearly shows is that the trajectory error increases with the decrease in the true robot-source distance. Roughly speaking, the trajectory error reaches the maximum when the true robot-source distance approaches the minimum. Therefore, it can be assumed that the trajectory error is associated with the robot-source distance.

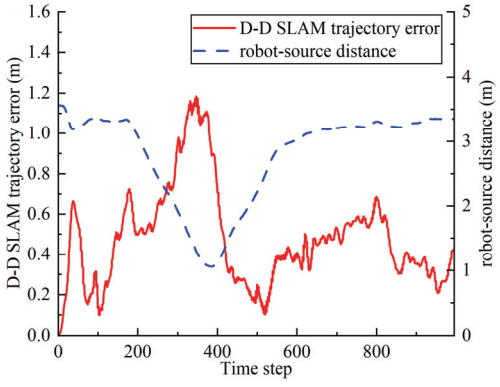

Figure 12. The robot-source distance and the trajectory error of D-D SLAM.

Using (16), the estimation of the robot-source distance depends on the critical distance. The critical distance should be fixed when the reverberation field is stable. However, the reverberation field may vary if there are moving objects. The closer the robot is to the source, the larger its influence on the reverberation field. The reason is that when they are close, the multiple diffractions and the multiple reflections they cause will become stronger, and the influence on the reverberation field is also heavier, and vice versa.

As shown in Figure 10, when the robot is still far from the source, the critical distance estimation has already converged to a stable value, leading to particle dilution of the critical distance. After that, the variation in the reverberation field caused by the change in distance between the robot and the source can no longer be considered with the diluted particle filter. As a result, the outdated estimation of the critical distance will affect the estimation of the robot-source distance, according to (16). The deviation of the robot-source distance finally causes an increase in the trajectory estimation error.

7. Conclusions

Focusing on the solution of indoor SLAM with acoustic data and an IMU, D-D SLAM is proposed. With the keyframe method, D-D SLAM performs well in mapping regardless of whether the robot moves or remains stationary. The use of the DRR for the estimation of the source's distance from the robot as a new constraint in D-D SLAM effectively eliminates the nonlinear noise of the IMU measurements. As the key factor to calculate the source's distance from the DRR estimates, the critical distance is unknown initially, so a particle filter is applied to estimate the critical distance online, and the estimation of the critical distance converges to a stable value.

According to the results, D-D SLAM has good performance in both simulations and experiments. For the first time, an acoustic SLAM algorithm is validated with a real indoor dataset containing only acoustic data and IMU measurements. Different from previous

work, D-D SLAM is designed for three-dimensional motion and rotation. On the real indoor dataset, the proposed D-D SLAM can locate the robot with an average accuracy of 0.48 m and build a source map with an average accuracy of 0.25 m. Even though the initial source position is random, the error of the source position converges to less than 0.25 m within 2.8 s.

These results demonstrate the effectiveness of the proposed D-D SLAM in real-world indoor scenes. In the future, D-D SLAM may contribute to robot localization and map building when conventional optical sensors are not suitable for special indoor environments, for example, foggy rooms where light and lasers cannot penetrate during navigation missions.

Author Contributions: W.Q., G.W. and W.Z.; conceptualization, W.Q., G.W. and W.Z.; methodology, W.Q.; software W.Q.; validation, W.Q. and W.Z.; formal analysis, W.Q.; writing—original draft preparation, W.Q.; writing—review and editing, G.W. All authors have read and agreed to the published version of the manuscript.

Funding: This work was supported by the National Natural Science Foundation of China grant number 11772123.

Institutional Review Board Statement: Not applicable.

Informed Consent Statement: Not applicable.

Data Availability Statement: The DREGON dataset is available at http://dregon.inria.fr/datasets/dregon/ (accessed on 26 October 2020).

Acknowledgments: This paper was supported by the National Natural Science Foundation of China. We thank the National Natural Science Foundation of China.

Conflicts of Interest: The authors declare no conflict of interest.

References

1. Qin, T.; Li, P.; Shen, S. VINS-Mono: A Robust and Versatile Monocular Visual-Inertial State Estimator. *IEEE Trans. Robot.* **2018**, *34*, 1004–1020. [CrossRef]
2. Chen, L.; Yang, A.; Hu, H.; Naeem, W. RBPF-MSIS: Toward Rao-Blackwellized Particle Filter SLAM for Autonomous Underwater Vehicle With Slow Mechanical Scanning Imaging Sonar. *IEEE Syst. J.* **2020**, *14*, 3301–3312. [CrossRef]
3. Shim, Y.; Park, J.; Kim, J. Relative navigation with passive underwater acoustic sensing. In Proceedings of the 2015 12th International Conference on Ubiquitous Robots and Ambient Intelligence (URAI), Goyang, Republic of Korea, 28–30 October 2015; pp. 214–217.
4. Ribas, D.; Ridao, P.; Tardós, J.D.; Neira, J. Underwater SLAM in Man-Made Structured Environments. *J. Field Robot.* **2008**, *25*, 898–921. Available online: https://onlinelibrary.wiley.com/doi/abs/10.1002/rob.20249 (accessed on 3 July 2021). [CrossRef]
5. Hu, J.S.; Chan, C.Y.; Wang, C.K.; Lee, M.T.; Kuo, C.Y. Simultaneous Localization of a Mobile Robot and Multiple Sound Sources Using a Microphone Array. *Adv. Robot.* **2011**, *25*, 135–152. [CrossRef]
6. Kallakuri, N.; Even, J.; Morales, Y.; Ishi, C.; Hagita, N. Probabilistic Approach for Building Auditory Maps with a Mobile Microphone Array. In Proceedings of the 2013 IEEE International Conference on Robotics and Automation (ICRA), Karlsruhe, Germany, 6–10 May 2013; pp. 2270–2275.
7. Evers, C.; Naylor, P.A. Acoustic SLAM. *IEEE/ACM Trans. Audio Speech Lang. Process.* **2018**, *26*, 1484–1498. [CrossRef]
8. Evers, C.; Naylor, P.A. Optimized Self-Localization for SLAM in Dynamic Scenes Using Probability Hypothesis Density Filters. *IEEE Trans. Signal Process.* **2018**, *66*, 863–878. [CrossRef]
9. Joly, C.; Rives, P. Bearing-only sam using a minimal inverse depth parametrization—Application to Omnidirectional SLAM. In Proceedings of the 7th International Conference on Informatics in Control, Automation and Robotics, Funchal, Portugal, 15–18 June 2010; pp. 281–288. [CrossRef]
10. Rascon, C.; Meza, I. Localization of sound sources in robotics: A review. *Robot. Auton. Syst.* **2017**, *96*, 184–210. [CrossRef]
11. Sobhdel, A.; Shahrivari, S. Few-Shot Sound Source Distance Estimation Using Relation Networks. *arXiv* **2019**, arXiv:2109.10561. [CrossRef]
12. Yiwere, M.; Rhee, E.J. Sound Source Distance Estimation Using Deep Learning: An Image Classification Approach. *Sensors* **2019**, *20*, 172. [CrossRef]
13. Portello, P.; Danès, P.; Argentieri, S. Acoustic models and Kalman filtering strategies for active binaural sound localization. In Proceedings of the 2011 IEEE/RSJ International Conference on Intelligent Robots and Systems, San Francisco, CA, USA, 25–30 September 2011; pp. 137–142. [CrossRef]
14. Zahorik, P. Direct-to-reverberant energy ratio sensitivity. *J. Acoust. Soc. Am.* **2002**, *112*, 2110–2117. [CrossRef]

15. Strauss, M.; Mordel, P.; Miguet, V.; Deleforge, A. DREGON: Dataset and Methods for UAV-Embedded Sound Source Localization. In Proceedings of the 2018 IEEE/RSJ International Conference on Intelligent Robots and Systems (IROS), Madrid, Spain, 1–5 October 2018; pp. 1–8. [CrossRef]
16. Zohourian, M.; Martin, R. Binaural Direct-to-Reverberant Energy Ratio and Speaker Distance Estimation. *IEEE/ACM Trans. Audio Speech Lang. Process.* **2020**, *28*, 92–104. [CrossRef]
17. Forster, C.; Carlone, L.; Dellaert, F.; Scaramuzza, D. IMU Preintegration on Manifold for Efficient Visual-Inertial Maximum-a-Posteriori Estimation. *Robotics Sci. Syst.* **2015**. [CrossRef]
18. Le Gentil, C.; Vidal-Calleja, T.A.; Huang, S. Gaussian Process Preintegration for Inertial-Aided State Estimation. *IEEE Robot. Autom. Lett.* **2020**, *5*, 2108–2114. [CrossRef]
19. Communication Acoustics; Springer: Berlin/Heidelberg, Germany. Available online: https://link.springer.com/book/10.1007/b139075 (accessed on 7 July 2021).
20. Schwartz, O.; Plinge, A.; Habets, E.A.P.; Gannot, S. Blind microphone geometry calibration using one reverberant speech event. In Proceedings of the 2017 IEEE Workshop on Applications of Signal Processing to Audio and Acoustics (WASPAA), New Paltz, NY, USA, 15–18 October 2017; pp. 131–135. [CrossRef]
21. Khairuddin, R.; Talib, M.; Haron, H. Review on simultaneous localization and mapping (SLAM). In Proceedings of the 2015 IEEE International Conference on Control System, Computing and Engineering (ICCSCE), Penang, Malaysia, 27–29 November 2015; pp. 85–90. [CrossRef]
22. Vo, B.-N.; Ma, W.-K. The Gaussian Mixture Probability Hypothesis Density Filter. *IEEE Trans. Signal Process.* **2006**, *54*, 4091–4104. [CrossRef]
23. Ristic, B.; Vo, B.-N.; Clark, D. A Metric for Performance Evaluation of Multi-Target Tracking Algorithms. *IEEE Trans. Signal Process.* **2011**, *59*, 3452–3457. [CrossRef]
24. Casella, G.; Robert, C.P. Rao-Blackwellisation of Sampling Schemes. *Biometrika* **1996**, *83*, 81–94. [CrossRef]
25. Schon, T.; Gustafsson, F.; Nordlund, P.-J. Marginalized particle filters for mixed linear/nonlinear state-space models. *IEEE Trans. Signal Process.* **2005**, *53*, 2279–2289. [CrossRef]
26. Jwo, D.-J.; Cho, T.-S. Critical remarks on the linearised and extended Kalman filters with geodetic navigation examples. *Measurement* **2010**, *43*, 1077–1089. [CrossRef]
27. Salmond, D.J. Mixture Reduction Algorithms for Point and Extended Object Tracking in Clutter. *IEEE Trans. Aerosp. Electron. Syst.* **2009**, *45*, 667–686. [CrossRef]
28. Arulampalam, M.; Maskell, S.; Gordon, N.; Clapp, T. A tutorial on particle filters for online nonlinear/non-Gaussian Bayesian tracking. *IEEE Trans. Signal Process.* **2002**, *50*, 174–188. [CrossRef]
29. Lehmann, E.A.; Johansson, A.M. Diffuse Reverberation Model for Efficient Image-Source Simulation of Room Impulse Responses. *IEEE Trans. Audio Speech Lang. Process.* **2010**, *18*, 1429–1439. [CrossRef]
30. Vincent, C.E.; Roomsimove, A. Matlab Toolbox for the Computation of Simulated Room Impulses Responses for Moving Sources. Available online: http://www.irisa.fr/metiss/members/evincent/software (accessed on 27 October 2020).
31. DiBiase, J.H.; Silverman, H.; Brandstein, M.S. Robust localization in reverberant rooms. In *Microphone Arrays: Signal Processing Techniques and Applications*; Springer: Berlin/Heidelberg, Germany, 2001.
32. Liang, Y.; Feng, Y.; Quan, P.; Yan, L. Adaptive Particle Filter: Tuning Particle Number and Sampling Interval. In Proceedings of the 24th Chinese Control Conference, Guangzhou, China, 15 June–18 July 2005; Volumes 1 and 2, pp. 803–807.
33. Kuptametee, C.; Aunsri, N. A review of resampling techniques in particle filtering framework. *Measurement* **2022**, *193*, 110836. [CrossRef]

drones

MDPI

Article

Optimum Flight Height for the Control of Desert Locusts Using Unmanned Aerial Vehicles (UAV)

Violet Ochieng' [1,2,*], Ivan Rwomushana [1], George Ong'amo [2], Paul Ndegwa [2], Solomon Kamau [3], Fernadis Makale [1], Duncan Chacha [1], Kush Gadhia [4] and Morris Akiri [1]

[1] CAB International (CABI), P.O. Box 633, Nairobi 00621, Kenya
[2] Faculty of Science and Technology, Department of Biology, University of Nairobi, P.O. Box 30197, Nairobi 00625, Kenya
[3] Faculty of Agriculture, Department of Land Resource Management and Agricultural Technology (LARMAT), University of Nairobi, P.O. Box 29053, Nairobi 00625, Kenya
[4] Astral Aerial Solutions, P.O. Box 594, Nairobi 00606, Kenya
* Correspondence: veeochieng@students.uonbi.ac.ke

Abstract: Desert locust is one of the most destructive migratory pest in the world. Current methods of control rely on conventional chemical insecticides during invasion. Some environmentally friendly biopesticides based on *Metarhizium acridum* and insect growth regulators have also been deployed in preventive control operations. They have been tested in sprayers mounted on commonly used platforms such as vehicles, aircraft, and human. However, despite being used successfully, these tools present many challenges, hence the need to supplement them with suitable alternatives. The successful use of drones to control pests such as fall armyworm, planthoppers, aphids, among others, makes it an attractive technology that has the potential to improve locust management, especially in inaccessible areas. However, key parameters for the safe and optimal use of drones in desert locust control are not documented. This study established the key parameters for spraying desert locusts with a drone. To test the optimum height for spraying *Metarhizium acridum* on the locusts, the drone was flown at five different heights: 2.5, 5, 7.5, 10, and 12.5 m. At each height, the drone sprayed the ink mixture on spray cards pinned to the ground to approximate the droplet density and compare it to the standard droplet density recommended for desert locust control. To assess the efficacy of *M. acridum* and the effectiveness of drones in its application, 50 g of spores were mixed in 1 L of diesel and sprayed on caged live locusts of different stages (3rd and 4th instars, as well as the adults); they were monitored for twenty-one days in a controlled room, and their mortality was determined. Variation in droplet density between the tested heights was significant. A height of 10 m agrees with the recommended standard droplet density within the 45 droplets/cm^2 range. Mortality varied among the locusts' developmental stages within and between heights. Survival probability varied between heights for 3rd instar, 4th instar, and adults. All the developmental stages of the desert locust were susceptible to Novacrid and the recommended target stage is the 3rd instar. Management of desert locusts by the use of drone technology appears promising when the pesticides are applied at an optimum height and standard operating procedures are followed. Further research could explore the gap in the effects of environmental parameters on flight application efficiency.

Keywords: drones; *Metarhizium*; pesticides application; optimum height; droplets density; mortality rate

Citation: Ochieng', V.; Rwomushana, I.; Ong'amo, G.; Ndegwa, P.; Kamau, S.; Makale, F.; Chacha, D.; Gadhia, K.; Akiri, M. Optimum Flight Height for the Control of Desert Locusts Using Unmanned Aerial Vehicles (UAV). *Drones* **2023**, *7*, 233. https://doi.org/10.3390/drones7040233

Academic Editors: Andrzej Łukaszewicz, Wojciech Giernacki, Zbigniew Kulesza, Jaroslaw Alexander Pytka and Andriy Holovatyy

Received: 17 February 2023
Revised: 19 March 2023
Accepted: 20 March 2023
Published: 28 March 2023

1. Introduction

Desert locust, *Schistocerca gregaria* Forskål (Orthoptera: Acrididae), is one of the most destructive migratory pest in the world [1] and exhibits solitary and gregarious phases that vary in biology and behavior [2–5]. Upsurge of desert locusts have prompted the use of chemical pesticides such as organochlorines, carbamates, organophosphates, and

pyrethroids as the main control measures [6,7]. However, although these chemical pesticides may provide an effective means of control, there are risks to the environment and human health and safety [8]. Moreover, invasion sometimes occurs in sensitive areas, such as near human settlements, and to some extent in protected areas with numerous beneficial organisms, which limits their use [9,10].

Consequently, safe and environment-friendly biopesticides based on *Metarhizium acridum* (Novacrid® and Green Muscle®) were developed [11–13] as oil formulations suitable for ultra-low volume (ULV) application. They have been tested in a range of commonly used spinning-disk sprayers, including the hand-held Micron Ulva-Plus and vehicle-mounted Ulva-Mast [14]. These sprayers were used successfully on various pesticide application platforms during the 2019–2022 desert locust invasions but presented some challenges, such as the accessibility of hard-to-reach areas and economic cost, both of which required improvements for the effective management of locusts [15,16].

Modern approaches and technologies, such as the use of UAVs, have the potential to complement the existing methods of desert locust management [1]. An UAV is an aircraft that flies without a human pilot onboard [1,17–22], whose development has become more practically feasible and affordable in precision agriculture [18,23,24]. The application of pest control products using UAV has been increasing over the years [25]. Importance is ascribed to the correctness of the process and application, taking into account the effects of sprayed liquid on the environment [26]. The fundamental issue in these processes is quality and efficiency, since they determine the efficacy and deposition of the pesticide [27]. One of the critical parameters to be optimized and considered for the effectiveness of UAV-enabled spraying is droplet deposition, measured by droplet density [18].

The efficiency of UAVs in spraying aphids and spider mites in cotton [28], brown plant hoppers [26], cowpea thrips [29], rice plant hoppers [30], fall armyworm in sugarcane [31], and wheat aphids [32] has been demonstrated. There have also been suggestions that UAVs can be used to apply pesticides on desert locusts [16,33], even though much remains to be completed in terms of research and implementation, or operationalization. Nonetheless, the parameters optimized in the studies on other insect pest species may not apply to desert locusts because of the differences in biology and behavior of the latter. There is a need to explore the potential of UAV technologies to improve locust management before populations build up and swarms invade extensive farming areas. One of the important factors to be considered for the effectiveness of UAV-enabled spraying is the droplet deposition. The parameters used for measuring the effectiveness of droplet deposition include droplets density. This measure is used to understand how the field is covered with pesticide and how well the pesticide is dispersed. The droplet density deposition is the number of droplets deposited per unit area and is often measured using water-sensitive papers. Effective control of pests requires the optimum dose of the pesticide applied so that droplets on the target surface can have the best coverage, spread, attachment, and absorption [18]. Droplets deposited on water-sensitive papers are counted through an automated solution, such as a swath kit, Dropscan, Agroscan, Dropleaf, and Image J software, among others. Flight altitude affects the effectiveness of a drone significantly [27,28,34] and it is logical that as the flight altitude increases, the droplet density reduces and droplet uniformity increases [34]; therefore, the goal is to achieve the highest possible flight altitude to increase effectiveness. At present, there is little information available on the optimum flight height when drones are used for desert locust control. Therefore, scientific-based field testing is required. This study established the optimum height for the application of pesticides for the control of desert locusts.

2. Materials and Methods

2.1. Field Site for the Experiment

The trials were conducted at the Kenya Agricultural and Livestock Research Organization (KALRO) Station, located at the Muguga Research Centre (1°13′ S, 36°38′ E), which lies 30 km from Nairobi, off the Nairobi–Nakuru highway. This study was conducted during

the second week of October (2021) on a day when the weather was sunny and cloudless with a low relative humidity of 65%, with temperatures varying between 26 and 29 °C and wind speeds varying between 3.0 and 3.6 m s^{-1}. Temperature and wind conditions, as well as site characteristics, were similar to conditions required during some actual locust survey and control operations [13,35].

2.2. Parameters for Spraying Pesticides Using a Drone

A DJI Agras T20 drone fitted with an ultra-low volume (ULV) atomizer was used to assess the effect of spray application heights on droplet density on the ground. The drone was fitted with a Micronair 12 ULV spraying boom with three atomizers and a 20 L spray tank. White A4 papers measuring 210 × 297 mm were used as spray cards to estimate the deposition of droplets at different spray heights. The spray tank was filled to its maximum volume with a mixture of water-soluble black ink and water in a ratio of 1:3 (v/v) to produce the payload of 20 L at the start of the trial and was reloaded when the tank was empty. The spray cards were placed and pinned on the ground at intervals of 1 m in three equal and parallel rows that were 50 m apart. The drone's flight path bisected the three rows in the middle at right angles. A total of 61 spray cards were pinned on each row, 30 on the left and 30 on the right, with one card at the mid-line that marked the drone flight path (Figure 1). The spray cards were appropriately labelled according to the spray height tested and distance from the drone flight path. The flight trajectory was programmed using the drone's software to spray the ink mixture at five different heights: 2.5 m, 5.0 m, 7.5 m, 10.0 m, and 12.5 m. At each height, the drone sprayed the ink mixture at a constant flow rate of 1 L/min at a constant speed of 14 km/h. After every flight, the pinned spray cards were collected sequentially for analysis. This procedure was repeated three times for each flight height. The sprayed papers were scanned using a scanner (LaserJet Pro MFP MI30NW, Hewlett Packard) at 600 dpi and stored in Joint Photographic Group (JPG) format. The images (Figure 2) were imported to the Dropleaf app, which processed and analyzed droplet density through five steps: color space conversion to grayscale, binarization by threshold for noise removal, dilation and erosion, production of contours, and droplet identification [36]. The spread factor was assumed to be such that the values calculated by the app were the ones used for analysis.

A primary progeny of 140 desert locust hoppers in different developmental stages was obtained from the University of Nairobi, Department of Biology, and reared at the KALRO Muguga Center for six months, during which they were able to breed and generate a total of 1280 individuals in various developmental stages. A total of 324 individuals were selected for this experiment, comprising 108 individuals at the 3rd and 4th instars and adults. The temperature and relative humidity maintained in the insectary were 33 °C and 60%, respectively.

To test the efficacy of the Novacrid® biopesticide sprayed by a drone on live desert locusts, a total of 324 desert locusts were placed in 54 cages, each measuring 30 × 30 × 30 cm, with six locusts per cage. Each developmental stage had a total of 18 designated cages, of which 15 were for treatment (one treatment per drone flight height, repeated twice) and three were untreated controls.

A total of 500 g of Novacrid® biopescide was mixed with 20 L of diesel to form a homogenous solution and loaded into the drone's container. At each of the five different flight heights, one cage for each developmental stage was randomly placed in a 1 ha area, parallel to the flight route (Figure 3). The drone was launched to spray at the selected height, and this process was replicated three times. After spraying, the labelled cages were transferred to a quarantine room at the insectary, while the untreated locusts (the control) were left at the main insectary for observation, with a daily mortality recorded for a period of 21 days. The dead locusts were removed on a daily basis from the experimental cages and incubated in the laboratory at a temperature of 28 °C and 80% relative humidity to encourage external growth and sporulation of the fungus.

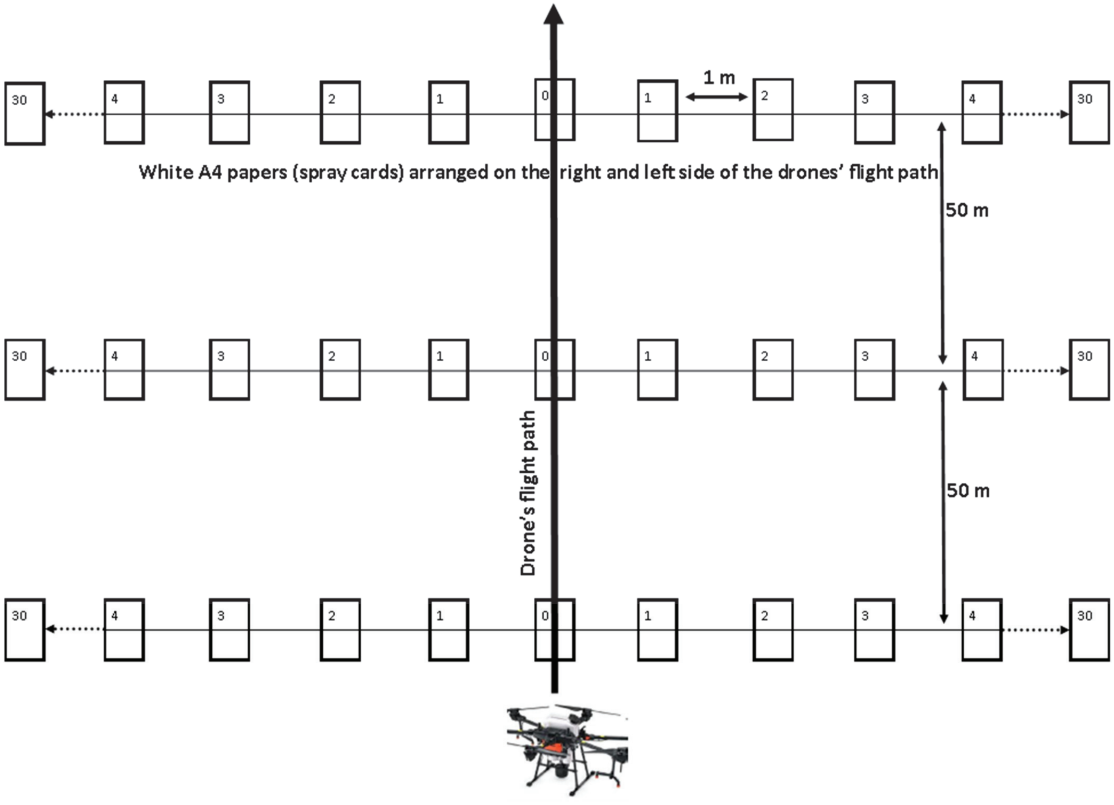

Figure 1. Illustration of the experimental layout of spray cards for establishing optimum droplet density by spraying at different heights using an Agras T20 drone fitted with a Micronair 12 ultra-low volume (ULV) spraying boom.

Figure 2. Samples of papers with droplets.

Figure 3. Wire mesh cages (objects arranged within the yellow circle) with live locusts arranged parallel to the drone flight path (object within the red circle).

2.3. Data Management and Analysis of Optimum Droplet Density at Different Flight Heights

The recorded density of the droplets was subjected to the Hampel filter in the R statistical software to identify outliers as part of data management. The Hampel filter considers outliers as values outside the interval (I) formed by the median, plus or minus 3 median absolute deviations (MAD);

$$I = [median - 3.MAD;\ median + 3.MAD], \tag{1}$$

where MAD is defined as the median of the absolute deviations from the data's median $\widetilde{x} = median(x)$:

$$MAD = median(|x_i - \widetilde{x}|). \tag{2}$$

To compute the optimum density of droplets, one litre sprayed in one hectare was converted to cubic micrometres (1.0×10^{15}). This was because it was known that during desert locust control, about 0.5–1.0 L of ULV insecticide was optimally sprayed in 1 hectare using rotary atomizers (spinning discs or rotating cages) to produce droplets in a small size range (50–100 μm) in diameter [13,34]. For optimization, a compromised diameter of 75 μm was used to estimate the volume of each droplet:

$$\text{Volume of each droplet} = \frac{4}{3}\pi r^3 = \frac{4}{3} \times \left(\frac{22}{7}\right) \times \left(\frac{75}{2}\right)^3 = 220,982\ \mu m^3. \tag{3}$$

Estimated droplet volume was used to estimate the number of droplets in 1 L,

$$\text{No. droplets} = \frac{1 \text{ litre } (\mu m^3)}{\text{Droplet size } (\mu m^3)} = \frac{1.0 \times 10^{15}}{220,982} = 4,525,252,525. \quad (4)$$

It was assumed that droplets were homogenously distributed in 1 ha (=100,000,000 cm^2), and then from this assumption, the optimum density of standard droplets Ø75 µm in one hectare was estimated from the following calculation, resulting in 45 droplets/cm^2:

$$\text{No. droplets } /cm^2 = \frac{4,525,252,525}{100,000,000} = 45 \text{ droplets}/cm^2. \quad (5)$$

The data on droplet density obtained from the dropleaf app was subjected to statistical analysis using R statistical software(Version 4.1.1). Anova was used to test the effect of flight height on droplet deposition. Tukey's honest significant difference (HSD) test was used where significant effects of flight heights on droplet density were observed ($p < 0.05$). One sample *t*-test was used to compare the standard calculated density against densities at different spray heights.

2.4. Efficacy of Metarhizium on Desert Locusts

Mortality in respective cages was transformed into percentages and corrected using Abbotts's correction formula to eliminate natural mortality as follows [37]:

$$Corrected\ mortality(\%) = \left(\frac{Trt - Co}{100 - Co}\right), \quad (6)$$

where *Trt* and *Co* are the daily treatment and control mortality, respectively.

Data were subjected to the Shapiro–Wilk test to test for normality. Mortalities in the 3rd instar, 4th instar, and adult stages in all the cages were subjected ANOVA to test the effect of spraying height on mortality. The Cox proportional hazard model was used to assess the statistical difference in survival probability of different developmental stages between flight heights. Survival distribution curves were generated using the Kaplan–Meier estimator.

3. Results

3.1. Variation in Droplet Density among Different Drone Flight Heights

Droplet density varied significantly among the tested heights ($F_{4,40} = 7.2$; $p < 0.001$) (Table 1). The highest and lowest mean droplet densities (152.2 ± 4.8 and 24.8 ± 6.51) were recorded at the lowest (2.5 m) and highest tested flight height (12.5 m), respectively. Droplet density observed at 5.0 m, 7.5 m, 10.0 m, and 12.5 m did not vary significantly, but at 2.5 m it was significantly different from other tested flight heights except for 7.5 m (Table 1).

Table 1. Mean (±SE) spray droplet density at different drone flight heights.

Flight Height (m)	Mean (±SE) Droplet Density
2.5	152.2 ± 24.8 [b]
5.0	75.3 ± 11.1 [a]
7.5	96.0 ± 29.4 [ab]
10.0	40.2 ± 10.1 [a]
12.5	24.8 ± 6.51 [a]
$F_{4,40}$	7.2
p-Value	0.0002

Same letters indicate no significant difference.

3.2. Optimum ULV Spraying Heights Using a Drone

One sample comparison between standard droplet density and observed mean droplet density varied among different heights (Table 2). Mean droplet densities were significantly

higher than the standard density (45 droplets/cm^2) at 2.5 m (t_{227} = 6.02; $p < 0.05$) and 5 m (t_{289} = 3.63; $p < 0.05$). The mean droplet density at 10 m was not different from the standard droplet density (t_{308} = 1.031; $p > 0.05$). Mean droplet density at a flight height of 10 m was concordant with the volume application rate (VAR) recommended by the manufacturer because the mean droplet density observed was within the standard range of 45 droplets/cm^2. However, the droplet density was lower than the standard at 12.5 m (t_{343} = 6.39; $p < 0.05$).

Table 2. One sample *t*-test comparison of the standard droplet density (45 droplets/cm^2) against droplet densities observed at different spray heights using a drone.

Spray Heights	Mean Droplet Density	One Sample *t*-Test (Mu = 45 Droplets/cm^2)		
(m)	($\bar{x} \pm$ SE)	*t*-Value	*Df*	*p*-Value
2.5	152.2 ± 24.8	6.02	227	7.07×10^{-9} ***
5.0	75.3 ± 11.1	3.63	289	0.0003 ***
7.5	96.0 ± 29.4	2.07	369	0.039 *
10.0	40.2 ± 10.1	1.03	308	0.304
12.5	24.8 ± 6.51	6.39	343	5.61×10^{-10} ***

*** shows strong significant difference of mean droplet density from the standard droplet density. * show least significant difference.

3.3. Effects of Drone Spraying Height on Mortality of Desert Locusts

Mortality varied among the locusts' developmental stages at different heights ($F_{2,30}$ = 25.71; $p < 0.0001$) (Table 3). Variation in mortality between different developmental stages was evident at 10.0 m ($F_{2,6}$ = 16.73; p = 0.0035) and 12.5 m ($F_{2,6}$ = 27.97; $p < 0.0009$). At 10.0 m, the mortality of the 3rd and 4th instars was similar and high compared to the adults, while at 12.5 m, the mortality of the third instar was high, followed by the fourth and lowest in adults. Mortality of all the locusts' stages was similar at 2.5 m ($F_{2,6}$ = 1.22; p = 1.00), 5.0 m ($F_{2,6}$ = 2.04; p = 0.21), and 7.5 m ($F_{2,6}$ = 1.53; p = 0.29).

Table 3. Mortality of different life cycle stages of desert locusts sprayed with Novacrid® biopesticide at different spray heights using an Agras T20 drone fitted with an ULV atomizer.

Stages of Desert Locusts	Drone Spraying Height (Metres above Ground Level)						
	2.5	5.0	7.5	10.0	12.5	$F_{4,10}$	*p*-Value
Third	100.00 ± 0.00 ^{cA}	100.00 ± 0.00 ^{cA}	86.66 ± 6.67 ^{bA}	80.00 ± 0.00 ^{bB}	40.00 ± 0.00 ^{aC}	68.50	<0.0001
Fourth	100.00 ± 0.00 ^{cA}	86.66 ± 6.67 ^{bcA}	86.66 ± 6.67 ^{bcA}	73.33 ± 6.66 ^{bB}	26.66 ± 6.67 ^{aB}	22.74	<0.0001
Adults	100.00 ± 0.00 ^{dA}	83.33 ± 8.33 ^{cA}	75.00 ± 0.00 ^{cA}	50.01 ± 0.00 ^{bA}	0.00 ± 0.00 ^{aA}	109.00	<0.0001
$F_{2,6}$	1.22	2.04	1.53	16.73	27.97		
p-value	1.00	0.21	0.29	0.0035	0.0009		

The same superscripted lowercase letters in the same row indicate no significant difference in the mortality among different spray heights, while the same superscripted uppercase letters in the column indicate no significant difference in the mortality across life cycle stages; Turkey test (HSD), p = 0.05.

Mortality of all the locusts' stages varied between heights ($F_{4,30}$ = 143.39; $p < 0.0001$) (Table 3). Variation of mortality between heights was evident in the third instar ($F_{4,10}$ = 68.50; $p < 0.0001$), with the highest and similar mortality at 2.5 m and 5.0 m (100 ± 0.00), followed by 7.5 m (86.66 ± 6.67), 10.0 m (80.00 ± 0.00), and lowest at 12.5 m (40.00 ± 0.00). Similar variation was observed at the fourth instar ($F_{4,10}$ = 22.74; $p < 0.0001$) and adults ($F_{4,10}$ = 109.00; $p < 0.0001$). Both the fourth instar and adults exhibited the same trend of reduced mortality with an increase in spray height, except at 5.0 m and 7.5 m, where mortality was the same. Interaction between spray heights and different stages of locusts also had a significant effect on mortality ($F_{8,30}$ = 3.6745; p = 0.004271).

3.4. Effects of Drone Spraying Height on Survival Rates of Desert Locusts

The survival rate of different locusts' developmental stages (3rd, 4th, and adults) varied between different heights (Figure 4). Survival probability varied between heights for the 3rd instar ($\chi^2_4 = 56.84$; $p < 0.0001$), the 4th instar ($\chi^2_4 = 54.17$; $p < 0.0001$), and adults ($\chi^2_4 = 47.57$; $p < 0.0001$). In the 3rd and 4th instars, locusts sprayed at 2.5 m and 5.0 m did not survive and all died by the 12th and 15th days, respectively. High survival probability was observed at 12.5 m, followed by 10.0 m, and least at 7.5 m, where some treated locusts remained alive after 21 days of monitoring. On the other hand, all the adults sprayed at 2.5 m died, while a high survival rate was observed at 12.5 m, followed by 10.0 m, 7.5 m, and 5.0 m, respectively.

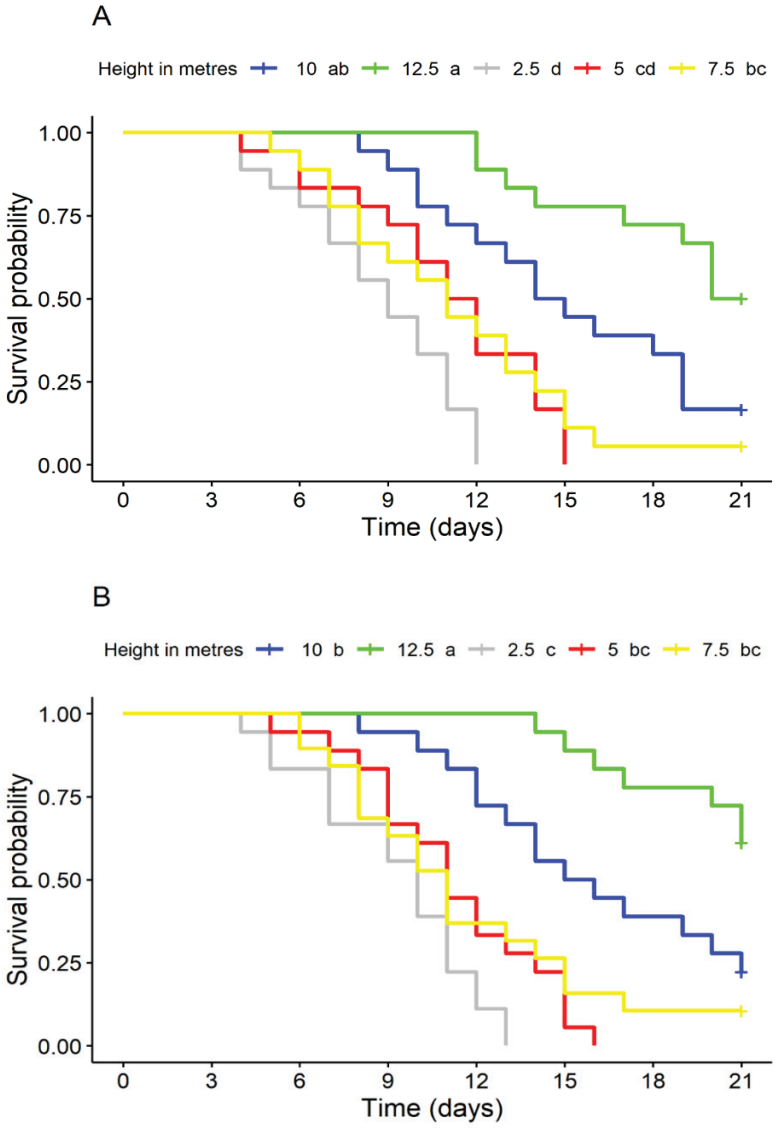

Figure 4. *Cont.*

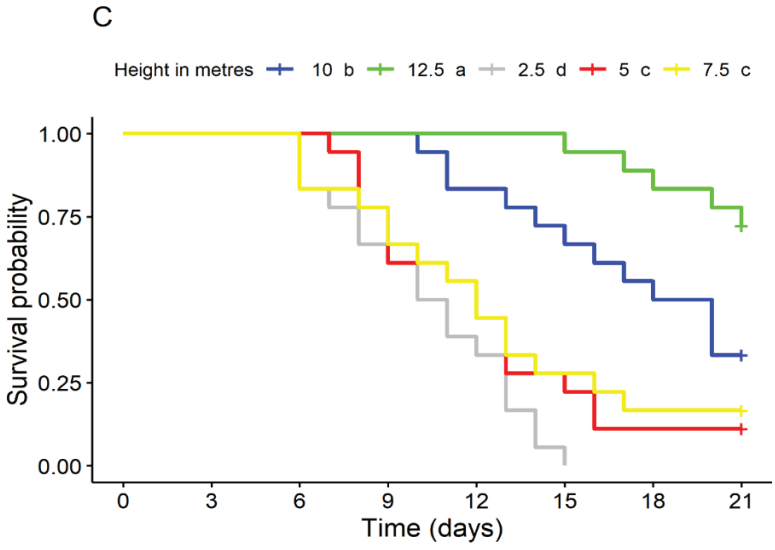

Figure 4. Kaplan—Meier survival curves for different stages of desert locusts sprayed with Novacrid® at different drone flight heights. The same small letters adjacent to the legend indicate no significant difference in the survival distribution curve at $p > 0.05$. (**A**) Survival curve of the 3rd instar, (**B**) survival curve of the 4th instar, and (**C**) survival curve of adults. "+" indicates right censorship.

4. Discussion

According to the formula derived from the information provided by Dobson [35], the recommended optimum droplet density for use in the management of desert locust is 45 droplets/cm^2. In this study, the droplet densities at the selected heights of 2.5 m, 5.0 m, 7.5 m, 10.0 m, and 12.5 m were 152.2 ± 4.8, 96.0 ± 29.4, 75.3 ± 11.1, 40.2 ± 10.1, and 24.8 ± 6.51, respectively. In reference to the optimum droplet density as provided by Dobson [35], the droplets were deposited more uniformly and sufficiently at the flight height of 10.0 m (40.2 ± 10.1). When the flight height was lower or higher than 10.0 m, the droplet densities indicated either over- or under-spraying, respectively. At lower heights (2.5 m, 5.0 m, and 7.5 m), the droplet density was higher near the nozzle area, resulting in an uneven distribution of droplets. Additionally, the swirling airflow caused by the flight effect of the drone flying perpendicular to the ground resulted in increased downward pressure on the droplets when the flight height was too low.

The variation of droplet densities with spray heights reported in this study matches the findings of earlier experiments in which a higher density of droplets was reported at lower heights than at higher heights [34,38–40]. High volumes and droplet densities at lower heights can also be the result of a strong downward swirling airflow that makes the air below sway substantially and affects the distribution and density of the droplets [26,40,41]. Lower droplet density at 12.5 m can be attributed to the downwash wind field above the ground, which is weakened when this flight height is maintained. Additionally, the weakened wind field in a vertical orientation causes an increase in the horizontal wind field that aggravates droplet transfer and drift to non-target areas, resulting in a sharp reduction in the density of droplets deposited on the target. These results are similar to a recent observation that an increase in height changes the downwash wind field, leading to a gradual reduction in droplet deposition within the effective target area [39,40]. The increased distance and time required for the spray to reach the targeted area also cause it to be dragged by the ambient air at higher heights compared to lower heights [41].

Drones have been identified as a potential platform for the application of pesticides in pest and weed management [24]. Their use in the management of desert locusts has been

challenged by a lack of data on optimum spraying height and the efficacy of biopesticides on different development stages of locusts in a field setting. This study demonstrated that although the application of Novacrid® at all the spraying heights tested caused mortality in the three different developmental stages of the desert locust, there were variances in the mortality rate and survival probability. In this experiment, lower spray heights produced a high rate of mortality and a lower survival probability in all the tested locust's lifecycle stages compared to higher spray heights (12.5 m), which was comparable to other similar studies conducted to assess effects of spraying heights on mortality of other pests upon application of synthetic pesticides using a drone [26,39,42,43]. For example, a significantly higher mortality of wheat hoppers was reported when sprayed with chlorpyrifos pesticides at lower flight heights [26]. The high concentration of conidia at a lower height can be attributed to reduced drift that maximized pesticide deposition in the target. Depending on the pesticide used, accuracy in deposition and distribution is dependent on application height [40], which could affect the penetration of the active ingredients of the pesticides [43]. Furthermore, as the height increases, droplet dispersion increases and deposition decreases, causing pesticides to be carried to non-target areas [39].

Our findings on the mortality and survival of the desert locust can also be explained by the mode of action of *Metarhizium acridum*, which is through direct contact and germinates, invading the hemocoel within 24 h after application of conidia to the insect's cuticle. The rate of mortality achieved is dependent on the dosage of conidia that is in contact with the locusts [11].

In this study, it was observed that at all heights, the 3rd instar was more susceptible to Novacrid®, followed by the 4th instar, and finally adults. The comparatively lower dose received at 12.5 m lengthened the infection period and lowered the mortality rate, leading to a high survival probability after 21 days of application. This finding was similar to those of other studies that treated desert locusts of different stages with *Metarhizium acridum* [44–46]. For example, experimental studies in a laboratory setting have previously reported the highest mortality (50%) in the 3rd instar, followed by the 5th instar (43%), and adults (33%) [44]. In this study, at the selected height of 10.0 m that deposited the standard droplet density, mortality was highest in the 3rd instar (80%), followed by the 4th instar (73%) and adults (50%). The high percentage of mortality observed at the 3rd nymphal stage could be due to a weakened immune system coupled with a soft exoskeleton that enabled the biopesticide to penetrate faster compared to the 4th instar and adults. At the hopper stage, their behavior includes banding and marching, and the band densities tend to reduce with the increase in size (30,000 hoppers per m^2 for the first instar and 50 to 100 hoppers per m^3 for the late instars) [4]. Therefore, targeting the most susceptible early stages is also cost-effective in terms of the density of bands that will be controlled at once unlike the female adult desert locusts which can lay at least one egg pod before dying after an estimated 21 days of Novacrid® application. Therefore, drones can be used to improve the control of desert locusts.

5. Conclusions

This study has demonstrated that spraying desert locusts using a drone at any height below 10.0 m may lead to over-deposition of the pesticide, while heights above 10.0 m may lead to under-application, which may limit exposure of the locusts to *Metarhizium* spores or pesticide molecules. This study demonstrated that spraying a control agent from a specific height is more effective than other heights tested.

Despite all the developmental stages of the desert locust being susceptible to Novacrid®, the recommended target stage for management using this biopesticide is the 3rd instar stage because of the higher mortality rate and lower survival probability at this stage.

Further studies could explore the gap in the effects of environmental parameters on application efficacy and the effectiveness of using more than one drone (drone swarms), which allow greater area coverage at the same time.

Author Contributions: Conceptualization, V.O. and I.R.; Methodology, V.O., I.R., G.O. and P.N.; Software, V.O. and K.G.; Validation, V.O., I.R., K.G., G.O. and P.N.; Formal Analysis, V.O., I.R., G.O., P.N. and S.K.; Investigation, V.O.; Resources, I.R., M.A. and K.G.; Data Curation, V.O., I.R., G.O., P.N. and S.K.; Writing—Original Draft Preparation, V.O; Writing—Review & Editing, I.R., G.O., P.N., S.K, F.M. and D.C.; Visualization, V.O. and I.R.; Supervision, I.R., G.O. and P.N.; Project Administration, I.R. and M.A.; Funding Acquisition, I.R. All authors have read and agreed to the published version of the manuscript.

Funding: The project was funded by the UKaid from the UK government through the support of Frontier Technologies. Additional financial support was received from the Carol Ellison Science Award for 2021.

Data Availability Statement: Data is available upon request.

Acknowledgments: We acknowledge CABI and Astral Aerial Solutions management and teams for the support they rendered toward this project. We also acknowledge KALRO Muguga for granting permission to use their facility for rearing desert locusts and conducting the drone experimental work. We deeply appreciate the University of Nairobi for providing the initial stock of locusts for rearing and the Ministry of Agriculture for providing the Novacrid® biopesticide. We are also grateful to Ruth McPake, Paul Miller, David Vigoureux, and Tristan Eagling for their contributions to this project.

Conflicts of Interest: The author declare no conflict of interest.

References

1. FAO. Desert locust upsurge; Global response plan, January–December 2020. In *Appeal for Rapid Response and Anticipatory Action*; FAO: Rome, Italy, 2020.
2. Cullen, D.; Ceace, A.; Latchinisky, A.; Ayali, A.; Berry, K.; Buhl, J.; Keyser, R.; Foquet, B.; Hadrich, J.; Matheson, T.; et al. From molecules to management: Mechanisms and consequences of locust phase polyphenism. *Adv. Insect Physiol.* **2017**, *53*, 167–285. [CrossRef]
3. Sword, G.; Lecoq, M.; Simpson, S. Phase polyphenism and preventative locust management. *J. Insect Physiol.* **2010**, *56*, 949–957. [CrossRef] [PubMed]
4. Symmons, P.M.; Cressman, K. *Desert Locust Guidelines, Biology and Behaviour*; Food and Agriculture Organization of the United Nations: Rome, Italy, 2001.
5. Cressman, K.; Stefanski, R. *Weather and Desert Locusts*; WMO: Geneva, Switzerland, 2016.
6. Githae, E.W.; Kuria, E.K. Biological control of desert locust (*Schistocerca gregaria* Forskål). *CAB Rev.* **2021**, *16*, 1–8. [CrossRef]
7. Shrestha, S.; Thakur, G.; Gautam, J.; Acharya, N.; Pandey, M. Desert locust and its management in Nepal. *J. Agric. Nat. Resour.* **2021**, *4*, 1–28. [CrossRef]
8. Lomer, C.; Bateman, B.; Johnson, D.; Langewald, J.; Thomas, M. Biological Control of Locusts and Grasshoppers. *Annu. Rev. Entomol.* **2001**, *46*, 667. [CrossRef]
9. Magor, I.; Lecoq, M.; Hunter, D. Preventive control and Desert Locust plagues. *Crop Prot. J.* **2008**, *27*, 1527–1533. [CrossRef]
10. Mullie, W.C.; Robert, A.C.; Robert, A.; Young, S.; Ibrahim, A.B.; Murk, A.J. Increased and sex-selective avian predation of desert locusts *Schistocerca gregaria* treated with *Metarhizium acridum*. *PLoS ONE* **2021**, *16*, e0244733. [CrossRef]
11. Kassimatis, E.J.M. Evaluation of *Metarhizium anisopliae* Mycoinsecticide as an Alternative Locust Control Measure in Southern Africa. Ph.D. Thesis, University of Pretoria, Pretoria, South Africa, 2000; pp. 1–80. [CrossRef]
12. Hunter, D.M.; Latchininsky, A.V.; Abashidze, E.; Gapparov, F.A.; Nurzhanov, A.A. The Efficacy of *Metarhizium acridum* against nymphs of the Italian locust, *Calliptamus italicus* (L.) (Orthoptera: Acrididae) in Uzbekistan and Georgia. *J. Orthoptera Res.* **2016**, *25*, 61–65. [CrossRef]
13. FAO. *Field Efficacy Trials with Entomopathogen Metarhiiizum anisopliae Var. Acridum against Desert Locusts*; FAO: Rome, Italy, 2007.
14. Owuor, A.; McRae, H. Desert Locust Control in Somalia between 2019 and 2021. *Outlooks Pest Manag* **2022**, *33*, 132–136. [CrossRef]
15. FAO. dLocusts; Potential of Drones for Locusts Early Warning and Prevention Control. 2018. Available online: https://www.fao.org/3/CA1073EN/ca1073en.pdf (accessed on 16 February 2023).
16. Fischer, N.; Koning, R.; de Ngwenyaman, B.; Slenders, L.; Wools, L. Detecting Desert Locusts: The UAV Way. 2020. Available online: https://www.fao.org/ag/locusts/common/ecg/2245/en/PosterTeamLocustWeb.pdf (accessed on 16 February 2023).
17. Shuvo, S.B.; Tusher, M.A.; Ghosh, M. A technical approach to prevent locust swarm. *Team Tetrahedron* **2020**, 1–4. [CrossRef]
18. Subramanian, K.S.; Pazhanivelan, S.; Srinivasan, G.; Santhi, R.; Sathiah, N. Drones in insect pest management. *Front. Agron.* **2021**, *3*, 1–12. [CrossRef]
19. Mroczkwoski, D.B. Development of a System for Detection, Control and Prevention of Locust Pests Using UAV Platforms. Bachelor's Thesis, Universitat Politechnica De Catalunya, Barcelona, Spain, 2018.
20. FAO. *The Potential Use of Drones in Locust Early Warning and Preventive Control*; FAO: Rome, Italy, 2016.
21. Matthews, G.A. New Technology for Desert Locust Control. *Agronomy* **2011**, *11*, 1052. [CrossRef]

22. Sharma, A. Locust Control Management: Moving from traditional to new technologies–An empirical analysis. *Entomol. Ornithol. Herpetol.* **2014**, *4*, 1–7. [CrossRef]
23. Beloev, I.H. A review on current and emerging application possibilities for unmanned aerial vehicles. *Acta Technol. Agric.* **2016**, *19*, 70–76. [CrossRef]
24. Filho, F.H.I.; Heldens, W.B.; Kong, Z.; De Lange, E.S. Drones: Innovative technology for use in precision pest management. *J. Econ. Entomol.* **2019**, *113*, 1–25. [CrossRef]
25. Mogili, U.M.R.; Deepak, B.B.V.L. Review on application of drone systems in precision agriculture. *Procedia Comput. Sci.* **2018**, *133*, 502–509. [CrossRef]
26. Qin, W.; Qiu, B.; Xue, X.; Chen, C.; Xu, Z.; Zhou, Q. Droplet deposition and control effect of insecticides sprayed with an unmanned aerial vehicle against plant hoppers. *Crop Prot.* **2016**, *85*, 79–88. [CrossRef]
27. Martin, D.E.; Woldt, W.E.; Latheef, M.A. Effect of application height and ground speed on spray pattern and droplet spectra from remotely piloted aerial application systems. *Sensors* **2019**, *3*, 83. [CrossRef]
28. Lou, Z.; Xin, F.; Han, X.; Lan, Y.; Duan, T.; Fu, W. Effect of unmanned aerial vehicle flight height on droplet distribution, drift and control of cotton aphids and spider mites. *Agronomy* **2018**, *8*, 87. [CrossRef]
29. Yan, X.; Zhou, Y.; Liu, X.; Yang, D.; Yuan, H. Minimizing occupational exposure to pesticide and increasing control efficacy of pests by unmanned aerial vehicle application on cowpea. *Appl. Sci.* **2021**, *11*, 9597. [CrossRef]
30. Chen, P.; Lan, Y.; Huang, X.; Qi, H.; Wang, G.; Wang, J.; Wang, L.; Xiao, H. Droplet deposition and control of planthoppers of different nozzles in two-stage rice with a quadrotor unmanned aerial vehicle. *Agronomy* **2020**, *10*, 303. [CrossRef]
31. Song, X.P.; Liang, Y.J.; Qui, Z.X.; Qiang, Q.Z.; Ju, W.J.; Rui, L.Y.; Wu, J.M. Intrusion of fall armyworm (*Spodoptera frugiperda*) in sugarcane and its control by drone in China. *Sugar Tech.* **2020**, *22*, 734–737. [CrossRef]
32. Wang, G.; Lan, Y.; Yuan, H.; Qi, H.; Chen, P.; Ouyang, F.; Han, Y. Comparison of spray deposition, control efficacy on wheat aphids and working efficiency in the wheat field of the unmanned aerial vehicle with boom sprayer and two conventional knapsack sprayers. *Appl. Sci.* **2019**, *9*, 218. [CrossRef]
33. Retkute, R.; Hinton, R.G.K.; Cressman, K.; Gilligan, C.A. Regional differences in control operations during the 2019–2021 desert locust upsurge. *Agronomy* **2021**, *11*, 2529. [CrossRef]
34. Bock, C.H.; Hotchkiss, M.W.; Cottrell, T.E.; Wood, B.W. The Effect of sample height on spray coverage in mature Pecan trees. *Plant Dis.* **2015**, *99*, 916–925. [CrossRef]
35. Dobson, H.M. Control. In *Desert Locust Guidelines*; FAO: Rome, Italy, 2001.
36. Machado, B.B.; Spadon, G.; Arruda, M.S.; Goncalves, W.N.; Carvalho, A.C.P.L.F.; Rodrigues-Jr, J.F. A smartphone application to measure the quality of pest control spraying machines via image analysis. In Proceedings of the 33rd Annual ACM Symposium on Applied Comuting, Pau, France, 9–13 April 2016; ACM: New York, NY, USA, 2018; pp. 956–963.
37. Abbott, W.S. A method of computing the effectiveness of an insecticide. *J. Econ. Entomol.* **1925**, *18*, 265–267. [CrossRef]
38. Wang, J.; Lan, Y.; Zhang, H.; Zhang, Y.; Wen, S.; Yao, W. Drift and deposition of pesticide applied by UAV on pineapple plants under different meteorological conditions. *Int. J. Agric. Biol. Eng.* **2018**, *11*, 5–12. [CrossRef]
39. Wang, C.; Zeng, A.; He, X.; Song, J.; Herbst, A.; Gao, W. Spray drift characteristics test of unmanned aerial vehicle spray unit under wind tunnel conditions. *Int. J. Agric. Biol. Eng.* **2020**, *13*, 13–21. [CrossRef]
40. Lan, Y.; Qian, S.; Chen, S.; Zhao, Y.; Deng, X.; Wang, G.; Zang, Y.; Wang, J.; Qiu, X. Influence of the downwash wind field of plant protection uav on droplet deposition distribution characteristics at different flight heights. *Agronomy* **2021**, *11*, 2399. [CrossRef]
41. OECD. *Report on the State of the Knowledge–Literature Review on Unmanned Aerial Spray Systems in Agriculture*; OECD: Paris, France, 2021; No. 105.
42. Qin, W.; Xue, X.; Zhou, L.; Zhang, S.; Sun, Z.; Kong, W.; Wang, B. Effects of spraying parameters of unmanned aerial vehicle on droplets deposition distribution of maize canopies. *Trans. Chin. Soc. Agric. Eng.* **2014**, *30*, 50–56.
43. Qin, W.; Xue, X.; Zhang, S.; Wei, G.; Baokun, W. Droplet deposition and efficiency of fungicides sprayed with small UAV against wheat powdery mildew. *Int. J. Agric. Biol. Eng.* **2018**, *11*, 27–32. [CrossRef]
44. Bashir, E.M.; El Shafie, H. Laboratory evaluation of the effects of neem (*Azadirachta indica*) oil and *Metarhizium anisopliae* against some immature stages of the desert locust *Schistocerca gregaria* (Forskal) (Orthoptera: Acrididae) Ebtisam. *J. Agric. Vet. Sci.* **2017**, *18*, 116–126.
45. Youssef, N.A. Effect of certain entomopathogenic fungi and nematode on the desert locust *Schistocerca gregaria* (Forskal). *Ann. Agric. Sci.* **2014**, *59*, 125–131. [CrossRef]
46. Wakil, W.; Ghazanfar, M.U.; Usman, M.; Hunter, D.; Shi, W. Fungal-based biopesticide formulation to control nymphs and adults of the desert locusts, *Schistocerca gregaria* Forkal(Orthoptera: Acrididae): A labaratory and field cage study. *Agronomy* **2022**, *12*, 1160. [CrossRef]

drones

MDPI

Article

Design and Experiment of Ecological Plant Protection UAV Based on Ozonated Water Spraying

Hang Xu [1,2,3,†], Lili Yi [1,2,3,†], Chuanyong Li [1,2,3], Yuemei Sun [1,2,3], Liangchen Hou [1,2,3], Jingbo Bai [4], Fanxia Kong [1,2,3], Xin Han [1,2,3,*] and Yubin Lan [1,2,3,5,*]

1 College of Agricultural Engineering and Food Science, Shandong University of Technology, Zibo 255000, China
2 Shandong Provincial Engineering Technology Research Center for Agricultural Aviation Intelligent Equipment, Zibo 255000, China
3 National Sub-Center for International Collaboration Research on Precision Agricultural Aviation Pesticide Spraying Technology, Zibo 255000, China
4 Shandong Siyuan Agricultural Development Co., Ltd., Zibo 255400, China
5 National Center for International Collaboration Research on Precision Agricultural Aviation Pesticides Spraying Technology, College of Engineering, South China Agricultural University, Guangzhou 510642, China
* Correspondence: sdut_hanxin@163.com (X.H.); ylan@sdut.edu.cn (Y.L.)
† These authors contributed equally to this work.

Abstract: With the development of pesticide substitution technology, ozonated water has been gradually applied in agricultural plant protection. This paper describes our development of an ecological plant protection unmanned aerial vehicle (UAV) that can produce and spray ozonated water while flying. Firstly, this paper carries out the design of the ozonated water system, including the selection of the ozone generator and the gas-liquid mixing method. Secondly, the conceptual design method of the ecological plant protection UAV is introduced, including total weight estimation, propulsion system selection, layout and structure design, battery modeling, center of gravity evaluation, and control system. Then, static analysis was computed in ANSYS Workbench on the UAV fuselage. Finally, the field test verified that the hovering time of the UAV could reach the design requirement of 10 min when it was fully loaded. The effective spraying width (with a height of 2 m and a speed of 3 m/s) is 5.25 m. The UAV was used to spray ozonated water with a concentration of 17 ppm continuously once a day; on day 7, the control effect could reach 76.4% and the reduction rate of the larvae population was 59.3%. Therefore, spraying ozonated water with a concentration of 17 ppm every day by using the ecological plant protection UAV can effectively control broccoli diamondback moth larvae and achieve the control effect of traditional pesticides (Chlorantraniliprole SC).

Keywords: plant protection UAV; ozonated water; conceptual design; finite element analysis (FEA); field tests

Citation: Xu, H.; Yi, L.; Li, C.; Sun, Y.; Hou, L.; Bai, J.; Kong, F.; Han, X.; Lan, Y. Design and Experiment of Ecological Plant Protection UAV Based on Ozonated Water Spraying. *Drones* **2023**, *7*, 291. https://doi.org/10.3390/drones7050291

Academic Editors: Andrzej Łukaszewicz, Wojciech Giernacki, Zbigniew Kulesza, Jaroslaw Alexander Pytka and Andriy Holovatyy

Received: 6 March 2023
Revised: 21 April 2023
Accepted: 22 April 2023
Published: 26 April 2023

1. Introduction

In recent years, under the support and guidance of the state, pesticide substitution technologies and green prevention and control technologies have been continuously developed, resulting in a continuous reduction in the use of pesticides in China [1,2]. As one of the most important technologies in green prevention and control, ozone plant protection technology causes no pollution to the environment or pesticide damage.

At present, ozonated water plant protection equipment has been widely studied by researchers in the field of pest control. The ozonated water plant protection is mainly carried out in the form of backpack, fixed, and ground-mounted mobile vehicles. Chai et al. developed a backpack ozonated water sprayer that used a gas-liquid mixing pump as the ozonated water mixing method, and manual spraying was required during operation [3]. Kenji et al. developed a portable ozone spray sterilization system to prevent and control pests in agricultural management. Studies showed that the ozone derivative free radicals

produced in ozone spray could improve the rate of aphid destruction, and all aphids were destroyed within 30 min [4]. Steffen et al. developed the PHYTO3-tech PCRO protection system, which can be mounted on a tractor to spray ozonated water with a concentration of 8 ppm to control yeast, mold, and insect damage, forming a field green plant protection operation equipment [5]. Fan et al. developed a crawler-type ozonated water plant protection unmanned vehicle that used PLC and single-chip microcomputer control technology to integrate the ozonated water preparation and spraying system with the crawler vehicle [6]. When the unmanned vehicle was operating, it could produce ozonated water in real time and spray it out. The plant protection test in the vineyard shows that the control effect is not significantly different from that of traditional pesticides when spraying with 20 ppm ozonated water for 6 days. Hu et al. developed an ozonated water spray system that could be mounted on a high-clearance vehicle [7]. The ozonated water spray system in the vehicle could produce ozonated water in real time and spray it during operation. In the rice control effect test, the combined use of ozone and pesticides can better control the leaf roller pests. The above ozonated water plant protection equipment is mainly aimed at greenhouse and orchard crops and is not suitable for open-field vegetables such as broccoli.

In recent years, the plant protection UAV and agricultural aviation industries have developed rapidly [8–11]. The literature [12] pointed out that using the DJI T20 plant protection UAV to spray ozonated water with a concentration of 1 ppm and a half-life of 8 min can be used for disinfection outdoors, but this concentration of ozonated water has no significant effect on the survival rate of diamondback moth larvae. The disadvantage of using traditional plant protection UAVs to spray ozonated water is that the ozonated water decomposes quickly, and the concentration of the ozonated water produced on the ground will decrease after being transported. Therefore, we put forward the idea of mounting the ozonated water production equipment into the UAV. Due to the high requirements of the UAV on the weight and position of the load, it is necessary to consider the concentration of ozonated water prepared, the load weight, and the center of gravity of the UAV when designing an ecological plant protection UAV.

This paper introduces an ecological plant protection UAV that will continuously produce and spray ozonated water during the flight, which is suitable for plant protection operations in vegetable fields.

Section 2 proposes the design process of the ecological plant protection UAV and determines the design parameters of the UAV.

Section 3 presents the conceptual design method of the ecological plant protection UAV, including selection of ozonated water system components, total weight estimation, propulsion system selection, layout and structure design, battery modeling, control system, center of gravity evaluation, and static structural analysis of the UAV.

Section 4 introduces the field tests of the UAV, including the hovering time test, the effective spraying width test, and the control efficacy test on diamondback moth larvae.

2. Design Process and Requirements

2.1. Design Process

When designing the ecological plant protection UAV, first of all, it is necessary to determine the design goals and parameters of the ecological plant protection UAV. Secondly, the ozone generator and the gas-liquid mixing device were selected. Thirdly, the weight of the plant protection UAV was estimated according to the weight of the workload (the ozonated water system), and the suitable propulsion system was selected. Then, the structure of the UAV fuselage was designed, the model of the UAV was built using Solidworks, lithium-polymer (Li-Po) battery capacity was calculated according to the power consumption of the UAV, and the center of gravity was viewed through Solidworks. Finally, the static structural analysis of the UAV fuselage was performed in ANSYS Workbench to verify the structural reliability of the UAV. The design process for ecological plant protection UAVs is shown in

Figure 1. The major parameters of the ecological plant protection UAV after the test are shown in Table 1.

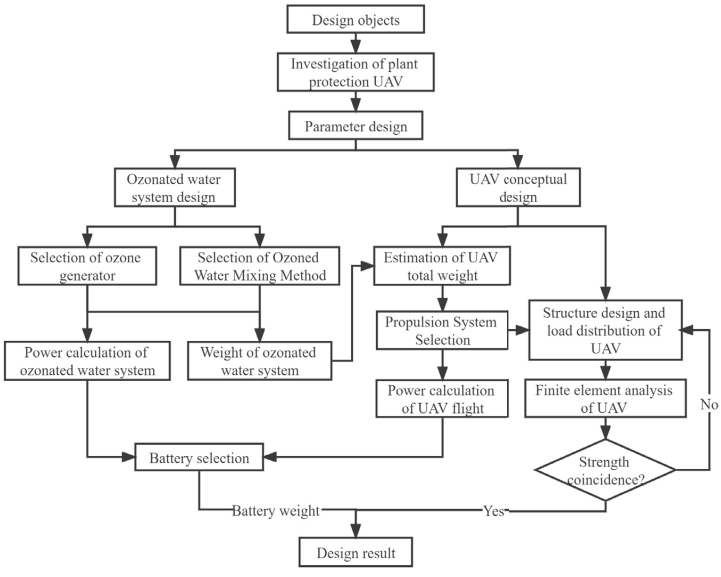

Figure 1. The design process for ecological plant protection UAV.

Table 1. Major parameters of ecological plant protection UAV after the test.

Parameter	Value
Flight speed (m/s)	1–7
Maximum take-off weight (kg)	58.3
Battery capacity (mAh)	44,000
Hover time at full load (min)	10.2
Total capacity of the water tank (L)	16
Ozone production (g/h)	0–24
Ozonated water concentration (ppm)	0–17
Dimensions (mm)	2100 × 2100 × 600
Total flow (L/min)	0–4.5
Number of nozzles	4
Effective spraying width (m) (with a height of 2.0 m and a speed of 3.0 m/s)	5.25

The ecological plant protection UAV is composed of the flight control system, ground control system, propulsion system, power system, and ozonated water system. The flight control system is the brain of the UAV, which is mainly responsible for the autonomous flight of the UAV. The ground control system cooperates with the flight control system to control the flight of the UAV and one can choose automatic flight settings or manual operation. The propulsion system is responsible for powering the UAV to climb, hover, fly, and land. The power system consists of the battery and a power distribution unit (PDU), and the battery supplies power to the propulsion system, ozonated water system, and flight control system. The ozonated water system consists of production and spraying equipment, and ozonated water can be produced and sprayed in real time. Figure 2 shows the UAV composition and each system's workflow.

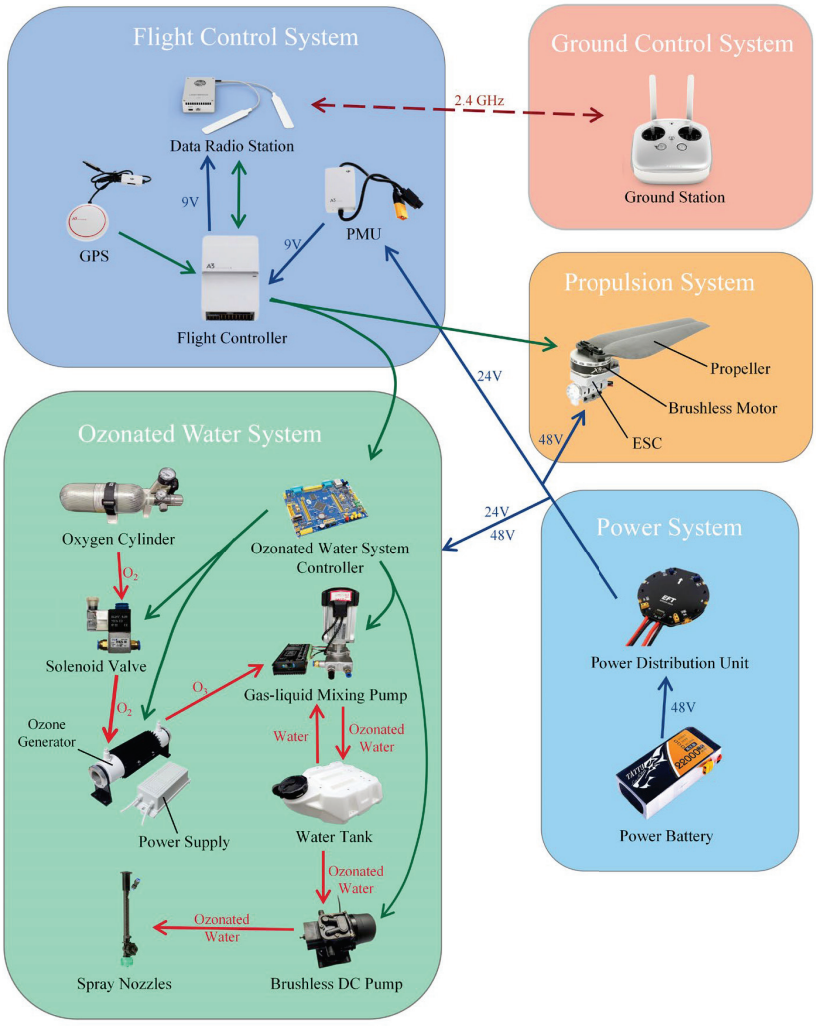

Figure 2. The UAV composition and each system's workflow.

2.2. Design Requirements and Objectives

Before starting to design the UAV, it is necessary to determine the design requirements and objectives. We put forward the design requirements and objectives, as shown in Table 2. Taking the technical parameters of conventional plant protection UAVs as a reference, the design objectives of the ecological plant protection UAV were determined. We selected a number of plant protection UAVs from SZ DJI Technology Co., Ltd. (Shenzhen, China) and Guangzhou XAG Technology Co., Ltd (Guangzhou, China). The parameters of these UAVs were counted [13,14]. The hovering time of plant protection UAVs is shown in Figure 3.

Table 2. Design requirements and objectives for the UAV.

S/N	Requirement	Value
1	Hover time at full load (min)	10
2	Endurance flight time (min)	7
3	Maximum take-off weight (kg)	60
4	Flight altitude (m)	0–6
5	Flight speed (m/s)	0–7
6	Capacity of the water tank (L)	15
7	Spraying efficiency (hm^2/h)	4
8	Ozonated water concentration (ppm)	15
9	Effective spraying width (m)	4

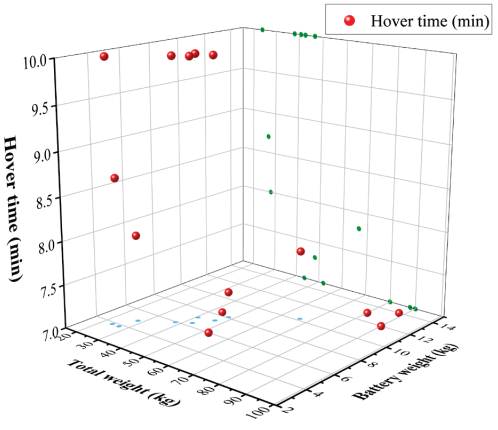

Figure 3. Statistics of the hovering time of plant protection UAV. Green balls represent the projection on the plane composed of the "Hover time" axis and the "Total weight" axis, and blue balls represent the projection on the plane composed of the "Total weight" axis and the "Battery weight" axis.

Figure 3 shows that the hovering time of plant protection UAVs with full loads is 7–10 min. Therefore, the ecological plant protection UAV is required to hover for at least 10 min under full load. Considering that the ecological plant protection UAV needs to carry the ozonated water workload, the capacity of the water tank should not be too high, and the minimum capacity is 15 L. The UAV's spraying area per sortie formula is as follows:

$$E_{spray} = t_f \times D_{width} \times v_f \quad (1)$$

where E_{spray} is the UAV's spraying area per sortie, t_f is endurance flight time, D_{width} is effective spraying width, and v_f is flight speed of the UAV.

According to Formula (1), when the endurance flight time is 7 min, the flight speed is 4 m/s, the effective spraying width is 4 m, and the UAV's spraying efficiency per sortie is 6720 m^2. If the spraying efficiency is to reach 4 hm^2/h, the UAV needs to fly 6 sorties per hour. Therefore, the preset operating parameters of the UAV are reasonable.

The literature [6] indicates that the concentration cannot be too low when working with the ozonated water system. The literature [15] indicates that ozonated water with a concentration of 15 ppm has a better control effect on aphids and cabbage caterpillar. Guo et al. explored the control of pests of green vegetables by ozonated water and found that ozonated water with a concentration of 6.0 ppm had a significant effect on preventing the occurrence of vegetable pests [16]. In order to ensure the control effect of ozonated water on insect pests, the concentration of ozonated water should reach 15 ppm. Because the concentration of ozonated water decays quickly, the ozonated water system needs to work continuously during the flight to maintain the concentration within a certain range.

3. Conceptual Design Method of UAV for Ecological Plant Protection

3.1. Selection of Ozonated Water System Components

The ozonated water system consists of the controller, the ozonated water production device, and the spraying device. The ozonated water production device is composed of an oxygen cylinder, an oxygen solenoid valve, a water outlet solenoid valve, two sets of ozone generators, and a gas-liquid mixing pump. The spraying device consists of a brushless DC pump and four nozzles. The ozone generator's output and the gas-liquid mixing efficiency are necessary conditions for producing high-concentration ozonated water. The weight and cost of each component in the ozonated water system are shown in Table 3.

Table 3. The weight and cost of each component in the ozonated water system.

S/N	Component	Weight (kg)	Cost (CNY)
1	Ozonated water system controller	0.22	500
2	Oxygen cylinder (with pressure reducing valve)	1.53	1300
3	Gas flowmeter	0.11	950
4	Cylinder solenoid valve	0.16	49
5	Water outlet solenoid valve	0.55	38
6	Relay module	0.20	42
7	Two sets of ozone generators	1.23	700
8	Ozone high voltage power supply	0.90	300
9	Gas-liquid mixed pump and its controller	3.24	2100
10	Water tank (full load)	17.27	259
11	Brushless DC pump	0.36	280
12	Four nozzles	0.40	180
	Total	26.17	6698 (CNY)/975 (USD)

The SQ-12 ozone generator (Suiquan Electromechanical Co., Ltd., Guangzhou, China) was selected as the device for producing ozone. The device uses a dielectric barrier discharge method, as shown in Figure 4. After oxygen molecules are introduced into a high-frequency and high-voltage electric field, high-energy electrons decompose oxygen into oxygen atoms, and eventually the oxygen atoms collide to form ozone. Two sets of SQ-12 ozone generators were connected in series to increase the production efficiency of ozone gas. The total output of the two sets of ozone generators is 24 g/h, and the combined power of the two sets of ozone generators is 240 W.

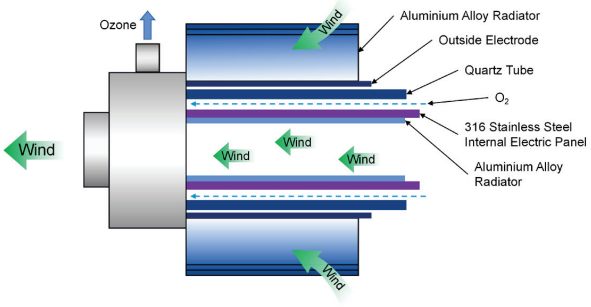

Figure 4. The ozone generator's working concept.

There are generally three ways to mix ozone and water: the direct aeration method, the Venturi jet method, and the gas-liquid mixing pump method [6]. The gas-liquid mixing pump method uses a gas-liquid mixing pump to mix ozone gas with water. The high-speed rotating turbine generates negative pressure through the gas-liquid mixing pump, sucking ozone gas into the pump chamber where it can be fully mixed with water under pressure. The dissolving effectiveness ranges from 70–90%. The gas-liquid mixing pump

(type 8ZTDB-40, Lingbo Electromechanical Pump Industry Co., Ltd., Yangjiang, China) was used in the design of the ozonated water system. Its rated flow and rated power are 0.77 m^3/h and 200 W, respectively.

In order to compare the production efficiency and attenuation of ozonated water under different gas-liquid mixing methods, the above three mixing methods were used to conduct tests. The three groups of tests used ozone generators with a total output of 24 g/h and supplied oxygen with the 0.8 L carbon fiber oxygen cylinder (Tianhai Industrial Co., Ltd., Beijing, China). After the gas cylinder was filled with oxygen, the pressure was 13 Mpa, and the oxygen concentration was 99.5%. In the ozonated water production and attenuation test, the ozone analyzer (type PM8200CL, GreenPrima Instruments Ltd., London, UK) was used to detect the ozone concentration in real-time, with the measurement range of 0–20 ppm, and the resolution of 0.01 ppm. The ozone concentration was recorded every 30 s and were repeated 3 times for each group of experiments, as shown in Figure 5.

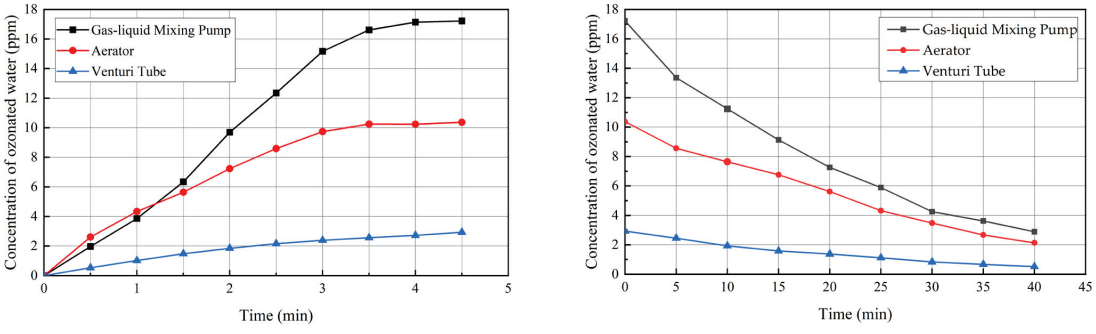

Figure 5. Variation of ozonated water concentration in different production modes: (**a**) generation of ozonated water concentration; (**b**) attenuation of ozonated water concentration.

Figure 5a shows that the gas-liquid mixing pump method can prepare ozonated water with a concentration of up to 17 ppm at 4.5 min, which is greater than the aeration method and the Venturi jet method. Figure 5b shows that the half-life of the ozonated water concentration is around 15 min.

3.2. Estimation of Total Weight

The total weight of the ecological plant protection UAV is expressed as W_{total}, which is composed of the frame structure weight W_S, propulsion system weight W_P, power system weight W_B, flight control system and other electronic equipment weight W_{EL}, and the workload weight W_L. The formula for the total weight of the UAV can be obtained:

$$W_{total} = W_S + N_{motor} W_P + W_B + W_{EL} + W_L \quad (2)$$

At present, we only know the weight of the ozonated water system, and other parts of the UAV have not been finalized, so it is necessary to estimate the total weight of the UAV. We counted the total weight and workload weight of plant protection UAVs from DJI and XAG. Figure 6 shows the fitting results of the total weight and the workload weight.

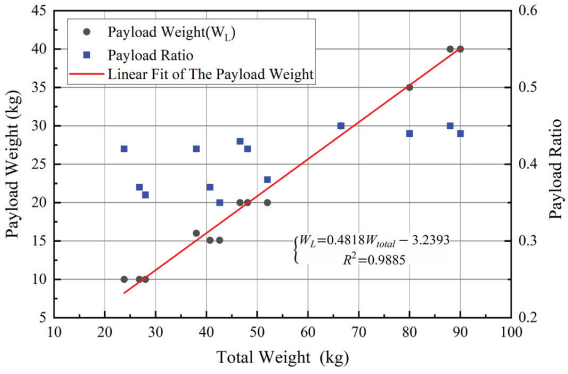

Figure 6. Statistics of workload weight and the total weight of plant protection UAV.

The fitting formula of the total weight and the workload weight is:

$$W_L = 0.4818W_{total} - 3.2393 \quad (3)$$

where W_{total} is the total weight of the ecological plant protection UAV, and W_L is the workload weight.

The workload of the ecological plant protection UAV includes the ozonated water system and the water contained in the water tank. The sum of the weight of each component is 26.17 kg, as shown in Table 3. The workload also includes other accessories, such as water pipes, so the total weight is 27 kg. According to Formula (3), the total weight of the ecological plant protection UAV is 62.92 kg.

3.3. Selection of Propulsion System

The propulsion system of the UAV consists of brushless motors, brushless electric controllers (ESC), and propellers. With a greater total weight of the plant protection UAV, the larger-sized propeller and the motor with a lower KV value need to be selected. KV represents the ratio of the motor's speed per minute to voltage. With a larger diameter of the paddle, the lower KV motor is more efficient than the higher KV motor [17]. The XRotor-X9 propulsion system (Hobbywing Technology Co., Ltd., Shenzhen, China) was selected, and its specifications are shown in Table 4. This system is equipped with 34.7 inch high-efficiency folding propellers, using FOC electric adjustment, and the maximum pulling force of a single axis can reach 22 kg.

Table 4. XRotor-X9 propulsion system specifications.

Specification	Value
Total weight of propulsion system (kg)	1.4
KV (rpm/V)	100
Size of the stator (mm)	96 × 16
Supported Battery Type	Li-Po (6–12 cells)
Electrical signal frequency modulation (Hz)	50–500
Working pulse width of electrical modulation (us)	1100–1940
Maximum allowable voltage (V)	52.2
Maximum allowable current (A)	120

According to the data of the XRotor-X9 propulsion system given on the official website [18], we plotted the load performance diagram of the propulsion system as shown in

Figure 7. The fitting formulas of pulling force and motor rotational speed, and current and motor rotational speed, are as follows:

$$T_p = 4.89e^{n_m/2121.74} - 6.46 \tag{4}$$

$$I_p = 2.92e^{n_m/1057.85} - 6.1 \tag{5}$$

where T_p represents the weight of propulsion by each propulsion system, n_m represents the rotational speed of the motor, and I_p represents current for the propulsion system.

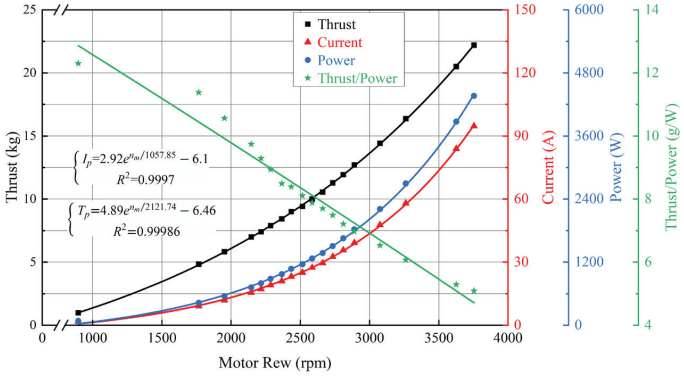

Figure 7. The load performance diagram of the propulsion system.

3.4. Layout Design

The layout of the fuselage and propulsion system must be considered in the design of the plant protection UAV. Common fuselage layouts for plant protection UAVs include four-rotor, six-rotor, and eight-rotor aircraft. The plant protection UAV's tolerance for the propulsion system failure increases with the number of rotors. By redistributing the control output signals in the event of a single power motor failure, the flight control system can maintain the stability of the plant protection UAV, increase its safety, and prevent damage to people or property. More rotors, however, are not necessarily better. The distance between the geometric center of gravity of the plant protection UAV and the center of gravity of the rotors will increase as the number of rotors does as well. In light of these factors, the plant protection UAV's fuselage uses a six-rotor layout.

From the literature [19], the number of arms and the size of the blades are closely attached to the dimensions of the plant protection UAV in the standard multi-rotor layout. The following relationship exists between the angle of the arms θ, the number of arms N_{motor}, the radius of the UAV fuselage R, the radius of the propeller R_p, and the maximum radius of the propeller R_{max}:

$$\begin{cases} R = \frac{R_{max}}{\sin\frac{\theta}{2}} \\ \theta = \frac{360^\circ}{N_{motor}} \\ 1.05R_p \le R_{max} \le 1.2R_p \end{cases} \tag{6}$$

The output tension of the propulsion systems keeps a dynamic balance relationship with the take-off weight while the UAV is hovering. In order to make the model simpler, each propulsion system's pulling weight is stated as 1/6 of the six-rotor UAV's take-off weight [20–22]. Since the weight of the UAV estimated above is 62.92 kg, the 6 sets of XRotor-X9 propulsion systems meet the flight requirements of the UAV for plant protection.

The number of arms is 6, the radius of the propeller is 44 cm, and the maximum radius of the propeller is 1.15 times the radius of the propeller. The UAV fuselage radius may be calculated using Formula (6) to be 101.2 cm.

In terms of material selection, carbon fiber reinforced polymer (CFRP) is frequently used in the plant protection UAV's fuselage structure. Both the specific strength and the specific modulus of this material are high. Under conditions of equal quality, the material has a large bearing capacity and minimal deformation as compared to other metal materials. The UAV's fuselage structure used CFRP T300, and the connecting parts used aluminum alloy 6061-T6.

The 3D model of the ecological plant protection UAV was designed using Solidworks, as shown in Figure 8. The material properties were assigned to each component, and the software will calculate the weight of each part. The material properties used are shown in Table 5.

Figure 8. The 3D model and the layout design of the ecological plant protection UAV.

Table 5. Material properties of aluminum alloy and carbon fiber.

Materials	Poisson Ratio	Density (kg/m^3)	Young Modulus (GPa)	Yield Strength (MPa)
Aluminum Alloy 6061-T6	0.33	2.7	69	275
CFPR T300	0.3	1.76	230	3530

The center frame is the core of the UAV fuselage, and its interior is mainly equipped with a flight control system and power distribution unit. The center frame's upper and lower carbon fiber panels are supported by several aluminum columns and six arm bases. The propulsion system is connected to the center frame by the UAV arm. The folding components are positioned in the middle of the arm and attached to the carbon fiber tubes on either side to make it easier to fold the UAV arm.

A 16 L water tank is chosen for the ozonated water system, and several threaded holes are set aside on the exterior of the water tank. Components such as the ozone generator, oxygen cylinder, brushless DC pump, relay, and controller are firmly connected to the water tank through bolts. Under the center frame, the water tank is attached to the UAV's landing gear via 4 aluminum alloy connectors that are 20° inclined. Install the gas-liquid mixing pump vertically behind the UAV's center frame using fasteners such as aluminum columns and bolts, and attach the controller of the mixing pump to the water tank. The bottom of each propulsion system can be equipped with a nozzle. The nozzles in the center and back of the plant protection UAV will spray ozonated water when it is flying ahead, but they will not spray it on other equipment. The battery is preset on top of the center frame to keep the plant protection UAV's center of gravity as close to the module's center as possible.

3.5. Battery Selection and Endurance of Flight

The ecological plant protection UAV's battery capacity, total weight, and flying power consumption all have a major impact on the UAV's endurance. Currently, 90% of UAVs use Li-Po batteries, which have a high energy density and discharge rate [23]. The rated voltage of a LiPo battery's Cell is 3.7 V, and the fully charged voltage of the battery is 4.2 V/Cell. The battery state of charge (SOC) is zero, which indicates that the battery is entirely discharged, when the Li-Po battery voltage is less than 3.5 V/cell [24]. Only 80% of the battery's capacity can be utilized when using Li-Po batteries to ensure battery longevity [25]. Therefore, the minimum remaining capacity set by the battery discharge protection is 20% of the battery capacity.

The actual battery discharge process must be simplified while carrying out battery modeling. Assuming that the voltage stays constant throughout the discharge process and that the battery's remaining capacity shifts linearly [20,23], the battery model formula can be obtained as follows:

$$\begin{cases} t_b = \frac{C_b - C_{min}}{I_b} \frac{60}{1000} \\ C_{min} = 0.2 C_b \\ I_b = N_{motor} I_p + I_{EL} + I_L \end{cases} \tag{7}$$

where t_b is the hovering time of the plant protection UAV, I_b is the total current of the plant protection UAV in the hovering state, I_p is the current for a single propulsion system, I_{EL} is the current of the flight control system, I_L is the current of the ozonated water system, C_b is the battery capacity, and C_{min} is the minimum remaining capacity set by the battery discharge protection.

In order to calculate the required capacity of the batteries, the current of the propulsion system needs to be known. The current of the plant protection UAV changes during flight. Choose the total current of the plant protection UAV's hovering condition for quick calculations. The power parameters of the flight control system and ozonated water system are shown in Table 6.

Table 6. The power parameters of the flight control system and ozonated water system.

System	Device	Power (W)	Voltage (V)	Current (A)
Flight control system	Main control module	8	24	0.33
	Data link communication module	7.8	12	0.65
Ozonated water system	Cylinder solenoid valve	6	24	0.25
	Water outlet solenoid valve	20	24	0.83
	Brushless DC pump	60	48	1.25
	Two sets of ozone generators	240	24	10
	Gas-liquid mixing pump	200	24	8.33

The relationship between the weight propelled by each propulsion system and the total weight in the hovering state is as follows:

$$W_{hover} = \frac{W_{total}}{N_{motor}} \tag{8}$$

where W_{hover} is the weight of propulsion by each propulsion system in the hover state.

We have estimated the total weight of the UAV at 62.92 kg and assumed the hovering time of the UAV is 10 min. The current of the flight control system is 0.98 A, and the current of the ozonated water system is 20.66 A. From Formulas (4), (5), (7), and (8), the weight of propulsion by each propulsion system in the hover state is 10.49 kg, the rotational speed of the propeller is 2640 rpm, the current for the propulsion system is 29.32 A, the total current of the plant protection UAV in the hovering state is 197.56 A, and the battery capacity is 41,158 mAh.

To meet the requirement that the plant protection UAV must hover for at least 10 min, the battery capacity is at least 41,158 mAh. Therefore, by connecting the batteries in series and parallel, we can make a Li-Po battery pack (44,000 mAh, 12 cells, 44.4 V) using 4 Li-Po batteries (22,000 mAh, 6 cells, 22.2 V). The weight of a Li-Po battery (22,000 mAh, 6 cells, 22.2 V) produced by Shenzhen Grepow Battery Co., Ltd. (Shenzhen, China) is 2.55 kg.

In order to ensure the safety of battery discharge, the maximum working current of the UAV must be less than the maximum discharge current of the battery. The formula for the maximum discharge current and the maximum discharge rate is as follows:

$$K_b = 1000 \frac{I_{bMax}}{C_b} \tag{9}$$

where K_b is the maximum discharge rate, and I_{bMax} is the battery's maximum allowable discharge current.

The battery should be able to operate safely under the full-throttle mode of the propulsion system [26]. The maximum discharge current should meet the following:

$$I_{bMax} \geq I_{b1} = N_{motor} I_{pMax} + I_{EL} + I_L \tag{10}$$

where I_{b1} is the maximum working current of the UAV, and I_{pMax} is the maximum current for the propulsion system.

From Table 4, the propulsion system's maximum current is 120 A. The maximum discharge rate is 25 C. It can be obtained that the maximum discharge current of the battery is 1100 A, and the maximum working current of the UAV is 741.64 A. As a result, the Li-Po battery's maximum discharge current satisfies the requirement of Formula (10), and the UAV can work safely under full-throttle mode.

3.6. Center of Gravity Evaluation

We could view weight properties in Solidworks. The center of gravity (CG), weight, and moment of inertia of the UAV are shown in Figure 9. The CG is located below the center frame. Among them, the x-axis and y-axis are 6.90 mm and 0.19 mm away from the central axis (z-axis) of the UAV, respectively; in the direction of the z-axis, the center of gravity is located at 75.69 mm on the center frame. The accurate weight of the UAV is 56.57 kg. The moments of inertia (MOIs) around CG are given as I_{xx} = 6.59 kgm^2, I_{yy} = 6.75 kgm^2, and I_{zz} = 10.21 kgm^2. The deviation of the CG position from the pitch axis and the roll axis is not large, which is within the controllable range of the flight control system.

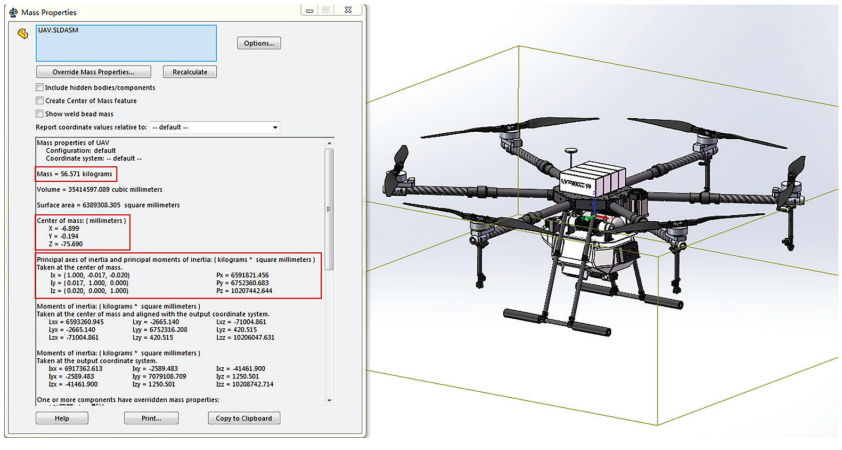

Figure 9. The 3D model and the layout design of the ecological plant protection UAV.

3.7. Control System

3.7.1. Flight Control System

The flight control system is in charge of the plant protection UAV's autonomous flying, which includes taking off and landing, route flight, and steady hovering. The DJI A3 flight control system is used, including the main control module (built-in IMU), GPS module, PMU, LED module, and data link communication module, as shown in Figure 10a. The rotation of the motors (1, 3, and 5) is counterclockwise, and the rotation of the motors (2, 4, and 6) is clockwise, as shown in Figure 10b.

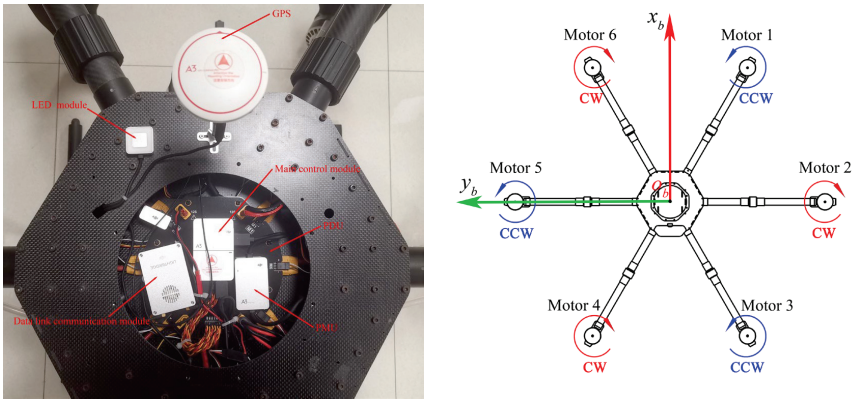

(**a**) (**b**)

Figure 10. (**a**) The direction of motor rotation; (**b**) The layout of the flight control system.

3.7.2. Control of Ozonated Water Production and Spraying

The ozonated water system uses the STM32F407 microprocessor (STMicroelectronics) as the main controller, integrating electronic switches, relay modules, and voltage conversion. The system realizes the control of the working status of the solenoid valve, ozone generator power supply, and gas-liquid mixing pump, thereby remotely controlling the production of ozonated water.

The input and output channels of the PWM signal in the flight control are the F5 to F8 channels, and the F5 and F6 channels of the flight control are connected, respectively, to the signal terminals of the electronic switch and the brushless DC pump. Control of the lever of the remote controller is on the ground, the PWM signal is input from the flight controller to the electronic switch, and the electronic switch is controlled to be turned on. The 24 V direct current provided by the power distribution unit passes through the voltage conversion module and supplies 5 V to the single-chip microcomputer. At this time, the single-chip microcomputer is started. The I/O port of the single-chip microcomputer outputs a high-level 3.3 V to power the gas-liquid mixing pump, the solenoid valve, the ozone generator, and the multi-channel relay module after it has received the instructions. At this point, the system started to produce ozone and ozonated water. Once the concentration of ozonated water has been reached, the UAV can begin spraying. The spraying flow can be adjusted by turning the knob on the remote control. When the spraying process is finished, the ozonated water system is turned off by operating the remote control's lever and knob. The control block diagram of the ozonated water system is shown in Figure 11.

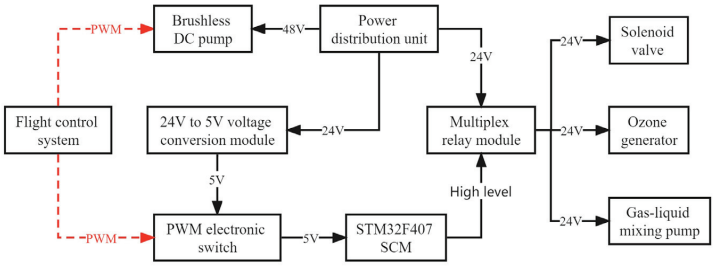

Figure 11. Control block diagram of the ozonated water system.

3.8. Static Structural Analysis

After the structural design is complete, we need to conduct the structural static analysis on the plant protection UAV's fuselage to verify the dependability of the UAV's overall structure. Simplify the plant protection UAV's 3D model in Solidworks before importing it into ANSYS Workbench. Add the properties from Table 5 to the engineering data in ANSYS Workbench, assign materials to the parts, and set the contact type based on how the parts are connected.

Combining the global automatic meshing setting with the local mesh refinement pattern was used to mesh the UAV fuselage, as shown in Figure 12a. After meshing, the element size of the arm bases, the aluminum alloy connectors for the landing gear, and the connectors for the water tank, is 2 mm. The element size of the others is 4 mm. There are 648,268 elements, and the average value of mesh quality is 0.8, which is greater than 0.7. As a result, the mesh quality satisfies the requirements for meshing. When setting the boundary conditions, a fixed support was applied to the center frame's lower carbon fiber panels, an upward force was applied to the ends of each arm, and downward pressure was applied to the connectors for the water tank, as shown in Figure 12b.

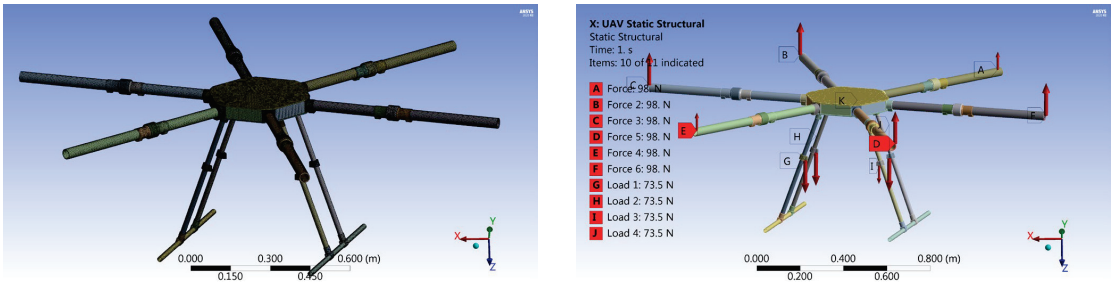

(**a**) (**b**)

Figure 12. (**a**) Mesh model of the UAV; (**b**) the boundary conditions.

The largest deformation of the plant protection UAV is at the end of the arm, with a maximum displacement of 1.0587 mm, which has little effect on the flight posture and control of the UAV, as shown in Figure 13a. The maximum equivalent stress of the UAV is 26.213 MPa, which is located on the arm base, as shown in Figure 13b. The allowable stress condition for parts is as follows:

$$\sigma_{max} \leq \frac{[\sigma]}{n_s} \tag{11}$$

where σ_{max} is the maximum equivalent stress, $[\sigma]$ is the yield strength, and n_s is the safety factor.

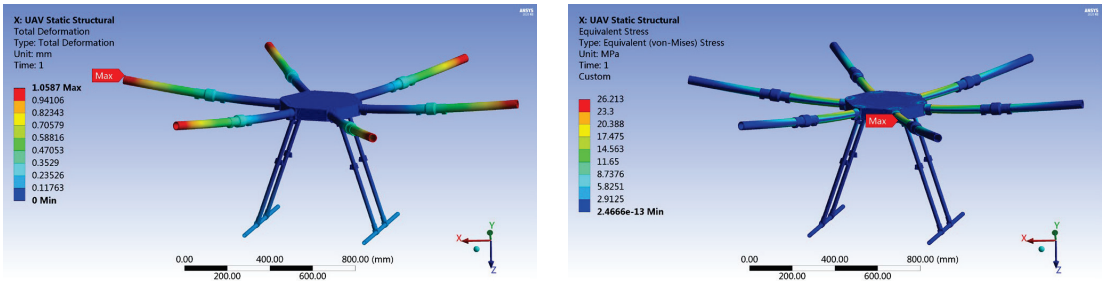

(**a**) (**b**)

Figure 13. The results of UAV statics analysis: (**a**) total deformation of the UAV; (**b**) equivalent stress of the UAV.

The yield strength of aluminum alloy 6061-T6 is 240 MPa, and the safety factor is taken as 1.5. From Formula (11), the maximum stress on the fuselage is less than the yield strength. As such, fatigue failure will not occur in the structure of the UAV fuselage.

4. Field Tests and Discussion

4.1. Hovering Time Test

The hovering time test of the plant protection UAV was carried out on the South Lawn, Shandong University of Technology. The temperature was around 20 °C during the test, and the ground wind speed was 0–1 m/s, which met the test conditions. According to the characteristics of lithium batteries, the battery voltage cannot be lower than 3.6 V/cell [27]. Therefore, the lowest voltage for the UAV was set to 43.2 V.

Before the test, we used an electronic scale to get the weight of the ecological plant protection UAV (no load) to be 42.3 kg and charged the Li-Po battery pack to the full voltage of 50.4 V. Then, we installed two power meters to measure the discharge energy and controlled the UAV to keep hovering after take-off, as shown in Figure 14. The UAV landed automatically when the lowest voltage was reached. Finally, the power meters were viewed and the discharge energy was recorded. Each time the UAV's weight was increased by 4 kg, the weight values for the five groups were 42.3 kg, 46.3 kg, 50.3 kg, 54.3 kg, and 58.3 kg, respectively.

(**a**) (**b**)

Figure 14. The hovering time test of the ecological plant protection UAV: (**a**) install the power meter; (**b**) the UAV stays in hover.

Figure 15 shows that the actual hovering time under different weights is lower than the theoretical hovering time. The battery pack's rated discharge energy (44,000 mAh,

12 cells, 44.4 V) is 2006.4 Wh. The test results show that the ecological plant protection UAV can hover for longer than 10 min when fully loaded, which meets the design requirements.

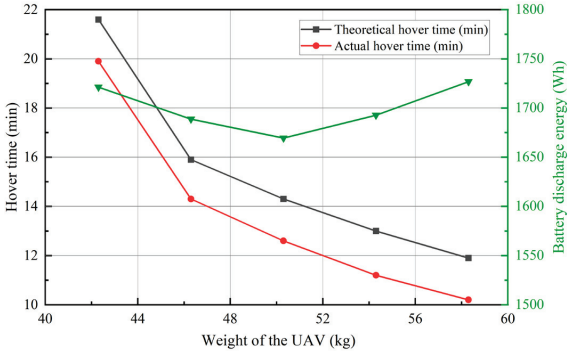

Figure 15. Comparison of hover times at different weights.

4.2. Effective Spraying Width Test

The accurate assessment of the effective spraying width of the plant protection UAV is the premise of precision agricultural aviation operations and plays an essential role in ensuring and improving the operation's efficiency and quality [28].

The effective spraying width test was carried out on the South Lawn, Shandong University of Technology. During the test, the ground wind speed was between 0–1 m/s, which met the test conditions. Referring to Technical Specifications of Quality Evaluation for Crop Protection UAV (NY/T 3213–2018) issued by the Ministry of Agriculture of the PRC, we placed 2 rows of sampling points in the middle of the lawn, 5 m apart, with 36 sampling points in each row. The interval between 2 sampling points was 0.2 m, and a droplet test card was fixed at each sampling point. The layout plan is shown in Figure 16a.

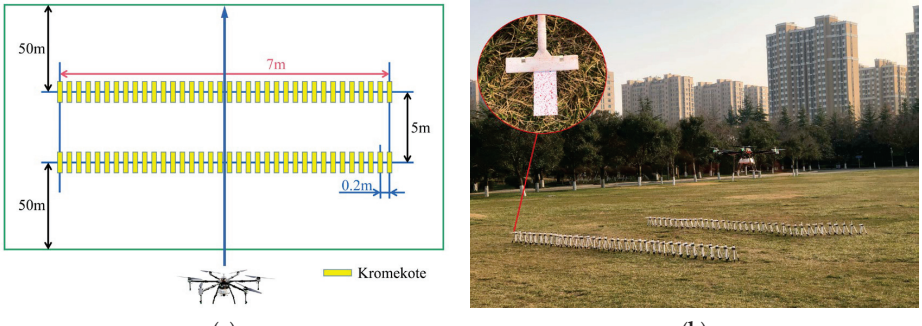

Figure 16. The effective spraying width test: (**a**) the layout plan; (**b**) the test site.

The Kromekote card was used as the droplet test card [29]. After adding Allura Red as a tracer to the liquid, the droplets sprayed by the UAV could be displayed on Kromekote cards [30,31]. The UAV flight speed was 3.0 m/s and the height was 2.0 m, and the spraying flow rate was 3.5 L/min, as shown in Figure 16b. The UAV started spraying 50 m before the sampling point and stopped spraying 50 m behind. The test was repeated twice, and the collected Kromekote cards were brought back to the laboratory. We used the scanner (type Epson DS-1610, Epson Co., Ltd., Beijing, China) to scan the droplets on the Kromekote card at a grayscale resolution of 600 dpi, and then used the image processing software DepositScan (USDA, Wooster, OH, USA) to measure the droplet deposition density [32,33]. The droplet deposition density diagram obtained in two flights is shown in Figure 17.

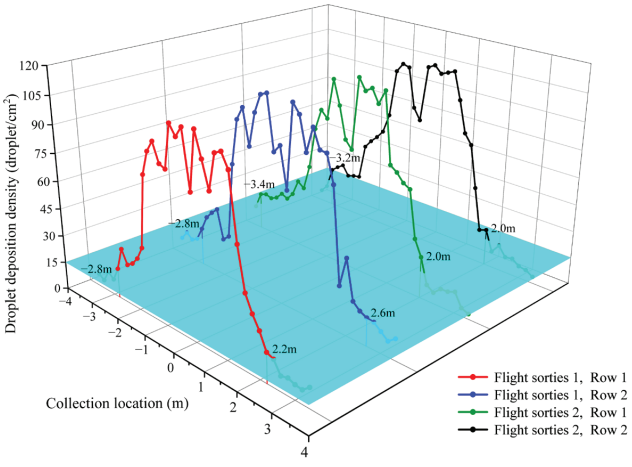

Figure 17. The effective spraying width of the UAV in two flights (a total of four rows).

According to the droplet density determination method, when the aircraft performs ultra-low-capacity agricultural spraying, the effective spraying width is defined as the droplet density of the operation object reaching 15 droplets/cm^2 or more [28]. Figure 17 shows that the effective spraying widths of 2 flight sorties (4 rows total) are 5.0 m, 5.4 m, 5.4 m, and 5.2 m. With the average value, the effective spraying width of the plant protection UAV is 5.25 m (with a height of 2.0 m and a speed of 3.0 m/s).

4.3. Control Efficacy Test on Diamondback Moth Larvae

4.3.1. Test Methods

The test was conducted on diamondback moth larvae in broccoli fields to test the effect of ecological plant protection UAV on pest insects. The test was carried out at the Siyuan Agricultural Experimental Base in Shandong, China, for 8 days (from 23 to 30 September 2022). During the test period, the weather was clear, the temperature varied between 23 and 30 °C, the wind direction was southwest, and the wind speed was 1–2 m/s.

The test plots were divided into four treatments: (a) the ecological plant protection UAV spraying ozonated water with a concentration of 17 ppm and spraying continuously for 6 days; (b) the ecological plant protection UAV spraying ozonated water with a concentration of 17 ppm, spraying at intervals of 1 day, and spraying 3 times in total; (c) X8 large-load plant protection UAV spraying 20% Chlorantraniliprole SC, with a dosage of 150 mL/hm^2, diluting with water and spraying once in total; and (d) X8 large-load plant protection UAV spraying water (control). Treatments (a), (b), and (c) were set up in 3 test plots, respectively; treatment (d) was set up in 1 test plot, for a total of 10 test plots, each with an area of 840 m^2. When dividing the test plots, the control treatment was placed upwind to prevent the impact of environmental wind on the drift of fog droplets. The ecological plant protection UAV and X8 large-load plant protection UAV were used to spray ozonated water and pesticides, respectively, as shown in the Figure 18. The X8 large-load plant protection UAV was developed by the Precision Agricultural Aviation Team of Shandong University of Technology [34]. Its full-load take-off weight is 54 kg, the capacity of the medicine box is 25 L, and the effective spray width is 4.5 m (height 2.0 m, speed 3.0 m/s).

(**a**) (**b**)

Figure 18. (**a**) The ecological plant protection UAV; (**b**) X8 large-load plant protection UAV.

In each test plot, 10 plants were randomly selected for fixed-point investigation, and the investigated plants were marked. Before the first spraying, the number of diamondback moth larvae was investigated. During the test, two plant protection UAVs were operated at a flying height of 2.0 m, a flying speed of 3.0 m/s, and a spraying flow rate of 3.5 L/min, as shown in Figure 19. After the first spraying, the number of larvae was investigated on days 1, 3, and 7. The calculation formulas for the reduction rate of larvae population and control effect are as follows [35]:

$$R = \frac{C_1 - C_2}{C_1} \times 100\% \tag{12}$$

$$E = \frac{R_1 - R_2}{1 - R_2} \times 100\% \tag{13}$$

where C_1 is the number of larvae before spraying, C_2 is the number of larvae after spraying, R is mortality, R_1 is observed mortality, R_2 is control mortality, and E is control effect.

Figure 19. Ecological plant protection UAV spraying operation.

4.3.2. Results and Discussion

The mean number (±SE) of diamondback moth larvae collected from four treatments is shown in Figure 20. According to Figure 20, we know that the mean number of diamondback moth larvae in treatments (a) and (b) continued to decrease, and the mean number of larvae in treatment (d) gradually increased. It shows that spraying 17 ppm ozonated water every day or every other day has the effect of killing larvae. In treatment (c), the mean number of larvae showed a downward trend on days 1 and 3 after spraying Chlorantraniliprole SC, but the mean number of larvae on day 7 was slightly higher than that on day 3. This shows that on day 7 after spraying Chlorantraniliprole SC, the larvae tend to break out, so it is necessary to spray Chlorantraniliprole SC in time.

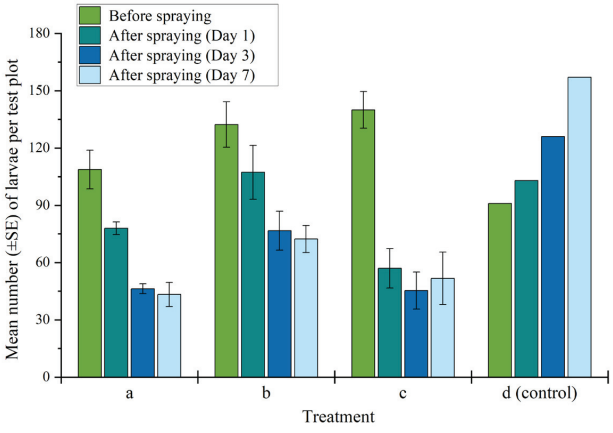

Figure 20. During the testing period, mean number (±SE) of diamondback moth larvae collected from four treatments.

The reduction rate of diamondback moth larvae population is shown in Table 7. From Table 7, treatments (a) and (b) had the lowest reduction rates on day 1, at 27.2 ± 3.7% and 19.4 ± 5.0%, respectively, and increased on days 3 and 7. The reduction rates on days 3 and 7 of treatment (a) were 56.3 ± 4.9% and 59.3 ± 7.1%, respectively, while those of treatment (b) were 42.2 ± 5.2% and 44.6 ± 6.1%, respectively. However, the reduction rate of treatment (c) on days 1, 3, and 7 did not change much, being 60.2 ± 4.4%, 68.4 ± 4.7%, and 64.1 ± 7.4%, respectively. It can be seen from the insect population reduction rate that, on day 1 after spraying, the reduction rate of spraying pesticides is much higher than that of spraying ozonated water. As the number of times of ozonated water spraying increased, the decline rate was also increasing.

Table 7. Reduction rate of diamondback moth larvae population in broccoli.

Treatment	Mean Number of Larve before Spraying	Reduction Rate of Larvae Population (%)		
		Day 1	Day 3	Day 7
a	108.7 ± 10.1	27.2 ± 3.7	56.3 ± 4.9	59.3 ± 7.1
b	132.3 ± 11.9	19.4 ± 5.0	42.2 ± 5.2	44.6 ± 6.1
c	140.0 ± 9.6	60.2 ± 4.4	68.4 ± 4.7	64.1 ± 7.4
d (CK)	91.0	−13.2	−38.0	−72.5

The control effect of different treatments on broccoli diamondback moth larvae is shown in Table 8. The control effects of treatments (a), (b), and (c) all reached their highest value on day 7, and treatment (c) with Chlorantraniliprole SC once in total had the highest control effect (79.2 ± 4.3%). On day 7, the control effect of treatment (a) was 76.4 ± 4.1%, which was not significantly different from the control effect of treatment (c). The control effect of treatment (b) was the worst (67.9 ± 3.6%), and was significantly different from treatments (a) and (c). The control effect of treatment (c) was 77.1 ± 3.4% on day 3, which had little change compared with the control effect on day 7. The tests have shown that spraying 17 ppm of ozonated water every day by using the ecological plant protection UAV can effectively control broccoli diamondback moth larvae and achieve the control effect of pesticides (Chlorantraniliprole SC). Although the use of the ecological plant protection UAV has increased, its advantages lie in the fact that it causes no pollution and no chemical damage.

Table 8. Control effect of diamondback moth larvae in broccoli.

Treatment	Control Effect (%)		
	Day 1	Day 3	Day 7
a	35.7 ± 3.3 b	68.5 ± 3.5 b	76.4 ± 4.1 a
b	28.8 ± 4.4 c	58.2 ± 3.7 c	67.9 ± 3.6 b
c	64.8 ± 3.9 a	77.1 ± 3.4 a	79.2 ± 4.3 a

The same lowercase letters in the same column indicate no significant difference in the control effect among different treatments, $p < 0.05$.

4.4. Cost Effectiveness of UAV for Ecological Plant Protection

We assessed the manufacturing cost of the ecological plant protection UAV prototype, which cost $6379 (USD), as shown in Table 9. The detailed cost of each component of the ozonated water system is shown in Table 3. We selected 4 UAVs with a load capacity of 20–30 kg: V40 (XAG), XP-2020 (XAG), T20 (DJI), and T30 (DJI); their prices are $5369, $7569, $5822, and $7278 (USD), respectively. Compared with the prices of these four UAVs, the cost of our ecological plant protection UAV is in the middle.

Table 9. Cost of each component of ecological plant protection UAV.

Component	Cost (CNY)
Flight control system	5500
Propulsion system (6 sets)	7130
Power system (4 batteries and a PDU)	8300
Ozonated water system	6698
Ground control system and data transmission	12,999
UAV fuselage	3200
Total	43,827 (CNY)/6379 (USD)

5. Conclusions

This paper describes an ecological plant protection UAV that will continuously produce and spray ozonated water during the flight, which is suitable for plant protection operations in vegetable fields. This paper carried out the design of the ozonated water system, the conceptual design of the UAV, and the structural strength analysis. Finally, the pilot production and field tests were conducted. As a result, the hovering time of the UAV could reach the design requirement of 10 min when it was fully loaded. The effective spraying width (with a height of 2.0 m and a speed of 3.0 m/s) is 5.25 m. The control effect test on broccoli diamondback moth larvae showed the ecological plant protection UAV was used to spray ozonated water with a concentration of 17 ppm once a day, and the control effect could reach 76.4%. It is proven that spraying 17 ppm ozonated water with the ecological plant protection UAV can effectively prevent and control some pests at certain concentrations. The ecological plant protection UAV can be used for plant protection in fields and orchards, meeting the requirements for the prevention and control of common diseases and pest larvae caused by harmful agricultural microorganisms such as bacteria and fungi. In the future, our work needs to be improved, and we need to explore the optimal spraying parameters for different crops and different pests and diseases. We also need to study the impact of high-concentration ozonated water on crop yield and pest reproduction.

6. Patents

A patent has been applied for and granted for this research. The patent issued as Luxembourg Patent LU101533 [36] on 14 April 2020.

Author Contributions: Conceptualization, H.X., L.Y., X.H. and Y.L.; methodology, H.X., L.Y. and X.H.; software, H.X. and C.L.; validation, H.X., C.L., J.B. and X.H.; formal analysis, H.X., C.L. and Y.S.; investigation, H.X., L.Y., C.L. and Y.S.; resources, X.H., L.Y. and Y.L.; data curation, H.X., L.H. and F.K.; writing—original draft preparation, H.X., L.Y. and X.H.; writing—review and editing, H.X., Y.S., L.H. and X.H.; visualization, H.X. and F.K.; supervision, Y.L. and X.H.; project administration, H.X., J.B., X.H. and Y.L.; funding acquisition, X.H., L.Y. and Y.L. All authors have read and agreed to the published version of the manuscript.

Funding: This research was funded by Top Talents Program for One Case One Discussion of Shandong Province, Academy of Ecological Unmanned Farm (2019ZBXC200), and Zibo School-City Integration Development Project (2019ZBXC053, 2019ZBXC143).

Data Availability Statement: The data are available upon request.

Conflicts of Interest: The authors declare no conflict of interest.

References

1. Zhou, Z.; Zang, Y.; Luo, X.; Lan, Y.; Xue, X. Technology innovation development strategy on agricultural aviation industry for plant protection in China. *Trans. Chin. Soc. Agric. Eng.* **2013**, *29*, 1–10. [CrossRef]
2. Zhou, Z.; Ming, R.; Zang, Y.; He, X.; Luo, X.; Lan, Y. Development status and countermeasures of agricultural aviation in China. *Trans. Chin. Soc. Agric. Eng.* **2017**, *33*, 1–13. [CrossRef]
3. Chai, X. The Performance of the Portable Ozone Sprayer Optimization and Experimental Research. Master's Thesis, Xinjiang Agricultural University, Urumqi, China, 2015.
4. Ebihara, K.; Mitsugi, F.; Ikegami, T.; Nakamura, N.; Hashimoto, Y.; Yamashita, Y.; Baba, S.; Stryczewska, H.D.; Pawlat, J.; Teii, S.; et al. Ozone-mist spray sterilization for pest control in agricultural management. *Eur. Phys. J. Appl. Phys.* **2013**, *61*, 24318. [CrossRef]
5. Steffen, H.; Rice, R.G. The PhytO3 Tech Crop Protection Technology for Microorganism and Insect Control using Ozone, UV, and Dipole-Electrical Air Jet Spray Technologies–Technical Basis and Possible Chemistries Involved. *Ozone Sci. Eng.* **2008**, *30*, 216–227. [CrossRef]
6. Fan, X. Design and Experimental Research of Tracked Plant Protection Vehicle Based on Ozonated Water. Master's Thesis, Shandong University of Technology, Zibo, China, 2021.
7. Hu, X. Design and Experiment of Spray System for Synthesis of Strong Oxidizing Free Radical Solution. Master's Thesis, Jiangsu University, Zhenjiang, China, 2022.
8. Lan, Y.; Chen, S. Current status and trends of plant protection UAV and its spraying technology in China. *Int. J. Precis. Agric. Aviat.* **2018**, *1*, 1–9. [CrossRef]
9. Wang, J.; Lan, Y.; Zhang, H.; Zhang, Y.; Wen, S.; Yao, W.; Deng, J. Drift and deposition of pesticide applied by UAV on pineapple plants under different meteorological conditions. *Int. J. Agric. Biol. Eng.* **2018**, *11*, 5–12. [CrossRef]
10. Kong, H.; Yi, L.; Lan, Y.; Kong, F.; Han, X. Exploring the operation mode of spraying cotton defoliation agent by plant protection UAV. *Int. J. Precis. Agric. Aviat.* **2018**, *1*, 43–48. [CrossRef]
11. Zhu, H.; Jiang, Y.; Li, H.; Li, J.; Zhang, H. Effects of application parameters on spray characteristics of multi-rotor UAV. *Int. J. Precis. Agric. Aviat.* **2019**, *2*, 18–25. [CrossRef]
12. Albert, S.; Amarilla, A.A.; Trollope, B.; Sng, J.D.J.; Setoh, Y.X.; Deering, N.; Modhiran, N.; Weng, S.-H.; Melo, M.C.; Hutley, N.; et al. Assessing the potential of unmanned aerial vehicle spraying of aqueous ozone as an outdoor disinfectant for SARS-CoV-2. *Environ. Res.* **2021**, *196*, 110944. [CrossRef]
13. DJI Agriculture UAV. Available online: https://ag.dji.com (accessed on 20 February 2023).
14. XAG Agricultural UAV. Available online: https://www.xa.com (accessed on 20 February 2023).
15. Zhang, Y.; Zhao, J.; Zhang, G.; Wang, Y.; Li, Y.; Zhuang, F. Application effect test of ozonated water in the control of dragon fruit diseases and insect pests. *Shanghai Agric. Sci. Technol.* **2020**, *2*, 100–103.
16. Guo, Z. Effects of Ozonated Water on Controlling of Greenhouse Vegetable Disease and Underlying Physiological Mechanism. Ph.D. Thesis, Shanghai Normal University, Shanghai, China, 2017.
17. Bershadsky, D.; Haviland, S.; Johnson, E.N. Electric Multirotor Propulsion System Sizing for Performance Prediction and Design Optimization. In Proceedings of the 57th AIAA/ASCE/AHS/ASC Structures, Structural Dynamics, and Materials Conference, San Diego, CA, USA, 4–8 January 2016.
18. Hobbywing XRotor-X9 Propulsion System. Available online: https://www.hobbywing.com (accessed on 20 February 2023).
19. Quan, Q. *Introduction to Multicopter Design and Control*; Springer: Singapore, 2017.
20. Li, J.; Zhan, Y.; Ouyang, F.; Li, Y.; Lan, Y. Optimization of rotor spacing and energy consumption test for multi-rotor single arm tandem electric UAV. *Trans. Chin. Soc. Agric. Eng.* **2019**, *35*, 87–95. [CrossRef]
21. Li, J.; Zhou, Z.; Lan, Y.; Hu, L. Distribution of canopy wind field produced by rotor unmanned aerial vehicle pollination operation. *Trans. Chin. Soc. Agric. Eng.* **2015**, *31*, 77–86. [CrossRef]

22. Li, J.; Long, B.; Wu, H.; Hu, X.; Wei, X.; Zhang, Z.; Chai, L.; Xie, J.; Mei, H. Rapid Evaluation Model of Endurance Performance and Its Application for Agricultural UAVs. *Drones* **2022**, *6*, 186. [CrossRef]
23. Hassanalian, M.; Abdelkefi, A. Classifications, applications, and design challenges of drones: A review. *Prog. Aerosp. Sci.* **2017**, *91*, 99–131. [CrossRef]
24. Krznar, M.; Piljek, P.; Kotarski, D.; Pavkovic, D. Modeling, Control System Design and Preliminary Experimental Verification of a Hybrid Power Unit Suitable for Multirotor UAVs. *Energies* **2021**, *14*, 2669. [CrossRef]
25. Vu, N.A.; Dang, D.K.; Dinh, T.L. Electric propulsion system sizing methodology for an agriculture multicopter. *Aerosp. Sci. Technol.* **2019**, *90*, 314–326. [CrossRef]
26. Dai, X.; Quan, Q.; Ren, J.; Cai, K. An Analytical Design-Optimization Method for Electric Propulsion Systems of Multicopter UAVs with Desired Hovering Endurance. *IEEE/ASME Trans. Mechatron.* **2019**, *24*, 228–239. [CrossRef]
27. Lin, J. Research on Energy Load Matching Technology of Multi Rotor Agricultural UAV. Master's Thesis, South China Agricultural University, Guangzhou, China, 2019.
28. Chen, S.; Lan, Y.; Li, J.; Xu, X.; Wang, Z.; Peng, B. Evaluation and test of effective spraying width of aerial spraying on plant protection UAV. *Trans. Chin. Soc. Agric. Eng.* **2017**, *33*, 82–90. [CrossRef]
29. Qin, W.; Xue, X.; Zhou, Q.; Cai, C.; Wang, B.; Jin, Y. Use of RhB and BSF as fluorescent tracers for determining pesticide spray distribution. *Anal. Methods* **2018**, *10*, 4073–4078. [CrossRef]
30. Gao, S.; Wang, G.; Zhou, Y.; Wang, M.; Yang, D.; Yuan, H.; Yan, X. Water-soluble food dye of Allura Red as a tracer to determine the spray deposition of pesticide on target crops. *Pest Manag. Sci.* **2019**, *75*, 2592–2597. [CrossRef] [PubMed]
31. Chen, P.; Lan, Y.; Huang, X.; Qi, H.; Wang, G.; Wang, J.; Wang, L.; Xiao, H. Droplet Deposition and Control of Planthoppers of Different Nozzles in Two-Stage Rice with a Quadrotor Unmanned Aerial Vehicle. *Agronomy* **2020**, *10*, 303. [CrossRef]
32. Lan, Y.; Shan, C.; Wang, Q.; Liu, Q.; Yang, C.; Xie, Y.; Wang, G. Effects of different spray additives on droplet deposition characteristics during plant protection UAV spraying operations. *Trans. Chin. Soc. Agric. Eng.* **2021**, *37*, 31–38. [CrossRef]
33. Zhu, H.; Salyani, M.; Fox, R.D. A portable scanning system for evaluation of spray deposit distribution. *Comput. Electron. Agric.* **2011**, *76*, 38–43. [CrossRef]
34. Zhang, R.; Yi, L.; Lan, Y.; Zhang, F.; Han, X.; Kong, F.; Yu, W. Structural Design and Simulation of Coaxial Double Propeller Plant Protection UAV. *J. Agric. Mech. Res.* **2023**, *45*, 29–35. [CrossRef]
35. Qin, W.; Qiu, B.; Xue, X.; Chen, C.; Xu, Z.; Zhou, Q. Droplet deposition and control effect of insecticides sprayed with an unmanned aerial vehicle against plant hoppers. *Crop Prot.* **2016**, *85*, 79–88. [CrossRef]
36. Han, X.; Shang, D.; Lan, Y.; Fan, X.; Li, X.; Fu, J.; Yi, L.; Kong, F. Electric Plant-Protection Drone Capable of Adding Water and No Pesticide. Luxembourg Patent LU101533, 14 April 2020.

drones

MDPI

Article

Noise Impact Assessment of UAS Operation in Urbanised Areas: Field Measurements and a Simulation

Filip Škultéty *, Erik Bujna, Michal Janovec and Branislav Kandera

Faculty of Operation and Economics of Transport and Communications, University of Žilina, Univerzitná 8215/1, SK-010-26 Žilina, Slovakia
* Correspondence: filip.skultety@uniza.sk

Abstract: This article's main topic is an assessment of unmanned aircraft system (UAS) noise pollution in several weight categories according to Regulation (EU) 2019/947 and its impact on the urban environment during regular operation. The necessity of solving the given problem is caused by an increasing occurrence of UASs in airspace and the prospect of introducing unmanned aircraft into broader commercial operations. This work aims to provide an overview of noise measurements of two UAS weight categories under natural atmospheric conditions to assess their impact on the surrounding environment. On top of that, modelling and simulations were used to observe and assess the noise emission characteristics. The quantitative results contain an assessment of the given noise restrictions based on the psychoacoustic impact and actual measured values inserted into the urban simulation scenario of the Zilina case study located in northwest Slovakia. It was preceded by a study of noise levels in certain areas to evaluate the variation level after UAS integration into the corresponding airspace. Following a model simulation of the C2 category, it was concluded that there was a marginal rise in the level of noise exposure, which would not exceed the prescribed standards of the Environmental Noise Directive.

Keywords: drone; UAS noise measurement; noise emission characteristics; noise modelling; noise simulation; Zilina case study

Citation: Škultéty, F.; Bujna, E.; Janovec, M.; Kandera, B. Noise Impact Assessment of UAS Operation in Urbanised Areas: Field Measurements and a Simulation. *Drones* **2023**, *7*, 314. https://doi.org/10.3390/drones7050314

Academic Editors: Andrzej Łukaszewicz, Wojciech Giernacki, Zbigniew Kulesza, Jaroslaw Alexander Pytka and Andriy Holovatyy

Received: 21 March 2023
Revised: 2 May 2023
Accepted: 3 May 2023
Published: 9 May 2023

1. Introduction

In the near future, the concept of parcel and medicine delivery by drones, increasingly associated especially with the perceptions of global shipping carriers, is a challenge for many research areas. It is expected that there will be an enormous increase in the number of unmanned aerial vehicles (UAVs) used not only for commercial operations but also for recreational purposes. With increased unmanned aircraft system (UAS) traffic, there is also a presumption of increased noise in the surrounding environment and the adverse impact of psychoacoustic phenomena on humans or animals.

The significance of this work lies in assessing the characteristics of the noise spreading by multirotor drones regarding the risks of psychological influences and negative impact on the population. The intention is to create a background for the future investigation of regular UAS operations through the practical introduction of the case study via a simulation environment. At present, there is no uniform rule for measuring and assessing the noise of drones, and each Member State has its regulations for this purpose, which are mostly based on a uniform ISO standard. Therefore, our future work will contain the assessment of whether actual legislation is adequate and whether there will be a necessity to implement new harmonised rules for EU member states.

The noise assessment was based on previous measurements and results used in our measurements and assumptions in determining the characteristics of sound spreading in space. These measurements were preceded by studies and examinations of the UAV noise sources and the influence of the external environment, which had to be considered

in other contexts. It is necessary to focus on a specific location when assessing noise, even when putting unmanned vehicles into operation. A study of legislation, current restrictions, and impacts on humans and wildlife preceded it. Based on information on legislation and measurements of sound propagation in the environment, it is possible to assess the effects on humans and provide data for further research and model situations in the natural environment.

1.1. Theory of Sound and Rotor Noise

The production of sound is achieved through the transmission of vibrations that propagate through the layers of air. This process involves the disturbance of air particles, which can be visualised as sinusoidal waves with varying amplitudes that correspond to the intensity of the sound. The peaks of the sinusoidal waves occur when the air particles are compressed and subsequently expanded.

1.1.1. Equations

The gap between the repeating wave period of sound waves is wavelength λ (m), tightly connected with the frequency of the sound f (Hz) and speed of sound c ($m.s^{-1}$), which is the speed of spreading of acoustical waves in air. It depends on actual atmospheric conditions with the most significant influence on temperature [1].

$$\lambda = c/f \tag{1}$$

The sound can be transferred from the source, which could be a monopole, dipole, or quadrupole. This statement forms the basis of the theory of sound developed by Lord Rayleigh in the nineteenth century [2].

The sound source emits the tones with some power. This is called sound power, with the unit watt (W). This energy is transmitted through the air per unit of time. The air serves as a surface through which the sound is transferred, which is the sound intensity with the unit (W/m^2). Since the sound intensity is a relation between sound power and the surface of wave propagation whose sound is transported, the equation is:

$$I = W/S \tag{2}$$

Moreover, when the sound is transferred in every direction, it is possible to write the equation for sound power:

$$W = 4\pi r^2 I \tag{3}$$

where r is the radius in a sphere (m); during observation, this is one of the minor variables of sound pressure. During measurement, microphones do it all the time. This pressure is responsible for the displacement of air molecules in all directions [1]. The relation between sounds we hear with exact power and the reference power is called the sound power level, L_W. It is measured in decibels and could be expressed via logarithmic function [2]. The reference power is considered to be 10–12 W. This is because it represents the lowest sound humans may discern. This parameter is used to measure overall noise regardless of the location because sound power level is not a function of distance from the sound source.

$$L_W = 10\log W/W_{ref} \tag{4}$$

In the same way, as shown in Equation (4), it is possible to identify sound intensity levels where sound power W and reference power W_{ref} are replaced by sound intensity I (Wm^2) and reference sound intensity I_{ref}. Sound intensity is a parameter showing the direction and amount of acoustic energy in a specific area. However, sound pressure level (SPL) L_p is used to identify how loud the source of sound is. It is the difference between a sound wave and the ambient pressure the sound travels through. Before expressing the

equation for SPL, it is necessary to mention that it is feasible to express sound intensity in Equation (1)

$$I = p^2/\rho c \quad (5)$$

where p^2 is the root mean square pressure (RMS), ρ is the density of air ($kg.m^{-3}$), and c is the speed of sound ($m.s^{-1}$). Additionally, the RMS pressure is used in the equation for SPL, which is proportional to the PWL equation and can be expressed as "ten times logarithm to the base 10 of the square of sound pressure p, to the square of a reference value $p_{ref,}$ expressed in decibels" [3]

$$L_p = 10\log p^2/{p_{ref}}^2 \quad (6)$$

$$L_p = 20\log p/p_{ref} \quad (7)$$

Reference values for both sound intensity and sound power are known. Reference sound intensity was set as I_{ref} equals 10–12 W/m and reference sound power was set as W_{ref} equals 10–12 W. In a numerical way, intensity and sound pressure levels are almost equal in room temperature and sea level pressure. When the area of the surface is taken into account, sound pressure level and sound power level are related to each other as:

$$L_p = L_W - 10\log S \quad (8)$$

where S is the surface through which sound is transported. From this relation, P_{ref} is taken as equivalent with sound power but, generally, it is known as the limit of audibility, 20 (μPa).

The last variable that it is important to incorporate during the measurement process is the distance of the source of the sound from the receiver. Distance has to be included when the sound of the exact source is measured due to the inverse square law [4].

1.1.2. Rotational Propeller Noise

Noise radiating from the rotor consists of three components: blade slap, rotational noise, and vortex noise. In the case of rotors, it is caused by a lack of symmetry. The advancing blade meets air with higher velocities during a forward flight than the retreating blade. Another essential feature of the rotor aerodynamic is the rotor wake from a noise and vibration point of view. Amplitudes of higher harmonics specific to helicopters or UAVs vary and also depend on flight conditions. A large part of the detectable noise observed is related to vortex effects.

External inputs also affect every numerical calculation, which limits the accuracy of calculations. However, blade slap noise is more complex for hand calculations and more sophisticated software is necessary for its calculations. Assumptions made by M.V. Lowson, which help to analyse and calculate trends of the behaviour of rotational noise generated by rotors during steady flight, can be used to achieve and use reasonable and valuable results of noise harmonies, which differ from computer calculations by no more than 2 dB [1].

1.2. Literature Review

Literature synthesis contributes to developing new insights and perspectives and helps identify gaps or inconsistencies in the previous research. In the databases, it is possible to reveal a trend and the frequency of the occurrence of scientific works on similar topics. Leslie, Wong, and Auld were among the first to focus on noise from UAS operations. They published a 2008 conference paper on broadband propeller noise reduction [5]. Massey and Gaeta dealt with noise measurements of tactical UAVs in 2010 [6]. Similar research was carried out in 2013 by Sinibaldi and Marino, particularly focused on experimental analysis of the noise of propellers for small UAVs [7]. The investigation involved generating an acoustic signature profile of a small multirotor UAS conducted by Kloet, Watkins, and Clothier [8]. Acoustic measurements carried out in an anechoic room were performed by Papa et al. as part of the research for a conference paper in 2016 [9].

We can include a computational study on the aeroacoustics of a multirotor unmanned aerial system by Heydari, Sadat, and Singh [10], and a combined experimental and numerical assessment of UAV noise emissions by Cussen, Garruccio and Kennedy [11] among the latest works that prove the relevance of the issue. Several works are also devoted, for instance, to noise certifications, such as [12], or preliminary research on transverse noise topics [13–21]. Nevertheless, there are only a few works conducted on real measurements according to official regulations on the noise of rotorcraft, followed by acoustic maps or simulation of noise propagation in a natural environment, which is the area of our interest. For example, Treichel et al. [22] conducted in 2022 a series of eight UAV noise measurements according to ISO standard 3744. However, the authors did not visualise the noise maps or directional characteristics of frequency analysis. On the other hand, Kenedy, Garruccio and Cussen [23] investigated the suitability of the software package 'iNoise' for modelling noise emission by drones. Relatively recent activity in the area of investigating the UAS impact as part of the U-space system is addressed by Deliverable D4.2 of DACUS Project [24]. The project has recognised the necessity of consolidating the concept of a social impact hotspot, which refers to a specific area where the demand for drone traffic results in noise and visual exposure that exceeds acceptable thresholds for a predetermined duration or frequency within a given period.

2. Materials and Methods

When the measurements were conducted, it was necessary to comply with specific conditions. Results of measurement might be affected by factors that cause them to deviate from results measured in an ideal reference area with specific reference conditions. These reference conditions are given and must be in compliance with approval by the certificating authority. Measurement in compliance with the reference procedure should follow reference atmospheric conditions:

- Sea level atmospheric pressure of 1013.25 hPa;
- Ambient temperature of 20 °C (ISA may be used);
- Relative humidity of 65%;
- Zero wind.

If the maximum rotor speed is given, the maximum operating rotor speed shall be taken as the highest speed, tolerance should be given on this speed, and measurement shall be conducted using this rotor speed. In case the rotor speed is adjustable maximum operating rotor speed for the reference conditions shall be used for the purpose of measurement and certification [25]. Test criteria, especially in case the measurement is in a non-airport area, should include criteria affecting results such as terrain, residual sound, weather conditions, microphone placement, and pilot sight [6]. Irregularities in terrain, such as mounds and furrows, can result in reflections and these surface anomalies may influence measured sound levels. Not only the terrain surface but also the highness of vegetation may influence the reflection of sound waves from ground level. Vegetation can result in the variation of sound level, more frequently with decreasing sound level, but the sound level may be higher. The surface of the measured area is also important, and the hardness of the surface is an important factor because hard surfaces, such as paved areas, may result in higher measured sound levels than soft ones.

Obstructions, for example, buildings, trees, vehicles, and even test personnel, may cause reflections that influence noise levels. For this reason, obstructions of this character are unacceptable in the vicinity of the measuring point. During measurement, there should not be any obstacle causing reflection in a conical shape area above the measurement device. Figure 1, created according to the ICAO standards [25], depicts this conical shape area defined as the axis normal to the ground and the axis formed by the angle of 80° around the vertical axis. Besides material, the object's width is important in reflection consideration and environmental correction can be negligible.

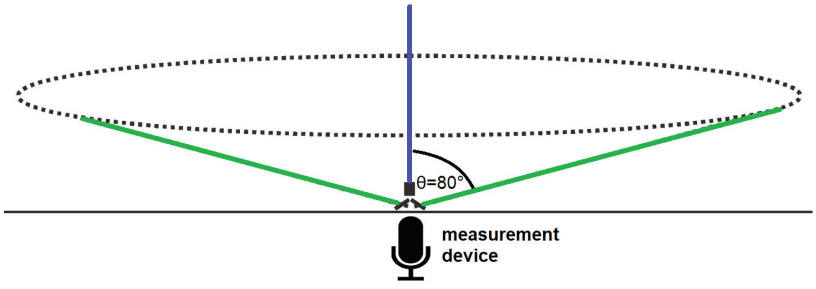

Figure 1. Conical area without obstructions during measurement.

2.1. Measurement Devices

For our experiment, NORSONIC Nor-140 measuring devices were used. Every chosen device is a hand-held device. They are composed of a microphone cartridge, microphone preamplifier, display, keyboard, sockets, and battery compartment. Our measurements were important mapping levels versus time display and level versus frequency. The display is possible to set as a dual view to observe more parameters at the same time. Nor-140 can also measure in the 120 dB range for one or one-third of an octave band. Every one of these three sound level meters is a measuring device class 1. It is possible to make a frequency analysis using the range within measuring devices depending on octave bands. The octave band has a wider span range than the third-octave bands. Nor-140 measures the range for frequency analysis in the one-third octave band from 0.4 Hz to 20 kHz. These span ranges are satisfactory for our experiment due to measuring frequencies which are hearable for the human ear. Basic measurement parameters are SPL, L_{Max}, L_{Min}, L_{Leq}, and L_{peak}. Results from measurements can be easily scanned through captured recordings in a measurement device without transferring data to a PC. However, it is more convenient to use a PC afterwards and post-process data in reporting software [26–28].

These data, which are measured in decibels referenced to 20 μPa, are updated at least once per second. In the settings, if necessary, it is always possible to switch measurements to another weighting. It is crucial because sound level meters respond differently to different sound frequencies compared with human hearing sensitivity. The most usable weighting is A because it measures the noise similarly, as humans are sensitive to sound. A-weighting is common for almost all environmental noise measurements. The analysis software may assess the result of equivalent sound-level data. Method, which is suitable for assessing noise audibility of tones, uses 1/3 octave measurements. One-third octave bands provide a more precise outlook on noise levels regarding frequency composition.

2.2. Evaluated UAVs

In our experiment, two types of drones were chosen, each representing a specific weight category. For each weight there are specified rules of flight determined in Regulation (EU) 2019/947. DJI Mavic 2 Pro and DJI Inspire 2 quadcopters were chosen for the experiment. The aforementioned regulation outlines the specific conditions under which the selected UAVs may be operated. Both are classified under the A2 sub-category of the 'open' category, which obtains the primary framework for most recreational drones and low-risk commercial operations. The elementary specifications of UAVs used in this evaluation are shown in Table 1. Size, weight and velocity data were obtained from the official store [29].

Table 1. Basic specifications of UAVs.

	DJI Mavic 2 Pro	DJI Inspire 2
Take-off weight (g)	907	3440
Dimensions with unfolded propellers (mm)	322 × 242 × 84	605 × 605 × 300
Max speed (km/h)	72	108
Weight category	C1	C2

2.3. Methodology

The methodology of outdoor measurements of UAS is described in the Commission delegated regulation (EU) 2020/1058 from 27 April 2020. This regulation should ensure the same conditions for measurement and it is based on ISO 3744 2010, where general conditions of measurement are described and methods of counting sound power levels are described. Part 13 describes the noise measurement prescription, which describes the determination of the A-weighted sound pressure level in the area surrounding the source of the sound.

The A-weighted time-averaged sound pressure level is measured at least three times for UAV configuration. Suppose a couple of these three measurements differ from the results by 1 dB. Measurements are repeated. The acoustic sound pressure level is the arithmetic mean of the two highest results. DJI Mavic 2 Pro belongs to category C1, whereas DJI Inspire, whose weight is 3440 g, belongs to category C2.

According to the Annex to Delegated Regulation (EU) 2019/945—Part 13 "The measurement surface shall have its origin at the point O lying in the ground plane directly below the UA". The minimum flight and hovering height above ground level of selected DJI UAVs is 0.5 m. Therefore, the UAVs shall hover above a hard acoustic surface at a sufficient distance from any reflecting wall or ceiling, or any reflecting object so that the requirements given in Annex A of EN ISO 3744:2010 will be satisfied on the measurement surface. The measurement surface is the hemisphere with one origin point O, in the middle, shown in Figure 2. This figure shows the displacement of microphones during measurements. The displacement was managed according to Annex F of ISO 3744 2010 standard, where A determines the measurement surface, B determines the reference surface, and r determines the measurement surface radius which is 4 m.

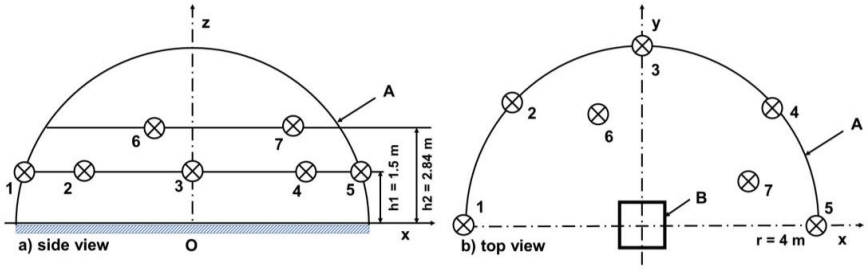

Figure 2. Microphone array on a hemispherical measurement surface for measurement.

According to the Commission delegated regulation (EU) 2020/1058 from 27 April 2020, the measurement of A-weighted sound power level L_{WA} shall be executed above a hard surface with minimal sound absorption. This provides objective results compared to sound pressure measurements. It allows for determining the acoustic power emitted by the device regardless of the direction of noise from the source. Knowing the sound power level is very useful and it allows the sound output of different devices to be objectively compared.

For this reason, the former local airstrip mainly used for agricultural works in Rosina village was chosen, as shown in Figure 3. Fields surrounded the place where the measurement was executed and the highest possible permanent source of the sound, the highway, was distanced 3 km from the measuring place. Measurements were partially interrupted

by non-permanent sources of sound, e.g., passenger cars. In these times, measurements were paused and results were not included with these non-desirable factors.

Figure 3. Microphone array at the airstrip.

The placement of the microphones is displayed according to ISO 3744 2010 Annex F in Figure 3. According to regulations, microphones are needed for measurement purposes at positions 2, 4, 6, 8, 10, and 12. However, our measurement was a round base divided by two with microphones in positions 6, 8, 12. Turning the UAV and flying with UAVs back and forth created perception from both sides of UAVs and made the imaginary hemispherical area. The *x*-axis served as an overflight line with a hard pad in the middle of the axis and the centre of the thought circle served as starting pad during hovering measurements. Microphones 6 and 8 were deployed according to ISO 3744 2010 Annex F conditions in the *x*- and *y*-axes from the circle's centre point. These two were distanced from the *x*- and *y*-axis 2.62 m. These two microphones were placed at 1.5 m height AGL. The third microphone was distanced from the *x*-axis 2.6 m and from the *y*-axis 1.08 m. Its height deployment was 2.84 m AGL. This placement was used to measure equivalent sound pressure level LAeq and count sound power levels L_{WA} of each UAV.

The values of the A-weighted sound power levels, the sound power levels in the third-octave bands, and the A-level sound exposure level were measured with sound level meter strings based on Nor-140 sound analysers. NORSONIC N1225 measuring microphones with NORSONIC Nor1209 measuring preamplifiers were used to record audio signals. A total of three measurement strings were used to measure acoustic performance, four to measure flights, and sound exposure levels A were determined. The microphones were equipped with wind and dust covers with a diameter of 60 mm. The monitored quantities were determined based on measuring the time course of the values of short-term A-weighted equivalent sound pressure levels and equivalent sound pressure levels on third-octave bands with mean frequencies in the range of 20 Hz to 20 kHz. The averaging period was T = 125 ms. The particular periods were continuously linked to each other during the time intervals of measurement of the respective flight operations, overflights, and hovering.

The determination of the value of the quantity describing the residual sound, the background noise, was determined from the values of the measured quantities at time intervals when no overflights were performed.

Verification of the correct sensitivity setting of the measurement strings was performed before and after all series of measurements were performed. Verification was performed using a reference signal source (microphone calibrator) NORSONIC Nor1251.

Sound analysers and specified elements of measuring chains, at the time of measurement, had valid verifications in accordance with the Act of the National Council of the Slovak Republic No. 157/2018 Coll. on metrology and related regulations, as amended.

2.4. Calibration

When measuring the level of the assessed source and the noise of the assessed source, there is background noise, which is included in the total SPL level. If the difference between the total level and the background noise level is in the range from 3 dB to 18 dB, then the noise level of the assessed source is determined by level L_{Aeq} which is deducted by the correction K_1 determined according to the equation:

$$K_1 = -10 \log(1 - 10^{-0,1(L_S - L_B)}) \quad (9)$$

where L_S means time-averaged sound pressure level, with source gained from the array of microphones in the measurement surface, and L_B means SPL of the background noise. If the difference exceeds 18 dB, the background noise negligibly affects the source level under consideration. The assessed value is then measured (resp. determined and adjusted for the length of exposure to noise sources), and the value of the determining quantity is increased by the measurement uncertainty adjusted by corrections and determined for the relevant reference time interval. Then:

$$L_{R,Aeq} = (L_{Aeq} + K_1 + K_T) \quad (10)$$

where $L_{R,Aeq}$ is the assessed equivalent sound level A for the reference time interval, LAeq is equivalent sound level A for the reference time interval, K_1 is the correction factor for background noise, and K_T is the assessed value for specific noise determined by adding the correction K_T = +5 dB to the equivalent sound level A unless otherwise stated. The day and evening K_T correction only applies if the total duration of the specific noise exceeds 10 min per day or 5 min per evening.

When 50 dB residual sound was recorded during measurements, the difference in Figure 4 illustrates the adjustment between the residual sound and the sound from the source in the 20 to 25 dB range. This means that the correction for K_1 is negligible and, after substituting the values into Equation (9), the correction for K_1 is up to 0.1 dB.

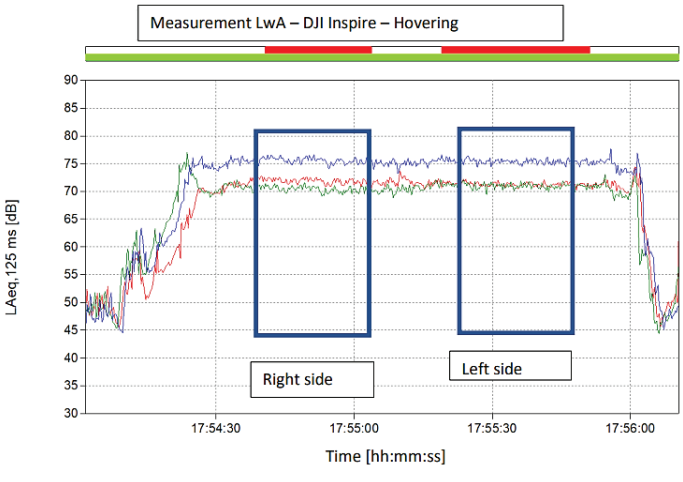

Figure 4. Equivalent sound pressure levels in time of DJI Inspire during hovering.

3. Results

Figures 4 and 5 describe L_{Aeq} during hovering and overflight of the DJI Inspire from UAV weight category C2, which provide an illustrative view of the perception of microphones during two flight modes. As mentioned, the microphones were placed on half the measuring surface. Therefore, the measurements were performed twice with the UAV rotated in both directions. The rotation of the UAV concerning the microphones is shown in both figures by dark blue rectangles. Each side was measured with three microphones. Therefore, for both figures, the record on the right contains microphones M2 marked in red, M6 marked in blue, and M4 marked in green, and the record on the left contains microphones M1 marked in green, M7 marked in blue, and M3 marked in red colour. In this way, the entire surface needed to perform the measurements was covered.

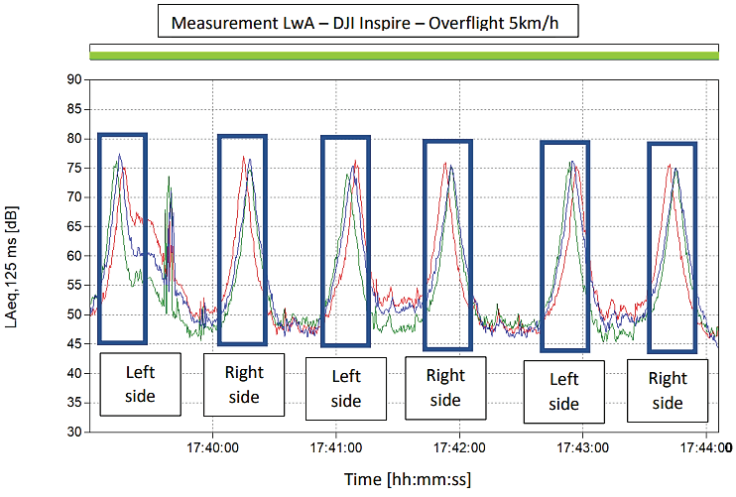

Figure 5. Equivalent sound pressure levels in time of DJI Inspire during the overflight.

From Figure 4, it is possible to observe the value of the residual sound before the UAV takes off over a solid surface of 0.5 m. From the graph, it is possible to find that the microphones at positions 6 and 7 recorded a higher level of L_{Aeq} than the four microphones distributed along the edges of the area at a lower height. This value differs from the values measured on four microphones while hovering by approximately 5 dB.

In Figure 5 are expressed the results of six DJI Inspire overflights at a speed of 5 km/h. The depicted L_{Aeq} noise levels present three flyovers in each direction along the specified section of the asphalt runway. In the time period between 17:39 and 17:40 you can spot the discrepancy in the measurement, which was caused by passage of the motorcycle on the road located right next to the airfield.

Measurements when UAVs were hovering above the hard surface and overflying the measuring area were performed for weight categories C1 and C2 with their representatives DJI Mavic 2 Pro and DJI Inspire 2. Measurements evaluated the A-weighted equivalent sound pressure level LAeq. However, in order to compare the noise load for comparison between chosen weight categories, it is necessary to convert the averaged equivalent sound pressure levels to sound power levels L_{WA}, using Equation (11), where S is the area of the measurement surface and S_0 equals 1 m^2. Results for DJI Inspire are displayed in Table 2 and for DJI Mavic 2 Pro in Table 3. These results compare the L_{WA} of UAVs from the C1 category, mostly used in the hobby sphere, and C2, which might also be used in commercial operations, from both categories; this is described as maximal L_{WA} in the Commission delegated regulation (EU) 2020/1058.

$$L_{WA} = L_{Aeq} + 10\log S/S_0 \quad (11)$$

Table 2. Corrected equivalent sound pressure levels of DJI Inspire 2.

Middle Filter Frequency (Hz)	Acoustic Sound Power Level Corrected with L_{WA} Equation (dB)			
	5 kmh^{-1}	10 kmh^{-1}	20 kmh^{-1}	Hovering
20	13.9	6.4	9.3	11.2
40	24.9	23.6	22.0	22.5
80	40.3	40.7	44.1	36.9
160	65.1	65.5	71.9	56.2
315	75.6	76.4	80.2	63.1
630	78.2	81.8	81.7	69.2
1250	83.0	83.9	85.3	73.1
2500	83.5	83.8	85.6	72.7
5000	79.9	82.6	84.4	69.5
10,000	71.6	75.3	77.3	62.5
20,000	58.8	64.2	67.6	51.3

Table 3. Corrected equivalent sound pressure levels of DJI Mavic 2 Pro.

Middle Filter Frequency (Hz)	Acoustic Sound Power Level Corrected with L_{WA} Equation (dB)			
	5 kmh^{-1}	10 kmh^{-1}	20 kmh^{-1}	Hovering
20	8.4	8.2	13.2	14.7
40	21.4	20.2	24.8	36.3
80	33.9	38.0	39.3	40.3
160	53.0	57.6	63.9	53.3
315	64.1	66.4	67.8	60.9
630	66.5	70.2	73.7	67.0
1250	70.0	73.6	76.1	70.7
2500	68.6	72.4	75.1	70.0
5000	67.8	70.3	73.7	68.9
10,000	65.0	65.5	67.7	64.7
20,000	55.8	54.5	55.8	54.2

Both Tables 2 and 3 show the A-weighted sound power levels during overflights at the height of 0.5 m, which is intended for measurements for this purpose of two drones at different speeds, as well as the values measured at 0.5 m above the ground during hovering. The measured values of L_{WA} are displayed in the range of the audible spectrum of the human ear from 20 Hz to 20 kHz.

Figures 6 and 7 depict a comparison of two drones, DJI Inspire 2 and DJI Mavic 2 Pro, during hovering and during overflight at a speed of 10 km/h. It is possible to see from a comparison of the graphs that, during hovering, the values of both categories are approximately the same when it is possible to observe similar levels of acoustic power at the same frequencies. However, as can be seen from Figure 6 at 10 km/h overflights, the DJI Inspire has been shown to reach higher L_{WA} than the DJI Mavic 2 Pro. However, during flights with DJI Mavic 2 Pro, higher frequencies were recorded at the same L_{WA}, which was audible with listening as "buzzing", which may have the effect of annoyance of people around. The following case study focuses on the DJI Inspire 2 only.

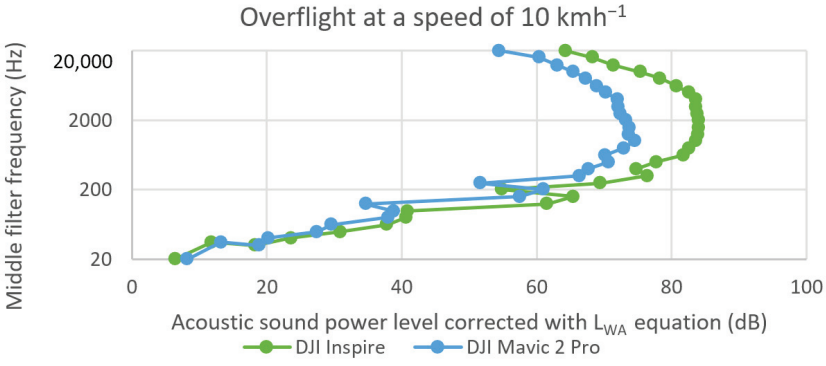

Figure 6. Comparison of L_{WA} for the two drones during overflight at a speed of 10 kmh^{-1} at 0.5 m height.

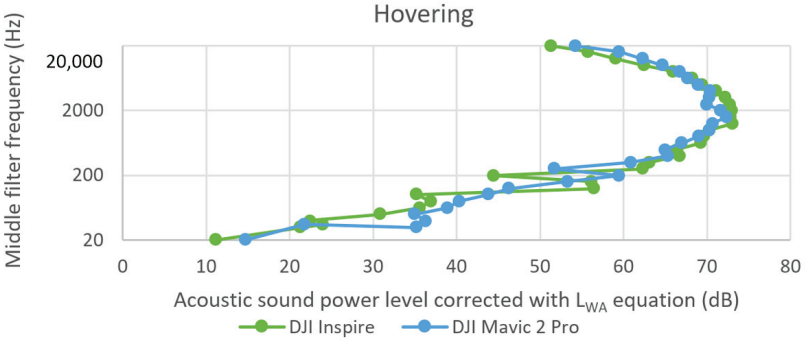

Figure 7. Comparison of L_{WA} for the two drones during hovering at 0.5 m height.

Simulation for Zilina Case Study

Based on the results, the implementation of the DJI Inspire 2 operation of weight category C2, which has the prerequisites to carry smaller goods, was considered according to cooperation with Mr. Kamenický [30]. The operation was intentionally simulated in the noise-sensitive environment of the University Hospital in Zilina. During this simulation, it was considered that DJI Inspire 2 might be able to transfer medication or blood from two pre-designated areas of the Faculty Hospital with the Polyclinic of Zilina.

The operation was simulated so that the UAV takes off from a place near the regional public health office building to a height of 50 m, the minimum height for flights over non-participants. According to the marked blue route, it will fly to the place near the building of the faculty hospital at the prescribed height and end its flight there.

The model situation was designed so that the UAV operation with one drone, DJI Inspire, with a speed of 20 kmh^{-1}, took place during the day reference time interval (12 h), defined from 6:00 to 18:00 with an average of 10 flights per hour with a total of 120 flights per day. The flight distance in this case study was 640 m. The duration of one UAV flight in the simulation was 120 s, excluding take-off and landing time.

For the visualisation of the case study, DataKustik GmbH CadnaA software was used. We started with the simulation of light rotorcraft (Robinson R22 Beta helicopter) noise propagation, which was modified according to our previously measured parameters. The aircraft database was based on the Integrated Noise Model (INM 7.0d), which is also recommended for noise mapping in the vicinity of airports. The ECAC Doc. 29 and AzB 2008 standards were alternatively considered. The noise model for the DJI Inspire 2 was modified and subsequently simulated for its flight path, taking into account the effects of atmospheric conditions and ground reflection. Both 2D and 3D visualisations were developed by the PlotDesigner function combined with the Eurosence Digital Terrain Model, including buildings and road corridors in the investigated geographical area.

Figures 8 and 9 graphically express the noise load of the selected place of operation, at a height of 1.5 m above the ground, which can be considered the ears' level. The difference between the two visualisations is as follows. The 2D visualisation contains a simulation of sound propagation in the given corridor. Figure 8 does not include residual sound, so it is possible to see that the noise load in the given area of the flight reaches the equivalent level of A-weighted sound from 40 to 45 dB. Due to the fact that the flight altitude is 50 m, the noise load at higher buildings in the area may be higher. The 3D visualisation (Figure 9) represents the resulting state of the investigated environment regarding road traffic noise, which was obtained based on the long-term measurements of the Euroakustik Ltd. Company, (Bratislava, Slovakia).

Since the noise load must be assessed based on the category of the specific area and the reference time interval, for this model situation, the operation in the first category of the territory with special noise protection during the day reference time interval is shown in which the maximum L_{Aeq} from other sources is defined by the Decree of the Ministry of Health of the Slovak Republic 549/2007 by 45 dB.

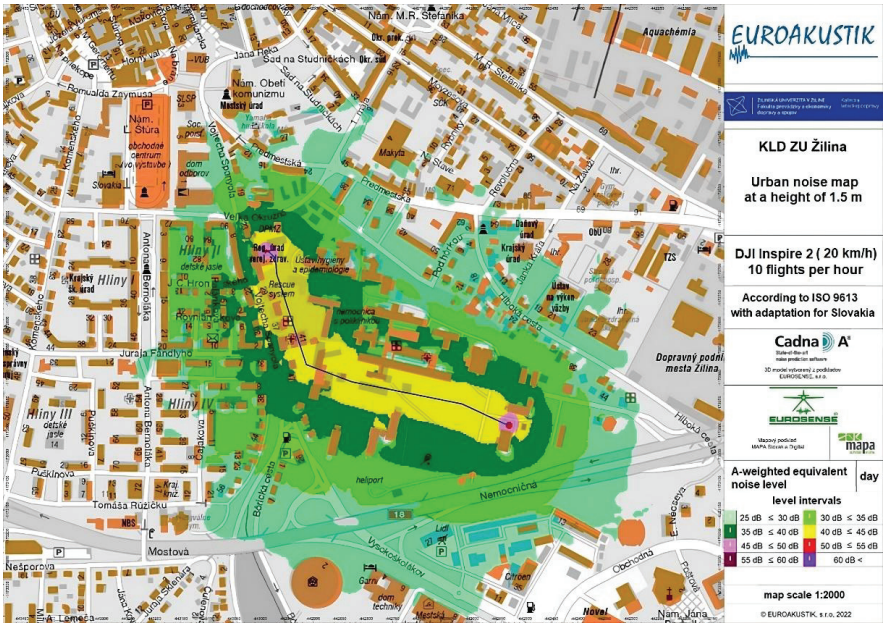

Figure 8. Noise load around flight corridor at 2D visualisation.

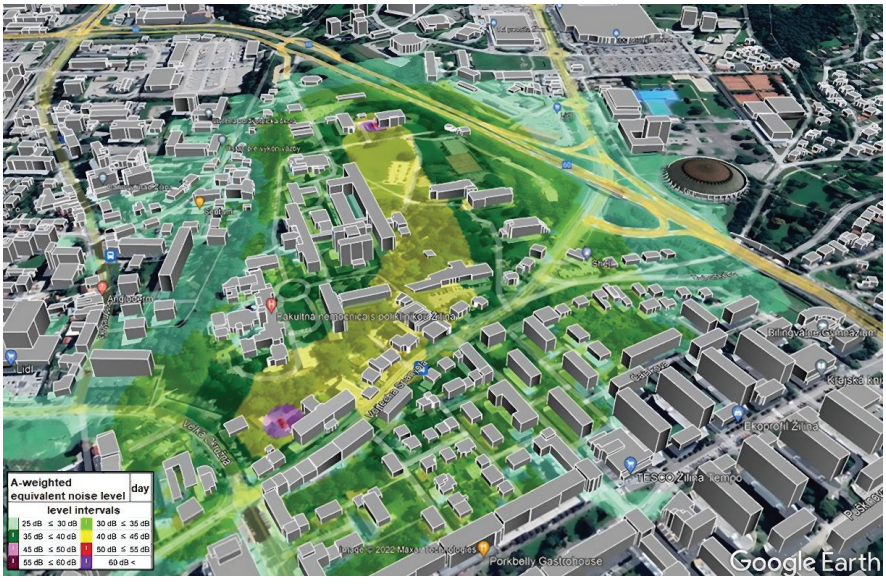

Figure 9. Noise load around flight corridor at 3D visualisation.

Concerning residual noise, it is necessary to assess the impact of whether the noise load of the examined sound source exceeds the noise load of surrounding objects such as roads. The impact of road noise was assessed in a 3D visualisation model situation in which it was found that the possible introduction of the UAV DJI Inspire 2 operation into the selected environment does not contribute to increasing the noise load.

From the model situation as well as the measured values, it is also possible to say that the commissioning of UAV DJI Inspire 2 will in no way cause health problems for people in the specific area and its short flight time over non-participants, which lasts only a few seconds, will not cause any long-term medical consequences associated with migraine headache or other problems.

4. Conclusions

This work confirmed the source of sound sources radiated by drones, which can be encountered in the hobby and commercial spheres. The precondition for the creation of the manuscript was the vision that, in the future, drones could, in increased numbers, affect people's mental health and annoyance. In this work, we confirmed the parameters of sound propagation of drones in the environment that have been estimated or known so far. Following the evaluation of frequency analyses from indoor measurements were outdoor measurements, which were not affected by excessive ambient sound undesirable to detect the noise load. These measurements were performed to determine and compare UAVs' sound power levels during hovering and overflights at increased RPM corresponding to the operation. Based on the provided data, the L_{WA} of UAVs from the C1 and C2 categories were evaluated. The corrected equivalent sound pressure levels of DJI Inspire 2 and DJI Mavic 2 Pro were measured at different speeds and frequencies. At a middle filter frequency of 160 Hz, the L_{WA} of the DJI Inspire 2 ranges from 65.1 dB to 71.9 dB, while the L_{WA} of the DJI Mavic 2 Pro ranges from 53.0 dB to 63.9 dB, indicating that the Mavic 2 Pro produces less noise than the Inspire 2 at this frequency.

Based on the measured values, we found that UAVs used for hobby flying do not exceed the limits listed in the category of other sources in the decree of the Ministry of Health of the Slovak Republic. Also, after a model simulation in the specific area of the

commissioning of the UAV DJI Inspire, no significant increase in the noise load on the population was found.

In this work, the data were provided for implementing measurements and subsequent assessment of the impact of noise on the external environment in introducing unmanned aerial vehicles into actual operation. Based on spectral analyses, a graphic model of sound propagation from an unmanned aerial vehicle could be designed in the future and, with an assessment of its radiation characteristics, placed in the map base of a specific model situation from which the consequences for broad-spectrum use would be derived.

Author Contributions: Introduction F.Š. and E.B.; literature review F.Š., M.J., and B.K.; materials and methods E.B. and F.Š.; data curation F.Š. and B.K.; results F.Š., E.B., and B.K.; writing—original draft F.Š., E.B., and M.J.; visualisation M.J. and F.Š.; internal review and editing B.K. All authors have read and agreed to the published version of the manuscript.

Funding: This publication was realized with the support of Operational Program Integrated Infrastructure 2014–2020 of the project: Intelligent operating and processing systems for UAVs, code ITMS 313011V422, co-financed by the European Regional Development Fund.

Institutional Review Board Statement: Not applicable.

Informed Consent Statement: Not applicable.

Data Availability Statement: The article includes the original contributions presented in the study. Further inquiries can be directed to the corresponding author.

Conflicts of Interest: The authors declare no conflict of interest.

Abbreviations

Abbreviations

AGL	Above ground level
EU	European Union
ISA	International standard atmosphere
ISO	International Organization for Standardization
PC	Computer
PWL	Sound power level
RMS	Root mean square
RPM	Revolutions per minute
SPL	Sound pressure level
UAS	Unmanned aircraft system
UAV	Unmanned aerial vehicle

List of symbols

λ	Wavelength
f	Frequency
Hz	Hertz
c	Phase velocity
dB	Decibel
W	Watt
m	Meter
Pa	Pascal
P_{rms}	Root mean square pressure
ρ	Density
L_{Aeq}	A-weighted equivalent continuous sound level
L_{WA}	A-weighted sound power level
L_W	Sound power level
L_p	Sound pressure level

References

1. Marte, J.E.A.; Kurtz, D.W. *A Review of Aerodynamic Noise from Propellers, Rotors, and Lift Fans*, 1st ed.; NASA: Pasadena, CA, USA, 1970; pp. 11–47.
2. Sound_Theory: Acoustics. Available online: https://acoustics.no/sound-measurement/sound-theory (accessed on 9 January 2023).
3. *ISO 3744:2010*; Acoustics—Determination of Sound Power Levels and Sound Energy Levels of Noise Sources Using Sound Pressure—Engineering Methods for an Essentially Free Field over a Reflecting Plane. ISO: Geneva, Switzerland, 2015. Available online: https://www.iso.org/standard/52055.html (accessed on 9 January 2023).
4. Longhurst, R.S. *Geometrical and Physical Optics*; Wiley: New York, NY, USA, 1967.
5. Leslie, A.; Wong, K.C.; Auld, D. Broadband noise reduction on a mini-UAV propeller. In Proceedings of the 14th AIAA/CEAS Aeroacoustics Conference (29th AIAA Aeroacoustics Conference), Vancouver, BC, Canada, 5–7 May 2008.
6. Massey, K.; Gaeta, R. Noise measurements of tactical UAVs. In Proceedings of the 16th AIAA/CEAS Aeroacoustics Conference, Stockholm, Sweden, 7–9 June 2010.
7. Sinibaldi, G.; Marino, L. Experimental analysis on the noise of propellers for small UAV. *Appl. Acoust.* **2013**, *74*, 79–88. [CrossRef]
8. Kloet, N.; Watkins, S.; Clothier, R. Acoustic signature measurement of small multi-rotor Unmanned Aircraft Systems. *Int. J. Micro Air Veh.* **2017**, *9*, 3–14. [CrossRef]
9. Papa, U.; Del Core, G.; Giordano, G. Determination of sound power levels of a small UAS during flight operations. In Proceedings of the 45th International Congress and Exposition on Noise Control Engineering (INTER-NOISE): Towards a Quieter Future, Hamburg, Germany, 21–24 August 2016; pp. 216–226.
10. Heydari, M.; Sadat, H.; Singh, R. A computational study on the aeroacoustics of a multi-rotor unmanned aerial system. *Appl. Sci.* **2021**, *11*, 9732. [CrossRef]
11. Cussen, K.; Garruccio, S.; Kennedy, J. UAV noise emission—A combined experimental and numerical assessment. *Acoustics* **2022**, *4*, 297–312. [CrossRef]
12. Senzig, D.A.; Marsan, M. UAS Noise Certification. In Proceedings of the Inter-Noise 2018 Impact of Noise Control Engineering Conference, Chicago, IL, USA, 6–29 August 2018.
13. Siljak, H.; Kennedy, J.; Byrne, S.; Einicke, K. Noise mitigation of UAV operations through a complex networks approach. In Proceedings of the INTER-NOISE and NOISE-CON Congress and Conference Proceedings, Glasgow, Scotland, 21–24 August 2022.
14. Roger, M.; Moreau, S. Tonal-noise assessment of quadrotor-type UAV using source-mode expansions. *Acoustics* **2020**, *2*, 674–690. [CrossRef]
15. Kim, D.H.; Park, C.H.; Moon, Y.J. Aerodynamic analyses on the steady and unsteady loading-noise sources of drone propellers. *Int. J. Aeronaut. Space Sci.* **2019**, *20*, 611–619. [CrossRef]
16. Schäffer, B.; Pieren, R.; Heutschi, K.; Wunderli, J.M.; Becker, S. Drone noise emission characteristics and noise effects on humans—A systematic review. *Int. J. Environ. Res. Public Health* **2021**, *18*, 5940. [CrossRef] [PubMed]
17. Park, C.H.; Kim, D.H.; Moon, Y.J. Computational study on the steady loading noise of drone propellers: Noise source modeling with the lattice Boltzmann method. *Int. J. Aeronaut. Space Sci.* **2019**, *20*, 858–869. [CrossRef]
18. Roy, M. Evaluation of Environmental Noise in urban areas: A noise pollution assessment approach. *Med. Agric. Environ. Sci.* **2022**, *2*, 21–40. [CrossRef]
19. Ramos-Romero, C.; Green, N.; Roberts, S.; Clark, C.; Torija, A.J. Requirements for drone operations to minimise community noise impact. *Int. J. Environ. Res. Public Health* **2022**, *19*, 9299. [CrossRef] [PubMed]
20. Alkmim, M.; Cardenuto, J.; Tengan, E.; Dietzen, T.; Van Waterschoot, T.; Cuenca, J.; De Ryck, L.; Desmet, W. Drone noise directivity and psychoacoustic evaluation using a hemispherical microphone array. *J. Acoust. Soc. Am.* **2022**, *152*, 2735–2745. [CrossRef] [PubMed]
21. Bian, H.; Tan, Q.; Zhong, S.; Zhang, X. Assessment of UAM and drone noise impact on the environment based on virtual flights. *Aerosp. Sci. Technol.* **2021**, *118*, 106996. [CrossRef]
22. Treichel, J.; Foerster, J.; Lieb, J.; Volkert, A. Anwendbarkeit der ISO 3744 Zur Ermittlung von Drohnengeräuschen/applicability of ISO standard 3744 for the determination of drone noise. *Lärmbekämpfung* **2023**, *18*, 50–54. [CrossRef]
23. Kennedy, J.; Garruccio, S.; Cussen, K. Modelling and mitigation of drone noise. *Vibroeng. Procedia* **2021**, *37*, 60–65. [CrossRef]
24. DACUS Research; Deliverable VALR D4.2: Brussels, Belgium. 2022. Available online: https://dacus-research.eu/wp-content/uploads/2022/10/DACUS-VALR-D4.2_00.01.01-1.pdf (accessed on 15 April 2023).
25. ICAO. *Doc 9501 Environmental Technical Manual. Procedures for the Noise Certification of Aircraft*, 3rd ed.; ICAO: Montreal, QC, Canada, 2018; Volume 3.
26. Sound Analyser NOR118. Available online: https://www.norsonic.asia/product/nor118 (accessed on 15 January 2023).
27. Sound Analyser NOR140. Available online: https://web2.norsonic.com/product_single/soundanalyser-nor140 (accessed on 15 January 2023).
28. Sound Level Meter-Analyser NOR145. Available online: https://web2.norsonic.com/product_single/sound-level-meter-nor145 (accessed on 15 January 2023).

29. DJI Store—Official Store for DJI Drones, Gimbals and Accessories (Europe). Available online: https://store.dji.com (accessed on 15 January 2023).
30. Kamenický, M.; (Euroakustik Ltd, Bratislava, Slovakia); Bujna, E.; (University of Zilina). Personal communication, 2022.

drones

MDPI

Article

Analysis of Aerodynamic Characteristics of Propeller Systems Based on Martian Atmospheric Environment

Wangwang Zhang [1,2], Bin Xu [1,2,*], Haitao Zhang [1], Changle Xiang [1], Wei Fan [1,2] and Zhiran Zhao [2]

[1] Vehicle Research Center, School of Mechanical Engineering, Beijing Institute of Technology, Beijing 100081, China; 3220205055@bit.edu.cn (W.Z.); zhanght15@tsinghua.org.cn (H.Z.); xiangcl@bit.edu.cn (C.X.); fanweixx@bit.edu.cn (W.F.)

[2] Beijing Institute of Technology Chongqing Innovation Center, Chongqing 401120, China; zhaozhiranhwe@163.com

* Correspondence: bitxubin@bit.edu.cn; Tel.: +86-13811490606

Abstract: Compared to detection methods employed by Mars rovers and orbiters, the employment of Mars UAVs presents clear advantages. However, the unique atmospheric conditions on Mars pose significant challenges to the design and operation of such UAVs. One of the primary difficulties lies in the impact of the planet's low air density on the aerodynamic performance of the UAV's rotor system. In order to determine the aerodynamic characteristics of the rotor system in the Martian atmospheric environment, a rotor system suitable for the Martian environment was designed under the premise of fully considering the special atmospheric environment of Mars, and the aerodynamic characteristics of the rotor system in the compressible and ultra-low Reynolds number environment were numerically simulated by means of a numerical calculation method. Additionally, a bench experiment was conducted in a vacuum chamber simulating the Martian atmospheric environment, and the aerodynamic characteristics of the UAV rotor system in the Martian environment were analyzed by combining theory and experiments. The feasibility of the rotor system applied to the Martian atmospheric environment was verified, and the first generation of Mars unmanned helicopters was developed and validated via hovering experiments, which thereby yielded crucial data support for the design of subsequent Mars UAV models.

Keywords: Martian atmospheric environment; low air density; compressed; ultra-low Reynolds number; aerodynamic characteristics; vacuum chamber experiment

Citation: Zhang, W.; Xu, B.; Zhang, H.; Xiang, C.; Fan, W.; Zhao, Z. Analysis of Aerodynamic Characteristics of Propeller Systems Based on Martian Atmospheric Environment. *Drones* **2023**, *7*, 397. https://doi.org/10.3390/drones7060397

Academic Editors: Andrzej Łukaszewicz, Wojciech Giernacki, Zbigniew Kulesza, Jaroslaw Alexander Pytka and Andriy Holovatyy

Received: 7 May 2023
Revised: 30 May 2023
Accepted: 8 June 2023
Published: 15 June 2023

1. Introduction

In the solar system, Mars and Earth have a high degree of similarity, with both having obvious changes in seasons, atmosphere and water. As such, the exploration of Mars is not only conducive to the exploration of the origin of life, but also has a considerable significance in respect of expanding human living space. Peijian Ye and Jing Peng [1] summarized some activities and plans for human deep space exploration, including the exploration of Mars, and introduced the significance and development process of deep space exploration; Weiren Wu and Dengyun Yu [2] elaborated on the development and future key technologies of deep space exploration, and provided a detailed introduction to the exploration process of the moon and Mars. In the past, Mars rovers or orbiters have been used for the exploration of Mars, but both have obvious drawbacks. Since the surface of Mars is full of hills and ravines, which is a major obstacle for rover exploration, there is a considerably limited exploration range and slow exploration speed. With regard to orbiters, due to the high distance from the surface of Mars, there are difficulties in exploring the surface of Mars in-depth. Due to the aforementioned factors, airborne platforms are particularly significant, owing to the higher exploration speed, wider detection range, and broader field of view. Further, areas that are inaccessible to Mars rovers can be accessed, and superior imaging and sensing resolution can be provided compared to orbiters. Anubhav

Datta [3] described the necessity of using a Mars unmanned aerial vehicle and described the design of an autonomous rotor vehicle (MARV) for Mars exploration. Thus, when considering such factors comprehensively, the airborne platform appears to be the most efficient means of detection.

Revolutionary changes have taken place in the future of Mars exploration. On 9 April 2021, the American Mars Helicopter "MH" successfully landed on Mars, completed the first test flight of human beings on Mars, and unveiled the new chapter of Mars exploration—Cheng, C. [4]. Ruiz, M.C. [5] and Balaram, J. [6], respectively, described the Mars helicopter "MH" to varying degrees, and based on this, conducted deeper research on the aerodynamic characteristics of the Mars propeller. The 1.8 kg "MH" Mars UAV is an unloaded aerodynamic demonstrator, the main purpose of which is to verify the possibility of flying UAVs in the Martian atmosphere and to facilitate understanding of the basic aeronautics of Mars—this is introduced in Balaram, J.'s [7] article; Pipenberg T.B. [8] described the design and testing process of the Mars helicopter rotor system, including the aerodynamic performance, structural strength, vibration characteristics, control strategy, and environmental adaptability of the rotor. To further scientific exploration, the air dynamic performance of Mars rotor systems needs to be more explored.

In recent years, increasing numbers of countries and institutions have begun to explore Mars UAV systems. Due to the unique atmospheric environment of Mars, the rotor blades of Mars UAVs rotate under low Reynolds numbers and compressible flow conditions, which poses new challenges for the design of Mars rotor systems and is a relatively new field for aerodynamics, with few numerical simulations and experimental data currently available. Takaki et al. [9] simulated and calculated the lift–drag characteristics of various airfoils in the Martian environment and found that the effect of a low Reynolds number on the lift–drag characteristics of airfoils was much greater than that of a Mach number on the lift–drag characteristics of airfoils; Shrestha et al. [10] conducted hovering performance experiments on a 200 g Martian coaxial helicopter propeller in a vacuum chamber, and the quality factor of the propeller at different Reynolds numbers was further explored; Kakeru et al. [11] studied the aerodynamic characteristics of an airfoil in the propeller slipstream at low Reynolds numbers and elucidated the effect of propeller slipstream on the control surface efficiency through aerodynamic measurements and particle image velocimetry measurements; Benjamin et al. [12] presented a detailed description of the rotor system and landing gear system of the MH Mars helicopter; KONING et al. [13] calculated the instability points, laminar separation points, and excess points on the surface of the C81Gen airfoil to approximate the two-dimensional rotor boundary layer state during hovering, and used the results on turbulence modeling in fluid dynamics; Kunz et al. [14], Liu et al. [15], and Bohorquez et al. [16] optimized the propeller airfoil for Re < 10,000 based on the theory of lobe element momentum; Oyama et al. [17] used finite element simulations to conclude that unconventional airfoils with considerably thin airfoil thickness and large airfoil curvature can significantly improve the lift-to-drag ratio and mechanical efficiency of Mars propellers in the Martian atmospheric environment; the Ames Research Center of NASA provided a performance comparison between several low Reynolds number airfoils, finding that the cambered airfoil can outperform conventional airfoils [18]; T. Désert analyzed the effects of Reynolds numbers and Mach numbers on the flow through airfoils in a low Reynolds number compressible flow, and proved the significant effect on flow separation and subsequent wake shape [19].

While the aerodynamics of rotor systems in the Martian atmosphere have been investigated in several studies, most rely on numerical simulations, with few experiments conducted to replicate the vacuum conditions of the Martian environment. Such experiments still fall short in comparison to the distant and unknown Martian environment. In order to further explore the aerodynamic characteristics of the propeller in the Martian atmospheric environment, the special atmospheric environment of Mars was fully considered in the present study. In addition, a lightweight Mars UAV rotor system was designed, and strength and stiffness analyses of the lightweight propeller were combined with finite

element software. The method of combining numerical simulation calculations and simulations of the vacuum chamber bench experiments of the Martian atmospheric environment was used to further study the aerodynamic characteristics of the rotor system in the Martian atmospheric environment, analyzed the influence of different Reynolds numbers and Mach numbers on the aerodynamic performance of Mars propellers, and established a Blade Element Theory inflow ratio model for the Martian atmospheric environment, so as to provide more sufficient data support for the design of Mars UAVs.

2. Materials and Methods

2.1. Dynamic Conditions in the Atmospheric Environment of Mars

2.1.1. Martian Atmosphere

Compared with the atmospheric environment of the Earth, the Martian atmospheric environment is undoubtedly much worse in the drone flight environment, posing a significant challenge to the design of Mars UAVs. The atmospheric density of Mars is about 1/80 of that of the Earth, which has been identified as the biggest obstacle to the design of Mars UAV rotor systems. Although the gravity acceleration on Mars is only 1/3 of that of the Earth, the impact of the low air density cannot be offset. At the same time, the sound speed on Mars is much lower than that on Earth, further limiting the tip speed of the propeller and increasing the difficulty of propeller design. The proportion of carbon dioxide in the Martian atmosphere is as high as 95%, but because the thinner atmosphere cannot bind the heat energy of the sun, there is a particularly low temperature on Mars. Notably, the lowest temperature reaches minus 140 °C, while the highest temperature is only 20 °C. Low temperature is another challenge that needs to be considered for Mars UAVs, especially for the electronic components inside, which need to be able to withstand low temperatures and other harsh environments. Moreover, in the design of Mars UAV avionics systems, a thermal insulation system needs to be set up so that the electronic components on the Mars UAV can be properly insulated, and the thermal insulation system needs to consume a lot of electric energy, which greatly shortens the endurance of the Mars UAV. As previously reported, the US "MH" Mars UAV has about 2/3 of the electrical energy for internal system insulation, and only 1/3 of the electrical energy is used for flight. Owing to the condensation and sublimation of the polar CO_2 of Mars, the atmospheric environment on Mars shows seasonal changes. In fact, these comparisons between the Martian and Earth atmospheric environments are presented in Braun, Refs. [20,21] Detailed descriptions were provided in all studies. Table 1 presents a comparison of the atmospheric environment characteristics of Mars and Earth.

Table 1. Characteristics of Martian and Earth's Atmospheric Environment.

Features	Mars	Earth
Acceleration of gravity (m/s^2)	3.72	9.78
Atmospheric pressure (Pa)	756	101,300
Air density (kg/m^3)	0.0167	1.22
Mean temperature (°C)	−63	15
Sound velocity (m/s)	227	340
Atmospheric dynamic viscosity (kg/(m·s))	1.289×10^{-5}	1.789×10^{-5}
Gas constants (J/kg/K)	188	287
Specific heat capacity ratioγ	1.29	1.40
Molar mass (g/mol)	44.01	28.96

2.1.2. Air Dynamics under Low Reynolds Numbers

Due to the relatively thin density of the atmosphere on the surface of Mars, a simple calculation of the aerodynamic conditions in the Martian atmospheric environment is needed before the propeller design so that the numerical simulation can be conducted more accurately. The Knudsen number (Kn) [22] is the ratio of the mean free path of gas

molecules to the characteristic scale. In rarefied gas mechanics, the size of the Knudsen number is often used to determine whether a fluid is suitable for the continuity hypothesis. Generally, in fluid mechanics, when $Kn < 0.01$, the flow of gas belongs to a continuous medium flow, and the Navier–Stokes equation can be used. The Knudsen number can be calculated using Equation (1):

$$Kn = \frac{kT}{\sqrt{2}\pi\sigma_1{}^2 PL} \tag{1}$$

where k is the Boltzmann constant, with a value of $1.3806498 \times 10^{-23}$; T is the thermodynamic temperature; σ_1 is the particle diameter, because 95% of the Martian atmospheric environment is carbon dioxide, so the diameter of carbon dioxide can be used instead of the diameter of the Martian atmosphere example diameter; P is the total pressure; and L is the characteristic length, with the propeller diameter considered here being 1.21 m. The indicators present in the Martian atmosphere suggest that the Knudsen number is significantly below 0.01, indicating that the continuity assumption is applicable to the Martian atmospheric environment.

2.1.3. Effect of Reynolds Number on the Aerodynamic Performance of Mars Propellers

The low air density and relatively small rotor size in the Martian atmosphere result in a low Reynolds number for the propeller, and the general chord-based Reynolds number range is Re = 10^3~10^4—this is reflected in Desert [23] research. There is a scarcity of research on Reynolds numbers in such a range. However, Ref. [24] research suggests that the flight of insects and birds on Earth notably falls within such range. In the Earth environment, propellers generally operate in a Reynolds number range greater than 10^4, with low-speed propellers corresponding to lower Mach numbers, and high-speed propellers corresponding to higher Mach numbers and Reynolds numbers. The common Reynolds number and Mach number research range is shown in Figure 1 [25–27].

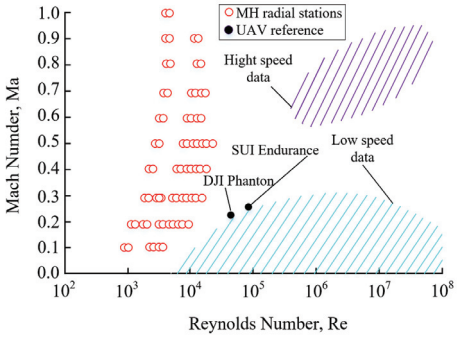

Figure 1. General Mach–Reynolds number research areas.

A low Reynolds number leads to a significant decrease in the lift-to-drag ratio of Martian propellers, which increases the difficulty of flight mainly because a low Reynolds number increases the viscous drag of the blades, resulting in a significant increase in the power consumed by the propeller [10]. G. K. Ananda [28] developed the external platform force balance device LRN-FB, which solved the deficiencies in the field of low Reynolds number aerodynamics and ten flat wings were tested at a low Reynolds number (60,000~160,000); the results show that no hysteresis phenomenon is observed on all flat wings, and the slope of the thrust curve shows a strong Reynolds number effect.

To summarize the relationship between the airfoil lift–drag ratio and Reynolds number in the larger Reynolds number range, McMasters and Henderson summarized the experimental results of the aerodynamic characteristics of different airfoils, as shown in Figure 2 [25]. The critical point for the Reynolds number is Re = 10^5. When Re < 10^5, rough airfoils exhibit better aerodynamic performance than smooth airfoils, which is due

to the contribution of roughness in promoting boundary layer transition and slowing down laminar flow separation on the rough airfoil surface. Controlled turnaround is the key to mitigating the adverse effects of air bubbles at laminar flow separation points and designing airfoils in low Reynolds number regions. Therefore, when designing Martian propellers, the appropriate roughness of the propeller surface is conducive to improving the aerodynamic performance of Mars propellers.

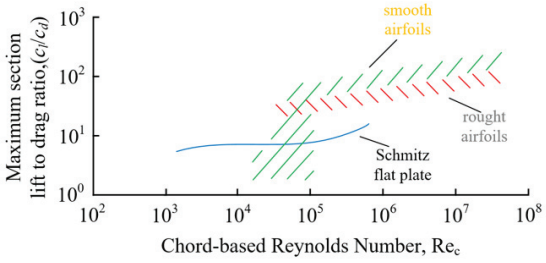

Figure 2. Maximum section lift-to-drag ratio versus Reynolds number.

2.2. Mars UAV Rotor System Design

The unique atmospheric environment on Mars has brought new challenges to the design of propellers, and propellers suitable for the Earth's atmospheric environment will no longer be suitable for the Martian atmosphere. Okamoto et al. [29] analyzed various airfoils when the Reynolds number was less than 10^4 and found that the airfoil suitable for such a low Reynolds number range had a thin airfoil, a sharp leading edge, and even an insect-like corrugated shape. In a study conducted by Hervé et al. [30], it was determined that a corrugated wing demonstrated superior performance as a flapping wing, but was not suitable for rotor applications, particularly in the hovering state. Thus, for hovering in the Martian atmospheric environment, airfoils with thin profiles and high camber are typically favored. In view of such circumstances, the clf5605 airfoil developed by AeroVironment was selected as the base airfoil for the propeller design in the present study.

In order to maximize the efficiency of the Martian propeller, the minimum energy loss method was used to design the propeller. Figure 3 shows the blade element force analysis diagram of the clf5605 airfoil, in which *L*, *D*, *T*, and F are the lift, drag, thrust, and tangential forces of the airfoil, respectively. *W* and W_1 are the combined velocity and induced combined velocity; V_a, V_t, and V' indicate axial inducted speed, circulation induced speed and induced angle of attack, respectively; α, β, φ_0, and φ, respectively, represent the actual angle of attack, interference angle, geometric inflow angle, and actual inflow angle.

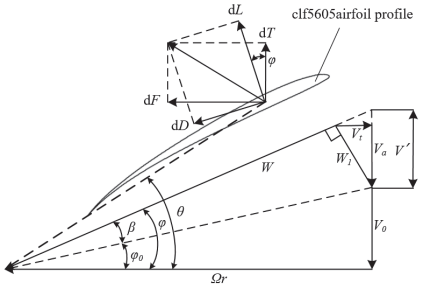

Figure 3. Force analysis of blade element.

The actual inflow angle φ can be calculated using Equation (2):

$$\tan\varphi = \frac{V_0 + V_a}{\Omega r - V_t} = \frac{V_t}{V_a} = \frac{V' \cos^2\varphi}{V' \cos\varphi \sin\varphi} \tag{2}$$

When the amount of the blade element circulation at the radial position r of the propeller blade increases $\Delta\Gamma$, the thrust and torque of the corresponding propeller will increase ΔT and ΔM. The ratio of the propeller's useful work to absorbed energy can then be calculated using Equation (3):

$$k = \frac{V_0 \Delta T}{\Omega \Delta M} \tag{3}$$

$$\begin{cases} \Delta M = \rho \Delta\Gamma (V_0 + V_a) r dr \\ \Delta T = \rho \Delta\Gamma (\Omega r - V_t) dr \end{cases} \tag{4}$$

By substituting Equation (4) into Equation (3) and then combining Equation (2), the following can be obtained:

$$k = \frac{V_0 \Delta T}{\Omega \Delta M} = \frac{V_0}{\Omega} \frac{(\Omega r - V_t)}{(V_0 + V_a) r} = \frac{V_0}{V_0 + V'} \tag{5}$$

The minimum energy loss is required to be constant along the blade k distribution [31]. From Equation (5), the induced angle of attack distribution along the blade is a constant value, but the induced pitch corresponding to each blade element section is different. First, the size of the induced pitch needs to be determined. The total thrust force of the propeller can be calculated using Equation (6):

$$T = \int_{r\min}^{r\max} f \frac{4\pi r \rho}{N_b} \left(V_0 + V' \cos^2\varphi \right) V' \cos^2\varphi dr \tag{6}$$

The induced angle of attack can be obtained by iterating Equation (6). Then, according to the Kutta–Joukowski theorem, the distribution of circulation quantities can be obtained:

$$\Gamma(r) = \frac{1}{2} W C_1 b = f \frac{4\pi r}{N_b} V' \cos\varphi \sin\varphi \tag{7}$$

Through iterating Equation (7), the chord length and twist angle distribution at different values of radial r of the impeller can be obtained. Then, the obtained chord length and torsion angle can be smoothed to obtain the torsion angle distribution and chord length distribution in different parts of the Martian propeller, as shown in Figure 4.

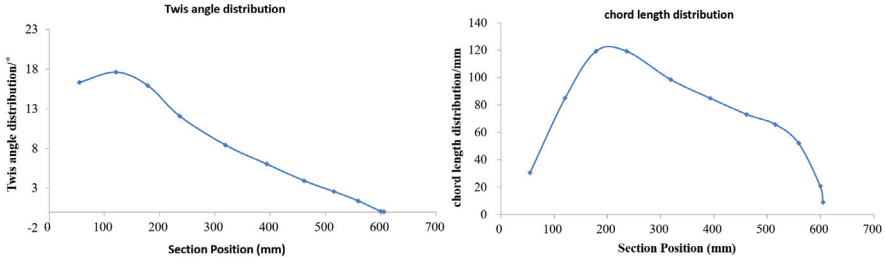

(**a**) (**b**)

Figure 4. Torsion angle and chord length distribution of different parts of propeller: (**a**) twist angle distribution; (**b**) chord length distribution.

The shape of the final propeller is shown in Figure 5.

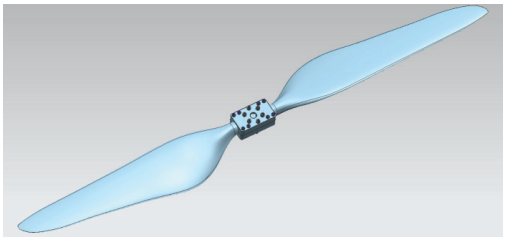

Figure 5. Propeller model.

2.3. Numerical Simulation

2.3.1. Unsteady Compressible Streams

In fluid mechanics, the weak form of the mass conservation equation affected by the momentum conservation equation and the state equation is equivalent to the strong form of the governing equation of unsteady compressed flow [32].

The weak form of the mass conservation equation can be calculated using Equation (8):

$$\iint \delta p dV \mathrm{d}t = \iint \left(\frac{\partial \phi}{\partial t} + \frac{1}{2}v_j^2\right)^{1/(k-1)} \delta \left(\frac{\partial \phi}{\partial t} + \frac{1}{2}v_j^2\right)^{1/(k-1)} \mathrm{d}V \mathrm{d}t = 0 \tag{8}$$

where p is pressure; V is volume; ϕ is velocity potential; v_j is the component of velocity in the j direction; k is the ideal gas constant; and t is time.

An equation of the state for an ideal gas can be calculated using Equation (9):

$$\frac{p}{p_0} = \left(\frac{\rho}{\rho_0}\right)^k \tag{9}$$

where p is the pressure; ρ is the gas density; and $(\cdot)_0$ is the initial state.

The momentum equation can be calculated using Equation (10):

$$\frac{\partial v_i}{\partial t} + v_j \frac{\partial v_i}{\partial x_j} = \frac{1}{\rho}\frac{\partial p}{\partial x_i} \tag{10}$$

where v_i is the ith component of velocity; x_i is the ith component of the spatial coordinates; x_j is the jth component of the spatial coordinates; p is pressure; and t is time. v_i can be calculated as follows:

$$v_i = \frac{\partial \phi}{\partial x_i}, v_j = \frac{\partial v_j}{\partial x_j} \tag{11}$$

By bringing Equation (11) into Equation (10) and then integrating x_i, one has:

$$\int \frac{1}{\rho}\mathrm{d}p = -\frac{\partial \phi}{\partial t} - \frac{\partial \phi}{\partial x_j}\frac{\partial \phi}{\partial x_j} = -\frac{\partial \phi}{\partial t} - \frac{1}{2}v^2 \tag{12}$$

According to Equation (9), it can be obtained that:

$$\int \frac{1}{\rho}\mathrm{d}p = (1 - \frac{1}{k})\left(\frac{p_0^{1/k}}{\rho_0}\right) p^{(1-\frac{1}{k})} = c p^{(1-\frac{1}{k})} \tag{13}$$

where c is a constant. Therefore, substituting Equation (13) into Equation (12) and solving for pressure:

$$p = -\left(-\frac{1}{c}\right)^{k/(k-1)} \left(\frac{\partial \phi}{\partial t} + \frac{1}{2}v_j^2\right)^{k/(k-1)} \tag{14}$$

One can drop the constant coefficient $-\left(-\frac{1}{c}\right)^{k/(k-1)}$, then, δp can be calculated using Equation (15):

$$\delta p = \delta\left(\frac{\partial \phi}{\partial t} + \frac{1}{2}v_j^2\right)^{k/(k-1)} = \left(\frac{k}{k-1}\right)\left(\frac{\partial \phi}{\partial t} + \frac{1}{2}v_j^2\right)^{1/(k-1)}\delta\left(\frac{\partial \phi}{\partial t} + \frac{1}{2}v_j^2\right) \tag{15}$$

For the convenience of the later calculations, A can be introduced, which is defined as follows:

$$\begin{cases} A = \left(\frac{\partial \phi}{\partial t} + \frac{1}{2}v_j^2\right)^{1/(k-1)} = \left(-\frac{a^2}{k-1}\right)^{1/(k-1)} \\ a^2 = -(k-1)\left(\frac{\partial \phi}{\partial t} + \frac{q_i^2}{2}\right) \\ q_i = \frac{\partial \phi}{\partial x_i} \end{cases} \tag{16}$$

where a is the speed of sound. Equation (16) can be brought into Equation (15) and further into Equation (8), so as to obtain the following:

$$\begin{aligned} \iint \delta p dV dt = \iint \left(-\tfrac{a^2}{k-1}\right)^{1/(k-1)} \frac{\partial^2 \phi}{\partial x_j^2} - \iint \tfrac{1}{k-1}\left(\tfrac{a^2}{1-k}\right)^{k/(1-k)}\left(\tfrac{\partial^2 \phi}{\partial t^2} + \tfrac{\partial \phi}{\partial x_i}\tfrac{\partial^2 \phi}{\partial x_j \partial t}\right)\delta\phi dt dV \\ -\iint \left(\tfrac{1}{k-1}\right)\left(\tfrac{a^2}{1-k}\right)^{k/(1-k)} \tfrac{\partial \phi}{\partial x_j}\left(\tfrac{\partial^2 \phi}{\partial t \partial x_j} + \tfrac{\partial \phi}{\partial x_i}\tfrac{\partial^2 \phi}{\partial x_i \partial x_j}\right)\delta\phi dt dV \end{aligned} \tag{17}$$

Assuming that $\delta\phi$ is arbitrary, the following is established:

$$\begin{aligned} \tfrac{1}{k-1}\left(\tfrac{a^2}{1-k}\right)^{k/(1-k)}\left(\tfrac{\partial^2 \phi}{\partial t^2} + \tfrac{\partial \phi}{\partial x_j}\tfrac{\partial^2 \phi}{\partial x_j \partial t}\right) - \left(-\tfrac{a^2}{k-1}\right)^{1/(k-1)}\tfrac{\partial^2 \phi}{\partial x_j^2} \\ +\left(\tfrac{1}{k-1}\right)\left(\tfrac{a^2}{1-k}\right)^{k/(1-k)}\tfrac{\partial \phi}{\partial x_j}\left(\tfrac{\partial^2 \phi}{\partial t \partial x_j} + \tfrac{\partial \phi}{\partial x_i}\tfrac{\partial^2 \phi}{\partial x_i \partial x_j}\right) = 0 \end{aligned} \tag{18}$$

After multiplying Equation (18) by $-(1-k)^{1/(1-k)}a^{-2/(1-k)}$, under the action of the equation of state and the equation of conservation of momentum, the unsteady, compressible, potential flow equation is:

$$\frac{1}{a^2}\frac{\partial^2 \phi}{\partial t^2} + \frac{2}{a^2}\frac{\partial \phi}{\partial x_j}\frac{\partial^2 \phi}{\partial x_j \partial t} - \frac{\partial^2 \phi}{\partial x_j^2} + \frac{1}{a^2}\left(\frac{\partial \phi}{\partial x_j}\frac{\partial \phi}{\partial x_i}\frac{\partial^2 \phi}{\partial x_i \partial x_j}\right) = 0 \tag{19}$$

2.3.2. Numerical Simulation Calculations

The current cost of sending UAVs to Mars is considerably expensive, therefore, before proceeding to Mars propeller manufacturing, extensive finite element simulations are required to ensure the dynamics of the propeller system. Since there are difficulties in determining the aerodynamic properties of propellers designed for the Martian environment using purely empirical formulas, Fluent software was used to perform aerodynamic analysis of the Mars propeller. In the numerical simulation, different angles of attack and rotational speeds of the Mars propeller were considered, and the range of angles of attack was taken from 0° to 12°, being calculated every 2° (the results were only taken from 0° to 10° due to the poor convergence of the calculation results at 12° angle of attack). Meanwhile, the range of rotational speeds could be roughly derived from the speed of sound and Mach number of the Martian atmosphere. The range of rotational speeds can be calculated using Equation (20):

$$n < \frac{Ma * a * 60}{D * \pi} \tag{20}$$

where n is the rotational speed in RPM (Revolutions Per Minute); Ma is the Mach number, which is taken as 0.85 to avoid transonic effects; a is the speed of sound in the Martian atmosphere, which is taken as 230 m/s; and D is the propeller diameter, which is taken as 1.21 m. The maximum rotational speed of the designed Mars propeller was calculated to be 3087 RPM. Because the air density on Mars is low, when the speed is small, the lift

provided by the propeller is small; therefore, the simulated speed was selected as 1200 RPM to 3000 RPM, being calculated every 200 RPM.

In order to simulate the Martian atmosphere as much as possible, the atmospheric density was set to the atmospheric density of Mars (0.0167 kg/m^3). Figure 6 shows the scheme of the whole computational domain. The whole computational domain is divided into a static domain (a) and a rotating domain (b). These two domains are connected by three pairs of interfaces, namely interface-prop-up and interface-far-up, interface-prop-down and interface-far-down, and interface-prop-wall and interface-far-wall. The static domain is a cylinder with a diameter of 20D and a height of 15D, which is used to simulate the outflow field of the Martian propeller. Figure 6c shows the mesh details of the propeller surface and the blade tip near the wall of the rotating domain. It can be seen that the leading and trailing edges of the propeller and the tip of the blade near the rotating field have a more dense grid, which is done to have more accurate calculation results. Numerical calculations of lift coefficients and power coefficients were performed for the Mars propeller at different angles of attack and rotational speeds, and the results were compared and analyzed with the results obtained from the simulated Mars atmospheric bench experiments in Section 3.2.

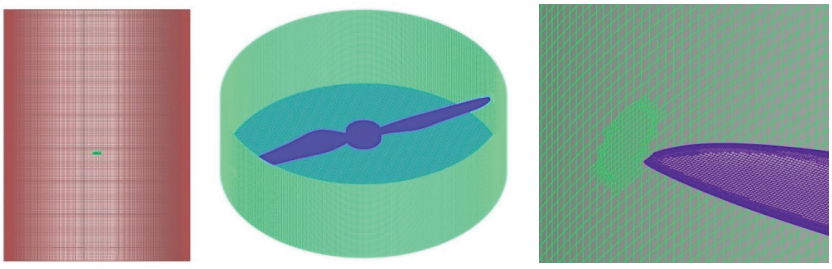

(**a**) (**b**) (**c**)

Figure 6. Mars propeller three-dimensional mesh: (**a**) static zone; (**b**) rotating zone; (**c**) blade tip area mesh.

In order to investigate the influence of the number of grids on the calculation results, 3 different densities of grids were selected, and then the thrust and torque of the propeller were calculated at a 0° angle of attack and 3000 RPM under the Martian atmosphere. The calculation results are shown in Table 2.

Table 2. Results of the grid dependency test for prototype.

	Mesh Density (10^4)	Simulation Time (h)	Thrust Error	Torque Error
Coarse	1237	*15*	5.77%	6.228%
Medium	2506	*26*	0.985%	2.076%
Fine	5032	*38*	0%	0%

Numerical simulation analysis was conducted by means of the same method for the aforementioned three grid density models. From the results, an observation can be made that the difference between the results calculated by the medium density grid and the high density grid was considerably small, while the error of the results calculated by the low density grid was relatively large. As such, considering the calculation accuracy and calculation efficiency, the medium density grid was ultimately chosen for the numerical calculation. Figure 7 visualizes the vortex structure of the flow field at a high speed rotation of the propeller with a 0° angle of orientation in the Martian atmospheric environment by extracting the equivalent surface of the Q-criterion = 5000, and also shows the pressure (Unit: Pa) distribution on the propeller blade. It can be seen that as the propeller speed increases, the vortex volume generated at the tip of the propeller blade becomes larger

and thicker below the blade, and at the same time, the vortex core increases. The pressure contour diagram shows that the pressure on the propeller blade increases as the speed increases, and the closer the tip, the greater the negative pressure, while the maximum positive pressure is found at the leading edge of the blade near the tip, which is due to the interaction with the air when the propeller rotates at high speed.

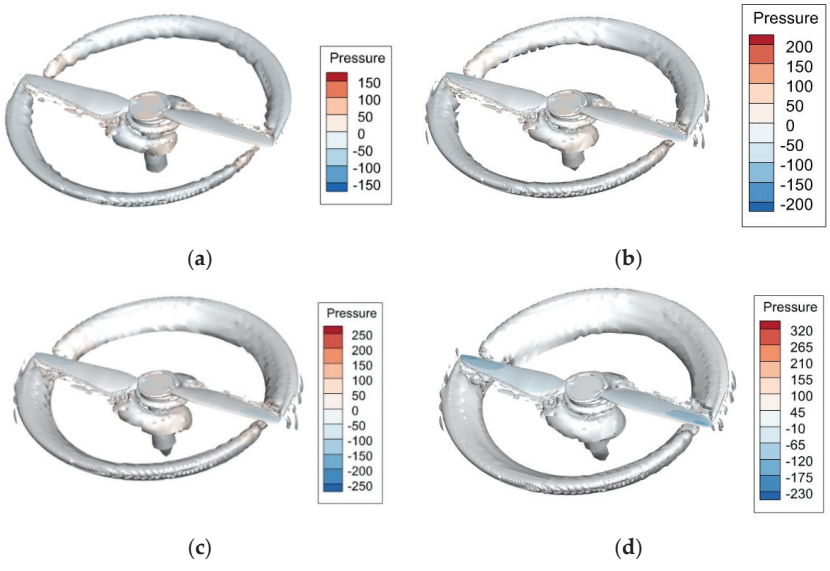

Figure 7. Diagram of propeller vorticity structure on the iso−surface of the Q−criterion = 5000 in Martian: (**a**) 2000 RPM; (**b**) 2400 RPM; (**c**) 2600 RPM; (**d**) 3000 RPM.

2.4. Lightweight Design and Strength Calibration of Mars Propellers

The low air density and low Reynolds number of the Martian atmospheric environment poses a significant challenge in propeller design and fabrication. The low density reduces the available thrust for a given size rotor and increases the power required to fly the vehicle relative to the Earth's atmospheric environment. Thus, as a critical factor, the overall weight of the vehicle must be kept as low as possible. Obviously, reducing the weight of the propeller is more simple and logical than reducing the weight of the electronics. To ensure optimal performance in the Martian environment, a propeller must possess sufficient lift-to-weight ratio, which necessitates a lightweight design. Consequently, the pursuit of reduced weight has emerged as a significant challenge in the development and production of propellers intended for Mars.

In order to reduce the weight of the propeller, a foam sandwich structure was adopted, with the propeller having foam in the middle and the outside being covered with carbon fiber fabric, as shown in Figure 8a. The yellow part is the PMI (Polymethacrylimide) foam core part, and the gray part is the T300 carbon fiber covered part. The surface area of the whole propeller is 0.098 m^2, and local reinforcement was performed at the root of the propeller to ensure the strength of the propeller. The density of the fabric prepreg is 1600 kg/m^3, the thickness of the single layer is 0.2 mm, and the lay-up direction is 0°/90°/45°. The total weight of a single propeller was calculated to be 100 g when laying 3 layers of carbon fiber fabric.

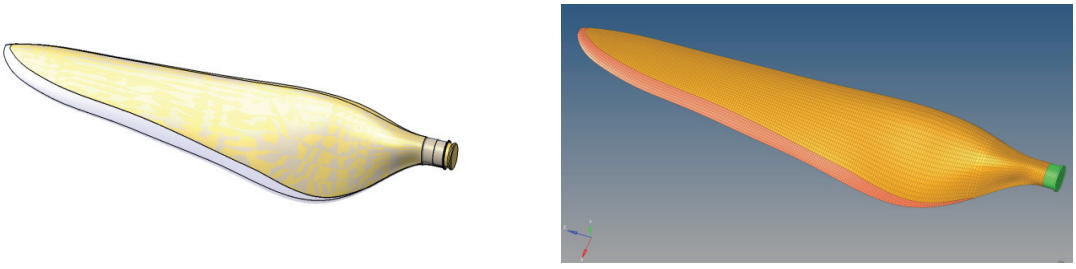

(**a**) (**b**)

Figure 8. Propeller structure and the finite element model: (**a**) structure diagram of the foam sandwich of the Mars propeller; (**b**) finite element model of the Mars propeller.

Although the foam sandwich structure largely reduced the weight of the Mars propeller, the strength and stiffness of the propeller were inevitably weakened while satisfying the lightweight requirements. Thus, the propeller must be calibrated for strength and other aspects before manufacturing. In this study, the HyperMesh and Nastran finite element software were used for joint simulation to check the deformation and failure factor of the propeller. The finite element model of the propeller is shown in Figure 8b.

The aerodynamic force (aerodynamic force at 10° angle of attack, 3000 RPM) obtained from aerodynamic simulation of the propeller under the Martian atmosphere was loaded onto the surface of the propeller, and the deformation of the propeller under the Martian atmosphere (as shown in Figure 9a) and the failure factor of the carbon fiber layup on the surface of the propeller (as shown in Figure 9b) could be obtained. From the deformation diagram, an observation can be made that the main deformation of the propeller was concentrated in the tip part of the propeller blade, and the maximum deformation was 19.8 mm, which was only 3.3% of the radius of the Mars propeller. As such, the stiffness of the propeller meets the requirements. As the trailing edge part of the propeller is considerably thin and is seriously affected by the trailing vortex during high speed rotation, the failure factor of the trailing edge part was also the largest. From the simulation results, the maximum failure factor was 0.11, much less than 1, meaning that the strength of the blade had a large surplus.

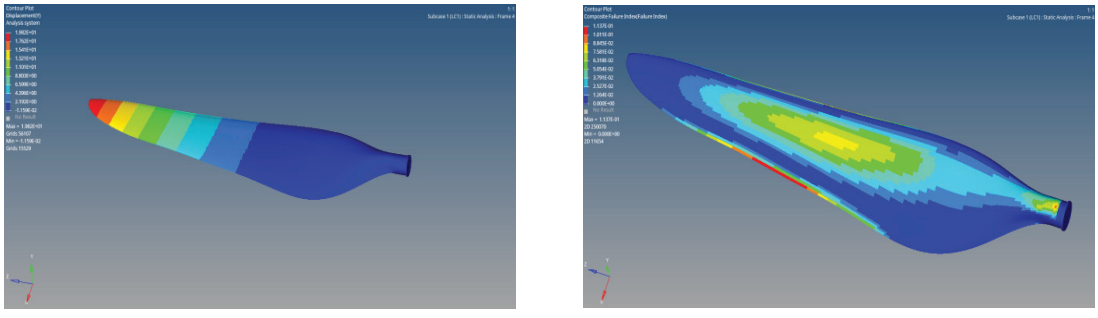

(**a**) (**b**)

Figure 9. Finite element analysis results of Mars Propeller: (**a**) axial direction deformation of the Mars propeller; (**b**) failure factors of the Mars propeller.

2.5. First-Generation Mars UAV Flight

The harsh Martian atmosphere poses a significant challenge in the design of unmanned helicopters, while the spatial size of the lander further limits the size of the Mars UAV. A reasonable structural layout can satisfy the structural size while minimizing the weight of

the UAV. The co-axial twin propellers were chosen as the initial structure form for the Mars UAV, as illustrated in Figure 10.

Figure 10. Mars unmanned helicopter model.

2.5.1. Dynamical Equations and Equations of Motion of an Unmanned Helicopter on Mars

Assuming that the Mars unmanned helicopter is a rigid body, ignoring the Martian curvature, and considering the Martian coordinate system as an inertial coordinate system, the equations of motion of the Mars unmanned helicopter can be divided into two parts to describe the translational and rotational motion, and according to the Newton-Euler equation, the translational motion of the Mars unmanned helicopter can be expressed as:

$$\dot{\boldsymbol{V}}=\frac{\boldsymbol{F}}{\boldsymbol{m_b}}-\boldsymbol{\omega_b}\times\boldsymbol{V_b} \tag{21}$$

$$\dot{\boldsymbol{\omega}}_{\boldsymbol{b}}=\boldsymbol{I}^{-1}[\boldsymbol{M}-\boldsymbol{\omega_b}\times(\boldsymbol{I}\boldsymbol{\omega_b})] \tag{22}$$

where m_b indicates the total mass of the Mars unmanned helicopter; $\boldsymbol{V_b} = (\boldsymbol{u},\boldsymbol{v},\boldsymbol{w})^{\boldsymbol{T}}$ represents the linear velocity of the Mars unmanned helicopter; $\boldsymbol{\omega_b} = (\boldsymbol{p},\boldsymbol{q},\boldsymbol{r})^{\boldsymbol{T}}$ represents the angular velocity of the Mars unmanned helicopter; $\boldsymbol{F}$ and $\boldsymbol{M}$ represent the combined external force and moment of the Mars unmanned helicopter; and I indicates the moment of inertia of the Mars unmanned helicopter.

$$\boldsymbol{I}=\begin{pmatrix} I_{xx} & -I_{xy} & -I_{xz} \\ -I_{xy} & I_{yy} & -I_{yz} \\ -I_{xz} & -I_{yz} & I_{zz} \end{pmatrix} \tag{23}$$

Due to the peculiarities of the Martian unmanned helicopter in structure, the belief of the present authors is that the symmetry in both the transverse plane and the longitudinal plane had $I_{xy} = I_{xz} = I_{yz} = 0$, and Equation (24) can be converted to:

$$\boldsymbol{I}=\begin{pmatrix} I_{xx} & 0 & 0 \\ 0 & I_{yy} & 0 \\ 0 & 0 & I_{zz} \end{pmatrix} \tag{24}$$

By bringing the linear velocity, angular velocity, and resultant force of the three axes of the Mars unmanned helicopter into Equation (21), the linear motion equation of the Mars unmanned helicopter can be obtained:

$$\begin{aligned} m\left(\tfrac{du}{dt}+wq-vr\right)+mg\sin\theta &= X \\ m\left(\tfrac{dv}{dt}+ur-wp\right)+mg\cos\theta\cos\phi &= Y \\ m\left(\tfrac{dw}{dt}+vp-uq\right)-mg\cos\theta\sin\phi &= Z \end{aligned} \tag{25}$$

where u, v, w are the linear velocities along the O_bX_b, O_bY_b, O_bZ_b axes, respectively; p, q, r are the angular velocities around the O_bX_b, O_bY_b, O_bZ_b axes, respectively; X, Y, Z are the net forces acting on the O_bX_b, O_bY_b, O_bZ_b axes, respectively.

The velocity differential equation can be obtained by sorting out Equation (26):

$$\begin{bmatrix} \dot{u} \\ \dot{v} \\ \dot{w} \end{bmatrix} = \frac{1}{m_b} \begin{bmatrix} X \\ Y \\ Z \end{bmatrix} + \begin{bmatrix} -g\sin\theta \\ g\cos\theta\sin\phi \\ g\cos\theta\cos\phi \end{bmatrix} + \begin{bmatrix} 0 & -r & q \\ -r & 0 & -p \\ -q & p & 0 \end{bmatrix} \begin{bmatrix} u \\ v \\ w \end{bmatrix} \tag{26}$$

The linear velocity, angular velocity, and moment of inertia of the three axes of the Mars unmanned helicopter were brought into Equation (22) to obtain the angular motion equation of the UAV around the center of mass:

$$\begin{array}{l} I_x \frac{dp}{dt} + (I_z - I_y)qr = L \\ I_y \frac{dq}{dt} + (I_x - I_z)pr = M \\ I_z \frac{dr}{dt} + (I_y - I_x)pq = N \end{array} \tag{27}$$

where I_x, I_y, I_z are, respectively, the rotational inertia of the unmanned helicopter on the O_bX_b, O_bY_b, O_bZ_b axes, respectively; L, M, N are the sum of the torques rotating about the O_bX_b, O_bY_b, O_bZ_b axes, respectively.

According to Equation (27), the angular rate differential equation can be calculated using Equation (28):

$$\begin{bmatrix} \dot{p} \\ \dot{q} \\ \dot{r} \end{bmatrix} = I^{-1} \left(\begin{bmatrix} L \\ M \\ N \end{bmatrix} - \begin{bmatrix} 0 & -r & q \\ r & 0 & -p \\ -q & p & 0 \end{bmatrix} \times I \begin{bmatrix} p \\ q \\ r \end{bmatrix} \right) \tag{28}$$

According to the relationship between attitude angle and angular rate, the rotation kinematics equation can be written as follows:

$$\begin{bmatrix} \dot{\phi} \\ \dot{\theta} \\ \dot{\psi} \end{bmatrix} = \begin{bmatrix} 1 & \sin\phi\tan\theta & \cos\phi\tan\theta \\ 0 & \cos\phi & \sin\phi \\ 0 & \sin\phi\sec\theta & \cos\phi\sec\theta \end{bmatrix} \begin{bmatrix} p \\ q \\ r \end{bmatrix} \tag{29}$$

2.5.2. System Nonlinear Model

For Mars unmanned helicopters, the lift thrust moment on the O_bZ_b axis is provided by the reverse torque of the upper and lower propellers—that is, $N = N_T = -N_{D1} + N_{D2}$—and the torque on the O_bX_b axis and O_bY_b axis is mainly provided by the servos—that is, $L = L_T, M = M_T$. Assuming that the angular velocity of the upper and lower rotors is Ω_1, Ω_2, the thrust generated by the upper and lower rotors can be expressed as:

$$\begin{array}{l} F_1 = b\Omega_1^2 \\ F_2 = b\Omega_2^2 \end{array} \tag{30}$$

where b is the thrust coefficient. The motion characteristics of the Mars unmanned helicopter in the previous section could be sorted out and simplified, because the test flight was mainly aimed at simulating the vacuum chamber environment of the Martian atmosphere, ignoring external interference, such as strong winds. When hovering in a vacuum chamber, the air resistance is relatively small and, therefore, negligible, resulting in a simplified mathematical model:

$$\begin{cases} \ddot{x} = \dot{u} = (\sin\theta\cos\phi\cos\psi + \sin\phi\sin\psi)\frac{b(\Omega_1^2+\Omega_2^2)}{m} \\ \ddot{y} = \dot{v} = (\sin\theta\cos\phi\cos\psi - \sin\phi\cos\psi)\frac{b(\Omega_1^2+\Omega_2^2)}{m} \\ \ddot{z} = \dot{w} = \cos\phi\cos\theta\frac{b(\Omega_1^2+\Omega_2^2)}{m} - g \\ \ddot{\phi} = \frac{(I_y-I_z)}{I_x}\dot{\theta}\dot{\psi} + \frac{L}{I_x} \\ \ddot{\theta} = \frac{(I_z-I_x)}{I_y}\dot{\phi}\dot{\psi} + \frac{M}{I_y} \\ \ddot{\psi} = \frac{(I_x-I_y)}{I_z}\dot{\phi}\dot{\theta} + \frac{N}{I_z} \end{cases} \tag{31}$$

3. Results

3.1. Experimental Protocol

Due to the large differences between the Martian environment and the Earth environment, the designed propeller needed to be further verified experimentally, and the Martian atmospheric environment needed to be restored as much as possible during the experiment. In the hovering experiments, the UAV hovering performance test device was used to measure the aerodynamic parameters of the Mars rotor system simulating the Martian atmospheric environment, and the feasibility of UAV flight in the Martian environment was evaluated. Such methods can verify the rationality of the model of the simulation method, intuitively reflect the dynamic performance of the UAV, and realize the evaluation of the aerodynamic characteristics of the rotor system of the Mars UAV. The experiment was conducted at the Vacuum Chamber Experimental Base of the China Academy of Aerospace, as illustrated in Figure 11. The chamber has a diameter of 4 m and a depth of 10 m, and can maintain a pressure below 10 Pa. However, notably, the experiment could not entirely replicate the Martian environment. The atmospheric density could only be reduced to approximate that of the Martian atmosphere. The temperature and gravitational acceleration could not simulate the Martian atmospheric environment. Additionally, due to the limitations of the experimental conditions, the composition of the atmosphere could not be the same as that of Mars.

Figure 11. A vacuum chamber simulating the atmospheric environment of Mars.

During the experiment, the propeller test bench was placed in a vacuum chamber for fixation, and then the air density in the vacuum chamber was reduced to be comparable to the density of air on Mars. The test bench was designed according to the size of the interface in the vacuum chamber. In order to reduce the wall effect, the diameter of the propeller disc was parallel to the diameter of the vacuum chamber when designing the bench, and at the same time, the propeller was placed 4 m away from the outlet during installation, so as to reserve as much space as possible for the tail and minimize flow recirculation. During the experiment, a T-Motor MN7005 brushless motor was used, which could increase the speed of the propeller to 3000 RPM at the density of the Martian atmosphere, reaching the subcritical acoustic velocity. The test bench of the propeller in the vacuum chamber was installed, as shown in Figure 12, and the propeller retention frame was connected to the aisles on both sides of the cabin to fix the entire test bench. The main performance parameters of each sensor on the test bench are shown in Table 3. Under conditions of air density equivalent to that of the Martian atmosphere, the propeller generated a relatively small pull force at a low speed. As a result, the measured value of the pull force at a low speed was not significantly high. Additionally, due to the limited accuracy of the thrust sensor, the thrust error measured at a low speed was relatively large. Therefore, the final rotation speed range of 1200 RPM to 3000 RPM was chosen to measure the pull and torque of the propeller.

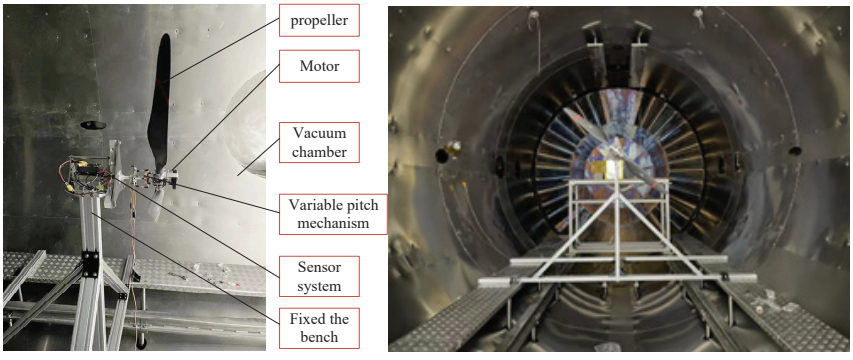

Figure 12. The test system of the Mars propeller in the vacuum chamber.

Table 3. Main performance parameters of each sensor.

	Range	Accuracy
Force sensor/kg	0~3	0.2% ± 20 g
Temperature sensor/°C	−40~350	±1% ± 1.5
Voltage sensor/V	11~55	±0.03% ± 0.03
Current sensor/A	0.2~80	±0.4% ± 0.1
Speed sensor/rpm	1500~3000	±0.5% ± 20

Figure 13 shows a schematic diagram of the data acquisition system. The force sensor, torque sensor, temperature sensor, current and voltage sensor are connected to the Arduino mega development board. The pulse signal output by the rotary encoder is also transmitted to the Arduino mega development board through the speed acquisition card, and then communicated with the personal computer through the serial port and the information interaction port on the vacuum bin.

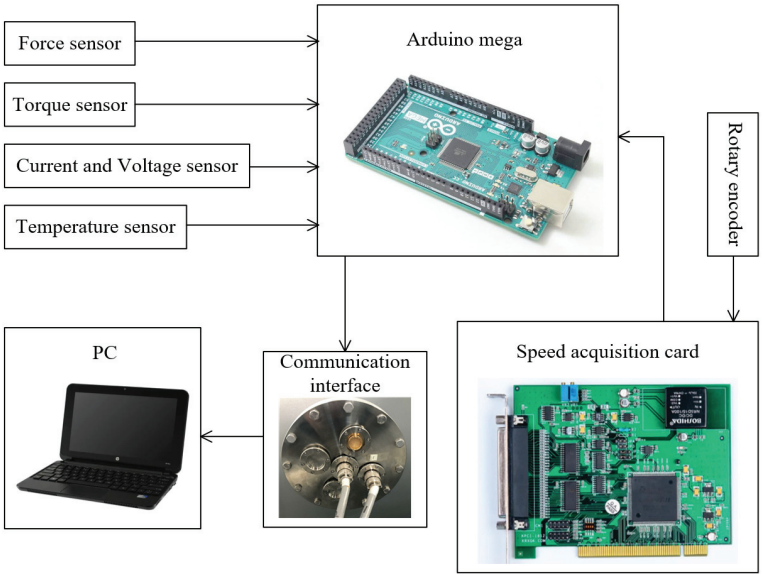

Figure 13. Data collection system of the test bench.

During the experiment, the propeller was subjected to thrust and torque tests at different speeds and different angles of attack. The rotation speed range was 1200 RPM to 3000 RPM, being measured every 200 RPM, and the angle of attack was 0° to 10°, being measured every 2°. The reason for the angle of attack only being 10° is that when using commercial software CFD for aerodynamic simulation, the convergence of the calculation results was not good when the angle of attack was greater than 10°, and the aerodynamic performance of the propeller was reduced. Such findings could be attributed to the fact that with the increase in the angle of attack, laminar flow separation occurs on the surface of the blade, thereby reducing the aerodynamic efficiency of the propeller. During the experiment, the pitch mechanism could be used to change the angle of attack of the propeller, thereby significantly saving costs and avoiding uneven air density in the vacuum chamber after each air extraction caused by multiple openings. Each set of data was measured four times, and then the average data were obtained by adopting the average method.

3.2. Experimental Results and Analysis

The lift thrust coefficient is the main parameter for characterizing the thrust characteristics of propellers, and the data obtained by the vacuum chamber bench test simulating the Martian atmospheric environment were compared with the data calculated by CFD numerical simulation. The results measured by the experiment obviously have the same trend as the results obtained by the CFD simulation, but there were certain errors between the two.

The difference in rotational speed caused the Reynolds number on the surface of the blade to change, which affected the thrust coefficient. As shown in Figure 14, as the rotational speed increases, the thrust coefficient would also slowly increase. However, the changes observed were notably not significant, and the thrust coefficient of the propeller demonstrated nearly identical changes with speeds at different angles of attack. The experimental results indicate that the thrust coefficient of the propeller exhibited varying changes at different angles of attack, and on average, the magnitude of the changes observed was greater than those shown by numerical simulation results.

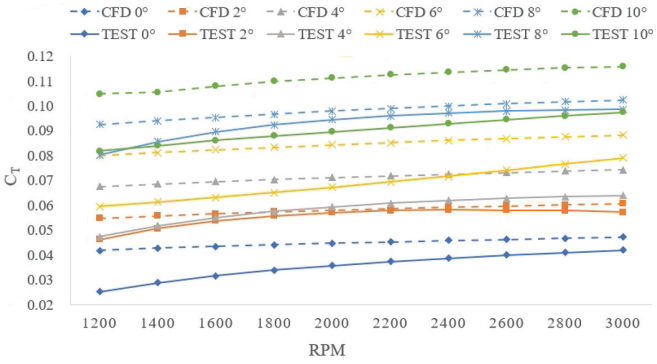

Figure 14. Thrust coefficient at different rotating speeds and angles of attack.

Undoubtedly, the angle of attack has the most significant influence on the thrust coefficient. In general, as the angle of attack increases, the thrust coefficient also increases. However, when the angle of attack exceeds a certain threshold, the laminar flow over the surface of the propeller separates, resulting in a reduction of the thrust coefficient. Therefore, changes in the angle of attack should be within a reasonable range. During the CFD numerical simulation of the propeller, the convergence effect of the thrust coefficient calculation was found to deteriorate significantly when the angle of attack exceeded 10°. Therefore, the aerodynamic performance of the propeller was analyzed only in the range of angle of attack between 0° and 10°. The CFD numerical simulation results show that

with the increase in the angle of attack, the thrust coefficient almost increased in the form of an equal difference series, and the maximum thrust coefficient was achieved when the angle of attack was 10° and the speed was 3000 RPM. Compared with the numerical simulation results, the experimental results were more volatile. In the range of 0° to 8°, with the increase in the angle of attack, the thrust coefficient increased, but unlike the CFD simulation results, when the angle of attack was 10°, the thrust coefficient was smaller than the thrust coefficient when the angle of attack is 8°. At the same time, the changes in the thrust coefficient between adjacent angles of attack did not show equal differences compared with the numerical simulation, which was caused by equipment and environmental errors during the test.

The thrust coefficient can be calculated using Equation (32):

$$C_T = \frac{3600T}{\rho n^2 D^4} \tag{32}$$

where T is the thrust generated by the propeller during rotation; ρ is the density of the Martian atmosphere; n is the rotational speed of the propeller in the Martian atmospheric environment; and D is the diameter of the paddle disc of the Mars propeller.

The power factor Cp is a performance indicator that measures the efficiency of propellers. The increase in the angle of attack means that the windward area of the propeller when rotating at high speed also increases, the resistance is correspondingly increased, and the power consumed is greater. As shown in Figure 15, comparing the CFD numerical simulation results and the vacuum chamber bench experimental results, an observation can be made that, in respect of numerical terms, the difference between the two was considerably large, and the results measured by the vacuum chamber bench test were obviously much larger than the CFD numerical simulation results; but, in terms of trends, the two were similar. As shown in Figure 15, with the increase in the angle of attack, the difference in the power coefficient between the adjacent angles of attack also increased, and at the same angle of attack, the speed increased, but the power coefficient showed a slight decrease, which is because the larger the rotational speed, the greater the inertia generated when the propeller rotates. In this way, the power loss can be reduced to a certain extent. The experimental data indicate that under the same angle of attack, the power coefficient of the propeller gradually decreases with an increase in speed. Moreover, within the range of 0° to 8° blade angles, the power coefficient increased with the angle of attack. Additionally, the greater the angle of attack, the more the power coefficient was affected by the increase in rotational speed. Notably, the power coefficient obtained from the experimental test was markedly different from the power coefficient obtained by CFD simulation. Specifically, under the same angle of attack, the power coefficient changed only slightly with an increase in rotational speed in the CFD simulation, while the experimental data showed a substantial change in the power coefficient with the increase in rotational speed. The biggest difference still occurred in the case of an angle of attack of 10°, and the experimental data show that when the rotational speed was less than 2400 RPM, the power coefficient at an angle of attack of 10° was significantly smaller than the power coefficient at an angle of attack of 8°. However, when the rotational speed was greater than 2400 RPM, the opposite trend could be seen, and as the rotational speed increased, the power coefficient at an angle of attack of 8° further decreased.

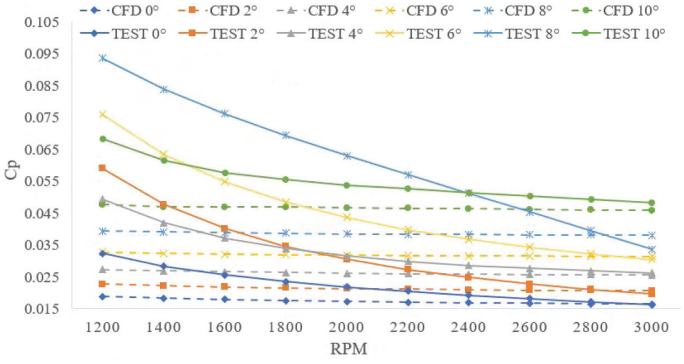

Figure 15. Power coefficient at different speeds and angles of attack.

The power factor can be calculated using Equation (33):

$$C_p = \frac{3600P}{\rho n^3 D^5} \tag{33}$$

where P is the power consumed by the Martian propeller as it rotates in the Martian atmosphere.

The merit factor is one of the main factors in evaluating the performance of the propeller, and the higher the merit factor, the higher the efficiency of the propeller in such states. The CFD numerical simulation results shown in Figure 16 indicate that, with the increase in propeller angle of attack, the merit factor also increased, but the increase became increasingly smaller. When the angle of attack was 8° and 10°, the merit factor of the propeller was roughly equal. At the same time, with the increase in speed, the merit factor also increased correspondingly; and, under the same angle of attack, the merit factor increases linearly with the increase in speed. There was a significant difference between the merit factor obtained from the vacuum warehouse bench experiment and the CFD numerical simulation. Not only was there a difference in value, but also in trend. The merit factor measured by the vacuum warehouse bench experiment did not increase with the angle of attack, but presented a disorderly pattern. However, the merit factor under the same angle of attack still increased with the increase in speed. At an angle of attack of 8° and a speed of 3000 RPM, the merit factor was optimal. Considering the thrust coefficient and power coefficient, it can be concluded that the optimal performance could be achieved at an angle of attack of 8°.

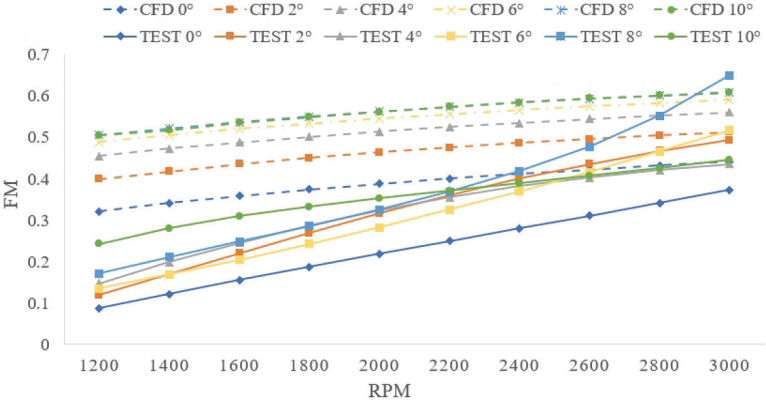

Figure 16. Merit factors at different speeds and angles of attack.

The merit factor can be calculated using Equation (34):

$$FM = \frac{1}{\sqrt{2}} \frac{C_l^{3/2}}{C_p} \tag{34}$$

where C_l and C_p indicate the thrust coefficient and power coefficient, respectively.

From the comparison of the experimental data and CFD simulation data, although there were errors therebetween, the general trend was the same. Therefore, to some extent, the CFD simulation results can be used to judge the quality of propeller design. In order to verify whether there was an increase in error caused by the vacuum chamber environment, we attempted to conduct outdoor experiments using the same experimental equipment in a calm environment, and conducted CFD simulations using the same numerical simulation methods. Comparing the numerical results with the simulation results, the errors of the thrust coefficient and torque coefficient are both within 10%. The specific experimental data will be presented in another manuscript. Therefore, we believe that the factor causing significant errors is the significant difference between the vacuum chamber environment and the open environment on Mars. The belief of the present authors is that the following reasons could have caused the errors:

(1) In the process of pumping the density of air in the vacuum chamber to the same as that of the Martian atmosphere, there were errors, and there were difficulties in achieving exactly the same between the two;
(2) The accuracy of force and torque sensors was not enough, leading to the deviation of the tested data;
(3) Due to the mechanism of the experimental bench, a great centrifugal force will be generated when the propeller rotates at a high rotational speed, which will lead to the vibration of the test bench in the process of testing, and then produce a certain deviation;
(4) Due to the existence of an idle stroke (due to mechanical structural gaps), the angle of attack will produce a certain deviation in each variation of pitch, which will affect the experimental results to a great extent;
(5) The vacuum chamber is a closed container. In the process of the experiment, certain wall effects and air reflux will be formed.

3.3. Mars Unmanned Helicopter Hover Experiment

The limited space within the vacuum chamber makes it challenging to perform maneuvering flight experiments. Therefore, the primary goal for the original Mars unmanned helicopter was to verify its hovering performance in the vacuum chamber. Notably, the gravitational acceleration on Mars is only one-third of that on Earth, and to simulate the Martian environment, the other two-thirds of Earth's gravitational acceleration were counterbalanced by lifting heavy objects at one end of the pulley set. As the vacuum chamber equipment was unable to fully simulate the Martian atmospheric environment—with the temperature in the chamber being maintained at Earth's room temperature—there was a failure to replicate the significantly lower temperature on Mars. In order to ensure that the Mars unmanned helicopter achieved hovering in an environment similar to the Mars air density, the pressure in the vacuum chamber was extracted to a pressure of approximately 1950 Pa instead of the Martian atmospheric pressure of 756 Pa. To achieve control, the hovering of the Mars unmanned helicopter was realized using a PID control, as shown in Figure 17, which illustrates the hovering state of the first generation of a Mars unmanned helicopter in the vacuum chamber simulating the Martian atmospheric environment.

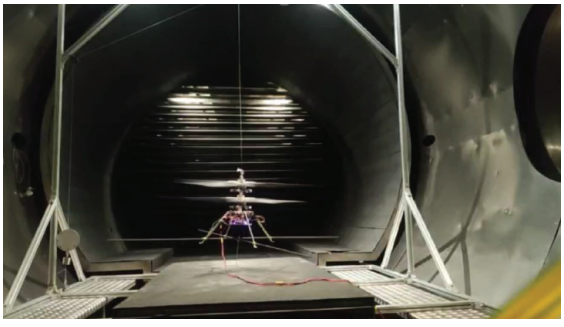

Figure 17. Hovering experiment of mars unmanned helicopter in vacuum chamber.

4. Conclusions

In the present study, by analyzing the dynamic conditions of the Martian atmospheric environment, a rotor system suitable for the Martian atmospheric environment was designed and a strength test of the lightweight Martian propeller was conducted by means of the finite element method. At the same time, the aerodynamic characteristics of the Martian propeller in the Martian atmospheric environment were explored by combining numerical simulations and vacuum chamber experiments. The following conclusions could be drawn:

(1) In order to reduce the weight of the Martian propeller, the adopted foam sandwich structure had a good weight reduction effect, and through finite element calculation and Earth environment bench experiments, the three-layer carbon fiber ply was verified to not only meet the lightweight and strength requirements, but also meet the requirements of the manufacturing process, which is the most suitable manufacturing method of the Mars propeller at present.

(2) Under the CFD numerical simulation, when the angle of attack was fixed, the thrust coefficient of the Martian propeller increased with the increase in speed, and the power coefficient decreased accordingly. The merit factor also increased with the increase in the propeller speed. When the propeller speed was constant, the thrust coefficient and power coefficient of the propeller increased accordingly with the increase in angle of attack, and the merit factor also increased accordingly. However, at 8° and 10° angles of attack, it had almost the same quality factor.

(3) A vacuum chamber experiment simulating the Martian atmospheric environment was conducted on the Martian propeller, and the aerodynamic characteristics of the Martian propeller in the Martian atmospheric environment were further explored. There was an error between the experimental results and the numerical simulation results, mainly because the numerical simulation was a simulation calculation in an ideal environment, while the experimental test had many external interferences, but the two exhibited roughly the same trend.

(4) The numerical simulation method considered the unsteady compressible flow and the vacuum chamber experiment of the simulated Martian atmospheric environment verified that the designed propeller system had good aerodynamic performance in the Martian atmospheric environment. On this basis, the initial design of the Mars unmanned helicopter was formulated, and the relevant hover experiments were conducted, providing reference and theoretical support for the design of subsequent Mars UAV sequences.

Author Contributions: Conceptualization, W.Z. and B.X.; methodology, W.Z.; validation, W.Z., B.X. and C.X.; formal analysis, C.X.; investigation, W.F.; resources, W.Z.; data curation, H.Z.; writing—original draft preparation, W.Z.; writing—review and editing, W.Z.; visualization, Z.Z.; supervision, B.X.; project administration, H.Z.; funding acquisition, W.F. All authors have read and agreed to the published version of the manuscript.

Funding: This work was supported in part by the National Natural Science Foundation of China Youth Fund under Grant 52102432, in part by the National Key Research and Development Program No. 2020YFC1512500 and the National Natural Science Foundation of Chongqing under Grant CSTB2022NSCQ-MSX1101, and Sponsored by the Natural Science Foundation of Chongqing, China, cstc2021jcyj-msxmX0792.

Data Availability Statement: Not applicable.

Acknowledgments: We sincerely thank the reviewers who contributed their expertise and time on reviewing this manuscript. Thank you very much to the China Academy of Space Technology 502 Research Institute for providing the vacuum chamber environment and technical support in this experiment.

Conflicts of Interest: The authors declare no conflict of interest.

References

1. Petritoli, E.; Leccese, F. Unmanned Autogyro for Mars Exploration: A Preliminary Study. *Drones* **2021**, *5*, 53. [CrossRef]
2. Wu, W.R.; Yu, D.Y. Development of deep space exploration and its future key technologies. *J. Deep Space Explor.* **2014**, *1*, 5–17.
3. Datta, A.; Roget, B.; Griffiths, D.; Pugliese, G.; Sitaraman, J.; Bao, J.; Liu, L.; Gamard, O. Design of a Martian autonomous rotary-wing vehicle. *J. Aircr.* **2015**, *40*, 461–472. [CrossRef]
4. Chi, C.; Lumba, R.; Su Jung, Y.; Datta, A. Aeromechanical Analysis of a Next-Generation Mars Helicopter Rotor. *J. Aircr.* **2022**, *59*, 1463–1477. [CrossRef]
5. Ruiz, M.C.; D'Ambrosio, D. Aerodynamic optimization and analysis of quadrotor blades operating in the Martian atmosphere. *Aerosp. Sci. Technol.* **2023**, 132.
6. Balaram, J.; Aung, M.; Golombek, M.P. The Ingenuity Helicopter on the Perseverance Rover. *Space Sci. Rev.* **2021**, *217*, 2–11. [CrossRef]
7. Balaram, J.; Daubar, I.J.; Bapst, J.; Tzanetos, T. Helicopters on Mars: Compelling Science of Extreme Terrains Enabled by an Aerial Platform. In Proceedings of the 9th International Conference on Mars, Pasadena, CA, USA, 22–25 July 2019; Volume 2089.
8. Pipenberg, B.T.; Keennon, M.T.; Langberg, S.A.; Tyler, J.D.; Balaram, J. Development of the Mars Helicopter Rotor System. In *Vertical Flight Society Annual Forum and Technology Display, Proceedings of the 75th American Helicopter Society Annual Forum, Philadelphia, PA, USA, 13–16 May 2019*; Vertical Flight Society: Fairfax, VA, USA, 2019; Volume 382.
9. Takaki, R. Aerodynamic characteristics of NACA4402 in low Reynolds number flows. *Jpn. Soc. Aeronaut. Space Sci.* **2006**, *54*, 367–373.
10. Shrestha, R.; Benedict, M.; Chopra, I. Hover Performance of a Small-Scale Helicopter Rotor for Flying on Mars. *J. Aircr.* **2016**, *53*, 1160–1167. [CrossRef]
11. Kurane, K.; Uechi, K.; Takahashi, K.; Fujita, K.; Nagai, H. Aerodynamic Characteristics of Mars Airplane Airfoils with Control Surface in Propeller Slipstream. In Proceedings of the 2018 AIAA Aerospace Sciences Meeting, AIAA-2018-2058, Kissimmee, FL, USA, 8–12 January 2018.
12. Pipenberg, B.T.; Keennon, M.; Tyler, J.; Hibbs, B.; Langberg, S.; Balaram, J.; Grip, H.F.; Pempejian, J. Design and Fabrication of the Mars Helicopter Rotor, Airframe, and Landing Gear Systems. In Proceedings of the AIAA Scitech 2019 Forum, AIAA-2019-0620, San Diego, CA, USA, 7–11 January 2019.
13. Koning, W.J.; Johnson, W.; Grip, H.F. Improved Mars Helicopter Aerodynamic Rotor Model for Comprehensive Analyses. *AIAA J.* **2019**, *57*, 3969–3979. [CrossRef]
14. Kunz, P.J. *Aerodynamics and Design for Ultra-Low Reynolds Number Flight*; Stanford University: Stanford, CA, USA, 2003.
15. Liu, Z.; Albertani, R.; Moschetta, J.M.; Thipyopas, C.; Xu, M. Experimental and Computational Evaluation of Small Microcoaxial Rotor in Hover. *J. Aircr.* **2011**, *48*, 220–229. [CrossRef]
16. Bohorquez, F. *Rotor Hover Performance and System Design of an Efficient Coaxial Rotary Wing Micro Air Vehicle*; University of Maryland: College Park, MD, USA, 2007.
17. Oyama, A.; Fujii, K. Airfoil design optimization for airplane for Mars exploration. In Proceedings of the J-55, the Third China-Japan-Korea Joint Symposium on Optimization of Structual and Mechanical Systems, CJK-OSM3, Kanazawa, Japan, 30 October–2 November 2004; pp. 1–3.
18. Koning, W.J.; Romander, E.A.; Johnson, W. Low Reynolds number airfoil evaluation for the Mars helicopter rotor. In Proceedings of the American Helicopter Society 74th Annual Forum, Phoenix, AZ, USA, 14–17 May 2018; pp. 1–17.
19. Désert, T.; Jardin, T.; Bézard, H.; Moschetta, J. Numerical predictions of low Reynolds number compressible aerodynamics. *Aerosp. Sci. Technol.* **2019**, *92*, 211–223. [CrossRef]
20. Braun, R.D.; Wright, H.S.; Croom, M.A.; Levine, J.S.; Spencer, D.A. Design of the ARES Mars Airplane and Mission Architecture. *J. Spacecr. Rockets* **2006**, *43*, 1026–1034. [CrossRef]
21. Marko, Ž.; Ekmedzic; Aleksandar, B.; Boško, R. Conceptual Design and Flight Envelopes of a Light Aircraft for Mars Atmosphere. *Teh. Vjesn.* **2018**, *25*, 375–381.

22. Chen, S.T. *Lift Drag Characteristics and Experimental Study of Mars Probe Rotor Uav*; Harbin Institute of Technology: Harbin, China, 2019; pp. 13–17.
23. Desert, T.; Moschetta, J.M.; Bezard, H. Numerical and experimental investigation of an airfoil design for a Martian micro rotorcraft. *Int. J. Micro Air Veh.* **2018**, *10*, 262–272. [CrossRef]
24. Jung, J.; Yee, K.; Misaka, T.; Jeong, S. Low Reynolds Number Airfoil Design for a Mars Exploration Airplane Using a Transition Mode. *Jpn. Soc. Aeronaut. Space Sci.* **2017**, *60*, 333–340.
25. Mcmasters, J.H.; Henderson, M.L. Low-Speed Single-Element Airfoil Synthesis. *Tech. Soar.* **1979**, *6*, 19–23.
26. Drela, M. Transonic low-Reynolds number airfoils. *J. Aircr.* **1992**, *29*, 1106–1113. [CrossRef]
27. Anyoji, M.; Numata, D.; Nagai, H.; Asai, K. Effects of Mach Number and Specific Heat Ratio on Low-Reynolds-Number Airfoil Flows. *AIAA J.* **2014**, *53*, 1640–1654. [CrossRef]
28. Ananda, G.K.; Sukumar, P.P.; Selig, M.S. Measured aerodynamic characteristics of wings at low Reynolds numbers. *Aerosp. Sci. Technol.* **2015**, *42*, 392–406. [CrossRef]
29. Okamoto, M. *An Experimental Study in Aerodynamic Characteristics of Steady and Unsteady Airfoils at Low Reynolds Number*; Nihon University: Tokyo, Japan, 2005.
30. Bézard, H.; Désert, T.; Jardin, T.; Moschetta, J.M. Numerical and Experimental Aerodynamic Investigation of a Micro-UAV for Flying on Mars. In Proceedings of the 76th Annual Forum & Technology Display, Online, 5–8 October 2020; Volume 17.
31. Liu, P.Q. *Theory and Application of Air Propeller*; Beijing University of Aeronautics and Astronautics Press: Beijing, China, 2006; pp. 148–234.
32. Zahra, S.; Hwang, Y.; Sotoudeh, Z. A Variational Principle for Unsteady Compressible Flow. In Proceedings of the 54th AIAA Aerospace Sciences Meeting, San Diego, CA, USA, 4–8 January 2016; pp. 4–8.

materials

MDPI

Article

Experimental Characterization of Composite-Printed Materials for the Production of Multirotor UAV Airframe Parts

Tomislav Šančić [1], Marino Brčić [2], Denis Kotarski [1,*] and Andrzej Łukaszewicz [3,*]

[1] Department of Mechanical Engineering, Karlovac University of Applied Sciences, 47000 Karlovac, Croatia; tomislav.sancic@vuka.hr
[2] Department of Engineering Mechanics, Faculty of Engineering, University of Rijeka, 51000 Rijeka, Croatia; marino.brcic@riteh.hr
[3] Institute of Mechanical Engineering, Faculty of Mechanical Engineering, Bialystok University of Technology, 15-351 Bialystok, Poland
* Correspondence: denis.kotarski@vuka.hr (D.K.); a.lukaszewicz@pb.edu.pl (A.Ł.)

Abstract: In this paper, the characterization of 3D-printed materials that are considered in the design of multirotor unmanned aerial vehicles (UAVs) for specialized purposes was carried out. The multirotor UAV system is briefly described, primarily from the aspect of system dynamics, considering that the airframe parts connect the UAV components, including the propulsion configuration, into a functional assembly. Three additive manufacturing (AM) technologies were discussed, and a brief overview was provided of selective laser sintering (SLS), fused deposition modeling (FDM), and continuous fiber fabrication (CFF). Using hardware and related software, 12 series of specimens were produced, which were experimentally tested utilizing a quasi-static uniaxial tensile test. The results of the experimental tests are provided graphically with stress–strain diagrams. In this work, the focus is on CFF technology and the testing of materials that will be used in the production of mechanically loaded airframe parts of multirotor UAVs. The experimentally obtained values of the maximum stresses were compared for different technologies. For the considered specimens manufactured using FDM and SLS technology, the values are up to 40 MPa, while for the considered CFF materials and range of investigated specimens, it is shown that it can be at least four times higher. By increasing the proportion of fibers, these differences increase. To be able to provide a wider comparison of CFF technology and investigated materials with aluminum alloys, the following three-point flexural and Charpy impact tests were selected that fit within this framework for experimental characterization.

Keywords: multirotor UAV airframe parts; additive manufacturing; continuous fiber fabrication; fiberglass reinforcement; material experimental characterization; uniaxial tensile test

Citation: Šančić, T.; Brčić, M.; Kotarski, D.; Łukaszewicz, A. Experimental Characterization of Composite-Printed Materials for the Production of Multirotor UAV Airframe Parts. *Materials* **2023**, *16*, 5060. https://doi.org/10.3390/ma16145060

Academic Editor: Antonio Mattia Grande

Received: 27 June 2023
Revised: 13 July 2023
Accepted: 16 July 2023
Published: 18 July 2023

1. Introduction

Technologies of rapid prototyping enabled a great step forward in various fields. Additive manufacturing technologies, which are widely used in biomedicine [1,2] to mechatronic systems such as unmanned aerial vehicles (UAVs), play a major role. The advantages of AM technologies come to full expression in the development sector or the production of small series. Nowadays, there are numerous types of research and applications of aircraft in various sectors, such as aerial photography [3], surveillance [4], precision agriculture [5,6], transport and logistics [7], research [8,9], and many others. Due to the possibility of vertical take-off and landing (VTOL), and therefore stationary flight and moderate-speed flight, multirotor UAVs are suitable for missions that require a high degree of system autonomy. Furthermore, the performance of the propulsion system consisting of several rotors enables greater agility and maneuverability, which consequently enables precise and complex movements. That fact places them in the category of aerial robotic systems and, in general, for specialized purposes. Major manufacturers mostly offer conventional multirotor configurations that are intended for specific applications. For example, the largest multirotor

UAV manufacturer DJI has several aircraft sizes that are intended for aerial photography, from the Mini to the Inspire UAV. In addition, there is a series of Agras UAVs that are intended for smart spraying tasks. These are large series of aircraft for which the frame parts are produced by conventional technologies, such as injection molding.

The multirotor type of UAV is used in more and more specific applications, and small series or unique aircraft are often required. The development of rapid prototyping technology is correlated with the development of specialized multirotor UAVs, where the key area is additive manufacturing (AM), 3D printing. There are many studies describing UAV systems that are built using additive technologies, such as fixed-wing type of UAVs [10] or considered multirotor [11]. With today's dynamic market demands based on shorter product life cycles that require smaller production batches, there is a need to move from traditional production systems to next-generation production systems [12]. Such systems must have high flexibility and reconfigurability in order to adapt to changes in the market, and this is exactly what is achieved with reconfigurable production systems (RMS) [13]. This is made possible by a quick response to the customer's needs by making products according to his requirements, which achieves his satisfaction. In contrast to the mass customization paradigm [14], where customers choose a product from a multitude of offered combinations, with mass individualization, the customer himself participates in the design of the product, which is suitable for the use of AM technologies, which gives advantages from the economic side due to the creation of a unique product adapted to an individual customer [15]. Increasing demands for unique customer-oriented products switch to the mass individualization paradigm, where the goal is to reduce the price of products to the level of products made by the mass customization paradigm.

AM technologies play a crucial role in the fourth industrial revolution by offering the ability to surpass the limitations of traditional production systems. Due to its flexibility, agility, and speed of placing new products on the market, AM is no longer used only for the creation of prototypes but also for the serial production of functional structural parts with the required accuracy and mechanical properties. With the development of new materials and forms of workpieces that ultimately lead to an increase in product quality, AM is used more and more often in research, especially in mechatronics, where production can be roughly divided into the design phase and the production phase itself. With this common approach, parts, or 3D objects, are created with the addition of materials, using technology by adding layers on top of each other. There are different AM technologies such as fused deposition modeling (FDM) [16], stereolithography (SLA) [17], selective laser sintering (SLS) [18], polyjet technology [19], laminated object manufacturing (LOM) [20], and others. Compared to other methods, FDM technology has its advantages, such as the variety of low-cost materials, which is why it is the most commonly used method, but there are always problems related to mechanical properties and dimensional accuracy. The most commonly used conventional materials are acrylonitrile butadiene styrene (ABS), polylactic acid (PLA), and polyethylene terephthalate glycol (PETG).

Additively manufactured polymers alongside polymer composites represent anisotropic materials [21]. With regard to the considered application of the parts, it is extremely important to identify the mechanical properties concerning the material and production parameters. In the research [22], the applicability of test methods for the mechanical characterization of test specimens manufactured with FDM technology was discussed. Furthermore, the numerical and experimental study of the PLA material compression uniaxial properties is presented in the research [23]. There are many types of research and works on the topic of improving the mechanical properties of materials that are made with FDM technology. One of the directions is joining polymer with composite materials that are widely used in research and the aerospace industry, where various types of materials and different purposes are represented, such as prototyping and production of wing structures shown in the papers [24,25]. The paper [26], gives an overview of strategies such as short fiber reinforcement (SFR), continuous fiber reinforcement (CFR), powder addition reinforcement (PAR), and other methods. Further related to the production of UAV parts,

in paper [27] a novel sandwich structure consisting of an ABS base laminated with carbon fiber-reinforced polymer (CFRP) layers was proposed. The main disadvantage of such materials is the time required to manufacture such parts. The solution is imposed with new 3D printers that are based on FDM technology, known as continuous fiber fabrication (CFF). In the paper [28], an experimental investigation of the additive manufacturing of continuous carbon fiber composites was carried out.

In this paper, experimental characterization was performed for 3D-printed specimens where three AM technologies were considered. The design of a multirotor type of UAV for specialized purposes is studied, and since the need for making prototypes or small series of UAVs, AM technologies are investigated for the production of airframe parts. To achieve the UAV assembly construction more efficiently integration of the process of characterizing the materials into the design process is examined. Results for the performed uniaxial tensile test are shown, and two more tests are being preliminarily investigated, which will also be integrated into the material characterization process. The goal is to enable a comprehensive comparison with aluminum alloys with high-reliability requirements such as in the automotive industry. To conduct experimental tests, 12 series of test specimens were produced using FDM, SLS, and CFF technologies. Test specimens are subjected to mechanical testing and experimental data are processed, saved, and graphically presented for each specimen. Since the emphasis in this study is on mechanically loaded airframe parts, particular attention is given to composite materials with reinforcement for enhancing the structural integrity of the airframe. The results for different reinforcement parameters are shown, and from the aspect of maximum stress, composite specimens have up to four times higher maximum stresses in the considered parameter range compared to conventional materials. At the same time, specimens with a higher proportion of fibers can be compared with aluminum alloys.

2. Multirotor UAV System Description

Multirotor-type UAVs represent an extremely complex system in terms of design and control. Such a type of aircraft is an inherently unstable system, which results from the fact that it cannot independently return to the point of balance (hover) if it loses the functionality of the control loops but will fall or begin to move uncontrollably in space. Furthermore, multirotor UAVs are nonlinear systems since rotor aerodynamic forces and moment characteristics are nonlinear functions with respect to angular velocities. The multirotor UAV is mathematically described by a rigid body dynamic model with 6 second-order differential equations, 12 state variables, and N input variables, which makes them a multivariable system. From the design point of view, it is important to emphasize that such UAVs are high energy-consumption systems, considering that for the needs of motion, rotary wings are used, which with their aerodynamic forces, among other effects, must cancel the gravity force.

The number of control variables depends on the aircraft configuration, which is determined by the geometric arrangement of the rotors. Conventional configurations are characterized by a planar arrangement of rotors. Typical designs are configured with four rotors, the quadrotor or quadcopter [29], with six rotors, a hexarotor, and with eight rotors (octorotor). Typical configurations are shown in Figure 1, the first heavy-lift quadrotor prototype and the 3D model of the hexarotor assembly that was presented within the modular configuration in the previous research [30].

Multirotor UAV dynamics are influenced by the forces and moments of the environment and of the propulsion subsystem. The equations of motion can be derived using the Newton–Euler method. The gravitational force, external disturbances, such as wind gusts, air resistance, gyroscopic effect, and others, act on the rigid body of the multirotor UAV. The only vector through which the dynamics of the aircraft can be directly influenced is the control vector, containing forces and moments of the propulsion configuration (subsystem, module). The multirotor UAV propulsion configuration is defined by the geometric arrangement and characteristics of the rotor. The configuration geometric arrangement is defined

by the position and orientation of each rotor in relation to the aircraft coordinate system, and a more detailed derivation is presented in the previous research [9,28]. In conventional propulsion configurations, the rotors are electric propulsion units (EPUs) whose central part is the brushless DC (BLDC) motor driven by an electronic speed controller (ESC). This type of electric propulsion converts electrical energy obtained from lithium-polymer (LiPo) batteries into mechanical work. Fixed-pitch propellers mounted on the rotor axis of the BLDC motor, with their rotation, create aerodynamic effects, from which it follows that the aircraft dynamics directly depend on the rotors' angular velocities.

(**a**) (**b**)

Figure 1. Multirotor UAV platform: (**a**) quadrotor heavy-lift prototype; (**b**) hexarotor 3D model.

When it comes to the design of specialized multirotor UAVs, such aircraft are produced in small series and often exist as unique systems designed to perform specific tasks. In small series production, the price per unit increases dramatically; therefore, it is important to consider technologies for rapid prototyping where manufacturing costs are not sensitive to changes in production volume. In general, it can be said that the design of the aircraft system primarily depends on the purpose, that is, the profile of the mission that the aircraft typically needs to perform. The aircraft system can be divided into subsystems, where from the aspect of designing and mass budgeting, each subsystem is defined by its mass. Payload (equipment and cargo) is determined by the UAV purpose and further dictates the choice of parameters and components of other subsystems. The total mass of the UAV obtained by adding the masses of the subsystems represents the take-off mass of the aircraft.

The basic performance of the multirotor UAV is defined by the ratio of the maximum thrust of the propulsion subsystem in the vertical aircraft axis and the take-off mass. The unwritten rule is that this thrust-to-mass ratio (TMR) is approximately two, except in extreme situations such as racing drones, and a more precise ratio can commonly be read from the specifications of the propulsion components manufacturers. As mentioned earlier, multirotor UAVs are characterized by high energy consumption, which in turn depends on the aircraft's mass. When designing a system, the ratio of battery mass and capacity is one of the key data. The propulsion and energy subsystems are mutually dependent because, for example, as the power of the aircraft increases, so does the need for energy, which results in a larger mass of the aircraft. The design of the propulsion subsystem is the most complex part of the overall design in terms of the mechanical properties that the parts of the assembly should possess. The multirotor type of UAV can be used in a wide power range, from several tens of watts to several tens of kilowatts, so it is necessary to choose materials and technologies concerning the selected propulsion components. In the aircraft design phase, the parts of the frame that connect everything into a functional assembly have to be modeled and manufactured based on the selected components, where the main requirements are high strength and absorption energy, and low specific mass (weight).

The production of parts for specialized multirotor UAVs can be divided into two main phases. The first phase represents the phase of designing the aircraft where various CAx techniques and tools are utilized, which are outlined through previous research [31–33]. In this phase, parts and assemblies are modeled using a 3D software package, and also simulations of airframe parts that need to meet certain mechanical properties can be carried out. The final versions of the 3D CAD model are exported performing a triangulation process to STL format, which is further used for the production of parts. In this research, the SOLIDWORKS software package (Dassault Systèmes SE, Vélizy-Villacoublay, France) is used for 3D modeling purposes. The next phase is the production, i.e., prototyping of the airframe parts. The first step of the prototyping phase is setting print parameters in accordance with the selected AM technology. The print parameters are adjusted in the software package, the slicer, which makes up the software package of a particular 3D printer. After setting the parameters, the G-code is generated for the 3D-printing execution, with which the 3D printer creates a physical model. The last step in this phase is the post-processing of the parts, such as removing the support, or sandblasting and cleaning the parts produced by the SLS technology.

Typically for a multirotor UAV, it can be stated that the mechanically loaded parts of the platform can be divided into propulsion airframe parts and landing gear. Whether it is the forces and moments of the propulsion units that act on airframe parts or the forces during landing that occur on the landing gear assembly, such parts are so far developed and tested using CFF technology. For a small UAV that can be classified as a micro aerial vehicle (MAV), landing airframe printed parts are depicted in Figure 2, alongside the heavy-lift multirotor UAV landing gear section. Heavy-lift multirotor UAV landing gear assembly consists of printed parts and prefabricated composite elements, such as tubes, and the whole assembly is shown in Figure 1a.

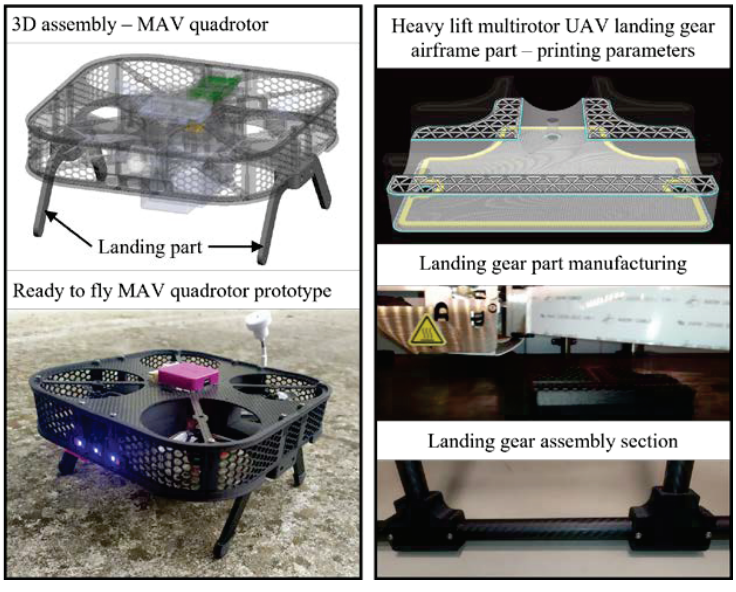

Figure 2. Examples of 3D-printed airframe parts.

3. Additive Manufacturing Considerations and Experimental Testing

Given that multirotor UAVs are used in various applications where small series or prototypes are used, it is important to consider rapid prototyping technologies in the system design phase. This is an additional benefit from the aspect of using such aircraft in engineering education and research. In addition to the fact that small series rapid

prototyping technologies are cheaper compared to conventional technologies, they also significantly reduce development time through rapid iteration and the possibility of early and frequent testing of many different designs or partial designs with critical features. The development of AM and new materials has led to an increase in the quality of the product; it is used more and more often in various industries, such as biomedicine, the automotive industry, and the space industry [34]. AM technology enables the production of structural parts with the required accuracy and mechanical properties at increased production speed, given that the development procedure is relatively simple for different technologies.

3.1. Considered Additive Manufacturing Technologies

In the field of making UAVs that are used mainly for research or education, FDM 3D-printing technology is mainly utilized, and recently, due to the availability of cheaper equipment and materials, SLS technology is prominent. In this paper, specimens made with SLS technology using the Lisa 3D printer by Sinterit (Sinterit sp. z o.o., Kraków, Poland), and using Sinterit Studio software (1.7.0.2), were investigated. For the considered FDM technology, a series of specimens can be made on a low-cost Prusa i3 MK3s 3D printer (Prusa Research a.s., Prague, Czech Republic) using the corresponding Prusa Slicer software (2.4.0). For UAV airframe parts that are mechanically loaded, composite materials are used, usually carbon fiber tubes and plates, from which structural parts can be quickly made. This means that it takes relatively little time from the design phase to the production of the aircraft, which is why it is cheaper. Although 3D printing is widely used, it is mostly for smaller UAVs. In the case of, for example, heavy-lift UAV, it is necessary to design parts that are mechanically more loaded, and most often, the propulsion airframe parts are made by processing aluminum. The development of CFF 3D-printing technology enabled the production of parts made of polymer-reinforced materials whose mechanical properties can be compared to aluminum parts, especially in combination with composite parts. In this work, the emphasis is on testing the specimens produced by CFF technology, where the Onyx Pro 3D printer (Markforged, Waltham, MA, USA) by Markforged is utilized.

Regardless of the type of AM technology, the production of the part is based on layer-by-layer construction, which is also the case with SLS technology. This AM technology uses powder materials that are sintered by thermal energy generated by a laser. Modeling by this process can be applied to all materials with powder particles that are sintered due to the application of heat. The most commonly used are polymer powder materials, the most important of which are polycarbonate (PC) and polyamide (PA). To further improve the mechanical and thermal properties of the material, reinforced polymers can be used, where fiber reinforcement is added to PA materials. Unlike other considered technologies in this work, SLS technology is suitable to produce small series of parts with complex geometry. A schematic representation of the working principle is shown in Figure 3, where the manufacturing process begins with the creation of a laser beam that is directed by the laser system to the exact desired position on the XY plane of the printed part. Changing the height of the layer is most often performed by lowering the build platform, the powdered material needed to create a new layer is added from the material feed chamber via a roller. The process of making the layer starts as a result of the action of the laser beam into the powder material. The required temperature applied to the powder particle must be between the crystallization temperature and the melting temperature of the particle [35]. In this research, test specimens were made from polyamide material with the trade name PA12 [36], using Sinterit Lisa Pro 3D printer Sinterit Studio software.

FDM 3D-printing technology is the most popular and most frequently used technology in research and development, education, and industry. It is based on the melting of solid polymer materials into a semiliquid that passes through a nozzle, forming objects by applying the polymer layer by layer. The working principle of FDM technology is schematically represented in Figure 4a. The created objects are made of thin layers of material whose direction of application defines the mechanical properties of the anisotropic material. Compared to other AM technologies, FDM has its advantages, such as the variety

of hardware/software and low material costs, which is why it is the most widely used. Since it is applied layer by layer, the support material is printed for parts with overhanging geometries [37]. Several issues need to be addressed related to mechanical properties, dimensional accuracy, consistency, and undetected defects within the structure of the products. The most used thermoplastic materials for FDM technology are ABS, PLA, and PETG. In this work, test specimens were made from PLA [38] and PETG [39] filament.

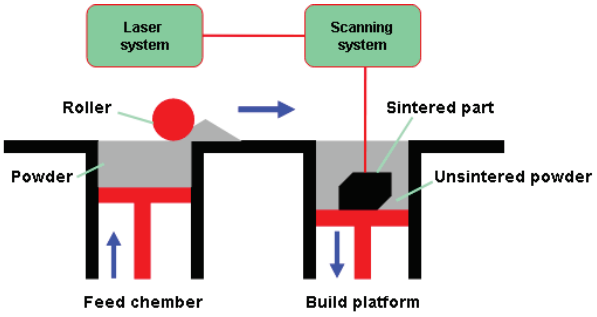

Figure 3. SLS technology—schematic overview.

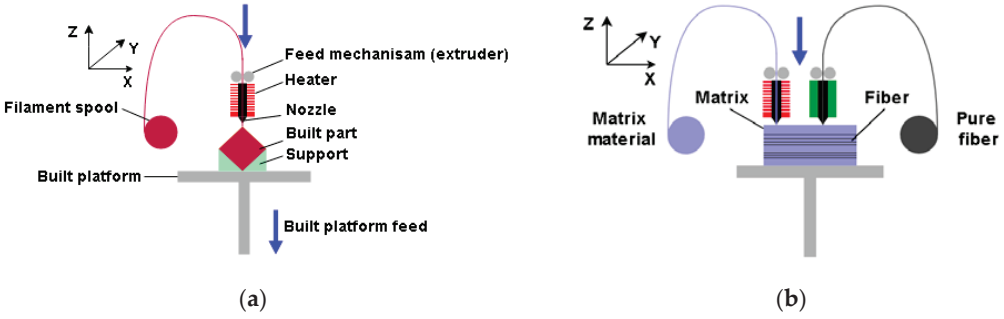

Figure 4. AM technologies—schematic overview: (**a**) FDM; (**b**) CFF.

Due to the FDM working principle, by adapting this technology it is possible to produce parts that are reinforced with composites. Considering the type of composite with which the polymer material is reinforced, they can be divided into fiber reinforcements, particle reinforcements, and nanoparticle reinforcements. Composite materials are usually synthetic carbon fiber (CF), glass fiber (GF), and Kevlar fiber. Additionally, more environmentally friendly natural biodegradable fibers can be produced [40]. Polymer materials with a reinforced matrix, have significantly increased strength and are used more and more, considering that at the same time they have a low mass [41]. In this paper, the CFF technology with direct reinforcement is discussed, which requires two nozzles, one for the matrix material and the other for the reinforcement fibers, where a composite sandwich structure is formed, as schematically shown in Figure 4b. The system with two nozzles can produce parts only from matrix materials (FDM), and the paper will examine a series of specimens produced from micro carbon fiber-filled nylon material, commercial name Onyx [42], using Markforged equipment and a slicer.

Utilizing the Onyx Pro 3D printer, this system of separate nozzles is used to produce parts of the sandwich structure of the composite, where the Onyx material is used as the matrix and the fiberglass as reinforcement. The mechanical properties of the parts depend on parameters that can be adjusted, such as the number of reinforcement layers and the different geometric arrangements of fibers. Models made with CFF technology have an advantage over those made with conventional FDM technology in terms of significantly

higher tensile strength, depending on the proportion of fibers in the composite structure. Test specimens with a different number of reinforcement layers and with various fiber orientations were considered in the testing phase.

3.2. Experimental Methods and Equipment

Numerous methods have been used so far to test the mechanical properties of printed materials, such as the Charpy test [43] or rotating bending fatigue analysis [44]; in this work, uniaxial tensile testing is utilized. Test specimens according to the ISO 527-2 standard (Figure 5), with a square cross-section, were modeled in the SOLIDWORKS software package, then exported in .stl format suitable for 3D printing. The print orientation of the test specimens placed on the XY plane of the 3D printer is shown in Figure 6. Researching the literature has determined that the print orientation where the direction of the layers is perpendicular to the direction of the test force gives the lowest values of tensile strength due to simple delamination of the layers. For this reason, such an orientation of the test specimens will not be examined. The data described by the 3D CAD model, according to which the test specimen is made, is inserted into the software called slicer, which is the link between the real and digital models.

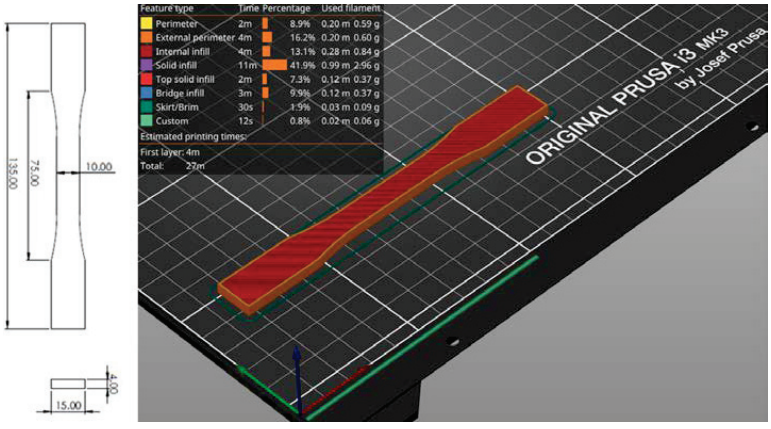

Figure 5. Test specimen (ISO 527-2 [45] standard test specimen for uniaxial quasi-static tensile testing)—G-code generation in a slicer.

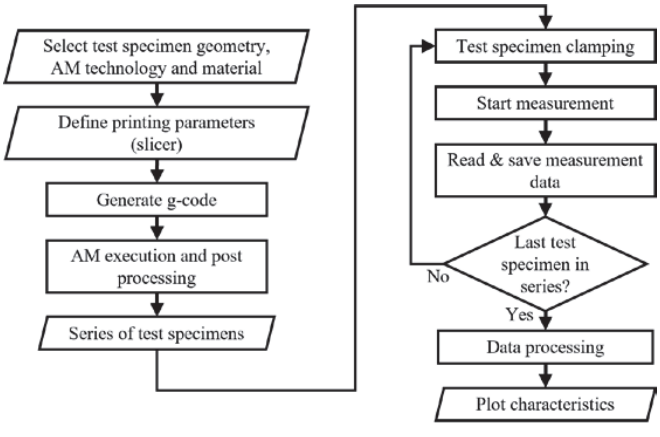

Figure 6. Additive manufacturing and experimental measurements flow chart.

Figure 6 shows the basic flowchart of the conducted experiments for one series of test specimens. In the first part, the process related to additive manufacturing is presented, where, regarding the experiment, specimen geometry is selected. Depending on the AM technology, in slicer software, printing parameters are defined. Steps and movements that the printer will perform during the creation of the physical part are described by G-code. The generated G-code is transferred to the printers where the manufacturing begins. It is possible to print one test specimen at a time, or it is possible to print the whole series at once, regardless of the AM technology. When printing test specimens with FDM and CFF technology, there is no post-processing because, due to the geometry of the test specimens, there are no support structures. With SLS technology, it is necessary to clean the test specimens of powder using sandblaster hardware. After the test specimens have been produced for one series, the second part of the process related to the implementation of experimental testing, data processing, and display begins. The first step in this part is the preparation of a test specimen in the clamp of the experimental hardware. After the specimen is clamped, the measurement can be started for the selected test parameters. During the test, data acquisition is performed, and raw data are obtained. Depending on the used equipment and software, in addition, experimental software can generate a report with a graphic display of the test results, as was the case in this research. After the last specimen in the series is tested, the raw data are further processed and interpreted. In this research, the MATLAB software package is used, and the results are graphically presented in the form of stress–strain diagrams.

The test specimens were subjected to a quasi-static uniaxial tensile test on a Shimadzu AG-X plus universal industrial equipment (Figure 7), which can achieve a tensile test force of up to 100 kN. The test was carried out at a constant speed of 30 mm/min without the use of external stress reading devices. The accompanying software of the equipment creates a stress–strain diagram from which the mechanical properties of the material and the critical points of the stress–strain diagram can be analyzed. Raw data measured over a certain time interval during the test are suitable for interpretation in the MS Excel or MATLAB software package. During the testing of polymer materials, clamping problems occur. Due to the lower tensile and compressive strength of the specimen, it is not possible to clamp the specimens into packs with the same force as aluminum and steel specimens because, during the test, the specimen breaks in a place that is not intended for it. These problems are especially pronounced when clamping composite test specimens because the highest values of tensile and compressive strength are expressed in the direction of the fibers, so such values should be achieved in the direction of the test axis, which is perpendicular to the forces that act when clamping the specimens. For this reason, by increasing the tensile strength of the composite specimen, a slip can occur between the packs and the clamped specimen.

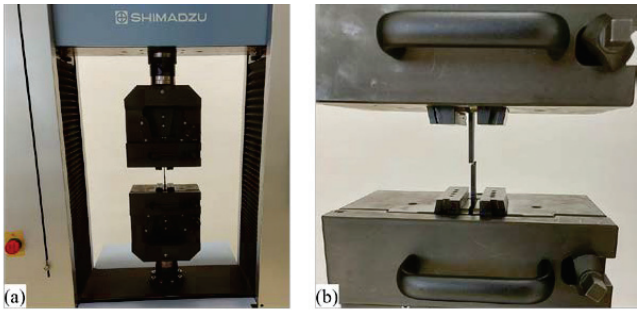

Figure 7. Experimental equipment: (**a**) SHIMADZU AG-X; (**b**) performing quasi-static uniaxial tensile stress on the test specimen.

3.3. Selection of Test Specimens Technological Parameters

In addition to striving to achieve the highest possible tensile strength of the tested specimens, it is more important to express the limit of elasticity. Due to the very small differences between the elastic limit and the maximum tensile strength of the printed specimens, the maximum tensile strength is used as an orientation value for testing purposes. The construction of unmanned aerial vehicles must ensure sufficient tensile strength and criteria of rigidity and stability. In order for the aircraft to be in a functional state, its structural parts must remain in the elastic region; that is, there must be no permanent deformations in the plastic region that would cause displacements of the structure that could adversely affect flight dynamics. The forces that occur due to thrust during flight would deform ductile materials, so it is desirable to have as much rigidity as possible in the construction material. To test the mechanical properties of airframe parts that are statically loaded with the load carried by aircraft, the best description is provided by the uniaxial static tensile test that was carried out in this research. The criteria that the material must meet are low mass, high stiffness, higher elastic limit, and orientation of composite fibers that will be satisfactory in different directions of force.

For this reason, a uniaxial quasi-static tensile test is performed on standard test specimens, from which a stress–strain diagram is obtained. During production, layer by layer, the anisotropic property of the material occurs. Due to the dimensional inaccuracy of the production, non-homogeneity also occurs, which results in different mechanical properties of the material and is present in all printing technologies, unlike mold-injected parts. This is why it is necessary to test several AM technologies using different materials and 3D-printing parameters. Five test specimens are produced for each specimen series (S01–S12). Low-cost PLA and PETG materials were considered, from which specimens (S01–S06) are produced by FDM technology using Prusa equipment and a slicer. Standard printing parameters were investigated, and furthermore, the infill percentage and the number of edge layers were varied. Table 1 shows the materials and parameters of 3D printing for test specimens manufactured using FDM technology. The test specimens (S01–S06) have four floor layers, six roof layers, and a triangles infill pattern. To make a test specimen (S07) with SLS technology, the factory parameters set in Sinterit Studio software are used, and the test specimens are composed of PA12 material.

Table 1. FDM print parameters.

Specimen Series	Material	Infill %	Wall Layer Number (Vertical Shells)	Mass (g)	Time (min)
S01	PLA	20	2	5.90	27
S02	PLA	40	2	6.62	30
S03	PLA	20	4	6.34	29
S04	PETG	20	2	6.04	27
S05	PETG	40	2	6.78	30
S06	PETG	20	4	6.50	29

The stiffness of the non-composite polymer materials used in the tests made by FDM and SLS technology is sufficient for the production of parts of UAVs, while their strength is low for the production of functional, structural airframe parts such as parts of the UAV propulsion assembly. The goal is to achieve the highest possible strength of the test specimens compared to conventional FDM and SLS technologies and to be comparable to aluminum alloys. Due to the most similar conditions when UAVs hit the ground or other unpredictable objects, a car chassis is compared as a reference, where it is tried to achieve a yield strength equal to or greater than the aluminum alloys used for the production of structural car chassis. This is made possible by CFF 3D-printing technology, where composite specimens are obtained by combining matrix and reinforcement materials. Then, micro carbon fiber-filled nylon matrix material is investigated, from which test specimens (S08) with default (factory) parameters (triangular infill 37%) are produced by a Markforged

Onyx 3D printer. Reinforcement materials are made from different fiber orientations with the aim of achieving the required values for the design of UAVs. The considered 3D-printing parameters of composite materials are shown in Table 2.

Table 2. CFF print parameters.

Specimen Series	Material	Number of Reinforcement Layers/Fill Type	Fiber Reinforcement Angles	Mass (g)	Time (min)
S08	Carbon fiber-filled nylon	None	-	6.14	33
S09	Carbon fiber-filled nylon + fiberglass reinforcement	8/Concentric	-	6.24	68
S10	Carbon fiber-filled nylon + fiberglass reinforcement	8/Isotropic	$[0/90/\pm45]_8$	6.95	80
S11	Carbon fiber-filled nylon + fiberglass reinforcement	8/Isotropic	$[30/45/60/0]_8$	6.95	82
S12	Carbon fiber-filled nylon + fiberglass reinforcement	12/Isotropic	$[30/45/60/0]_{12}$	7.52	92

The mechanical properties depend on the number of reinforcement layers, as well as the reinforcement fill type. Changes in mechanical properties with a change in the proportion of fibers in printed composites with fiberglass reinforcement are noted in the paper [46]. The initial specimen consisted of four layers of fiberglass with a total volume share of approximately 4%, so for subsequent specimens, 4 layers were added up to 30 layers of fiberglass (33% volume share). They did not reach the limit of 40% to 50% fiber content in CFF; however, it was clearly proven that with each increase in fiber content, the maximum tensile strength of the tested specimen increases. The arrangement of fibers can be divided into concentric, which is shown in Figure 8, and isotropic. The concentric fiber pattern orientation has fibers in the directions as the walls in the FDM technology following the wall of the model, and for that pattern, a series (S09) of test specimens were 3D printed according to standard Markforged parameters. Isotropic fiber orientation represents parallel fiber lines at different angles. Other test specimen series with different numbers and fiber orientations were made using this pattern approach.

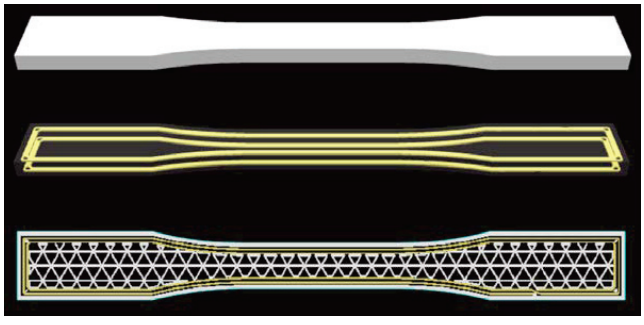

Figure 8. S09 test specimen with concentric fiber reinforcement.

Fibers in the axial direction have very high strength, but also composites with the action of force perpendicular to the direction of the fiber have the lowest strength, which is why it is necessary to make a compromise with the orientation of the fibers because, in reality, there are multiaxial forces acting on the structure. Placing the fibers longitudinally at 0 degrees in the load direction gives the highest tensile strength. By rotating the fibers (increasing the angles), the tensile strength of the composite material decreases because the applied force is no longer only longitudinal to the fibers but also to the layers of the matrix. By increasing the angles from 0° to 90°, more and more load is transferred to the matrix, which has a significantly lower tensile strength than the fibers, and thus the overall tensile strength of the composite material decreases. In the research [47], such behavior

of the material was shown, where the orientation of the fibers was varied by increasing the angle by 22.5° from 0° to 90°. When constructing the airframe of UAVs, the bending load on the rotor arms caused by the thrust of the propeller has a great influence on the airframe construction. When making such parts from composite structures, it is essential to take into account the anisotropic properties of CFF specimens that, due to bending, cause variations in the strain rate, increasing the shear stress between layers that lead to material failure [48]. The behavior of the flexural properties by testing the material is described in the work [49], where increasing the angle of the fibers increases the ductility of the tested specimens. With the structure of the specimens with angles [+45°/−45°], they could not break due to high ductility; however, by adding more layers, a more balanced structure is obtained [48], which is the reason for testing the orientation [30,45,60,0]. The test is carried out for three different setups (S10–S12) of isotropic reinforcement parameters, which are shown in Table 2. Figure 9 shows the geometric arrangement of fibers considered in the test.

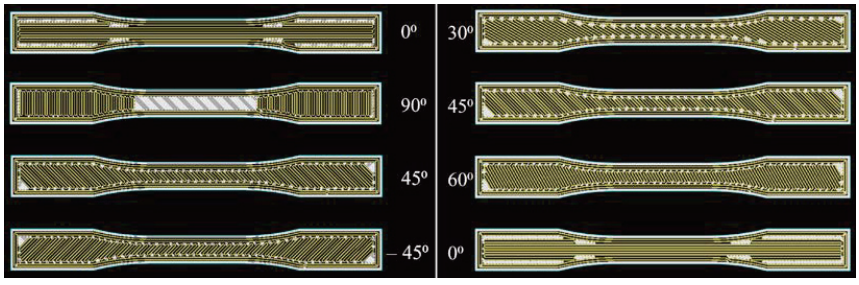

Figure 9. CFF—fiber reinforcement angles.

3.4. Experimental Testing Procedure Integration in Design Process

Technological parameters of test specimens are adjusted for certain technologies in software tools that come with 3D printers. This step is also the first step in the production of the airframe parts that make up the UAV system, and the output of the step is the G-code that is executed on the 3D printer. In general, after adjusting the considered parameters of the 3D model (part or test specimen), it is necessary to prepare the material in the additive manufacturing execution step, which is in the form of filament for FDM and CFF technologies and in powder form for SLS technology. With CFF technology, for the used material, it is necessary to dehumidify the box in which it is placed, and before starting printing, it is necessary to create a purge line of ejected material located between the dry box and the nozzle. With SLS technology, a sieve is used to prepare the material, which is fed into the feed chamber. After the material is ready for production, the G-code execution itself follows. The execution time depends on the technology and the parameters of individual technologies. After the end of printing, depending on the technology, the parts need to be post-processed.

When it comes to test specimens, after the production of a particular series is finished, the testing stage is approached. Figure 10 schematically shows the material testing process, the integration of which in the design process enables a more efficient design of structural parts and the aircraft assembly in general. Furthermore, the testing process may include other methods, such as the three-point flexural test or the Charpy impact test. In the next chapter, the test results and characterization for the considered series of specimens (S01–S12) are presented.

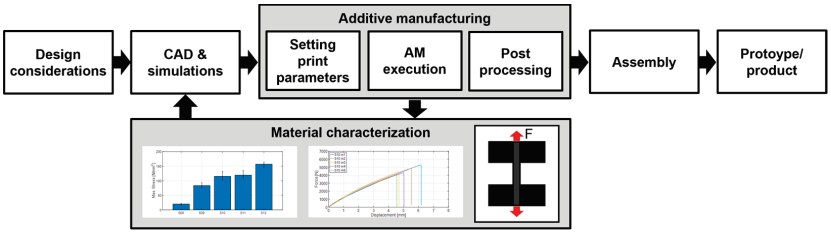

Figure 10. Integrated experimental procedure for material characterization.

4. Results of Experimental Testing

Investigation of the mechanical properties of the printed specimens by a uniaxial tensile test is shown by the stress–strain diagrams. For each series of different specimens that are shown in Tables 1 and 2, five test specimens were used to obtain more reliable results. Each specimen in the series from S01 to S12 is shown separately on the stress–strain diagrams.

4.1. Measurement Results Shown by Stress–Strain Diagrams

The first group of materials made by the FDM technology consists of specimens S01, S02, and S03, which are composed of PLA material. The mechanical properties depend on the parameters of the print, and this paper considers the infill (percentage) and the number of vertical shells. The first series of specimens use the default settings; in the second series, the percentage of infill has been doubled, while in the third series, the number of vertical shells has been doubled. From the measurement results (Figures 11–13), it can be seen that with an increase in the number of vertical shells, the mechanical properties improve more significantly in relation to an increase in the percentage of infill, which can further serve as a milestone in the design of airframe parts that will be made by the FDM technology from PLA material, which require higher tensile strength. Although slightly, S03 specimens are also lighter comparing S02 specimens, and the printing time is slightly shorter.

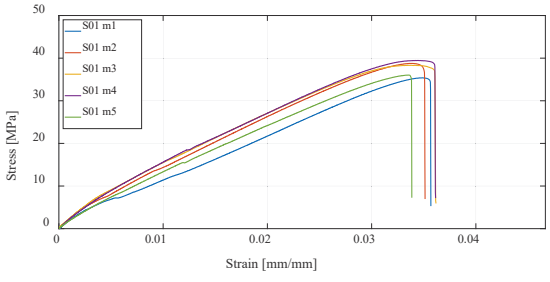

Figure 11. Stress–strain diagram for specimen 1 (S01) series experimental measurements.

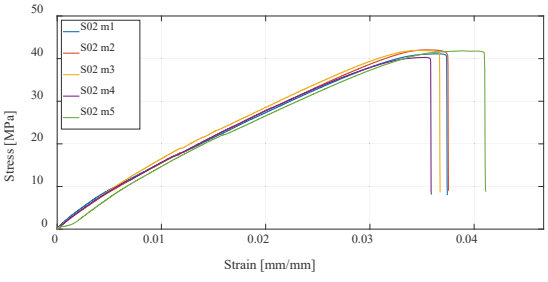

Figure 12. Stress–strain diagram for S02 experimental measurements.

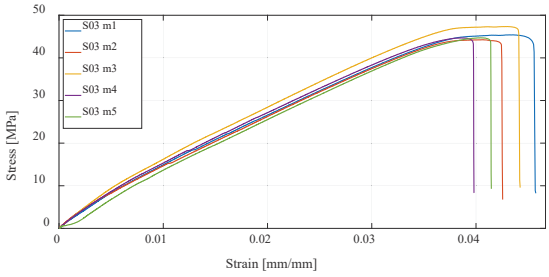

Figure 13. Stress–strain diagram for S03 experimental measurements.

The next three series of test specimens are also produced using the FDM technology but from PETG material. The same 3D-printing parameters were considered, and as with PLA material, it can be concluded that specimens with a higher percentage of infill have higher tensile strength than the default settings, while specimens with twice the number of vertical shells have the highest, as shown in Figures 14–16. In relation to PLA material, it is important to emphasize that PETG material generally has lower tensile strength but is more resistant to elevated temperatures and chemical influences.

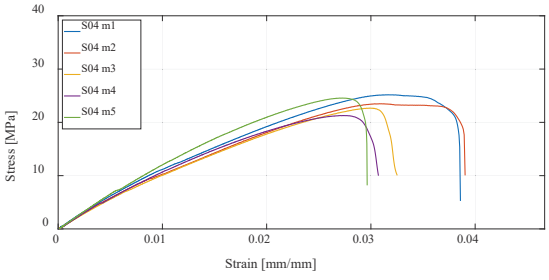

Figure 14. Stress–strain diagram for S04 experimental measurements.

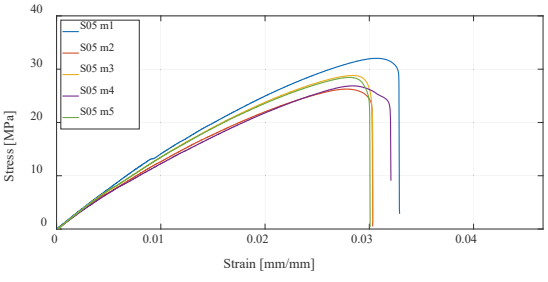

Figure 15. Stress–strain diagram for S05 experimental measurements.

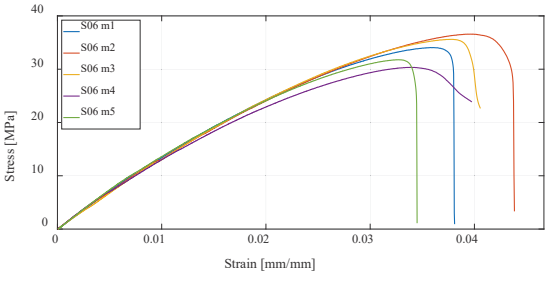

Figure 16. Stress–strain diagram for S06 experimental measurements.

Utilizing the SLS technology, one series of test specimens is manufactured using PA12 powder material. Compared to the test specimens made by the FDM technology from PLA and PETG materials, S07 has significantly higher ductility and higher tensile strength. Due to the manufacturing process, a greater homogeneity of the material is obtained compared to the FDM technologies; thus, there is greater independence of the direction of the force acting on the specimen, which is more credible for real structural UAV airframe parts, which are rarely loaded uniaxially. Figure 17 shows the results of the experimental test for S07 specimens.

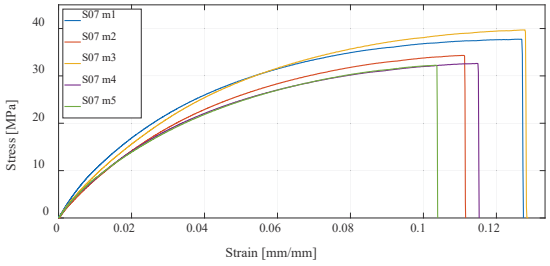

Figure 17. Stress–strain diagram for S07 experimental measurements.

The next series of test specimens will be produced using Markforged equipment and software, which, in addition to the classic FDM technology, also enable the production of parts using the CFF technology. First, a series of specimens made of Onyx carbon fiber-filled nylon material, without reinforcement, is tested. For this material, the highest ductility is obtained, but also the lowest tensile strength (Figure 18). Due to its high ductility, which causes displacement of the test specimen, and tensile strength values close to those of PETG and PLA specimens, a significantly larger area under the curve of the graph is obtained, i.e., absorption energy of the specimen. From the point of view of the impact of the UAV on the objects, it is very favorable; however, larger displacements at lower load forces would lead to problems in flight dynamics. Due to its high ductility, this material is suitable for use as a matrix of a composite structure that is tested further.

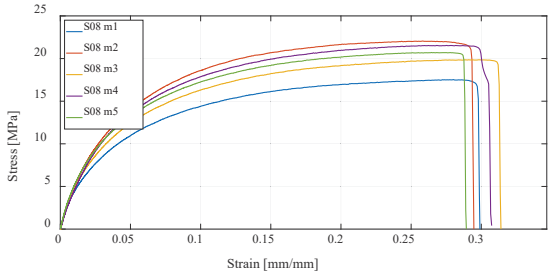

Figure 18. Stress–strain diagram for S08 experimental measurements.

Furthermore, the CFF technology is considered, which enables the production of reinforced composite materials such as parts reinforced with fiberglass. Anisotropy of printed parts is present regardless of how the printing parameters are selected in the slicer; however, in the case of composite structures, the printed polymer forms only a material matrix that is equally printed in all layers of the part. The second part of the composite structure, the fiberglass reinforcement, can be oriented differently to each printing layer. In this research, four series of test specimens were considered. The first composite structure of specimen S09 was made by concentric distribution of fibers in a standard test specimen, and Figure 19 shows the test results. All other specimens of series S10, S11, and S12 have an isotropic fiber arrangement with different fiber orientations, for which the results of

the experimental test are shown in Figures 20–22. As can be expected, the most significant increase in the value of the maximum tensile strength has the specimens with an increase in the number of fiberglass reinforcement layers.

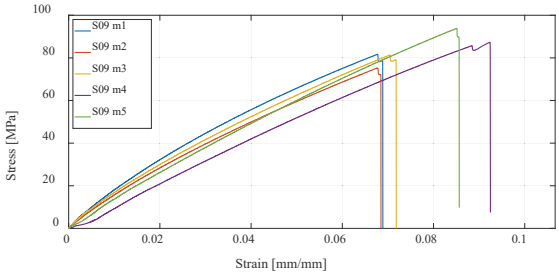

Figure 19. Stress–strain diagram for S09 experimental measurements.

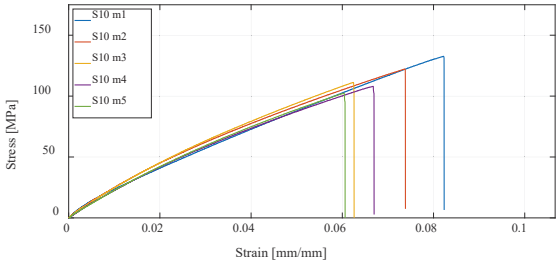

Figure 20. Stress–strain diagram for S10 experimental measurements.

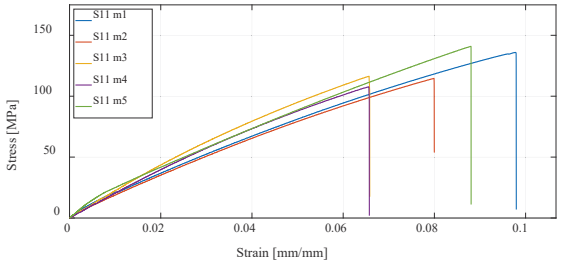

Figure 21. Stress–strain diagram for S11 experimental measurements.

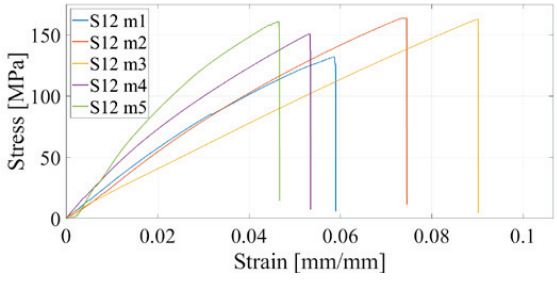

Figure 22. Stress–strain diagram for S12 experimental measurements.

As previously described, due to the problem of clamping composite materials into packs, increasing it to 16 layers makes clamping even more difficult. The higher the tensile strength of the specimen, the more difficult it is to clamp; that is, by increasing the fibers,

the tensile strength significantly increases in the axial direction of the test specimen but not so much in the radial direction of clamping, so the test specimens break due to excessive clamping. If it is not clamped enough, then slippage occurs, so there is a small range to clamp the test specimen so that it does not break and, on the other hand, so that it does not slip. Precisely because of these problems, only one specimen consisting of 16 layers was tested. As expected, that specimen had an even higher tensile strength. For this reason, in future work, testing on a different test device is planned.

4.2. Comparison of Maximum Stress for Different AM Technologies

For a better presentation and visualization of the results, bar charts are used with the mean values of the maximum stress of each series of tested specimens. In the first diagram shown in Figure 23, the values of maximum stress for specimens S01 to S06 made of PLA and PETG materials using FDM technology on the Prusa printer are compared. The diagram shown in Figure 24 shows specimens that actually represent the default parameters for three different technologies and three different printers. Therefore, specimens S01 (PLA) and S04 (PETG) regarding FDM, specimen S07 (PA12) regarding SLS, and finally, S08 (Onyx) regarding CFF/FDM are compared. The following is a comparison of the composite materials that are the main focus of this research. Figure 25 shows all five series of specimens that were produced on the Onyx 3D printer, including the unreinforced specimen S08 to compare with the reinforced specimens.

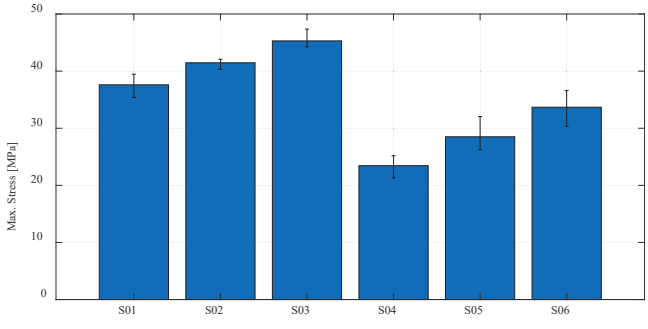

Figure 23. Mean values of the maximum stress regarding PLA and PETG materials.

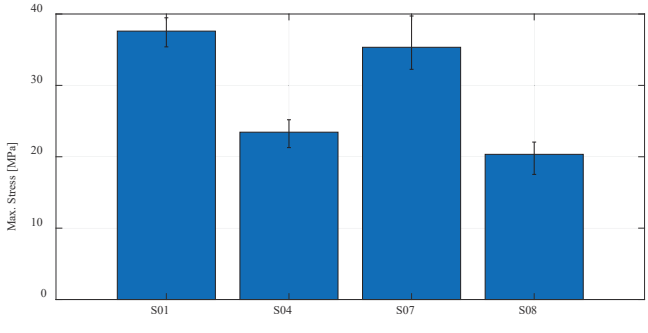

Figure 24. Mean values of the maximum stress regarding default print parameters for PLA, PETG, PA 12, and Onyx materials.

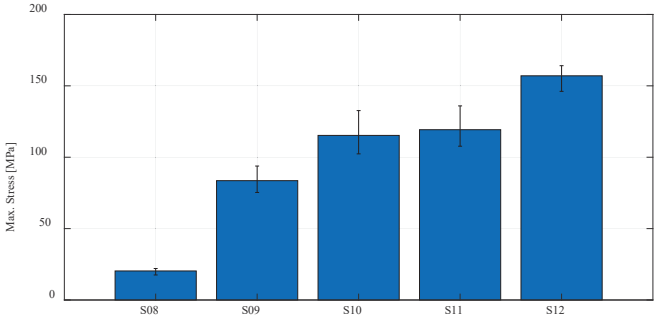

Figure 25. Mean values of the maximum stress regarding CFF technology using Onyx and fiberglass reinforcement.

Onyx material from which specimen series 8 was produced is further used as a matrix material for the production of series S09, S10, S11, and S12. Apart from the fact that the type of reinforcement (concentric or isotropic) and the orientation of the fibers affect the maximum stress, the number of layers in which the fibers are applied has the greatest influence. Considering that of the specimens (S09, S10, S11), which are reinforced with eight layers of fibers, specimen S11 with the highest maximum tensile strength, is further considered, and the proportion of fibers is increased to 12. The specimen S12 with 12 fiber layers orientation is obtained $[30/45/60/0]_{12,}$ which, as expected, gives the highest value of maximum tensile strength. With 12 layers of fibers, the tensile strength is up to 164 MPa. For one measurement that has been completed in the case of 16 fibers, the tensile strength of 174 MPa was recorded.

5. Discussion

In this paper, the focus was on CFF technology, which enables the production of multirotor UAV airframe parts more resilient to mechanical loads. For early development and prototyping, it is most advantageous to use FDM technology due to the low cost and faster model creation if mechanical properties are not crucial when prototyping and testing the assemblies and subassemblies. The price of PLA and PETG materials is almost equal and the lowest compared to other technologies, so it is taken as a reference for comparison in terms of costs. Comparing the materials of FDM technology, PLA has a higher tensile strength compared to PETG material for the same printing parameters. The difference between the lowest and highest obtained tensile strength values for the tested materials is not as significant as when changing the technology.

If higher tensile strength and stiffness of the structural airframe part are required, it is more advantageous to use CFF technology because higher values are achieved compared to FDM and SLS technologies. Although different mechanical properties can be obtained by combining the proportion and orientation of the fibers as shown by the experiment, when making the structural part, it is also necessary to consider the manufacturing costs [50]. Onyx material is approximately 10 times more expensive compared to PLA and PETG materials per kilogram. By adding fibers for making composites, this price increases even more, and compared to PLA is approximately 50 times higher. The powder material for SLS technology used in this work is 13 times more expensive than PLA.

Regarding CFF technology, first, tests were carried out on unreinforced specimens (S08), where the lowest values of tensile strength are obtained in relation to all considered AM technologies and materials in this research. However, the highest ductility is obtained for the same material as shown by experiments, which makes this material suitable as a matrix for composite connection applying fiberglass. As possible matrix reinforcements, Kevlar, carbon, and fiberglass can be used. According to the results in paper [51], the maximum tensile strength of the composite consisting of fiberglass reinforcement is higher than Kevlar reinforcement but lower than carbon reinforcement. From the aspect of mechanical

properties, carbon fiber reinforcements have better characteristics; however, compared to fiberglass reinforcements, they are between 1.5 and 2 times more expensive. The characterization of test specimens produced by CFF technology with different reinforcement parameters was presented. It is evident from the test results that the considered materials can be compared with aluminum alloys 5xxx and 6xxx, which are used for car frame production, as shown in the paper [52]. In Europe, aluminum alloy 6016-T4 is used for the outer panels of cars, whose yield strength is approximately 110 MPa.

In addition to the various technologies and materials examined in this paper and given that the integration of other experimental setups is considered in future work, preliminary testing of test specimens is conducted using a three-point flexural test [53]. Figure 26 shows the equipment and the execution of the test. Universal testing machine Shimadzu AGS-X 5kN (Shimadzu, Kyoto, Japan) is used, standard ISO 178 [54], with a distance of 62 mm, speed of 1%/min, and preload of 0.5N. Experimental testing of three series of three test specimens was carried out, and the flexural modulus for the tested specimens is presented in Table 3. Based on preliminary testing, a test framework will be established. Moreover, the Charpy impact test will also be integrated into the material characterization process.

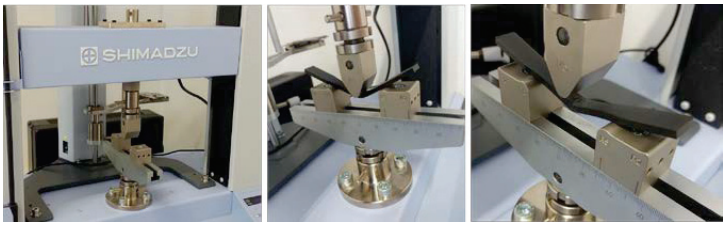

Figure 26. Three-point flexural test—equipment and test execution.

Table 3. Experimental data for three-point flexural test.

Specimen Series	Flexural Modulus (MPa)			
	Meas. 1	Meas. 2	Meas. 3	Mean
S03	2899	2860	2849	2869
S10	3638	3395	3581	3538
S11	3718	3726	3650	3698

6. Conclusions

It has been shown by experiments that even by using a concentric pattern of reinforced material, the mechanical properties are significantly improved concerning tensile strength and ductility, which is the goal of obtaining optimal construction of UAVs. The isotropic reinforcement pattern has a higher proportion of fibers; therefore, higher tensile strength and the orientation of the fibers can be modified. A typical way to elevate tensile strength is by increasing the number of reinforcement layers, as shown by the literature and experiments. This results in an increase in the price but also in an increase in production time. In this paper, a contribution to previous research is provided in the form that different fiber orientations were investigated with the aim of increasing the tensile strength for the same proportion of fibers. Three orientations were tested, and the results are presented for two, with the one having the lowest maximum tensile strength of 132 MPa and strain of 6% has S10—$[0/90/\pm45]_8$, which still exceeds the tensile strength properties of some aluminum alloys. The highest value of maximum tensile strength of 136 MPa is obtained for S11—$[30/45/60/0]_8$. To achieve higher tensile strength, comparable to the 5xxx and 6xxx series aluminum alloys, an isotropic reinforcement pattern with the highest tensile strength is investigated for the case of 12 and 16 reinforcement layers. For 12 layers, tensile strength is up to 164 MPa, and for 16 layers, one measurement was carried out, and a strength of 174 MPa was recorded, which is comparable to the considered aluminum alloys.

Due to the similar requirements of the construction of UAVs to those of the automotive industry, such as absorption energy, lower mass, and high strength, the composites tested in this paper will be subject to extensive testing, which, in addition to the uniaxial test, includes the three-point flexural test and the Charpy impact test. Moreover, the plan is to analyze the microstructure and the specimens' fracture. In future work, the goal is to enable a more diverse and extensive comparison with aluminum alloys.

Author Contributions: Conceptualization, T.Š. and D.K.; methodology, T.Š. and M.B.; software, D.K.; validation, T.Š. and M.B.; writing—original draft preparation, D.K.; writing—review and editing, A.Ł.; supervision, M.B. All authors have read and agreed to the published version of the manuscript.

Funding: This research was funded by European Regional Development Fund, Operational Programme Competitiveness and Cohesion 2014–2020, grant number KK.01.1.1.04.0092, and the APC was funded by KK.01.1.1.04.0092.

Institutional Review Board Statement: Not applicable.

Informed Consent Statement: Not applicable.

Data Availability Statement: The data presented in this study can be provided by the corresponding author upon reasonable request.

Conflicts of Interest: The authors declare no conflict of interest.

References

1. Sharma, S.K.; Saxena, K.K.; Dixit, A.K.; Singh, R.; Mohammed, K.A. Role of additive manufacturing and various reinforcements in MMCs related to biomedical applications. *Adv. Mater. Process. Technol.* **2022**, 1–18. [CrossRef]
2. Ahmad, M.N.; Tarmeze, A.A.; Rasib, A.H.A. Capability of 3D Printing Technology in Producing Molar Teeth Prototype. *Int. J. Eng. Appl. (IREA)* **2020**, *8*, 64. [CrossRef]
3. Morgan, J.L.; Gergel, S.E.; Coops, N.C. Aerial Photography: A Rapidly Evolving Tool for Ecological Management. *Bioscience* **2010**, *60*, 47–59. [CrossRef]
4. Yeom, S.; Cho, I.-J. Detection and Tracking of Moving Pedestrians with a Small Unmanned Aerial Vehicle. *Appl. Sci.* **2019**, *9*, 3359. [CrossRef]
5. Kim, J.; Kim, S.; Ju, C.; Son, H.I. Unmanned Aerial Vehicles in Agriculture: A Review of Perspective of Platform, Control, and Applications. *IEEE Access* **2019**, *7*, 105100–105115. [CrossRef]
6. Jannoura, R.; Brinkmann, K.; Uteau, D.; Bruns, C.; Joergensen, R.G. Monitoring of crop biomass using true colour aerial photographs taken from a remote controlled hexacopter. *Biosyst. Eng.* **2014**, *129*, 341–351. [CrossRef]
7. Villa, D.K.D.; Brandão, A.S.; Sarcinelli-Filho, M. A Survey on Load Transportation Using Multirotor UAVs. *J. Intell. Robot. Syst.* **2019**, *98*, 267–296. [CrossRef]
8. Budholiya, S.; Bhat, A.; Raj, S.A.; Sultan, M.T.H.; Shah, A.U.M.; Basri, A.A. State of the Art Review about Bio-Inspired Design and Applications: An Aerospace Perspective. *Appl. Sci.* **2021**, *11*, 5054. [CrossRef]
9. Puchalski, R.; Giernacki, W. UAV Fault Detection Methods, State-of-the-Art. *Drones* **2022**, *6*, 330. [CrossRef]
10. Carneiro, P.M.C.; Gamboa, P. Structural analysis of wing ribs obtained by additive manufacturing. *Rapid Prototyp. J.* **2019**, *25*, 708–720. [CrossRef]
11. Kotarski, D.; Piljek, P.; Pranjić, M.; Grlj, C.G.; Kasać, J. A Modular Multirotor Unmanned Aerial Vehicle Design Approach for Development of an Engineering Education Platform. *Sensors* **2021**, *21*, 2737. [CrossRef] [PubMed]
12. Bortolini, M.; Galizia, F.G.; Mora, C. Reconfigurable manufacturing systems: Literature review and research trend. *J. Manuf. Syst.* **2018**, *49*, 93–106. [CrossRef]
13. Koren, Y. *The Global Manufacturing Revolution: Product-Process-Business Integration and Reconfigurable Systems*, 1st ed.; John Wiley & Sons, Inc.: New York, NY, USA, 2010; ISBN 9780470618813.
14. Da Silveira, G.; Borenstein, D.; Fogliatto, F.S. Mass customization: Literature review and research directions. *Int. J. Prod. Econ.* **2001**, *72*, 1–13. [CrossRef]
15. Xiong, G.; Wang, F.-Y.; Nyberg, T.R.; Shang, X.; Zhou, M.; Shen, Z.; Li, S.; Guo, C. From mind to products: Towards social manufacturing and service. *IEEE/CAA J. Autom. Sin.* **2017**, *5*, 47–57. [CrossRef]
16. Kristiawan, R.B.; Imaduddin, F.; Ariawan, D.; Ubaidillah; Arifin, Z. A review on the fused deposition modeling (FDM) 3D printing: Filament processing, materials, and printing parameters. *Open Eng.* **2021**, *11*, 639–649. [CrossRef]
17. Huang, J.; Qin, Q.; Wang, J. A Review of Stereolithography: Processes and Systems. *Processes* **2020**, *8*, 1138. [CrossRef]
18. Kumar, S. Selective laser sintering: A qualitative and objective approach. *JOM* **2003**, *55*, 43–47. [CrossRef]
19. Patpatiya, P.; Chaudhary, K.; Shastri, A.; Sharma, S. A review on polyjet 3D printing of polymers and multi-material structures. *Proc. Inst. Mech. Eng. Part C J. Mech. Eng. Sci.* **2022**, *236*, 7899–7926. [CrossRef]

20. Mekonnen, B.G.; Bright, G.; Walker, A. A Study on State of the Art Technology of Laminated Object Manufacturing (LOM). In *CAD/CAM, Robotics and Factories of the Future. Lecture Notes in Mechanical Engineering*; Mandal, D.K., Syan, C.S., Eds.; Springer: New Delhi, India, 2016; pp. 207–216. [CrossRef]
21. Zohdi, N.; Yang, R. Material Anisotropy in Additively Manufactured Polymers and Polymer Composites: A Review. *Polymers* **2021**, *13*, 3368. [CrossRef]
22. García-Domínguez, A.; Claver, J.; Camacho, A.M.; Sebastián, M.A. Considerations on the Applicability of Test Methods for Mechanical Characterization of Materials Manufactured by FDM. *Materials* **2020**, *13*, 28. [CrossRef]
23. Mercado-Colmenero, J.M.; Rubio-Paramio, M.A.; la Rubia-Garcia, M.D.; Lozano-Arjona, D.; Martin-Doñate, C. A numerical and experimental study of the compression uniaxial properties of PLA manufactured with FDM technology based on product specifications. *Int. J. Adv. Manuf. Technol.* **2019**, *103*, 1893–1909. [CrossRef]
24. Grodzki, W.; Łukaszewicz, A. Design and manufacture of umanned aerial vehicles (UAV) wing structure using composite materials. *Mater. Werkst.* **2015**, *46*, 269–278. [CrossRef]
25. Basri, E.I.; Sultan, M.T.H.; Basri, A.A.; Mustapha, F.; Ahmad, K.A. Consideration of Lamination Structural Analysis in a Multi-Layered Composite and Failure Analysis on Wing Design Application. *Materials* **2021**, *14*, 3705. [CrossRef] [PubMed]
26. Pratama, J.; Cahyono, S.I.; Suyitno, S.; Muflikhun, M.A.; Salim, U.A.; Mahardika, M.; Arifvianto, B. A Review on Reinforcement Methods for Polymeric Materials Processed Using Fused Filament Fabrication (FFF). *Polymers* **2021**, *13*, 4022. [CrossRef]
27. Galatas, A.; Hassanin, H.; Zweiri, Y.; Seneviratne, L. Additive Manufactured Sandwich Composite/ABS Parts for Unmanned Aerial Vehicle Applications. *Polymers* **2018**, *10*, 1262. [CrossRef]
28. Lupone, F.; Padovano, E.; Venezia, C.; Badini, C. Experimental Characterization and Modeling of 3D Printed Continuous Carbon Fibers Composites with Different Fiber Orientation Produced by FFF Process. *Polymers* **2022**, *14*, 426. [CrossRef]
29. Espinoza-Fraire, T.; Saenz, A.; Salas, F.; Juarez, R.; Giernacki, W. Trajectory Tracking with Adaptive Robust Control for Quadrotor. *Appl. Sci.* **2021**, *11*, 8571. [CrossRef]
30. Kotarski, D.; Piljek, P.; Pranjić, M.; Kasać, J. Concept of a Modular Multirotor Heavy Lift Unmanned Aerial Vehicle Platform. *Aerospace* **2023**, *10*, 528. [CrossRef]
31. Lukaszewicz, A.; Panas, K.; Szczebiot, R. Design process of technological line for vegetables packaging using CAx tools. In Proceedings of the 17th International Scientific Conference on Engineering for Rural Development, Jelgava, Latvia, 23–25 May 2018; pp. 871–887. [CrossRef]
32. Mircheski, I.; Łukaszewicz, A.; Szczebiot, R. Injection process design for manufacturing of bicycle plastic bottle holder using CAx tools. *Procedia Manuf.* **2019**, *32*, 68–73. [CrossRef]
33. Lukaszewicz, A.; Szafran, K.; Jozwik, J. CAx Techniques Used in UAV Design Process. In Proceedings of the 2020 IEEE 7th International Workshop on Metrology for AeroSpace (MetroAeroSpace), Pisa, Italy, 22–24 June 2020; pp. 95–98. [CrossRef]
34. Saleh Alghamdi, S.; John, S.; Roy Choudhury, N.; Dutta, N.K. Additive Manufacturing of Polymer Materials: Progress, Promise and Challenges. *Polymers* **2021**, *13*, 753. [CrossRef]
35. Peyre, P.; Rouchausse, Y.; Defauchy, D.; Régnier, G. Experimental and numerical analysis of the selective laser sintering (SLS) of PA12 and PEKK semi-crystalline polymers. *J. Mater. Process. Technol.* **2015**, *225*, 326–336. [CrossRef]
36. PA12 Smooth Technical Data Sheet. Available online: https://sinterit.com/wp-content/uploads/2022/06/PA12-Smooth-EN.pdf (accessed on 11 July 2023).
37. Moghanizadeh, A. Development of 3D printing scaffolds by sacrificial ice support layers. *Manuf. Lett.* **2022**, *31*, 116–118. [CrossRef]
38. Devil Design PLA Ffilament Product Card. Available online: https://devildesign.com/download/PLA_-_product_card.pdf (accessed on 11 July 2023).
39. Devil Design PET-G Filament Product Card. Available online: https://devildesign.com/download/PET-G_-_product_card.pdf (accessed on 11 July 2023).
40. Nath, S.D.; Nilufar, S. An Overview of Additive Manufacturing of Polymers and Associated Composites. *Polymers* **2020**, *12*, 2719. [CrossRef] [PubMed]
41. Patel, H.V.; Dave, H.K. Effect of fiber orientation on tensile strength of thin composites. *Mater. Today Proc.* **2021**, *46*, 8634–8638. [CrossRef]
42. Markforged Material Datasheet. Available online: https://www-objects.markforged.com/craft/materials/CompositesV5.2.pdf (accessed on 11 July 2023).
43. Zisopol, D.G.; Ion, N.; Portoaca, A.I. Comparison of the Charpy Resilience of Two 3D Printed Materials: A Study on the Impact Resistance of Plastic Parts. *Eng. Technol. Appl. Sci. Res.* **2023**, *13*, 10781–10784. [CrossRef]
44. Brčić, M.; Kršćanski, S.; Brnić, J. Rotating Bending Fatigue Analysis of Printed Specimens from Assorted Polymer Materials. *Polymers* **2021**, *13*, 1020. [CrossRef]
45. *ISO E. 527-2*; Plastics—Determination of Tensile Properties—Part 2: Test Conditions for Moulding and Extrusion Plastics. International Organization of Standardization: Geneva, Switzerland, 2012.
46. Dickson, A.N.; Barry, J.N.; McDonnell, K.A.; Dowling, D.P. Fabrication of continuous carbon, glass and Kevlar fibre reinforced polymer composites using additive manufacturing. *Addit. Manuf.* **2017**, *16*, 146–152. [CrossRef]
47. Cordin, M.; Bechtold, T.; Pham, T. Effect of fibre orientation on the mechanical properties of polypropylene–lyocell composites. *Cellulose* **2018**, *25*, 7197–7210. [CrossRef]

48. Shanmugam, V.; Rajendran, D.J.J.; Babu, K.; Rajendran, S.; Veerasimman, A.; Marimuthu, U.; Singh, S.; Das, O.; Neisiany, R.E.; Hedenqvist, M.S.; et al. The mechanical testing and performance analysis of polymer-fibre composites prepared through the additive manufacturing. *Polym. Test.* **2021**, *93*, 106925. [CrossRef]
49. Parmiggiani, A.; Prato, M.; Pizzorni, M. Effect of the fiber orientation on the tensile and flexural behavior of continuous carbon fiber composites made via fused filament fabrication. *Int. J. Adv. Manuf. Technol.* **2021**, *114*, 2085–2101. [CrossRef]
50. Costabile, G.; Fera, M.; Fruggiero, F.; Lambiase, A.; Pham, D. Cost models of additive manufacturing: A literature review. *Int. J. Ind. Eng. Comput.* **2017**, *8*, 263–283. [CrossRef]
51. Cofaru, N.F.; Pascu, A.; Oleksik, M.; Petruse, R. Tensile Properties of 3D-printed Continuous-Fiber-Reinforced Plastics. *Mater. Plast.* **2021**, *58*, 271–282. [CrossRef]
52. Miller, W.S.; Zhuang, L.; Bottema, J.; Wittebrood, A.J.; De Smet, P.; Haszler, A.; Vieregge, A. Recent development in aluminium alloys for the automotive industry. *Mater. Sci. Eng. A* **2000**, *280*, 37–49. [CrossRef]
53. Moreno-Núñez, B.A.; Abarca-Vidal, C.G.; Treviño-Quintanilla, C.D.; Sánchez-Santana, U.; Cuan-Urquizo, E.; Uribe-Lam, E. Experimental Analysis of Fiber Reinforcement Rings' Effect on Tensile and Flexural Properties of Onyx™–Kevlar® Composites Manufactured by Continuous Fiber Reinforcement. *Polymers* **2023**, *15*, 1252. [CrossRef] [PubMed]
54. *ISO 178*; Plastics—Determination of Flexural Properties. International Organization for Standardization: Geneva, Switzerland, 2019.

drones

MDPI

Article

An Approach to the Implementation of a Neural Network for Cryptographic Protection of Data Transmission at UAV

Ivan Tsmots [1], Vasyl Teslyuk [1,*], Andrzej Łukaszewicz [2,*], Yurii Lukashchuk [1], Iryna Kazymyra [1], Andriy Holovatyy [3] and Yurii Opotyak [1]

[1] Department of Automated Control Systems, Lviv Polytechnic National University, 79013 Lviv, Ukraine; ivan.h.tsmots@lpnu.ua (I.T.); urijlukas@gmail.com (Y.L.); iryna.y.kazymyra@lpnu.ua (I.K.); yurii.v.opotiak@lpnu.ua (Y.O.)
[2] Department of Machine Design and Exploitation, Faculty of Mechanical Engineering, Bialystok University of Technology, 15-351 Bialystok, Poland
[3] Department of Computer-Aided Design Systems, Lviv Polytechnic National University, 79013 Lviv, Ukraine; andrii.i.holovatyi@lpnu.ua
* Correspondence: vasyl.m.teslyuk@lpnu.ua (V.T.); a.lukaszewicz@pb.edu.pl (A.Ł.)

Abstract: An approach to the implementation of a neural network for real-time cryptographic data protection with symmetric keys oriented on embedded systems is presented. This approach is valuable, especially for onboard communication systems in unmanned aerial vehicles (UAV), because of its suitability for hardware implementation. In this study, we evaluate the possibility of building such a system in hardware implementation at FPGA. Onboard implementation-oriented information technology of real-time neuro-like cryptographic data protection with symmetric keys (masking codes, neural network architecture, and matrix of weighting coefficients) has been developed. Due to the pre-calculation of matrices of weighting coefficients and tables of macro-partial products and the use of tabular-algorithmic implementation of neuro-like elements and dynamic change of keys, it provides increased cryptographic stability and hardware–software implementation on FPGA. The table-algorithmic method of calculating the scalar product has been improved. By bringing the weighting coefficients to the greatest common order, pre-computing the tables of macro-partial products, and using operations of memory read, fixed-point addition, and shift operations instead of floating-point multiplication and addition operations, it provides a reduction in hardware costs for its implementation and calculation time as well. Using a processor core supplemented with specialized hardware modules for calculating the scalar product, a system of neural network cryptographic data protection in real-time has been developed, which, due to the combination of universal and specialized approaches, software, and hardware, ensures the effective implementation of neuro-like algorithms for cryptographic encryption and decryption of data in real-time. The specialized hardware for neural network cryptographic data encryption was developed using VHDL for equipment programming in the Quartus II development environment ver. 13.1 and the appropriate libraries and implemented on the basis of the FPGA EP3C16F484C6 Cyclone III family, and it requires 3053 logic elements and 745 registers. The execution time of exclusively software realization of NN cryptographic data encryption procedure using a NanoPi Duo microcomputer based on the Allwinner Cortex-A7 H2+ SoC was about 20 ms. The hardware–software implementation of the encryption, taking into account the pre-calculations and settings, requires about 1 msec, including hardware encryption on the FPGA of four 2-bit inputs, which is performed in 160 nanoseconds.

Keywords: neural network (NN); cryptographic protection; UAV; UAS; onboard system; encryption; decryption; tabular-algorithmic method; scalar product; real time

Citation: Tsmots, I.; Teslyuk, V.; Łukaszewicz, A.; Lukashchuk, Y.; Kazymyra, I.; Holovatyy, A.; Opotyak, Y. An Approach to the Implementation of a Neural Network for Cryptographic Protection of Data Transmission at UAV. *Drones* **2023**, *7*, 507. https://doi.org/10.3390/drones7080507

Academic Editor: Diego González-Aguilera

Received: 1 July 2023
Revised: 27 July 2023
Accepted: 30 July 2023
Published: 2 August 2023

1. Introduction

Cryptographic protection of data transmission between the UAV and the remote-control centre is important to ensure the confidentiality and integrity of the information

transmitted. However, there are certain practical problems and influencing factors that must be taken into account when developing a cryptographic protection system for data transmission, specifically for UAVs. The main ones are limited computing resources; ensuring requirements for energy consumption, dimensions, and weight of equipment; provision of data transmission between the UAV and the remote control centre in real time; ensuring the requirements for the cost of the system of cryptographic protection of data transmission; algorithmic problems of cryptographic algorithms, which are associated with security vulnerabilities and malicious attacks; limitation of physical access to means of cryptographic protection; organization of an effective key management system; damage or loss of data in the wireless transmission channel; and change in altitude and environmental conditions that affect the quality of communication and data transmission.

The key problem is to guarantee the cryptographic security of data transmission in the management of UAVs [1,2], intelligent robots [3], microsatellites [4], and various mobile transport systems [5]. Due to the security vulnerabilities of UAVs and illegal and malicious attacks against UAVs, especially against communication data and UAV control, solutions to prevent such attacks are needed, and one of them is to encrypt UAV's communication data [6–8]. Unmanned aerial vehicles (UAVs) must be energy-efficient, especially in data processing, because of limited battery capacity [9]. Solving this problem requires the development of neural network (NN) technology [10–12] for cryptographic data protection, which is focused on use in UAV onboard communication systems. When developing onboard cryptographic data protection systems, it is necessary to provide a real-time mode, increase cryptographic resistance and noise immunity, and reduce power consumption, weight, size and cost [13–23]. The usage of an auto-associative NN of direct propagation, which is trained on the basis of the principal components analysis, helps to conform to such requirements. A specific feature of such neural networks is the ability of weight pre-calculation and to apply the tabular-algorithmic method for the implementation of neuro-like elements using the basis of elementary arithmetic operations. For NN cryptographic encryption and decryption of data, it is proposed to use symmetric keys, which include masking codes, NN architecture and a matrix of weights [24,25].

Through the extensive use of a modern component base and the development of new VLSI methods, algorithms, and structures, high technical and operational rates of onboard cryptographic data protection systems are achieved. Onboard systems for NN cryptographic protection of data must have variable hardware for rapid changes in NN architecture. The use of modern element base (microcontrollers, programmable logic integrated circuits FPGA) in the development of onboard and embedded systems makes it possible to reduce their weight, size, and power consumption [26,27] and, in the development of onboard systems of NN cryptographic, data protection provides a quick change of encryption and decryption keys.

NN cryptographic encryption and decryption of data in real-time is achieved through the application of parallel encryption and decryption of data, hardware implementation of neuro-like elements based on a multi-operand approach and macro-partial products tables.

Therefore, the urgent problem is to propose an approach to the implementation of NN for cryptographic data protection, focused on implementing onboard systems with high technical and operational characteristics. The objective of the work is to study how to implement the onboard NN for real-time cryptographic data protection. In order to achieve this goal, the following tasks have to be solved:

- Development of the approach to NN cryptographic data protection;
- Development of the structure of the system of NN cryptographic protection and real-time data transmission;
- Development of components of onboard systems of NN cryptographic encryption–decryption of data;
- Implementation of the specialized hardware components of NN cryptographic data encryption on FPGA.

This article is structured as follows. In the Introduction, we have considered the problem relevancy and the main objectives of this research. Section 2 contains a brief review of the related works (the research context). The structure of NN technology for cryptographic data protection is described in Section 3, and the main stages of NN data encryption/decryption are considered here as well. Section 4 presents the structure of the system for NN cryptographic data protection and transmission (stationery and UAV onboard parts) developed using an integrated approach. The components of the onboard system for NN cryptographic data encryption and decryption are proposed in Section 5, and the diagrams for the specialized hardware are given.

2. Related Works

The study of the main trends in the area of UAV onboard systems development for real-time cryptographic data protection shows that NN methods are increasingly used for performing data encryption and decryption in such systems [28–32]. These publications show that the implementation of NN methods of cryptographic data protection is generally performed by software. The critical drawback of software implementation of NN cryptographic data protection is the difficulty of providing a real-time mode and the constraints imposed on onboard systems in terms of weight, size, power consumption, and cost.

The possibilities of adapting the auto-associative NN with non-iterative learning for data protection tasks are considered in [28–32]. The peculiarity of the functioning of such an NN is the preliminary calculation of weights as a result of its training based on the principal component analysis (PCA). In this case, a system of eigenvectors is used that corresponds to the eigenvalues of the covariance matrix of input data [33]. To encrypt and decrypt data, the auto-associative NN with pre-calculated weights is applied. In [34], it was shown that for the masking codes, the architecture of the NN and the matrix of weights are the basis for cryptographic encryption and decryption of data in neural networks.

Publications [35–37] are devoted to the hardware implementation of neural networks, showing that they are based on neural elements. The feature of such neural elements is that the number of inputs and their bit length are determined by the NN architecture, which is one of the characteristics of the data encryption key. The main operation of the neuro element is the calculation of the scalar product using pre-calculated weights.

In [37–39], the methods for calculating the scalar product using the basis of elementary arithmetic operations, addition and shift, are considered. The peculiarity of these methods is the formation of macro-partial products, their shift, and addition to the previously accumulated amount. Hardware implementation of such methods requires significant equipment costs. The implementation of a tabular-algorithmic method for calculating the scalar product, which is reduced to the operations of reading macro-partial products, addition and shift, requires fewer equipment costs and less computation time. The disadvantage of this method is that it is limited to fixed-point data format (for input data and weights).

Analyzing the works [31,40,41], it can be noted that NN tools for cryptographic symmetric encryption and decryption of data [42] are implemented on the basis of microprocessors supplemented by hardware that implements time-consuming computational operations using FPGA [43]. The high speed of NN tools for cryptographic encryption and decryption of data is achieved through parallelization, pipeline computing processes, and hardware implementation of neural elements. The disadvantage of the existing NN tools for cryptographic data protection is the difficulty of changing the encryption and decryption key rapidly.

3. The Approach to NN Implementation for Cryptographic Data Protection

3.1. Structure of NN Technology of Cryptographic Data Protection

The implementation of NN for cryptographic protection of data transmission is focused on hardware and software implementation with high technical and operational

characteristics. It is proposed that to carry out such implementation on the basis of an integrated approach includes the following:

- Research and development of theoretical foundations of neuro-like cryptographic data protection;
- Research and development of new algorithms and structures of neuro-like encryption and decryption of data focused on modern element base;
- Modern element base with the ability to program the structure;
- The means for automated design of software and hardware.

Figure 1 shows the developed structure of NN technology for cryptographic data protection, which is focused on hardware implementation and provides encryption with symmetric keys. When implementing the symmetric cryptosystem, the encryption key and the decryption key are the same, or the decryption key is easily calculated from the encryption key.

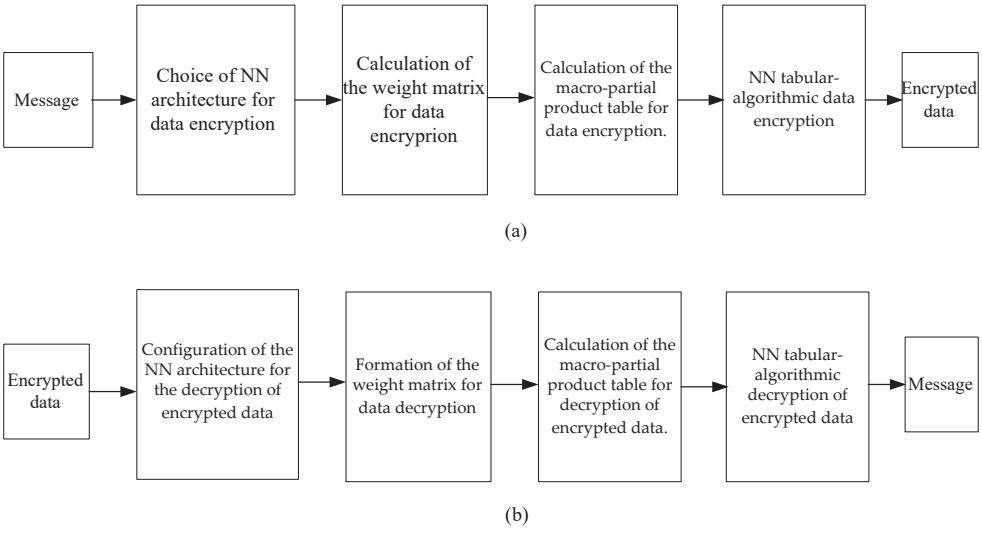

Figure 1. Structure of NN technology for cryptographic data protection: (**a**) the process of data encryption; (**b**) the process of decrypting data.

For hardware implementation, the proposed technology is based on the selection of auto-associative neural networks, which are trained non-iteratively. This allows us to calculate the matrix of weighting coefficients in advance and to store them in the lookup tables since they will be fixed for the selected NN configuration. The calculation of the output of the neuro-like element of this NN can be represented as the sum of the products of the weighting coefficients and the input data to be encrypted. To implement a quick calculation on the FPGA of the product of the fixed weighting coefficients and the input data, a table-algorithmic method of their calculation is applied. The tabular-algorithmic method makes it possible to implement high technical and operational characteristics of data encryption–decryption tools. A combination of these approaches ensures the effective implementation of FPGAs. The details of the above-mentioned steps are described further in the article.

A specific feature of the proposed technology is the pre-calculation of matrices of weighting coefficients for possible variants of neural networks and the use of the tabular-algorithmic method for the implementation of neuro elements. Such pre-calculation of matrices and tables provides the possibility of dynamically changing keys and, accordingly, increasing cryptographic stability. The use of elementary arithmetic operations in fixed-

point format for the hardware tabular-algorithmic implementation of the neuro element provides a reduction in hardware costs when building specialized hardware modules.

Ensuring the real-time mode when encrypting (decrypting) data can be achieved by selecting the necessary number of specialized hardware modules and reducing the time of calculating the scalar product in such modules. It is possible to reduce the time of calculating the scalar product by using an algorithm that provides for submitting g bit slices to the address inputs of g tables of macro-partial products. Using such an algorithm reduces the time of calculating the scalar product by g times.

3.2. Main Stages of NN Encryption

The encryption uses a key consisting of N neurons in the NN, a weight matrix, and masking operations. The main stages of message encryption are considered below.

Choice of NN architecture. The number of neuro elements N, the number of inputs k, and the bit inputs m determine the architecture of the NN. The number of neural elements is defined according to the following formula:

$$N = \frac{n}{m}, \tag{1}$$

where n is the bit length of the message, and m is the bit length of the inputs.

The incoming messages, which are encrypted, can have different bit lengths (n) and different inputs number (k), which is equal to the number of neuro elements N. The architecture of the NN depends on the value of the bit length of the message n and the number of inputs k. Such configuration of the NN architecture is available to encrypt the $n = 16$ bit message: $m = 2$, $k = 8$, $N = 8$; $m = 4$, $k = 4$, $N = 4$; $m = 8$, $k = 2$, $N = 2$, in case of $n = 24$ they are: $m = 2$, $k = 12$, $N = 12$; $m = 3$, $k = 8$, $N = 8$; $m = 4$, $k = 6$, $N = 6$, $m = 6$, $k = 4$, $N = 4$; $m = 8$, $k = 3$, $N = 3$; $m = 12$, $k = 2$, $N = 2$.

Calculation of the weight matrix. For data encryption–decryption, we will use an auto-associative NN, which learns non-iteratively using the principal components analysis (PCA), which performs a linear transformation following the formula

$$\overline{y} = W \cdot \overline{x} \tag{2}$$

According to Equation (2), the matrix $W \in R^{n \times n}$ is used to convert the input vector $\overline{x} \in R^n$ into the output vector $\overline{y} \in R^n$. The conversion is as follows. A system of linearly independent vectors selects an orthonormal system of eigenvectors corresponding to the eigenvalues of the covariance matrix of the input data.

The input data is a set of N vectors $\overline{x}_j, j = 1, \ldots N$, with dimension n, $\overline{x}_j = (x_{j1}, x_{j2}, \ldots, x_{jn})$:

$$X = (\overline{x}_1, \overline{x}_2, \ldots, \overline{x}_N)^t. \tag{3}$$

For N vectors, the autocovariance matrix $\overline{x}_j$ is

$$R = X^t \cdot X, \tag{4}$$

where each of the elements is expressed by

$$r_{jl} = \sum_{i=1}^{N} \overline{x}_{jl} \overline{x}_{il} = \sum_{i=1}^{N} (\overline{x}_{ji} - \mu_j)(\overline{x}_{il} - \mu_l), \tag{5}$$

where $j, l = 1, 2, \ldots, n$, and μ_j; μ_l—mathematical expectations of vectors $\overline{x}_j$, $\overline{x}_l$.

The eigenvalues of R symmetric non-negative matrix are real and positive numbers. They are arranged in descending order $\lambda_1 > \lambda_2 > \ldots > \lambda_n$. Similarly, the eigenvectors corresponding to λ_i are placed. Therefore, a linear transformation (2) is defined by the matrix W. Here, $\overline{y} = (y_1, y_2, \ldots, y_n)$ is a vector of the PCA principal components corresponding to the input data vector $\overline{x}$. The number of principal components vectors N conforms with

the number of input data vectors $\overline{x}$ [29]. The matrix of weights used to encrypt the data is as follows:

$$\begin{vmatrix} W_{11} & W_{12} & \cdots & W_{1k} \\ W_{21} & W_{22} & \cdots & W_{2k} \\ \vdots & \vdots & \cdots & \vdots \\ W_{N1} & W_{N2} & \cdots & W_{Nk} \end{vmatrix}. \quad (6)$$

The basic operation of the NN used to encrypt data is the operation of calculating the scalar product. This operation should be implemented using the tabular-algorithmic method because the matrix of weights W_{js}, where $j = 1, \ldots, N$, $s = 1, \ldots, k$, is pre-calculated.

Calculation of the table of macro-partial products for data encryption. The specificity of the scalar product calculation operation used in data encryption is that the weights are pre-calculated (constants) and set in floating point format, and the input data X_j is in fixed point format with its fixing before the high digit of a number. The scalar product is calculated by means of the tabular-algorithmic method according to the formula

$$Z = \sum_{j=1}^{N} W_j X_j = \sum_{i=1}^{n} 2^{-i} \sum_{j=1}^{N} W_j X_{ji} = \sum_{i=1}^{n} 2^{-i} \sum_{j=1}^{N} P_{ji} = \sum_{i=1}^{n} 2^{-i} P_{Mi}, \quad (7)$$

where N is the number of products; X_j is the input data; W_j is the j-th weight coefficient; n is the bit length of the input data; P_{ij} is the partial product; and P_{Mi} is the macro-partial product formed by adding N partial products P_{ij}, as follows: $P_{Mi} = \sum_{j=1}^{N} P_{ji}$.

Formation of the tables of macro-partial products for floating-point weights $W_j = w_j 2^{m_{W_j}}$ (where w_j is the mantissa of W_j weight coefficient; m_{W_j} is the order of W_j weight coefficient) foresees the following operations to be performed:

- Defining the largest common order of weights m_{Wmaxc};
- Calculation of the order difference for each W_j weight coefficient: $\Delta m_{W_j} = m_{Wmaxc} - m_{W_j}$;
- Shift the mantissa w_j to the right by a difference of orders Δm_{W_j};
- Calculation of P_{Mi} macro-partial product for the case when $x_{1i} = x_{2i} = x_{3i} = \ldots = x_{Ni} = 1$;
- Determining the number of overflow bits q in the P_{Mi} macro-partial product for the case when $x_{1i} = x_{2i} = x_{3i} = \ldots = x_{Ni} = 1$;
- Obtaining scalable mantissas w_j^h by shifting them to the right by the number of overflow bits;
- Adding to the largest common order of weight m_{Wmaxc} the number of overflow bits q, as per the formula $m_j = m_{Wmaxc} + q$.

The table of macro-partial products is calculated by the formula

$$P_{Mi} = \begin{cases} 0, \ if\ x_{1i} = x_{2i} = x_{3i} = \ldots = x_{Ni} = 0 \\ w_1^h, \ if\ x_{1i} = 1, \ x_{2i} = x_{3i} = \ldots = x_{Ni} = 0 \\ w_2^h, \ if\ x_{1i} = 0, x_{2i} = 1, x_{3i} = \ldots = x_{Ni} = 0 \\ w_1^h + w_2^h, \ if\ x_{1i} = 1, x_{2i} = 1, x_{3i} = \ldots = x_{Ni} = 0 \\ \vdots \\ w_2^h + \ldots + w_N^h, \ if\ x_{1i} = 0, x_{2i} = x_{3i} = \ldots = x_{Ni} = 1 \\ w_1^h + w_2^h + \ldots + w_N^h, \ if\ x_{1i} = x_{2i} = x_{3i} = \ldots = x_{Ni} = 1 \end{cases}, \quad (8)$$

where $x_{1i}, x_{2i}, x_{3i}, \ldots, x_{Ni}$ address inputs of the table, and w_j^h is the mantissa of W_j weight coefficient brought to the greatest common order.

The possible combinations number of P_{Mi} macro-partial products and the table size are as follows:

$$Q = 2^N. \quad (9)$$

By dividing all N products by parts $N1$ and $N2$, we can reduce the table size. For each of these parts, separate tables of macro-partial products P_{N1Mi} and P_{N2Mi} are formed and stored in separate memory blocks or a single memory block. When using two memory blocks, parts of the macro-partial products P_{N1Mi} and P_{N2Mi} are read in one clock cycle and in one memory block—in two clock cycles. The sum of two macro-partial products P_{N1Mi} and P_{N2Mi} gives us the macro-partial product P_{Mi}.

NN tabular-algorithmic data encryption. During the training of the NN, the matrix of weights W is determined. Figure 2 shows the structure of auto-associative NN used for data encryption. Here, M_j is the mask for the j-th input, x_j is the j-th input data, and XOR is the masking operation using the exclusive OR elements.

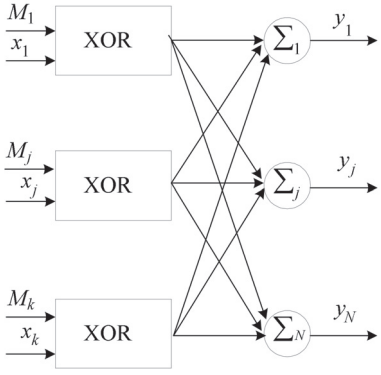

Figure 2. The structure of the data encryption NN.

To perform the NN data encryption, we multiply the W matrix by the input data vector x according to the formula

$$y_j = \begin{vmatrix} W_{11} & W_{12} & \cdots & W_{1k} \\ W_{21} & W_{22} & \cdots & W_{2k} \\ \vdots & \vdots & \cdots & \vdots \\ W_{N1} & W_{N2} & \cdots & W_{Nk} \end{vmatrix} \times \begin{matrix} x_1 \\ x_2 \\ \vdots \\ x_k \end{matrix}. \tag{10}$$

The multiplication of the matrix of weights W by the vector of input data x is reduced to performing N scalar product calculations:

$$y_j = \sum_{s=1}^{k} W_{js} x_s \tag{11}$$

where k—number of products, $s = 1, 2, \ldots, k; j = 1, 2, \ldots, N$.

The calculation of scalar products will be achieved using the tabular-algorithmic method, where the weights W_{js} are set in floating-point format, and the input data x_s is in a fixed-point format with fixation before the highest digit. Tabular-algorithmic calculation of the mantissa of the scalar product is reduced to reading the macro-partial product P_{Mi} from the j-th table (memory) at the address corresponding to the i-th bit slice of N input data, and adding it to the before accumulated sums according to

$$y_{Mji} = 2^{-1} y_{Mj(i-1)} + P_{Mji}, \tag{12}$$

where $y_{Mj0} = 0$, $i = 1, \ldots, m$, and m is the bit length of the input data. The number of tables of macro-partial products corresponds to N—the number of rows of the matrix (10). The result of calculating the scalar product y_j consists of the mantissa y_{Mj} and the order m_j.

The time required to compute the mantissa of the scalar product (SP) is determined by the formula

$$t_{SP} = m\left(t_{table} + t_{reg} + t_{add}\right), \tag{13}$$

where t_{SP} is the time of calculation of the scalar product, t_{table} is the time of reading from the table (memory), t_{reg} is the time of reading (writing) from the register, and t_{add} is the time of adding.

Data encryption can be performed either sequentially or in parallel, depending on the speed required. In the case of sequential encryption, the encryption time is the result of the formula

$$t_{encrypt} = Nm\left(t_{table} + t_{reg} + t_{add}\right), \tag{14}$$

where $t_{encrypt}$ is the time required for encryption. The encryption time can be reduced by performing N operations of calculating the scalar product in parallel.

As a result of NN data encryption, we obtain N encrypted data in the form $y_j = y_{Mj}2^{m_j}$, where y_{Mj} is the mantissa at the j-th output, and m_j is the order value at the j-th output. It is advisable to bring all encrypted data to the highest common order for transmission, and such reduction to the greatest common order is performed in three stages:

- Define the greatest order m_{encr};
- For each encrypted data y_j, calculate the difference between the orders $\Delta m_j = m_{encr} - m_j$;
- By performing shift of the mantissa y_{Mj} to the right by the difference of orders Δm_j, we obtain mantissa of the encrypted data y^h_{Mj} reduced to the greatest common order.

The mantissa of the encrypted data y^h_{Mj} reduced to the largest common order and the largest common order m_{encr} are sent for decryption.

3.3. The Main Stages of NN Cryptographic Data Decryption

Now the encrypted data presented by mantissa y^h_{Mj} reduced to the largest common order m_{encr} need to be decrypted. The encrypted data will be decrypted according to the following procedure.

Configuration of the NN architecture for the decryption of encrypted data. The architecture of the NN for the decryption of encrypted data, in terms of the number of neural elements, is the same as the architecture of the NN used for the encryption of data. In this NN, the number of inputs and the number of neurons corresponds to the number of the encrypted mantissa y^h_{Mj}. The NN architecture used to decrypt encrypted data is presented in Figure 3.

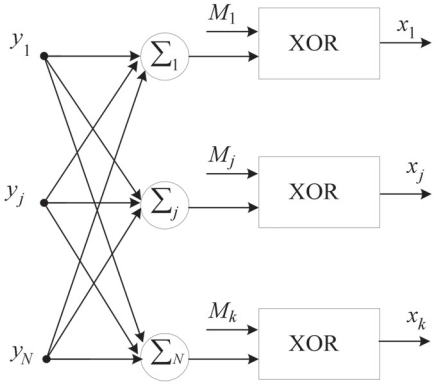

Figure 3. The NN architecture for decryption of encrypted data.

The bit rate of the inputs during decryption corresponds to the bit rate of the encrypted mantissa y^h_{Mj}. Its value determines the decryption time, and to reduce it, the lower bits of the mantissa may be discarded because they will not affect the original message recovery.

Formation of the weight matrix. The matrix of weights for decrypting encrypted data is formed from a matrix of weights for encrypting input data by transposing it:

$$\begin{vmatrix} W_{11} & W_{12} & \cdots & W_{1k} \\ W_{21} & W_{22} & \cdots & W_{2k} \\ \vdots & \vdots & \cdots & \vdots \\ W_{N1} & W_{N2} & \cdots & W_{Nk} \end{vmatrix}^{T} = \begin{vmatrix} W_{11} & W_{21} & \cdots & W_{N1} \\ W_{12} & W_{22} & \cdots & W_{N2} \\ \vdots & \vdots & \cdots & \vdots \\ W_{1k} & W_{2k} & \cdots & W_{Nk} \end{vmatrix}. \quad (15)$$

The basic operation for the encryption of input data and decryption of encrypted data is the calculation of the scalar product, which is implemented using a tabular-algorithmic method.

Calculation of the table of macro-partial products for decryption of encrypted data. A specific feature of the scalar product calculation operation used to decrypt encrypted data is that the weights are pre-calculated (constants) and set in floating-point format, while the encrypted data y_j are received in block-floating-point format. The calculation of the scalar product using the tabular-algorithmic method is performed by Equation (7). Preparation and calculation of possible variants of macro-partial products are performed as in the previous case under Equation (8).

The amount of encrypted data determines the number of macro-partial products P_{Mi} and the size of the table. The largest common order m_{Pms} is computed for each table.

NN tabular-algorithmic decryption of encrypted data. The NN decryption is specified by multiplying the W matrix by the encrypted data vector y:

$$x_s = \begin{vmatrix} W_{11} & W_{21} & \cdots & W_{N1} \\ W_{12} & W_{22} & \cdots & W_{N2} \\ \vdots & \vdots & \cdots & \vdots \\ W_{1k} & W_{2k} & \cdots & W_{Nk} \end{vmatrix} \times \begin{matrix} y_1 \\ y_2 \\ \vdots \\ y_N \end{matrix}. \quad (16)$$

The multiplication of the weights matrix W^T by the input data vector y is reduced to performing N scalar product calculations:

$$x_s = \sum_{j=1}^{N} W_{sj} y_j \quad (17)$$

where N is the number of products, and $s = 1, 2, \ldots, k; j = 1, 2, \ldots, N$.

Tabular-algorithmic calculation of the mantissa of the scalar product is reduced to reading the macro-partial product P_{Mi} from the table (memory) at the address corresponding to the i-th bit-slice of k input data, and adding it to the previously accumulated sums, according to the formula

$$x_{Msi} = 2^{-1} y_{Ms(i-1)} + P_{Msi}, \quad (18)$$

where $x_{s0} = 0, i = 1, \ldots, g$, and g is the bit rate of the encrypted data. The time necessary to calculate the scalar product mantissa is defined under the formula

$$t_{SP} = g\left(t_{table} + t_{reg} + t_{add}\right), \quad (19)$$

where t_{SP} is the time for scalar product calculation, t_{table} is the time for reading from a table (memory), t_{reg} is the time of reading (writing) from the register, and t_{add} is the time for adding. The result of the calculation of the x_s scalar product consists of a mantissa x_{Ms} and order, which is equal to $m_{decrs} = m_{PMs} + m_{encr}$.

At the output of the NN (see Figure 3), we obtain k decrypted data in the following form $x_s = x_{Ms} 2^{m_{decrs}}$, where x_{Ms} is the mantissa at the s-th output, and m_{decrs} is the value of the order at the s-th output. To obtain the input data, it is necessary to shift the s-th mantissa x_{Ms} by the value of the order m_{decrs}.

4. The Structure of the System for NN Cryptographic Data Protection and Transferring in Real-Time Mode

The development of the structure of the system for NN cryptographic data protection and transmission in real-time will be carried out using an integrated approach, which contains the following:

- Research and development of theoretical foundations of NN cryptographic data encryption and decryption;
- Development of new tabular-algorithmic algorithms and structures for NN cryptographic data encryption and decryption;
- Modern element base, development environment and computer-aided design tools.

A system for NN cryptographic data protection in real-time was developed using the following principles:

- Changeable composition of the equipment, which foresees the presence of the processor core and replaceable modules, with which the core adapts to the requirements of a particular application;
- Modularity, which involves the development of system components in the form of functionally complete devices;
- Pipeline and spatial parallelism in data encryption and decryption;
- The openness of the software, which provides opportunities for development and improvement, maximising the use of standard drivers and software;
- Specialising and adapting hardware and software to the structure of tabular algorithms for encrypting and decrypting data;
- The programmability of hardware module architecture through the use of programmable logic integrated circuits.

In order to provide neural-like encryption and decryption of data arrays in real time, it is necessary that encryption and decryption occur without accumulating delays. Encrypting (decrypting) an array of h messages in real time imposes a time limit for their encryption (decryption), which must meet the following:

$$ht_{E/De} \leq t_a, \tag{20}$$

where $t_{E/De}$ is the time of encryption (decryption) of one message, and t_a is the time of arrival of h messages, which is determined as follows:

$$t_a = \frac{hn}{F_d s n_k}, \tag{21}$$

where n is the bit rate of the message, s is the number of channels through which the message is received, n_k is the bit rate of the channels, and F_d is the frequency of message arrival.

Knowing the time t_a, it is possible to determine the encryption (decryption) time of one message $t_{E/De}$ according to the following formula:

$$t_{\text{Ш/Дш}} \leq \frac{n}{F_d s n_k}. \tag{22}$$

In the case of the NN approach to encryption (decryption), it is proposed to supplement the processor core with the specialized modules that implement neural elements in hardware to ensure real time. The number of specialized modules and the time of calculation of the scalar product in such modules should ensure the fulfilment of the condition $t_{E/De} \leq t_a/h$. It is possible to choose the time of calculation of the scalar product by using an algorithm that involves the use of q tables of macropartial products for calculation by applying q bit slices to their address inputs. The use of such an algorithm reduces the time of calculating the scalar product by q times.

The system of NN cryptographic real-time data protection and transmission consists of a stationary part, which is a remote-control centre, and a UAV onboard part. The structure of the stationary part of the system of NN cryptographic data protection and transmission is shown in Figure 4.

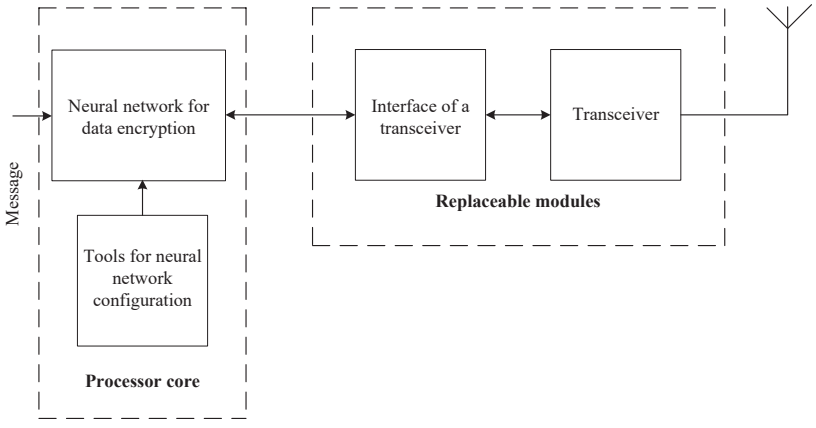

Figure 4. Structure of the stationary part of the system of NN cryptographic data protection and transmission.

The processor core of the remote-control center is implemented on the basis of a personal computer. The transceiver is used to transmit encrypted data; it communicates with the processor core through the interface based on a microcontroller.

The UAV onboard part of the system for NN cryptographic real-time data protection and transmission is implemented on the processor core, which is supplemented by dedicated hardware and software. The processor core of the UAV onboard part of the system is designed on a microcomputer. The structure of the onboard part of the system of NN cryptographic data protection and receiving is depicted in Figure 5.

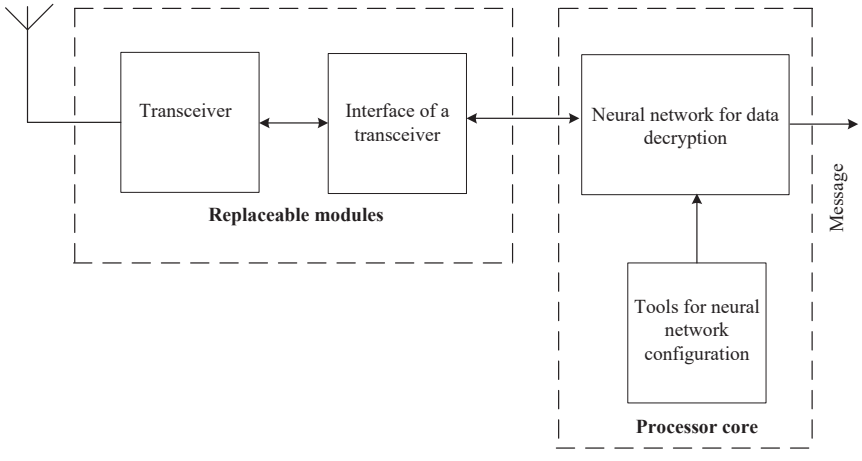

Figure 5. Structure of the UAV onboard part of the system of NN cryptographic data protection and transmission.

The effective implementation of NN encryption–decryption and encoding–decoding algorithms in real time is achieved by combining universal and customized software and hardware. The use of modern elements (microcomputer, microcontroller, FPGA) in the

development of the UAV onboard part ensures the accomplishment of the requirements for weight, dimensions and energy consumption.

The effectiveness of the system for NN cryptographic real-time data protection and transmission is directly associated with the choice of both hardware and software implementation.

5. Development of the Components of the Onboard System for NN Cryptographic Data Encryption and Decryption

In general, the problem of developing onboard systems for NN cryptographic encryption–decryption of data can be formulated as follows:

- To develop an algorithm for the onboard system of NN encryption–decryption of data and present it in the form of a specified flow graph;
- To design the structure of the onboard system for NN data encryption–decryption with the maximum efficiency of equipment use, taking into account all the limitations and providing real-time data processing;
- To determine the main characteristics of neural elements and carry out their synthesis;
- To choose exchange methods, determine the necessary connections and develop algorithms for exchange between system components;
- To determine the order of implementation in time of NN data encryption–decryption processes and develop algorithms for their management.

Components of the onboard system of NN cryptographic data encryption and decryption should provide the implementation of the selected NN, ability to change masks, and calculate matrices of weights W_j and tables of macro-partial products P_{Mi} for possible NN options. To effectively implement the components of the onboard system of NN cryptographic encryption–decryption of data, it is proposed to use hardware–software implementation of the algorithms based on a microcontroller supplemented by specialized hardware. The structure of the component of NN cryptographic data encryption, which meets such requirements, is presented in Figure 6, where MC is the microcontroller, MN is the mask node, MP is the macro-partial product, Rg is the register, and Add is the adder.

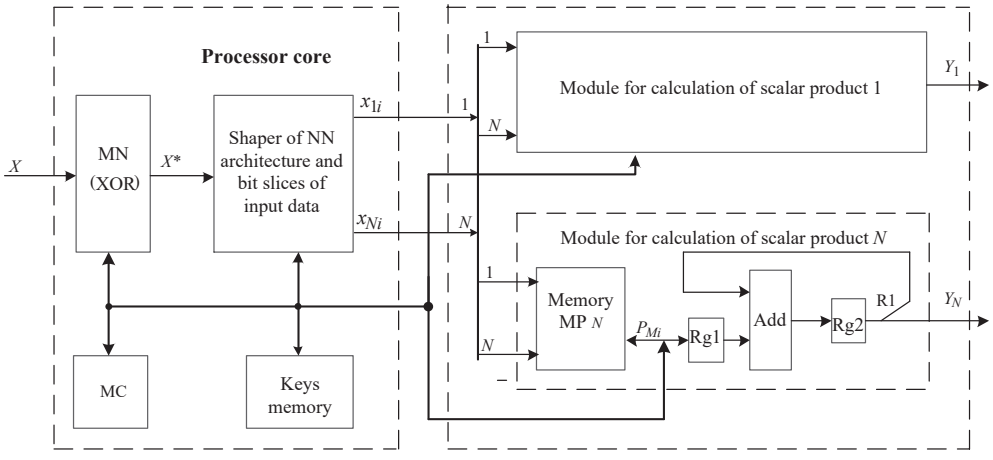

Figure 6. Structure of the component of NN cryptographic encryption of data.

The developed component of NN cryptographic data encryption has a variable composition of equipment, which is based on the core of the system and a set of modules for calculating the scalar product. The system core is constant for all applications and consists of microcontroller MC, mask node MN, keys memory, and module of the shaper of the NN architecture and bit slices of input data. The scalar product calculation modules implement

the basic operation of the tabular-algorithmic method of scalar product calculation under the formula

$$Z_i = 2^{-1} Z_{i-1} + P_{Mi}, \tag{23}$$

where $Z_0 = 0$.

The number of modules for calculating the scalar product depending on the required speed is determined by the following formula:

$$s = \frac{N}{2^v}, \tag{24}$$

where N is the number of neuro-like elements, and $v = 0, \ldots, d, d = log_2 N$. The system of NN cryptographic data encryption reaches its highest speed when the number of computational modules of the scalar product corresponds to the number of neural elements N. To ensure real-time data encryption, it is proposed to implement the scalar product calculation modules, mask node module (MN), and module of the shaper of NN architecture and bit slices of the input data in the form of specialized hardware.

The NN cryptographic data encryption component works as follows. Before encrypting the data, the MC configures the NN architecture (determines the number of neural elements N, the number of inputs k and their bit-size m). For the selected NN architecture matrix of weights W_j and tables of P_{Mi} macro-partial products are calculated by MC, and then they are written in the memory of MP. In addition, the masks selected from the keys' memory are stored in the MN node. The message X to be encrypted comes to input of MN in fixed-point format; here, it is masked. The masked message X^* from the output of MN comes to input of the module of the shaper of NN architecture and bit slices, where it is divided into N groups with m bit rate and bit slices are formed $x_{1i}, \ldots, x_{Ni}$. It should be noted that forming of bit slices $x_{1i}, \ldots, x_{Ni}$ begins with lower bits. The formed bit slices $x_{1i}, \ldots, x_{Ni}$ are the addresses for reading macro-partial products P_{Mi} from the MP memory. The read macro-partial product P_{Mi} is written to the Rg1 register. The adder (Add) performs a summation of macro-partial products P_{Mi} as per Equation (23). The number of cycles required to calculate the scalar product is determined by the bit size of input m. Control of the encryption process in the onboard system of NN cryptographic data encryption is performed by MC.

The structure of the component of NN cryptographic data decryption is shown in Figure 7, where DCSB is the decryption component setting block, and x_j^*–j-th masked initial data.

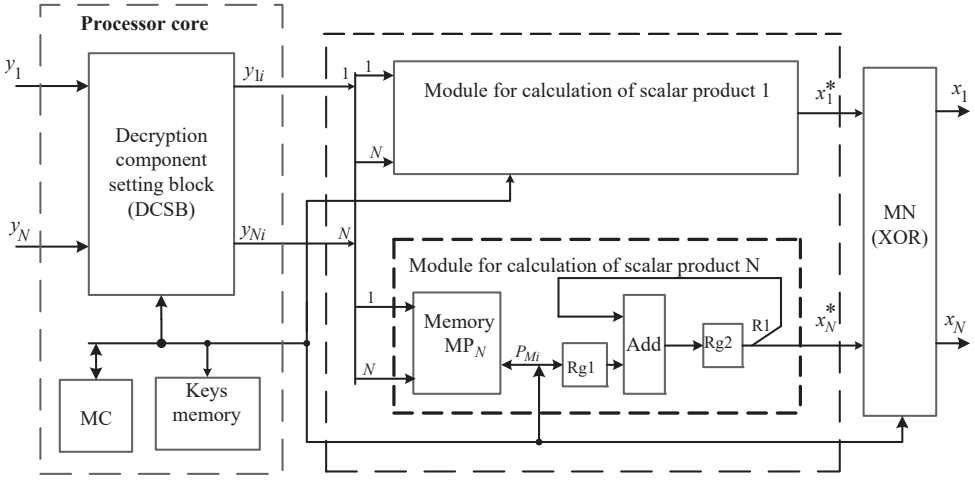

Figure 7. Structure of the component of NN cryptographic decryption of data.

The NN cryptographic data decryption component with symmetric keys works as follows. Before the start of data decryption, a key arrives, which, with the help of DCSB, configures the architecture (the number of N neuro-like elements) of the NN. For the selected NN architecture, the matrix of weighting coefficients W_j and the table of macro-partial products P_{Mi} are calculated using DCSB, and the mask digits are recorded in the MN node. Encrypted data $y_1, \ldots, y_N$ in floating-point format are sent to the input of the DCSB, in which the order alignment of the encrypted data and the formation of bit sections of the mantissas of the encrypted data $y_{1i}, \ldots, y_{Ni}$ are performed. Alignment of the orders of the encrypted data $y_1, \ldots, y_N$ is performed by determining the maximum order m_{maxy}, calculating the difference of orders for each y_j of the encrypted number $\Delta m_{y_j} = m_{maxy} - m_{y_j}$, and shifting the mantissa of each number to the right by the amount Δm_{y_j}. After the alignment of the orders, the formation of bit cuts of the mantissa of the encrypted numbers $y_{1i}, \ldots, y_{Ni}$ is performed, starting with the lowest digits.

The bit cuts $y_{1i}, \ldots, y_{Ni}$ obtained at the output of the DCSB are the address for reading from the MP memory of the macro-partial product P_{Mi}, which are used in the proposed table-algorithmic calculation of the scalar product. Calculated macro-partial P_{Mi} product is recorded in the register Rg1. With the help of the adder Add, the summation of macro-partial products P_{Mi} is performed according to Equation (23). The number of cycles required to calculate the scalar product is determined by the mantissas of encrypted numbers n_y. Management of the process of decryption of encrypted data is performed using MC. Decrypted masked initial data $x_1^*, \ldots, x_N^*$ are received at the inputs of the MN, at the output of which we receive the initial data $x_1, \ldots, x_N$.

The process of decrypting encrypted data takes much longer than the encryption process. The number of cycles required to calculate the scalar product during data decryption has increased by $q = \left\lceil \frac{n_y}{m} \right\rceil$ times, where $\lceil\ \rceil$—the sign of rounding up to a larger whole number, n_y is the digits number of the mantissa of the encrypted data, and m is the digits number of the input data $x_1, \ldots, x_N$. It is possible to reduce the time of calculating the scalar product by using an algorithm that provides for the submission of q bit slices to the address inputs of q tables of macro-partial products. The use of such an algorithm reduces the time of calculating the scalar product by q times.

6. Results and Discussion

For experimental verification of the proposed NN technology for cryptographic protection of data transmission system, the simulation was performed. Currently, the hardware description languages such as VHDL, VHDL-AMS, Verilog, and Verilog-AMS are widely used for creating behavioral descriptions and models of digital, analog, and mixed-signal devices and systems [44,45].

The design of specialized onboard hardware systems for NN cryptographic data encryption was performed in the VHDL hardware programming language in the Quartus II ver. 13.1 development environment using its libraries. The Quartus II development environment supports the entire process of designing specialized hardware, from user input to FPGA programming and debugging of both the chip itself and the tools as a whole.

A schematic diagram of the specialized hardware components of NN cryptographic data encryption is shown in Figure 8. The inputs of module XOR_Mask1_4_2: X [7..0]—are the input data; Clk—input sync for input data download; X_Mask [7..0]—8-bit mask. At the output of this block, N vectors with bit length m are formed. Synchronization is implemented on the leading edge of Clk pulses.

Block V_Cutter with $N = 4$ input vectors of bit length $m = 2$ consists of N registers of parallel-serial type and forms vertical bit slices. Input data: Data_1 [n-1..0], …, Data_N [n-1..0]—N input vectors with bit length n; Clk—pulses of synchronization of forming vertical bit slices; Reset—the signal of the initial reset in the "0" output of the registers R_Par_Ser; Load—the signal to allow data to be loaded into the R_Par_Ser registers. Outputs: V_Out1, …, V_OutN—vertical bit slice. The formation of vertical sections begins with the lower bit.

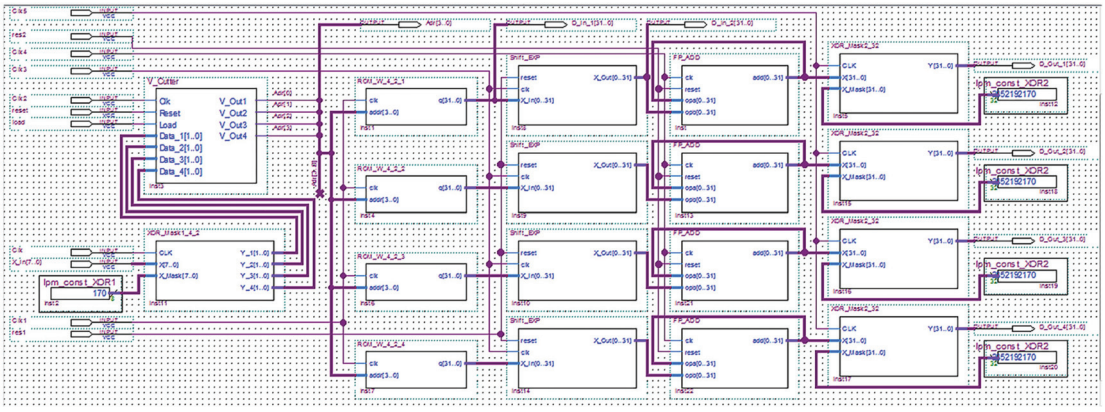

Figure 8. A circuit of the specialized hardware components of NN cryptographic data encryption.

The weights of the NN with $N = 4$ inputs with a bit length of $m = 2$ are stored in the FPGA ROM in the form of four tables. Each of them consists of 16 words with a bit length of 32 bits. Reading data from these tables is performed using blocks ROM_W_4_2_1, . . ., ROM_W_4_2_4.

Inputs of these blocks: addr [3..0]—the address of the cell of the table from which the data will be read; clk—synchronization pulses for reading data from the table. Synchronization is implemented on the leading edge of the pulses clk. Output: q [31..0]—data read from the cell with the input address.

The data read from the tables is transmitted to the input blocks Shift_EXP, which perform their multiplication by 2^j, where $j = 0, \ldots, n-1$. Upon receipt of this block of data corresponding to the zero digit, the bit counter is reset. Synchronization of this block is carried out by means of clock pulses Clk. At the output X_Out [0..31], we obtain the input data multiplied by 2^j.

From the output of the Shift_EXP blocks, the data are sent to one of the inputs of the adders FP_ADD. The other input of the adders is connected to their output. Adder input signals: clk—synchronization pulses; reset—signal to reset the input data opa when implementing the adder with the battery; opa [0..31], opb [0..31]—terms. On the leading edge of the first pulse clk, the adders are loaded into the adder, and on the leading edge of the second pulse, the received sum is displayed. Adder output: the sum add [0..31].

From the output of the adders, FP_ADD data is fed to the input of the block XOR_Mask2_32, which performs the overlay of the 32-bit mask. Inputs of the block XOR_Mask2_32: X [31..0]—encrypted output data; Clk—synchronization of input data download; X_Mask [31..0]—32-bit mask. Block output: vector Y [31..0]. Synchronization is implemented on the leading edge of Clk pulses. The encrypted data are obtained at the outputs D_Out_1, D_Out_2, D_Out_3, D_Out_4.

The timing diagram of the specialized hardware of NN cryptographic data encryption is presented in Figure 9.

The time diagram (Figure 9) shows an example of NN cryptographic encryption of eight-bit data, which are received in binary code at inputs X_In X [7..0]. An 8-bit mask 170 = 0xAA is received at the X_Mask [7..0] inputs, which is set using the lpm_const_XOR1 component (Figure 7). It is used to mask input data using the XOR operation. For input X_In_1—01001100 XOR 10101010 = 11100110; for input X_In_2—01010100 XOR 10101010 = 11111110. For the first number 01001100 at the outputs Y_1[1. . .0], Y_2[1. . .0], Y_3[1. . .0], Y_4[1. . .0] of the XOR_Mask1_4_2 block, we obtain 11, 10, 01, and 10, respectively. When encrypting the first vector of input data at the Adr outputs, we obtain 4-bit slices starting from the lowest bits, which are sent to the address inputs of ROM_W4_2_1,

ROM_W4_2_2, ROM_W4_2_3, and ROM_W4_2_4 blocks. These lookup tables contain pre-calculated neuro elements' weights.

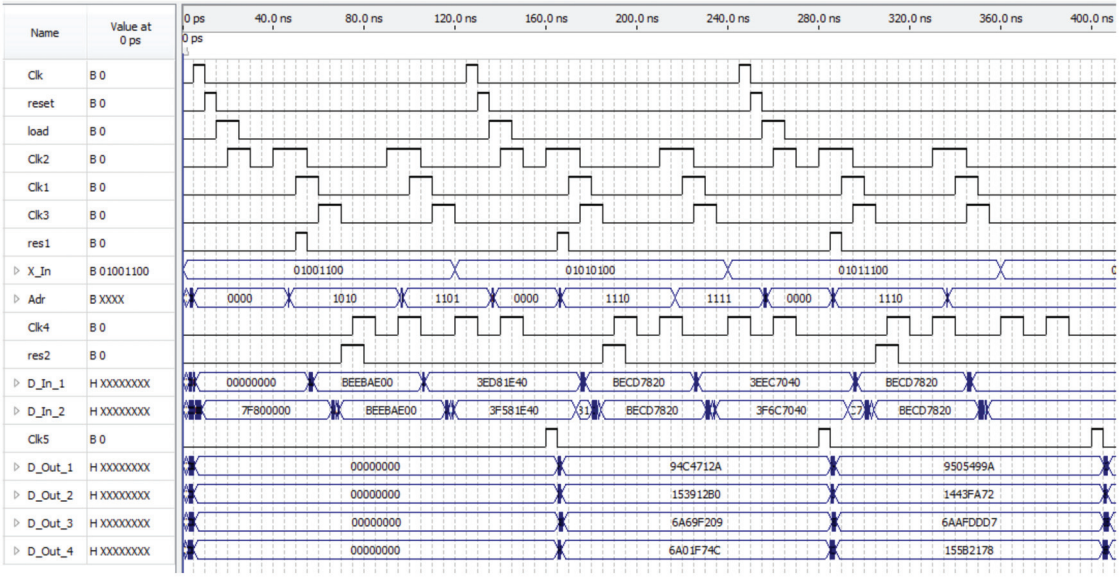

Figure 9. The timing chart of the specialized hardware of NN cryptographic data encryption.

For lower bits 1010 from ROM_W4_2_1 block, the 32-bit macro-partial product BEEBAE00 is read, which is fed to the input D_In_1 and to the input of the first block Shift_EXP, which performs the multiplication operation by shifting by 2^j, where $j = 0, \ldots, n-1$. At the output of the first block Shift_EXP and at the input D_In_2, we obtain BEEBAE00. For the next 1101 bits, the 32-bit macro-partial product 3ED81E40 is read from the ROM_W4_2_1 block. At the output of the first block Shift_EXP and at the input D_In_2, we obtain the macro-partial product multiplied by two, which is equal to 3F581E40.

In the first adder FP_ADD, we sum up the data from the outputs of the first block Shift_EXP and obtain the sum (its value is not displayed on the time charts), which is sent to the first block XOR_Mask2_32. In the first block, XOR_Mask2_32, the XOR operation is performed with the sum in IEEE 754 format and mask 2852192170 = 0xAA00FFAA. At the D_Out_1 output, we obtain the encrypted value 0x94C4712A.

For input data with a dimension of 1 byte X_In = {01001100}, we obtain an encrypted value with a dimension of 16 bytes D_Out_1 = 0x94C4712A; D_Out_2 = 0x153912B0; D_Out_3 = 0x6A69F209; D_Out_4 = 0x6A01F74C.

The implementation of the specialized hardware for NN cryptographic data encryption based on the FPGA EP3C16F484C6 Cyclone III family [46] requires 3053 logic elements and 745 registers. Approximately 160 nanoseconds are required to encrypt one input vector.

For comparison with the above-described hardware implementation on FPGA, the same components were implemented exclusively as the software. The components were created in the C language using the Code::Blocks development environment version 20.03. The execution time of a similar NN cryptographic data encryption procedure using a NanoPi Duo microcomputer based on the Allwinner Cortex-A7 H2+ SoC was about 20 ms. The results of the comparison allow us to see a significant gain in time for the implementation of NN cryptographic data encryption and decryption.

The authors understand the importance of the issue of cryptographic stability. However, this is beyond the scope of this study. The security of the neural network cryptographic approach mainly depends on the length of the key, which is determined by the masking codes, the neural network architecture, and the floating-point weighting matrix, as well

as on the frequency of its change. The length of the key depends on the number of neural elements N, which determine the size of the matrix of weighting coefficients.

The operation of onboard communication cryptographic systems for UAVs can be exposed to an attack on the secret key by breaking, through which it is possible to gain access to protected data. However, the time and resources required to crack the key and decrypt the encrypted data depend on the complexity of the algorithm for calculating the floating-point weighting matrix and the decryption algorithm. The number of operations required to calculate the matrix of weighting coefficients is approximately equal to N^2n arithmetic operations (where n is the data bit width), and the number of operations required to decrypt encrypted data approximately equals N^2 operations of multiplying floating-point numbers and N^2 operations of adding floating-point numbers. Therefore, the computational complexity of the proposed NN approach is high. Obviously, the evaluation of security analysis could be performed in further studies.

7. Conclusions

The approach to the implementation of neural networks for cryptographic protection of data transmission at UAV onboard communication systems has been presented in this work. This paper describes the UAV onboard system for NN cryptographic data protection in real-time using an integrated approach based on the following principles: variable equipment composition; modularity; conveyorization and spatial parallelism; software openness; and suitability for hardware implementation on FPGA.

The information technology of real-time neuro-like cryptographic data protection with symmetric keys (masking codes, neural network architecture, and matrix of weighting coefficients) oriented for onboard implementation has been developed. Due to the pre-calculation of matrices of weighting coefficients and tables of macro-partial products, use of tabular-algorithmic implementation of neuro-like elements, and dynamic change of keys, it provides increased cryptographic stability and hardware–software implementation on FPGA.

The table-algorithmic method of calculating the scalar product has been improved, by bringing the weighting coefficients to the greatest common order, pre-calculating the tables of macro-partial products and using instead of floating-point multiplication and summation the operations of reading from memory, fixed-point summation and shift, it provides a reduction hardware costs for its implementation and calculation time.

A real-time neural network cryptographic data protection system has been developed on the basis of a processor core supplemented with specialized hardware modules for calculating the scalar product, which, due to the combination of universal and specialized approaches, software and hardware, ensures the effective implementation of neuro-like algorithms for real-time cryptographic encryption and decryption of data.

The specialized hardware for NN cryptographic data encryption was developed in the VHDL equipment programming language in the Quartus II environment and implemented using family Cyclone III FPGA EP3C16F484C6.

Author Contributions: Conceptualization, I.T. and V.T.; methodology, I.T., Y.O. and Y.L.; software, Y.L. and Y.O.; validation, Y.L., Y.O. and I.K.; formal analysis, I.T. and V.T.; investigation, A.Ł. and A.H.; resources, A.Ł. and I.K.; data curation, Y.L. and I.K.; writing—original draft preparation, I.T., I.K. and Y.O.; writing—review and editing, I.K., A.H. and A.Ł.; visualization, I.K. and Y.O.; supervision, V.T. and A.Ł.; project administration, I.T. and V.T. All authors have read and agreed to the published version of the manuscript.

Funding: This research received no external funding.

Data Availability Statement: No new data were created or analyzed in this study. Data sharing is not applicable to this article.

Conflicts of Interest: The authors declare no conflict of interest.

References

1. Han, B.; Qin, D.; Zheng, P.; Ma, L.; Teklu, M.B. Modeling and performance optimization of unmanned aerial vehicle channels in urban emergency management. *ISPRS Int. J. Geo-Inf.* **2021**, *10*, 478. [CrossRef]
2. Śledź, S.; Ewertowski, M.W.; Piekarczyk, J. Applications of unmanned aerial vehicle (UAV) surveys and Structure from Motion photogrammetry in glacial and periglacial geomorphology. *Geomorphology* **2021**, *378*, 107620. [CrossRef]
3. Zhang, C.; Zou, W.; Ma, L.; Wang, Z. Biologically inspired jumping robots: A comprehensive review. *Robot. Auton. Syst.* **2020**, *124*, 103362. [CrossRef]
4. Li, D.; Ma, G.; He, W.; Ge, S.S.; Lee, T.H. Cooperative Circumnavigation Control of Networked Microsatellites. *IEEE Trans. Cybern.* **2020**, *50*, 4550–4555. [CrossRef]
5. Boreiko, O.; Teslyuk, V.; Zelinskyy, A.; Berezsky, O. Development of models and means of the server part of the system for passenger traffic registration of public transport in the "smart" city. *East.-Eur. J. Enterp. Technol.* **2017**, *1*, 40–47. [CrossRef]
6. Kim, K.; Kang, Y. Drone security module for UAV data encryption. In Proceedings of the 2020 International Conference on Information and Communication Technology Convergence (ICTC), Jeju, Republic of Korea, 21–23 October 2020; pp. 1672–1674. [CrossRef]
7. Samanth, S.; Prema, K.V.; Balachandra, M. Security in Internet of Drones: A Comprehensive Review. *Cogent Eng.* **2022**, *9*, 2029080. [CrossRef]
8. Kong, P.-Y. A survey of cyberattack countermeasures for unmanned aerial vehicles. *IEEE Access* **2021**, *9*, 148244–148263. [CrossRef]
9. Shafique, A.; Mehmood, A.; Elhadef, M.; Khan, K.H. A lightweight noise-tolerant encryption scheme for secure communication: An unmanned aerial vehicle application. *PLoS ONE* **2022**, *17*, e0273661. [CrossRef] [PubMed]
10. Verma, A.; Ranga, V. Security of RPL based 6LoWPAN Networks in the Internet of Things: A Review. *IEEE Sens. J.* **2020**, *20*, 5666–5690. [CrossRef]
11. Srivastava, S.; Bhatia, A. On the Learning Capabilities of Recurrent Neural Networks: A Cryptographic Perspective. In Proceedings of the 2018 IEEE International Conference on Big Knowledge (ICBK), Singapore, 17–18 November 2018; pp. 162–167. [CrossRef]
12. Zhu, Y.; Vargas, D.V.; Sakurai, K. Neural Cryptography Based on the Topology Evolving Neural Networks. In Proceedings of the 2018 Sixth International Symposium on Computing and Networking Workshops (CANDARW), Takayama, Japan, 27–30 November 2018; pp. 472–478. [CrossRef]
13. Duan, X.; Han, Y.; Wang, C.; Ni, H. Optimization of Encrypted Communication Length Based on Generative Adversarial Network. In Proceedings of the 2021 IEEE 4th International Conference on Big Data and Artificial Intelligence (BDAI), Qingdao, China, 2–4 July 2021; pp. 165–170. [CrossRef]
14. Grodzki, W.; Łukaszewicz, A. Design and manufacture of unmanned aerial vehicles (UAV) wing structure using composite materials. *Mater. Werkst.* **2015**, *46*, 269–278. [CrossRef]
15. Łukaszewicz, A.; Szafran, K.; Jóźwik, J. CAx techniques used in UAV design process. In Proceedings of the 2020 IEEE 7th International Workshop on Metrology for AeroSpace (MetroAeroSpace), Pisa, Italy, 22–24 June 2020; pp. 95–98. [CrossRef]
16. Łukaszewicz, A.; Skorulski, G.; Szczebiot, R. The main aspects of training in the field of computer aided techniques (CAx) in mechanical engineering. In Proceedings of the 17th International Scientific Conference on Engineering for Rural Development, Jelgava, Latvia, 23–25 May 2018; pp. 865–870. [CrossRef]
17. Łukaszewicz, A.; Miatluk, K. Reverse Engineering Approach for Object with Free-Form Surfaces Using Standard Surface-Solid Parametric CAD System. *Solid State Phenom.* **2009**, *147–149*, 706–711. [CrossRef]
18. Miatliuk, K.; Łukaszewicz, A.; Siemieniako, F. Coordination method in design of forming operations of hierarchical solid objects. In Proceedings of the 2008 International Conference on Control, Automation and Systems, ICCAS 2008, Seoul, Republic of Korea, 14–17 October 2008; pp. 2724–2727. [CrossRef]
19. Puchalski, R.; Giernacki, W. UAV Fault Detection Methods, State-of-the-Art. *Drones* **2022**, *6*, 330. [CrossRef]
20. Zietkiewicz, J.; Kozierski, P.; Giernacki, W. Particle swarm optimisation in nonlinear model predictive control; comprehensive simulation study for two selected problems. *Int. J. Control* **2021**, *94*, 2623–2639. [CrossRef]
21. Kownacki, C.; Ambroziak, L. Adaptation Mechanism of Asymmetrical Potential Field Improving Precision of Position Tracking in the Case of Nonholonomic UAVs. *Robotica* **2019**, *37*, 1823–1834. [CrossRef]
22. Kownacki, C.; Ambroziak, L.; Ciężkowski, M.; Wolniakowski, A.; Romaniuk, S.; Bożko, A.; Ołdziej, D. Precision Landing Tests of Tethered Multicopter and VTOL UAV on Moving Landing Pad on a Lake. *Sensors* **2023**, *23*, 2016. [CrossRef]
23. Basri, E.I.; Sultan, M.T.H.; Basri, A.A.; Mustapha, F.; Ahmad, K.A. Consideration of Lamination Structural Analysis in a Multi-Layered Composite and Failure Analysis on Wing Design Application. *Materials* **2021**, *14*, 3705. [CrossRef]
24. Al-Haddad, L.A.; Jaber, A.A. An Intelligent Fault Diagnosis Approach for Multirotor UAVs Based on Deep Neural Network of Multi-Resolution Transform Features. *Drones* **2023**, *7*, 82. [CrossRef]
25. Yang, J.; Gu, H.; Hu, C.; Zhang, X.; Gui, G.; Gacanin, H. Deep Complex-Valued Convolutional Neural Network for Drone Recognition Based on RF Fingerprinting. *Drones* **2022**, *6*, 374. [CrossRef]
26. Duan, X.; Han, Y.; Wang, C.; Ni, H. Optimization of Encrypted Communication Model Based on Generative Adversarial Network. In Proceedings of the 2022 International Conference on Blockchain Technology and Information Security (ICBCTIS), Huaihua City, China, 15–17 July 2022; pp. 20–24. [CrossRef]

27. Karakaya, B.; Celik, V.; Gulten, A. Realization of Delayed Cellular Neural Network model ON FPGA. In Proceedings of the 2018 Electric Electronics, Computer Science, Biomedical Engineerings' Meeting (EBBT), Istanbul, Turkey, 18–19 April 2018; pp. 1–4. [CrossRef]
28. Volna, E.; Kotyrba, M.; Kocian, V.; Janosek, M. Cryptography Based on Neural Network. In *Proceedings of the 26th European Conference on Modeling and Simulation (ECMS 2012), Koblenz, Germany, 29 May–1 June 2012*; Troitzsch, K.G., Moehring, M., Lotzmann, U., Eds.; European Council for Modeling and Simulation: Caserta, Italy, 2012; pp. 386–391. [CrossRef]
29. Shihab, K. A backpropagation neural network for computer network security. *J. Comput. Sci.* **2006**, *2*, 710–715. [CrossRef]
30. Sagar, V.; Kumar, K. A symmetric key cryptographic algorithm using counter propagation network (CPN). In Proceedings of the 2014 ACM International Conference on Information and Communication Technology for Competitive Strategies, (ICTCS'14), Udaipur, India, 14–16 November 2014. [CrossRef]
31. Arvandi, M.; Wu, S.; Sadeghian, A.; Melek, W.W.; Woungang, I. Symmetric cipher design using recurrent neural networks. In Proceedings of the IEEE International Joint Conference on Neural Networks, Vancouver, BC, Canada, 16–21 July 2006; pp. 2039–2046. [CrossRef]
32. Tsmots, I.; Tsymbal, Y.; Khavalko, V.; Skorokhoda, O.; Teslyuk, T. Neural-like means for data streams encryption and decryption in real time. In Proceedings of the 2018 IEEE Second International Conference on Data Stream Mining & Processing (DSMP), Lviv, Ukraine, 21–25 August 2018; pp. 438–443. [CrossRef]
33. Scholz, M.; Fraunholz, M.; Selbig, J. Nonlinear principal component analysis: Neural network models and applications. In *Principal Manifolds for Data Visualization and Dimension Reduction*; Gorban, A.N., Kégl, B., Wunsch, D.C., Zinovyev, A.Y., Eds.; Lecture Notes in Computational Science and Engineering; Springer: Berlin/Heidelberg, Germany, 2008; Volume 58. [CrossRef]
34. Rabyk, V.; Tsmots, I.; Lyubun, Z.; Skorokhoda, O. Method and Means of Symmetric Real-time Neural Network Data Encryption. In Proceedings of the 2020 IEEE 15th International Scientific and Technical Conference on Computer Sciences and Information Technologies (CSIT 2020), Zbarazh, Ukraine, 23–26 September 2020; Volume 1, pp. 47–50. [CrossRef]
35. Chang, A.X.M.; Martini, B.; Culurciello, E. Recurrent Neural Networks Hardware Implementation on FPGA. *arXiv* **2015**, arXiv:1511.05552. [CrossRef]
36. Nurvitadhi, E.; Venkatesh, G.; Sim, J.; Marr, D.; Huang, R.; Ong Gee Hock, J.; Tat Liew, Y.; Srivatsan, K.; Moss, D.; Subhaschandra, S.; et al. Can FPGAs beat GPUs in accelerating next-generation deep neural networks? In Proceedings of the 2017 ACM/SIGDA International Symposium on Field-Programmable Gate Arrays, Monterey, CA, USA, 22–24 February 2017; pp. 5–14. [CrossRef]
37. Misra, J.; Saha, I. Artificial neural networks in hardware: A survey of two decades of progress. *Neurocomputing* **2010**, *74*, 239–255. [CrossRef]
38. Guo, K.; Sui, L.; Qiu, J.; Yao, S.; Han, S.; Wang, Y.; Yang, H. From model to FPGA: Software-hardware co-design for efficient neural network acceleration. In Proceedings of the 2016 IEEE Hot Chips 28 Symposium (HCS), Cupertino, CA, USA, 21–23 August 2016; pp. 1–27. [CrossRef]
39. Ovtcharov, K.; Ruwase, O.; Kim, J.Y.; Fowers, J.; Strauss, K.; Chung, E.S. Accelerating Deep Convolutional Neural Networks Using Specialized Hardware. Microsoft Research Whitepaper. 2016. Available online: https://www.microsoft.com/en-us/research/wp-content/uploads/2016/02/CNN20Whitepaper.pdf (accessed on 29 April 2022).
40. Wang, Y.; Xu, J.; Han, Y.; Li, H.; Li, X. DeepBurning: Automatic generation of FPGA-based learning accelerators for the neural network family. In Proceedings of the 53rd Annual Design Automation Conference (DAC'16), Austin, TX, USA, 5–9 June 2016; Association for Computing Machinery: New York, NY, USA, 2016; pp. 1–6. [CrossRef]
41. Nurvitadhi, E.; Sheffield, D.; Sim, J.; Mishra, A.; Venkatesh, G.; Marr, D. Accelerating Binarized Neural Networks: Comparison of FPGA, CPU, GPU, and ASIC. In Proceedings of the 2016 International Conference on Field-Programmable Technology (FPT), Xi'an, China, 7–9 December 2016; pp. 77–84. [CrossRef]
42. Yayik, A.; Kutlu, Y. Neural Network Based Cryptography. *Neural Netw. World* **2014**, *24*, 177–192. [CrossRef]
43. Govindu, G.; Zhuo, L.; Choi, S.; Prasanna, V. Analysis of high-performance floating-point arithmetic on FPGAs. In Proceedings of the 18th International Parallel and Distributed Processing Symposium (IPDPS 2004), Santa Fe, NM, USA, 26–30 April 2004; p. 149. [CrossRef]
44. Khalil, K.; Dey, B.; Abdelrehim, M.; Kumar, A.; Bayoumi, M. An Efficient Reconfigurable Neural Network on Chip. In Proceedings of the 2021 28th IEEE International Conference on Electronics, Circuits, and Systems (ICECS), Dubai, United Arab Emirates, 28 November–1 December 2021; pp. 1–4. [CrossRef]
45. Dumesnil, E.; Beaulieu, P.-O.; Boukadoum, M. Fully parallel FPGA Implementation of an Artificial Neural Network Tuned by Genetic Algorithm. In Proceedings of the 2018 16th IEEE International New Circuits and Systems Conference (NEWCAS), Montreal, QC, Canada, 24–27 June 2018; pp. 365–369. [CrossRef]
46. *Cyclone III Device Handbook*; Altera Corporation: San Jose, CA, USA, 2012. Available online: https://www.intel.com/content/www/us/en/content-details/655197/cyclone-iii-device-handbook-volume-2-chapter-1-cyclone-iii-device-datasheet.html (accessed on 29 April 2022).

drones

MDPI

Article

Dynamic Analysis and Numerical Simulation of Arresting Hook Engaging Cable in Carried-Based UAV Landing Process

Haoyuan Shao [1], Zi Kan [1], Yifeng Wang [2], Daochun Li [1,*], Zhuoer Yao [1] and Jinwu Xiang [1]

[1] School of Aeronautic Science and Engineering, Beihang University, Beijing 100191, China
[2] AVIC Shenyang Aircraft Design and Research Institute, Shenyang 110087, China
* Correspondence: lidc@buaa.edu.cn

Abstract: Carrier-based unmanned aerial vehicles (UAVs) require precise evaluation methods for their landing and arresting safety due to their high autonomy and demanding reliability requirements. In this paper, an efficient and accurate simulation method is presented for studying the arresting hook engaging arresting cable process. The finite element method and multibody dynamics (FEM-MBD) approach is employed. By establishing a rigid–flexible coupling model encompassing the UAV and arresting gear system, the simulation model for the engagement process is obtained. The model incorporates multiple coordinate systems to effectively capture the relative motion between the rigid and flexible components. The model considers the material properties, arresting gear system characteristics, and UAV state during engagement. Verification is conducted by comparing simulation results with experimental data from a referenced arresting hook rebound. Finally, simulations are performed under different touchdown points and roll angles of the UAV to analyze the stress distribution of the hook, center of gravity variations, and the tire touch and rollover cable response. The proposed rigid–flexible coupling arresting dynamics model in this paper enables the effective analysis of the dynamic behavior during the arresting hook engaging arresting cable process.

Keywords: carrier-based UAV; engagement; FEM-MBD; rigid–flexible coupling model; dynamic analysis

Citation: Shao, H.; Kan, Z.; Wang, Y.; Li, D.; Yao, Z.; Xiang, J. Dynamic Analysis and Numerical Simulation of Arresting Hook Engaging Cable in Carried-Based UAV Landing Process. *Drones* **2023**, *7*, 530. https://doi.org/10.3390/drones7080530

Academic Editors: Andrzej Łukaszewicz, Wojciech Giernacki, Zbigniew Kulesza, Jaroslaw Alexander Pytka and Andriy Holovatyy

Received: 7 July 2023
Revised: 4 August 2023
Accepted: 11 August 2023
Published: 13 August 2023

1. Introduction

The engagement of the arresting hook with the arresting cable is a critical maneuver that most directly reflects the success of arrestment and serves as the most complex stage in terms of dynamics in the carrier-based aircraft landing process [1,2]. Carrier-based UAVs usually land in a collision [3]. To achieve a successful arrest on a carrier, UAVs must approach with the specified speed and attitude, and land precisely on the desired area of the carrier deck [4]. The arrested landing process of UAVs includes multiple intricate dynamic stages. The arresting hook, located at the tail of the aircraft, makes contact with the deck upon landing and rebounds to a limited height under the influence of the hook's damper. Subsequently, the arresting hook engages with the arresting cable on the deck, transferring the arresting force to the fuselage and bringing the aircraft to a rapid stop.

Due to the complexity of carrier arresting systems and the unique operational environment, it is challenging to accurately measure real-time loads via experiments [5]. During the design phase of a carrier-based aircraft, the analysis of the hook–cable engagement process plays an important role in confirming the safety area for deck landing [6]. The primary research employed analyzes the arresting performance through theoretical analysis and simulation methods [7,8]. Thomlinson [9] conducted research on the motion of the aircraft arresting hook within the plane of symmetry after impacting the deck. In the paper, it was assumed that the carrier-based aircraft had no yaw deviation during the arresting process. Jones [10] obtained a fitting equation and curve for the arresting force based on statistical data from the arresting system. Gao [11], Liu [12] and Peng [13,14] established the mechanical relationships among the aircraft, deck and arresting hook for

an arresting hook impacting the deck. Zhu [15] considered the influence of frictional force on the collision between the arresting hook and deck, and established a more accurate model for the arresting hook and deck collision. The previous research provides a better understanding of the interaction between the arresting hook and deck during the collision process. Additionally, the enhanced model proposed has a guiding effect on the design of the arresting hook system. However, it is acknowledged that the model assumptions in these studies limit the comprehensive analysis of the dynamics involved in the arresting process in different scenarios.

In order to conduct a comprehensive analysis of a hook's cable engagement process, it is essential to establish accurate model for both the aircraft and the arresting cable [16,17]. Various methods can be employed to model cable dynamics, including the absolute node coordinate method [18] and finite segment method [19,20]. Deng [21] developed a 2D non-material variable-domain co-rotational element to perform a nonlinear dynamic analysis of arresting gears, and the nonlinear equation of the hydraulic damper sub-system was formulated. The propagation mechanism of longitudinal waves and kink waves was investigated. Software such as LS-Dyna [22] and PAM-Crash [23] have also been widely used to simulate the dynamic characteristics of aircraft landing and arrest. Shen [24] established a full-scale dynamic model of an MK7-type arresting gear system based on the multi-body dynamics method. Zhang [25] adopted arbitrary Lagrangian–Eulerian formulation to efficiently simulate hook/pulley-cable moving contact in arresting cable systems. Zhang [26] developed a dynamic model for the rebound of the arresting hook during collision, using the numerical iteration calculation method to obtain the longitudinal safety envelope of the aircraft during the landing and arresting process. Peng [27] conducted an impact rebound test for the arresting hook and subsequently refined the coefficient of restitution for the deck coating based on the test results. The comprehensive examination of the arresting hook engaging cable process necessitates a meticulous analysis encompassing the model of landing gear shock absorbers and flexible tires, as well as the material properties and mechanical characteristics of the arresting cable and hook.

In this paper, a novel rigid–flexible coupling model of a carrier-based UAV for arresting engagement is established based on the FEM-MBD approach. The dynamic model is verified by comparing simulation results with experimental data from references, and simulations are conducted with different touchdown points and roll angles. The proposed simulation method can accurately capture the process of UAV arresting hook engagement, including the rebound motion of the hook upon deck impact, the bending of the cable during engagement and the stress distribution on the hook. The results obtained from this analysis offer valuable insights into the performance of the engagement process, which can be used to test various design configurations virtually and improve the design of carrier-based UAVs for carrier landing.

2. Dynamic Model of Carrier-Based UAV Landing and Engagement with Cable

2.1. Model Description

2.1.1. Finite Element Discretization and Contact

The finite element method primarily employs eight-node hexahedral elements and four-node shell elements to describe the structural components. The dynamic equation for each finite element is as follows:

$$m_i \ddot{u}_i^{t+\Delta t} + c_i \dot{u}_i^{t+\Delta t} + k_i u_i^{t+\Delta t} = f_i^{t+\Delta t} \tag{1}$$

where m_i, c_i, k_i are the mass, damping and stiffness matrices of node i, respectively, and $f_i^{t+\Delta t}$ is the external load at time, $t + \Delta t$. $u_i^{t+\Delta t}$, $\dot{u}_i^{t+\Delta t}$, $\ddot{u}_i^{t+\Delta t}$ are the displacement, velocity and acceleration matrices, respectively. $\dot{u}_i^{t+\Delta t}$, $u_i^{t+\Delta t}$ can be calculated via the central difference method.

The contact force between elements is illustrated in Figure 1. n_i represents the slave node, S_j represents the master surface, m_1, m_2, m_3, m_4 represents the master surface node,

H_{cont} represents contact thickness, δ_i represents the penetration between elements, v_i represents relative sliding velocity at the contact point with respect to the master surface, F_i represents the contact force acting on the slave node n_i, and f_1, f_2, f_3 and f_4 represent the equivalent force acting on the master node.

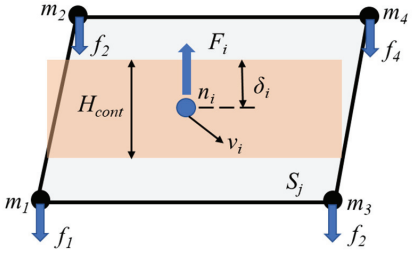

Figure 1. Schematic diagram of element contact.

The contact force, F_i, between elements can be resolved into the normal component f_s and tangential component f_c, which are determined via Equation (2).

$$\begin{aligned} F_i &= f_s + f_c \\ f_s &= |f_{s,e} + f_{s,v}| \cdot \overline{n} \\ f_c &= \min(|uf_s|, |f_{c,e}|) \cdot \overline{t} \end{aligned} \tag{2}$$

where $f_{s,e}$ is the normal elastic force, $f_{s,v}$ is the normal viscous force, $f_{c,e}$ is the tangential elastic, u is the coefficient of friction, $\overline{n}$ is the unit vector in the normal direction of contact, and $\overline{t}$ is the unit vector in the tangential direction of contact.

The normal elastic force, $f_{s,e}$, and normal viscous force, $f_{s,v}$, between elements are given by Equations (3) and (4), respectively.

$$f_{s,e} = k_{Ni}\delta_i = \left(1 + \frac{(\varepsilon - 1){\delta_i}^2}{H_{\text{cont}}^2}\right) k_i \delta_i \tag{3}$$

$$f_{s,v} = -c_{Ni} v_i \tag{4}$$

where k_i is the local contact stiffness, ε is the proportionality factor of the contact force, $c_{Ni} = 2\xi_i\sqrt{k_{Ni}m_i}$ is the internal damping, ξ_i is the contact damping coefficient, m_i is the mass of the slave node, and v_i is the relative velocity in the normal direction at the contact point.

The tangential elastic force, $f_{c,e}$, and tangential friction force, f_c, between elements are as follows.

$$f_{c,e} = \frac{3}{2(2-\nu)(1+\nu)} k_{Ni}\delta_j \tag{5}$$

$$f_c = uf_s \tag{6}$$

where k_{Ni} is the normal stiffness, ν is Poisson's ratio, and δ_j is the tangential relative displacement at contact nodes.

2.1.2. Model Description

Noticing a common technique to simplify system dynamic equations and reduce computational costs, this paper adopts the approach of connecting multiple rigid bodies through joints. The UAV model consists of the fuselage, landing gear, and arresting hook. The simulation model of the arresting gear system includes wire rope supports, a deck, an arresting cable, a damper and sheaves. The simulation model of the integrated UAV and arresting gear system is shown in Figure 2.

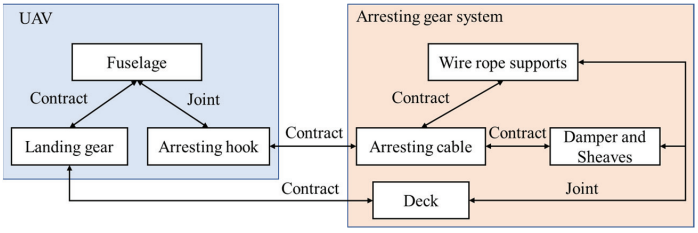

Figure 2. Schematic diagram of UAV and arresting gear system.

2.2. Model of Carrier-Based UAV

2.2.1. Configuration of UAV

The deformation and stress of the UAV structure are not the main concern. Therefore, it is modeled using rigid bodies described by the degree of freedom (DoF) kinematic and dynamic differential equations. The UAV model in this paper consists of the arresting hook, nose landing gear (NLG), main landing gear (MLG) and fuselage as shown in Figure 3a. Aerodynamic force is applied as a 6 DoF load (X, Y, Z, L, M, and N) on the fuselage rigid body, with the point of application being converted into the center of gravity. X, Y, Z, L, M, and N are calculated via Equation (7).

$$\begin{aligned} \mathrm{X} &= \tfrac{1}{2}\rho u^2 S_{ref} C_x \\ \mathrm{Y} &= \tfrac{1}{2}\rho u^2 S_{ref} C_y \\ \mathrm{Z} &= \tfrac{1}{2}\rho u^2 S_{ref} C_z \\ \mathrm{L} &= \tfrac{1}{2}\rho u^2 S_{ref} b C_l \\ \mathrm{M} &= \tfrac{1}{2}\rho u^2 S_{ref} c C_m \\ \mathrm{N} &= \tfrac{1}{2}\rho u^2 S_{ref} b C_n \end{aligned} \tag{7}$$

where ρ is the density of air, u is the UAV velocity, and C_x, C_y, C_z, C_l, C_m, and C_n are aerodynamic coefficients, respectively. c, b, and S_{ref} are the reference chord, reference span and reference wing area of the UAV, respectively.

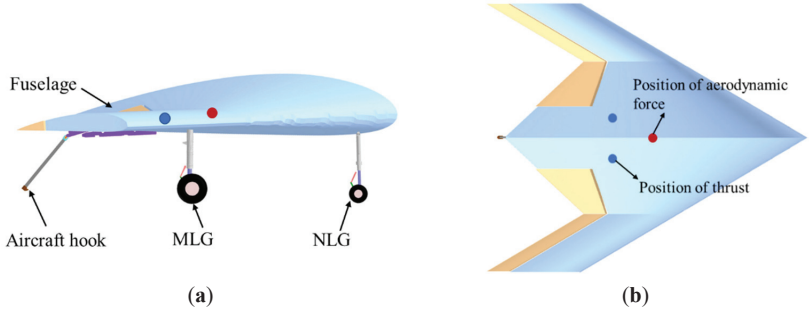

Figure 3. Main parts of UAV model: (**a**) Side view of carrier-based UAV; (**b**) Top view of carrier-based UAV.

The influence of the engine's rotational torque is neglected, and the engine thrust is decoupled into a three-axis force acting at a point in the fuselage's rigid body [28]. The thrust during this process remains constant at 14 tons in this paper. The relative positions of aerodynamic force and thrust with respect to the UAV body are depicted in Figure 3b.

2.2.2. Model of Landing Gear

The landing gear is the ground support system of the UAV and plays a crucial role as an energy-absorbing component during the landing process. As shown in Figure 4, the

dynamic model of the landing gear comprises the upper strut, lower strut, torque link, wheel axle and tire assemblies. The upper strut is collected in the same rigid body as the fuselage, while the lower strut is collected in the same rigid body as the wheel axle. Three revolute joints are set between the upper strut and upper torque link, the upper strut and lower torque link, and the lower strut and lower torque link, respectively.

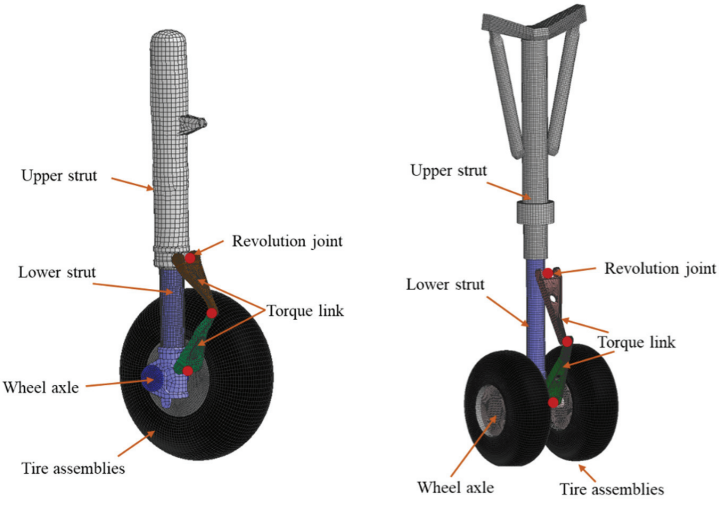

Figure 4. FEM model of landing gear. (**a**) MLG; (**b**) NLG.

The displacement of the shock absorber is determined via the relative motion of the upper and lower struts [23]. The hydraulic force, F_S, can be expressed as

$$F_S = F_a + F_u \tag{8}$$

where F_a is the air spring force, and F_u is the hydraulic damping force.

The air spring force, F_a, can be expressed as

$$F_a = \begin{cases} A_a^L \left[\frac{P_{a0}^L}{\left(1 - \frac{A_a^L S}{V_{a0}^L}\right)^{\gamma}} - P_{atm} \right], \; S \le S_{H0} \\ A_a^L \left[\frac{P_{a0}^L}{\left(1 - \frac{A_a^L S}{V_{a0}^L}\right)^{\gamma}} - P_{atm} \right] + A_a^H \left[\frac{P_{a0}^H - P_{a0}^L}{\left(1 - \frac{A_a^H (S - S_{H0})}{V_{a0}^H}\right)^{\gamma}} - P_{atm} \right], \; S > S_{H0} \end{cases} \tag{9}$$

where A_a^L is the initial pressure area of the low-pressure air chamber, A_a^H is the pressure area of the high-pressure air chamber, and P_{a0}^L is the initial pressure in the low-pressure air chamber. P_{a0}^H is the initial pressure in the low-pressure air chamber. P_{atm} is the atmospheric pressure, S is the stroke of the damper, *and* S_{H0} is the initial stroke of the high-pressure chamber. V_{a0}^L is the initial volume of the low-pressure chamber, V_{a0}^H is the initial volume of the high-pressure chamber, and γ is the polytropic exponent.

The hydraulic damping force can be expressed as follows:

$$F_u = \begin{cases} \frac{\rho_h A_h^3 \dot{S}^2}{2\left(C_d^+\right)^2 A_d^2} + \frac{\rho_h A_{hL}^3 \dot{S}^2}{2\left(C_{dL}^+\right)^2 \left(A_{dL}^+\right)^2}, \dot{S} \ge 0 \\ -\frac{\rho_h A_h^3 \dot{S}^2}{2\left(C_d^-\right)^2 A_d^2} - \frac{\rho_h A_{hL}^3 \dot{S}^2}{2\left(C_{dL}^-\right)^2 \left(A_{dL}^-\right)^2}, \dot{S} \le 0 \end{cases} \tag{10}$$

where ρ_h is the oil density, $\dot{S}$ is the stroke velocity, A_h is the effective area of the buffer, A_d is the main oil cavity oil hole area, C_d^+ and C_d^- are the flow coefficient of the main oil hole under the forward and reverse stroke, A_{hL} is the effective area of the back oil hole, A_{dL}^+ and A_{dL}^- are the effective flow areas of the oil return hole under the forward and reverse stroke, and C_{dL}^+ and C_{dL}^- are the flow coefficient of the back oil hole under the forward and reverse stroke.

In addition to the load of the shock absorber, the flexibility of the tire also contributes significantly to the impact load during UAV landing. The compression of the tire under the impact load constitutes a substantial proportion of the overall compression stroke of the landing gear's damping system. The internal structure of the tire is illustrated in Figure 5a. The inner layer of the tire is defined as the fabric material and the change of volume surrounded by the wheel rim and the inner fabric layer of the tire conforms to the ideal gas equation.

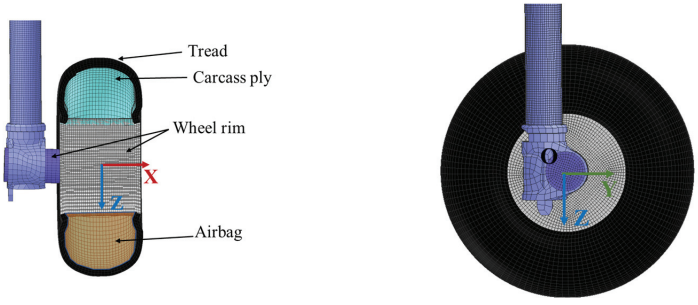

(**a**) (**b**)

Figure 5. Schematic of tire assemblies. (**a**) Internal structure of tire; (**b**) FEM model of tire and constraint.

The tread and the wheel rim share common nodes on the adjacent surface, and the rotational constraints of the tire are defined using a coordinate system, O-XYZ, located at the center of the wheel rim as shown in Figure 5b. The rubber material of the tire is modeled using eight-node hexahedral elements, employing the Mooney–Rivlin material model. The constitutive equation for this model is as follows:

$$W = \mathrm{A}(\mathrm{I}-3) + \mathrm{B}(\mathrm{II}-3) + \mathrm{C}\left(\mathrm{III}^{-2}-1\right) + \mathrm{D}(\mathrm{III}-1)^2 \tag{11}$$

where $\mathrm{C} = 0.5\mathrm{A} + \mathrm{B}$, $\mathrm{D} = \frac{\mathrm{A}(5v-2)+\mathrm{B}(11v-5)}{2(1-2v)}$, A and B are the Rivlin constants determined through uniaxial tensile testing, v is Poisson's ratio, and I, II and III are the Green–Lagrange strain tensor constants.

2.2.3. Model of Arresting Hook

The dynamic model of the arresting hook [29] is shown in Figure 6. The model of the arresting hook comprises fuselage assembly, the hold down damper, lateral damper, hook shank, hook, joint part and two revolute joints. Fuselage assembly and the fuselage are set to a rigid body. The hold down damper has one end node located at the fuselage assembly and the other end node located at the joint part. By defining revolute joints 1 and 2, the longitudinal and lateral rotations of the arresting hook are, respectively, determined.

Prior to engaging the arresting cable, the arresting hook collides with the deck and rebounds with a certain velocity. The rebound height of the arresting hook is limited by the hold down damper to ensure the successful engagement of the arresting hook with the cable. The hold down damper of the arresting hook plays a critical role in determining the height of the rebound [25], and it is modeled as a bar element.

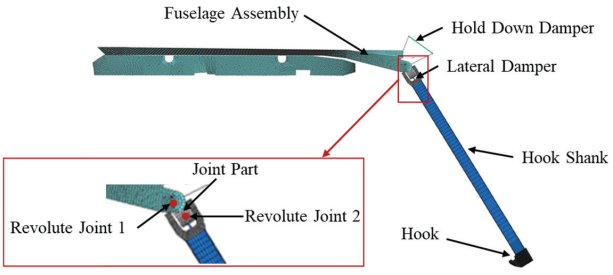

Figure 6. Schematic diagram of arresting hook.

2.3. Model of Arresting System

The deck is partitioned into the arresting hook contact area and non-contact area as shown in Figure 7. Additionally, the arresting gear system in this paper is based on the MK7-3 hydraulic arresting gear system [8]. The complete hydraulic arresting gear system model is divided into three components: the pulley system, the hydraulic system and arresting cable system. The pulley system comprises fixed pulleys, moving pulleys, and steering pulleys. The hydraulic system is composed of the damper sheave, main hydraulic cylinder and cable anchor damper system, which are modeled using the shell element and spring damper beam.

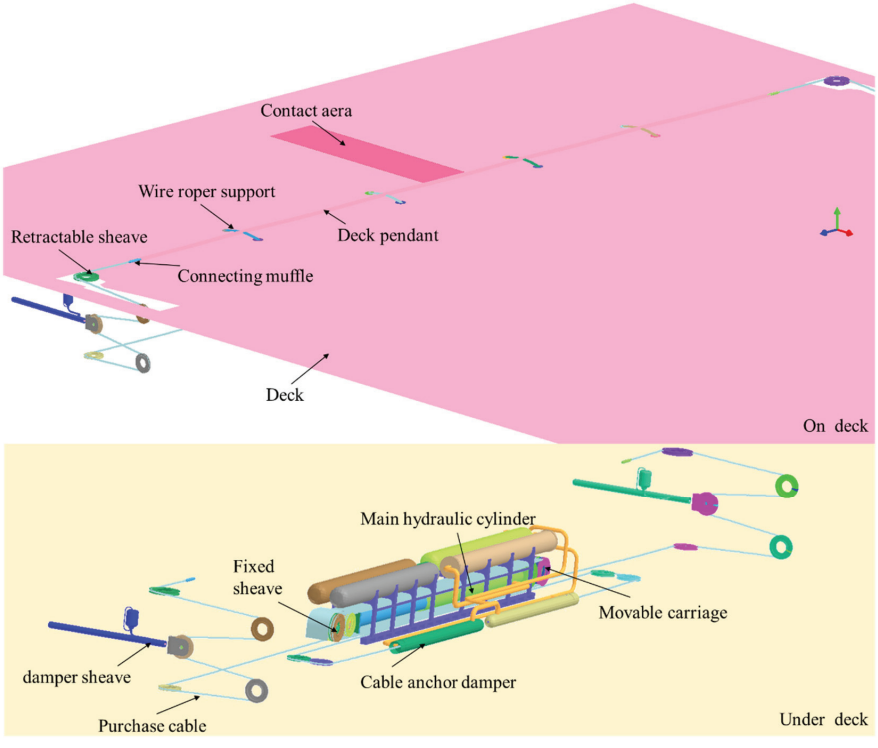

Figure 7. Diagram of arresting gear system.

2.3.1. Modeling of Rigid Bodies in the Arresting Cable System and Constraints

The arresting hook of a carrier-based UAV engages with the arresting cable, resulting in the cable being pulled out during the arresting process. The cable is threaded through the

arresting gear system, forming a block and tackle mechanism. This mechanism is designed to transfer the load from the UAV to the hydraulic machine. Within the hydraulic machine, the kinetic energy of the UAV is converted into heat and subsequently dissipates.

The arresting gear system is a complex mechanical hydraulic system. In this paper, the arresting gear system is modeled using three arresting cables (one deck pendant and two purchase cables), block and tackles (forty-eight sheaves), and five hydraulic dampers (two damper sheave installations, two cable anchor dampers and one hydraulic cylinder). In this research, the deformation and stress of the pulley, piston and cylinder system are not the main concern. Therefore, they are modeled as rigid bodies. The fixed sheave assembly is merged into the deck, which prevents there from being unnecessary fixed joints between the deck and itself. The other sheaves, piston and cylinder shown in Figure 7 undergo translation and rotation simultaneously.

2.3.2. Arresting Cable

The configuration of the pendant and wire rope support is shown in Figure 8. To improve computational efficiency, the arresting cable is divided into two parts based on the connecting muffle, the pendant and the purchase cable, as shown in Figure 8. The purchase cable is modeled using a nonlinear tension bar. This modeling approach takes into account the nonlinear dynamic characteristics of the cable under tension by accounting for factors such as material properties, cable diameter and applied tension force.

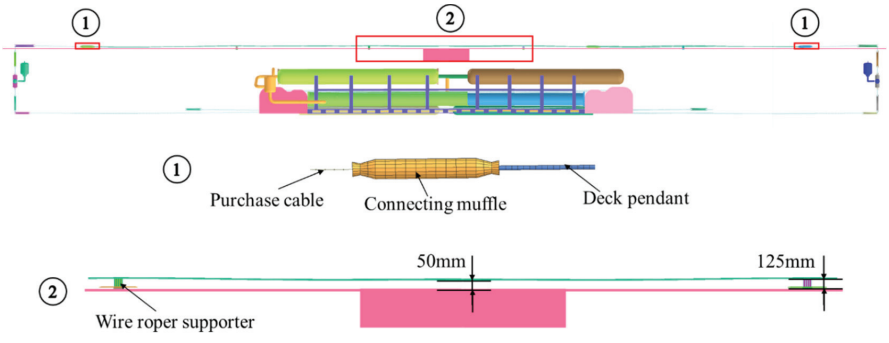

Figure 8. Diagram of arresting cable and wire rope supports.

The FEM model of the pendant is modeled using a shell and spring beam element with 6 DoF as shown in Figure 9. The beam element is connected to the shell element at the node N_i and the nodes N_{i1}–N_{i8} of the shell element. These nodes collectively form a rigid body. In the local coordinate system (N_i-$S_iR_iT_i$), N_i represents the origin point of the coordinate system, S_i denotes the direction vector along the beam axis, R_i represents the direction vector along the cross-sectional plane of the beam, and T_i represents the direction vector perpendicular to both R_i and S_i. Defining the constitutive characteristics of the beam in the local coordinate system enables an accurate representation of the beam's deformation and response to applied loads.

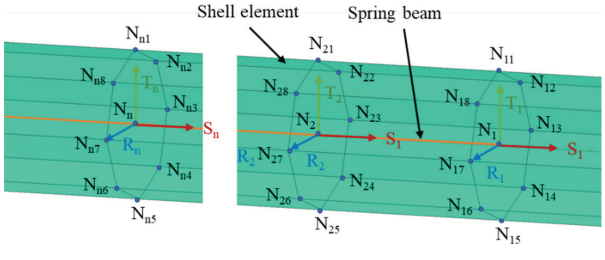

Figure 9. FEM model of pendant.

2.3.3. Wire Rope Supports

Wire rope supports serve as a means of elevating the cable above the deck to guarantee the engagement of the arresting cable on the incoming arresting hook. The four wire rope supports are equidistantly placed across the deck and maintain a minimum cross-deck cable height of 0.5 m, measured from the bottom of the cable to the deck at its lowest point (Figure 8). Each wire rope support is directly tied to the deck [30].

As shown in Figure 10, the model of the wire rope support is established based on a four-node shell element. The forward end of the wire rope support spring is secured using a cam mounted in a deck recess and a follower pinned at the end of the wire rope support. The aft end of the wire rope support is also pinned and set between adjustable forward stops as required.

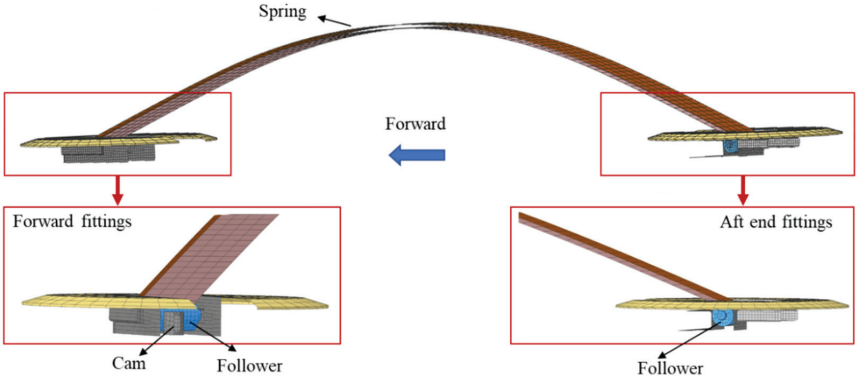

Figure 10. FEM model of wire rope support.

3. Verification of the Dynamic Model of the Collision and Rebound of the Arresting Hook

All the computations presented in this study are performed using an in-house-developed code solver and a combination of tools of PAM-Crash was utilized. The code solver solves the governing finite element equations based on a central difference explicit integration scheme in time [31]. Simulation is performed to verify the collision rebound of the arresting hook. As shown in Figure 11a, fuselage assembly and main landing gear sleeve are defined as a rigid body. Below the arresting hook is a rotating disc, and the collision point between the hook and disc is located at the edge of the disc. The rotation direction of the disc is shown in Figure 11b. In this simulation, the relative linear velocity between the hook and disc is equal to the velocity of the UAV at the collision of point. The simulation conditions including the sinking velocity, horizontal velocity and arresting hook configuration are consistent with the results of the collision rebound test in reference [27]. The elastic modulus of the hook and rotating disc material is 210 GPa, and Poisson's ratio is 0.3. The collision rebound height and distance are matched to the test in the reference by adjusting the spring and damping parameters of the arresting hook's longitudinal buffer.

The simulation results for the collision rebound height of the arresting hook, corresponding to sinking velocities of 3.6 m/s, 4 m/s, and 5 m/s, are presented in Figure 12. With the requirement of an increased sinking velocity, the bounce height on the aircraft hook increases correspondingly. The satisfactory agreement observed between the simulated and experimental data regarding the rebound height and rebound span of the arresting hook demonstrates the accuracy of the dynamic model established in this paper for the collision rebound process.

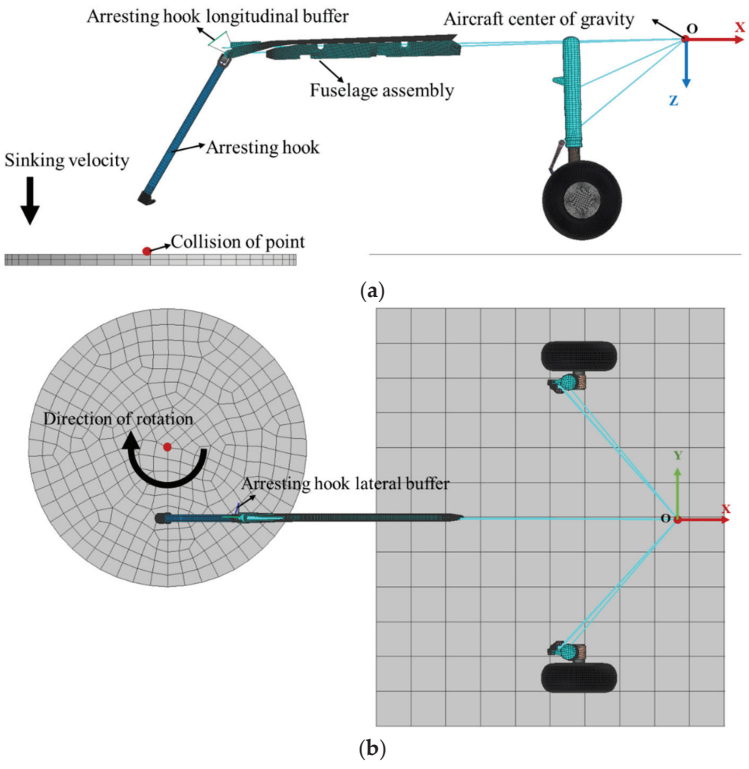

Figure 11. Diagram of simulation test of arresting hook bounce. (**a**) Left-side view (**b**); top-side view.

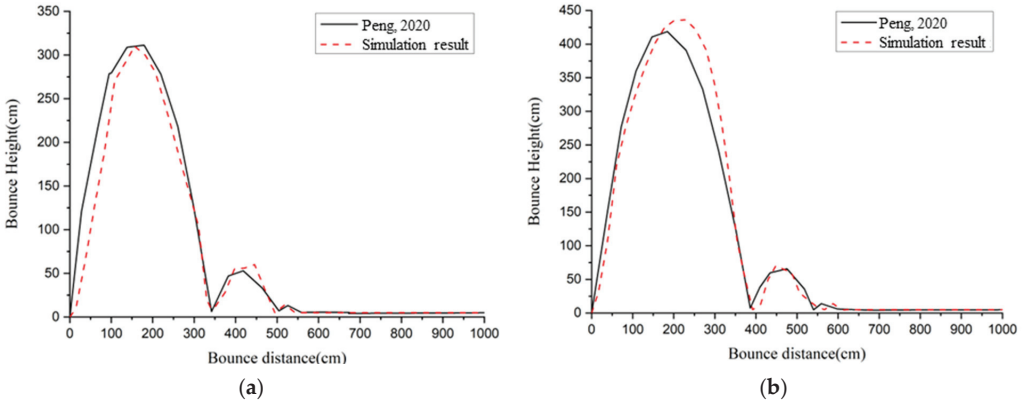

Figure 12. *Cont.*

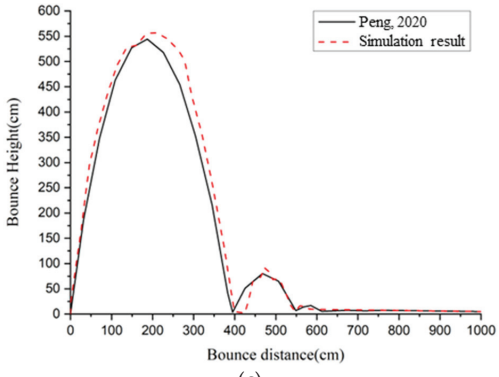

(**c**)

Figure 12. Comparison of bounce height of arresting hook between experiment and simulation. Sinking velocity = (**a**) 3.6 m/s; (**b**) 4 m/s; (**c**) 5 m/s [13].

4. Results and Discussion

4.1. Setting of Carrier-Based UAV Attitude

Figure 13a illustrates the initial condition of the UAV, and the mass of the fuselage's rigid body is set as 16,500 kg. The horizontal and sinking velocity of the carrier-based UAV at the moment the hook touches the deck are 60 m/s and 4.5 m/s, respectively. The diagram of the distance between the touchdown point, cable d and the roll angle, φ, is shown in Figure 13b,c. The position of the aerodynamic force and thrust is same as that described in Section 2.2.1. The control of variables facilitates a comparative study of the similarities and differences between different touchdown points and roll angles of an UAV.

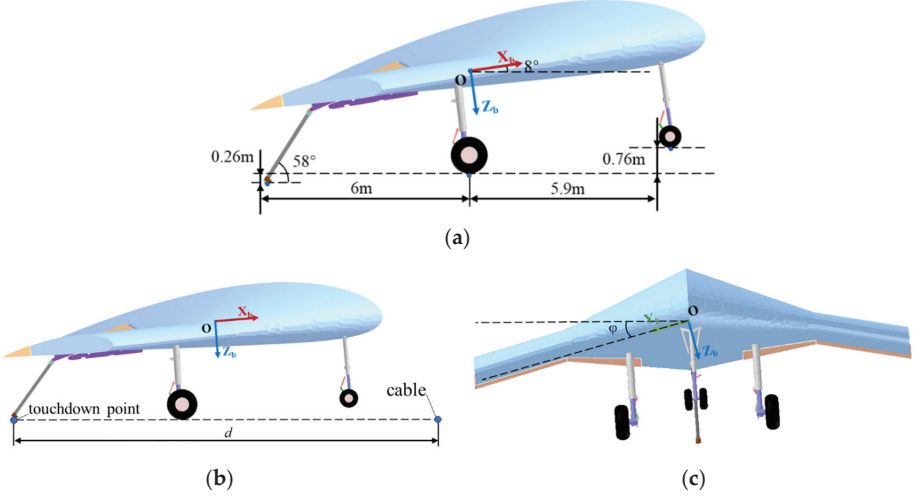

(**a**) (**b**) (**c**)

Figure 13. Carrier-based UAV model and parameters. (**a**) Configuration of UAV; (**b**) diagram of distance between touchdown point and cable d; (**c**) diagram of UAV roll angle, φ.

4.2. Influence of Touchdown Point on the Engagement of Hook with Cable

The hook engages with the arresting cable after the UAV hook touches down on the carrier deck. Subsequently, the UAV starts to slow down under the action of the arresting gear system. In this section, the influence of distance between the touch point and cable on the engagement process is studied. The initial condition of the UAV is represented in

Figure 13a, and the distance between the touchdown point and cable d is set at 0, 2 m, 4 m 6 m, 8 m and 10 m. The distance between the touchdown points and the cable significantly influences the rebound height of the arresting hook at the moment of engagement. The engagement location of the arresting hook with the arresting cable varies depending on the distance from the touchdown point to the arresting cable. However, the contact force between the arresting hook and cable are nearly equal, at approximately 54 kN, for different touchdown point distances.

The stress–strain situation of the arresting hook is depicted in Figure 14. At d = 1 m, the arresting hook rebounds and engages with the cable in the upward phase of the first rebound. The maximum stress, reaching 187 MPa, occurs at the groove of the arresting hook. At d = 2 m, the arresting hook rebounds and engages with the cable in the downward phase of the first rebound. The maximum stress at this point is 179 MPa. At d = 4 m, the arresting hook engages with the cable during the second rebound phase. The engagement location is in the upper part of the hook, resulting in a maximum stress of 172 MPa. When d = 6 m, the arresting hook engages with the cable during the third rebound phase. The engagement location is at the connection between the hook head and the hook shank, leading to a larger high-stress area. Additionally, the maximum stress in this case is 184 MPa. For d = 8 m, the arresting hook engages with the cable during the deck drag phase. The engagement location is at the connection between the hook head and the hook shank. Additionally, the maximum stress is 188 MPa. When d = 10 m, the arresting hook engages with the cable during deck drag on the deck. However, there is an occurrence of the cable being crushed by the tire, which significantly affects the location of the cable's engagement. The location of maximum stress in this case is at the point where the hook shank and the cable engage, with a maximum stress of 165 MPa.

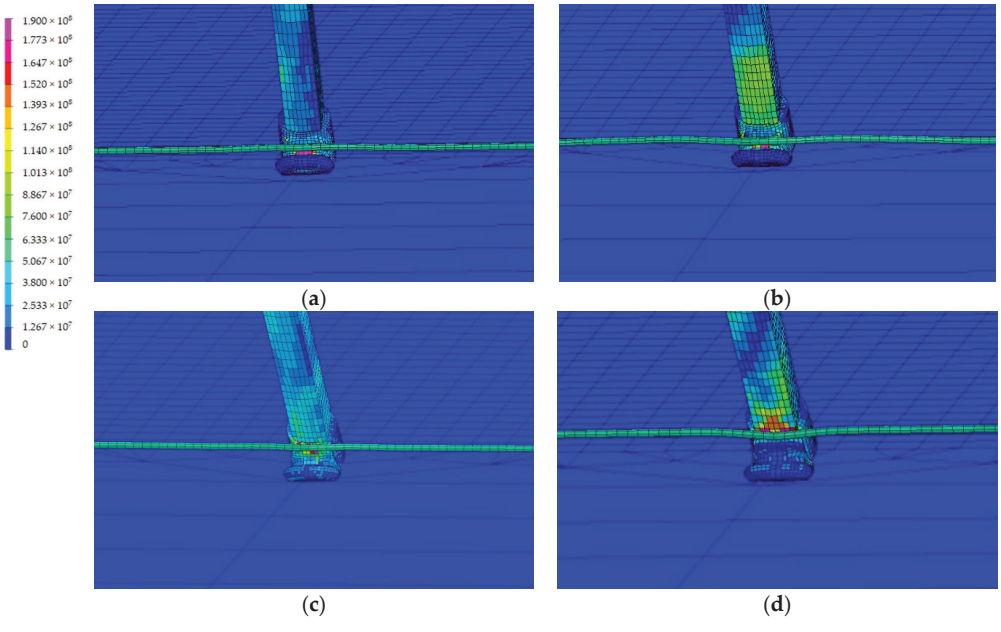

Figure 14. *Cont.*

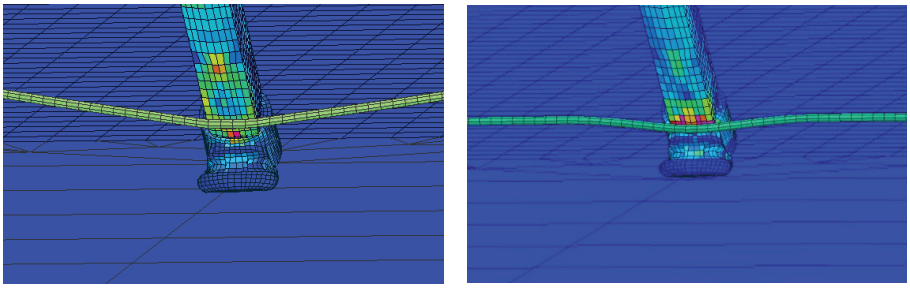

(**e**) (**f**)

Figure 14. Stress distribution of the arresting hook at the moment the hook engages the cable. (**a**) d = 1 m; (**b**) d = 2 m; (**c**) d = 4 m; (**d**) d = 6 m; (**e**) d = 8 m; (**f**) d = 10 m.

Figure 15 illustrates the process of the arresting cable being run over by the tire during the aircraft's arrest. As the tire rolls over the arresting cable, a significant bending effect occurs at the point of contact, leading to the propagation of bending waves along the cable's length. Notably, at 0.03 s, when the bending wave reaches the middle section of the arresting cable, it forcefully makes contact with the deck, resulting in a rebound effect. During the rebound, the cable momentarily loses tension at 0.04 s and then regains tension at 0.08 s. The simulation model effectively captures the dynamic behavior of the arresting cable after the tire rolls over, providing valuable insights into the engagement process of the cable and hook.

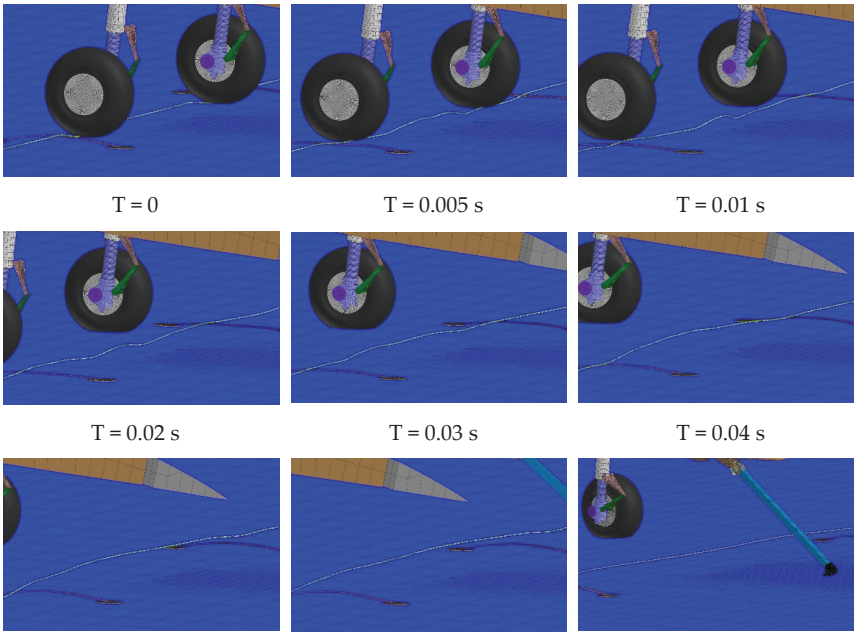

Figure 15. *Cont.*

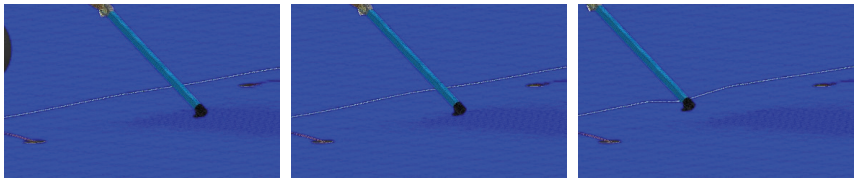

T = 0.08 s T = 0.1 s T = 0.12 s

Figure 15. Engagement process after tire rolling cable.

At a sinking velocity of 4.5 m/s, the bounce height of the arresting hook remains below the height of the arresting cable. Therefore, under the above conditions, no failures in engaging the cable were observed during UAV arrestment. The optimal distance between the touchdown point and cable for the UAV on the carrier deck is 4 m. At this distance, the arresting hook undergoes a secondary collision with the deck before engaging the cable, resulting in a low bounce height and a high success rate of engagement.

4.3. Influence of Roll Angle on the Engagement of Hook with Cable

In this section, the influence of roll angle on the engagement process is studied. The initial condition of UAV is represented in Figure 12. The distance between the touchdown point and cable d is 4 m and the roll angle, φ, is set at 0, 2°, 4° and 6°. Figure 16 depicts the change in the height of the UAV's center of gravity after the tire makes contact with the deck. One side of the landing gear touches down earlier, resulting in a higher altitude of the UAV's center of gravity at the moment of touchdown compared to that in the situation without any roll angle. The greater the roll angle, the larger the distance of the center of gravity descent.

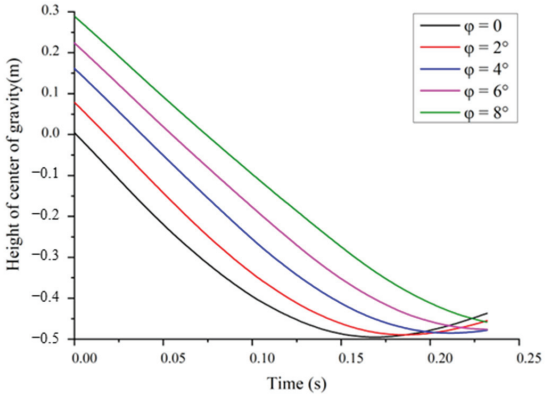

Figure 16. Time history of the height of the center of gravity after the landing gear touches the deck under different roll angles.

The stress distribution at the moment of the hook engaging the cable is shown in Figure 17. It can be observed that the roll angle has a minor influence on the contact force during cable engagement, which remains around 54 kN. However, the roll angle affects the contact area of the hook, resulting in an increased high-stress region in the arresting hook.

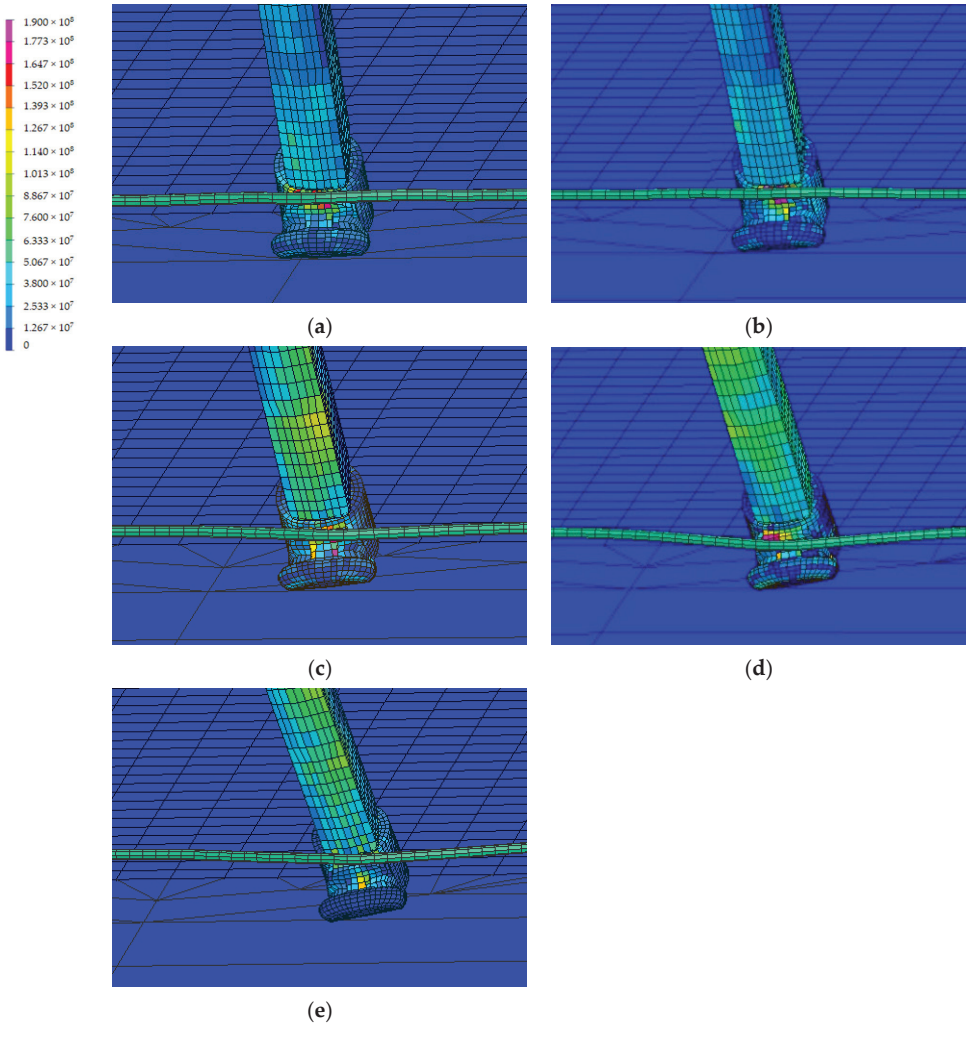

Figure 17. Stress distribution of the arresting hook at the moment the hook engages the cable: (**a**) $\varphi = 0$; (**b**) $\varphi = 2°$; (**c**) $\varphi = 4°$; (**d**) $\varphi = 6°$; (**e**) $\varphi = 8°$.

It is noteworthy that at a roll angle of 8°, one side of the tire makes contact with the arresting cable, and the engagement location of the arresting hook and the cable is at the connection between the hook and hook shank. This particular process of the tire touching the cable is depicted in Figure 18. Upon tire–cable contact, the arresting cable undergoes bending, leading to induced vertical movements. The arresting cable bends and transmits the force to the wire rope support. At 0.05 s, the bending is effectively transmitted to the wire rope support, resulting in the near elimination of the vertical movements of the arresting cable. Due to the impact from the tire collision, the arresting cable experiences a slight forward movement after 0.05 s until the hook engages with the cable.

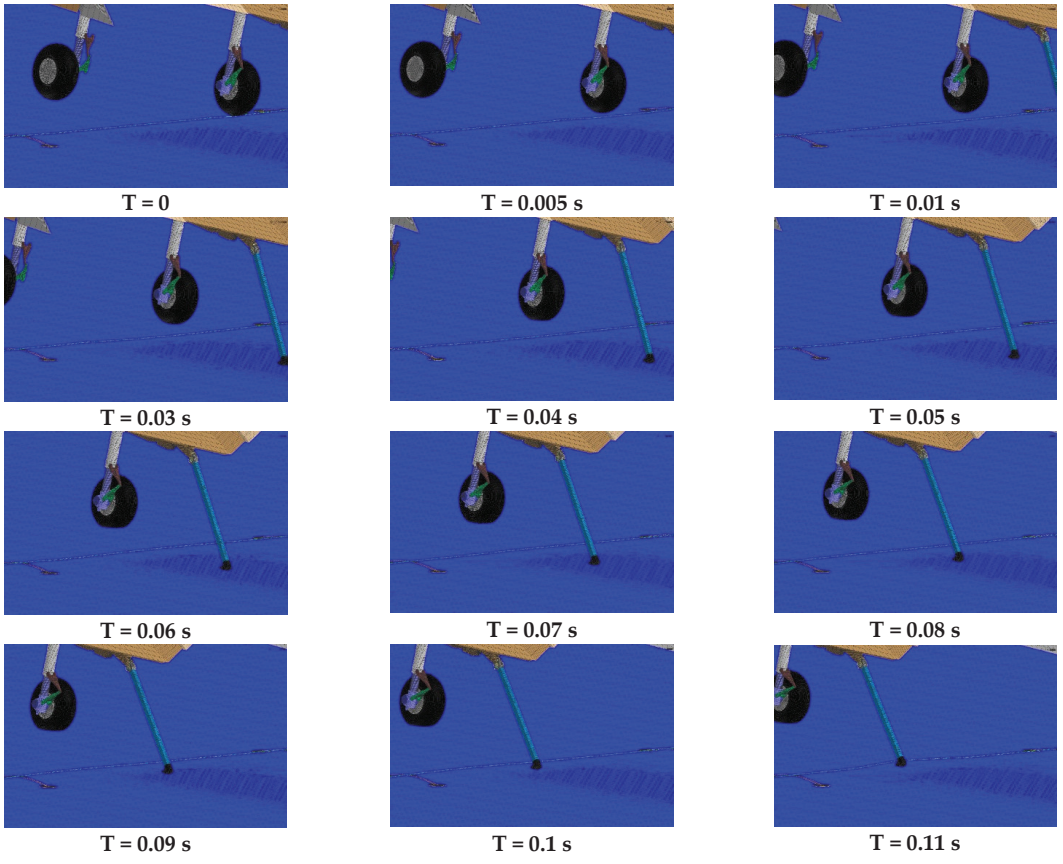

Figure 18. Hook engaging cable after one side of the tire touches the cable.

Furthermore, a scenario involving one side tire rolling over the cable is observed when the distance between the touchdown point and the cable is 8 m, and the UAV experiences a roll angle of 4°. As depicted in Figure 19 at 0.1 s after the tire makes contact with the cable, it is evident that tire rollover exerts a considerably larger interference on the motion of the arresting cable compared to the scenario where the tire touches the cable. Specifically, when the tire of the right landing gear rolls over the arresting cable, it applies a substantial bending force on the cable due to the pressure and friction at the contact point, leading to significant cable flexing and deformation along its length. Subsequently, the bending action propagates towards the wire rope supports on the other side, consequently impacting the cable's tension and dynamics. In this case, the bending is transmitted to the left-side wire rope support at 0.05 s. Simultaneously, the arresting cable undergoes a forward motion in the direction of the tire, affecting the engagement location of the hook and cable.

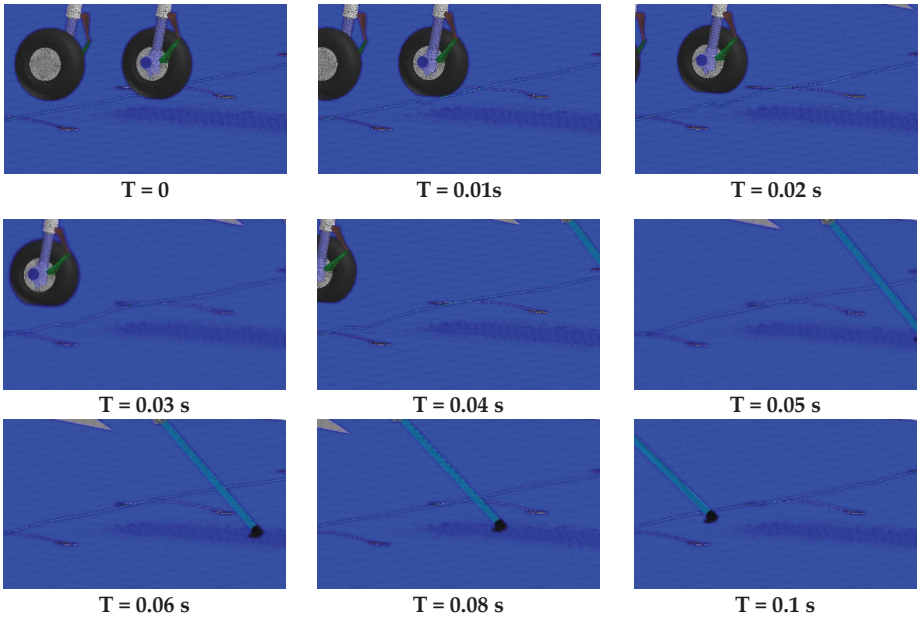

Figure 19. Hook engaging cable after one side of the tire rolls over the cable.

5. Conclusions

Successful engagement requires careful coordination and attention to detail, including aspects such as the configuration of a UAV and arresting cable setup, as well as a determination of the precise landing point for the UAV. In this paper, a FEM-MBD numerical method is used to study the dynamic characteristics of a carrier-based UAV. Simulation was conducted to investigate the engagement process under different touch down points and UAV roll angles. Analysis of the scenarios involving cable and tire contact was performed.

(1) A rigid–flexible coupling model of the hook–cable engagement process is established for a specific carrier-based UAV using the FEM-MBD method. To validate the rationality of the finite element model in solving the hook's rebound dynamics, the results are compared with experimental data from a relevant reference. The comprehensive model incorporates three key elements: the coupling of the carrier deck, aircraft body and the landing gears; a detailed arresting hook and cable model which considers their material properties and contact interactions; wire rope supports and a full-scale arresting gear system model. The established FEM-MBD model offers a framework for examining the dynamic behavior of the hook–cable engagement process.

(2) The touchdown position significantly influences the height of the arresting hook at the moment of hook and cable engagement, leading to variations in the maximum stress location on the arresting hook. When the touchdown point is 10 m away from the arresting cable, the cable is rolled over by the tires of the UAV. As a consequence, the arresting cable undergoes bending at the point of contact with the tires, and this bending effect is transmitted to both sides of the cable. The propagation of bending along the cable leads to the cable's contact with the deck and subsequent rebound. At the same time, the arresting cable experiences rapid movement in the direction of the tire roll-over. This movement has an impact on the engagement of the hook and cable, affecting the hook and cable's engagement location.

(3) In the case of an UAV carrier landing with a roll angle, the main landing gear on one side makes contact with the deck first, resulting in a more significant variation in the height of the UAV's center of gravity during hook engagement compared to

that in situations without any roll angle. As the roll angle increases, the downward displacement of the center of gravity increases. The roll angle has a minimal effect on the contact force at the moment of cable engagement, but it influences the location of cable contact at the engagement moment. A larger roll angle increases the high-stress area of the arresting hook at the engagement moment.

(4) The detailed analysis of this tire–cable interaction sheds light on the complex dynamics involved in the engagement process. Under a roll angle of 8° and distance of 4 m between the touch point and the cable, the tire makes contact with the cable. The cable undergoes bending at the point where the tire touches the cable, and the bending leads to the small-scale vertical movement of the arresting cable. Under the condition of a 4° roll angle and an 8 m distance between the touchdown point and the cable, the tire rolls over the arresting cable on one side. The bending caused by the tire rolling over is greater than that of the tire touching the cable. As the single tire rolls over the arresting cable, it causes a rapid movement of the cable in the direction of the UAV's motion and transmits force to the wire rope support. Simultaneously, this movement of the arresting cable amplifies the uncertainty of engagement.

Author Contributions: Conceptualization, H.S., Z.K. and Y.W.; methodology, H.S.; software, H.S. and D.L.; validation, H.S., Z.K. and Y.W.; formal analysis, H.S. and Z.K.; investigation, H.S. and Z.Y.; resources, Z.K. and Y.W.; data curation, H.S. and Z.K.; writing—original draft preparation, H.S.; writing—review and editing, H.S. and Z.Y.; visualization, H.S. and Z.K.; supervision, D.L.; project administration, D.L.; funding acquisition, J.X. and D.L. All authors have read and agreed to the published version of the manuscript.

Funding: This research was funded by National Natural Science Foundation of China (no. T2288101) and the National Key Research and Development Project, grant number 2020YFC1512500.

Institutional Review Board Statement: Not applicable.

Informed Consent Statement: Not applicable.

Data Availability Statement: Not applicable.

Conflicts of Interest: The authors declare no conflict of interest.

References

1. Wei, X.; Yin, Q.; Peng, Y.; Nie, H.; Liu, C. An overview of researches on deck-landing of carrier-based aircrafts. In Proceedings of the 2013 International Powered Lift Conferenc 2013 International Powered Lift Conferencee AIAA Aviation, Los Angles, CA, USA, 12–14 August 2013.
2. Ryan, J.C.; Cummings, M.L. A systems analysis of the introduction of unmanned aircraft into aircraft carrier operations. *IEEE Trans. Hum.-Mach. Syst.* **2016**, *46*, 209–220. [CrossRef]
3. Zhen, Z.; Tao, G.; Yu, C.; Xue, Y. A multivariable adaptive control scheme for automatic carrier landing of UAV. *Aerosp. Sci. Technol.* **2019**, *92*, 714–721. [CrossRef]
4. Wang, X.; Liu, J.; Su, X.; Peng, H.; Zhao, X.; Lu, C. A review on carrier aircraft dispatch path planning and control on deck. *Chin. J. Aeronaut.* **2020**, *33*, 3039–3057. [CrossRef]
5. Yang, Q. Research on flight measurement method of a carrier-based aircraft hook loads. *Acta Aeronaut. Astronaut. Sin.* **2015**, *36*, 1162–1168.
6. Lawrence, J.T. Milestones and developments in US naval carrier aviation-part II: AIAA-2005-6120. In Proceedings of the AIAA Atmospheric Flight Mechanics Conference and Exhibit, San Francisco, CA, USA, 15–18 August 2005.
7. Max, M.D.; Phillip, W.R.; Morgan, W.; Erickson, A.J. Carrier Landing Simulation using Detailed Aircraft and Landing. In Proceedings of the AIAA SciTech Forum, Orlando, FL, USA, 6–10 January 2020.
8. Naval Air Engineering Center. *Military Standard: Catapulting and Arresting Gear Forcing Functions for Aircraft Structural Design*; MIL-STD-2066 (AS); Navy Air Systems Command: Lakehurst, NJ, USA, 1981.
9. Thomlinson, J. A Study of the Aircraft Arresting Hook Bounce Problem. In *The Principal Director of Scientific Research (Air)*; Her majesty's Stationery Office: London, UK, 1954.
10. Jones, L.W. *Development of Curves for Estimating Aircraft Arresting Hook Loads: ADA119551*; Air Force Flight Test Center, Edwards Air Force Base: Edwards AFB, CA, USA, 1982; pp. 15–42.
11. Gao, Z.J. A discussion of bounce kinematics of aircraft arresting hook and cable dynamics. *Acta Aeronaut. Astronaut. Sin.* **1990**, *11*, B543–B548.

12. Liu, G.; Nie, H. Dynamics of arresting hook bounce after initial touchdown and impacting with deck. *Acta Aeronaut. Astronaut. Sin.* **2009**, *30*, 1672–1677.
13. Peng, Y.; Zhang, Z.; Wei, X.; Li, L.; Wang, Y.; Liu, X. Dynamics influence analysis of structural parameters on impact and rebound of arresting. *Acta Aeronaut. Astronaut. Sin.* **2020**, *41*, 107864.
14. Peng, Y.; Xie, P.; Wei, X.; Nie, H. Dynamics test research of bounce of carrier-based aircraft arresting hook. *Appl. Sci.* **2020**, *10*, 9033. [CrossRef]
15. Zhu, Q.D.; Meng, X.; Zhang, Z. Simulation research on motion law of arresting hook during landing. *Appl. Mech. Mater.* **2013**, *300–301*, 997–1002. [CrossRef]
16. Tony, W. F-35 Carrier Suitability Testing. In Proceedings of the AIAA Aviation Forum, Atlanta, GA, USA, 25–29 June 2018.
17. Yin, Y.; Nie, H.; Ni, H.; Zhang, M. Reliability analysis of landing gear retraction system influenced by multifactors. *J. Aircr.* **2016**, *53*, 713–724. [CrossRef]
18. Liang, L.; Wan, C. Xun Study on the dynamic performance of aircraft arresting cable. *Acta Aeronaut. Astronaut. Sin.* **2013**, *34*, 833–839.
19. Vetyukov, Y. Non-material finite element modelling of large vibrations of axially moving strings and beams. *J. Sound Vib.* **2018**, *414*, 299–317. [CrossRef]
20. Liu, J.; Cheng, Z.; Ren, G. An Arbitrary Lagrangian-Eulerian formulation of a geometrically exact timoshenko beam running through a tube. *Acta Mech.* **2018**, *229*, 3161–3188. [CrossRef]
21. Deng, L.; Zhang, Y. Nonlinear dynamic analysis of arresting gears using 2D non-material variable-domain corotational elements. *Mech. Mach. Theory* **2021**, *163*, 104377. [CrossRef]
22. Mikhaluk, D.; Voinov, I.; Borovkov, A. Finite element modeling of the arresting gear and simulation of the aircraft deck landing dynamics. In Proceedings of the European LS-DYNA Conference, Petersburg, Russia, 30 June–4 July 2008.
23. Liu, C.; Wang, B. Dynamics Modeling and Simulation Analysis of Coupled Carrier-Based Aircraft and Arresting Gear System. *J. Nanjing Univ. Aeronaut. Astronaut.* **2016**, *48*, 418–425.
24. Shen, W.; Zhao, Z.; Ren, G.; Liu, J. Modeling and Simulation of Arresting Gear System with Multibody Dynamic Approach. *Math. Probl. Eng.* **2013**, *2013*, 867012. [CrossRef]
25. Zhang, H.; Guo, J.; Liu, J.P.; Ren, G.-X. An efficient multibody dynamic model of arresting cable systems based on ALE formulation. *Mech. Mach. Theory* **2020**, *151*, 103892. [CrossRef]
26. Zhang, Z.; Peng, Y.; Wei, X.; Li, L.; Wang, Y.; Liu, X. Research on longitudinal dynamics safety boundary of carrier-based aircraft arresting. *Aerosp. Sci. Technol.* **2022**, *130*, 107864. [CrossRef]
27. Peng, Y.; Yin, Y.; Xie, P.; Wei, X.; Nie, H. Reliability analysis of arresting hook engaging arresting cable for carrier-based aircraft influenced by multifactors. *Chin. J. Aeronaut.* **2022**, *36*, 311–323. [CrossRef]
28. The Chief Committee of Aircraft Design Manual. *Aircraft Design Manual: Takeoff and Landing System Design*; Aviation Industry Press: Beijing, China, 2002; pp. 90–180.
29. Dou, Q.; Yang, Z.; Liu, J.; Li, X. Experimental research and analysis on dynamics characteristics of arresting hook buffer. *Mech. Sci. Technol. Aerosp. Eng.* **2019**, *38*, 1307–1312.
30. Johnny, E. *US Navy Aviation Boatswain's Mate E NAVEDTRA 14310: Chapter 3*; Naval Education and Training Professional Development and Technology Center: Saufley Field in Escambia County, FL, USA, 2001; pp. 33–34.
31. Bathe, K.J. Finite Element Procedures. Prentice Hall: Hoboken, NJ, USA, 1996.

drones

MDPI

Article

Research on Scenario Modeling for V-Tail Fixed-Wing UAV Dynamic Obstacle Avoidance

Peihao Huang [1,2], Yong Tang [3,4], Bingsan Yang [1,2] and Tao Wang [1,2,*]

[1] School of Intelligent Systems Engineering, Sun Yat-sen University, Shenzhen 518107, China; huangph26@mail2.sysu.edu.cn (P.H.); yangbs3@mail2.sysu.edu.cn (B.Y.)
[2] Southern Marine Science and Engineering Guangdong Laboratory (Zhuhai), Zhuhai 519000, China
[3] School of Civil Aviation, Northwestern Polytechnical University, Xi'an 710072, China; tangyonguas@163.com
[4] Unmanned Aerial System Co., Ltd., Aviation Industry Corporation of China (Chengdu), Chengdu 610091, China
* Correspondence: wangt339@mail.sysu.edu.cn

Abstract: With the advantages of long-range flight and high payload capacity, large fixed-wing UAVs are often used in anti-terrorism missions, disaster surveillance, and emergency supply delivery. In the existing research, there is little research on the 3D model design of the V-tail fixed-wing UAV and 3D flight environment modeling. The study focuses on designing a comprehensive simulation environment using Gazebo and ROS, referencing existing large fixed-wing UAVs, to design a V-tail aircraft, incorporating realistic aircraft dynamics, aerodynamics, and flight controls. Additionally, we present a simulation environment modeling approach tailored for obstacle avoidance in no-fly zones, and have created a 3D flight environment in Gazebo, generating a large-scale terrain map based on the original grayscale heightmap. This terrain map is used to simulate potential mountainous terrain threats that a fixed-wing UAV might encounter during mission execution. We have also introduced wind disturbances and other specific no-fly zones. We integrated the V-tail fixed-wing aircraft model into the 3D flight environment in Gazebo and designed PID controllers to stabilize the aircraft's flight attitude.

Keywords: fixed-wing UAV simulation; V-tail aircraft; 3D flight environment; threat scenario; simulation environment modeling; Gazebo

Citation: Huang, P.; Tang, Y.; Yang, B.; Wang, T. Research on Scenario Modeling for V-Tail Fixed-Wing UAV Dynamic Obstacle Avoidance. *Drones* **2023**, *7*, 601. https://doi.org/10.3390/drones7100601

Academic Editors: Mostafa Hassanalian, Andrzej Łukaszewicz, Wojciech Giernacki, Zbigniew Kulesza, Jaroslaw Alexander Pytka and Andriy Holovatyy

Received: 8 August 2023
Revised: 11 September 2023
Accepted: 21 September 2023
Published: 25 September 2023

1. Introduction

A V-tail aircraft is a distinct class of aircraft that features a V-shaped tail configuration. This unconventional design replaces the traditional horizontal stabilizer and vertical fin with two surfaces angled to form a V shape, which serve as both elevator and rudder control surfaces [1]. The V-tail design offers advantages such as reduced weight, improved maneuverability, and reduced drag [2]. Due to these advantages of the V-shaped tail, this tail design is widely used in large fixed-wing UAVs in various countries, such as the CAIG Wing Loong II, CASC Rainbow CH-4, and General Atomics MQ-9 Reaper [3].

The primary objective of this project is to create a realistic simulation framework using Gazebo and ROS for V-tail aircraft, allowing for the accurate modeling of their flight dynamics, control systems, and response to flight threat scenarios. Through leveraging the capabilities of Gazebo, a powerful physics-based simulator, and ROS, a flexible and widely used robotic framework [4–7], we can create a comprehensive and interactive simulation environment.

In existing research [8–10] on fixed-wing aircraft flight simulation, the majority of studies are based on developing flight dynamics models, control algorithms, and trajectory planning using MATLAB software. Scott et al. [11] developed a fixed-wing aircraft simulation tool that incorporates aerodynamics, structural dynamics, kinematics, and kinetics, but has only numerical simulation calculations and no visual scene interface. Deiler et al. [12]

proposed dynamic aircraft simulation models that cover the effects of local icing, but did not incorporate actual flight scenarios, only numerical calculations. Heesbeen et al. [13] proposed a multi-purpose aircraft simulation architecture, but it requires a lot of hardware equipment. These studies [14–18] combined MATLAB and FlightGear for the flight simulation of aircraft. Horri et al. [19] studied the co-simulation of an aircraft using MATLAB combined with Xplane, FlightGear, and VFTE simulation software. These studies [20–22] combined MATLAB and X-Plane for co-simulation to design and verify the performance of aircraft controllers. There are also some aircraft simulation studies based on the Gazebo simulation platform. Yang et al. [23] studied the hardware-in-the-loop simulation of fixed-wing UAVs in Gazebo. Irmawan et al. [24] studied the 3D simulation of a VTOL fixed wing in Gazebo. Lee et al. [25,26] combined the PX4 autopilot and Gazebo simulation environment to test the controller performance of a fixed-wing aircraft under control surface failure conditions. Ellingson et al. [27] designed a fixed-wing autopilot for education and research and used Gazebo for the remote flight simulation of an aircraft model. In these simulation studies, most of them use existing aircraft models to simulate flight, and many of them do not combine the corresponding flight scenarios, and the scalability of the simulation platform is poor.

Different from the existing aircraft simulation framework, this paper focuses on the model establishment of V-tail aircraft and flight simulation based on Gazebo, and uses the powerful performance of the Gazebo simulator to create the flight threat scenario of aircraft and support the flight control of multiple aircraft in the same scenario. It lays a foundation for subsequent research on aircraft route planning algorithms and multi-aircraft cooperative flight algorithms. Through this project, we aim to provide researchers, engineers, and aviation enthusiasts with a robust and customizable simulation framework for V-tail aircraft, enabling them to evaluate the aircraft's behavior under realistic conditions and explore novel flight threat scenarios. This simulation framework can serve as a valuable tool for performance analysis, algorithm development, and decision-making in V-tail aircraft-related research and development.

The paper is organized as follows. Section 2 introduces the simulation system framework used in this study. Section 3 provides the aerodynamics mathematical model of the fixed-wing aircraft and the establishment of the 3D model of the V-tail aircraft. Section 4 presents a simulation environment modeling approach tailored for obstacle avoidance in no-fly zones. Section 5 presents the attitude control of the V-tail aircraft in the Gazebo flight environment. Finally, Section 6 contains the conclusions.

2. Simulation System Framework

Gazebo and ROS are two powerful tools which are widely used in the field of robotics and simulation. Gazebo is an open-source, multi-robot simulator that provides a highly realistic and dynamic environment for simulating robots, UAVs, and complex systems. It allows for the simulation of physics-based interactions, sensor data, and control algorithms. ROS, on the other hand, is a flexible framework for building robotic systems. It provides a collection of software libraries, tools, and conventions that facilitate communication between different components of a robotic system. ROS enables the development of modular and scalable robotic applications through offering features such as message passing, service calls, and parameter management.

When combined, Gazebo and ROS form a powerful simulation environment that allows for the integration of realistic physics-based simulation with sophisticated robot control and interaction. This combination has become a standard in the robotics community for developing and testing robotic systems.

In the context of V-tail aircraft and flight threat scenario modeling, Gazebo provides a platform for creating a realistic simulation environment that accurately models the physics and dynamics of the aircraft. It enables the simulation of aerodynamic forces, environmental factors, and realistic sensor data. Gazebo's visualization capabilities also allow for the real-time monitoring and visualization of the simulation.

Through leveraging the capabilities of Gazebo and ROS, researchers and engineers can create comprehensive and interactive simulations of V-tail aircraft and flight threat scenarios. This allows for the in-depth analysis of the aircraft's behavior, performance evaluation, and the testing of control algorithms. The integration of Gazebo and ROS provides a seamless workflow, enabling users to develop and validate their models and algorithms in a realistic virtual environment before deploying them on real aircraft.

3. Fixed-Wing UAV Vehicle Modeling

3.1. Aircraft Aerodynamics

In the V-tail fixed-wing aircraft simulation environment created in this study, the primary reliance is on the aerodynamics plugin provided by Gazebo's official sources to simulate the aircraft's flight lift. Referring to existing literature [28–30], the following aerodynamics mathematical model is established.

Wind speed has a significant impact on UAV motion, which can have an impact on flight performance, flight trajectory, and control requirements. Taking the body coordinate system as a reference, the airspeed vector of the UAV is denoted as $\boldsymbol{v}_r^b$, the ground speed vector is denoted as $\boldsymbol{v}^b$, and the wind speed vector is denoted as $\boldsymbol{v}_\omega^b$. Then, the relationship between wind speed, ground speed, and airspeed can be obtained as follows:

$$\boldsymbol{v}_r^b = \boldsymbol{v}^b - \boldsymbol{v}_\omega^b \tag{1}$$

The relationship between the size of UAV airspeed V_a and the airspeed vector $\boldsymbol{v}_r^b$ of an UAV under the aircraft system is as follows:

$$v_r^b = \begin{pmatrix} u \\ v \\ w \end{pmatrix} = R_w^b \begin{pmatrix} V_a \\ 0 \\ 0 \end{pmatrix} = (R_b^w)^T \begin{pmatrix} V_a \\ 0 \\ 0 \end{pmatrix} = \begin{pmatrix} \cos\beta\cos\ \alpha & -\sin\beta\cos\ \alpha & -\sin\alpha \\ \sin\beta & \cos\beta & 0 \\ \cos\beta\sin\alpha & -\sin\beta\sin\alpha & \cos\ \alpha \end{pmatrix} \begin{pmatrix} V_a \\ 0 \\ 0 \end{pmatrix} \tag{2}$$

where R_w^b is the rotation matrix from the air flow coordinate system to the body coordinate system, α is the angle of attack, β is the sideslip angle, and V_a is the magnitude of the airspeed, which can be calculated using the following equation.

$$\begin{cases} \alpha = \arctan\left(\frac{w}{u}\right) \\ \beta = \arcsin\left(\frac{v}{V_a}\right) \\ V_a = \sqrt{u^2 + v^2 + w^2} \end{cases} \tag{3}$$

The translational kinematic equation of the UAV is given by

$$\dot{\boldsymbol{p}}_n = R_b^n \boldsymbol{v}^b \tag{4}$$

$$\boldsymbol{v}_r^b = \boldsymbol{v}^b - R_n^b \boldsymbol{v}_{wind}^n \tag{5}$$

where $\boldsymbol{p}_n$ represents the position of the UAV in the inertial frame, $\boldsymbol{v}^b$ represents the ground velocity vector of the UAV in the aircraft system, R_b^n represents the rotation matrix from the aircraft system to the inertial frame, and $\boldsymbol{v}_{wind}^n$ represents the wind speed vector in the inertial frame.

The wind speed is assumed to be constant or slowly varying. Newton's second law is applied to the UAV in translational motion, and the force and velocity under the UAV system are expressed as

$$\frac{\mathrm{d}\boldsymbol{v}_r^b}{\mathrm{d}t_b} = -S\left(\boldsymbol{w}_{n,b}^b\right)\boldsymbol{v}_r^b + \boldsymbol{f}^b/m \tag{6}$$

where m is the mass of the UAV, $\frac{\mathrm{d}}{\mathrm{d}t_b}$ is the time derivative in the body coordinate system, and $\boldsymbol{f}^b$ is the sum of all external forces acting on the UAV under the aircraft system, including gravity, aerodynamic force, and thrust. $w_{n,b}^b$ is the angular velocity between the machine system and the inertial frame.

$$\boldsymbol{f}^b = R_n^b \boldsymbol{f}_g^n + R_w^b \boldsymbol{f}_{aero}^w + \boldsymbol{f}_{thrust}^b \tag{7}$$

where $\boldsymbol{f}_g^n = [0\ 0\ mg]^T$ is the heavy force vector under inertial system, and g is the acceleration degree of heavy force. $\boldsymbol{f}_{thrust}^b = [T\ 0\ 0]^T$ is the thrust vector under the aircraft system. Most aircraft are designed with thrust directly along the aircraft body axis i^b. $\boldsymbol{f}_{aero}^w$ is the aerodynamic force vector under the flow system, which can be expressed as

$$\boldsymbol{f}_{aero}^w = \frac{1}{2}\rho S V_a^2 \begin{bmatrix} -\left(C_{D_0} + kC_L^2\right) \\ C_{Y_\beta}\beta \\ -\left(C_{L_0} + C_{L_\alpha}\alpha\right) \end{bmatrix} \tag{8}$$

where ρ is air density, S is the plane airfoil area, $C(\cdot)$ is the coefficient of aerodynamics, and $C_L = C_{L_0} + C_{L_\alpha}\alpha$. k is a constant scalar value that depends on the aircraft configuration.

The quaternion based rotational kinematics equation of aircraft is as follows:

$$\dot{\boldsymbol{q}}_{n,b} = \frac{1}{2}\boldsymbol{q}_{n,b} \otimes \begin{bmatrix} 0 \\ \boldsymbol{\omega}_{n,b}^b \end{bmatrix} \tag{9}$$

where $\boldsymbol{q}_{n,b}$ represents the quaternion of rotation from the body coordinate system to the inertial system.

Under the body coordinate system, Euler's momentum equation is applied to a rotating aircraft.

$$\frac{d\boldsymbol{h}^b}{dt_b} + \boldsymbol{\omega}_{n,b}^b \times \boldsymbol{h}^b = \boldsymbol{\tau}_{aero}^b \tag{10}$$

where $\boldsymbol{h}^b$ is the vector form of angular momentum under body coordinate system. $\boldsymbol{\tau}_{aero}^b$ is the aerodynamic torque vector of body coordinate system. For a rigid body, angular momentum is defined as the product of the moment of inertia matrix $\boldsymbol{J}$ and the angular velocity vector: $\boldsymbol{h}^b = \boldsymbol{J}\boldsymbol{\omega}_{n,b}^b$.

$$\boldsymbol{J} = \begin{pmatrix} J_{xx} & -J_{xy} & -J_{xz} \\ -J_{xy} & J_{yy} & -J_{yz} \\ -J_{xz} & -J_{yz} & J_{zz} \end{pmatrix} \tag{11}$$

Thus, Equation (10) can be rewritten as:

$$\dot{\boldsymbol{\omega}}_{n,b}^b = \boldsymbol{J}^{-1}[-S(\boldsymbol{\omega}_{n,b}^b)\boldsymbol{J}\boldsymbol{\omega}_{n,b}^b + \boldsymbol{\tau}_{aero}^b] \tag{12}$$

Aerodynamic torque is defined as:

$$\boldsymbol{\tau}_{aero}^b = \boldsymbol{f}(\alpha, \beta) - \boldsymbol{D}\boldsymbol{\omega}_{n,b}^n + \boldsymbol{B}\boldsymbol{u} \tag{13}$$

where $\boldsymbol{u} = [\delta_a \delta_e \delta_r]^T$ is a vector consisting of three control quantities used to control the rotation angles of the aileron, elevator, and rudder. $\boldsymbol{f}(\alpha, \beta)$ is the aerodynamic torque vector function, which can be expressed as:

$$f(\alpha, \beta) = \frac{1}{2}\rho S V_a^2 \begin{bmatrix} b\left(C_{l_0} + C_{l_\beta}\beta\right) \\ \bar{c}(C_{m_0} + C_{m_\alpha}\alpha) \\ b\left(C_{n_0} + C_{n_\beta}\beta\right) \end{bmatrix} \tag{14}$$

$\boldsymbol{D}$ is a positive definite matrix denoted by:

$$\boldsymbol{D} = \frac{1}{2}\rho S V_a^2 \begin{bmatrix} \frac{b^2}{2V_a}C_{l_p} & 0 & \frac{b^2}{2V_a}C_{l_r} \\ 0 & \frac{(\bar{c})^2}{2V_a}C_{m_q} & 0 \\ \frac{b^2}{2V_a}C_{n_p} & 0 & \frac{b^2}{2V_a}C_{n_r} \end{bmatrix} \tag{15}$$

$\boldsymbol{B}$ is the control matrix and is defined as:

$$\boldsymbol{B} = \frac{1}{2}\rho S V_a^2 \begin{bmatrix} bC_{l_{\delta_a}} & 0 & bC_{l_{\delta_r}} \\ 0 & \bar{c}C_{m_{\delta_e}} & 0 \\ bC_{n_{\delta_a}} & 0 & bC_{n_{\delta_a}} \end{bmatrix} \tag{16}$$

where b is the wingspan length and $\bar{c}$ is the average aerodynamic chord.

In summary, the following dynamic model can be obtained through combining the translational motion and rotational motion of the fixed-wing aircraft.

$$\begin{cases} \dot{\boldsymbol{p}}_n = R_b^n \boldsymbol{v}^b \\ \dot{\boldsymbol{v}}_r^b = -S(\boldsymbol{w}_{n,b}^b)\boldsymbol{v}_r^b + (R_n^b \boldsymbol{f}_g^n + R_w^b \boldsymbol{f}_{\text{aero}}^w + \boldsymbol{f}_{\text{thrust}}^b)/m \\ \dot{\boldsymbol{q}}_{n,b} = \frac{1}{2}\boldsymbol{q}_{n,b} \otimes [\ 0 \quad (\boldsymbol{\omega}_{n,b}^b)^T\ ]^T \\ \dot{\boldsymbol{\omega}}_{n,b}^b = \boldsymbol{J}^{-1}[-S(\boldsymbol{\omega}_{n,b}^b)\boldsymbol{J}\boldsymbol{\omega}_{n,b}^b + \boldsymbol{f}(\alpha,\beta) - \boldsymbol{D}\boldsymbol{\omega}_{n,b}^n + \boldsymbol{B}\boldsymbol{u}] \end{cases} \tag{17}$$

3.2. V-Tail Fixed-Wing UAV 3D Modeling

SolidWorks is a computer-aided design (CAD) software widely used for creating 3D models, assemblies, and drawings of various mechanical and engineering components, including aircraft. In the Gazebo simulation platform, there is no open-source V-tail aircraft available, and the official offering only includes the Cessna C-172 aircraft model. Therefore, we designed a V-tail aircraft using SolidWorks and configured the aerodynamics of our model through referencing the Cessna C-172 aircraft model files.

The aircraft model we built using SolidWorks is shown in Figure 1. This V-tail aircraft is modeled according to our reference to existing mainstream reconnaissance fixed-wing UAVs, such as the CAIG Wing Loong II and CASC Rainbow CH-4.

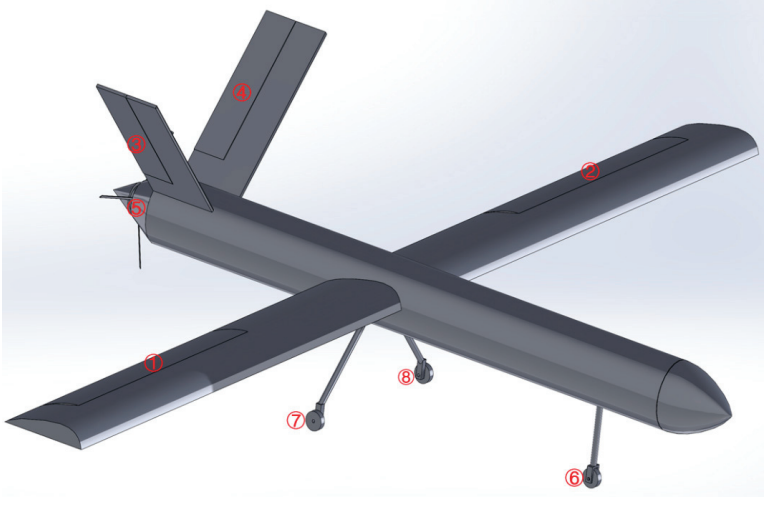

Figure 1. A 3D model of a V-tail fixed-wing UAV created using SolidWorks. The aircraft model has 8 moving parts, which are ① right aileron, ② left aileron, ③ right tail, ④ left tail, ⑤ propeller, ⑥ front wheel, ⑦ right wheel, and ⑧ left wheel.

We rely on the aerodynamic plugin provided by the Gazebo simulator for the flight simulation of our aircraft model, which does not require the aircraft model to have an accurate aerodynamic shape, so we do not consider aerodynamic appearance when modeling in SolidWorks. At the same time, we omit the moving part modeling of the aircraft flaps, and we incorporate the functions of the flaps into the ailerons of the aircraft model.

In the Gazebo simulator, model description files are used to describe the objects in the simulation, including robots, UAVs, buildings, etc. The model description file contains the geometry of the object, physical properties, sensor information, and controllers, among others. Gazebo uses SDF (Simulation Description Format) as the default model description file format. SDF is an XML format used to describe simulation scenarios, which has rich functions and flexibility. In addition, URDF (Unified Robot Description Format) is a model description file format used in ROS. Gazebo can import URDF files with ROS plugin support and use the model in simulations.

In this project, we use the SDF file format as the aircraft model description file, because using SDF allows us to use the latest plugin provided by Gazebo. Stephen Brawner et al. developed

a SolidWorks plugin for converting assembly models made in SolidWorks to URDF format [31]. Next, using the command line method provided by Gazebo [32], we can easily convert the model description file in URDF format to SDF format. Figure 2 shows the flow chart of converting a SolidWorks model to SDF format.

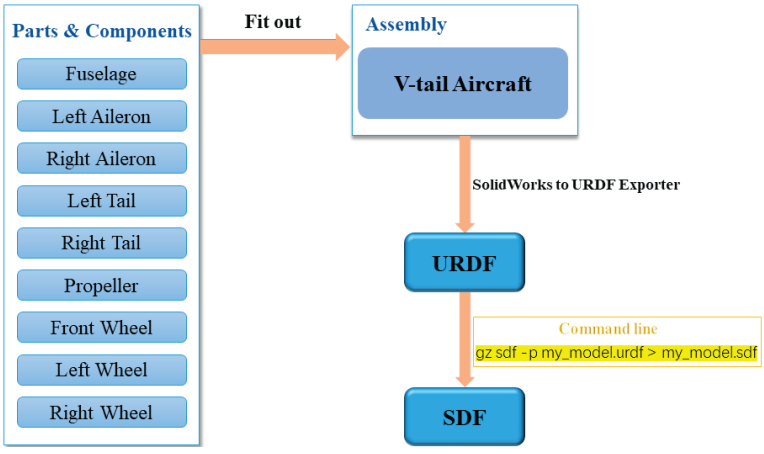

Figure 2. Flowchart of converting a SolidWorks model to SDF format. In SolidWorks, individual 3D models of different components of the aircraft are created separately. These components are then assembled to form a complete aircraft. A model format conversion plugin is used to convert this model into URDF format. Finally, the model is converted to the SDF format recommended by Gazebo using the format conversion command in the terminal.

In the generated aircraft model file, we introduced an open-source aerodynamics plugin provided by Gazebo's official sources [33]. This plugin's mathematical model aligns with the aerodynamics mathematical model proposed in Section 3.1. Figure 3 shows the aerodynamic plugin used in the SDF model description file. The plugin has the following parameters to configure:

```
<plugin name="left_wing" filename="./libLiftDragPlugin.so">
  <a0>0.05984281113</a0>
  <cla>4.752798721</cla>
  <cda>0.6417112299</cda>
  <cma>-1.8</cma>
  <alpha_stall>0.3391428111</alpha_stall>
  <cla_stall>-3.85</cla_stall>
  <cda_stall>-0.9233984055</cda_stall>
  <cma_stall>0</cma_stall>
  <cp>-0.7 5 0.01</cp>
  <area>15</area>
  <air_density>1.2041</air_density>
  <forward>1 0 0</forward>
  <upward>0 0 1</upward>
  <link_name>fuselage</link_name>
  <control_joint_name>
    left_aileron_joint
  </control_joint_name>
  <control_joint_rad_to_cl>-0.5</control_joint_rad_to_cl>
</plugin>
```

Figure 3. Add aerodynamic plugin to the SDF aircraft model description file. Using the official aerodynamics plugin provided by Gazebo, the figure displays the aerodynamic parameters of the left wing. In the aircraft model description file used in this study, the same plugin is also employed for the right wing and tails.

"a0" is the negative value of the zero-lift angle of attack.
"cla" is the slope of lift line.
"cda" is the slope of drag line.
"cma" is the slope of aerodynamic moment line.
"alpha_stall" is the stall angle of attack.
"cla_stall" is the slope of the lift line after stall.
"cda_stall" is the slope of the drag line after stall.
"cma_stall" is the slope of the aerodynamic torque line after stall.
"link_name" is the link applied by the aerodynamic force.
"cp" is the coordinate of the pressure center (in link coordinate system).
"aera" is the reference area of the aerodynamic surface.
"air_density" is the air density.
"forward" is the forward-direction vector (in link coordinate system).
"upward" is the up-direction vector (in link coordinates system).
"control_joint_name" is the name of the joint that controls the rudder axis.
"control_joint_rad_to_cl" is the rate of change of the lift coefficient with the control value.

If you intend to control models within Gazebo through an external program, there are typically two methods. The first involves creating a Gazebo plugin and embedding it into the model file you wish to control. However, this method lacks flexibility, and modifying plugin code can be cumbersome. The second method is for the external program to utilize Gazebo's provided external interface, combined with ROS for controlling models in Gazebo and managing real-time simulation data for the models. In this study, we are using the second method. To incorporate ROS into the Gazebo simulation, we need to create a ROS launch file following ROS standards. This ROS launch file includes our V-tail aircraft model file, environment model file, and certain initialization parameters for Gazebo. Running this ROS launch file opens our aircraft simulation. Figure 4 depicts the initialization interface of the successfully opened simulation, where the aircraft model can be observed positioned on the runway.

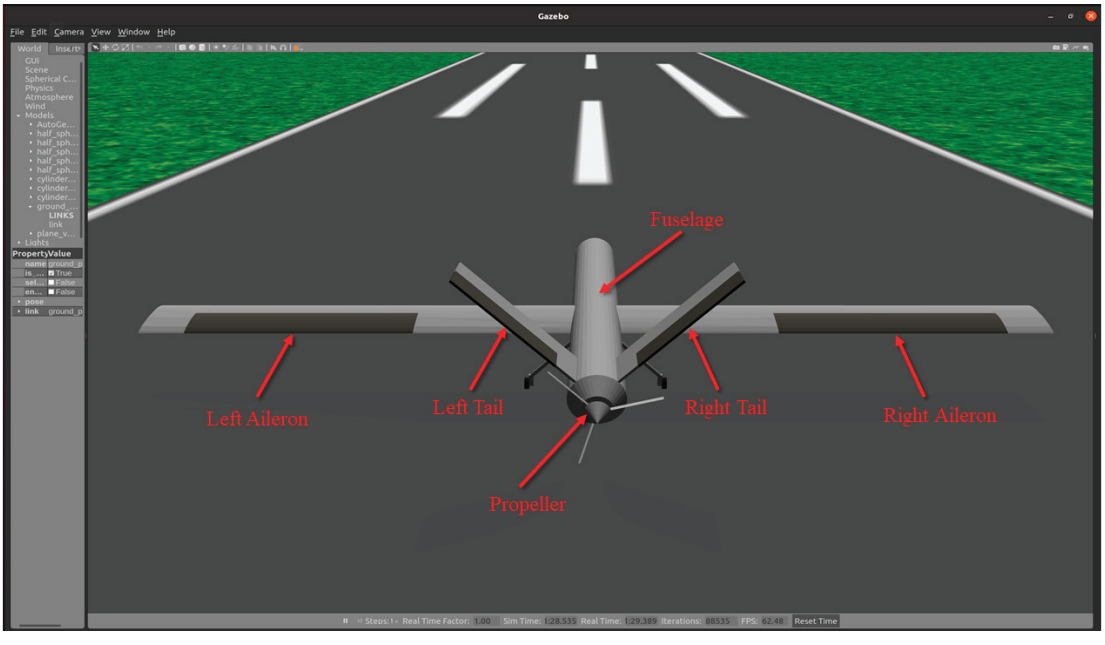

Figure 4. V-tail aircraft in Gazebo. After successfully launching the simulation program, the aircraft model will appear on the runway scene in Gazebo.

We have chosen Gazebo as our aircraft simulator not only due to its capacity for customizing various simulation scenarios, but also for its support of simulating multiple models within a single

scene. This feature provides a foundation for researching cooperative control algorithms for multi-agent systems. Figure 5 showcases our addition of nine V-tail aircraft within a single simulation scene.

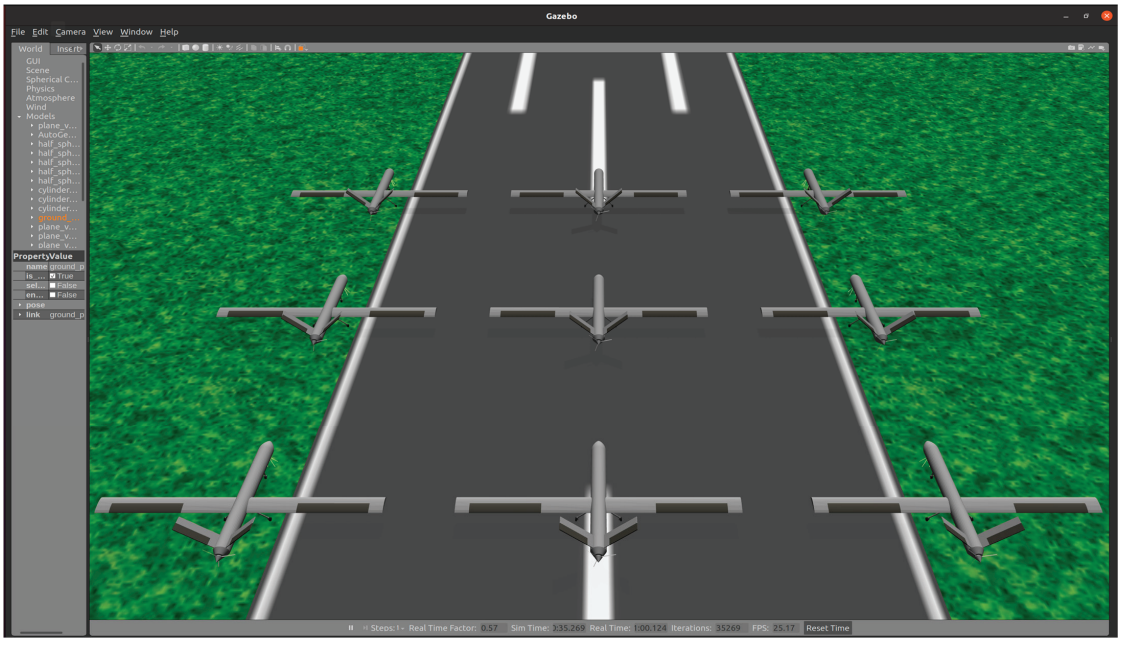

Figure 5. Multiple V-tail aircraft in Gazebo. Gazebo supports the simultaneous simulation of multiple aircraft models, which facilitates the research of multi-UAV formation flight algorithms.

4. 3D Flight Environment Design

Another focus of this study is the simulation modeling method tailored for obstacle avoidance in no-fly zones, providing a 3D flight scenario for aircraft models. The centerpiece of this scene is a large terrain model containing multiple mountain ranges. Custom no-fly zones are added, and wind disturbances are introduced to challenge the aircraft's safe flight. These environmental models pose a challenge to ensuring the aircraft's safe navigation.

4.1. Wind Disturbance

Wind disturbances can have significant effects on the behavior of an aircraft during flight, and it is crucial for pilots and control systems to account for these disturbances to ensure safe and stable operations. In this project, we mainly consider wind disturbances as gusts, steady wind, wind shear, and their combination.

Gusts refer to sudden and brief increases in wind speed that occur over a short period of time. These rapid changes in wind velocity can have significant effects on the flight performance and handling characteristics of aircraft. The mathematical representation of a discrete gust is:

$$V_{\text{gusts}} = \begin{cases} 0 & x < 0 \\ \frac{V_m}{2}\left(1 - \cos\left(\frac{\pi x}{d_m}\right)\right) & 0 \le x \le d_m \\ V_m & x > d_m \end{cases} \tag{18}$$

where V_m is the gust amplitude, d_m is the gust length, x is the distance traveled, and V_{gusts} is the resultant wind velocity in the body axis frame.

Steady wind refers to a constant and uniform wind flow with consistent speed and direction over time. In the context of atmospheric conditions, it means that the wind is blowing at a steady rate and maintaining a constant heading for a significant period.

Wind shear refers to the change in wind speed and/or direction with altitude. It is a meteorological phenomenon that occurs in the Earth's atmosphere and can affect aircraft during takeoff and landing. Strong wind shear can create turbulence and sudden changes in airspeed, making it challenging for pilots to maintain control and stability. The magnitude of the wind shear is given by the following equation for the mean wind profile as a function of altitude and the measured wind speed at 20 feet (6 m) above the ground.

$$V_{\text{shear}} = W_{20} \frac{\ln\left(\frac{h}{z_0}\right)}{\ln\left(\frac{20}{z_0}\right)}, 3ft < h < 1000ft \tag{19}$$

where V_{shear} is the mean wind speed, W_{20} is the measured wind speed at an altitude of 20 feet, h is the altitude, and z_0 is a constant equal to 0.15 feet for Category C flight phases and 2.0 feet for all other flight phases. Category C flight phases are defined in reference [34] to be terminal flight phases, which include takeoff, approach, and landing.

In Gazebo, SDF plugins are used to extend the functionality of the simulation environment and add custom behavior to models or the world. SDF plugins are written in C++ and are loaded by Gazebo during the simulation startup.

In the simulation, the effect of wind disturbance on the aircraft can be regarded as a continuous external force acting on the body coordinates, and the wind disturbance model is packaged into an SDF plugin to activate it during simulation. To create a wind disturbance SDF plugin and add it to the aircraft flight environment, we typically follow these steps:

Step 1: Write the Plugin Code.

Create a C++ source file for the plugin and define the desired forces generated by wind disturbances acting on the body coordinate system.

Step 2: Build the Plugin.

Compile the plugin into a shared library (.so file) using CMake. Ensure that the plugin is linked to Gazebo and its required libraries.

Step 3: Load the Plugin.

In the Gazebo SDF file, include a "<plugin>" element that references the compiled plugin library and specifies any necessary parameters.

Figure 6 shows a wind plugin provided by Gazebo, which needs to have the following parameters to configure:

```
<plugin name='wind_plugin' filename='libgazebo_wind_plugin.so'>
  <linkName>base_link</linkName>
  <xyzOffset>1 0 0</xyzOffset>
  <windDirection>0 1 0</windDirection>
  <windForceMean>0.7</windForceMean>
  <windGustDirection>0 0 0</windGustDirection>
  <windGustDuration>0</windGustDuration>
  <windGustStart>0</windGustStart>
  <windGustForceMean>0</windGustForceMean>
</plugin>
```

Figure 6. Add wind plugin to the SDF aircraft model description file. Using the officially provided wind disturbance plugin, you can set the wind direction and magnitude for both constant wind and gusts.

"linkName" is the link affected by the wind.

"xyzOffset" is the spatial offset of the link coordinate system to form the new coordinate system, which is the reference coordinate system for the wind.

"windDirection" is the force direction under the wind coordinate system.

"windForceMean" is the average value of the wind.

"windGustDirection" is the direction of the gust.

"windGustDuration" is the duration of the gust.

"windGustStart" is the start time of the gust.
"windGustForceMean" is the average value of the gust.

4.2. Terrain Model

Mountainous regions pose a threat to the safe flight of aircraft. When large fixed-wing UAVs are engaged in low-altitude penetration missions, their flight altitude is often relatively low. Aircraft must promptly adjust their flight altitude and course based on terrain obstacles to avoid collisions. In this section, we generate a large-scale terrain model using a heightmap.

In Gazebo, a heightmap is a type of terrain representation used to model the elevation and topography of the ground surface in a simulation environment. Heightmaps are an efficient way to create realistic and detailed terrains, especially for large outdoor scenes. A heightmap is essentially a 2D grid of elevation values, where each cell in the grid represents a point on the terrain, and the value in the cell determines the height or elevation of that point above a reference level, typically the ground level (Z = 0). The elevation values can be measured in meters, feet, or other units, depending on the scale of the simulation.

Figure 7 is a heightmap that we utilize. Essentially, it is a grayscale image. In the Gazebo environment model file, this heightmap can be configured to automatically generate the terrain model. In order for Gazebo to successfully load the heightmap and generate the terrain model, the original map needs to be cropped to the pixel size of (2n+1, 2n+1). In this project, the original heightmap was cropped to the pixel size of (1025, 1025).

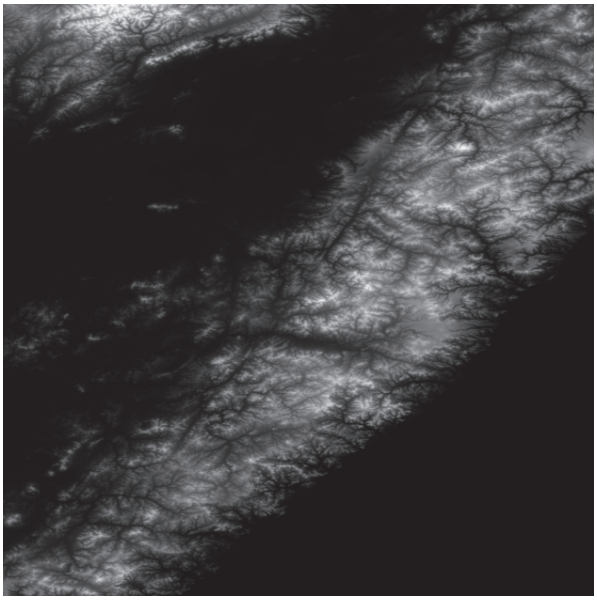

Figure 7. Original heightmap. Different grayscale values represent different altitudes, where higher grayscale values (whiter pixels) indicate higher elevations.

At the same time, in order to make the generated terrain model more realistic, maps are used on the surface of the terrain. In the terrain model shown in Figure 8, three maps of water, grass, and sand are used, and different maps are used in different height threshold ranges. Figure 9 is a partial enlargement of the terrain model in Gazebo. The mountains in the figure are automatically generated terrain, and the height of the mountains can be scaled in the model profile.

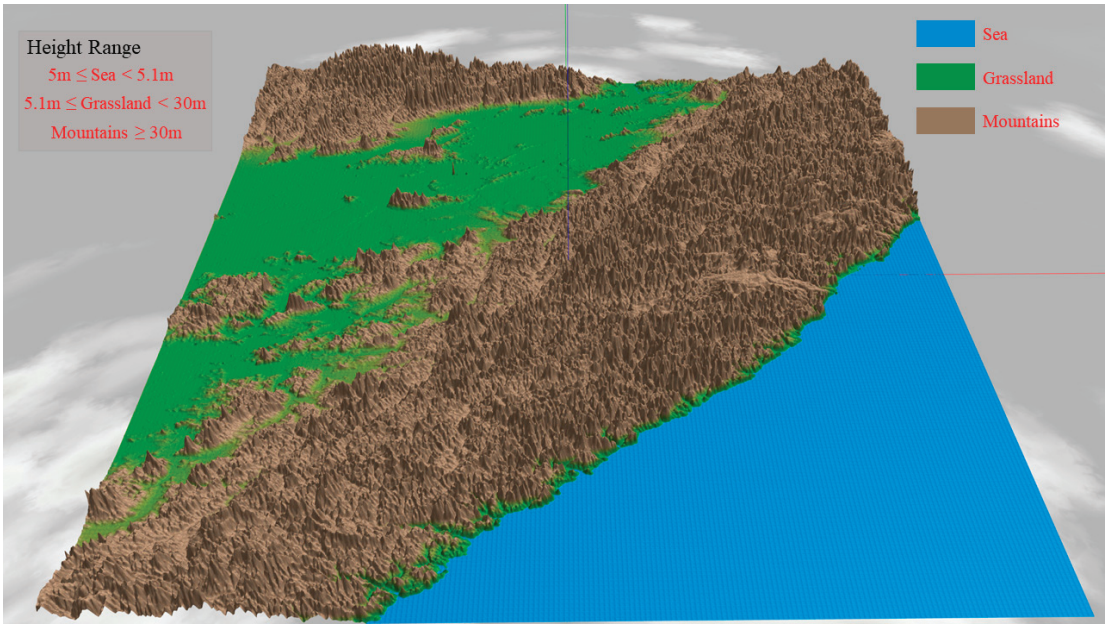

Figure 8. Terrain model in Gazebo. Different textures are applied to different altitudes: blue texture represents ocean areas, green texture represents grassland regions, and brown texture represents mountainous areas.

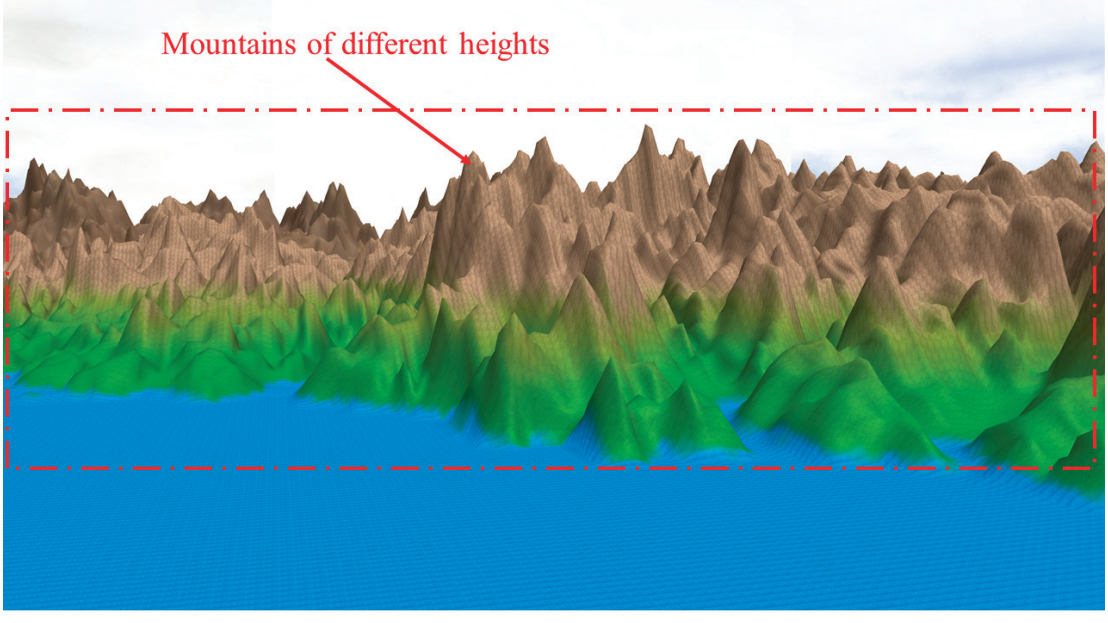

Figure 9. Terrain model in Gazebo (local zoom). The image displays details from Figure 8, where the red dashed box highlights mountains at different altitudes. These mountains pose a threat to low-altitude aircraft flight.

4.3. No-Fly Zones

There are some areas where the flying of aircraft, drones, or other aerial vehicles is restricted or prohibited due to safety, security, or regulatory concerns. These zones are often established to prevent potential conflicts with other air traffic, protect sensitive areas, maintain privacy, and ensure public safety.

The restricted airspace designed in this study consists of multiple hemisphere models and cylindrical models. In our simulation scenario, the size and coverage of these no-fly zones are not fixed and remain dynamically deployable. The no-fly zone models are dynamically generated based on the terrain model designed in Section 4.2. Prior to launching the simulation program, we have the flexibility to customize the number, type, coverage area, and world coordinates of the no-fly zones. Therefore, a wide variety of different no-fly zone configurations can be applied on the same terrain model. Furthermore, during the aircraft flight simulation, it is possible to dynamically add additional no-fly zones to the original simulation environment. These zones can also be specified to undergo certain changes, such as translation with a fixed speed, based on predefined rules.

For the aircraft, the information about these no-fly zones is known. It can either be known to the aircraft before takeoff, including all the no-fly zones and threat areas, or it can be received in real-time by external perception devices (such as satellite remote sensing) through a data link. Based on this known information about no-fly zones and threat areas, the aircraft can plan its flight path in advance. When encountering newly acquired information about no-fly zones, the aircraft needs to perform dynamic avoidance maneuvers and replan its flight path accordingly.

The hemispherical no-fly zone model is formulated as follows:

$$L_i(x, y, z) = \sum (x - x_i)^2 + (y - y_i)^2 + z^2 = R_{R_i max}^2 \qquad z \geq 0 \tag{20}$$

where the coordinate of the hemispherical no-fly zone i is $(x_i,\ y_i,\ z_i)$, and $R_{R_i max}$ is the maximum detection radius of the ground no-fly detector.

The Gazebo terrain model includes multiple hemispheres as no-fly zones, which can be customized in position, radius size, and color, as shown by the five red semi-transparent hemispheres in Figure 10.

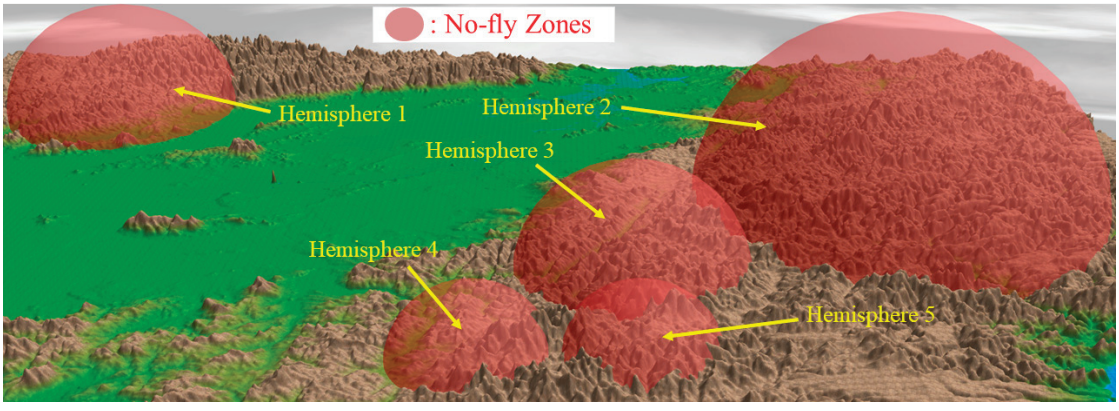

Figure 10. Hemisphere models in Gazebo. On the foundation of the terrain model, some custom semi-transparent red hemisphere regions are added as no-fly zones.

The cylindrical no-fly zone model is formulated as follows:

$$L_i(x, y, z) = (x - x_i)^2 + (y - y_i)^2 - R_{M_i max}^2 = 0 \qquad z_i = [0, Z_{ih}] \tag{21}$$

where $L_i(x, y, z)$ represents the hemispherical no-fly zone i, $(x_i,\ y_i)$ represents the center coordinate of the cylinder i, $R_{M_i max}$ represents the horizontal threat radius of the cylinder i, and Z_{ih} represents the vertical threat altitude of the cylinder i.

Multiple cylinders are added to the Gazebo terrain model as no-fly zones; these cylinders are customizable in position, radius size, and color, as shown by the five purple translucent cylinders in Figure 11.

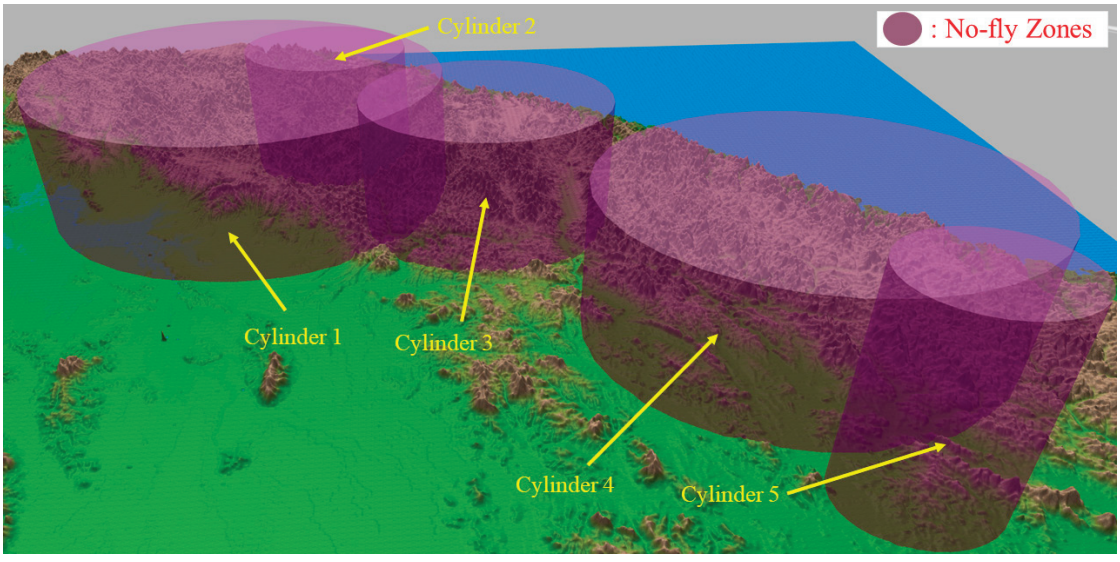

Figure 11. Cylinder models in Gazebo. On the foundation of the terrain model, some custom semi-transparent purple cylindrical regions are added as no-fly zones.

5. Comprehensive Simulation

In this section, we combine the V-tail aircraft designed in Section 3 with the flight threat scenario proposed in Section 4. The aircraft model performs flight simulation in the Gazebo simulator and collects and uses ROS to manage the data of the aircraft, such as position, attitude angle, angular velocity, and angular acceleration.

Figure 12 illustrates the main modules and primary data flow within the comprehensive simulation. Gazebo serves as the simulation platform for comprehensive control experiments of the V-tail aircraft, deployed within a large-scale 3D flight environment. We have designed two Python programs and use ROS for data management. The first program is utilized to retrieve the aircraft model's state data in Gazebo at each simulation time step. It extracts the aircraft's attitude and velocity data from the raw state data. The second program is responsible for controlling the desired state of the aircraft model. It includes attitude angle controllers and a flight speed controller, both employing PID control algorithms. These controllers output the deflection angles of the ailerons and V-tail, as well as the engine thrust magnitude, which are used to control the aircraft model in Gazebo.

The controller program for the V-tail fixed-wing UAV primarily consists of an attitude angle controller, flight speed controller, and altitude controller, as depicted in Figure 13. The attitude angle controller comprises three distinct control programs: pitch, roll, and yaw. The roll controller controls the aircraft's roll angle through adjusting the aileron control surface. Both the pitch and yaw controllers use the deflection angles of the V-tail's two control surfaces as outputs. Consequently, there is coupling between pitch and yaw control in V-tail aircraft. We use the pitch controller's output control surface angle as a baseline, and the control surface angle output from the yaw controller is added to this baseline. This approach allows us to achieve yaw control while maintaining the desired pitch angle.

The flight speed controller adjusts the engine thrust to maintain the desired flight speed. The altitude hold controller is a two-loop controller, where the outer loop takes the desired altitude as input and outputs the pitch angle magnitude. The inner loop is the pitch angle controller. In this study, these controllers all use PID control algorithms.

In order to control the aircraft model in Gazebo from an external program, we established a link between ROS and Gazebo, as shown in Figure 14, where the oval box represents the ROS node and the connecting line represents the ROS topic, "/gazebo_gui" is the visual simulation interface of Gazebo, and "/gazebo" contains a variety of Gazebo simulation data, which is used to obtain and set the state of the model. "/object_position_publisher" retrieves multiple state data of the model from "/gazebo/model_states", extracts the position and pose of the model, and publishes them through the topic "/plane_pose". "/aircraft_command" publishes the angle and throttle controls of

the aircraft, using three PID controllers to control the angles, corresponding to the pitch, roll, and yaw control of the aircraft. The desired angles are input by the keyboard key, and the controllers output the control values of the aircraft rudder surfaces.

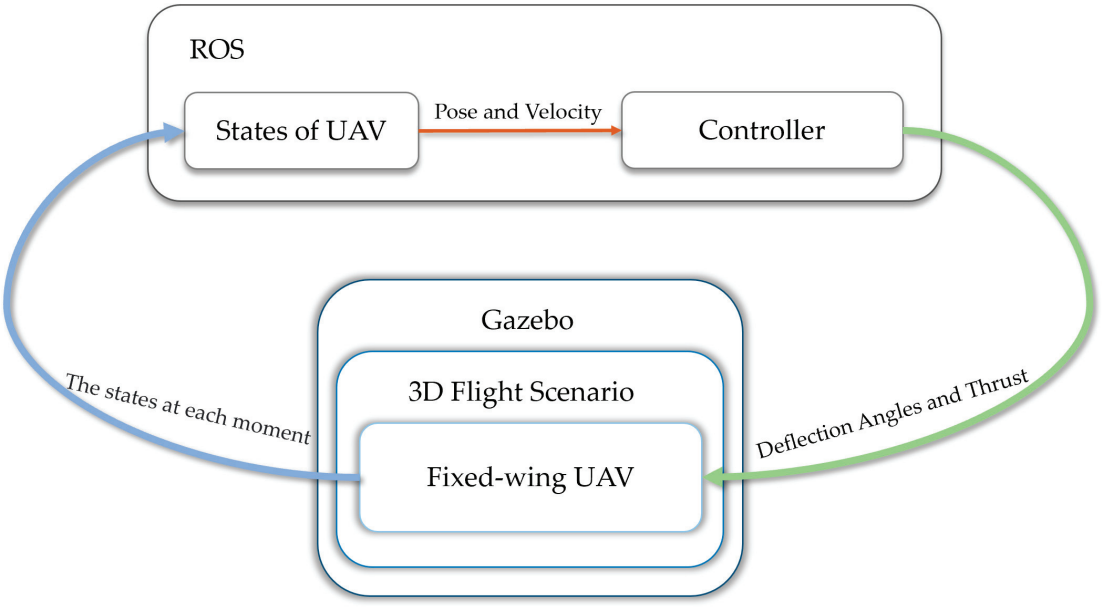

Figure 12. The comprehensive simulation system flowchart.

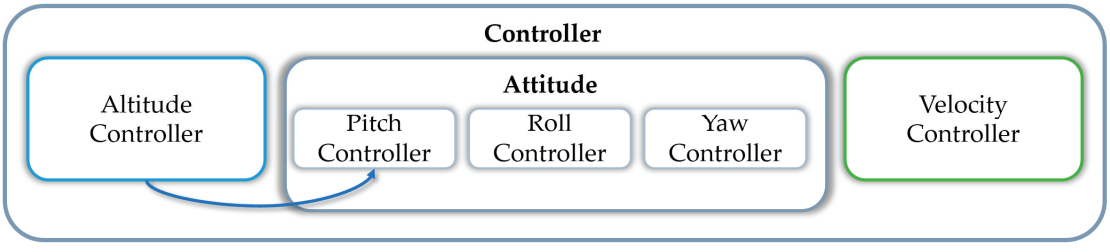

Figure 13. The block diagram for the V-tail aircraft controller design.

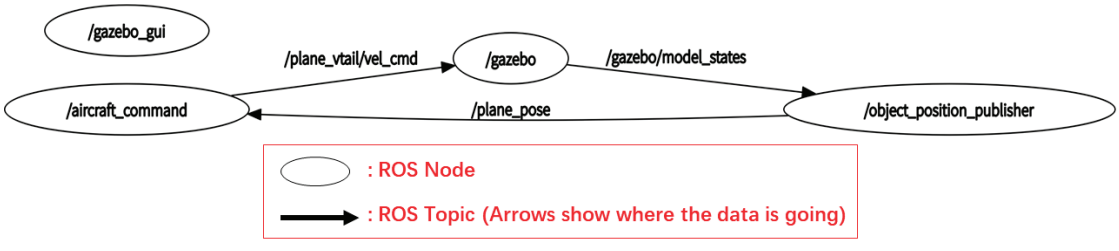

Figure 14. ROS node graph. Using the official ROS tool, "rqt_graph" generates a ROS node graph, where ellipses represent individual nodes and arrows indicate the direction of data transmission.

Figure 15 depicts the comprehensive simulated flight environment, primarily composed of two terrain models. One is the runway model, utilized for taxiing and takeoff, while the other is the mountainous terrain model, simulating potential mountain obstacles that the aircraft may encounter during flight missions. We have designed an aircraft flight state controller program that

enables control over the aircraft's flight attitude angles and throttle through keyboard commands, as shown in Figure 16. The program continuously prints expected and actual flight states in real time. Using this control program, we have accomplished fundamental aircraft maneuvers such as climbing and rolling.

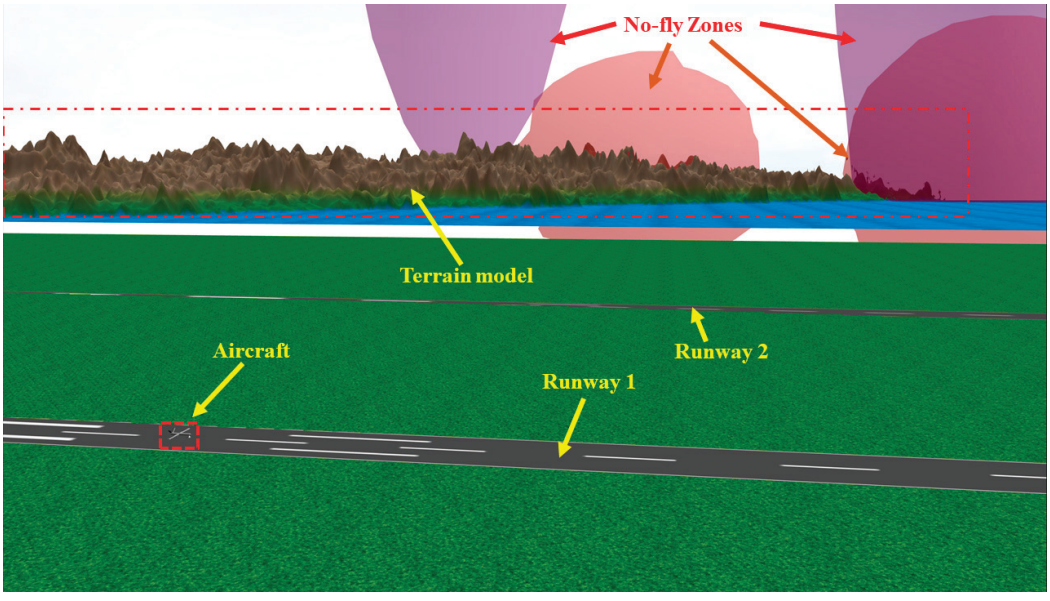

Figure 15. Comprehensive simulation flight scenario. The flight environment consists of two parts: one is the runway scene used for taxiing and takeoff of the aircraft, and the other is the terrain model used to simulate obstacles encountered by the aircraft during flight.

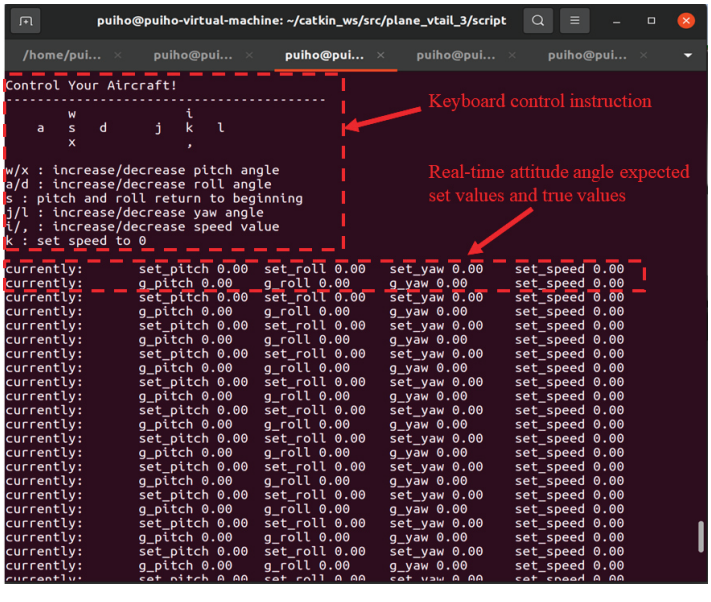

Figure 16. Keyboard control. The figure displays an aircraft control program we designed, which allows controlling the aircraft's attitude and throttle through keyboard inputs. It also prints the desired and actual values in real time.

Figure 17 illustrates the simulated aircraft's attitude angle data over a period of time. The deep blue line represents the roll angle data, the red line represents the pitch angle data, and the light blue line represents the yaw angle data. During the flight simulation, in conjunction with the flight controller program, the desired aircraft attitude angles are set through keyboard inputs. The attitude angle controller employs a PID control algorithm to manipulate the ailerons and V-tail to achieve the desired angles.

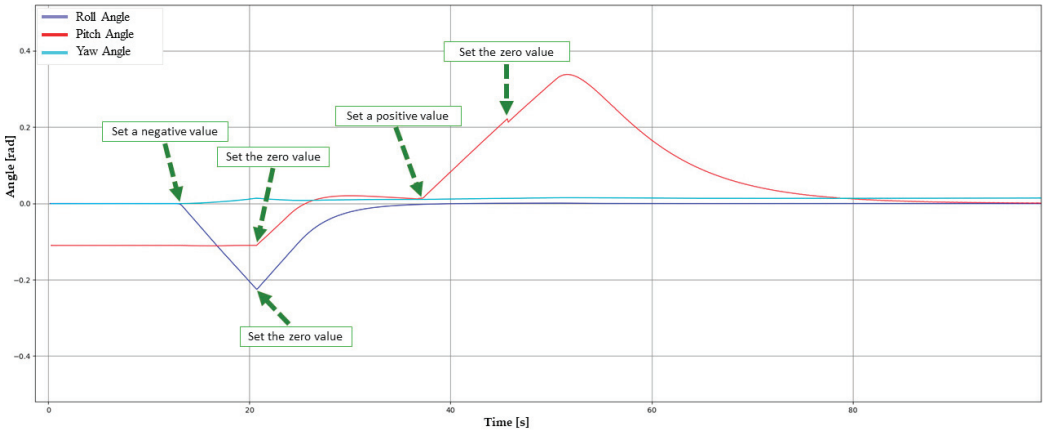

Figure 17. Attitude angle data of the aircraft. During flight testing, a segment of attitude angle data is recorded. Through configuring different desired attitude angles, the attitude angle controller steers the aircraft to reach the desired angles.

We tested the pitch angle controller of the aircraft. In the takeoff phase, the pitch angle was set to −0.3 radians, and the throttle was increased at the same time. The aircraft experienced overshoot and fluctuation in the pitch angle during the climbing phase, and finally stabilized at −0.3 radians as shown in Figure 18. Figure 19 shows the simulation screenshot of the aircraft in the climbing phase, and the PID controller of pitch angle outputs the maximum angular control (0.52 radians) to the tail. Figure 20 is a simulation screenshot of the aircraft reaching the pitch angle set point of −0.3 radians. In the pitch angle PID controller, set Kp = −3, Ki = −0.05, Kd = 0.05.

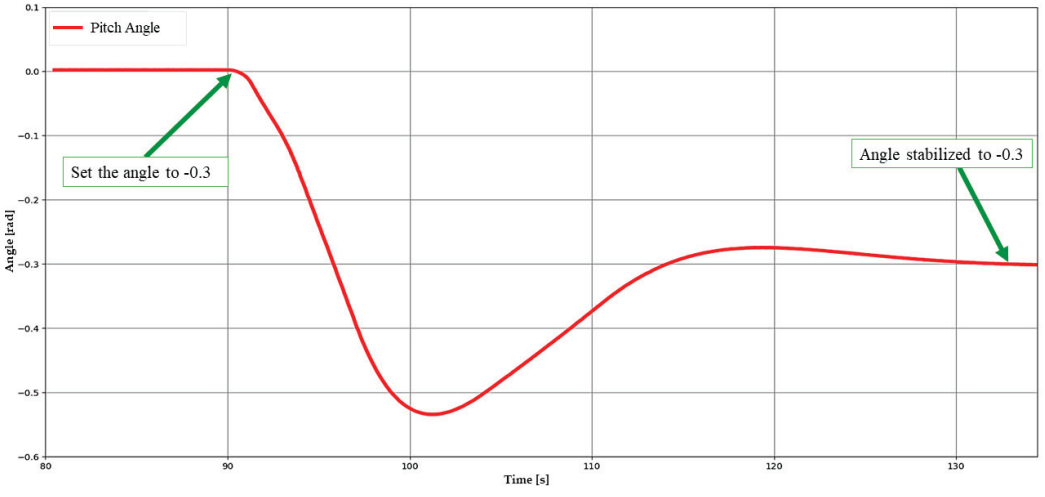

Figure 18. Pitch angle data of the aircraft. Pitch angle data during the aircraft's takeoff phase is recorded. At the moment of takeoff, the desired pitch angle is set to −0.3 radians. After a period of angular fluctuations, the pitch angle eventually stabilizes at −0.3 radians.

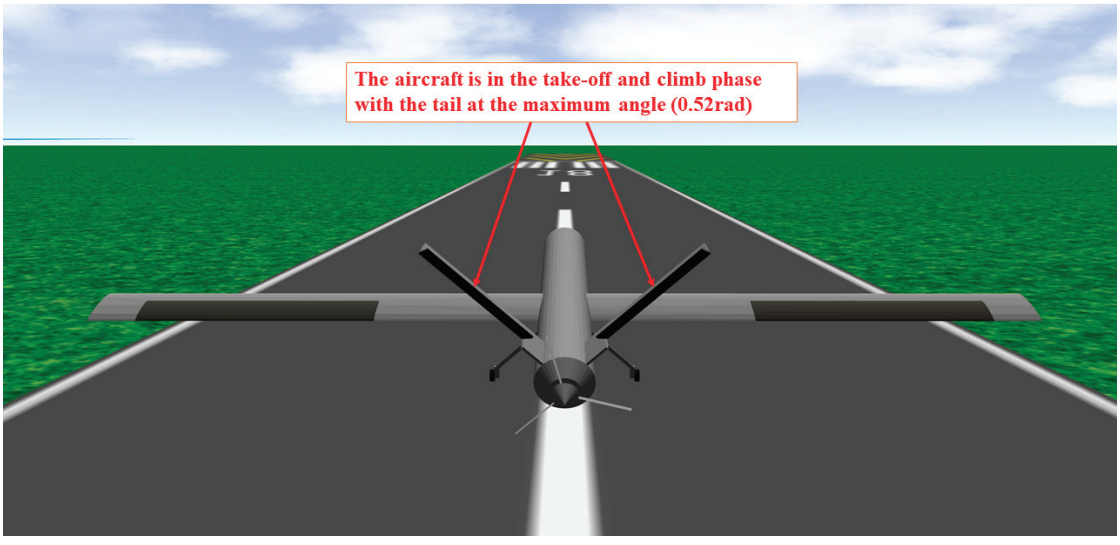

Figure 19. Aircraft is in the climbing phase. The aircraft's V-tail control surface is set to rotate within the range of −0.52 radians to 0.52 radians. At takeoff, the pitch angle is set to −0.3 radians, at which point the V-tail control surface is at its maximum deflection.

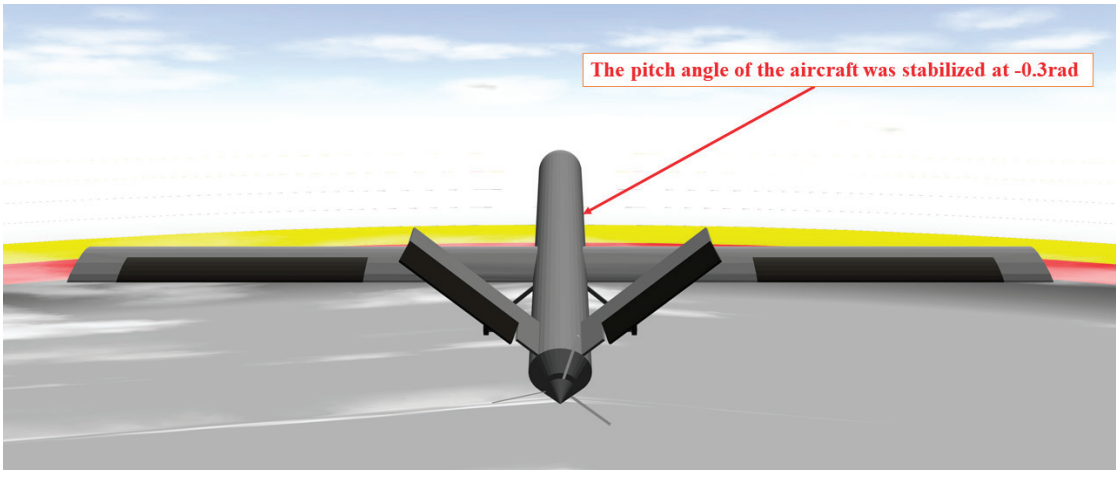

Figure 20. The pitch angle of the aircraft is stable at −0.3 radians. When the aircraft's pitch angle stabilizes at −0.3 radians, due to excessive lift, the V-tail control surface needs to rotate downward by a certain angle to maintain pitch stability.

A PD controller is employed for the aircraft's roll angle control, with PD controller parameters set as follows: Kp = −5 and Kd = −0.05. Figure 21 displays the roll angle curve of the aircraft, demonstrating that the use of the PD controller effectively stabilizes the aircraft's roll angle. It's important to note that the roll angle control involves a system with significant delays. This is why we opted not to introduce integral control, as it could potentially affect the stability of the control system. Figure 22 depicts a 3D simulation snapshot of the aircraft's roll angle stabilizing at 0.42 radians.

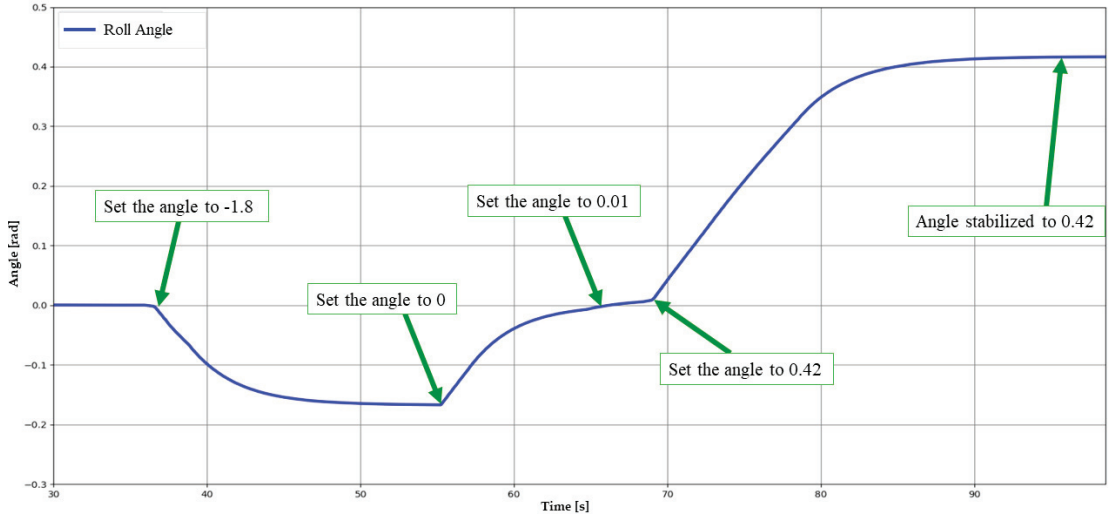

Figure 21. Roll angle data of the aircraft. During the stable flight phase, multiple desired roll angles for the aircraft are set to evaluate the performance of the roll angle controller.

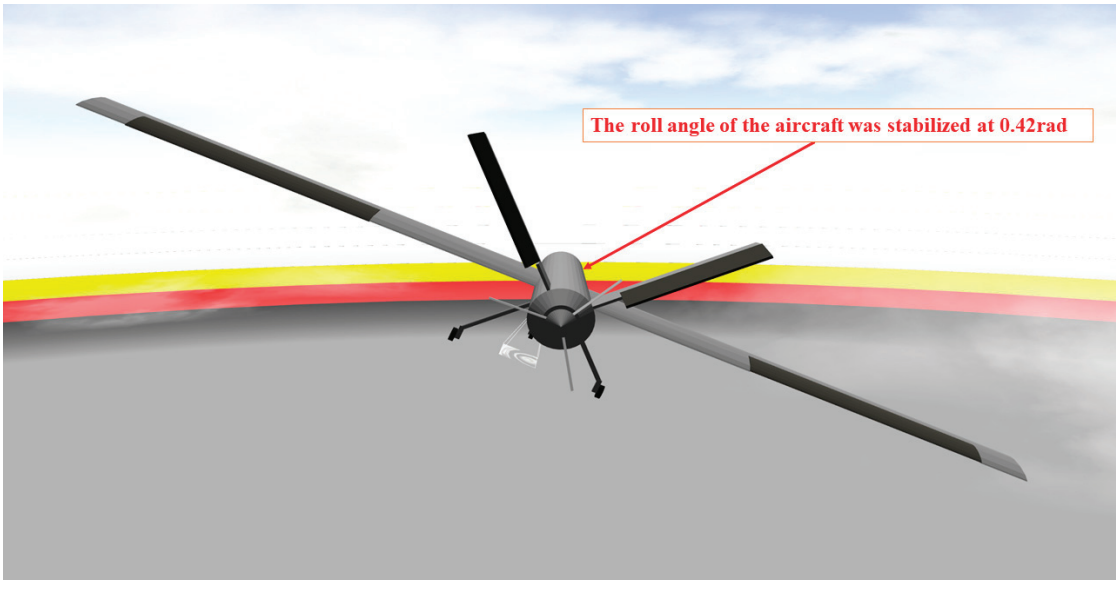

Figure 22. The roll angle of the aircraft is stable at 0.42 radians. A screenshot of the aircraft maintaining a roll angle of 0.42 radians is taken. At this moment, the aileron control surface is essentially not deflected. Due to excessive lift generated by the high aircraft speed, the V-tail control surface rotates downward by a certain angle to maintain pitch stability.

6. Conclusions

Nowadays, large fixed-wing UAVs are being utilized for a variety of tasks. Relevant research indicates that V-tail configurations can effectively reduce aerodynamic drag and enhance flight endurance. However, achieving efficient customized development and various intelligent functionalities in a specific domain remains an unresolved challenge. This study integrates SolidWorks model design with aircraft simulation technology, establishing a comprehensive aircraft simulation system

in Gazebo that encompasses kinematics, dynamics, and collision characteristics. Additionally, a simulation environment modeling approach for obstacle avoidance in no-fly zones is presented, creating a large-scale flight environment model that includes mountains, wind disturbances, and no-fly zones. Data communication and motion control are achieved through ROS, and the aircraft's attitude control is implemented using a PID algorithm. The primary contribution of this research lies in providing a 3D visualization simulation platform for dynamic obstacle avoidance, trajectory planning, and formation flying applications in the context of large-scale fixed-wing unmanned aircraft.

Currently, this research is at the initial stage, and there is still a lot of work to be done. The following outlines the future directions of the study:

(1) Develop trajectory planning and tracking algorithms for the research aircraft to achieve obstacle avoidance flight with minimal cost.
(2) Investigate multi-aircraft formation flying algorithms, aiming to maintain formation while avoiding threat areas as effectively as possible.

Author Contributions: Conceptualization, P.H. and T.W.; methodology, Y.T. and P.H.; software, P.H.; validation, B.Y. and P.H.; formal analysis, P.H.; investigation, P.H. and T.W.; resources, T.W. and Y.T.; writing—original draft preparation, P.H.; writing—review and editing, P.H. and T.W.; visualization, P.H. and B.Y.; supervision, T.W.; project administration, T.W.; funding acquisition, T.W. All authors have read and agreed to the published version of the manuscript.

Funding: This research received no external funding.

Data Availability Statement: The data are not publicly available.

Conflicts of Interest: The authors declare no conflict of interest.

References

1. Khan, M.U.; Khan, M.D.; Din, N.A.; Babar, M.Z.; Hussain, M.F. Aerodynamic Comparison of Unconventional Aircraft Tail Setup. In Proceedings of the 2019 22nd International Multitopic Conference (INMIC), Islamabad, Pakistan, 29–30 November 2019; pp. 1–5. [CrossRef]
2. Vatandas, O.E.; Anteplioglu, A. Aerodynamic performance comparison of V-tail and conventional tail for an unmanned vehicle. In Proceedings of the 2015 7th International Conference on Recent Advances in Space Technologies (RAST), Istanbul, Turkey, 16–19 June 2015; pp. 655–658. [CrossRef]
3. Zountouridou, E.; Kiokes, G.; Dimeas, A.; Prousalidis, J.; Hatziargyriou, N. A guide to unmanned aerial vehicles performance analysis—The MQ-9 unmanned air vehicle case study. *J. Eng.* **2023**, *2023*, e12270. [CrossRef]
4. Kim, S.; Park, J.; Yun, J.-K.; Seo, J. Motion Planning by Reinforcement Learning for an Unmanned Aerial Vehicle in Virtual Open Space with Static Obstacles. In Proceedings of the 2020 20th International Conference on Control, Automation and Systems (ICCAS), Busan, Republic of Korea, 13–16 October 2020; pp. 784–787. [CrossRef]
5. Rivera, Z.B.; De Simone, M.C.; Guida, D. Unmanned Ground Vehicle Modelling in Gazebo/ROS-Based Environments. *Machines* **2019**, *7*, 42. [CrossRef]
6. Sokolov, M.; Lavrenov, R.; Gabdullin, A.; Afanasyev, I.; Magid, E. 3D modelling and simulation of a crawler robot in ROS/Gazebo. In Proceedings of the 4th International Conference on Control, Mechatronics and Automation, Barcelona, Spain, 7–11 December 2016; pp. 61–65.
7. Bingham, B.; Agüero, C.; McCarrin, M.; Klamo, J.; Malia, J.; Allen, K.; Lum, T.; Rawson, M.; Waqar, R. Toward Maritime Robotic Simulation in Gazebo. In Proceedings of the OCEANS 2019 MTS/IEEE SEATTLE, Seattle, WA, USA, 27–31 October 2019; pp. 1–10. [CrossRef]
8. Niu, C.; Yan, X.; Chen, B. Control-oriented modeling of a high-aspect-ratio flying wing with coupled flight dynamics. *Chin. J. Aeronaut.* **2023**, *36*, 409–422. [CrossRef]
9. Jayaraman, B.; Saini, V.K.; Ghosh, A.K. Robust Time-Delayed PID Flight Control for Automatic Landing Guidance under Actuator Loss-Of-Control. *IFAC-PapersOnLine* **2022**, *55*, 189–194. [CrossRef]
10. Xu, B.; Zhang, Q.; Pan, Y. Neural network based dynamic surface control of hypersonic flight dynamics using small-gain theorem. *Neurocomputing* **2016**, *173*, 690–699. [CrossRef]
11. Morton, S.A.; McDaniel, D.R. A Fixed-Wing Aircraft Simulation Tool for Improving DoD Acquisition Efficiency. *Comput. Sci. Eng.* **2016**, *18*, 25–31. [CrossRef]
12. Deiler, C.; Kilian, T. Dynamic aircraft simulation model covering local icing effects. *CEAS Aeronaut. J.* **2018**, *9*, 429–444. [CrossRef]
13. Heesbeen, B.; Ruigrok, R.; Hoekstra, J. GRACE-a Versatile Simulator Architecture Making Simulation of Multiple Complex Aircraft Simple. In Proceedings of the AIAA Modeling and Simulation Technologies Conference and Exhibit, Keystone, CO, USA, 21–24 August 2006; p. 6477.
14. Aschauer, G.; Schirrer, A.; Kozek, M. Co-simulation of matlab and flightgear for identification and control of aircraft. *IFAC-PapersOnLine* **2015**, *48*, 67–72. [CrossRef]

15. Yang, L.; Hu, B.; Fu, J.; Fu, Y. Research on Longitudinal Control and Visual Simulation System for Civil Aircraft Based on Simulink/FlightGear. In Proceedings of the 2022 Chinese Intelligent Systems Conference. CISC 2022, Beijing, China, 15–16 October 2022; Lecture Notes in Electrical Engineering; Jia, Y., Zhang, W., Fu, Y., Zhao, S., Eds.; Springer: Singapore, 2022; Volume 951. [CrossRef]
16. Rostami, M.; Kamoonpuri, J.; Pradhan, P.; Chung, J. Development and Evaluation of an Enhanced Virtual Reality Flight Simulation Tool for Airships. *Aerospace* **2023**, *10*, 457. [CrossRef]
17. Marianandam, P.A.; Ghose, D. Vision based alignment to runway during approach for landing of fixed wing uavs. *IFAC Proc. Vol.* **2014**, *47*, 470–476. [CrossRef]
18. Henry, D. Application of the H∞ control theory to space missions in engineering education. *IFAC-PapersOnLine* **2020**, *53*, 17132–17137. [CrossRef]
19. Horri, N.; Pietraszko, M. A Tutorial and Review on Flight Control Co-Simulation Using Matlab/Simulink and Flight Simulators. *Automation* **2022**, *3*, 486–510. [CrossRef]
20. Bittar, A.; Figuereido, H.V.; Guimaraes, P.A.; Mendes, A.C. Guidance Software-In-the-Loop simulation using X-Plane and Simulink for UAVs. In Proceedings of the 2014 International Conference on Unmanned Aircraft Systems (ICUAS), Orlando, FL, USA, 27–30 May 2014; pp. 993–1002. [CrossRef]
21. Çetin, E.; Kutay, A.T. Automatic landing flare control design by model-following control and flight test on X-Plane flight simulator. In Proceedings of the 2016 7th International Conference on Mechanical and Aerospace Engineering (ICMAE), London, UK, 18–20 July 2016; pp. 416–420. [CrossRef]
22. Aláez, D.; Olaz, X.; Prieto, M.; Porcellinis, P.; Villadangos, J. HIL Flight Simulator for VTOL-UAV Pilot Training Using X-Plane. *Information* **2022**, *13*, 585. [CrossRef]
23. Yang, J.; Thomas, A.G.; Singh, S.; Baldi, S.; Wang, X. A Semi-Physical Platform for Guidance and Formations of Fixed-Wing Unmanned Aerial Vehicles. *Sensors* **2020**, *20*, 1136. [CrossRef] [PubMed]
24. Irmawan, E.; Harjoko, A.; Dharmawan, A. Model, Control, and Realistic Visual 3D Simulation of VTOL Fixed-Wing Transition Flight Considering Ground Effect. *Drones* **2023**, *7*, 330. [CrossRef]
25. Lee, J.; Spencer, J.; Paredes, J.A.; Ravela, S.; Bernstein, D.S.; Goel, A. An adaptive digital autopilot for fixed-wing aircraft with actuator faults. *arXiv* **2021**, arXiv:2110.11390.
26. Lee, J.; Spencer, J.; Shao, S.; Paredes, J.A.; Bernstein, D.S.; Goel, A. Experimental Flight Testing of a Fault-Tolerant Adaptive Autopilot for Fixed-Wing Aircraft. In Proceedings of the 2023 American Control Conference (ACC), San Diego, CA, USA, 31 May–2 June 2023; pp. 2981–2986. [CrossRef]
27. Ellingson, G.; McLain, T. ROSplane: Fixed-wing autopilot for education and research. In Proceedings of the 2017 International Conference on Unmanned Aircraft Systems (ICUAS), Miami, FL, USA, 13–16 June 2017; pp. 1503–1507. [CrossRef]
28. Stevens, B.L.; Lewis, F.L.; Johnson, E.N. *Aircraft Control and Simulation: Dynamics, Controls Design, and Autonomous Systems*; John Wiley & Sons: Hoboken, NJ, USA, 2015.
29. Babister, A.W. *Aircraft Dynamic Stability and Response: Pergamon International Library of Science, Technology, Engineering and Social Studies*; Elsevier: Amsterdam, The Netherlands, 2013.
30. Sinha, N.K.; Ananthkrishnan, N. *Elementary Flight Dynamics with an Introduction to Bifurcation and Continuation Methods*; CRC Press: Boca Raton, FL, USA, 2021.
31. SolidWorks to URDF Exporter. Available online: https://wiki.ros.org/sw_urdf_exporter (accessed on 15 July 2023).
32. Convert URDF to SDF. Available online: https://answers.gazebosim.org//question/2282/convert-urdf-to-sdf-or-load-urdf/ (accessed on 15 July 2023).
33. Gazebo's Aerodynamics Tutorial. Available online: https://classic.gazebosim.org/tutorials?tut=aerodynamics&cat=physics (accessed on 25 August 2023).
34. Moorhouse, D.J.; Woodcock, R.J. Background Information and User Guide for MIL-F-8785C, Military Specification: Flying Qualities of Piloted Airplanes. 1982. Available online: https://apps.dtic.mil/sti/citations/tr/ADA119421 (accessed on 10 September 2023).

applied sciences

MDPI

Article

Rapid Deployment Method for Multi-Scene UAV Base Stations for Disaster Emergency Communications

Rui Gao and Xiao Wang *

Electrical Engineering College, Guizhou University, Guiyang 550025, China; sdgr211@163.com
* Correspondence: xwang9@gzu.edu.cn

Abstract: The collaborative deployment of multiple UAVs is a crucial issue in UAV-supported disaster emergency communication networks, as utilizing these UAVs as air base stations can greatly assist in restoring communication networks within disaster-stricken areas. In this paper, the problem of rapid deployment of randomly distributed UAVs in disaster scenarios is studied, and a distributed rapid deployment method for UAVs´ emergency communication network is proposed; this method can cover all target deployment points while maintaining connectivity and provide maximum area coverage for the emergency communication network. To reduce the deployment complexity, we decoupled the three-dimensional UAV deployment problem into two dimensions: vertical and horizontal. For this small-area deployment scenario, a small area UAVs deployment improved-Broyden–Fletcher–Goldfarb–Shanno (SAIBFGS) algorithm is proposed via improving the Iterative step size and search direction to solve the high computational complexity of the traditional Broyden–Fletcher–Goldfarb–Shanno (BFGS) algorithm. In a large area deployment scenario, aiming at the problem of the premature convergence of the standard genetic algorithm (SGA), the large-area UAVs deployment elitist strategy genetic algorithm (LAESGA) is proposed through the improvement of selection, crossover, and mutation operations. The adaptation function of connectivity and coverage is solved by using SAIBFGS and LAESGA, respectively, in the horizontal dimension to obtain the optimal UAV two-dimensional deployment coordinates. Then, the transmitting power and height of the UAV base station are dynamically adjusted according to the channel characteristics and the discrete coefficients of the ground users to be rescued in different environments, which effectively improves the power consumption efficiency of the UAV base station and increases the usage time of the UAV base station, realizing the energy-saving deployment of the UAV base station. Finally, the effectiveness of the proposed method is verified via data transmission rate simulation results in different environments.

Keywords: disaster emergency communication; UAV connectivity; UAV deployment optimization; UAV coverage

Citation: Gao, R.; Wang, X. Rapid Deployment Method for Multi-Scene UAV Base Stations for Disaster Emergency Communications. *Appl. Sci.* **2023**, *13*, 10723. https://doi.org/10.3390/app131910723

Academic Editors: Jaroslaw Alexander Pytka, Andrzej Łukaszewicz, Zbigniew Kulesza, Wojciech Giernacki and Andriy Holovatyy

Received: 30 August 2023
Revised: 25 September 2023
Accepted: 25 September 2023
Published: 27 September 2023

1. Introduction

In recent decades, the frequency of all kinds of natural disasters has been increasing year by year, especially earthquakes, floods, and debris flows, which often bring incalculable losses to the affected areas [1]. In these disasters, the ground communication facilities in the accident area are often destroyed, which can make it difficult for information on the disaster situation in the accident area to be transmitted in time and makes the post-disaster relief work difficult to carry out effectively. Unmanned aerial vehicles (UAVs), which are characterized by their low cost, high flexibility, and high line-of-sight link probability [2], can be utilized to establish low altitude platforms (LAP) for emergency communication purposes [3], satisfying post-disaster communication needs [4–8].

However, given the urgency and timeliness of disasters, a UAV-assisted emergency communications network must be deployed in a timely manner [9], and the key challenges are the following. First, UAVs have limited computing power [10], and the dynamic

tracking of disaster areas to rescue ground users will consume a lot of computing resources, increasing the deployment time of UAVs. Second, the UAV's energy storage is limited [11]; the dynamic adjustment of the height of the UAV will further increase energy consumption, reducing the UAV emergency communications service time.

A reasonable channel model can improve the deployment effect of UAVs, minimizing the path loss, expanding the coverage area, and reducing the deployment time of the UAVs. In [12], the authors assumed that UAVs are fixed in a two-dimensional plane without seeking a balance between deployment range and link loss. In [13], the authors derived the air-to-air channel model among UAVs while considering height factors. In [14], the authors incorporated the characteristics of the air-to-ground propagation channel, the impact of co-channel interference from other UAV base stations, and energy constraints of the UAV base stations. In [15], the authors proposed a framework for evaluating flight height and area coverage using a fixed number of drones and area dimensions. In [16], the authors presented a distributed deployment algorithm specifically designed for line-of-sight (LoS) scenarios which allowed UAV base stations to determine their motion based solely on local information, making it suitable for large area UAVs deployments.

By integrating considerations of connectivity and coverage, the communication connectivity and area coverage challenges in the deployment of emergency communication UAVs can be effectively addressed, thereby enhancing the efficiency and accuracy of the emergency response. In [17], the authors proposed a three-dimensional UAV deployment scheme based on the improved genetic algorithm (IGA), which ensured the connectivity of the UAV network in both static and dynamic user scenarios. In [18], the authors investigated the maximum coverage deployment problem while maintaining connectivity conditions in the absence of user location information. In [19], the authors presented a combined approach using the steepest descent method and genetic algorithm to optimize the deployment scheme of wireless sensor nodes, aiming to achieve network connectivity while meeting coverage constraints. In [20], the authors proposed a graphic coalition formation game that combines UAV time-varying topology with a coalition formation game.

To reduce the complexity of the UAV deployment problem, some scholars have pursued some interesting research. In [21], the authors took into consideration the complexity of 3D UAV deployment by decoupling the UAV deployment problem into vertical and horizontal dimensions. In [22], the authors demonstrated the existence of an optimal vertical height that achieves a maximum coverage range for UAV energy efficiency.

Due to the limited endurance of UAVs, researchers have investigated the power allocation problem for UAVs. In [23], the authors proposed a new analysis model to study the key factors affecting UAV power consumption. In [24], the authors proposed a joint power allocation and deployment scheme in UAV-based IoT networks, aiming to optimize the deployment locations and power allocation of UAVs by maximizing network coverage and minimizing network interference. In [25], the authors proposed an adaptive UAV deployment scheme with the objective of optimizing UAV positions to cover as many navigation grids as possible while reducing communication energy consumption. In [26], the authors analyzed the effects of wind speed, wind direction, and turbulence on the endurance of UAVs. In [27], the authors studied the use of hybrid precoding to reduce hardware complexity and energy consumption in UAVs.

Applying the meta-heuristic optimization algorithm to solve the UAV deployment optimization problem can simplify the solution process, improve the deployment efficiency, and optimize the deployment effectiveness. The most common meta-heuristic methods include real-coded genetic algorithm (RCGA-rdn) [28], water strider algorithm (WSA) [29], thermal exchange optimization algorithm (TEO) [30], and so on.

Moreover, there exist several intriguing research directions. In [31], the authors presented a UAV emergency communication system architecture based on 5G and its subsequent technologies. This system exploits UAVs as communication relay nodes to provide communication services within disaster-stricken areas. In [32], the authors proposed a relay

deployment and network optimization framework based on non-orthogonal multiple access. The framework aims to maximize network coverage and service quality by optimizing the deployment locations and power allocation of relay nodes. In [33], the authors considered a facility location problem with drones. In [34], the authors proposed a new UAV or UAV platform that can connect a network of sensors and actuators on demand. In [35], the authors proposed a base station interference management method for UAVs based on affinity propagation and machine learning. In [36], the authors proposed a lightweight, privacy-preserving protocol for UAV internet environments. In [37], the authors developed a multi-UAV cooperative search model (MCSM) with communication cost and formation benefit as an optimization function to ensure the effectiveness of multi-UAV search.

The above research focuses on solving the problems of UAV energy consumption and UAV communication effect but does not consider the efficiency of UAV deployment. In view of the urgency and timeliness of disaster emergency communication, we design the rapid deployment method for UAV base stations which is suitable for small areas and large areas, respectively. Then, according to different disaster scenarios, the launch power and deployment height of the UAVs are dynamically adjusted to provide emergency communications for different disaster scenarios.

The main contributions of this paper are as follows:

- First, we decouple the UAV deployment problem for disaster emergency communication into two sub-problems: horizontal deployment and height regulation. We extract the horizontal deployment problem into the solution of UAV coverage rate and connectivity rate and calculate the optimal horizontal deployment coordinates of the UAV base stations, which effectively improves the deployment speed of UAV base stations after disasters. Then, the transmitting power and deployment height of the UAV base station are adjusted according to the channel model of urban, suburban, and rural environments and the distribution characteristics of the users waiting for rescue on the ground; in this way, energy-saving communication for the UAV base station is realized effectively.
- Secondly, we proposed the small-area UAV deployment improved-Broyden–Fletcher–Goldfarb–Shanno algorithm (SAIBFGS) to solve the UAV two-dimensional deployment problem for small-scale disaster scenarios, which reduces the complexity of the algorithm by improving the iterative step size and search direction. For large-scale disaster scenarios, we proposed a large area UAV deployment elitist strategy genetic algorithm (LAESGA) to solve the UAV two-dimensional deployment problem. By improving the selection, crossover, and mutation operations, the premature convergence of genetic algorithm is avoided. Simulation results show the convergence of the algorithm.

The remaining sections of this paper are as follows: Section 2 presents the system model and problem-solving approach for the rapid deployment of disaster emergency communication UAVs. Section 3 proposes deployment methods for unmanned UAVs applicable to different scales of disaster scenarios, along with the validation of the proposed algorithms' effectiveness in problem solving. Section 4 provides simulation results and analysis. Finally, Section 5 concludes the paper.

2. System Model

The present paper primarily investigates a UAVs-assisted model for disaster emergency communication networks, as depicted in Figure 1. We consider a disaster scenario with a square area of S. The system comprises I_{UAV} of UAVs, J_{person} of ground users awaiting rescue, and L target deployment points are located, the sets $I_{UAV} = \{1, 2, \ldots i\}$, $J_{person} = \{1, 2 \ldots j\}$ and $L = \{1, 2 \ldots l\}$. In the disaster scenario described in this paper, the target deployment point represents the damaged ground communication base station, and the UAV base stations replace these damaged ground communication base stations to provide emergency communications services for the rescue ground users. The communication links depicted in Figure 1 include UAV-to-UAV communication (U2U) and UAV-to-ground

communication (U2G) for interaction between unmanned aerial vehicles and ground users in need of rescue. In addition, Table 1 summarizes the main notations used in this paper.

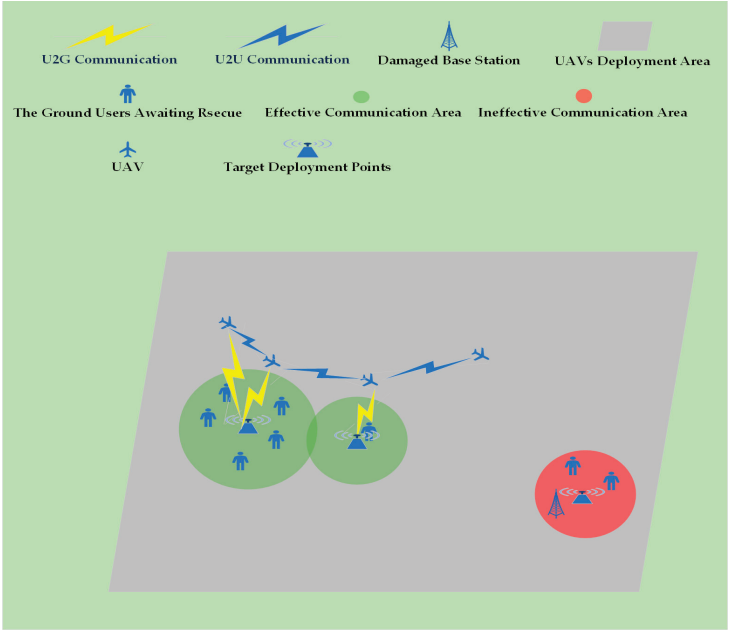

Figure 1. Communication network model of UAV base stations.

Table 1. Table of notations.

Notations	Description
I_{UAV}	UAVs' set
J_{person}	Sets of ground users awaiting rescue
D	The horizontal distance between the user's equipment antenna on the rescue surface and the UAV´s station antenna
$\mathbb{Z}(h_{msta})$	The antenna parameter calibration factor
$\mathbb{k}$	The scenario type calibration factor
R_{u_i,l_i}	Euclid distance between UAVs and target deployment points
R_{u_i,Z_i}	Euclid distance between a UAV and any point
u_i	The horizontal coordinates of a UAV
l_i	The horizontal coordinates of the target deployment points
Z_i	The coordinates of any point in the rectangular area
f_1	The connectivity fitness function
f_2	The coverage fitness function
fit_{final}	Fitness function
P_{loss}	Pathloss
ϑ	Random variable
a_k	Step size
d_k	The search direction
N	Number of UAVs
L	Number of target deployment points
M	Number of the ground users awaiting rescue
d_{min}	UAVs safe distance
d_{max}	Maximum communication distance of UAVs
f_0	Carrier frequency
T_1	Path loss threshold

Table 1. *Cont.*

Notations	Description
h_{msta}	The effective height of the user equipment antenna on the rescue surface
h_{sta}	The effective height of the UAVs station antenna
ω	The number of chromosomes
C_i	The offspring chromosome
F_i	The parent chromosome
$\lhd$	The crossover probability
$\rhd$	The mutation probability
γ_1, γ_2	Number of iterations
P_t	UAVs launch power
P_r	Power received by ground users to be rescued
C_{target}	The coordinates of the target deployment points
C_{final}	The final deployment coordinates
M_i	The number of users in need of rescue within the coverage range of the UAVs
M_{COV}	The user coverage ratio
$\mathbb{S}$	The accuracy of deployment
F_{BW}	Bandwidth frequency
$\mathfrak{M}$	Data transmission rate
$SINR$	The signal-to-noise ratio of the communication.
σ,τ	Random variable
erf	Error function
U	A random number uniformly distributed over an interval (0,1)
C_D	The discrete coefficient of user distribution on the ground to be rescued
$Z_{Jperson}$	The coordinates of the ground users to be rescued
P_{extra}	A power loss function

2.1. Channel Model

For the recovery of UAV communications in the disaster area, we assume that the people who survived in the disaster area can still use their smartphones, but because the ground base stations in the disaster area are overloaded or damaged, it makes it impossible for smartphones to communicate with the outside world. At this time, UAV can be used as a mobile node in the communication network to provide emergency communications for disaster areas. We hypothesized two scenarios that would require UAVs deployment. One scenario would be a large event space, where the large number of user communications requests exceed the load of the ground base station, and the UAVs would overcome geographic barriers that limit communication at the event horizon, providing temporary emergency communications to the region. In the other scenario, where ground base stations are damaged by a disaster such as an earthquake or mudslide [5], UAVs are deployed immediately to provide a temporary emergency communications network in open areas. The Hata–Okumura model [38] is employed to evaluate path loss and signal enhancement. This model enables the assessment of path loss in urban, suburban, and rural environments, and can be represented as follows:

$$P_{loss} = 69.55 + 26.16lg(f_{\,o}) - 13.82lg(h_{\,sta}) - \mathbb{Z}(h_{msta}) + (44.9 - 6.55lg(h_{\,sta})) \times lg(D) + \mathbb{k} \quad (1)$$

$$\mathbb{Z}(h_{msta}) = \begin{cases} 3.2 \times (lg(11.75 \times h_{msta}))^2 - 4.97 \; f_0 > 300MHz \\ 8.29 \times (lg(1.54 \times h_{msta}))^2 - 1.1 f_0 \leq 300MHz \\ (1.11\, lgf_0 - 0.7)h_{msta} - 1.56 lgf_0 + 0.8 \; others \end{cases} \quad (2)$$

$$\mathbb{k} = \begin{cases} 0 & urban \\ -2 \times (lg(f_{\,0}/28))^2 - 5.4 & suburban \\ -4.78 \times (lg(f_{\,0}))^2 + 18.33 \times lg(f_{\,0}) - 40.98 & rural \end{cases} \quad (3)$$

In the equation, h_{msta} represents the effective height of the user equipment antenna on the rescue surface, h_{sta} represents the effective height of the UAVs station antenna, D represents the horizontal distance between the users equipment antenna on the rescue surface and the UAVs station antenna, $\mathbb{Z}(h_{msta})$ is the antenna parameter calibration factor, $\mathbb{k}$ is the scenario type calibration factor, and f_0 is the carrier frequency of the U2U channel. Due to the requirement of setting a certain redundancy value for path loss in disaster scenarios, this paper does not consider the path loss generated by the transmission and reception signals between the UAV and the ground user equipment. The relationship curve between path loss P_{loss} and horizontal distance D is plotted using Equations (1) to (3), as shown in Figure 2:

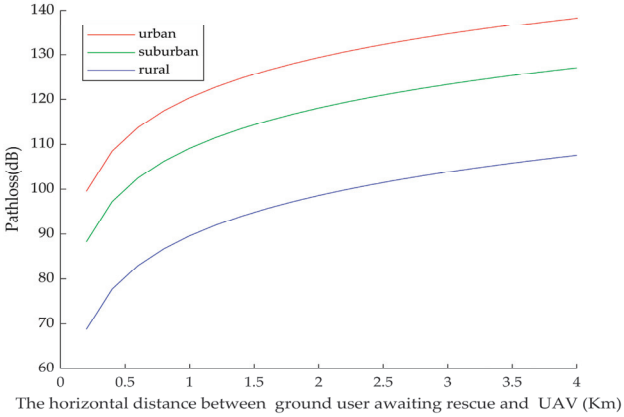

Figure 2. Plot of path loss versus horizontal distance.

When the path loss P_{loss} is less than or equal T_1 to the threshold, it can be inferred that the quality of customer service (QoS) of all ground users [39] under the coverage of UAV i_{th} in need of rescue is ensured.

2.2. Connectivity and Coverage Model

Assume a rectangular area R, within which L target deployment points are located, denoted by the set $L = \{1, 2 \ldots l\}$, $l_i = (lx_l, ly_l)$ representing the horizontal coordinates of the target deployment points. Let N UAVs be distributed within this area, $u_i = (x_i, y_i)$ representing the horizontal coordinates of the i_{th} UAV. R_i represent the communication radius of the i_{th} UAV. Let $Z_i = (zx_i, zy_i)$ represent the coordinates of any point in the rectangular area. The distance between any two UAVs must not be less than the UAVs safe distance, nor exceed the maximum communication distance. The distance between UAVs can be expressed as follows:

$$d_{i,k} = \sqrt{(h_{sta} - h_k)^2 + (u_i - u_k)^2} \geq d_{min} \tag{4}$$

where d_{min} represents the UAVs safe distance.

Modeling the connectivity rate as a function of Euclid distance R_{u_i,l_i} between UAVs u_i and target deployment points l_i: max

$$P_{u_i,l_i} = \begin{cases} 1, 0 \leq R_{u_i,l_i} \leq d_{max} \\ 0, R_{u_i,l_i} > d_{max} \end{cases} \tag{5}$$

$$R_{u_i,l_i} = \sqrt{{h_{sta}}^2 + (lxi - xi)^2 + (lyi - yi)^2} \tag{6}$$

where d_{max} represented the maximum communication distance of UAVs.

The connectivity fitness function is:

$$f_1 = \sum_{l_i \in R} P_{u_i, l_i} \tag{7}$$

Modeling coverage as the Euclid distance R_{u_i,l_i} between a UAV u_i and any point Z_i within a given region:

$$P_{u_i,Z_i} = \begin{cases} 1, 0 \le R_{u_i,Z_i} \le d_{max} \\ 0, R_{u_i,Z_i} > d_{max} \end{cases} \tag{8}$$

$$R_{u_i,Z_i} = \sqrt{(zxi - xi)^2 + (zyi - yi)^2} \tag{9}$$

The coverage fitness function is:

$$f_2 = \sum_{Z_i \in R} P_{u_i,Z_i} \tag{10}$$

The connectivity fitness function and the coverage fitness function are specified as follows:

$$Maximize: fit_{final} = \left[\vartheta \times \frac{f_1}{L \times L} + (1 - \vartheta) \times \frac{f_2}{S} \right], \vartheta \in (0, 1) \tag{11}$$

3. UAVs Deployment Methods for Disaster Scenarios of Different Scales

According to the requirement in disaster emergency response that UAVs must be deployed precisely and timely at the target point, this paper designs SAIBFGS, which is suitable for small-area UAV deployment, and LAESGA, which applies to large area UAV deployment.

3.1. Small Area UAVs Deployment Improved-Broyden–Fletcher–Goldfarb–Shanno

The quasi-Newton method is one of the most efficient approaches for solving nonlinear optimization problems, initially proposed by American physicist W. C. Davidon in the 1950s. Presently, the prevalent variants of the quasi-Newton method are the well-established Broyden–Fletcher–Goldfarb–Shanno (BFGS) method. Additionally, the steepest descent methods (SD) are frequently employed to tackle nonlinear optimization problems [19].

The conventional BFGS quasi-Newton method, due to its excessive computational demands, is not suitable for application in disaster emergency communications UAV deployment tasks. Therefore, this paper proposes the low-complexity and low-storage-demand SAIBFGS method. The SAIBFGS algorithm process is defined in Algorithm 1.

The standard iterative form of the BFGS algorithm is as follows:

$$x_{k+1} = x_k + a_k d_k = x_k - a_k b_k g_k \tag{12}$$

From the above equation, it can be observed that the computational burden of the standard BFGS algorithm primarily lies in the search direction d_k and iteration step a_k. In order to cater to the exigent communication scenarios during disaster emergencies, improvements need to be made in these two aspects.

Firstly, we consider the iteration step size a_k. In the quasi-Newton method, in order to ensure the convergence of the function, it is required that the line search be monotonic. Considering the requirement of conserving computational resources in disaster emergency communication, we made the following improvements.

Exact search step size:

$$a_k = \frac{(d_k)^T (g_k)}{(d_k)^T B (d_k)} \tag{13}$$

Simplify the direction of the search:

$$d_{k+1} = -g_{k+1} + \frac{(a_k d_k)(a_k B d_k)^T}{(a_k d_k)^T (a_k B d_k)} g_{k+1} \tag{14}$$

In the equation, B is a positive definite matrix.

Compared to the standard BFGS algorithm, the SAIBFGS algorithm obviates the need for direct calculation of the inverse Hessian matrix b_k, thereby effectively reducing computational complexity. The computational complexity of the standard BFGS algorithm is $L(6k^2 + 6k)$, while that of the SAIBFGS algorithm is $L(2k^2 + 7k)$.

Algorithm 1 Small-Area UAV Deployment Improved-Broyden–Fletcher–Goldfarb–Shanno (SAIBFGS)

Input: The starting coordinates of the UAV and the coordinates of the ground users awaiting rescue.
Output: The final coordinates for the deployment of the unmanned aerial vehicle.
Step1: Initialize the two-dimensional coordinate points for the unmanned aerial vehicle, initialize the step size, and store the data of the nearest m iterations.
Step2: While it is less than the iteration number and greater than the error, do the following.
Step3: Calculate the iterative step size: a_k.
Step4: Modify and refine key points: $x_{k+1} = x_k + a_k d_k$
Step5: Compute the correction operator: $p_k = a_k d_k, q_k = a_k B d_k$.
Step6: Calculate the updated gradient value: $g_{k+1} = g_k + q_k$.
Step7: Compute a novel trajectory for the search: d_{k+1}.
Step8: Update: $k = k + 1$
Step9: End

The accuracy of SAIBFGS is high, but as the number of UAVs increases and the deployment range expands, it is prone to getting trapped in local optima. Additionally, SAIBFGS further reduces computational complexity, making it suitable for small-scale UAV deployment.

3.2. Large Area UAVs Deployment Elitist Strategy Genetic Algorithm

The standard genetic algorithm (SGA), proposed by John Holland of the United States in the 1970s, is a computational technique that utilizes mathematical methods and computer simulations to transform the problem-solving process into a series of chromosome-based genetic operations such as selection, crossover, and mutation, similar to biological evolution. Genetic algorithms can be encoded using either binary or real-number representations, and this article adopts the real-number encoding scheme. The LAESGA algorithm process is defined as shown in Algorithm 2.

Selection operation: The common selection method for genetic algorithms is binary tournament selection; because only two individuals are compared at a time, the mechanism of this method is simple, reducing diversity. In view of the defects of the binary tournament, we made some improvements to the selection operation. First, the fitness function values of each individual in the population are calculated and ranked from large to small. Then, an elite strategy is applied to the first two ranked individuals, which are preserved and directly copied to the next generation; the remaining ranked individuals were equally divided into two groups, and the individuals with the same rank in each group were cross-operated, thus avoiding limiting the population to a local optimal solution. Since only a comparison between two individuals is involved at a time, the calculation is simple and fast. To understand the selection operation more clearly, below is a schematic of a selection operation with a chromosome number of 10, as shown in Figure 3:

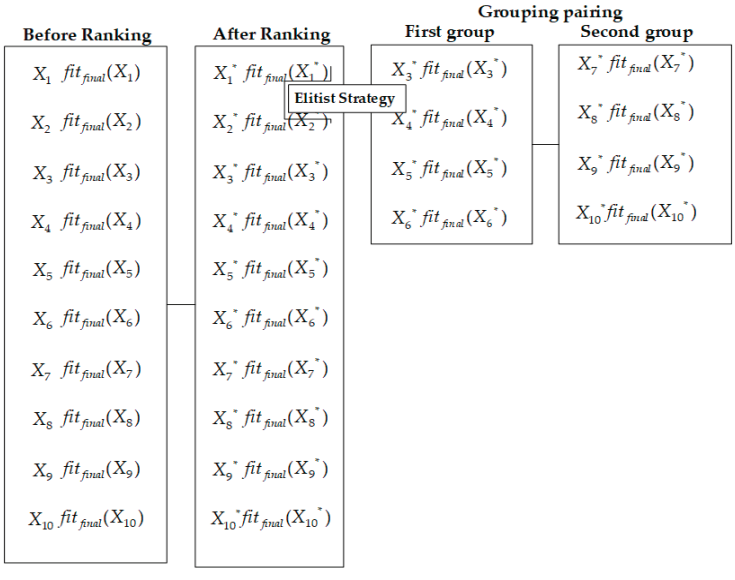

Figure 3. Schematic of the selected operation.

The chromosome before ranking is $X = (X_1, X_2, \ldots, X_\omega)$; after ranking, it becomes $X^* = (X_1^*, X_2^*, \ldots, X_\omega^*)$ and satisfies $fit_{final}(X_1^*) \geq fit_{final}(X_2^*) \geq \ldots \geq fit_{final}(X_\omega^*)$.

Crossover operation: The uniform crossover operation based on random weights is adopted. In each crossover process, two parent individuals are selected from the mating pool, denoted as F_i and F_{i+1} respectively. Then, the decision of whether to perform crossover is determined based on the probability of the crossover rate P_C. If the randomly generated number is less than P_C, the crossover operation is executed. The crossover operator is expressed as follows:

$$C_i = \sigma F_i + (1 - \sigma) F_{i+1} \tag{15}$$

$$C_{i+1} = \tau F_{i+1} + (1 - \tau) F_i \tag{16}$$

C_i is the offspring chromosome, F_i is the parent chromosome, and σ and τ are random values between 0 and 1. The crossover probability $\lhd$ is set at 0.9, the mutation probability $\rhd$ is set at 0.09, and the number of chromosomes ω is 30.

Mutation operation: Gauss's mutation method can generate continuous variation, which allows the genetic algorithm to fine-tune and search in solution space and provides a mechanism for global search, so it is widely used in genetic algorithms for unconstrained optimization problems.

The genetic algorithm has shown promising results in the application of UAV deployment. However, the standard genetic algorithm suffers from lengthy computation times and premature convergence. To address these limitations, LAESGA was devised to enhance the overall convergence capability of the standard genetic algorithm. Consequently, the deployment accuracy of UAVs is significantly improved, making it suitable for extensive UAV deployments.

Algorithm 2 Large-Area UAV Deployment Elitist Strategy Genetic Algorithm (LAESGA)

Input: The starting coordinates of the UAV and the coordinates of the ground users awaiting rescue.
Output: The final coordinates for the deployment of the unmanned aerial vehicle.
Step1: Initialization, establishing maximum number of iterations.
Step2: Initialize the population, initialize the parameters.
Step3: If the number of iterations is less than and the error is greater than the number.
Step4: Calculate the fitness value and perform the elitist selection operation.
Step5: For the paternal chromosomes in the mating pool, the crossover operator generates offspring.
Step6: For all offspring generated, do the following.
Step7: If mutation operation.
Step8: Then, the current progeny is undergoing mutation.
Step9: End
Step10: End
Step11: End
Step12: Calculate the fitness value and update the next offspring.
Step13: Update the iteration number.
Step14: End

4. Simulation Results and Discussion

In this section, we conducted simulations to validate the convergence and effectiveness of the proposed methodology. The specific simulation parameters are presented in the following Table 2:

Table 2. Simulation parameter settings.

Parameter	Description	Value
N	Number of UAVS	8–12
M	Number of the ground users awaiting rescue	200
$d_{\min}$	UAVs safe distance	100 m
$d_{\max}$	Maximum communication distance of UAVs	100–750 m
f_0	Carrier frequency	1440 MHz
T_1	Path loss threshold	150 dB
h_{msta}	The effective height of the user equipment antenna on the rescue surface	1.5 m
h_{sta}	The effective height of the UAVs station antenna	30–200 m
ω	The number of chromosomes	30
$\lhd$	The crossover probability	0.9
$\rhd$	The mutation probability	0.09
γ_1, γ_2	Number of iterations	1500, 4000
P_t	UAVs launch power	20–60 dBm
P_r	Power received by ground users to be rescued	−80 dBm
F_{BW}	Bandwidth frequency	40 MHz
σ,τ	Random variable	0~1
E_{UAV}	The power of a single UAV base station	600 Wh

4.1. Convergence Performance

To delve into the convergence performance of algorithms, we conducted simulations in both small-area (500 m × 500 m) and large-area (4000 m × 4000 m) scenarios. In the 500 m × 500 m area scenario, we envision a short-lived communications outage in this small area, which would be suitable for the deployment of subminiature UAVs. Eight UAVs were deployed to execute mission tasks, with a communication radius set at 100 m. To assess the effectiveness of the UAV deployment, we set the error threshold between the UAV's horizontal coordinates and the Euclidean distance of the target deployment point to 10m. In the 4000 m × 4000 m area scenario, 10 UAVs were deployed, with a

communication radius of 750 m. To assess the effectiveness of the UAV deployment, we set the error threshold between the UAV's horizontal coordinates and the Euclidean distance of the target deployment point to 50 m.

Figure 4a–c shows the fitness curve of UAV deployment in the small area scenario, where Figure 4d depicts the fitness curve in the large area scenario. It is observed that our proposed algorithm converges after a certain number of iterations, which demonstrates the effectiveness of our method in achieving rapid deployment for emergency communication UAVs. As illustrated in Figure 4a, both the SAIBFGS algorithm and the LAESGA algorithm achieve higher accuracy in solving the 500 m × 500 m area deployment, enabling more accurate deployment overall. In Figure 4c, the SAIBFGS is difficult to converge in a 2500 m × 2500 m area. In contrast, Figure 4d shows that the SAIBFGS algorithm struggles to handle large area deployment tasks, while the LAESGA algorithm effectively solves such tasks. Although SGA converges quickly, its convergence time is too early to reach the specified accuracy. So, while the area is less than 1500 m × 1500 m, we recommend using the SAIBFGS algorithm to calculate the optimal horizontal deployment coordinates of UAV base stations.

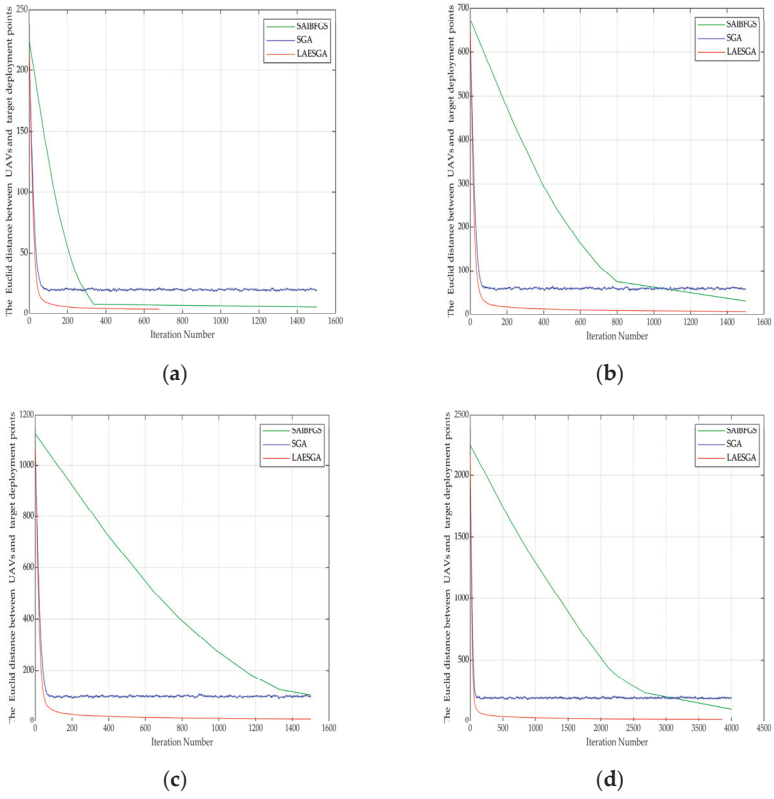

Figure 4. Fitness curve of iteration number and the Euclid distance between UAVs and target deployment points. (**a**) Fitness curve for 500 m × 500 m area UAV deployment (eight UAVs); (**b**) fitness curve for 1500 m × 1500 m area UAV deployment (eight UAVs); (**c**) fitness curve for 2500 m × 2500 m area UAV deployment (eight UAVs); (**d**) fitness curve for 4000 m × 4000 m area UAV deployment (10 UAVs).

4.2. Efficiency Analysis of the Algorithm

In a rectangular area with dimensions of 500 m × 500 m, UAVs are randomly deployed. Within area R, there are, respectively, 6, 8, 10, and 12 targets that require priority emergency

communication. Simulation experiments are conducted to compare the single search CPU average computation times of the SD algorithm, SAIBFGS algorithm, LAESGA algorithm, and SGA algorithm. The aim is to validate the efficiency of these algorithms in solving the problem at hand. Each algorithm is run 10 times for different numbers of targets, and the average values are obtained, as shown in Figure 5 for statistical analysis.

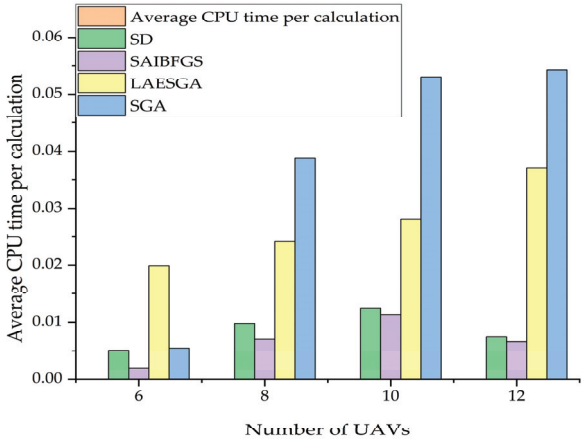

Figure 5. Comparison of average computing time.

As depicted in Figure 5, the line search method, such as the SD algorithm and SAIBFGS algorithm, showcases remarkable advantages in terms of computational efficiency when compared to genetic algorithms. The improved genetic algorithm, compared to the standard genetic algorithm, demands less computational time, thereby conserving computing resources.

4.3. Small Area UAV Deployment Simulation

Eight UAVs are randomly deployed within a rectangular area of 500 m × 500 m. Additionally, eight target deployment points are set for UAV redeployment, while 200 users in need of rescue are distributed within the area. The fitness function for redeployment is calculated using three algorithms: SABFGS, LAESGA, and SGA. The coordinates of the target deployment points are denoted as $C_{target} = (x_{target}, y_{target})$, and the final deployment coordinates calculated with the three algorithms are denoted as $C_{final} = (x_{final}, y_{final})$. The number of users in need of rescue within the coverage range of the UAVs is denoted as M_i, and the user coverage ratio is calculated using the following formula:

$$M_{COV} = \frac{M_i}{M} \times 100\% \tag{17}$$

We evaluate the accuracy of deployment by normalizing the error between the final coordinates of the UAV deployment and the coordinates of the target deployment point:

$$\mathbb{S} = (100 - \frac{1}{2 \times N} \sum_{i=1}^{N} \sqrt{(x_{target} - x_{final})^2 + (y_{target} - y_{final})^2}) \times 100\% \tag{18}$$

We configure the maximum number of iterations γ_1 for the three algorithms as 1500. To ensure user QoS in the small-scale UAV deployment scenario, we establish a UAV communication radius of 100 m.

As depicted in Figure 6, the pink circle represents UAV communication radius. And demonstrated by Tables 3 and 4, all targets are encompassed within the UAV's coverage area. This indicates that all three algorithms are capable of achieving redeployment of the unmanned aerial vehicles within a limited range. In terms of connectivity and coverage,

all three algorithms are capable of achieving 100% connectivity. The SAIBFGS algorithm yields a user coverage rate of 91%, while the LAESGA algorithm achieves a user coverage rate of 92%, and the SGA algorithm achieves a user coverage rate of 88.5%. Regarding deployment accuracy, the SAIBFGS algorithm boasts a deployment accuracy of 89.85%, the LAESGA algorithm exhibits a deployment accuracy of 90.85%, and the SGA algorithm demonstrates a deployment accuracy of 90.83%.

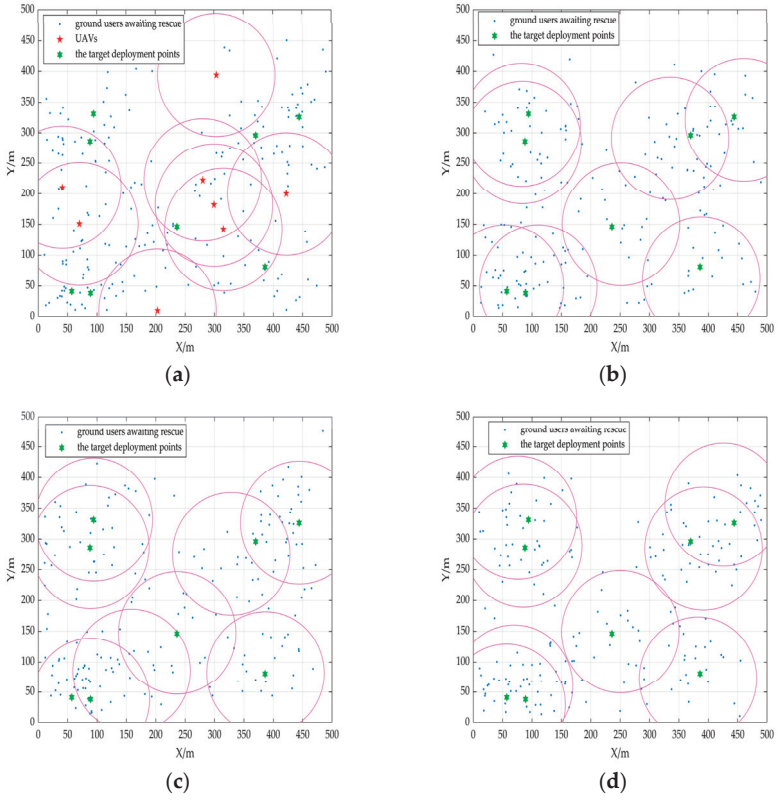

Figure 6. A simulated representation of the deployment of small area UAVs. (**a**) UAVs initial deployment of small area; (**b**) UAVs final deployment results under the small area LAESGA algorithm; (**c**) UAVs final deployment results under the small area SAIBFGS algorithm; (**d**) UAVs final deployment results under the small area SGA algorithm.

Table 3. Small-area deployment coordinate parameters.

Coordinate	SAIBFGS	LAESGA	SGA
(444, 326)	(444.17, 326.74)	(460.60, 321.16)	(426.14, 355.8)
(88, 286)	(88.65, 286.77)	(83.91, 283.83)	(85.16, 289.06)
(94, 331)	(94.68, 331.65)	(82.27, 313.19)	(76.08, 334.73)
(370, 296)	(328.45, 275.85)	(334.97, 290.48)	(391.88, 284.28)
(386, 81)	(386.72, 81.39)	(388.15, 62.04)	(382.45, 72.84)
(89, 38)	(89.47, 38.46)	(110.57, 48.95)	(69.59, 60.12)
(57, 41)	(158.88, 85.38)	(54.15, 48.96)	(56.75, 29.28)
(236, 146)	(236.42, 146.79)	(251.43, 150.47)	(250.42, 148.75)

Table 4. Performance comparison of three algorithms for small-area deployment.

Indicators	Initial	SAIBFGS	LAESGA	SGA
Connectivity	100%	100%	100%	100%
Coverage of ground users awaiting rescue	65.5%	91%	92%	88.5%
Accuracy of deployment	/	89.85%	90.85%	90.83%

4.4. Large Area UAV Deployment Simulation

In a rectangular area of 4000 m × 4000 m, we arrange 10 UAVs randomly and set up 10 target deployment points for the deployment of the UAVs. Within the area, there are 200 ground users in need of rescue. We employ the SAIBFGS algorithm, LAESGA algorithm, and SGA algorithm to compute the fitness function for the deployment. We set the maximum iteration count γ_2 for the three algorithms as 4000. In order to ensure user QoS during the large-area deployment, we set the communication radius of the UAVs to be 750 m.

As depicted in Figure 7, the pink circle represents UAV communication radius. All the targets presented in Tables 5 and 6 lie within the coverage range of the UAVs, illustrating that all three algorithms can facilitate large-scale redeployment of UAVs. In terms of connectivity and coverage, all three algorithms achieve 100% connectivity. The SAIBFGS algorithm attains a user coverage rate of 92%, the LAESGA algorithm a user coverage rate of 86.5%, and the SGA algorithm a user coverage rate of 85.5%. Concerning deployment accuracy, the SAIBFGS algorithm exhibits a deployment accuracy of 45.87%, the LAESGA algorithm a deployment accuracy of 90.36%, and the SGA algorithm a deployment accuracy of 89.26%.

Table 5. Large area deployment coordinate parameters.

Coordinate	SAIBFGS	LAESGA	SGA
(2807, 1496)	(2807.36, 1496.75)	(2807.33, 1495.58)	(2825.22, 1478.14)
(2673, 113)	(2465.86, 692.99)	(2608.97, 282.28)	(2678.63, 108.52)
(2508, 640)	(2544.33, 625.63)	(2507.94, 641.11)	(2493.34, 621.13)
(73, 2026)	(464.17, 2080.26)	(76.40, 2023.19)	(81.51, 2034.20)
(3193, 399)	(3193.26, 3972.49)	(3193.15, 3972.21)	(3225.98, 3972.82)
(3329, 1845)	(3329.76, 1845.79)	(3328.76, 1844.83)	(3363.03, 1854.57)
(882, 740)	(882.63, 740.26)	(881.94, 742.02)	(880.13, 741.81)
(3250, 3570)	(3250.36, 3570.79)	(3248.72, 3569.72)	(3250.04, 3582.09)
(2285, 1643)	(2280.70, 1669.93)	(2284.94, 1642.83)	(2283.87, 1598.43)
(2032, 2681)	(2031.29, 2682.36)	(2031.90, 2682.67)	(2020.11, 2666.59)

Table 6. Performance comparison of three algorithms for large area deployment.

Indicators	Initial	SAIBFGS	LAESGA	SGA
Connectivity	100%	100%	100%	100%
Coverage of ground users awaiting rescue	66.5%	92%	86.5%	85.5%
Accuracy of deployment	/	45.87%	90.36%	89.26%

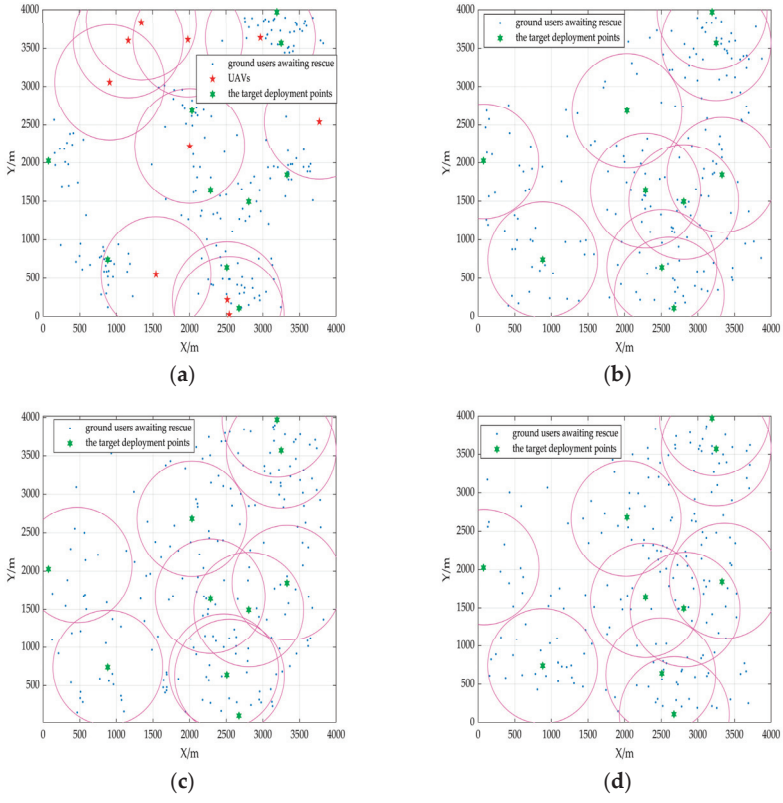

Figure 7. A simulated representation of the deployment of large-area UAVs. (**a**) UAVs´ initial deployment in the large area; (**b**) UAVs´ final deployment results under the large area LAESGA algorithm; (**c**) UAVs´ final deployment results under the large area SAIBFGS algorithm; (**d**) UAVs´ final deployment results under the large area SGA algorithm.

4.5. Minimum Power Consumption Simulation of UAVs Base Station

We set the simulation environment in a rectangular area of 4000 m × 4000 m, arrange 10 UAVs randomly, and set up 10 target deployment points for the deployment of the UAVs. Within the area, there are 200 ground users in need of rescue. In order to describe the distribution of users on the ground to be rescued, a properly defined measure of distance between points [40] is used to represent the deviation from uniformity. We define the coordinates of the ground users to be rescued as:

$$Z_{Jperson} = l_i + (\frac{1}{2} \times (1 + erf(\frac{U}{\sqrt{2}})))^{-1} \times C_D \tag{19}$$

where erf is the error function, U is a random number uniformly distributed over an interval (0, 1), C_D represents the discrete coefficient of user distribution on the ground to be rescued.

After the disaster environment and the UAV deployment location are determined, all the ground users who are waiting for rescue have the same path loss. On the premise of satisfying the communication service quality of all ground users to be rescued within the coverage range of UAV base stations, the efficiency of UAV base station power consumption can be improved by enabling the UAV base stations to cover the rescue ground users with

a minimum transmission power. The minimum launch power of the UAV base stations is expressed as:

$$P_t = P_r + P_{loss} - P_{extra} \tag{20}$$

where P_{extra} is a power loss function that varies according to different environments.

In order to study the specific energy-saving situation of UAVs based on the UAV power consumption model [41], we express the single UAV base station energy consumption as follows:

$$E_{UAV} = P_t \times t + (13.0397h_{sta} + 196.894) \times t + 4.6817h_{sta}^2 - 11.9708h_{sta} + 135.3118 \tag{21}$$

where E_{UAV} represents the energy of a single UAV base station and t represents the usage time of the UAV base station.

Figure 8 shows a fixed UAV base station with a launch power of 20 dBm. We study the minimum UAV altitude for urban, suburban, and rural environments with a given ground user dispersion coefficient.

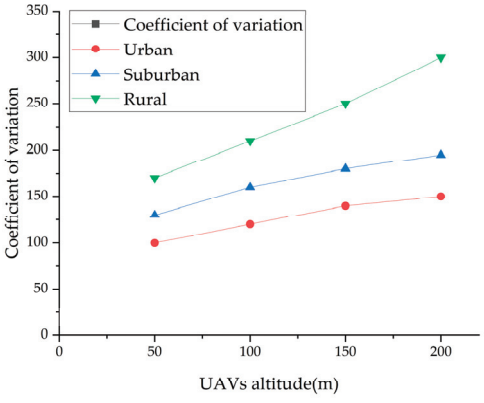

Figure 8. The relationship between the height of the UAV base station and the discrete coefficient of ground users to be rescued.

Figure 9 shows a fixed UAV base station with a height of 200 m. We study the minimum UAV launch power in urban, suburban, and rural environments to meet the specified ground user dispersion coefficient.

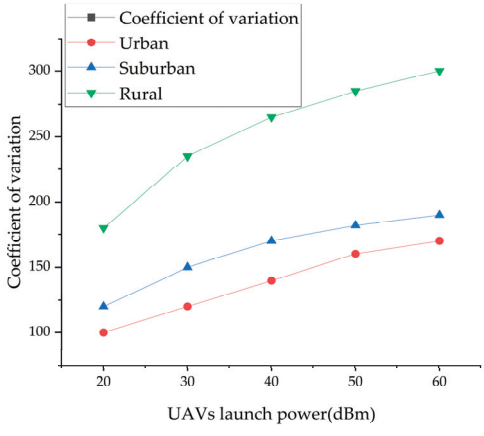

Figure 9. The relationship between the launch power of UAVs base station and the discrete coefficient of ground users to be rescued.

In previous studies, we found that the higher the base station deployment height, the greater the coverage radius, and the higher the base station deployment height, the greater the path loss between the UAV and the user on the ground to be rescued. As shown in Figure 8, we found that the height of UAV base stations needs to be increased to some extent with the increase of the dispersion coefficient of ground users to be rescued in urban, suburban, and rural environments. As shown in Figure 9, we found that with the increase of the dispersion coefficient of ground users to be rescued in urban, suburban, and rural environments, the launch power of UAV base stations needs to be increased to varying degrees. The dispersion coefficient of the ground users in an urban environment is much larger than that in a rural environment, and the dispersion coefficient of the ground users in a suburban environment is between the other two. Based on this, we can conclude that UAV base stations in rural environments can choose larger deployment heights and smaller transmitting power, such as a 200 m hover height deployment and a transmitting power of 20 dBm. UAV base stations can be deployed at a moderate altitude and transmit power, for example, at a hovering altitude of 150 m and transmit power of 30 dBm. UAV base stations in urban environments can be deployed at a lower altitude and with a larger launch power, such as a 100 m hover deployment with a launch power of 40 dBm. Thus, the QoS can be maintained while covering a large area of ground users to be rescued, and the power consumption efficiency of the UAV base station can be improved.

4.6. Simulating the Data Transmission Rate in Diverse Environments

To verify the effectiveness of the rapid deployment approach for UAV communications restoration in disaster-affected areas, we performed a data transmission rate verification in Figures 10–12. We divide the disaster areas into three types: urban, suburban, and rural. The actual data transmission rate of deployed drones will vary because the density of ground users awaiting rescue varies from disaster to disaster. Specifically, we first calculated the distance between each ground user awaiting rescue and a nearby target deployment point, calculated the signal quality index $SINR$ based on the distance, calculated the data transmission rate of each location based on $SINR$, and finally, a contour map of the data transmission rate based on the minimum data transmission rate. The bandwidth frequency is expressed as F_{BW}. By calculating the distance between each ground user and the nearest ground base station, the value of $SINR$ is obtained, where a value $\mathfrak{M}$ greater than or equal to 1 Mbps is considered effective communication. The formula for calculating the data transmission rate is as follows:

$$\mathfrak{M} = F_{BW} \times \log 2(1 + SINR) \tag{22}$$

We set the initial hover height of the UAVs base station to 200 m, and the initial launch power of the UAVs base station to 60 dBm. At this time, in urban environments, the deployment of the central data transmission rate reaches 900 Mbps, with the deployment of the edge data transmission rate being 100 Mbps (Figure 10b); we assume a single UAV base station energy of 600 Wh and, according to Formula (21), calculated the UAV base station usage time as being 519.08 s. Then, we adjusted the hover height of the UAV base station to 100 m and the launch power of the UAV base station to 40 dBm. At this time, in urban environments, the deployment of the central data transmission rate also reaches 900 Mbps, with the deployment of the edge data transmission rate also being 100 Mbps (Figure 10a); thus, according to Formula (21), we calculated the UAV base station usage time as 1399.39 s. In urban environments, our approach increases the usage time of UAV base stations while maintaining the data transmission rate.

We set the initial hover height of the UAVs base station to 200 m, and the initial launch power of the UAVs base station to 60 dBm. At this time, in suburban environments, the deployment of the central data transmission rate reaches 700 Mbps, with the deployment of the edge data transmission rate being 100 Mbps (Figure 11b); we assume a single UAV base station energy of 600 Wh, so, according to Formula (21), we calculated the UAV base station usage time as 519.08 s. Then, we adjusted the hover height of the UAV base station

to 160 m and the launch power of the UAV base station to 30 dBm. At this time, in suburban environments, the deployment of the central data transmission rate also reaches 700 Mbps, with the deployment of the edge data transmission rate also being 100 Mbps (Figure 11a); thus, according to Formula (21), we calculated the UAV base station usage time is 893.93 s. In suburban environments, our approach increases the usage time of UAV base stations while maintaining the data transmission rate.

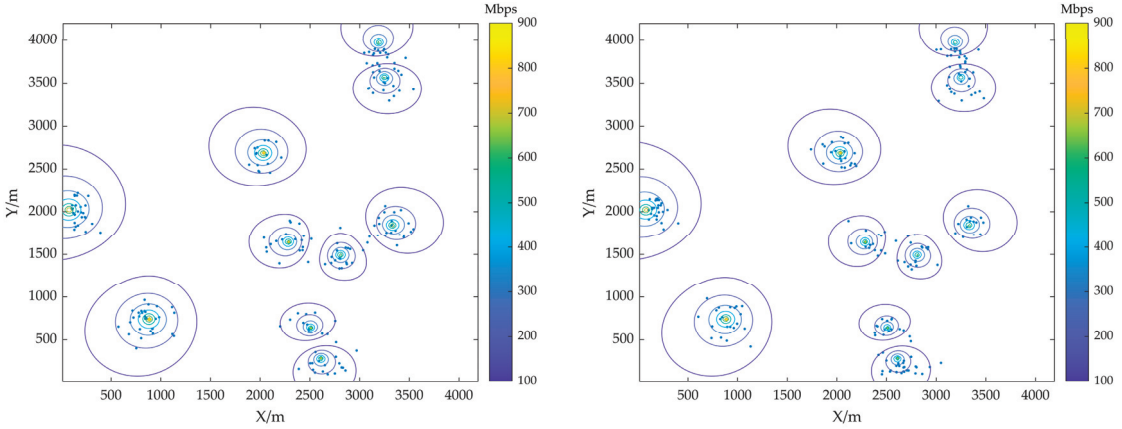

Figure 10. The data transmission rate of UAVs base station in urban environment: (**a**) 100 m hover height deployment and 40 dBm launch power; (**b**) 200 m hover height deployment and 60 dBm launch power.

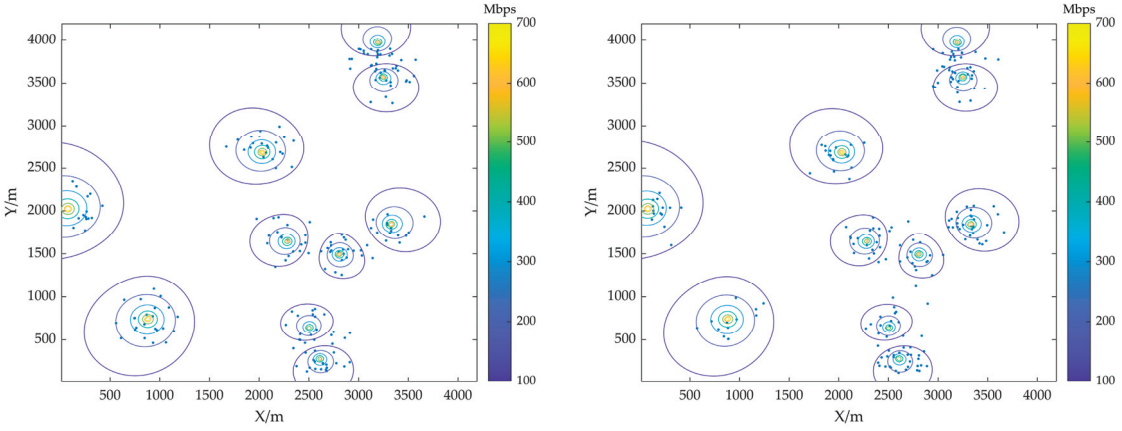

Figure 11. The data transmission rate of UAVs base station in suburban environment: (**a**) 160 m hover height deployment and 30 dBm launch power; (**b**) 200 m hover height deployment and 60 dBm launch power.

We set the initial hover height of the UAVs base station to 200 m, and the initial launch power of the UAVs base station to 60 dBm. At this time, in rural environments, the deployment of the central data transmission rate reaches 500 Mbps, with the deployment of the edge data transmission rate being 50 Mbps (Figure 12b); we assume a single UAV base station energy of 600 Wh, so, according to Formula (21), we calculated the UAV base station usage time as 519.08 s. Then, we adjusted the hover height of the UAV base station

to 200 m and the launch power of the UAV base station to 20 dBm. At this time, in rural environments, the deployment of the central data transmission rate also reaches 500 Mbps, with the deployment of the edge data transmission rate also being 50 Mbps (Figure 12a); thus, according to Formula (21), we calculated the UAV base station usage time as 704.12 s. In rural environments, our approach increases the usage time of UAV base stations while maintaining the data transmission rate.

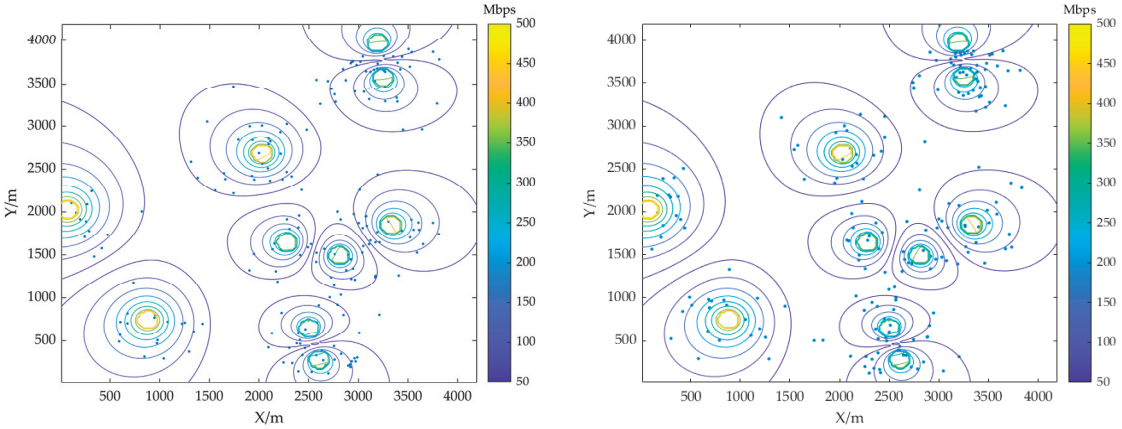

Figure 12. The data transmission rate of UAVs base station in rural environment: (**a**) 200 m hover height deployment and 20 dBm launch power; (**b**) 200 m hover height deployment and 60 dBm launch power.

5. Conclusions

In order to address the issues of low efficiency and insufficient accuracy in the deployment of disaster emergency communication UAVs, this paper presents a method for the rapid deployment of disaster emergency communication UAV base stations. This method utilizes efficient algorithms tailored to different scale scenarios, greatly improving deployment efficiency, and the feasibility of the proposed algorithms is validated through simulations. By dynamically adjusting the launch power and deployment height of UAVs to provide emergency communication for different disaster scenarios, the power consumption efficiency of the UAVs is improved, the usage time of the UAV base stations is increased, and the energy-saving deployment of the UAV base stations is realized. From the perspective of data transmission rate in urban, suburban, and rural environments after UAVs´ deployment, this method effectively provides emergency communication services for disaster areas with multiple scenarios.

Although the algorithm in this paper allows for the rapid deployment of UAVs to restore emergency communication in disaster areas, it does have certain limitations. Specifically, it does not consider complex dynamic environmental interference factors. Therefore, further improvement of the proposed algorithm and the consideration of the interrelation between rapid UAV deployment and multi-hop self-organizing communication of relay UAVs should be explored in future research.

Author Contributions: Conceptualization R.G.; methodology, R.G.; formal analysis, R.G.; investigation, R.G.; resources, R.G.; data curation, R.G.; writing—original draft preparation, R.G.; writing—review and editing, R.G.; visualization, X.W.; supervision, X.W.; project administration, R.G.; funding acquisition, X.W. All authors have read and agreed to the published version of the manuscript.

Funding: This work was supported in part by the National Natural Science Foundation of China under grant 61861007 and 61640014; in part by the Guizhou Province Science and Technology Planning Project ZK [2021]303; in part by the Guizhou Province Science Technology Support Plan under grant [2022]017, [2023]096 and [2022]264; in part by the Guizhou Education Department Innovation Group Project under grant KY [2021]012; in part by the Talent Introduction Project of Guizhou University (2014)-08.

Institutional Review Board Statement: Not applicable.

Informed Consent Statement: Not applicable.

Data Availability Statement: All data used to support the findings of the study is included in this paper.

Conflicts of Interest: The authors declare no conflict of interest.

References

1. Zheng, Y.J.; Chen, Q.Z.; Ling, H.F.; Xue, J.Y. Rescue wings: Mobile computing and active services support for disaster rescue. *IEEE Trans. Serv. Comput.* **2015**, *9*, 594–607. [CrossRef]
2. Cheng, F.; Zhang, S.; Chen, Y.F.; Zhao, N.; Yu, F.R.; Leung, V.C.M. UAV trajectory optimization for data offloading at the edge of multiple cells. *IEEE Trans. Veh. Technol.* **2018**, *67*, 6732–6736. [CrossRef]
3. Al-Hourani, A.; Kandeepan, S.; Lardner, S. Optimal LAP altitude for maximum coverage. *IEEE Wirel. Commun. Lett.* **2014**, *3*, 569–572. [CrossRef]
4. Otto, A.; Agatz, N.; Campbell, J.; Golden, B.; Pesch, E. Optimization approaches for civil applications of unmanned aerial vehicles (UAVs) or aerial drones: A survey. *Netw. J.* **2018**, *72*, 411–458. [CrossRef]
5. Giagkos, A.; Wilson, M.S.; Tuci, E.; Charlesworth, P.B. Comparing approaches for coordination of autonomous communications UAVs. In Proceedings of the 2016 International Conference on Unmanned Aircraft Systems (ICUAS), Arlington, VA, USA, 7–10 June 2016; pp. 1131–1139.
6. Rupasinghe, N.; Ibrahim, A.S.; Guvenc, I. Optimum Hovering Locations with Angular Domain User Separation for Cooperative UAV Networks. In Proceedings of the 2016 IEEE Global Communications Conference (GLOBECOM), Washington, DC, USA, 4–8 December 2016; pp. 1–6.
7. Zhu, J.; Zhao, H.; Wei, Y.M.; Ma, C.M.; Lv, Q. Unmanned aerial vehicle computation task scheduling based on parking resources in post-disaster rescue. *Appl. Sci.* **2023**, *13*, 289. [CrossRef]
8. Montanari, R.; Tozadore, D.C.; Fraccaroli, E.S.; Romero, R.A.F. Ground Vehicle Detection and Classification by an Unmanned Aerial Vehicle. In Proceedings of the 2015 12th Latin American Robotics Symposium and 2015 3rd Brazilian Symposium on Robotics (LARS-SBR), Uberlandia, Brazil, 29–31 October 2015; pp. 253–258.
9. Erdelj, M.; Natalizio, E.; Chowdhury, K.R.; Akyildiz, I.F. Help from the Sky: Leveraging UAVs for Disaster Management. *IEEE Pervasive Comput.* **2017**, *16*, 24–32. [CrossRef]
10. He, X.F.; Jin, R.C.; Dai, H.Y. Multi-hop task offloading with on-the-fly computation for multi-UAV remote edge computing. *IEEE Trans. Commun.* **2021**, *70*, 1332–1344. [CrossRef]
11. Qin, Y.J.; Kishk, M.A.; Alouini, M.S. Performance evaluation of UAV-enabled cellular networks with battery-limited drones. *IEEE Commun. Lett.* **2020**, *24*, 2664–2668. [CrossRef]
12. Akram, T.; Awais, M.; Naqvi, R.; Ahmed, A.; Naeem, M. Multicriteria UAV base stations placement for disaster management. *IEEE Syst. J.* **2020**, *14*, 3475–3482. [CrossRef]
13. Safwat, N.E.D.; Newagy, F.; Hafez, I.M. Air-to-Air channel model for UAVs in dense urban environments. In Proceedings of the 2021 5th International Conference on Electrical, Electronics, Communication, Computer Technologies and Optimization Techniques (ICEECCOT), Mysuru, India, 10–11 December 2021; pp. 204–209.
14. Hydher, H.; Jayakody, D.N.K.; Hemachandra, K.T. Intelligent UAV deployment for a disaster-resilient wireless network. *Sensors* **2020**, *20*, 6140. [CrossRef]
15. Munawar, H.S.; W A Hammad, A.; Waller, S.T. Disaster region coverage using drones: Maximum area coverage and minimum resource utilisation. *Drones* **2022**, *6*, 96. [CrossRef]
16. Huang, H.L.; Savkin, A.V. Deployment of heterogeneous UAV base stations for optimal quality of coverage. *IEEE Internet Things J.* **2022**, *9*, 16429–16437. [CrossRef]
17. Wen, X.T.; Ruan, Y.H.; Li, Y.Z.; Xia, H.X.; Zhang, R.; Wang, C.; Liu, W.; Jiang, X.Y. Improved Genetic Algorithm based 3-D deployment of UAVs. *Commun. Netw. J.* **2022**, *24*, 223–231. [CrossRef]
18. Zhao, H.T.; Wang, H.J.; Wu, W.Y.; Wei, J.B. Deployment algorithms for UAV airborne networks toward on-demand coverage. *IEEE Sel. Area Commun. J.* **2018**, *36*, 2015–2031. [CrossRef]
19. Sheikh-Hosseini, M.; Hashemi, S.R.S. Connectivity and coverage constrained wireless sensor nodes deployment using steepest descent and genetic algorithms. *Expert Syst. Appl.* **2022**, *190*, 116164. [CrossRef]
20. Huang, Y.T.; Qi, N.; Huang, Z.Q.; Jia, L.L.; Wu, Q.H.; Yao, R.G.; Wang, W.J. Connectivity Guarantee Within UAV Cluster: A Graph Coalition Formation Game Approach. *IEEE Open J. Commun. Soc.* **2023**, *4*, 79–90. [CrossRef]

21. Zhong, X.K.; Huo, Y.M.; Dong, X.D.; Liang, Z.H. QoS-compliant 3-D deployment optimization strategy for UAV base stations. *IEEE Syst. J.* **2021**, *15*, 1795–1803. [CrossRef]
22. Alzenad, M.; El-Keyi, A.; Lagum, F.; Yanikomeroglu, H. 3-D placement of an unmanned aerial vehicle base station (UAV-BS) for energy-efficient maximal coverage. *IEEE Wirel. Commun. Lett.* **2017**, *6*, 434–437. [CrossRef]
23. Citroni, R.; Di Paolo, F.; Livreri, P. A Novel Energy Harvester for Powering Small UAVs: Performance Analysis, Model Validation and Flight Results. *Sensors* **2019**, *19*, 1771. [CrossRef]
24. Chen, R.R.; Sun, Y.J.; Liang, L.P.; Cheng, W.C. Joint power allocation and placement scheme for UAV-assisted IOT with QOS guarantee. *IEEE Trans. Veh. Technol.* **2021**, *71*, 1066–1071. [CrossRef]
25. Lin, N.; Liu, Y.H.; Zhao, L.; Wu, D.O.; Wang, Y.F. An adaptive UAV deployment scheme for emergency networking. *IEEE Trans. Wirel. Commun.* **2021**, *21*, 2383–2398. [CrossRef]
26. Chu, T.X.; Starek, M.J.; Berryhill, J.; Quiroga, C.; Pashaei, M. Simulation and Characterization of Wind Impacts on sUAS Flight Performance for Crash Scene Reconstruction. *Drones* **2021**, *5*, 67. [CrossRef]
27. Mir, T.; Waqas, M.; Tu, S.; Fang, C.; Ni, W.; MacKenzie, R.; Xue, X.; Han, Z. Relay hybrid precoding in uav-assisted wideband millimeter-wave massive mimo system. *IEEE Trans. Wirel. Commun.* **2022**, *21*, 7040–7054. [CrossRef]
28. Song, Y.Y.; Wang, F.L.; Chen, X.X. An improved genetic algorithm for numerical function optimization. *Appl. Intell.* **2019**, *49*, 1880–1902. [CrossRef]
29. Kaveh, A.; Eslamlou, A.D. Water strider algorithm: A new metaheuristic and applications. *Structures* **2020**, *25*, 520–541. [CrossRef]
30. Kaveh, A.; Dadras, A. A novel meta-heuristic optimization algorithm: Thermal exchange optimization. *Adv. Eng. Softw.* **2017**, *110*, 69–84. [CrossRef]
31. Shah, A.F.M.S. Architecture of emergency communication systems in disasters through UAVs in 5G and beyond. *Drones* **2022**, *7*, 25. [CrossRef]
32. He, Y.X.; Nie, L.; Guo, T.; Kaur, K.; Hassan, M.; Yu, K. A NOMA-enabled framework for relay deployment and network optimization in double-layer airborne access VANETs. *IEEE Trans. Intell. Transp. Syst.* **2022**, *23*, 22452–22466. [CrossRef]
33. Zhu, T.K.; Boyles, S.D.; Unnikrishnan, A. Two-stage robust facility location problem with drones. *Transp. Res. Part C Emerg. Technol.* **2022**, *137*, 103563. [CrossRef]
34. Bae, M.; Yoo, S.; Jung, J.; Park, S.; Kim, K.; Lee, J.Y.; Kim, H. Devising Mobile Sensing and Actuation Infrastructure with Drones. *Sensors* **2018**, *18*, 624. [CrossRef]
35. Wang, L.C.; Chao, Y.S.; Cheng, S.H.; Han, Z. An Integrated Affinity Propagation and Machine Learning Approach for Interference Management in Drone Base Stations. *IEEE Trans. Cogn. Commun. Netw.* **2019**, *6*, 83–94. [CrossRef]
36. Pu, C.; Wall, A.; Choo, K.-K.R.; Ahmed, I.; Lim, S. A Lightweight and Privacy-Preserving Mutual Authentication and Key Agreement Protocol for Internet of Drones Environment. *IEEE Internet Things J.* **2022**, *9*, 9918–9933. [CrossRef]
37. Fei, B.W.; Bao, W.D.; Zhu, X.M.; Liu, D.Q.; Men, T.; Xiao, Z.L. Autonomous Cooperative Search Model for Multi-UAV With Limited Communication Network. *IEEE Internet Things J.* **2022**, *9*, 19346–19361. [CrossRef]
38. Hata, M. Empirical formula for propagation loss in land mobile radio services. *IEEE Trans Veh. Technol.* **1980**, *29*, 317–325. [CrossRef]
39. Hayat, S.; Yanmaz, E.; Bettstetter, C.; Brown, T.X. Multi-Objective Drone Path Planning for Search and Rescue with Quality-of Service Requirements. *Auton. Robot.* **2020**, *44*, 1183–1198. [CrossRef]
40. Mirahsan, M.; Schoenen, R.; Yanikomeroglu, H. HetHetNets: Heterogeneous Traffic Distribution in Heterogeneous Wireless Cellular Networks. *IEEE J. Sel. Areas Commun.* **2015**, *33*, 2252–2265. [CrossRef]
41. Abeywickrama, H.V.; Jayawickrama, B.A.; He, Y.; Dutkiewicz, E. Empirical Power Consumption Model for UAVs. In Proceedings of the 2018 IEEE 88th Vehicular Technology Conference (VTC-Fall), Chicago, IL, USA, 27–30 August 2018; pp. 1–5.

applied sciences

MDPI

Article

Curved-Line Path-Following Control of Fixed-Wing Unmanned Aerial Vehicles Using a Robust Disturbance-Estimator-Based Predictive Control Approach

Weiwei Qi [1,2], Mingbo Tong [1,*], Qi Wang [3], Wei Song [3] and Hunan Ying [2]

[1] College of Aerospace Engineering, Nanjing University of Aeronautics and Astronautics, Nanjing 211106, China; 70720@nchu.edu.cn
[2] School of General Aviation, Nanchang Hangkong University, Nanchang 330063, China; 58102@nchu.edu.cn
[3] School of Aircraft Engineering, Nanchang Hangkong University, Nanchang 330063, China; wangqi439@126.com (Q.W.); songwei@nchu.edu.cn (W.S.)
* Correspondence: tongw@nuaa.edu.cn

Abstract: In this research, the design of a robust curved-line path-following control system for fixed-wing unmanned aerial vehicles (FWUAVs) affected by uncertainties on the latitude plane is studied. This is undertaken to enhance closed-loop system robustness under unknown uncertainties and derive the control surface deflection angle directly used to control FWUAVs, which has rarely been studied in previous works. The system is formed through the mass center position control (MCPC) and yaw angle control (YAC) subsystems. In the MCPC, the desired yaw angle, which is treated as the reference signal for the YAC subsystem, is calculated analytically using path-following errors, current flow angles, and the yaw angle. In the YAC, a disturbance estimator is designed to estimate uncertainties such as nonlinearities, couplings, time variations, model parameter perturbations, and unmodeled dynamics. Predictive functional controllers are designed to target nominal systems in the absence of uncertainties, such that the estimations of the uncertainties can be incorporated through feedback for closed-loop system robustness enhancement. The simulation results show that higher path-following precision and stronger robustness for the FWUAVs based on the proposed approach can be achieved using only rough model parameters compared with the conventional nonlinear dynamic inversion, which requires detailed model information.

Keywords: fixed-wing unmanned aerial vehicles; path following; disturbance estimator; predictive functional control; nonlinear dynamic inversion

Citation: Qi, W.; Tong, M.; Wang, Q.; Song, W.; Ying, H. Curved-Line Path-Following Control of Fixed-Wing Unmanned Aerial Vehicles Using a Robust Disturbance-Estimator-Based Predictive Control Approach. *Appl. Sci.* **2023**, *13*, 11577. https://doi.org/10.3390/app132011577

Academic Editors: Andrzej Łukaszewicz, Wojciech Giernacki, Zbigniew Kulesza, Jaroslaw Alexander Pytka and Andriy Holovatyy

Received: 25 September 2023
Revised: 12 October 2023
Accepted: 19 October 2023
Published: 23 October 2023

1. Introduction

Due to the advantages of long endurance, fast flight, and high energy availability, fixed-wing unmanned aerial vehicles (FWUAVs) have become increasingly attractive in many areas, such as reconnaissance, patrol inspection, and monitoring. When executing missions, FWUAVs are required to follow a prescribed reference path. The mission execution effect relies on the path-following control performance, making the design of the path-following control system important with engineering significance.

Path-following errors are adjusted via attitude angles. According to the path-following errors, the mass center position controller generates the desired attitude angles, which are regarded as the references for the attitude controller so that the control surface deflection angles as well as the control laws of FWUAVs can be derived.

In the MCPC, establishing a motion model is quite important. By considering aerodynamic complexities, variable couplings, fast time variations, and high nonlinearities, the geometric approach and control technique are mainly applied for model establishment. The two approaches have the advantages of a simple model structure and irrelevant model

information, such that their superiority is obvious when compared with conventional modeling methods [1].

The commonly utilized geometric approaches include the line-of-sight (LOS) [2–7], vector field [8–14], virtual target following [15–21], and L_1 guidance approaches [22–28]. Analytical solutions of the desired attitude angles or body rates regarded as reference signals can be derived through the relationships among the path-following errors, the current flow angles, and the current attitude angles.

Being different from the geometric approach, the control technique assumes that there is a virtual target point attached to the prescribed reference path. A natural frame also named the Frenet frame [21,29–32], whose origin coincides with the virtual target point, is established; in this case, the Frenet frame overlaps with the body frame if the FWUAV can strictly follow the path. In the control technique, path-following error kinematic models whose inputs are the error angles (also called error attitude angles) between the Frenet frame and the body frame are built without using any plant model information. The advantages of the control technique are that the error attitude angles can be designed through different control theories, such as L_1 adaptive control [33], L_1 state feedback control [34], nested saturation control [35], linear model-based predictive control [36], optimal control [37], and nonlinear model predictive control [38], and that the approach has been studied widely.

By considering that FWUAVs are easily influenced via external wind fields, approaches such as a new guidance law combined with pure pursuit and the LOS [39], a VTP-based nonlinear guidance law [15], optimal control with the wind amplitude available [16], feedback control with wind estimation and compensation [37], and adaptive backstepping control [40] have been presented.

However, the existing path-following control schemes are incomplete since they mainly focus on the establishment of a path-following error kinematic model and the design of mass center position controllers. Once the desired attitude angles/body rates have been obtained, the studies are ceased, meaning that the design of the attitude controllers is ignored and that the final deflection laws of the control surfaces actually used to steer the FWUAVs are not given. It is well known that attitude control plays a decisive role not only in path-following control but also in the field of flight control. Hence, the design of an attitude control system and control performance enhancement cannot be ignored.

To address these problems, targeting the movement of FWUAVs on the latitude plane, a robust path-following control approach is presented in this paper. The path-following control performance can be improved using only a small amount of rough dynamic model information. The main outcomes and contributions of this paper are twofold:

(1) A path-following control scheme for FWUAVs is perfected.

Being different from most existing studies, this paper aims to improve attitude system performance via improving path-following control performance. Effective deflection angles of the control surfaces as well as the control laws are designed;

(2) A robust control approach is proposed for attitude control.

A novel disturbance estimator (DE) [41,42] is applied to estimate uncertainties, such as nonlinearities, strong couplings, and system unmodeled dynamics, so that, in the design of controllers, only a small amount of model information is used. As pointed out in the two literatures, the novel DE has better performance than the commonly used extended state observer [43–48]. In addition, a predictive functional controller (PFC) is designed for the nominal system in the absence of uncertainties to improve system input/output performance. The estimation of the uncertainties is incorporated into the PFC for feedback compensation so that the closed-loop system's robustness can be improved.

2. System Modeling

In this section, a movement model based on the latitude plane is established. The fundamentals of the curved path following the latitude plane are illustrated in Figure 1.

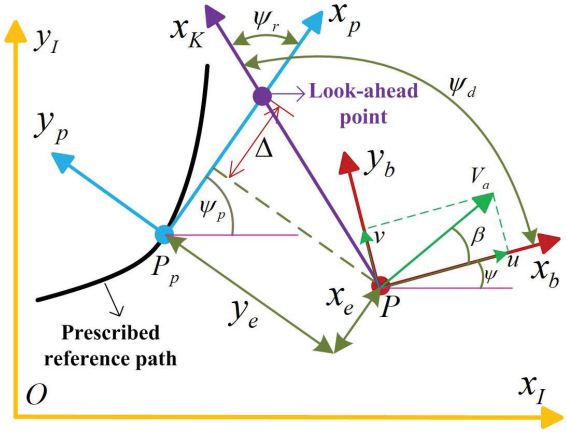

Figure 1. Path following on the latitude plane.

Here, Ox_Iy_I and Px_by_b represent the inertia frame and body frame, respectively. P represents the current mass center position of the FWUAV, which is denoted as (x, y). P_p represents the desired position denoted as (x_p, y_p), which the FWUAV should locate. u and v are the velocities along Px_b and Py_b, respectively. $\beta = \arctan\frac{v}{u}$ represents the side-slip angle. $V_a = \sqrt{u^2 + v^2}$ is the air speed. ψ is the yaw angle. x_e and y_e represent the components between the current position P and the desired position P_p in the frame $P_px_py_p$. Δ is the look-ahead distance, which is a positive number.

2.1. Computation of Desired Attitude Angles

The prescribed reference path is denoted as $P_p = [x_p(s), y_p(s)]^T$, with s representing the path parameter and $x_p(s)$ and $y_p(s)$ being the second-order derivatives with respect to s. Then, the desired path angle can be written as

$$\psi_p = \arctan2\big(y_p(s), x_p(s)\big) \tag{1}$$

where $\arctan2(*)$ represents the quadrant function.

The transformation matrix from Ox_Iy_I to $P_px_py_p$ can be given using

$$L_{pg} = \begin{bmatrix} \cos\psi_p & -\sin\psi_p \\ \sin\psi_p & \cos\psi_p \end{bmatrix} \tag{2}$$

The following errors can be computed using Figure 1:

$$e = [x_e, y_e]^T = L_{pg}(P - P_p) \tag{3}$$

Differentiating Formula (3) relative to time yields

$$\dot{e} = \dot{L}_{pg}(P - P_p) + L_{pg}\left(\dot{P} - \dot{P}_p\right) \tag{4}$$

One can also have

$$\dot{L}_{pg} = S_p L_{pg} \tag{5}$$

$$S_p = \begin{bmatrix} 0 & \dot{\psi}_p \\ -\dot{\psi}_p & 0 \end{bmatrix} \tag{6}$$

The transformation matrix from Px_Ky_K to $P_px_py_p$ can be given using

$$L_{pk} = \begin{bmatrix} \cos\psi_r & \sin\psi_r \\ -\sin\psi_r & \cos\psi_r \end{bmatrix} \tag{7}$$

By considering the wind velocities along Px_b and Py_b denoted as u_w and v_w, respectively, the perturbed airspeed denoted by V_g can be calculated using $V_g = \sqrt{(u+u_w)^2 + (v+v_w)^2}$.

Since $V_{kg} = \left[V_g, 0\right]^T$, we can have

$$\dot{P} = L_{pg}^T L_{pk} V_{kg} \tag{8}$$

The velocity of the desired path in $P_px_py_p$ can be expressed as $V_{pg} = [V_p, 0]^T$; then, we can derive

$$\dot{P_p} = L_{pg}^T V_{pg} \tag{9}$$

and

$$\left|\dot{P_p}\right| = \left|L_{pg}^T V_{pg}\right| \tag{10}$$

where $|*|$ represents the norm of a vector.

It can be determined from Formula (10) that

$$\dot{s} = \frac{V_p}{\sqrt{{x'_p}^2(s) + {y'_p}^2(s)}} \tag{11}$$

where $x'_p(s) = \frac{\partial x_p(s)}{\partial s}$ and $y'_p(s) = \frac{\partial y_p(s)}{\partial s}$.

Bringing Formulas (5), (8), and (9) into (4) yields

$$\begin{aligned} \dot{e} &= S_p L_{pg}(P - P_p) + L_{pg}\left(L_{pg}^T L_{pk} V_{kg} - L_{pg}^T V_{pg}\right) \\ &= S_p e + L_{pk} V_{kg} - V_{pg} \end{aligned} \tag{12}$$

Then, the desired yaw angle can be calculated as

$$\psi_d = \psi_r + \psi_p - \beta \tag{13}$$

with ψ_r defined as

$$\psi_r = \arctan\left(\frac{-y_e}{\Delta}\right) \tag{14}$$

Take the following Lyapunov function:

$$V_e = \frac{1}{2} e^T e \tag{15}$$

Differentiating the Lyapunov function relative to time yields

$$\begin{aligned} \dot{V_e} &= e^T \dot{e} \\ &= e^T\left(S_p e + L_{pk} V_{kg} - V_{pg}\right) \end{aligned} \tag{16}$$

It is easy to prove that $e^T S_p e = 0$. Then, via carrying out a simple mathematical operation, one can derive

$$\dot{V_e} = x_e\left(V_g \cos\psi_r - V_p\right) + y_e V_g \sin\psi_r \tag{17}$$

To guarantee $\dot{V_e} \leq 0$, we can take

$$V_p = V_g \cos \psi_r + \tau x_e \tag{18}$$

where $\tau > 0$ is a tuning variable.

Bringing Formula (18) into (11) yields

$$\dot{s} = \frac{V_g \cos \psi_r + \tau x_e}{\sqrt{x_p'^2(s) + y_p'^2(s)}} \tag{19}$$

Bringing Formulas (14) and (18) into (17) yields

$$\dot{V_e} = -\tau x_e^2 - V_g \frac{\Delta {y_e}^2}{\sqrt{\Delta^2 + {y_e}^2}} < 0 \tag{20}$$

It can be seen from the definition that the velocity V_g must be a positive number. Δ is the look-ahead distance, which is a positive number and has also been defined before. Thus,$V_g > 0$ and $\Delta > 0$ can guarantee $-V_g \frac{\Delta {y_e}^2}{\sqrt{\Delta^2 + {y_e}^2}} < 0$, which also implies $\dot{V_e} < 0$. Formula (20) indicates that the real flight path of the FWUAV can converge gradually to the prescribed reference path under the designed desired yaw angle (14).

The complete curved path-following scheme can be summarized as follows:

$$\begin{cases} \dot{s} = \frac{V_g \cos \psi_r + \tau x_e}{\sqrt{x_p'^2(s) + y_p'^2(s)}} \\ \psi_r = \arctan\left(\frac{-y_e}{\Delta}\right) \\ \psi_d = \psi_r + \psi_p - \beta \end{cases} \tag{21}$$

Equation (21) describes the path-following error of the center of mass of the FWUAV. The first equation $\dot{s}$ describes the changing rate of the path variable s relative to time so that the desired path to be followed can be digitalized and programmed in the flight control hardware. The rest of the two equations afford reference signals to the yaw angle system to design the deflection laws of the rudder.

2.2. Yaw System Model

In the yaw movement, the force acting on the FWUAV is mainly the yaw torque, which depends on the rudder. The expression of the yaw torque N is given by [49]:

$$\begin{cases} N = \frac{1}{2}\rho V_a^2 S b C_n \\ C_n = C_{n_0} + C_{n_\beta}\beta + C_{n_r}\frac{br}{2V_a} + C_{n_{\delta_r}}\delta_r \end{cases} \tag{22}$$

where ρ, S, b, and δ_r are the air density, wing area, wing span, and rudder deflection angle, respectively. r is the yaw rate. C_{n_0} is the zero yaw moment coefficient. C_{n_β}, C_{n_r}, and $C_{n_{\delta_r}}$ are derivatives of the yaw moment with respect to the side-slip angle, yaw rate, and rudder, respectively, which can also be seen in [49].

Then, by referring to [49] and considering uncertainties, the yaw movement model is given using

$$\begin{cases} \dot{\psi} = r \\ \dot{r} = \frac{N}{I_z} + d_s \\ \quad = \underbrace{\frac{C_{n_0} + C_{n_\beta}\beta}{I_z} + \frac{C_{n_r} br}{2V_a I_z} + d_s}_{f_r} + \underbrace{\frac{C_{n_{\delta_r}}}{I_z}}_{b_r} \delta_r \\ \quad = f_r + b_r \delta_r \end{cases} \tag{23}$$

where I_z is the moment of inertia. d_s represents the uncertainties, including the unmodeled dynamics and model parameter perturbations.

Then, the remaining task of this paper is to design the deflection angle of the rudder δ_r so that the yaw angle of the FWUAV ψ in Formula (23) can track the desired value of ψ_d derived from Formula (21) using the dynamic model (23).

2.3. Existing Approaches and Defects

To highlight the approach proposed in the paper, the existing approaches and their defects are summarized in Table 1.

Table 1. The existing approaches and their defects.

Approach Category	Literatures	Defects
LOS	[2–7]	Poor robustness, no attitude control system
vector field	[8–14]	Complicated theories, Poor robustness, no attitude control system
virtual target following	[15–21]	Too many virtual targets, poor robustness, no attitude control system
L_1 guidance	[22–28]	Poor robustness, no attitude control system
Frenet	[21,29–32]	Poor robustness, no attitude control system

3. Yaw Angle Control Design

In this section, based on the desired yaw angle derived in Section 2.1, a control scheme for the yaw movement can be designed.

3.1. Design of DE

By referring to the literature [41], the design of the DE for estimating the nonlinear term f_r can be divided into the following steps:

Step 1: design of the nominal model

In the absence of f_r in Formula (23), the nominal model in the continuous-time domain can be given using

$$\dot{r}_m = b_r \delta_r \tag{24}$$

The discrete-time version is written as

$$r_m(k+1) = r_m(k) + T b_r \delta_r(k) \tag{25}$$

where r_m is the state of the nominal model, and T is the sampling period;

Step 2: DE formulation

The DE is designed as follows:

$$\begin{cases} \hat{f}_r(k) = \frac{\Delta \varepsilon_r(k)}{T} + \hat{\phi}(k) \cdot \Delta \delta_r(k) \\ \hat{\phi}(k) = \hat{\phi}(k-1) + \frac{\eta \left[\Delta r(k) - \hat{\phi}(k-1) \Delta \delta_r(k-1) \right] \Delta \delta_r(k-1)}{\mu + |\Delta \delta_r(k-1)|^2} \end{cases} \tag{26}$$

where $\hat{f}_r$ is the estimated value of f_r, $\varepsilon_r(k) = r(k) - r_m(k)$, $\Delta\varepsilon_r(k) = \varepsilon_r(k) - \varepsilon_r(k-1)$, $\Delta\delta_r(k) = \delta_r(k) - \delta_r(k-1)$, $\Delta r(k) = r(k) - r(k-1)$, $\mu > 0$, $\eta \in (0, 2]$, and $\hat{\phi}(0)$ is specified by users.

A stability analysis of the DE can be seen in Appendix C in [42].

3.2. Controller Design

In Formula (23), the desired yaw rate for manipulating the yaw angle is designed as follows:

$$r_d(k) = \omega_1[\psi_d(k) - \psi(k)] \tag{27}$$

According to the predictive functional control theory [50,51], the system input can be formulated using

$$\begin{cases} \delta_r(k+i) = \delta_1 + i \cdot \delta_2 \\ \Delta\delta_r(k+i) = \delta_2 \end{cases} \tag{28}$$

Then, in Formula (23), in the absence of f_r, a predictive model for the yaw rate model can be given using

$$\begin{cases} r(k+1) = r(k) + Tb_r\delta_1 \\ r(k+2) = r(k) + Tb_r(\delta_1 + \delta_2) \\ r(k+3) = r(k) + Tb_r(\delta_1 + 2\delta_2) \\ \quad\vdots \\ r(k+n) = r(k) + Tb_r[\delta_1 + (n-1)\delta_2] \end{cases} \tag{29}$$

The following receding horizon performance index function is selected:

$$J(k) = \frac{1}{2}\sum_{j=1}^{2}\left[r\left(k+n_j\right) - r_d\left(k+n_j\right)\right] \tag{30}$$

where n_1 and n_2, which are two positive integers, are the lengths of the receding horizon.

Denote $u(k) = [\delta_1, \delta_2]^T$. Then, by letting $\frac{\partial J(k)}{\partial u(k)} = 0$, the optimal rudder deflection angle can be derived as follows:

$$\delta_r(k) = [1, 0]\begin{bmatrix} Tb_r & Tb_r(n_1 - 1) \\ Tb_r & Tb_r(n_2 - 1) \end{bmatrix}^{-1}\begin{bmatrix} r_d(k+n_1) - r(k) \\ r_d(k+n_1) - r(k) \end{bmatrix} \tag{31}$$

Through combing Formulas (26) and (31), the final control law is summarized as

$$\delta_r(k) = [1, 0]\begin{bmatrix} Tb_r & Tb_r(n_1 - 1) \\ Tb_r & Tb_r(n_2 - 1) \end{bmatrix}^{-1}\begin{bmatrix} r_d(k+n_1) - r(k) \\ r_d(k+n_1) - r(k) \end{bmatrix} - \frac{1}{b_r}\hat{f}_r(k) \tag{32}$$

4. Numerical Simulations

In this section, two groups of numerical simulations are carried out to demonstrate the effectiveness and superiority of the proposed control scheme via a comparison with the conventional nonlinear dynamic inversion (NDI) approach [52–54], which is commonly used in flight control. The conventional nonlinear dynamic inversion controller for the yaw angle control is designed as follows:

$$\begin{cases} r_d(k) = \rho_1[\psi_d(k) - \psi(k)] \\ \delta_r(k) = \frac{1}{b_r}\{\rho_2[r_d(k) - r(k)] - f_r(k)\} \end{cases} \tag{33}$$

where $\rho_1 > 0$ and $\rho_2 > 0$ are two tuning parameters.

The geometry and aerodynamic parameters in Formulas (22) and (23) are $I_z = 1.759\ \text{kg} \cdot \text{m}^2$, $C_{n_0} = 0$, $C_{n_\beta} = 0.25$, $C_{n_r} = -0.35$, and $C_{n_{\delta_r}} = -0.032$. The trimmed conditions of the FWUAV are $V_a = 30\ \text{m/s}$, $x_p = y_p = 0$, $\psi = r = 0$, and $\delta_r = 0$. The values of the controller parameters for the NDI are $\rho_1 = 5$ and $\rho_2 = 10$. The values of the controller

parameters for the proposed approach are $\mu = 0.1$, $\eta = 0.1$, $\hat{\phi}(0) = 1$, $\omega_1 = 2$, $n_1 = 5$, and $n_2 = 10$. The uncertainty term is $d_s = 4\sin(0.5t) + 3\cos(t)$ when 45 s $\leq t \leq$ 90 s, and the wind velocities along Ox_I and Oy_I are 0 and 3 m/s when 15 s $\leq t \leq$ 30 s, respectively. Actually, the wind disturbances along Ox_I would not have great effects on the flight path of the FWUAV since the wind can only decrease the flight speed and prolong the mission accomplishment time of the path following. However, the wind along Oy_I has entirely different effects on the FWUAV since it affects the airplane from the side direction, which would influence the stability of the FWUAV.

The prescribed reference path (unit: m) is given using

$$\begin{cases} x_d(s) = -450\sin(s) \\ y_d(s) = 450\cos(s) + 450 \end{cases} \tag{34}$$

4.1. Case Study 1

In this group, wind disturbances along Ox_I and Oy_I and the uncertainty of d_s regeared as unmodeled dynamics are considered. The unmodeled dynamics d_s would affect the flight stability of the FWUAV since it can cause unstable poles.

The simulation results are illustrated below.

Figures 2 and 3 clearly prove that the proposed approach is superior to the NDI approach. The absolute maximum following errors of the proposed scheme along Ox_I and Oy_I are only 0.02 m and 2 m, respectively, compared with the ones based on the NDI approach, which are up to 0.12 m and 12 m along Ox_I and Oy_I, respectively. The path-following errors of the proposed approach are much smaller than those of the NDI. Additionally, the two figures also indicate that the NDI approach has a trend of divergence after 45 s when the unmodeled dynamics are encountered, since the NDI approach does not have any anti-disturbance mechanisms. However, the situations are different in the proposed scheme due to the existence of the DE, which has a strong disturbance estimation capability and superb estimation accuracy.

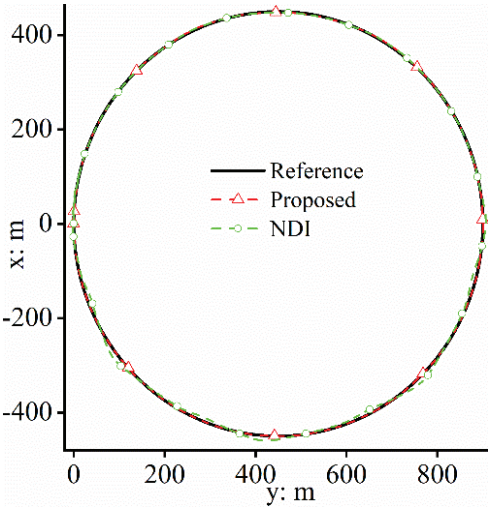

Figure 2. Path−following effect.

Figure 4 shows that, when dealing with wind disturbances, the controllers of the proposed approach generate more effective control inputs than those of the NDI approach to guarantee path-following precision. However, to deal with the unknown unmodeled dynamics, too-frequent deflection for the rudder occurs in the NDI-based closed-loop system, which places a heavy burden on the actuator of the FWUAV. The reason for this

is that the closed-loop system based on the proposed control scheme has a disturbance rejection mechanism that enables the FWUAV's strong robustness. Figure 5 shows the accurate estimation capability of the DE, which is the fundamental reason for the proposed control approach being superior to the conventional NDI approach.

Figures 6–8 show the attitude control performance of the FWUAV during flight. In the flight control field, attitude maintenance capability plays a decisive role and determines path-following performance. In Figures 7 and 8, the NDI approach-based path-following control system is incapable of steering the yaw movement when unmodeled dynamics are encountered. It can be seen in Figure 7 that the yaw angle of the NDI approach has frequent fluctuations. In Figure 8, the FWUAV has large changing rates, which reach up to 30 degrees (should be around zero) for the yaw movement. A poor attitude control capability would cause large path-following errors for the FWUAV, which results in unsatisfying control performance in path-following missions. The situations are quite different in the proposed approach, as shown in Figure 6, due to the disturbance rejection function because the unmodeled dynamics can be estimated and compensated successfully.

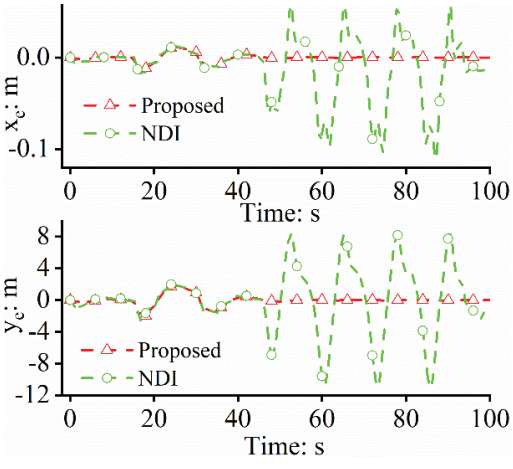

Figure 3. Path−following errors.

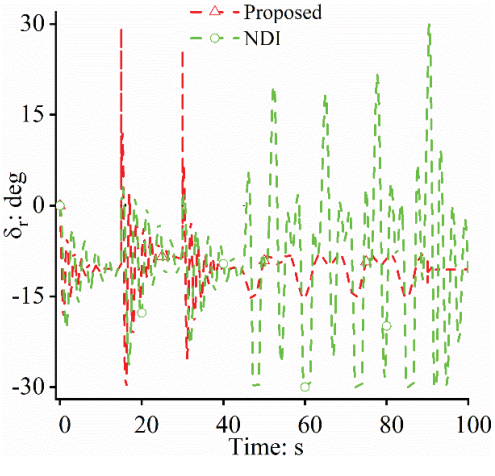

Figure 4. Control laws.

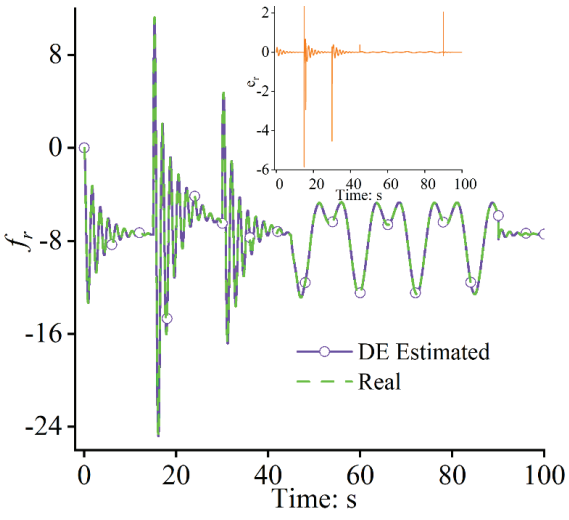

Figure 5. Uncertainty estimation and estimation error $e_r = f_r - \hat{f}_r$.

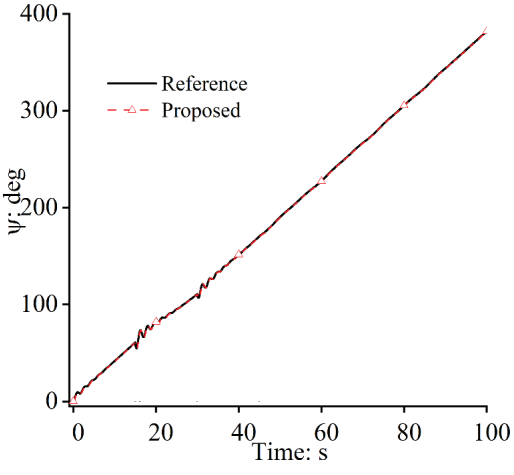

Figure 6. Yaw angles: proposed approach.

4.2. Case Study 2

In this group, all uncertainties, including wind disturbances along Ox_I and Oy_I, the model parameter perturbations for b_r, and uncertainty d_s, are considered. To validate the proposed scheme completely, +30% and −30% perturbations of b_r are considered. Furthermore, the results of the two perturbation cases are also combined with those of the case without any perturbations to show the effectiveness of the proposed scheme.

The simulation results are illustrated below.

It can be determined from Figures 9 and 10 that the proposed approach-based path-following control system can achieve great flight performance regardless of whether the important model parameter has perturbations. The absolute maximum following error of the proposed approach in the two situations along Oy_I is only 0.02 m, and the mean path-following errors are all very close to zero. Additionally, when recalling the results in Section 4.1, it is found that, even when the model parameter perturbs within a wide range, the control performance of the proposed approach is much better than that of the NDI.

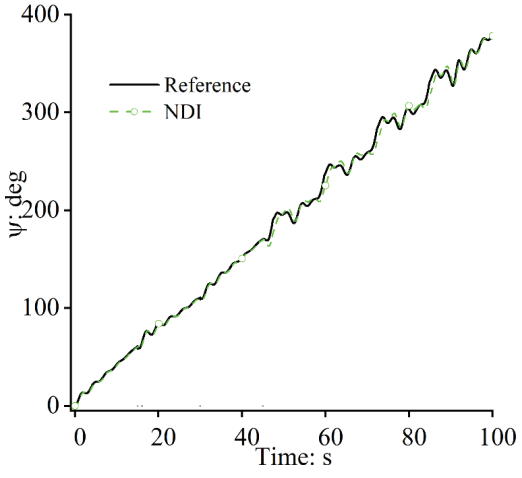

Figure 7. Yaw angles: the NDI approach.

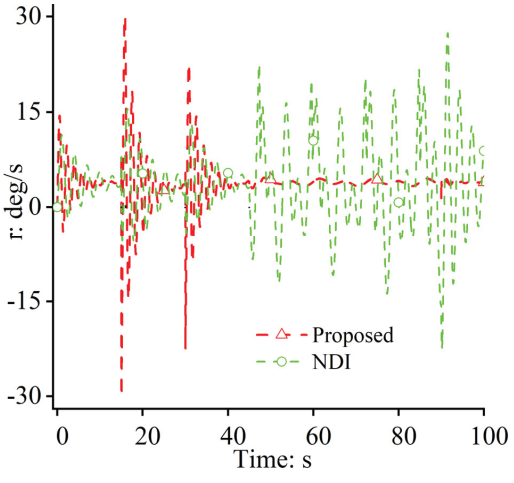

Figure 8. Yaw rates.

Figure 11 shows that the control law can be designed requiring only a small amount of rough model information. In addition, due to the existence of the DE, the dynamics of the model perturbation can be observed accurately and compensated effectively so that even slight changes in the characteristics of the closed-loop system would not happen. Thus, the trends of the rudder deflection angles in the two situations are similar, which means that even the model parameter undergoes large perturbations, and the rudder deflection angles similar to those in the case without any perturbations can be used to steer the FWUAV. Figures 12 and 13 show that the DE can estimate the uncertainties accurately, even when large perturbations occur in the model parameter. It has an advantage in that the design of the control system for the FWUAV is mildly correlated with the system modeling and model parameter measurement.

Figures 14–16 show that similar yaw movements in the two situations can be achieved during path following. Under the uncertainties induced via the unmodeled dynamics and the parameter perturbation, the yaw angle changes stably without any jumping or fluctuation, which proves that the frame stability of the FWUAV can be guaranteed and

that the closed-loop system's robustness can be significantly enhanced under large model parameter perturbations.

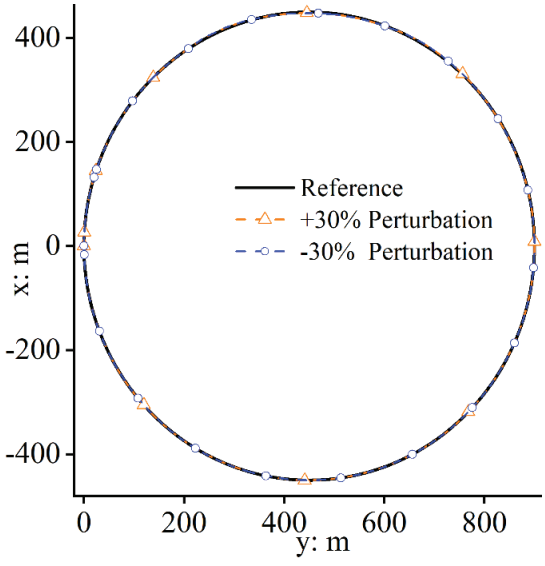

Figure 9. Path−following effects.

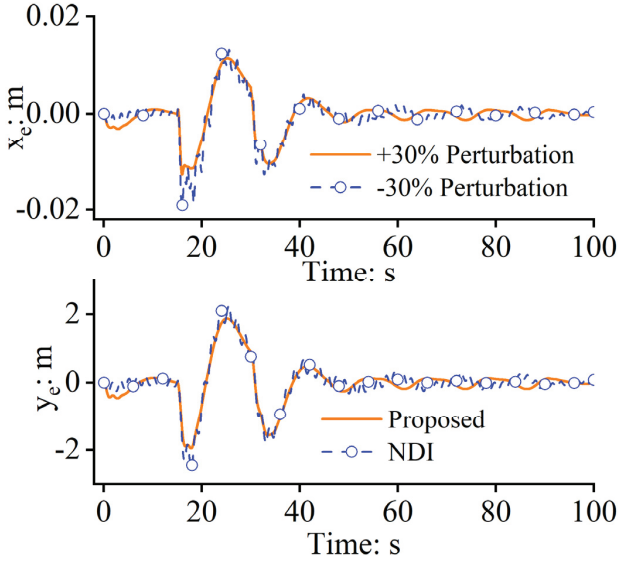

Figure 10. Path−following errors.

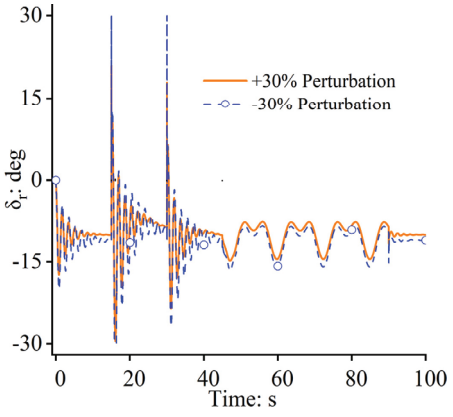

Figure 11. Control laws.

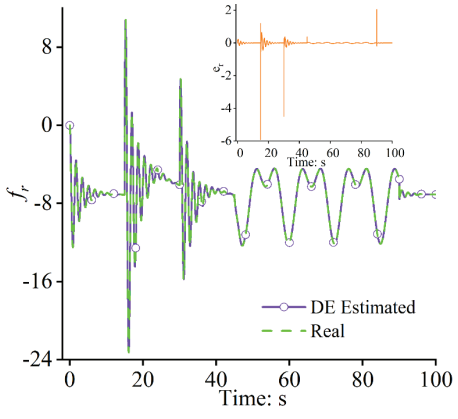

Figure 12. Uncertainty estimation: +30% and estimation error $e_r = f_r - \hat{f}_r$.

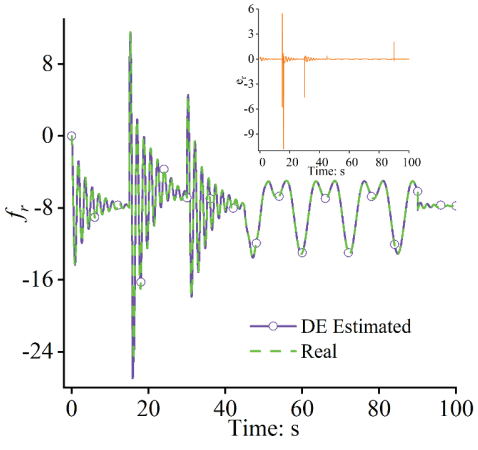

Figure 13. Uncertainty estimations: −30% and estimation error $e_r = f_r - \hat{f}_r$.

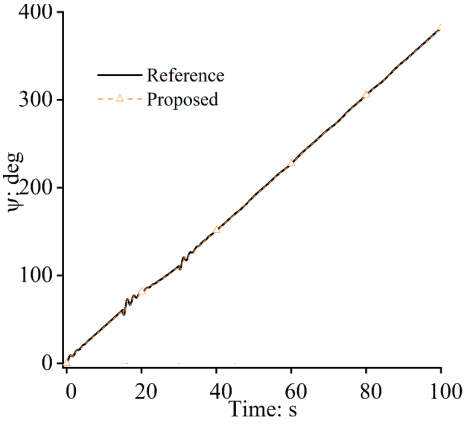

Figure 14. Yaw angles: +30%.

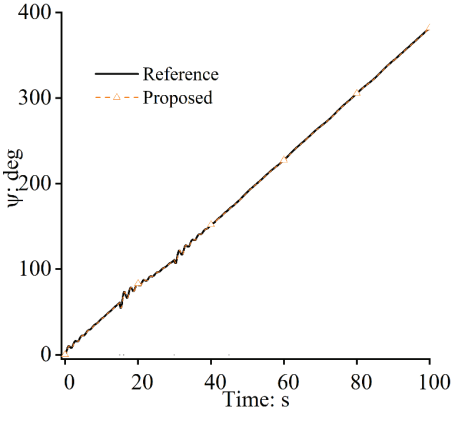

Figure 15. Yaw angles: −30%.

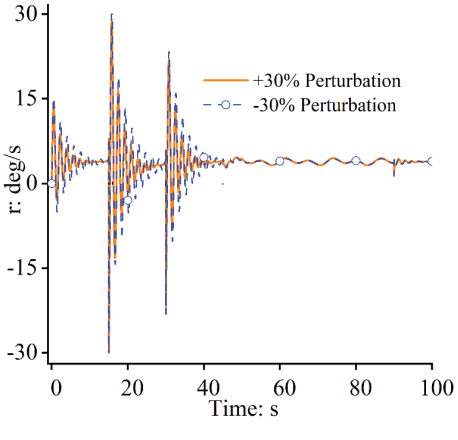

Figure 16. Yaw rates.

5. Conclusions

In this study, a novel, robust flight control system was designed for FWUAVs following curved paths under uncertainties on the latitude plane. Without using any model information, the desired yaw angle can be derived by using path-following errors, flow angles, and the current yaw angle. The model-free approach for deriving the desired yaw angle is easy to implement in hardware for engineering applications, and it dramatically reduces the burden of flight control computers. For the yaw angle control, firstly, though the yaw movement system is full of nonlinearities, couplings, time variations, and external winds, which would seriously degrade flight performance, the designed disturbance estimator can estimate all the uncertainties existing in the yaw movement model accurately for feedback compensation such that the path-following accuracy can be improved significantly. The path-following errors for the x and y directions are only 0.02 m and 2 m, respectively, compared with 0.12 m and 12 m for the NDI approach. Secondly, due to the existence of the disturbance estimator, the frame parameters of FWUAVs are allowed to perturb within a wide range between −30% and +30%. Through consuming quite a similar amount of input power (the deflection angles of the rudder), almost the same path-following control performance with very small path-following errors can be achieved. The yaw system has strong robustness in dealing with uncertainties, which allows the desired yaw angle of the position system to be tracked precisely. The yaw rate has small fluctuations in situations where external wind fields are encountered. However, the yaw rate can return to a stable value within a short time period.

Author Contributions: Conceptualization, M.T. and W.Q.; Methodology, W.Q.; Validation, W.Q.; Formal analysis, W.Q.; Investigation, Q.W.; Resources, W.S.; Writing—original draft, W.Q.; Writing—review & editing, M.T.; Supervision, H.Y. All authors have read and agreed to the published version of the manuscript.

Funding: This research received no external funding.

Institutional Review Board Statement: Not applicable.

Informed Consent Statement: Not applicable.

Data Availability Statement: The supporting information is shared and available online by visiting https://github.com/maggie48dy/english-nal (accessed on 22 October 2023).

Conflicts of Interest: The authors declare no conflict of interest.

References

1. Nelson, R.C. *Flight Stability and Automatic Control*; The McGraw-Hill Companies Press: New York, USA, 1989.
2. Ambrosino, G.; Ariola, M.; Ciniglio, U.; Corraro, F.; De Lellis, E.; Pironti, A. Path generation and tracking in 3-D for UAVs. *IEEE Trans. Control Syst. Technol.* **2009**, *17*, 980–988. [CrossRef]
3. Woo, J.W.; An, J.Y.; Cho, M.G.; Kim, C.J. Integration of path planning, trajectory generation and trajectory tracking control for aircraft mission autonomy. *Aerosp. Sci. Technol.* **2021**, *118*, 107014. [CrossRef]
4. Tan, G.Y.; Luo, H.B.; Liao, F.; Wang, X.H.; Ji, H.B. Cooperative Strategy for Aircraft Defense Line-of-Sight Guidance in Three-Dimensional Space. In Proceedings of the 2022 41st Chinese Control Conference (CCC), Hefei, China, 25–27 July 2022; pp. 3398–3403.
5. Gu, J.C.; Ding, G.R.; Xu, Y.T.; Wang, H.C.; Wu, Q.H. Proactive optimization of transmission power and 3D trajectory in UAV-assisted relay systems with mobile ground users. *Chin. J. Aeronaut.* **2021**, *34*, 129–144. [CrossRef]
6. Rymer, N.; Moore, A.J.; Young, S.; Glaab, L.; Smalling, K.; Consiglio, M. Demonstration of Two Extended Visual Line of Sight Methods for Urban UAV Operations. In Proceedings of the AIAA AVIATION 2020 Forum, Virtual, 15–19 June 2020; p. 2889.
7. Li, S.W.; Gu, Y.X.; Subedi, B.; He, C.Y.; Wan, Y.; Miyaji, A.; Higashino, A. Beyond Visual Line of Sight UAV Control for Remote Monitoring using Directional Antennas. In Proceedings of the 2019 IEEE Globecom Workshops, Waikoloa, HI, USA, 9–13 December 2019; pp. 1–6.
8. Nelson, D.R.; Blake Barber, D.; McLain, T.W.; Beard, R.W. Vector Field Path Following for Miniature Air Vehicles. *IEEE Trans. Robot.* **2007**, *23*, 519–529. [CrossRef]
9. Wilhelm, J.; Clem, G.; Casbeer, D.; Gerlach, A. Circumnavigation and obstacle avoidance guidance for UAVs using Gradient Vector Fields. In Proceedings of the AIAA Sci tech 2019 Forum, San Diego, CA, USA, 7–11 January 2019; pp. 1–15.

10. Wilhelm, J.P.; Clem, G. Vector Field UAV Guidance for Path Following and Obstacle Avoidance with Minimal Deviation. *J. Guid. Control Dyn.* **2019**, *42*, 1848–1856. [CrossRef]
11. Chang, K.; Ma, D.L.; Han, X.B.; Liu, N.; Zhang, B.B. Lyapunov vector-based formation tracking control for unmanned aerial vehicles with obstacle/collision avoidance. *Trans. Inst. Meas. Control* **2020**, *42*, 1–8. [CrossRef]
12. Luo, Y.L.; Huang, X.Y.; Wu, C.F.; Leng, S.P. Enhanced Artificial Potential Field-based Moving Obstacle Avoidance for UAV in Three-Dimensional Environment. In Proceedings of the 2020 IEEE 16th International Conference on Control & Automation (ICCA), Singapore, 9–11 October 2020; pp. 177–182.
13. Zheng, X.; Galland, S.; Tu, X.; Yang, Q.; Lombard, A.; Gaud, N. Obstacle avoidance model for UAVs with joint target based on multi-strategies and follow-up vector field. In Proceedings of the 11th International Conference on Ambient Systems, Networks and Technologies (ANT), Warsaw, Poland, 6–9 April 2020; pp. 257–264.
14. Wang, X.; Wang, H.; Lun, Y.B. Shortest Path Planning of UAV for Target Tracking and Obstacle Avoidance in 3D Environment. In Proceedings of the 39th Chinese Control Conference, Shenyang, China, 27–29 July 2020; pp. 3385–3390.
15. Park, S.; Deyst, J.; How, J.P. Performance and Lyapunov stability and of a nonlinear path following guidance method. *J. Guid. Control Dyn.* **2007**, *30*, 1718–1728. [CrossRef]
16. Rucco, A.; Aguiar, A.P.; Pereira, F.L.; de Sousa, J.B. A Predictive Path-Following Approach for Fixed-Wing Unmanned Aerial Vehicles in Presence of Wind Disturbances. In Proceedings of the Robot 2015: Second Iberian Robotics Conference, Lisbon, Portugal, 2 December 2015; pp. 623–634.
17. Yamasaki, T.; Balakrishnan, S.N.; Takano, H. Separate-Channel Integrated Guidance and Autopilot for Automatic Path-Following. *J. Guid. Control Dyn.* **2013**, *36*, 25–34. [CrossRef]
18. Rysdyk, R. Unmanned Aerial Vehicle Path Following for Target Observation in Wind. *J. Guid. Control Dyn.* **2006**, *29*, 1092–1100. [CrossRef]
19. Chen, Q.; Wang, X.G.; Yang, J.; Wang, Z.Y. Trajectory-following guidance based on a virtual target and an angle constraint. *Aerosp. Sci. Technol.* **2019**, *87*, 448–458. [CrossRef]
20. Cai, Z.H.; Wang, L.H.; Zhao, J.; Wu, K.; Wang, Y.X. Virtual target guidance-based distributed model 4 predictive control for formation control of multiple 5 UAVs. *Chin. J. Aeronaut.* **2020**, *33*, 1037–1056. [CrossRef]
21. Chen, H.; Wang, X.K.; Shen, L.C.; Cong, Y.R. Formation flight of fixed-wing UAV swarms: A 4 group-based hierarchical approach. *Chin. J. Aeronaut.* **2021**, *34*, 504–515. [CrossRef]
22. Mao, Y.H.; Chen, Q.Y.; Hou, Z.X.; Zheng, G. An improved nonlinear guidance law for unmanned aerial vehicles path following. In Proceedings of the 2015 34th Chinese Control Conference (CCC), Hangzhou, China, 28–30 July 2015; pp. 5271–5276.
23. Park, S.; Deyst, J.; How, J. A New Nonlinear Guidance Logic for Trajectory Tracking. In Proceedings of the AIAA Guidance, Navigation, and Control Conference and Exhibit, Providence, RI, USA, 16–19 August 2004; pp. 1–16.
24. Zhou, W.H.; Li, J.; Liu, Z.H.; Shen, L.C. Improving multi-target cooperative tracking guidance for UAV swarms using multi-agent reinforcement learning. *Chin. J. Aeronaut.* **2022**, *35*, 100–112. [CrossRef]
25. Ueba, M.; Takaku, Y.; Takahashi, K.; Kamata, T. Design and Tests of Guidance and Control Systems for Autonomous Flight of a Low-Speed Model Airplane for Application to a Small-Scale Unmanned Supersonic Airplane. *Trans. Jpn. Soc. Aeronaut. Space Sci. Aerosp. Technol. Jpn.* **2019**, *17*, 220–226. [CrossRef]
26. Modali, S.; Ghosh, S. Terminal-Angle-Constrained Guidance based on Sliding Mode Control for UAV Soft Landing on Ground Vehicles. *Electr. Eng. Syst. Sci.* **2020**, *2009*, 14748.
27. Yin, H.; Li, D.G.; Wang, Y.; Li, X.P. Adaptive Dynamic Occupancy Guidance for Air Combat of UAV. *Unmanned Syst.* **2023**, *11*, 1–18. [CrossRef]
28. Tan, Y.Y.; Tang, W.X. Guidance Strategy for UAV Tracking Target Based on Reference Point Guidance Method. *J. Northwest. Polytech. Univ.* **2020**, *38*, 176–182. [CrossRef]
29. Cui, Z.Y.; Wang, Y. Nonlinear Adaptive Line-of-Sight Path Following Control of Unmanned Aerial Vehicles considering Sideslip Amendment and System Constraints. *Math. Probl. Eng.* **2020**, *2020*, 1–11. [CrossRef]
30. Wang, Y.Z.; Wang, D.W.; Zhu, S.Q. Cooperative moving path following for multiple fixed-wing unmanned aerial vehicles with speed constraints. *Automatica* **2019**, *100*, 82–89. [CrossRef]
31. Ma, C.; Yang, J.; Chen, J.Y.; Zhou, C. Path following identification of unmanned aerial vehicles for navigation spoofing and its application. *ISA Trans.* **2021**, *108*, 393–405. [CrossRef]
32. Sedlmair, N.; Theis, J.; Thielecke, F. Design and Experimental Validation of UAV Control Laws—3D Spline-Path-Following and Easy-Handling Remote Control. In Proceedings of the 5th CEAS Conf. Guid., Navigation, Control, Milano, Italy, 3–5 April 2019; pp. 1–20.
33. Kaminer, I.; Pascoa, A.; Xargay, E.; Hovakimyan, N.; Cao, C.Y.; Dobrokhodov, V. Path following for unmanned aerial vehicles using L1 adaptive augmentation of commercial autopilots. *J. Guid. Control Dyn.* **2010**, *33*, 550–564. [CrossRef]
34. Liu, C.J.; McAree, O.; Chen, W.H. Path-following control for small fixed-wing unmanned aerial vehicles under wind disturbances. *Int. J. Robust. Nonlinear Control* **2013**, *23*, 1682–1698. [CrossRef]
35. Beard, R.W.; Ferrin, J.; Humpherys, J. Fixed wing UAV path following in wind with input constraints. *IEEE Trans. Control Syst. Technol.* **2014**, *22*, 2103–2117. [CrossRef]
36. Gavilan, F.; Vazquez, R.; Camacho, E.F. An iterative model predictive control algorithm for UAV guidance. *IEEE Trans. Aerosp. Electron. Syst.* **2015**, *51*, 2406–2419. [CrossRef]

37. Yang, J.; Liu, C.J.; Coombes, M.; Yan, Y.D.; Chen, W.H. Optimal path following for small fixed-wing UAVs under wind disturbances. *IEEE Trans. Control Syst. Technol.* **2020**, *29*, 996–1008. [CrossRef]
38. Jackson, S.; Tisdale, J.; Kamgarpour, M.; Basso, B.; Karl Hedrick, J. Tracking controllers for small UAVs with wind disturbances: Theory and flight results. In Proceedings of the 2008 47th IEEE Conference on Decision and Control, Cancun, Mexico, 9–11 December 2008; pp. 564–569.
39. Kothari, M.; Postlethwaite, I.; Gu, D.W. A suboptimal path planning algorithm using rapidly-exploring random trees. *Int. J. Aerosp. Innov.* **2010**, *2*, 93–104.
40. Brezoescu, A.; Espinoza, T.; Castillo, P.; Lozano, R. Adaptive trajectory following for a fixed-wing UAV in presence of crosswind. *J. Intell. Robot. Syst.* **2013**, *69*, 257–271. [CrossRef]
41. Wang, Y.; Cai, H.M.; Zhang, J.M.; Li, X.B. Disturbance attenuation predictive optimal control for quad-rotor transporting unknown varying payload. *IEEE Access* **2020**, *8*, 44671–44686. [CrossRef]
42. Wang, Y.; Zheng, Y.M. Path following of Nano quad-rotors using a novel disturbance observer-enhanced dynamic inversion approach. *Aeronaut. J.* **2019**, *123*, 1122–1134. [CrossRef]
43. Abro, G.E.M.; Zulkifli, S.A.B.M.; Asirvadam, V.S. Dual-loop single dimension fuzzy-based sliding mode control design for robust tracking of an underactuated quadrotor craft. *Asian J. Control* **2023**, *25*, 144–169. [CrossRef]
44. Zhao, S.L.; Wang, X.K.; Zhang, D.B.; Shen, L.C. Curved Path Following Control for Fixed-wing Unmanned Aerial Vehicles with Control Constraint. *J. Intell. Robot. Syst.* **2017**, *89*, 107–119. [CrossRef]
45. Abro, G.E.M.; Zulkifli, S.A.B.M.; Ali, Z.A.; Asirvadam, V.S.; Chowdhry, B.S. Fuzzy Based Backstepping Control Design for Stabilizing an Underactuated Quadrotor Craft under Unmodelled Dynamic Factors. *Electronics* **2022**, *11*, 999. [CrossRef]
46. Chen, H.; Wang, X.; Shen, L.; Yu, Y. Coordinated path following control of fixed-wing unmanned aerial vehicles in wind. *ISA Trans.* **2022**, *122*, 260–270. [CrossRef] [PubMed]
47. Sujit, P.B.; Saripalli, S.; Sousa, J.B. Unmanned aerial vehicle path following: A survey and analysis of algorithms for fixed-wing unmanned aerial vehicles. *IEEE Control Syst. Mag.* **2014**, *34*, 42–59.
48. Mustafa Abro, G.E.; Ali, Z.A.; Zulkifli, S.A.; Asirvadam, V.S. Performance evaluation of different control methods for an underactuated quadrotor unmanned aerial vehicle (QUAV) with position estimator and disturbance observer. *Math. Probl. Eng.* **2021**, *2021*, 1–22. [CrossRef]
49. Beard, R.W.; Mclain, T.W. *Small Unmanned Airplane: Theory and Practice*; Princeton University Press: Princeton, NJ, USA, 2012.
50. Zhou, L.; Lin, J.; Sun, J.Z.; Fu, H.M.; Wan, Q. Predictive Functional Control for Linear Motor Speed System Based on Repetitive Sliding Mode Observer. In Proceedings of the 2021 40th Chinese Control Conference (CCC), Shanghai, China, 26–28 July 2021; pp. 2633–2638.
51. Xiang, Y.; Liu, Z.L.; Wang, L.M. Genetic-algorithm-optimization-based predictive functional control for chemical industry processes against partial actuator faults. *IEEE Access* **2020**, *8*, 214586–214595. [CrossRef]
52. Zhou, Y.; Ho, H.W.; Chu, Q.P. Extended incremental nonlinear dynamic inversion for optical flow control of micro air vehicles. *Aerosp. Sci. Technol.* **2021**, *116*, 106889. [CrossRef]
53. Fan, Z.H.; Liu, L. The high angle of attack aerodynamic modeling and nonlinear dynamic inversion flight control law design. In Proceedings of the 2012 IEEE 10th International Conference on Industrial Informatics, Beijing, China, 25–27 July 2012; pp. 901–905.
54. Jayaraman, B.; Ghosh, A.K. Cascaded and Non-Cascaded Incremental Nonlinear Dynamic Inversion Flight Control Applied to a Light Aircraft. In Proceedings of the 2021 Australian & New Zealand Control Conference (ANZCC), Gold Coast, Australia, 25–26 November 2021; pp. 189–194.

applied sciences

MDPI

Review

Power Sources for Unmanned Aerial Vehicles: A State-of-the Art

Yavinaash Naidu Saravanakumar [1], Mohamed Thariq Hameed Sultan [1,2,3,*], Farah Syazwani Shahar [1], Wojciech Giernacki [4], Andrzej Łukaszewicz [5], Marek Nowakowski [6,*], Andriy Holovatyy [7] and Sławomir Stępień [8]

[1] Department of Aerospace Engineering, Faculty of Engineering, University Putra Malaysia, UPM Serdang, Serdang 43400, Selangor, Malaysia; yavinaash1399@gmail.com (Y.N.S.); farahsyazwani@upm.edu.my (F.S.S.)
[2] Laboratory of Biocomposite Technology, Institute of Tropical Forestry and Forest Products (INTROP), University Putra Malaysia, UPM Serdang, Serdang 43400, Selangor, Malaysia
[3] Aerospace Malaysia Innovation Centre (944751-A), Prime Minister's Department, MIGHT Partnership Hub, Jalan Impact, Cyberjaya 63000, Selangor, Malaysia
[4] Institute of Robotics and Machine Intelligence, Faculty of Control, Robotics and Electrical Engineering, Poznan University of Technology, 60-965 Poznan, Poland; wojciech.giernacki@put.poznan.pl
[5] Institute of Mechanical Engineering, Faculty of Mechanical Engineering, Bialystok University of Technology, 15-351 Bialystok, Poland; a.lukaszewicz@pb.edu.pl
[6] Military Institute of Armoured and Automotive Technology, 05-070 Sulejowek, Poland
[7] Department of Computer-Aided Design Systems, Lviv Polytechnic National University, 79013 Lviv, Ukraine
[8] Airplanes and Helicopters Division, Air Force Institute of Technology, 01-494 Warszawa, Poland
* Correspondence: thariq@upm.edu.my (M.T.H.S.); marek.nowakowski@witpis.eu (M.N.)

Abstract: Over the past few years, there has been an increasing fascination with electric unmanned aerial vehicles (UAVs) because of their capacity to undertake demanding and perilous missions while also delivering advantages in terms of flexibility, safety, and expenses. These UAVs are revolutionizing various public services, encompassing real-time surveillance, search and rescue operations, wildlife assessments, delivery services, wireless connectivity, and precise farming. To enhance their efficiency and duration, UAVs typically employ a hybrid power system. This system integrates diverse energy sources, such as fuel cells, batteries, solar cells, and supercapacitors. The selection of an appropriate hybrid power arrangement and the implementation of an effective energy management system are crucial for the successful functioning of advanced UAVs. This article specifically concentrates on UAV platforms powered by batteries, incorporating innovative technologies, like in-flight recharging via laser beams and tethering. It provides an all-encompassing and evaluative examination of the current cutting-edge power supply configurations, with the objective of identifying deficiencies, presenting perspectives, and offering recommendations for future consideration in this domain.

Keywords: UAV; power supply; battery swapping; laser beam inflight charging; tethered UAV; batteries; battery systems; materials of batteries; efficiency; duration; hybrid power system; energy management system

Citation: Saravanakumar, Y.N.; Sultan, M.T.H.; Shahar, F.S.; Giernacki, W.; Łukaszewicz, A.; Nowakowski, M.; Holovatyy, A.; Stępień, S. Power Sources for Unmanned Aerial Vehicles: A State-of-the Art. *Appl. Sci.* **2023**, *13*, 11932. https://doi.org/10.3390/app132111932

Academic Editor: Yutaka Ishibashi

Received: 18 August 2023
Revised: 13 October 2023
Accepted: 28 October 2023
Published: 31 October 2023

1. Introduction

An unmanned aerial vehicle (UAV), also referred to as a flying robot or drone, possesses the ability to operate independently or under remote control for specific missions [1]. In recent times, UAVs have garnered considerable attention as a result of advancements in microprocessors [2,3] and artificial intelligence (AI) [4–7], sensors [8–14], and the design [15–18] and manufacturing process [16–20], facilitating the creation of intelligent UAVs. The term "intelligent UAVs" refers to these drones' capacity to operate autonomously or semi-autonomously, making real-time decisions based on data from their sensors and AI algorithms. These intelligent UAVs can adapt to changing environments, navigate with precision, and perform tasks with a level of autonomy that was once reserved for science fiction [21]. Moreover, the UAV wireless charging system represents a significant departure

from conventional cable-based charging methods. This innovation has attracted substantial interest in the field [22], as it offers a promising alternative to traditional charging mechanisms, further enhancing the appeal of UAV technology. These technologically advanced UAVs offer a multitude of benefits, including cost efficiency and exceptional maneuverability, leading to their utilization in diverse military and civilian domains such as mine clearance, surveillance, delivery services, wireless connectivity, and agriculture [23,24]. It is crucial to highlight that UAVs have significant advantages over UGV operational requirements [25], but UGVs are preferred for heavy-load missions due to their ability to carry substantial payloads [26]. Prominent multinational corporations are making substantial investments to enhance UAV capabilities and expand their application spectrum. Nowadays detection techniques improve safe and reliable UAV operations due to fault detection methods [27]. It is estimated that the market value of UAVs will reach a staggering USD 127 billion by 2022 [28,29]. This surge is propelled by remarkable advancements in microprocessors, artificial intelligence (AI), sensors, design, and manufacturing processes. Recent statistics and trends underscore their growing significance, as UAVs have become integral in numerous real-world applications. For instance, in 2021, the global drone market was valued at USD 22.5 billion, and it is projected to reach a staggering USD 42.8 billion by 2026 [28,29]. These numbers reflect not only the market's explosive growth but also the increasing adoption of UAVs across various sectors. From precision agriculture to search and rescue missions, surveillance, and even package delivery services, the ubiquity of UAVs is a testament to their versatile and dynamic role in modern society.

UAVs exhibit diverse features and configurations that are tailored to meet specific mission demands. Consequently, the literature provides multiple classifications that emphasize various parameters [30,31]. In terms of their physical structure, UAVs can be classified into distinct categories such as fixed-wing, rotary-wing, flapping-wing, hybrid, or balloon configurations. When considering their dimensions, UAVs come in different sizes, including mini, micro, and nano variations. The North Atlantic Treaty Organization (NATO) has established a classification system for UAVs, grouping them into three classes based on their maximum take-off weight (MTOW). Each class is further divided into subcategories, which take into account factors such as altitude and mission radius [32].

Electric UAVs are favored for their advantageous characteristics, such as their reliability [33], reduced noise, disturbance rejection [34] and thermal signatures [35,36], high efficiency [5], absence of pollutant emissions, self-starting capabilities, and advanced control mechanisms that enable exceptional maneuverability. For instance, electric UAVs have excelled in urban environments where noise and emissions regulations are stringent. They are being utilized for tasks like monitoring traffic, delivering medical supplies, or capturing aerial footage with minimal disruption. On the other hand, internal combustion engine (ICE)-based UAVs offer longer endurance due to the high power and energy densities of ICE. Thus, ICE-based UAVs, with their extended endurance, still have their place in missions requiring long flight durations, such as search and rescue operations in remote areas or the surveillance of large, sparsely populated regions. The choice between electric and ICE-based UAVs often depends on the specific demands of the mission and the environmental considerations [35]. However, they necessitate an auxiliary starting motor, involve more complex control demands [37], and generate high acoustic and thermal signatures. Some researchers [38,39] have explored hybrid architectures that combine electric motors with ICE to harness the advantages of both engine types. Nevertheless, the depletion of fossil fuels and the growing concerns regarding greenhouse gas (GHG) emissions have diminished the appeal of thermal engines, prompting the adoption of electric propulsion as a sustainable technology across various sectors, including transportation [40]. International policies and market trends that aim to phase out ICE vehicles [41] are expected to extend to UAVs in the foreseeable future, fostering the development of environmentally friendly devices. The shift away from ICE in UAVs, particularly for tasks that do not require extensive endurance, can be attributed to these factors.

Batteries serve as the primary source of electric power, but their flight durations in UAVs are limited by their low energy density and long-lasting charging time [41] similar to all unmanned types of unmanned vehicles [42]. These challenges are common to various types of unmanned vehicles. In addition to energy density and charging time concerns, the safety of battery energy storage systems has become a paramount consideration, especially in light of the increasing use of electric vehicles [43]. Monitoring the state of charge (SOC) and battery temperature has proven to be instrumental in enabling comprehensive decision-making within the system, ultimately enhancing safety and performance. Furthermore, batteries may not offer the required power response for rapid maneuvers due to their slow power dynamics. To address these limitations, supercapacitors present a suitable option for balancing the constraints imposed by batteries [44]. It should be noted that flight endurance can be improved through aerodynamic optimization during the UAV design phase [45]. Recent advancements in battery technology have slightly extended endurance to approximately 90 min using lithium polymer (LiPo) batteries [46]. However, increasing the number of batteries becomes impractical due to weight and space limitations. One of the key challenges is the limited energy density of batteries, which constrains the amount of energy that can be stored within a given weight and volume [47]. This limitation impacts the flight duration and payload capacity of electric UAVs, making it a critical consideration in mission planning. Additionally, batteries exhibit slow power dynamics, meaning they may not provide the rapid power response required for sudden maneuvers or emergencies. These challenges are central to the quest for improving the endurance and overall capabilities of electric UAVs [22]. To enhance UAV endurance, additional power sources must be employed to supplement batteries while adhering to weight and space constraints. In this regard, fuel cells offer a promising solution due to their high specific energy and near instantaneous refueling capability. They can typically achieve up to five times higher energy density than LiPo batteries, significantly enhancing the endurance of hybrid UAVs [48]. It is worth mentioning that many existing electric UAVs utilize fuel cells as their primary power source. Supercapacitors can also contribute to the power supply process due to their high-power density and rapid response to peak power demands during UAV take-off and sudden maneuvers. They excel in providing high power density, enabling electric UAVs to execute swift maneuvers and respond promptly to changing flight conditions. Additionally, supercapacitors boast a longer cycle life, meaning they can endure a higher number of charge and discharge cycles without significant degradation. The combination of batteries and supercapacitors in a hybrid system capitalizes on the strengths of both technologies, optimizing energy storage and delivery for UAVs. Fixed-wing UAVs have the advantage of incorporating solar cells and harnessing solar energy, which can reduce fuel consumption and greatly enhance endurance when combined with an energy storage system [49].

Therefore, in order to achieve longer endurance for UAVs, it becomes necessary to employ hybrid power supply systems that combine multiple power sources. The selection of the power supply system structure is crucial and depends not only on the characteristics of the power sources but also on the specific mission requirements of the UAV. To effectively manage the distribution of power among the onboard power sources and ensure optimal performance and efficiency for the intended mission, the implementation of an energy management system (EMS) is essential. An EMS is a sophisticated control system that plays a pivotal role in efficiently managing the distribution of power among the UAV's onboard power sources. It employs a combination of current and voltage sensors for monitoring power flow, converters for regulating the power source outputs, and a processing unit responsible for executing the adopted power management strategy. The EMS ensures that power is allocated optimally, enabling the UAV to meet its specific mission requirements. In addition to hybridization, there are alternative techniques available to extend the endurance of battery-based UAVs. These techniques include battery swapping [50,51], in-flight recharging using laser beams [52–55], and tethered UAVs [56–58]. Battery swapping involves replenishing depleted batteries of a UAV during its mission by

utilizing ground stations located at specific locations. In-flight recharging utilizes a laser beam transmitted from a generator at a ground station to provide light power, enabling recharging without the need for landing. Tethered UAVs have the advantage of unlimited endurance as they receive a continuous power supply through connection lines that link the UAV to a ground-based power supply station.

Numerous review papers in the literature have extensively covered various aspects of UAVs. These include topics such as fuel storage and generation in small fixed-wing UAVs [41], the classification, advancements, and research trends in small-scale UAVs [58], the classification and design challenges of UAVs [30], path planning algorithms for fixed-wing UAVs [59], the guidance, navigation, and control of rotorcraft unmanned aircraft systems [60], and the modeling and control of quadrotors [61]. However, the specific focus of this review is centered on the energy aspect of UAVs. Its objective is to provide a comprehensive and critical assessment of the existing power supply structures [62] and their corresponding energy management systems. This review will not only identify any existing gaps but also provide valuable recommendations and prospects to guide future research in this field.

2. Unmanned Aerial Vehicle (UAV)

Prior to discussing the various power sources, it is important to provide a brief introduction to the two main types of UAVs, as illustrated in Figure 1. These types are rotary-wing UAVs and fixed-wing UAVs. Rotary-wing UAVs are characterized by a body structure that incorporates multiple rotors for propulsion. In contrast, fixed-wing UAVs resemble conventional aircraft, featuring fixed wings on either side of the body. Rotary-wing UAVs, also known as rotorcraft types, have gained popularity due to their ability to perform vertical take-off and landing, eliminating the need for a runway or launcher. They are capable of hovering in the air and exhibit exceptional agility, making them well-suited for precise maneuvering tasks. However, the design of rotary-wing UAVs involves mechanical and electronic complexities, resulting in more intricate maintenance procedures, reduced operational time, and increased costs. Additionally, rotary-wing UAVs generally have lower payload capacities, higher power requirements, shorter operational durations, and even higher costs.

(**a**) (**b**)

Figure 1. Two types of drones: (**a**) fixed-wing drone, (**b**) rotary-wing drone.

Fixed-wing UAVs present several advantages over rotary-wing UAVs. They possess a simpler structure, leading to easier maintenance and improved aerodynamics, resulting in reduced operational costs and increased flight time. The presence of fixed wings enables natural gliding capabilities, leading to lower power consumption. Additionally, fixed-wing UAVs can carry larger payloads over longer distances with less power, enhancing efficiency and cost-effectiveness. However, they require a runway or launching device for take-off and landing, lack the hovering capability of rotary-wing UAVs, and tend to be larger and bulkier, compromising maneuverability. In addition to rotary-wing and fixed-wing UAVs, there is a unique type of drone that combines the characteristics of both. This hybrid drone

offers the stability and maneuverability of a rotary-wing drone along with the extended flight range of a fixed-wing drone. Importantly, it does not require a runway or additional equipment for take-off. Figure 2 provides an illustration of this combination drone. Each type of UAV—rotary-wing, fixed-wing, and hybrid—has its own applications that align with their respective advantages and disadvantages. Moreover, various power sources are employed in these drones.

Rotary-wing UAVs are highly versatile, excelling in tasks that require precision and agility, such as surveillance, search and rescue, and monitoring. They are ideal for stable and controlled aerial observation in confined spaces and urban environments. On the other hand, fixed-wing UAVs are preferred for endurance and long-range missions, making them suitable for tasks like precision agriculture, mapping, wildlife tracking, border patrols, and high-speed data collection in expansive areas. The choice between these UAV types depends on the specific mission requirements and operational constraints.

The unmanned aerial vehicle (UAV) platform, depicted in Figure 2, comprises several essential components. Firstly, there is an onboard flight control system encompassing processing units that handle various tasks, including implementing guidance, navigation, and control (GNC) algorithms, collecting and analyzing in-flight data, establishing communication with the ground station, and planning mission activities. Secondly, a propulsion system is integrated, which consists of multiple elements such as power supply sources, speed controllers, converters, energy management systems, motors, and propellers. These components work together to generate the required thrust and control the UAV's speed. Thirdly, the UAV is equipped with sensors that enable autonomous flight by providing crucial feedback and accurate measurements about the surrounding environment. Lastly, there is the payload, which includes additional equipment necessary for specific missions. This may comprise actuators, cameras, radar systems, or other specialized tools and instruments [63].

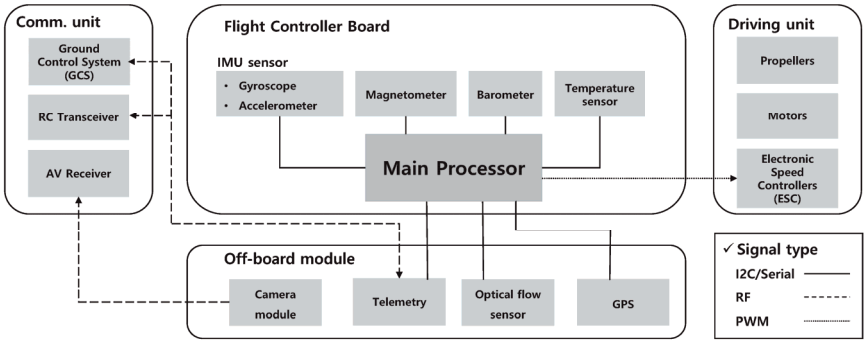

Figure 2. A typical UAV block diagram [64].

The propulsion system of a UAV plays a critical role as it consumes a significant portion of the onboard power. Its main purpose is to convert stored electrical energy into mechanical power, which propels the UAV through the motor propeller system called a propulsion unit. In fact, the propulsion system can constitute more than half of the total weight of the UAV. Figure 3 provides a typical schematic diagram of a UAV propulsion system. The power from the onboard sources is supplied to the DC bus through unidirectional and bidirectional converters, allowing for battery charging and discharging. These converters enable control over the power flow and receive control signals from the energy management system (EMS), which manages power distribution. Among the various motor types utilized in small UAVs, the brushless DC (BLDC) motor is widely preferred. This motor type offers significant advantages, including high efficiency and power density [65], as well as features such as high speed, favorable torque characteristics, reliability, ease of control via electronic speed controllers, ESCs, and long lifespan [66]. While induction motors are cost-effective

and robust, they have limitations such as relatively low efficiency, cooling challenges, and lower torque output.

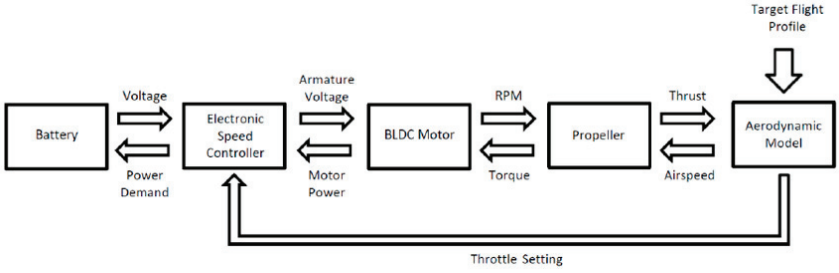

Figure 3. UAV propulsion system block diagram.

2.1. Unmanned Aerial Vehicle (UAV) Power Sources

Gas turbine engines have been widely used in aircraft propulsion systems due to their favorable power-to-weight ratio [67] and extended operational duration [30]. Gas turbine engines operate on the principle of air compression, combustion, and exhaust propulsion. They intake air, compress it, mix it with fuel for combustion, and then release the high-velocity exhaust gases to produce thrust. These engines are known for their high power-to-weight ratio, making them suitable for fast and agile UAVs. However, their optimal performance is limited to high-power ranges [68], typically above 100 hp [69]. As a result, they are not suitable for small-scale UAV applications, as they exhibit drawbacks such as inefficiency in fuel consumption, low overall efficiency, and high noise levels [70]. In contrast, the internal combustion engine (ICE) has traditionally served as the cornerstone of aircraft propulsion systems [71,72]. These engines are characterized by their energy density, making them suitable for long-endurance missions in UAVs. Compared to electric motors (EMs), ICEs offer advantages in terms of higher fuel energy and power densities, enabling longer flight times and larger payload capacities, which are crucial factors in flight missions. However, the multi-step energy production process in ICEs results in decreased system efficiency [56]. EMs are the preferred choice for UAVs due to their distinct characteristics, including minimal thermal and acoustic signatures, well-established electronic control systems, adaptability to automatic control, self-starting capabilities [37], cost-effectiveness, and higher reliability, which minimizes the risk of crashes caused by motor shutdown or failure. It should be noted that electric propulsion systems may encounter electronic speed controller (ESC) failures due to issues such as overheating and melting of the ESC casing. One potential solution to mitigate this problem is duplicating components [73].

A research paper [37] introduced a novel hybrid power propulsion prototype for unmanned aircraft systems (UAS), aiming to combine the advantages of thermal and electric engines. Although simulation results showed a 13% improvement in endurance, the system was considered complex and not environmentally friendly. Other researchers [73] have also discussed hybrid parallel powertrain architectures using electric motors (EMs) and internal combustion engines (ICEs). However, the incorporation of ICEs in UAVs is currently not the preferred solution due to limitations in fuel usage and endurance optimization. Therefore, this section will solely focus on electric propulsion-based UAVs and provide a critical evaluation of available electric power sources for UAV applications. Additionally, alternative supply strategies including swapping, laser beam inflight recharging, and tethered UAVs will be discussed, particularly for UAVs relying on a single power source.

2.2. Battery-Based Supply Techniques

2.2.1. Battery-Powered Unmanned Aerial Vehicles (UAVs)

Battery power is widely utilized in small UAVs, especially quadrotors, as it offers simplicity and flexibility to the propulsion system [71]. Battery-based platforms, particularly those using lithium batteries, such as LiPo batteries, are popular in hobbyist and

commercial applications due to their flight time capabilities and cost effectiveness. However, the endurance of small battery-powered UAVs is limited by the weight constraints of the battery pack, typically allowing for a maximum flight time of around 90 min using LiPo batteries [46]. LiPo batteries are preferred for small UAVs due to their lightweight nature and relatively high specific energy. In fact, LiPo batteries power the majority of micro aerial vehicles weighing less than 2 kg and with a length below 100 cm [30].

In selecting the appropriate battery technology for a given UAV application and mission, various characteristics such as specific energy, energy density, and specific power are taken into consideration. Table 1 provides detailed information on these characteristics for four different battery technologies, aiding in the battery technology selection process [44]. Additionally, in a specific study, different battery technologies were assessed based on the state of charge (SOC) for a particular mission, further emphasizing the importance of considering mission requirements when choosing battery technologies [58].

Table 1. Comparison of different batteries with their characteristics [57,58].

Characteristics	Ni-Cd	Ni-Mh	LiPo	Li-S
Specific energy (Wh/kg)	40	80	180	350
Energy density (Wh/L)	100	300	300	350
Specific power (W/kg)	300	900	2800	600

Ref. [74] focused on examining the factors that affect the performance of UAVs powered by batteries. Mathematical equations were developed to assess the UAV's range and endurance, taking into consideration the discharge conditions of the battery. The study establishes relationships to estimate the range and endurance of battery-powered aircraft, considering battery discharge rate and voltage drop effects. The research demonstrates that the Peukert effect can enhance range and endurance, particularly when battery capacity significantly exceeds current demand. Conversely, when the current draw approaches the battery's nominal capacity, effective capacity decreases. In situations with geometric constraints and a fixed battery weight as a fraction of the total aircraft weight, increasing battery capacity can lead to reduced performance due to higher power requirements and current draw.

One of the main challenges encountered by electric vehicles relying on battery power, including UAVs, is the limited autonomy they possess. Extensive efforts have been devoted to enhancing the performance of batteries in order to prolong operational duration and enable extended missions for electric vehicles. Despite the advancements made in battery technology, the specific energy of current batteries still poses limitations on the endurance and range of UAVs, which may not meet the requirements of numerous UAV applications. Additionally, improvements in energy density can have implications for the stability and safety levels [75]. To tackle these limitations, various solutions have been proposed in the existing body of literature. Fuel cells have emerged as a promising alternative due to their higher specific energy. Furthermore, numerous existing UAVs employ a hybrid configuration in their power supply, utilizing multiple energy sources such as batteries, fuel cells, solar cells, and supercapacitors. In practice, hybrid configurations integrate various power sources, such as batteries, fuel cells, solar cells, or generators, to work in harmony. The energy management system (EMS) plays a crucial role in optimizing power distribution among these sources to achieve enhanced efficiency and endurance [76].

The advantages of hybrid configurations over single-source systems are numerous. They offer improved endurance, as different sources can complement each other. For example, batteries can provide immediate power for take-off, while fuel cells or generators can sustain operations for longer durations. They enhance reliability by providing redundancy—if one source fails, others can take over. Additionally, hybrid systems can be more environmentally friendly, using cleaner energy sources in combination with traditional ones [76,77].

2.2.2. Swapping Method Algorithm

The technique known as swapping is employed to recharge the batteries of a UAV while it is in the midst of its mission. This process involves the exchange of depleted batteries with fully charged ones, which can be performed either autonomously or with human intervention. A specific type of swapping, called hot swapping, enables the immediate replacement of a depleted battery with a fully charged one, allowing the UAV to maintain power and continue its operation without interruption. Subsequently, the UAV can return to its assigned operational area and resume its tasks. By deploying multiple UAVs and coordinating their actions, a multi-agent system can ensure uninterrupted coverage of a specific area [34]. To successfully carry out a swapping operation, three important conditions must be fulfilled: (1) the presence of a ground recharge station where UAVs can land for battery charging or replacement, (2) a group of UAVs capable of continuous operation, and (3) a management system that facilitates cooperation among the swarm of UAVs. Figure 4 illustrates the techniques of swapping and hot swapping.

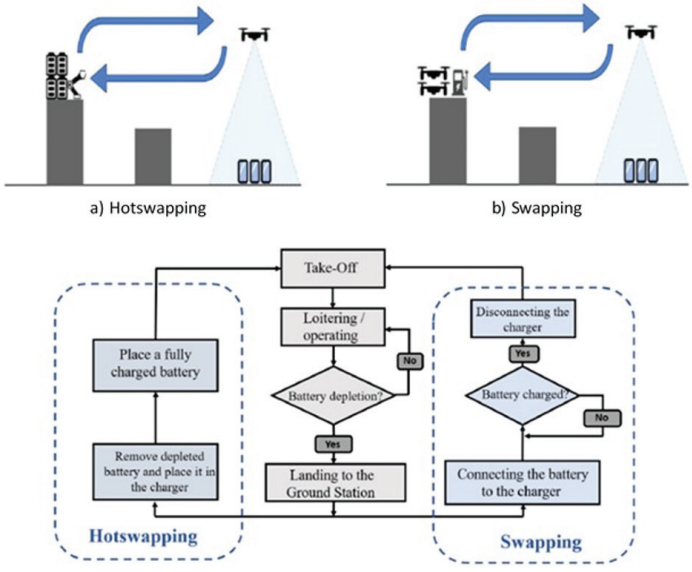

Figure 4. The swapping and hot swapping algorithms.

In the infrastructure network for UAVs, ground stations (GS), are strategically placed in various locations, such as cities or along connecting paths between cities. These GS can be installed on different structures like cell towers, streetlights, rooftops, power poles, or standalone pylons. As part of this infrastructure, battery swap stations are established, which consist of several components including ground electronics, an onboard circuit, a landing frame, and a contact mechanism. The batteries can be recharged through contact-based pathways or by utilizing inductive coupling. The docking platforms at the swap stations can be powered through a combination of power lines, large batteries, and solar cells, especially for stations located in remote areas.

There was also research that developed a multi-rotor aerial prototype specifically designed for long-duration missions using the swapping approach. The main goal of their study was to ensure the uninterrupted operation of the airborne platform by monitoring the battery's state of charge (SOC). Their concept involved having three quadcopters in a rotating system, with one quadcopter always in a loiter position. When the SOC of a quadcopter drops below a predetermined threshold, it is replaced by another quadcopter, allowing the former to return to the ground station for battery charging. This cycle continues until all batteries are depleted or the mission is completed. The number of batteries required

for sustainable operation depends on the discharge time and the duration needed for charging, rather than the number of UAVs. However, a larger number of batteries increases the system's resilience and reliability [34–36].

However, it is important to mention that the process of battery swapping and charging on the launch platform was not automated and still relied on human intervention. Additionally, the field test conducted in the study did not involve specific missions that required the use of sensors; instead, only static loitering was performed. In a separate study, researchers conducted an economic comparison of battery refilling and recharging platforms. They developed three stations based on axiomatic design principles, which allowed them to analyze and establish relationships between cost, complexity, and coverage levels [78]. This analysis provided valuable insights into the various factors associated with the implementation of battery refilling and recharging platforms.

The comparison between refilling and exchange stations has indicated that refilling stations are suitable for low-coverage scenarios, while exchange stations are preferable when higher coverage levels are required. In [79], research was conducted on a comparison of battery charging and replacement systems using a Petri net model. A Petri net model is a mathematical tool used to model and analyze systems with concurrent processes, making it relevant in designing efficient battery management systems. The authors also discussed in detail the design options for autonomous swapping stations, aiming to achieve precise UAV positioning for swapping regardless of landing errors. However, it is worth noting that the estimated swap time in their study was approximately one minute, which is relatively long compared to other studies researches. Moreover, the system was not fully operational, as certain modules were not prototyped or tested. In a separate study [57], a ground recharge station was designed for battery-powered quadrotor helicopters, and an algorithm was implemented to reduce the battery recharge duration. It can significantly reduce downtime and enhance the efficiency of quadrotor helicopters in applications like search and rescue, surveillance, delivery services, agriculture, infrastructure inspection, environmental monitoring, film production, and security. The proposed autonomous charging process utilized safer electrical contacts and a balancer specifically designed for swarm applications. It is important to mention that similar to the majority of the conducted studies, no experiments or flight tests were performed, and the study did not consider battery lifetime as a factor.

An automated refueling station for small-scale UAVs was designed and implemented in a study [80] to enable long-duration autonomous missions with multi-agent UAV systems. The study developed a planning and learning algorithm and tested it in a 3 h persistent flight involving 3 UAVs and over 100 battery swaps. The battery recharger mechanism used a linear sweeping motion, resulting in a simple and robust design. However, the cost of the system was not taken into account, and it should be noted that increasing the number of batteries and UAVs could potentially lead to a more expensive and complex system to manage. In a study [81], a swapping system based on online algorithms for energy management, UAV health monitoring, and accurate landing was proposed. The system utilized a servo-based lift for battery swaps and placed the batteries onto a horizontally mounted hexagonal mat for charging. However, this swap mechanism introduced power losses in the UAVs. While individual tests were conducted for all the components, the entire system was not tested as a whole. In another study [82], an autonomous docking platform was designed using active infrared imaging. The system operated during both day and night and incorporated a camera and an infrared filter to achieve high-precision landing.

In a study [73], a hardware platform was introduced featuring a dual-drum structure for efficient hot swapping of batteries. The platform included a buffer of eight batteries, and experimental work provided insights into the average time required for battery swapping. A flight test was conducted, focusing on a search and track mission with communication constraints. However, the maximum operational time achieved for this mission using the developed station with three quadrotors was approximately 70 min. In a recent paper [83], the focus was on cyclically repeated missions, such as aerial delivery services. They

proposed the use of mobile battery swapping stations (MBS) that would move to designated swapping points according to a preset timetable. UAVs could then join the appropriate station for battery replacement and cargo loading/unloading. The study addressed the optimization of the number of UAVs and the distance traveled by proposing a declarative model for routing UAVs and MBS. However, it should be noted that this approach is applicable to only a limited range of missions, and the feasibility of mobile swapping stations may vary. The study primarily focused on the routing task, and no specific experiments related to swapping were conducted. Table 2 provides a critical analysis of the various swapping approaches discussed in the literature.

Table 2. The critical evaluation of available swapping studies [78–80,84].

Main Contribution	Advantages	Limitations
An aerial prototype utilizing multiple rotors designed for surveillance missions of extended duration by employing battery health monitoring.	The hardware prototype enables uninterrupted operation by taking into account battery health considerations.	The system does not include autonomous swapping, and its operation is managed using a laptop instead of an embedded controller.
The design, testing, and construction of an autonomous ground recharge station were carried out, incorporating a balancer and safer electrical contacts.	A hardware platform was developed that enabled autonomous swapping, utilizing an embedded controller. An optimization algorithm was implemented to minimize the recharge duration.	Although no flight test was conducted, the hardware platform focused on autonomous swapping and did not consider battery health as a factor in its design.
A planning and learning algorithm was developed and tested during a 3 h long persistent flight involving 3 UAVs and over 100 battery swaps.	The design and hardware implementation of an automated refueling system was carried out, and flight tests were conducted to evaluate its performance.	The discussion of system cost and the consideration of landing accuracy were not included in the analysis.
An automated swapping mechanism was implemented, incorporating online algorithms for energy management, vehicle health monitoring, and accurate landing. The system aimed to optimize the swapping process by efficiently managing energy resources, monitoring the health of the vehicles, and ensuring precise landing during the swapping operation.	The constructed platform is designed to sustain the continuous operation of a single UAV indefinitely. It incorporates algorithms for precision landing, ensuring accurate and safe landing during the swapping process. Additionally, the platform includes battery health tracking algorithms to monitor and manage the condition of the batteries, optimizing their performance and lifespan.	The entire system, including all its components and functionalities, was not tested as a whole. While individual tests were conducted for specific aspects of the system, such as precision landing and battery health tracking, a comprehensive test involving the complete system was not performed.
A design for an autonomous docking platform was developed, incorporating the use of active infrared imaging. The system utilized a combination of a camera and an infrared filter to achieve precise and accurate docking between the unmanned aerial vehicle (UAV) and the docking platform. The active infrared imaging technology enabled the system to operate effectively both during the day and at night, enhancing the reliability and versatility of the docking process.	A hardware platform was created to enable accurate and fast swapping of components, specifically targeting an impressive swapping time of 8 s. The platform was designed to operate seamlessly during both daytime and nighttime conditions, ensuring its usability in various environments and lighting conditions. This capability allows for continuous and efficient operations, minimizing downtime and maximizing the overall efficiency of the system.	No flight tests were conducted to evaluate the performance of the hardware platform. Additionally, the study did not focus on discussing the specific improvements in endurance achieved through the implemented technology.

Table 2. *Cont.*

Main Contribution	Advantages	Limitations
A dual-drum structure was implemented in the hardware platform to enable fast and efficient hot swapping. This design feature allows for the quick replacement of batteries, enhancing the efficiency of the swapping process.	A flight test was conducted to evaluate the performance of the system, taking into account communication constraints. During the test, the system was assessed under real-world conditions, considering limitations in communication capabilities. This provided valuable insights into the system's performance and effectiveness in scenarios with communication constraints.	The study did not include tracking the health of the vehicle or monitoring its condition. Additionally, the experiments conducted had a maximum mission time of only 70 min. Therefore, the study did not focus on monitoring and assessing the overall health and performance of the vehicle throughout extended missions.
A declarative model was proposed to optimize the routing of a multi-agent system consisting of UAVs and mobile battery swapping stations (MBS) for delivery missions. The model aimed to efficiently plan the routes and schedules of UAVs and MBS to ensure timely battery replacements and loading/unloading of goods. However, it is important to note that the study primarily focused on the routing aspect and did not involve specific experiments or tests related to the functionality and feasibility of mobile battery swapping stations in the context of delivery missions.	The study focused on optimizing the distance traveled and the number of UAVs in the context of the proposed multi-agent system with mobile battery-swapping stations. The goal was to find an optimal configuration that minimizes the overall distance traveled by the UAVs and maximizes the efficiency of the system. By optimizing these factors, the study aimed to enhance the performance and cost-effectiveness of the system. However, it should be noted that the feasibility and practicality of implementing the proposed optimizations were not specifically tested or evaluated in the study.	The study presented computational results related to the optimization of the traveled distance and the number of UAVs in the context of the multi-agent system with mobile battery swapping stations. However, it did not include experimental validation or testing of the proposed techniques. The focus of the study was on computational modeling and analysis, providing insights into the potential benefits of the proposed optimizations. The specific details and mechanisms of the swapping technique were not discussed in the study, as it primarily concentrated on the computational aspects of routing and optimization.
The study aimed to achieve precise UAV positioning after landing with minimal error. The researchers focused on developing techniques or algorithms that would ensure accurate positioning of the UAVs after the landing process. By minimizing the positioning error, they aimed to enhance the overall performance and efficiency of the system. However, it is important to note that the specific methods or approaches used to achieve precise UAV positioning after landing were not detailed in the information provided.	The research focused on achieving precise UAV positioning for swapping operations, regardless of any errors that may occur during the landing process. The objective was to develop techniques or strategies that would ensure accurate and reliable positioning of the UAVs during swapping, even if the initial landing had some degree of error. By addressing this challenge, the researchers aimed to enhance the efficiency and effectiveness of the swapping process, enabling seamless battery replacement and continuous operation of the UAVs. However, specific details about the methods or approaches employed to achieve precise positioning in the presence of landing errors were not provided in the given information.	The study reported a relatively long swapping duration, indicating that the process of replacing batteries in the system took a considerable amount of time. However, it should be noted that the entire system, including all its components and functionalities, was not tested as a whole. This means that while certain aspects of the swapping process may have been examined or validated individually, the complete integration and performance of the system were not assessed through comprehensive testing. As a result, the overall efficiency and effectiveness of the swapping mechanism, as well as its potential limitations or drawbacks, remain uncertain and require further investigation or evaluation.

2.2.3. Laser Beam Inflight Recharging

The swapping approach has shown promise in extending the operational time of battery-powered UAVs by utilizing ground stations for battery replacement or recharging. However, an alternative approach that has been proposed is wireless recharging, as discussed in the previous literature [51,85]. This method involves a ground station equipped with a primary power source, which generates a laser beam transmitted to the UAV while it is in flight. The UAV has an embedded optical receiver that converts the light into electricity, effectively powering the UAV. With wireless recharging, UAVs can remain airborne indefinitely without the need to land for battery recharging. When recharging is necessary, the UAV can access an aerial power link area to receive energy. This approach enhances

safety by eliminating risks associated with take-off and landing. Laser transmitters can be strategically positioned on tall building rooftops to ensure an unobstructed laser beam path, or they can be installed on a mobile station, as depicted in Figure 5. This establishes a radiative link between the UAV and the nearest energy source, enabling fast power transfer. Companies like LaserMotive (Washington, DC, USA) have developed working prototypes capable of transferring hundreds of watts of power [54]. Furthermore, experiments described in [53] have demonstrated the feasibility of this technique, achieving flight times of over 12 h for a quadcopter. Wireless recharging offers the potential for continuous operation and extended flight durations, addressing limitations associated with battery capacity and swapping cycles. However, further research and development efforts are necessary to optimize the technology and overcome challenges related to power efficiency, safety, and scalability.

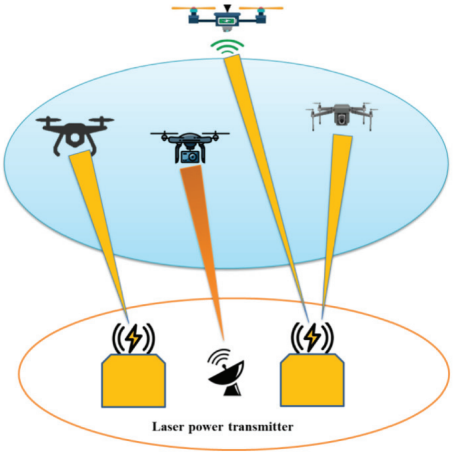

Figure 5. A laser-powered UAV inflight charging system [54,58,68].

While the laser beam inflight recharging approach offers potential benefits, it also introduces certain constraints and considerations that need to be taken into account. One such constraint is the need for UAVs to operate at reduced heights and within a limited area to maintain a reliable power transfer from the laser transmitter. This limitation is influenced by regulations, such as those imposed by the FAA, which set a maximum altitude of 400 feet for small UAVs weighing less than 26 kg. Compliance with these regulations is crucial for safe and legal operations. Another consideration is that each UAV utilizing laser beam inflight recharging requires its own dedicated laser transmitter. This can pose limitations on the number of UAVs that can be deployed in a given area, as multiple transmitters would be needed to support a larger fleet. Additionally, the individual transmitters can significantly increase the overall cost of implementing the laser beam inflight recharging system [34]. Therefore, the scalability and economic feasibility of this approach should be carefully evaluated before widespread adoption. It is important to conduct a comprehensive assessment of the operational and regulatory aspects, as well as the economic implications, when considering the integration of laser beam inflight recharging for UAVs. This evaluation should involve a careful balance between the benefits of extended flight time and the potential limitations and costs associated with this technology. By addressing these considerations, researchers and industry professionals can make informed decisions regarding the practical implementation of laser beam inflight recharging in UAV operations.

2.2.4. Tethered UAVs

Tethered UAVs offer a unique solution for achieving unlimited autonomy by connecting to a power supply station through tethering lines. This eliminates the need for

frequent recharging or battery replacement, enabling long-duration missions. Typically located on the ground, the power supply station continuously provides electricity to the UAV through the tethering lines, ensuring uninterrupted operation. Traditionally, copper wires have been used for the tethering lines of UAVs. However, there is a growing trend toward using fiber optic technology in this domain. Fiber optic cables allow for the transfer of kilowatts of power using high-intensity light, offering several advantages over copper wires. Optics-based power transfer reduces detectability by eliminating electrical signatures and significantly reduces both the payload weight of the UAV and the weight of the power lines compared to copper wires. In fact, fiber technology can reduce weight by up to eight times. Furthermore, power losses in fiber optic cables are minimal, making them more efficient for high-altitude operations.

Tethered UAVs have found applications in various fields. For instance, in maritime pollution monitoring, a tethered UAV can be deployed on a ship to detect oil spills in the sea, preventing contamination of the shoreline [57]. In data-gathering applications, tethered UAVs equipped with sensors can be utilized to collect information in specific areas [58]. However, one limitation of tethered UAVs is the restricted operating area imposed by the length of the connecting cable, which prevents the UAV from flying far from its ground station. To overcome this limitation, in some cases, a moving vehicle is used to carry the prime power source, allowing the UAV to cover a larger area. In missions requiring extremely long endurance, such as monitoring nuclear power plants, tethered UAVs can be deployed to provide continuous aerial surveillance for days or even months, as long as the tethered cable provides a continuous power supply [55]. Prototypes of tethered UAVs have been designed and successfully demonstrated in outdoor environments, showcasing the feasibility and potential of this technology. The use of fiber optic cables in tethered UAV systems presents unique advantages in terms of weight reduction, power efficiency, and reduced detectability, making them an attractive option for extended-duration missions in various applications.

2.3. Fuel Cell Powered UAVs

Hydrogen-powered UAVs offer significant benefits compared to traditional battery-powered UAVs, particularly in terms of flight duration and refueling time [86,87]. LiPo batteries, commonly used in UAVs, have a specific energy of up to 250 Wh/kg. In contrast, a fuel cell system with a compressed hydrogen tank can provide a specific energy of up to 1000 Wh/kg, allowing for much longer flight times [46,48]. This substantial increase in specific energy enables hydrogen-powered UAVs to fly for hours instead of just a few minutes.

Furthermore, refueling hydrogen-powered UAVs is nearly instantaneous compared to the time-consuming recharging process required for batteries. While batteries need a significant amount of time to recharge and replenish their energy, refueling a hydrogen-powered UAV involves simply replacing the depleted hydrogen tank with a fully charged one. This enables quick turnaround times and continuous operation. These advantages make hydrogen-powered UAVs highly desirable for applications that require extended flight durations and rapid refueling, such as long-range surveillance, mapping, and monitoring missions. However, it is essential to consider the infrastructure needed for hydrogen storage, transportation, and refueling, as well as the safety considerations associated with handling hydrogen gas [88]. Proper safety protocols and infrastructure development are necessary to ensure the efficient and secure use of hydrogen-powered UAVs. Thus, a comprehensive comparison of battery-based supplying techniques is presented in Table 3 for a better understanding on their advantages and limitations.

Table 3. A comparison between battery-based supplying techniques [54,58,78–80].

Power Supplying Technique	Advantages	Limitations and Drawbacks
Swapping	Hydrogen-powered UAVs offer the advantage of unlimited operating time, making them a viable option for long-range missions. Unlike battery-powered UAVs that require multiple battery packs or frequent recharging, hydrogen-powered UAVs rely on a single energy source, namely hydrogen fuel. This significantly reduces the weight and complexity of power management systems. With a hydrogen fuel cell system, the UAV can continuously generate electrical energy by combining hydrogen and oxygen, producing water vapor as a by-product. This continuous power generation eliminates the need for carrying multiple batteries or landing for recharging, allowing the UAV to operate for extended periods without interruption. The reduction in weight and complexity of power management systems brings several benefits. Firstly, the overall weight of the UAV is reduced, enabling increased payload capacity or longer flight durations. Secondly, the simplified power management system decreases the risk of component failures and improves overall reliability. Moreover, the reduced complexity also simplifies maintenance and servicing, contributing to more efficient operations. These advantages make hydrogen-powered UAVs particularly suitable for long-range missions where endurance and uninterrupted operation are crucial. Applications such as aerial surveillance, environmental monitoring, and remote sensing can greatly benefit from the extended operating time and reduced power management requirements of hydrogen-powered UAVs. However, it is important to consider the infrastructure for hydrogen storage, transportation, and refueling, as well as safety considerations associated with handling hydrogen gas. Proper infrastructure development, safety protocols, and regulations are necessary to support the widespread adoption of hydrogen-powered UAVs and ensure their safe and efficient operation.	The use of a ground station (GS) in the context of battery-powered UAVs can introduce certain challenges and considerations. While a GS can provide benefits, such as battery charging or swapping capabilities, it also brings along some limitations that impact operational efficiency. One of the major concerns is the increased cost associated with deploying and maintaining a GS. As the number of batteries and UAVs in operation increases, the infrastructure and resources required for the GS also need to scale accordingly. This can result in higher costs for equipment, maintenance, and operational management. Another challenge is the coordination and cooperation between UAVs and the GS. Efficient communication and synchronization are essential for smooth operations. UAVs need to interact with the GS to initiate battery charging or swapping processes, which requires effective communication protocols and coordination algorithms. Failure in communication or synchronization can disrupt operations and lead to inefficiencies. Autonomous swapping, which involves landing and battery-changing operations, can introduce additional issues. Precise UAV positioning during landing is crucial to ensure safe and accurate battery swapping. Any errors or discrepancies in landing can affect the efficiency and reliability of the swapping process. Designing and implementing robust algorithms and mechanisms to achieve precise positioning and seamless battery-changing operations is a complex task. Furthermore, autonomous swapping systems need to address concerns related to the compatibility of different UAV models and battery types. Ensuring that the swapping mechanism is compatible with a wide range of UAVs and batteries adds complexity to the system design and may require customization or adaptation for different configurations. Overall, while the concept of a ground station and autonomous swapping holds promise for extending UAV operational time, it is important to address the challenges associated with cost, cooperation between UAVs and the GS, and the technical issues related to landing and battery-changing operations. Thorough planning, system design, and testing are necessary to achieve efficient and reliable autonomous swapping systems in practical applications.

Table 3. *Cont.*

Power Supplying Technique	Advantages	Limitations and Drawbacks
Laser beam charging	The concept of wireless refueling offers significant advantages for UAVs, including the potential for unlimited operating time and extended mission durations. With this approach, UAVs can receive a continuous supply of power without the need to land or swap batteries. This eliminates the limitations imposed by battery capacity and enables persistent missions. By utilizing a wireless power transfer system, UAVs can remain in the air while receiving power from a ground station or an aerial power link area. This continuous power supply ensures that the UAVs can operate without interruption, effectively extending their operating range and mission capabilities. The use of a single energy source in wireless refueling simplifies the power management system of the UAV. There is no need to manage multiple batteries or swap them out, reducing the weight and complexity associated with power management. This streamlined approach enhances the overall efficiency and reliability of the UAV system. Wireless refueling also eliminates the need for UAVs to land, reducing the risks and challenges associated with take-off and landing operations. This improves safety and minimizes potential damage or wear and tear on the UAVs during landing and take-off maneuvers. With unlimited operating time and extended range, wireless refueling opens up possibilities for a wide range of applications. UAVs can be deployed for persistent surveillance, long-range mapping, remote sensing, and other missions that require continuous operation over extended periods. However, it is important to note that wireless refueling is still an emerging technology, and further research and development are needed to optimize its efficiency, safety, and scalability. Challenges such as power efficiency, regulatory considerations, and infrastructure requirements must be addressed to fully realize the potential of wireless refueling for UAVs.	While wireless refueling using laser beams offers potential benefits for UAVs, there are certain constraints and considerations that need to be addressed. One of these constraints is the necessity of a ground station (GS) equipped with a laser transmitter to provide power to the UAVs. This means that the UAVs need to operate within a certain range of the GS to maintain a reliable power transfer. This range limitation can restrict the operating area of the UAVs and may not be suitable for missions that require long-range coverage or operations in remote areas. Another constraint is related to the operating heights of the UAVs during laser beam recharging. In order to maintain a consistent power transfer, the UAVs typically need to operate at reduced heights, which can be influenced by regulations and safety considerations. For instance, the Federal Aviation Administration (FAA) sets maximum altitude restrictions for small UAVs, limiting their operating height to 400 feet. Compliance with these regulations may further restrict the altitude range for UAVs using laser beam refueling. Obstruction of the laser beam is another consideration. The laser beam used for refueling needs a clear path between the GS and the UAV. This means that obstacles such as buildings, trees, or other structures can obstruct the beam, potentially interrupting the power transfer. Careful planning and positioning of the GS and the UAVs are required to minimize the risk of obstruction and ensure a reliable power supply. Furthermore, the range of laser beams used for wireless refueling is typically limited compared to the range of traditional propulsion systems. This can impact the operational range of the UAVs, especially for missions that require long-distance coverage or operations in remote areas. Overall, while wireless refueling using laser beams offers advantages, such as extended flight duration and continuous operation, the necessity of a GS, constraints related to operating heights and beam obstruction, and reduced range need to be carefully considered when evaluating its suitability for specific UAV missions. Proper planning, regulatory compliance, and technological advancements are necessary to overcome these constraints and fully leverage the benefits of laser beam refueling for UAVs.

Table 3. *Cont.*

Power Supplying Technique	Advantages	Limitations and Drawbacks
Tethered UAVs	Wireless refueling using laser beams offers the potential for unlimited operating time for UAVs without the need to land. By utilizing a single energy source, such as a ground station equipped with a laser transmitter, the UAVs can receive a continuous and uninterrupted power supply while in flight. This eliminates the need for frequent battery changes or recharging, allowing for persistent operation and extended mission durations. In addition to providing power, wireless refueling also enables safe and effective data transfer between the UAV and the ground station. Along with power, the laser beam can be used to transmit data and communication signals, ensuring seamless connectivity and information exchange between the UAV and the ground control. The ability to operate continuously and receive power and data transfer wirelessly offers several advantages. It enables UAVs to perform long-duration missions without interruption, making them suitable for applications that require persistent surveillance, monitoring, or data gathering. It also reduces the logistical challenges and risks associated with manual battery replacement or refueling operations, as the UAVs can remain in the air and operational throughout their mission. Moreover, wireless refueling contributes to increased safety by eliminating the need for frequent take-offs and landings, which can be risky maneuvers for UAVs. The continuous operation and avoidance of landing procedures minimize the chances of accidents or incidents during mission execution. Overall, wireless refueling with a single energy source provides UAVs with the capability for unlimited operating time, persistent operation, safe data transfer, and reduced reliance on ground-based support. These advantages make it an attractive solution for various applications where extended flight durations, continuous operation, and efficient data transfer are essential.	While wireless refueling offers the advantage of unlimited operating time and eliminates the need for landing or battery replacement, it comes with certain limitations. One of these limitations is the necessity of a ground station (GS) to provide the power supply or laser transmitter. The GS serves as the central hub for supplying power or transmitting the laser beam to the UAV in flight. Additionally, wireless refueling methods often have constraints related to the operating area of the UAV. For example, laser beams used for power transfer may have a limited range or be affected by obstructions, such as buildings or other objects that can block or interfere with the transmission. This can restrict the operational altitude and area of the UAV, requiring it to operate within a specific range from the GS to maintain a consistent power supply. Another concern with wireless refueling is the potential for UAV damage in case of tethering loss. In some cases, UAVs may be tethered to the power source or laser transmitter through physical connections, such as cables or beams. If the tethering connection is lost or severed, it can lead to a sudden loss of power or disruption in the energy transfer, which may result in the UAV losing control or experiencing a sudden shutdown. This can potentially lead to damage to the UAV or compromise the mission's success. To mitigate these limitations and concerns, careful planning, system redundancy, and safety measures need to be implemented. This may involve the use of backup power sources or redundant laser transmitters to ensure uninterrupted operation and minimize the risk of power loss. Additionally, thorough risk assessments and safety protocols should be in place to prevent or mitigate potential damage to the UAV in case of tethering loss or system failures. Overall, while wireless refueling offers advantages, such as unlimited operating time and no landing requirements, it is important to consider the necessity of a GS, the limitations on operating area, and the potential risks associated with tethering loss. Proper planning, robust systems, and safety measures can help address these concerns and ensure the efficient and safe operation of UAVs using wireless refueling methods.

In a study [89], a comparison of various battery types (Li-ion, Ni-Cd, Ni-Mh) and fuel cells was conducted, considering criteria such as energy and power densities, discharging characteristics, temperature effects, efficiency, and endurance. However, it is important to note that flight tests were not conducted to evaluate the actual behavior, capabilities, and performance of these power sources in real flight conditions. Figure 6 in the study presents a comparison of specific power versus specific energy for batteries, fuel cells, and supercapacitors. It indicates that fuel cells demonstrate higher specific energy compared

to other power sources, which makes them a promising option for achieving extended endurance in UAVs while maintaining a given weight [57]. Nevertheless, it should be acknowledged that fuel cells may have lower energy density compared to lithium batteries due to the additional volume required for hydrogen storage in the form of a tank.

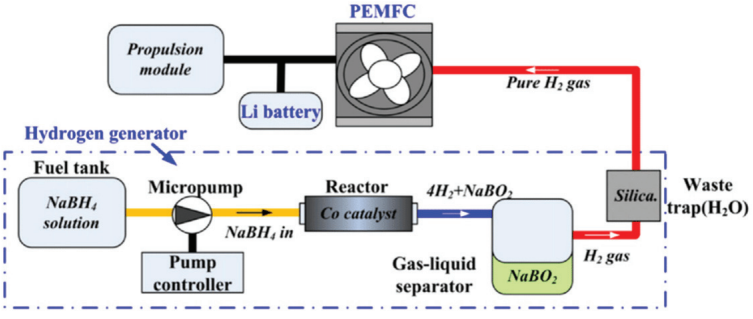

Figure 6. The fuel cell system auxiliaries.

In a separate study, the development of a UAV for mobile crane inspection was explored, with a focus on proton exchange membrane fuel cells [90] and lithium-ion batteries [91]. The research involved an economic analysis and a life cycle assessment to compare the two power sources. One of the main conclusions drawn from the study was that from a commercial standpoint, fuel cells, being a niche product, tend to be more expensive compared to lithium-ion batteries. This fact emphasizes the trade-offs between fuel cells and batteries in terms of specific energy, energy density, cost, and commercial viability. The selection of the appropriate power source for UAV applications relies on specific requirements, mission profiles, and considerations such as flight endurance, weight limitations, cost constraints, and the availability of infrastructure.

2.3.1. Fuel Cell Efficiency Issues

The process of electricity generation from fuel cells involves certain elements. Fuel cells can achieve an efficiency level of up to 60% [89]. However, this efficiency is lower compared to lithium batteries, which can exceed 90%. One of the reasons for the lower efficiency of fuel cells is the presence of auxiliary equipment required for the operation of the fuel cell stack. These auxiliary components add complexity to the system and can contribute to energy losses, thus reducing overall efficiency [80]. Additionally, the onboard hydrogen generation system, which is necessary for fuel cell operation, can also introduce complexity and potentially decrease efficiency. While fuel cells may have lower efficiency compared to lithium batteries, they offer advantages in terms of specific energy and longer operational duration. While proton exchange Membrane fuel cells (PEMFCs) hold promises for enhancing the endurance of drones and hydrogen–lithium composite energy storage systems prove adaptable to specialized working conditions, certain challenges must be addressed for their large-scale commercialization. Notably, PEMFCs require higher power and current densities to meet the demands of commercial applications. However, at elevated operating current densities, issues such as the accumulation of liquid water in the Gas Diffusion Layer (GDL) can lead to flooding and impede gas diffusion, resulting in a rapid degradation of cell performance [92]. Consequently, the improvement of water management capabilities is imperative to unlock the full potential of PEMFCs and achieve better cell output performance. The choice between fuel cells and batteries depends on specific application requirements, taking into account factors such as flight endurance, weight limitations, cost considerations, and the availability of infrastructure. The cost of implementing fuel cells in drones varies based on factors such as fuel cell type, size, and specific application requirements. While fuel cells offer advantages in terms of extended endurance and reduced environmental impact, their cost is a significant consideration in

the adoption of this technology. Cost reduction efforts, advancements in research and development, and economies of scale are expected to make fuel cells more cost-effective in the future. The decision to use fuel cells as the primary means of power generation and energy supply in drones will depend on the specific drone applications, regulatory support, competition with evolving battery technology, and a comprehensive evaluation of the total cost of ownership, taking into account initial purchase, maintenance, and operational costs.

2.3.2. Fuel Storage

Hydrogen has a low density at standard temperature and pressure, which poses a challenge for storing a sufficient amount of fuel for UAV missions. The low density means that hydrogen tanks need to be bulky to accommodate the required amount of fuel, which can impact the size and weight of the UAV. In addition to the size and weight considerations, safety is also a significant concern when it comes to storing hydrogen. Pure hydrogen cannot be stored under extremely high pressure and low temperatures due to safety reasons. Therefore, alternative techniques are employed for hydrogen storage in UAVs.

The three main techniques currently used for hydrogen storage in UAVs are as follows:

1. **Compressed hydrogen gas:** Hydrogen gas is stored in tanks under high pressure. This method allows for easier storage and refueling compared to other techniques. However, it requires high-pressure tanks, which can add weight and volume to the UAV.
2. **Liquid hydrogen:** Hydrogen is stored in a liquid state at very low temperatures. This method provides a higher energy density compared to compressed gas storage. However, it requires specialized cryogenic storage systems and insulation, which can add complexity and weight to the UAV.
3. **Chemical hydrogen generation:** Hydrogen is generated onboard the UAV through chemical reactions, such as the reaction between a metal hydride and water. This method offers the advantage of generating hydrogen as needed, eliminating the need for storing large quantities of hydrogen. However, it requires additional components and can have limitations in terms of hydrogen generation rate.

Table 4 in the referenced study likely provides a detailed analysis of the advantages and drawbacks of each hydrogen storage technique in UAV applications, allowing for a comprehensive comparison and evaluation of the different options.

Table 4. Comparison between compressed and liquid hydrogen storage [80,89].

	Compressed H_2	**Liquid H_2**
Properties	The most commonly used method for hydrogen storage in UAV applications is high-pressure storage. Hydrogen is stored at pressures ranging from 35 to 70 megapascals (MPa). At these high pressures, the density of hydrogen increases, reaching approximately 42 kg/m^3 at 70 MPa	Hydrogen has a density of approximately 71 kg/m^3 at 1 bar and a temperature of −252.87 °C, which is extremely low. To store hydrogen in its liquid form, a thermal insulation system is necessary to maintain such low temperatures. While hydrogen storage has benefits for large-scale applications, it can be challenging on a smaller scale. The liquefaction process requires extremely low temperatures, making it costly and energy intensive. It is more practical for large-scale production and distribution systems rather than small-scale applications.

Table 4. *Cont.*

	Compressed H_2	Liquid H_2
Advantages	High-pressure storage offers several advantages. It is a relatively simple method, requiring a pressure vessel to contain the hydrogen gas. The storage mass penalty, or the additional weight of the storage system, is relatively low compared to other storage methods. Additionally, high-pressure storage allows for rapid refueling capability, enabling quick turnaround times for UAV operations. However, there are certain drawbacks to high-pressure storage. One significant disadvantage is the low storage efficiency. The energy required to compress hydrogen to high pressures results in energy losses, reducing the overall storage efficiency. This can impact the range and endurance of the UAV.	There are several advantages to using hydrogen as a fuel despite its low density. One advantage is its high energy density, which means that a relatively small volume of hydrogen can store a large amount of energy. This high energy density enables longer flight durations and increased operational efficiency for UAVs. Hydrogen storage also offers improved safety compared to other fuel options. Hydrogen is non-toxic and non-polluting, and it dissipates rapidly in the event of a leak. However, safety measures are still necessary due to its flammability and the potential for embrittlement of materials in the presence of hydrogen.
Disadvantages	Safety risks are also a concern with high-pressure storage. The high pressures involved in the storage process increase the potential for leaks or ruptures, which can be hazardous. Proper safety measures and precautions must be in place to mitigate these risks. Another consideration is the larger volume required for high-pressure storage systems. The pressure vessels need to be sized to accommodate the required amount of hydrogen at the specified pressure. This can increase the overall size and volume of the UAV, affecting its aerodynamics and payload capacity. In summary, high-pressure storage is a commonly used method for hydrogen storage in UAVs. It offers simplicity, low storage mass penalty, and rapid refueling capabilities. However, it has drawbacks such as low storage efficiency, safety risks, and the need for larger storage volumes. These factors should be carefully considered when selecting the appropriate storage method for UAV applications.	Handling and transporting hydrogen in its liquid form can be difficult due to the low temperatures involved and the need for specialized storage and transportation infrastructure. Additionally, the weight of the storage tanks can be significant, impacting the overall weight of the UAV. In summary, while hydrogen offers advantages, such as high energy density, improved safety, and the potential for long-duration flights, there are challenges associated with its low density, high liquefaction energy requirements, impractical small-scale production, and the need for careful handling and storage. These factors must be carefully considered in the design and implementation of hydrogen storage systems for UAV applications.

2.4. Hybrid Power Sources (Fuel Cell and Battery)

Fuel cells face limitations when used as the sole power source for UAVs. Their time constant is relatively long, typically in the range of seconds, due to the requirements of fuel and air supply facilitated by pumps, valves, and compressors. This sluggish response is primarily attributed to the mechanical characteristics of the pumps, flow delay, thermodynamic properties, and the effect of capacitance [93]. Consequently, when there are significant fluctuations in current demand, there is a potential risk of fuel shortage,

which can negatively impact the fuel cell system's lifetime, reliability, and efficiency [94]. To tackle these challenges, researchers have explored the integration of fuel cells with batteries to form hybrid power supply systems, which have emerged as a promising solution. By harnessing the strengths of both power sources and mitigating their weaknesses, hybrid systems can deliver enhanced performance and efficiency for UAV propulsion [48,95,96]. The battery can swiftly provide power for sudden changes in demand, while the fuel cell can supply sustained power for extended durations. This approach enables superior power management, heightened system dependability, and overall improved UAV performance.

In a hybrid UAV propulsion system, the battery plays a crucial role in supplying power during high-demand maneuvers, like take-off and climbing. Its higher power density, quicker response time, and greater efficiency make it well-suited for such tasks compared to a fuel cell. On the other hand, the fuel cell takes over as the primary power source during cruise or descent phases, providing sustained power and also recharging the battery to maintain its state of charge (SOC) above a certain threshold. To evaluate the performance of hybrid UAV propulsion systems, researchers have employed hardware-in-the-loop (HIL) simulations. These simulations analyze the behavior of each power source in various test scenarios, considering factors such as endurance and hydrogen consumption.

The role of the battery in the hybrid system has been extensively considered in studies, such as [63]. These experiments have specifically focused on analyzing the battery's performance during different flight mission phases and under varying demands. Additionally, ref. [75] provides a comprehensive characterization of the hybrid propulsion system using diverse mission profiles and speeds. However, it should be noted that these studies mainly concentrated on passive power-splitting methods and did not delve into the development of an active energy management strategy. The implementation of an energy management strategy is a crucial aspect of hybrid UAV propulsion systems. It involves actively regulating the power flow between the fuel cell and battery to optimize the overall performance, efficiency, and longevity of the system. This strategy determines the appropriate utilization of each power source based on the prevailing flight conditions, load requirements, and the battery's state of charge. By employing intelligent power management algorithms, the hybrid system can achieve enhanced efficiency and prolong the UAV's mission endurance. Table 5 in this review paper offers a comprehensive comparison between batteries and supercapacitors, providing a detailed analysis of their characteristics and performance. Moving forward, Table 6 provides a comprehensive overview of the advantages and disadvantages associated with batteries and supercapacitors, aiding in the assessment of their suitability for various applications. Lastly, Table 7 is dedicated to a thorough comparison of diverse power supply configurations, facilitating a nuanced understanding of the various options available for power delivery in different contexts. These tables, with their respective data and insights, play a pivotal role in elucidating key aspects of energy storage and power supply solutions.

Table 5. Comparison between batteries and supercapacitors [48,95,96].

Type	Energy Density (Wh/kg)	Power Density (W/kg)	Cycle Life (Times)	Efficiency (%)
Lead-acid battery	30–40	200–300	300–400	75
Ni-MH battery	60–80	800–1500	1000	75
Li-ion battery	100–120	600–2000	1000	90
Supercapacitor	4–15	1000–100,000	100,000	85–98

Table 6. Batteries and supercapacitor advantages and disadvantages.

Type	Advantages	Disadvantages
Lead-acid battery	Affordable, rapid discharging rate, and high recyclability.	Inadequate performance in low-temperature conditions.
Ni-MH battery	High energy density, quick charging and discharging, and extended lifespan.	Pronounced self-discharge rate, the necessity for a cooling system, and higher manufacturing expenses.
Li-ion battery	Elevated voltage, superior energy density, lightweight, durable cycle life, minimal self-discharge, absence of memory effect, and eco-friendly.	Reduced lifespan in high-temperature environments, susceptibility to overcharging and over-discharging, and stringent security requirements.
Supercapacitor	Swift charging and discharging capabilities, absence of pollution, and remarkability.	Limited energy density.

Table 7. Comparison of power supply configurations.

Energy Sources	Architecture	Advantages	Limitations and Drawbacks
Thermal energy	Gas turbine engine	Impressive ratio of power to weight, coupled with extended duration of operation.	Extremely poor fuel efficiency and elevated noise levels.
	ICE	Exceptionally high power and energy densities, extended endurance, and significant payload range.	Decreased efficiency, thermal and acoustic signatures, greenhouse gas emissions, and high fuel costs.
One electrical source	Battery	Significant energy density and storage (rather than generation), resulting in a rapid response to power demand.	Limited power density, decreased endurance, and prolonged recharging time with the presence of a "memory effect" in certain battery types. To enhance autonomy, additional batteries need to be added, leading to increased weight and cost.
	Fuel cell	Significant energy density and, instant refueling without the presence of a "memory effect," allowing for increased autonomy using more fuel within the same stack, resulting in weight reduction.	Due to the process of energy generation, there is a slower response to power demand in fuel cells. Additionally, auxiliary equipment, such as compressors and regulators, are required for their operation. Challenges related to the lack of hydrogen distribution infrastructure, issues with hydrogen storage, safety concerns, and the high cost of hydrogen production are also present.

Table 7. *Cont.*

Energy Sources	Architecture	Advantages	Limitations and Drawbacks
Hybrid power supply	Fuel cell and battery	The high energy and power densities of the hybrid power supply result in increased endurance and faster response time. This allows for efficient energy generation and storage, enhancing the overall performance of the system.	The use of a hybrid power supply system leads to an increase in weight, as additional components, such as controllers and converters, are required to manage the system. This introduces added complexity to the UAV, further contributing to the overall weight.
	Fuel cell, battery, and solar cells	The inclusion of an additional energy source in a hybrid power supply system results in improved endurance for the UAV. This extra source provides clean and readily available energy, which leads to a decrease in energy costs and saves on hydrogen usage.	Large UAV wings are necessary for the implementation of a hybrid power supply system. However, this configuration is not suitable for rotary-wing UAVs. Additionally, an energy storage device is required to store and manage the energy generated by the system. The hybrid system also necessitates the use of an energy management system (EMS) and Maximum Power Point Tracking (MPPT) to optimize the power flow and ensure efficient operation.
	Fuel cell, battery, and supercapacitor	The hybrid system consisting of a fuel cell, battery, and supercapacitor offers several advantages. It provides very-high-power density, enabling efficient and rapid charging. It also contributes to reduced weight and minimized fluctuations in the direct current (DC) bus. The system exhibits a very long lifetime, thanks to its reduced internal resistance, and experiences minimal heat loss. These features make the hybrid system highly desirable for various applications, ensuring optimal performance and reliability.	The integration of an energy management system (EMS) is essential in the hybrid system, which includes a fuel cell, battery, and supercapacitor. The EMS plays a crucial role in coordinating and regulating the power flow between these components. It ensures efficient utilization of the energy sources, manages charging and discharging processes, and maintains the stability of the system. Additionally, the voltage regulation of the supercapacitor is necessary to ensure its proper operation and prevent any voltage-related issues. The EMS and supercapacitor voltage regulation contribute to the overall performance and reliability of the hybrid system.

3. Conclusions

The primary focus of this research paper is to examine and evaluate the energy aspects of onboard propulsion systems in UAV platforms. By conducting a comprehensive review and analysis of different power supply architectures and energy management strategies, the objective is to establish a foundation for the development of high-performance UAV propulsion systems. This assessment aims to facilitate the assessment of trade-offs and considerations when selecting suitable power sources for UAVs.

Relying solely on a single power source can be limiting for UAVs, as different power sources exhibit diverse performance characteristics under varying operating conditions. Therefore, the integration of hybrid power sources with complementary capabilities is increasingly recognized as a standard approach for designing UAV electric power systems. The selection and sizing of hybrid power sources depend on the specific mission requirements and associated weight/duration constraints of the UAV.

By comparing and analyzing various power supply architectures and energy management strategies, this research paper aims to contribute to the advancement of efficient and reliable UAV propulsion systems. The objective is to enable UAVs to operate optimally in different mission scenarios, enhance overall performance, extend mission durations, and improve the adaptability of the propulsion system to changing operating conditions.

Therefore, some key points regarding the advantages and limitations of different power sources for UAV propulsion systems are highlighted. Combustion engines, although robust, are typically heavier and more commonly used in fixed-wing UAVs. On the other hand, fuel cells (FCs) and batteries, such as lithium polymer (Li-Po) batteries, offer longer flight times and greater maneuverability. However, they may struggle to supply peak current when required and can deplete their energy rapidly. Hybrid systems, which combine multiple power sources, offer significant advantages over single-source systems. By leveraging the specific strengths of each power source, hybrid systems can address issues such as prolonged charging times, short flight durations, and limited peak power supply. Supercapacitors (SCs) are commonly used in hybrid systems due to their ability to overcome the drawbacks of other power sources. SCs have high energy density, short recharge periods, and virtually unlimited cycle life, making them a promising replacement for Li-Po batteries in hybrid systems.

Hydrogen fuel cells, often incorporating Li-Po batteries, can be considered a type of hybrid system. However, Li-Po batteries present several disadvantages in drone applications, including low energy density, short flight times, long recharge times, environmental hazards, and limited lifespan compared to other power sources. SCs, with their high energy density, short recharge periods, and long cycle life, offer a potential solution as a replacement for Li-Po batteries in hybrid systems. Further research is necessary to evaluate the impact of SCs on the effectiveness of fuel cell systems in drone applications. Overall, the implementation of hybrid systems with SCs shows promise in improving the flight time and efficiency of UAVs. To truly advance current systems, hybrid systems need to be comparable in weight and size to existing drones while providing enhanced performance and addressing the limitations of single-source power systems. Further research and development are required to optimize the integration and performance of hybrid power systems in UAV applications.

Author Contributions: Conceptualization, Y.N.S. and W.G.; writing—original draft preparation, Y.N.S.; writing—review and editing, Y.N.S., M.T.H.S., F.S.S., M.N., W.G., S.S., A.Ł. and A.H.; visualization, Y.N.S.; supervision, M.T.H.S. and A.Ł.; project administration, F.S.S., M.N., W.G., A.Ł. and A.H.; funding acquisition, M.T.H.S., M.N, W.G. and A.Ł. All authors have read and agreed to the published version of the manuscript.

Funding: The authors are grateful for the financial support given by The Ministry of Higher Education Malaysia (MOHE) under the Higher Institution Centre of Excellence (HICOE2.0/5210004) at the Institute of Tropical Forestry and Forest Products. The research was financially supported as a statutory work of the Poznan University of Technology (No. 0214/SBAD/0241). This research was partially financed by the Ministry of Science and Higher Education of Poland with allocation to the Faculty of Mechanical Engineering, Bialystok University of Technology, for the WZ/WM-IIM/5/2023 academic project in the mechanical engineering discipline.

Institutional Review Board Statement: Not applicable.

Informed Consent Statement: Not applicable.

Data Availability Statement: Data sharing does not apply to this article as no new data were created or analyzed in this study.

Acknowledgments: The authors would like to thank the Department of Aerospace Engineering, Faculty of Engineering, Universiti Putra Malaysia, and the Laboratory of Biocomposite Technology, the Institute of Tropical Forestry and Forest Product (INTROP), Universiti Putra Malaysia, for the close collaboration in this research.

Conflicts of Interest: The authors declare no conflict of interest.

References

1. Zhai, Q.; Meng, K.; Dong, Z.Y.; Ma, J. Modeling and Analysis of Lithium Battery Operations in Spot and Frequency Regulation Service Markets in Australia Electricity Market. *IEEE Trans. Ind. Inform.* **2017**, *13*, 2576–2586. [CrossRef]
2. Horla, D.; Giernacki, W.; Báča, T.; Spurny, V.; Saska, M. AL-TUNE: A Family of Methods to Effectively Tune UAV Controllers in In-flight Conditions. *J. Intell. Robot. Syst.* **2021**, *103*, 5. [CrossRef]
3. Tsmots, I.; Teslyuk, V.; Łukaszewicz, A.; Lukashchuk, Y.; Kazymyra, I.; Holovatyy, A.; Opotyak, Y. An Approach to the Implementation of a Neural Network for Cryptographic Protection of Data Transmission at UAV. *Drones* **2023**, *7*, 507. [CrossRef]
4. Holovatyy, A.; Łukaszewicz, A.; Teslyuk, V.; Ripak, N. Development of AC Voltage Stabilizer with Microcontroller-Based Control System. In Proceedings of the 2022 IEEE 17th International Conference on Computer Sciences and Information Technologies (CSIT), Lviv, Ukraine, 10–12 November 2022; Institute of Electrical and Electronics Engineers: Piscataway, NJ, USA, 2022; pp. 527–530.
5. Pytka, J.; Budzynski, P.; Tomilo, P.; Laskowski, J.; Michalowska, J.; Gnapowski, E.; Blazejczak, D.; Lukaszewicz, A. IMUMETER—AI-based sensor for airplane motion measurements. In Proceedings of the 2021 IEEE International Workshop on Metrology for AeroSpace, MetroAeroSpace 2021, Naples, Italy, 23–25 June 2021; pp. 692–697.
6. Pytka, J.; Budzyński, P.; Łyszczyk, T.; Józwik, J.; Michałowska, J.; Tofil, A.; Błażejczak, D.; Laskowski, J. Determining wheel forces and moments on aircraft landing gear with a dynamometer sensor. *Sensors* **2020**, *20*, 227. [CrossRef]
7. Chandran, N.K.; Sultan, M.T.H.; Łukaszewicz, A.; Shahar, F.S.; Holovatyy, A.; Giernacki, W. Review on Type of Sensors and Detection Method of Anti-Collision System of Unmanned Aerial Vehicle. *Sensors* **2023**, *23*, 6810. [CrossRef]
8. Łukaszewicz, A.; Szafran, K.; Józwik, J. CAx techniques used in UAV design process. In Proceedings of the 2020 IEEE 7th International Workshop on Metrology for AeroSpace (MetroAeroSpace), Pisa, Italy, 22–24 June 2020; pp. 95–98. [CrossRef]
9. Kotarski, D.; Piljek, P.; Pranjić, M.; Grlj, C.G.; Kasać, J. A Modular Multirotor Unmanned Aerial Vehicle Design Approach for Development of an Engineering Education Platform. *Sensors* **2021**, *21*, 2737. [CrossRef]
10. Krznar, M.; Piljek, P.; Kotarski, D.; Pavković, D. Modeling, Control System Design and Preliminary Experimental Verification of a Hybrid Power Unit Suitable for Multirotor UAVs. *Energies* **2021**, *14*, 2669. [CrossRef]
11. Turk, I.; Ozbek, E.; Ekici, S.; Karakoc, T.H. A conceptual design of a solar powered UAV and assessment for continental climate flight conditions. *Int. J. Green Energy* **2022**, *19*, 638–648. [CrossRef]
12. Rodríguez-Sevillano, Á.A.; Casati-Calzada, M.J.; Bardera-Mora, R.; Nieto-Centenero, J.; Matías-García, J.C.; Barroso-Barderas, E. Rapid Parametric CAx Tools for Modelling Morphing Wings of Micro Air Vehicles (MAVs). *Aerospace* **2023**, *10*, 467. [CrossRef]
13. Ozbek, E.; Ekici, S.; Karakoc, T.H. Unleashing the Potential of Morphing Wings: A Novel Cost Effective Morphing Method for UAV Surfaces, Rear Spar Articulated Wing Camber. *Drones* **2023**, *7*, 379. [CrossRef]
14. Kotarski, D.; Piljek, P.; Pranjić, M.; Kasać, J. Concept of a Modular Multirotor Heavy Lift Unmanned Aerial Vehicle Platform. *Aerospace* **2023**, *10*, 528. [CrossRef]
15. Miatliuk, K.; Lukaszewicz, A.; Siemieniako, F. Coordination method in design of forming operations of hierarchical solid objects. In Proceedings of the 2008 International Conference on Control, Automation and Systems, ICCAS 2008, Seoul, Republic of Korea, 14–17 October 2008; art. no. 4694220; pp. 2724–2727. [CrossRef]
16. Grodzki, W.; Łukaszewicz, A. Design and manufacture of unmanned aerial vehicles (UAV) wing structure using composite materials. *Mater. Werkst.* **2015**, *46*, 269–278. [CrossRef]
17. Parparita, M.; Bere, P.; Józwik, J.; Biruk-Urban, K. Design and Manufacturing of a Small Sized UAV Wing. In Proceedings of the 2023 IEEE 10th International Workshop on Metrology for AeroSpace (MetroAeroSpace), Milan, Italy, 19–21 June 2023; pp. 187–192. [CrossRef]
18. Leleń, M.; Józwik, J. Analysis of technological parameters of hydroabrasive cutting of multilayer aerospace structures of aluminium alloy-carbon composite type. In Proceedings of the 2023 IEEE 10th International Workshop on Metrology for AeroSpace (MetroAeroSpace), Milan, Italy, 19–21 June 2023; pp. 638–643. [CrossRef]
19. Šančić, T.; Brčić, M.; Kotarski, D.; Łukaszewicz, A. Experimental Characterization of Composite-Printed Materials for the Production of Multirotor UAV Airframe Parts. *Materials* **2023**, *16*, 5060. [CrossRef]
20. Tomiło, P.; Pytka, J.; Józwik, J.; Gnapowski, E.; Muszyński, T.; Łukaszewicz, A. Latent Neural Network for Recognition of Annomalies in 3D-Print of a Scale Model for Wind Tunnel Measurements. In Proceedings of the 2023 IEEE 10th International Workshop on Metrology for AeroSpace (MetroAeroSpace), Milan, Italy, 19–21 June 2023; pp. 688–692. [CrossRef]
21. Alwateer, M.; Loke, S.W.; Fernando, N. Enabling drone services: Drone crowdsourcing and drone scripting. *IEEE Access* **2019**, *7*, 110035–110049. [CrossRef]
22. Yang, F.; Jiang, J.; Sun, C.; He, A.; Chen, W.; Lan, Y.; Song, K. Efficiency Improvement of Magnetic Coupler with Nanocrystalline Alloy Film for UAV Wireless Charging System with a Carbon Fiber Fuselage. *Energies* **2022**, *15*, 8363. [CrossRef]
23. Pan, Z.F.; An, L.; Wen, C.Y. Recent advances in fuel cells based propulsion systems for unmanned aerial vehicles. *Appl. Energy* **2019**, *240*, 473–485. [CrossRef]
24. Berger, G.S.; Teixeira, M.; Cantieri, A.; Lima, J.; Pereira, A.I.; Valente, A.; Castro, G.G.R.d.; Pinto, M.F. Cooperative Heterogeneous Robots for Autonomous Insects Trap Monitoring System in a Precision Agriculture Scenario. *Agriculture* **2023**, *13*, 239. [CrossRef]
25. Nowakowski, M.; Kurylo, J. Usability of Perception Sensors to Determine the Obstacles of Unmanned Ground Vehicles Operating in Off-Road Environments. *Appl. Sci.* **2023**, *13*, 4892. [CrossRef]

26. Silarski, M.; Nowakowski, M. Performance of the SABAT Neutron-Based Explosives Detector Integrated with an Unmanned Ground Vehicle: A Simulation Study. *Sensors* **2022**, *22*, 9996. [CrossRef]
27. Puchalski, R.; Giernacki, W. UAV Fault Detection Methods, State-of-the-Art. *Drones* **2022**, *6*, 330. [CrossRef]
28. Alwateer, M.; Loke, S.W.; Zuchowicz, A.M. Drone services: Issues in drones for location-based services from human-drone interaction to information processing. *J. Locat. Based Serv.* **2019**, *13*, 94–127. [CrossRef]
29. Tang, L.; Shao, G. Drone remote sensing for forestry research and practices. *J. For. Res.* **2015**, *26*, 791–797. [CrossRef]
30. Ruan, L.; Wang, J.; Chen, J.; Xu, Y.; Yang, Y.; Jiang, H.; Zhang, Y.; Xu, Y. Energy-efficient multi-UAV coverage deployment in UAV networks: A game-theoretic framework. *China Commun.* **2018**, *15*, 194–209. [CrossRef]
31. Claesson, A.; Svensson, L.; Nordberg, P.; Ringh, M.; Rosenqvist, M.; Djarv, T.; Samuelsson, J.; Hernborg, O.; Dahlbom, P.; Jansson, A.; et al. Drones may be used to save lives in out of hospital cardiac arrest due to drowning.pdf. *Resuscitation* **2017**, *114*, 152–156. [CrossRef] [PubMed]
32. Loke, S.W.; Alwateer, M.; Abeysinghe Achchige Don, V.S. Virtual space boxes and drone-as-reference-station localisation for drone services: An approach based on signal strengths. In Proceedings of the DroNet 2016—2nd Workshop on Micro Aerial Vehicle Networks, Systems, and Applications for Civilian Use, Co-Located with MobiSys 2016, Singapore, 26 June 2016; pp. 45–48.
33. Shukla, A.; Xiaoqian, H.; Karki, H. Autonomous tracking and navigation controller for an unmanned aerial vehicle based on visual data for inspection of oil and gas pipelines. In Proceedings of the 2016 16th International Conference on Control, Automation and Systems (ICCAS), Gyeongju, Republic of Korea, 16–19 October 2016; pp. 194–200.
34. Michałowska, J.; Tofil, A.; Józwik, J.; Pytka, J.; Legutko, S.; Siemiątkowski, Z.; Łukaszewicz, A. Monitoring the risk of the electric component imposed on a pilot during light aircraft operations in a high-frequency electromagnetic field. *Sensors* **2019**, *19*, 5537. [CrossRef] [PubMed]
35. Bacco, M.; Berton, A.; Ferro, E.; Gennaro, C.; Gotta, A.; Matteoli, S.; Paonessa, F.; Ruggeri, M.; Virone, G.; Zanella, A. Smart farming: Opportunities, challenges and technology enablers. In Proceedings of the 2018 IoT Vertical and Topical Summit on Agriculture-Tuscany (IOT Tuscany), Tuscany, Italy, 8–9 May 2018; pp. 1–6.
36. Thakar, P.S.; Markana, A.; Miyani, P.B. Robust temperature tracking and estimation for resistive heater circuit board with implementation. *Adv. Control Appl.* **2023**, *5*, e147. [CrossRef]
37. Ding, G.; Wu, Q.; Zhang, L.; Lin, Y.; Tsiftsis, T.A.; Yao, Y.D. An Amateur Drone Surveillance System Based on the Cognitive Internet of Things. *IEEE Commun. Mag.* **2018**, *56*, 29–35. [CrossRef]
38. Yoo, S.; Kim, K.; Jung, J.; Chung, A.Y.; Lee, J.; Lee, S.K.; Lee, H.K.; Kim, H. A multi-drone platform for empowering drones' teamwork. In Proceedings of the Annual International Conference on Mobile Computing and Networking, MOBICOM 2015, Paris, France, 7–11 September 2015; pp. 275–277.
39. Lee, J.; Kim, K.; Yoo, S.; Chung, A.Y.; Lee, J.Y.; Park, S.J.; Kim, H. Constructing a reliable and fast recoverable network for drones. In Proceedings of the 2016 IEEE International Conference on Communications (ICC), Kuala Lumpur, Malaysia, 22–27 May 2016.
40. Zhou, J.; Zhang, B.; Xiao, W.; Qiu, D.; Chen, Y. Nonlinear Parity-Time-Symmetric Model for Constant Efficiency Wireless Power Transfer: Application to a Drone-in-Flight Wireless Charging Platform. *IEEE Trans. Ind. Electron.* **2019**, *66*, 4097–4107. [CrossRef]
41. Lu, M.; Bagheri, M.; James, A.P.; Phung, T. Wireless Charging Techniques for UAVs: A Review, Reconceptualization, and Extension. *IEEE Access.* **2018**, *6*, 29865–29884. [CrossRef]
42. Sato, A.; Naknishi, H. Observation and measurement in disaster areas using industrial use unmanned helicopters. In Proceedings of the 12th IEEE International Symposium on Safety, Security and Rescue Robotics, SSRR 2014, Hokkaido, Japan, 27–30 October 2014.
43. Zhang, R.; Li, X.; Sun, C.; Yang, S.; Tian, Y.; Tian, J. State of Charge and Temperature Joint Estimation Based on Ultrasonic Reflection Waves for Lithium-Ion Battery Applications. *Batteries* **2023**, *9*, 335. [CrossRef]
44. Mikołajczyk, T.; Mikołajewski, D.; Kłodowski, A.; Łukaszewicz, A.; Mikołajewska, E.; Paczkowski, T.; Macko, M.; Skornia, M. Energy Sources of Mobile Robot Power Systems: A Systematic Review and Comparison of Efficiency. *Appl. Sci.* **2023**, *13*, 7547. [CrossRef]
45. Afridrones Aviation CC. Afridrones. 2020. Available online: https://afridrones.com/home_190315/ (accessed on 15 June 2023).
46. Vanchiappan, A.; Joe, G.; Lee, Y.S.; Srinivasan, M. Insertion-type electrodes for nonaqueous Li-ion capacitors. *Chem. Rev.* **2014**, *114*, 11619–11635.
47. Ci, S.; Lin, N.; Wu, D. Reconfigurable Battery Techniques and Systems: A Survey. *IEEE Access.* **2016**, *4*, 1175–1189. [CrossRef]
48. Rajashekara, K. Present status and future trends in electric vehicle propulsion technologies. *IEEE J. Emerg. Sel. Top. Power Electron.* **2013**, *1*, 3–10. [CrossRef]
49. Vidal, C.; Gross, O.; Gu, R.; Kollmeyer, P.; Emadi, A. XEV Li-Ion Battery Low-Temperature Effects-Review. *IEEE Trans. Veh. Technol.* **2019**, *68*, 4560–4572. [CrossRef]
50. Wagner, F.T.; Lakshmanan, B.; Mathias, M.F. Electrochemistry and the Future of the Automobile. *J. Phys. Chem. Lett.* **2010**, *1*, 2204–2219. [CrossRef]
51. Karden, E.; Ploumen, S.; Fricke, B.; Miller, T.; Snyder, K. Energy storage devices for future hybrid electric vehicles. *J. Power Sources* **2007**, *168*, 2–11. [CrossRef]
52. Kim, T.; Qiao, W.; Qu, L. Power electronics-enabled self-X multicell batteries: A design toward smart batteries. *IEEE Trans. Power Electron.* **2012**, *27*, 4723–4733.

53. Song, M.; Zhu, D.; Zhang, L.; Wang, X.; Chen, Y.; Mi, R.; Liu, H.; Mei, J.; Lau, L.W.M. Improved charging performances of Li2O2 cathodes in non-aqueous electrolyte lithium-air batteries at high test temperatures. In Proceedings of the ICMREE 2013—Proceedings: 2013 International Conference on Materials for Renewable Energy and Environment, Chengdu, China, 19–21 August 2013; pp. 513–515.
54. Meng, J.; Luo, G.; Gao, F. Lithium polymer battery state-of-charge estimation based on adaptive unscented kalman filter and support vector machine. *IEEE Trans. Power Electron.* **2016**, *31*, 2226–2238. [CrossRef]
55. Kranjec, B.; Sladic, S.; Giernacki, W.; Bulic, N. PV System Design and Flight Efficiency Considerations for Fixed-Wing Radio-Controlled Aircraft—A Case Study. *Energies* **2018**, *11*, 2648. [CrossRef]
56. RS Components. Fiamm 12V Faston F1 Sealed Lead Acid Battery, 2Ah. Available online: https://za.rs-online.com/web/p/lead-acid-batteries/8431308/ (accessed on 18 May 2023).
57. RS Components. RS PRO 12V NiMH Rechargeable Battery Pack, 2Ah—Pack of 1. Available online: https://za.rs-online.com/web/p/rechargeable-battery-packs/7770400/ (accessed on 18 May 2023).
58. RS Components. Samsung, INR-18650 20R, 3.6V, 18650, Lithium-Ion Rechargeable Battery, 2Ah. Available online: https://za.rs-online.com/web/p/speciality-size-rechargeable-batteries/8182992/ (accessed on 18 May 2023).
59. RS Components. RS PRO Alkaline AA Battery 1.5V. Available online: https://za.rs-online.com/web/p/aa-batteries/7442199/ (accessed on 18 May 2023).
60. NASA. Technology Readiness Level Definitions. 1989; Volume 1. Available online: https://www.nasa.gov/pdf/458490main_TRL_Definitions.pdf (accessed on 22 September 2023).
61. RS Components. RS PRO PR44 Button Battery, 1.4 V, 11.6 mm Diameter. Available online: https://za.rs-online.com/web/p/button-batteries/8010730 (accessed on 18 May 2023).
62. Mantech Electronics. LITHIUM CELL / BATTERY AA 3V6 2.2AH 14×50. Available online: https://www.mantech.co.za/ProductInfo.aspx?Item=15C5860%20-%20CPT (accessed on 18 May 2023).
63. RS Components. RS PRO 12V NiCd Rechargeable Battery Pack, 1.8Ah—Pack of 1. Available online: https://za.rs-online.com/web/p/rechargeable-battery-packs/1253427 (accessed on 18 May 2023).
64. Kim, S.-G.; Lee, E.; Hong, I.-P.; Yook, J.-G. Review of Intentional Electromagnetic Interference on UAV Sensor Modules and Experimental Study. *Sensors* **2022**, *22*, 2384. [CrossRef]
65. RS Components. RS PRO, 3.7V, Lithium Polymer Rechargeable Battery, 2Ah. Available online: https://za.rs-online.com/web/p/speciality-size-rechargeable-batteries/1251266 (accessed on 18 May 2023).
66. Kalogirou, S.A. Industrial Process Heat, Chemistry Applications, and Solar Dryers. *Sol. Energy Eng.* **2009**, 391–420.
67. DRONEII.com. Drone Energy Sources—Pushing the Boundaries of Electric Flight. Available online: https://droneii.com/drone-energy-sources (accessed on 30 July 2020).
68. Ganguly, S.; Das, S.; Kargupta, K.; Bannerjee, D. Optimization of Performance of Phosphoric Acid Fuel Cell (PAFC) Stack using Reduced Order Model with Integrated Space Marching and Electrolyte Concentration Inferencing. *Comput. Aided Chem. Eng.* **2012**, *31*, 1010–1014.
69. Kumar, V.; Rudra, R.; Hait, S.; Kumar, P.; Kundu, P.P. Performance trends and status of microbial fuel cells. In *Progress and Recent Trends in Microbial Fuel Cells*; Elsevier: Amsterdam, The Netherlands, 2018; pp. 7–24.
70. Haile, S.M.; Boysen, D.A.; Chisholm, C.R.I.; Merie, R.B. Solid acids as fuel cell electrolytes. *Nature* **2001**, *410*, 910–913. [CrossRef] [PubMed]
71. Chen, B.; Li, X.; Evangelou, S. Comparative Study of Hybrid Powertrain Architectures from a Fuel Economy Perspective. In Proceedings of the 14th International Symposium on Advanced Vehicle Control, AVEC, Beijing, China, 16–20 July 2018; Volume 14.
72. Haile, S.M.; Chisholm, C.R.I.; Sasaki, K.; Boysen, D.A.; Uda, T. Solid acid proton conductors: From laboratory curiosities to fuel cell electrolytes. *Faraday Discuss.* **2007**, *134*, 17–39. [CrossRef]
73. Shah, S.D. Electrification of Transport and Oil Displacement: How Plug-Ins Could Lead to a 50 Percent Reduction in U.S. Demand for Oil. In *Plug-In Electric Vehicles: What Role for Washington?* Sandalow, D.B., Ed.; Brookings Institution Press: Washington, DC, USA, 2009; pp. 22–44. Available online: http://www.jstor.org/stable/10.7864/j.ctt1262t0.7 (accessed on 23 September 2023).
74. Traub, L.W. Range and endurance estimates for battery-powered aircraft. *J. Aircr.* **2011**, *48*, 703–707. [CrossRef]
75. Rajabi, M.S.; Beigi, P.; Aghakhani, S. Drone Delivery Systems and Energy Management: A Review and Future Trends. 2022. Available online: http://arxiv.org/abs/2206.10765 (accessed on 23 September 2023).
76. Gong, A.; MacNeill, R.; Verstraete, D.; Palmer, J.L. Analysis of a Fuel-Cell/Battery /Supercapacitor Hybrid Propulsion System for a UAV Using a Hardware-in-the-Loop Flight Simulator. In Proceedings of the 2018 AIAA/IEEE Electric Aircraft Technologies Symposium (EATS), Cincinnati, OH, USA, 12–14 July 2018.
77. Yilmaz, M.; Krein, P.T. Review of battery charger topologies, charging power levels, and infrastructure for plug-in electric and hybrid vehicles. *IEEE Trans. Power Electron.* **2013**, *28*, 2151–2169. [CrossRef]
78. Wang, Y.; Chen, K.S.; Mishler, J.; Cho, S.C.; Adroher, X.C. A review of polymer electrolyte membrane fuel cells: Technology, applications, and needs on fundamental research. *Appl. Energy* **2011**, *88*, 981–1007. [CrossRef]
79. Burke, A.; Miller, M. Comparisons of Ultracapacitors and Advanced Batteries for Pulse Power in Vehicle Applications: Performance, Life, and Cost. Proc. 19th Int. Electr. Vehicle Symp (pp. 19–23). October 2002. Available online: https://www.researchgate.net/publication/286065134_Comparisons_ultracapacitors_and_advanced_batteries_for_pulse_power_in_vehicle_applications_Performance (accessed on 23 September 2023).

80. Suzuki, K.A.O.; Kemper Filho, P.; Morrison, J.R. Automatic Battery Replacement System for UAVs: Analysis and Design. *J. Intell. Robot. Syst.* **2011**, *65*, 563–586. [CrossRef]
81. Jain, A.K.; Mathapati, S.; Ranganathan, V.T.; Narayanan, V. Integrated starter generator for 42-V powernet using induction machine and direct torque control technique. *IEEE Trans. Power Electron.* **2006**, *21*, 701–710. [CrossRef]
82. Swieringa, K.A.; Hanson, C.B.; Richardson, J.R.; White, J.D.; Hasan, Z.; Qian, E.; Girard, A. Autonomous battery swapping system for small-scale helicopters. In Proceedings of the 2010 IEEE International Conference on Robotics and Automation, Anchorage, AK, USA, 3–7 May 2010; pp. 3335–3340.
83. Kraemer, D.; Hu, L.; Muto, A.; Chen, X.; Chen, G.; Chiesa, M. Photovoltaic-thermoelectric hybrid systems: A general optimization methodology. *Appl. Phys. Lett.* **2008**, *92*, 243503. [CrossRef]
84. Galkin, B.; DaSilva, L.A. UAVs as Mobile Infrastructure: Addressing Battery Lifetime. *arXiv* **2018**, arXiv:1807.00996. [CrossRef]
85. Bocewicz, G.; Nielsen, P.; Banaszak, Z.; Thibbotuwawa, A. A declarative modelling framework for routing of multiple UAVs in a system with mobile battery swapping stations. In *Advances in Intelligent Systems and Computing*; Springer: Cham, Switzerland, 2019; pp. 429–441.
86. Emadi, A.; Rajashekara, K.; Williamson, S.S.; Lukic, S.M. Topological overview of hybrid electric and fuel cell vehicular power system architectures and configurations. *IEEE Trans. Veh. Technol.* **2005**, *54*, 763–770. [CrossRef]
87. Steilen, M.; Jörissen, L. Hydrogen Conversion into Electricity and Thermal Energy by Fuel Cells. In *Electrochemical Energy Storage for Renewable Sources and Grid Balancing*; Elsevier: Amsterdam, The Netherlands, 2015; pp. 143–158.
88. Thanomjit, C.; Patcharavorachot, Y.; Arpornwichanop, A. Design and Thermal Analysis of a Solid Oxide Fuel Cell System Integrated with Ethanol Steam Reforming. *Comput. Aided Chem. Eng.* **2012**, *30*, 287–291.
89. Uzunoglu, M.; Alam, M.S. Fuel-Cell Systems for Transportations. In *Power Electronics Handbook*, 4th ed.; Butterworth-Heinemann: Oxford, UK, 2017; pp. 1091–1112.
90. Dharmalingam, S.; Kugarajah, V.; Sugumar, M. Membranes for microbial fuel cells. In *Biomass, Biofuels, Biochemicals: Microbial Electrochemical Technology: Sustainable Platform for Fuels, Chemicals and Remediation*; Elsevier: Amsterdam, The Netherlands, 2018; pp. 143–194.
91. Fathabadi, H. Plug-In Hybrid Electric Vehicles: Replacing Internal Combustion Engine with Clean and Renewable Energy Based Auxiliary Power Sources. *IEEE Trans. Power Electron.* **2018**, *33*, 9611–9618. [CrossRef]
92. Yan, S.; Yang, M.; Sun, C.; Xu, S. Liquid Water Characteristics in the Compressed Gradient Porosity Gas Diffusion Layer of Proton Exchange Membrane Fuel Cells Using the Lattice Boltzmann Method. *Energies* **2023**, *16*, 6010. [CrossRef]
93. Mehta, V.; Cooper, J.S. Review and analysis of PEM fuel cell design and manufacturing. *Fuel Cells Compend.* **2005**, *114*, 469–501. [CrossRef]
94. Mohammed, O.A.; Lowther, D.A.; Lean, M.H.; Alhalabi, B. On the creation of a generalized design optimization environment for electromagnetic devices. *IEEE Trans. Magn.* **2001**, *37*, 3562–3565. [CrossRef]
95. Rhoads, G.D.; Wagner, N.A.; Taylor, B.J.; Keen, D.B.; Bradley, T.H. Design and flight test results for a 24 hour fuel cell unmanned aerial vehicle. In Proceedings of the 8th Annual International Energy Conversion Engineering Conference, Nashville, TN, USA, 25–28 July 2010.
96. Barreras, F.; Lozano, A.; Valiño, L.; Marín, C.; Pascau, A. Flow distribution in a bipolar plate of a proton exchange membrane fuel cell: Experiments and numerical simulation studies. *J. Power Sources* **2005**, *144*, 54–66. [CrossRef]

MDPI
St. Alban-Anlage 66
4052 Basel
Switzerland
www.mdpi.com

MDPI Books Editorial Office
E-mail: books@mdpi.com
www.mdpi.com/books

Academic Open
Access Publishing

mdpi.com

ISBN 978-3-7258-0980-6